10TH Years
ANNIVERSARY
2015 - 2025

International Journal of BIOPRINTING

ISSN: 2424-7723 (Print)
ISSN: 2424-8002 (Online)
Volume 11 • Issue 1
February 2025

ACCSCIENCE PUBLISHING

ACCSCIENCE PUBLISHING

International Journal of Bioprinting

Print ISSN: 2424-7723

Online ISSN: 2424-8002

International Journal of Bioprinting is an international journal covering the technology, science and clinical application of the broadly defined field of Bioprinting. Bioprinting is defined as the use of 3D printing technology with materials that incorporate viable living cells or biological elements to produce tissue or biotechnological products. We are interested in the scientific topics spanning all stages of bioprinting process from concept creation to fabrication and beyond.

Scan to access website:

Scan to submit papers:

About the Publisher

AccScience Publishing is a publishing company based in Singapore. We publish a range of high-quality, open-access, peer-reviewed journals and books from a broad spectrum of disciplines.

Contact Us

Managing Editor
ijb.office@accscience.sg

AccScience Publishing
8 Burn Road, #15-03 Trivex, Singapore 369977.

Volume 11 • Issue 1 • February 2025
ISSN 2424-7723 (print) ISSN 2424-8002 (online)

INTERNATIONAL JOURNAL OF BIOPRINTING

Editor-in-Chief

Chee Kai Chua

Singapore University of Technology and Design, Singapore

ACCSCIENCE PUBLISHING

Access Science Without Barriers

Full issue copyright © 2025 AccScience Publishing
All rights reserved. Without permission in writing from the publisher, this full issue publication in its entirety may not be reproduced or transmitted for commercial purposes in any form or by any means, electronic or mechanical, including photocopying, recording, or any information storage and retrieval system. Permissions may be sought from ijb.office@accscience.sg.

Article copyright © Respective Author(s)
See articles for copyright year. All articles in this full issue publication are open-access. There are no restrictions in the distribution and reproduction of individual articles, provided the original work is properly cited. However, permission to reuse copyrighted materials of an article for commercial purposes is applicable if the article is licensed under Creative Commons Attribution-NonCommercial License. Check the specific license before reusing.

INTERNATIONAL JOURNAL OF BIOPRINTING

ISSN: 2424-7723 (print)
ISSN: 2424-8002 (online)

Editorial and Production Credits

Publisher: AccScience Publishing
Managing Editor: Cathy Huang
Editorial Assistants: Puva Ramakrishnan, Flora Kang
Production Editor: Puva Ramakrishnan
Special Issue Commissioning Editors: Shirley Song, Terra Shi
Article Layout and Typeset: Bsmart Publishing (India)

For all advertising queries, contact ijb.office@accscience.sg.

Supplementary file

Supplementary files of articles can be obtained at https://accscience.com/journal/IJB/11/1.

Disclaimer

AccScience Publishing is not liable to the statements, perspectives, and opinions contained in the publications. The appearance of advertisements in the journal shall not be construed as a warranty, endorsement, or approval of the products or services advertised and/or the safety thereof. AccScience Publishing disclaims responsibility for any injury to persons or property resulting from any ideas or products referred to in the publications or advertisements. AccScience Publishing remains neutral with regard to jurisdictional claims in published maps and institutional affiliations.

International Journal of Bioprinting

Editorial Board

Editor-in-Chief

Chee Kai Chua
Singapore University of Technology and Design, Singapore

Associate Editors

Wai Yee Yeong
Nanyang Technological University, Singapore

Jiankang He
Xi'an Jiaotong University, China

Liliang Ouyang
Tsinghua University, China

Maling Gou
Sichuan University, China

Yongqiang Hao (Clinician)
Shanghai Jiao Tong University School of Medicine, China

*Editorial Board Members**

Jason A. Burdick, *USA*

Shweta Agarwala, *Denmark*

Eben Alsberg, *USA*

Anthony Atala, *USA*

Douglas B. Chrisey, *USA*

Amit Bandyopadhyay, *USA*

Andrea Barbetta, *Italy*

Mikhael Bechelany, *France*

Martin Birchall, *UK*

Paulo J.D.S. Bártolo, *Singapore*

Christian Celia, *Italy*

Maria Chatzinikolaidou, *Greece*

Jun Chen, *Australia*

Daniel Chen, *Canada*

Boris Chichkov, *Germany*

Gianluca Ciardelli, *Italy*

Jeremy Crook, *Australia*

Cédric Delattre, *France*

Rui Domingues, *Portugal*

Dennis Douroumis, *UK*

Tal Dvir, *Israel*

Eleonora Ferraris, *Belgium*

Sanjay Garg, *Australia*

Antonio Gloria, *Italy*

Manuela Gomes, *Portugal*

Brunella Grigolo, *Italy*

Michinao Hashimoto, *Singapore*

Charlotte Hauser, *Saudi Arabia*

Dong Nyoung Heo, *Korea*

Raymund E. Horch, *Germany*

Geun Hyung Kim, *Korea*

Richard James Bibb, *UK*

Jinah Jang, *South Korea*

Jingchao Jiang, *China*

Qing Jiang, *China*

Hyun-Do Jung, *Korea*

Lifeng Kang, *Australia*

Ali Khademhosseini, *USA*

Moon Suk Kim, *South Korea*

Jangho Kim, *South Korea*

Bahattin Koç, *Turkey*

Dimitrios A. Lamprou, *UK*

Junmin Lee, *South Korea*

Khoon Lim, *Australia*

Ki-Taek Lim, *South Korea*

Fengyuan Liu, *UK*

Veronica MacChi, *Italy*

Carmelo De Maria, *Italy*

Elena Martínez Fraiz, *Spain*

Laurence Meagher, *Australia*

Ferry Melchels, *Australia*

Nikolaos Michailidis, *Greece*

David K. Mills, *USA*

Vladimir Mironov, *Russia*

Mario Moisés Alvarez, *Mexico*

Maurice N Collins, *Ireland*

Makoto Nakamura, *Japan*

Roger Narayan, *USA*

Insup Noh, *Korea*

Ali Nokhodchi, *UK*

J.M.A.C. de Oliveira, *Portugal*

Aleksandr Ovsianikov, *Austria*

Sang-Hyug Park, *Korea*

Alokesh Pramanik, *Australia*

Aldo R. Boccaccini, *Germany*

Michael Raghunath, *Switzerland*

Anabela Raymundo, *Portugal*

Shinji Sakai, *Japan*

Thomas Scheibel, *Germany*

Cijun Shuai, *China*

Swee Leong Sing, *Singapore*

Kedong Song, *China*

Jie Sun, *China*

Zhonghua Sun, *Australia*

Ergün Süleyman, *Germany*

Ibrahim Tarik Ozbolat, *USA*

Savas Tasoglu, *Turkey*

S. Vijayavenkataraman, *UAE*

Giovanni Vozzi, *Italy*

Liqiang Wang, *China*

Yin Xiao, *Australia*

Seung-Schik Yoo, *USA*

Barbara Zavan, *Italy*

Ioanna Zergioti, *Greece*

Yu Shrike Zhang, *USA*

Yi Zhang, *China*

Hala Zreiqat, *Australia*

Assistant Editor

Jia An, *Singapore*

Youth Editorial Board Members

Tanveer Ahmad, *Saudi Arabia*

Shivesh Anand, *Denmark*

Gokhan Bahcecioglu, *USA*

Gianluca Cidonio, *Italy*

Giovanni Falcone, *Italy*

Ruben Foresti, *Italy*

Gabriele Maria Fortunato, *Italy*

Paola Serena Ginestra, *Italy*

Xulin Hu, *China*

Anna Jezierski, *Canada*

Yiting Lei, *China*

Lan Li, *China*

Huixin Liang, *China*

Elena Marcello, *Italy*

Wei Long Ng, *Singapore*

Egor Osidak, *Russia*

Chenxi Peng, *Australia*

Rúben Pereira, *Portugal*

Mohammadmajid Sepantafar, *USA*

João Carlos Silva, *Portugal*

Yogendra Pratap Singh, *USA*

Thiago Domingues Stocco, *Brazil*

Binbin Sun, *China*

Aitor Tejo-Otero, *Spain*

Danlei Zhao, *China*

Hui Zhu, *China*

*Editorial Board Members as of February 19, 2025

ACCSCIENCE PUBLISHING

Volume 11 | Issue 1 | February 2025 | Page 1 – 630 |

International Journal of Bioprinting

https://accscience.com/journal/IJB

CONTENTS

REVIEW ARTICLES

1 **A perspective on transformative bioprinting**
Chee Kai Chua, Jia An, Shiyuan Fan, Xuening Zhang, Liliang Ouyang, Haofan Liu, Li Zhang, Ya Ren, Maling Gou, Wei Long Ng, Wai Yee Yeong, Hui Zhu, Zijie Meng, Jiankang He

30 **Miniature modeling while aiming for transplantation: Current challenges and future perspectives of lung bioprinting**
Judit Bovari-Biri, Kitti Garai, Borbala Lovaszi, Zoltan Vereb, Judit E. Pongracz

57 **Scaling liver bioprinting: A guide for usage of the hepatic extracellular matrix as a bioink**
Valentin A. Brumberg, Polina Yu. Bikmulina, Artem A. Pozdnyakov, Zahra Heydari, Darya R. Zimulkina, Olga A. Smirnova, Frederico David Alencar de Sena Pereira, Anastasiia M. Nesterova, Svetlana L. Kotova, Massoud Vosough, Anastasia I. Shpichka, Peter S. Timashev

84 **Designing methacrylic anhydride-based hydrogels for 3D bioprinting**
Naisi Shen, Zhen Li, Pu Yang, Xiangjun Liu, Yikun Ju, Yue Hu, Bairong Fang, Liangle Liu

139 **The application prospects of 4D printing tissue engineering materials in oral bone regeneration**
Wenlu Song, Weihua Huang, Junzhuo Qu, Chujie Xiao, Huinan Yin, Xiangzhen Liu, Weikang Xu

192 **Application of three-dimensional printing in bacterial detection**
Tingting Cui, Ziye Xu, Ting Cao

210 **Revolutionizing regenerative rehabilitation: 3D printing for musculoskeletal regeneration**
Ai-Jia Guan, Yong-Chao Zhao, Xiao-Na Xiang, Ma-Ling Gou, Hong-Chen He

RESEARCH ARTICLES

233 **Patient-specific design and fabrication of a trapeziometacarpal joint orthosis using a computed tomography image-based finite element model**
Chan Beom Park, Ji Sup Hwang, Hyun Sik Gong, Hyung-Soon Park

246 **3D-printed scaffolds with controlled-releasing compounds for ectopic activation of dormant ovarian follicles**
Yali Yang, Huashan Zhao, Mingming Wu, Lei Ge, Meiyue Wang, Feifei Du, Zhonglin Xiao, Li Xue, Pinpin Wang, Jie Chen, Tianxia Xiao, Pei-Gen Ren, Changshun Ruan, Jian V. Zhang

259 **Heterotopically differentiated PDLSCs-laden 3D-bioprinted scaffolds for concurrent oral hard and soft tissue regeneration**
Huilin Zhu, Ke Yi, Zhihui Tang, Qing Li

284 **Osteocytic PGE2 receptors EP2/4 signaling create a physiological osteogenic microenvironment in polycaprolactone 3D modules**
Jingjing Chen, Qiuling Guo, Jinling Zhang, Ying Zhang, Yangxi Liu, Pengtao Wang, Chengzhu Zhao, Linda F. Bonewald, Xiaolin Tu

301 **Design, fabrication, and evaluation of a novel 3D-printed temporomandibular joint prosthesis enhanced with elastic layers**
Junqi Jiang, Zhiwei Jiao, Bingxue Cheng, Jianmin Han, Xiangliang Xu, Chuanbin Guo

314 **3D bioprinting of biomimetic trachea with interspersed cartilage and vascularized connective tissue for prompt segmental tracheal reconstruction**
Pengli Wang, Ziming Wang, Bohui Li, Lei Xie, Liang Guo, Yong Xu, Dan Li, Jiaoyu Yi, Bo Tao

327 **Sericin improves alginate-gelatin hydrogels' mechanical properties, porosity, durability, and viability of fibroblasts in cardiac spheroids**
Martine Tarsitano, Clara Liu Chung Ming, Dana Idais, Hadi Mahmodi, Kaitlin Wyllie, Benedetta Isella, Thomas R. Cox, Irina Kabakova, Donatella Paolino, Carmine Gentile

347 Parametric computational modeling of melt electrowritten scaffolds: Predicting the cellular micromechanical environment for gradient tissue engineering in rotator cuff repair
Sam E. Winston, Lynn M. Pezzanite, Steven Dow, Kirk C. McGilvray

363 Toward robust and reproducible pluripotent stem cell expansion in bioprinted GelMA constructs
Elizabeth R. Komosa, Wei-Han Lin, Brenda M. Ogle

382 A 3D-bioprinted neuroinflammatory co-culture model for *in vitro* study of Parkinson's disease pathology
Hongliang Mao, Liangchen Yu, Yang Qiao, Menghui Liu, Xingliang Dai, Hongwei Cheng

400 Optimizing printability and mechanical properties of poly(3-hydroxybutyrate) biocomposite blends and their biological response to Saos-2 cells
Štěpán Krobot, Přemysl Menčík, Kateřina Chaloupková, Ján Bočkaj, Sára Vach Agócsová, Michala Klusáček Rampichová, Věra Hedvičáková, Pavol Alexy, Radek Přikryl, Veronika Melčová

418 Polydopamine-modified 3D-printed polycaprolactone scaffolds for promoting bone regeneration
Qian Zhong, Shuai Huang, Weihua Huang, Hengpeng Wu, Yang Wang, Zhenyu Wen, Huinan Yin, Yixiao Wang, Weikang Xu, Qingde Wa

439 Prevascularized cell sheets enhance therapeutic effect of extracellular matrix scaffolds in a one-stage skin grafting rat model
Fei Zhou, Ning Liu, Shuying Chen, Yahui Xiong, Zhaoqiang Zhang, Lei Chen, Yingbin Xu

453 Collagen-sodium alginate-silk fibroin 3D-printed scaffold loaded with polydatin promotes cartilage regeneration by improving lipid metabolism and cell apoptosis
Weibin Du, Wenxiang Zeng, Zhenwei Wang, Huahui Hu, Yanghua Tang, Wei Zhuang, Guoping Cao, Gang Qu

470 Replication of an intervertebral disc using an in-house bioprinter: A proof-of-concept study
Emmaëlle Carrot, Perrine de Villemagne, Paul Humbert, Sébastien Grastilleur, Benoit Rosa, Boris Halgand, Yoan Le Guennec, Johann Clouet, Vianney Delplace, Pierre Weiss, Franck Halary, Jean-Yves Hascoët, Marion Fusellier, Luciano Vidal, Jérôme Guicheux, Catherine Le Visage

485 3D-printed biomimetic liposomal hydrogels for localized and targeted treatment of drug-resistant *Candida albicans* vaginitis
Lina Dong, Wenyan Wang, Bixing Fang, Meixuan Liu, Miao Pan, Xiaoqi Li, Aobuliaximu Yakupu, Chunmao Han, Qiong Li, Xingang Wang

501 Gradient hydroxyapatite nanoparticles with spatial distribution facilitate the healing of tendon-to-bone interface
Lei Wang, Liguo Sun, Zhennan Qiu, Zhao Zhang, Yubo Shi, Jingyi Dang, Weidong Tao, Jiankang He, Hongbin Fan

517 Improved osseointegration and segmental stability of 3D-printed porous tantalum cages with micro-scale structures for spinal fusion
Hang Liang, Jingyao Tu, Bingjin Wang, Kun Wang, Xiaobo Feng, Wenbin Hua, Shuai Li, Xinyi Chen, Lei Tan, Cao Yang

532 3D-printed cardiac patch coated with human extracellular matrix hydrogel: Significant improvement of cell adhesion and immune reaction
Marjan Enayati, Christopher Riedmüller, Sabrina Rohringer, Lukas Weber, Felix Pointner, Luis Pichelkastner, Marta Bonora, Ana Isabel Antunes Goncalves, Francesco Moscato, Ewald Unger, Emir Benca, Marvin Dötzlhofer, Bruno K. Podesser, Karl H. Schneider, Helga Bergmeister

556 Establishing a framework for the design and fabrication of patient-specific scaffolds targeting partial meniscal defects
Francklin Trindade da Silva, Willian Gonçalves Tsumura, Millena de Cassia Sousa e Silva, Anderson Oliveira Lobo, Thiago Domingues Stocco

573 Biomimetically hierarchical scaffolds drive critical-sized osteochondral tissue regeneration
Farnaz Ghorbani, Joaquim Miguel Oliveira, Zhi Qian, Chongjing Zhang, Yi Zhang, Behafarid Ghalandari, Dejian Li, Zeyuan Zhong, Zichen Liu, Yuanyuan Liu, Baoqing Yu

598 3D-printed artificial cornea featuring aligned fibrous structure and enhanced mechanical strength
Priyanka Chaudhary, Dun-Heng Tan, Chia-Hsien Lee, Chun-Yu Chang, Ting-Han Lin, Ming-Chung Wu, Wei-Fang Su, Meng-Fang Lin, Yu-Ching Huang

614 Primitive regenerated-tissue evolution *in situ* after implantation of a 3D-printed tracheal graft
Sen-Ei Shai, Yi-Ling Lai, Yi-Wen Hung, Chi-Wei Hsieh, Kuo-Chih Su, Chun-Hsiang Wang, Te-Hsin Chao, Yung-Tsung Chiu, Chia-Ching Wu, Shih-Chieh Hung

ACCSCIENCE PUBLISHING

International Journal of Bioprinting

REVIEW ARTICLE

A perspective on transformative bioprinting

Chee Kai Chua[1]*, Jia An[1], Shiyuan Fan[2], Xuening Zhang[2], Liliang Ouyang[2]*, Haofan Liu[3], Li Zhang[3], Ya Ren[3], Maling Gou[3]*, Wei Long Ng[4], Wai Yee Yeong[4]*, Hui Zhu[5,6], Zijie Meng[5,6], and Jiankang He[5,6]*

[1]Centre for Healthcare Education, Entrepreneurship and Research @ SUTD (CHEERS), Singapore University of Technology and Design, Singapore, Singapore

[2]Department of Mechanical Engineering, Tsinghua University, Beijing, China

[3]State Key Laboratory of Biotherapy and Cancer Center, West China Hospital, Sichuan University, Chengdu, China

[4]Singapore Centre for 3D Printing, Nanyang Technological University, Singapore, Singapore

[5] State Key Laboratory for Manufacturing Systems Engineering, Xi'an Jiaotong University, Xi'an, Shaanxi, China

[6]NMPA Key Lab for Research and Evaluation of Additive Manufacturing Medical Devices, Xi'an Jiaotong University, Xi'an, Shaanxi, China

Abstract

Our understanding of bioprinting originated from tissue engineering and 3D printing. Over the last two decades, 3D printing has been serving tissue engineering to fulfill its goal of solving the worldwide challenge of human organ shortage. Fundamental research and translation to clinical settings are currently the mainstream and have led to the emergence of translational bioprinting. However, as bioprinting evolves with more refined capabilities such as spatial and temporal controls of multiple biological materials at the microscale, perhaps it is time to reflect on a reciprocal approach, i.e., tissue engineering, to serve 3D printing with the hope to address problems more than or other than organ shortage. Recent examples of cultivated meat, digital bioprinting, bioelectronics, and space exploration may have just revealed the tip of the iceberg, though some still overlap with the goal of tissue engineering. Whenever a new material is introduced to the realm of 3D printing and becomes printable, it always leads to versatile or even unforeseen applications. This has happened to metals, ceramics, composite, and electronics. Although it has been known for a long time that biological cells are 3D-printable, the application of such concept has been always perceived from the angle of tissue engineering with human organ shortage as the sole motivation. Therefore, in this review based on existing evidence, we offer an innovative perspective of bioprinting, termed "transformative bioprinting," to emphasize the role of an enabling tool of bioprinting and its alternative motivations.

Keywords: Additive manufacturing; Bioprinting; Tissue engineering; *In situ* bioprinting; Cultivated meat; Bioelectronics

***Corresponding authors:**
Liliang Ouyang (ouy@tsinghua.edu.cn)

Maling Gou (goumaling@scu.edu.cn)

Wai Yee Yeong (wyyeong@ntu.edu.sg)

Jiankang He (jiankanghe@mail.xjtu.edu.cn)

Chee Kai Chua (cheekai_chua@sutd.edu.sg)

Citation: Chua CK, An J, Fan S, et al. A perspective on transformative bioprinting. *Int J Bioprint.* 2025;11(1):1-29. doi: 10.36922/ijb.3525

Received: April 29, 2024
Accepted: June 21, 2024
Published Online: August 15, 2024

Copyright: © 2024 Author(s). This is an Open Access article distributed under the terms of the Creative Commons Attribution License, permitting distribution, and reproduction in any medium, provided the original work is properly cited.

Publisher's Note: AccScience Publishing remains neutral with regard to jurisdictional claims in published maps and institutional affiliations.

1. Introduction

Three-dimensional (3D) printing, also known as additive manufacturing or rapid prototyping, has revolutionized the landscape of tissue engineering by introducing

automation and control.[1] This technique was initially employed for fabricating customized porous scaffolds,[2] but further evolution of the technique to encompass living cells has given rise to the field of organ printing or 3D bioprinting.[3–5] Like the basic 3D printing process chain, 3D bioprinting comprises three sequential segments: preprocessing, processing, and post-processing.[4] Preprocessing includes 3D model generation (e.g., computer-aided design [CAD] or 3D reconstruction from computed tomography [CT] or magnetic resonance imaging [MRI] images), material and cell selection, and all other preparation works before printing. Processing is the layer-by-layer automated fabrication of tissue analogues inside a bioprinter. Postprocessing refers to the accelerated tissue maturation enabled by various types of stimulations (chemical, mechanical, electrical, magnetic, etc.) applied to the as-printed constructs. To meet the requirements of clinical applications, most research works are carried out around enhancing structural designs, printing stem cells, refining bioink formulations, improving bioprinter capabilities, optimizing bioreactor conditions, as well as vascularizing large constructs. At present, a number of bioprinted transplants such as cartilage and skin have been successfully implemented in a clinical setting.[6] To further reduce time and accelerate clinical translation, the interest in *in situ* or *in vivo* bioprinting, in which the printed tissue capitalizes on the human body as a bioreactor, has been rapidly growing over recent years.[6] Recently, a framework of technological readiness level for bioprinting has been proposed to measure how far a bioprinting project has progressed from the early stage towards clinical application.[7]

Creating functional tissues and organs with biological and physiological performance has long been a shared goal between tissue engineering and bioprinting.[8–10] However, recent advancements in bioprinting have showcased a shift in focus towards various other priorities, revealing the enabling capabilities of bioprinting to solve problems beyond organ shortage. For example, animal cells have been bioprinted into meat for human consumption,[11] which solves meat shortage instead. Likewise, plant cells have been bioprinted into wood analogue to explore a solution to wood shortage.[12] In fact, these developments encompass a broad spectrum of applications, including bioelectronics,[13] soft robotics,[14] space exploration,[15] plant biology,[16] and sustainability.[17] All the above have changed our perspective and understanding of bioprinting fundamentally, and we see bioprinting becoming more and more separated from tissue engineering in terms of goals and capabilities. To describe this recent trend, we would like to propose a term "transformative bioprinting," in contrast to "translational bioprinting," for all the missions of bioprinting going beyond organ shortage. In transformative bioprinting, the research motivation is not necessarily human organ shortage. Rather, the ability to manipulate the spatial and temporal organization of biological materials at micro-scales becomes pivotal, and bioprinting serves as an enabling method or tool to solve many new problems ahead.

This article aims to provide, from the perspective of editors, an overview of recent developments in bioprinting, meant for stimulating further discussions on the future of bioprinting. To facilitate the discussion, we classify bioprinting into three categories (Figure 1): fundamental bioprinting, translational bioprinting, and transformative bioprinting. Fundamental bioprinting and translational bioprinting differ in application readiness level while transformative bioprinting is distinct in motivation. Currently, the mainstream of bioprinting lies in fundamental bioprinting and translational bioprinting while the transformative emerges as a side stream only.

2. Fundamental bioprinting

This section reviews the fundamental concepts in bioprinting and the current status of the two main uses of bioprinted human tissues: tissue repair and *in vitro* models.

2.1. Bioprinting technologies and bioinks: fundamentals and trends

The inclusion of living cells in the manufacturing process differentiates 3D bioprinting from conventional 3D printing technologies. Since the first trials of cell printing in the early 2000s, various bioprinting technologies have emerged, including droplet-based (e.g., inkjet printing, microvalve-based jetting), filament-based (e.g., extrusion-based printing), and plane-based (e.g., digital light processing [DLP]) approaches.[18] With the capacity to rapidly construct 3D structures with considerable integrity, extrusion-based and light projection-based bioprinting technologies have been the major players in both academia and industry considering the number of relevant publications and commercial bioprinter products. One major trend in technological advances is the further enhancement of structural complexity. For example, extrusion bioprinting in a supporting bath has emerged as a significant technique since 2015,[19] which allows for the printing of free-form structures with intrinsic support from yield-fluid supporting baths. This approach also makes it possible for the printing of less-viscous ink formulations, which might not self-support well in the conventional printing paradigm in the air. The use of light-based 3D printing technologies (e.g., DLP, stereolithography) to print cells has only been highlighted in the past decade, before which the hazardous effects of ultraviolet (UV) light and

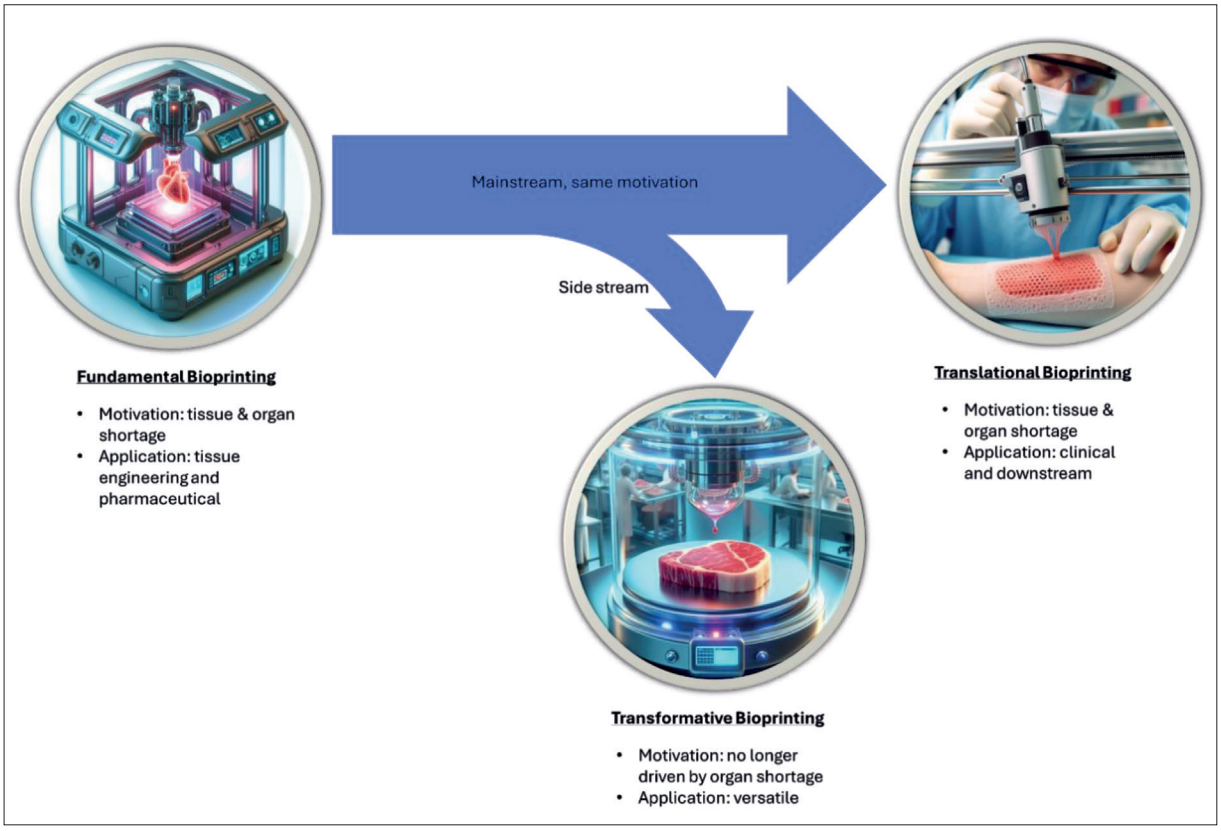

Figure 1. An overview of bioprinting.

photo-related chemicals were believed to cause cell death. The use of visible light, high-efficiency photoinitiators, and biocompatible photo absorbers have all contributed to the progress of cell printing using light-based 3D printing techniques. Moreover, the recent advances in volumetric 3D printing have added to the capacity to fabricate free-standing complex structures rapidly. For example, the computer tomography light projection technique can be used to print centimeter-sized cell-laden constructs in tens of seconds in a rotation vat.[20]

Bioinks are typically referred to as the cell-laden formulations to be printed. The progress of bioinks is greatly associated with the advances of hydrogels, the major cell carrier materials due to the mimicry of the extracellular matrix (ECM). The primary considerations for bioinks include structural printability and cell survivability during the printing process. The rheological requirements for bioinks differ from printing technologies. Inkjet bioprinting can only deal with low-viscosity ink formulation to avoid clogging, while extrusion-based bioprinting usually favors viscous formulation to maintain structural integrity. To date, less-viscous bioink and soft bioprints can also be extrusion-printed by developing novel materials and technological strategies, such as complementary network bioinks, suspension bioprinting, and *in situ* crosslinking strategies.[21,22] Beyond its bulk form for cell encapsulation, the hydrogel has also been processed into different forms of bioinks, such as granular microgels. Based on the success of hydrogel microparticles in non-invasive injectable applications, researchers first introduced granular microgels to 3D bioprinting in 2019.[23] Since then, granular bioinks have drawn much attention considering their wide applicability of materials and potential protection of cells from the flow-induced shearing force. Nevertheless, it is still challenging to achieve the bio-functionality of printed constructs beyond structural printability. To this end, decellularized extracellular matrices (dECM) have been massively studied to formulate tissue-specific bioinks in favor of engineering different tissues. In general, efforts are still needed to enable the bioinks with the replication of tissue microenvironments, covering mechanical, topological, and biochemical aspects.

More detailed information on the development of bioprinting technologies[24] and bioinks[21] can be obtained in several review articles.

2.2. Tissue engineering applications

The initial motivation for cell printing was to fabricate tissues and organs for transplantation, considering the significant shortage of organ donors. The customization and heterogeneity capacities of 3D printing perfectly align with the anatomical features of native tissues. To date, tissue engineering and regenerative medicine are still the major applications for 3D bioprinting, with musculoskeletal tissue engineering being the most widely studied area. Back in the 1990s, 3D printing was used to fabricate polymer or metal bone tissue scaffolds and cell-free bone grafts. With the development of cell printing technology, cell-laden living grafts have made it possible to directly repair bone defects. For example, to evaluate the ability of hypertrophic cartilage grafts to regenerate critical-size bone defects, Pitacco et al. incorporated human mesenchymal stem/stromal cells (hMSC) into fibrin-based bioinks and bioprinted them into polycaprolactone (PCL) framework to produce mechanically reinforced structures. Through the formation of early hypertrophic grafts in *in vitro* and animal experiments, it was verified that the early hypertrophic bioprinted structure supports higher levels of vascularization and bone formation in the body.[25] In another example, Xie et al. designed a portable concrete-like bioink made of cell-laden microgels and gelatin methacryloyl (GelMA) solutions for bone repair in emergencies. The composite bioink formulations containing bone marrow stromal cells were demonstrated to promote endogenous bone regeneration in the skull of rats.[26] For cartilage tissue engineering, developing cartilage grafts with biomimetic natural cartilage anisotropy remains a major challenge. Sun et al. achieved anisotropic cartilage regeneration through the combination of PCL scaffolds and growth factor-loaded composite bioinks. The hybrid graft can promote the differentiation of human mesenchymal stem cells and the formation of tissue with a cartilage matrix that can eventually form a cartilage-like anistropic tissue.[27] Since native bone and cartilage are usually load-bearing, it is highly important for the bioprinted constructs to achieve a mechanical match with the native tissues. However, too high mechanical properties of the scaffolds has been shown to hinder the growth of osteoblasts and chondrocytes and thus tissue formation. Currently, a common strategy is to adopt a composite structure with both soft and hard components, where a soft hydrogel domain could carry cells and support the fast ingrowth of native tissues while the hard domain provide necessary mechanical strength. Osteoarthritis is often accompanied by defects of cartilage and subchondral bone, thus making the integrated osteochondral tissue regeneration another important development direction. To this end, Zhang et al. developed a bioink consisting of dECM and silk fibroin for 3D bioprinting of the bilayered scaffold with distinct mechanical properties and growth factor release profile for each layer. Scaffolds encapsulating transforming growth factor-β (TGF-β) and bone morphogenetic protein-2 (BMP-2) can serve as a controlled-release system to promote the directional differentiation of bone marrow-derived mesenchymal stem cells (Figure 2a).[28]

Skin tissue engineering is another major application field for bioprinting. Conventional tissue-engineered dermal products available in the market fail to customize the personalized wound in depths or shapes. To this end, Albanna et al. combined scanning imaging and inkjet cell printing technology to build an *in situ* skin bioprinting system. This system allows for rapid imaging, trauma model generation, and then deposition of biomaterials and cells to a specific area of the wound.[29] To better mimic the skin tissue microenvironment, Yang et al. adapted recombinant human type III collagen (rhCol3) to formulate a skin-specific bioink and created a full-thickness skin equivalent using extrusion-based bioprinting.[30] The inclusion of rhCol3 was shown to promote epidermal keratinocytes at early stages and contribute to would healing process *in vivo*. Despite the progress, the engineering of skin tissues with functional skin appendages (e.g., hair, sweat glands) is still challenging.

The engineering of other organs like heart and liver is likely more challenging considering the highly complex and heterogeneous structures and compositions. A general methodology is to engineer functional microtissues or organ units first and scale it up with advanced biofabrication technologies. Taking cardiac tissue engineering as an example, Noor et al. used cardiomyocytes and endothelial cells (ECs) derived from human pluripotent stem cells (hiPSCs) to formulate a bioink to construct cardiac patches containing blood vessels, which showed to match the anatomy of a native heart.[31] They also demonstrated the possibility of printing a mini heart model with anatomic similarity using suspension bioprinting technologies, though no biofunctional evidence was shown. Furthermore, Lee et al. printed a left ventricular model made of collagen and high-density cardiomyocytes by using an improved suspension bioprinting technique, as shown in Figure 2b. During the 28-day culture process, the ventricular model maintained its integrity and showed synchronized contractions, directional action potential propagation, and wall thickening up to 14% during peak systole.[32] The authors also showed the creation of vascular network of anatomic mimicry. Vascularization is indeed an enduring challenge for large-scale tissue engineering. Although it is possible to fabricate complex 3D channel networks as vascular beds, the current post cell seeding approach for endothelialization is time-consuming and of low efficiency.[33] To this end, an *in situ* endothelialization approach was developed to pre-load ECs in the sacrificial

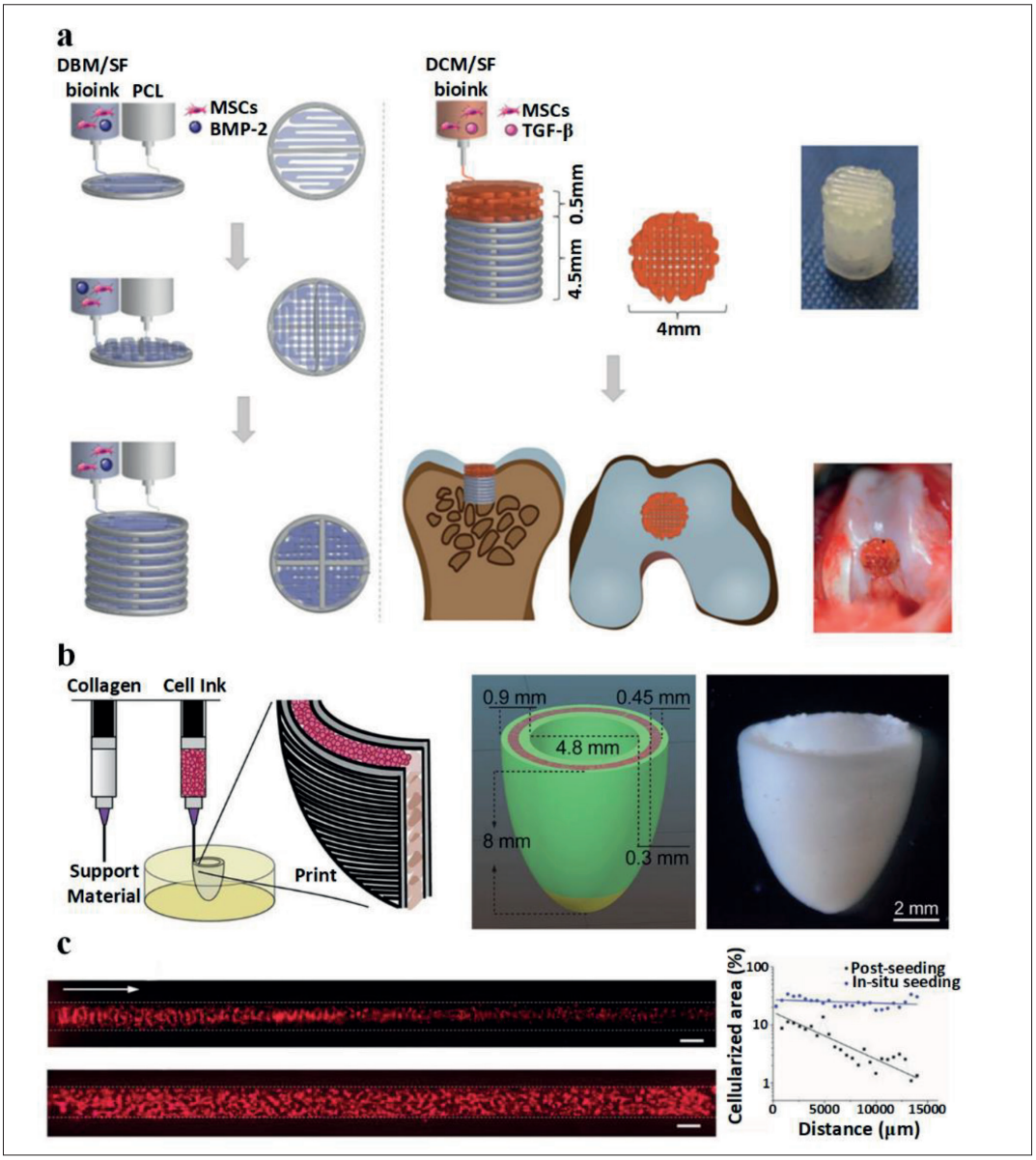

Figure 2. Tissue engineering applications. (a) The design and fabrication of a bilayered osteochondral tissue engineering scaffold.[28] Reprinted under the Creative Commons license. (b) 3D-bioprinted human cardiac ventricle model by printing collagen ink and a high-concentration cell ink in baths. Reprinted with permission from Lee et al.[32] Copyright © 2019, the American Association for the Advancement of Science. (c) Comparison of conventional post-seeding and *in situ* seeding of endothelial cells in solo channels indicates the potential of *in situ* endothelization approach. Reprinted with permission from Ouyang et al.[34] Copyright © 2020, Wiley-VCH GmbH.

phase, which will template vascular channels during the culturing process (see Figure 2c).[34] Technically, this approach can allow for the delivery of ECs to every single channel of the networks independent of size and geometry.

Despite the progress, there is a gap between engineering and the natural development of life, which remains a major challenge to combine the two ends towards physiological function. Organoid is a miniaturized and simplified version of an organ generated *in vitro* by following developmental principles. The combination of the cutting-edge organoid technologies with bioprinting might be able to address the problems of complex tissue engineering. For example, Lawlor et al. used extrusion-based bioprinting technology to produce kidney organoids with highly reproducible, consistent cell numbers and viability in a high-throughput manner, facilitating the fabrication of uniformly patterned kidney tissue sheets with functional proximal tubular segments.[35] In another example, Brassard

et al. took advantage of the principle that small organoids can be forced to fuse and reorganize based on the geometry and constraints imposed by 3D printing, and used bioprinting-assisted tissue emergence (BATE) technology to bioprint organoids into the ECM to form centimeter-sized organoids.[36] Some research teams have also reported using aspiration-assisted bioprinting (AAB) technology to move spheres for bioprinting with or without scaffolds to minimize cell damage during the printing process.[37,38]

2.3. Pharmaceutical applications

The development of commercial drugs requires a significant amount of investment, including drug optimization and toxicity testing before clinical trials to reduce late-stage failures.[39] Commonly used drug screening models include monolayer cell models and animal models. While the planar cell platform allows for high-throughput screening and easy manipulation, it cannot fully replicate *in vivo* physiology and pathology due to the lack of cell–cell contact and interactions with the ECM.[40] Animal models have the potential to show *in vivo* reactions, but they may result in pharmacological mismatches due to genetic differences from humans.[41] During phase I clinical trials, drug candidates often face high failure rates, partly due to the inherent limitations of 2D cell culture and animal models in predicting the clinical performance of drug candidates.

The limitations of previous models have spurred interest in biofabrication techniques for creating improved predictive human *in vitro* models. 3D bioprinting enables the fabrication of 3D biological structures with multiple functional, structural, and mechanical properties that better mimic the *in vivo* microenvironment.[42] The bioprinting models used in pharmaceutics mainly divided into two groups according to usage purpose: organ toxicity test and drug screening (for novel drug development or drug optimization). The organ toxicity test is conventionally based on organ-on-a-chip systems. For example, Miller et al. reported a 3D-bioprinted cardiac model using iPSC-derived cardiomyocyte to assess CuO nanoparticles toxicity.[43] In the realm of drug screening, bioprinting has shown great potential in the application of cancer modeling. Bioprinting models primarily concentrate on constructing multiple components to allow for the study of tumor microenvironment, tumor–matrix interactions, and tumor–immune interactions. The diverse selection of bioinks enables precise recreation of these environments through bioprinting techniques. For instance, Zhao et al. achieved 3D printing of tumor cells for the first time and verified the advantages of 3D tumor models over traditional 2D models.[44] Dai et al. reported a glioma stem cell model made with bioprinting using modified porous gelatin/alginate/fibrinogen hydrogel to mimic the ECM. The results showed that the 3D-printed model had higher drug resistance than 2D model[45] (Figure 3a). Wang et al. created a breast cancer model using 3D bioprinting techniques to modify adipose-derived mesenchymal stem/stromal cells in the surrounding area and breast cancer cells in the middle, mimicking the *in vivo* tumor microenvironment. They investigated the supportive effect of the stromal cells on breast cancer and studied the response to the chemotherapy drug doxorubicin.[46] Wu et al. employed a renal cell carcinoma model by utilizing decellularized porcine kidney powder combined with GelMA as the bioink for extrusion printing, facilitating novel drug screening[47] (Figure 3b). Moreover, the utilization of multicellular 3D bioprinting offers significant advantages in targeting gene expression, particularly in tumor model development. Comparisons between 3D and 2D drug screening models revealed significant differences, underscoring chemotherapy resistance.

Furthermore, advancements in printing methods have enhanced model-shaping capabilities. Huang et al. introduced a dot extrusion printing (DEP) system capable of printing GelMA beads containing human pancreatic cancer cells and stromal fibroblasts, thus providing ECM-mimetic microenvironments that mimic native cell–cell junctions and interactions with the ECM[48] (Figure 3c). Additionally, bioprinting perfusion systems have been developed for drug screening purposes, particularly for evaluating antiangiogenic drugs crucial in cancer treatment as angiogenesis is essential for the expansion of tumor. Gu et al. devised a reliable antiangiogenic drug screening chip integrated for long-term perfusion and real-time monitoring, which demonstrated distinct differences in human umbilical vein endothelial cell sprouting after 3 days of perfusion screening, indicating the efficacy and reliability of the drug screening perfusion system.[49] Several reviews on cancer models are recommended for the readers if more information is required.[50,51]

With the development of stem cell technology, the self-renewal and pluripotent features of patient-derived pluripotent stem cells make precision medicine possible and can even allow the drug discovery for congenital diseases.[52] The iterations of 3D bioprinting enable a closer mimicry of *in vivo* 3D structures, making high-throughput fabrication of multiple models realistic. 3D bioprinting demonstrates the combined effect of seeding cells, chosen biomaterials, and model design, and might address some of the key challenges in drug screening.

3. Translational bioprinting

3D printing has a wide range of applications in many fields, and medical 3D printing has gradually become a research

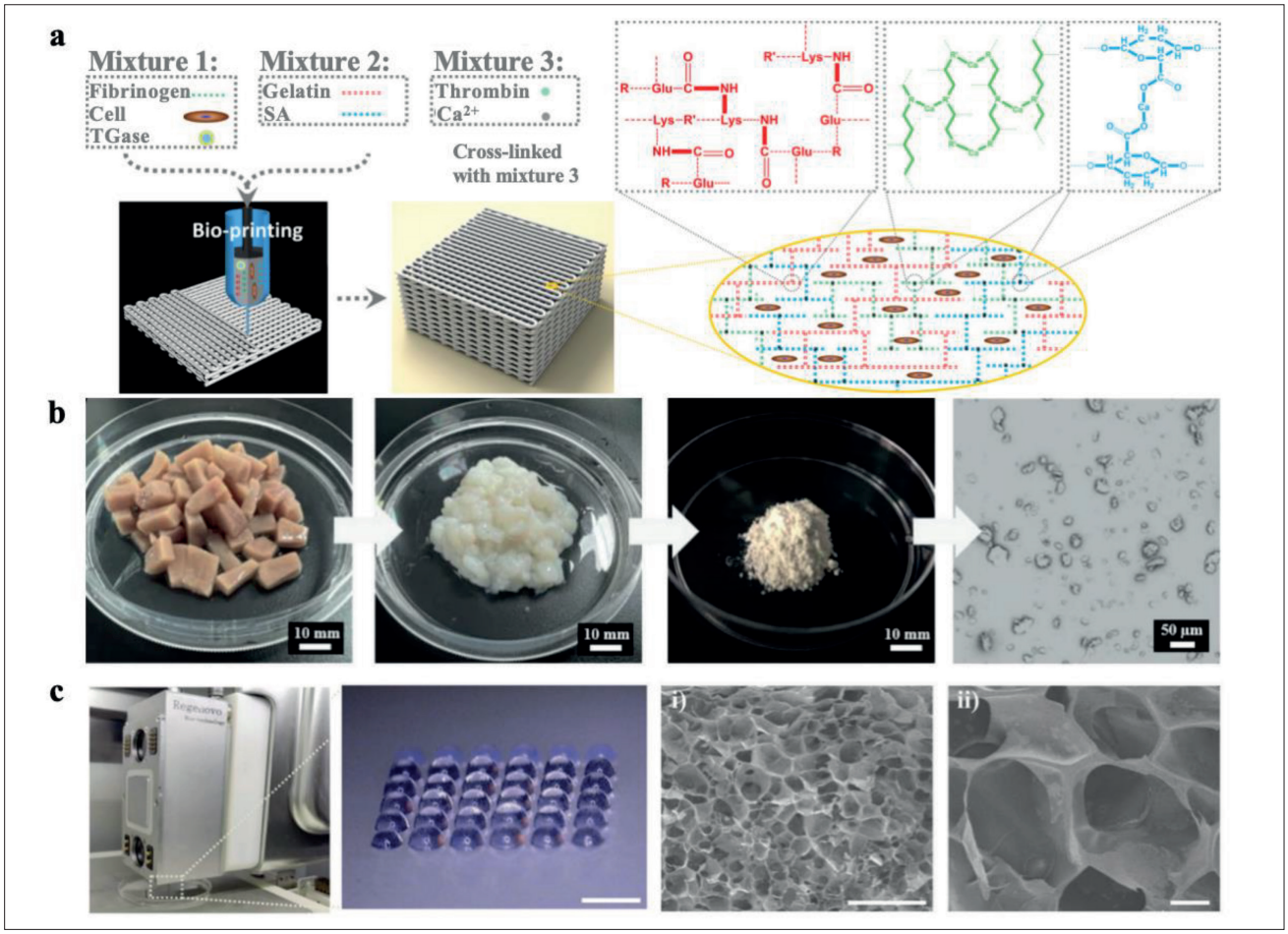

Figure 3. *In vitro* models. (a) The schematic of the printing process of hydrogel-based glioma stem cell model. Reprined with permission from Dai et al.[45] Copyright © 2016, IOP Publishing. (b) The decellularized porcine kidney powder for the bioprinting of renal cell carcinoma model.[47] Reprinted under the Creative Commons license. (c) Bioprinting of hydrogel beads containing human pancreatic cancer cells and stromal fibroblasts.[48] Reprinted under the Creative Commons license.

hotspot,[53–56] including personalized customization of drug,[57] medical devices,[58–62] and medical prosthesis[63–70] that are suitable for complex situations. However, applying 3D printing to clinical practice remains a key challenge.[6,71] It is necessary to develop 3D printing technology based on clinical demands[72] and consider the development of 3D printing according to the development path of pharmaceutical products. To expand the application of 3D printing technology in clinical settings, it is essential to develop advanced 3D printing technologies that can achieve faster speed, higher resolution, and multi-material precise fabrication (Figure 4). In addition, some novel 3D printing technologies are emerging in response to future medical development trends, including four-dimensional (4D) printing technology that can perform treatment according to the changing environment and *in situ* 3D printing that can provide rapid treatment.

3.1. Research progress of high-resolution 3D printing

In the process of translating 3D bioprinting into clinical applications, improving resolution is an important and meaningful goal because it directly affects the quality and functionality of 3D-printed medical products. High-precision biomimetic structures have great application potential in the pharmaceutical field. Some studies have explored approaches for improving the resolution of 3D printing (Figure 5a), mainly including optimization of prototyping technology,[73] materials,[74] printing parameters,[75] and post-processing methods.[76] Two-photon polymerization, a technology widely used in the processing of micro- and nano-structures (Figure 5b), has emerged as a hot research topic in recent years.[74,77] Notably, You et al. improved the resolution of cell-containing 3D-printed structures by adjusting the refractive index of the bioink,

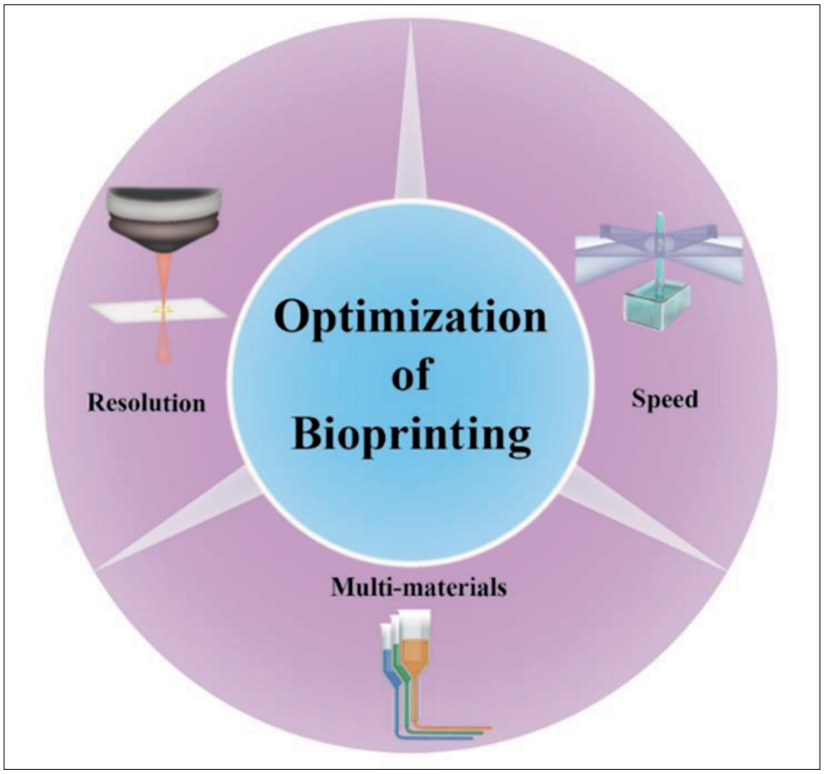

Figure 4. Optimization of bioprinting for medicine.

which can minimize the scattering effect caused by cells in the bioink.[74] This work also achieved high-resolution bioprinting of high-density cells.

3.2. Improving the speed of 3D printing

Increasing speed is another challenge for the clinical translation of 3D printing. Increasing the manufacturing speed of 3D printing can reduce damage to cells and bioactive substances during the printing process, thereby better maintaining their activity.[9,10,65,78] At the same time, in the commercialization process of 3D-printed products, increasing the printing speed can improve production efficiency and significantly reduce manufacturing costs. Currently, different methods have been developed to increase the speed of 3D printing across various technology paths. Changing from layer-by-layer printing to continuous printing represents a technical optimization. Utilizing volumetric molding instead of point or surface stacking can also improve the speed. Based on the active control of mass transport principle, Lipkowitz et al. reported a novel 3D printing method called injection continuous liquid interface production (iCLIP) (Figure 6a), which can accelerate printing speeds to 5- to 10-fold over current methods such as conventional CLIP.[79] In addition, Regehly et al. introduced a volumetric two-color 3D printing technology called xolography, which is based on molecular photoswitches. The volumetric generation rate is four to five orders of magnitude higher than that of two-photon photopolymerization (Figure 6b).[80,81] It provides a potential shortcut for the preparation of large-size and high-precision biomimetic structures.

3.3. Multi-material 3D printing for medicine

In the clinical treatment process, there is often a demand for heterogeneous materials and structures. However, 3D printing usually requires a single material to manufacture structures, which limits the functional diversity and complexity of 3D-printed medical products. To achieve multidimensional control of the products and create heterogeneous 3D structures with various properties and functions, it is urgent to develop multi-material 3D printing technology. In addition to the common multi-nozzle fused deposition modeling, some researchers have explored different multi-material preparation strategies for different 3D printing methods. Cheng *et al.* reported a DLP-based multi-material 3D printing method that used centrifugal force to achieve non-contact cleaning of residual materials caused by the multi-material switching process. This method can realize large-volume heterogeneous 3D objects of multiple materials,[82] providing a solution for the preparation

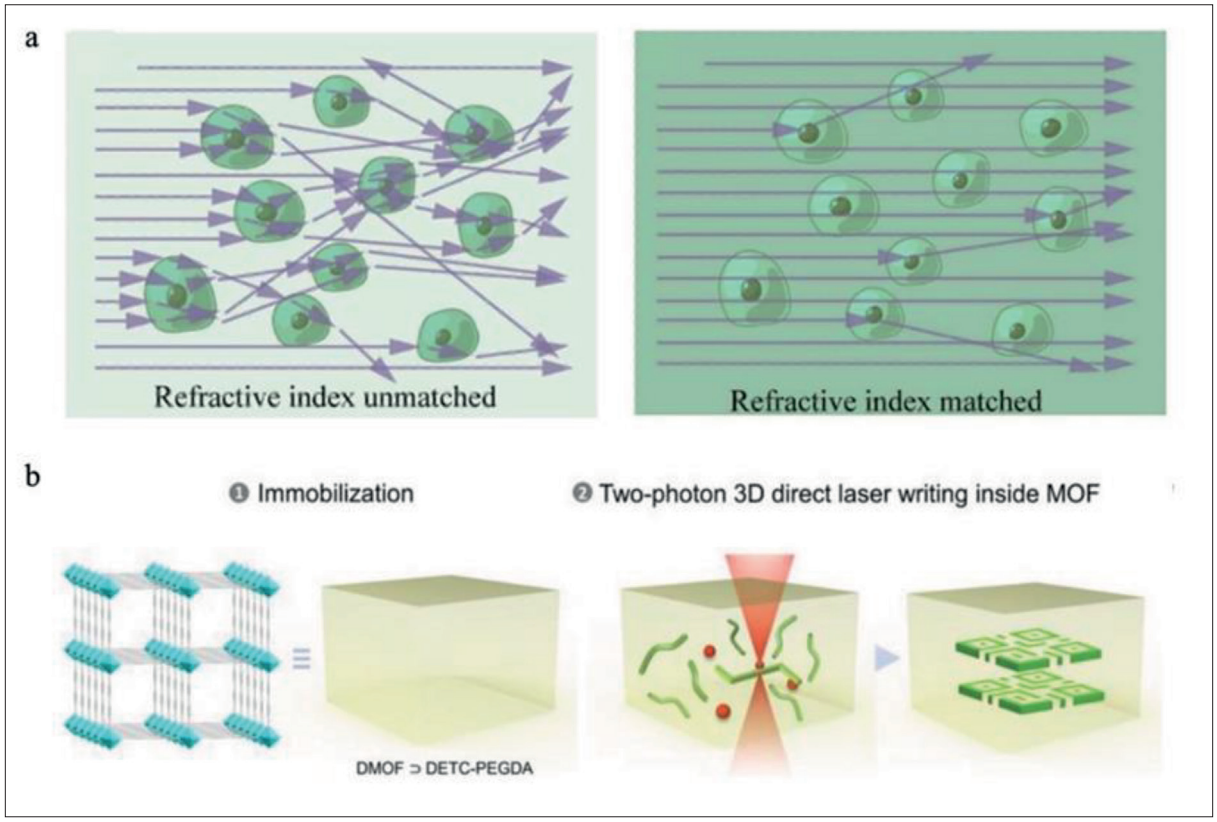

Figure 5. Improving the resolution of 3D printing. (a) Adjusting the refractive index of matrix and matched the cells.[74] Reprinted under the Creative Commons license. (b) Strategy of two-photon polymerization for creating a microstructure-in-crystal hybrid. Reprinted with permission from Zhang et al.[77] Copyright © 2022, John Wiley & Sons.

of heterogeneous structures by photopolymerization, which is difficult due to the residual monomer materials. Larson et al. developed a rotational multi-material 3D printing method that programmatically controls the local orientation of heterogeneous features in the azimuthal angle of multi-material functional and structural filaments at the sub-voxel level.[83] Buchner et al. proposed a vision-controlled jetting inkjet deposition process, which can be used for a wider range of multi-material systems.[84] In addition to the improvement of the process methods for each 3D printing technology, the combination of different 3D printing technologies will also become a feasible method for the preparation of large-size and heterogeneous complex biological structures in the future.

3.4. Research progress of 4D printing in medicine

In the process of bioprinting customized medical products, complex requirements usually arise, such as simulating dynamic physiological environments and responding to biological signals. 4D printing is a new manufacturing technology developed based on 3D printing, which adds a time dimension to the process. 4D printing can be defined as the ability of the structures prepared by 3D printing to change their shapes, properties, or functions on their own in a specific environment or under a specific stimulus.[85,86] Due to the variable characteristics of 4D-printed products, they hold promising applications in personalized medicine. At present, most research focuses on achieving 4D effects through external stimuli, aiming to change the shapes or properties of the products. These stimuli mainly include chemical,[87] light,[88] heat,[89] or magnetism.[90] Additionally, some 4D printing products have self-healing properties,[91] which have potential application value in tissue repair. Some teams have also reported using 4D printing characteristics to mimic tissue growth and induce cell growth into functional tissues.[92] Since the human body itself is in a dynamic state, these 4D-printed products that can adapt to the environment also have great potential in the future development of medicine.

3.5. Research progress of *in situ* 3D printing

In future, personalized treatment necessitates doctors to make temporary judgments based on the actual condition of the patients and perform rapid treatment through

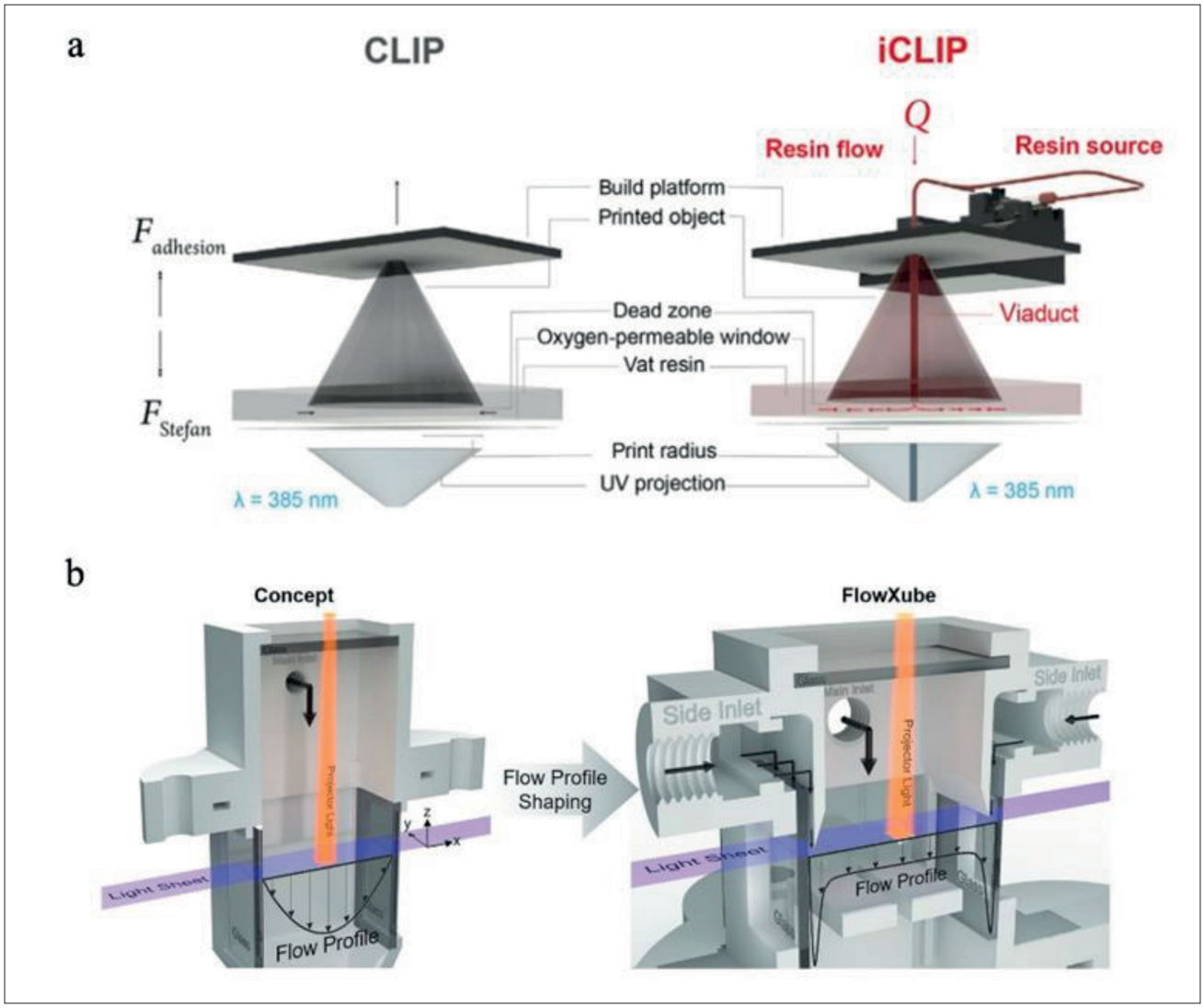

Figure 6. Improving the speed of 3D printing. (a) Printing speed is increased by injection continuous liquid interface production (iCLIP) technology.[79] Reprinted under the Creative Commons license. (b) Continuous volumetric 3D printing technology.[81] Reprinted under the Creative Commons license.

bedside printing. In recent years, the concept of *in situ* 3D printing has been proposed. *In situ* 3D printing can print at the treatment site during the treatment process, thereby optimizing the traditional method of implantation after completing 3D printing. This method is more suitable when dealing with different treatment needs in personalized treatment. It can also greatly shorten the treatment cycle and reduce the possibility of contamination.[93] Recently, many *in situ* 3D bioprinting strategies have been developed. In addition to common extrusion-based 3D printing technology,[26,94] smartphones have also been used to perform *in situ* DLP-based 3D printing, providing a variety of potential options for personalized clinical treatment.[95] Furthermore, some researchers have attempted combining 3D printing with endoscopy to achieve *in situ* printing at the deep level of the organism.[96]

Moreover, in response to the demands of minimally invasive medicine, some non-invasive *in situ* 3D printing strategies were explored. In 2020, Gou's team first reported non-invasive bioprinting *in vivo* (Figure 7a). They developed a digital near-infrared (NIR) photopolymerization (DNP)-based 3D printing technology. The patterned NIR was created to penetrate through the skin to induce the spatially polymerization of the injected bioink. Tissue structures with potential to mature into tissues were customized *in vivo* without surgery implantation.[97] Recently, laser,[98] magnetic fields (Figure 7b),[99] or ultrasound[100] were also employed to develop novel strategies for non-invasive *in*

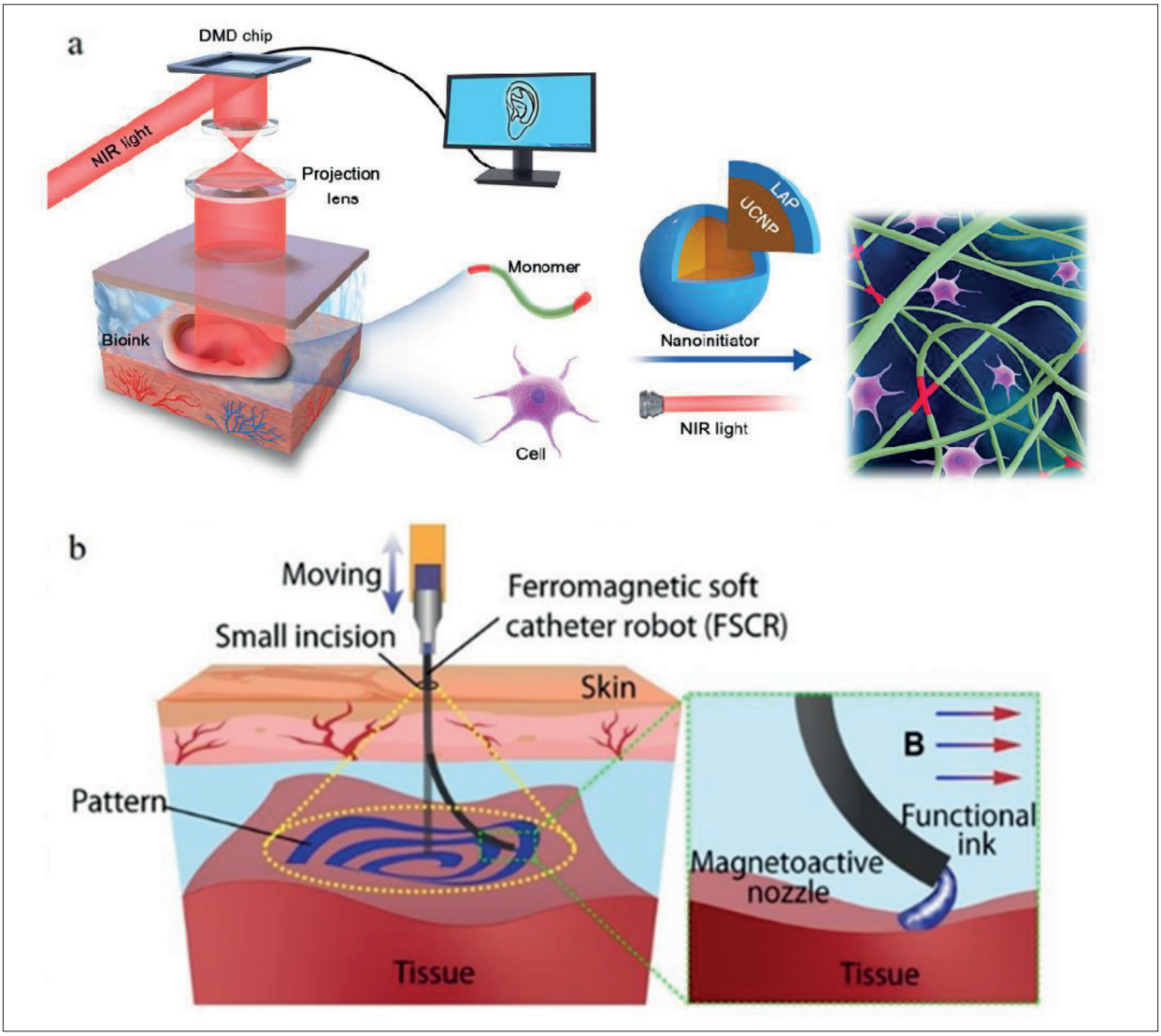

Figure 7. Strategy of 3D printing *in vivo*. (a) A digital near-infrared photopolymerization-based 3D printing for non-invasive *in vivo* 3D bioprinting.[97] Reprinted under the Creative Commons license. (b) *In situ* computer-controlled bioprinting in a minimally invasive manner based on magnetic actuation.[99] Reprinted under the Creative Commons license.

vivo bioprinting. These studies could provide new sight for the future treatment of tissue and organ damage, expanding the 3D bioprinting research avenue and enriching the connotation of minimally invasive/non-invasive medicine.

3.6. The prospect of translational bioprinting for medicine

In the process of translating 3D printing to clinical practice, there are some other challenges besides the 3D printing technology itself. 3D-printed medical products must consider whether they can benefit patients, including their efficacy, safety, and accessibility. First, 3D printing technology needs continuous optimization to meet clinical requirements. Moreover, since medical 3D printing involves personalized customization service, traditional regulatory schemes for medical products may not be applicable.[6] Encouraging the establishment of group and enterprise standards would be more conducive to its development. In addition, since the process and structure of 3D-printed medical products always change during the personalized preparation process, their effectiveness and safety may also change. Therefore, a reasonable quality evaluation system is needed. Long-term research is also required to determine the effectiveness of living tissues constructed by 3D printing. Finally, due to the uniqueness of 3D-printed medical products, new modes of medical product supply

need to be explored, so they can be more reasonably applied to treatment. Undoubtedly, published research results concerning medical 3D printing have demonstrated its potential for developing novel strategies for clinical treatment. We also look forward to more relevant clinical trials focusing on the utilization of 3D-printed medical products in the future.

4. Transformative bioprinting

The section of transformative bioprinting revolves around the principles of bioprinting in other areas such as the fabrication of cultivated meat, the development of more sustainable bioinks, the integration of machine learning (ML) into the 3D bioprinting processes (optimization of bioink formulation and printing parameters, evaluation of cell viability, and prediction of number of printed cells), bioprinting of bioelectronics and bioprinting in space. In-depth discussion of these various aspects of "transformative bioprinting" will be presented in the subsequent sections.

4.1. Cultivated meat

Bioprinting, an advanced technology at the convergence of biology and 3D printing, is transforming the landscape of future food production. A particularly promising application of bioprinting involves the fabrication of cultivated meat, offering a sustainable and ethical alternative to traditional livestock farming. Bioprinted cultivated meat addresses various environmental challenges associated with conventional agriculture, significantly reducing resource-intensive practices such as land use, water consumption, and greenhouse gas emissions. This technology enables controlled and efficient meat production within the necessity for large-scale animal farming, thereby contributing to a more sustainable and eco-friendly food supply chain. Furthermore, bioprinting holds the promise to address ethical concerns related to animal welfare by utilizing a small number of cells harvested from an animal, which can be multiplied to generate cultivated meat without the need to slaughter the animals. This aligns with the growing societal awareness of ethical animal treatment, providing a viable option for cruelty-free diet. The ultimate goal is to develop a sustainable and ethical approach to conventional meat production, addressing the escalating concerns associated with traditional practices.[101]

This innovative process of bioprinting cultivated meat offers three key advantages: (1) depositing bioinks and multiple types of living cells (muscle satellite cells, adipose-derived cells) at precise pre-defined spatial positions; (2) printing highly viable cells that continue to undergo proliferation and differentiation; and (3) inducing protein/cell alignment within the 3D-bioprinted cultivated meat. Numerous recent studies on 3D bioprinting of cultivated meat[11,102–107] have explored various techniques (Table 1), such as jetting-based,[102] extrusion-based,[11,103–106] and vat photopolymerization-based bioprinting.[107] The extrusion-based bioprinting approach are commonly used and different printable protein matrices such zein/hordein or zein/secalin,[102] alginate-based bioinks enriched with plant-based protein isolates,[103,104] gelatin/alginate,[11] and GelMA[107] have been utilized for fabrication of cultivated meat. These protein-based bioinks are typically printed within a supporting bath to facilitate the formation of highly-aligned protein matrices, crucial for mimicking meat texture and promoting cell attachment, proliferation, and myogenic differentiation.[11,102–104]

In a recent study, the effectiveness of two different bioink compositions [arginyl-glycyl-aspartic acid (RGD)-modified alginate with pea protein isolate and RGD-modified alginate with soy protein isolate] as 3D-bioprinted matrices for bovine satellite cell cultivation was evaluated.[103] These plant-based protein isolates offer high nutritional value and carry a low risk of allergic reactions. During the printing process, an edible agar support bath containing calcium chloride solution as a crosslinker was utilized to enhance the fidelity of the printed meat constructs. Additionally, porogens were incorporated into the composite bioinks to increase the overall porosity of the printed constructs, facilitating better nutrient and oxygen diffusion to the encapsulated cells. This research demonstrates the feasibility of incorporating plant-based protein isolates as part of the scaffold component for cultivated meat production. Another study showcased that the use of hydrolysate-enriched bioinks resulted in enhanced myogenesis.[11] Furthermore, research efforts have also concentrated on inducing adipogenesis within 3D-bioprinted cultivated meat.[105–107] In addition to employing standard muscle satellite cells, adipose-derived stem cells were introduced into the 3D-bioprinted cultivated meat, and adipogenic components were supplemented in the culture medium to induce adipogenic differentiation (Figure 8).

Remarkably, recent studies have showcased the utilization of ML across various facets of 3D-bioprinted cultivated meat, revealing its potential for optimization and enhancement.[108,109] These applications span from refining culture medium formulations,[110,111] to predicting and regulating food flavor,[112] and implementing quality control measures.[113] A critical stage in cultivated meat production revolves around cell production within bioreactors, where ML emerges as a valuable tool for real-time adjustments. ML enables the dynamic optimization of parameters such as temperature, pH, oxygen levels, and nutrient circulation, facilitating optimal cell growth. Lastly, ML also plays an important role in the optimization of printing parameters and the prediction of the number of

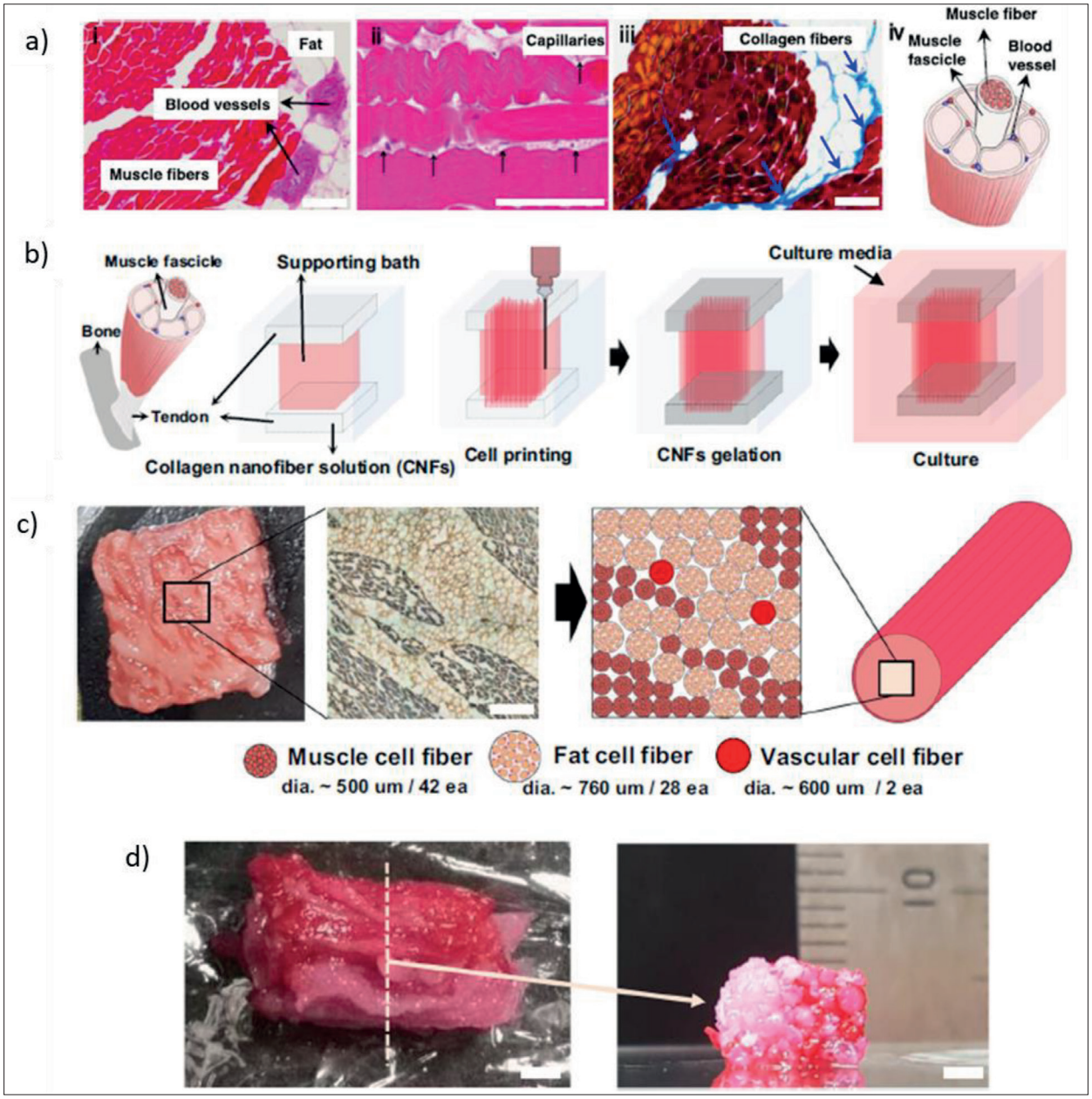

Figure 8. Cultivated meat. (a) Structure of the steak. Representative images to demonstrate hematoxylin and eosin (H&E) staining (i, ii) and Azan staining (iii) on a section of steak. Scale bars: 100 μm. (iv) An illustration of the hierarchical structure within muscle tissue. (b) Tendon-gel integrated bioprinting (TIP) for the fabrication of muscle, fat, and vascular tissues. (c) Analysis of a commercial steak depicting sarcomeric α-actin- (blue) and laminin- (brown) stained images. Scale bar: 1 mm. (d) Integration of fibrous muscle, fat, and vascular tissues to create a cultivated steak, in which the muscle and vascular tissue (red color; stained with carmine), as well as fat tissues (white color), were stained. Scale bar: 2 mm. Reproduced under the Creative Commons license.[105]

printed cells.[114] A recent study exemplified the application of ML in optimizing the development of serum-free media, determining the optimal media compositions that balance yield, environmental considerations, and cost-effectiveness for the production of cultivated meat.[110]

The bioprinting of cultivated meat signifies a paradigm shift in meat production, promising a more sustainable, ethical, and secure future for the food industry. Advanced technique such as ML can play a crucial role in different facets of 3D cultivated meat production, contributing to development, optimization, and scale-up of the entire process. By analyzing data on different cell types, ML identifies the most suitable cells for cultivated meat production based on factors like growth rate, nutrient

Table 1. A summary of research on 3D-printed meat.

Meat	Printing approach	Materials	Cells	Results	Ref.
Cultivated meat	Jetting bioprinting (electrohydrodynamic printing)	Zein/hordein, zein/secalin	Mouse skeletal muscle (C_2C_{12}), porcine skeletal muscle cells (PSCs)	Fibrous matrix induced cell differentiation – upregulation of myogenic proteins	[102]
Cultivated meat	Extrusion bioprinting (1.5% agar support bath containing 10 mM $CaCl_2$)	Pea protein isolate (PPI), soy protein isolate (SPI) and RGD-modified alginate	Bovine satellite cells (printed cell viability of ~80–90%)	Plant proteins supported the attachment and maturation of multiple cell types	[103]
Cultivated meat	Extrusion bioprinting (1.5% agar support bath containing 10 mM $CaCl_2$)	13.4% w/v pea protein isolate, 0.54% w/v alginate (pH 7)	Bovine satellite cells	Protein-rich pea scaffold supported cell attachment, proliferation, and differentiation	[104]
Steak-like structure	Extrusion bioprinting (30% w/v Pluronic pre-gel supporting bath containing 50 mM $CaCl_2$)	6% w/v alginate/ and 4% w/v gelatin supplemented with naturally derived protein hydrolysates	Bovine muscle satellite cells (bMSCs)	Presence of antioxidative protein hydrolysates improved bMSC proliferation *in vitro*	[11]
Steak-like structure	Extrusion bioprinting (support bath mixed with granular particles of gelatin or gellan gum and thrombin)	20 mg/mL fibrinogen and Matrigel	Bovine satellite cells, bovine adipose-derived stem cells	Engineered steak-like structure containing muscle, adipose and blood capillary cell fibers	[105]
Fish-like structure	Extrusion bioprinting	10% fish gelatin/1% sodium alginate with 1% $CaCl_2$ for 10 min or 5% $CaCl_2$ for 5 min	Pax7+/Myf5- piscine satellite cells, piscine adipose-derived stem cells (printed cell viability of ~86.2%)	Muscle tissue formation was achieved under the guidance of biomimetic structures	[106]
Steak-like structure	Vat photopolymerization (digital light processing)	10% w/v GelMA, 0.5% w/v LAP photoinitiator, 1% v/v tartrazine pigment photo absorber	Immortalized bovine embryonic fibroblasts	Cooked culture meat maintained its size and shape upon cutting	[107]

requirements, and flavor profile, ensuring the production of high-quality cultured meat products.[115] Envisioning further progress in the field of cultivated meat, we anticipate that the widespread adoption of cultivated meat is increasingly feasible, ushering in a new era marked by the evolution of global food systems.

4.2. Sustainable bioinks

In recent years, there has been a notable push towards sustainable solutions across diverse industries, including the field of bioink development. This momentum is driven by the heightened awareness of environmental issues and the urgent need to mitigate ecological footprints. As society becomes increasingly conscious of environmental issues, there is a growing recognition of the necessity for sustainable practices in bioink development. In response to this, the field of bioink development has witnessed a surge in interest towards creating environmentally friendly solutions.

The concept of sustainable bioinks revolves around using biomaterials and processes that are environmentally friendly and resource efficient. This holistic approach considers the entire lifecycle of bioinks, from raw material sourcing to disposal. It emphasizes the importance of adopting practices that minimize waste generation, energy consumption, and environmental pollution. By prioritizing sustainability, researchers aim to create bioinks that not only meet the technical requirements but also contribute positively to environmental preservation and resource conservation.

Achieving sustainability in bioink formulation requires sourcing materials from sustainable sources, wastes, and their by-products, and even recombinant proteins. This multifaceted approach involves evaluating the environmental impact of each component and process involved in bioink production. A promising strategy involves utilizing plant-derived biomaterials as fundamental components of sustainable bioinks. These biomaterials, such as alginate-based,[116–118] agarose-based,[119] and cellulose-based[120,121] bioinks, have attracted attention due to their abundance, biocompatibility, and tunable

mechanical properties. Traditional production processes for these biomaterials typically involve pre-treatment, extraction, separation, and purification.[122,123] However, with a growing emphasis on sustainable development, greener technologies have been employed to enhance extraction yield and product quality. Numerous studies have explored innovative methods like ultrasound-assisted,[124] microwave-assisted,[125,126] extrusion-assisted,[127] autoclaving,[128] bio-ionic liquid,[129,130] and enzymatic[131,132] approaches for more environmentally friendly extraction methods (Table 2). These advancements in extraction techniques improve the environmental sustainability of bioink production and reduce the environmental footprint of bioprinting processes.

Valorization of wastes or by-products into useful bioinks is essential for a more sustainable future. By repurposing materials that would otherwise be discarded, researchers can reduce waste generation and minimize environmental pollution. Collagen,[133–136] chitosan,[137] silk,[138] and keratin[139–141] are examples of biomaterials that can be extracted from waste sources and used to create bioinks with desirable properties. Collagen, a major structural protein in most animal tissues, can be sustainably extracted from various sources such as fish (scales and skin) and animal waste (skins, hides, bones, and connective tissues).[133–135] Chitosan is primarily derived from marine-species such as shrimp shells, crab shells, and lobster/crayfish shells, providing a renewable source for chitosan extraction.[137] Emerging methods also enable the utilization of silk waste or by-products (collecting discarded silk fibers from textile manufacturing processes or extracting silk proteins from waste sources) to produce silk-based bioinks in a more sustainable manner.[142,143] Keratin is commonly found in industrial wastes such as low-grade wool and trimmings, and feathers that are often disposed through incineration or landfill. These unwanted waste products offer an abundant protein source that can be repurposed into printable bioinks.[144]

Additionally, recombinant protein-based bioinks have been developed for various bioprinting applications.[30,145–150] These recombinant protein-based bioinks include collagen,[30,145–147] elastin,[148] and spider silk.[149,150] Recombinant proteins, produced through recombinant DNA technology, offer advantages such as large-scale production with high purity and consistency. They also allow for standardized manufacturing processes and quality control, as well as the production of proteins that are difficult to obtain from natural sources or modified for improved efficacy and safety. These recombinant proteins are typically produced using host organisms such as bacteria (*Escherichia coli*),[151] yeast (*Saccharomyces cerevisiae*),[152,153] or mammalian cells.[154] When selecting the appropriate host organisms

Table 2. A summary of greener methods for extracting biomaterials.

Materials	Extraction method	Extraction parameters	Extraction yield	Ref.
Alginate	Ultrasound-assisted	pH 12 using Na_2CO_3, loading ratio of 1:100, 40 min of ultrasound at 25 kHz, 150 W	~54.1%	[124]
Alginate	Microwave-assisted	Initial drying at 80–94°C for 24 min with vacuum, pre-treatment with HCl (95°C for 15 min), and extraction with Na_2CO_3 (100°C for 10 min)	~23.1%	[125]
Alginate	Microwave-assisted	Pre-treatment temperature of 67°C, microwave power of 400 W, and a biomass loading ratio of 1:30 (w/v) for 19 min	~31.4%	[126]
Alginate	Extrusion-assisted	Extraction was performed using an intermeshing co-rotating twin-screw extruder at an alginate to solution ratio of 1:5, feed rate (27.5 rpm), and pH 12	~45.5%	[127]
Agarose	Sonication pretreatment with autoclaving	Seaweed-to-solvent ratio of 1:20, sonication frequency of 35 Hz, power intensity of 30% for 30 min	~56.5%	[128]
Agarose	Bio-ionic liquids	Alkali treatment with NaOH (10% w/v) at 80°C for 2 h, followed by autoclaving at 120°C at a seaweed-to-solvent ratio of 1:20 for 2 h, and lastly the use of 4% w/w choline laurate bio-ionic liquid for 4 h at 80°C	~14%	[129]
Agarose	Enzymatic-assisted	Pre-treatment with enzyme (0.5 g cellulase) at 50°C for 2 h and hydrogen-peroxide prior to alkali treatment with NaOH (7% w/v) at 90°C for 3 h and washing to reach a neutral pH	~16.1%	[131]
Cellulose	Enzymatic hydrolysis	Alkali treatment with NaOH (10% w/w) at 80°C under mechanical stirring for 2 h, followed by washing with distilled water until neutral pH and drying at 50°C for 24 h, and lastly enzymatic hydrolysis in sodium citrate buffer (0.1 M, pH 5) with a 10% w/v solid loading and an enzyme loading of 10 mg of protein per gram of treated fiber	~16.2%	[132]

for recombinant protein production, critical factors to consider include protein quality, functionality, production speed, and yield.[155] Through the thoughtful selection of sustainable and renewable biomaterials, adoption of eco-friendly manufacturing techniques, and innovative utilization of wastes and its by-products, researchers strive to pave the way for a more sustainable future in bioink development.

4.3. Machine learning in bioprinting

Machine learning stands out for its remarkable capability to discern and model intricate relationships within extensive, multi-factor datasets, representing an invaluable technique across various applications.[156] Particularly in bioprinting, ML has attracted attention for optimizing processes,[157] including extrusion-based,[158–161] jetting-based,[162–164] vat photopolymerization-based bioprinting.[165] By leveraging ML, researchers aim to expedite material formulation, fine-tune printing parameters, enhance printing quality, and enhance the viability of printed cells, all in pursuit of creating biomimetic 3D tissue-engineered constructs.[8,166–171] A significant focus in this domain lies on optimization of printing parameters through ML techniques.[172,173] These ML models, trained on large datasets that may be complex to interpret manually, unveil the intricate relationships between various printing parameters, streamlining the optimization process.

Given that cells serve as the fundamental building units in tissue-engineered constructs, maintaining their viability and inherent abilities to proliferate and differentiate is paramount. Numerous studies have delved into understanding the influence of different printing parameters on cell viability. Various critical factors that are known to affect the viability of printed cells include shear stress, nozzle size in extrusion-based bioprinting,[174,175] shear stress, droplet impact velocity, droplet volume, and polymer concentration in jetting-based bioprinting,[176–180] the wavelength and intensity of light, exposure time, type and concentration of photo-initiators, and the presence of unreacted free radicals in vat photopolymerization-based bioprinting.[181]

Recent advances have seen ML approaches accurately predicting cell viability during bioprinting processes.[182,183] Various parameters were evaluated in the extrusion-based bioprinting system[182] and vat photo-polymerization bioprinting,[183] and the live-dead assays provided the dataset for ML training to predict cell viability post-printing. For instance, in extrusion-based bioprinting, factors such as cell type, printing pressure, crosslinker concentration were identified as crucial for cell viability.[182] Similarly, in stereolithography-based bioprinting, parameters such as UV exposure time, layer thickness, GelMA concentration, and UV intensity were found to significantly influence cell viability.[183]

Furthermore, ML has been employed for optimization of bioink formulations and printing parameters in 3D bioprinting.[184–186] Particularly, ML models have been employed to predict the number of printed cells in inkjet-based bioprinting, based on the droplet velocity profiles captured using a high-speed camera,[114] a critical aspect for scalable and reproducible fabrication of 3D tissue constructs. The integration of ML techniques in bioprinting not only streamlines the optimization of bioink formulations and printing parameters but also holds promise for enhancing the quality and viability of printed cells, thus advancing the field towards the realization of complex, functional 3D tissue constructs.

4.4. Bioprinting in bioelectronics

Bioelectronic devices can range from wearable sensors and diagnostic tools for monitoring biological activities, to therapeutic and implantable devices for the characterization and treatment of deep tissues. Generally, bioelectronics developed are operated as translators between the electric signals of biology and human-made electronic devices or systems. On the one hand, the bioelectronics can regulate the physiology and behaviors of cells and tissues at high spatiotemporal resolution by electric stimulation. On the other hand, the electric activities of biological systems can be sensed and recorded by the bioelectronics, as well as transcoded to electronic readout for diagnosis and treatment. To obtain desired properties and functions of bioelectronic devices, electronic materials need to be designed and possessed in specific way followed by ingenious manufacturing process. However, traditional fabrication methods such as photolithograph, electroless platin, or vacuum deposition are not able to construct 3D structures or combine multiple material during the processing procedure, which often impedes the applications of those electronics on biological aspects.[187] 3D printing as a bottom-up technique allows for patterning electronic systems in three dimensions with customized materials, structures, and performance in a biomimetic way. Electronic elements can be integrated with complex geometries by 3D printing to form flexible and biocompatible systems for both *in vitro* and *in vivo* use.[188]

Bioelectronic devices which mostly integrate 3D bio-/printing techniques are the biological regenerative scaffolds coupled with electronic components, with the potential to modulate and improve tissue regenerative processes combined with electric stimulation. For example, Gao et al. reported bioprinted electrically conductive biomanufactured scaffolds using PEDOT:LS/GelMA/HAMA hydrogel encapsulated with neural stem cells

(NSCs), demonstrating promoted neuronal differentiation of NSCs *in vitro* (Figure 9a).[189] Furthermore, nerve axon regeneration and myelination were detected after implantation of the bioprinted scaffolds into spinal cord injury sites. Alternatively, the electrically conductive and biological devices can be created by multiscale 3D printing approaches as well, assembling electronic components and bioprinted constructs together. For instance, a bionic ear was created by printing with hydrogel matrix with living chondrocytes according to the shape of ear, and a coiled antenna was co-printed inside the ear using silver nanoparticles (Figure 9b).[190] The hybrid printing approach paves a new way for fabrication of functional electronics integrated with living cells, showcasing superior biocompatibility and seamless integration of tissues and electronics.

In addition, microelectrodes and biosensors with specific topographical features are often engineered to interface electronics with biological electrical signals. The employment of printing techniques like inkjet printing significantly simplifies the fabrication of electrodes (Figure 9c-i),[191] and can regulate the sensing capacities by tuning the surface properties of biosensors.[192,193] In a recent work, Tomaskovic-Crook et al. reported that PEDOT:PSS micropillars were direct-write printed in an array format on top of microelectrode arrays for 3D electrical stimulation of human neural stem cells, as shown in Figure 9c-ii.[194] Enhanced electrical performance was detected compared to flat films, and electrical signal feedback was recorded from the functional neural network by the fabricated 3D electrode. Recently, with the development of lab-on-chip technology, various sensors can be 3D-printed and

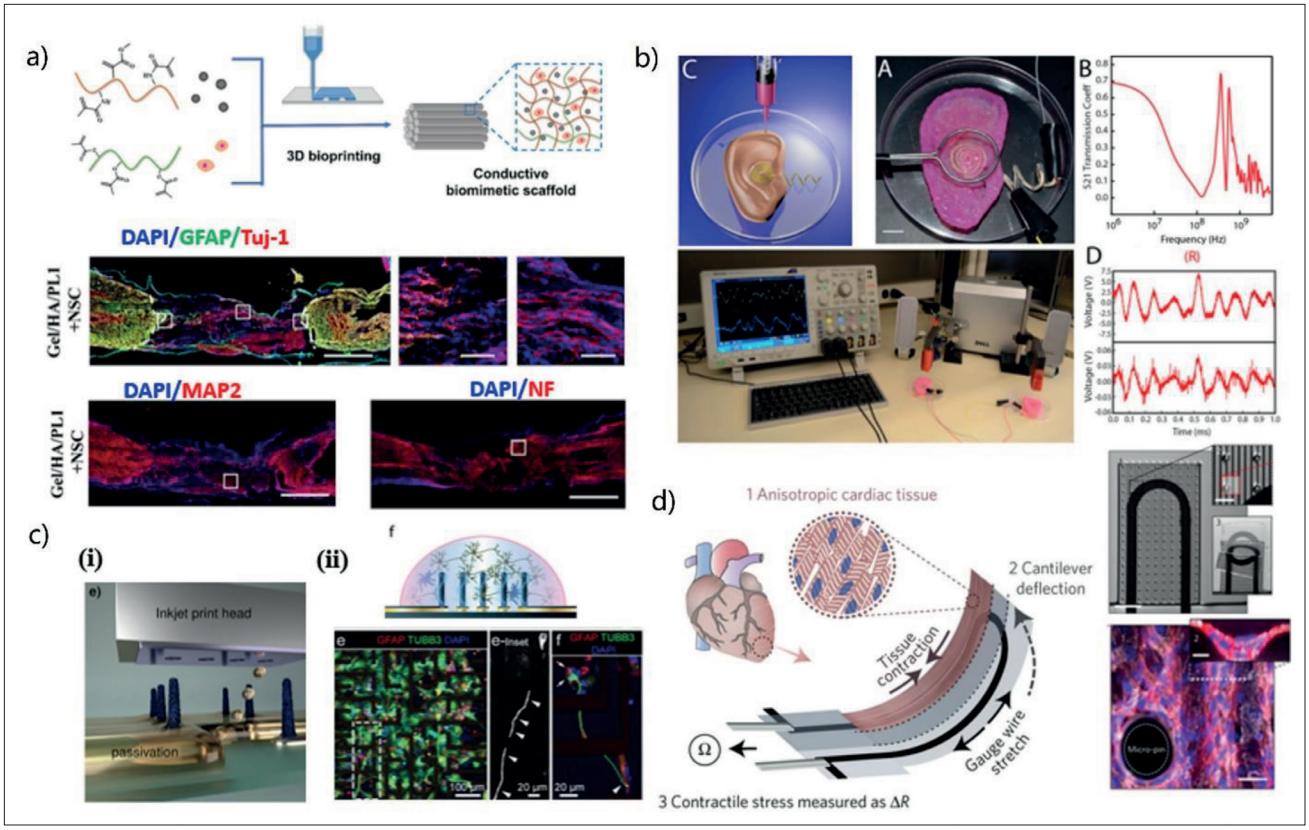

Figure 9. Illustrations of 3D-printed bioelectronics. (a) Schematic diagram of 3D-bioprinted conductive spinal cord biomimetic scaffolds using GelMA/HAMA/PEDOT:LS and neural stem cells for repairing of spinal cord injury. The bioprinted conductive scaffolds promotes neurogenesis shown by the immunofluorescence staining of the longitudinal sections implanted in the injured spinal cords. Scale bars: 100 μm. Reprinted with permission from Gao et al.[189] Copyright © 2023, Elsevier B.V. (b) Illustration of the 3D-printed bionic ear, and the tested output signal via connections to two electrodes on the cochlea. Transmitted and received audio signals can be collected when exposed to stereophonic audio music. Scale bar: 1 cm. Reprinted with permission from Mannoor et al.[190] Copyright © 2013, American Chemical Society. (c) (i) Inject-printing of μ-needle electrode arrays. Reprinted with permission from Zips et al.[191] Copyright © 2019, American Chemical Society. (ii) Schematic illustrating the integration of printed CP pillar microelectrode arrays with conductive neural cell-laden biogel for neural differentiation. Neural stem cell (NSC) differentiation after 7 days at the interface of Matrigel-coated Au electrodes under 3D electrical stimulation. Reprinted with permission from Tomaskovic-Crook et al.[194] Copyright © 2019, Wiley-VCH GmbH. (d) Sketch map of an anisotropic engineered cardiac tissue an dpicture showing modified device with micro-pin and micro-well supporting thicker laminar tissue. Scale bar: 30 μm. Reprinted with permission from Lind et al.[197] Copyright © 2016, Springer Nature Limited.

assembled for better customization and biocompatibility.[195] Furthermore, bioprinting was combined in chips for an unprecedented control over biomimetic cell arrangement to generate anisotropic constructs (Figure 9d).[196,197]

While healthcare and biotechnology are indeed primary areas of application for 3D-printed bioelectronics, there emerge several other fields where this technology can be leveraged for innovative solutions. For instance, 3D-printed biosensors could be employed in the food industry for rapid detection of pathogens, toxins, or contaminants in food products.[198] Besides, 3D-printed bioelectronics provide a novel solution for smart and precision agriculture.[199] The microenvironment of plants in both air and soil can be monitored to reflect the growth condition of single plant, and simultaneously, the key parameters on plant growth and production can be detected as well for promotion of farm industry. Besides, 3D-printed bioelectronics can play a role in environmental remediation efforts. For example, bioelectrochemical systems consisting of 3D-printed electrodes and microbial fuel cells can be used to degrade organic pollutants or recover valuable resources from wastewater.[200,201] These systems harness the power of microorganisms to catalyze electrochemical reactions, offering a sustainable approach to environmental remediation. By leveraging the flexibility and customization capabilities of 3D printing technology, researchers and innovators can develop innovative solutions to address complex challenges in various domains.

Despite the advanced progress of 3D-printed bioelectronics, seamless merging of the electronic devices with biological constructs still poses difficulties. It is difficult to combine bioprinting with electric components, considering simultaneous maintenance of the long-term cell viability and bio-functionality, as well as the electronic sensitivity of the whole system in the complex ECM-like microenvironment. In addition, ideal interfacing of bioelectronics requires biomimetic structure in cell-level scale and mechanical modules similar to native tissues, which bring huge challenges to the printing technology with high precision and development of suitable materials. Nevertheless, continued research on 3D printing, especially bioprinting in multi-scale with multi-material, will shed light on the freeform fabrication of bioelectronics endowed with customized and versatile properties in the future.

4.5. Three-dimensional bioprinting in space

The advancement of manned spaceflight technology has facilitated the feasibility of long-term and long-distance planetary exploration missions. However, prolonged exposure to microgravity and increased radiation environment in space leads to musculoskeletal loss, reduced cardiovascular activity, altered motor functions, diminished visual acuity, as well as impaired wound healing capabilities.[202–204] Therefore, the initial motivation for developing in-space 3D bioprinting strategies was to provide tools for building *in vitro* models to investigate the effects of in-space environments on living cells/tissues, as well as to develop artificial tissue constructs for potential organ transplantation in injured astronauts.[205]

To this goal, the world's first bio-fabrication equipment, the magnetic bioassembler Bioprinter Organ. Aut (Figure 10a-i) was delivered to the International Space Station (ISS) in February 2019 by the Russian Federal Space Agency Roscomos.[206] By utilizing low concentrations of paramagnetic nanoparticles, 3D tissue constructs were successfully assembled via magnetic levitation for the first time in the microgravity environment (Figure 10a-ii). As shown in Figure 10a-iii, the assembled tissue spheroids possessed a simple spherical structure and exhibited agreement with predictive mathematical models. The fabricated tissue constructs demonstrated robust viability and development potentials for the subsequent tissue spheroid fusion process.[15] However, the precise magnetic manipulation of tissue spheroids for the formation of tissue analogs with biomimetic structural and compositional configurations remains a substantial challenge. In the same year, another pioneer in-space bioprinter, the 3D BioFabrication Facility (BFF), was shipped to the ISS (Figure 10b-i). The BFF was equipped with four independently controlled ink-extrusion systems for depositing different cell-laden hydrogels (Figure 10b-ii), which had been proven effective in building cardiac tissue-like structures that encompassed specific cell types and components related to cardiac, nerve, and vascular tissues with a total volume of ≈19.3 cm^3. The bioprinted constructs were further functionalized into tissue analogs by culturing in ingeniously designed bioreactor cassettes, as depicted in Figure 10b-iii, which incorporated thermal, chemical, mechanical, and electrical stimuli cues to guide the *in vivo* tissue development.[207,208] Although promising, the missing gravity effects in space make the bioprinting of *in vitro* 3D models and tissue analogs with high-resolution and intricate biomimetic architectures still challenging. More recently, a miniaturized and automated space 3D bioprinter was developed by Mo *et al.* for unmanned satellite platforms (Figure 10c-i).[209] The device comprised a 3D printing module for the embedded bioprinting of cell-laden bioinks, a biological module for cell culture, a microscope module for visualization, and a control module for regulating the functions of the other three modules. Based on the embedded bioprinting configuration, biphasic thermosensitive bioink and suspension medium derived from the microgel phase and continuous phase were formed to support the precise in-

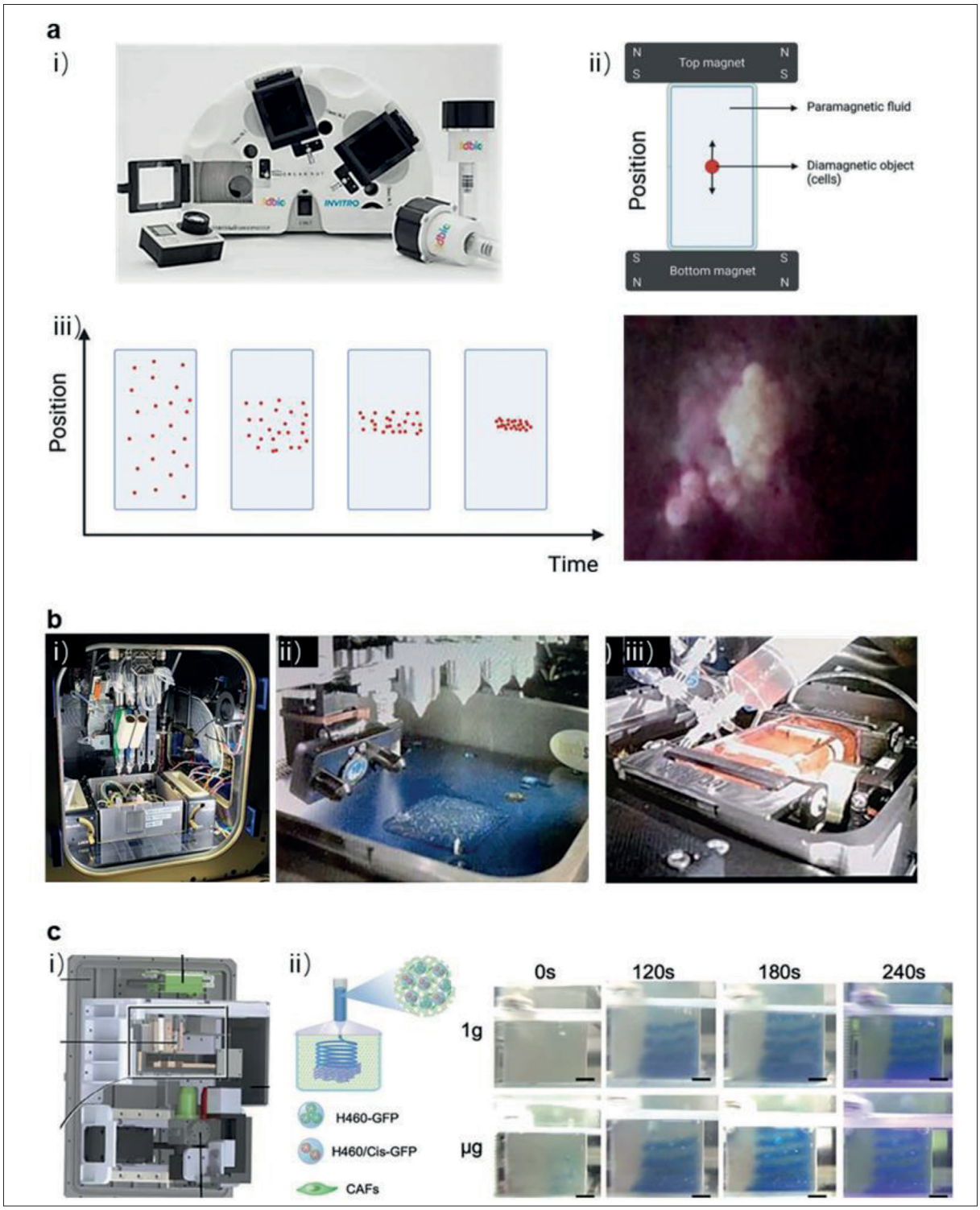

Figure 10. Existing 3D bioprinting explorations in space. (a) (i) Magnetic bioassembler and cuvettes of Bioprinter Organ.Aut[206]; (ii) principle of magnetic levitation[207]; (iii) aggregating the tissue spheroids to form a tissue construct. Reprinted with permission from Parfenov et al. and Tabury et al.[206,207] Copyright © 2020, the American Association for the Advancement of Science. Copyright © 2023, Wiley-VCH GmbH. (b) (i) The 3D BioFabrication Facility (BFF)'s interior print volume; (ii) bioprinting on the International Space Station using a cell-laden hydrogel; (iii) filling the BFF's bioreactor cassette post-bioprinting. Reprinted with permission from Chang and Boland.[208] Copyright © 2022, Wiley-VCH GmbH. (c) (i) Schematic diagram of the 3D embedded bioprinting device with four modules; (ii) Schematic design of on-orbit 3D bioprinting of complex tumor model and images of the 3D bioprinting process in space and on Earth. Reprinted with permission from Mo et al.[209] Copyright © 2023, Wiley-VCH GmbH.

space bioprinting and subsequent *in situ* culture. It was found that the process of embedded bioprinting itself did not exhibit significant differences in space compared with that on Earth, and complex tumor models with a square spiral structure were successfully 3D-bioprinted in orbit (Figure 10c-ii). The in-space bioprinted tumor cells exhibited spatial heterogeneity in the expression of tumor markers and are more sensitive to antitumor drugs than those printed on Earth. This exploration may open up a new avenue for 3D bioprinting in space and offer new possibilities for future research in space life science and medicine.

Besides addressing the pressing clinical requirements for human tissue and organ regeneration, in-space 3D bioprinting may also revolutionize the paradigm for space exploration through the utilization of living materials as the building blocks. As sustaining the supporting supply chains becomes increasingly challenging in deep space, the effective utilization of *in situ* and sustainable resources becomes progressively crucial. On Earth, living microorganisms such as fungal mycelia and bacteria have long been used as sustainable materials for engineering needs.[210] Therefore, leveraging living microorganisms might offer unprecedented possibilities for more sustainable manufacturing practices and raw material fabrication in resource-poor space environments.[210,211] For example, the combination of living microorganisms with abiotic sand-gelatin scaffolds has demonstrated the potential to develop self-healing concretes, which could be utilized for constructing human habitats on other planets.[212] Fungal mycelia have been used to bioprint living complex materials that possess self-repair, regeneration, and adaptability capabilities while serving an engineering purpose.[213] The 3D-bioprinted mycelium-based living constructs exhibit mechanical robustness, softness, self-healing capability, and waterproof nature, making them suitable as protective skin with multiple functionalities. It can be envisioned that the 3D bioprinting of living microorganisms with intricate adaptive properties may present a distinctive opportunity to fabricate functional materials for building construction purposes or synthesize chemicals on demand, and potentially inspiring more biomanufacturing approaches into the realm of space exploration.

5. Conclusion

Bioprinting has been rapidly growing and evolving over the past two decades. This review summarizes the recent developments of bioprinting in various applications and reflects on the future of bioprinting from a fresh new angle. The key argument of this review is that bioprinting has become a versatile enabling tool, capable of addressing problems beyond human organ shortage. Thinking outside the box of tissue engineering, coupled with harnessing the capabilities of bioprinting for alternative applications, is crucial for conceptualizing new directions for the field to thrust. In light of this, we coin a new term "transformative bioprinting" to describe this trend, as well as to highlight a new distinction between bioprinting and tissue engineering in addition to their inherent differences in automation and control. Although predicting the future trajectories of transformative bioprinting remains challenging at present, and the initial developments in this realm may not necessarily translate into real-life clinical applications, we are confident that the continuous developments of transformative bioprinting would potentially circle back to clinical applications or pave the way for unforeseen advancements, for example, bioelectronics and space exploration, while others can lead to exploration of new, uncharted territories, potentially shaping a different future trajectory for the field, such as cultivated meat.

Acknowledgments

The authors would like to thank AccScience Publishing for the invitation to write a review on the recent developments in bioprinting.

Funding

None.

Conflict of interest

All authors declare that there is no financial conflict of interest during the preparation of this manuscript.

Author contributions

Conceptualization: Chee Kai Chua, Liliang Ouyang, Wai Yee Yeong, Maling Gou, Jiankang He

Writing – original draft: Jia An, Shiyuan Fan, Xuening Zhang, Haofan Liu, Li Zhang, Ya Ren, Wei Long Ng, Hui Zhu, Zijie Meng

Writing – review & editing: All authors

Ethics approval and consent to participate

Not applicable.

Consent for publication

Not applicable.

Availability of data

Not applicable.

References

1. Yeong W-Y, Chua C-K, Leong K-F, Chandrasekaran M. Rapid prototyping in tissue engineering: challenges and potential. *Trends Biotechnol*. 2004;22(12):643-652. doi: 10.1016/j.tibtech.2004.10.004
2. Yeong W, Sudarmadji N, Yu H, et al. Porous polycaprolactone scaffold for cardiac tissue engineering fabricated by selective laser sintering. *Acta Biomater*. 2010;6(6):2028-2034. doi: 10.1016/j.actbio.2009.12.033
3. Mironov V, Kasyanov V, Drake C, Markwald RR. Organ printing: promises and challenges Regen Med. 2008; 3(1):93-103. doi: 10.2217/17460751.3.1.93
4. Mironov V, Boland T, Trusk T, Forgacs G, Markwald RR. Organ printing: computer-aided jet-based 3D tissue engineering. *Trends Biotechnol*. 2003;21(4):157-161. doi: 10.1016/S0167-7799(03)00033-7
5. Ng WL, An J, Chua CK. Process, material, and regulatory considerations for 3D printed medical devices and tissue constructs. *Engineering*. 2024. doi: 10.1016/j.eng.2024.01.028
6. Murphy SV, De Coppi P, Atala A. Opportunities and challenges of translational 3D bioprinting. *Nat Biomed Eng*. 2020;4(4):370-380. doi: 10.1038/s41551-019-0471-7
7. O'Connell CD, Dalton PD, Hutmacher DW. Why bioprinting in regenerative medicine should adopt a rational technology readiness assessment. *Trends Biotechnol.* 2024. doi: 10.1016/j.tibtech.2024.03.006
8. He J, Mao M, Li X, Chua CK. Bioprinting of 3D functional tissue constructs. *Int J Bioprint*. 2021;7(3):1-2. doi: 10.18063/ijb.v7i3.395
9. Bertassoni LE. Bioprinting of complex multicellular organs with advanced functionality—recent progress and challenges ahead. *Adv Mater*. 2022;34(3):e2101321. doi: 10.1002/adma.202101321
10. Lee J, Park D, Seo Y, Chung JJ, Jung Y, Kim SH. Organ-level functional 3D tissue constructs with complex compartments and their preclinical applications. *Adv Mater*. 2020;32(51):e2002096. doi: 10.1002/adma.202002096
11. Dutta SD, Ganguly K, Jeong M-S, et al. Bioengineered lab-grown meat-like constructs through 3D bioprinting of antioxidative protein hydrolysates. *ACS Appl Mater Interfaces*. 2022;14(30):34513-34526. doi: 10.1021/acsami.2c10620
12. Beckwith AL, Borenstein JT, Velásquez-García LF. Physical, mechanical, and microstructural characterization of novel, 3D-printed, tunable, lab-grown plant materials generated from Zinnia elegans cell cultures. *Mater Today*. 2022;54:27-41. doi: 10.1016/j.mattod.2022.02.012
13. Simon DT, Gabrielsson EO, Tybrandt K, Berggren M. Organic bioelectronics: bridging the signaling gap between biology and technology. *Chem. Rev*. 2016;116(21): 13009-13041. doi: 10.1021/acs.chemrev.6b00146
14. Zhang H, Wen H, Zhu J, Xia Z, Zhang Z. 3D printing dielectric elastomers for advanced functional structures: a mini-review. *J Appl Polym Sci*. 2024; 141(15):e55015. doi: 10.1002/app.55015
15. Sarabi MR, Yetisen AK, Tasoglu S. Magnetic levitation for space exploration. *Trends Biotechnol*. 2022;40(8):915-917. doi: 10.1016/j.tibtech.2022.03.010
16. Landerneau S, Lemarié L, Marquette C, Petiot E. Green 3D bioprinting of plant cells: a new scope for 3D bioprinting. *Bioprinting*. 2022;27:e00216. doi: 10.1016/j.bprint.2022.e00216
17. Whenish R, Ramakrishna S, Jaiswal AK, Manivasagam G. A framework for the sustainability implications of 3D bioprinting through nature-inspired materials and structures. *Bio-Design Manuf*. 2022;5(2):412-423. doi: 10.1007/s42242-021-00168-x
18. Zhou D, Dou B, Kroh F, Wang C, Ouyang L. Biofabrication strategies with single-cell resolution: a review. *Int J Extreme Manuf*. 2023;5(4):042005. doi: 10.1088/2631-7990/ace863
19. Hinton TJ, Jallerat Q, Palchesko RN, et al. Three-dimensional printing of complex biological structures by freeform reversible embedding of suspended hydrogels. *Sci Adv*. 2015;1(9):e1500758. doi: 10.1126/sciadv.1500758
20. Bernal PN, Delrot P, Loterie D, et al. Volumetric bioprinting of complex living-tissue constructs within seconds. *Adv Mater*. 2019;31(42):e1904209. doi: 10.1002/adma.201904209
21. Ouyang L. Pushing the rheological and mechanical boundaries of extrusion-based 3D bioprinting. *Trends Biotechnol*. 2022;40(7):891-902. doi: 10.1016/j.tibtech.2022.01.001
22. Wu Y, Yang X, Gupta D, et al. Dissecting the interplay mechanism among process parameters toward the biofabrication of high-quality shapes in embedded bioprinting. *Adv Funct Mater*. 2024;34(21):2313088. doi: 10.1002/adfm.202313088
23. Highley CB, Song KH, Daly AC, Burdick JA. Jammed microgel inks for 3D printing applications. *Adv Sci*. 2019;6(1):1801076. doi: 10.1002/advs.201801076
24. Yuan X, Wang Z, Che L, et al. Recent developments and challenges of 3D bioprinting technologies. *Int J Bioprinting*. 2024;10(2):1752. doi: doi.org/10.36922/ijb.1752

25. Pitacco P, Sadowska JM, O'Brien FJ, Kelly DJ. 3D bioprinting of cartilaginous templates for large bone defect healing. *Acta Biomater*. 2023;156:61-74.
doi: 10.1016/j.actbio.2022.07.037

26. Xie M, Shi Y, Zhang C, et al. In situ 3D bioprinting with bioconcrete bioink. *Nature communications*. 2022;13(1):3597.
doi: 10.1038/s41467-022-30997-y

27. Sun Y, You Y, Jiang W, Wang B, Wu Q, Dai K. 3D bioprinting dual-factor releasing and gradient-structured constructs ready to implant for anisotropic cartilage regeneration. *Sci Adv*. 2020;6(37):eaay1422.
doi: 10.1126/sciadv.aay1422

28. Zhang X, Liu Y, Zuo Q, et al. 3D bioprinting of biomimetic bilayered scaffold consisting of decellularized extracellular matrix and silk fibroin for osteochondral repair. *Int J Bioprint*. 2021;7(4):401.
doi: 10.18063/ijb.v7i4.401

29. Albanna M, Binder KW, Murphy SV, et al. In situ bioprinting of autologous skin cells accelerates wound healing of extensive excisional full-thickness wounds. *Sci Rep*. 2019;9(1):1856.
doi: 10.1038/s41598-018-38366-w

30. Yang Y, Xu R, Wang C, Guo Y, Sun W, Ouyang L. Recombinant human collagen-based bioinks for the 3D bioprinting of full-thickness human skin equivalent. *Int J Bioprint*. 2022;8(4):611.
doi: 10.18063/ijb.v8i4.611

31. Noor N, Shapira A, Edri R, Gal I, Wertheim L, Dvir T. 3D printing of personalized thick and perfusable cardiac patches and hearts. *Adv Sci*. 2019;6(11):1900344.
doi: 10.1002/advs.201900344

32. Lee A, Hudson A, Shiwarski D, et al. 3D bioprinting of collagen to rebuild components of the human heart. *Science*. 2019;365(6452):482-487.
doi: 10.1126/science.aav9051

33. Lammers A, Hsu H-H, Sundaram S, et al. Rapid tissue perfusion using sacrificial percolation of anisotropic networks. *Matter*. 2024;7(6):2184-2204.
doi: 10.1016/j.matt.2024.04.001

34. Ouyang L, Armstrong JP, Chen Q, Lin Y, Stevens MM. Void-free 3D bioprinting for in situ endothelialization and microfluidic perfusion. *Adv Funct Mater*. 2020;30(1):1908349.
doi: 10.1002/adfm.201908349

35. Lawlor KT, Vanslambrouck JM, Higgins JW, et al. Cellular extrusion bioprinting improves kidney organoid reproducibility and conformation. *Nat Mater*. 2021;20(2):260-271.
doi: 10.1038/s41563-020-00853-9

36. Brassard JA, Nikolaev M, Hübscher T, Hofer M, Lutolf MP. Recapitulating macro-scale tissue self-organization through organoid bioprinting. *Nat Mater*. 2021;20(1):22-29.
doi: 10.1038/s41563-020-00803-5

37. Ayan B, Heo DN, Zhang Z, et al. Aspiration-assisted bioprinting for precise positioning of biologics. *Sci Adv*. 2020;6(10):eaaw5111.
doi: 10.1126/sciadv.aaw5111

38. Daly AC, Davidson MD, Burdick JA. 3D bioprinting of high cell-density heterogeneous tissue models through spheroid fusion within self-healing hydrogels. *Nat Commun*. 2021;12(1):753.
doi: 10.1038/s41467-021-21029-2

39. Egawa N, Kitaoka S, Tsukita K, et al. Drug screening for ALS using patient-specific induced pluripotent stem cells. *Sci Transl Med*. 2012;4(145):145ra104.
doi: 10.1126/scitranslmed.3004052

40. Griffith LG, Swartz MA. Capturing complex 3D tissue physiology in vitro. *Nat Rev Mol Cell Biol*. 2006;7(3):211-224.
doi: 10.1038/nrm1858

41. Nelson CM, Bissell MJ. Of extracellular matrix, scaffolds, and signaling: tissue architecture regulates development, homeostasis, and cancer. *Annu Rev Cell Dev Biol*. 2006;22:287-309.
doi: 10.1146/annurev.cellbio.22.010305.104315

42. Nie J, Gao Q, Fu J, He Y. Grafting of 3D bioprinting to in vitro drug screening: a review. *Adv Healthc Mater*. 2020;9(7):1901773.
doi: 10.1002/adhm.201901773

43. Miller KL, Sit I, Xiang Y, et al. Evaluation of CuO nanoparticle toxicity on 3D bioprinted human iPSC-derived cardiac tissues. *Bioprinting*. 2023;32:e00284.
doi: 10.1016/j.bprint.2023.e00284

44. Zhao Y, Yao R, Ouyang L, et al. Three-dimensional printing of Hela cells for cervical tumor model in vitro. *Biofabrication*. 2014;6(3):035001.
doi: 10.1088/1758-5082/6/3/035001

45. Dai X, Ma C, Lan Q, Xu T. 3D bioprinted glioma stem cells for brain tumor model and applications of drug susceptibility. *Biofabrication*. 2016;8(4):045005.
doi: 10.1088/1758-5090/8/4/045005

46. Wang Y, Shi W, Kuss M, et al. 3D bioprinting of breast cancer models for drug resistance study. *ACS Biomater Sci Eng*. 2018;4(12):4401-4411.
doi: 10.1021/acsbiomaterials.8b01277

47. Wu M, Zhou H, Hu J, et al. Decellularized porcine kidney-incorporated hydrogels for cell-laden bioprinting of renal cell carcinoma model. *Int J Bioprint*. 2024;10(2):1413.
doi: 10.36922/ijb.1413

48. Huang B, Wei X, Chen K, Wang L, Xu M. Bioprinting of hydrogel beads to engineer pancreatic tumor-stroma microtissues for drug screening. *Int J Bioprint*. 2023;9(3):676.
doi: 10.18063/ijb.676

49. Gu Z, Xie M, Lv S, et al. Perfusable vessel-on-a-chip for antiangiogenic drug screening with coaxial bioprinting. *Int J Bioprint*. 2022;8(4):619. doi: 10.18063/ijb.v8i4.619

50. Fang L, Liu Y, Qiu J, Wan W. Bioprinting and its use in tumor-on-a-chip technology for cancer drug screening: a review. *Int J Bioprint*. 2022;8(4):603. doi: 10.18063/ijb.v8i4.603

51. Liu C, Chen Y, Chen H, Zhang P. Droplet-based bioprinting for fabrication of tumor spheroids. *Int J Bioprint*. 2024;10(1):1214. doi: 10.36922/ijb.1214

52. Maizels L, Huber I, Arbel G, et al. Patient-specific drug screening using a human induced pluripotent stem cell model of catecholaminergic polymorphic ventricular tachycardia type 2. *Circ Arrhythm Electrophysiol*. 2017;10(6):e004725. doi: 10.1161/CIRCEP.116.004725

53. Akbari M, Khademhosseini A. Tissue bioprinting for biology and medicine. *Cell*. 2022;185(15):2644-2648. doi: 10.1016/j.cell.2022.06.015

54. Fonseca AC, Melchels FP, Ferreira MJ, et al. Emulating human tissues and organs: a bioprinting perspective toward personalized medicine. *Chem Rev*. 2020;120(19): 11093-11139. doi: 10.1021/acs.chemrev.0c00342

55. Wang Z, Liang X, Wang G, Wang X, Chen Y. Emerging bioprinting for wound healing. *Adv Mater*. 2023:e2304738. doi: 10.1002/adma.202304738

56. Liu H, He L, Kuzmanović M, et al. Advanced nanomaterials in medical 3D printing. *Small Methods*. 2024;8(3):e2301121. doi: 10.1002/smtd.202301121

57. Eisenstein M. First 3D-printed pill. *Nat Biotechnol*. 2015;33:1014. doi: 10.1038/nbt1015-1014a

58. Loh JM, Lim YJL, Tay JT, Cheng HM, Tey HL, Liang K. Design and fabrication of customizable microneedles enabled by 3D printing for biomedical applications. *Bioactive Mater*. 2024;32:222-241. doi: 10.1016/j.bioactmat.2023.09.022

59. Li R, Liu X, Yuan X, et al. Fast customization of hollow microneedle patches for insulin delivery. *Int J Bioprint*. 2022;8(2):553. doi: 10.18063/ijb.v8i2.553

60. Wang Z, Fu R, Han X, et al. Shrinking fabrication of a glucose-responsive glucagon microneedle patch. *Adv Sci*. 2022;9(28):2203274. doi: 10.1002/advs.202203274

61. Joo SH, Kim J, Hong J, Fakhraei Lahiji S, Kim YH. Dissolvable self-locking microneedle patches integrated with immunomodulators for cancer immunotherapy. *Adv Mater*. 2023;35(10):2209966. doi: 10.1002/adma.202209966

62. Li R, Zhang L, Jiang X, et al. 3D-printed microneedle arrays for drug delivery. *J Control Release*. 2022;350:933-948. doi: 10.1016/j.jconrel.2022.08.022

63. Yadid M, Oved H, Silberman E, Dvir T. Bioengineering approaches to treat the failing heart: from cell biology to 3D printing. *Nat Rev Cardiol*. 2022;19(2):83-99. doi: 10.1038/s41569-021-00603-7

64. Tao J, Liu H, Wu W, et al. 3D-printed nerve conduits with live platelets for effective peripheral nerve repair. *Adv Funct Mater*. 2020;30(42):2004272. doi: 10.1002/adfm.202004272

65. Choi S, Lee KY, Kim SL, et al. Fibre-infused gel scaffolds guide cardiomyocyte alignment in 3D-printed ventricles. *Nat Mater*. 2023;22(8):1039-1046. doi: 10.1038/s41563-023-01611-3

66. Chen S, Luo J, Shen L, et al. 3D printing mini-capsule device for islet delivery to treat type 1 diabetes. *ACS Appl Mater Interfaces*. 2022;14(20):23139-23151. doi: 10.1021/acsami.2c02487

67. Bertsch P, Diba M, Mooney DJ, Leeuwenburgh SC. Self-healing injectable hydrogels for tissue regeneration. *Chem Rev*. 2022;123(2):834-873. doi: 10.1021/acs.chemrev.2c00179

68. Daly AC, Riley L, Segura T, Burdick JA. Hydrogel microparticles for biomedical applications. *Nat Rev Mater*. 2020;5(1):20-43. doi: 10.1038/s41578-019-0148-6.

69. Liu X, Tao J, Liu J, et al. 3D printing enabled customization of functional microgels. *ACS Appl Mater Interfaces*. 2019;11(13):12209-12215. doi: 10.1021/acsami.8b18701.

70. Muir VG, Qazi TH, Weintraub S, Torres Maldonado BO, Arratia PE, Burdick JA. Sticking together: injectable granular hydrogels with increased functionality via dynamic covalent inter-particle crosslinking. *Small*. 2022;18(36):e2201115. doi: 10.1002/smll.202201115

71. Tang M, Xie Q, Gimple RC, et al. Three-dimensional bioprinted glioblastoma microenvironments model cellular dependencies and immune interactions. *Cell Res*. 2020;30(10):833-853. doi: 10.1038/s41422-020-0338-1.

72. Prendergast ME, Burdick JA. Recent advances in enabling technologies in 3D printing for precision medicine. *Adv Mater*. 2020;32(13):e1902516. doi: 10.1002/adma.201902516

73. Wen X, Zhang B, Wang W, et al. 3D-printed silica with nanoscale resolution. *Nat Mater*. 2021;20(11):1506-1511. doi: 10.1038/s41563-021-01111-2

74. You S, Xiang Y, Hwang HH, et al. High cell density and high-resolution 3D bioprinting for fabricating vascularized tissues. *Sci Adv*. 2023;9(8):eade7923. doi: 10.1126/sciadv.ade7923

75. Guan J, You S, Xiang Y, et al. Compensating the cell-induced light scattering effect in light-based bioprinting using deep learning. *Biofabrication*. 2021;14(1):015011. doi: 10.1088/1758-5090/ac3b92.

76. Bauer J, Crook C, Baldacchini T. A sinterless, low-temperature route to 3D print nanoscale optical-grade glass. *Science*. 2023;380(6648):960-966. doi: 10.1126/science.abq3037

77. Zhang Y, Su Y, Zhao Y, Wang Z, Wang C. Two-photon 3D printing in metal–organic framework single crystals. *Small*. 2022;18(18):e2200514. doi: 10.1002/smll.202200514

78. Xu H-Q, Liu J-C, Zhang Z-Y, Xu C-X. A review on cell damage, viability, and functionality during 3D bioprinting. *Mil Med Res*. 2022;9(1):70. doi: 10.1186/s40779-022-00429-5

79. Lipkowitz G, Samuelsen T, Hsiao K, et al. Injection continuous liquid interface production of 3D objects. *Sci Adv*. 2022;8(39):eabq3917. doi: 10.1126/sciadv.abq3917

80. Regehly M, Garmshausen Y, Reuter M, et al. Xolography for linear volumetric 3D printing. *Nature*. 2020;588(7839): 620-624. doi: 10.1038/s41586-020-3029-7

81. Stüwe L, Geiger M, Röllgen F, et al. Continuous volumetric 3D printing: xolography in flow. *Adv Mater*. 2024;36(4):e2306716. doi: 10.1002/adma.202306716

82. Cheng J, Wang R, Sun Z, et al. Centrifugal multimaterial 3D printing of multifunctional heterogeneous objects. *Nat Commun*. 2022;13(1):7931. doi: 10.1038/s41467-022-35622-6

83. Larson NM, Mueller J, Chortos A, Davidson ZS, Clarke DR, Lewis JA. Rotational multimaterial printing of filaments with subvoxel control. *Nature*. 2023;613(7945):682-688. doi: 10.1038/s41586-022-05490-7

84. Buchner TJ, Rogler S, Weirich S, et al. Vision-controlled jetting for composite systems and robots. *Nature*. 2023;623(7987):522-530. doi: 10.1038/s41586-023-06684-3

85. Wang Y, Cui H, Esworthy T, Mei D, Wang Y, Zhang LG. Emerging 4D printing strategies for next-generation tissue regeneration and medical devices. *Adv Mater*. 2022;34(20):e2109198. doi: 10.1002/adma.202109198

86. Bedell ML, Navara AM, Du Y, Zhang S, Mikos AG. Polymeric systems for bioprinting. *Chem Rev*. 2020;120(19): 10744-10792. doi: 10.1021/acs.chemrev.9b00834

87. Hao XP, Xu Z, Li CY, Hong W, Zheng Q, Wu ZL. Kirigami-design-enabled hydrogel multimorphs with application as a multistate switch. *Adv Mater*. 2020;32(22):e2000781. doi: 10.1002/adma.202000781

88. Cui H, Miao S, Esworthy T, et al. A novel near-infrared light responsive 4D printed nanoarchitecture with dynamically and remotely controllable transformation. *Nano Res*. 2019;12:1381-1388. doi: 10.1007/s12274-019-2340-9

89. Miao S, Cui H, Esworthy T, et al. 4D self-morphing culture substrate for modulating cell differentiation. *Adv Sci*. 2020;7(6):1902403. doi: 10.1002/advs.201902403

90. Zhang F, Wang L, Zheng Z, Liu Y, Leng J. *Magnetic Programming of 4D Printed Shape Memory Composite Structures*. Elsevier. 2019;125:105571. doi: 10.1016/j.compositesa.2019.105571

91. Bai Y, Zhang J, Wen D, et al. A reconfigurable, self-healing and near infrared light responsive thermoset shape memory polymer. *Compos Sci Technol*. 2020;187:107940. doi: 10.1016/j.compscitech.2019.107940

92. Lee YB, Jeon O, Lee SJ, Ding A, Wells D, Alsberg E. Induction of four-dimensional spatiotemporal geometric transformations in high cell density tissues via shape-changing hydrogels. *Adv Funct Mater*. 2021;31(24):2010104. doi: 10.1002/adfm.202010104.

93. Samandari M, Mostafavi A, Quint J, Memić A, Tamayol A. In situ bioprinting: intraoperative implementation of regenerative medicine. *Trends Biotechnol*. 2022;40(10):1229-1247. doi: 10.1016/j.tibtech.2022.03.009

94. Duchi S, Onofrillo C, O'Connell CD, et al. Handheld co-axial bioprinting: application to in situ surgical cartilage repair. *Sci Rep*. 2017;7(1):5837. doi: 10.1038/s41598-017-05699-x

95. Li W, Wang M, Mille LS, et al. A smartphone-enabled portable digital light processing 3D printer. *Adv Mater*. 2021;33(35):e2102153. doi: 10.1002/adma.202102153

96. Thai MT, Phan PT, Tran HA, et al. Advanced soft robotic system for in situ 3D bioprinting and endoscopic surgery. *Adv Sci*. 2023;10(12):2205656. doi: 10.1002/advs.202205656

97. Chen Y, Zhang J, Liu X, et al. Noninvasive in vivo 3D bioprinting. *Sci Adv*. 2020;6(23):eaba7406. doi: 10.1126/sciadv.aba7406

98. Urciuolo A, Poli I, Brandolino L, et al. Intravital three-dimensional bioprinting. *Nat Biomed Eng*. 2020;4(9):901-915. doi: 10.1038/s41551-020-0568-z

99. Zhou C, Yang Y, Wang J, et al. Ferromagnetic soft catheter robots for minimally invasive bioprinting. *Nat Commun*. 2021;12(1):5072. doi: 10.1038/s41467-021-25386-w

100. Kuang X, Rong Q, Belal S, et al. Self-enhancing sono-inks enable deep-penetration acoustic volumetric printing. *Science*. 2023;382(6675):1148-1155. doi: 10.1126/science.adi1563

101. Post MJ, Levenberg S, Kaplan DL, et al. Scientific, sustainability and regulatory challenges of cultured meat. *Nat Food*. 2020;1(7):403-415.
doi: 10.1038/s43016-020-0112-z

102. Su L, Jing L, Zeng X, et al. 3D-printed prolamin scaffolds for cell-based meat culture. *Adv Mater*. 2023;35(2):2207397.
doi: 10.1002/adma.202207397

103. Ianovici I, Zagury Y, Redenski I, Lavon N, Levenberg S. 3D-printable plant protein-enriched scaffolds for cultivated meat development. *Biomaterials*. 2022;284:121487.
doi: 10.1016/j.biomaterials.2022.121487

104. David S, Ianovici I, Guterman Ram G, Shaulov Dvir Y, Lavon N, Levenberg S. Pea protein-rich scaffolds support 3D bovine skeletal muscle formation for cultivated meat application. *Adv Sustain Syst*. 2024;8(6):2300499.
doi: 10.1002/adsu.202300499

105. Kang D-H, Louis F, Liu H, et al. Engineered whole cut meat-like tissue by the assembly of cell fibers using tendon-gel integrated bioprinting. *Nat Commun*. 2021;12(1):5059.
doi: 10.1038/s41467-021-25236-9

106. Xu E, Niu R, Lao J, et al. Tissue-like cultured fish fillets through a synthetic food pipeline. *NPJ Sci Food*. 2023;7(1):17.
doi: 10.1038/s41538-023-00194-2

107. Jeong D, Seo JW, Lee HG, Jung WK, Park YH, Bae H. Efficient myogenic/adipogenic transdifferentiation of bovine fibroblasts in a 3D bioprinting system for steak-type cultured meat production. *Adv Sci*. 2022;9(31):2202877.
doi: 10.1002/advs.202202877

108. Ng WL, Tan JS. Application of machine learning in 3D bioprinting of cultivated meat. *Int J AI Mater Design*. 2024;1(1):2279.
doi: 10.36922/ijamd.2279

109. Ng WL, Goh GL, Goh GD, Sheuan TJJ, Yeong WY. Progress and opportunities for machine learning in materials and processes of additive manufacturing. *Adv Mater*. 2024:202310006.
doi: 10.1002/adma.202310006

110. Nikkhah A, Rohani A, Zarei M, et al. Toward sustainable culture media: Using artificial intelligence to optimize reduced-serum formulations for cultivated meat. *Sci Total Environ*. 2023;894:164988.
doi: 10.1016/j.scitotenv.2023.164988

111. Cosenza Z, Block DE, Baar K. Optimization of muscle cell culture media using nonlinear design of experiments. *Biotechnol J*. 2021;16(11):2100228.
doi: 10.1002/biot.202100228

112. Ji H, Pu D, Yan W, Zhang Q, Zuo M, Yuyu Z. Recent advances and application of machine learning in food flavor prediction and regulation. *Trends Food Sci Technol*. 2023;138:738-751.
doi: 10.1016/j.tifs.2023.07.012

113. Soni A, Dixit Y, Reis MM, Brightwell G. Hyperspectral imaging and machine learning in food microbiology: developments and challenges in detection of bacterial, fungal, and viral contaminants. *Compr Rev Food Sci Food Saf*. 2022;21(4):3717-3745.
doi: 10.1111/1541-4337.12983

114. Huang X, Ng WL, Yeong WY. Predicting the number of printed cells during inkjet-based bioprinting process based on droplet velocity profile using machine learning approaches. *J Intell Manuf*. 2023;35(5).
doi: 10.1007/s10845-023-02167-4

115. Wang J, Ding S, Da C, et al. Morphology-based prediction of proliferation and differentiation potencies of porcine muscle stem cells for cultured meat production. *J Agric Food Chem*. 2023;71(47):18613-18621.
doi: 10.1021/acs.jafc.3c06919

116. Axpe E, Oyen ML. Applications of alginate-based bioinks in 3D bioprinting. *Int J Mol Sci*. 2016;17(12):1976.
doi: 10.3390/ijms17121976

117. Jia J, Richards DJ, Pollard S, et al. Engineering alginate as bioink for bioprinting. *Acta Biomater*. 2014;10(10):4323-4331.
doi: 10.1016/j.actbio.2014.06.034

118. Gao Q, Kim B-S, Gao G. Advanced strategies for 3D bioprinting of tissue and organ analogs using alginate hydrogel bioinks. *Marine Drugs*. 2021;19(12):708.
doi: 10.3390/md19120708

119. López-Marcial GR, Zeng AY, Osuna C, Dennis J, García JM, O'Connell GD. Agarose-based hydrogels as suitable bioprinting materials for tissue engineering. *ACS Biomater Sci Eng*. 2018;4(10):3610-3616.
doi: 10.1021/acsbiomaterials.8b00903

120. Wang X, Wang Q, Xu C. Nanocellulose-based inks for 3d bioprinting: key aspects in research development and challenging perspectives in applications—a mini review. *Bioengineering*. 2020;7(2):40.
doi: 10.3390/bioengineering7020040

121. Athukoralalage SS, Balu R, Dutta NK, Roy Choudhury N. 3D bioprinted nanocellulose-based hydrogels for tissue engineering applications: a brief review. *Polymers*. 2019;11(5):898.
doi: 10.3390/polym11050898

122. Saji S, Hebden A, Goswami P, Du C. A brief review on the development of alginate extraction process and its sustainability. *Sustainability*. 2022;14(9):5181.
doi: 10.3390/su14095181

123. Chew KW, Juan JC, Phang SM, Ling TC, Show PL. An overview on the development of conventional and alternative extractive methods for the purification of agarose from seaweed. *Sep Sci Technol*. 2018;53(3):467-480.
doi: 10.1080/01496395.2017.1394881

124. Youssouf L, Lallemand L, Giraud P, et al. Ultrasound-assisted extraction and structural characterization by NMR of alginates and carrageenans from seaweeds. *Carbohydr Polymers*. 2017;166:55-63.
doi: 10.1016/j.carbpol.2017.01.041

125. Yuan Y, Macquarrie DJ. Microwave assisted step-by-step process for the production of fucoidan, alginate sodium, sugars and biochar from Ascophyllum nodosum through a biorefinery concept. *Bioresourc Technol*. 2015;198:819-827. doi: 10.1016/j.biortech.2015.09.090

126. Torabi P, Hamdami N, Keramat J. Microwave-assisted extraction of sodium alginate from brown macroalgae Nizimuddinia zanardini, optimization and physicochemical properties. *Sep Sci Technol*. 2022;57(6):872-885. doi: 10.1080/01496395.2021.1954020

127. Sugiono S, Masruri M, Estiasih T, Widjanarko SB. Optimization of extrusion-assisted extraction parameters and characterization of alginate from brown algae (Sargassum cristaefolium). *J Food Sci Technol*. 2019;56(8):3687-3696. doi: 10.1007/s13197-019-03829-z

128. Din SS, Chew KW, Chang Y-K, Show PL, Phang SM, Juan JC. Extraction of agar from Eucheuma cottonii and Gelidium amansii seaweeds with sonication pretreatment using autoclaving method. *J Oceanol Limnol*. 2019;37(3):871-880. doi: 10.1007/s00343-019-8145-6

129. Sharma M, Chaudhary JP, Mondal D, Meena R, Prasad K. A green and sustainable approach to utilize bio-ionic liquids for the selective precipitation of high purity agarose from an agarophyte extract. *Green Chem*. 2015;17(5):2867-2873. doi: 10.1039/C4GC02498B

130. Rieland JM, Love BJ. Ionic liquids: a milestone on the pathway to greener recycling of cellulose from biomass. *Resources Conserv Recycl*. 2020;155:104678. doi: 10.1016/j.resconrec.2019.104678

131. Chen H, Xiao Q, Weng H, Zhang Y, Yang Q, Xiao A. Extraction of sulfated agar from Gracilaria lemaneiformis using hydrogen peroxide-assisted enzymatic method. *Carbohydr Polym*. 2020;232:115790. doi: 10.1016/j.carbpol.2019.115790

132. de Aguiar J, Bondancia TJ, Claro PIC, Mattoso LHC, Farinas CS, Marconcini JM. Enzymatic deconstruction of sugarcane bagasse and straw to obtain cellulose nanomaterials. *ACS Sustain Chem Eng*. 2020;8(5):2287-2299. doi: 10.1021/acssuschemeng.9b06806

133. Morimura S, Nagata H, Uemura Y, Fahmi A, Shigematsu T, Kida K. Development of an effective process for utilization of collagen from livestock and fish waste. *Process Biochem*. 2002;37(12):1403-1412. doi: 10.1016/S0032-9592(02)00024-9

134. Ahmed M, Verma AK, Patel R. Collagen extraction and recent biological activities of collagen peptides derived from sea-food waste: a review. *Sustain Chem Pharm*. 2020;18:100315. doi: 10.1016/j.scp.2020.100315

135. Noorzai S, Verbeek CJR, Lay MC, Swan J. Collagen extraction from various waste bovine hide sources. *Waste Biomass Valoriz*. 2020;11:5687-5698. doi: 10.1007/s12649-019-00843-2

136. Lee JM, Suen SKQ, Ng WL, Ma WC, Yeong WY. Bioprinting of collagen: considerations, potentials, and applications. *Macromolecular Biosci*. 2020;21(1):2000280. doi: 10.1002/mabi.202000280

137. Taghizadeh M, Taghizadeh A, Yazdi MK, et al. Chitosan-based inks for 3D printing and bioprinting. *Green Chem*. 2022;24(1):62-101. doi: 10.1039/d1gc01799c

138. Chawla S, Midha S, Sharma A, Ghosh S. Silk-based bioinks for 3D bioprinting. *Adv Healthc Mater*. 2018;7(8): 1701204. doi: 10.1002/adhm.201701204

139. Yu K-F, Lu T-Y, Li Y-CE, et al. Design and synthesis of stem cell-laden keratin/glycol chitosan methacrylate bioinks for 3D bioprinting. *Biomacromolecules*. 2022;23(7): 2814-2826. doi: 10.1021/acs.biomac.2c00191

140. Brodin E, Boehmer M, Prentice A, et al. Extrusion 3D printing of keratin protein hydrogels free of exogenous chemical agents. *Biomed Mater*. 2022;17(5):055006. doi: 10.1088/1748-605X/ac7f15

141. Navarro J, Clohessy RM, Holder RC, et al. In vivo evaluation of three-dimensional printed, keratin-based hydrogels in a porcine thermal burn model. *Tissue Eng Part A*. 2020; 26(5-6):265-278. doi: 10.1089/ten.tea.2019.0181

142. Aramwit P, Siritientong T, Srichana T. Potential applications of silk sericin, a natural protein from textile industry by-products. *Waste Manage Res*. 2012;30(3):217-224. doi: 10.1177/0734242X11404733

143. Reddy R, Jiang Q, Aramwit P, Reddy N. Litter to leaf: the unexplored potential of silk byproducts. *Trends Biotechnol*. 2021;39(7):706-718. doi: 10.1016/j.tibtech.2020.11.001

144. Shavandi A, Silva TH, Bekhit AA, Bekhit AE-DA. Keratin: dissolution, extraction and biomedical application. *Biomater Sci*. 2017;5(9):1699-1735. doi: 10.1039/C7BM00411G

145. Wang Z, Yang Y, Gao Y, Xu Z, Yang S, Jin M. Establishing a novel 3D printing bioinks system with recombinant human collagen. *Int J Biol Macromol*. 2022;211:400-409. doi: 10.1016/j.ijbiomac.2022.05.088

146. Tytgat L, Dobos A, Markovic M, et al. High-resolution 3D bioprinting of photo-cross-linkable recombinant collagen to serve tissue engineering applications. *Biomacromolecules*. 2020;21(10):3997-4007. doi: 10.1021/acs.biomac.0c00386

147. Sorkio A, Koch L, Koivusalo L, et al. Human stem cell based corneal tissue mimicking structures using laser-assisted 3D bioprinting and functional bioinks. *Biomaterials*. 2018;171:57-71. doi: 10.1016/j.biomaterials.2018.04.034

148. Dai M, Belaïdi J-P, Fleury G, et al. Elastin-like polypeptide-based bioink: a promising alternative for 3D bioprinting. *Biomacromolecules*. 2021;22(12):4956-4966. doi: 10.1021/acs.biomac.1c00861

149. Lechner A, Trossmann VT, Scheibel T. Impact of cell loading of recombinant spider silk based bioinks on gelation and printability. *Macromol Biosci*. 2022;22(3):2100390. doi: 10.1002/mabi.202100390

150. Schacht K, Jüngst T, Schweinlin M, Ewald A, Groll J, Scheibel T. Biofabrication of cell-loaded 3D spider silk constructs. *Angew Chemie Int Ed*. 2015;54(9):2816-2820. doi: 10.1002/anie.201409846

151. Buechter DD, Paolella DN, Leslie BS, Brown MS, Mehos KA, Gruskin EA. Co-translational incorporation of trans-4-hydroxyproline into recombinant proteins in bacteria. *J Biol Chem*. 2003;278(1):645-650. doi: 10.1074/jbc.M209364200

152. Toman PD, Chisholm G, McMullin H, et al. Production of recombinant human type I procollagen trimers using a four-gene expression system in the yeast Saccharomyces cerevisiae. *J Biol Chem*. 2000;275(30):23303-23309. doi: 10.1074/jbc.M002284200

153. Vaughan PR, Galanis M, Richards KM, Tebb TA, Ramshaw JA, Werkmeister JA. Production of recombinant hydroxylated human type III collagen fragment in Saccharomyces cerevisiae. *DNA Cell Biol*. 1998;17(6):511-518. doi: 10.1089/dna.1998.17.511

154. Barnes LM, Bentley CM, Dickson AJ. Stability of protein production from recombinant mammalian cells. *Biotechnol Bioeng*. 2003;81(6):631-639. doi: 10.1002/bit.10517

155. Demain AL, Vaishnav P. Production of recombinant proteins by microbes and higher organisms. *Biotechnol Adv*. 2009;27(3):297-306. doi: 10.1016/j.biotechadv.2009.01.008

156. LeCun Y, Bengio Y, Hinton G. Deep learning. *Nature*. 2015;521(7553):436-444. doi: 10.1038/nature14539

157. Ng WL, Chan A, Ong YS, Chua CK. Deep learning for fabrication and maturation of 3D bioprinted tissues and organs. *Virtual Phys Prototyping*. 2020;15(3):340-358. doi: 10.1080/17452759.2020.1771741

158. Zhuang P, Ng WL, An J, Chua CK, Tan LP. Layer-by-layer ultraviolet assisted extrusion-based (UAE) bioprinting of hydrogel constructs with high aspect ratio for soft tissue engineering applications. *PLoS One*. 2019;14(6):e0216776. doi: 10.1371/journal.pone.0216776

159. Ozbolat IT, Hospodiuk M. Current advances and future perspectives in extrusion-based bioprinting. *Biomaterials*. 2016;76:321-343. doi: 10.1016/j.biomaterials.2015.10.076

160. Ng WL, Yeong WY, Naing MW. Potential of bioprinted films for skin tissue engineering. In: *Proceedings of the 1st International Conference on Progress in Additive Manufacturing*; 2014:441-446. doi: 10.3850/978-981-09-0446-3_065

161. Ng WL, Yeong WY, Naing MW. Development of polyelectrolyte chitosan-gelatin hydrogels for skin bioprinting. *Procedia CIRP*. 2016;49:105-112. doi: 10.1016/j.procir.2015.09.002

162. Suntornnond R, Ng WL, Huang X, Yeow ECH, Yeong WY. Improving printability of hydrogel-based bio-inks for thermal inkjet bioprinting applications via saponification and heat treatment process. *J Mater Chem B*. 2022;10(31):5989-6000. doi: 10.1039/D2TB00442A

163. Ng WL, Yeong WY, Naing MW. Microvalve bioprinting of cellular droplets with high resolution and consistency. *Proc Int Conf Prog Additive Manuf*. 2016; 2016:397-402. doi: 10.3850/2424-8967_V02-236

164. Ng WL, Lee JM, Yeong WY, Win Naing M. Microvalve-based bioprinting – process, bio-inks and applications. *Biomater Sci*. 2017;5(4):632-647. doi: 10.1039/C6BM00861E

165. Li W, Mille LS, Robledo JA, Uribe T, Huerta V, Zhang YS. Recent advances in formulating and processing biomaterial inks for vat polymerization-based 3D printing. *Adv Healthc Mater*. 2020;9(15):2000156. doi: 10.1002/adhm.202000156

166. Ng WL, Chua CK, Shen Y-F. Print me an organ! Why we are not there yet. *Prog Polymer Sci*. 2019;97:101145. doi: 10.1016/j.progpolymsci.2019.101145

167. Levato R, Jungst T, Scheuring RG, Blunk T, Groll J, Malda J. From shape to function: the next step in bioprinting. *Adv Mater*. 2020;32(12):1906423. doi: 10.1002/adma.201906423

168. Ng WL, Wang S, Yeong WY, Naing MW. Skin bioprinting: impending reality or fantasy? *Trends Biotechnol*. 2016;34(9):689-699. doi: 10.1016/j.tibtech.2016.04.006

169. Lee JM, Ng WL, Yeong WY. Resolution and shape in bioprinting: strategizing towards complex tissue and organ printing. *Appl Phys Rev*. 2019;6(1):011307. doi: 10.1063/1.5053909

170. Ng WL, Lee JM, Zhou M, Yeong WY. Hydrogels for 3-D bioprinting-based tissue engineering. In: Narayan R, ed. *Rapid Prototyping of Biomaterials*. Elsevier; 2020:183-204. doi: 10.1016/B978-0-08-102663-2.00008-3

171. Ng WL, Tan ZQ, Yeong WY, Naing MW. Proof-of-concept: 3D bioprinting of pigmented human skin constructs. *Biofabrication*. 2018;10(2):025005. doi: 10.1088/1758-5090/aa9e1e

172. Lu Y, Rai R, Nitin N. Image-based assessment and machine learning-enabled prediction of printability of polysaccharides-based food ink for 3D printing. *Food Res Int*. 2023;173:113384.
doi: 10.1016/j.foodres.2023.113384

173. Chen H, Liu Y, Balabani S, Hirayama R, Huang J. Machine learning in predicting printable biomaterial formulations for direct ink writing. *Research*. 2023;6:0197.
doi: 10.34133/research.0197

174. Han S, Kim CM, Jin S, Kim TY. Study of the process-induced cell damage in forced extrusion bioprinting. *Biofabrication*. 2021;13(3):035048.
doi: 10.1088/1758-5090/ac0415

175. Fischer L, Nosratlo M, Hast K, et al. Calcium supplementation of bioinks reduces shear stress-induced cell damage during bioprinting. *Biofabrication*. 2022;14(4):045005.
doi: 10.1088/1758-5090/ac84af

176. Ng WL, Shkolnikov V. Optimizing cell deposition for inkjet-based bioprinting. *Int J Bioprint*. 2024;10(2):2135.
doi: 10.36922/ijb.2135

177. Blaeser A, Duarte Campos DF, Puster U, Richtering W, Stevens MM, Fischer H. Controlling shear stress in 3D bioprinting is a key factor to balance printing resolution and stem cell integrity. *Adv Healthc Mater*. 2016; 5(3):326-333.
doi: 10.1002/adhm.201500677

178. Ng WL, Huang X, Shkolnikov V, Goh GL, Suntornnond R, Yeong WY. Controlling droplet impact velocity and droplet volume: key factors to achieving high cell viability in sub-nanoliter droplet-based bioprinting. *Int J Bioprint*. 2022;8(1):424.
doi: 10.18063/ijb.v8i1.424

179. Ng WL, Huang X, Shkolnikov V, Suntornnond R, Yeong WY. Polyvinylpyrrolidone-based bioink: influence of bioink properties on printing performance and cell proliferation during inkjet-based bioprinting. *Bio-Design Manufacturing*. 2023;6:676-690.
doi: 10.1007/s42242-023-00245-3

180. Ng WL, Yeong WY, Naing MW. Polyvinylpyrrolidone-based bio-ink improves cell viability and homogeneity during drop-on-demand printing. *Materials*. 2017;10(2):190.
doi: 10.3390/ma10020190

181. Ng WL, Lee JM, Zhou M, et al. Vat polymerization-based bioprinting–process, materials, applications and regulatory challenges. *Biofabrication*. 2020;12(2):022001.
doi: 10.1088/1758-5090/ab6034

182. Mohammadrezaei D, Podina L, De Silva J, Kohandel M. Cell viability prediction and optimization in extrusion-based bioprinting via neural network-based Bayesian optimization models. *Biofabrication*. 2024;16(2).
doi: 10.1088/1758-5090/ad17cf

183. Xu H, Liu Q, Casillas J, et al. Prediction of cell viability in dynamic optical projection stereolithography-based bioprinting using machine learning. *J Intell Manuf*. 2022;33(4):995-1005.
doi: 10.1007/s10845-020-01708-5

184. Ruberu K, Senadeera M, Rana S, et al. Coupling machine learning with 3D bioprinting to fast track optimisation of extrusion printing. *Appl Mater Today*. 2021;22:100914.
doi: 10.1016/j.apmt.2020.100914

185. Fu Z, Angeline V, Sun W. Evaluation of printing parameters on 3D extrusion printing of pluronic hydrogels and machine learning guided parameter recommendation. *Int J Bioprint*. 2021;7(4):434.
doi: 10.18063/ijb.v7i4.434

186. Oh D, Shirzad M, Kim MC, Chung E-J, Nam SY. Rheology-informed hierarchical machine learning model for the prediction of printing resolution in extrusion-based bioprinting. *Int J Bioprinting*. 2023;9(6):1280.
doi: 10.36922/ijb.1280

187. Hales S, Tokita E, Neupane R, et al. 3D printed nanomaterial-based electronic, biomedical, and bioelectronic devices. *Nanotechnology*. 2020;31(17):172001.
doi: 10.1088/1361-6528/ab5f29

188. Kong YL, Gupta MK, Johnson BN, McAlpine MC. 3D printed bionic nanodevices. *Nano Today*. 2016;11(3): 330-350.
doi: 10.1016/j.nantod.2016.04.007

189. Gao C, Li Y, Liu X, Huang J, Zhang Z. 3D bioprinted conductive spinal cord biomimetic scaffolds for promoting neuronal differentiation of neural stem cells and repairing of spinal cord injury. *Chem Eng J*. 2023;451:138788.
doi: 10.1016/j.cej.2022.138788

190. Mannoor MS, Jiang Z, James T, et al. 3D printed bionic ears. *Nano Lett*. 2013;13(6):2634-2639.
doi: 10.1021/nl4007744

191. Zips S, Grob L, Rinklin P, et al. Fully printed µ-needle electrode array from conductive polymer ink for bioelectronic applications. *ACS Appl Mater Interfaces*. 2019;11(36):32778-32786.
doi: 10.1021/acsami.9b11774.

192. Su C-K, Chen J-C. One-step three-dimensional printing of enzyme/substrate–incorporated devices for glucose testing. *Anal Chim Acta*. 2018;1036:133-140.
doi: 10.1016/j.aca.2018.06.073

193. Hussain A, Abbas N, Ali A. Inkjet printing: a viable technology for biosensor fabrication. *Chemosensors*. 2022;10(3):103.
doi: 10.3390/chemosensors10030103

194. Tomaskovic-Crook E, Zhang P, Ahtiainen A, et al. Human neural tissues from neural stem cells using conductive biogel and printed polymer microelectrode arrays for 3D electrical stimulation. *Adv Healthc Mater*. 2019;8(15):1900425.
doi: 10.1002/adhm.201900425

195. Moya A, Ortega-Ribera M, Guimerà X, et al. Online oxygen monitoring using integrated inkjet-printed sensors in a

liver-on-a-chip system. *Lab Chip*. 2018;18(14):2023-2035. doi: 10.1039/C8LC00456K

196. Rothbauer M, Eilenberger C, Spitz S, et al. Recent advances in additive manufacturing and 3D bioprinting for organs-on-a-chip and microphysiological systems. Review. *Front Bioeng Biotechnol*. 2022;10. doi: 10.3389/fbioe.2022.837087
197. Lind JU, Busbee TA, Valentine AD, et al. Instrumented cardiac microphysiological devices via multimaterial three-dimensional printing. *Nat Mater*. 2017;16(3):303-308. doi: 10.1038/nmat4782
198. Liu Z, Zhang Y, Xu S, et al. A 3D printed smartphone optosensing platform for point-of-need food safety inspection. *Anal Chim Acta*. 2017;966:81-89. doi: 10.1016/j.aca.2017.02.022
199. Dufil G, Bernacka-Wojcik I, Armada-Moreira A, Stavrinidou E. Plant bioelectronics and biohybrids: the growing contribution of organic electronic and carbon-based materials. *Chem Rev*. 2022;122(4):4847-4883. doi: 10.1021/acs.chemrev.1c00525
200. Yamashita T, Yamashita Y, Takano M, Sato N, Nakano S, Yokoyama H. 3D printed lattice-structured metal electrodes for enhanced current production in bioelectrochemical systems. *Environ Technol*. 2023;44(21):3229-3235. doi: 10.1080/09593330.2022.2056083
201. Baş F, Kaya MF. 3D printed anode electrodes for microbial electrolysis cells. *Fuel*. 2022;317(6):123560. doi: 10.1016/j.fuel.2022.123560
202. Hoffmann M, Elwany A. In-space additive manufacturing: a review. *J Manuf Sci Eng*. 2023;145(2). doi: 10.1115/1.4055603
203. Rezapour Sarabi M, Yetisen AK, Tasoglu S. Bioprinting in microgravity. *ACS Biomater Sci Eng*. 2023;9(6):3074-3083. doi: 10.1021/acsbiomaterials.3c00195
204. Yang J-Q, Jiang N, Li Z-P, et al. The effects of microgravity on the digestive system and the new insights it brings to the life sciences. *Life Sci Space Res*. 2020;27:74-82. doi: 10.1016/j.lssr.2020.07.009
205. Mao M, Meng Z, Huang X, et al. 3D printing in space: from mechanical structures to living tissues. *Int J Extreme Manuf*. 2024;6(2):023001. doi: 10.1088/2631-7990/ad23ef
206. Parfenov VA, Khesuani YD, Petrov SV, et al. Magnetic levitational bioassembly of 3D tissue construct in space. *Sci Adv*. 2020;6(29):eaba4174. doi: 10.1126/sciadv.aba4174
207. Tabury K, Rehnberg E, Baselet B, Baatout S, Moroni L. Bioprinting of cardiac tissue in space: where are we? *Adv Healthc Mater*. 2023;12(23): 2203338. doi: 10.1002/adhm.202203338
208. Chang CC, Boland ED. 3D bioprinting aboard the international space station using the techshot biofabrication facility. In: Hessel V, Stoudemire J, Miyamoto H, Fisk I D, eds. *In-Space Manufacturing and Resources*; 2022:303-317. doi: 10.1002/9783527830909.ch16
209. Mo XW, Zhang YM, Wang ZX, et al. Satellite-based on-orbit printing of 3D tumor models. *Adv Mater*. 2023: e2309618. doi: 10.1002/adma.202309618
210. Averesch NJH, Berliner AJ, Nangle SN, et al. Microbial biomanufacturing for space-exploration—what to take and when to make. *Nat Commun*. 2023;14(1):2311. doi: 10.1038/s41467-023-37910-1
211. Duraj-Thatte AM, Manjula-Basavanna A, Rutledge J, et al. Programmable microbial ink for 3D printing of living materials produced from genetically engineered protein nanofibers. *Nat Commun*. 2021;12(1):6600. doi: 10.1038/s41467-021-26791-x
212. Heveran CM, Williams SL, Qiu J, et al. Biomineralization and successive regeneration of engineered living building materials. *Matter*. 2020;2(2):481-494. doi: 10.1016/j.matt.2019.11.016
213. Gantenbein S, Colucci E, Käch J, et al. Three-dimensional printing of mycelium hydrogels into living complex materials. *Nat Mater*. 2022;22(1):128-134. doi: 10.1038/s41563-022-01429-5

ACCSCIENCE PUBLISHING

International Journal of Bioprinting

REVIEW ARTICLE

Miniature modeling while aiming for transplantation: Current challenges and future perspectives of lung bioprinting

Judit Bovari-Biri[1], Kitti Garai[1], Borbala Lovaszi[2], Zoltan Vereb[2], and Judit E. Pongracz[1]*

[1]Department of Pharmaceutical Biotechnology, Faculty of Pharmacy, University of Pécs, Pécs, Baranya, Hungary

[2]Department of Dermatology and Allergology, Albert Szentgyorgyi Clinical Centre, University of Szeged, Szeged, Hungary

(This article belongs to the Special Issue: *3D Printing for tissue engineering and regenerative medicine*)

Abstract

The development of three-dimensional (3D) lung organs or tissues using gravitational methods and bioprinting technologies displays significant promise for producing lung tissue for research, pharmaceutical, and clinical applications. The advancement of innovative technologies can improve our understanding of lung diseases and, if necessary, enable the production of replacement lungs for transplantation. The development of functional organs-on-a-chip and disease-specific lung tissues could provide a deep understanding of the molecular mechanisms underlying lung diseases and aid the identification of drug targets. This knowledge has the potential to enhance our understanding of lung tissue regeneration processes, potentially leading to the development of more effective treatments for human lung diseases. This could eliminate the need for lung transplants in most disease-induced cases, as appropriate medications could induce regeneration of the damaged organ. This review highlights the importance of using a variety of materials, preparation methods, and sizes of lung tissues in 3D bioprinting technologies to better understand lung function, facilitate drug selection during therapy, and ultimately produce transplantable organs if needed. The review also emphasizes the need for improvements in legislation and guidelines for researchers aiming to achieve quality-assured biomanufacturing.

Keywords: Lung diseases; Lung bioprinting; Lung tissue aggregates; Personalized medicine; Drug testing; Organ-on-a-chip

***Corresponding author:**
Judit E. Pongracz
(pongracz.e.judit@pte.hu)

Citation: Bovari-Biri J, Garai K, Lovaszi B, Vereb Z, Pongracz JE. Miniature modeling while aiming for transplantation: Current challenges and future perspectives of lung bioprinting. *Int J Bioprint*. 2025;11(1):30-56. doi: 10.36922/ijb.4673

Received: August 28, 2024
Revised: September 28, 2024
Accepted: October 7, 2024
Published Online: October 7, 2024

Copyright: © 2024 Author(s). This is an Open Access article distributed under the terms of the Creative Commons Attribution License, permitting distribution, and reproduction in any medium, provided the original work is properly cited.

Publisher's Note: AccScience Publishing remains neutral with regard to jurisdictional claims in published maps and institutional affiliations.

1. Introduction

Lung diseases represent a significant global health concern (The main types of lung diseases and the applicable therapies are collected in Table 1). According to the World Health Organization, over four million people succumb to respiratory diseases annually, with nearly two million additional deaths attributed to various types of lung cancers.[1] Despite the wide prevalence of a broad range of lung diseases, public attention and health concerns are primarily focused on different diseases, including heart diseases,

Table 1. Main types of lung diseases and the applicable therapy

Main types of lung diseases	Transplantation might be necessary	Medication
Asthma	+	+
Acute respiratory distress syndrome (ARDS)	+	+
Chronic obstructive pulmonary disease (COPD)	+	+
Emphysema	+	+
Cystic fibrosis	+	+/−
Interstitial lung disease (ILD)	+	−
Infections	−	+
Infection induced fibrosis	+	−
Lung cancers	−	+

Note: "+" denotes likely medical intervention; "-" denotes unlikely medical intervention.

stroke, and cancers, which present more prominent and early symptoms. The delayed diagnosis of lung diseases highlights the crucial need to identify early diagnostic markers and therapeutic targets for timely intervention during the initial disease stages. It is evident that to address all the demands, a thorough understanding of healthy lung anatomy and function is just as crucial as understanding the diseases and therapy responses, clinical needs, and regulatory issues. Understanding the development and progression of lung diseases, identifying potential therapeutic targets, and evaluating drugs to find effective treatments or stimulate regenerative processes for damaged lung tissue present complex challenges for the research community and clinicians. While treating lung cancers require a different approach, lung modeling is equally important in lung cancer modeling as it is for other lung diseases. Additionally, in cases of severe, end-stage lung tissue damage, lung transplantation may be the only, albeit extremely challenging, option.

Bioprinting is pivotal to numerous applications in research laboratories, including understanding disease mechanisms, identifying drug targets, testing medications, and producing transplantation-ready organs. Bioprinting dates back to the late 1980s[2] and started to gain significance in the 1990s[2] when 3D bioprinting technology became associated with the broader field of tissue engineering (TE) to create increasingly complex structures. Technical approaches were broad and included inkjet-based bioprinting, extrusion-based bioprinting, and laser-assisted (e.g., stereolithography) bioprinting[3] mostly to create tissue models for understanding organogenesis, diseases, and drug reactions, as well as organ regeneration processes. With technological advancements, the creation of patient-specific tissues and organs tailored to individual needs became possible. Over the past few decades, the field of 3D bioprinting has experienced significant advancements in terms of the types of tissue models that can be constructed, including normal proximal and distal lung tissue assembly, blood vessel infiltration into the tissue, and lung disease modeling (e.g., cancer, chronic obstructive pulmonary disease [COPD], cystic fibrosis), which offer various benefits and applications beyond lung transplantation. Considering the complex structure and dynamic characteristics of the lung, various reviews have described the construction of artificial lung tissues, mostly focusing on specific lung tissue segments, mostly on the microscale, and discussed precise tissue compositions at the macroscale. Although extensive work has been done on portraying lung bioprinting, our review is the first one to associate the challenges posed by clinical procedures and the application of model tissues that aid the clinical application of microscale lung printing. While numerous reviews have delved into the details of printing technologies and the myriad applications currently available, our review uniquely focuses on the obstacles still hindering the integration of lung tissue printing into clinical practice. Moreover, we draw attention to the overlooked aspect of lung transplantation, noting the absence of bioprinting technologies in understanding the clinical requirements necessary for making bioprinted tissues or organs viable for surgical manipulation. Consequently, we offer a summary of the current challenges in clinically applicable bioprinting, diverging from the usual summaries that tend towards an optimistic portrayal of solutions for the hurdles encountered in the development of printing processes. Public expectations often lean towards a swift readiness of sophisticated solutions, particularly the bioprinting of soft tissues like the lung, anticipated to supply donor organs within a few years. Despite the enthusiasm from the scientific community to foster such expectations, the

reality falls short. This is partly due to unresolved issues such as the sourcing of the trillions of cells necessary for bioprinted lung tissue, the regulation of cellular subtype differentiation, the integration of functional capabilities, and the quality control of transplantation-ready tissues that are safe for surgical handling. In addition to technical and biological challenges, we also highlight another critical facet often sidelined—the regulatory and legislative framework governing bioprinting. These regulatory aspects, crucial for the advancement of bioprinting applications, are not keeping pace with the technological and procedural innovations in the field. While bioprinting of solid scaffold-based tissue seems to have achieved a level of clinical applicability, recent discoveries point to emerging challenges. For instance, different scaffold materials, pore sizes, growth and differentiation factors, and cell sources are necessitated for the regeneration of lung tissues—a nuance that may not hold significant importance in a research lab but is of utmost relevance from the perspectives of clinicians and patients alike. Accordingly, we have divided the present manuscript into two main areas:

(i) Bioprinting macro-sized, transplantation-ready lung tissue, addressing the challenges and recent discoveries necessary before printing full transplantable lungs.

(ii) Bioprinting micro-sized lung tissue for research and clinical applications to evaluate personalized therapy effectiveness as well as for pharmaceutical applications to test drug candidates for toxicology, drug–drug interactions, and efficacy.

Finally, we highlight the prospects for *in vitro* production of lung tissue and the incorporation of all knowledge obtained from bioprinted lung tissue models into personalized clinical applications.

2. Transplantation-ready—macroscale-lung tissue

2.1. Lung transplantation

Lung transplantation is only considered for patients who have advanced and progressively declining lung function (e.g., interstitial lung disease) and those with no other treatment options available. Candidates typically experience symptoms during their daily activities and have a limited life expectancy. Ideally, they should not have any other organ dysfunctions and preferably no other underlying health conditions.[4,5] In recent years, there has been an increased demand for lung transplants due to severe fibrosis resulting from Coronavirus disease 2019 (COVID-19) infections. This has led to more potential recipients without a proportional increase in available transplantable organs, boosting the interest in lung bioprinting. Theoretically, organs, including the lungs, can be printed *in vitro*. However, several factors must be considered when creating a functional organ.

The anatomical structure of the lung poses the first challenge for clinical application. The airways (proximal lung)[6] begin with the trachea, which bifurcates into the main bronchi and finally into bronchioles. The trachea and upper airways are lined with columnar ciliated and mucous secretory cells. These cells coordinate to trap inhaled particles in mucus, which is then expelled by the cilia. Additionally, cuboidal secretory club cells can be found in the bronchioles producing mucus. They secrete various proteins to protect the bronchiolar epithelium. The transition from terminal bronchioles to the alveoli marks the beginning of the distal respiratory zone (Figure 1).

The distal airways of a healthy human lung have around 300–700 million alveoli,[7] and each alveolus is surrounded by a homogenous mesh of capillary vessels, forming the vast surface area of gas exchange. An alveolar septum separates each alveolus. Previously, it was believed that there were only three main cell types in alveoli: type 1 pneumocytes (AT1), type 2 pneumocytes (AT2), and alveolar macrophages. In recent years, single-cell sequencing identified dozens more subtypes of cells in the gas exchange area.[8] In general, AT1 cells cover 70%–95% of the internal surface of each alveolus as thin, squamous cells with surfactant proteins to decrease surface tension and form an air-blood barrier for gas exchange. They are connected via tight junctions, creating an almost impermeable barrier to fluid infiltration into the alveoli. The cuboidal AT2 cells cover 7% of the internal surface of each alveolus and have apical microvilli and characteristic lamellar bodies. AT2 cells produce surfactant proteins to decrease alveolar surface tension and serve as tissue-specific progenitor cells to trans-differentiate into AT1 cells when regeneration of the gas-exchange surface is necessary following tissue damage.[9] Recently, it was discovered that the alveolar capillary network is composed of two intermingled, stable cell types, the general capillary cells and the aCap (aerocytes) cells.[10] The aCap cells are complex, large cells (diameter: >100 μm; mean volume: 21 $\times 10^3$ μm^3) with ramified extensions surrounding the pores (mean of six pores per cell). The cells have a variety of sizes and shapes, and a single cell frequently spans multiple alveoli to increase the efficiency of gas exchange. A similar morphological complexity has also been described for AT1 cells.[11] Alveolar macrophages are mononuclear phagocytes resident in the alveoli and play a key role in protecting the distal lung tissue from infections.[12]

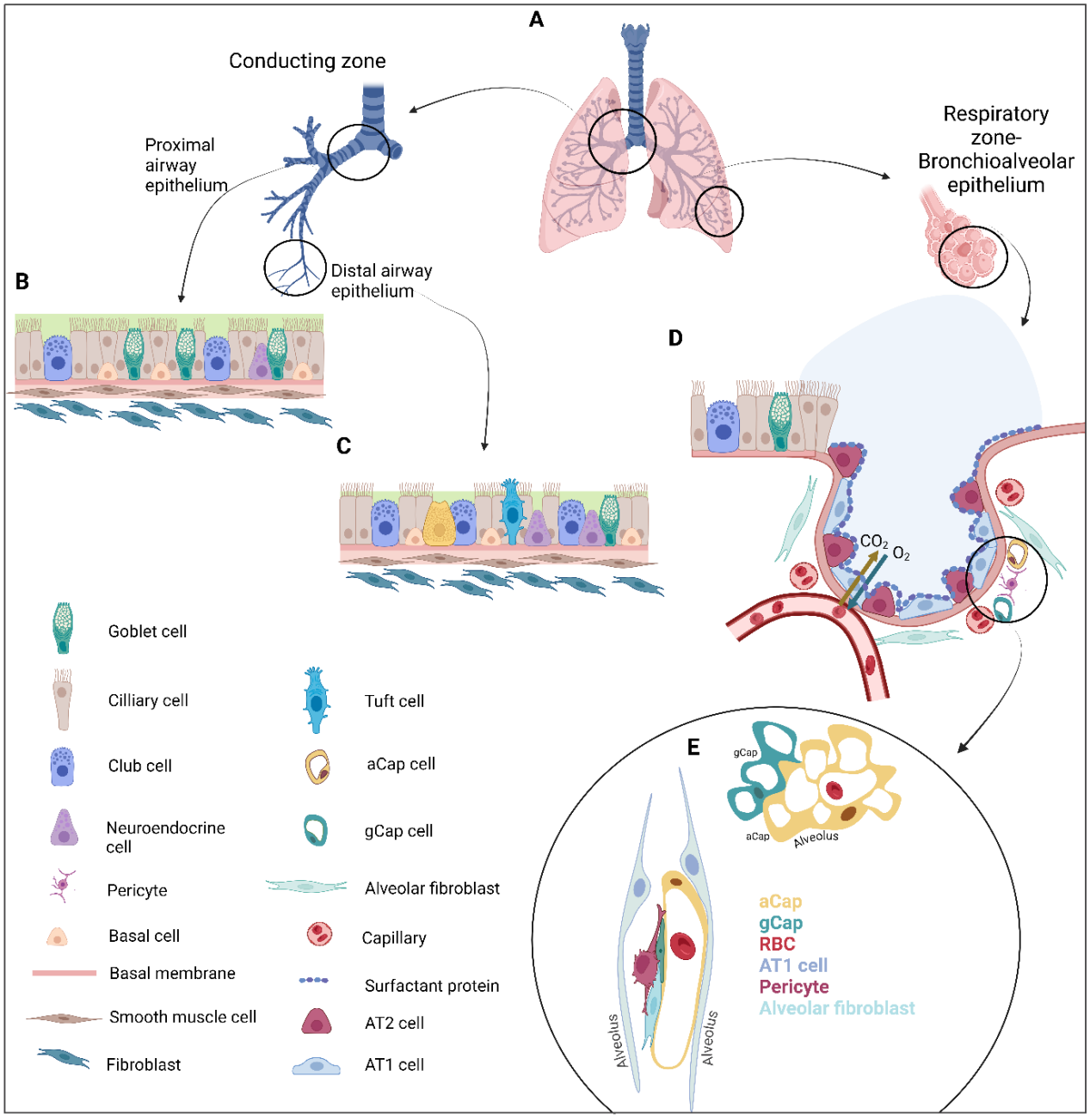

Figure 1. Anatomical characterization of the different tissue types of the lungs. (A) The main functional roles of the lung tissue are conducting and respiratory zones. (B) Characteristic cell types of the proximal airway epithelium. (C) Characteristic cell types of the distal airway epithelium. (D) Characteristic cell types of the bronchioalveolar epithelium. (E) The relative position of the different types of capillary cells. Abbreviations: gCap, general capillary cells; aCap, aerocyte capillary cells; RBC, red blood cell; AT1, alveolar epithelial cell type 1; AT2, alveolar epithelial cell type 2.

The total thickness of the interstitium together with an ultrathin basement membrane (BM) is about 1 μm, while the BM is less than 100 nm.[13] The BM is elastic and porous, allowing for up to 10% linear strain under physiological conditions, and has Young's modulus of 3–7 kPa,[14] making the lung tissue resilient to constant inflation and deflation.

In vitro production of the lung presents unique challenges. Preparing lung tissues for transplantation includes dealing with large tissue sizes spanning from dozens of centimeters (trachea) to nanometers (alveoli) and establishing a complex vascular network for such a large organ to maintain the appropriate and coordinated blood supply.

Without computer-aided design (CAD) and computer-aided manufacturing (CAM),[15] it would not be possible to create human-sized tissues with the complexity required for organs such as the lungs. The CAD/CAM technology and the development of degradable scaffolds and bioinks are crucial for advancing lung bioprinting. This involves using medical imaging and anatomical knowledge (Figure 1) to identify tissue types and translate scanned frameworks into suitable computer programs for printing.

2.2. Criteria for bioprinting lung and tracheal constructs

Recently, several reviews have summarized the technical issues associated with lung tissue bioprinting,[16,17] including cell sources, cell cultures, growth and differentiation factors and markers, and the various printing methodologies (e.g., extrusion-based, inkjet-based, pressure-assisted, and laser-assisted bioprinting).[18–22] Based on existing knowledge, the challenges of printing a transplant-ready lung include (Figure 2):

(i) The massive number of cells required. Therefore, the number and the origin of the cells are essential (primary human organ-specific tissue cells, stem cells, tissue-specific progenitor cells, induced pluripotent stem cells [iPSCs]).

(ii) The required cell types must be able to differentiate reliably and be scalable for further differentiation within the appropriate microenvironment (including scaffold material, other cells, secured nutrition, and oxygen supply). It poses an additional challenge if the interactions between cells do not initiate the differentiation process and the organ produced *in vitro* requires additional proteins (growth and differentiation factors) at the appropriate concentration and timing (Figure 3).

(iii) The cells must differentiate into the required and appropriate cell subtypes. Suitable mechanical parameters and an air–liquid interface are required for complete cellular differentiation and polarization.

(iv) Ability to print a nanoscale scaffold with appropriate grooves where the cells attach, proliferate, and create the necessary cytoskeleton.

(v) The matrices where the cells are grown and then printed must be reproducible and adjustable.

(vi) The bioprinter should be suitable for printing structures as small as an alveolus (with a diameter of 200 μm) and as large as a full lung (with three lobes, approximately 1.3 kg, and a total respiratory surface area of about 70–100 m^2).

(vii) Time is crucial—the tissue needs to be printed and matured at an accelerated pace.

(viii) The tissue needs to be maintained in a differentiated, oxygenated, and fully formed state *in vitro* under sterile conditions to make it suitable to be considered for human surgery.

(ix) The organ designated for transplantation must undergo a quality assurance test to rapidly determine its clinical suitability.

(x) The *in vitro*-produced organ being considered for transplant must meet all legal requirements.

It is important to emphasize that generating a healthy clone of a damaged lung for transplantation is not achievable with a small number of stem cells alone. Growing a fully functional organ from such a limited starting point would require several months or even years. Given the urgent demand for the organ and the absence of a defined timeline, it is crucial to explore alternative solutions.

2.3. Sources of cells

Human-sized organs necessitate an astounding number of cells, hovering around the trillion mark. To bioprint a complete lung, approximately 11×10^9 cells are required, and these cells must be healthy and capable of proliferation and differentiation into dozens of subtypes necessary to produce the functional organ. While many lung tissue printing techniques are tested using cancer cell lines, determining how applicable these techniques are for primary tissue is challenging.

Primary cells can be forced to proliferate, but only a limited number of replication cycles can be expected, while genetic changes cannot be ruled out, and the ability to re-differentiate is questionable. The best source to achieve the required trillions of cells for a full organ transplant appears to be iPSCs, preferentially created from isolated progenitor cells. Any kind of tissue replacement therapy could use iPSCs for either autologous or carefully tested allogeneic applications. While the creation of iPSCs sounds like an easy and straightforward process based on the protocol created by Yamanaka et al.,[23] who identified the transcription factors (Oct3/4, Sox2, Klf4, c-Myc) that play a vital role in the creation of iPSCs, several factors need to be considered to use human donor cells for making a transplantation-ready iPSC-based organ. Even for iPSC, the quality of the donated cells is essential. Quality assurance of iPSCs includes observation of iPSC colony morphology, cell surface and internal protein immunochemistry-based markers, metabolic function testing, karyotyping chromosome anomalies, and endotoxin testing. Nevertheless, the question remains: how many of the

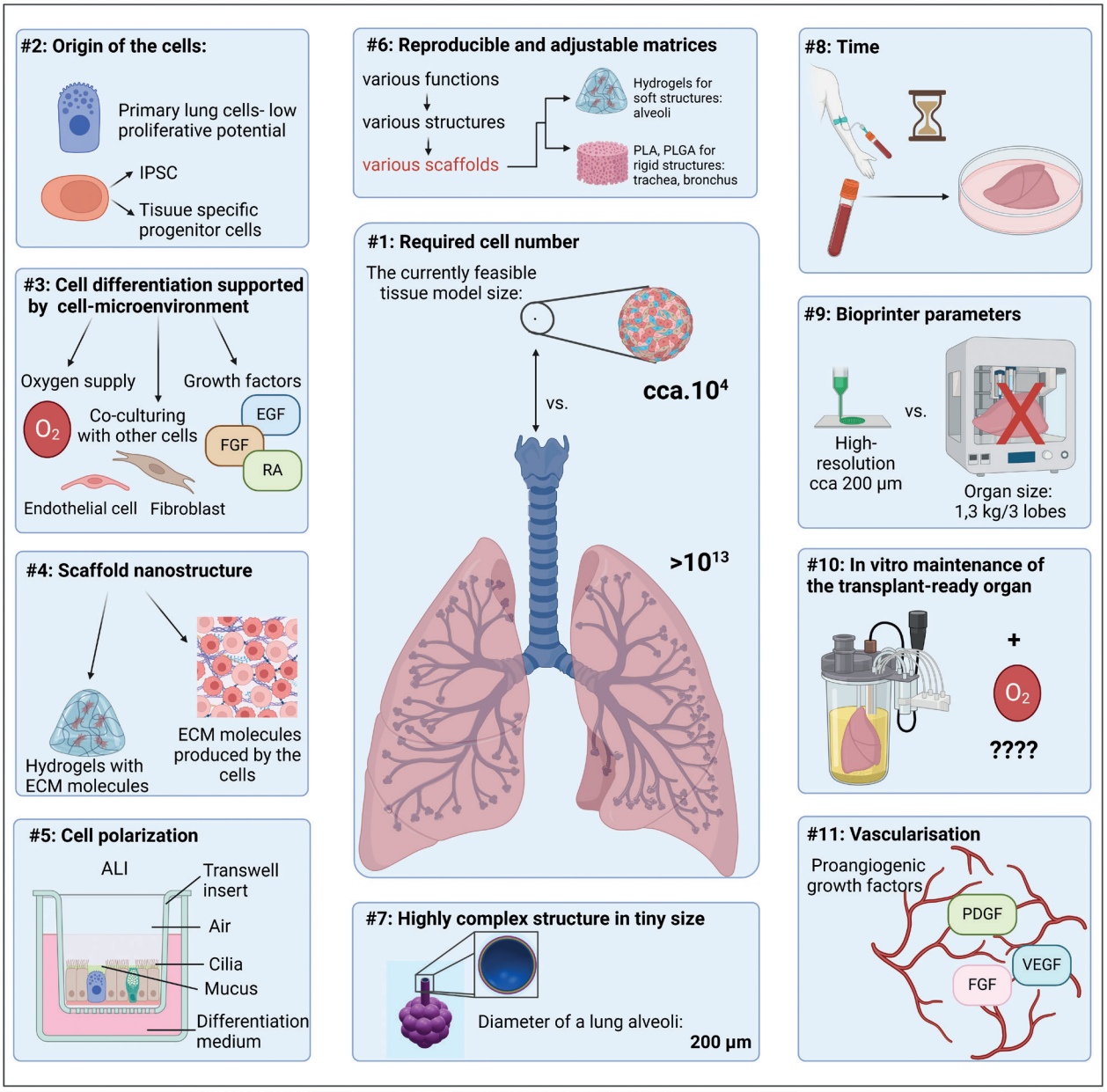

Figure 2. Summary of the challenges of transplant-ready lung tissue bioprinting. #1 Required cell number: The size of the currently feasible and reproducible tissue model is only a fraction of the size of transplant-ready lung tissue. #2 Origin of the cells: The proliferation of the primary cells is slow and limited; induced pluripotent stem cells (IPSCs) are genetically modified cells and may not be suitable for transplantation; tissue-specific progenitor cells are difficult to isolate in large quantities, especially from a diseased lung. #3 Cell differentiation supported by cell-microenvironment: Cell differentiation is influenced by various microenvironmental factors, such as other co-cultured cell types, growth factors, and oxygenation. #4 Scaffold nanostructure: Extracellular matrix molecules characteristic of the lungs must be applied during tissue culturing, or these molecules need to be produced by the cultured and printed cells themselves. #5 Cell polarization: Cell polarization of the epithelial cells in various airway sections is crucial for transplant-ready lung tissue; the air-liquid interface (ALI) promotes cell differentiation and cell polarization. #6 Reproducible and adjustable matrices: Various regions of lung tissue have different functions and structures, necessitating the use of various scaffold materials for tissue engineering; e.g., hydrogels in the case of lung alveoli, poly(lactic-co-glycolic) acid (PLGA) or poly-lactic acid (PLA) in the case of the conducting zone. #7 Highly complex structure in tiny size: To reproduce the highly complex, three-layered structure of the lung alveoli in a relatively tiny size (200 µm) is also challenging. #8 Time: One of the biggest challenges in creating a transplant-ready lung model is the time-consuming nature of the process; the upscaling of the isolated autologous cells itself would take an invaluable amount of time, if feasible at all, not to mention the additional time required for the printing process. #9 Bioprinter parameters: Printing a transplant-ready lung model would require a 3D bioprinter with high-resolution capabilities that can also print large tissue models; such a printer is currently not available on the market. #10 In vitro maintenance of the transplant-ready organ: Researchers have to solve the maintenance problem of transplant-ready lung tissue, i.e., nutrition and oxygenation. #11 Vascularization: Vascularization is also a crucial point in tissue engineering protocols, while complex tissues in a larger size start to necrotize without proper vascularization.

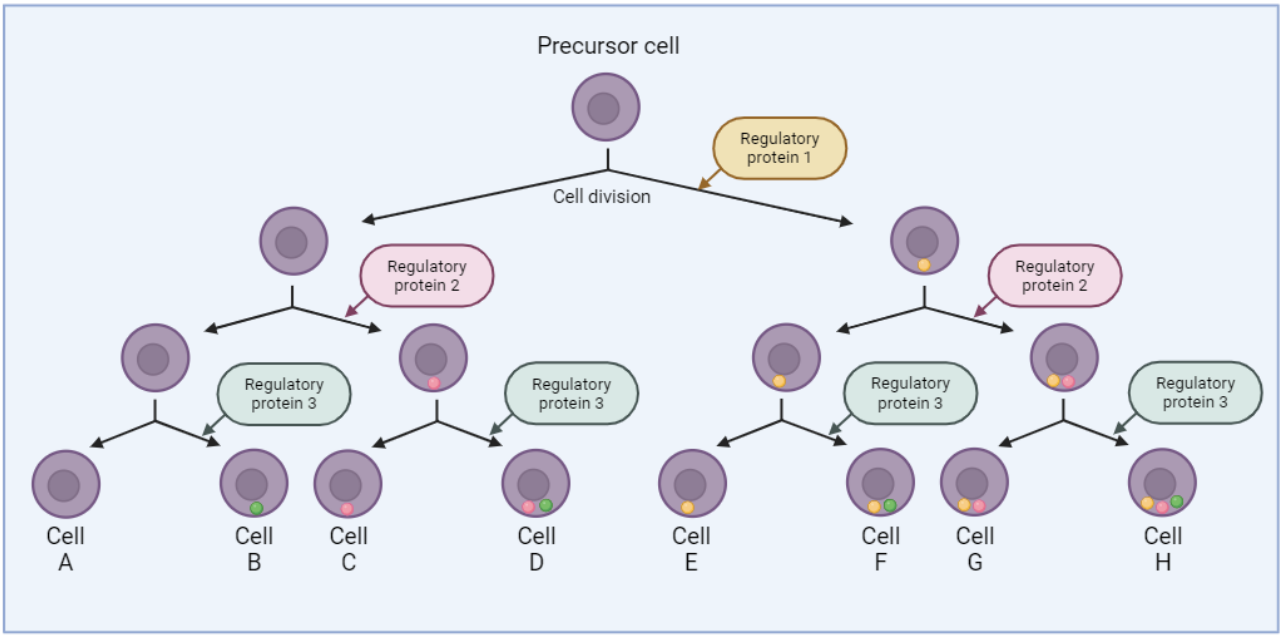

Figure 3. Exposure to various combinations of regulatory factors changes the direction of cellular subtype differentiation.

iPSCs can be printed directly on scaffolds, and how many pre-differentiation steps need to be performed to speed up functional organ production? How can we ensure that no de-differentiation will occur in the transplant-ready tissue? Additionally, the dedifferentiation of reprogrammed cells may not be the sole issue in the clinical use of iPSCs. The potential risk factors associated with iPSC-based applications include the cell source, the process of *in vitro* culturing, and the reprogramming method. A major risk is the teratoma-forming capability of the undifferentiated and pluripotent cells of the iPSC-derived donor organ.[24,25] To produce safe iPSC-derived transplant organs, quantifying undifferentiated iPSCs with a real-time monitoring system is necessary. The genetic instability of the iPSCs can be traced back to the reprogramming method or to the extended culturing of the cells *in vitro*.[26] The gene transfer of the reprogramming factors can result in the accumulation of pre-existing mutations, reprogramming factor integration-induced mutagenesis, and the resetting of the epigenetic codes of the genome.[27] A further problem is the spontaneous reactivation of reprogramming factors in the daughter cells of differentiated cells, which can result in tumor generation. The origin of the reprogrammed cell is also a crucial risk factor (Figure 4). In animal research, the transplanted, autologous murine embryonic stem (ES) cells induced teratocarcinoma formation, while xenotransplantation of ES cells did not induce tumor growth. The patient's reprogrammed cells can also carry disease-causing genes with expanded repeat regions, that can cause further genetic instability.[28] Hence, careful characterization of the donor cells is essential before any further steps are taken. From a clinical perspective, the origin and cell number remain unresolved issues for producing human transplantation—ready lung tissue.

2.4. Matrices

When the problem of cell numbers is resolved, it is essential to use degradable scaffolds and bioinks with the right biochemical and mechanical properties to support region-specific lung cells and the hierarchical lung structure.

In the proximal conducting airways, the trachea is the major airway that connects the larynx and bronchi, allowing air to enter and exit the lungs. Although the trachea is an airway, it is morphologically different from the distal airways of the lung. The trachea is composed of 16–20 cartilage rings that prevent it from collapsing. These rings are surrounded by smooth muscle and connective tissue.[29] Natural proteins, like collagen, elastin, fibronectin, and laminin, are commonly used in TE and regenerative medicine. Scaffolds and bioinks must be biocompatible and promote cell adhesion, proliferation, and differentiation.[30–32] Several scaffolds have been implemented to print a trachea, such as biodegradable reticular polycaprolactone (PCL), chitosan-based nanofiber membrane (CHIM), or a 1-day cell self-aggregation technique using a synthesized zwitterionic polymer.[33–35] The trachea scaffold has been suspended or immersed in human bronchial epithelial cells (hBECs), iPSC-derived mesenchymal stem cells (iPSC-MSCs), and iPSC-derived chondrocytes (iPSC-Chds)

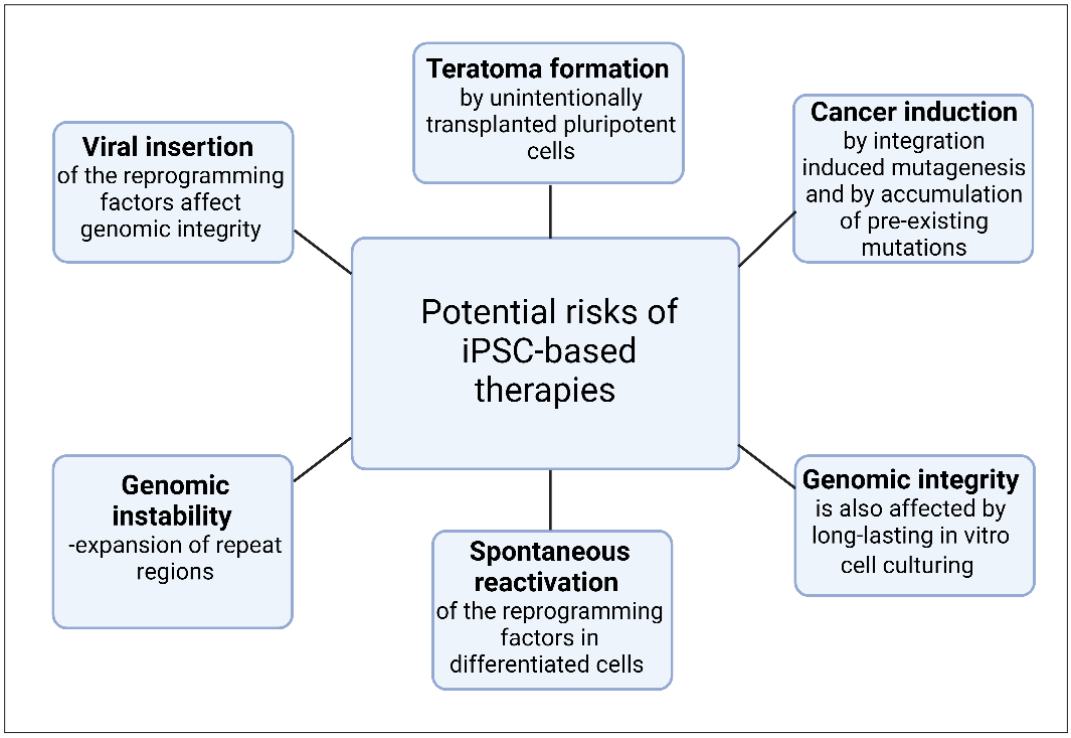

Figure 4. Overview of potential risks of reprogrammed stem cell-based therapies. Abbreviation: iPSC, induced pluripotent stem cell.

to maximize the regeneration of tracheal mucosa and cartilage cells to create the suitable tissue that is functional *in vivo*. Similarly to trachea printing, PCL and chitosan were combined with hydrogels to print bronchi and to create a lung-like structure.[36] Differentiation of the cells on the scaffolds also requires mechanical stimuli. Hence, the cells on the inner surface, for example, on the bronchi, must be exposed to air to initiate ciliated differentiation and mucus production. Practically, creating a tissue-size air–liquid interface[37] is a technique frequently used in the *in vitro* modeling of lung tissues for experimentation.

The distal respiratory airways provide different challenges for bioprinting. There are multiple modalities, but the two main categories are (i) acellular scaffold printing with subsequent recellularization and (ii) direct printing with cells suspended in a "bioink." Bioinks directly printed for the final shape with or without live cells, often include additional biomaterials, including growth factors (Figure 3), chemicals, microfactors, etc., that are mixed into hydrogels. While these hydrogels are generally soft due to naturally high water content, they can be gelled or reinforced to create functional scaffolds.[38] Hydrogels, mechanically weaker than conventional 3D-printed substrates, allow bioprinters to incorporate cells into the construct. Hydrogels are often used with the supportive scaffold, which is also necessary for producing a human-size, functional lung. The hydrogels are polymers and are made from natural or synthetic components. Components of natural polymers are designed to mimic the extracellular matrix (ECM) and include gelatin, collagen, laminin, and fibronectin, and other natural polymers such as alginate, chitosan, silk fibrin, and hyaluronic acid (HA).[39] When used alone, the hydrogels lack the mechanical strength required as bioinks, particularly for stereolithography bioprinting,[40,41] which is gaining recognition in lung bioprinting. Chemical modifications are often performed to make bioinks suitable for printing specific tissues. The mechanical properties of bioprinted constructs directly depend on the chemical composition of the bioink. HA is a widely used material that is present in the ECM and provides mechanical support and is also prone to undergo fairly rapid degradation, which might leave the maturing tissue construct without structural support before the cells can build their matrixes. Methacrylated HA (MeHA) is a chemically modified HA that can be further crosslinked by adding a photoinitiator under ultraviolet (UV) light exposure.[42] By chemically modifying gelatin with unsaturated methacrylamide groups, a crosslinkable polymer, gelatin-methacrylamide (GelMA), is created that can then be tailored for various mechanical properties and can encapsulate cells and drugs for TE.[43,44] GelMA has been used as the primary bioink to print human blood-derived endothelial colony-forming cells (ECFCs) and MSCs,

which could form a vascular network.[45] Hybrid bioinks are designed to improve the individual materials' disadvantages and desired properties. The hybrid bioink containing HA and gelatin can mimic ECM and its role in the mechanical support of native human tissues. A crosslinkable hybrid hydrogel containing GelMA and MeHA can be tailored for different TE applications.[46,47] By changing the crosslinkers and their concentrations, the storage modulus could be shifted from 100 Pa to 20 kPa, making such hybrid bioink suitable for printing several tissues, including the lung. The aforementioned matrices, cell types, and ECM molecules are summarized in Table 2.

2.5. Vascularization

The main challenge in human lung bioprinting is the development of vasculature, essential for the *in vitro*-produced lung to fulfill its primary function of gas exchange. Vasculature formation involves advancing bioinks and printing techniques to construct a viable vascular network within an engineered construct. The vasculature in the lung construct plays a crucial role in oxygen and nutrient delivery, as well as waste product transportation during maturation until the organ achieves functionality. Physiologically, cells must not be farther than 200 μm[48–50] from capillary blood vessels. The primary challenge lies in reliably printing capillaries. Capillary-sized networks have not yet been successfully printed, and there have been limitations in printing blood vessels smaller than 6 mm in diameter.[51] To address this issue, the microextrusion technique,[52] in combination with innovative and established methodologies, appears to be the most promising direction for resolving challenges in capillary network generation. Despite advancements in creating blood vessels, the techniques are slow to produce a functional vascular network and have several limitations, such as restricted sizes, shapes, and stable bifurcations.[53,54] To ensure cell survival in this environment, cellular metabolism needs to be slowed down by adding adenosine[55,56] and/or extra oxygen supplied transiently using particulate oxygen generators within the construct. However, achieving a safe and fully functional vascularization solution remains unrealized. Additionally, tissue vascularization is another challenge that should be addressed.[57–59] During the bioprinting process, the use of scaffolds and bioinks is inevitable. The goal is for the implanted scaffolds to degrade into non-toxic components, as high concentrations of waste components can be detrimental to cellular health, creating necrotic zones within the bioprinted organ, thus failing quality assurance. The extensive blood vessel network is paramount for the lung, and until this issue is resolved, clinically applicable transplant-ready lungs cannot be produced.[57,58,60–63]

2.6. Surgical suitability

While the technical challenges of creating laboratory-based organs are significant, additional requirements must be met for transplant-ready printed organs to be suitable for handling in the operating theatre (Figure 5). Therefore, additional factors must be considered alongside the challenges associated with producing a surgery-ready, transplantable lung:

(i) The tissue must be suitable for surgical procedures, e.g., suitable for suturing.

(ii) The lung must have connectable airways (bronchi).

(iii) The lung must be connectable to appropriately sized blood vessels (pulmonary artery and vein); therefore, a transplantable organ ready for surgery should also be designed and printed, bearing the above steps in mind.

After the organ is printed, the transplantation procedure will follow the standard protocol for any transplant surgery. Lung transplantation surgery typically lasts 3–8 h under

Table 2. Matrices of the airways

Airway	Airway section	Tissue-type	ECM	Scaffold-types	Cell-types
Proximal conducting airway	Trachea	Cartilage, smooth muscle, connective tissue, ciliated epithelium	Fibronectin, elastin, collagen, laminin	PCL, CHIM, CAT	hBECs, iPSC-MSCs, iPSC-Chds
	Larynx				
	Bronchi			PCL, CHIM, CAT, PCL+chitosan	
Distal respiratory airway	Bronchioles	Smooth muscle, connective tissue, ciliated epithelium	Gelatin, collagen, laminin, fibronectin, alginate, chitosan, silk fibrin, hyaluronic acid	HA or meHA hydrogels+ supportive scaffold (optional); GelMA	ECFC, MSCs
	Alveoli	Squamous epithelium, connective tissue			

Abbreviations: ECM, extracellular matrix; PCL, polycaprolactone; CHIM, chitosan-based nanofiber membrane; CAT, catalase chitosan; hBEC, human bronchial epithelial cell; iPSC, induced pluripotent stem cell; MSC, mesenchymal stem cells; Chds, chitosan derivatives; HA, hyaluronic acid; meHA, Methacrylated HA; GelMA, gelatin-methacrylamide; ECFC, endothelial colony-forming cells.

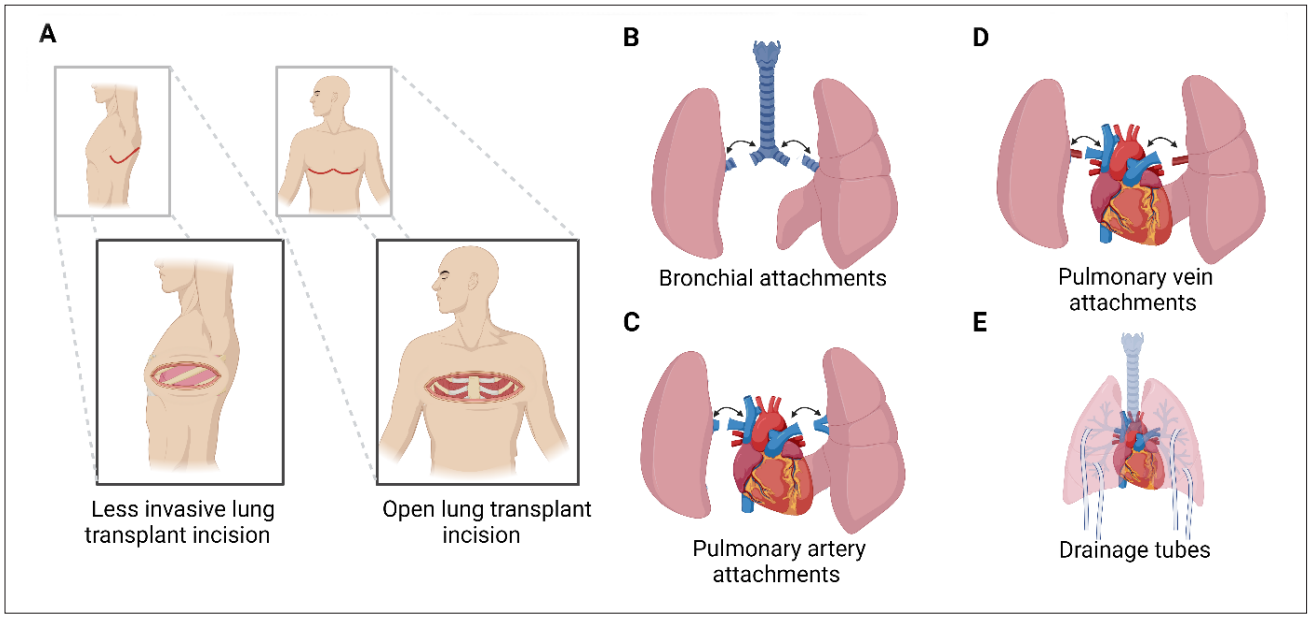

Figure 5. The process of a lung transplantation surgery. (A) Various types of lung transplant incisions. (B) The surgeon attaches the bronchial section of the donor's lung and the recipient's bronchial stub is attached by the surgeon. (C and D) The surgeon also connects the pulmonary artery (C) and veins (D) of the donor and recipient. (E) Drainage tubes are placed in the transplanted lungs.

general anesthesia, depending on the number of lung lobes being transplanted.

During the surgery, the damaged lung's bronchi and pulmonary blood vessels are cut and removed. Then, a healthy lung from a donor or, in the present case, from the tissue bioreactor is inserted. The new lung must have strong and fully formed airways and blood vessels, like those of a healthy human lung, to be connected to the recipient's airways and blood vessels. The surgery is completed by closing the incision. While all surgeries have risks, organ transplant surgeries carry high risks of infection, bleeding, and death. Even if a well-prepared and tested lung transplant is created using the patient's cells, there is still a potential risk shared with donated lungs. This risk is primary graft dysfunction, which is the most common cause of death after lung transplantation. Recent data from the International Society for Heart and Lung Transplantation Registry revealed that adult lung transplant recipients since 2010 have a 1-year survival rate of 85% and a 5-year survival rate of 59%. Despite ongoing advancements in patient and donor selection, surgical techniques, and pre- and postoperative care, lung transplantation survival rates still fall short of expectations.[64] The main reason why the development of macroscale printed organs is pursued, apart from the shortages of transplantable organs, is to avoid the additional risks associated with organ transplantation. If the printed organ is created from the recipient's cells, donor lung rejection is not expected, eliminating the need for immunosuppressant medications. Consequently, complications after surgery (e.g., kidney damage[65] or increased cancer and infection risks[66]) can be avoided.

2.7. Quality assurance

When printing a therapy-ready and clinical-grade organ, quality assurance must begin by ensuring the quality of the cell source, testing the donor and the harvested cells, and then scaling up the process to increase the cell numbers. First, the patients or donors must be screened for health and cleared to undergo the biopsy in a suitable operating room. Documentation of the entire process must follow each step. Biopsies have to be transported to a manufacturing facility for cell extraction. Using an iPSC-based therapy, somatic cell isolation will be followed by cell expansion to initiate the reprogramming procedure for the iPSC line. The entire process should utilize good manufacturing practice (GMP)-grade reagents, consumables, and facilities to ensure clinical compliance. GMP is critical for cell therapy, as it ensures the consistency, safety, and quality of therapeutic products. By adhering to GMP standards, risks such as contamination, variability, and errors in production are minimized, which is essential for patient safety and the efficacy of cell-based treatments. Compliance with GMP also meets regulatory requirements, facilitating the approval process and ensuring that the cell therapy product can be reliably and safely scaled for clinical use.

Once the organ is printed and matured, quality assurance of the functionality of the printed organ would be essential before even attempting surgical application of the *in vitro*-prepared lung.[67,68] Due to the unresolved challenges of biomanufacturing transplant-ready organs, relatively little attention is given to quality assurance in biomanufacturing. Quality assurance must be an independent field that develops in parallel with transplantation ready organs and rigorously scrutinizes every aspect of organ production, function, and transplant surgery. The *in vitro*-prepared lung tissue must have all the functional cell types, cultured most likely from iPSCs to complete organ cultures; cells and tissues must be infection-free (including mycoplasma) throughout the preparation. The final tissue must have a tight capillary network, culminating in pulmonary blood vessels. Test methods for building such organs and testing the complete biostructure before surgery require further development of bioreactors, allowing continuous oxygen and nutrition supply until the organ is mature enough to be used in surgery. Hence, the engineering requirements of *in vitro* organ production have to be developed in parallel with TE, focusing on the final product. Currently, we can only anticipate the primary requirements for quality assurance. Firstly, preliminary biocompatibility and safety testing will be required on animals to ensure that the 3D-bioprinted materials are not harmful and that the printed lung functions effectively, essentially validating that the protocol to print a functional lung is potentially suitable for human lung bioprinting. Thereafter, the printed organs will need to undergo clinical trials with human subjects, provided that the quality assurance protocol for each newly produced lung proves that the organ is functional. The key question is how the quality assurance will be carried out. As there is currently no fully functional bioprinted human lung, a standard quality assurance methodology has not yet been developed, hindering bioprinted lung tissue production and its clinical application.

2.8. Legislative regulation

The primary principle to conduct organ production for human beings involves the clear determination of ethical principles. Countries have developed ethical guidelines for conducting and evaluating research involving human participants, and many of these are necessary for organ production. The main guidelines are outlined in the World Medical Association's Declaration of Helsinki[69] and the Council for International Organizations of Medical Sciences (CIOMS) International Ethical Guidelines for Health-Related Research Involving Humans.[70]

In most countries, the country-specific biomedical research councils have adopted the CIOMS guidelines,[70] regulating the collection, storage, and use of biological materials and related data. Additionally, in the European Union (EU), the EU Tissues, and Cells Directive[71] sets quality and safety standards for the donation, procurement, testing, processing, preservation, storage, and distribution of human tissues and cells. In the United Kingdom (UK), the Human Tissue Act 2004[72] regulates the application of human cells and tissues; in the United States of America (USA), this is governed by the Code of Federal Regulations[73]; and in Australia, the guidelines are covered by the National Health and Medical Research Council.[74] Human biospecimens in laboratory-based research or transplantation are well-established. However, the challenge of personalized tissue production for patients in need of *in vitro*-made transplantable organs is compounded by the lack of well-defined administrative regulations for *in vitro*-produced, complex, functional tissues. To streamline regulatory pathways, it is crucial to establish clear and expeditious legislation for this relatively novel biomanufacturing process. The laws should facilitate the rapid implementation of organ production methods that can be brought to the market. Furthermore, the biotech industry requires support to navigate the regulatory framework and to scale up from research to biomanufacturing.[75] Although attention is given to the issue in the EU,[76] the series of overarching recommendations do not yet provide clear, step-by-step protocols for the research and biomanufacturing community to follow and implement the legal and ethical aspects of their work. Certainly, ethical and legal issues must be addressed, and solutions must be clearly communicated to the research and biomanufacturing community. This community is working on establishing regulations for biomanufacturing and approving biomanufactured products, especially when creating complex organs like the lung. In the USA, permissions are granted by the Institutional Review Boards; in Canada, by the Research Ethics Boards; and in Australia, by the Human Research Ethics Committees. These institutions must collaborate with administrative agencies for approval of drugs, devices, or diagnostic tools for sale or use in clinical settings, which is overseen by national drug and therapeutic goods regulators such as the US Food and Drug Administration (FDA) or the Australian Therapeutic Goods Administration. In Europe, the EU Medical Device Regulations also apply; in China, several agencies control the regulatory field.[77] It is important to note that not only the procedures but also the tools used in the process need to comply with standards and regulations. Currently, the biggest challenge in creating engineered tissues is that neither bioprinters nor bioreactors have medical device

Conformité Européenne (CE) certification (CE, EU) or GMP certification.

3. Aggregates and organoids for *in vitro* microscale lung tissue for clinical applications

It is crucial to study cell–cell interactions and differentiation processes in the normal lung to comprehend deviations from health and to gain insights into the development and progression of lung diseases. These studies can aid in creating lung tissue models that replicate lung diseases and in testing drugs for safety and efficacy. Furthermore, these investigations offer the opportunity to explore differences in therapy responses among various populations and to tailor medicine accordingly. Understanding the regenerative potential of specific tissues is also vital for promoting the generation of healthy, self-derived cells in the regenerative process, thereby reducing the reliance on complex medication and surgery as therapy (Figure 6). Hence, microscale lung tissue models can be just as clinically relevant as the transplantation-ready, functional lung.

3.1. Normal physiology

Based on the knowledge of lung anatomy and molecular studies, it has been realized that cell functions are governed by internal processes and various external factors, including direct and indirect interactions with neighboring cells, ECM, and soluble factors that shape and differentiate cells into specific tissues by additional physical forces.

In the initial 3D pulmonary models, a significant advancement was the use of mixed cell tissue cultures comprising primary human small airway epithelial cells (SAECs), normal human lung fibroblasts (NHLFs), and human microvascular endothelial cells (HMVECs). Together, these cells create the necessary ECM and restore specific tissue differentiation markers characteristic of the proximal or distal respiratory tract (Figure 7A), including surfactant proteins.[78] These markers are lost when lung epithelial cells are cultured in 2D environments. If the above primary cell types are simply incubated (natural gravitation) or forced (centrifuged together) to sediment in a low-affinity tissue culture plate, they form an aggregate culture within 24 h. The simplest distal airway model is

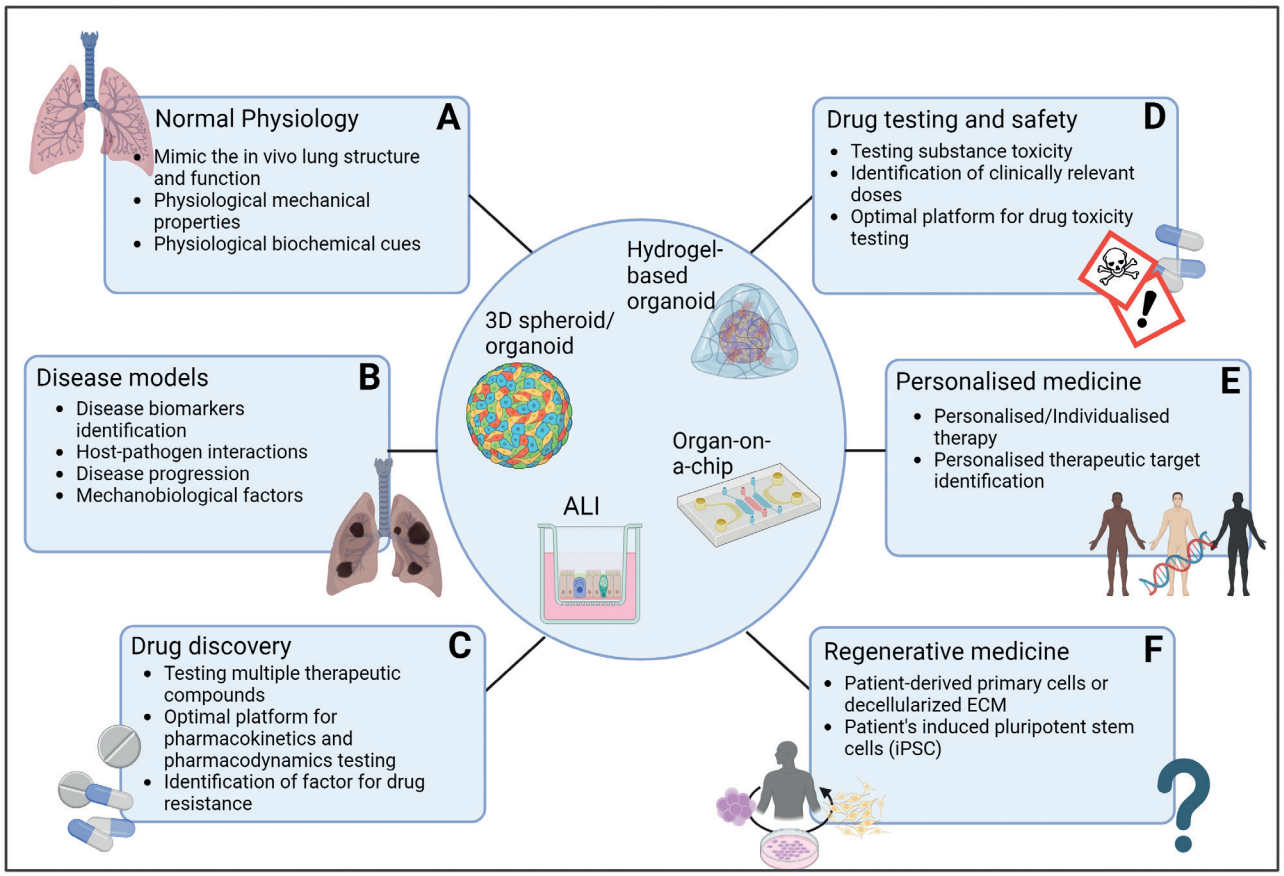

Figure 6. Summary of various applications of lung micro-tissue models. Abbreviations: ALI, air–liquid interface; ECM, extracellular matrix.

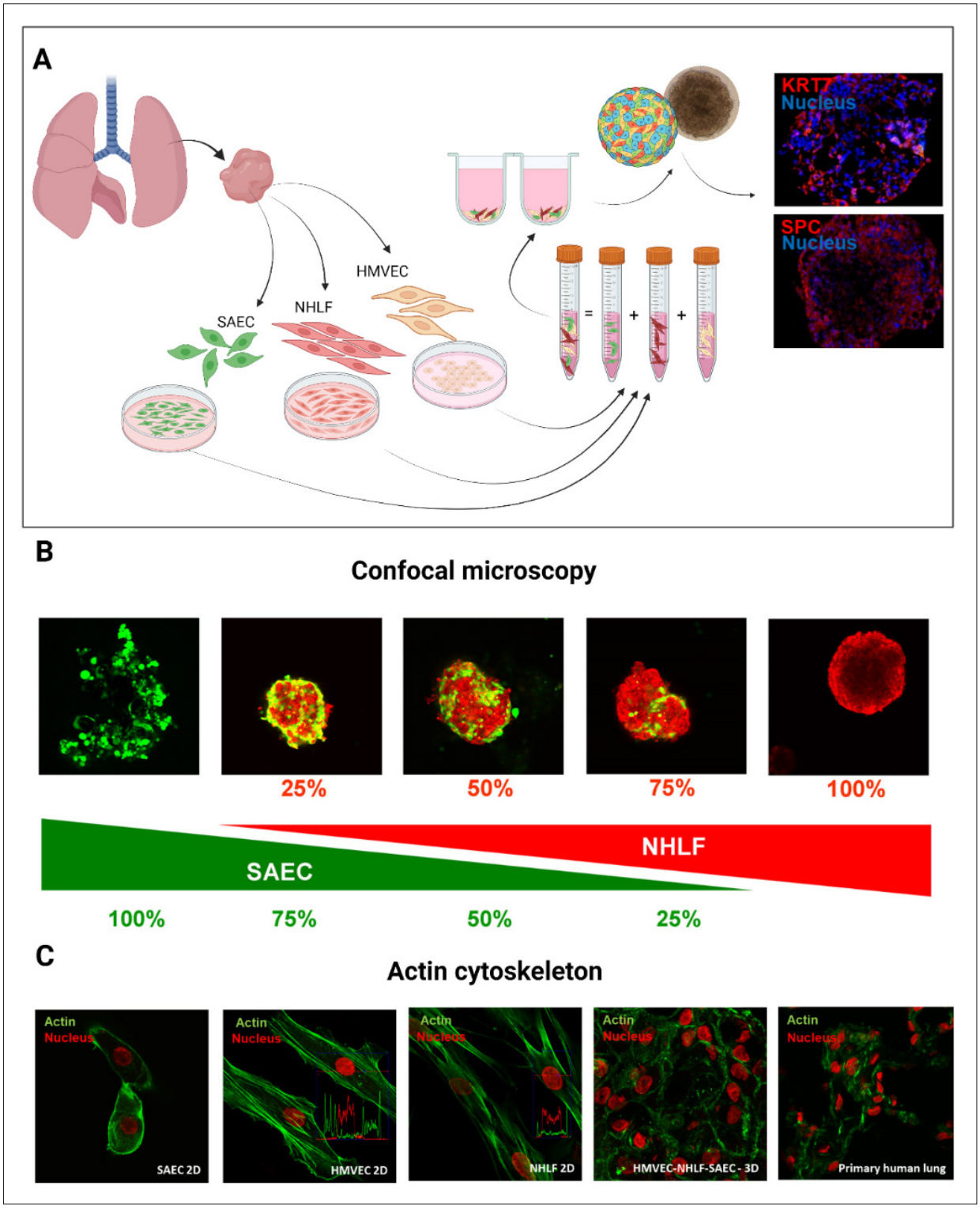

Figure 7. The production and characterization of 3D aggregation cultures. (A) The visualized protocol of the 3D aggregate models, with three different cell types. The fluorescent microscopic images display the molecular characteristics of the cells (red: KRT7 and SPC; blue: nuclear staining). (B) Confocal microscopic images of 3D aggregate models of SAEC and NHLF cells in different relative ratios. Cells in 2D monolayers were washed twice in PBS and incubated with CFSE, DiI, or DiD at the concentration of 0.5 μg/mL at 37°C for 10 min. (C) Confocal microscopic images of the actin cytoskeleton of various cell cultures versus human primary lung (green: actin; red: nuclear staining). Abbreviations: SAEC, small airway epithelial cells; NHLF, normal human lung fibroblasts; PBS, phosphate-buffered saline; CFSE, Carboxyfluorescein succinimidyl ester.

the combination of SAEC and NHLF at varying ratios, followed by the incubation of the aggregates for various lengths of time, depending on the purpose of the tissue model. The maximum size of such aggregate culture cannot exceed 500 μm in diameter and contain no more than about 30,000 cells in total. Otherwise, the inner core of the aggregate becomes necrotic due to a lack of nutrition and oxygen. The inner structure of such 3D aggregates maintains a certain arrangement due to the cell type-specific surface tension of cells.[79,80] Tracing the location of SAECs and NHLFs specifically within the aggregate, the individual 2D monocultures were first stained with fluorescent physiological dyes (carboxyfluorescein succinimidyl ester [CFSE], DiI (orange fluorescence) [DiIC18(3) or 3H-Indolium] and DiD (red fluorescence) [DiIC18(5) a longer-wavelength DiI analog], respectively). Within the aggregates, SAECs formed the outer layer on the surface of the inner NHLF core network.[81] The tissue size depends on the epithelial cell-to-fibroblast ratio and the total cell number (Figure 7). During the 24-h time frame, differentiation cannot be detected; instead, only the preferential location of each cell type in the aggregate can be observed (Figure 7B). This arrangement is based on the cell surface tension and biophysical parameters mentioned above. The arrangement of the cytoskeleton also changes depending on the type of cell culture and the cell types used creating the lung model. Adding endothelial and smooth muscle cells to the model can enhance its complexity. In 2D monolayers, the actin cytoskeleton demonstrates the stretched-out formation of the cells; in 3D aggregate cultures, the actin cytoskeleton takes on the formation that is highly similar to normal primary lung tissue pattern (Figure 7C), which becomes detectable after 72 h in culture.[82] The presence of endothelial cells was also found to stimulate the expression of functional molecules such as ABC drug transporters.[83] This makes the aggregate models easy to create and suitable for investigating biochemical mechanisms and molecular regulation of healthy and diseased lung tissues.[84] Such tissue structures are also suitable for testing the functionality of the expressed molecules and drug response.

Cells in the airways are exposed to mechanical effects; hence, the most effective models for producing tissues closely resembling normal human airways are those subjected to constant dynamic stress and oxygen tension. Among the various methodologies currently available, the air–liquid interface (ALI) method stands out for its simplicity and ability to promote cell differentiation and optimize the morphological and histological characteristics of airway epithelial cells.[37]

The epithelial layer exhibits various functional phenotypes, such as tightly packed cells forming a barrier to external elements through tight intercellular junctions, cilia growth, and mucus secretion. These phenotypes depend on the tissue type and mechanical effects. This model requires exposure to air to develop these properties. The mechanical environment within the bronchial airway model, whether normal or modified (e.g., constricted airways), is distinct.[85] In order to replicate constricted airways, we need to apply lateral compressive strain to the model, inducing buckling folds similar to those observed *in vivo*. This compression can lead to matrix deformation affecting hBECs and human fetal fibroblasts (HLFs), which are in direct communication via the ECM. It is crucial to analyze the system's response to mechanical strain and the interaction between different cell types sharing the same ECM. This investigation can shed light on normal development, the effects of mechanical strains, disease development, or any other stimuli and associated molecular changes.

The 3D lung models previously mentioned generate their own ECM. However, in creating intricate tissue models, hydrogels[37] are frequently used. Hydrogels are gel-like materials containing networks of interconnected polymers that are swollen with water. They are available in various forms and are employed to mimic the functions of the ECM, which surrounds and sustains cells in our tissues. Hydrogels can help create complex tissues and provide experimental systems to modify molecules that affect tissue differentiation and natural physiology. This is important for gaining a better understanding of normal human lung physiology and for creating controls for disease models.

3.2. Disease models

Understanding the mechanisms that drive human disease pathologies is essential for developing effective treatments. However, this is a complex task due to the lack of biologically relevant disease models. Rodents have been extensively used to attempt to replicate human diseases for many years, owing to their status as mammalian models that lend themselves to experimental assessment and genetic engineering. The fundamental interspecies differences render it impossible for rodent models to precisely mirror or fully reproduce human clinical pathophysiology.[86]

Several companies offer the same cell types (SAEC, NHLF, HMVC, etc.) isolated from patients suffering from lung complications (e.g., asthma and COPD). By applying the same model system for the controls as for the donated cells, and using the same growth and air–liquid interface media, researchers can create disease models that reflect the great variety of human lung diseases using the techniques mentioned in the previous section. However, primary cell types are not as readily available, which may

limit the cell numbers available to generate the required quantity of tissue aggregates. As a result, more tests and analyses could be conducted using recently developed methods involving iPSCs derived from patients suffering from various lung diseases.

Human iPSCs (hiPSCs) have emerged as an attractive platform for overcoming the conventional limitations of animal models and primary lung cells from patients with lung diseases. The simple aggregate or hydrogel models using iPSCs are suitable for studying a great variety of lung diseases, gaining spatial and temporal data on tissue morphology, and providing the opportunity to identify disease biomarkers and factors that induce disease progression. The aggregate and hydrogel cultures described above are easy to create and use in the laboratory, while the whole arsenal of molecular technology[87] and clinical and open databases support the analysis of disease progression.

For example, hydrogels could provide the necessary binding capacity[88] and a more comprehensive *in vitro* model of the airway wall as a dynamic system. Due to its ability to support multiple cell types without contracting the matrix, this model is suitable for observing and understanding the long-term effects of factors, such as inflammation and mechanical stress, on remodeling. It is especially relevant for studying remodeling events associated with asthma.[89] The development of appropriate disease models, such as ALI, for investigating asthma and identifying drug targets is essential to streamline the drug discovery and test process. As the models work similarly to the human body, the developed medications are likely to be more effective with fewer adverse reactions. It is essential to have non-invasive methods for measuring cellular functionality and maturation in tissue model systems (e.g., ALI) to ensure their reliability. A commonly used technique for this purpose is trans-epithelial electrical resistance, which assesses the permeability of the cell or tissue layer to monitor barrier integrity. Preserving intact barriers is crucial for evaluating the transport of small molecules or drugs across the barrier in these model systems.[90]

3.3. Drug discovery

Understanding and confirming potential drug targets involves delving into the intricate mechanisms and specific points where intervention can be effective for a particular disease or condition. It is essential to ascertain that a potential target plays a pivotal role in initiating and perpetuating the disease. According to the hypothesis, there are diverse potential targets to consider for intervention, including genes, epigenetic factors, proteins, RNA, miRNA, and other components involved in the disease's pathogenesis that could be targeted for treatment or modulation.

Despite a surge in investments in drug research, most drugs fail during clinical stages due to various reasons. One significant factor contributing to this translational gap is the heavy reliance on animal-derived data[91,92] to make decisions about advancing a drug candidate into clinical trials. Consequently, biomedical research is currently undergoing a significant shift toward approaches centered on human disease models, including micro-tissue lung models, such as organoids, functionality models, and the cutting-edge technology of organs-on-chips (OOCs).[93] This paradigm shift has been fueled by the notably high failure rates of the current drug development process.

Organ-on-a-chip (OOC) microfluidic cultures represent a groundbreaking advancement in human tissue mimicry, simulating the intricate cellular interactions, molecular regulations, and mechanical influences that cells experience within real organs (Figure 8A). This innovative technology is revolutionizing our ability to replicate organ-level functions and responses, offering a more accurate model of physiological systems. On a chip, the microfluidic form of a microphysiological system can be of different sizes and shapes, but all contain hollow channels lined with living cells and tissues cultured under dynamic fluid flow (Figure 8B). Several different fluid systems have been built from suitable materials and miniature pumps and the application of microphysical forces to move fluids and attached detection systems.[94] While microfluidic systems involve tiny volumes, they also ensure fast interactions between fluids and cells. The pulmonary alveolus model was created using a soft lithography-based[95,96] manufacturing approach, adapted from the microchip industry. The microfluidic lung alveolar chip device was made from optically clear, elastomeric polydimethylsiloxane material[97] that contains two parallel hollow channels separated initially by a porous membrane,[98] which was eventually replaced by an ECM gel to support tissue ECM formation.[99,100] The channels coated with ECM and lined with epithelial (SAECs differentiated into AT1) cells on one side and endothelial cells (HMVEC-L) on the other to mimic the alveolar–capillary interface. The suitable culture medium is perfused through the endothelium-lined channel to mimic vascular perfusion, while air is introduced into the epithelial channel to mimic the air–liquid interface in the lung, promoting polarization, and differentiation of the epithelial cell lining. It also instigates cyclic aspiration on the hollow side chambers, allowing cyclic tissue deformation to occur at the flexible tissue–tissue interface, and mimicking respiratory movement.

Human-based models are invaluable tools in every stage of the drug development process, including high-throughput screening to identify target or lead molecules, efficacy and safety testing in preclinical stages, and

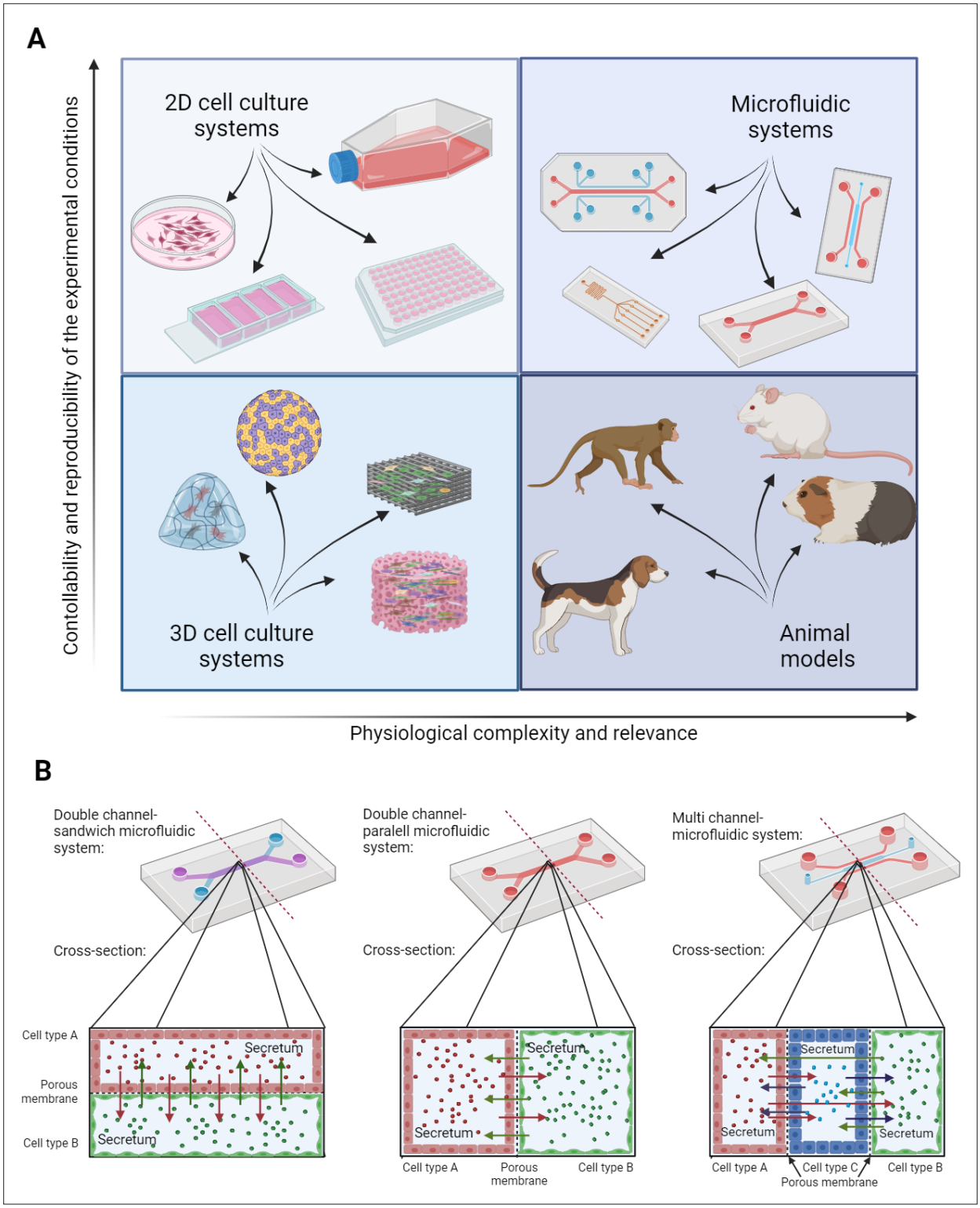

Figure 8. Complexity and reproducibility of disease models. (A) *In vitro* and *in vivo* techniques used in the pharmaceutical industry for testing toxicology and efficacy. (B) Various complexities of microchips using fully human tissue mimicking microfluidic systems for reproducible testing.

implementation in clinical trials and decision-making. Rational drug design and development require a proper understanding of the underlying disease mechanism. The need for *in vitro* human lung modeling became apparent during the COVID-19 pandemic. For instance, central disease mechanisms, such as endothelial dysfunction, the "cytokine storm," and the variability of infection susceptibility between cells, were identified using organoids and lung-on-a-chip models.[101–104] It was discovered that exposure to Sars-CoV-2 (Severe acute respiratory syndrome coronavirus 2) significantly reduces endothelial barrier function, leading to increased release of pro-inflammatory cytokines. Endothelial dysfunction is aggravated upon the introduction of peripheral blood mononuclear cells, resulting in excessive inflammation. Organoids also exhibit inefficient interferon responses after COVID-19 infection, highlighting the value and predictivity of human micro-tissue models. Organoids of the lung and other tissues, such as the brain, kidneys, and heart, have facilitated the identification of SARS-CoV-2 tropism[105] and receptor angiotensin-converting enzyme 2 preferences, making it easier to identify the most likely target organs. Similar examples include allergic asthma[106] and influenza. It was found that organoids can be supplemented with primary immune cells to closely mimic the host microenvironment following infection, aiding the understanding of disease mechanisms and drug target identification. The 3D human cell-based infection models were extremely valuable in identifying new antiviral treatments and repurposing drugs. Over a thousand drugs were tested using high-throughput screening against COVID-19, and some have been approved by the United States (US) FDA. Interestingly, when physiological breathing mechanics were applied in alveoli-on-chip models, it was found that mechanical stimuli increased the expression of interferon-related genes and improved the host's defense, indicating antiviral activity.[107]

Significant progress has been made in the fight against cancer through the use of human disease models. In human-derived organoids, MCLA-158, a bispecific antibody that targets the epidermal growth factor receptor (EGFR) and leucine-rich repeat-containing G-protein-coupled receptor 5, emerged as the most effective antibody against wild-type and KRAS (Kirsten rat sarcoma virus)-mutant colorectal cancer (CRC) after screening a large biobank of patient-derived CRC organoids; the research results have reached clinical application within 3 years.[108] A similar result was achieved in the treatment of non-small cell lung cancer (NSCLC), where the efficacy of amivantamab, a bispecific antibody against EGFR and the mesenchymal-epithelial transition receptor, was preclinically tested in patient-derived cells and organoids with EGFR Exon20ins mutations.[109] Patients with this mutation have an extremely poor prognosis because standard tyrosine kinase inhibitors are not effective in therapy. These results were validated in clinical trials, leading to the approval of amivantamab by the European Medicines Agency for the treatment of EGFR mutant NSCLC.

3.4. Drug testing and safety

Pharmaceutical applications of human tissue models were considered early on when the 3Rs (Replacement, Reduction, and Refinement) of animal testing were introduced as a concept over 60 years ago.[110,111]

Due to strict regulations in the pharmaceutical industry, implementation remains difficult despite billions of dollars being spent on drugs, vaccines, and advanced therapeutic products that fail in humans after successful pre-clinical animal testing. Some fail to demonstrate efficacy, like the tuberculosis drug MV85a[112]; while others, like the monoclonal antibody Hu5c8 (CD40L), exhibit life-threatening toxicity[113,114] and unexpected thrombotic complications. Researchers are working relentlessly to make human tissue systems available for human disease research and drug testing.[115] Certainly, the USA has recently taken a bold step forward, evidenced by the US FDA Modernization Act of 2021[116] and the Humane Research and Testing Act (HR 1744).[117,118] Unfortunately, neither Act that was passed by the 117th Congress makes *in vitro* drug testing compulsory for human drugs before clinical trials commence.

Nevertheless, researchers are working to develop a great variety of pre-clinical *in vitro* models to address the challenges posed by the safety and efficacy testing of human medications. The use of 3D cultures in drug target identification, drug efficacy testing, and toxicity assessment is high on the agenda, as selecting the most effective compound for clinical trials is in the interest of the pharmaceutical industry.

The recently developed multicompartment nasal-bronchial-acinar-on-chip has demonstrated cytokine responses in lower lung compartments upon administration of an aerosolized virus to the nasal chamber.[45] However, this study has not applied cell stretch, which could enhance aerosolized nanoparticles' cellular uptake and transport.[46] The development of complex *in vitro* models to emulate the interplay between various lung compartments with aerosolized drug delivery could improve the predictive capacity of lung models to study the fate of aerosol inhalation.

The microfluidic-based platform for lungs suffers from a lack of high throughput, which, albeit not harmful during the initial drug discovery phase, poses a severe challenge

in the later stages of drug development. Adapting the outcome of current microphysiological systems to the drug development pipeline is challenging due to the inaccurate extrapolation and scaling-up of data to the *in vivo* level. Potential strategies would be cell assay standardization, scaling up the microvolume size of these platforms using parallel cell culture chambers,[47] or applying milli-scale systems, such as the newly developed mini-lung model.[36]

The establishment of healthy/disease *in vitro* models based on isolated human primary cells or hiPSCs using organoid technology[57–59] or organotypic cells from patients (disease-specific) could enhance the mimicry of the models, such as cell–cell interactions and cellular responses. It could also improve the prediction of drug pharmacodynamics and pharmacokinetics, thereby facilitating *in vitro–in vivo* translation. It has been reported that the culture of ATII cell-derived organoids under physiologic stretch conditions (10% strain) using alveolus-on-chip could preserve the ATII phenotype (such as supported by the expression of SPC [Surfactant Protein C]).[60] Likewise, a lower expression level of vimentin as an epithelial-mesenchymal transition-related marker was observed compared to the static Transwell inserts. Hence, combining the lung-on-chip models with primary cell-derived organoids[61,62] could enhance the predictive capacity of the preclinical models for at least some clinically relevant aspects to levels higher than those obtained with animal models.

The developed systems involve aggregate cultures (often called spheroids or organoids) as well as OOCs or body-on-a-chip (BOCs) microfluidic cultures by fluidically coupling two or more organ chips.[119] A microfluidic lung model was used, for example, to investigate drug-induced pulmonary edema[120] by mimicking the physiology of the distal lung as OOC.

The advances in stem-cell technology have enabled the cultivation of personalized stem cells that can now be integrated into OOCs for studying disease progression, identifying drug targets, and testing developed drugs for safety and efficacy.[121]

As the sophistication of the models increases, advancements in OOC technology can shift the focus to complex human tissue tests instead of animal testing before clinical trials in the future.[122] This shift is important in personalized medicine, as the need for personalized therapy is highlighted by inter-racial disparities in drug response, stressing the importance of considering diverse genetic factors in optimizing treatment outcomes.[123]

3.5. Personalized therapy selection

A broad variation in individual response to the same therapy can be caused by differences in the molecular microenvironment within the affected tissue, personal variability in the patient's genetics, environmental effects, etc., influencing the treatment selection and therapy outcome.

Currently, the most widely studied therapy response is investigated in cancer therapy, where a well-identifiable altered tissue can be removed from the affected person to identify drug sensitivity, drug administration sequence, and selection of the best sequence of combination therapy.[124,125]

By preserving or recreating the individual tumor microenvironment *in vitro*, we can test drug responses and identify the most effective drug combinations for therapy. Creating these test systems is easy to understand, as they are similar to the methods used to identify specific antibiotics for microbial infections. Just as antimicrobial resistance remains the world's most urgent public health concern,[126] cancer cells can also inherently possess or develop drug resistance.[127]

In clinical applications, the use of 3D lung micro-tissues serves as groundbreaking test systems for the precise selection of cancer therapy. This innovative approach promises to revolutionize cancer treatment by providing a more tailored and effective strategy. For example, in NSCLC,[128] a suspension of solid cancer tissue is created, which is then reaggregated and exposed to recommended chemotherapeutic drugs and combinations; the results can be compared with patient therapy responses. The importance of personalized drug response testing became evident through an analysis conducted by the Evidence-based Synthesis Program, which reviewed over 820 trials and published meta-analyses.[129–132] The conclusions were ambiguous and determined mostly what was already known; doublet chemotherapy with a platinum agent has a slight advantage over non-platinum doublets[133]; cisplatin combinations may have a slight advantage over carboplatin combinations in terms of survival and response rate.[134] However, carboplatin generally has a milder toxicity than cisplatin.[135] Triplet cytotoxic therapy might have some slight advantages in terms of response rate but at an increased risk of toxicity; doublet chemotherapy probably has slight benefits in terms of survival compared to singlet therapy but causes more toxicity. The question remains: why are the drugs not chosen more effectively? According to general treatment guidelines (www.cancer.org), in NSCLC, the most commonly used chemotherapeutic drugs include cisplatin, carboplatin, paclitaxel, albumin-bound paclitaxel, docetaxel, gemcitabine, vinorelbine, irinotecan, etoposide, vinblastine, and pemetrexed.[136] The 11 different kinds of chemotherapeutic drugs are most often applied as a combination, typically involving two selected drugs—either two chemotherapeutic drugs or in combination

with targeted therapy drugs, such as afatinib, gefitinib,[137] crizotinib, certinib,[138] bevacizumab,[139] cetuximab, and ramucirumab.[140] These therapies target specific small molecules in signaling pathways or the immune system, including nivolumab and ipilimumab.[141]

The unpredictable efficacy of therapy is not surprising, as over 140 driver mutations[142–145] and an unknown number of passenger mutations[146–148] have been identified, both of which may impact carcinogenesis. Effectively, at least two to eight driver mutations per cancer sample regulate

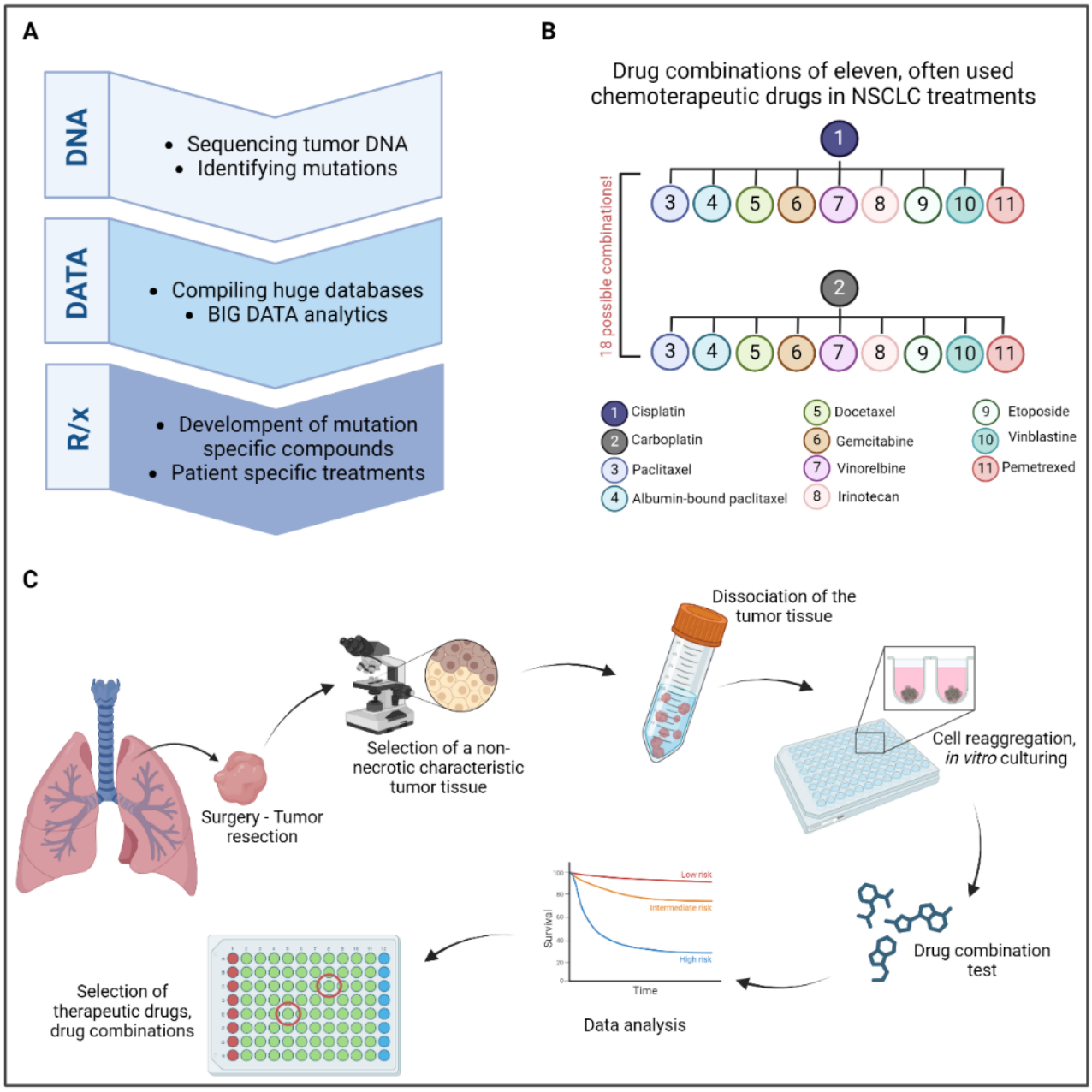

Figure 9. Lung models in personalized medicine. (A) The response of the biotech industry to the challenges of cancer genetics. Analyzing sequenced tumor DNAs and identified mutations can form the basis of personalized medicine. (B) The combinational options of different chemotherapeutic drugs used in the treatment of NSCLC. The listed drugs can be applied in 18 different combinations to treat the disease. (C) Resected dissociated, reaggregated, and *in vitro* cultured tumor cells can provide a useful platform for finding the best combination of chemotherapeutic drugs to treat cancer in a personalized way. Abbreviation: NSCLC, non-small cell lung cancer.

cancer progression. Additionally, non-mutation-induced metabolic changes and personalized environmental factors can also modulate therapy response, making therapy selection extremely challenging for the clinical team (Figure 9).

Hence, clinicians could determine the best combination of drugs—those with the most efficacy and the least adverse effects—on an individual level if the potential drug combinations were tested on the tumor tissue *in vitro* after surgery and before therapy selection (Figure 9), while the patient recovers from surgery and becomes ready for chemotherapy, targeted therapy, or immunotherapy.[149]

3.6. Lung tissue regeneration

The key therapeutic promise of investigating lung tissue regeneration is its potential to cure acute lung failure and reduce the need for lung transplantation surgery. Lung tissue possesses a natural regenerative ability, initiating repair processes following injury. Under controlled conditions, lung tissue can fully restore its normal structure and function. Disruptions in this process can lead to respiratory system failure and even death. The primary types of respiratory diseases include COPD, idiopathic pulmonary fibrosis, and acute respiratory distress syndrome. Various cells, such as lung epithelial cells, endothelial cells, fibroblasts, and immune cells, are involved in regulating lung injury repair. Although the regulatory mechanism of lung repair has not yet been fully elucidated, clinical trials are targeting different cells and signaling pathways to achieve therapeutic effects. For example, primary lung stem cell-like ATII cells were induced to transdifferentiate into ATI (AT1-like) cells[9] by changing the wingless (WNT) ligand microenvironment in 3D lung microtissues. While WNT4 and WNT5A downregulated ATII-type characteristics, the presence of WNT7A strengthened ATI-like markers, including aquaporin 5 (AQ5). Identification of all the markers, cytokines, miRNAs, and other factors involved in the process of lung tissue regeneration is still in its early stages. However, the establishment of healthy and disease *in vitro* models based on isolated human primary cells or hiPSCs using 3D lung microtissue technology enhances the mimicry of the models, such as the cell–cell interactions and cellular responses. This approach can facilitate combination therapies for faster recovery of lung tissue after disease-induced damage. Most available *in vitro* lung models investigating regenerative processes rely on primary or iPSCs to mimic proximal or distal pulmonary cells during tissue damage. These models also help identify the best combinations of factors for tissue regeneration.

4. Conclusion

The intricate 3D structure of the lung tissue, characterized by thin boundaries and interconnected pores, presents significant challenges for bioprinting. Technical limitations and unresolved ethical and legal issues complicate the process. While research laboratories are making progress in overcoming these technical challenges, the prospect of a transplant-ready organ currently remains distant from clinical reality. However, researchers and engineers in the TE sector are relentlessly advancing lung bioprinting, committed to developing fully functional, transplantation-ready lungs. They are also determined to overcome the significant challenges, while fully recognizing that achieving this milestone may take several decades. Nonetheless, at present, the growing understanding of lung tissue complexity suggests that regenerative therapy could become a more effective and safer alternative for specific disease types.

Meanwhile, advances in lung bioprinting technologies and discoveries are enhancing our understanding of molecular interactions in healthy lungs. Disease-specific lung models are crucial for identifying new drug targets, improving our understanding of metabolic changes, and offering robust systems to test new drug candidates' safety and efficacy. These accomplishments are driving drug development and regenerative therapy forward. Additionally, further research in various fields, including bioink development, chemistry, materials science, bioprinter, and bioreactor engineering, is crucial to effectively model the lung for individual clinical applications. The most promising human-based preclinical *in vitro* lung models with high clinical translational capacity include detailed, complex tissue models derived from patient-specific cells, and leading *in vitro* platforms that mimic more physiological and pathological conditions through non-invasive functional analysis. There is significant potential in modern fabrication technology and approaches to achieve truly biomimetic material designs, integrating tissue-specific multicellularity with structural and mechanical biomimicry. This approach can produce biologically functional and realistic *in vitro* lung tissue models suitable for clinical applications, ultimately improving the health of individuals with lung diseases.

Acknowledgments

None.

Funding

This work was funded by a grant from the University of Pécs (grant number POC/2024).

Conflict of interest

The authors declare they have no competing interests.

Author contributions

Conceptualization: Judit E Pongracz
Visualization: Judit Bovari-Biri, Borbala Lovaszi
Writing–original draft: Judit Bovari-Biri, Judit E Pongracz
Writing–review & editing: All authors

Ethics approval and consent to participate

Not applicable.

Consent for publication

Not applicable.

Availability of data

Not applicable.

Further disclosure

Part of or the entire set of findings has been presented at a conference (The role of 3D bioprinting in drug testing (in Hungarian). 2018, Partner Day Conference, Pécs, Hungary).

References

1. Barnes-Harris M, Allingham S, Morgan D, et al. Comparing functional decline and distress from symptoms in people with thoracic life-limiting illnesses: lung cancers and non-malignant end-stage respiratory diseases. *Thorax.* 2021;76:989-995. doi: 10.1136/thoraxjnl-2020-216039.
2. Dey M, Ozbolat IT. 3D bioprinting of cells, tissues and organs. *Sci Rep.* 2020;10:14023. doi: 10.1038/s41598-020-70086-y
3. Derakhshanfar S, Mbeleck R, Xu K, Zhang X, Zhong W, Xing M. 3D bioprinting for biomedical devices and tissue engineering: a review of recent trends and advances. *Bioact Mater.* 2018;3:144-156. doi: 10.1016/j.bioactmat.2017.11.008
4. Tuppin MP, Paratz JD, Chang AT, et al. Predictive utility of the 6-minute walk distance on survival in patients awaiting lung transplantation. *J Heart Lung Transplant.* 2008;27:729-734. doi: 10.1016/j.healun.2008.03.017
5. Nathan SD. Lung transplantation: disease-specific considerations for referral. *Chest.* 2005;127;1006-1016. doi: 10.1378/chest.127.3.1006
6. Van Scott MR, Chandler J, Olmstead S, Brown JM, Mannie M. Airway anatomy, physiology, and inflammation. In: Weggs WJ, ed. The Toxicant Induction of Irritant Asthma, Rhinitis, and Related Conditions; 2013:19–61. doi: 10.1007/978-1-4614-9044-9_2
7. Ochs M, Nyengaard JR, Jung A, et al. The number of alveoli in the human lung. *Am J Respir Crit Care Med.* 2004;169:120-124. doi: 10.1164/rccm.200308-1107OC
8. Travaglini KJ, Nabhan AN, Penland L, et al. A molecular cell atlas of the human lung from single-cell RNA sequencing. *Nature.* 2020;587:619-625. doi: 10.1038/s41586-020-2922-4
9. Abdelwahab EMM, Rapp J, Feller D, et al. Wnt signaling regulates trans-differentiation of stem cell like type 2 alveolar epithelial cells to type 1 epithelial cells. *Respir Res.* 2019;20:204. doi: 10.1186/s12931-019-1176-x
10. Gillich A, Zhang F, Farmer CG, et al. Capillary cell-type specialization in the alveolus. *Nature.* 2020;586:785-789. doi: 10.1038/s41586-020-2822-7
11. Kadur Lakshminarasimha Murthy P, Sontake V, Tata A, et al. Human distal lung maps and lineage hierarchies reveal a bipotent progenitor. *Nature.* 2022;604:111-119. doi: 10.1038/s41586-022-04541-3
12. Woo YD, Jeong D, Chung DH. Development and functions of alveolar macrophages. *Mol Cells.* 2021;44:292-300. doi: 10.14348/molcells.2021.0058
13. Weibel ER. What makes a good lung? *Swiss Med Wkly.* 2009;139:375-386. doi: 10.4414/smw.2009.12270
14. Doryab A, Tas S, Taskin MB, et al. Evolution of bioengineered lung models: recent advances and challenges in tissue mimicry for studying the role of mechanical forces in cell biology. *Adv Funct Mater*. 2019;29:1903114. doi: 10.1002/adfm.201903114
15. Bonassar LJ, Vacanti CA. Tissue engineering: the first decade and beyond. *J Cell Biochem.* 1998;72(Suppl 30–31):297-303. doi:10.1002/(SICI)1097-4644(1998)72:30/31+<297::AID-JCB36>3.0.CO;2-6
16. Fan P, Jin F, Qin Y, et al. Multiscale 3D bioprinting for the recapitulation of lung tissue. *IJB.* 2023;9:1166. doi: 10.36922/ijb.1166
17. Mahfouzi SH, Hamid S, Ghassem, A. 3D bioprinting for lung and tracheal tissue engineering: criteria, advances, challenges, and future directions. *Bioprinting.* 2021;21:e00124. doi: 10.1016/j.bprint.2020.e00124
18. Papaioannou TG, Manolesou D, Dimakakos E, Tsoucalas G, Vavuranakis M, Tousoulis D. 3D bioprinting methods and techniques: applications on artificial blood vessel fabrication. *Acta Cardiol Sin.* 2019;35:284-289. doi: 10.6515/ACS.201905_35(3).20181115A
19. Roche CD, Brereton RJL, Ashton AW, Jackson C, Gentile C. Current challenges in three-dimensional bioprinting

heart tissues for cardiac surgery. *Eur J Cardiothorac Surg.* 2020;58:500-510.
doi: 10.1093/ejcts/ezaa093

20. Li J, Chen M, Fan X, Zhou H. Recent advances in bioprinting techniques: approaches, applications and future prospects. *J Transl Med.* 2016;14:271.
doi: 10.1186/s12967-016-1028-0

21. Gudapati H, Dey M, Ozbolat I. A comprehensive review on droplet-based bioprinting: past, present and future. *Biomaterials.* 2016;102:20-42.
doi: 10.1016/j.biomaterials.2016.06.012

22. Hinton TJ, Jallerat Q, Palchesko RN, et al. Three-dimensional printing of complex biological structures by freeform reversible embedding of suspended hydrogels. *Sci Adv.* 2015;1:e1500758.
doi: 10.1126/sciadv.1500758

23. Takahashi K, Yamanaka S. Induction of pluripotent stem cells from mouse embryonic and adult fibroblast cultures by defined factors. *Cell.* 2006;126:663-676.
doi: 10.1016/j.cell.2006.07.024

24. Ben-David U, Nudel N, Benvenisty N. Immunologic and chemical targeting of the tight-junction protein Claudin-6 eliminates tumorigenic human pluripotent stem cells. *Nat Commun.* 2013;4:1992.
doi: 10.1038/ncomms2992

25. Cunningham JJ, Ulbright TM, Pera MF, Looijenga LH. Lessons from human teratomas to guide development of safe stem cell therapies. *Nat Biotechnol.* 2012;30:849-857.
doi: 10.1038/nbt.2329

26. Herberts CA, Kwa MS, Hermsen HP. Risk factors in the development of stem cell therapy. *J Transl Med.* 2011;9:29.
doi: 10.1186/1479-5876-9-29

27. Blasco MA, Serrano M, Fernandez-Capetillo O. Genomic instability in iPS: time for a break. *EMBO J.* 2011;30:991-993.
doi: 10.1038/emboj.2011.50

28. Haston KM, Finkbeiner S. Clinical trials in a dish: the potential of pluripotent stem cells to develop therapies for neurodegenerative diseases. *Annu Rev Pharmacol Toxicol.* 2016;56:489-510.
doi: 10.1146/annurev-pharmtox-010715-103548

29. Holbert JM, Strollo DC. Imaging of the normal trachea. *J Thorac Imaging.* 1995;10:171-179.
doi: 10.1097/00005382-199522000-00003

30. Xing H, Lee H, Luo L, Kyriakides TR. Extracellular matrix-derived biomaterials in engineering cell function. *Biotechnol Adv.* 2020;42:107421.
doi: 10.1016/j.biotechadv.2019.107421

31. Morwood AJ, El-Karim IA, Clarke SA, Lundy FT. The role of extracellular matrix (ECM) adhesion motifs in functionalised hydrogels. *Molecules.* 2023;28(12):4616.
doi: 10.3390/molecules28124616

32. Noro J, Vilaça-Faria H, Reis RL, Pirraco RP. Extracellular matrix-derived materials for tissue engineering and regenerative medicine: a journey from isolation to characterization and application. *Bioact Mater.* 2024;34:494-519.
doi: 10.1016/j.bioactmat.2024.01.004

33. Gao M, Zhang H, Dong W, et al. Tissue-engineered trachea from a 3D-printed scaffold enhances whole-segment tracheal repair. *Sci Rep.* 2017;7:5246.
doi: 10.1038/s41598-017-05518-3

34. Kim H, Lee JY, Han H, et al. Improved chondrogenic performance with protective tracheal design of Chitosan membrane surrounding 3D-printed trachea. *Sci Rep.* 2021;11:9258.
doi: 10.1038/s41598-021-88830-3

35. Hiwatashi S, Iwai R, Nakayama Y, Moriwaki T, Okuyama H. Successful tracheal regeneration using biofabricated autologous analogues without artificial supports. *Sci Rep.* 2022;12:20279.
doi: 10.1038/s41598-022-24798-y

36. Rezaei FS, Khorshidian A, Beram FM, et al. 3D printed chitosan/polycaprolactone scaffold for lung tissue engineering: hope to be useful for COVID-19 studies. *RSC Adv.* 2021;11:19508-19520.
doi: 10.1039/d1ra03410c

37. Silva S, Bicker J, Falcão A, Fortuna A. Air-liquid interface (ALI) impact on different respiratory cell cultures. *Eur J Pharm Biopharm.* 2023;184:62-82.
doi: 10.1016/j.ejpb.2023.01.013

38. Sears NA, Seshadri DR, Dhavalikar PS, Cosgriff-Hernandez E. A review of three-dimensional printing in tissue engineering. *Tissue Eng Part B Rev.* 2016;22:298-310.
doi: 10.1089/ten.TEB.2015.0464

39. Aazmi A, Zhang D, Mazzaglia C, et al. Biofabrication methods for reconstructing extracellular matrix mimetics. *Bioact Mater.* 2024;31:475-496.
doi: 10.1016/j.bioactmat.2023.08.018

40. Kumar H, Kim K. Stereolithography 3D bioprinting. *Methods Mol Biol.* 2020;2140:93-108.
doi: 10.1007/978-1-0716-0520-2_6

41. Li W, Wang M, Ma H, Chapa-Villarreal FA, Lobo AO, Zhang YS. Stereolithography apparatus and digital light processing-based 3D bioprinting for tissue fabrication. *iScience.* 2023;26:106039.
doi: 10.1016/j.isci.2023.106039

42. GhavamiNejad A, Ashammakhi N, Wu XY, Khademhosseini A. Crosslinking strategies for 3D bioprinting of polymeric hydrogels. *Small.* 2020;16:e2002931.
doi: 10.1002/smll.202002931

43. Schuurman W, Levett PA, Pot MW, et al. Gelatin-methacrylamide hydrogels as potential biomaterials for fabrication of tissue-engineered cartilage constructs. *Macromol Biosci.* 2013;13:551-561.

doi: 10.1002/mabi.201200471

44. Galliger Z, Vogt CD, Panoskaltsis-Mortari A. 3D bioprinting for lungs and hollow organs. *Transl Res.* 2019;211:19-34. doi: 10.1016/j.trsl.2019.05.001

45. Chen YC, Lin RZ, Qi H, et al. Functional human vascular network generated in photocrosslinkable gelatin methacrylate hydrogels. *Adv Funct Mater.* 2012;22: 2027-2039. doi: 10.1002/adfm.201101662

46. Camci-Unal G, Cuttica D, Annabi N, Demarchi D, Khademhosseini A. Synthesis and characterization of hybrid hyaluronic acid-gelatin hydrogels. *Biomacromolecules.* 2013;14:1085-1092. doi: 10.1021/bm3019856

47. Skardal A, Devarasetty M, Kang HW, et al. A hydrogel bioink toolkit for mimicking native tissue biochemical and mechanical properties in bioprinted tissue constructs. *Acta Biomater.* 2015;25:24-34. doi: 10.1016/j.actbio.2015.07.030

48. Kaully T, Kaufman-Francis K, Lesman A, Levenberg S. Vascularization--the conduit to viable engineered tissues. *Tissue Eng Part B Rev.* 2009;15:159-169. doi: 10.1089/ten.teb.2008.0193

49. Bertassoni LE, Cecconi M, Manoharan V, et al. Hydrogel bioprinted microchannel networks for vascularization of tissue engineering constructs. *Lab Chip.* 2014;14:2202-2211. doi: 10.1039/c4lc00030g

50. Nashimoto Y, Hayashi T, Kunita I, et al. Integrating perfusable vascular networks with a three-dimensional tissue in a microfluidic device. *Integr Biol (Camb.)* 2017;9:506-518. doi: 10.1039/c7ib00024c

51. L'Heureux N, McAllister TN, de la Fuente LM. Tissue-engineered blood vessel for adult arterial revascularization. *N Engl J Med.* 2007;357:1451-1453. doi: 10.1056/NEJMc071536

52. Eduardo DT, Ana SE, José BF. A micro-extrusion 3D printing platform for fabrication of orodispersible printlets for pediatric use. *Int J Pharm.* 2021;605:120854. doi: 10.1016/j.ijpharm.2021.120854

53. Bos GW, Poot AA, Beugeling T, van Aken WG, Feijen J. Small-diameter vascular graft prostheses: current status. *Arch Physiol Biochem.* 1998;106:100-115. doi: 10.1076/apab.106.2.100.4384

54. Seifu DG, Purnama A, Mequanint K, Mantovani D. Small-diameter vascular tissue engineering. *Nat Rev Cardiol.* 2013;10:410-421. doi: 10.1038/nrcardio.2013.77

55. Boison D, Yegutkin GG. Adenosine metabolism: emerging concepts for cancer therapy. *Cancer Cell.* 2019;36:582-596. doi: 10.1016/j.ccell.2019.10.007

56. Wirth AN, Tsutsui K, Maltsev VA, Lakatta EG. Adenosine reduces sinoatrial node cell action potential firing rate by uncoupling its membrane and calcium clocks. *Front Physiol.* 2022;13;977807. doi: 10.3389/fphys.2022.977807

57. Dall'Olmo L, Zanusso I, Di Liddo R, et al. Blood vessel-derived acellular matrix for vascular graft application. *Biomed Res Int.* 2014;2014:685426. doi: 10.1155/2014/685426

58. L'Heureux N, Pâquet S, Labbé R, Germain L, Auger FA. A completely biological tissue-engineered human blood vessel. *FASEB J.* 1998;12:47-56. doi: 10.1096/fasebj.12.1.47

59. McAllister TN, Maruszewski M, Garrido SA, et al. Effectiveness of haemodialysis access with an autologous tissue-engineered vascular graft: a multicentre cohort study. *Lancet.* 2009;373:1440-1446. doi: 10.1016/S0140-6736(09)60248-8

60. Gao G, Lee JH, Jang J, et al. Tissue engineered bio-blood-vessels constructed using a tissue-specific bioink and 3d coaxial cell printing technique: a novel therapy for ischemic disease. *Adv Funct Mater.* 2017;27:1700798. doi: 10.1002/adfm.201700798

61. Ju YM, Choi JS, Atala A, Yoo JJ, Lee SJ. Bilayered scaffold for engineering cellularized blood vessels. *Biomaterials.* 2010;31:4313-4321. doi: 10.1016/j.biomaterials.2010.02.002

62. Assmann A, Delfs C, Munakata H, et al. Acceleration of autologous in vivo recellularization of decellularized aortic conduits by fibronectin surface coating. *Biomaterials.* 2013;34:6015-6026. doi: 10.1016/j.biomaterials.2013.04.037

63. Jung Y, Ji H, Chen Z, et al. Scaffold-free, human mesenchymal stem cell-based tissue engineered blood vessels. *Sci Rep.* 2015;5:15116. doi: 10.1038/srep15116

64. Bos S, Vos R, Van Raemdonck DE, Verleden GM. Survival in adult lung transplantation: where are we in 2020? *Curr Opin Organ Transplant.* 2020;25:268-273. doi: 10.1097/MOT.0000000000000753

65. Kędzierska K, Sindrewicz K, Sporniak-Tutak K, et al. Does immunosuppressive therapy affect markers of kidney damage? *Ann Transplant.* 2016;21:137-144. doi: 10.12659/aot.895275

66. Engels EA, Pfeiffer RM, Fraumeni JF, et al. Spectrum of cancer risk among US solid organ transplant recipients. *JAMA.* 2011;306;1891-1901. doi: 10.1001/jama.2011.1592

67. Kirillova A, Bushev S, Abubakirov A, Sukikh G. Bioethical and Legal Issues in 3D Bioprinting. *Int J Bioprint.* 2020;6:272. doi: 10.18063/ijb.v6i3.272

68. Ricci G, Gibelli F, Sirignano A. Three-dimensional bioprinting of human organs and tissues: bioethical and medico-legal implications examined through a scoping review. *Bioengineering (Basel).* 2023;10:1052.

doi: 10.3390/bioengineering10091052

69. Association WM. World Medical Association Declaration of Helsinki: ethical principles for medical research involving human subjects. *JAMA*. 2013;310:2191-2194. doi: 10.1001/jama.2013.281053

70. van Delden JJ, van der Graaf R. Revised CIOMS International ethical guidelines for health-related research involving humans. *JAMA*. 2017;317:135-136. doi: 10.1001/jama.2016.18977

71. Directive 2004/23/EC of the European Parliament and of the Council of 31 March 2004 on Setting Standards of Quality and Safety for the Donation, Procurement, Testing, Processing, Preservation, Storage and Distribution of Human Tissues and Cells; 2004.

72. Human Tissue Act; 2004.

73. Code of Federal Regulations. *Part 1271: Human Cells, Tissues, and Cellular and Tissue-Based Products*; 2024.

74. National Health and Medical Research Council. Australian Research Council and Universities Australia (2007, Updated 2018) National Statement on Ethical Conduct in Human Research; 2018.

75. Garielchyk T. Biotech Boost without Extra Money, Vol. 23, *Summer ed.*; 2024.

76. Kritikos M. 3D Bio-Printing for Medical and Enhancement Purposes: Legal and Ethical Aspects; 2018. doi: 10.2861/923327

77. Li Y, Verter F, Wang B, Gu N. Regulations on cell therapy products in China: a brief history and current status. *Regen Med.* 2019;14:791-803. doi: 10.2217/rme-2019-0069

78. Kovacs T, Csongei V, Feller D, et al. Alteration in the Wnt microenvironment directly regulates molecular events leading to pulmonary senescence. *Aging Cell.* 2014;13:838-849. doi: 10.1111/acel.12240

79. Foty RA, Pfleger CM, Forgacs G, Steinberg MS. Surface tensions of embryonic tissues predict their mutual envelopment behavior. *Development.* 1996;122:1611-1620. doi: 10.1242/dev.122.5.1611

80. Forgacs G. Surface tension and viscoelastic properties of embryonic tissues depend on the cytoskeleton. *Biol Bull.* 1998;194:328-329; discussion 329-330. doi: 10.2307/1543103

81. JE, Pongracz, 2009. Unpublished observations

82. JE, Pongracz, 2016. Unpublished observations

83. Vesel M, Rapp J, Feller D, et al. ABCB1 and ABCG2 drug transporters are differentially expressed in non-small cell lung cancers (NSCLC) and expression is modified by cisplatin treatment via altered Wnt signaling. *Respir Res.* 2017;18:52. doi: 10.1186/s12931-017-0537-6

84. Rapp J, Kiss E, Meggyes M, et al. Increased Wnt5a in squamous cell lung carcinoma inhibits endothelial cell motility. *BMC Cancer.* 2016;16:915. doi: 10.1186/s12885-016-2943-4

85. Kilic O, Yoon A, Shah SR, et al. A microphysiological model of the bronchial airways reveals the interplay of mechanical and biochemical signals in bronchospasm. *Nat Biomed Eng.* 2019;3:532-544. doi: 10.1038/s41551-019-0366-7

86. Sayed N, Liu C, Wu JC. Translation of human-induced pluripotent stem cells: from clinical trial in a dish to precision medicine. *J Am Coll Cardiol.* 2016;67: 2161-2176. doi: 10.1016/j.jacc.2016.01.083

87. Baxter A, Thain S, Banerjee A, et al. Targeted omics analyses, and metabolic enzyme activity assays demonstrate maintenance of key mucociliary characteristics in long term cultures of reconstituted human airway epithelia. *Toxicol In Vitro.* 2015;29:864-875. doi: 10.1016/j.tiv.2015.03.004

88. Shafiee A, Norotte C, Elham G. Cellular bioink surface tension: a tunable biophysical parameter for faster maturation of bioprinted tissue. *Bioprinting.* 2017;8:13-21. doi: 10.1016/j.bprint.2017.10.001

89. Nizamoglu M, Joglekar MM, Almeida CR, et al. Innovative three-dimensional models for understanding mechanisms underlying lung diseases: powerful tools for translational research. *Eur Respir Rev.* 2023;32(169):230042. doi: 10.1183/16000617.0042-2023.

90. Felix K, Tobias S, Jan H, Nicolas S, Michael M. Measurements of transepithelial electrical resistance (TEER) are affected by junctional length in immature epithelial monolayers. *Histochem Cell Biol.* 2021;156:609-616. doi: 10.1007/s00418-021-02026-4

91. Golding H, Khurana S, Zaitseva M. What is the predictive value of animal models for vaccine efficacy in humans? The importance of bridging studies and species-independent correlates of protection. *Cold Spring Harb Perspect Biol.* 2018;10(4):a028902. doi: 10.1101/cshperspect.a028902

92. Franco R, Cedazo-Minguez A. Successful therapies for Alzheimer's disease: why so many in animal models and none in humans? *Front Pharmacol.* 2014;5:146. doi: 10.3389/fphar.2014.00146

93. Si L, Bai H, Rodas M, et al. A human-airway-on-a-chip for the rapid identification of candidate antiviral therapeutics and prophylactics. *Nat Biomed Eng.* 2021;5:815-829. doi: 10.1038/s41551-021-00718-9

94. Iakovlev AP, Erofeev AS, Gorelkin PV. Novel pumping methods for microfluidic devices: a comprehensive review. *Biosensors (Basel).* 2022;12(11):956. doi: 10.3390/bios12110956.

95. Xia Y, Whitesides GM. Soft lithography. *Angew Chem Int Ed Engl.* 1998;37:550-575. doi: 10.1002/(SICI)1521-3773(19980316)37:5<550::AID-ANIE550>3.0.CO;2-G

96. Bhatia SN, Ingber DE. Microfluidic organs-on-chips. *Nat Biotechnol.* 2014;32:760-772. doi: 10.1038/nbt.2989

97. Miranda I, Souza A, Sousa P, et al. Properties and applications of pdms for biomedical engineering: a review. *J Funct Biomater.* 2021;13(1):2. doi: 10.3390/jfb13010002

98. Huh D, Matthews BD, Mammoto A, et al. Reconstituting organ-level lung functions on a chip. *Science.* 2010;328:1662-1668. doi: 10.1126/science.1188302

99. Saldin LT, Cramer MC, Velankar SS, White LJ, Badylak SF. Extracellular matrix hydrogels from decellularized tissues: structure and function. *Acta Biomater.* 2017;49:1-15. doi: 10.1016/j.actbio.2016.11.068

100. Pouliot RA, Link PA, Mikhaiel NS, et al. Development and characterization of a naturally derived lung extracellular matrix hydrogel. *J Biomed Mater Res A*. 2016;104:1922-1935. doi: 10.1002/jbm.a.35726

101. Zhang M, Wang P, Luo R, et al. Biomimetic human disease model of SARS-CoV-2-induced lung injury and immune responses on organ chip system. *Adv Sci (Weinh).* 2021;8:2002928. doi: 10.1002/advs.202002928

102. Katsura H, Sontake V, Tata A, et al. Human lung stem cell-based alveolospheres provide insights into SARS-CoV-2-mediated interferon responses and pneumocyte dysfunction. *Cell Stem Cell.* 2020;27(6):890-904.e898. doi: 10.1016/j.stem.2020.10.005

103. Lamers MM, van der Vaart J, Knoops K, et al. An organoid-derived bronchioalveolar model for SARS-CoV-2 infection of human alveolar type II-like cells. *EMBO J.* 2021;40:e105912. doi: 10.15252/embj.2020105912

104. Thacker VV, Sharma K, Dhar N, Mancini GF, Sordet-Dessimoz J, McKinney JD. Rapid endotheliitis and vascular damage characterize SARS-CoV-2 infection in a human lung-on-chip model. *EMBO Rep.* 2021;22:e52744. doi: 10.15252/embr.202152744

105. Ramani A, Müller L, Ostermann PN, et al. SARS-CoV-2 targets neurons of 3D human brain organoids. *EMBO J.* 2020;39:e106230. doi: 10.15252/embj.2020106230

106. Nawroth JC, Lucchesi C, Cheng D, et al. A microengineered airway lung chip models key features of viral-induced exacerbation of asthma. *Am J Respir Cell Mol Biol.* 2020;63:591-600. doi: 10.1165/rcmb.2020-0010MA

107. Bai H, Si L, Jiang A, et al. Mechanical control of innate immune responses against viral infection revealed in a human lung alveolus chip. *Nat Commun.* 2022;13:1928. doi: 10.1038/s41467-022-29562-4

108. Herpers B, Eppink B, James MI, et al. Functional patient-derived organoid screenings identify MCLA-158 as a therapeutic EGFR × LGR5 bispecific antibody with efficacy in epithelial tumors. *Nat Cancer.* 2022;3:418-436. doi: 10.1038/s43018-022-00359-0

109. Yun J, Lee SH, Kim SY, et al. Antitumor activity of amivantamab (JNJ-61186372), an EGFR-MET bispecific antibody, in diverse models of. *Cancer Discov.* 2020;10:1194-1209. doi: 10.1158/2159-8290.CD-20-0116

110. Hubrecht RC, Carter E. The 3Rs and humane experimental technique: implementing change. *Animals (Basel).* 2019;9(10):754. doi: 10.3390/ani9100754

111. Russel WMS, Burch RL. The Principles of Human Experimental Technique; 1992.

112. Tameris MD, Hatherill M, Landry BS, et al. Safety and efficacy of MVA85A, a new tuberculosis vaccine, in infants previously vaccinated with BCG: a randomised, placebo-controlled phase 2b trial. *Lancet.* 2013;381:1021-1028. doi: 10.1016/S0140-6736(13)60177-4

113. Arpinati M, Chirumbolo G, Rondelli D. Enhancement of T cell activation by immobilized hu5C8 (anti-CD40L) monoclonal antibody. *Eur J Haematol.* 2008;80: 322-330. doi: 10.1111/j.1600-0609.2007.01015.x

114. Shock A, Burkly L, Wakefield I, et al. CDP7657, an anti-CD40L antibody lacking an Fc domain, inhibits CD40L-dependent immune responses without thrombotic complications: an in vivo study. *Arthritis Res Ther.* 2015;17:234. doi: 10.1186/s13075-015-0757-4

115. Breslin S, O'Driscoll L. Three-dimensional cell culture: the missing link in drug discovery. *Drug Discov Today.* 2013;18:240-249. doi: 10.1016/j.drudis.2012.10.003

116. Han JJ. FDA Modernization Act 2.0 allows for alternatives to animal testing. *Artif Organs*. 2023;47(3):449-450. doi: 10.1111/aor.14503

117. Administration F.a.D. HR-1744 Human Research and Testing Act of 2021 117th Congress; 2021–2022.

118. Wadman M. FDA no longer has to require animal testing for new drugs. *Science.* 2023;379:127-128. doi: 10.1126/science.adg6276

119. Kimura H, Sakai Y, Fujii T. Organ/body-on-a-chip based on microfluidic technology for drug discovery. *Drug Metab Pharmacokinet.* 2018;33:43-48. doi: 10.1016/j.dmpk.2017.11.003

120. Huh D, Leslie DC, Matthews BD, et al. A human disease model of drug toxicity-induced pulmonary edema in a lung-on-a-chip microdevice. *Sci Transl Med.* 2012;4:159ra147. doi: 10.1126/scitranslmed.3004249

121. Palasantzas VEJM, Tamargo-Rubio I, Le K, et al. iPSC-derived organ-on-a-chip models for personalized human genetics and pharmacogenomics studies. *Trends Genet.* 2023;39:268-284. doi: 10.1016/j.tig.2023.01.002

122. Ma C, Peng Y, Li H, Chen W. Organ-on-a-chip: a new paradigm for drug development. *Trends Pharmacol Sci.* 2021;42:119-133. doi: 10.1016/j.tips.2020.11.009

123. Chen ML. Ethnic or racial differences revisited: impact of dosage regimen and dosage form on pharmacokinetics and pharmacodynamics. *Clin Pharmacokinet.* 2006;45:957-964. doi: 10.2165/00003088-200645100-00001

124. Driehuis E, Kretzschmar K, Clevers H. Establishment of patient-derived cancer organoids for drug-screening applications. *Nat Protoc.* 2020;15:3380-3409. doi: 10.1038/s41596-020-0379-4.

125. Papp E, Steib A, Abdelwahab EM, et al. Feasibility study of in vitro drug sensitivity assay of advanced non-small cell lung adenocarcinomas. *BMJ Open Respir Res.* 2020;7(1):e000505. doi: 10.1136/bmjresp-2019-000505

126. Holmes AH, Moore LS, Sundsfjord A, et al. Understanding the mechanisms and drivers of antimicrobial resistance. *Lancet.* 2016;387:176-187. doi: 10.1016/S0140-6736(15)00473-0

127. Weng WH, Wang CY, Yan ZY, Lee HT, Kao CY, Chang CW. Isolation and characterizations of multidrug-resistant human cancer cells by a biodegradable nano-sensor. *Biosens Bioelectron.* 2024;249:115985. doi: 10.1016/j.bios.2023.115985

128. Gridelli C, Rossi A, Carbone DP, et al. Non-small-cell lung cancer. *Nat Rev Dis Primers.* 2015;1:15009. doi: 10.1038/nrdp.2015.9

129. Yang X, Yang K, Kuang K. The efficacy and safety of EGFR inhibitor monotherapy in non-small cell lung cancer: a systematic review. *Curr Oncol Rep.* 2014;16:390. doi: 10.1007/s11912-014-0390-4

130. Tajarernmuang P, Aliaga F, Alwakeel AJ, et al. Accuracy of cytologic vs histologic specimens for assessment of programmed cell death Ligand-1 expression in non-small cell lung cancer: a systematic review and meta-analysis. *Chest.* 2024;165:461-474. doi: 10.1016/j.chest.2023.09.013

131. Bremnes RM, Camps C, Sirera R. Angiogenesis in non-small cell lung cancer: the prognostic impact of neoangiogenesis and the cytokines VEGF and bFGF in tumours and blood. *Lung Cancer.* 2006;51:143-158. doi: 10.1016/j.lungcan.2005.09.005

132. Xue C, Zheng S, Dong H, et al. Association between efficacy of immune checkpoint inhibitors and sex: an updated meta-analysis on 21 trials and 12,675 non-small cell lung cancer patients. *Front Oncol.* 2021;11:627016. doi: 10.3389/fonc.2021.627016

133. Boni C, Tiseo M, Boni L, et al. Triplets versus doublets, with or without cisplatin, in the first-line treatment of stage IIIB-IV non-small cell lung cancer (NSCLC) patients: a multicenter randomised factorial trial (FAST). *Br J Cancer.* 2012;106:658-665. doi: 10.1038/bjc.2011.606

134. Griesinger F, Korol EE, Kayaniyil S, et al. Efficacy and safety of first-line carboplatin-versus cisplatin-based chemotherapy for non-small cell lung cancer: a meta-analysis. *Lung Cancer.* 2019;135:196-204. doi: 10.1016/j.lungcan.2019.07.010

135. Rajeswaran A, Trojan A, Burnand B, Giannelli M. Efficacy and side effects of cisplatin- and carboplatin-based doublet chemotherapeutic regimens versus non-platinum-based doublet chemotherapeutic regimens as first line treatment of metastatic non-small cell lung carcinoma: a systematic review of randomized controlled trials. *Lung Cancer.* 2008;59:1-11. doi: 10.1016/j.lungcan.2007.07.012

136. Tsvetkova D, Ivanova S. Application of approved cisplatin derivatives in combination therapy against different cancer diseases. *Molecules.* 2022;27(8):2466. doi: 10.3390/molecules27082466

137. van der Wekken AJ, Saber A, Hiltermann TJ, Kok K, van den Berg A, Groen HJ. Resistance mechanisms after tyrosine kinase inhibitors afatinib and crizotinib in non-small cell lung cancer, a review of the literature. *Crit Rev Oncol Hematol.* 2016;100:107-116. doi: 10.1016/j.critrevonc.2016.01.024

138. Li J, Knoll S, Bocharova I, Tang W, Signorovitch J. Comparative efficacy of first-line ceritinib and crizotinib in advanced or metastatic anaplastic lymphoma kinase-positive non-small cell lung cancer: an adjusted indirect comparison with external controls. *Curr Med Res Opin.* 2019;35:105-111. doi: 10.1080/03007995.2018.1541443

139. Socinski MA, Nishio M, Jotte RM, et al. IMpower150 final overall survival analyses for atezolizumab plus bevacizumab and chemotherapy in first-line metastatic nonsquamous NSCLC. *J Thorac Oncol.* 2021; 16:1909-1924. doi: 10.1016/j.jtho.2021.07.009

140. Vacchelli E, Pol J, Bloy N, et al. Trial watch: tumor-targeting monoclonal antibodies for oncological indications. *Oncoimmunology.* 2015;4:e985940. doi: 10.4161/2162402X.2014.985940

141. Stoff R, Grynberg S, Asher N, et al. Efficacy and toxicity of Ipilimumab-Nivolumab combination therapy in

elderly metastatic melanoma patients. *Front Oncol.* 2022;12:1020058.
doi: 10.3389/fonc.2022.1020058

142. Tan AC, Tan DSW. Targeted therapies for lung cancer patients with oncogenic driver molecular alterations. *J Clin Oncol.* 2022;40:611-625.
doi: 10.1200/JCO.21.01626

143. Harrison PT, Vyse S, Huang PH. Rare epidermal growth factor receptor (EGFR) mutations in non-small cell lung cancer. *Semin Cancer Biol.* 2020;61:167-179.
doi: 10.1016/j.semcancer.2019.09.015

144. Lim TKH, Skoulidis F, Kerr KM, et al. KRAS G12C in advanced NSCLC: prevalence, co-mutations, and testing. *Lung Cancer.* 2023;184:107293.
doi: 10.1016/j.lungcan.2023.107293

145. Wu J, Lin Z. Non-small cell lung cancer targeted therapy: drugs and mechanisms of drug resistance. *Int J Mol Sci.* 2022;23:15056.
doi: 10.3390/ijms232315056

146. Daniels MG, Bowman RV, Yang IA, Govindan R, Fong KM. An emerging place for lung cancer genomics in 2013. *J Thorac Dis.* 2013;5(Suppl 5):S491-497.
doi: 10.3978/j.issn.2072-1439.2013.10.06

147. Merlotti A, Sadacca B, Arribas YA, et al. Noncanonical splicing junctions between exons and transposable elements represent a source of immunogenic recurrent neo-antigens in patients with lung cancer. *Sci Immunol.* 2023;8:eabm6359.
doi: 10.1126/sciimmunol.abm6359

148. Vokes NI, Galan Cobo A, Fernandez-Chas M, et al. ATM mutations associate with distinct co-mutational patterns and therapeutic vulnerabilities in NSCLC. *Clin Cancer Res.* 2023;29:4958-4972.
doi: 10.1158/1078-0432.CCR-23-1122

149. Bartfeld S, Clevers H. Stem cell-derived organoids and their application for medical research and patient treatment. *J Mol Med (Berl).* 2017;95:729-738.
doi: 10.1007/s00109-017-1531-7

ACCSCIENCE PUBLISHING

International Journal of Bioprinting

REVIEW ARTICLE

Scaling liver bioprinting: A guide for usage of the hepatic extracellular matrix as a bioink

Valentin A. Brumberg[1], Polina Yu. Bikmulina[1]*, Artem A. Pozdnyakov[1], Zahra Heydari[1], Darya R. Zimulkina[1], Olga A. Smirnova[1], Frederico David Alencar de Sena Pereira[1], Anastasiia M. Nesterova[1], Svetlana L. Kotova[1], Massoud Vosough[2,3], Anastasia I. Shpichka[1], and Peter S. Timashev[1,4,5]*

[1]Institute for Regenerative Medicine, Sechenov University, Moscow, Russia

[2]Department of Regenerative Medicine, Cell Science Research Center, Royan Institute for Stem Cell Biology and Technology, ACECR, Tehran, Iran

[3]Experimental Cancer Medicine Group, Institution for Laboratory Medicine, Karolinska Institute, Stockholm, Sweden

[4]World-Class Research Center "Digital biodesign Biodesign and Personalized Healthcare", Sechenov University, Moscow, Russia

[5]Chemistry Department, Lomonosov Moscow State University, Moscow, Russia

(This article belongs to the Special Issue: *Made-to-order Organ*)

Abstract

Hydrogels derived from the decellularized extracellular matrix (dECM) are widely used in three-dimensional (3D) bioprinting, mainly because they recapitulate the native tissue microenvironment and retain key growth factors and cytokines. Hence, they are characterized by adequate biocompatibility for use in 3D bioprinting. In liver tissue engineering, these materials, along with liver-derived cell types, can serve as appropriate *in vitro* hepatic models for drug efficiency testing and liver metabolism studies. These hydrogels can also be considered as good manufacturing practice-compliant systems for liver cell and organoid expansion, unlike routinely used basal membrane extract products derived from tumorigenic cell lines. Although weak mechanical properties and poor printability hinder the direct usage of dECM hydrogels as bioinks, various modifications of dECM and the bioprinting process are applied to overcome these problems. However, there are several complications regarding the scale-up and good laboratory practice-compliant manufacturing of these hydrogels: (i) the manufacturing standards for dECM hydrogels are not well established; (ii) the methods for obtaining these hydrogels are slightly varying, resulting in decreased reproducibility; and (iii) since these hydrogels are traditionally produced from animal tissue, the animal-to-animal variability, different harvesting conditions, and bioburden reduction need to be thoroughly considered. This review examines the essential properties of dECM hydrogels for biomedical applications, focusing on biocompatibility, mechanical strength, and bioactivity. Additionally, this review discusses production methods and modifications for 3D bioprinting, highlights case studies of dECM-based liver constructs, and addresses challenges in scalability and regulatory hurdles for clinical translation.

Keywords: Bioprinting; Decellularized extracellular matrix; Hydrogels; Liver biofabrication; Crosslinking; Photopolymerization; Large-scale manufacturing

***Corresponding author:**
Peter S. Timashev
(timashev_p_s@staff.sechenov.ru)

Citation: Brumberg VA, Bikmulina PY, Pozdnyakov AA, et al. Scaling liver bioprinting: A guide for usage of the hepatic extracellular matrix as a bioink. *Int J Bioprint*. 2025;11(1):57-83. doi: 10.36922/ijb.4343

Received: July 26, 2024
Revised: September 19, 2024
Accepted: September 26, 2024
Published Online: September 26, 2024

Copyright: © 2024 Author(s). This is an Open Access article distributed under the terms of the Creative Commons Attribution License, permitting distribution, and reproduction in any medium, provided the original work is properly cited.

Publisher's Note: AccScience Publishing remains neutral with regard to jurisdictional claims in published maps and institutional affiliations.

1. Introduction

Hydrogels can be defined as highly hydrated polymeric materials (with a water content of more than 30% of the wet weight), the structure of which is maintained by physical and/or chemical crosslinking of polymer chains. These three-dimensional (3D) networks of hydrophilic polymers undergo a phase transition (volume phase transition or sol–gel transition) under certain physical or chemical stimuli.[1] The polymers may be synthetic (polyethylene oxide, polyvinyl alcohol, polyacrylic acid, poly[propylene fumarate-co-ethylene glycol], etc.), natural (alginate, chitosan, collagen, hyaluronic acid [HA], etc.), or combined. Hydrogels of all origins are actively used as systems for drug and cell delivery to stimulate regenerative processes.

Natural hydrogels may be based upon a specific component (alginate, fibrin, chitosan, etc.) or composite mixtures of the extracellular matrix (ECM) components (e.g., a hydrogel of pig small intestine submucosa [SIS]). Hydrogels derived from decellularized ECM (dECM) stand out among natural hydrogels. These hydrogels are generally obtained by enzymatic hydrolysis, with crosslinking occurring at a physiological temperature and pH.[2] Unlike other hydrogels, which are represented by a single ECM component, these materials can reproduce the native microenvironment of cells. The ECM is known to be one of the universal components of the stem cell niche, along with the supporting cells and autocrine and paracrine factors.[3]

This review examines the essential properties that dECM hydrogels must retain to ensure their efficacy in biomedical applications. We begin by outlining the critical characteristics that are necessary for optimal functionality, including biocompatibility, mechanical strength, and bioactivity. Next, we delve into the various production methods for dECM, highlighting both conventional techniques and innovative modifications that enhance the material's performance. We explore strategies for modifying and crosslinking these hydrogels to improve their suitability for 3D bioprinting applications, emphasizing the importance of achieving the right balance between viscosity and printability. In addition, we provide a detailed analysis of different bioprinting approaches, discussing the unique features and advantages of each method. This section includes case studies and exemplary models of bioprinted dECM-based liver constructs, showcasing the potential of these technologies in tissue engineering and regenerative medicine. Finally, we address the challenges associated with large-scale manufacturing of dECM hydrogels, including scalability, reproducibility, and cost-effectiveness. We also consider the clinical translation of dECM-based products, discussing regulatory hurdles and the need for rigorous testing to ensure safety and efficacy in human applications. Through this review, we aim to highlight both the potential and complexities of utilizing dECM hydrogels in advanced biomedical applications.

2. Desired properties of liver dECM for bioink applications

2.1. Mechanical and structural properties

Stiffness is a key factor influencing cell behavior, impacting various cell functions like signaling, proliferation, differentiation, and metabolic activity. The normal liver has an average stiffness of approximately 1.5–2 kPa. However, healthy liver stiffness is reported in the literature to be within a wide range between 150 Pa and 6 kPa due to different measurement techniques. For example, the lowest stiffness value of 150 Pa was produced by indentation using atomic force microscopy, while 6 kPa was measured by the non-invasive FibroScan® method utilized in the clinic.[4,5]

It has been revealed that the porosity and pore sizes have a significant influence on the regeneration and function of cells. Introducing a more complex construct geometry with pores via bioprinting enhanced cell metabolic activity and spheroid sprouting.[6] Additionally, angiogenesis can be affected by the scaffold pore size and porosity, which may be designed in different ranges.[7] Numerous studies have suggested that an ideal scaffold requires an interconnected pore structure with high porosity to ensure adequate diffusion of nutrients for cells and waste products within the scaffold. Using different protocols to obtain dECM scaffolds and hydrogels, various pore sizes and porosity can be achieved.[4–8] Mao et al.[9] developed a bioink by combining methacrylated gelatin (GelMA) with dECM to encapsulate human-induced hepatocytes (hiHep cells). The obtained data indicated that porosity and hepatic-specific functions of the printed liver microtissues were significantly increased in GelMA/dECM bioinks compared to GelMA bioinks. It has been demonstrated that hepatocytes require a scaffold with at least 95% porosity to maintain high metabolic functions[10]; pore sizes of 10 or 80 μm improve the hepatic function in rat hepatocytes. Moreover, the metabolic function increased with 80 μm pore sizes, especially at a high cell concentration, due to the increased cell–cell interaction resulting from larger pore sizes.[11] The impact of different dECM hydrogel properties on cellular behaviors is summarized in Table 1.

2.2. Chemical composition and matrisome

Baptista et al. reported that the total composition of decellularized liver contained ≈0.5% of sulfated glycosaminoglycans (sGAG), ≈73% of collagen, and ≈23% of elastin (by dry weight).[14] However, in recent

Table 1. Impact of different dECM hydrogel properties on cellular behaviors.

Property	Material	Impact on cellular behavior	Ref.
Pore size	Collagen foam	The pore size of 10 or 80 μm improves the viability of rat hepatocytes	[11]
Porosity	GelMA/liver dECM	Higher porosity maintains the increased viability of HiHeps after 5 days of cultivation	[9]
Normalized storage modulus	Porcine lung dECM hydrogel	Gels with higher storage modulus can contain more cells (PVECs, hLFs, or hMSCs)	[32]
Elastic modulus	Porcine UBM Pocine and SIS	dECM hydrogels with high elastic modulus maintained viable and elongated cells for 5 days	[12]
Stiffness	Collagen hydrogel with genipin	Mouse mesenchymal stromal cells on 10 mM genipin-mixed collagen gels: mouse mesenchymal stromal cells differentiated to vascular smooth muscle cells; 0 mM genipin-mixed collagen gels (≈0.0292 kPa): mouse mesenchymal stromal cells differentiated to visceral smooth muscle cells.	[13]

Abbreviations: AM, a*cetyl methoxy methyl ester group;* dECM, decellularized extracellular matrix; GelMA, gelatin methacryloyl; HiHep, human induced hepatocytes; *PVECs, pulmonary vascular endothelial cells; UBM, urinary bladder matrix; SIS, small intestine submucosa.*

years, detailed studies of the ECM and the discovery of new interactions led to the emergence of the "matrisome" concept. Matrisome is defined as a set of all ECM elements and ECM-associated proteins.[15] It is important to consider the main structural units of the normal liver matrisome to justify the choice of composition when creating tissue-engineered structures.

The matrisome is divided into the main matrisome of the ECM, consisting of collagens, glycoproteins, proteoglycans (PGs), and other components, such as matrix-bound vesicles (MBVs[16]), and matrisome-associated molecules, which are divided into ECM-secreted proteins (e.g., transmembrane PGs, collagen-related proteins, cytokines, transforming growth factor β [TGFβ]) and ECM regulators (enzymes that destroy or change the structure of the ECM, e.g., matrix metalloproteinases [MMPs], α1-antitrypsin).[15,17] Therefore, the ECM is not only responsible for maintaining the structure and supporting cells, but also provides a reservoir for growth factors and cytokines and acts as a signaling core, where each cell can communicate with its environment and other cells.[18,19] The most important ECM components include PGs, glycosaminoglycans (GAGs), glycoproteins, collagens, bioactive collagen fragments, and integrins.

Proteoglycans (PGs) are divided into four main subclasses, which determine their various functions: extracellular, intracellular, pericellular, and cell surface-associated.[18–20] Their main functions are similar to the co-receptors of signaling molecules, regulating the integral properties of cells, such as adhesion, migration, proliferation, angiogenesis, and viability. The subclasses and functions of PGs are summarized in Table 2.

Glycosaminoglycans (GAGs) represent a part of PGs and an important component of the ECM, usually not found in free form. In the liver tissue matrisome, the main representatives of the class are heparin sulfate and HA[21]; HA is synthesized by stellate cells of the liver and immediately released into the extracellular space.[15] This is a process highly controlled by enzymes located on the inner surface membranes of stellate cells.[22] HA plays an important role in the formation of the normal structure of the ECM, controlling tissue hydration and maintaining the osmotic balance.[22]

The typical representatives of glycoproteins are adhesive proteins, e.g., fibronectin, laminin, and elastin. They ensure cell adhesion inside the ECM through the interaction with membrane receptors. In the liver tissue, glycoproteins are mainly represented by fibronectin 1 (FN1), elastin and elastin microfibril interface located protein 1 (EMILIN1), periostin, tenascin, fibrillin (FBN1), fibrinogen alpha, beta and gamma chains (FGA, FGB, FGG, respectively).[17] Laminin, a component of the basement membrane of the liver, is represented by seven different chains, but is often found in large quantities in pathological liver tissues, e.g., fibrosis.[17,23]

Different types of collagens are a part of both the basement membrane and interstitial tissue. The components of the basement membrane are chains of collagen IV and collagen VI.[17] The other collagens are detected in different concentrations, depending on the specific sample, the accuracy of the study, and other factors. In a mass spectrometry study, fibrillar collagens I, III, V, and XXVII were detected (and considered the most common); fibril-associated collagens with interrupted triple helices (FACIT) IX, XII, XIV, XVI, XIX, XXI, and XXII (the least common and variable in their presence in the liver tissue); collagens VIII and X form networks.[17] The origin and roles of the various proteins are only partially

understood. For example, collagen VIII is synthesized by endothelial cells and vascular smooth muscle cells.[15]

Moreover, collagen fragments are the key players in cell signaling and tissue remodeling. The most well-known molecules of this class are MMPs (matrixins), tissue inhibitors of metalloproteinases (TIMPs), and disintegrins and metalloproteinases with thrombospondin motifs (ADAMTS).[15,24] MMP and TIMP are in physiological equilibrium in the normal liver tissue. MMPs degrade various types of extracellular collagen, while TIMPs regulate MMP activity through hydrolysis.[22] Thus, a normal ratio of MMP and TIMP regulates the ECM composition and inhibits the process of liver fibrosis.[24] Eight types of MMPs are found in the liver tissue, namely, MMP-1, MMP-2, MMP-3, MMP-7, MMP-8, MMP-9, MMP-12, and MMP-13, each of which performs specific functions in maintaining the normal ECM composition.[12] The role of the ADAMTS2, ADAMTS3, and ADAMTS14 enzymes is to cleave aminopropeptides of fibrillar procollagens, promoting collagen maturation and formation of normal ECM.[15]

The function of integrins (transmembrane cellular proteins) is to bind the ECM and cell cytoskeleton, transmit signals into cells, and interact with other ECM molecules.[15] They consist of alpha and beta subunits, which are further divided into different types, determining their role in modeling the liver tissue.[15,25]

3. Preparation of dECM hydrogels for 3D bioprinting

3.1. Classic preparation methods for dECM hydrogels

Methods for producing dECM hydrogels can be divided into the following groups: (i) solubilization of the prepared dECM in the form of a fine powder with pepsin in hydrochloric acid (Freytes et al. method[26]), or pepsin in acetic acid (Voytik-Harbin method[27]); and (ii) the Uriel method,[28] which consists of isolating the ECM as a product of tumor tissues (Figure 1).

In Freytes et al.[26] method, pepsin is used to release collagen monomers into the solution, since pepsin cleaves the terminal telopeptides present in the triple helix of collagen with "unfolding" of collagen fibrils. The dECM, according to the Freytes et al.[26] method, is first crushed to a fine powder (recommended particle size: 0.2–0.4 mm[29,30]), after which it is cleaved with pepsin in 0.1 or 0.01 N HCl for 48 h at room temperature (RT)[31] or predominantly for 72 h.[8] An alternative is the Voytik-Harbin method, which uses 0.5 M acetic acid as a medium for pepsin.[27] The duration of enzymatic hydrolysis is a key parameter; insufficient hydrolysis leaves most collagen in the form of dissolved aggregates, while excessive hydrolysis leads to predominance of low molecular weight products (less than 250 kDa) over high molecular weight products (above 250 kDa).[32] Other important parameters include the factors affecting collagen polymerization, such as temperature, ionic strength, and pH. Johnson et al.[31] studied the effect of changing one of the neutralization parameters of the myocardial dECM hydrogel and revealed that the gelation time can range from 20 min at low salt concentrations (0.5× phosphate-buffered saline [PBS]) to more than 8 h at high salt concentrations (1.5× PBS). In addition, increasing the salt concentration led to a two- to three-fold decrease in the storage modulus (G'). The same authors demonstrated that gelation slows down at 22°C, in contrast to collagen hydrogels, which have a gelation temperature range of 4–37°C.

The Uriel method involves the extraction of proteins and glycoproteins by homogenization in a high-salt buffer, disintegrating ECM particles, and collagen fibers at neutral pH.[33] The tissue is cut into small sections

Table 2. PGs of the liver and related organs.

Group	ECM molecule	Matrix phenotype	Functions
Pericellular/BM PGs	Collagen XVIII (liver)	Basement membrane	Inflammation; cell adhesion
	Agrin (gallbladder)	Basement membrane	Postsynaptic differentiation; depolarization at CNS synapses
Cell surface PGs	Syndecan-1 (liver)	Interstitial connective tissue	Angiogenesis; wound healing; cell invasion; and survival
	Syndecan-2 (liver)	Interstitial connective tissue	Actin cytoskeleton; cell adhesion
	Syndecan-4 (liver)	Interstitial connective tissue	Wound healing; cell invasion and survival; focal adhesion and stress fibers
	GPC-6 (liver)	Interstitial connective tissue	Cell growth; cell division
Intracellular PGs	SRGN (endothelial cells)	Interstitial connective tissue	Secretion of inflammatory regulator; formation of mast cell secretory granules; storage of growth factors and cytokines in secretory vesicles; tumor growth

Abbreviations: BM, basal membrane; CNS, central nervous system; GPC-6, glypican-6; PGs, proteoglycans; SRGN, serglycin.

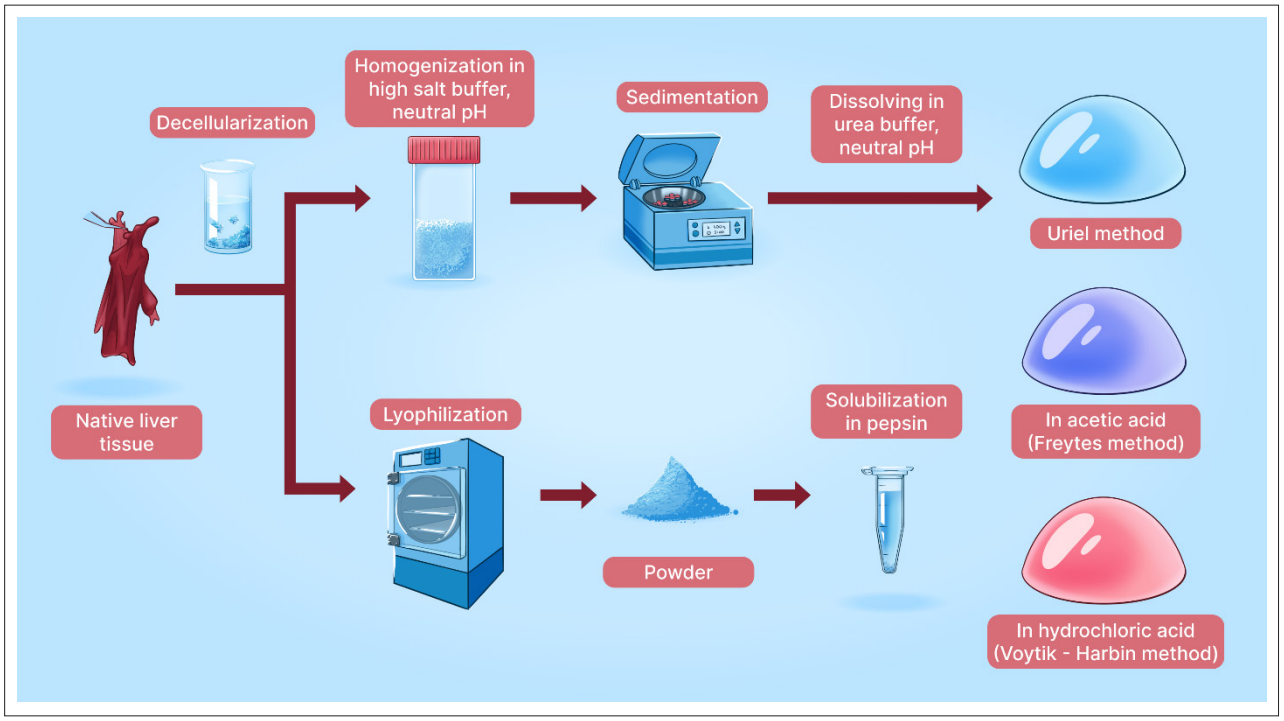

Figure 1. Approaches to obtain decellularized extracellular matrix (dECM) hydrogel via tissue homogenization in buffers (top) or solubilization in pepsin (bottom).

(1–2 mm thick), suspended in a dispase solution at a 2 mL/g tissue concentration, and incubated for 15 min at 4°C. The sections are passed through a cell sieve to separate cells from the remaining tissue. The tissue is homogenized in a high-salt buffer solution (0.05 µM Tris, pH 7.4, 3.4 M sodium chloride, 4 µM EDTA, and 2 µM N-ethylmaleimide), containing protease inhibitors (0.001 µg/mL pepstatin, 0.01 µg/mL aprotonin, 0.001 µg/mL leupeptin, 2 mM sodium orthovanadate, and 1 mM phenylmethylsulfonyl fluoride [PMSF]). The homogenate is centrifuged three times at 7000 × *g* for 15 min, and the supernatant is removed. The sediment is dissolved in a 2 M urea buffer (with the addition of 0.15 M sodium chloride and 0.05 M Tris, pH 7.4) at the amount of 1 mL of buffer per 1 g of tissue and stirred overnight at 4°C. They are then centrifuged again at 14,000 × *g* for 20 min; the supernatant is saved, and the sediment is resuspended in the urea buffer. The sediment is homogenized and centrifuged again at 14,000 × *g* for 20 min. The supernatants from both centrifugation steps are used in subsequent experiments.[33]

3.2. Alternative methods for producing dECM hydrogels

Considering the original method of Freytes et al.[26] without modifications reveals inconsistencies regarding the potential clinical translation of dECM-derived hydrogels. For instance, although porcine mucosa pepsin is irreversibly denatured at pH 7.0–7.4, it should be completely removed, as residual pepsin can cause allergy and inflammation. Additionally, pepsin cleaves collagen in non-helical regions where telopeptides are located, suggesting that collagen telopeptides with pepsin should also be removed. Besides that, the decellularization and lyophilization processes should be as mild and accurate as possible to ensure cell removal and preservation of GAGs, PGs, basement membrane components, and secreted factors.

3.2.1. Modified preparation methods for dECM hydrogels

Modifications to the methods for producing dECM hydrogels include the enzymatic breakdown of the ECM with acidic pepsin. For example, Simsa et al.[30] used the Freytes et al. method in their study. Briefly, lyophilized pig brain tissue was ground to a powder using a knife mill with a 60-mesh sieve to sift particles with a size of 250 µm, followed by enzymatic hydrolysis of the ECM in 0.1 M HCl and pepsin (enzyme:substrate ratio = 1:10). After 72 h of hydrolysis, the suspension was centrifuged at 13,000 rpm for 10 min; the supernatant was collected and neutralized to pH 7.2–7.8 in an ice bath with the addition of 1/10 volume of 10× PBS. The solution was then quickly frozen and lyophilized. The lyophilizate of the porcine brain dECM hydrogel was also ground using a knife mill and a 60-mesh (250 µm) sieve, after which the resulting

particles were dissolved in distilled water and vortexed, then incubated at 37°C to form a hydrogel (Figure 2). The final G' of hydrogels were 0.7, 12.8, and 36.4 Pa at concentrations of 5, 10, and 15 mg/mL, respectively. A linear dependence of the G' on the strain was observed up to 10% strain, and the change in the G' did not exceed 5% within this range. This value is similar to that of Matrigel, which has a linearity range of up to 13%.[30] However, regarding this particular modification, it should be noted that the second lyophilization step could lead to gelation failure in case of poor lyophilization post-digestion.

Another modification of the standard Freytes et al.[26] method was proposed for the preparation of porcine intestinal hydrogels for an endodermal organoid model.[34] Decellularized porcine intestinal matrix was lyophilized for 72 h, ground to a fine powder using a knife mill and a 40-mesh (0.4 mm) sieve, then sterilized by γ-irradiation and stored at −20°C until use. For solubilization, various concentrations (4, 6, 8, and 10 mg/mL) of porcine intestinal dECM powder were dissolved in a solution of pepsin in hydrochloric acid (1 mg/mL in 0.1 M HCl) at RT for a 72-h incubation. The acidic pre-gel was centrifuged at 200–400 × g for 5 min to remove incompletely cleaved particles. To mix with isolated intestinal crypts, the pre-gel solution was brought to an isotonic salt concentration by adding 10% 10× DMEM F/12 or 10× PBS, then titrated with 10 N NaOH with thorough mixing; neutralization was carried out using cut tips (Figure 3). The gel was mixed with cell sediments and aliquoted in 30–40 µL into a Petri dish, and the gelation time was not longer than 30 min. The authors emphasize that the pre-gel stored at RT was not able to form a gel, unlike the one stored at 4°C. The 6 mg/mL dECM gel had properties similar to those of Matrigel (storage and loss [G''] moduli; elastic modulus) and was used for culturing organoids.[34]

Ijima et al.[35] used the Freytes et al.[26] method to produce liver dECM hydrogel; 10 mg of the lyophilized liver matrix was hydrolyzed in 1 mL of pepsin at a concentration of 1 mg/mL in 0.1 N HCl, and the hydrolysis was carried out for 72 h at 4°C. The pH of the acidic pre-gel was

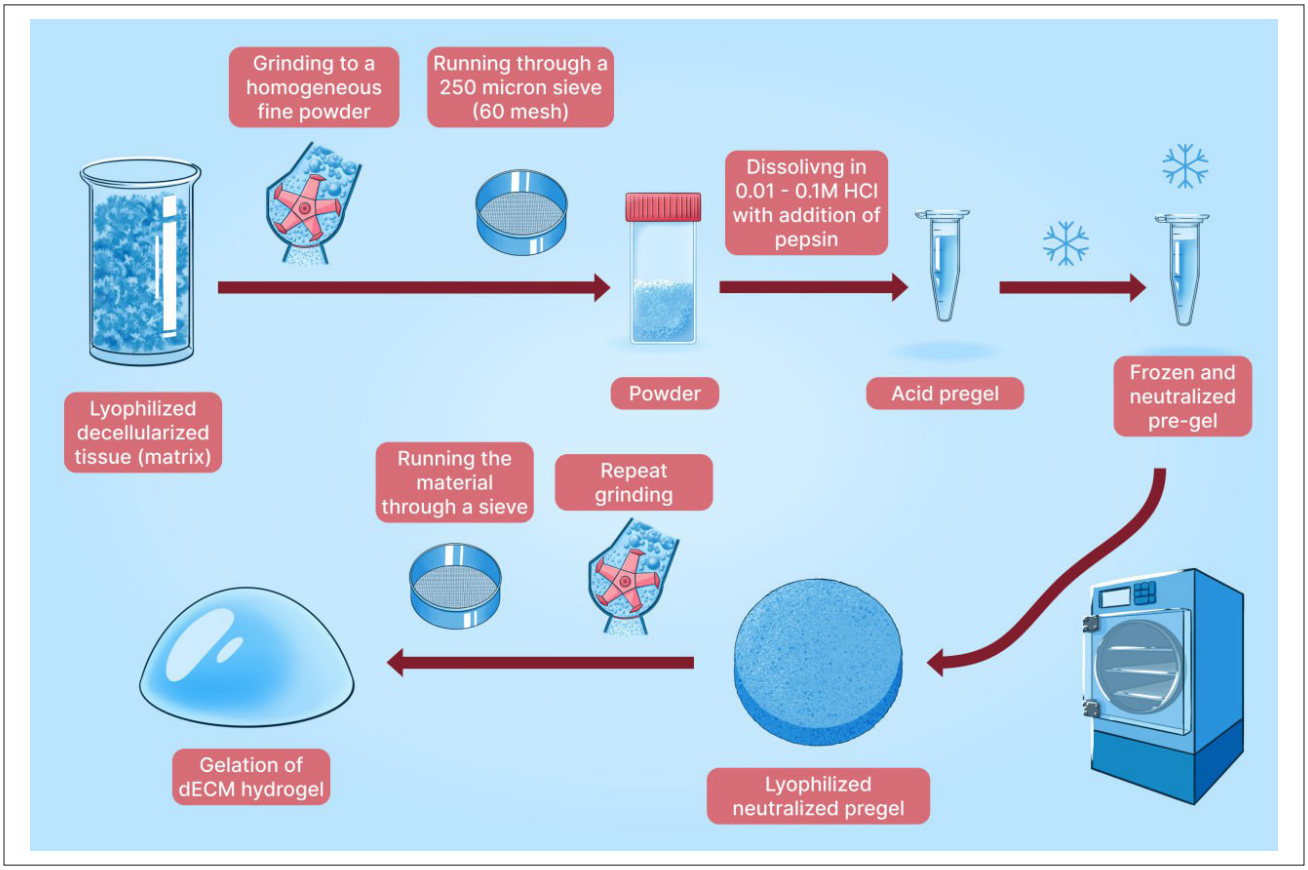

Figure 2. A modification of the Freytes method by Simsa et al.[30] This modification was used for the porcine brain decellularized extracellular matrix (dECM) hydrogel formation and the subsequent culture of cerebral organoids inside the hydrogel. Notably, the authors used a second lyophilization step after the acid pre-gel neutralization, balancing the salt concentration.

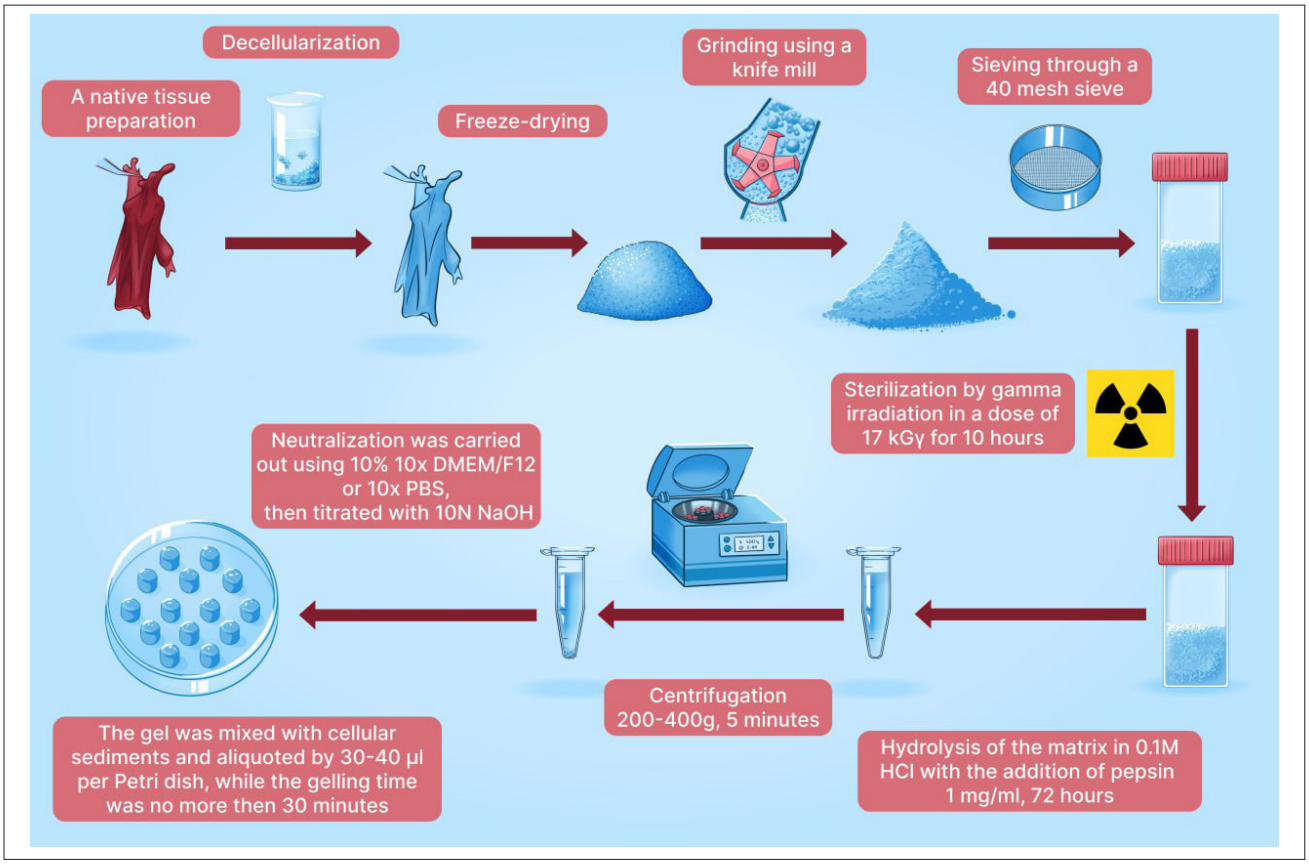

Figure 3. A modification of the Freytes method used by Giobbe et al.[34] Lyophilized, ground, and sieved porcine small intestinal matrix was sterilized by gamma irradiation for 10 h at 17 kGy. Gamma sterilization is a distinct step in this protocol as it is generally excluded in most studies.

adjusted to 3.0 by dialysis. The pre-gel was mixed with the neutralization buffer (47.7 mg/mL HEPES; 0.08 N NaOH) and concentrated nutrient medium (10× MEM, in a volume ratio of 8:1:1) and incubated in an ice bath. Gelation was observed during a 30-min incubation at 37°C. The authors conducted studies using three groups of samples: (i) acid-soluble telocollagen; (ii) pepsin-soluble collagen, and (iii) porcine liver dECM. Pepsin-soluble collagen had a constant G' value in the strain range of 0.1%–20%. However, when the strain was increased above 20%, G' decreased sharply with a simultaneous increase in G'', and this phenomenon was concentration-dependent. Porcine atelocollagen at a concentration of 1 mg/mL did not exhibit G' crossing G'', indicating a relatively viscous state. However, at a concentration of 2 mg/mL, an intersection of G' and G'' was observed, demonstrating that elastic behavior became more pronounced with increasing concentration. For the liver dECM hydrogel, the range of linear viscoelasticity appeared narrower, ranging at 0.1%–10%. In addition, an increase in G' and G'' at high frequencies was recorded for both telocollagen and liver dECM. In comparison with pepsin-soluble collagen, the G' and G'' did not intersect in the measured frequency range. When comparing acid-soluble collagen type I (3 mg/mL) and liver extracellular matrix (L-ECM; 10 mg/mL), comparable fiber densities were noted. The fiber diameter in the 3 mg/mL collagen gel sample was larger compared to that for the liver dECM, but the fiber density in the 20 mg/mL liver dECM hydrogel was higher compared to that for the 10 mg/mL hydrogel. The authors suggest that the diameter of the fibers depended on the presence of additional ECM components other than collagen, while the density depended on the concentration.

3.2.2. Alternative methods to obtain dECM

Higher-quality dECM hydrogels can be produced using alternative decellularization methods instead of chemical techniques. For instance, a custom laboratory-scale ultrafiltration system was used to concentrate a porcine dermis atelocollagen solution and remove both telopeptide and pepsin.[36] The dermis layer of the porcine skin was sliced and then placed in a $scCO_2$ vessel system containing 75% ethanol as a co-solvent. After the decellularization step, the obtained dermal membrane was freeze-dried and sterilized by γ-irradiation. After that, the minced dermal membrane

was treated with a continuous flow of liquid nitrogen and fed to a freeze-miller. Sieved particles of 50–200 μm sizes were collected and sterilized again by γ-irradiation. Freeze-milled powders were soaked in pepsin (1 mg/mL in 10 mM HCl, pH 2.0) and shaken for 16–18 h at 25°C. The obtained acidified atelocollagen solution was filtered using the lab-built ultrafiltration unit consisting of two columns; the first column blocked and removed particles larger than 1.4 μm, and the second one retained proteins with molecular mass higher than 150 kDa. With the use of the second column, the atelocollagen solution was concentrated by successive runs of 0.1 N HCl. To adjust pH to 7 and induce the fibrillogenesis, nine parts of the sterilized atelocollagen solution were mixed with one part of 0.2 M phosphate buffer, and the obtained precipitate was centrifuged to form an atelocollagen slurry, which was then freeze-dried to form an atelocollagen powder. This process of atelocollagen preparation can be considered as a process with minimal manipulation, unlike traditional laborious and time-consuming processes, where salting-out, alkali, acid, and enzymatic treatments, as well as ion-exchange chromatography, were used.

Interestingly, Hussey et al.[37] proposed a new method for the preparation of dECM hydrogels using ultrasonic cavitation instead of the traditional mild-acidified pepsin digestion. Lyophilized and milled dECM was used as a starting material; dECM was resuspended in a neutral buffered salt solution and dissolved by sonication.[37]

In dECM stock production, apart from removing pepsin and telopeptides, there is a need to streamline the process for clinical translation. For example, a second lyophilization step is proposed to standardize and ease the manufacturing process.[30] This modification of the Freytes et al.[26] method facilitates the formation of stock material for dECM hydrogel preparation and long-term storage of the stock dECM material.

3.3. Gelation process of dECM hydrogels

After the preparation steps, dECM-based hydrogels undergo polymerization under standard conditions of neutral pH and a temperature of 37ºC. It should be noted that the exact mechanism of gelation of ECM hydrogels, as well as the role of pH and temperature factors, have not been precisely established. Although the kinetics of the self-assembly of collagen fibers upon changes in the pH and temperature are known, the role of other ECM components in collagen assembly cannot be ignored. Voytik-Harbin and Brightman[27] demonstrated that ECM hydrogels are characterized by self-assembly kinetics, network structure, and fiber morphology different from those of purified type I collagen. For example, the addition of sGAG, heparin in particular, or PGs (decorin), to purified type I collagen revealed that heparin promotes faster collagen gelation and fiber thickening. Decorin also increases the rate of collagen gelation, but does not affect either the thickness of fibers or their compaction.[27] These results are consistent with the known function of heparin as a nucleation site for collagen fibrillogenesis, and of decorin as a regulator of collagen fiber self-assembly.[38] In addition to heparin and decorin, many other ECM proteins also affect collagen assembly; fibronectin and minor types of collagens (collagen V and XI) are known as nucleation sites, the presence of which is necessary for *in vivo* collagen fibrillogenesis.[39]

However, dECM hydrogels, similar to type I collagen, are subject to *in vitro* degradation to a greater extent compared to composite hydrogels. For example, Kayabölen[40] measured the degradation kinetics of decellularized adipose tissue hydrogels with the addition of silk fibroin (3:1, 1:1, and 1:3, respectively) and indicated that the 1:3 gel was much more resistant to degradation compared to the 1:1 gel.

Secondly, these biomaterials, depending on the duration of enzymatic hydrolysis and other parameters, may exhibit insufficient elasticity. Low G' was reported for porcine lung dECM hydrogel obtained after 72 h of hydrolysis in acidic pepsin. A rheological study revealed higher and more stable G' for aliquots of the hydrogel taken at 4, 12, and 24 h of hydrolysis, while a drop in G' was recorded for aliquots from 48 to 72 h of hydrolysis.[32]

Thirdly, furthermore, dECM-based hydrogels can harden unevenly and slowly during the bioprinting process, which, combined with a significant nozzle diameter (0.4 mm) and high printing speed, can lead to the collapse of the construct. Additionally, slower gelation of dECM hydrogels has been reported with excess NaOH.[41]

3.4. Modifications used to control the viscosity/ crosslinking of dECM hydrogel

The above circumstances emphasize the need for modifications of dECM hydrogels, which may have a physical or chemical mechanism.

3.4.1. Genipin crosslinking of collagen

The mechanism of crosslinking of collagen and dECM by genipin has not been fully understood. One of the proposed mechanisms includes two stages; in the first stage, a nucleophilic attack of an amino group in the collagen chain on the olefinic part of the α,β-unsaturated ester in the genipin molecule takes place, opening of the genipin ring; then, an amino group of another collagen chain attacks the methoxycarbonyl group to form an amide bond, thus crosslinking the two collagen chains.[42,43]

Genipin, due to its low toxicity compared to glutaraldehyde, is used in the preparation of crosslinked

dECM hydrogels. For example, Boso et al.[44] lyophilized a decellularized diaphragm powder (1%, 2%, and 3%), which was subjected to enzymatic hydrolysis with the addition of up to 10% pepsin in 0.5 M acetic acid for 48 h. To restore the osmolarity and physiological conditions, the pre-gel was titrated to pH 7.4, followed by the addition of 10% 1× PBS. After hydrogel formation, 1 mM genipin in 1× PBS was immediately added and incubated overnight; the hydrogels were washed three times with 1× PBS to remove the residual genipin. Crosslinking using genipin can be monitored by recording fluorescence at an excitation wavelength of 590 nm and an emission wavelength of 630 nm. The same authors indicated that hydrogels crosslinked with genipin demonstrated denser organization of fibers compared to non-crosslinked hydrogels; a twofold increase in viscosity was observed compared to the non-crosslinked hydrogel of the same concentration. In addition, the crosslinked hydrogels exhibited elastic properties to a greater extent than the non-crosslinked gel.[44]

3.4.2. Crosslinking with "zero-length" chain agents

Another frequently used method is crosslinking with bifunctional crosslinkers, 1-ethyl-3-(3-dimethylaminopropyl)carbodiimide (EDC), and N-hydroxysuccinimide (NHS) esters.

EDC, the former reacts with a carboxyl group to form an active O-acylurea intermediate, which is then displaced by the nucleophilic attack of a primary amine. The primary amine then forms an amide bond with this initial carboxyl group, releasing a soluble urea derivative. The O-acylisourea intermediate is unstable in aqueous solutions. NHS and its water-soluble analog (sulfo-NHS) are often used to react with EDC, creating more stable NHS esters. These NHS esters react with primary amines, forming an amide bond and subsequently releasing NHS.

Although EDC and NHS esters both are "zero chain length" crosslinkers, the mechanism of crosslinking cannot be considered biocompatible, since cell culture media contain primary amines. Nevertheless, EDC and NHS were used to crosslink a polyamidoamine dendrimer into which HeLa and 3T3 cells were encapsulated, and cell survival on the second day was 80%.[45]

3.4.3. Photopolymerization

Photopolymerization is a common method for crosslinking of bioprinted hydrogels, allowing for high-precision polymerization control of 3D structures. In order to induce free radical polymerization with chain growth, as well as step-growth polymerization, additional functional groups are introduced into the ECM, like acryloyl chloride, methacryloyl chloride, methacrylic anhydride, 2-isocyanato-ethyl methacrylate, glycidyl methacrylate, 5-norbornene-2-carboxylic acid, cysteine derivatives, dithiothreitol, 3-mercaptopropionic acid, etc.[46]

The first mechanism to be considered is free radical photopolymerization with chain growth. It is known that macromolecules containing a vinyl group are capable of photopolymerization as the chain grows.[46] Irradiation at the appropriate wavelength leads to the absorption of light energy by the photoinitiator and its dissociation with free radical formation. These free radicals attack the vinyl groups of the macromolecular precursor, leading to the homolytic opening of the π bond, thereby forming new free radicals. Therefore, the reaction center spreads as covalent bonds between precursors are completed, which contributes to the formation of a polymer chain from several seconds to minutes. Typically, photopolymerization occurs under ultraviolet (UV; 365 nm) or high-energy visible light (405 nm). Although free radical chain growth photopolymerization has been successfully used to obtain 3D cell constructs, the photopolymerization conditions must be carefully selected. It was reported that cell survival in the presence of several photoinitiators depends on the cell type and growth rate. Irgacure 2959 (2-hydroxy-1-(4-(2-hydroxyethoxy)phenyl)-2-methylpropan-1-one) turned out to be one of the least cytotoxic photoinitiators and the most commonly used for cell encapsulation. However, Fedorovich et al.[47] observed unfavorable effects of this photoinitiator on mesenchymal stromal cells (MSC) monolayer. Similarly, Rouillard et al.[48] demonstrated that free radicals generated by this photoinitiator negatively affected cell survival, which was reduced by up to 70%. Another commonly used photoinitiator, lithium phenyl(2,4,6-trimethylbenzoyl)phosphinate (LAP), is less toxic due to its maximum absorption in the near-UV region (i.e., 365 nm).

The second mechanism, step-growth photopolymerization, is used conventionally to produce collagen-based hydrogels. It is known also as thiol-ene polymerization and requires the presence of two functional groups, vinyl and thiol.[46] Thiol-ene is conducted under the same conditions as free radical polymerization, often photochemically induced. It resembles a typical chain process with three stages: initiation, propagation, and termination. Initiation involves the decomposition of the photoinitiator into free radicals, which attack the thiol group and forms thiyl radicals (RS) and other byproducts. Propagation consists of two stages; a thiyl radical attacks C=C double bond, forming the intermediate carbon-centered alkane radical that attacks another thiol group to obtain the thiol-ene addition product, regenerating the thiyl radical. The termination reactions involve radical–radical coupling processes. The step-growth photopolymerization process is considered to be more

cell-compatible compared to radical chain growth polymerization,[46,49] as it is associated with low reactive oxygen species (ROS) levels. When choosing (meth) acrylate as a vinyl group for thiol-ene polymerization, step-growth polymerization is not the only approach, as free radicals of the photoinitiator can interact with both thiol and methacrylate groups. Anseth et al.[50] studied the formation of thiol-methacrylate networks during mixed polymerization, as well as the mechanical properties and degradation kinetics of the resulting gels; these gels were used to encapsulate MSCs. As a result, the gel was obtained by mixed polymerization with the addition of cell adhesion peptides containing cysteine. Additionally, the preparation of a hydrogel consisting of thiolated heparin and methacrylated HA, which polymerizes under visible light, has also been reported.[50,51]

Regarding dECM hydrogels, slightly different approaches are used, the essence of which is to introduce functional groups into the dECM (most often [meth] acrylate) or by mixing with materials that improve the micromechanical properties of dECM. For example, Brew[52] functionalized placenta dECM after decellularization and enzymatic hydrolysis using methacrylation.

3.4.4. Physical modifications with interpenetrating polymer networks

The interpenetrating polymer network (IPN) is a polymer network consisting of two different polymer networks that are bound to each other at least partially but non-covalently. The hydrophobic, ionic, or hydrogen bonding inside the IPN is responsible for the improved mechanics and degradation behavior. There are some examples of generating IPNs with collagen and dECM. For instance, Shi et al.[53] utilized GelMA hydrogel to encapsulate chondrocytes and construct a phase transition 3D cell culture system, in which gelatin microspheres created micropores within the hydrogel. They demonstrated that after 28 days of culture, the GelMA phase transition culture system forms an ECM predominantly composed of collagen type II, collagen type I, and fibronectin. After decellularization, the protein types and mechanical properties are well preserved, fabricating a dECM-GelMA IPN that consists of GelMA hydrogel as the first-level network and the ECM secreted by chondrocytes as the second-level network. Crosby et al.[54] have synthesized an IPN hydrogel comprised of collagen and norbornene-modified HA (NorHA) (1 wt% NorHA and 0.25 wt% collagen). The approaches to modifications of dECM hydrogel are summarized in Figure 4.

4. Bioprinting of dECM-based constructs

As mentioned above, dECM hydrogels can reproduce the native microenvironment of stem cells and possess a biochemically unique signature of tissue-specific ECM. Hence, these hydrogels can be considered a base for bioink and a medium for expanding cells, spheroids, or organoids. Moreover, they can be regarded as GMP-compliant systems for 3D cell culture, in contrast to routinely used basement membrane extracts (BME)-related products obtained from tumorigenic cell lines.

The replication of bioprinted microtissues or structures depends on how close their architecture is to the anatomical features of their native counterparts. The complexity of the anatomical organization of tissues and organs, including multiple repeating functional units and at least several types of cells, defines bioprinting resolution as a crucial parameter for 3D tissue engineering. For liver lobule representation, the printing resolution should be high enough to generate a hexagon structure with 12 radial channels (liver sinusoids) and a central cavity; the total size of the lobule should not exceed 1.5 mm. For instance, this was achieved by Mao et al.,[9] who used a customized digital light processing (DLP) setup with a resolution of 200–500 μm.

The resolution of bioprinting is largely related to the technical characteristics of the bioprinter platform and the physicochemical properties of the bioink. Three main 3D bioprinting technologies include inkjet, microextrusion, and laser-based methods, namely laser-induced direct transfer (LIFT) technology, DLP, and stereolithography (SLA) technology. The resolution of inkjet bioprinting is determined by the contact angle of the surface; the speed of the nozzle in conjunction with the nonlinearity of viscoelastic properties has a decisive influence on microextrusion; and the resolution of printers with laser-based technology depends on the photo-crosslinking parameters and light characteristics.

The application of 3D printing technologies for organ-on-a-chip platforms has encountered difficulties in creating constructs that are physiologically comparable to native tissues at the desired resolutions, which are dictated by the detailed anatomical and physiological features of biological tissues. An ideal ECM-like microenvironment should have the following properties: (i) the pore size several times larger than the size of cells, which is necessary to create an adequate contractile force for cell motility; (ii) the pores must communicate with each other to ensure the diffusion of nutrients and metabolites; (iii) the appropriate surface chemistry must be maintained. In addition, it is crucial to maintain the accuracy of cell distribution, especially when using organs-on-a-chip for drug resistance research. The broad spectrum of approaches employed to create tissue-engineered liver via 3D bioprinting is summarized in Table 3.

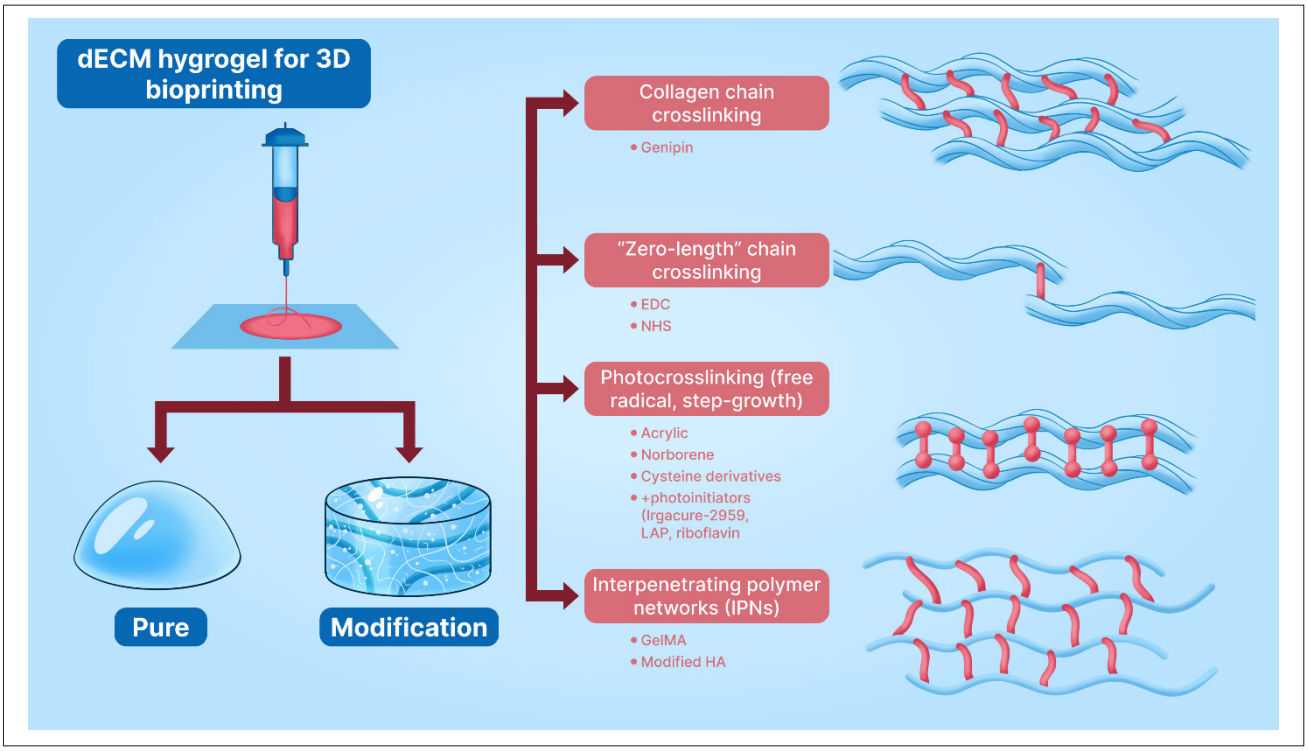

Figure 4. Major techniques of decellularized extracellular matrix (dECM) hydrogel modifications to improve mechanical properties. Abbreviations: EDC, 1-ethyl-3-(3-dimethylaminopropyl)carbodiimide; GelMA, gelatin methacrylate; HA, hyaluronic acid; LAP, lithium phenyl(2,4,6-trimethylbenzoyl) phosphinate; NHS, N-hydroxysuccinimide.

The cell patterning and organization in bioprinting are further complicated by multi-component designs required to reproduce highly vascularized organs and tissues (e.g., the liver). Cell patterning plays a critical role in liver tissue biofabrication because a functional liver is composed of multiple cell types, which necessitates the use of bioinks made from various materials and cell types in liver bioprinting. Liver sinusoids are distinct microvascular systems (less than 10 μm in diameter) lined by sinusoidal endothelial cells that form a radial pattern; they are critical for the survival and function of liver hepatocytes.[65] Accordingly, a similar resolution of about 10 μm is required to reproduce hepatic and liver sinusoidal cell patterns.

In addition to the difficulties associated with reproducing cellular patterns and microenvironments, bioprinting is also challenged from other aspects, such as increased printing speed, printing using multiple types of materials and cells, and the need to minimize shear strain on cells. Taken together, these factors may contribute to the loss or reduction of resolution in the final construct. When bioprinting is used to generate support structures and microfluidic channels, the resolution provided by the technology platform, as well as the viscoelastic properties of the biomaterial, play a key role in the functioning of the organ-on-a-chip platform. The influence of various 3D bioprinting parameters on the resolution of constructs is discussed in detail below.

4.1. Inkjet bioprinting systems

In the case of droplet-jet bioprinting, the bioink is pressed through a nozzle with a small diameter, leading to bioink deposition in the form of individual droplets (Rayleigh–Plateau instability). These droplets become charged, and accordingly, an electric field is used to precisely position the droplets. For bioprinting of materials, drop-on-demand (DOD) bioprinters are used, which can be divided depending on the method of droplet formation: printers with a temperature or piezoelectric print head,[66] as well as inkjet printers that use ultrasound to form droplets of the material.[67]

The resolution of inkjet, mainly DOD, printers is determined by the size of a drop on a flat surface, from which the vertical and lateral resolution can be determined.[68] Several studies have demonstrated the ability of DOD bioprinting to generate high-resolution cell constructs with limitations on hydrogel viscosity (≤10 mPa/s) and cell number (≤10 million/mL).[69] Additionally, DOD inkjet bioprinting has been used to fabricate a liver-on-a-chip by patterning liver organoids.[70] Bioequivalents were represented by layers of human umbilical vein

Table 3. Summary of methodical approaches used for 3D bioprinting of liver constructs.

Bioprinting method	Material	Cells	Physiological activity	Printing parameters	Resolution (μm)	Ref.
DMD	(i) 5% GelMA for supporting hiPSC-HPCs; (ii) 2.5% GelMA with 1% GMHA for supporting cells	HPCs and HUVECs-ADSCs (50:1; 4×10^7 HUVECs and 8×10^5 ADSCs)	76% viable cells within 2 h following printing; 65% viable cells after a week; higher expression levels of HNF4α, TTR, and ALB in triculture	Size: 500 μm; height: 200 μm; first layer: HPCs in a 1:1 prepolymer of 10% GelMA; second layer: supportive cells in a prepolymer of 5% GelMA and 2% Glycidyl methacrylate-hyaluronic acid (GMHA)	50–200	[55]
Extrusion	3% alginate with 1% $CaCl_2$	Primary rat hepatocytes (4×10^7 cells/mL)	Viable culture after 14 days	Size: 25 × 25 mm (square); seven layers	200–500	[56]
	dECM with 10% GelMA and 0.5% LAP	hiHep cells ($2.5–3.0 \times 10^6$ cells/mL)	More live cells in dECM-incorporated bioink after 1 and 3 days of culture	Size: ~10 mm (round); height: 2 mm; protrusions (gear-like form)	200–500	[9]
	2% alginate with 3% gelatin and liver dECM (0, 0.25, 0.5, 1, and 2 mg/mL)	HepaRG (7×10^6 cells/mL)	Impairment of cellular metabolism at 2 mg/mL dECM	Size: 10 × 10 mm; H (height): 1 mm; regular pores	200–500	[57]
	Porous gelatin scaffold	Huh 7 (3.3×10^6/mL)	Higher ALB secretion for a layer orientation of 60° (compared to 90° and 2D control on day 7)	Size: 15 × 15 mm; nozzle diameter: 200 μm; *D* (distance) between filaments: 700 μm; *L* (layer thickness): 156 μm		[58]
	4% alginate; 20% gelatin	HepaRG (1×10^6 cells/mL)	Higher gene expression of differentiated HepaRG	Nozzle: 23G; printing speed: 150 mm^3/min.		[59]
	liver Liver dECM hydrogel; Pluronic F127 as a FRESH substrate	Immortalized cholangiocytes and Huh 7 spheroids	Cholangiocytes remained viable after 7 days of cultivation; the morphology (proliferation and branching) depended on Huh7 spheroid concentration in the area	Nozzle: 200 or 150 μm		[60]
	15% alginate; 6% Pluronic F-127	75% hepatoblasts, 20% induced endothelial cells, and 5% induced MSCs (1×10^7 cells/mL)	High levels of urea secretion in liver spheroids compared to a suspension of single cells	Size: 10 mm (donut-shaped); *H* (height): 5 mm; n (Needle): 20G	-	[61]
	GelXA LAMININK: gelatin, alginate, xanthan gum, and LAMININ 521	HepG2 (3×10^7 cells/mL)	Highest cell viability and proliferation capacity when printed with GelXA LAMININK521	Size: 3 mm (hexagonal); height: 2 mm; Nnozzle: 25G	-	[62]

(*Continue...*)

doi: 10.36922/ijb.4343

Table 3. Continue...

Bioprinting method	Material	Cells	Physiological activity	Printing parameters	Resolution (μm)	Ref.
	10% GelMA; PEG-bis-acryloyloxyacetate	HepaRG and human liver stellate cells (10×10^7 cells/mL)	High viability for 14 days of culture; Ki-67+ cells were detected, but their number decreased during cultivation	Size: 4 mm (hexagonal); height: 5 mm; 12 hollow channels inside every hexagonal structure	67.2	[63]
SLA	20% PEGDA (3400 MW) with 20 μM/mL acryloyl-PEG-RGDS	Hepatocytes ($5–15 \times 10^6$)	Inclusion of the synthetic RGDS peptide led to a 5-fold increase in ALB secretion	Size: 34 mm	-	[64]

Abbreviations: ADSCs, adipose derived stem cells; ALB, albumin; dECM, decellularized extracellular matrix; DMD: Digital micromirror device; FRESH, freeform reversible embedding of suspended hydrogels; GelMA, gelatin methacrylate; GMHA, glycidyl methacrylate-hyaluronic acid; GST, glutathione S-transferase; hiHep, human-induced hepatocytes; hiPSC-HPCs, human induced pluripotent stem cells-hepatic progenitor cells; HPCs, hepatocyte progenitor cells; HUVECs, human umbilical vein endothelial cells; LDH, lactate dehydrogenase; MRP-2, multidrug resistance-associated protein 2; MSCs, mesenchymal stromal cells; MW, molecular weight; PEGDA, polyethylene glycol diacrylate; PEG, polyethylene glycol; RGDS, Arg-Gly-Asp-Ser peptide; SLA, stereolithography; TTR, Transthyretin.

endothelial cells (HUVECs) and HepG2 cells, while layers of fibronectin and gelatin were used as scaffolds. The authors reported that, by using DOD in printed organoids, a resolution of about 400 μm was achieved. This resolution can be improved by using hydrophobic surfaces (i.e., those with a large contact angle).[70]

An important advantage of inkjet DOD bioprinting is that bioprinting is performed in a virtually non-contact manner, which reduces the risk of contamination.[71] Another advantage of inkjet bioprinting is the ability to reproduce cellular patterns with multiple cell types and hydrogels using different types of printing heads. Despite these examples, the main disadvantage of DOD bioprinting remains its low resolution in the context of 3D models and organs-on-a-chip.

4.2. Extrusion bioprinting systems

Microextrusion bioprinting is a biofabrication technology that uses compressed air pressure or a syringe pump to extrude a highly viscous liquid (or gel) containing biomaterials and/or cells. An ideal biomaterial for microextrusion bioprinting should exhibit pseudoplasticity and thixotropy.

Among the physical properties of bioinks, the dynamic viscosity plays an important role in achieving a good resolution, along with the "printing threshold" (initiating the release of the bioink from the nozzle and stable formation on the surface of the platform). Extrusion bioprinting supports hydrogels with a viscosity range from 1×10^2 to 1×10^9 mPa/s.[72] Another important factor determining the resolution of microextrusion bioprinting is the speed of a material passing through the nozzle (extrusion speed), which is influenced by the pneumatic pressure or plunger stroke speed. The extrusion speed also affects cell survival; for example, an extrusion speed of 0.5 mm^3/s (0.5 μL/s) was reportedly optimal for cell survival, considering factors such as the extrusion time and shear strain.[73]

In general, it is known that the maximum resolution of microextrusion bioprinting is 50 μm.[74] However, this resolution can only be achieved under near-ideal model conditions using non-biocompatible materials without a cellular component. Typically, when the cell suspension density is 10^7 cells/mL or higher, a nozzle with a minimum diameter of 200 μm should be used; accordingly, the final resolution of the construct is expected to be in the range of 200–500 μm.[74] Microextrusion bioprinting is often used to generate functional liver constructs (Table 4).

4.3. Laser-based bioprinting systems

Laser-based bioprinting systems include stereolithography, two-photon polymerization, digital light projection, and

Table 4. Analysis of extrusion printing of liver constructs.

Bioink type	Hydrogel composition	Cells	Results	Ref.
Liver-specific hydrogel/liver-specific cells	Gelatin/porcine liver matrix microparticles (size: 13.4 μm)	Fibroblasts 3T3, HUVECs, mouse hepatocytes	The addition of microparticles improved the mechanical properties and printability; cell survival and ALB secretion were higher compared to gelatin without microparticles	[75]
	Pig liver ECM hydrogel combined with type I collagen (pig dermis)	HepG2, bone marrow MSCs	Liver dECM hydrogel contributed to the survival of cells and more pronounced (compared to type I collagen) differentiation of MSCs into liver cells (assessed using markers HNF1α, HNF3β, HNF4α, ALB, AFP, TTR, and CK18)	[76]
	HA/gelatin/liver ECM crosslinked with PEG-based crosslinkers	Primary human hepatocytes, primary stellate cells, Kupffer cells	Constructs maintained a high survival rate and detectable levels of ALB and urea on day 14 of culture	[77]
Non-specific hydrogel/liver-specific cells	AlgianteAlginate/gelatin/human lung dECM	HepaRG	Cells maintained good viability, and metabolic and functional activities (ALB, CYP3A4); HepaRG cells were successfully transduced with AAV serotype 6 vectors	[57]
	Col I-MA/HA-SH	Liver stellate cells LX2, activated fetal HSCs, human hepatocytes	Functional activity (secretion of ALB and urea) was observed for 15 days	[78]
	Alginate	HepG2	Cells encapsulated in alginate proliferated (Ki67+) and expressed metabolic markers (ALB, ASGPR1, AFP, CYP1A2, TAT) during 21 days of culture	[79]
	Alginate	Mouse hepatocytes	Functional activity of cells (expression of ALB, CK18, ASGPR1, HNF4α, Foxa3) during 14 days of culture	[56]
	PCL (substrate)/atelocollagen (cell encapsulation)	Rat hepatocytes, HUVECs, human lung fibroblasts	Maintained cell functionality for 10 days; co-culture with HUVECs improved the functional properties of the constructs	[80]

Abbreviations: ALB, albumin; AAV 6, adeno-associated virus type 6 vectors; ASGPR1, Asialoglycoprotein receptor 1; CK18, Cytokeratin 18; Col I-MA/HA-SH, Collagen I-methacrylated/thiolated hyaluronic acid; dECM, decellularized extracellular matrix; ECM, extracellular matrix; HA, hyaluronic acid; HSCs, hepatic stellate cells; HUVECs, human umbilical vein endothelial cells; MSCs, mesenchymal stromal cells; PCL, polycaprolactone; PEG, polyethylene glycol; TAT, tyrosine aminotransferase; TTR, transthyretin.

volumetric methods.[81,82] Unlike microextrusion and inkjet methods, bioprinting using visible or UV light involves the delivery of the photon energy to the desired point, which leads to local polymerization of the construct at that point. Moreover, the resolution of these bioprinting methods ranges from a micrometer or less than a micrometer.[81,82] The features of each of these methods, as well as their disadvantages, advantages, and resolution, are summarized in Table 5.

4.3.1. Laser-induced forward transfer

In general, a LIFT bioprinter comprises three elements: a laser that generates pulsed beams, a radiation-absorbing layer, and the material on the back of the latter. Laser radiation is absorbed by a thin layer of absorbent material on a transparent substrate. Absorption of pulsed laser energy at the interface between the transparent donor and the absorbent layer results in the formation of vapor bubbles or mechanical waves that destroy the donor layer around the irradiated area, transferring the bioink dropwise to the collector.[84,85]

In a study conducted by Leva et al.,[82] LIFT technology was used to print Huh7 tumor cells on porous scaffolds made of collagen and GAGs. Scaffolds were prepared by lyophilizing a collagen suspension (5 mg/mL fibrillated collagen; 0.44 mg/mL chondroitin 6-sulfate dissolved in 0.5 M acetic acid). To deposit cells onto the surface of the scaffold, the following parameters were used: the diameter of the round laser spot was 60 μm, the distance between the donor layer and the substrate was 500 μm, and the laser pulse density required for printing cells on the scaffold was 530 mJ/cm^2. The authors demonstrated that the LIFT method allowed precise positioning of cellular patterns, as each drop deposited on the matrix had a diameter of 100 μm and included 16–20 cells; the cell viability was 100% within 2 h after the completion of printing.

However, the difficulty of controlled deposition of individual droplets is a major challenge of LIFT technology,

Table 5. Summary of laser-based bioprinting methods in liver tissue engineering.

Bioprinting method	Resolution (μm)	Viability (%)	Hydrogel composition	Examples of liver constructs	Ref.
LIFT	>>100	90–100	Porous collagen and GAGs as the substrate	Porous scaffolds made of collagen and GAGs	[82]
SLA	>50	85–90	GelMA GelMA/GMHA	3D hexagonal lobule-like liver structures with iPSC-derived hepatocytes, HUVECs, and AT-MSCs	[55]
DMD/DLP	<100	75–90	5% liver dECM with 5% GelMA	Liver constructs (3 × 3 × 250 μm) with hexagonal lobules containing round elements (portal triad and central vein); each hexagonal lobe (diameter: 1 mm) had sinusoidal sections with a width of 35 μm	[83]

Abbreviations: AT-MSCs, adipose tissue-derived mesenchymal stem cells; dECM, decellularized extracellular matrix; DLP, digital light processing; DMD, digital micromirror device; GAGs, glycosaminoglycans; GelMA, gelatin methacrylate; GMHA, glycidyl methacrylate-hyaluronic acid; HUVECs, human umbilical vein endothelial cells; iPSCs, induced pluripotent stem cells; LIFT, laser-induced forward transfer; SLA, stereolithography.

which limits its resolution to 100 μm. In addition, one of the problems with LIFT is the unwanted deposition of a "residue" from the absorbent layer.[85,86]

4.3.2. Stereolithography

Most SLA printers are configured in such a way that a light source cures a vat filled with liquid photoresin on a moving platform. As soon as one of the layers is polymerized, the stand is lowered to a specified distance (depending on the vertical resolution of the SLA printer) to polymerize the next layer. SLA bioprinting was originally used to generate bone tissue models. For example, an SLA bioprinter with a resolution of 100 μm was used to cure a biodegradable photopolymer, represented by diethyl fumarate, poly(polypropylene fumarate), and bisacylphosphine oxide (with an absorption maximum of 325 nm) as a model for the regeneration of a critical bone defect with a thickness of about 4 mm and a diameter of 50 mm.[87] Another study reported the use of SLA technology to fabricate 1 mm neural conduits with a resolution greater than 50 μm.[88] SLA is used in the rapid fabrication of microfluidic systems using transparent photopolymers. The main advantages of the SLA method include eliminating the need for substrates and enabling rapid prototyping. However, in general, the SLA method is rarely used in bioprinting and tissue engineering due to low resolution and poor biocompatibility.

4.3.3. Laser printing using a digital micromirror device or digital light processing

New technologies, such as continuous DLP or digital micromirror device (DMD), make it possible to generate dynamic masks through personal computer (PC)-controlled control of micromirrors, where polymerization occurs per unit volume of the photopolymer, accelerating the photo-crosslinking process. A DMD consists of millions of mirrors arranged in columns and rows. Upon exposure, the DMD mirrors can reflect or project the light, resulting in a light pattern. Each layer is cured based on the light pattern generated by the DMD chip, and the light is then modulated and passed through reduction lenses onto the photopolymer. After patterning each layer, the substrate is lowered by a movable stand into a container with the photopolymer; thus, the light pattern falls on the next layer. The resolution of this method is comparable to the size of single cells, which can reach up to 5 μm just by adjusting the laser power. This method allows the use of high-density cell suspensions (from several million/mL) compared to methods that use nozzles.[88]

Using DLP technology, Mao et al.[9] utilized 10% GelMA in combination with 3% or 1.5% porcine liver dECM as a composite bioink containing hiHep cells. All bioink types were characterized by remarkable cell viability, but the addition of liver decellularized extracellular matrix (ldECM) increased the number of living cells compared to pure GelMA.[9]

Ma et al.[89] used liver dECM as a bioink in conjunction with the DLP approach to engineer a hepatocellular carcinoma model. For bioink formulation, 5% GelMA and 5% liver dECM were mixed with HepG2/C3A cells. Hexagonal constructs with a height of 200 μm were fabricated using a custom DMD-based system.[89] Using DMD, Zhu et al.[90] produced pre-vascularized constructs with complex geometries and varying widths (<50 μm) and 50–100 μm, more than 50 μm, using endothelial cells that were encapsulated in a mixture of HA glycidyl methacrylate and GelMA.

4.3.4. Laser bioprinting using two-photon lithography

Two-photon lithography (TPL) is an emerging laser-assisted bioprinting (LAB) technology that provides the

highest resolution in the biofabrication of 3D scaffolds. Unlike traditional LAB technologies, TPL does not require composite optical systems or photomasks. On the contrary, this method uses a near-infrared ultrafast femtosecond laser. Multiphoton absorption occurs in a medium that transmits the emitted light and does not absorb the light of the specified laser length. With two-photon polymerization, the fabrication of 3D objects is not limited to the layer-by-layer method. Microstructures are created from a transparent photosensitive material that has high absorption in the UV range and is transparent in the infrared region. Thus, 3D free-form constructs can be reproduced using a high-intensity femtosecond laser when the simultaneous energy of two photons exceeds the absorption energy threshold of the photosensitive material.[90,91]

In particular, using polyethylene glycol (PEG) tetrabicyclonine as a sensitive photopolymer, channel structures were generated by the photodegradation of the photopolymer in accordance with the given pattern, with a lateral resolution in the 1 μm order.[91,92] TPL is a promising technology in the field of 3D bioprinting because it can reproduce microtissue patterns at submicron resolution.

5. Large-scale manufacturing of dECM hydrogels and clinical translation

Although many dECM-derived materials still require evaluation at the pre-clinical stage, numerous decellularized products have become commercially available (Apligraf, GraftJacket, AlloDerm, etc.). These decellularized materials are most commonly manufactured in the form of sheets. Implantation of decellularized sheets requires more invasive procedures compared to injectable forms of decellularized materials. In particular, ECM hydrogels have been increasingly studied for their potential for minimally invasive delivery. Their gel form is advantageous for filling abnormally shaped defects. In addition, dECM pre-gel can be injected into the surgical site, and at a human body temperature (37°C), the dECM pre-gel can rapidly form a dECM hydrogel, highlighting the use of these hydrogels as an injectable substance to treat local trauma or disease. However, there is only one clinical trial conducted to evaluate the safety/efficacy of dECM hydrogels, i.e., a decellularized myocardial matrix from Ventrix, Inc. (ClinicalTrials.gov identifier: NCT02305602). The study findings support the initial safety and feasibility of injecting VentriGel, an ECM hydrogel derived from porcine myocardium, in post-myocardial infarction patients with left ventricular dysfunction.[93] They conducted a first-in-man, single-arm, multicenter trial to demonstrate the safety, feasibility, and preliminary efficacy of percutaneous trans-endocardial delivery of VentriGel. The safety (absence of adverse events) and efficacy (i.e., treatment with VentriGel significantly increased the maximum walk distance with time post-injection at 3 and 6 months) of the injection therapy of MI with Ventrigel were validated.[93] Hence, dECM hydrogels can be potentially applied as hemostatic materials[94] because of their good temperature sensitivity and ability to form irregular porous reticular scaffolds at 37°C that mechanically seal the vascular breach and form a physical barrier. However, they have poor mechanical properties, which hinder their application in the field. Despite their disadvantages, dECM hydrogels are extensively studied and used in regenerating various types of tissues *in vivo*. The progress of translating dECM hydrogels towards clinical applications is summarized in Table 6.

Although dECM hydrogels are extensively studied and are attractive for clinical translation (Table 6), only one product has reached clinical trials. This circumstance could be related to the existence of many specific challenges in the clinical translation of these materials. Firstly, manufacturing standards are not well established for dECM hydrogels. Challenges may also arise from laboratory processes related to dECM hydrogel preparation, such as the absence of a standardized protocol for tissue decellularization (although there are standardized criteria for effective tissue decellularization, cell nuclei are not visible on histological slides and residual double-stranded DNA [dsDNA] content is less than 50 ng/mg dry mass[115]), the need for complete pepsin and telopeptides removal, sterilization of the dECM material, and adequate source of dECM. Additionally, challenges associated with upscaling from laboratory to manufacturing include inter-animal differences, the need for reducing biological burden, and the influence of different harvesting conditions on product quality.

5.1. Challenges in scaling up from laboratory to manufacturing

When designing biomaterials for regenerative medicine applications, including dECMs, it is important to consider the implications for manufacturing, namely, increased costs, availability of raw materials, or difficulty of production. Animal-to-animal variability, bioburden reduction, and different harvesting conditions are challenges that need to be considered when scaling up the dECM hydrogel production from the laboratory to the GMP-graded manufacturing scale.[116] When scaling up to a manufacturing-scale batch, a certain number of donors or animals is required to eliminate batch effects; bioburden reduction is a necessary step that alters the properties and quality of the final product. Hence, the final product must

Table 6. Progress toward clinical translation.

Tissue target	Tissue source	*In vitro* studies	Biocompatability/ Biocompatibility/ histological assessment	Functional studies	Clinical trials	Functional outcomes
Myocardium	Porcine myocardium	[95,96]	[97]	[98–100]	[93]	Clinical trial results support the safety and feasibility of transendocardial injection of VentriGel in post-MI patients with LV dysfunction and introduce a new potential treatment for patients with heart failure[93]
	Human placenta	[101]	[101]	[101]	-	Compared to sham-treated animals, hpECM-injected rat hearts displayed a significant reduction in scar volume and normal electrical activity of the surviving tissue[101]
Skeletal muscle	Porcine hindlimb skeletal muscle	[102]	[102]	-	-	Obtained hydrogels were characterized by superior biocompatibility and low immunogenicity[102]
	Human umbilical cord	[103]	[103]	[103]	-	Improved hindlimb tissue vascularization and perfusion[103]
	Porcine dermis	[104]	[104]	-	-	ECM hydrogels were fully infiltrated with CD68+ cells within 3 days of implantation; CD68+ cells continued to populate the hydrogels at all timepoints and remained in the remodeled tissue after the hydrogel had degraded[104]
Tendon	Human tendon	[105]	[105]	[105]	-	Both fetal bovine serum and hydrogel injection in rats led to more cells inside the tendon compared with culturing[105]
Articular cartilage	Porcine articular cartilage	[106]	-	-	-	Human MSCs cultured on hydrogels from shark skull cartilage, as well as pig articular and auricular cartilage ECM, had increased expression of chondrocyte markers and decreased secretion of angiogenic factors VEGF-A and FGF2[106]
Meniscus	Bovine meniscus	[107]	-	-	-	Region-depended increase of collagen type I and type II and aggrecan expressions in the presence of ECM[107]
Liver	Porcine liver	[108]	-	-	-	Immortalized human hepatocytes were encapsulated in the hydrogels and survived for a week[108]
	Porcine and human livers	[109]	-	-	-	Proliferation rates of organoids cultured in liver ECM hydrogels were lower, but the differentiation capacity of the cholangiocyte organoids towards hepatocyte-like cells is not altered by the presence of tissue-specific ECM components[109]

(*Continue...*)

doi: 10.36922/ijb.4343

Table 6. Continue...

Tissue target	Tissue source	*In vitro* studies	Biocompatability/ Biocompatibility/ histological assessment	Functional studies	Clinical trials	Functional outcomes
Lung	Porcine lung	[32]	-	-	-	A 12-h pepsin digestion of pig lung dECM provides an optimal balance between desirable physical ECM hydrogel properties and effects on lung cell behaviors[32]
Brain	Porcine brain	[30,110]	-	-	-	Rheological results revealed stable hydrogel formation, starting from 5 mg/mL hydrogel; hESCs cultured in ECM exhibited gene expression and differentiation outcomes similar to those cultured in Matrigel[30]
	Human umbilical cord	[111]	[111]	-	-	Injection of umbilical cord-ECM hydrogels into a photothrombotic cortical ischemic lesion in rats resulted in *in vivo* gelation and infiltration with host macrophages[111]
Adipose tissue	Human adipose	[112, 113]	[114]	-	-	From histological assessment, the vascularization process in the hydrogels implanted with adipogenic and endothelial pre-differentiated ASCs was faster than observed in the empty hydrogels[114]

Note: Citations in columns indicate studies on dECM hydrogel in: (i) *in vitro* studies only (least translated), (ii) biocompatibility/histological assessment (i.e., hydrogel injected *in vivo*), (iii) functional study (animal model), and (iv) clinical trials. Abbreviations: ASCs, adipose stem cells; B-ECM, brain extracellular matrix hydrogel; ECM, extracellular matrix; FGF-2, fibroblast growth factor 2; hESCs, human embryonic stem cells; hpECM, human placenta extracellular matrix; LivMA, methacrylated liver extracellular matrix hydrogel; LV, left ventricular; mECM, meniscus extracellular matrix; MI, myocardial infarction; MSCs, mesenchymal stem cells; VEGF-A, vascular endothelial growth factor A.

be evaluated for any changes in its material properties. Different harvesting conditions are also a major factor that can result in inferior quality of the final product.

5.1.1. Challenges associated with the source of dECM

A major concern for large-scale dECM manufacturing is the tissue/organ source used for dECM hydrogel preparation. Three main sources should be considered: patient-derived cells, animal tissues/organs, and human tissues/organs.[117] Cell-derived ECM (CD-ECM) contains a complex and organized mixture of macromolecules that can mimic all aspects of the natural tissue microenvironment.[117] Both primary cells and cell lines have been used to produce CD-EDM. MSCs are easily obtained and are usually used to prepare cell-derived ECM[118] or MBVs (extracellular vesicles bound to ECM crucial for regeneration, especially in 3D conditions).[119] An autologous MSC-derived dECM hydrogel would be an ideal product for clinical translation. Stromal cell-derived ECMs are rich in collagens,[118] while endothelial/epithelial CD-ECMs contain laminin-rich basement membrane-like ECMs.[118] CD-ECM can be generated by scaffold-free 2D and 3D cell cultures.[120] For example, a bioink derived from primary human neonatal dermal fibroblast cell sheets is suitable for 3D bioprinting applications; more importantly, CD-ECM-derived hydrogel retains matrix-deposited growth factors, including EGF, bFGF, NGF, PDGF (A, B, C, and D), IGF-1, TGF-β, and VEGF, in contrast to a dECM hydrogel produced by the standard mild acidified pepsin digestion.[121,122] However, a potential limitation of CD-ECM is its inadequate mechanical properties.

Various tissues from different animals have been widely used to create dECM, such as pig bladder and heart,[123] lung,[32] small intestine,[124] liver,[109] bovine tendons,[125] goat kidney,[126] and rat liver and lungs.[127,128] A major source of heterogeneous dECM is pigs, and the use of swine tissue/organs is superior to other animal sources in many aspects, but one should consider the risk of infection with porcine endogenous retrovirus (PERV).[108]

An animal-to-animal variability as well as different harvesting conditions can significantly affect the resulting properties of the final product, i.e., dECM hydrogels. Evenmore, source variability raises a challenge to a reproducible and standardized manufacturing of dECM materials. Hernandez[116] assessed the effect of animal-to-animal variability and different harvesting conditions on properties of the final dECM hydrogels. The properties of the final dECM hydrogels were evaluated by dsDNA and sGAG quantification, SDS-PAGE gel electrophoresis, and quantitative mass spectrometry. In another study, conducted by Di Francesco et al.,[129] to represent animal-to-animal variability, three out of nine

representative decellularized bovine pericardia were used for experiments, and the properties of the resulting dECM hydrogels prepared from pericardia were assessed by SDS-PAGE gel electrophoresis, rheological characterization, scanning electron microscopy (SEM), and additionally, the influence of animal-to-animal variability on cell viability was assessed by MTS assay. They have shown that although there was a difference in protein composition revealed by mass spectrometry between three different batches, all batches showed the same gelation kinetics, rheological properties, surface structure and same effect in inducing cell viability.[129] Tottey et al.[130] studied the effects of pig source tissue different in age upon extracellular matrix scaffold properties. They have found that the structural, mechanical, and compositional properties of small intestinal submucosa - decellularized extracellular matrix (SIS - dECM) were dependent on the animals' age. For instance, strength (peak load per unit width in uniaxial tensile test) and growth factors content of ECM from 3-week-old animals were less than that of ECM harvested from 12, 26, or >52-week-old animals.[130]

For assessing the effects of animal-to-animal variability on dECM hydrogel properties, longissimus dorsi muscles from four different Yorkshire farm pigs were obtained. Throughout the entire process, including tissue preparation, decellularization, lyophilization, milling, and mild acidified pepsin digestion, all animals were kept separated; but to compare the full batch of a material, the four unfiltered dECM powders from each pig were combined. To assess the effects of different harvesting conditions on the properties of the final dECM hydrogel, longissimus dorsi muscles were obtained from Yorkshire pigs from one source, cross-bred pigs from another source, and boneless pork loin chops from a grocery store. Regarding animal-to-animal variability, there were significant changes in dsDNA and the remaining sGAG content (0.12–1.17 ng dsDNA/mg ECM; 9.13–13.74 μg sGAGs/mg ECM), but these differences fall within the expected ranges for dsDNA and sGAGs. SDS-PAGE did not reveal any differences in the band intensity compared between the four animals. The results of quantitative mass spectrometry revealed that the largest fractions of ECM proteins classified by function were consistent across all the animals, but the amount for each protein was different for each animal. Taken together, it can be concluded that there were minimal effects accounted for animal-to-animal variability; the scaling up from the laboratory to the manufacturing scale would require a larger number of animals to decrease the batch-to-batch variability. However, these differences are still important for the laboratory setting, especially concerning reproducibility. Regarding different harvesting conditions, no significant differences in the residual dsDNA content were found between the three different sources. However, the grocery store batch did not exhibit peptide bands at ~80 and ~90 kDa. The quantitative mass spectrometry data also revealed that, for the grocery store material, the fibrillar collagen and other ECM protein percentages were higher in comparison with the other two sources, while the fractions for the basement membrane were lower. These findings indicate the importance of identifying a feasible raw tissue source and performing quality control experiments.[116]

In order to avoid the spread of disease from animals, i.e., associated with the application of xenogenic dECM, human tissues would be the best choice to produce dECM for clinical applications.[131] Human-derived dECM can be obtained from cadavers, diseased or damaged tissues and organs of patients, and tissues from human tissue biobanks.[131,132] Various tissues and organs from the human body have been used to create dECM. For example, the entire heart,[133] cartilage,[134] ovarian tissue,[135] adipose tissue,[136] pancreas,[137] kidney,[138] liver,[109] skin,[139] teeth,[140] and lungs[141] have been successfully decellularized. However, in the case of cadaveric donors, age is uncontrollable, which leads to great variations in different batches, as non-enzymatic tissue crosslinks tend to increase towards age. Therefore, it is not possible to achieve the industrial-scale production of dECM hydrogels from human tissue sources. Moreover, the sources of autologous and allogeneic tissues are extremely limited.

Interestingly, Willemse et al.[108] prepared dECM hydrogels from porcine and human livers and found differences in Young's modulus and G' depending on the species; porcine liver ECM had a higher G' than human liver ECM. Additionally, by measuring the total protein content, they demonstrated that porcine ECM was digested more efficiently than human ECM, which could be associated with the accumulation of age-related damage and/or non-enzymatic crosslinking of ECM molecules in aged human livers.[108]

5.1.2. Challenges associated with sterilization

For bioburden reduction, sterilization treatment is mandatory and can be achieved via several means throughout the process of dECM hydrogel preparation, among which γ-irradiation is the most frequently used. Typical conditions are presented by an approximate dose of 15 kGy and a duration of about 10 h.[34] There are protocols involving two-step sterilization, on stages of the acellular membrane and milled powder.[36] Another approach is tissue treatment in 0.1% peracetic acid (PAA) solution to reduce bioburden.[116,142,143] Several studies employed a decontamination by soaking the tissue sample in PBS supplemented with penicillin – streptomycin throughout all the decellularization process.[144] However, this may be

insufficient if the dECM source is obtained under unsterile conditions.

6. Future prospects

Currently, several challenges need to be addressed to translate dECM hydrogels into manufacturing and clinical practice. Batch-to-batch variability can affect the manufacturing process of dECM hydrogels slightly.[116] The printability of dECM hydrogels depends on the tissue source, the relative concentration of dECM (i.e., the concentration of pepsin-soluble collagen), and manipulations associated with decellularization and acid hydrolysis. For instance, the G' for 1.37 mg/mL oligomeric collagen is 235 Pa, while that of an 8 mg/mL hydrogel liver dECM is 30 kPa.[145] However, its influence on the printability of dECM hydrogels should not be neglected, as dECM hydrogel batches from different animals of the same species can exhibit different rheological and biomechanical properties. There are no available publications regarding this issue; hence, it is a prospective area for extensive research.

To increase the stability and printability of dECM hydrogels, biorthogonal crosslinking agents should be used, or dECM should be chemically modified with the addition of various functional monomers (acrylate, methacrylate, glycidyl methacrylate, etc.). It should be noted that some "popular" crosslinkers are not biorthogonal. For example, crosslinking using EDC and NHS esters affects the glutamate residue in the GFOGER sequence of collagen, which disrupts cell adhesion.[146] At certain concentrations (IC_{50} = 0.166 mM), genipin has a cytotoxic effect.[147] For these reasons, crosslinking using stepwise (thiol-ene) photopolymerization seems more relevant. An alternative to chemical modification may be the FRESH method.

Unlike microextrusion bioprinting, DMD and DLP bioprinting do not have clear viscosity and viscoelastic property requirements, allowing for the use of suspensions with a higher cell density and is characterized by fewer artifacts compared to extrusion. However, the DMD method requires hydrogel modifications, such as the introduction of functional monomers using photoinitiators, preferably with absorption in the near-UV region (e.g., LAP). The cytotoxicity of hydrogels used in the DMD method is determined mainly by the concentration of the photoinitiator, but practically does not depend on the concentration of the photopolymerized hydrogel.[148]

Therefore, the use of liver dECM as a bioink is promising, as liver dECM hydrogels may contain residual growth factors and GAGs, which serve to deposit growth factors and as nucleation sites during gelation. However, since the process of decellularization and preparation of dECM hydrogels is difficult to standardize, studying the composition of dECM hydrogels in connection with their viscoelastic properties and printability is of high interest.[45,83,129]

Based on the discussion above, the following guidelines for generating dECM hydrogel-based products can be established:

(i) Pre-processing: The source of dECM should be carefully considered in relation to—potential endogenous viral load and—the volume of material required. To minimize batch-to-batch variation, multiple samples should be combined. Additionally, proper sterilization and storage protocols must be implemented.

(ii) Processing: The decellularization technique should be tailored to the specific source material used. Non-chemical decellularization methods are preferable to maintain the integrity of the ECM. Modifications to traditional hydrogel preparation techniques should be selected to preserve essential matrix compounds. The choice of crosslinking mechanisms and bioink composition should align with the desired mechanical properties of the final product.

(iii) 3D bioprinting: The type of bioprinting technology employed should be chosen based on the required resolution and volume of the construct. The geometry of the construct must mimic the structural characteristics of liver components, incorporating pores to facilitate cell function and nutrient exchange.

(iv) Quality control: Each batch of dECM-based products must undergo rigorous quality control assessments, including evaluations of mechanical properties, biocompatibility, and sterility. This ensures consistency and reliability across different production runs.

(v) Application: The final application of dECM hydrogel-based products should be clearly defined, considering factors such as the target tissue or organ system, intended therapeutic outcomes, and regulatory requirements. Understanding the specific application will guide design choices, such as bioink formulation and printing parameters, to optimize functionality and integration within the host environment. This application-focused approach ensures that the developed products effectively meet both scientific and clinical needs.

7. Conclusion

The transition of dECM hydrogels from laboratory research to clinical application presents several significant challenges that must be addressed. The inherent batch-

to-batch variability, influenced by factors such as tissue source and processing techniques, underscores the need for standardized protocols to ensure consistent rheological and biomechanical properties across different hydrogel batches. The potential of liver dECM as a bioink, enriched with growth factors and GAGs, highlights its therapeutic promise, yet necessitates further exploration into its composition and functionality. By adhering to guidelines for producing dECM bioinks, it is feasible to pave the way for the successful integration of dECM hydrogels into clinical practices.

Acknowledgments

The research was conducted at the scientific base of the laboratory established within the framework of the Academic Leadership Program "Priority 2030."

Funding

The work was carried out with financial support from the Ministry of Science and Higher Education of the Russian Federation (grant agreement no. 075-15-2024-640; Sechenov University).

Conflict of interest

Peter S. Timashev serves as a guest editor for the journal but was not in any way (directly or indirectly) involved in the editorial and peer-review process conducted for this paper. The other authors declare they have no competing interests.

Author contributions

Conceptualization: Anastasia I. Shpichka, Anastasiia M. Nesterova, Peter S. Timashev, Massoud Vosough

Figures Visualization: Olga A. Smirnova

Writing – original draft: Valentin A. Brumberg, Zahra Heydari, Polina Yu. Bikmulina, Artem A. Pozdnyakov, Darya R. Zimulkina, Frederico David Alencar de Sena Pereira

Writing – review & editing: Anastasia I. Shpichka, Svetlana L. Kotova, Anastasiia M. Nesterova, Peter S. Timashev

Ethics approval and consent to participate

Not applicable.

Consent for publication

Not applicable.

Availability of data

None.

References

1. Kaur S, Kaur I, Rawal P, Tripathi DM, Vasudevan A. Non-matrigel scaffolds for organoid cultures. *Cancer Lett*. 2021;504:58-66. doi: 10.1016/j.canlet.2021.01.025

2. Bustamante-Torres M, Romero-Fierro D, Arcentales-Vera B, Palomino K, Magaña H, Bucio E. Hydrogels classification according to the physical or chemical interactions and as stimuli-sensitive materials. *Gels*. 2021;7(4):182. doi: 10.3390/gels7040182

3. Chaplenko AA, Khorolsky MD, Melnikova EV, Merkulov VA. Current trends in the use of cell therapy in regenerative medicine. *Bio Prod Prev Diag Treat*. 2020;20(2):82–88. doi: 10.30895/2221-996X-2020-20-2-82-88

4. Ruoß M, Vosough M, Königsrainer A, et al. Towards improved hepatocyte cultures: Progress and limitations. *Food Chem Toxicol*. 2020;138:111188. doi: 10.1016/j.fct.2020.111188

5. Heydari Z, Zarkesh I, Ghanian MH, et al. Biofabrication of size-controlled liver microtissues incorporated with ECM-derived microparticles to prolong hepatocyte function. *Bio-des Manuf*. 2021;4:790-805. doi: 10.1007/s42242-021-00137-4

6. Bikmulina P, Kosheleva N, Efremov Yu, et al. Building a tissue: gingiva- and adipose-derived mesenchymal cell spheroids' survivability and functionality after 3D extrusion bioprinting. *Bioprinting*. 2023;32: e00279. doi: 10.1016/j.bprint.2023.e00279.

7. Mirdamadi ES, Kalhori D, Zakeri N, Azarpira N, Solati-Hashjin M. Liver tissue engineering as an emerging alternative for liver disease treatment. *Tissue Eng Part B Rev*. 2020;26(2):145-163. doi: 10.1089/ten.TEB.2019.0233

8. Ergun C, Parmaksiz M, Vurat MT, Elçin AE, Elçin YM. Decellularized liver ECM-based 3D scaffolds: compositional, physical, chemical, rheological, thermal, mechanical, and in vitro biological evaluations. *Int J Biol Macromol*. 2022;200:110-123. doi: 10.1016/j.ijbiomac.2021.12.086

9. Mao Q, Wang Y, Li Y, et al. Fabrication of liver microtissue with liver decellularized extracellular matrix (dECM) bioink by digital light processing (DLP) bioprinting. *Mater Sci Eng C Mater Biol Appl*. 2020;109:110625. doi: 10.1016/j.msec.2020.110625

10. Heydari Z, Najimi M, Mirzaei H, et al. Tissue engineering in liver regenerative medicine: insights into novel translational technologies. *Cells*. 2020;9(2):304. doi: 10.3390/cells9020304

11. Ranucci CS, Kumar A, Batra SP, Moghe PV. Control of hepatocyte function on collagen foams: sizing matrix pores toward selective induction of 2-D and 3-D cellular morphogenesis. *Biomaterials*. 2000;21(8):783-793.

doi: 10.1016/s0142-9612(99)00238-0

12. Kobayashi M, Kadota J, Hashimoto Y, et al. Elastic modulus of ECM hydrogels derived from decellularized tissue affects capillary network formation in endothelial cells. *Int J Mol Sci*. 2020;21(17):6304.
doi: 10.3390/ijms21176304

13. Ishihara S, Kurosawa H, Haga H. Stiffness-modulation of collagen gels by genipin-crosslinking for cell culture. *Gels*. 2023; 9(2):148.
doi: 10.3390/gels9020148

14. Baptista PM, Siddiqui MM, Lozier G, Rodriguez SR, Atala A, Soker S. The use of whole organ decellularization for the generation of a vascularized liver organoid. *Hepatology*. 2011;53(2):604-617.
doi: 10.1002/hep.24067

15. Karamanos NK, Theocharis AD, Piperigkou Z, et al. A guide to the composition and functions of the extracellular matrix. *FEBS J*. 2021;288(24):6850-6912.
doi: 10.1111/febs.15776

16. Hussey GS, Pineda Molina C, Cramer MC, et al. Lipidomics and RNA sequencing reveal a novel subpopulation of nanovesicle within extracellular matrix biomaterials. *Sci Adv*. 2020;6(12):eaay4361.
doi: 10.1126/sciadv.aay4361

17. Arteel GE, Naba A. The liver matrisome - looking beyond collagens. *JHEP Rep*. 2020;2(4):100115.
doi: 10.1016/j.jhepr.2020.100115

18. Rozario T, DeSimone DW. The extracellular matrix in development and morphogenesis: a dynamic view. *Dev Biol*. 2010;341(1):126-140.
doi: 10.1016/j.ydbio.2009.10.026

19. Heydari Z., Pooyan P, Bikmulina P, et al. Mimicking the liver function in micro-patterned units: challenges and perspectives in 3D bioprinting. *Bioprinting*. 2022;27:e00208.
doi: 10.1016/J.BPRINT.2022.E00208

20. Whiteford JR, Arokiasamy S, De Rossi G. Translating the matrix. *Br J Pharmacol*. 2019;176(1):3-4.
doi: 10.1111/bph.14517

21. Kim J, Seki E. Hyaluronan in liver fibrosis: basic mechanisms, clinical implications, and therapeutic targets. *Hepatol Commun*. 2023;7(4):e0083.
doi: 10.1097/HC9.0000000000000083

22. Gudowska M, Cylwik B, Chrostek L. The role of serum hyaluronic acid determination in the diagnosis of liver fibrosis. *Acta Biochim Pol*. 2017;64(3):451-457.
doi: 10.18388/abp.2016_1443

23. Matsuda M, Seki E. The liver fibrosis niche: Novel insights into the interplay between fibrosis-composing mesenchymal cells, immune cells, endothelial cells, and extracellular matrix. *Food Chem Toxicol*. 2020;143:111556.
doi: 10.1016/j.fct.2020.111556

24. Shan L, Wang F, Zhai D, Meng X, Liu J, Lv X. Matrix metalloproteinases induce extracellular matrix degradation through various pathways to alleviate hepatic fibrosis [published correction appears in Biomed Pharmacother. 2023 Jun;162:114632]. *Biomed Pharmacother*. 2023;161:114472.
doi: 10.1016/j.biopha.2023.114472

25. Hintermann E, Christen U. The many roles of cell adhesion molecules in hepatic fibrosis. *Cells*. 2019;8(12):1503.
doi: 10.3390/cells8121503

26. Freytes DO, O'Neill JD, Duan-Arnold Y, Wrona EA, Vunjak-Novakovic G. Natural cardiac extracellular matrix hydrogels for cultivation of human stem cell-derived cardiomyocytes. *Methods Mol Biol*. 2014;1181:69-81.
doi: 10.1007/978-1-4939-1047-2_7

27. Voytik-Harbin SL, Brightman AO. Small intestinal submucosa: a tissue derived extracellular matrix that promotes tissue-specific growth and differentiation of cells in vitro. *Tissue Eng*. 1998;4:157-174.
doi: 10.1089/ten.1998.4.157

28. Uriel S, Huang JJ, Moya ML, et al. The role of adipose protein derived hydrogels in adipogenesis. *Biomaterials*. 2008;29(27):3712-3719.
doi: 10.1016/j.biomaterials.2008.05.028

29. Kao CY, Nguyen HQ, Weng YC. Characterization of Porcine Urinary Bladder Matrix Hydrogels from Sodium Dodecyl Sulfate Decellularization Method. *Polymers (Basel)*. 2020;12(12):3007.
doi: 10.3390/polym12123007

30. Simsa R, Rothenbücher T, Gürbüz H, et al. Brain organoid formation on decellularized porcine brain ECM hydrogels. *PLoS One*. 2021;16(1):e0245685.
doi: 10.1371/journal.pone.0245685

31. Johnson TD, Lin SY, Christman KL. Tailoring material properties of a nanofibrous extracellular matrix derived hydrogel. *Nanotechnology*. 2011;22(49):494015.
doi: 10.1088/0957-4484/22/49/494015

32. Pouliot RA, Young BM, Link PA, et al. Porcine lung-derived extracellular matrix hydrogel properties are dependent on pepsin digestion time. *Tissue Eng Part C Methods*. 2020;26(6):332-346.
doi: 10.1089/ten.TEC.2020.0042

33. Uriel S, Labay E, Francis-Sedlak M, et al. Extraction and assembly of tissue-derived gels for cell culture and tissue engineering. *Tissue Eng Part C Methods*. 2009;15(3):309-321.
doi: 10.1089/ten.tec.2008.0309

34. Giobbe GG, Crowley C, Luni C, et al. Extracellular matrix hydrogel derived from decellularized tissues enables endodermal organoid culture. *Nat Commun*. 2019;10(1):5658.
doi: 10.1038/s41467-019-13605-4

35. Ijima H, Nakamura S, Bual R, Shirakigawa N, Tanoue S. Physical properties of the extracellular matrix of

decellularized porcine liver. *Gels*. 2018;4(2):39.
doi: 10.3390/gels4020039

36. Hsieh DJ, Srinivasan P. Protocols for accelerated production and purification of collagen scaffold and atelocollagen from animal tissues. *Biotechniques*. 2020;69(3):220-225.
doi: 10.2144/btn-2020-0070

37. Hussey GS, Nascari DG, Saldin LT, et al. Ultrasonic cavitation to prepare ECM hydrogels. *Acta Biomater*. 2020;108:77-86.
doi: 10.1016/j.actbio.2020.03.036

38. Hulmes DJS. *Collagen Diversity, Synthesis, and Assembly*. New York: Springer; 2008.
doi: 10.1007/978-0-387-73906-9_2

39. Kadler KE, Hill A, Canty-Laird EG. Collagen fibrillogenesis: fibronectin, integrins, and minor collagens as organizers and nucleators. *Curr Opin Cell Biol*. 2008;20(5):495-501.
doi: 10.1016/j.ceb.2008.06.008

40. Kayabölen A. *Development of Vascularized Adipose Tissue Construct Based on Adipose Tissue Extracellular Matrix and Silk Fibroin*. M.S. - Master of Science, Middle East Technical University; 2015.

41. Stepanovska J, Otahal M, Hanzalek K, Supova M, Matejka R. pH modification of high-concentrated collagen bioinks as a factor affecting cell viability, mechanical properties, and printability. *Gels*. 2021;7(4):252.
doi: 10.3390/gels7040252

42. Riacci L, Sorriento A, Ricotti L. Genipin-based crosslinking of jellyfish collagen 3D hydrogels. *Gels*. 2021;7(4):238.
doi: 10.3390/gels7040238

43. Utami Nike D, Md Fadilah NI, Sallehuddin N, et al. Genipin-crosslinking effects on biomatrix development for cutaneous wound healing: a concise review. *Front Bioeng Biotechnol*. 2022;10:865014.
doi: 10.3389/fbioe.2022.865014

44. Boso D, Carraro E, Maghin E, et al. Porcine decellularized diaphragm hydrogel: a new option for skeletal muscle malformations. *Biomedicines*. 2021;9(7):709.
doi: 10.3390/biomedicines9070709

45. Zhu H, Cai X, Wu L, Gu Z. A facile one-step gelation approach simultaneously combining physical and chemical cross-linking for the preparation of injectable hydrogels. *J Mater Chem B*. 2017;5(17):3145-3153.
doi: 10.1039/c7tb00396j

46. Cécile E, Laurine V, Jean M, Ahmad M, Gilles S. Chemical cross-linking methods for cell encapsulation in hydrogels. *Materials Today Commun*. 2019; 20:100536, ISSN 2352-4928.
doi: 10.1016/j.mtcomm.2019.05.012

47. Fedorovich NE, Oudshoorn MH, van Geemen D, Hennink WE, Alblas J, Dhert WJ. The effect of photopolymerization on stem cells embedded in hydrogels. *Biomaterials*. 2009;30(3):344-353.
doi: 10.1016/j.biomaterials.2008.09.037

48. Rouillard AD, Berglund CM, Lee JY, et al. Methods for photocrosslinking alginate hydrogel scaffolds with high cell viability. *Tissue Eng Part C Methods*. 2011;17(2):173-179.
doi: 10.1089/ten.TEC.2009.0582

49. Roberts JJ, Bryant SJ. Comparison of photopolymerizable thiol-ene PEG and acrylate-based PEG hydrogels for cartilage development. *Biomaterials*. 2013;34(38):9969-9979.
doi: 10.1016/j.biomaterials.2013.09.020

50. Rydholm AE, Bowman CN, Anseth KS. Degradable thiol-acrylate photopolymers: polymerization and degradation behavior of an in situ forming biomaterial. *Biomaterials*. 2005;26(22):4495-4506.
doi: 10.1016/j.biomaterials.2004.11.046

51. Gwon K, Kim E, Tae G. Heparin-hyaluronic acid hydrogel in support of cellular activities of 3D encapsulated adipose derived stem cells. *Acta Biomater*. 2017;49:284-295.
doi: 10.1016/j.actbio.2016.12.001

52. Brew L. *Development of a Crosslinkable Hydrogel Derived from Placental Tissue*. Master of Philosophy thesis, Queensland University of Technology; 2019.

53. Shi J, Yao H, Wang B, et al. Construction of a decellularized multicomponent extracellular matrix interpenetrating network scaffold by gelatin microporous hydrogel 3d cell culture system. *Macromol Rapid Commun*. 2024;45(5):e2300508.
doi: 10.1002/marc.202300508.

54. Crosby CO, Hillsley A, Kumar S, et al. Phototunable interpenetrating polymer network hydrogels to stimulate the vasculogenesis of stem cell-derived endothelial progenitors. *Acta Biomater*. 2021;122:133-144.
doi: 10.1016/j.actbio.2020.12.041

55. Ma X, Qu X, Zhu W, et al. Deterministically patterned biomimetic human iPSC-derived hepatic model via rapid 3D bioprinting. *Proc Natl Acad Sci U S A*. 2016;113(8):2206-2211.
doi: 10.1073/pnas.1524510113

56. Kim Y, Kang K, Jeong J, et al. Three-dimensional (3D) printing of mouse primary hepatocytes to generate 3D hepatic structure. *Ann Surg Treat Res*. 2017;92(2):67-72.
doi: 10.4174/astr.2017.92.2.67

57. Hiller T, Berg J, Elomaa L, et al. Generation of a 3D liver model comprising human extracellular matrix in an alginate/gelatin-based bioink by extrusion bioprinting for infection and transduction studies. *Int J Mol Sci*. 2018;19(10):3129.
doi: 10.3390/ijms19103129

58. Lewis PL, Green RM, Shah RN. 3D-printed gelatin scaffolds of differing pore geometry modulate hepatocyte function and gene expression. *Acta Biomater*. 2018;69:63-70.
doi: 10.1016/j.actbio.2017.12.042

59. Yang H, Sun L, Pang Y, et al. Three-dimensional bioprinted hepatorganoids prolong survival of mice with liver failure. *Gut*. 2021;70(3):567-574.
doi: 10.1136/gutjnl-2019-319960

60. Lewis PL, Yan M, Su J, Shah RN. Directing the growth and alignment of biliary epithelium within extracellular matrix hydrogels. *Acta Biomater*. 2019;85:84-93. doi: 10.1016/j.actbio.2018.12.039

61. Goulart E, de Caires-Junior LC, Telles-Silva KA, et al. 3D bioprinting of liver spheroids derived from human induced pluripotent stem cells sustain liver function and viability in vitro. *Biofabrication*. 2019;12(1):015010. doi: 10.1088/1758-5090/ab4a30

62. Kang HK, Sarsenova M, Kim DH, et al. Establishing a 3D in vitro hepatic model mimicking physiologically relevant to in vivo state. *Cells*. 2021;10(5):1268. doi: 10.3390/cells10051268

63. Grix T, Ruppelt A, Thomas A, et al. Bioprinting perfusion-enabled liver equivalents for advanced organ-on-a-chip applications. *Genes* (Basel). 2018;9(4):176. doi: 10.3390/genes9040176

64. Liu Tsang V, Chen AA, Cho LM, et al. Fabrication of 3D hepatic tissues by additive photopatterning of cellular hydrogels. *FASEB J*. 2007;21(3):790-801. doi: 10.1096/fj.06-7117com

65. Gibert-Ramos A, Sanfeliu-Redondo D, Aristu-Zabalza P, et al. The hepatic sinusoid in chronic liver disease: the optimal milieu for cancer. *Cancers (Basel)*. 2021;13(22):5719. doi: 10.3390/cancers13225719

66. Murphy SV, Atala A. 3D bioprinting of tissues and organs. *Nat Biotechnol*. 2014;32(8):773-785. doi: 10.1038/nbt.2958

67. Saunders RE, Derby B. Inkjet printing biomaterials for tissue engineering: bioprinting. *Int Mater Rev*. 2014;*59*(8):430-448. doi: 10.1179/1743280414Y.0000000040

68. Cui X, Breitenkamp K, Finn MG, Lotz M, D'Lima DD. Direct human cartilage repair using three-dimensional bioprinting technology. *Tissue Eng Part A*. 2012;18(11-12):1304-1312. doi: 10.1089/ten.TEA.2011.0543

69. Matsusaki M, Sakaue K, Kadowaki K, Akashi M. Three-dimensional human tissue chips fabricated by rapid and automatic inkjet cell printing. *Adv Healthc Mater*. 2013;2(4):534-539. doi: 10.1002/adhm.201200299

70. Dababneh AB, Ozbolat IT. Bioprinting technology: a current state-of-the-art review. *J Manuf Sci Eng*. 2014;136(6):061016. doi: 10.1115/1.4028512

71. Jungst T, Smolan W, Schacht K, Scheibel T, Groll J. Strategies and molecular design criteria for 3D printable hydrogels. *Chem Rev*. 2016;116(3):1496-1539. doi: 10.1021/acs.chemrev.5b00303

72. Chua CK, Yeong WY. *Bioprinting: Principles and Applications*. World Scientific Publishing Co Inc; 2014.

73. You S, Li J, Zhu W, Yu C, Mei D, Chen S. Nanoscale 3D printing of hydrogels for cellular tissue engineering. *J Mater Chem B*. 2018;6(15):2187-2197. doi: 10.1039/C8TB00301G

74. Grigoryan B, Paulsen SJ, Corbett DC, et al. Multivascular networks and functional intravascular topologies within biocompatible hydrogels. *Science*. 2019;364(6439): 458-464. doi: 10.1126/science.aav9750

75. Kim MK, Jeong W, Lee SM, Kim JB, Jin S, Kang HW. Decellularized extracellular matrix-based bio-ink with enhanced 3D printability and mechanical properties. *Biofabrication*. 2020;12(2):025003. doi: 10.1088/1758-5090/ab5d80

76. Lee H, Han W, Kim H, et al. Development of liver decellularized extracellular matrix bioink for three-dimensional cell printing-based liver tissue engineering. *Biomacromolecules*. 2017;18(4):1229-1237. doi: 10.1021/acs.biomac.6b01908

77. Skardal A, Devarasetty M, Kang HW, et al. A hydrogel bioink toolkit for mimicking native tissue biochemical and mechanical properties in bioprinted tissue constructs. *Acta Biomater*. 2015;25:24-34. doi: 10.1016/j.actbio.2015.07.030

78. Mazzocchi A, Devarasetty M, Huntwork R, Soker S, Skardal A. Optimization of collagen type I-hyaluronan hybrid bioink for 3D bioprinted liver microenvironments. *Biofabrication*. 2018;11(1):015003. doi: 10.1088/1758-5090/aae543

79. Jeon H, Kang K, Park SA, et al. Generation of multilayered 3D structures of HepG2 cells using a bio-printing technique. *Gut Liver*. 2017;11(1):121-128. doi: 10.5009/gnl16010

80. Lee JW, Choi YJ, Yong WJ, et al. Development of a 3D cell printed construct considering angiogenesis for liver tissue engineering. *Biofabrication*. 2016;8(1):015007. doi: 10.1088/1758-5090/8/1/015007

81. Bernal PN, Delrot P, Loterie D, et al. Volumetric bioprinting of complex living-tissue constructs within seconds. *Adv Mater*. 2019;31(42):e1904209. doi: 10.1002/adma.201904209

82. Leva V, Chatzipetrou M, Alexopoulos L, Tzeranis DS, Zergioti I. Direct laser printing of liver cells on porous collagen scaffolds. *J Laser Micro Nanoeng*. 2018;13(3):234-237. doi: 10.2961/jlmn.2018.03.0015

83. Yu C, Ma X, Zhu W, et al. Scanningless and continuous 3D bioprinting of human tissues with decellularized extracellular matrix. *Biomaterials*. 2019;194:1-13. doi: 10.1016/j.biomaterials.2018.12.009

84. Antoshin AA, Churbanov SN, Minaev NV, et al. LIFT-bioprinting, is it worth it? *Bioprinting*. 2019;15,2019, doi: 10.1016/j.bprint.2019.e00052.

85. Antoshin A, Minaeva E, Koteneva P, et al. LIFT of cell spheroids: proof of concept. *Bioprinting*. 2023;34: e00297. doi: 10.1016/j.bprint.2023.e00297.

86. Catros S, Fricain JC, Guillotin B, et al. Laser-assisted bioprinting for creating on-demand patterns of human osteoprogenitor cells and nano-hydroxyapatite. *Biofabrication*. 2011;3(2):025001. doi: 10.1088/1758-5082/3/2/025001

87. Koch L, Deiwick A, Schlie S, et al. Skin tissue generation by laser cell printing. *Biotechnol Bioeng*. 2012;109(7):1855-1863. doi: 10.1002/bit.24455

88. Miri AK, Mirzaee I, Hassan S, et al. Effective bioprinting resolution in tissue model fabrication. *Lab Chip*. 2019;19(11):2019-2037. doi: 10.1039/c8lc01037d

89. Ma X, Yu C, Wang P, et al. Rapid 3D bioprinting of decellularized extracellular matrix with regionally varied mechanical properties and biomimetic microarchitecture. *Biomaterials*. 2018;185:310-321. doi: 10.1016/j.biomaterials.2018.09.026

90. Zhu W, Qu X, Zhu J, et al. Direct 3D bioprinting of prevascularized tissue constructs with complex microarchitecture. *Biomaterials*. 2017;124:106-115. doi: 10.1016/j.biomaterials.2017.01.042

91. Zhang X, Zhang X, Li Y, Zhang Y. Applications of light-bBased 3D bioprinting and photoactive biomaterials for tissue engineering. *Materials (Basel)*. 2023;16(23):7461. doi: 10.3390/ma16237461

92. Ovsianikov A, Mühleder S, Torgersen J, et al. Laser photofabrication of cell-containing hydrogel constructs. *Langmuir*. 2014;30(13):3787-3794. doi: 10.1021/la402346z

93. Traverse JH, Henry TD, Dib N, et al. First-in-man study of a cardiac extracellular matrix hydrogel in early and late myocardial infarction patients. *JACC Basic Transl Sci*. 2019;4(6):659-669. doi: 10.1016/j.jacbts.2019.07.012

94. Cai D, Weng W. Development potential of extracellular matrix hydrogels as hemostatic materials. *Front Bioeng Biotechnol*. 2023;11:1187474. doi: 10.3389/fbioe.2023.1187474

95. Fong AH, Romero-López M, Heylman CM, et al. Three-dimensional adult cardiac extracellular matrix promotes maturation of human induced pluripotent stem cell-derived cardiomyocytes. *Tissue Eng Part A*. 2016;22(15-16):1016-1025. doi: 10.1089/ten

96. Gaetani R, Yin C, Srikumar N, et al. Cardiac-derived extracellular matrix enhances cardiogenic properties of human cardiac progenitor cells. *Cell Transplant*. 2016;25(9):1653-1663. doi: 10.3727/096368915X689794

97. Wang RM, Johnson TD, He J, et al. Humanized mouse model for assessing the human immune response to xenogeneic and allogeneic decellularized biomaterials. *Biomaterials*. 2017;129:98-110. doi: 10.1016/j.biomaterials.2017.03.016

98. Pok S, Stupin IV, Tsao C, et al. Full-thickness heart repair with an engineered multilayered myocardial patch in rat model. *Adv Healthc Mater*. 2017;6(5):10.1002/adhm.201600549. doi: 10.1002/adhm.201600549

99. Efraim Y, Sarig H, Cohen Anavy N, et al. Biohybrid cardiac ECM-based hydrogels improve long term cardiac function post myocardial infarction. *Acta Biomater*. 2017;50:220-233. doi: 10.1016/j.actbio.2016.12.015

100. Jang J, Park HJ, Kim SW, et al. 3D printed complex tissue construct using stem cell-laden decellularized extracellular matrix bioinks for cardiac repair. *Biomaterials*. 2017;112:264-274. doi: 10.1016/j.biomaterials.2016.10.026

101. Francis MP, Breathwaite E, Bulysheva AA, et al. Human placenta hydrogel reduces scarring in a rat model of cardiac ischemia and enhances cardiomyocyte and stem cell cultures. *Acta Biomater*. 2017;52:92-104. doi: 10.1016/j.actbio.2016.12.027

102. Barajaa MA, Otsuka T, Ghosh D, Kan HM, Laurencin CT. Development of porcine skeletal muscle extracellular matrix-derived hydrogels with improved properties and low immunogenicity. *Proc Natl Acad Sci USA*. 2024;121(19):e2322822121. doi: 10.1073/pnas.2322822121

103. Ungerleider JL, Johnson TD, Hernandez MJ, et al. Extracellular matrix hydrogel promotes tissue remodeling, arteriogenesis, and perfusion in a rat hindlimb ischemia Model. *JACC Basic Transl Sci*. 2016;1(1-2):32-44. doi: 10.1016/j.jacbts.2016.01.009

104. Wolf MT, Daly KA, Brennan-Pierce EP, et al. A hydrogel derived from decellularized dermal extracellular matrix. *Biomaterials*. 2012;33(29):7028-7038. doi: 10.1016/j.biomaterials.2012.06.051

105. Long C, Galvez MG, Legrand A, et al. Intratendinous injection of hydrogel for reseeding decellularized human flexor tendons. *Plast Reconstr Surg*. 2017;139(6):1305e-1314e. doi: 10.1097/PRS.0000000000003359

106. Burnsed OA, Schwartz Z, Marchand KO, Hyzy SL, Olivares-Navarrete R, Boyan BD. Hydrogels derived from cartilage matrices promote induction of human mesenchymal stem cell chondrogenic differentiation. *Acta Biomater*. 2016;43:139-149. doi: 10.1016/j.actbio.2016.07.034

107. Shimomura K, Rothrauff BB, Tuan RS. Region-specific effect of the decellularized meniscus extracellular matrix on mesenchymal stem cell-based meniscus tissue engineering. *Am J Sports Med*. 2017;45(3):604-611. doi: 10.1177/0363546516674184

108. Ravichandran A, Murekatete B, Moedder D., et al. Photocrosslinkable liver extracellular matrix hydrogels for the generation of 3D liver microenvironment models. *Sci Rep*. 2021;11:15566. doi: 10.1038/s41598-021-94990-z

109. Willemse J, van Tienderen G, van Hengel E, et al. Hydrogels derived from decellularized liver tissue support the growth and differentiation of cholangiocyte organoids. *Biomaterials*. 2022;284:121473.
doi: 10.1016/j.biomaterials.2022.121473

110. Faust A, Kandakatla A, van der Merwe Y, et al. Urinary bladder extracellular matrix hydrogels and matrix-bound vesicles differentially regulate central nervous system neuron viability and axon growth and branching. *J Biomater Appl*. 2017;31(9):1277-1295.
doi: 10.1177/088532821769806

111. Kočí Z, Výborný K, Dubišová J, et al. Extracellular matrix hydrogel derived from human umbilical cord as a scaffold for neural tissue repair and its comparison with extracellular matrix from porcine tissues. *Tissue Eng Part C Methods*. 2017;23(6):333-345.
doi: 10.1089/ten.TEC.2017.0089

112. van Dongen JA, Getova V, Brouwer LA, et al. Adipose tissue-derived extracellular matrix hydrogels as a release platform for secreted paracrine factors. *J Tissue Eng Regen Med*. 2019;13(6):973-985.
doi: 10.1002/term.2843

113. Mahoney CM, Kelmindi-Doko A, Snowden MJ, Peter Rubin J, Marra KG. Adipose derived delivery vehicle for encapsulated adipogenic factors. *Acta Biomater*. 2017;58:26-33.
doi: 10.1016/j.actbio.2017.05.046

114. Kayabolen A, Keskin D, Aykan A, Karslıoglu Y, Zor F, Tezcaner A. Native extracellular matrix/fibroin hydrogels for adipose tissue engineering with enhanced vascularization. *Biomed Mater*. 2017;12(3):035007.
doi: 10.1088/1748-605X/aa6a63

115. Neishabouri A, Soltani Khaboushan A, Daghigh F, Kajbafzadeh AM, Majidi Zolbin M. Decellularization in tissue engineering and regenerative medicine: evaluation, modification, and application methods. *Front Bioeng Biotechnol*. 2022;10:805299.
doi: 10.3389/fbioe.2022.805299

116. Hernandez MJ. *Translation of an Injectable Decellularized Extracellular Matrix Hydrogel for Promoting Skeletal Muscle Regeneration*. University of California San Diego; 2019.

117. Zhang W, Du A, Liu S, Lv M, Chen S. Research progress in decellularized extracellular matrix-derived hydrogels. *Regen Ther*. 2021;18:88-96.
doi: 10.1016/j.reth.2021.04.002

118. Zhu W, Cao L, Song C, Pang Z, Jiang H, Guo C. Cell-derived decellularized extracellular matrix scaffolds for articular cartilage repair. *Int J Artif Organs*. 2021;44(4):269-281.
doi: 10.1177/0391398820953866

119. Peshkova M, Korneev A, Revokatova D, et al. Four sides to the story: A proteomic comparison of liquid-phase and matrix-bound extracellular vesicles in 2D and 3D cell cultures. *Proteomics*. 2024;24(18):e2300375.
doi: 10.1002/pmic.202300375

120. Assunção M, Dehghan-Baniani D, Yiu CHK, Später T, Beyer S, Blocki A. Cell-derived extracellular matrix for tissue engineering and regenerative medicine. *Front Bioeng Biotechnol*. 2020;8:602009.
doi: 10.3389/fbioe.2020.602009

121. Sharma D, Ferguson M, Zhao F. A step-by-step protocol for generating human fibroblast cell-derived completely biological extracellular matrix scaffolds. *Methods Cell Biol*. 2020;156:3-13.
doi: 10.1016/bs.mcb.2019.10.010

122. Lee JS, Nah H, Lee D, et al. Immediately implantable extracellular matrix-enriched osteoinductive hydrogel-laden 3D-printed scaffold for promoting vascularized bone regeneration in vivo. *Mater Des Vol*. 2022; 219:110801.
doi: 10.1016/j.matdes.2022.110801

123. Shin YJ, Shafranek RT, Tsui JH, Walcott J, Nelson A, Kim DH. 3D bioprinting of mechanically tuned bioinks derived from cardiac decellularized extracellular matrix. *Acta Biomater*. 2021;119:75-88.
doi: 10.1016/j.actbio.2020.11.006

124. Casarin M, Fortunato TM, Imran S, et al. Porcine small intestinal submucosa (SIS) as a Suitable Scaffold for the creation of a tissue-engineered urinary conduit: decellularization, biomechanical and biocompatibility characterization using new approaches. *Int J Mol Sci*. 2022;23(5):2826.
doi: 10.3390/ijms23052826

125. Toprakhisar B, Nadernezhad A, Bakirci E, Khani N, Skvortsov GA, Koc B. Development of bioink from decellularized tendon extracellular matrix for 3D bioprinting. *Macromol Biosci*. 2018;18(10):e1800024.
doi: 10.1002/mabi.201800024

126. Vishwakarma SK, Bhavani PG, Bardia A, et al. Preparation of natural three-dimensional goat kidney scaffold for the development of bioartificial organ. *Indian J Nephrol*. 2014;24(6):372-375.
doi: 10.4103/0971-4065.133008

127. Geerts S, Ozer S, Jaramillo M, Yarmush ML, Uygun BE. Nondestructive methods for monitoring cell removal during rat liver decellularization. *Tissue Eng Part C Methods*. 2016;22(7):671-678.
doi: 10.1089/ten.TEC.2015.0571

128. Ren X, Moser PT, Gilpin SE, et al. Engineering pulmonary vasculature in decellularized rat and human lungs. *Nat Biotechnol*. 2015;33(10):1097-1102.
doi: 10.1038/nbt.3354

129. Di Francesco D, Marcello E, Casarella S, et al. Characterization of a decellularized pericardium extracellular matrix hydrogel for regenerative medicine: insights on animal-to-animal variability. *Front Bioeng Biotechnol*. 2024;12:1452965.
doi: 10.3389/fbioe.2024.1452965

130. Tottey S, Johnson SA, Crapo PM, et al. The effect of source animal age upon extracellular matrix scaffold properties. *Biomaterials*. 2011;32(1):128-136.

doi: 10.1016/j.biomaterials.2010.09.006

131. Porzionato A, Stocco E, Barbon S, Grandi F, Macchi V, De Caro R. Tissue-engineered grafts from human decellularized extracellular matrices: a systematic review and future perspectives. *Int J Mol Sci*. 2018;19(12):4117. doi: 10.3390/ijms19124117

132. Meran L, Massie I, Campinoti S, et al. Engineering transplantable jejunal mucosal grafts using patient-derived organoids from children with intestinal failure. *Nat Med*. 2020;26(10):1593-1601. doi: 10.1038/s41591-020-1024-z

133. Garreta E, de Oñate L, Fernández-Santos ME, et al. Myocardial commitment from human pluripotent stem cells: rapid production of human heart grafts. *Biomaterials*. 2016;98:64-78. doi: 10.1016/j.biomaterials.2016.04.003

134. Chen Y, Chen J, Zhang Z, et al. Current advances in the development of natural meniscus scaffolds: innovative approaches to decellularization and recellularization. *Cell Tissue Res*. 2017;370(1):41-52. doi: 10.1007/s00441-017-2605-0

135. Hassanpour A, Talaei-Khozani T, Kargar-Abarghouei E, Razban V, Vojdani Z. Decellularized human ovarian scaffold based on a sodium lauryl ester sulfate (SLES)-treated protocol, as a natural three-dimensional scaffold for construction of bioengineered ovaries. *Stem Cell Res Ther*. 2018;9(1):252. doi: 10.1186/s13287-018-0971-5

136. Brown CF, Yan J, Han TT, Marecak DM, Amsden BG, Flynn LE. Effect of decellularized adipose tissue particle size and cell density on adipose-derived stem cell proliferation and adipogenic differentiation in composite methacrylated chondroitin sulphate hydrogels. *Biomed Mater*. 2015;10(4):045010. doi: 10.1088/1748-6041/10/4/045010

137. Tremmel DM, Sackett SD, Feeney AK, et al. A human pancreatic ECM hydrogel optimized for 3-D modeling of the islet microenvironment. *Sci Rep*. 2022;12(1):7188. doi: 10.1038/s41598-022-11085-z

138. Peloso A, Petrosyan A, Da Sacco S, et al. Renal extracellular matrix scaffolds from discarded kidneys maintain glomerular morphometry and vascular resilience and retains critical growth factors. *Transplantation*. 2015;99(9):1807-1816. doi: 10.1097/TP.0000000000000811.

139. Milan PB, Lotfibakhshaiesh N, Joghataie MT, et al. Accelerated wound healing in a diabetic rat model using decellularized dermal matrix and human umbilical cord perivascular cells. *Acta Biomater*. 2016;45:234-246. doi: 10.1016/j.actbio.2016.08.053

140. Matoug-Elwerfelli M, Duggal MS, Nazzal H, Esteves F, Raïf E. A biocompatible decellularized pulp scaffold for regenerative endodontics. *Int Endod J*. 2018;51(6):663-673. doi: 10.1111/iej.12882

141. Nichols JE, La Francesca S, Vega SP, et al. Giving new life to old lungs: methods to produce and assess whole human paediatric bioengineered lungs. *J Tissue Eng Regen Med*. 2017;11(7):2136-2152. doi: 10.1002/term.2113

142. Yamanaka H, Morimoto N, Yamaoka T. Decellularization of submillimeter-diameter vascular scaffolds using peracetic acid. *J Artif Organs*. 2020;23(2):156-162. doi: 10.1007/s10047-019-01152-0

143. Jiwangga D, Mahyudin F, Mastutik G, Juliana, Meitavany EN. Current Strategies for Tracheal Decellularization: A Systematic Review. *Int J Biomater.* 2024;2024:3355239. doi: 10.1155/2024/3355239

144. Sackett SD, Tremmel DM, Ma F, et al. Extracellular matrix scaffold and hydrogel derived from decellularized and delipidized human pancreas. *Sci Rep*. 2018;8:10452. doi: 10.1038/s41598-018-28857-1

145. Pankajakshan D, Voytik-Harbin SL, Nör JE, Bottino MC. Injectable highly tunable oligomeric collagen matrices for dental tissue regeneration. *ACS Appl Bio Mater*. 2020;3(2):859-868. doi: 10.1021/acsabm.9b00944

146. Kojima H, Kushige H, Yagi H, et al. Combinational treatment involving decellularized extracellular matrix hydrogels with mesenchymal stem cells increased the efficacy of cell therapy in pancreatitis. *Cell Transplant*. 2023;32:9636897231170437. doi: 10.1177/09636897231170437

147. Davidenko N, Schuster CF, Bax DV, et al. Control of crosslinking for tailoring collagen-based scaffolds stability and mechanics. *Acta Biomater*. 2015;25:131-142. doi: 10.1016/j.actbio.2015.07.034

148. Shie MY, Lee JJ, Ho CC, Yen SY, Ng HY, Chen YW. Effects of gelatin methacrylate bio-ink concentration on mechano-physical properties and human dermal fibroblast behavior. *Polymers (Basel)*. 2020;12(9):1930. doi: 10.3390/polym12091930

149. Singh RK, Seliktar D, Putnam AJ. Capillary morphogenesis in PEG-collagen hydrogels. Biomaterials. 2013;34(37):9331-9340. doi: 10.1016/j.biomaterials.2013.08.016

150. Antebi B, Zhang Z, Wang Y, Lu Z, Chen XD, Ling J. Stromal-cell-derived extracellular matrix promotes the proliferation and retains the osteogenic differentiation capacity of mesenchymal stem cells on three-dimensional scaffolds. *Tissue Eng Part C Methods*. 2015;21(2):171-181. doi: 10.1089/ten.TEC.2014.0092

151. Madrid-Wolff J, Boniface A, Loterie D, Delrot P, Moser C. Controlling light in scattering materials for volumetric additive manufacturing. *Adv Sci (Weinh)*. 2022;9(22):e2105144. doi: 10.1002/advs.202105144

ACCSCIENCE PUBLISHING

International Journal of Bioprinting

REVIEW ARTICLE

Designing methacrylic anhydride-based hydrogels for 3D bioprinting

Naisi Shen[1], Zhen Li[1], Pu Yang[1], Xiangjun Liu[1], Yikun Ju[1], Yue Hu[1], Bairong Fang[1]*, and Liangle Liu[2]*

[1]Department of Plastic and Aesthetic (Burn) Surgery, The Second Xiangya Hospital of Central South University, Changsha, Hunan, China

[2]Department of Spinal Surgery, The Third Affiliated Hospital of Wenzhou Medical University, Wenzhou, Zhejiang , China

(This article belongs to the Special Issue: *New matrix materials for 3D Bioprinting*)

Abstract

Methacrylic anhydride (MA)-based hydrogels, derived by introducing methacryloyl groups to various polymer side chains, are promising bioinks for three-dimensional (3D) printing in medical applications. These hydrogels combine the inherent biocompatibility and therapeutic benefits of their parent polymers with the unique photocrosslinking properties conferred by the methacryloyl groups, allowing precise control over their mechanical properties through light-curing parameters. Using 3D biological compression, these hydrogels serve as bioinks for producing scaffolds with optimal porosity, facilitating cell adhesion, proliferation, and differentiation. This technology enables the precise spatial distribution of bioactive substances, offering targeted therapeutic treatment and controlled release. This review delved into recent advancements in bioprinting technologies, outlined the preparation of MA-based bioinks, and summarized factors influencing the resulting biological and mechanical properties of bioscaffolds. Additionally, the properties and applications of methylpropionic anhydride-based hydrogels in various medical fields were discussed, addressing current limitations and future challenges in integrating these hydrogels with 3D bioprinting for clinical applications.

Keywords: 3D printing; 3D-printed scaffold; Bioink; Light curing; Methacrylic anhydride-based compound

***Corresponding authors:**
Bairong Fang
(fbrfbr2004@csu.edu.cn)

Liangle Liu
(liuliangle@wmu.edu.cn)

Citation: Shen N, Li N, Yang P, et al. Designing methacrylic anhydride-based hydrogels for 3D bioprinting. *Int J Bioprint*. 2025;11(1):84-138. doi: 10.36922/ijb.4650

Received: August 24, 2024
Revised: October 3, 2024
Accepted: October 14, 2024
Published Online: October 15, 2024

Copyright: © 2024 Author(s). This is an Open Access article distributed under the terms of the Creative Commons Attribution License, permitting distribution, and reproduction in any medium, provided the original work is properly cited.

Publisher's Note: AccScience Publishing remains neutral with regard to jurisdictional claims in published maps and institutional affiliations.

1. Introduction

Three-dimensional (3D) bioprinting employs bioactive materials and biounits, such as bioink, as well as 3D printing technology, to create personalized biofunctional scaffolds. From a macrostructural perspective, conventional 2D cell culture technology cannot replicate the intricate complexity of actual tissues and organ systems. On a molecular and cellular level, the absence of mechanical induction and signaling crosslinking in 2D cultures results in a cellular state that significantly diverges from the physiological morphology observed in the human body compared with *in vivo* and 3D cell cultures. The 2D cellular environment lacks essential nutrients, as well as cellular and other factors present in native tissues, thus eliminating crucial stimuli that guide cell behavior. Moreover, 2D cell cultures exhibit a flat morphology, are limited by single growth

conditions, and display minimal cellular connections, resulting in inadequate differentiation and proliferation. Consequently, a higher incidence of apoptosis, reduced drug resistance, and diminished resilience to mechanical stress are observed in 2D cultures.[1]

Spatially distributed cells cultured in 3D not only exhibit different signaling cascades and drug sensitivities, but can also be induced to adhere, proliferate, and differentiate. Moreover, 3D culture enables the spatial localization and co-cultivation of different cell populations to observe their interactions. With the aid of microengineering (microfluidics), the effects of pathway modulators on tissue compartmentalization, cellular differentiation, and sequential sorting can be quantitatively and systematically investigated.[2] The assembly of multilayered 3D cellular structures can only be achieved through the use of scaffolds. In recent years, increasing research has centered around the advancement of 3D cell culture techniques to circumvent the limitations of 2D cell culture. Microtissue cellular scaffolds, such as scaffolds based on hydrogel, polymer rigid material, or hydrophilic glass fiber, have an enormous influence on cell differentiation and proliferation.[3] Notably, 3D printing technology can be used to generate 3D structures with adequate precision and mechanical performance, which can be combined with substrates, cells, and bioactive cues to produce 3D bioscaffolds.

The biomaterials used for 3D printing are called bioinks. Aqueous formulations of polymers or hydrogel precursors that contain biological factors would be considered biomaterial inks. Bioink varies from biomaterial ink as it contains cells. This is important because this biological component significantly restricts the choice of biomaterials and processing methods.[4] Bioink can also be loaded with microcarriers, such as cell-active substances, drugs, and various types of nanoparticles, which can be used to release functional drugs or improve the rheological and mechanical properties of bioink.[5] Bioinks need to have good biocompatibility and mechanical properties. The former ensures that printed cells can survive and establish connections, whereas the latter provides good fluidity during the printing process, enables rapid curing and molding after printing, and supports subsequent applications. Emerging bioprinting technologies allow the printing process to personalize the distribution of bioink on the x–y axes and form biological scaffolds with 3D spatial microscopic properties through multilayer print stacking on the z-axis. The power source for the droplets generated by inkjet 3D printing is the deformation of the printer head, which is squeezed against the bioink to generate tiny, discontinuous hydrogel droplets that are deposited on the receiving plane. In contrast to inkjet printing, laser-assisted printing uses focused laser pulses to stimulate a small area of the absorbing layer and generate high-pressure bubbles that propel the bioink to avoid direct contact with the dispenser. This printing method can maintain high cell viability (typically above 95%) because it does not subject cells to high mechanical stress.[6] Extrusion 3D printing utilizes a syringe-needle style nozzle that, by applying constant pressure to it, can produce a continuous filamentary hydrogel that is deposited on the receiving table. Based on extrusion 3D printing, fused deposition 3D printing introduces individualized temperature regulation of the nozzle and receiving panel, which is more suitable for bioinks with different mechanical properties at different temperatures.

Furthermore, digital light processing (DLP) and stereolithography (SLA) employ photocurable hydrogels, which are cured by using light sources of varying wavelengths; each corresponding layer of bioink is light-cured layer by layer to obtain high-precision 3D scaffolds. In addition, 4D printing, an emerging technology, employs 3D printing technology to print biological scaffolds that can change properties over time or have adjustable stability.[7] The power source for the property change can be a smart reactive hydrogel or living cells.[8] This holds significant potential for the engineering of tissues and organs whose primary function is mechanical, such as skeletal and smooth muscles. These 3D printing methods have their respective merits and demerits. Notably, 3D printing using light-cured hydrogels provides enhanced maneuverability, yielding reactive scaffolds that better simulate biological tissues in terms of mechanical strength. Notably, the light-curing process can be combined with different printing modalities at various stages: pretreatment of the bioink, curing upon completion of each layer, and consolidation curing after the print.

Methacrylic anhydride (MA)-based hydrogels, derived from MA and various polymers, serve as photosensitive biohydrogel materials suitable to be used as 3D printing bioinks. Upon ultraviolet (UV) or visible light exposure, the methacrylate side chains generate free radicals, promoting crosslinking and transitioning from sol–gel to gel. Variations in ink concentrations, UV wavelengths, and irradiation concentrations yield hydrogels with differing elastic modulus, hardness modulus, and adhesion strength, making them suitable for various biological tissue replacements. Methacryloyl anhydride group-modified bioactive substances, notably gelatin methacrylate (GelMA), feature a universal arginine-glycine-aspartic acid (RGD) tripeptide similar to that in extracellular matrix (ECM) proteins, enhancing cellular activities. Through meticulous control of reaction conditions, the substitution rate of methacryloyl anhydride groups can be adjusted, influencing scaffold physical properties

under identical light conditions. The light curing process allows for manipulation of the mechanical strength of each printed layer and overall scaffold by selecting photoinitiators and adjusting the light source's wavelength, intensity, duration, and distance. In summary, MA-based hydrogels used as bioinks offer versatility in 3D printing methods, enabling the customization of mechanical properties for personalized, biocompatible 3D tissues in medical applications.

By choosing different compounds for polymerization, different biological properties and therapeutic significance can be obtained. The spatial distribution of cells, drugs, bioactives, exosomes, or other factors introduced into the MA-based hydrogel can be managed through 3D printing technology, enabling the construction of 3D tissues that better resemble the structure of target tissues. By changing the printing and light-curing parameters or mixing polymer hydrogels with high mechanical strength but poor bioactivity with MA-based hydrogels, it is possible to create bioscaffolds with high mechanical strength that meet the varying mechanical modulus requirements of the human body, from skin to bone.

In this paper, we first introduce 3D printing technology and the associated materials used and systematically summarize the preparation methods of MA hydrogels. We then introduce MA-modifiable compounds or active substances, followed by the biological potential of these precursors, which provides insights and guidance for the future application and development of MA hydrogel. By applying MA-based bioink in 3D printing technology, we can directionally distribute cells and other active components to produce 3D scaffolds with good biocompatibility and mechanical properties. We not only review the applications of these 3D scaffolds in tissue engineering but also discuss their use in organ-on-a-chip systems, organoids, biosensors, and bioglues. These applications can provide ideas for clinical treatment of various systemic diseases. Ultimately, we highlight the trends and shortcomings of MA-based hydrogels for 3D bioprinting and provide directions for their future development.

2. 3D printing technology and materials

2.1. 3D printing technology and characteristics

2.1.1. Inkjet 3D printing

As one of the earliest printing technologies,[9] inkjet 3D printing can be traced back to traditional inkjet 2D printers used for text printing. In fact, as early as 1988, Klebe used collagen as bioink and inkjet 3D printing technology in his experiments.[10] Similar to the construction of traditional 2D inkjet printers, the cartridge containing the bioink is connected to the printer head. During the electronically controlled printing process, the printer head is deformed and extruded, producing average-sized droplets (resolution can be as high as 50 μm). Depending on the power source, the printer head can be categorized as a piezoelectric, thermal, or electrostatic inkjet[11] (Figure 1A). Piezoelectric actuators work by utilizing the vibration of a polycrystalline piezoelectric ceramic actuator when energized, causing the head to eject ink. A major problem with this method is that the high frequencies (15–25 kHz) used in this bioprinter may disrupt cell membranes, leading to cell damage.[12] Thermal piezoelectrics operate by heating the printer head to create small bubbles inside the bioink; the kinetic energy generated by these bubbles squeezes and ejects the bioink. Even after being exposed to temperatures up to 300°C in the nozzle, cells can still be ejected with up to 90% viability, as they are only heated for 2 μs, resulting in a temperature increase of 4–10°C.[13] Electrostatic inkjets exploit the deformation of the platen when the circuit is turned on or off to extrude ink droplets. The advantages of inkjet printing are as follows: (i) low cost due to a commercial printer-like construction; (ii) high print speed; and (iii) relatively high cell viability. However, current printer heads are based on microelectromechanical system devices; hence, thermal or piezoelectric actuation at the nozzle opening produces relatively small deformation blockages.[14] Another disadvantage of inkjet printing is the settling effect.[15] When the bioinks are initially loaded into the cartridges, they typically mix well. However, throughout the printing process, cells begin to deposit in the cartridge, increasing the viscosity of the bioinks during subsequent printing and often clogging the printer head. In terms of material selection, the non-contact nature of inkjet printing and its reliance on gravity limit the utilization of biomaterials to those with low viscosity, restricting its ability to create fine 3D structures with suitable mechanical properties. Additionally, a certain degree of splattering may occur during the printing process, thus affecting the accuracy of inkjet printing (Table 1).[11]

2.1.2. Laser-assisted 3D printing

Laser-assisted printing is a 3D printing method based on the principle of focused laser-induced transfer of bioink in bioink carriers (cartridges). Laser-assisted 3D printing produces discontinuous droplets of bioink similar to inkjet 3D printing. The difference with inkjet 3D printing lies in its power source during the printing process: focused laser pulses generate high-pressure bubbles at the boundary of the bioink layer, propelling the bioink particles suspended within.[16] Accordingly, laser-assisted printing circumvents many of the drawbacks of inkjet 3D printing by eliminating the need for physical contact and mechanical pressure on cells, leading to optimal cell survival rates, typically

above 95%.[6] Experiments have demonstrated that mesenchymal stem cells (MSCs) can survive and maintain their function throughout the printing process.[17] In addition, laser-assisted printing allows for the printing of more diverse types of bioinks. However, as no nozzles are used to deliver the bioink to the desired plane, the entire cartridge is filled with bioink, leading to material wastage. Moreover, high-resolution and high-intensity laser diodes are expensive. Laser-assisted 3D printing instruments are also bulkier than other 3D printers due to the complexity of the control technology (Table 1).

2.1.3. Extrusion 3D printing

As one of the most common biological 3D printing methods, extrusion 3D printing, also known as pressure-assisted 3D printing, involves assembling bioink in a printer head. By applying pressure to it, the bioink is extruded out of the printer head to form a continuous strand that is deposited onto a surface, forming a 2D structure[18]; a 3D structure is then created layer by layer. The pressure applied to the bioink during the deposition and extrusion process can be carried out using either pneumatic, piston, or screw systems[19] (Figure 1B). To build complex tissue structures, more advanced extrusion bioprinting fabrication methods, such as multi-dispenser printing, coaxial bioprinting, and hybrid bioprinting, have been developed.[19] By using multi-dispenser printing and hybrid bioprinting, simultaneous printing of multiple bioinks can be achieved for constructing complex organ tissues; however, the key to this method is to prevent contact and mixing between the different bioinks.[20] Coaxial bioprinting utilizes different diameters of print heads on the same longitudinal axis to print hollow structures and vertical filament structures (e.g., blood vessels[21] and small intestine villi[22]). A wide range of bioinks are available for extrusion bioprinting. The cost and commercial availability of this printing method are also among its advantages. Extrusion-based bioprinting can also result in cell damage, primarily due to shear stress exerted on the hydrogel and cells, which is the main force leading to this damage. Other influencing factors include needle type and size, dispensing pressure, and bioink concentration.[23,24] A larger print head diameter would reduce the shear stress and print precision (>100 nm), limiting the ability to print finer biological tissues; when the dispensing pressure, which is the pressure exerted directly on the bioink, is increased, shear stress increases; in addition, when printing bioink with higher viscosity, the increased pressure exerted by the machine leads to greater shear stress, increasing the risk of damaging the cell membrane (Table 1).

2.1.4. Depositional 3D printing

Currently, depositional 3D printing, also called fused deposition modeling (FDM), is the most common, economical, and commercially available form of 3D printing.[25] The key characteristic of FDM is the temperature difference between the nozzle and platform, which enables the bioink to exhibit varying mechanical properties at different spatial and temporal scales (Figure 1C). Before being extruded by the nozzle, the bioink is heated to a semi-solid state at a relatively high temperature, and after being deposited on the relatively low-temperature platform, it reverts back to a solid state. Other polymerization methods, such as photopolymerization, can also help improve the mechanical properties of bioink. The printing process, akin to extrusion 3D printing, involves nozzle movement along the x–y axes to follow the in-plane shape of the final object, while stacking layers on the z-axis. Temperature control is critical in depositional printing, as the heat-sensitive bioink can lead to poor material connectivity if the printed filament cools too quickly after extrusion. This cooling may create gaps in the material, affecting its mechanical properties.[26] If the printing process requires an extended duration of elevated temperature, this can affect the activity of the active bioink ingredients; for example, some industrial sectors require nozzle temperatures of up to 400°C.[27] However, various studies have attempted to minimize the potential negative effects of thermal conditions through different approaches, such as adding polymers or excipients to lower the temperature or scaling down the heating time (Table 1).

2.1.5. Stereolithography

SLA differs from traditional extrusion and inkjet printing technologies, as it does not require a nozzle or extrusion head to stack the bioink; it relies on a light source to cure the bioink. The fundamental principle of SLA molding technology involves utilizing a UV laser (350–410 nm). Under the programmable instructions, a vibrating mirror system is employed to scan the liquid surface point by point, gradually curing 2D hydrogel layers. After stacking along the z-axis, a 3D scaffold is formed through this curing process[28] (Figure 1E). Compared with the aforementioned 3D printing methods, SLA has more stringent material requirements, as the utilized bioinks must be easily photocrosslinked upon light exposure. As most light-sensitive materials require photoinitiators during the curing process, the potential toxicity of these initiators can also affect the bioactives in bioinks. The main advantages of this method are its enhanced precision and print quality, as the precise movement and tiny dimensions of the laser enable improved detail and resolution. However, this enhanced quality comes at the cost of print speed, as plotting each layer can be more time-consuming (Table 1).

2.1.6. Digital light processing

The process of DLP, also called projection-based 3D printing, involves the construction of a 2D hydrogel image

on the x–y axes, followed by layer-by-layer printing to realize the superposition on the z-axis, ultimately obtaining a 3D hydrogel body. DLP and SLA differ mainly in the way that each layer of hydrogel is constructed due to the difference in the light sources used. If the SLA's light source is a dot-shaped light source moving relative to the bioink, the DLP's light source is a static, surface-shaped light source with image properties relative to the bioink. The DLP system projects a 2D light image onto the bioink layer, triggering a photopolymerization reaction in the hydrogel solution, allowing for personalized single-material 3D printing.[35] A simple projected 3D printing device uses a UV emitter at the bottom as the light source, with the hydrogel being contained in a solution chamber above and separated from the UV emitter by a glass substrate (Figure 1E).[36] The light source of the DLP device is capable of emitting light at a wavelength range of 350–450 nm, with corresponding intensities varying according to wavelength, peaking at 405 nm (Figure 1E).[37] Due to its high manufacturing speed and resolution, DLP has become a significant focus in biomanufacturing technology. Compared to extrusion 3D printing, which has the smallest extrusion diameter of 100 μm, DLP can reach resolutions of up to 10 μm or less, resulting in significantly higher print quality,[38] allowing

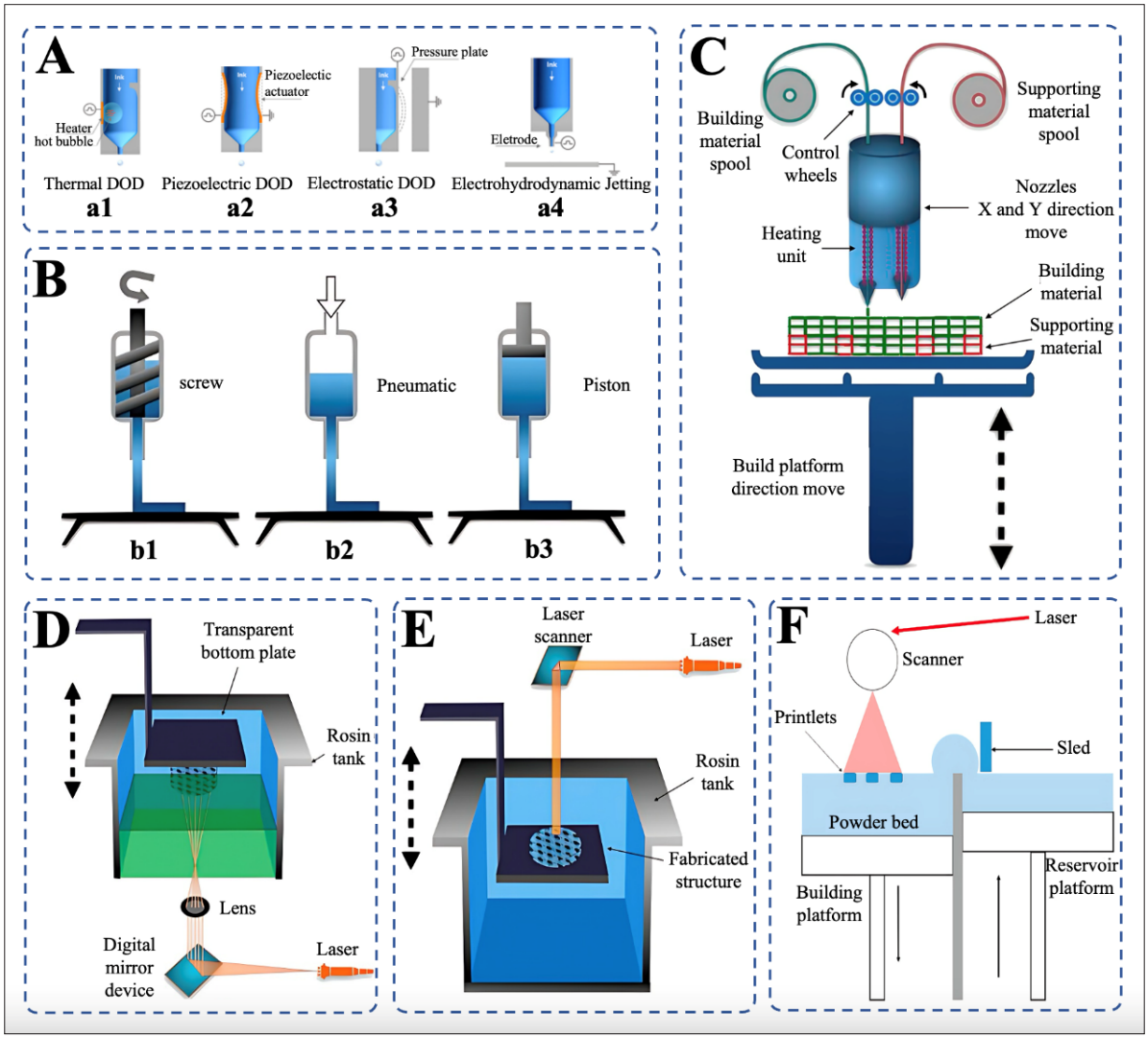

Figure 1. Overview of 3D printing. (A) Simple nozzle models for inkjet 3D printing: (a1) hot inkjet produces water droplets by heating bubbles; (a2) piezoelectric inkjet produces droplets by the vibration of the piezoelectric actuator; (a3) electrostatic inkjet ejects droplets through deformation of the pressure plate; (a4) high voltage electric field produces droplet. Adapted with permission from Li et al.[11] (B) Power sources of extruded heads: (b1) screw, (b2) pneumatic, (b3) piston. (C) FDM 3D printing with two different materials. (D) SLA printing model. (E) DLP printing model. Adapted with permission from Su et al.[32] (F) SLS printing model. Adapted with permission from Kafle et al.[33] Abbreviations: DOD, drop-on-demand; FDM, fused deposition modeling; SLA, stereolithography; SLS, selective laser sintering.

for the printing of finer tissues.[39] Additionally, projection-based 3D printing is more efficient than SLA, with manufacturing speeds typically ranging from 0.5 to 15 mm/s, allowing cell viability to be consistently maintained at 85–95%.[38] By assessing the adenosine triphosphate (ATP) content, Tahouni et al. demonstrated that DLP produced the highest number of viable cells compared with extrusion and inkjet 3D printing.[40] However, DLP has its drawbacks, such as potential DNA inducibility of the light source and photoinitiator toxicity (Table 1).[41]

2.1.7. Selective laser sintering

Selective laser sintering (SLS), known as solid-state sintering, is a process that uses one or more lasers to produce an object from a powder material. Any powder material that can be heated to form an atomic bond can be used as a molding material for SLS. A computer-controlled laser heats the powder, causing the particles in the powder to polymerize into a solid form. After sintering layer by layer, the 3D structure is successfully printed. Once the process is complete, the remaining powder is extracted from the platform (Figure 1F). The unsintered material can be reused, thus reducing waste and costs. Due to its distinct printing principle and process, SLS is seldom used to print cell-laden bioinks. SLS employs thermoplastic polymer, similar to fused deposition 3D printing; the material precursor for the former is powder, whereas for the latter, it is filament. SLS can achieve high printing accuracy with a minimum resolution of 20 μm if the laser is tightly focused.[29] However, its application is currently limited by its high cost and slow printing speed, which prevents rapid printing over large areas (Table 1).[30,31]

2.1.8. 4D printing

4D printing introduces a new dimension to the *x*–*y*–*z* spatial dimensions of 3D printing, i.e., time. By applying stimulus-responsive bioink, 4D bioprinting can create dynamic biostructures that can alter their shapes or behaviors in reaction to a range of stimuli (Figure 2A), more closely resembling the biological state of the original tissue (Figure 2B),[34] thereby offering significant promise for tissue engineering of tissues and organs with mechanical primary functions (Figure 2C). One such example is the use of electrical stimulation to activate cardiomyocytes cultured in 3D fibrin hydrogel environments that mimic the natural environment of these cells and enable the reshaping of their structure to produce contractility under electrical pacing conditions.[35] However, one of the limitations of 4D bioprinting also stems from its dependence on external stimuli, as excessive stimulation may damage and kill living cells; therefore, stimuli must be adapted. One of the simplest mechanisms that can be employed in 4D printing is using non-homogeneous materials with different properties to enable folding and unfolding under different conditions (e.g., swelling). The power source for 4D-printed biomaterials to undergo a trait change can be an intelligent hydrogel substance or cells. The available hydrogel substances are categorized into light-responsive hydrogels,[36] temperature-responsive hydrogels,[37,38] acidity-responsive hydrogels,[39] humidity-responsive hydrogels,[40] magnetic,[41] and electric[42] reactive hydrogels, and acoustic reactive hydrogels,[43] or combinations of these. Additionally, material changes can also be achieved using cellular forces, where cells can generate traction in their matrix, originating from intracellular actin polymerization and antiglobulin interactions.[44] Kuribayashi-Shigetomi et al. cultured cells on microtiter plates and then used cellular traction to fold these cells into 3D microstructures.[45]

2.2. Materials

Bioinks typically comprise a solution of hydrogel prepolymer and cells (Figure 3A). In the 3D printing process, cells interact with the hydrogel material. Hence, choosing suitable biomaterials to simulate the physiological *in vivo* environment is essential for cells to proliferate in the microenvironment provided by the hydrogel.[49] However, the printing properties of the hydrogel vary to a certain extent due to the incorporation of cells (Figure 3B).[50] Therefore, selecting suitable hydrogel solutions and cells, and using proper printing and crosslinking methods are significant.

2.2.1. Hydrogel solutions

Hydrogel solutions play a critical role in bioinks because they provide the immediate environment on which cells depend on and must have the required physical and chemical properties.

Given that most current 3D printing approaches support dispensing liquid materials and that subsequent cell proliferation necessitates a scaffold with adequate mechanical strength, the printability of the hydrogel solution in both liquid and gel states while maintaining its solidity after printing is essential. Consequently, hydrogels designed for 3D printing must exhibit responsiveness to specific optical,[51] chemical,[52] and thermal[53] stimuli. This responsiveness is crucial for forming solid scaffolds with the requisite mechanical strength under controlled conditions. Moreover, these hydrogel properties should remain relatively stable in a biological environment, minimizing susceptibility to changes.

The interaction between hydrogels and cells is dynamic, which is important for cell adhesion and growth.[54] The hydrogel's mechanical characteristics, including shear stress, mass expansion, strain, and compression modulus, precisely determine its interaction with cells. For some soft

Table 1. Comparison of various 3D printing technologies

3D printing method	Printing form	Printing speed	Resolution (μm)	Vertical stability	Cell viability	Cell density	Printing cost	Ref.
Inkjet 3D printing	Droplet	Fast	50–100	Poor	>85%	Low	Low	[11]
Laser-assisted 3D printing	Punctiform	Medium	10–100	Good	>95%	Medium	High	[46]
Extruded 3D printing/ FDM	Filamentous	Slow	200–1000	Good	40–90%	High	Medium	[23,47]
DLP/SLA	Layered	Fast	<50	Good	>85%	Medium	High	[29,48]

Abbreviations: FDM, fused deposition modeling; DLP, digital light processing; SLA, stereolithography.

tissues, tissue functionality lies in the mechanical properties they provide; therefore, the resulting hydrogel must first be well-adapted and can withstand the stresses and tensions that the tissue would otherwise be subjected to.

Biocompatibility requires that cells survive, differentiate, and proliferate in the hydrogel after 3D printing. Hydrogels need to have good porosity to facilitate nutrient delivery. The problem of vascularization is a major limitation for printing structures on a large scale.[55] These are just the basic requirements for *in vitro* applications. When hydrogels are used *in vivo*, they not only need to have the basic requirements for *in vitro* applications described above but also avoid adversely affecting the organism or being metabolized to produce toxic by-products. In addition, the ideal implantable tissue needs to have good degradability, gradually combining with human tissue through metabolic degradation.[56]

2.2.2. Cells

Cells selected for bioink production are typically divided into two main categories: differentiated functional or support cells[57,58] and stem cells with differentiation potential.[59,60] such as induced pluripotent stem cells (iPSCs), MSCs, neural stem cells (NSCs), adipose-derived stem cells (ADSCs), embryonic stem cells (ESCs), or embryoid bodies (EBs) made up of multiple ESCs.[61] When using differentiated cells, parallel printing is needed as multiple cell types must be embedded in one or more hydrogels concurrently or sequentially. This complicates real-time alignment and printing control, introducing challenges in preventing interference between bioinks due to varied excitation conditions, potentially leading to errors in bioprinting processes. Stem cell printing streamlines the variety of bioinks but increases complexity in subsequent steps, particularly in inducing differentiation. Precise deposition of growth factors and differentiation stimulators is essential for controlling differentiation during subsequent post-printing culturing. Currently, two methods exist for cell insertion during printing: (i) mixing a hydrogel solution with cells in a cartridge and acting as a bioink, or (ii) applying cells directly to a scaffold of cured material after printing with a hydrogel solution.[50] Notably, a reliable cell source remains a long-term challenge for bioprinting, especially for clinical applications, where cells should ideally be isolated from the body of the patient to prevent immune reactions.[62]

3. MA-based hydrogel bioinks

3.1. Preparation

3.1.1. Introduction of methacryloyl groups

The preparation of MA-based hydrogels involves grafting methacryloyl anhydride groups to the hydroxyl or carboxyl

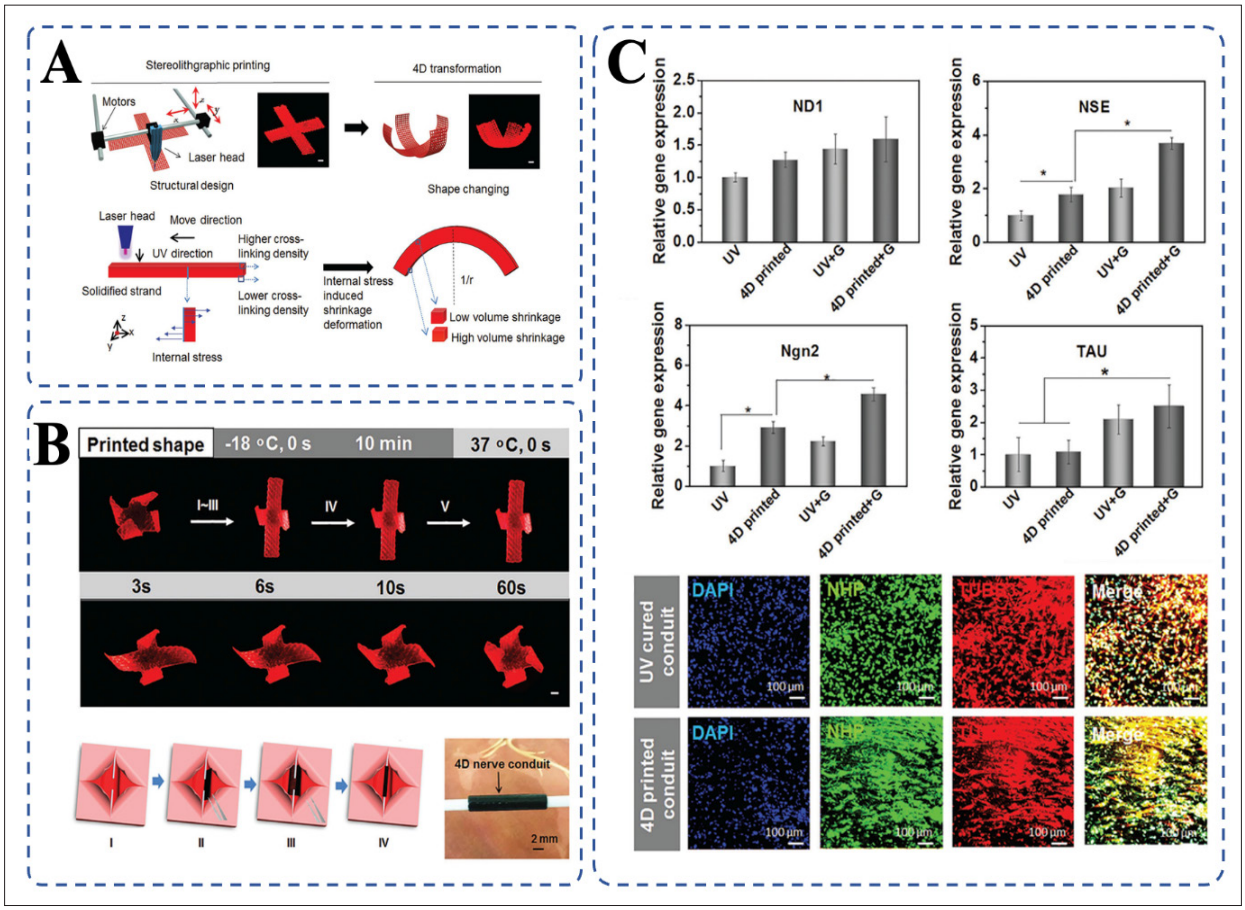

Figure 2. A novel multi-responsive architecture through stereolithography (SLA)-based 4D bioprinting, using a naturally derived, photocrosslinkable monomer (soybean oil epoxidized acrylate [SOEA]). (A) A claw structure obtained by SLS printing technology and its deformation mechanism. (B) Images displaying the reversible shape change process of a 4D-printed structure and its application in nerve repair. (C) The 4D-printed graphene hybrid conduit significantly improved the neurogenic differentiation of hMSCs. Adapted with permission from ref.[36] Abbreviations: SLS, selective laser sintering; hMSCs, human mesenchymal stem cells.

groups on their side chains by mixing different hydrogels with compounds capable of introducing MA groups under certain conditions, generating an amidation or an esterification reaction. At present, owing to simplicity and cost, the most common modification reaction used is the esterification of MA or glycidyl methacrylate (GMA).[64] Alternatively, aminoethyl methacrylate (AEMA) and hydroxyethyl methacrylate (HEMA) may be used.[64] AEMA, HEMA,[65] and methacryloyl chloride[66] can also be used for the introduction of methacryloyl anhydride groups. Different concentrations of MA can result in different methacrylic acid (MAA) graft substitution conversions in the resulting material (Table 2). The substitution conversion ratio of MAA is a key parameter for measuring GelMA performance. When the substitution rate is low, the formed MA compounds can better retain their original biocompatibility and other active properties; however, when the substitution rate increases, the crosslinking and mechanical properties increase significantly; when the rate of substitution exceeds 15% for light-curing crosslinking, the degree of methacrylation can reach up to 90%.[67] By adjusting the GMA content and reaction time, the degree of methacrylation can also be changed, reaching up to 90%.[68] Nichol et al.[69] prepared three batches of GelMA with methacrylation degrees of 81.4% (high), 53.8% (middle), and 19.7% (low) by adding 20, 1.25, and 0.25 vol.% MAA, respectively, into the synthesis reaction. The compressive modulus was significantly higher for low, medium, and high degrees of methacrylation at both the 15% and 10% (w/v) GelMA concentrations. Holding the hydrogel percentage constant, the mass swelling ratio increased significantly with a decreasing degree of methacrylation at all three hydrogel concentrations, demonstrating that the degree of methacrylation had a significant effect on the material's ability and propensity for attracting and storing water within the polymer network (Figure 4B).[69]

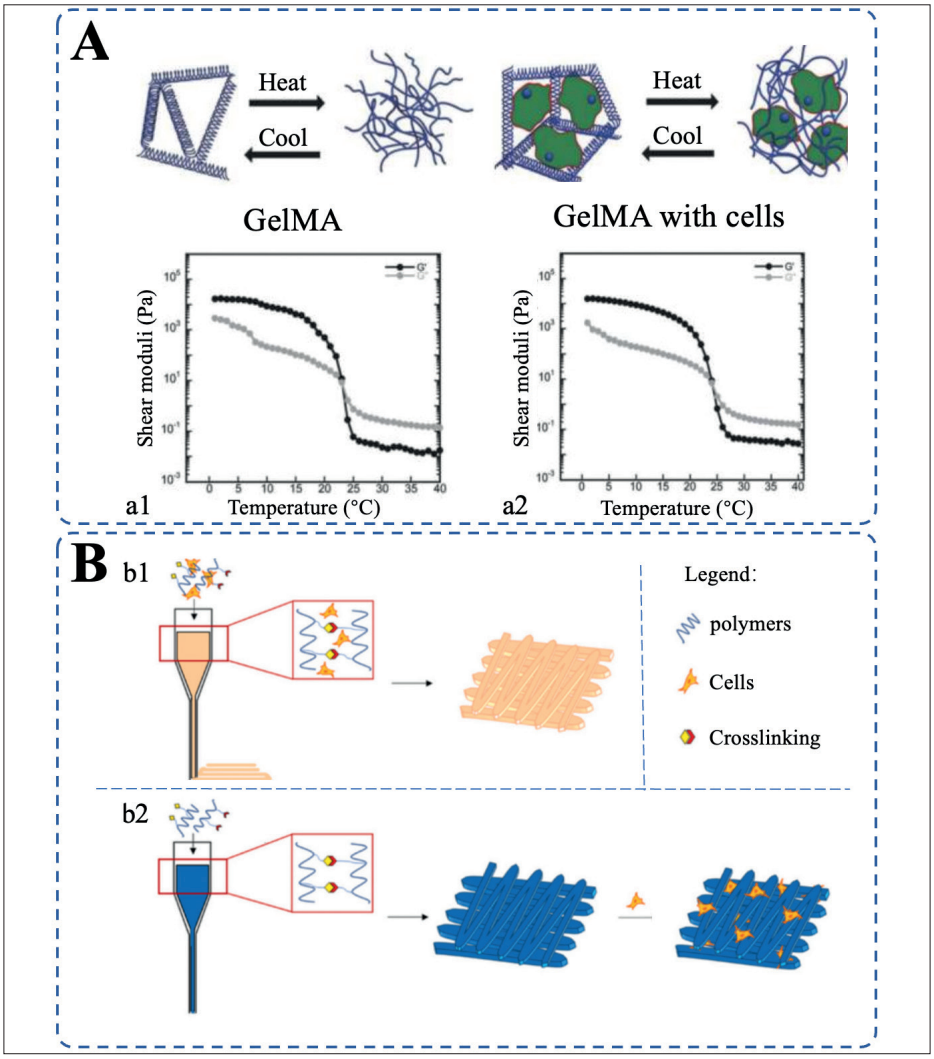

Figure 3. Basic form of a bioink. (A) Schematic representation of temperature-responsive gels (top); corresponding shear elasticity and loss modulus of pure GelMA (a1) and fibroblast-containing GelMA bioink (a2). Adapted with permission from Kolesky et al.[63] (B) Cell coating methods for 3D printing using bioink: printing with cells (b1), or using scaffold adhesion cells (b2). Adapted with permission from Cadamuro and Nicotra.[50] Abbreviation: GelMA, methacrylated gelatin.

3.1.2. Photocrosslinking reactions and photoinitiators

MA-based hydrogels can be crosslinked and molded by light reactions because they contain many photosensitive groups, usually unsaturated double bonds. Unlike the polymerization process of traditional materials that form a 1D linear structure, photosensitive hydrogels require a certain light wavelength and photoinitiator to polymerize. This reaction mainly consists of three steps: proliferation, termination, and closure reaction (Figure 4C).

Only two factors influence the formation of light-cured hydrogels: hydrogel precursor properties and crosslinking conditions. The latter include temperature, exposure time and intensity, and light wavelength.[72] The printability of hydrogel materials is mainly determined by the degree of crosslinking. He et al. found that utilizing fast crosslinking printing and slow crosslinking followed by printing can improve the printability of hydrogels by two to four times. Fast crosslinking printing refers to a printing method that utilizes high exposure intensity and short exposure time, forming a hydrogel with a lower crosslinking degree. By contrast, slow crosslinking post-printing utilizes low exposure intensity and long exposure time, forming a hydrogel with a higher crosslinking degree underneath. By adjusting the exposure parameters, this strategy achieves higher cell viability. Hence, the properties of cured materials can be improved to a large extent by personalizing the light reaction parameters in the photocrosslinking reaction.[73]

Table 2. Common MA reactants

Reactants	Reaction solvent	Reactant concentration	Reaction pH	Reaction temperature	Response time (h)	Ref.
MA	Water, PBS	4–6%	8–10	Indoor temperature	2–4	[68,70]
GMA	PBS	1%	3.5–5.5	50–60°C	24	[64]
AEMA	MES buffer	0.38%	6.5	Indoor temperature	24	[64]
HEMA	DMAP, Boc_2O	-	-	45°C	20	[65]
Methacryloyl chloride	Anhydrous chloroform	-	-	0°C to room temperature	14	[66]

Abbreviations: AEMA, aminoethyl methacrylate; Boc_2O, di-tert-butyl decarbonate; DMAP, dimethyl sulfoxide; GMA, glycidyl methacrylate; HEMA, hydroxyethyl methacrylate; MA, methacrylic anhydride; PBS, phosphate-buffered saline.

Photosensitizers can absorb energy at a certain wavelength and produce free radicals and cations, triggering the polymerization of monomers, crosslinking, and curing. Lithium phenyl-2,4,6-trimethylbenzoylphosphinate (LAP), a kind of phosphine derivative with good spectral properties and high water-solubility, is the most commonly used photoinitiator in the photopolymerization of MA-based hydrogel. Studies have reported that using different types of photosensitizers results in varying resolutions. Using a high-intensity light source that is scattered or refracted by other substances amplifies the effect of the photosensitizer.[74] Additionally, certain photoinitiators may pose potential toxicity to cells. Therefore, when designing a photocrosslinking reaction, the choice of photoinitiator and its absorbance properties should be cautiously considered.

3.1.3. Advantages and disadvantages of modified hydrogel bioinks

Most hydrogels crosslinked by ionic, chemical, or temperature reactions have poor mechanical strength and reversible crosslinking disadvantages. Photopolymerization offers numerous advantages over other methods. Firstly, light is non-invasive and can be manipulated remotely without additional reagents. Secondly, by adjusting the illumination parameters (intensity, wavelength, and illumination time), the irradiation dose can be controlled, thereby imparting precise regulation of the degree of light reaction.[75] Under certain light reaction conditions, a gum can form quickly and be crosslinked in a few seconds. This can greatly improve the efficiency of 3D printing. However, this poses challenges for 3D printing; for example, in extrusion 3D printing, the extrusion speed of the precursor solution of hydrogel needs to be controlled to match the gelation speed of the hydrogel. Otherwise, if the extrusion speed is too fast while the gelation time is too little, this will cause the collapse of the stent; conversely, if the extrusion speed is too slow while the gelation time is too long, the pre-cured hydrogel will block the nozzle. The UV light utilized in the photocrosslinking process also affects cell viability and DNA stability. When cells are exposed to UV light for more than 10 min, up to 90% of cells can be damaged.[76] Although UV light and free radicals may attack the cell membrane during crosslinking, this can be easily controlled by adjusting the light source and dose of photoinitiator.

To maintain cell viability during and after printing, the low toxicity and high biocompatibility of the printed scaffolds are imperative, especially for implantable tissue structures. From a materials science perspective, the biggest factor that influences the biocompatibility of biological scaffolds is their microscopic morphology.

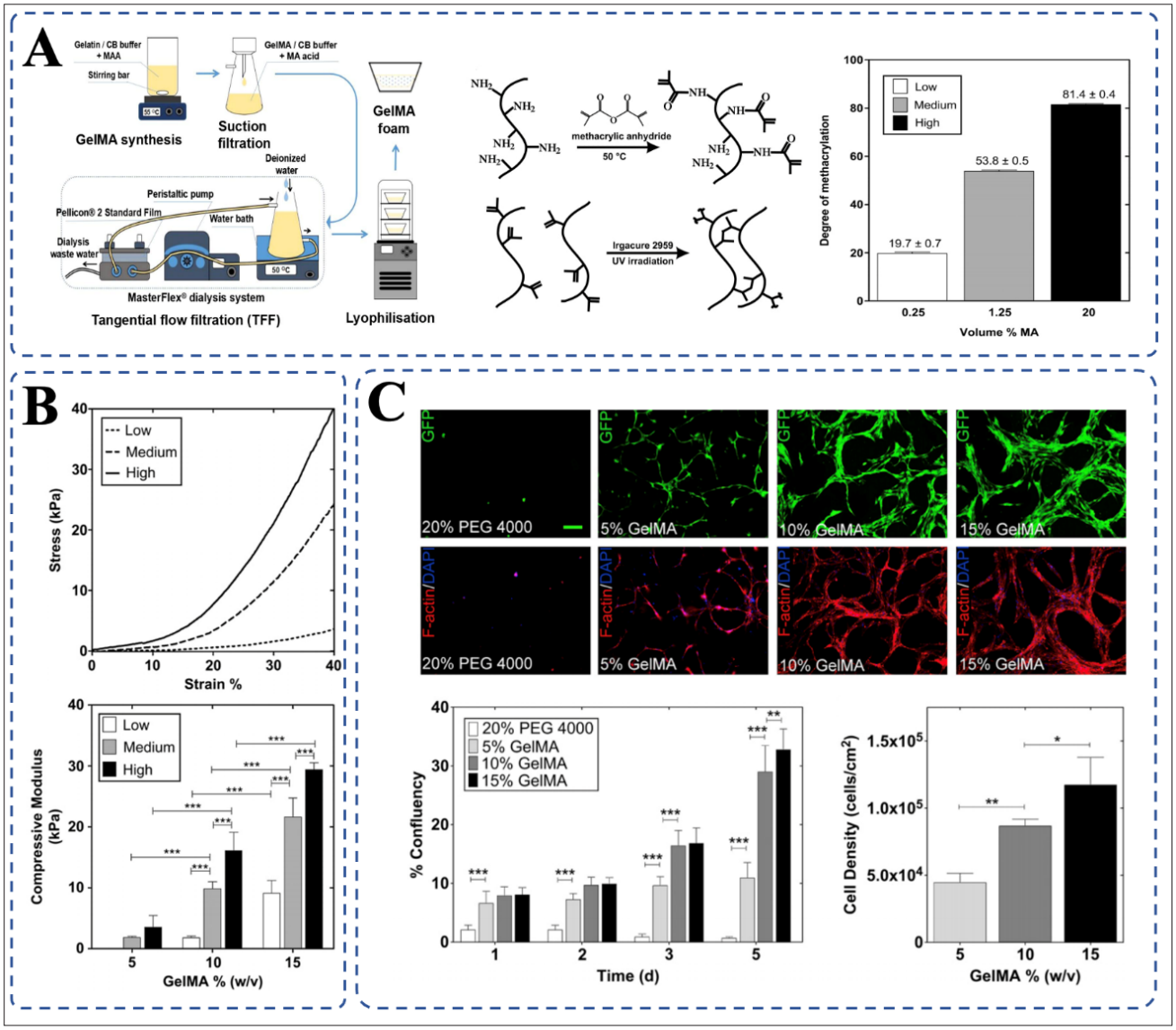

Figure 4. Gelatin methacrylate (GelMA) hydrogels with different substitution rates have different properties. (A) GelMA hydrogels with different substitution rates can be obtained by changing the feed ratio. Adapted with permission from Zhu et al.[71] (B) GelMA hydrogels with different substitution rates have different physical properties. (C) GelMA hydrogels with different concentrations have different biocompatibility. Adapted with permission from Nichol et al.[69] Abbreviations: CB, carbonate-bicarbonate; MAA, methacrylic acid; MA, methacrylic anhydride; PEG, polyethylene glycol, GelMA, methacrylated gelatin.

Thus, by adjusting the printing parameters and methods, 3D printing and photoreactive hydrogels can be utilized to develop bionic cues that favor cell adhesion.[77]

Regarding the microscopic morphology, the pore size and porosity of hydrogels are critical for cell migration, nutrient and oxygen distribution, and cell–cell interactions. Of note, adequate pore size and porosity mediate vascularization, as they provide an optimal physical microenvironment for human umbilical vein endothelial cell (HUVEC) migration. When pore size ranges from 200 to 250 μm, cell migration and proliferation are favored.[78] Porosity and pore size are largely determined by the precision of the printing process and material properties. The fidelity of the printed hydrogel determines whether the subsequent scaffold can maintain these biological cues. With the increasing number of layers, the geometry of the hydrogel may collapse under its own weight. As bioink cannot sustain unsupported fibers, vertical pores may close as they expand, whereas lateral pores may collapse.[79] The final filament width in a hydrogel material increases due to its water-absorbing and swelling properties, resulting in a

decrease in the final filament spacing when exposed to body fluids. The swelling of hydrogels in simulated body fluid environments leads to notable pore closure, affecting cell migration and nutrient penetration. However, advocating solely for high porosity is not that simple, as increased porosity and pore size inevitably diminish the mechanical properties of the hydrogel. Therefore, a balance must be achieved to optimize both porosity and mechanical strength based on specific tissue load-bearing requirements.

3.2. Material classification and finishing

3.2.1. Proteins

GelMA: Gelatin has an amino acid sequence similar to that of its precursor, collagen, and is widely utilized in the food manufacturing and pharmaceutical sectors. Unmodified gelatin can self-form a crosslinked network under chemical or enzymatic crosslinking conditions, though exhibiting poor mechanical properties.[80] By introducing methacryloyl substituents to the reactive groups on its side chains, GelMA can be obtained, which can be crosslinked and cured into a gel using photoinitiators and UV/visible light. GelMA has good biocompatibility because the gelatin backbone contains biologically active sequences of collagen for cell attachment, such as RGD peptides and matrix metalloproteinase-sensitive degradation sites.[67] 3D GelMA hydrogels closely resemble some of the fundamental properties of natural ECM.[81] In addition, GelMA possesses good temperature-sensitive gel properties and degradability, while a broad spectrum of stiffness and viscoelastic characteristics can be provided by controlling the methacryloyl substitution rate. With the increasing methacryloyl substitution rate, hydrogels exhibit increased stiffness and smaller pore sizes, but they are also less favorable to cellular translocation. As no accurate standard method exists for determining and quantifying the substitution rate of MAA in hydrogels, the amount of MAA used to synthesize GelMA macromolecules is generally used as a measure of the degree of GelMA functionalization.[82] Typically, the compression modulus of hydrogels is in the range of 5–180 kPa, as the concentration of macromolecules varies from 5% to 20%.[83] GelMA, the most widely used MA-based hydrogel, has been used in tissue engineering of various systems of the human body.[70]

Silk protein- and silk gelatin-methacrylate: As a natural fiber, silk mainly comprises silk fibroin (SF) and silk sericin (SS) proteins, both of which have good biocompatibility and biodegradability. Silk fibers have a core–shell structure, with the inner core made up of sericin protein and the outer shell comprising silk gelatin protein. SF protein makes up the central fiber of silk, comprising approximately 75% of the total weight; SS can be used as an adhesive to maintain the structural integrity of the fiber, accounting for approximately 25% of the total weight.[84] SF, derived from the degumming of silk, is a polymer polypeptide composed of various amino acids, with serine, aspartic acid, and glycine being the three most significant amino acids.[85] The SF polypeptide comprises a hydrophobic light chain (with a molecular weight of 26 kDa) and a hydrophilic heavy chain (with a molecular weight of 390 kDa). This structure allows the generation of various secondary conformations of proteins and interconversion between them. Moreover, the degradation products of SF, primarily amino acids and peptides, can serve as nutrients for cells, rendering SF a promising candidate for tissue engineering. As the heavy chain of SF contains more repetitive sequences, which gives it excellent mechanical properties (maximum elongation at break: 4%; ultimate Young's modulus: 300–700 MPa; toughness: 70–78 MJ/m^3), it has been used in bone, blood vessel, and wound dressings.[86] SF solution is a semi-stable colloidal solution that can undergo gelation when induced by various factors, including shear force, ultrasound, temperature, and organic solvents. However, controlling the gelation process is challenging, limiting its adaptation to cell culture and 3D printing.[87] Methacryloylated SF (SilMA) is a methacryloylated modification of SF by glycidyl methacrylate, which introduces a double bond on the SF molecule. SilMA possesses excellent mechanical and rheological properties.[88] SilMA bioinks are ideally suited for DLP printing processes, enabling the construction of highly complex organ structures with excellent structural stability and biocompatibility.[89] In contrast, SS hydrogels exhibit inherent biological properties that support wound healing, moisturization, anticoagulation, and epithelial and connective tissue repair. They are widely applied as antioxidants, food additives, cosmetic additives, drug delivery carriers, polymer grafting devices, chemical protectors, UV radiation protectants (sunscreens), and anticancer compounds.[90] The antioxidant activity of methacryloylated SS (SerMA) is considered a fundamental property contributing to its biological effects, though the exact mechanism remains unclear. Reportedly, SerMA hydrogels have excellent biocompatibility. Moreover, they have demonstrated mechanical properties and degradation rates similar to those of other hydrogels. Diverse restoration needs can be readily accommodated by altering the extent of methacryloyl modification of SS.[91]

Bovine serum albumin (BSA) methacrylate: BSA is a non-glycosylated protein in the circulatory system that is ubiquitous in the human serum. BSA can function as a pH buffer to maintain homeostasis in the internal environment. Given the biodegradability, non-immunogenicity, cost-effectiveness, and remarkable biocompatibility of BSA, it has gained significant attention for biomedical applications,

especially in the treatment of various diseases and tissue engineering.[92] BSA can form hydrogel crosslinking networks under acid-based excitation, photoinitiation, and thermal excitation. However, the high cost and complexity of photoinitiation and temperature excitation can lead to cell inactivation and protein denaturation; thus, acid-based excitation is the optimal choice.[93] The introduction of a methyl amide group enables the synthesis of photoreactive BSA methacrylate (BSAMA), which exhibits slower gelation kinetics and enzymatic degradation than GelMA. In a study by Chen et al., BSAMA demonstrated higher cell survival than GelMA (BSAMA: 99.43 ± 0.57%; GelMA: 97.14 ± 0.69%). However, BSAMA gels were not as suitable as GelMA gels for cell proliferation and migration.[94] The group synthesized and formulated an aqueous resin using BSAMA to print precise 3D objects, exhibiting favorable cell viability after 21 days of incubation.

Methacrylate collagen: Collagen is the main component of animal connective tissue and the most abundant and widely distributed functional protein in mammals, as it can be found in skin, bones, joints, and hair.[95] Conventional collagen mainly derives from animal tissues such as pig skin, cow Achilles tendon, and fish skin. However, these sources entail inherent disease risks and may lead to human exclusivity and reduced efficacy due to structural disruption during extraction. By comparison, recombinant collagen presents no viral risk, demonstrating outstanding biological compatibility and efficacy, along with low immunogenicity. Collagen, which cannot directly support cells, can only be bioprinted by modifying it or mixing it with other hydrogels to form hybrid bioinks, posing a challenge in achieving the proper spatial distribution of cells. Furthermore, collagen exhibits low printability and stability. Toxic chemicals used in the crosslinking process limit cell viability in the bioprinting process.[96] Human recombinant collagen modified with MAA is crosslinked under photoexcitation and initiator conditions with better biocompatibility, printability, and mechanical strength, demonstrating great potential in tissue engineering and regenerative medicine.[97] Cardiomyocytes and cardiac fibroblasts can survive in MAA-modified human recombinant collagen for >14 days, allowing stiffness control of the 3D microenvironment and monitoring of cardiac cellular responses.[98]

3.2.2. Polysaccharides

Methacrylate chitosan: Chitosan, also known as deacetylated or soluble chitin, is derived through deacetylation (removal of the acetyl group from C2) of chitin. Chitosan presents a novel nanomedicine carrier, with a core factor being its unique mucosal property. The biodegradability, low toxicity, and good biocompatibility of chitosan have led to its widespread use in biomedicine and formulations.[99] It exhibits antimicrobial activity against various bacterial, fungal, and viral pathogens, as well as antacid, antiulcer, and wound healing properties.[100–102] Chitosan possesses hydroxyl and amino groups that facilitate intermolecular hydrogen bonding and enable chemical modification of chitosan chains.[103] However, the robust hydrogen bonding between chitosan molecules renders its solubility in both water and organic solvents challenging, thereby restricting its practical utility. Modification of chitosan with MAA involves introducing methacrylic groups into the chitosan molecular chain, enabling light curing.[104] This modification results in chitosan methacrylate, which exists in solution form, possesses injectability and favorable physicochemical properties, and can be rapidly light-cured into a glue.[105] Another derivative, methacrylated carboxymethyl chitosan (CMCSMA), is obtained through the carboxymethyl substitution of active hydrogen on chitosan, retaining the excellent properties of chitosan, including its biocompatibility, biodegradability, and bioadhesion, while enhancing its water solubility.[134] Structurally, CMCSMA, in addition to its light-curing ability from the methacrylic group, contains abundant –COOH and $–NH_2$ groups, allowing for multifunctionalities through chemical modification. Chitosan methacrylate and CMCSMA biohydrogels retain the strong adhesion, good biocompatibility, and antimicrobial properties of chitosan, while also enhancing the versatility of the hydrogel base. This allows for mixing with other drugs or compounds, making them applicable in wound healing,[106–108] bone tissue engineering,[109,110] nerve repair,[111] and other biomedical applications.

Methacryloylated dextran: Glucans are homopolysaccharides composed of glucose connected by glycosidic bonds. The structure of dextran, a complex glucan, varies depending on the microbial species and growth conditions. Based on the type of glycosidic bond, glucans can be categorized into α- and β-glucans. β-glucan is more physiologically active and plays more roles than α-glucan.[112] Additionally, dextran can obtain multifunctional active derivatives through modification of the groups on its side chain. Based on these characteristics, dextran has been widely used in tissue repair,[113] wound dressings,[114] and drug delivery.[112] Compared with other polysaccharides, dextran is popular for its relative bioinertness, biodegradability, and modifiability. However, pure dextran hydrogels exhibit poor mechanical properties.[115] MAA has been utilized to introduce MA groups and generate dextran methacryloyl (DexMA), which can be photocrosslinked to improve its mechanical strength. DexMA is characterized by transparency, flexibility, excellent physical morphology, and high viscosity, as well as stable gel-forming properties

and good biocompatibility.[116] It also exhibits stable adhesive properties and retains biophilicity. In practical applications, DexMA is not only combined with other biopolymers to form macroporous scaffolds for drug delivery, but it is also made into hydrogel microneedles for subcutaneous release.[117,118] DexMA has also been utilized as a platform for angiogenesis and tissue repair.[118,119] In contrast to other derivatives, DexMA retains its beneficial properties in the crosslinked network and possesses tunable mechanical properties that facilitate the renewal and use of composite systems.

Sodium alginate methacrylate: Sodium alginate (Alg) possesses favorable characteristics such as good biocompatibility, stability, solubility, inertness, low cost, and ease of production.[120] Sodium Alg exhibits versatility and can be employed under both extreme and gentle conditions. It can readily form gels through chemical crosslinking. The gelation process under mild conditions is advantageous in preventing the inactivation of active substances.[121] However, the lower mechanical strength of sodium Alg crosslinked hydrogels limits their range of application.[122] Methacrylated sodium Alg (AlgMA) can greatly compensate for this shortcoming, as their crosslinking is highly versatile, and they exhibit good internal gel homogeneity. The introduction of methacrylate groups into AlgMA enables dual crosslinking, which enhances its mechanical properties. Tests revealed that at the same concentration, AlgMA hydrogel mesh scaffolds exhibited enhanced molding fidelity and mechanical strength compared with those of Alg hydrogels.[123,124] Currently, AlgMA is extensively used in the biomedical field as an effective scaffolding material for loading cells, drugs, or other active substances.[125,126]

Methacrylated chondroitin: Chondroitin sulfate (Chs) is a sulfated linear glycosaminoglycan widely distributed in mammalian cells and crucial for the function of the extracellular matrix methacrylate (ECMMA).[127] Chs is found in large quantities in tissues where it serves crucial physiological functions.[128] Chs is most commonly used in combination with glucosamine in the treatment of osteoarthritis.[129] Chs can regulate growth factors and promote injury healing.[130] It acts as a neuroprotective agent[131,132] and possesses anti-inflammatory, antioxidant,[133,134] and antitumor[133,135] activities. Incorporation of a methacrylate group into the molecular chain of Chs forms methacryloylated Chs (ChSMA) with light-curing capability. Utilizing a versatile crosslinking molding method and exhibiting excellent biocompatibility, ChSMA-based material systems have found extensive applications in various biomedical research areas, including serving as effective drug carriers.[136] ChSMA has displayed promise in osteoarthritis treatment,[137] cartilage and heart regeneration,[68] neurological repair,[138] and bone–tendon interface reconstruction.[139]

Methacrylated hyaluronic acid: Hyaluronic acid (HA) is the simplest glycosaminoglycan and a major component of ECM.[140] The chain length of HA can range from 0.200 to 10 MDa, with the most common size range being 2–5 MDa. HA is a scaffolding material secreted *in vivo* by cells and has good water retention and moisturizing properties. The distinctive characteristic of reduced viscosity under shear makes HA suitable as a lubricant. In static conditions, HA offers elasticity. Additionally, apart from creating a hydration space around cells, HA influences the transport of growth factors and other signals through its pore size and charge density. Hyaluronic acrylate methacrylate (HAMA) imparts HA with a light-curing ability. Due to their versatile molding method and good biocompatibility, HAMA-based materials have been used in many biomedical research areas, including chondrocyte and cartilage regeneration,[141,142] infection or diabetic wound repair,[143,144] anti-inflammation, antioxidative stress,[145] corneal reconstruction,[146] tumor modeling,[147] drug-controlled release,[148] biosensors,[149] and post-surgery anti-adhesion.[150]

3.2.3. Other substances

In addition to the natural proteins and polysaccharides mentioned above, numerous substances can be modified with MA groups. Theoretically, as long as a substance is rich in amino and hydroxyl groups, it can potentially incorporate the methacrylate group, thus acquiring photocurable properties. ECM is a natural scaffold prepared from a tissue or organ by removing cellular components and retaining the 3D structure and some natural fiber components of the tissue or organ. As the living environment of cells, it contains various proteins, polysaccharides, and a large number of bioactive factors. ECM can be potentially modified with MA. Growth factors are keys to the biological function of ECM. A study comparing ECM and ECMMA hydrogels revealed that most growth factors and cytokines were retained in ECMMA hydrogels.[151]

Liu et al. prepared polyamide-amine by introducing the MA group into the side chain of polyamides and prepared cartilage repair scaffolds by adding GelMA and ADSCs. The obtained hydrogel displayed sufficient potential for promoting cartilage regeneration.[152] In the study by Lim et al.,[153] a new type of biological resin was constructed by adding GelMA to polyvinyl alcohol polyvinyl methacrylate. Using a visible photoinitiator system that displays high Mohr absorbance, constructs with high-resolution features were bioprinted in the 25–50 μm range. Simaan-Yameen et al.[154] synthesized FibMA by methacrylation of

denatured fibrinogen using MA. Studies have reported that MAA does not alter the important biological properties of fibrinogen, including the ability to support cell adhesion, 3D cell culture, and proteolysis.[154]

4. Applications

4.1. Tissue engineering scaffolds

We summarize the application of various types of methacrylic anhydride hydrogel 3D printing scaffolds in biological tissue engineering in Table 3.

4.1.1. Skin trauma

The main focus in skin tissue engineering is the treatment of chronic ulcers, which are a leading cause of death worldwide.[155]. Chronic wounds are caused by hypoxia and lack of tissue nutrition, with pathogenic infections often being responsible for prolonged non-healing.[156] For example, impaired angiogenesis in patients with diabetes leads to reduced infiltration of inflammatory cells, while growth factors and elevated glucose levels make wounds more susceptible to infection.[185] Furthermore, severe injuries may cause impaired wound healing in the skin, with excessive and sustained myofibroblast activation further leading to scar tissue formation.[157] In summary, a more effective treatment for skin wound tissues is necessary.

Tissue-engineered scaffolds for skin healing should provide isolation and protection to the wound bed by exerting anti-inflammatory and anti-infection effects. Additionally, the scaffolds should promote vascularization, thereby accelerating skin tissue regeneration while concurrently inhibiting scar tissue formation. The bioengineering approach to skin regeneration primarily relies on the utilization of hydrogels and factors, such as vascular endothelial growth factor (VEGF) or stem cells of diverse origins, including human skin fibroblasts,[157] adipose-derived stem cells, and epidermal stem cells. These components are mixed to create bioinks for the formation of hydrogel scaffolds through a combination of extrusion and light-cured printing (Figure 5A). In a study by Chen et al., *in situ* printing on a whole skin incision mice model was achieved using a robot.[158] Multiple animal experiments have demonstrated that 3D scaffolds can attenuate inflammatory response, increase periwound blood perfusion, and promote re-epithelialization, collagen deposition and alignment, and angiogenesis, thereby facilitating wound regeneration. Moreover, the addition of skin-derived precursors (SKPs) printed in a hydrogel incorporating stem cells not only maintains their properties but also promotes their proliferation.[158] By printing the epidermis, dermis, and vascular network in layers, constructing a structure that approximates a full skin layer is made possible.[159] The regenerated skin contains the epidermis, dermis, blood vessels, hair follicles, and sebaceous glands similar to natural skin. These approaches provide an effective strategy for *in vitro* epidermal reconstruction.

4.1.2. Bone defects

Bone tissue consists of a mixture of living cells and minerals (mainly calcium and phosphorus) that provide support and protection. Due to the high mechanical properties that bone tissues possess, the biological replacement of large volumes of bone tissue is still limited to inorganic compounds. In addition to inorganic metallic materials, many organic materials have been used in clinical bone defect repair due to their superior biological properties. For example, synthetic hydroxyapatite (HAp), β-tricalcium phosphate (β-TCP), and their composites have been widely used in orthopedic reconstructive surgeries due to their similar composition to normal bone.[160] Polycaprolactone (PCL) scaffolds regulate cell proliferation and differentiation by promoting cellular senescence, cell cycle, and deoxyribonucleic acid replication pathways, accelerating osteogenesis, and healing tissue formation within cartilage. Bioceramic (e.g., β-TCP) scaffolds specifically enhance osteoclast differentiation and extracellular fluid pathway gene expression, promoting osteoclast differentiation and bone remodeling. During these processes, specific biomaterial properties can be used to direct cell behavior and regulate molecular networks in the symbiotic microenvironment, thus minimizing the existing regeneration and repair barriers.[161]

In recent years, efforts have been made to combine methacrylate-based hydrogels with biologically active and functionalized nanomaterials to enhance the physicochemical and biological properties of methacrylate-based hydrogels (Figure 5B). Currently, the mainstream application is to print 3D scaffolds with high mechanical properties, utilizing the aforementioned nanomaterials, and then apply surface coating[162] or fill the interior with[163] methacrylamide hydrogels. The benefits of this approach are as follows:

(i) Enhanced mechanical properties.[164,165]

(ii) Modulation of viscoelastic properties to allow 3D printing of bioinks.

(iii) Presentation of electro/magnetic properties to produce electro/magnetically active hydrogels for the repair of specific tissues (e.g., muscles, nerves). In particular, MXene exhibits a robust photothermal and sterile effect under infrared irradiation. In addition, GelMA/β-TCP/sodium alginate (Sr2+)/MXene (Ti3C2) (GTAM) scaffolds constructed in

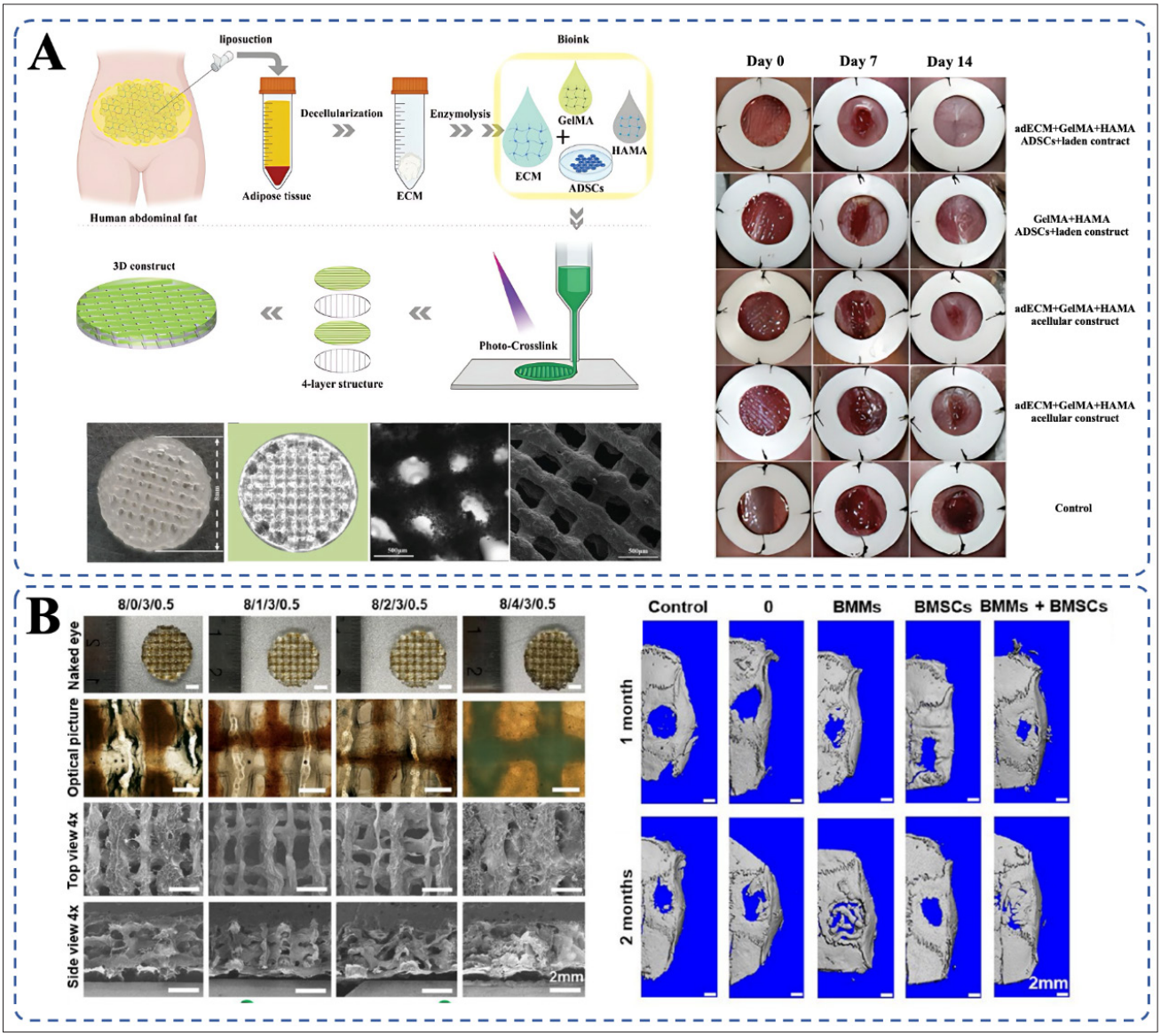

Figure 5. The application of bioink composed of GelMA and HAMA in wound healing and bone repair. (A) The adECM-GelMA-HAMA 3D-printed scaffold loaded with ADSCs can accelerate wound healing. Adapted with permission from Zhang et al.[173] (B) 3D-bioprinted GelMA-HAMA scaffolds encapsulated with rat bone marrow-derived macrophages (BMMs) and bone marrow mesenchymal stem cells (BMSCs) can promote bone repair. Adapted with permission from Yu et al.[174] Abbreviations: adECM, adipose derived extracellular matrix; ADSC, adipose-derived stem cell; GelMA, gelatin methacrylate; HAMA, hyaluronic acrylate methacrylate.

conjunction with GelMA have antimicrobial and osteogenic applications.[166]

(iv) Active delivery of therapeutic molecules, including HAp, MnCO, and desferrioxamine nanoparticles (DFO), to hinder osteoclast differentiation. The Fenton-like reaction between MnCO delivered by GelMA hydrogel and endogenous hydrogen peroxide generated at the implantation site triggers the sustained release of CO and Mn^{2+}. This process significantly reduces inflammatory responses by upregulating the macrophage M2 phenotype. Furthermore, DFO contributes to inflammation reduction by promoting the M2 phenotype of macrophages, thereby synergizing with it to promote vascularization and inhibit osteoclast differentiation.[166]

(v) Therapeutic capabilities, such as antioxidant effects, during tissue repair. 3D-printed GelMA-

g-glutathione scaffolds not only scavenge reactive oxygen species (ROS) by delivering glutathione, but also accelerate bone repair under diabetic conditions by activating the PI3K/Akt signaling pathway to promote osteoblast proliferation and differentiation.[167] Dutta et al. prepared polyphenolic carbon quantum dots (CQDs)-GelMA loaded with antitumor drugs (≈49%), which effectively killed osteosarcoma cells and treated bone defects caused by malignant osteosarcoma.[168]

(vi) Enhanced oxygen transport and erythrocyte development to improve angiogenesis, thereby stimulating tissue regeneration and reconstruction.[169]

(vii) Enhanced osteoblast proliferation and differentiation and mineral salt deposition. Specifically, strontium mesoporous bioactive glass nanoparticles (Sr-MBGNs)-GelMA bioscaffolds release Sr, Ca, and Si ions to enhance osteogenesis, angiogenesis, and immunomodulatory properties. They also regulate ECM reconstruction, promoting cellular adhesion through the activation of lysyl oxidase to form healthy, enzymatically crosslinked collagen, modulate osteoblast differentiation, and mimic biomineralization.[170] By loading and releasing parathyroid hormone (PTH), ultrastructural PCL/GelMA- methacryloylated SF (SilMA) scaffolds can repair bone defects by promoting angiogenesis and osteogenic processes.[171]

(viii) Inhibition of osteoclastogenesis.[172] In addition, more biosimilar-rich spatially distributed bioscaffolds can be constructed using coaxial 3D printing. Ghahri et al. utilized quadruple coaxial extrusion 3D bioprinting with polyethylene glycol as the hollowing agent. The layers mimicked blood vessels, VEGF, and bone, respectively. This approach improved osteoblast differentiation and increased mechanical modulus from 35 to 80 kPa.[164]

4.1.3. Cartilage defect

Due to the complexity of its tissue structure and the absence of blood vessels, nerves, and lymphatic vessels, osteochondral tissue regeneration is challenging.[175] The use of 3D printing enables the construction of a 3D biomimetic structure that mimics cartilage tissue (Figure 6A). By manipulating and adjusting the bioink during the 3D printing process and incorporating diverse cell types, active substances, drugs, and hormone-binding peptides, various induction pathways can be employed. This approach prompts chondrocyte proliferation and facilitates the generation of cartilage material (Figure 6B). Currently, the primary cells incorporated into bioinks consist of chondrocytes from different sources and stem cells with the potential for chondrocyte differentiation. The addition of ECM stroma or MA-based modified ECM stroma to bioink not only enhances its biocompatibility but also promotes chondrocyte maturation. This process can also make the printed 3D structures more viscous and elastic, with enhanced microfinesse[176,177] (Figure 6C). Furthermore, the addition of bioactive factors to bioinks can induce the chemotaxis and differentiation of chondrocyte stem cells. For example, transforming growth factor (TGF)-β1 is a potent chondrogenic cytokine and the most widely utilized biofactor for articular cartilage bioscaffold construction.[178,179] Incorporating platelet-derived growth factor-BB (PDGF-BB), chondro-inducing molecules (e.g., kartogenin [KGN],[175] interleukin [IL]-4,[180] bioglass [BG], and Mn^{2+} [181]), hormones,[182] drugs, and exosomes[183] to bioinks enables their continuous delivery through hydrogel constructs. These additions exert anti-inflammatory effects, contributing to the treatment of arthritic cartilage defects. Moreover, bioinks can carry various bioactive substances, such as platelet-rich plasma (PRP). A PRP-GelMA hydrogel was reported to be involved in macrophage immunomodulation and M1-M2 conversion, showcasing excellent properties for cartilage and subchondral bone repair.[184,185]

Methacrylic compounds provide robust crosslinking and mechanical properties for the construction of cartilage scaffolds with good biocompatibility. Methacryloyl anhydride-based compounds can be constructed with good fineness, fidelity, and biocompatibility for cartilage tissues, including ear and nasal cartilages,[51,76,176] providing a novel source of biostructures for otoplasty and rhinoplasty, which typically use rib cartilage. The most significant challenge in this process is to ensure the good mechanical properties of the bioscaffold. Cartilage is structurally composed of several regions (superficial, transitional, intermediate, and calcified) from superficial to deep. The compression modulus of the layers in a gradient scaffold increases gradually from the topmost layer 3 to the bottom layer 1, forming a gradient structure. The compressive modulus of the superficial and deeper layers is 1–7 MPa, and articular cartilage should ideally have a compressive modulus of 10 MPa.[186] To mimic the realistic structure of cartilage, a layered printing approach is often employed in studies. The bottom layer is simulated using a bioink with good mechanical properties, whereas the middle or top layer utilizes an ink with similar characteristics (cell recruitment and differentiation-inducing biofactors).[187,188] Alternatively, bioinks with anti-inflammatory properties, such as HAMA, can be directly applied.[189]

Currently, the main bioinks utilized are based on GelMA and HAMA; the addition of HAMA to GelMA improves cartilage formation compared with GelMA alone

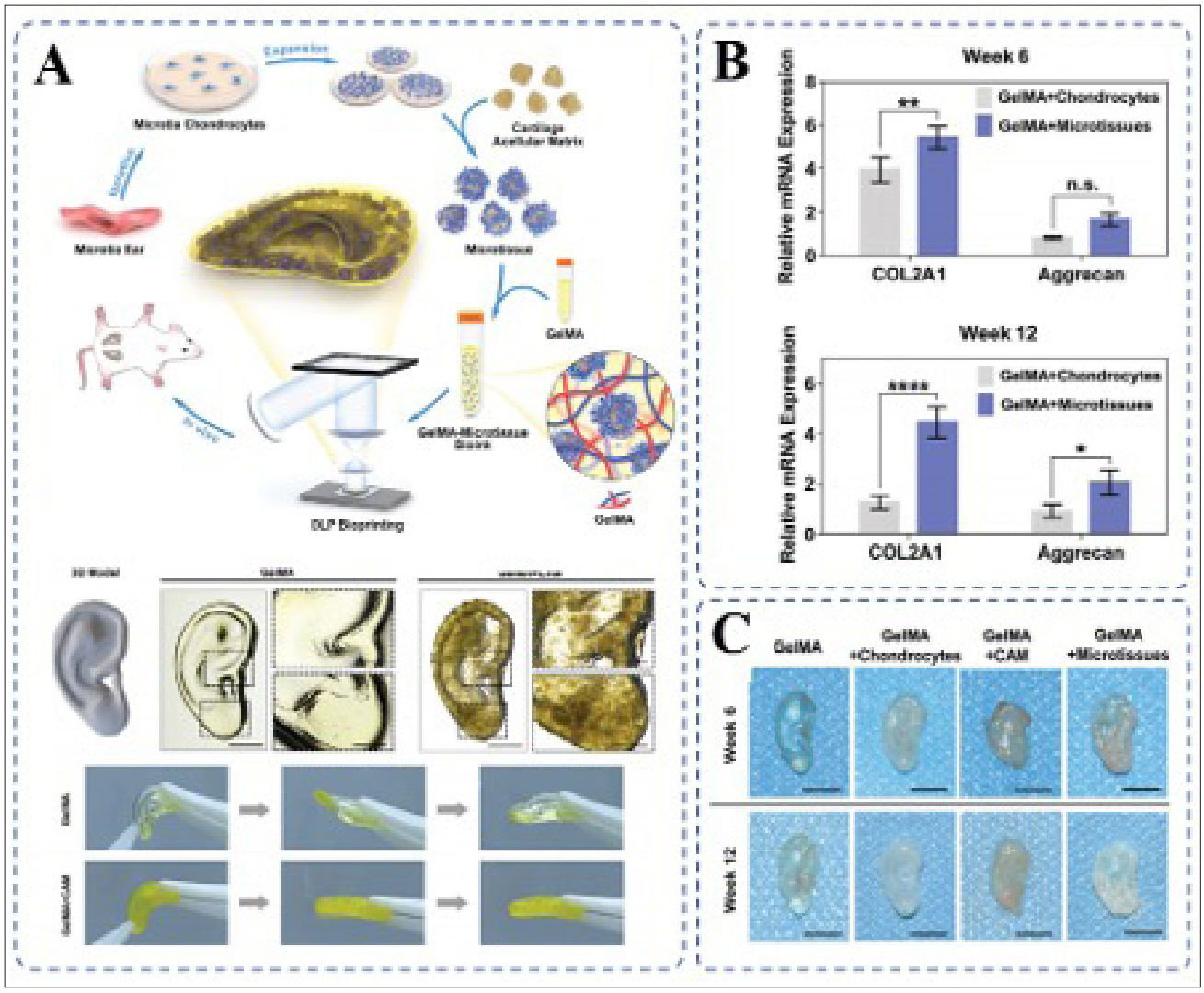

Figure 6. GelMA can be used as bioink to print ear-shape 3D scaffolds with good performance. (A) The bioink was prepared by mixing microtia chondrocytes and cartilage acellular matrix (CAM) with GelMA solution, printed to the auricular shape by a DLP-based 3D bioprinter. The printed auricular scaffold displayed flexibility. (B) The mRNA expression analysis of chondrocytes in auricular constructs at weeks 6 and 12 revealed good biocompatibility of the 3D-printed scaffolds. (C) Images of *in vivo* constructs at weeks 6 and 12 demonstrate the stability of the 3D-printed scaffolds. Adapted with permission from Xie et al.[176] Abbreviations: DLP, digital light processing; GelMA, gelatin methacrylate.

(15%).[190] However, their physical and biological properties need improvement, which is often achieved by blending the hydrogel with other more durable, less hydrophilic polymers.[191] Research suggests that the addition of polyesters (PCL,[76] PEDGA,[178,186,192] poly(propyleneglycolide)-glycolide[193]), bacterial nanocellulose (BNC), and HAp[187,188] to the original methacryloyl anhydride-based hydrogels increase the mechanical strength to better simulate the complex structure of osteochondral tissue. Furthermore, Xia et al. utilized GelMA with HAMA to develop a lyophilized hydrogel preparation method, which further increased the mechanical strength of 3D-printed hydrogels and reduced their degradation rate to match cartilage regeneration.[194]

Moreover, Wang et al. utilized electrostatically spun polylactic acid (PLA) staple fibers, ammonolyzed them to generate PLA crushed microfibers, and incorporated them into oxidized Alg and GelMA bioinks. The inclusion of polylactic acid (PLA) staple fibers improved printing fidelity and resulted in structures with higher mechanical strength. By optimizing the bioink composition, constructs with a compressive stress of approximately 150 kPa were obtained even after 100 cycles of compressive loading (up to 40% strain). This mechanically enhanced

sodium Alg/gel dual network bioink demonstrated good biocompatibility and supported *in vitro* BMSC cartilage formation.[195] These findings suggested that this method is capable of printing engineered grafts with irregular sizes and mechanical properties similar to cartilage, making it a promising approach for functional tissue regeneration.

4.1.4. Skeletal muscle defects

The muscle is one of the few organs that maintains the lifelong ability to regenerate. However, when a large portion of muscle mass is lost due to trauma, disease, or surgical ablation, the natural regenerative capacity of the muscle is overwhelmed. Conversely, when skeletal muscle heals excessively, active fibrosis can lead to volumetric muscle loss, resulting in scar tissue formation. The primary goal of tissue engineering for skeletal muscle repair is to promote myocyte survival and alignment and functional reconstruction of myofibers. Currently, the most utilized hydrogel for tissue engineering reconstruction of skeletal muscle defects is GelMA, followed by AlgMA[196] and SilMA.[197] Using 3D-printing technology, cell-containing GelMA constructs were processed with a functional nozzle featuring topographical cues and an optic-fiber-assisted bioprinting process, which induced the uniaxial alignment of C2C12 and human ASCs. A significantly higher degree of cellular alignment and myogenic activity was observed in cell-loaded GelMA structures compared with cellular constructs printed using conventional crosslinking methods.[198] The GelMA constructs were printed in a light-responsive hydrogel. In addition, by adding iron oxide to the photo-responsive hydrogel, the cells in the hydrogel were mechanically stretched in a 3D manner using a magnetic bioreactor to ensure that cell differentiation could mimic the 3D human environment. The magnetic bioreactor system promoted the differentiation of mouse adult myoblasts in the hydrogel by increasing the diameter and length of myotubes.[197] By incorporating gold nanoparticles (AuNPs)/2D transition metal carbides (MXene nanosheets), which led to an increase in the electrical conductivity of GelMA (up to 0.8 ± 0.07 and 0.9 ± 0.12 S/m, respectively), an enhancement in the differentiation ability of encapsulated adult myoblasts was observed that enabled the printing of a highly viable (97%) stable construct.[199]

4.1.5. Spinal cord repair

Due to the poor self-regeneration ability of damaged neurons, no effective treatments are currently available for neurological impairments. With the in-depth development of stem cell therapy, NSCs, with their self-renewal ability and potential to differentiate into various neural cells, have become ideal candidates for spinal cord injury repair. Bioengineered spinal cord-like scaffolds with microchannel structures are prepared using 3D bioprinting technology. Different types of neural progenitor cells are precisely placed in the scaffolds, which can promote the regeneration and functional reconstruction of the spinal cord. In addition to low cell survival, transplanted NSCs often tend to differentiate into glial cells rather than neurons in the complex pathological microenvironment of spinal cord injury, which is another major cause of nerve regeneration failure.[200] Therefore, a substantial increase in the survival rate and neuronal differentiation of transplanted NSCs is necessary for the effective treatment of spinal cord injury.

Many bioscaffolds have been investigated for therapeutic effects using a wide range of nerve injury models. These bioscaffolds are neuroprotective, promote repair, reduce injury volume, and improve functional recovery in animal models; however, many challenges remain before they can be routinely applied in clinical practice. One of the most pressing challenges is the fabrication of 3D scaffolds capable of maintaining the survival and guiding the proliferation, functional differentiation, and transplantation of replacement or supportive cells.[201] OSMI-4, acrylic β-cyclodextrin (Ac-β-CD), and GelMA bioscaffolds constructed using GelMA significantly enhanced intrinsic neuronal differentiation of neural stem cells by inhibiting Notch signaling through sustained delivery of OsMI-4. This promoted neuronal regeneration and axon growth in a spinal cord injury rat model, leading to significant motor recovery.[202] PCL-GelMA-Alg builds EBs that give rise to neural progenitor cells, which are responsive to morphogenic factors and can differentiate into different neuronal identities. PCL scaffolds constructed using 3D printing technology displayed a regular tubular structure consisting of two concentric cylinders in micro-computed tomography (μCT) images. To enable the availability of oxygen and nutrients for the cells within the hydrogel cylinder supply, the internal PCL cylinder was printed as a macroporous structure. Macropores were generated on the cylinder surface by printing specific patterns of discontinuous and continuous PCL layers, with the well-organized biopores promoting cell migration, adhesion, and proliferation.[203]

4.1.6. Respiratory system

Tissue engineering for the heart has focused on myocardial tissue and heart valves, and to a lesser extent on coronary arteries.[204] The myocardial layer of the heart is a complex 3D laminar myofibrillar tissue containing multiple cardiomyocytes and collagen fibers that gradually shift in the direction of their transmural depth, contributing to the unique cardiac biomechanical behavior. Ischemic damage to the myocardium leads to cardiomyocyte death, with the limited regenerative capacity of cardiomyocytes resulting in scar tissue formation. Cardiac scar tissue, once formed,

persists for a lifetime, reducing the pumping ability of the heart and increasing stress on the remaining myocardium. 3D printing with MA-based compounds aims to create a cardiac patch or mesh tissue with specific mechanical strength, electrical conductivity, and the ability to support cardiomyocytes, human cardiac progenitor cells, and human-induced multifunctional stem cells.[205,206] Currently, two main methods for increasing and maintaining cell viability exist; one is the simultaneous use of biocompatible substances, such as ECM[205] and methacryloyl-substituted recombinant human parasomatic elastin (MeTro),[207] and methacryloyl anhydride-based compounds in one bioink.

Moreover, the oxygen concentration of hydrogels can be enhanced through low-intensity pulsed ultrasound (LIPUS) irradiation, effectively increasing hydrogel permeability and facilitating substance exchange in a non-invasive manner. Ultrasound-controlled release of oxygen, achieved through LIPUS, reportedly improved the viability of transplanted cells and expedited the repair of infarcted tissues.[207,208] In 3D structures created from microsphere tissues using calcium peroxide and IL-10-containing GelMA, microspheres could sustain oxygen availability to support cell viability in hypoxic environments for at least five days, concurrently modulating the macrophage M2 phenotype to exert an anti-inflammatory effect (Figure 7).[209] Functional tissue-engineered heart valves have

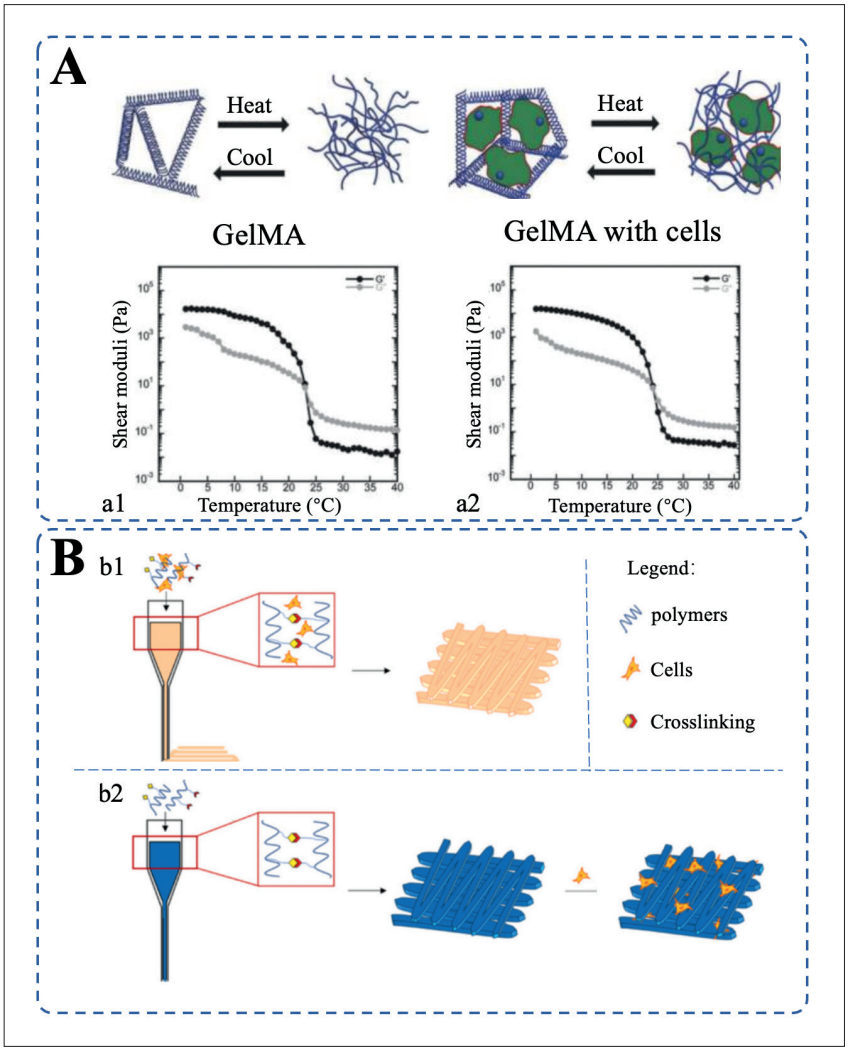

Figure 7. XXX. (A) A 3D-bioprinted scaffold printed from a silk-based bioink comprising non-mulberry silk fibroin (nSF), polyethylene glycol dimethacrylate (PEGDMA), gelatin methacrylate (GelMA), and carbon nanotubes (CNTs). (B) DNA content quantification and live dead assay of human umbilical vein endothelial cell (HUVECs) survival. (C) Beating signal of neonatal rat cardiomyocytes on the 3D-bioprinted scaffold. (D) *In vivo* immune-compatibility assessment of conductive 3D-printed constructs indicates the presence of macrophages and the formation of new blood vessels in the implants. Adapted with permission from Mehrotra et al.[209] Abbreviations: CPO, calcium peroxide; HRP, horseradish; HT, host tissue; IC, implanted construct.

been an elusive goal for approximately 30 years. Among the ongoing challenges is the requirement that engineered valve leaflets have nonlinear elastic tissue biomechanical properties, support a quiescent fibroblast phenotype, and resist calcification.[210] Scaffolds constructed using PCL-MAA with GelMA and polyethylene glycol diacrylate not only withstood the flow and pressure conditions of the aortic valve but also maintained and promoted cell viability in the spongiosum/ventricular layer and increased type I collagen production.[211] These results are summarized in Table 3. Notably, cells cultured on TEMPO-modified nanocrystalline cellulose (mNCC)-GelMA scaffolds demonstrated resistance to calcification.[210]

4.1.7. Pancreas

3D liver bioprinting is a promising technique for creating 3D liver models that can be used for *in vitro* drug testing, hepatotoxicity studies, and transplantation. Several 3D-printed MA-based bioinks, such as incorporating hepatocytes, primary human hepatocytes, and hepatic stellate cells utilizing ColMA\thioHA, have been utilized in liver tissue engineering; these bioinks maintain cell viability for more than 2 weeks and can respond to appropriate drug (acetaminophen) treatment.[212] Moreover, bioinks utilizing GelMA and antioxidant mixtures of vitamin C and vitamin E demonstrated improved cell–cell interactions and liver-specific functions, such as albumin and urea secretion, which were increased by 5- and 2.5-folds, respectively.[213] By utilizing GelMA with liver decellularized ECM (dECM) via DLP, a novel liver microtissue with an endodentate structure was constructed to achieve a larger body surface area for improved recovery of liver functions.[214] In 3D structures printed with bioinks constructed using Alg (1%), cellulose nanocrystals (CNC) (3%), and GelMA (5%), a clear cell migration was observed: fibroblasts colonized the hard 135ACG matrix and aligned themselves at the 135ACG/GelMA border due to chemotaxis, whereas HepG2 only formed spheres in the soft GelMA matrix.[215]

4.2. Bioactive factor loading

By loading hydrogels with various bioactive factors, not only the functionality of the scaffold can be increased, but also the acting time of these substances can be prolonged. These bioactive factors are summarized in Table 4.

4.2.1. Growth factors

Cytokines are a class of small or low-molecular-weight proteins that transmit information between cells and exert immunoregulatory and effector functions. Their levels in the body are low; as they are stimulants (immunogens, mitogens, or other), they can induce cells to produce low-molecular-weight soluble proteins (polypeptides), which can regulate intrinsic and adaptive immunity, promote the generation and growth of blood cells, and repair damaged tissues among other functions. Cytokines can be divided into IL, interferons, tumor necrosis factor, colony-stimulating factor, growth factors, and chemotactic cytokines.

Adding growth factors to 3D-printed hydrogel scaffolds, either by mixing them in bioink or adhering them to the surface of the final scaffolds, can promote cell growth and migration. For instance, GelMA combined with VEGF reportedly promoted wound healing, collagen deposition, and angiogenesis.[216] The addition of epidermal growth factor (EGF) to GelMA-SilMA promoted wound healing in the epidermis and dermis and enhanced the proliferation of keratinocytes and fibroblasts.[273] The addition of insulin-like growth factor-I (IGF-1) to GelMA promoted myoblast alignment and differentiation into myotubes, with the synthesized microfluidic-assisted polymer particles exhibiting successful adsorption and sustained release of IGF-1 at physiological pH for at least 21 days.[274] Regarding TGFs, the sustained release of TGF-β1[219] and TGF-β3[175] from the scaffold successfully directed the migration and differentiation of endogenous stem/progenitor cells. Short peptide cell regulatory protein-10, a TGF-β1 analog, along with KGN, promotes endogenous stem/progenitor cell migration and differentiation by upregulating the expression of RUNX1 and SOX9 at both the mRNA and protein levels.[275] IL-4[276] and IL-10[209] exert their functions in 3D-printed scaffolds primarily by modulating inflammatory responses, while also mediating the conversion of macrophages from a proinflammatory M1 phenotype to an anti-inflammatory M2 phenotype for immunomodulation.

4.2.2. Drug delivery

The physical properties of hydrogels are favorable for drug delivery, as they enable the sustained release of encapsulated drugs. Hydrogels are capable of maintaining high localized drug concentrations over long periods of time through appropriate release mechanisms, which can be based on diffusion, swelling, chemical, or other environmental stimuli. The macrostructure, microstructure (e.g., porosity), and degree of polymer crosslinking of a hydrogel affect its lattice pore size, while the hydrodynamic diameter and number of lattices in a hydrogel affect the degree of drug movement. The mechanism of drug release from hydrogels is ultimately regulated by the grid size. A drug with a smaller relative grid size can diffuse rapidly through the hydrogel, resulting in a shorter drug release time. When the size of the drug is close to the grid size, the drug release slows down significantly; when it is larger than the grid size, the drug is physically encapsulated in the grid. Constructing hydrogel scaffolds through 3D printing not only enables the precise control of scaffold dimensions and

Table 3. Application of 3D-printed methacrylic anhydride (MA) hydrogel in tissue engineering

Tissue type	MA-based biomaterials	Biological factor	3D printing method	Light curing parameters	Animal models	Effects	Ref.
Skin	GelMA	HdFs	Extrusion 3D printing	405 nm UV light for 3 min	-	Promotes the activity of healthy fibroblasts; inhibits myofibroblast activation to accelerate healing and reduce scar regeneration	[157]
	GelMA, HAMA, adECM	ADSCs	Extrusion 3D printing	405 nm UV light for 3–5 s	Mouse total skin excision model	Promotes faster neoangiogenesis, collagen production, and remodeling to accelerate wound healing	[173]
	GelMA	Epi-SCs	Extrusion, robot-assisted *in situ* printing	405 nm UV light for 10–30 s	Mouse total skin excision model	Supports SKP proliferation and maintains their properties; promotes wound healing and functional tissue skin regeneration	[158]
	GelMA, ADM	Fibroblasts, HUVECs	Extrusion 3D printing	Blue light for 30 s	Mouse total skin excision model	Promotes cell viability and proliferation and supports *in vitro* epidermal reconstruction	[159]
	GelMA	VEGF	Extrusion 3D printing	365 nm UV light for 5 min	Porcine skin wound model	Promotes wound healing, collagen deposition, and angiogenesis	[216]
Cartilage	GelMA	PRP	DLP	405 nm visible light at 30 mW/cm^2 for 30 s	Rabbit cartilage defect model	Promotes migration, osteogenic, and chondrogenic differentiation of bone marrow MSCs	[184]
	GelMA	ECM, MSCs, exosomes	DLP	405 nm visible light at 11 mW/cm^2 for 30 s	Rabbit cartilage defect model	Repairs chondrocyte mitochondrial dysfunction; enhances chondrocyte migration	[183]
	GelMA, ACMMA	dECM, auricular chondrocytes	Extrusion 3D printing	405 nm UV light at 20 mW/cm^2 for 10 s	Subcutaneous transplantation in nude mice	Microporous lugs with precise shapes and satisfactory mechanical strength	[51]
	GelMA, HAMA	Meniscus ECMMA MECM, PDGF-BB, KGN	Extrusion 3D printing	405 nm blue light at 90 mW/cm^2 for 30 s	Medial meniscus defect model in rabbit knee joint	Promotes chondrocyte migration and differentiation	[175]
	GelMA, HAMA	Chondrocytes	DLP	385–405 nm blue light for 30 s	-	Promotes chondrocyte differentiation	[217]
	GelMA, alginate	Chondrocytes	Extrusion 3D printing	-	Subcutaneous transplantation in nude mice	Promotes sustained release of nutrients and medications	[218]
	GelMA-PLA SFs, OMA	BMSCs	Extrusion 3D printing	365 nm UV light at 10 mW/cm^2 for 1 min	-	Printed structures have high mechanical strength and good biocompatibility	[195]
	GelMA, alginate	TGF-β1, chondrocytes	Extrusion 3D printing	365 nm UV light at 7 mW/cm^2 for 15 s	Subcutaneous transplantation in nude mice	Promotes chondrocyte differentiation into cartilage	[218]

(Continue...)

Table 3. Continue...

Tissue type	MA-based biomaterials	Biological factor	3D printing method	Light curing parameters	Animal models	Effects	Ref.
Cartilage	GelMA, CAM	Microtia chondrocytes	DLP	365 nm UV light at 14 mW/cm^2 for 35 s	Subcutaneous transplantation in nude mice	Auricular structures with high elasticity, high printing precision, and low swelling rate	[176]
	PACG, GelMA	Mn^{2+}, BG	Inkjet printing	-	Rat cartilage defect model	Promotes cell attachment and spreading; enhances gene expression for chondrocyte- and osteogenic-related differentiation of human bone marrow stem cells	[181]
	GelMA, HAMA, ChSMA	TGF-β1, synovial-derived MSCs	Extrusion 3D printing	405 nm blue light for 60 s	Rat model of patellar notch osteochondral defects	With good shape fidelity, it improves the biological properties and cartilage formation of synovial-derived MSCs	[219]
	GelMA	BNC	Extrusion 3D printing	405 nm UV source at 30 mW/cm^2 for 10 s	Subcutaneous transplantation in nude mice	Facilitates the secretion of GAG from regenerated cartilage; improves biomechanical properties.	[219]
	GelMA	PRP, adipose tissue-derived MSCs	Extrusion 3D printing	300–500 nm UV light at 200 mW/cm^2	-	Increases glycosaminoglycan and calcium content, mineralization, and ECM production; promotes *in vitro* osteochondral tissue formation	[185]
	GelMA	Chondrocytes	Extrusion 3D printing	405 nm UV light for 90 s	-	Promotes human chondrocyte proliferation and expression of markers related to chondrogenesis	[220]
	GelMA, PEGMA	BMSCs	Extrusion 3D printing	-	-	Supports the development of more fibrocartilage-like tissue	[221]
	GelMA, PEGDA, ChSMA	BMSCs	Extrusion 3D printing	405 nm blue light at 30 mW/cm^2 for 30 s	-	Promotes differentiation, proliferation, and extracellular mesenchymal production of bone marrow MSCs	[193]
	GelMA, PCL	Chondrocytes	Extrusion 3D printing	UV light for 20 s	-	Construction of new cartilage with mechanical properties similar to nasal cartilage	[76]
	GelMA, PEGDA, RNTK	ADSCs	DLP	355 nm UV light	-	Promotes cell growth, differentiation, and proliferation; promotes collagen II, glycosaminoglycan, and total collagen synthesis	[192]
	GelMA	ADSCs, aptamer HM69 and TGF-β3	Extrusion 3D printing	-	Rabbit femoral synovial osteochondral defect model	Recruited MSCs promote cell adhesion and proliferation, and cartilage formation	[222]

(Continue...)

Table 3. Continue...

Tissue type	MA-based biomaterials	Biological factor	3D printing method	Light curing parameters	Animal models	Effects	Ref.
Cartilage	GelMA, HAMA	Chondrocytes	Extrusion 3D printing	405 nm UV light at 30 mW /cm^2 for 4 s	Subcutaneous transplantation in nude mice	Lyophilization further improved the mechanical strength of the 3D-printed hydrogel and reduced its degradation rate	[194]
	GelMA	Human BMSCs	Extrusion 3D printing	365 nm UV light at 200 mW/cm^2 for 60 s	-	Microspheres are capable of randomly assembling into large tissues, which form dense large tissues after 72 h of incubation	[223]
	GelMA, HAMA	Human chondrocytes	Extrusion 3D printing	405 nm UV light at 300 mW/cm^2	-	Addition of HAMA to GelMA improves cartilage formation over GelMA alone (15%)	[223]
	GelMA	MSCs, TGF-β1 binding peptide, Hap	Extrusion 3D printing	-	Osteochondral defect model of rat femoral talus	Promotes chondrogenesis; induces cartilage (repair and formation) better without triggering significant inflammatory responses	[187]
	GelMA, alginate	Chondrocytes,	DLP	365 nm UV light for 120 s	-	Improves the scaffolds' mechanical properties	[186]
	Functionalized alginate, GelMA	BMSCs	Extrusion 3D printing	365 nm UV light at 5 mW/cm^2 for 15 min	-	Promoted robust cartilage formation; increases stiffness while maintaining elasticity and toughness	[224]
	GelMA-PEGDA	MSCs	DLP	-	-	Promotes the differentiation of embedded MSCs to chondrocytes	[178]
	GelMA	-	Extrusion 3D printing	UV light at 0.09 mW/cm^2 for 1 min	Chinchilla ear tympanic membrane defect model	Promotes cell invasion and proliferation	[225]
	GelMA	$CaCO_3$ granules, TGFβ1, human meniscal chondrocytes	DLP	UV light at 50 mW/cm^2 for 8 s	Longitudinal tears in human meniscus slices	Produces an organized cellular arrangement that promotes meniscus-like tissue formation	[179]
	GelMA, SFMA	PTH, Acs articular chondrocytes, BMSCs	Extrusion 3D printing	405 nm blue light for 10 s	Rabbit osteoarticular defect model	Inhibition of chondrocyte hypertrophy favors hyaline chondrocyte ECMMA production	[182]
	SilMA	Human chondrocytes	DLP	365 nm UV light for 5 s	Subcutaneous transplantation in nude mice	Ensures cell viability; promotes proliferation and differentiation	[226]

(Continue...)

Table 3. Continue...

Tissue type	MA-based biomaterials	Biological factor	3D printing method	Light curing parameters	Animal models	Effects	Ref.
Cartilage	SilMA, PEGDA	Porcine chondrocytes	Extrusion 3D printing	405 nm blue light at 1000 mW for 20 s	-	Expression of collagen II and aggregated proteoglycans is consistent with the formation of cartilage tissue	[227]
	HAMA, PCL	BMSCs	Extrusion 3D printing	-	Medial meniscectomy-induced osteoarthritis animal model	BMSCs in scaffolds survive and proliferate; BMSC-loaded brace significantly improved the joint function of the injured lower leg	[189]
	ECMMA	Rabbit ear chondrocyte	Extrusion 3D printing	UV light at 200 mW/cm^2 for 2 min	-	Promotes cell proliferation and generation of cartilage tissue	[228]
	AlgMA, PCL	BMSCs	Extrusion 3D printing	405 nm blue light for 30 s	-	Good cell survival, proliferation, morphology, type II collagen deposition, and differentiation into cartilage	[229]
	ChsMA	Chondrocytes	Extrusion 3D printing	UV light at 103 mW/cm^2 for 3 s	-	Promotes cell proliferation	[230]
	HAMA	-	Robot-assisted in-situ printing	-	Rabbit talipes cartilage defect model	Bioink can properly fill the defective area and repair cartilage damage after 12 weeks	[231]
	HAMA, ChsMA	Bovine chondrocytes	Extrusion 3D printing	365 nm UV light at 6.09 mW/cm^2 for 10 s	-	Promotes cell proliferation	[232]
Bone	PLA, HAp, GelMA	MnCO, deferoxamine NPs	FDM	365 nm UV light for 5.5 h	Rat femoral defect model	Scaffold with strong immunomodulation and angiogenesis, weak osteoclastogenesis, and superior osteogenic capacity	[233]
	GelMA, HA	Rat BMSCs, β-TCP, Sr^{2+}, MXene	Extrusion 3D printing	405 nm UV light	Chronic osteomyelitis model of rat jawbone	Promotes infection healing and bone regeneration	[166]
	GelMA, HAMA	BMMs, BMSCs	Extrusion 3D printing	405 nm blue light at 0.5 W/cm^2	Rat cranial defect model	Promotes M2-type polarization of macrophages in the microenvironment of early bone defects and further promotes bone repair	[174]
	GelMA, PEGDA, Fullon f 127 bis-acrylate F127DA	Mouse embryonic osteoblast precursor cells, rabbit BMSCs	DLP	405 nm blue light at 20 mW/cm^2 for 4 s	Rabbit femoral condylar defect model	Effective promotion of osteogenic differentiation of BMSCs	[234]
	GelMA	Rabbit BMSCs	Extrusion 3D printing	UV light at 365 nm	/	Promotes cell growth to support and effectively maintain the osteogenic process	[235]

(Continue...)

doi: 10.36922/ijb.4650

Table 3. Continue...

Tissue type	MA-based biomaterials	Biological factor	3D printing method	Light curing parameters	Animal models	Effects	Ref.
Bone	GelMA	DFO	Extrusion 3D printing	405 nm blue light for 120 s	Rat cranial defect model	Significantly promotes endothelial cell migration and tube formation, mineralized matrix deposition, and ALP expression in osteoblasts	[236]
	GelMA/PCL	BMSC ST2	FDM	405 nm blue light for 5 s	Rat cranial defect model	Promotes cell proliferation, osteogenic differentiation, and mineralization of ST2 in *in vitro* scaffold, enhancing angiogenesis and osteogenesis	[237]
	Ti-6Al-4V alloy, GelMA	BMSCs	SLS	UV light at 7.1 mW/cm^2 for 80 s	Rabbit radial bone defect model	Promotes osteogenesis and angiogenesis	[163]
	Graphene, GelMA	BMSCs	Extrusion 3D printing	405 nm blue light for 60 s	Subcutaneous transplantation in nude mice	Promotes synergistic regeneration of nerves and bone	[238]
	GelMA, PEGDA, poly aluminum silicate	HUVECs	Extrusion 3D printing	-	Rat cranial defect model	Promotes angiogenesis and osteogenesis	[239]
	GelMA	Graphene oxide, MSCs	Extrusion 3D printing	UV light for 30 s	-	Enhances cell proliferation and adhesion, and osteogenic differentiation properties	[240]
	PLA, GelMA	MSCs	FDM	-	-	Promotes osteoblast differentiation	[241]
	nHAp, GelMA	BMSCs	Extrusion 3D printing	405 nm	Subcutaneous grafting in nude mice/rabbit cranial defect model	Initiates early osteogenesis and angiogenesis by recruiting endogenous stem cells *in situ*	[242]
	Alginate, C3S, GelMA	MSCs	Extrusion 3D printing	365 nm irradiation for 4 min	-	Promotes cell adhesion, spreading, proliferation, and osteogenic differentiation while possessing good mechanical qualities	[162]
	GelMA	MC3T3-E1, glutathione	Extrusion 3D printing	UV light at 405 nm for 30 s	Rat cranial defect model	Clears ROS; promotes osteoblast proliferation and differentiation for bone repair in diabetes	[167]
	GelMA, HAp	BMSCs	Extrusion 3D printing	410 nm blue light for 1 min	Rabbit cranial defect	Promotes BMSC migration, proliferation, and osteogenic differentiation *in vitro*; promotes targeted migration of endogenous stem cells, early osteogenesis, and angiogenesis	[243]

(Continue...)

doi: 10.36922/ijb.4650

Table 3. Continue...

Tissue type	MA-based biomaterials	Biological factor	3D printing method	Light curing parameters	Animal models	Effects	Ref.
Bone	PL/GelMA/BCP	HUVECs	DLP	UV light at 405 nm for 30 s	Subcutaneous implantation on the back of rats	Regulates cell behavior and promotes the formation of vascular-like structures	[169]
	GelMA-HM5, GelMA-HZ5 (Mg/Zn-modified HAp)	-	Extrusion 3D printing	UV light at 360 nm for 5 min	-	Supports the bone	[244]
	GelMA, SilMA, GelDA, graphene oxide	BMSCs	Extrusion 3D printing	UV light at 405 nm for 2 min.	Rat cranial defect model	Effectively promotes osteogenesis *in vitro* and *in vivo*	[245]
	GelMA, Laponite	BMSCs	Extrusion 3D printing	UV light at 100 mW/cm^2 for 5 min.	-	Promotes cell proliferation and osteogenic differentiation	[246]
	GelMA, dECM	DFCs	Extrusion 3D printing	405 nm UV light for 30 s	Rat subcutaneous graft, Beagle mutt alveolar fossa bone defect model	Promotes regeneration of periodontal tissues, especially anchoring structures at the bone–ligament interface	[247]
	GelMA, BP	BP cells	Extrusion 3D printing	405 nm UV light for 1 min	-	Ensures cell migration and colonization	[248]
	Mg-PCL-GelMA	MSCs	FDM	405 nm UV light at 30 mW/cm^2 for 3 min.	-	Enhances osteogenic differentiation of encapsulated MSCs; supports bone ECM deposition; promotes mineralized nodule formation, OCN, and Col I expression	[249]
	Polyphenol CQDs, GelMA	MG-63 cells	Extrusion 3D printing	365 nm	Rat cranial defect model	Promotes angiogenesis, bone regeneration, and anti-tumor	[250]
	Sr-MBGNs, GelMA	BMSCs	Extrusion 3D printing	-	Rat cranial defect model	Releases Sr, Ca, and Si ions to enhance osteogenesis, angiogenesis, and immunomodulatory properties; promotes cell adhesion and regulates osteoblast differentiation	[170]
	MSNcapDex, GelMA	Human BMSCs	Extrusion 3D printing	UV light at 0.86 mW/cm^2 for 5 min	-	Cells survived and exhibited osteogenic differentiation biomarkers	[251]
	Nifedipine-containing alcohol plasmas and tumblestone, sodium alginate, GelMA	BMSCs	Extrusion 3D printing	405 nm	Rat cranial defect model	Promoted osteogenic differentiation and migration of bone marrow MSCs; inhibits osteoclastogenesis *in vitro*	[172]

(Continue...)

doi: 10.36922/ijb.4650

Table 3. Continue...

Tissue type	MA-based biomaterials	Biological factor	3D printing method	Light curing parameters	Animal models	Effects	Ref.
Bone	Gelatin, GelMA, alginate, nHAp	HUVECs and osteoblasts (MC3T3)	Extrusion 3D printing	360–480 nm UV light at 6.9 mW/cm^2 for 40 s	-	Promotes cell growth, angiogenesis, and gene expression	[252]
	GelMA, HAMA	hMSCs, MXene	Extrusion 3D printing	-	-	Promotes spontaneous differentiation of human BMSCs into osteoblasts	[253]
	GelMA, PEGDA	PDLSCs	Extrusion 3D printing	UV light at 2.9 mW/cm^2 for 30 s	Rat alveolar bone defect model	Promotes new bone formation	[254]
	GelMA, sodium alginate, BGM	mBMSCs, BMP2, PDGF	Extrusion 3D printing	365 nm UV light for 30 s	Rat subcutaneous graft, Beagle mutt alveolar fossa bone defect model	Promotes osteogenic differentiation and soft tissue repair.	[255]
	GelMA, nHAP	MC3T3-E1	Extrusion 3D printing	450 nm UV light for 3 min	Mouse cranial defect model	Effective repair of cranial defects and promotion of MC3T3-E1 osteogenic differentiation in mice	[256]
	GelMA, nHAP	MG63 cells, human BMSCs	DLP	440 nm blue light at 8 mW/cm^2 for 1 min	-	Promotes expression of cellular osteogenic genes	[257]
	GelMA, alginate	HUVECS, hBMSCs	Extrusion 3D printing	30 s of UV exposure	-	Induction of osteoblast differentiation and enhancement of mechanical properties	[164]
	LDH-GelMA	Osteoblasts	Extrusion 3D printing	360–480 nm UV light at 6.9 W/cm^2 for 40 s	-	Supports the survival, spreading, and proliferation of encapsulated osteoblasts in the absence of osteoinductive factors utilizing LDH	[165]
	SilMA	MRC5 cells	DLP, pneumatic extrusion	370 nm UV light at 45 W/m^2 for 60 s	-	Supports cell metabolism, adhesion, proliferation, and osteogenic differentiation	[258]
	MeGC	MG-63 cells	Extrusion 3D printing	430–485 nm UV light	-	Promotes cell proliferation and differentiation	[259]
	meHA-HAp-PEEK scaffolds	Human MSCs	FDM	UV light for 5–10 min	-	Promotes MSC adhesion and proliferation; contributes to osteogenic differentiation and extracellular mesenchymal mineralization	[260]
BLI	ColMA, BG	MSCs	Extrusion 3D printing	UV light for 1 min	Rabbit anterior cruciate ligament stripping model	Promotes specific cell differentiation, regeneration of the bone–ligament interface, and functional grafting to osseointegration	[261]

(Continue...)

Table 3. Continue...

Tissue type	MA-based biomaterials	Biological factor	3D printing method	Light curing parameters	Animal models	Effects	Ref.
Medulla spinalis	Ac-β-CD, GelMA	Neural stem cells, OSMI-4	Extrusion 3D printing	405 nm UV light at 0.6 mW/cm^2 for 14 s	Rat whole-sectional SCI model	Enhances intrinsic neuronal differentiation of neural stem cells; promotes neuronal regeneration and axonal growth in spinal cord injury model rats, leading to significant motor recovery	[202]
Medulla spinalis	GelMA	Human amniotic AEC neural-like cells	DLP	-	Rat whole-sectional SCI model	Promotes the recovery of nervous system function and motor function in rats	[262]
	PCL, GelMA, alginate	RA	Extrusion 3D printing	UV light for 1 min	-	Supports neural differentiation and patterning of EBs in response to co-printing with 1 μM RA	[203]
Coronary artery	Carbon nanotubes, ColMA	HCAECs	Extrusion 3D printing	365 nm UV light at 6.1 mW/cm^2	-	Significantly improves viscoelastic behavior and conductivity	[204]
Heart valve	PCL-MAA holder, GelMA/PEGDA	MSCs	FDM	-	-	Maintains and promotes cell viability; increases the production of type I collagen	[211]
	mNCC-GelMA	Human ADMSCs	Extrusion 3D printing	365 nm UV light for 4 min	/	Cells cultured in mNCC-GelMA demonstrate resistance to calcification	[210]
Myocardium	nSF, PEGDMA, GelMA	Cardiomyocyte, IL-10	Extrusion 3D printing	UV light for 60 s	Subcutaneous transplantation in nude mice	Upregulation of mature cardiac biomarkers, sarcomere formation, and heartbeat; regulates macrophage anti-inflammatory M2 phenotype	[209]
	GelMA-PEDOT:PSS	Cardiomyocyte	Extrusion 3D printing	450–550 nm UV light for 80 s	Subcutaneous transplantation in nude mice	Maintains high cytocompatibility and cell-spreading ability	[209]
	GeMA	Human cardiomyocytes, human cardiac fibroblasts	Extrusion 3D printing	UV light for 3–5 min	Rat AMI model	Improves long-term survival, angiogenesis, and stability of AMI rat grafts; reduces fibrosis, increases left ventricular thickness, and enhances cardiac function	[263]
	GelMA, MeTro	Cardiomyocytes	Extrusion 3D printing	405 nm blue light for 3 min	Rat subcutaneous transplantation	Displays endothelial barrier function and spontaneous beating of cardiomyocytes; reduces inflammatory response	[207]
	GelMA	Cardiomyocytes (H9C2s)	Extrusion 3D printing	365 nm UV light	-	Optimizes culture of cardiomyocytes through ERK1/2 and PI3K-Akt signaling pathways in 3D bioprinted cell-loaded GelMA scaffolds	[264]

(Continue...)

Table 3. Continue...

Tissue type	MA-based biomaterials	Biological factor	3D printing method	Light curing parameters	Animal models	Effects	Ref.
Myocardium	GelMA, collagen, fibronectin	Human iPSC-CM	Extrusion 3D printing	-	-	Creation of a pre-vascular pathway with the shape of an anterior interventricular artery within the myocardial structure that maintains cell viability	[265]
	GelMA	ND-Hb	Extrusion 3D printing	405 nm blue light	Rat myocardial infarction model	Improvement of cell viability in ND-Hb patches	[208]
	cECM, GelMA	hCPCs	Extrusion 3D printing	White light for 5 min	Rat AMI model	Promotes cell survival and vascularization	[205]
	PCL-GelMA	Human iPSCs	FDM	-	-	Supports iPSC-CM function in a 14-day culture	[206]
Biliary system	PCL, GelMA	USPIO NPs	FDM	405 nm, 3 W light source for 50 s	-	Protecting and supporting the stent improves the biocompatibility of the printed bile ducts; USPIO NPs dispersed in GelMA were used as a contrast agent for real-time monitoring of lesion repair and bile duct degradation by MRI	[266]
	GelMA	Hepatocytes, fibroblasts	DLP	25 mW/cm^2	-	Maintains >90% cell viability; enhances albumin secretion	[267]
	Alginate, CNC, GelMA	HepG2, NIH/3T3	Extrusion 3D printing	365 nm blue light for 2 min	-	Improves hepatocyte function; increases albumin production	[215]
	GelMA, liver dECM	Hepatocytes (hiHep cells)	DLP	365 nm UV light at 2.25 mW/cm^2	-	Enhances hepatocyte-specific functions and liver function recovery	[214]
	GelMA	Antioxidant mixture of vitamin C and vitamin E, HepG2 cell	Extrusion 3D printing	365 nm UV light for 3–5 min	Rabbit subcutaneous graft	Improves cell–cell interactions and liver-specific functions	[213]
	GelMA	Primary human HCC	Extrusion 3D printing	405 nm UV light at 7 mW/cm^2 for 1 min	Mouse subcutaneous transplantation	Survival for at least 28 days, albumin secretion, and debromoisoquin metabolism	[268]
	ColMA, thio hyaluronic acid	Primary human hepatocytes, hepatic stellate cells	Extrusion 3D printing	-	-	Cells remained active and responded to appropriate medication (acetaminophen) therapy for more than 2 weeks	[212]
Muscle tissue	GelMA, fibrinogen	C2C12 myoblasts	Extrusion 3D printing	365 nm UV light for 15 s	Rat subcutaneous implantation, rat bulk muscle loss model	Promotes cell growth, differentiation, and *in situ* regeneration of functional skeletal muscle	[269]
	GelMA	C2C12 myoblasts	Extrusion 3D printing	821 mJ/cm^2 light for 30 s	Tibialis anterior muscle injury mouse model	Demonstrates significant functional recovery and muscle volume restoration	[270]

(Continue...)

doi: 10.36922/ijb.4650

Table 3. Continue...

Tissue type	MA-based biomaterials	Biological factor	3D printing method	Light curing parameters	Animal models	Effects	Ref.
Muscle tissue	GelMA, collagen, decellularized ECMMA	C2C12, human ASCs	Extrusion 3D printing	20 mW/cm^2 light for 6 s	Mouse tibialis anterior muscle defect injury model	Constructs carrying ASCs significantly induced greater muscle regeneration than cellular constructs without topographical cues	[198]
	GelMA,	Mouse myoblasts (C2C12), MPT of skeletal muscles	Extrusion 3D printing	405 nm UV light	-	Maintains cell survival; cells exhibited a higher degree of cellular alignment	[271]
	SilMA	Mouse myoblasts (C2C12)	DLP	365 nm UV light	-	Promotes the differentiation of mouse adult myoblasts in hydrogels; increases the diameter and length of myotubes	[197]
	GelMA, CMCMA, AlgMA-PEGDA	Mouse myoblasts (C2C12)	Extrusion 3D printing	365 nm UV light at 3 W/cm^2	-	Provides structure and supports the formation and alignment of myotubes	[196]
	GelMA	Mouse myoblasts (C2C12), PEDOT NPs	Extrusion 3D printing	UV light for 2 min	-	Promotes proliferation, migration, and differentiation of C2C12 cells and myofiber formation	[272]
	GelMA	Mouse myoblasts (C2C12), AuNPs/ MXene nanosheets	Extrusion 3D printing	UV light for 4 min	-	Improved electrical and rheological properties led to enhanced differentiation of encapsulated myoblasts and allowed printing of highly viable (97%) stable constructs	[199]

Abbreviations: adECM, adipose derived extracellular matrix; ADSCs, adipose-derived stem cell; ADM, acellular dermal matrix; AlgMA, methacrylated sodium Alg; ALP, alkaline phosphatase; AMI, acute myocardial infarction; BCP, bidirectional calcium phosphate; BG, bioactive glass; BGM, bioactive glass microspheres; BLI, bone–ligament interface; BMMs, bone marrow-derived macrophages; BMSCs, bone marrow mesenchymal stem cells; BNC, bacterial nanocellulose; BP, bone particles; C3S, calcium trisilicate; CAM, cartilage acellular matrix; cECM, chondrocyte extracellular matrix; ChSMA, methacryloylated Chondroitin sulfate; CNC, cellulose nanocrystals; Col I, Collagen I; ColMA, methacrylated collagen; CQD, carbon quantum dot; dECM, decellularized extracellular matrix; DFCs, dental follicle cells; DLP, digital light processing; ECM, extracellular matrix; ECMMA, methacryloylated extracellular matrix; Epi-SCs, epidermal stem cells; FDM, fused deposition modeling; GAG, glycosaminoglycan; GelDA, gelatin-dopamine; GelMA, methacrylated gelatin; HA, hyaluronic acid; HAMA, hyaluronic acrylate methacrylate; Hap, hydroxyapatite; HCAECs, human coronary artery endothelial cells; HCC, hepatocellular carcinoma; hCPCs, human cardiac progenitor cells; HdFs, human skin fibroblasts; HUVECs, human umbilical cord vascular endothelial cells; iPSCs, induced pluripotent stem cells; iPSC-CM, induced pluripotent stem cell-derived cardiomyocytes; KGN, Kartogenin; LDH, layered double hydroxides; MAA, methacrylic acid; MBGN, mesoporous bioactive glass nanoparticle; mBMSCs, mouse bone marrow-derived stromal cells; MeGC, methacrylic acid glycol chitosan; MECM, mesenchymal stem cell-derived extracellular matrix; meHA, hyaluronic acid methacrylate; MeTro, methacryloyl-substituted recombinant human para-somatic elastin; mNCC, TEMPO-modified nanocrystalline cellulose; mNG, mNCC-GelMA; MPT, minimal processing tissue; MRI, magnetic resonance imaging; MSCs, mesenchymal stem cells; MSNCaPDex, mesoporous silica nanoparticles functionalized with calcium, phosphate, and dexamethasone; ND-Hb, hemoglobin wrapped into nanodroplets; nHAP, nanohydroxyapatite; NPs, nanoparticles; nSF, non-mulberry silk fibroin; OCN, osteocalcin; OMA, oxidized methacrylate; PACG, N-acryloyl-2-glycine; PCL, polycaprolactone; PDGF-BB, platelet-derived growth factor-BB; PDLSCs, periodontal membrane stem cells; PEDOT, poly(3,4-ethylenedioxythiophene); PSS, polystyrene sulfonate; PEEK, polyetheretherketone; PEGDA, polyethylene glycol diacrylate; PEGDMA, polyethylene glycol dimethacrylate; PEGMA, poly(ethylene glycol) methacrylate; PL, platelet lysate; PLA, polylactic acid; PRP, platelet-rich plasma; PTH, parathyroid hormone; RA, retinoic acid; RNTK, rosette nanotubes; ROS, reactive oxygen species; SCI, spinal cord injury; SF, silk fibroin; SilMA, methacryloylated SF; SKPs, skin-derived precursors; SLS, selective laser sintering; USPIO, ultrasmall superparamagnetic iron oxide; UV, ultraviolet; VEGF, vascular endothelial growth factor.

doi: 10.36922/ijb.4650

pore sizes to match drug sizes, but also facilitates a targeted drug delivery system for precision therapy.

Hydrogel scaffolds for controlling the release of Mn^{2+}, Sr^{2+}, Si^{4+}, and B^{3+} were constructed using GelMA. A burst release was observed during the first 3 days due to the rapid leakage of ions near the surface. These ions gradually diffused out of the printed porous hydrogel scaffolds over approximately 25 days.[181] Zhang et al.[233] used 3D printing to construct 3D GelMA scaffolds loaded with MnCO, which could trigger a sustained release of CO and Mn^{2+} through a Fenton-like reaction with endogenous hydrogen peroxide produced at the implanted tissue site, thereby significantly reducing the inflammatory response by upregulating the M2 macrophage phenotype. MXenes have a favorable photothermal effect. Under near-infrared light irradiation, they kill both Gram-positive and Gram-negative bacteria and can be used to treat infected bone defects by constructing 3D scaffolds for delivery to infected bones.[166,253] The addition of antitumor cells to these scaffolds can kill tumor cells through targeted transport. Dutta et al. constructed 3D scaffolds that could release antitumor drugs (≈49%) to kill osteosarcoma cells.[168] Vitamins are a class of essential organic compounds that play a critical role in the metabolism of substances. Retinoic acid (RA) promoted the neural differentiation of EBs incorporated in PCL-GelMA-Alg.[203] Additionally, RA exhibited the ability to scavenge intracellular ROS generated during photocrosslinking, a property further enhanced by incorporating an antioxidant mixture of vitamin C and vitamin E into GelMA.[213]

4.2.3. Exosomes

Exosomes are membranous vesicles released into the ECM by intracellular multivesicular bodies fused to the cell membrane. Almost all types of cells can produce and release exosomes. They possess a nanosized lipid inclusion structure with a diameter of 30–100 nm and contain proteins, mRNAs, and microRNAs. Exosomes have been recognized as biomarkers of diagnostic/drug responses or as intercellular communication vectors for transferring biologically active noncoding RNA or proteins between cells. Compared with the use of cells combined with hydrogels, this cell-free treatment avoids immune rejection and loss of cell viability for achieving therapeutic effects.

Several studies have combined exosomes with hydrogels for the treatment of various conditions, such as diabetes, chronic wound healing,[277] regeneration of cartilage defects,[278] and spinal cord repair.[279] However, *in situ* crosslinking is utilized for the generation of most hydrogel constructs, resulting in hydrogels with low porosity. The preparation of scaffolds using physical freeze-drying and crosslinking methods allows for the generation of hydrogel scaffolds with higher porosity, yielding promising results in terms of cellular encapsulation. Emerging technologies, such as 3D printing, enable the synthesis of radically oriented channels that guide cell migration for therapeutic purposes.[280] Two key issues are associated with the 3D printing of scaffolds delivering exosomes using methacryloyl compounds: survival of exosomes (toxicity of photoinitiators and physical extrusion of the printing process can affect exosome survival) and the rate of exosome release (exosomes are characterized by rapid clearance from the bloodstream, limiting the duration of their therapeutic effect). In a study by Born et al., a deliverable MSC-derived GelMA hydrogel scaffold demonstrating anti-inflammatory and pro-angiogenic effects was constructed using an extrusion printer. This study also demonstrated that the initial release rate of exosomes can be controlled by different photoinitiator concentrations and that the bioactivity of MSC extracellular vesicles (EV) in endothelial gap closure assays was retained after bioprinting.[281] In a study by Chen et al., GelMA hydrogel scaffolds loaded with exosomes from ADSCs were constructed using SLA printing and demonstrated effectiveness in repairing mitochondrial dysfunction in chondrocytes, enhancing chondrocyte migration, and polarizing synovial macrophages toward the M2 phenotype, thereby promoting cartilage regeneration.[183] Hu et al. utilized DLP printing to construct a GelMA hydrogel scaffold loaded with exosomes derived from epidermal stem cells of human umbilical cord mesenchymal stem cells (hUC-MSCs-sEVs) and demonstrated that hUC-MSCs-sEVs, by delivering miR-23a-3p, activated the PTEN/AKT signaling pathway, subsequently promoting calcium deposition, endothelial network formation, and osteogenic differentiation.[282]

4.2.4. Bioactive substances

Introducing bioactive tissues into hydrogel scaffolds not only increases the biocompatibility of hydrogels but also increases the bioactive factors and primitive cell colonization in hydrogels. Many bioactive substances can work well combined with cell-active substrates in bioinks. PRP contains a large number of growth factors, such as PDGF, TGF-β, and IGF-1, which play a significant role in maintaining cell activity and inducing differentiation and colonization.[184,283] If bone particles (BPs) are included in GelMA for co-printing, the cells initially contained in BPs can migrate and colonize the bioprinted scaffolds while maintaining their ability to express early osteogenic markers for bone regeneration purposes. Similarly, Tavares-Negrete et al. developed GelMA hydrogels supplemented with minimal processing tissue (MPT) constructs to create dense skeletal muscle-like tissue.[271] Constructs supplemented with MPT also maintained

their 3D integrity for 28 days. In contrast, similar original GelMA constructs only maintained their structure for 14 days or less. C2C12 cells embedded in MPT-supplemented constructs exhibited a higher degree of cellular alignment and achieved significantly higher densities than cells loaded in the original GelMA constructs. Their findings suggested that the addition of MPT contains abundant biochemical and topological cues such as growth factors, glycosaminoglycans, and structurally conserved proteins (e.g., collagen).[271]

4.2.5. Other functional substances

The recruitment of the above functional substances to enable the therapeutic effect can be achieved by loading some other recruiting substances. For example, Yang et al. constructed a 3D-bioprinted bifunctional scaffold made of GelMA and PCL based on the MSC-specific recruitment mediated by the aptamer HM69 and the cellular cartilage formation enhanced by growth factors; this aptamer specifically recognizes and recruits MSCs.[222] Ding et al. revealed that a hydrogel scaffold carrying a bioactive peptide linkage that selectively adsorbs TGF-β1 not only provides cell growth space but also induces endogenous TGF-β1 recruitment to promote cartilage formation.[187]

4.3. Organoids/organ-on-chip

An organ-on-chip is a microfluidic cell culture device created using microchip fabrication methods (Figure 8A). This device incorporates continuous perfusion chambers with multicell layer structures, tissue interfaces, physicochemical microenvironments, and a simulated human vascular circulation. Organ-on-chip have diverse applications, including high-throughput drug screening, drug uptake and metabolism studies, drug development, modeling the human circulatory system, drug toxicology assessments, artificial biomimetic microenvironments, studying intercellular interactions, ECM interactions, and serving as a novel *in vitro* culture platform.

Notably, organ-on-chip addresses the limitations of animal models by offering controlled experimental conditions. Organoids, with their unique advantages in drug absorption, metabolism, and toxicity studies, enable the determination of key pharmacokinetic parameters, such as drug absorption, distribution, metabolism, elimination, and toxicity. This approach allows for rapid screening of various drugs for antitumor effects and assessments of liver and kidney toxicity. Moreover, organ-on-chip offers low sample usage, high throughput, safety, and minimal environmental impact.

In addition, an organoid is a 3D *in vitro* cell culture system that is highly similar to the source tissue or organ *in vivo*. These culture systems can replicate the complex spatial morphology of differentiated tissues and exhibit cell-to-cell and cell-to-surrounding matrix interactions and spatial location patterns. In turn, they are capable of achieving similar physiological responses to differentiated tissues and organs *in vivo*, with a high degree of similarity to the source tissue. Compared with the traditional 2D cell culture model, the 3D cultured organoid contains multiple cell types, breaking through the pure physical contact between cells, forming closer cell-to-cell and cell-to-matrix interactions. These results in the formation of functional "micro-organs" that better simulate organogenesis and physiology, making them valuable in basic research. Moreover, it can be used to better simulate the process of organogenesis and the physiological and pathological state of organs and tissues and thus has a broad application prospect in basic research and clinical diagnosis and treatment.

Furthermore, 3D bioprinting technology can be employed to precisely control cell distribution and differentiation through layered printing, enabling the construction of human organ-like structures with high fidelity. This can expand our knowledge of human development and tissue and organ regeneration mechanisms and promote the application of organ-like and organ chips in tissue biology, disease model construction, toxicology, pharmacology, and personalized medicine.[286] Currently, the use of MA-based compounds has been realized in the liver,[287,288] pancreas,[283] blood vessels,[289] myocardium,[290] atrioventricular nodes,[291] malignant tumors,[292,293] skeletal muscle,[291] bones and joints,[294] and periodontal ligament-alveolar bone (Table 5).[295]

MA-based hydrogels are gradually being used in the 3D printing of biological scaffolds due to their robust biological properties and flexible, tunable properties, with strong potential in organoid construction. Reportedly, structures obtained by 3D printing can provide topographical cues for cell migration, differentiation, and proliferation. Further, dECM and GelMA structures with topographical cues displayed increased gene expression levels by 1.5–1.8 fold,[296] providing cues for gene expression and proliferation.

Van der Valk et al. employed GelMA/HAMA and extrusion 3D printing to construct biomodels that enhance microcalcification by mimicking the mechanical environment of the natural Aortic valve (AV) node.[291] The median Young's modulus of the atrioventricular node midlayer was 37.1, 15.4, and 26.9 kPa for fiber, sponge, and ventricle, respectively. By adjusting the ratio of the bioinks, they observed that the modulus of the fibers and sponges matched that of the 3D 5% GelMA/1% HAMA UV-crosslinked hydrogel. Their study revealed the effective use

Table 4. Application of 3D-printed methacrylic anhydride (MA) hydrogel in active biological factor loading

Active biological factor	MA biomaterials	3D printing	Light curing parameters	Effect	Ref.
Cytokine					
VEGF	GelMA	Extrusion 3D printing	365 nm UV light for 5 min	Promotes wound healing, collagen deposition, and angiogenesis	[216]
EGF	GelMA, SilMA	DLP	365 nm UV light for 4 s at 6.09 mW/cm^2	Enhanced wound healing in the epidermis and dermis with proliferation of keratinocytes and fibroblasts	[273]
IGF-1	GelMA	Extrusion 3D printing	365 nm UV light for 25 s at 180 mW/cm^2	Promotes alignment of myoblasts and differentiation into myotubes	[274]
PDGF-BB, chondro-inducible KGN	GelMA, HAMA	-	-	Promotion of cell migration and synergistic promotion of MSC chondrogenic differentiation	[175]
TGF-β1	GelMA, HAMA, ChsMA	Extrusion 3D printing	405 nm blue light for 60 s	Enhanced the aggregation, proliferation, and differentiation of SMSCs	[219]
TGF-β1 binding peptide	GelMA	Extrusion 3D printing		Promotes the recruitment of TGF-β1, with favorable therapeutic effects	[187]
TGF-β3	GelMA, HAMA	Extrusion 3D printing	405 nm blue light for 60 s	Sustained release of TGF-β3 from scaffolds successfully directs migration and differentiation of endogenous stem/progenitor cells	[219]
IL-4	GelMA, dextrose (PGelDex)	Extrusion 3D printing, handheld, DLP	360–480 nm UV light for 30 s at 10 mW/cm^2	Mediates the conversion of macrophages from a pro-inflammatory M1 phenotype to an anti-inflammatory M2 phenotype for immunomodulation	[276]
IL-10	GelMA, SilMA	Extrusion 3D printing	405 nm UV light for 20 s at 1000 mW	Mediates the conversion of macrophages from pro-inflammatory M1 phenotype to anti-inflammatory M2 phenotype for immunomodulation; cell viability maintained in anoxic environment for at least 5 days	[209]
Therapeutic drugs					
Mn^{2+}, Sr^{2+}, Si^{4+}, B^{3+}	GelMA, PACG	Inkjet	-	Promotes bone regeneration	[181]
MXene	GelMA	Extrusion 3D printing	405 nm UV light for 15 s	MXene has a good photothermal effect and kills both Gram-positive and Gram-negative bacteria under near-infrared light	[166]
DOXH	GelMA	Extrusion 3D printing	400 nm UV light for 2 min	DOXH facilitates diabetic wound regeneration by regulating ROS scavenging and macrophage polarization to the M2 phenotype	[284]
DC	HAMA	Extrusion 3D printing	-	Anti-cancer properties	[189]
Anti-tumor drugs	GelMA	Extrusion 3D printing	365 nm UV light for 60 s	Release of anti-tumor drugs (≈49%), which kill osteosarcoma cells	[168]
RA	GelMA, PCL	Extrusion 3D printing	UV light for 60 s	Induction of neural differentiation in EBs	[203]

(Continue...)

Table 4. Continue...

Active biological factor	MA biomaterials	3D printing	Light curing parameters	Effect	Ref.
Antioxidant mixture of vitamin C and E	GelMA	Extrusion 3D printing	365 nm UV light for 3–5 min	Enhances scavenging of intracellular ROS formed during photocrosslinking	[213]
Exosomes					
HADSC exosomes	GelMA	SLA	405 nm UV light for 30 s at 11 mW/cm^2	Effective repair of chondrocyte mitochondrial dysfunction, enhancement of chondrocyte migration, and polarization of synovial macrophages toward the M2 phenotype	[281]
MSCs exosomes	GelMA	Extrusion 3D printing	UV light at 850 mW/cm^2	Anti-inflammatory and pro-angiogenic	[183]
hUC-MSCs-sEVs	GelMA, nanoclay hydrogel	DLP	365 nm UV light for 2 min	Activates the PTEN/AKT signaling via miR-23a-3p; promotes calcium deposition and endothelial network formation; induces osteogenic differentiation and angiogenesis	[282]
Human MSC exosomes	HAMA	Extrusion 3D printing	-	Improves proliferation, migration, and angiogenic capacity of human fibroblasts and human endothelial cells; enhances expression of markers associated with wound healing	[285]
Nucleic acid					
Fitness HM69	GelMA	Extrusion 3D printing	-	This aptamer specifically recognizes and recruits MSCs, provides a favorable microenvironment for cell adhesion and proliferation, and promotes cartilage formation, improving the repair of total cartilage defects in rabbits	[222]
Bioactive substance					
BP	GelMA	Extrusion 3D printing	-	Cells migrate and colonize the bioprinted scaffold while maintaining their ability to express early osteogenic markers	[248]
MPT of skeletal muscles	GelMA	Extrusion 3D printing	405 nm UV light	MPT contains abundant biochemical and topological clues such as growth factors, GAGs, and structurally conserved proteins (e.g., collagen)	[271]
Cytoplasm					
MSCs	GelMA-dextrose (PGelDex)	Extrusion, DLP, handheld printing	360–480 nm UV light for 30 s at 10 mW/cm^2	Inhibits the activation and proliferation of immune cells (e.g., monocytes and macrophages) through the paracrine release of bioactive molecules, particularly interleukins	[276]

Abbreviations: BP, bone pellets; ChsMA, methacryloylated Chondroitin sulfate; DC, diclofenac sodium; DLP, digital light processing; DOXH, doxycycline hyclate; EBs, embryoid bodies; EGF, endothelial growth factor; GAG, glycosaminoglycans; GelMA, methacrylated gelatin; HADSC, human adipose-derived stem cell; HAMA, hyaluronic acrylate methacrylate; hUC-MSCs-sEVs, human umbilical cord mesenchymal stem cell-derived small extracellular vesicle; IGF-1, insulin-like growth factor-I; KGN, Kartogenin; MSC, mesenchymal stem cell; MPT, minimal processing tissue; PACG, poly(*N*-acryloyl 2-glycine); PDGF-BB, platelet-derived growth factor-BB; RA, retinoic acid; ROS, reactive oxygen species; SilMA, methacryloylated SF; SLA, stereolithography; SMSCs, synovial mesenchymal stem cells; UV, ultraviolet; VEGF, vascular endothelial growth factor.

doi: 10.36922/ijb.4650

of heart valve mechanobiology for high-throughput drug screening in calcific aortic valve disease (Figure 8B).[291]

For the vascular system, Zhang et al. utilized sacrificial 3D bioprinting to fabricate hollow microchannel-like vascular chips containing a fused endothelial layer. The microchannels were embedded in GelMA hydrogel with human endothelial cells attached to the surface. Human whole blood was injected into the microchannel to form a thrombus, and tissue plasminogen activator (tPA) was continuously infused as a thrombolytic agent, demonstrating potential lysis of nonfibrotic thrombi. They further observed that in hydrogels containing fibroblasts and damaged endothelium, fibroblast migration into the clot and type I collagen deposition had occurred, confirming the mimicry of the model in generalizing the fibrotic process *in vivo*.[289]

For malignant tumors, Sanchez-Salazar et al. utilized GelMA and reported >75% survival of microtumors cultured with Caco2 cells during a 10-day incubation period.[292] Microtumors treated with 5-fluorouracil displayed <20% cell survival and lower VEGF-A and E-cadherin expression than untreated controls. The tumor microarray device was demonstrated to be suitable for studying cancer biology and performing drug response assays.[292] Furthermore, Chen et al. utilized MDA-MB-231 and MCF7 human breast cancer cell lines, HT-29 human colon cancer cell lines, and NCI-H23 human lung cancer cell lines co-printed with GelMA; they demonstrated that GelMA exhibits similar properties to matrix gel in tumorsphere cultures and 3D tumor invasiveness studies.[293] This established the effectiveness of the 3D GelMA culture in multiple tumors and its potential for replacing stromal gel in tumor invasiveness assessments.[293]

Based on the mechanical strength of 5% (wt/vol) GelMA similar to that of healthy liver tissue, Ma et al. utilized photopolymerization of the hydrogel matrix to encapsulate hiPSC-derived hepatocytes along with endothelial and mesenchymal supporting cells.[297] This complementary pattern mimicked the hepatic lobular structure, resulting in a patient-specific liver model that closely resembled the natural tissue structure and cellular composition. Furthermore, 2% (wt/vol) glyceryl methacrylate-hyaluronate mixed with 5% (wt/vol) GelMA in a 1:1 ratio for encapsulating supporting endothelial and mesenchymal cells was found to promote endothelial cell proliferation and support blood vessel formation.[297] In a study by Gu et al., acoustic differential bioassembly was utilized to differentially assemble hiPSC-derived hepatospheres and endothelial cells and porous GelMA-encapsulated HUVECs in a microgel into a hexagonal cellular structure that mimicked the umbilical and sinusoidal structures in the liver lobule. This hepatic lobule model reconstructed hepatic metabolic and synthetic functions, such as albumin secretion and urea production.[298]

4.4. Adhesive tissue engineering scaffolds

Adhesive tissue engineering scaffolds (ATES) have emerged as an innovative alternative to sutures and bio-adhesives for ensuring implantation into target tissues. Relying on their inherent tissue adhesion properties, ATES systems enable minimally invasive delivery of various scaffolds. Here, we present the development of first-in-class 3D-bioprinted ATES constructs using functionalized hydrogel bioinks (Table 6). Two ATES delivery strategies—*in situ* printing and post-printing transfer—were tested using two bioprinting methods: embedded- versus air-printing. Dopamine-modified HA methacrylate and GelMA were used as the main bioink components, allowing for the fabrication of scaffolds with enhanced adhesion and crosslinking properties. Dopamine modification improved the adhesive properties of the HAMA-dopa/GelMA constructs under different loading conditions while maintaining their structural fidelity, stability, mechanical properties, and biocompatibility. While direct printing onto the adhesive yielded superior bond strength, embedded printing followed by transfer to the target tissue displayed greater potential for translational applications. In summary, these results demonstrated the potential of bioprinted ATES as off-the-shelf medical devices for different biomedical applications.[300]

The robust adhesive properties of an adhesive bioink consisting of gelatin methacryloyl, gelatin, HA methacrylate, and skin secretions of Chinese giant salamander enabled good extrusion bioprinting under humid conditions. This bioink also demonstrated strong adhesion to various surfaces with different chemistries, likely due to the different bonds presented in the bioink formulation. Thus, this bioink is capable of fabricating complex planar and volumetric structures using extrusion bioprinting.[301]

4.5. Biosensor

A biosensor is an analytical device consisting of a biosensitive element (sensing element) and a signal converter (transducer) (Table 6). The role of the biosensitive element is to recognize the target material, mainly antibodies, enzymes, nucleic acids, cells, and other biological substances, as well as similar molecules, such as aptamer, peptide, and molecularly imprinted polymers. Signal conversion devices serve to convert the interaction between a biosensitive element and a target molecule into a different signal. For example, an enzyme catalyzes a chemical reaction with a specific substance, which is then

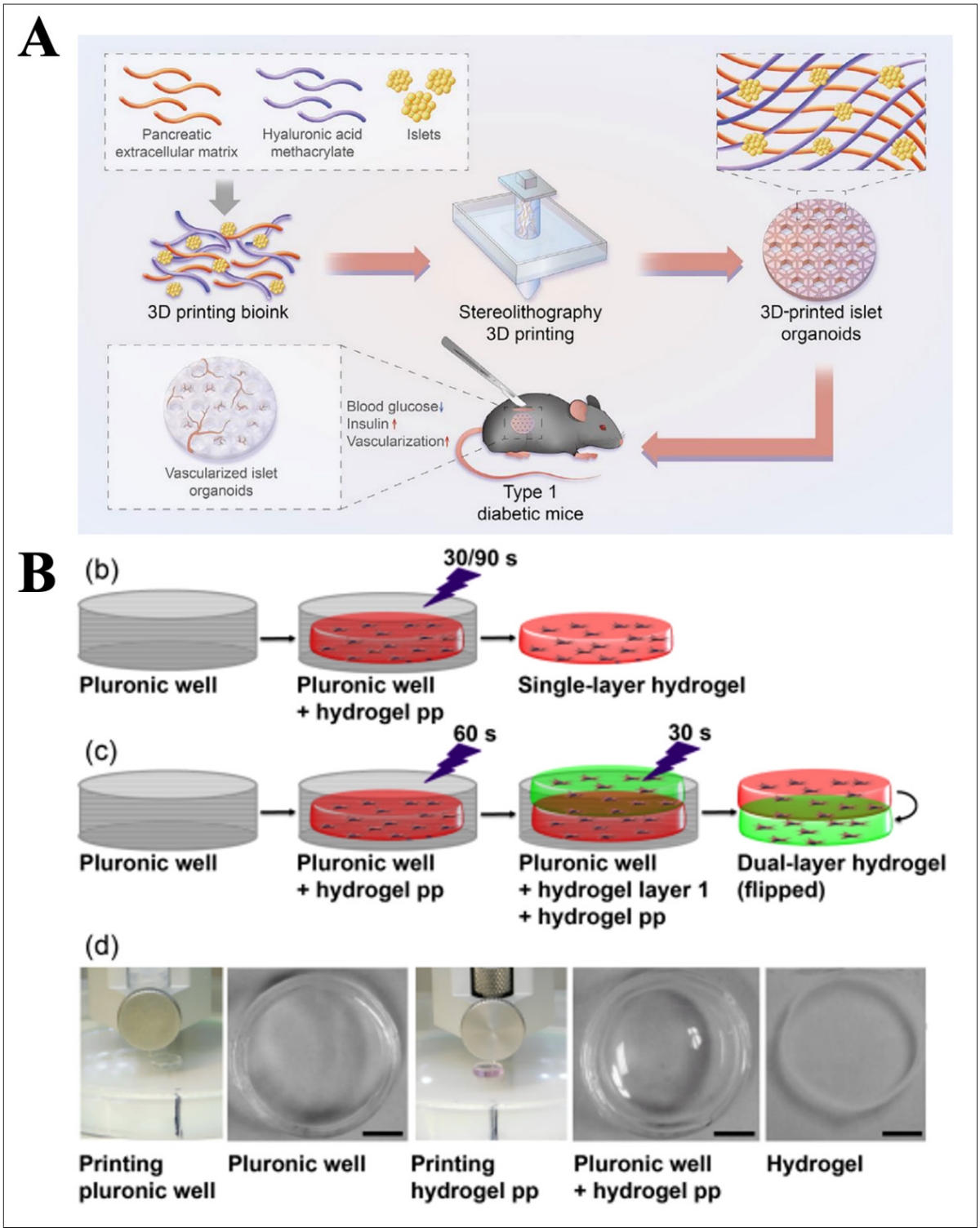

Figure 8. Organoids and organ chips. (A) 3D-printed HAMA/pECM pancreatic islet organoids. Adapted with permission from Wang et al.[299] (B) A 3D-printed model of calcific aortic valve disease (CAVD) prepared by encapsulating human aortic valvular interstitial cells (VICs) with GelMA and HAMA. Adapted with permission from van der Valk et al.[291] Abbreviations: GelMA, methacrylated gelatin; HAMA, hyaluronic acrylate methacrylate; pECM, pancreatic extracellular matrix.

converted into an electrical signal; a biological antibody captures a specific antigen, which is then converted into a light signal through labeled fluorescence.

Electrochemical biosensors based on 3D printing technology can prevent artificial errors and provide high-throughput detection. Wei et al. utilized a carbon nanofiber (CN)/GelMA conductive composite hydrogel printed on eight-channel screen-printed carbon electrodes to form tight intercellular contacts that maintain cell viability.[302] To improve the conductivity of the biosensors, they chose a 3D honeycomb-printed filler pattern. The electrochemical impedance spectroscopy technique was used to evaluate the toxicity of fungal toxins. The electrochemical method is simple, effective, and functions in real-time, which provides a new direction for cytotoxicity evaluation tools that can be used for producing toxins in bulk. Differences in the print fill pattern and number of graphically printed layers during extrusion-based 3D bioprinting can lead to the formation of different morphological structures of composite hydrogels on screen-printed electrodes, which can affect the electrochemical signals of the constructed sensors. Therefore, they explored the effects of five common print fill patterns and different graphic print layers on the electrical signals.[302] In addition, it was observed that different concentrations of GelMA hydrogels would exhibit different processing performance and biocompatibility characteristics. The electrical conductivity of different concentrations of GelMA hydrogels and their effects on cell viability were evaluated, revealing a survival rate of cells in 5–7.5% concentrations of GelMA hydrogels greater than 93%. Finally, the combined toxicity of deoxynivalenol (DON), 3-acetyldeoxynivalenol (3-ADON), and 15-acetyldeoxynivalenol (15-ADON) was analyzed by employing the combined index method, and the type of toxic combined effect was determined. Accordingly, a new method for evaluating the combined toxicity of mycotoxins was proposed, which has potential applications in food safety and evaluation.[302]

Wan et al. designed a green, rapid, and efficient method for constructing fluorescent nanosystems based on polyethyleneimine (PEI) and functionalized HAp using simple physical adsorption.[303] First, HAp nanorods were

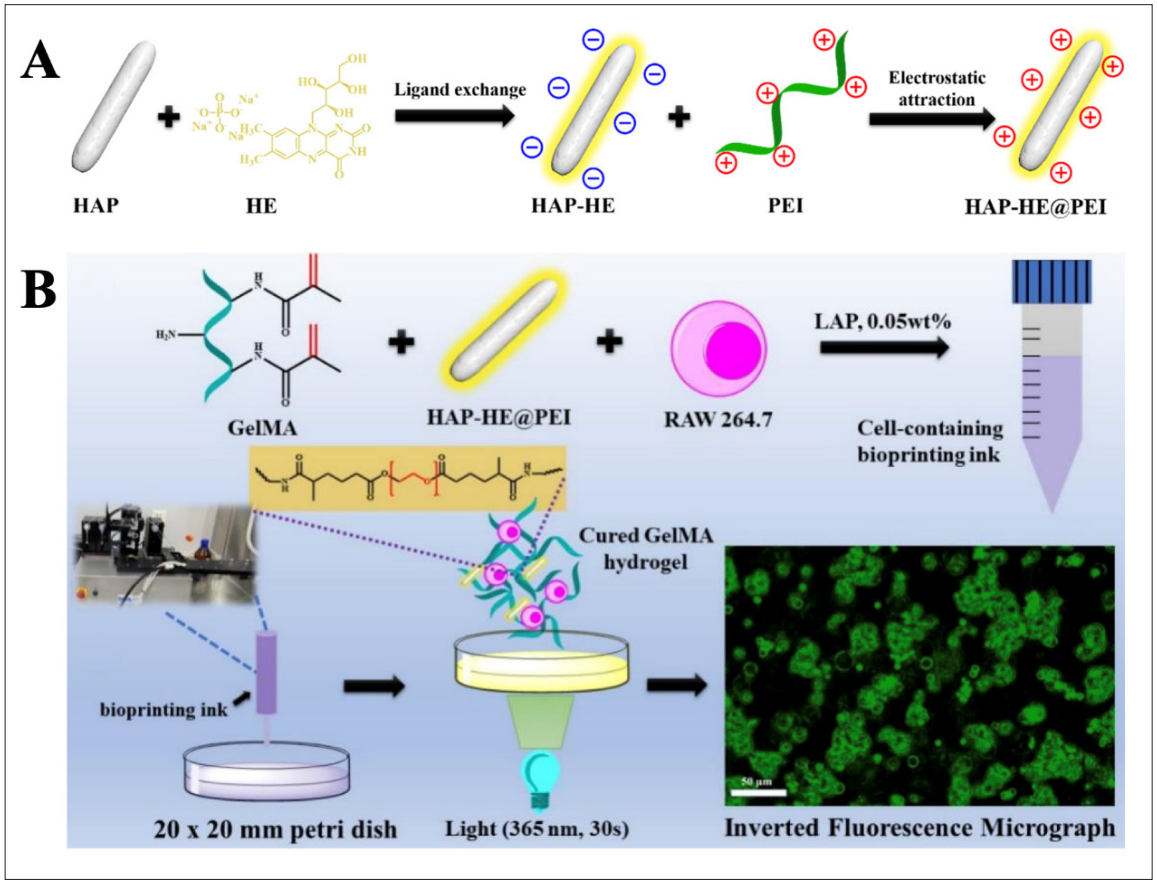

Figure 9. A fluorescent nanosystem based on PEI and functionalized HAP. (A) Preparation of HAP-HE@PEI with a positively charged surface. (B) Bioink preparation and printing for 3D cell imaging. Adapted with permission from Wan et al.[303] Abbreviations: GelMA, methacrylated gelatin; HAP, hydroxyapatite; HE, riboflavin sodium phosphate; LAP, lithium phenyl-2,4,6-trimethylbenzoylphosphinate; PEI, polyethyleneimine.

Table 5. Application of 3D-printed methacrylic anhydride (MA) hydrogel in organoid/organ chip

Organoid/ organ-on-chip	MA biomaterials	Bioactive substances	3D printing	Light curing parameters	Effects	Ref.
Aortic valve organoid	GelMA, HAMA	VIC	Extrusion 3D printing	365 nm UV light for 60 s at 2.5 mW/cm^2	Potentiates microcalcification by mimicking the native AV mechanical environment; reveals valvular mechanobiology and facilitates high-throughput drug screening in CAVD	[291]
Heart-on-a-chip	GelMA, PCL	Cardiac myocytes	Extrusion 3D printing; electrospinning	UV light for 30 s at 12 mW/cm^2	Established a 3D anisotropic HoC platform for evaluating DIC and cardioprotective efficacy; the 3D-printed micrometer-scale scaffold frames mimic the interwoven myocardium anatomical structure and the branched-aligned nanofibers network to guide cellular arrangements	[304]
	GelMA, PCL	Neonatal mouse cardiomyocytes	DLP	365 nm UV light for 18 s at 6 mW/cm^2	The constructed 3D cardiac microtissue *in vitro* modeling system has great potential for cardiac disease modeling and drug screening	[305]
Thrombosis-on-a-chip	GelMA	Endothelial cell	Extrusion 3D printing	UV light at 850 mW/cm^2	Injection of human whole blood into microchannels to form thrombi and continuous infusion of tPA as a thrombolytic agent demonstrated the potential lysis of nonfibrotic thrombi	[289]
Liver organoid	GelMA	Huh7, HepaRG stem cells	Extrusion 3D printing	365 nm UV light for 60 s at 2.5 mW/cm^2	Promotes fibrillar collagen deposition for liver fibrosis studies	[287]
Liver-on-a-chip	GelMA	HepG2/C3A cells	Extrusion 3D printing	UV light for 15 s at 850 mW	Treatment with 15 mM acetaminophen induces a toxic response in liver constructs, suggesting this liver microarray platform for toxicity assessment	[288]
Islet organoid	GelMA	Pancreatic ECM, PRP, mouse islet β cells (MIN6)	Extrusion 3D printing	405 nm UV light for 30 s	Specific bioinks with coordinated immunomodulatory responses, indicated by abundant M2-polarized macrophages, were prepared and characterized to attenuate inflammation; maintains cellular activity, enhances glucose sensitivity, and promotes angiogenesis.	[283]
	HAMA	Pancreatic dECM	SLA	405 nm UV light for 10 s	Maintenance of islet cell adhesion and morphology through the Rac1/ROCK/MLCK signaling pathway improved islet function and activity; favors the formation of a new vascular network	[299]
Bone organoid	GelMA, AlgMA, HAP	BMSCs	DLP	-	Guides osteogenesis, mineralization, cell layer formation, modeling, and remodeling, ultimately promoting bone organoid development	[306]

(Continue...)

Table 5. Continue...

Organoid/ organ-on-chip	MA biomaterials	Bioactive substances	3D printing	Light curing parameters	Effects	Ref.
Skeletal muscle organoid	GelMA, dECM-MA	Myoblasts (C2C12)	Extrusion 3D printing	UV light at 300 mW/cm^2	3D-printed dECM-based structures with topographical cues have the potential to bioengineer functional skeletal muscle tissuev	[296]
Knee joint-on-a-chip	GelMA	Cartilage, synovium, and adipose tissue	Extrusion 3D printing	395 nm UV light for 60 s	Drugs can be tested by systemic administration in all mid-streams or intra-articular administration by adding the drug to a shared synovial analog stream; perfusion of a shared stream through cartilage, synovium, and adipose tissue enables tissue crosstalk	[294]
Knee joint adipose tissue-on-a-chip	GelMA	ASCs	-	-	Adipose tissue-like organ could be constructed to study the role of the infrapatellar fat pad in the pathobiology of knee OA	[307]
PDL-AB-on-a-chip	GelMA, HAp magnetic iron oxide nanoparticles	Human PDL fibroblasts, human osteoblasts	Extrusion 3D printing	365 nm UV light for 120 s	Preliminary tetracycline interaction studies suggest that 3D microtissue cells within the model can uptake the drug	[307]
Tumor-on-a-chip	GelMA/alginate hydrogel microspheres	Caco2 cells	Extrusion 3D printing, DLP	365 nm UV light for 30 s	An organ chip suitable was constructed for studying cancer biology and performing drug response assays	[307]
	GelMA-hydrolyzed collagen	Lung cancer cell	Extrusion 3D printing	-	The efficacy of this hydrogel in 3D tumor cultures is demonstrated, as well as its potential to replace stromal gels in the assessment of tumor aggressiveness	[293]
	GelMA	Adipocyte- and iPSC-derived MSCs\endothelial cells, patient-derived neuroblastoma spheroids	Extrusion 3D printing	365 nm UV light for 125 s	Created a novel medium-throughput bio-fabrication platform suitable for studying tumor angiogenesis and metastasis in future precision medicine; demonstrated that micro-vessels are attracted to and grow into tumors by tumor spheres and that neuroblastoma cells invade the tumor environment once the spheres are destroyed	[308]

Abbreviations: AlgMA, methacrylated sodium Alg; ASCs, adipose tissue-derived mesenchymal stem cells; AV, aortic valve; BMSCs, bone marrow mesenchymal stem cells; CAVD, calcific aortic valve disease; dECM, decellularized extracellular matrix; DIC, disseminated intravascular coagulation; DLP, digital light processing; ECM, extracellular matrix; GelMA, methacrylated gelatin; HAMA, hyaluronic acrylate methacrylate; HAP, hydroxyapatite; Hoc, Heart-on-a-chip; iPSC, induced pluripotent stem cells; PCL, polycaprolactone; PDL, periodontal ligament; AB, alveolar bone; PRP, platelet-rich plasma; SLA, stereolithography; UV, ultraviolet; VIC, valvular interstitial cell.

doi: 10.36922/ijb.4650

Table 6. Application of 3D-printed methacrylic anhydride (MA) hydrogel in adhesive tissue engineering scaffolds (ATESs) and biosensors

Component	MA biomaterials	Bioactive substances	3D printing	Light curing parameters	Effects	Ref.
ATESs	Dopa-HAMA, GelMA	-	Extrusion 3D printing	365 nm UV light	Dopamine modification improved adhesive properties while maintaining structural fidelity, stability, mechanical properties, and biocompatibility	[289]
	GelMA, HAMA	Skin secretion of *Andrias davidianus*	Extrusion 3D printing	360–480 nm UV light for 30 s at 10 mW/cm^2	Promotes adhesion of the scaffold in wet conditions; maintains high cell viability	[301]
Biosensors	GelMA, CN	Human lung cancer cell A549	Extruded	405 nm UV light for 10–20 s	A new method for evaluating the combined toxicity of mycotoxins	[302]
	GelMa, HAP-HE@PEI	Macrophages RAW 264.7 cells	Inkjet	UV light for 30 s	A promising candidate for bioimaging, drug delivery, and bioprinting; can be rapidly taken up by NIH-3T3 fibroblasts and successfully applied to cellular imaging	[303]

Abbreviations: CN, carbon nanofiber; Dopa, dopamine; GelMA, methacrylated gelatin; HAMA, hyaluronic acrylate methacrylate; HAP, hydroxyapatite; HE, riboflavin sodium phosphate; PEI, polyethyleneimine; UV, ultraviolet.

functionalized with riboflavin sodium phosphate (HE) to impart fluorescent properties based on the ligand exchange process. Next, PEI was attached to the surface of HE-functionalized HAP (HAP-HE@PEI) using electrostatic attraction. The fluorescent HAP-HE@PEI nanosystems were rapidly absorbed by NIH-3T3 fibroblasts and successfully applied to cellular imaging. Additionally, they prepared doxorubicin hydrochloride (DOX) with a high loading of HAp-HE@PEI; the *in vitro* release results revealed that the maximum release of DOX at pH 5.4 was significantly higher (31.83%) than that at pH 7.2 (9.90%). Consequently, DOX can be employed as a drug delivery vehicle for cancer therapy. Finally, a 3D cell culture of RAW 264.7 macrophages using GelMA hydrogel-printed HAP-HE@PEI as 3D inkjet printing ink displayed good biocompatibility. In conclusion, due to the enhanced affinity of HAP-HE@PEI for cell membranes, this method has potential in bioimaging, drug delivery, and bioprinting (Figure 9).[303]

5. Conclusion

Among the currently used MA-based bioinks, GelMA remains the mainstream choice with established and reproducible printing parameters. While the preparation and 3D printing processes of GelMA hydrogels are well-established, a systematic research framework for other MA-based bioinks, encompassing nomenclature, preparation, light-curing processes, and applications, is lacking. In this review, although many MA hydrogels have demonstrated significant therapeutic and clinical potential, further research on their application is warranted. In addition, the biological potential of the precursor compounds remains underexplored, presenting opportunities for future investigation and advancement.

In this review, we introduced various 3D printing technologies for use in bioclinical applications. The current conventional method is extrusion printing combined with light curing, followed by DLP and SLA. We discussed the advantages and disadvantages of various printing modalities, among which extrusion printing stood out due to the lightweight and low cost of the device; however, it exhibits a low printing speed and poor cell activity of printed cells. To promote the development of translational medicine, future research should utilize other bioprinting modalities and explore methods that are more economical and compatible with clinical applications. Moreover, results on 3D-printed scaffolds are limited to *in vitro* or animal experiments; 3D printing should be tested in clinical settings. Some emergent studies proposed *in situ* printing, handheld 3D pens, and other emerging 3D printing technologies.[309] This enables the combination of computer-aided technology with 3D printing to obtain personalized 3D-printed stents.

In summation, the fusion of MA-based compounds with 3D biotechnology yields bioscaffolds with high biocompatibility and customizable mechanical properties. These versatile scaffolds can be utilized in tissue engineering, drug delivery, organoids, organ chips, biosensing, and more applications. Future advancements in this technology can be achieved by employing multifaceted and multiparameter methods to better support both research and clinical treatment.

Acknowledgments

None

Funding

This work was supported by the Hunan Provincial Health Commission Scientific Research Project, China (C202304106744).

Conflict of interest

The authors declared no potential conflicts of interest with respect to the research, authorship, and publication of this article.

Author contributions

Conceptualization: Naisi Shen, Bairong Fang, Liangle Liu
Investigation: Naisi Shen, Zhen Li, Pu Yang, Xiangjun Liu, Yikun Ju, Yue Hu
Writing – original draft: Naisi Shen
Writing – review & editing: All authors

Ethics approval and consent to participate

Not applicable.

Consent for publication

Not applicable.

Availability of data

Not applicable.

References

1. Ravi M, Paramesh V, Kaviya SR, Anuradha E, Solomon FD. 3D cell culture systems: advantages and applications. *J Cell Physiol*. 2015;230:16-26. doi: 10.1002/jcp.24683
2. Shankar V, van Blitterswijk C, Vrij E, Giselbrecht S. Automated, high-throughput phenotypic screening and analysis platform to study pre- and post-implantation morphogenesis in stem cell-derived embryo-like structures. *Adv Sci (Weinh)*. 2023;11(4):2304987. doi: 10.1002/advs.202304987
3. Jensen C, Teng Y. Is it time to start transitioning from 2D to 3D cell culture?, *Front Mol Biosci*. 2020;7:33. doi: 10.3389/fmolb.2020.00033
4. Groll J, Burdick JA, Cho DW, et al. A definition of bioinks and their distinction from biomaterial inks. *Biofabrication*. 2018;11:013001. doi: 10.1088/1758-5090/aaec52
5. Raja IS, Kang MS, Hong SW, et al. State-of-the-art techniques for promoting tissue regeneration: combination of three-dimensional bioprinting and carbon nanomaterials. *Int J Bioprint*. 2023;9:635. doi: 10.18063/ijb.v9i1.635
6. Mandrycky C, Wang Z, Kim K, Kim DH. 3D bioprinting for engineering complex tissues. *Biotechnol Adv*. 2016;34:422-434. doi: 10.1016/j.biotechadv.2015.12.011
7. Peng X, Wu S, Sun X, et al. 4D printing of freestanding liquid crystal elastomers via hybrid additive manufacturing. *Adv Mater*. 2022;34:e2204890. doi: 10.1002/adma.202204890
8. Mainik P, Spiegel CA, Blasco E. Recent advances in multi-photon 3D laser printing: active materials and applications. *Adv Mater.* 2024;36(11):e2310100. doi: 10.1002/adma.202310100
9. Tuan RS, Boland G, Tuli R. Adult mesenchymal stem cells and cell-based tissue engineering. *Arthritis Res Ther*. 2003;5:32-45. doi: 10.1186/ar614
10. Klebe RJ. Cytoscribing: a method for micropositioning cells and the construction of two- and three-dimensional synthetic tissues. *Exp Cell Res*. 1988;179:362-373. doi: 10.1016/0014-4827(88)90275-3
11. Li X, Liu B, Pei B, et al. Inkjet bioprinting of biomaterials. *Chem Rev*. 2020;120:10793-10833. doi: 10.1021/acs.chemrev.0c00008
12. Miri AK, Mirzaee I, Hassan S, et al. Effective bioprinting resolution in tissue model fabrication. *Lab Chip*. 2019;19: 2019-2037. doi: 10.1039/c8lc01037d
13. Cui X, Boland T, D'Lima DD, Lotz MK. Thermal inkjet printing in tissue engineering and regenerative medicine. *Recent Pat Drug Deliv Formul*. 2012;6:149-155. doi: 10.2174/187221112800672949
14. Guillemot F, Souquet A, Catros S, et al. High-throughput laser printing of cells and biomaterials for tissue engineering. *Acta Biomater*. 2010;6:2494-2500. doi: 10.1016/j.actbio.2009.09.029
15. Pepper ME, Seshadri V, Burg TC, Burg KJ, Groff RE. Characterizing the effects of cell settling on bioprinter output. *Biofabrication*. 2012;4:011001. doi: 10.1088/1758-5082/4/1/011001
16. Courson R, Bratash O, Maziz A, et al. Rapid prototyping of a polymer MEMS droplet dispenser by laser-assisted 3D printing. *Microsyst Nanoeng*. 2023;9:85. doi: 10.1038/s41378-023-00559-3
17. Gruene M, Deiwick A, Koch L, et al. Laser printing of stem cells for biofabrication of scaffold-free autologous grafts. *Tissue Eng Part C Methods*. 2011;17:79-87.

doi: 10.1089/ten.TEC.2010.0359

18. Daly AC, Prendergast ME, Hughes AJ, Burdick JA. Bioprinting for the biologist. *Cell*. 2021;184:18-32. doi: 10.1016/j.cell.2020.12.002

19. Askari M, Afzali Naniz M, Kouhi M, Saberi A, Zolfagharian A, Bodaghi M. Recent progress in extrusion 3D bioprinting of hydrogel biomaterials for tissue regeneration: a comprehensive review with focus on advanced fabrication techniques. *Biomater Sci*. 2021;9:535-573. doi: 10.1039/d0bm00973c

20. Rocca M, Fragasso A, Liu W, Heinrich MA, Zhang YS. Embedded multimaterial extrusion bioprinting. *SLAS Technol*. 2018;23:154-163. doi: 10.1177/2472630317742071

21. Xu L, Varkey M, Jorgensen A, et al. Bioprinting small diameter blood vessel constructs with an endothelial and smooth muscle cell bilayer in a single step. *Biofabrication*. 2020;12:045012. doi: 10.1088/1758-5090/aba2b6

22. Lian L, Zhou C, Tang G, et al. Uniaxial and coaxial vertical embedded extrusion bioprinting. *Adv Healthc Mater*. 2022;11(9):e2102411. doi: 10.1002/adhm.202102411

23. Malekpour A, Chen X. Printability and cell viability in extrusion-based bioprinting from experimental, computational, and machine learning views. *J Funct Biomater*. 2022;13(2):40. doi: 10.3390/jfb13020040

24. Lan X, Adesida A, Boluk Y. Rheological and viscoelastic properties of collagens and their role in bioprinting by micro-extrusion. *Biomed Mater*. 2022;17(6). doi: 10.1088/1748-605X/ac9b06

25. Tappa K, Jammalamadaka U. Novel biomaterials used in medical 3D printing techniques. *J Funct Biomater*. 2018;9(1):17. doi: 10.3390/jfb9010017

26. Ismail KI, Yap TC, Ahmed R. 3D-printed fiber-reinforced polymer composites by fused deposition modelling (FDM): fiber length and fiber implementation techniques. *Polymers (Basel)*. 2022;14(21):4659. doi: 10.3390/polym14214659

27. Krueger L, Miles JA, Popat A. 3D printing hybrid materials using fused deposition modelling for solid oral dosage forms. *J Control Release*. 2022;351:444-455. doi: 10.1016/j.jconrel.2022.09.032

28. Kumar H, Kim K. Stereolithography 3D bioprinting. *Methods Mol Biol*. 2020;2140:93-108. doi: 10.1007/978-1-0716-0520-2_6

29. Morano C, Pagnotta L. Additive manufactured parts produced using selective laser sintering technology: comparison between porosity of pure and blended polymers. *Polymers (Basel)*. 2023;15(22):4446. doi: 10.3390/polym15224446

30. Mazzoli A. Selective laser sintering in biomedical engineering. *Med Biol Eng Comput*. 2013;51(3):245-256. doi: 10.1007/s11517-012-1001-x

31. Shirazi SF, Gharehkhani S, Mehrali M, et al. A review on powder-based additive manufacturing for tissue engineering: selective laser sintering and inkjet 3D printing. *Sci Technol Adv Mater*. 2015;16:033502. doi: 10.1088/1468-6996/16/3/033502

32. Su X, Wang T, Guo S. Applications of 3D printed bone tissue engineering scaffolds in the stem cell field. *Regen Ther*. 2021;16:63-72. doi: 10.1016/j.reth.2021.01.007

33. Kafle A, Luis E, Silwal R, Pan HM, Shrestha PL, Bastola AK. 3D/4D printing of polymers: fused deposition modelling (FDM), selective laser sintering (SLS), and stereolithography (SLA). *Polymers (Basel)*. 2021;13(18):3101. doi: 10.3390/polym13183101

34. Li YC, Zhang YS, Akpek A, Shin SR, Khademhosseini A. 4D bioprinting: the next-generation technology for biofabrication enabled by stimuli-responsive materials. *Biofabrication*. 2016;9:012001. doi: 10.1088/1758-5090/9/1/012001

35. Ong CS, Nam L, Ong K, et al. 3D and 4D bioprinting of the myocardium: current approaches, challenges, and future prospects. *Biomed Res Int*. 2018;2018: 6497242. doi: 10.1155/2018/6497242

36. Miao S, Cui H, Nowicki M, et al. Stereolithographic 4D bioprinting of multiresponsive architectures for neural engineering. *Adv Biosyst*. 2018;2(9):1800101. doi: 10.1002/adbi.201800101

37. Hua M, Wu D, Wu S, Ma Y, Alsaid Y, He X. 4D printable tough and thermoresponsive hydrogels. *ACS Appl Mater Interfaces*. 2021;13:12689-12697. doi: 10.1021/acsami.0c17532

38. Guo Y, Belgodere JA, Ma Y, Jung JP, Bharti B. Directed printing and reconfiguration of thermoresponsive Silica-pNIPAM nanocomposites. *Macromol Rapid Commun*. 2019;40(13):e1900191. doi: 10.1002/marc.201900191

39. Pan HM, Goto A. Topology-dependent pH-responsive actuation and shape memory programming for biomimetic 4D printing. *Macromol Rapid Commun*. 2023;44:e2300074. doi: 10.1002/marc.202300074

40. Tahouni Y, Cheng T, Lajewski S, et al. Codesign of biobased cellulose-filled filaments and mesostructures for 4D printing humidity responsive smart structures. *3D Print Addit Manuf*. 2023;10(1):1-14. doi: 10.1089/3dp.2022.0061

41. Wychowaniec JK, Brougham DF. Emerging magnetic fabrication technologies provide controllable hierarchically-structured biomaterials and stimulus response for biomedical applications. *Adv Sci (Weinh)*. 2022;9:e2202278.

doi: 10.1002/advs.202202278.

42. Capakova Z, Radaszkiewicz KA, Acharya TH, et al. The biocompatibility of polyaniline and polypyrrole 2: doping with organic phosphonates. *Mater Sci Eng C Mater Biol Appl*. 2020;113:110986. doi: 10.1016/j.msec.2020.110986.

43. Noroozi R, Bodaghi M, Jafari H, Zolfagharian A, Fotouhi M. Shape-adaptive metastructures with variable Bandgap regions by 4D printing. *Polymers (Basel)*. 2020;12(3):519. doi: 10.3390/polym12030519

44. Ashammakhi N, Ahadian S, Zengjie F, et al. Advances and future perspectives in 4D bioprinting. *Biotechnol J*. 2018;13:e1800148. doi: 10.1002/biot.201800148

45. Kuribayashi-Shigetomi K, Onoe H, Takeuchi S. Cell origami: self-folding of three-dimensional cell-laden microstructures driven by cell traction force. *PLoS One*. 2012;7:e51085. doi: 10.1371/journal.pone.0051085

46. Devillard R, Pages E, Correa MM, et al. Cell patterning by laser-assisted bioprinting. *Methods Cell Biol*. 2014;119:159-174. doi: 10.1016/B978-0-12-416742-1.00009-3

47. Placone JK, Engler AJ. Recent advances in extrusion-based 3D printing for biomedical applications. *Adv Healthc Mater*. 2018;7:e1701161. doi: 10.1002/adhm.201701161.

48. Hwang HH, Zhu W, Victorine G, Lawrence N, Chen S. 3D-printing of functional biomedical microdevices via light- and extrusion-based approaches. *Small Methods*. 2018;2(2):1700277. doi: 10.1002/smtd.201700277

49. Murphy SV, Atala A. 3D bioprinting of tissues and organs. *Nat Biotechnol*. 2014;32:773-785. doi: 10.1038/nbt.2958

50. Cadamuro F, Nicotra F, Russo L. 3D printed tissue models: from hydrogels to biomedical applications. *J Control Release*. 2023;354:726-745. doi: 10.1016/j.jconrel.2023.01.048

51. Jia L, Hua Y, Zeng J, et al. Bioprinting and regeneration of auricular cartilage using a bioactive bioink based on microporous photocrosslinkable acellular cartilage matrix. *Bioact Mater*. 2022;16:66-81. doi: 10.1016/j.bioactmat.2022.02.032

52. Ojansivu M, Rashad A, Ahlinder A, et al. Wood-based nanocellulose and bioactive glass modified gelatin-alginate bioinks for 3D bioprinting of bone cells. *Biofabrication*. 2019;11:035010. doi: 10.1088/1758-5090/ab0692

53. Moncal KK, Ozbolat V, Datta P, Heo DN, Ozbolat IT. Thermally-controlled extrusion-based bioprinting of collagen. *J Mater Sci Mater Med*. 2019;30:55. doi: 10.1007/s10856-019-6258-2

54. Benson K, Galla HJ, Kehr NS. Cell adhesion behavior in 3D hydrogel scaffolds functionalized with D- or L-aminoacids. *Macromol Biosci*. 2014;14:793-798. doi: 10.1002/mabi.201300485

55. Sigaux N, Pourchet L, Breton P, Brosset S, Louvrier A, Marquette CA. 3D bioprinting:principles, fantasies and prospects. *J Stomatol Oral Maxillofac Surg*. 2019;120:128-132. doi: 10.1016/j.jormas.2018.12.014

56. Yao B, Hu T, Cui X, Song W, Fu X, Huang S. Enzymatically degradable alginate/gelatin bioink promotes cellular behavior and degradation in vitro and in vivo. *Biofabrication*. 2019;11:045020. doi: 10.1088/1758-5090/ab38ef

57. Duan B, Hockaday LA, Kang KH, Butcher JT. 3D bioprinting of heterogeneous aortic valve conduits with alginate/gelatin hydrogels. *J Biomed Mater Res A*. 2013;101:1255-1264. doi: 10.1002/jbm.a.34420

58. Michael S, Sorg H, Peck CT, et al. Tissue engineered skin substitutes created by laser-assisted bioprinting form skin-like structures in the dorsal skin fold chamber in mice. *PLoS One*. 2013;8:e57741. doi: 10.1371/journal.pone.0057741

59. Visser J, Peters B, Burger TJ, et al. Biofabrication of multi-material anatomically shaped tissue constructs. *Biofabrication*. 2013;5:035007. doi: 10.1088/1758-5082/5/3/035007

60. Owens CM, Marga F, Forgacs G, Heesch CM. Biofabrication and testing of a fully cellular nerve graft. *Biofabrication*. 2013;5:045007. doi: 10.1088/1758-5082/5/4/045007

61. Xiao S, Zhao T, Wang J, et al. Gelatin methacrylate (GelMA)-based hydrogels for cell transplantation: an effective strategy for tissue engineering. *Stem Cell Rev Rep*. 2019;15:664-679. doi: 10.1007/s12015-019-09893-4

62. Ozbolat IT, Yu Y. Bioprinting toward organ fabrication: challenges and future trends. *IEEE Trans Biomed Eng*. 2013;60:691-699. doi: 10.1109/TBME.2013.2243912

63. Kolesky DB, Truby RL, Gladman AS, Busbee TA, Homan KA, Lewis JA. 3D bioprinting of vascularized, heterogeneous cell-laden tissue constructs. *Adv Mater*. 2014;26:3124-3130. doi: 10.1002/adma.201305506

64. Abdollahi Baghban S, Ebrahimi M, Bagheri-Khoulenjani S, Khorasani M. A highly efficient microwave-assisted synthesis of an LED-curable methacrylated gelatin for bio applications. *RSC Adv*. 2021;11:14996-15009. doi: 10.1039/d1ra01269j

65. Purcell BP, Elser JA, Mu A, Margulies KB, Burdick JA. Synergistic effects of SDF-1alpha chemokine and hyaluronic acid release from degradable hydrogels on directing bone marrow derived cell homing to the myocardium. *Biomaterials*. 2012;33:7849-7857.

doi: 10.1016/j.biomaterials.2012.07.005

66. Burkhart A, Ritter H. Influence of cyclodextrin on the UCST- and LCST-behavior of poly(2-methacrylamido-caprolactam)-co-(N,N-dimethylacrylamide). *Beilstein J Org Chem*. 2014;10:1951-1958.
doi: 10.3762/bjoc.10.203

67. Yue K, Trujillo-de Santiago G, Alvarez MM, Tamayol A, Annabi N, Khademhosseini A. Synthesis, properties, and biomedical applications of gelatin methacryloyl (GelMA) hydrogels. *Biomaterials*. 2015;73:254-271.
doi: 10.1016/j.biomaterials.2015.08.045

68. Schuurmans CCL, Mihajlovic M, Hiemstra C, Ito K, Hennink WE, Vermonden T. Hyaluronic acid and chondroitin sulfate (meth)acrylate-based hydrogels for tissue engineering: synthesis, characteristics and pre-clinical evaluation. *Biomaterials*. 2021;268:120602.
doi: 10.1016/j.biomaterials.2020.120602

69. Nichol JW, Koshy ST, Bae H, Hwang CM, Yamanlar S, Khademhosseini A. Cell-laden microengineered gelatin methacrylate hydrogels. *Biomaterials*. 2010;31:5536-5544.
doi: 10.1016/j.biomaterials.2010.03.064

70. Sun M, Sun X, Wang Z, Guo S, Yu G, Yang H. Synthesis and properties of gelatin methacryloyl (GelMA) hydrogels and their recent applications in load-bearing tissue. *Polymers (Basel)*. 2018;10(11):1290.
doi: 10.3390/polym10111290

71. Zhu M, Wang Y, Ferracci G, Zheng J, Cho NJ, Lee BH. Gelatin methacryloyl and its hydrogels with an exceptional degree of controllability and batch-to-batch consistency. *Sci Rep*. 2019;9:6863.
doi: 10.1038/s41598-019-42186-x

72. Janmaleki M, Liu J, Kamkar M, Azarmanesh M, Sundararaj U, Nezhad AS. Role of temperature on bio-printability of gelatin methacryloyl bioink in two-step cross-linking strategy for tissue engineering applications. *Biomed Mater*. 2020;16:015021.
doi: 10.1088/1748-605X/abbcc9

73. He Q, Cheng Y, Deng Y, Wen F, Lai Y, Li H. Conductive hydrogel for flexible bioelectronic device: current progress and future perspective. *Adv Funct Mater*. 2024;34(1):2308974.
doi: 10.1002/adfm.202308974

74. Goodarzi Hosseinabadi H, Dogan E, Miri AK, Ionov L. Digital light processing bioprinting advances for microtissue models. *ACS Biomater Sci Eng*. 2022;8:1381-1395.
doi: 10.1021/acsbiomaterials.1c01509

75. Li L, Scheiger JM, Levkin PA. Design and applications of photoresponsive hydrogels. *Adv. Mater*. 2019;31:e1807333.
doi: 10.1002/adma.201807333

76. Ruiz-Cantu L, Gleadall A, Faris C, Segal J, Shakesheff K, Yang J. Multi-material 3D bioprinting of porous constructs for cartilage regeneration. *Mater Sci Eng C Mater Biol Appl*. 2020;109:110578.
doi: 10.1016/j.msec.2019.110578

77. Raees S, Ullah F, Javed F, et al. Classification, processing, and applications of bioink and 3D bioprinting: a detailed review. *Int J Biol Macromol*.2023;232:123476.
doi: 10.1016/j.ijbiomac.2023.123476.

78. Lu D, Zeng Z, Geng Z, et al. Macroporous methacrylated hyaluronic acid hydrogel with different pore sizes for in vitro and in vivo evaluation of vascularization. *Biomed Mater*. 2022;17.
doi: 10.1088/1748-605X/ac494b

79. Chimene D, Kaunas R, Gaharwar AK. Hydrogel bioink reinforcement for additive manufacturing: a focused review of emerging strategies. *Adv Mater*. 2020;32:e1902026.
doi: 10.1002/adma.201902026

80. Klotz BJ, Gawlitta D, Rosenberg A, Malda J, Melchels FPW. Gelatin-methacryloyl hydrogels: towards biofabrication-based tissue repair. *Trends Biotechnol*. 2016;34:394-407.
doi: 10.1016/j.tibtech.2016.01.002

81. Kurian AG, Singh RK, Patel KD, Lee JH, Kim HW. Multifunctional GelMA platforms with nanomaterials for advanced tissue therapeutics. *Bioact Mater*. 2022;8:267-295.
doi: 10.1016/j.bioactmat.2021.06.027

82. Dong Z, Yuan Q, Huang K, Xu W, Liu G, Gu Z. Gelatin methacryloyl (GelMA)-based biomaterials for bone regeneration. *RSC Adv*. 2019;9:17737-17744.
doi: 10.1039/c9ra02695a.

83. Schuurman W, Levett PA, Pot MW, et al. Gelatin-methacrylamide hydrogels as potential biomaterials for fabrication of tissue-engineered cartilage constructs. *Macromol Biosci*. 2013;13:551-561.
doi: 10.1002/mabi.201200471

84. Zheng H, Zuo B. Functional silk fibroin hydrogels: preparation, properties and applications. *J Mater Chem B*. 2021;9:1238-1258.
doi: 10.1039/d0tb02099k

85. Liu H, Sun Z, Guo C. Chemical modification of silk proteins: current status and future prospects. *Adv Fiber Mater*. 2022;4:705-719.
doi: 10.1007/s42765-022-00144-9.

86. Sun W, Gregory DA, Tomeh MA, Zhao X. Silk fibroin as a functional biomaterial for tissue engineering. *Int J Mol Sci*. 2021;22(3):1499.
doi: 10.3390/ijms22031499

87. Kim SH, Hong H, Ajiteru O, et al. 3D bioprinted silk fibroin hydrogels for tissue engineering. *Nat Protoc*. 2021;16:5484-5532.
doi: 10.1038/s41596-021-00622-1

88. Kim SH, Seo YB, Yeon YK, et al. 4D-bioprinted silk hydrogels for tissue engineering. *Biomaterials*. 2020;260:120281.

doi: 10.1016/j.biomaterials.2020.120281.

89. Kim SH, Yeon YK, Lee JM, et al. Precisely printable and biocompatible silk fibroin bioink for digital light processing 3D printing. *Nat Commun*. 2018;9:1620. doi: 10.1038/s41467-018-03759-y

90. Liu J, Shi L, Deng Y, et al. Silk sericin-based materials for biomedical applications. *Biomaterials*. 2022;287: 121638. doi: 10.1016/j.biomaterials.2022.121638

91. Qi C, Liu J, Jin Y, et al. Photo-crosslinkable, injectable sericin hydrogel as 3D biomimetic extracellular matrix for minimally invasive repairing cartilage. *Biomaterials*. 2018;163:89-104. doi: 10.1016/j.biomaterials.2018.02.016

92. Spada A, Emami J, Tuszynski JA, Lavasanifar A. The uniqueness of albumin as a Carrier in Nanodrug Delivery. *Mol Pharm*. 2021;18:1862-1894. doi: 10.1021/acs.molpharmaceut.1c00046

93. Khanna S, Singh AK, Behera SP, Gupta S. Thermoresponsive BSA hydrogels with phase tunability. *Mater Sci Eng C Mater Biol Appl*. 2021;119:111590. doi: 10.1016/j.msec.2020.111590.

94. Chen Y, Zhai MJ, Mehwish N, et al. Comparison of globular albumin methacryloyl and random-coil gelatin methacryloyl: preparation, hydrogel properties, cell behaviors, and mineralization. *Int J Biol Macromol*. 2022;204:692-708. doi: 10.1016/j.ijbiomac.2022.02.028

95. Patrawalla NY, Kajave NS, Albanna MZ, Kishore V. Collagen and beyond: a comprehensive comparison of human ECM properties derived from various tissue sources for regenerative medicine applications. *J Funct Biomater*. 2023;14(7):363. doi: 10.3390/jfb14070363

96. Marques CF, Diogo GS, Pina S, Oliveira JM, Silva TH, Reis RL. Collagen-based bioinks for hard tissue engineering applications: a comprehensive review. *J Mater Sci Mater Med*. 2019;30:32. doi: 10.1007/s10856-019-6234-x

97. Wang Z, Yang Y, Gao Y, Xu Z, Yang S, Jin M. Establishing a novel 3D printing bioinks system with recombinant human collagen. *Int J Biol Macromol*. 2022;211:400-409. doi: 10.1016/j.ijbiomac.2022.05.088

98. Mostert D, Jorba I, Groenen BGW, et al. Methacrylated human recombinant collagen peptide as a hydrogel for manipulating and monitoring stiffness-related cardiac cell behavior. *iScience*. 2023;26:106423. doi: 10.1016/j.isci.2023.106423

99. Zhou J, Wen B, Xie H, et al. Advances in the preparation and assessment of the biological activities of chitosan oligosaccharides with different structural characteristics. *Food Funct*. 2021;12:926-951. doi: 10.1039/d0fo02768e

100. Yang M, Wang H, Li K, Chen Z, Seamirumi DT. A new soft tissue constructed with chitosan for wound dressings-incorporating nanoparticles for medical and nursing therapeutic efficacy. *Regen Ther*. 2023;24:103-111. doi: 10.1016/j.reth.2023.06.005

101. Ailincai D, Cibotaru S, Anisiei A, et al. Marin, mesoporous chitosan nanofibers loaded with norfloxacin and coated with phenylboronic acid perform as bioabsorbable active dressings to accelerate the healing of burn wounds. *Carbohydr Polym*. 2023;318:121135. doi: 10.1016/j.carbpol.2023.121135.

102. Yang Y, Ma Y, Wang J, et al. Chitosan-based mussel-inspired hydrogel for rapid self-healing and high adhesion of tissue adhesion and wound dressings. *Carbohydr Polym*. 2023;316:121083. doi: 10.1016/j.carbpol.2023.121083

103. Wang W, Xue C, Mao X. Chitosan: structural modification, biological activity and application. *Int J Biol Macromol*. 2020;164:4532-4546. doi: 10.1016/j.ijbiomac.2020.09.042

104. Shen Y, Tang H, Huang X, et al. DLP printing photocurable chitosan to build bio-constructs for tissue engineering. *Carbohydr Polym*. 2020;235:115970. doi: 10.1016/j.carbpol.2020.115970

105. Aguirre G, Billon L. Water-borne synthesis of multi-responsive and biodegradable chitosan-crosslinked microgels: towards self-assembled films with adaptable properties. *Carbohydr Polym*. 2023;318:121099. doi: 10.1016/j.carbpol.2023.121099

106. Song F, Kong Y, Shao C, et al. Chitosan-based multifunctional flexible hemostatic bio-hydrogel. *Acta Biomater*. 2021;136:170-183. doi: 10.1016/j.actbio.2021.09.056

107. He X, Liu X, Yang J, et al. Tannic acid-reinforced methacrylated chitosan/methacrylated silk fibroin hydrogels with multifunctionality for accelerating wound healing. Carbohydr Polym. 2020;247:116689. doi: 10.1016/j.carbpol.2020.116689

108. Wei H, Yu S, Zhang Y, et al. Injectable chitosan/xyloglucan composite hydrogel with mechanical adaptivity and endogenous bioactivity for skin repair. *Carbohydr Polym*. 2023;313:120904. doi: 10.1016/j.carbpol.2023.120904

109. Yoon SJ, Kim SH, Choi JW, Chun HJ, Yang DH. Guided cortical and cancellous bone formation using a minimally invasive technique of BMSC- and BMP-2-laden visible light-cured carboxymethyl chitosan hydrogels. *Int J Biol Macromol*. 2023;227:641-653. doi: 10.1016/j.ijbiomac.2022.12.137

110. Chen Y, Sheng W, Lin J, et al. Magnesium oxide nanoparticle coordinated phosphate-functionalized chitosan injectable hydrogel for osteogenesis and angiogenesis in bone regeneration. *ACS Appl Mater Interfaces*. 2022;14:7592-7608.

doi: 10.1021/acsami.1c21260

111. Carvalho CR, Wrobel S, Meyer C, et al. Gellan Gum-based luminal fillers for peripheral nerve regeneration: an in vivo study in the rat sciatic nerve repair model. *Biomater Sci*. 2018;6:1059-1075. doi: 10.1039/c7bm01101f

112. Chen F, Huang G, Huang H. Preparation and application of dextran and its derivatives as carriers. *Int J Biol Macromol*. 2020;145:827-834. doi: 10.1016/j.ijbiomac.2019.11.151

113. Sun G, Mao JJ. Engineering dextran-based scaffolds for drug delivery and tissue repair. *Nanomedicine (Lond)*. 2012;7:1771-1784. doi: 10.2217/nnm.12.149

114. Yang R, Xue W, Liao H, et al. Injectable polylysine and dextran hydrogels with robust antibacterial and ROS-scavenging activity for wound healing. *Int J Biol Macromol*. 2022;223:950-960. doi: 10.1016/j.ijbiomac.2022.11.065

115. Zhao B, Zhang Y, Li D, Mo X, Pan J. Hofmeister effect-enhanced gelatin/oxidized dextran hydrogels with improved mechanical properties and biocompatibility for wound healing. *Acta Biomater*. 2022;151:235-253. doi: 10.1016/j.actbio.2022.08.009

116. Kolahdoozan M, Rahimi T, Taghizadeh A, Aghaei H. Preparation of new hydrogels by visible light cross-linking of dextran methacrylate and poly(ethylene glycol)-maleic acid copolymer. *Int J Biol Macromol*. 2023;227:1221-1233. doi: 10.1016/j.ijbiomac.2022.11.309

117. Huang S, Liu H, Huang S, Fu T, Xue W, Guo R. Dextran methacrylate hydrogel microneedles loaded with doxorubicin and trametinib for continuous transdermal administration of melanoma. *Carbohydr Polym*. 2020;246:116650. doi: 10.1016/j.carbpol.2020.116650

118. Wang H, Zhou L, Liao J, et al. Cell-laden photocrosslinked GelMA-DexMA copolymer hydrogels with tunable mechanical properties for tissue engineering. *J Mater Sci Mater Med*. 2014;25:2173-2183. doi: 10.1007/s10856-014-5261-x

119. Sun G, Zhang X, Shen YI, et al. Dextran hydrogel scaffolds enhance angiogenic responses and promote complete skin regeneration during burn wound healing. *Proc Natl Acad Sci U S A*. 2011;108: 20976-20981. doi: 10.1073/pnas.1115973108

120. Dhamecha D, Movsas R, Sano U, Menon JU. Applications of alginate microspheres in therapeutics delivery and cell culture: past, present and future. *Int J Pharm*. 2019;569:118627. doi: 10.1016/j.ijpharm.2019.118627

121. Rastogi P, Kandasubramanian B. Review of alginate-based hydrogel bioprinting for application in tissue engineering. *Biofabrication*. 2019;11:042001. doi: 10.1088/1758-5090/ab331e

122. Charron PN, Fenn SL, Poniz A, Oldinski RA. Mechanical properties and failure analysis of visible light crosslinked alginate-based tissue sealants. *J Mech Behav Biomed Mater*. 2016;59:314-321. doi: 10.1016/j.jmbbm.2016.02.003

123. Samorezov JE, Morlock CM, Alsberg E. Dual ionic and photo-crosslinked alginate hydrogels for micropatterned spatial control of material properties and cell behavior. *Bioconjug Chem*. 2015;26:1339-1347. doi: 10.1021/acs.bioconjchem.5b00117

124. Gao Y, Jin X. Dual crosslinked methacrylated alginate hydrogel micron fibers and tissue constructs for cell biology. Mar Drugs. 2019;17:557. doi: 10.3390/md17100557

125. Garcia-Lizarribar A, Villasante A, Lopez-Martin JA, et al. 3D bioprinted functional skeletal muscle models have potential applications for studies of muscle wasting in cancer cachexia. *Biomater Adv*. 2023;150:213426. doi: 10.1016/j.bioadv.2023.213426

126. Fenn SL, Miao T, Scherrer RM, Floreani RA. Dual-cross-linked methacrylated alginate sub-microspheres for intracellular chemotherapeutic delivery. *ACS Appl Mater Interfaces*. 2016;8:17775-17783. doi: 10.1021/acsami.6b03245

127. Wang Y, Li S, Xu X, Tan Y, Liu XW, Fang J. Chemoenzymatic synthesis of homogeneous chondroitin polymers and its derivatives. *Carbohydr Polym*. 2020;232:115822. doi: 10.1016/j.carbpol.2019.115822

128. Bishnoi M, Jain A, Hurkat P, Jain SK. Chondroitin sulphate: a focus on osteoarthritis. *Glycoconj J*. 2016;33:693-705. doi: 10.1007/s10719-016-9665-3

129. Mencio CP, Hussein RK, Yu P, Geller HM. The role of chondroitin sulfate proteoglycans in nervous system development. *J Histochem Cytochem*. 2021;69:61-80. doi: 10.1369/0022155420959147

130. Ida-Yonemochi H, Takeuchi K, Ohshima H. Role of chondroitin sulfate in the developmental and healing process of the dental pulp in mice. *Cell Tissue Res*. 2022;388:133-148. doi: 10.1007/s00441-022-03575-3

131. Lin JZ, Duan MR, Lin N, Zhao WJ. The emerging role of the chondroitin sulfate proteoglycan family in neurodegenerative diseases. *Rev Neurosci*. 2021;32:737-750. doi: 10.1515/revneuro-2020-0146

132. Yang S, Gigout S, Molinaro A, et al. Chondroitin 6-sulphate is required for neuroplasticity and memory in ageing. *Mol Psychiatry*. 2021;26:5658-5668. doi: 10.1038/s41380-021-01208-9

133. Morla S. Glycosaminoglycans and glycosaminoglycan mimetics in cancer and inflammation. *Int J Mol Sci*. 2019;20(8):1963. doi: 10.3390/ijms20081963

134. Grzanna MW, Au RY, Au AY, Rashmir AM, Frondoza CG. Avocado/soybean unsaponifiables, glucosamine and chondroitin sulfate combination inhibits proinflammatory cox-2 expression and prostaglandin e2 production in tendon-derived cells. *J Med Food*. 2020;23:139-146. doi: 10.1089/jmf.2019.0022

135. Pudelko A, Wisowski G, Olczyk K, Kozma EM. The dual role of the glycosaminoglycan chondroitin-6-sulfate in the development, progression and metastasis of cancer. *FEBS J*. 2019;286:1815-1837. doi: 10.1111/febs.14748

136. Ornell KJ, Lozada D, Phan NV, Coburn JM. Controlling methacryloyl substitution of chondroitin sulfate: injectable hydrogels with tunable long-term drug release profiles. *J Mater Chem B*. 2019;7:2151-2161. doi: 10.1039/c8tb03020k

137. He Y, Sun M, Wang J, et al. Chondroitin sulfate microspheres anchored with drug-loaded liposomes play a dual antioxidant role in the treatment of osteoarthritis. *Acta Biomater*. 2022;151:512-527. doi: 10.1016/j.actbio.2022.07.052

138. Liu C, Fan L, Xing J, et al. Inhibition of astrocytic differentiation of transplanted neural stem cells by chondroitin sulfate methacrylate hydrogels for the repair of injured spinal cord. *Biomater Sci*. 2019;7:1995-2008. doi: 10.1039/c8bm01363b

139. Silva ED, Babo PS, Costa-Almeida R, et al. Multifunctional magnetic-responsive hydrogels to engineer tendon-to-bone interface. *Nanomedicine*. 2018;14:2375-2385. doi: 10.1016/j.nano.2017.06.002

140. Le HV, Le Cerf D. Colloidal polyelectrolyte complexes from hyaluronic acid: preparation and biomedical applications. *Small*. 2022;18:e2204283. doi: 10.1002/smll.202204283.

141. Xia C, Chen P, Mei S, et al. Photo-crosslinked HAMA hydrogel with cordycepin encapsulated chitosan microspheres for osteoarthritis treatment. *Oncotarget*. 2017;8: 2835-2849. doi: 10.18632/oncotarget.13748

142. Mouser VH, Abbadessa A, Levato R, et al. Development of a thermosensitive HAMA-containing bio-ink for the fabrication of composite cartilage repair constructs. *Biofabrication*. 2017;9:015026. doi: 10.1088/1758-5090/aa6265

143. Wei S, Wang Z, Liang X, et al. A composite hydrogel with antibacterial and promoted cell proliferation dual properties for healing of infected wounds. *Am J Transl Res*. 2023;15:4467-4486.

144. Xu Z, Liu G, Liu P, et al. Hyaluronic acid-based glucose-responsive antioxidant hydrogel platform for enhanced diabetic wound repair. *Acta Biomater*. 2022;147:147-157. doi: 10.1016/j.actbio.2022.05.047

145. Shen J, Chen A, Cai Z, et al. Exhausted local lactate accumulation via injectable nanozyme-functionalized hydrogel microsphere for inflammation relief and tissue regeneration. *Bioact Mater*. 2022;12:153-168. doi: 10.1016/j.bioactmat.2021.10.013

146. Shen X, Li S, Zhao X, et al. Dual-crosslinked regenerative hydrogel for sutureless long-term repair of corneal defect. *Bioact Mater*. 2023;20:434-448. doi: 10.1016/j.bioactmat.2022.06.006

147. Jung M, Han Y, Woo C, Ki CS. Pulmonary tissue-mimetic hydrogel niches for small cell lung cancer cell culture. *J Mater Chem B*. 2021;9:1858-1866. doi: 10.1039/d0tb02609c

148. Schuurmans CCL, Abbadessa A, Bengtson MA, et al. Complex coacervation-based loading and tunable release of a cationic protein from monodisperse glycosaminoglycan microgels. *Soft Matter*. 2018;14:6327-6341. doi: 10.1039/c8sm00686e

149. Wang L, Cao H, Jiang H, Fang Y, Jiang D. A novel 3D bio-printing "liver lobule" microtissue biosensor for the detection of AFB(1). *Food Res Int*. 2023;168:112778. doi: 10.1016/j.foodres.2023.112778

150. Huang YC, Liu ZH, Kuo CY, Chen JP. Photo-crosslinked hyaluronic acid/carboxymethyl cellulose composite hydrogel as a dural substitute to prevent post-surgical adhesion. *Int J Mol Sci*. 2022;23:6177. doi: 10.3390/ijms23116177

151. Yu Y, Xiao H, Tang G, et al. Biomimetic hydrogel derived from decellularized dermal matrix facilitates skin wounds healing. *Mater Today Bio*. 2023;21:100725. doi: 10.1016/j.mtbio.2023.100725

152. Liu F, Wang X, Li Y, et al. Dendrimer-modified gelatin methacrylate hydrogels carrying adipose-derived stromal/stem cells promote cartilage regeneration. *Stem Cell Res Ther*. 2022;13:26. doi: 10.1186/s13287-022-02705-6

153. Lim KS, Levato R, Costa PF, et al. Bio-resin for high resolution lithography-based biofabrication of complex cell-laden constructs. *Biofabrication*. 2018;10:034101. doi: 10.1088/1758-5090/aac00c

154. Simaan-Yameen H, Bar-Am O, Saar G, Seliktar D. Methacrylated fibrinogen hydrogels for 3D cell culture and delivery. *Acta Biomater*. 2023;164:94-110. doi: 10.1016/j.actbio.2023.03.046

155. Powers JG, Higham C, Broussard K, Phillips TJ. Wound healing and treating wounds: chronic wound care and management. *J Am Acad Dermatol*. 2016;74:607-625; quiz625-606. doi: 10.1016/j.jaad.2015.08.070

156. Wilkinson HN, Hardman MJ. Wound healing: cellular mechanisms and pathological outcomes. *Open Biol*. 2020;10:200223.

doi: 10.1098/rsob.200223

157. R Ibañez RI, do Amaral R, Reis RL, Marques AP, Murphy CM, O'Brien FJ. 3D-printed gelatin methacrylate scaffolds with controlled architecture and stiffness modulate the fibroblast phenotype towards dermal regeneration. *Polymers (Basel)*. 2021;13(15):2510. doi: 10.3390/polym13152510

158. Chen H, Ma X, Gao T, Zhao W, Xu T, Liu Z. Robot-assisted in situ bioprinting of gelatin methacrylate hydrogels with stem cells induces hair follicle-inclusive skin regeneration. *Biomed Pharmacother*. 2023;158:114140. doi: 10.1016/j.biopha.2022.114140

159. Jin R, Cui Y, Chen H, et al. Three-dimensional bioprinting of a full-thickness functional skin model using acellular dermal matrix and gelatin methacrylamide bioink. *Acta Biomater*. 2021;131:248-261. doi: 10.1016/j.actbio.2021.07.012

160. Zhang L, Yang G, Johnson BN, Jia X. Three-dimensional (3D) printed scaffold and material selection for bone repair. *Acta Biomater*. 2019;84:16-33. doi: 10.1016/j.actbio.2018.11.039

161. Ji C, Qiu M, Ruan H, et al. Transcriptome analysis revealed the symbiosis niche of 3d scaffolds to accelerate bone defect healing. *Adv Sci (Weinh)*. 2022;9:e2105194. doi: 10.1002/advs.202105194

162. Beheshtizadeh N, Farzin A, Rezvantalab S, et al. 3D printing of complicated GelMA-coated Alginate/Tri-calcium silicate scaffold for accelerated bone regeneration. *Int J Biol Macromol*. 2023;229:636-653. doi: 10.1016/j.ijbiomac.2022.12.267

163. Ma L, Wang X, Zhou Y, et al. Biomimetic Ti-6Al-4V alloy/gelatin methacrylate hybrid scaffold with enhanced osteogenic and angiogenic capabilities for large bone defect restoration. *Bioact Mater*. 2021;6:3437-3448. doi: 10.1016/j.bioactmat.2021.03.010

164. Ghahri T, Salehi Z, Aghajanpour S, et al. Development of osteon-like scaffold-cell construct by quadruple coaxial extrusion-based 3D bioprinting of nanocomposite hydrogel. *Biomater Adv*. 2023;145:213254. doi: 10.1016/j.bioadv.2022.213254

165. Alarcin E, Izbudak B, Yuce E, et al. Optimization of methacrylated gelatin /layered double hydroxides nanocomposite cell-laden hydrogel bioinks with high printability for 3D extrusion bioprinting. *J Biomed Mater Res A*. 2023;111:209-223. doi: 10.1002/jbm.a.37450

166. Nie R, Sun Y, Lv H, et al. 3D printing of MXene composite hydrogel scaffolds for photothermal antibacterial activity and bone regeneration in infected bone defect models. *Nanoscale*. 2022;14:8112-8129. doi: 10.1039/d2nr02176e

167. Wang L, Shen M, Hou Q, Wu Z, Xu J, Wang L. 3D printing of reduced glutathione grafted gelatine methacrylate hydrogel scaffold promotes diabetic bone regeneration by activating PI3K/Akt signaling pathway. *Int J Biol Macromol*. 2022;222:1175-1191. doi: 10.1016/j.ijbiomac.2022.09.236

168. Dutta SD, Ganguly K, Hexiu J, Randhawa A, Moniruzzaman M, Lim KT. A 3D bioprinted nanoengineered hydrogel with photoactivated drug delivery for tumor apoptosis and simultaneous bone regeneration via macrophage immunomodulation. *Macromol Biosci*. 2023;23(9):e2300096. doi: 10.1002/mabi.202300096

169. Liu G, Zhang B, Wan T, et al. A 3D-printed biphasic calcium phosphate scaffold loaded with platelet lysate/gelatin methacrylate to promote vascularization. *J Mater Chem B*. 2022;10:3138-3151. doi: 10.1039/d2tb00006g

170. Xu Z, Qi X, Bao M, et al. Biomineralization inspired 3D printed bioactive glass nanocomposite scaffolds orchestrate diabetic bone regeneration by remodeling micromilieu. *Bioact Mater*. 2023;25:239-255. doi: 10.1016/j.bioactmat.2023.01.024

171. Yang J, Fatima K, Zhou X, He C. Meticulously engineered three-dimensional-printed scaffold with microarchitecture and controlled peptide release for enhanced bone regeneration. *Biomater Transl*. 2024;5:69-83. doi: 10.12336/biomatertransl.2024.01.007

172. Li S, Li Z, Yang J, Ha Y, Zhou X, He C. Inhibition of sympathetic activation by delivering calcium channel blockers from a 3D printed scaffold to promote bone defect repair. *Adv Healthc Mater*. 2022;11:e2200785. doi: 10.1002/adhm.202200785

173. Zhang D, Fu Q, Fu H, Zeng J, Jia L, Chen M. 3D-bioprinted human lipoaspirate-derived cell-laden skin constructs for healing of full-thickness skin defects. *Int J Bioprint*. 2023;9:718. doi: 10.18063/ijb.718

174. Yu K, Huangfu H, Qin Q, et al. Application of bone marrow-derived macrophages combined with bone mesenchymal stem cells in dual-channel three-dimensional bioprinting scaffolds for early immune regulation and osteogenic induction in rat calvarial defects. *ACS Appl Mater Interfaces*. 2022;14:47052-47065. doi: 10.1021/acsami.2c13557

175. Yang Z, Cao F, Li H, et al. Microenvironmentally optimized 3D-printed TGFbeta-functionalized scaffolds facilitate endogenous cartilage regeneration in sheep. *Acta Biomater*. 2022;150:181-198. doi: 10.1016/j.actbio.2022.07.029

176. Xie X, Wu S, Mou S, Guo N, Wang Z, Sun J. Microtissue-based bioink as a chondrocyte microshelter for DLP bioprinting. *Adv Healthc Mater*. 2022;11:e2201877.

doi: 10.1002/adhm.202201877

177. Galliger Z, Vogt CD, Helms HR, Panoskaltsis-Mortari A. Extracellular matrix microparticles improve GelMA bioink resolution for 3D bioprinting at ambient temperature. *Macromol Mater Eng*. 2022;307(10):2200196. doi: 10.1002/mame.202200196

178. Zhu W, Cui H, Boualam B, et al. 3D bioprinting mesenchymal stem cell-laden construct with core-shell nanospheres for cartilage tissue engineering. *Nanotechnology*. 2018;29:185101. doi: 10.1088/1361-6528/aaafa1

179. Grogan SP, Chung PH, Soman P, et al. Digital micromirror device projection printing system for meniscus tissue engineering. *Acta Biomater*. 2013;9:7218-7226. doi: 10.1016/j.actbio.2013.03.020

180. Gong L, Li J, Zhang J, et al. An interleukin-4-loaded bi-layer 3D printed scaffold promotes osteochondral regeneration. *Acta Biomater*. 2020;117:246-260. doi: 10.1016/j.actbio.2020.09.039

181. Gao F, Xu Z, Liang Q, et al. Osteochondral regeneration with 3d-printed biodegradable high-strength supramolecular polymer reinforced-gelatin hydrogel scaffolds. *Adv Sci (Weinh)*. 2019;6:1900867. doi: 10.1002/advs.201900867

182. Deng C, Yang J, He H, et al. 3D bio-printed biphasic scaffolds with dual modification of silk fibroin for the integrated repair of osteochondral defects. *Biomater Sci*. 2021;9:4891-4903. doi: 10.1039/d1bm00535a

183. Chen P, Zheng L, Wang Y, et al. Desktop-stereolithography 3D printing of a radially oriented extracellular matrix/mesenchymal stem cell exosome bioink for osteochondral defect regeneration. *Theranostics*. 2019;9:2439-2459. doi: 10.7150/thno.31017

184. Jiang G, Li S, Yu K, et al. A 3D-printed PRP-GelMA hydrogel promotes osteochondral regeneration through M2 macrophage polarization in a rabbit model. *Acta Biomater*. 2021;128:150-162. doi: 10.1016/j.actbio.2021.04.010

185. Irmak G, Gumusderelioglu M. Patients- and tissue-specific bio-inks with photoactivated PRP and methacrylated gelatin for the fabrication of osteochondral constructs, *Mater Sci Eng C Mater Biol Appl*. 2021;125:112092. doi: 10.1016/j.msec.2021.112092

186. Zhang X, Yan Z, Guan G, et al. Polyethylene glycol diacrylate scaffold filled with cell-laden methacrylamide gelatin/alginate hydrogels used for cartilage repair. *J Biomater Appl*. 2022;36:1019-1032. doi: 10.1177/08853282211044853

187. Ding X, Gao J, Yu X, et al. 3D-printed porous scaffolds of hydrogels modified with TGF-beta1 binding peptides to promote in vivo cartilage regeneration and animal gait restoration. *ACS Appl Mater Interfaces*. 2022;14:15982-15995. doi: 10.1021/acsami.2c00761

188. Gao J, Ding X, Yu X, et al. Cell-free bilayered porous scaffolds for osteochondral regeneration fabricated by continuous 3D-printing using nascent physical hydrogel as ink. *Adv Healthc Mater*. 2021;10:e2001404. doi: 10.1002/adhm.202001404

189. Liu Y, Peng L, Li L, et al. 3D-bioprinted BMSC-laden biomimetic multiphasic scaffolds for efficient repair of osteochondral defects in an osteoarthritic rat model. *Biomaterials*. 2021;279:121216. doi: 10.1016/j.biomaterials.2021.121216

190. Martyniak K, Lokshina A, Cruz MA, Karimzadeh M, Kemp R, Kean TJ. Biomaterial composition and stiffness as decisive properties of 3D bioprinted constructs for type II collagen stimulation. *Acta Biomater*. 2022;152:221-234. doi: 10.1016/j.actbio.2022.08.058

191. Ege D, Hasirci V. Is 3D printing promising for osteochondral tissue regeneration? *ACS Appl Bio Mater*. 2023;6:1431-1444. doi: 10.1021/acsabm.3c00093

192. Zhou X, Tenaglio S, Esworthy T, et al. Three-dimensional printing biologically inspired DNA-based gradient scaffolds for cartilage tissue regeneration. *ACS Appl Mater Interfaces*. 2020;12:33219-33228. doi: 10.1021/acsami.0c07918

193. Guan J, Yuan FZ, Mao ZM, et al. Fabrication of 3D-printed interpenetrating hydrogel scaffolds for promoting chondrogenic differentiation. *Polymers (Basel)*. 2021;13(13):2146. doi: 10.3390/polym13132146

194. Xia H, Zhao D, Zhu H, et al. Lyophilized scaffolds fabricated from 3d-printed photocurable natural hydrogel for cartilage regeneration. *ACS Appl Mater Interfaces*. 2018;10:31704-31715. doi: 10.1021/acsami.8b10926

195. Wang M, Zhao J, Luo Y, et al. 3D contour printing of anatomically mimetic cartilage grafts with microfiber-reinforced double-network bioink. *Macromol Biosci*. 2022;22:e2200179. doi: 10.1002/mabi.202200179

196. Garcia-Lizarribar A, Fernandez-Garibay X, Velasco-Mallorqui F, Castano AG, Samitier J, Ramon-Azcon J. Composite biomaterials as long-lasting scaffolds for 3D bioprinting of highly aligned muscle tissue. *Macromol Biosci*. 2018;18:e1800167. doi: 10.1002/mabi.201800167.

197. Ajiteru O, Choi KY, Lim TH, et al. A digital light processing 3D printed magnetic bioreactor system using silk magnetic bioink. *Biofabrication*. 2021;13(3). doi: 10.1088/1758-5090/abfaee

198. Lee J, Lee H, Jin EJ, Ryu D, Kim GH. 3D bioprinting using a new photo-crosslinking method for muscle tissue restoration. *NPJ Regen Med*. 2023;8:18. doi: 10.1038/s41536-023-00292-5

199. Boularaoui S, Shanti A, Lanotte M, et al. Nanocomposite conductive bioinks based on low-concentration gelma and mxene nanosheets/gold nanoparticles providing enhanced printability of functional skeletal muscle tissues. *ACS Biomater Sci Eng*. 2021;7:5810-5822.
doi: 10.1021/acsbiomaterials.1c01193

200. Koffler J, Zhu W, Qu X, et al. Biomimetic 3D-printed scaffolds for spinal cord injury repair. *Nat Med*. 2019;25:263-269.
doi: 10.1038/s41591-018-0296-z

201. Poongodi R, Chen YL, Yang TH, et al. Bio-scaffolds as cell or exosome carriers for nerve injury repair. *Int J Mol Sci*. 2021;22(24):13347.
doi: 10.3390/ijms222413347

202. Liu X, Song S, Chen Z, et al. Release of O-GlcNAc transferase inhibitor promotes neuronal differentiation of neural stem cells in 3D bioprinted supramolecular hydrogel scaffold for spinal cord injury repair, *Acta Biomater*. 2022;151:148-162.
doi: 10.1016/j.actbio.2022.08.031

203. Hamid OA, Eltaher HM, Sottile V, Yang J. 3D bioprinting of a stem cell-laden, multi-material tubular composite: an approach for spinal cord repair. *Mater Sci Eng C Mater Biol Appl*. 2021;120:111707.
doi: 10.1016/j.msec.2020.111707

204. Izadifar M, Chapman D, Babyn P, Chen X, Kelly ME. UV-assisted 3D bioprinting of nanoreinforced hybrid cardiac patch for myocardial tissue engineering. *Tissue Eng Part C Methods*. 2018;24:74-88.
doi: 10.1089/ten.TEC.2017.0346

205. Bejleri D, Streeter BW, Nachlas ALY, et al. A bioprinted cardiac patch composed of cardiac-specific extracellular matrix and progenitor cells for heart repair. *Adv Healthc Mater*. 2018;7:e1800672.
doi: 10.1002/adhm.201800672

206. Brazhkina O, Park JH, Park HJ, et al. Designing a 3D printing based auxetic cardiac patch with hiPSC-CMs for heart repair. *J Cardiovasc Dev Dis*. 2021;8(12):172.
doi: 10.3390/jcdd8120172

207. Lee S, Sani ES, Spencer AR, et al. Human-recombinant-elastin-based bioinks for 3D bioprinting of vascularized soft tissues. *Adv Mater*. 2020;32:e2003915.
doi: 10.1002/adma.202003915

208. Wang H, Guo Y, Hu Y, et al. Ultrasound-controlled nano oxygen carriers enhancing cell viability in 3D GelMA hydrogel for the treatment of myocardial infarction. *Int J Biol Macromol*. 2023;244:125139.
doi: 10.1016/j.ijbiomac.2023.125139

209. Mehrotra S, Singh RD, Bandyopadhyay A, Janani G, Dey S, Mandal BB. Engineering microsphere-loaded non-mulberry silk-based 3D bioprinted vascularized cardiac patches with oxygen-releasing and immunomodulatory potential. *ACS Appl Mater Interfaces*. 2021;13:50744-50759.
doi: 10.1021/acsami.1c14118

210. Ma N, Cheung DY, Butcher JT. Incorporating nanocrystalline cellulose into a multifunctional hydrogel for heart valve tissue engineering applications. *J Biomed Mater Res A*. 2022; 110:76-91.
doi: 10.1002/jbm.a.37267

211. Nachlas ALY, Li S, Streeter BW, et al. A multilayered valve leaflet promotes cell-laden collagen type I production and aortic valve hemodynamics. *Biomaterials*. 2020;240:119838.
doi: 10.1016/j.biomaterials.2020.119838

212. Mazzocchi A, Devarasetty M, Huntwork R, Soker S, Skardal A. Optimization of collagen type I-hyaluronan hybrid bioink for 3D bioprinted liver microenvironments. *Biofabrication*. 2018;11:015003.
doi: 10.1088/1758-5090/aae543

213. S. J, S. Velayudhan, A.K. Pr, Biocompatibility evaluation of antioxidant cocktail loaded gelatin methacrylamide as bioink for extrusion-based 3D bioprinting, *Biomed Mater*. 2023;18(4).
doi: 10.1088/1748-605X/acd82f

214. Mao Q, Wang Y, Li Y, et al. Fabrication of liver microtissue with liver decellularized extracellular matrix (dECM) bioink by digital light processing (DLP) bioprinting. *Mater Sci Eng C Mater Biol Appl*. 2020;109:110625.
doi: 10.1016/j.msec.2020.110625

215. Wu Y, Wenger A, Golzar H, Tang XS. 3D bioprinting of bicellular liver lobule-mimetic structures via microextrusion of cellulose nanocrystal-incorporated shear-thinning bioink. Sci Rep. 2020;10:20648.
doi: 10.1038/s41598-020-77146-3

216. Jang MJ, Bae SK, Jung YS, et al. Enhanced wound healing using a 3D printed VEGF-mimicking peptide incorporated hydrogel patch in a pig model. *Biomed Mater*. 2021;16(4).
doi: 10.1088/1748-605X/abf1a8

217. Lam T, Dehne T, Kruger JP, et al. Photopolymerizable gelatin and hyaluronic acid for stereolithographic 3D bioprinting of tissue-engineered cartilage. *J Biomed Mater Res B Appl Biomater*. 2019:107:2649-2657.
doi: 10.1002/jbm.b.34354

218. Yin P, Su W, Li T, et al. A modular hydrogel bioink containing microsphere-embedded chondrocytes for 3D-printed multiscale composite scaffolds for cartilage repair. iScience 2023;26:107349.
doi: 10.1016/j.isci.2023.107349

219. Sang S, Mao X, Cao Y, et al. 3D Bioprinting Using Synovium-Derived MSC-Laden Photo-Cross-Linked ECM Bioink for Cartilage Regeneration. *ACS Appl Mater Interfaces*. 2023.
doi: 10.1021/acsami.2c19058

220. Chen YW, Lin YH, Lin TL, et al. 3D-biofabricated chondrocyte-laden decellularized extracellular matrix-contained gelatin methacrylate auxetic scaffolds under cyclic tensile stimulation for cartilage regeneration, *Biofabrication*. 2023;15(4).
doi: 10.1088/1758-5090/ace5e1

221. Daly AC, Critchley SE, Rencsok EM, Kelly DJ. A comparison of different bioinks for 3D bioprinting of fibrocartilage and hyaline cartilage. *Biofabrication*. 2016;8:045002. doi: 10.1088/1758-5090/8/4/045002

222. Yang Z, Zhao T, Gao C, et al. 3D-bioprinted difunctional scaffold for in situ cartilage regeneration based on aptamer-directed cell recruitment and growth factor-enhanced cell chondrogenesis. *ACS Appl Mater Interfaces*. 2021;13:23369-23383. doi: 10.1021/acsami.1c01844

223. De Moor L, Fernandez S, Vercruysse C, et al. Hybrid bioprinting of chondrogenically induced human mesenchymal stem cell spheroids. *Front Bioeng Biotechnol*. 2020;8:484. doi: 10.3389/fbioe.2020.00484

224. Wang B, Diaz-Payno PJ, Browe DC, et al. Affinity-bound growth factor within sulfated interpenetrating network bioinks for bioprinting cartilaginous tissues. *Acta Biomater*. 2021;128:130-142. doi: 10.1016/j.actbio.2021.04.016

225. Kuo CY, Wilson E, Fuson A, et al. Repair of tympanic membrane perforations with customized bioprinted ear grafts using Chinchilla models. *Tissue Eng Part A*. 2018;24:527-535. doi: 10.1089/ten.TEA.2017.0246

226. Hong H, Seo YB, Kim DY, et al. Digital light processing 3D printed silk fibroin hydrogel for cartilage tissue engineering. *Biomaterials*. 2020;232:119679. doi: 10.1016/j.biomaterials.2019.119679

227. Bandyopadhyay A, Mandal BB, Bhardwaj N. 3D bioprinting of photo-crosslinkable silk methacrylate (SilMA)-polyethylene glycol diacrylate (PEGDA) bioink for cartilage tissue engineering. *J Biomed Mater Res A*. 2022;110:884-898. doi: 10.1002/jbm.a.37336

228. Visscher DO, Lee H, van Zuijlen PPM, et al. A photo-crosslinkable cartilage-derived extracellular matrix bioink for auricular cartilage tissue engineering. *Acta Biomater*. 2021;121:193-203. doi: 10.1016/j.actbio.2020.11.029

229. Cao Y, Cheng P, Sang S, et al. Mesenchymal stem cells loaded on 3D-printed gradient poly(epsilon-caprolactone)/methacrylated alginate composite scaffolds for cartilage tissue engineering. *Regen Biomater*. 2021;8:rbab019. doi: 10.1093/rb/rbab019

230. Abbadessa A, Blokzijl MM, Mouser VH, et al. A thermo-responsive and photo-polymerizable chondroitin sulfate-based hydrogel for 3D printing applications. *Carbohydr Polym*. 2016;149:163-174. doi: 10.1016/j.carbpol.2016.04.080

231. Ma K, Zhao T, Yang L, et al. Application of robotic-assisted in situ 3D printing in cartilage regeneration with HAMA hydrogel: an in vivo study. *J Adv Res*. 2020;23:123-132. doi: 10.1016/j.jare.2020.01.010

232. Kesti M, Muller M, Becher J, et al. A versatile bioink for three-dimensional printing of cellular scaffolds based on thermally and photo-triggered tandem gelation. *Acta Biomater*. 2015;11:162-172. doi: 10.1016/j.actbio.2014.09.033

233. Zhang J, Tong D, Song H, et al. Osteoimmunity-regulating biomimetically hierarchical scaffold for augmented bone regeneration. *Adv Mater*. 2022;34:e2202044. doi: 10.1002/adma.202202044

234. Gao J, Li M, Cheng J, et al. 3D-printed GelMA/PEGDA/F127DA scaffolds for bone regeneration. *J Funct Biomater*. 2023;14:96. doi: 10.3390/jfb14020096

235. Leu Alexa R, Cucuruz A, Ghitulica CD, et al. 3D printable composite biomaterials based on GelMA and hydroxyapatite powders doped with cerium ions for bone tissue regeneration. *Int J Mol Sci*. 2022;23:1841. doi: 10.3390/ijms23031841

236. Li Z, Li S, Yang J, et al. 3D bioprinted gelatin/gellan gum-based scaffold with double-crosslinking network for vascularized bone regeneration. *Carbohydr Polym*. 2020;290:119469. doi: 10.1016/j.carbpol.2022.119469

237. Liu G, Chen J, Wang X, Liu Y, Ma Y, Tu X. Functionalized 3D-printed ST2/gelatin methacryloyl/polcaprolactone scaffolds for enhancing bone regeneration with vascularization. Int J Mol Sci. 2022;23(15):8347. doi: 10.3390/ijms23158347

238. Zhang X, Zhang H, Zhang Y, et al. 3D printed reduced graphene oxide-GelMA hybrid hydrogel scaffolds for potential neuralized bone regeneration. *J Mater Chem B*. 2023;11:1288-1301. doi: 10.1039/d2tb01979e

239. Xu C, Chang Y, Xu Y, et al. Silicon-phosphorus-nanosheets-integrated 3D-printable hydrogel as a bioactive and biodegradable scaffold for vascularized bone regeneration. *Adv Healthc Mater*. 2022;11:e2101911. doi: 10.1002/adhm.202101911

240. Jiang Y, Zhou D, Yang B. 3D bioprinted GelMA/GO composite induces osteoblastic differentiation. *J Biomater Appl*. 2022;37:527-537. doi: 10.1177/08853282221098235

241. Ashwin B, Abinaya B, Prasith TP, et al. 3D-poly (lactic acid) scaffolds coated with gelatin and mucic acid for bone tissue engineering. *Int J Biol Macromol.* 2020;162:523-532. doi: 10.1016/j.ijbiomac.2020.06.157

242. Tong L, Pu X, Liu Q, et al. Nanostructured 3D-printed hybrid scaffold accelerates bone regeneration by photointegrating nanohydroxyapatite. *Adv Sci (Weinh)*. 2023;10:e2300038. doi: 10.1002/advs.202300038

243. Pu X, Tong L, Wang X, et al. Bioinspired hydrogel anchoring 3DP GelMA/HAp scaffolds accelerates bone reconstruction. *ACS Appl Mater Interfaces*. 2022;14:20591-20602.

doi: 10.1021/acsami.1c25015

244. Leu Alexa R, Cucuruz A, Ghitulica CD, et al. 3D printed composite scaffolds of GelMA and hydroxyapatite nanopowders doped with Mg/Zn ions to evaluate the expression of genes and proteins of osteogenic markers. *Nanomaterials (Basel)*. 2022;12(19):3420. doi: 10.3390/nano12193420

245. Sun X, Yang J, Ma J, et al. Three-dimensional bioprinted BMSCs-laden highly adhesive artificial periosteum containing gelatin-dopamine and graphene oxide nanosheets promoting bone defect repair. *Biofabrication*. 2023;15(2). doi: 10.1088/1758-5090/acb73e

246. Dong L, Bu Z, Xiong Y, et al. Facile extrusion 3D printing of gelatine methacrylate/Laponite nanocomposite hydrogel with high concentration nanoclay for bone tissue regeneration. *Int J Biol Macromol*. 2021;188:72-81. doi: 10.1016/j.ijbiomac.2021.07.199

247. Yang X, Ma Y, Wang X, et al. A 3D-bioprinted functional module based on decellularized extracellular matrix bioink for periodontal regeneration. *Adv Sci (Weinh)*. 2023;10:e2205041. doi: 10.1002/advs.202205041

248. Ratheesh G, Vaquette C, Xiao Y. Patient-specific bone particles bioprinting for bone tissue engineering. *Adv Healthc Mater*. 2020;9(23):e2001323. doi: 10.1002/adhm.202001323

249. Alcala-Orozco CR, Mutreja I, Cui X, Hooper GJ, Lim KS, Woodfield TBF. Hybrid biofabrication of 3D osteoconductive constructs comprising Mg-based nanocomposites and cell-laden bioinks for bone repair. *Bone*. 2022;154:116198. doi: 10.1016/j.bone.2021.116198

250. Dutta SD, Ganguly K, Hexiu J, Randhawa A, Moniruzzaman M, Lim KT. A 3D bioprinted nanoengineered hydrogel with photoactivated drug delivery for tumor apoptosis and simultaneous bone regeneration via macrophage immunomodulation. *Macromol Biosci*. 2023;23:e2300096. doi: 10.1002/mabi.202300096

251. Tavares MT, Gaspar VM, Monteiro MV, S Farinha JP, Baleizão C, Mano JF. GelMA/bioactive silica nanocomposite bioinks for stem cell osteogenic differentiation. *Biofabrication*. 2021;13(3). doi: 10.1088/1758-5090/abdc86

252. Shahabipour F, Tavafoghi M, Aninwene GE, et al. Coaxial 3D bioprinting of tri-polymer scaffolds to improve the osteogenic and vasculogenic potential of cells in co-culture models. *J Biomed Mater Res A*. 2022;110:1077-1089. doi: 10.1002/jbm.a.37354

253. Lee SH, Kang MS, Jeon S, et al. 3D bioprinting of human mesenchymal stem cells-laden hydrogels incorporating MXene for spontaneous osteodifferentiation. *Heliyon*. 2023;9:e14490. doi: 10.1016/j.heliyon.2023.e14490

254. Ma Y, Ji Y, Zhong T, et al. Bioprinting-based PDLSC-ECM screening for in vivo repair of alveolar bone defect using cell-laden, injectable and photocrosslinkable hydrogels. *ACS Biomater Sci Eng*. 2017;3:3534-3545. doi: 10.1021/acsbiomaterials.7b00601

255. Miao G, Liang L, Li W, et al. 3D bioprinting of a bioactive composite scaffold for cell delivery in periodontal tissue regeneration. *Biomolecules*. 2023;13(7):1062. doi: 10.3390/biom13071062

256. Guo L, Chen H, Li Y, Zhou J, Chen J. Biocompatible scaffolds constructed by chondroitin sulfate microspheres conjugated 3D-printed frameworks for bone repair. *Carbohydr Polym*. 2023;299:120188. doi: 10.1016/j.carbpol.2022.120188

257. Su JJ, Lin CH, Chen H, Lee SY, Lin YM. Biofabrication of cell-laden gelatin methacryloyl hydrogels with incorporation of silanized hydroxyapatite by visible light projection. *Polymers (Basel)*. 2021;13(14):2354. doi: 10.3390/polym13142354

258. Bucciarelli A, Petretta M, Grigolo B, et al. Methacrylated silk fibroin additive manufacturing of shape memory constructs with possible application in bone regeneration. *Gels*. 2022;8(12):833. doi: 10.3390/gels8120833

259. Chang HK, Yang DH, Ha MY, et al. 3D printing of cell-laden visible light curable glycol chitosan bioink for bone tissue engineering. *Carbohydr Polym*. 2022;287:119328. doi: 10.1016/j.carbpol.2022.119328

260. Ferroni L, D'Amora U, Leo S, et al. PEEK and hyaluronan-based 3d printed structures: promising combination to improve bone regeneration. *Molecules*. 2022;27(24):8749. doi: 10.3390/molecules27248749

261. Kajave NS, Schmitt T, Patrawalla NY, Kishore V. Design-build-validate strategy to 3D print bioglass gradients for anterior cruciate ligament enthesis reconstruction. *Tissue Eng Part C Methods*. 2022;28:158-167. doi: 10.1089/ten.TEC.2022.0035

262. Qiu C, Sun Y, Li J, et al. Therapeutic effect of biomimetic scaffold loaded with human amniotic epithelial cell-derived neural-like cells for spinal cord injury. *Bioengineering (Basel)*. 2022;9(10):535. doi: 10.3390/bioengineering9100535

263. Kim KS, Joo HJ, Choi SC, et al. Transplantation of 3D bio-printed cardiac mesh improves cardiac function and vessel formation via ANGPT1/Tie2 pathway in rats with acute myocardial infarction. *Biofabrication*. 2021;13(4). doi: 10.1088/1758-5090/ac1e78

264. Hu Y, Jia Y, Wang H, et al. Low-intensity pulsed ultrasound promotes cell viability and inhibits apoptosis of H9C2 cardiomyocytes in 3D bioprinting scaffolds via PI3K-Akt and ERK1/2 pathways. *J Biomater Appl*. 2022; 37:402-414. doi: 10.1177/08853282221102669

265. Ainsworth MJ, Chirico N, de Ruijter M, et al. Convergence of melt electrowriting and extrusion-based bioprinting for vascular patterning of a myocardial construct. *Biofabrication*. 2023;15(3). doi: 10.1088/1758-5090/ace07f

266. Li H, Yin Y, Xiang Y, Liu H, Guo R. A novel 3D printing PCL/GelMA scaffold containing USPIO for MRI-guided bile duct repair. *Biomed Mater*. 2020;15:045004. doi: 10.1088/1748-605X/ab797a

267. Cui J, Wang H, Shi Q, Sun T, Huang Q, Fukuda T. Multicellular co-culture in three-dimensional gelatin methacryloyl hydrogels for liver tissue engineering. *Molecules*. 2019;24(9):1762. doi: 10.3390/molecules24091762

268. Cuvellier M, Rose S, Ezan F, et al. In vitrolong term differentiation and functionality of three-dimensional bioprinted primary human hepatocytes: application forin vivoengraftment. *Biofabrication*. 2022;14(3). doi: 10.1088/1758-5090/ac7825

269. Li T, Hou J, Wang L, et al. Bioprinted anisotropic scaffolds with fast stress relaxation bioink for engineering 3D skeletal muscle and repairing volumetric muscle loss. *Acta Biomater*. 2023;156:21-36. doi: 10.1016/j.actbio.2022.08.037

270. Hwangbo H, Lee H, Jin EJ, et al. Bio-printing of aligned GelMa-based cell-laden structure for muscle tissue regeneration. *Bioact Mater*. 2022;8:57-70. doi: 10.1016/j.bioactmat.2021.06.031

271. Tavares-Negrete JA, Pedroza-Gonzalez SC, Frias-Sanchez AI, et al. Supplementation of GelMA with minimally processed tissue promotes the formation of densely packed skeletal-muscle-like tissues. *ACS Biomater Sci Eng*. 2023;9:3462-3475. doi: 10.1021/acsbiomaterials.2c01521

272. Wang Y, Wang Q, Luo S, et al. 3D bioprinting of conductive hydrogel for enhanced myogenic differentiation. *Regen Biomater*. 2021;8:rbab035. doi: 10.1093/rb/rbab035

273. Choi KY, Ajiteru O, Hong H, et al. A digital light processing 3D-printed artificial skin model and full-thickness wound models using silk fibroin bioink. *Acta Biomater*. 2023;164:159-174. doi: 10.1016/j.actbio.2023.04.034

274. de Barros NR, Darabi MA, Ma X, et al. Enhanced maturation of 3D bioprinted skeletal muscle tissue constructs encapsulating soluble factor-releasing microparticles. *Macromol Biosci*. 2023;23(12):e2300276. doi: 10.1002/mabi.202300276

275. Liu G, Guo Q, Liu C, et al. Cytomodulin-10 modified GelMA hydrogel with kartogenin for in-situ osteochondral regeneration. *Acta Biomater*. 2023;169:317-333. doi: 10.1016/j.actbio.2023.08.013

276. Wang M, Li W, Luo Z, et al. A multifunctional micropore-forming bioink with enhanced anti-bacterial and anti-inflammatory properties. *Biofabrication*. 2022;14(2). doi: 10.1088/1758-5090/ac5936

277. Wang C, Wang M, Xu T, et al. Engineering bioactive self-healing antibacterial exosomes hydrogel for promoting chronic diabetic wound healing and complete skin regeneration. *Theranostics*. 2019;9:65-76. doi: 10.7150/thno.29766

278. Zhang FX, Liu P, Ding W, et al. Injectable mussel-inspired highly adhesive hydrogel with exosomes for endogenous cell recruitment and cartilage defect regeneration. *Biomaterials*. 2021;278:121169. doi: 10.1016/j.biomaterials.2021.121169

279. Fan L, Liu C, Chen X, et al. Exosomes-loaded electroconductive hydrogel synergistically promotes tissue repair after spinal cord injury via immunoregulation and enhancement of myelinated axon growth. *Adv Sci (Weinh)*. 2022;9:e2105586. doi: 10.1002/advs.202105586

280. Khayambashi P, Iyer J, Pillai S, Upadhyay A, Zhang Y, Tran SD. Hydrogel encapsulation of mesenchymal stem cells and their derived exosomes for tissue engineering. *Int J Mol Sci*. 2021;22(2):684. doi: 10.3390/ijms22020684

281. Born LJ, McLoughlin ST, Dutta D, et al. Sustained released of bioactive mesenchymal stromal cell-derived extracellular vesicles from 3D-printed gelatin methacrylate hydrogels. *J Biomed Mater Res A*. 2022;110:1190-1198. doi: 10.1002/jbm.a.37362

282. Hu H, Zhang H, Bu Z, et al. Small extracellular vesicles released from bioglass/hydrogel scaffold promote vascularized bone regeneration by transferring miR-23a-3p. *Int J Nanomedicine*. 2022;17:6201-6220. doi: 10.2147/IJN.S389471

283. Zhu B, Wang D, Pan H, et al. Three-in-one customized bioink for islet organoid: GelMA/ECM/PRP orchestrate pro-angiogenic and immunoregulatory function. *Colloids Surf B Biointerfaces*. 2023;221:113017. doi: 10.1016/j.colsurfb.2022.113017

284. Cao W, Peng S, Yao Y, et al. A nanofibrous membrane loaded with doxycycline and printed with conductive hydrogel strips promotes diabetic wound healing in vivo. *Acta Biomater*. 2022;152:60-73. doi: 10.1016/j.actbio.2022.08.048

285. Ferroni L, Gardin C, D'Amora U, et al. Exosomes of mesenchymal stem cells delivered from methacrylated hyaluronic acid patch improve the regenerative properties of endothelial and dermal cells. *Biomater Adv*. 2022;139:213000. doi: 10.1016/j.bioadv.2022.213000

286. Liu H, Wang Y, Cui K, Guo Y, Zhang X, Qin J. Advances in hydrogels in organoids and organs-on-a-chip. *Adv Mater*. 2019;31:e1902042. doi: 10.1002/adma.201902042

287. Cuvellier M, Ezan F, Oliveira H, et al. 3D culture of HepaRG cells in GelMa and its application to bioprinting of a multicellular hepatic model. *Biomaterials*. 2021;269:120611. doi: 10.1016/j.biomaterials.2020.120611

288. Bhise NS, Manoharan V, Massa S, et al. A liver-on-a-chip platform with bioprinted hepatic spheroids. *Biofabrication*. 2016;8:014101. doi: 10.1088/1758-5090/8/1/014101

289. Zhang YS, Davoudi F, Walch P, et al. Bioprinted thrombosis-on-a-chip. *Lab Chip*. 2016;16:4097-4105. doi: 10.1039/c6lc00380j

290. Liu S, Wang Z, Chen X, et al. Multiscale anisotropic scaffold integrating 3D printing and electrospinning techniques as a heart-on-a-chip platform for evaluating drug-induced cardiotoxicity. *Adv Healthc Mater*. 2023;12(24):e2300719. doi: 10.1002/adhm.202300719

291. van der Valk DC, van der Ven CFT, Blaser MC, et al. Engineering a 3D-bioprinted model of human heart valve disease using nanoindentation-based biomechanics. *Nanomaterials (Basel)*. 2018;8(5):296. doi: 10.3390/nano8050296

292. Sanchez-Salazar MG, Crespo-Lopez Oliver R, Ramos-Meizoso S, et al. 3D-printed tumor-on-chip for the culture of colorectal cancer microspheres: mass transport characterization and anti-cancer drug assays. *Bioengineering (Basel)*. 2023;10(5):554. doi: 10.3390/bioengineering10050554

293. Chen Z, Wang F, Zhang J, et al. Study on development of composite hydrogels with tunable structures and properties for tumor-on-a-chip research. *Front Bioeng Biotechnol*. 2020;8:611796. doi: 10.3389/fbioe.2020.611796

294. Makarcyzk MJ, Li ZA, Yu I, et al. Creation of a knee joint-on-a-chip for modeling joint diseases and testing drugs. *J Vis Exp*. 2023;(191):10.3791/64186. doi: 10.3791/64186

295. Vurat MT, Seker S, Lalegul-Ulker O, et al. Development of a multicellular 3D-bioprinted microtissue model of human periodontal ligament-alveolar bone biointerface: towards a pre-clinical model of periodontal diseases and personalized periodontal tissue engineering. *Genes Dis*. 2022;9:1008-1023. doi: 10.1016/j.gendis.2020.11.011

296. Kim W, Lee H, Lee J, et al. Efficient myotube formation in 3D bioprinted tissue construct by biochemical and topographical cues. *Biomaterials*. 2020;230:119632. doi: 10.1016/j.biomaterials.2019.119632

297. Ma X, Qu X, Zhu W, et al. Deterministically patterned biomimetic human iPSC-derived hepatic model via rapid 3D bioprinting. *Proc Natl Acad Sci U S A*. 2016;113:2206-2211. doi: 10.1073/pnas.1524510113

298. Gu L, Jiang S, Xu X, et al. Size- and density-dependent acoustic differential bioassembly of spatially-defined heterocellular architecture. *Biofabrication*. 2022;15(1). doi: 10.1088/1758-5090/aca79c

299. Wang D, Guo Y, Zhu J, et al. Hyaluronic acid methacrylate/pancreatic extracellular matrix as a potential 3D printing bioink for constructing islet organoids. *Acta Biomater*. 2023;165:86-101. doi: 10.1016/j.actbio.2022.06.036

300. Chen S, Tomov ML, Ning L, et al. Extrusion-based 3D bioprinting of adhesive tissue engineering scaffolds using hybrid functionalized hydrogel bioinks. *Adv Biol (Weinh)*. 2023;7:e2300124. doi: 10.1002/adbi.202300124

301. Li W, Wang M, Wang S, et al. An adhesive bioink toward biofabrication under wet conditions. *Small*. 2023;19(50):e2205078. doi: 10.1002/smll.202205078

302. Wei K, Sun J, Gao Q, et al. 3D "honeycomb" cell/carbon nanofiber/gelatin methacryloyl (GelMA) modified screen-printed electrode for electrochemical assessment of the combined toxicity of deoxynivalenol family mycotoxins. *Bioelectrochemistry*. 2021;139:107743. doi: 10.1016/j.bioelechem.2021.107743

303. Wan W, Li Z, Wang X, Tian F, Yang J. Surface-fabrication of fluorescent hydroxyapatite for cancer cell imaging and bio-printing applications. *Biosensors (Basel)*. 2022;12(6):419. doi: 10.3390/bios12060419

304. Liu S, Wang Z, Chen X, et al. Multiscale anisotropic scaffold integrating 3D printing and electrospinning techniques as a heart-on-a-chip platform for evaluating drug-induced cardiotoxicity. *Adv Healthc Mater*. 2023;12:e2300719. doi: 10.1002/adhm.202300719

305. Liu J, Miller K, Ma X, et al. Direct 3D bioprinting of cardiac micro-tissues mimicking native myocardium. *Biomaterials*. 2020;256:120204. doi: 10.1016/j.biomaterials.2020.120204

306. Wang J, Wu Y, Li G, et al. Engineering large-scale self-mineralizing bone organoids with bone matrix-inspired hydroxyapatite hybrid bioinks. *Adv Mater*. 2024;36:e2309875. doi: 10.1002/adma.202309875

307. O'Donnell BT, Al-Ghadban S, Ives CJ, et al. Adipose tissue-derived stem cells retain their adipocyte differentiation potential in three-dimensional hydrogels and bioreactors (dagger). *Biomolecules*. 2020;10:1070. doi: 10.3390/biom10071070

308. Nothdurfter D, Ploner C, Coraca-Huber DC, et al. 3D bioprinted, vascularized neuroblastoma tumor environment in fluidic chip devices for precision medicine drug testing. *Biofabrication*. 2022;14(3). doi: 10.1088/1758-5090/ac5fb7.

309. Bhattacharyya A, Ham HW, Sonh J, et al. 3D bioprinting of complex tissue scaffolds with in situ homogeneously mixed alginate-chitosan-kaolin bioink using advanced portable biopen. *Carbohydr Polym*. 2023;317:121046. doi: 10.1016/j.carbpol.2023.121046

ACCSCIENCE PUBLISHING

International Journal of Bioprinting

REVIEW ARTICLE

The application prospects of 4D printing tissue engineering materials in oral bone regeneration

Wenlu Song[1,2,3,4], Weihua Huang[2,4,5,6], Junzhuo Qu[1,3], Chujie Xiao[7], Huinan Yin[6], Xiangzhen Liu[1,3]*, and Weikang Xu[2,4,8]*

[1]Department of Stomatology, The Sixth Affiliated Hospital, Sun Yat-sen University, Guangzhou, Guangdong, China

[2]Institute of Biological and Medical Engineering, Guangdong Academy of Sciences, Guangzhou, Guangdong, China

[3]Biomedical Innovation Center, The Sixth Affiliated Hospital, Sun Yat-sen University, Guangzhou, Guangdong, China

[4]Guangdong Key Lab of Medical Electronic Instruments and Polymer Material Products, National Engineering Research Center for Healthcare Devices, Guangdong Institute of Medical Instruments, Guangzhou, Guangdong, China

[5]Department of Orthopaedic Surgery, Affiliated Qingyuan Hospital, Guangzhou Medical University, Qingyuan People's Hospital, Qingyuan, Guangdong, China

[6]Department of Orthopaedic Surgery, The Second Affiliated Hospital of Guangzhou Medical University, Guangzhou, Guangdong, China

[7]School of Biology and Biological Engineering, South China University of Technology, Guangzhou, Guangdong, China

[8]Guangdong Chinese Medicine Intelligent Diagnosis and Treatment Engineering Technology Research Center, Guangzhou, Guangdong, China

***Corresponding authors:**
Weikang Xu
(weikangxu1987@hotmail.com)

Xiangzhen Liu
(lxzh3@mail2.sysu.edu.cn)

(This article belongs to the Special Issue: *Bioprinting of Dental Tissues and Materials*)

Citation: Song W, Huang W, Qu J, et al. The application prospects of 4D printing tissue engineering materials in oral bone regeneration. *Int J Bioprint*. 2025;11(1):139-191. doi: 10.36922/ijb.4450

Received: August 6, 2024
Revised: September 30, 2024
Accepted: October 1, 2024
Published Online: October 4, 2024

Copyright: © 2024 Author(s). This is an Open Access article distributed under the terms of the Creative Commons Attribution License, permitting distribution, and reproduction in any medium, provided the original work is properly cited.

Publisher's Note: AccScience Publishing remains neutral with regard to jurisdictional claims in published maps and institutional affiliations.

Abstract

Researchers have developed smart shape-memory materials that adapt their structure or function to external stimuli. The demand for dynamic oral bone tissue repair is driven by continuous changes in bone and surrounding tissues during the repair process, such as tooth growth, movement, reconstruction of oral soft tissues, and skeletal differences in alveolar and craniofacial bones. These changes challenge the mechanical stability of bone implants and the precision of printing. Consequently, 4D printing technology introduces "time," allowing pre-programmed changes in material shape or functionality, which enables scaffolds to respond to complex oral environments intelligently, achieving dynamic repair of bone and surrounding tissues. Despite its theoretical benefits in oral bone tissue engineering, the study and use of 4D printing technology is still in its infancy. This review explores the recent advances in 4D printing in dentistry, discussing skeletal structure, etiology of bone defects, and bone repair mechanisms. It also provides an overview of the materials, cells, and growth factors used in 4D printing bone tissue engineering. Thus, by reviewing existing studies, this review provides valuable insights for the future development of 4D printing technology in oral bone tissue engineering.

Keywords: 4D printing; Smart responsive materials; Bone tissue engineering; Bone regeneration; Dentistry

1. Introduction

The musculoskeletal system consists of bones, connective tissues, joints, and muscles, which enable complex interaction and effective movement. Aside from providing mechanical and structural support, bones serve as reservoirs for growth factors (GFs) and cells, storing calcium and phosphate salts, maintaining mineral homeostasis, and safeguarding internal organs and structures.[1] However, due to diseases, traumas, or bone defects, the skeletal structure may incur damage beyond its self-repair capacity.

Autologous bone grafting is currently the preferred method for repairing defective bone due to its exceptional biocompatibility, lack of immune response, and impressive osteoinductive and osteoconductive properties. However, it has several limitations, including the potential risks related to donor site surgery, postoperative bone resorption, and complications from infection. Allogeneic bone grafts can also be utilized for cancellous or structural bone transplantation, with performance closely resembling autologous bone repair, serving as an alternative option. Nonetheless, they are challenged by immune rejection, disease transmission, and inadequate supply.[2] A range of biomaterial scaffolds, regenerative cells, and GFs that direct morphogenesis are used in bone tissue engineering to repair, regenerate, and restore abnormalities in bone tissue. Tissue engineering has demonstrated effective repair outcomes in the laboratory and preclinical settings.[3,4] Osteoblasts, mesenchymal stem cells (MSCs), vascular cells, and inflammatory cells are involved in the multistep process of repairing and regenerating bone tissues. Present strategies for promoting osteogenesis emphasize osteoinduction, frequently utilizing GFs, like BMP-2 and BMP-7, to enhance self-renewal and maintain homeostasis and differentiation. However, the involvement of numerous cell factors in the osteogenic process is extensive, and the complexity of bone morphogenetic proteins (BMPs) and other cell factor signaling pathways warrants further research.[5] Meanwhile, the potential for the proliferation of bone marrow MSCs (BMSCs) limits their use in bone defect repair treatment. Meanwhile, prolonged separation and in vitro cultivation or the aging or disease of donor patients can impair the osteogenic properties of BMSCs. These will lead to a decrease in the proliferation potential of BMSCs, thus limiting their use in bone defect repair treatment.[6] Hence, it is crucial to thoroughly assess the bone defect's location and size, the surrounding tissues, and the patient's overall health for personalized and accurate treatment, which in turn leads to more effective clinical bone repair.

Conventional 3D printing methods only consider the initial static state of the printed structure and are limited to non-intelligent materials in material selection. These materials cannot dynamically adjust their shape and function according to environmental changes, so the resulting samples cannot change shape over time to better simulate the dynamic behavior of natural bone tissue (Figure 1). This results in 3D-printed bone scaffolds lacking the necessary mechanical strength and elastic modulus to match natural bone tissue, especially in load-bearing areas, which can cause the scaffold to disintegrate or deform prematurely after implantation. 3D printing technology manufactures complex structures, but the accuracy is still limited at the microscopic level, particularly regarding pore size, shape, and distribution. This affects cell attachment, growth, and functionalization and is not conducive to tissue regeneration. Traditional 3D printing is unable to keep pace with medical advancements due to our growing understanding of dynamic biological settings and the rising demand for precision treatment.[5,7] With advancements in programmable functional biomaterials, 4D printing technology is gaining traction in bone tissue engineering. Skylar Tibbits announced the notion of 4D printing at the 2013 technology, entertainment, design (TED) TALKs conference,[8] extending 3D printing by incorporating a temporal dimension. This allows printed artificial bones or orthopedic implants to gradually alter their form or function in reaction to specific stimuli.[9-11] Compared with 3D printing, 4D printing technology uses smart materials that can respond to external stimuli (temperature, humidity, pH, light, etc.). These materials can dynamically adjust their shape and function in response to environmental changes and mechanical stress after implantation, inducing self-reinforcement or softening. This capability helps reduce the disintegration and deformation of materials after implantation, prolongs the scaffold's service life, and better simulates the dynamic behavior of natural bone tissue. This dynamic response can also provide technical support for the targeted or timed release of GFs or other bioactive molecules. 4D-printed scaffolds can self-adjust and optimize their structure over time after printing. For example, 4D-printed scaffolds can automatically change their shape or pore structure under certain conditions to better support cell growth and tissue reconstruction. This self-regulation creates a microenvironment with better compatibility between the scaffold and cells. In 2014, Ge et al.[12] brought 4D printing to reality by performing active origami through this technology. In 2016, Miao et al.[13] created biomedical scaffolds with notable shape-memory properties by polymerizing epoxide acrylates using 4D printing technology. With 4D printing, Bodaghi et al.[14] created triple shape-memory polymers (SMPs) for biomedical devices. Likewise, 4D-printed components were used to repair spinal bones.[15] This technology opens new possibilities for manufacturing custom implants. The field of orthopedics anticipates the use of 4D-printed

scaffolds, with predetermined shapes and functions, to progressively conform to the shape of bone defects in response to stimuli, i.e., undergo functional changes after printing, resembling the natural healing process and promoting dynamic bone remodeling. Furthermore, the original shape of scaffolds produced by 4D printing can be introduced into the host through minimally invasive methods.[16] Upon receiving appropriate stimuli, they gradually assemble into a complex hierarchical structure that resembles natural bone tissue, attracting new osteoblasts, inducing the differentiation of resident cells, and regulating cellular functions post-implantation. The capacity of these structures to modify and undergo functional maturation offers significant advantages for bone tissue engineering. 4D printing technology is widely used in other tissue engineering applications besides bone tissue engineering. For example, Lin et al.[17] designed and fabricated a cardiac implant, i.e., a 4D-printed absorbable left atrial appendage occluder (LAAO), as an alternative to Nitinol occluders that can be remotely driven by a magnetic field to perform left atrial appendage occlusion via a catheter. Researchers have also utilized 4D printing technology to create T-shaped vascular bifurcation with an inner surface inoculated with endothelial cells and an expandable diameter. This is achieved by precisely controlling the hydrogel structural parameters and shape transformations, offering a novel approach to creating biomimetic vascular grafts with different geometries.[18] 4D printing shares technological and procedural similarities with 3D printing, such as computer-aided design (CAD) modeling and the use of a 3D printer.[19-21] The key distinctions lie in the design of the selected shape-memory materials (SMMs) and the functional structures, both crucial for shape and function transformations.[22-24] Pre-programming smart material structures allow 4D-printed objects to react to certain stimuli and alter over time, following predetermined protocols.

Shape-memory materials (SMMs), such as shape-memory alloys (SMAs), shape-memory ceramics (SMCs), SMPs, and shape-memory hydrogels (SMHs), play a key role in 4D printing. These materials exhibit bionic qualities, including reasonable mechanical strength and concentrated homeostatic regulation for the bone microenvironment in bone tissue engineering, along with rapid response, good recovery, ease of manufacture, and high repeatability. Consequently, SMMs are increasingly utilized in the creation of bone scaffolds as potentially stimulus-responsive, programmable biomaterials.

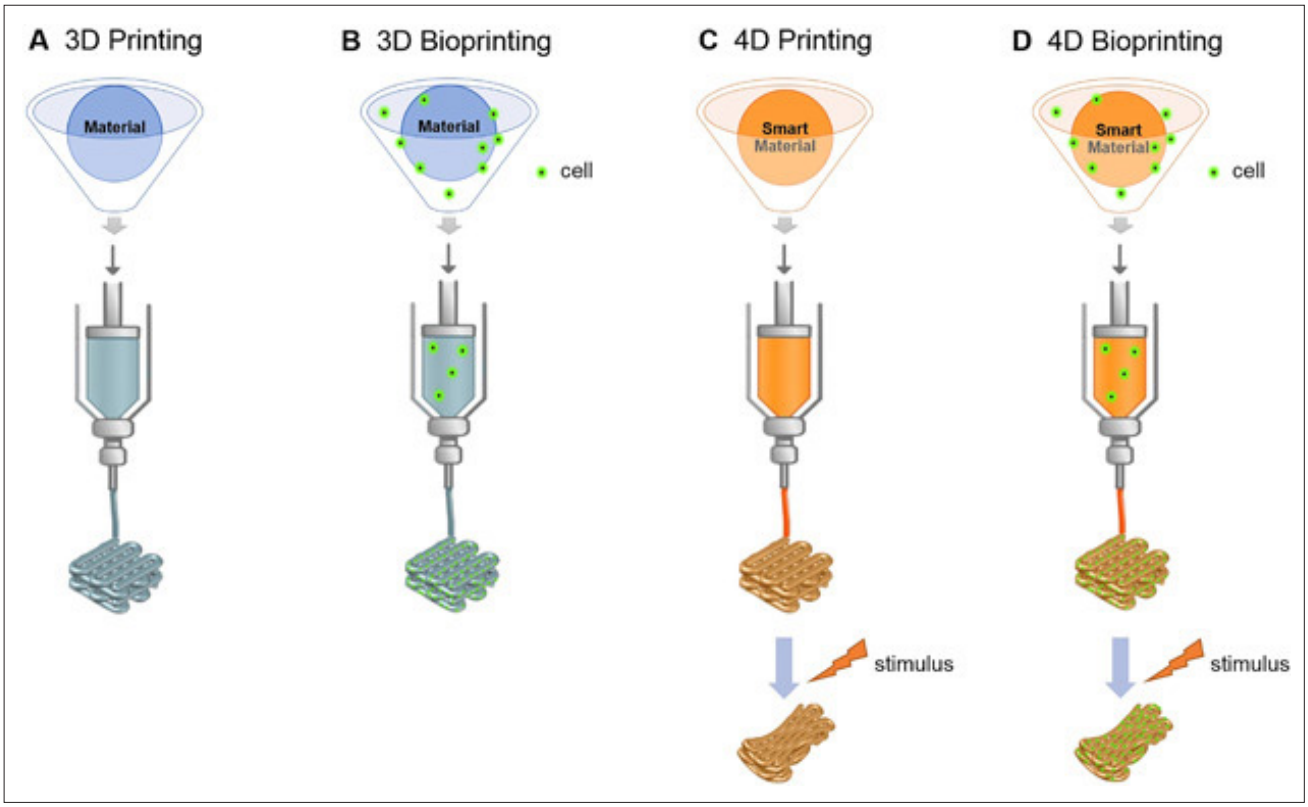

Figure 1. Schematic of different printing technologies (3D printing [A], 3D bioprinting [B], 4D printing [C], and 4D bioprinting [D]) using conventional and smart materials; cells are only involved in bioprinting technologies. Adapted with permission from Ashammakhi et al.[25]

In oral bone tissue, the bones and surrounding tissues are constantly changing, such as tooth growth, movement, reconstruction of oral soft tissues, and skeletal differences between alveolar and craniofacial bones. 4D printing technology can pre-program materials to ensure that the scaffold can intelligently respond to the complex oral environment through changes in shape or function, achieving dynamic repair of bones and surrounding tissues. Despite the theoretical benefits of 4D printing technology in oral bone tissue engineering, its research and use are still in their infancy. This review explores the latest advances in 4D printing in dentistry and discusses bone structure, the etiology of bone defects, and bone repair mechanisms. The review also outlines the materials, cells, and GFs used in 4D printing for bone tissue engineering. By examining existing research, this review provides valuable insights into the future development of 4D printing technology in oral bone tissue engineering.

2. Bone defect and repair

2.1. Bone defect

Bone defects and fractures are frequently encountered clinically, arising from intrinsic or extrinsic factors, such as autoimmune diseases, degenerative diseases, bone cancer, hereditary conditions, sports injuries, congenital anomalies, or traffic accidents.[26] Various conditions, including osteogenesis imperfecta, rheumatoid arthritis, hyperparathyroidism, hyperprolactinemia, osteomyeloma, and osteosarcoma, as well as medications like chemotherapeutics, immunosuppressants, glucocorticoids, and antipsychotics, can influence bone mass.[27,28] Based on the extent of bone loss, defects in bones are categorized as either segmental (major bone loss) or cavitary (minor bone loss).[1] The primary focus in treating bone defects is to promote bone regeneration, with approaches varying according to the type and cause of the defect. This includes medication[29-31] and bone grafting surgical interventions.[32] At present, to completely repair fractures and bone defects due to the above factors, especially the regeneration of large bone defects, bone grafting is still required.[33-36] Bone grafting is the second most common tissue transplantation procedure in the clinical setting.[36] In bone grafting, autologous iliac bone fragments are still used as the gold standard for grafts, owing to their reticular structure, presence of osteoblasts, osteogenesis-promoting cytokines, and favorable osteogenic conditions, as using an autologous donor eliminates the risk of immune rejection. However, autologous bone grafting is limited by the need for donor region surgery, insufficient donor volume, and complications such as bone resorption, tissue mismatch, and infection due to insufficient blood supply post-surgery. As a substitute for autologous bone, allograft bone is also widely used, but it is equally constrained by problems such as immune rejection and disease transmission.[2] Bone graft substitutes support osteoblast osteogenesis with osteogenic tissue architecture, vascularization, and mechanical properties.[37] Designing bone graft materials with properties superior to those of autogenous and allogeneic bone is a key focus in current and future research. The absence of bone extracellular matrix (ECM) in large segmental bone defects often makes it challenging to achieve rapid and effective healing. Therefore, when the native ECM is absent, the bionic ECM of bone can be temporarily established by tissue engineering.[38]

2.2. Bone repair

2.2.1. Bone structure and function

Bone is a highly ordered composite substance consisting of 50–70% inorganic components, 20–40% organic components, 5–10% water, and 3% lipids.[39] All biological tissues, including bone tissue, are made up of an ECM that is rich in biologically active chemicals that surround distinctive cells. ECM can be viewed as a scaffold in bone tissue engineering and is composed of 60% inorganic and 40% organic components with the main organic components including collagen (Col), glycoproteins, proteoglycans, and hyaluronic acid.[40,41] Hydroxyapatite, the primary inorganic component, consists of calcium phosphate crystals, which provide support and stiffness while serving as a calcium ion reservoir.[41-43] Bone ECM is crucial in regulating cell activity in bone tissue through various molecules.

Bone tissue cell types (Figure 2) include BMSCs, bone lining cells, osteocytes, bone marrow-derived macrophages, osteoblasts, osteoclasts, and bone progenitor cells.[1,41] Osteoblasts originate from MSCs, bone lining cells, or chondrocytes and are essential for bone formation. *Runx2* is a key gene for osteoblast differentiation, and its activation via the Wnt/β-catenin pathway is essential for osteoblast function and bone formation.[1] *Runx2* activation increases the expression of osteoblast-related genes.[44] Additionally, macrophage colony-stimulating factor (MCSF), osteoclastogenesis inhibitory factor (OPG), and receptor activator of nuclear factor-κ B ligand (RANKL) are produced to promote osteoblast differentiation.[28] During osteogenic differentiation, a pool of osteoblast progenitors expressing *Runx2* and *COL1A1* forms, leading to a proliferative stage where progenitors exhibit alkaline phosphatase (ALP) activity (i.e., classified as pre-osteoblasts).[1] Apoptosis or differentiation into osteocytes or bone-lining cells are the two possible outcomes for mature osteoblasts.[1]

Osteoblasts communicate through cell surface protrusions and promote bone remodeling by sensing the local mechanical environment while stimulating osteoclastogenesis and regulating the coordination of osteoblasts and osteoclasts. Numerous juvenile cells are present in the surrounding progenitor cell pools, and osteoblasts can attract these immature cells in the pools and develop into mature osteoblasts.[45] They also express sclerostin, a negative regulator of bone formation.[46] Bone marrow-derived macrophages, or intraosseous macrophages, stimulate osteoclastogenesis and matrix mineralization by secreting oncostatin M.[45] Bone lining cells, which are flat and inactive osteoblasts, cover areas of the bone's surface that do not undergo resorption or creation. Although their specific function is unknown, bone lining cells can differentiate into osteoblasts and release RANKL and OPG, which govern osteoclast differentiation.[1] Hematopoietic stem cells give rise to multinucleated, terminally differentiated cells called osteoclasts. Research has demonstrated that the RANKL/RANK/OPG system is crucial for osteoclastogenesis.[1] Several bone resorption disorders, including osteoporosis and alveolar bone resorption, can result from an abnormally high increase in osteoclast activity during bone remodeling. Bone cells can perform distinct functions during normal bone formation and resorption, but they work in coordination and are important for maintaining homeostasis in the bone remodeling process.

2.2.2. Bone remodeling and regeneration

Bone remodeling and regeneration is a continuous and highly complex process. It involves alterations to the volume and structure of bones, with bone resorption and formation occurring at different sites in different individuals. In normal individuals, bone remodeling maintains skeletal integrity through homeostasis. In the human skeleton, there are approximately 1 million remodeling sites, replacing approximately 10% of adult bone each year.[28] In bone regeneration, the collaboration between osteoblasts and osteoclasts is crucial. The process starts with bone tissue responding to changes in the local mechanical environment. Osteoblasts initiate bone formation by secreting an osteoid matrix, which undergoes mineralization[28] and is tightly regulated by various cytokines.[47] Osteocytes detect minor injuries

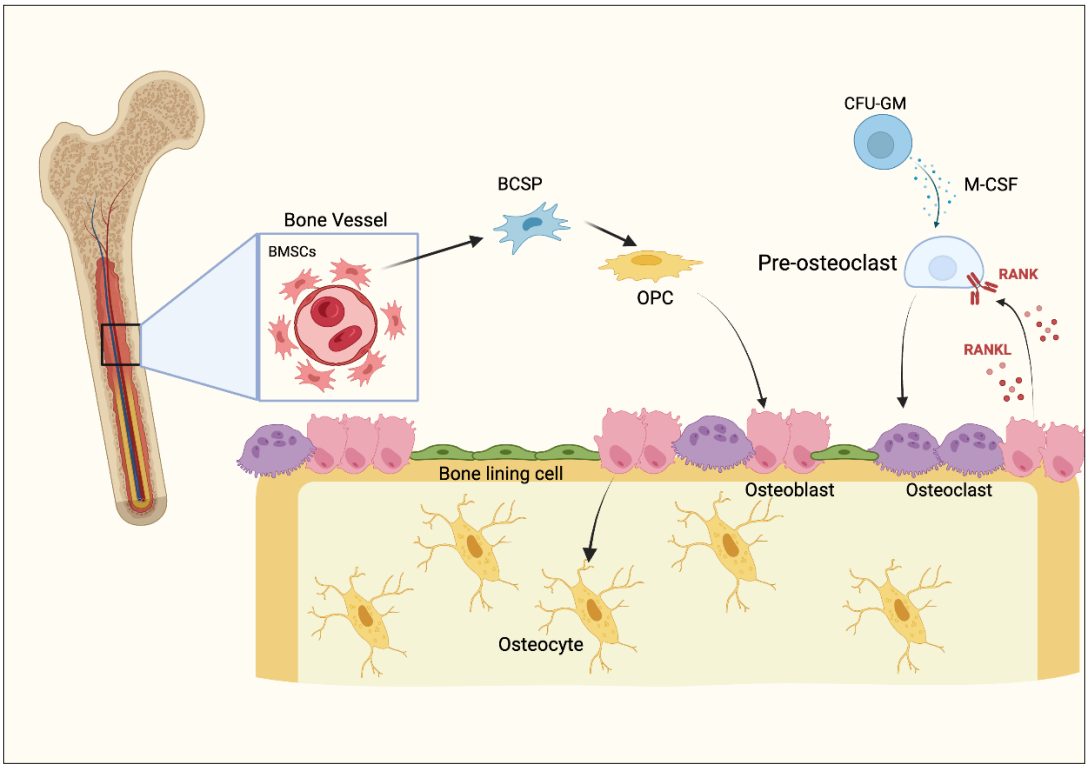

Figure 2. Bone tissue cell types. RANKL and M-CSF activate colony-forming unit granulocyte-macrophage (CFU-GM) precursors that differentiate from osteoclasts. Osteoblasts, bone lining cells, and osteoclasts are present on the bone surface. Osteocytes are present in the bone matrix. Abbreviations: BCSP: Bone, cartilage, and stromal progenitor cells; BMSCs: Bone marrow mesenchymal stem cells; OPC: bone progenitor cells; RANK: Receptor activator of nuclear factor kappa-β; RANKL: Receptor activator of nuclear factor-κB-ligand; M-CSF: Macrophage colony-stimulating factor. Created by BioRender.com.

to the bone, prompting osteoblasts to recruit osteoclast precursors to the injury site, where osteoclasts resorb old and damaged bone[28] by secreting H^+ ions and proteases, leading to acidification and protein hydrolysis of the Col-rich bone matrix and hydroxyapatite.[48,49] A transition period follows, where bone resorption and new formation occur, culminating in osteoblasts forming new bone.[1] Disruptions in the balance between osteoclast and osteoblast activity during bone regeneration can result in decreased bone mineral density, increased risk of fractures, and bone defects.[28]

Despite bone tissue possessing regenerative and self-repair capabilities for bone defects beyond a certain size, significant bone defects cannot undergo self-repair. Non-bone tissues, such as fibrous tissue, may infiltrate the defect site. Furthermore, the need for the regeneration and repair of significant bone defects has increased as bone abnormalities caused by trauma, tumor excision, and accidents are becoming more common.[50]

Examining the bone structure reveals that coordination among different cell types is essential for maintaining homeostasis in the bone regeneration process. The mechanisms of bone repair and remodeling are elucidated, emphasizing the synergistic roles of osteoblasts and osteoclasts. The continuous nature of bone regeneration and alterations in the mechanical environment is critical for osteoblasts to initiate bone formation.[51]

Nonetheless, this section has provided important insights into bone tissue biology and establishes the osteological foundation for engineering bone tissue for repair purposes.

3. 4D printing materials for bone tissue engineering

The dynamic modulation of matrix microstructure is an effective strategy for controlling the fate of stem cells in tissue engineering and cell differentiation.[52,53] 3D printing can mimic natural bone tissue by personalized modeling and layered fabrication of different-sized (nano and micron) pores to improve cell adhesion, migration, differentiation, ECM secretion, mineral deposition, and vascularization.[54] However, 3D-printed materials exist only in a static state and cannot intelligently deform over time to fully adapt to the dynamically changing structure of natural bone tissue,[10,55] indicating the limitations of 3D printing for bone repair. Printed bioscaffolds need to mimic the osteoconductive, osteoinductive, osteogenic, and vascularization properties of bone.[4] Tissue-engineered osteogenesis typically attempts to initiate and enhance the innate ability of cells to form tissues, thus creating a 3D structural ECM, where multiple cells form a 3D microenvironment similar to the natural developmental state *in vivo*. This environment controls how cells adhere, proliferate, differentiate, and respond to GFs, facilitating the restoration of bone tissue's natural developmental ability *in vivo*.[40] Optimal biomaterial scaffolds for bone regeneration should exhibit osteoconductive characteristics, i.e., nourish osteoblasts, promote blood vessel growth, and release GFs that facilitate the differentiation of MSCs and the mineralization of bone matrix. *In vitro*, osteogenic differentiation is based on a variety of factors, including scaffold design, novel technologies, signaling molecule integration, and high-quality biomaterials.[56,57] In contrast, scaffolds fabricated by 4D printing can be made into temporary shapes that undergo dynamic deformation in response to specific stimuli to adapt to the complex physiological environment inside the bone defect. This process forms complex layers similar to the ECM in bone tissue engineering, thus mimicking the natural bone tissue environment to form bone tissue.[58,59] The three main components constituting bone tissue engineering – biomaterial scaffolds, cells, and GFs – are discussed in this review. These components are combined through various fabrication methods to build 4D-printed bioscaffolds that modulate composition and structure to facilitate cellular interactions and directed bone repair.[13,60]

3.1. Scaffold materials

Biomaterial scaffolds are an important part of bone tissue engineering for osteogenesis that are essentially made of natural or synthetic materials. The potential of different biomaterials – including metals, ceramics, polymers, and hydrogels – to enhance osseointegration and bone repair has been explored. These materials are valuable in biomedicine, as they aid in restoring normal bone functions and repairing soft tissues and organs. 4D printing SMMs not only have self-assembling and -repairing characteristics but also include shape changes that are directly related to the functionalization of the programs. Smart biomaterials and living cells have been recognized as the most promising bioinks for 4D printing.[61,62] Their advantages include the possibility of time control,[63,64] improved product adaptability for ease of application,[65,66] and the possibility of minimally invasive procedures, which could reduce secondary trauma and improve patient compliance.[67-72] Herein, we discuss the different types of smart materials suitable for 4D printing.

3.1.1. Smart shape-memory materials

Smart SMMs exhibit a shape-memory effect, allowing them to alter their size, shape, and physical strength in response to external stimuli.[73] They can be categorized as SMPs, SMHs, SMAs, and SMCs.[39] An ideal programmable SMM should exhibit a rapid response, high recovery rate, self-healing

abilities, ease of manufacture, and strong reproducibility. In bone tissue engineering, there is a significant demand for smart materials due to their biomimetic nature. Likewise, these materials offer adequate mechanical strength, multi-anisotropic properties, and homeostatic regulation to mimic the bone microenvironment.[74] At present, SMPs and SMHs are widely utilized in 4D printing due to their tunable mechanical properties and desirable biodegradability.[74] Similarly, SMAs and SMCs are also employed in bone and cartilage tissue engineering for their mechanical strength (Table 1).[75]

3.1.1.1. Shape-memory polymers

Shape-memory polymers (SMPs) are lightweight and biodegradable, with good shape-memory recovery, simple stimulation conditions, and low to non-toxic cytotoxicity, making them widely used in 4D printing of bone repair materials.[76] 4D-printed SMP scaffolds can often be co-cultured with cells for subsequent bone tissue engineering. SMPs undergo shape change in response to a specific stimulus at a specific time; this change is transmitted to the cultured cells, influencing the shape of adherent cells and guiding osteogenic differentiation.[77,78]

Table 1. Classification of smart shape-memory material in 4D printing.

Material classification	Shape-memory process	Applications	Ref.
SMP			
PCL	PCLDA: 60°C warm saline heating; temporary softening; adaptation to the borders of the bone defect; cooling fixation	Self-adaptive scaffolds for treating critical-sized bone defects; recruitment of progenitor cells for osteoinduction	79
	50:50 PCL/Pellethane: heating above T_m; material stretching; cooling to obtain a temporary shape (PCL in compression; Pellethane in stretch); addition of lipase (PCL is degraded by the enzyme; Pellethane shrinks back to its original shape)	Enzyme responsive-programmed shape-changing materials; basic and applied materials sciences	80
PLA	PLA: 70°C water bath heating; PLA tubular structure cavity enlarged and internal herringbone origami scaffold expanded to simulate cancellous bone	Minimally invasive surgery to fill cavities	82
PU	PCPU: deformation at a specific temperature; at close to body temperature, 100% return to original shape within 20 s	Shape-memory and self-healing capabilities at body temperature	84
	PU: the stent is heated to 65°C; 50% strain is applied; temporary shape cooled and fixed at 4°C; at 37°C, maximum recovery in 30 min	Regeneration of tissues (e.g., bone, muscle, and cardiovascular tissue) with dynamically changing mechanical properties in response to physical activity	77
	ISO-PU: 60°C heating of ISO2-PU rectangular samples for 5 min; 360° twisting to obtain a temporary shape; cooling and fixation at 4°C for 5 min; shape recovery within 600 s at 60°C	Bone repair materials for minimally invasive implantation and bone regeneration	85
	SMPU/HA/RGD: 55°C heating for 10 min; compression into small diameter screws; room temperature for 10 min to fix the temporary shape; water bath at 55°C for 20 s to restore the original shape	Bone screw	86
PGDA	PGDA: fixed to a temporary shape by cooling at 20°C; returns to the original shape in 8 s when reaching transition temperature of 20–37°C	Vascular graft	87
PBF	PBF: bracket soaked in deionized water for 3 min; compressed to a temporary shape; dried to fix; soaked again in deionized water to restore the original shape	Hydroxyl and alkenyl functionalization; water-responsive shape-memory effects	38
PPF	Star PPF DP200 for 240 and 280 μm pillars heated to 40°C; 65 and 100% of original shape restored within 15 min	Minimally invasive surgery for regenerating major bone defects	89
SOEA	Strip folded 180° at 37°C to form a U-shape; cooled and fixed at 18°C for 10 min to obtain a temporary shape; strip soaked in 37°C PBS; original shape restored	Biomedical scaffolds combining renewable vegetable oils and 3D manufacturing technology	13

(*Continued*)

Table 1. Continued...

Material classification	Shape-memory process	Applications	Ref.
SMH			
Gelatin	NH-GS: scaffold moistened with distilled water; compressed into the syringe; lyophilized to determine the shape; injected into the petri dish with a 2 mm diameter needle syringe; added with 1 mL saline solution; scaffolds regained original 3D shape	Maxillary sinus lift and dilation	[95]
	UV-crosslinked gelatin samples form temporary shapes after freeze-drying; immersion in PBS restores the original shape	Tissue engineering; regenerative medicine	[96]
GelMA	GelMA: frozen gel exits syringe needle; original shape and size restored outside needle	Regeneration of vascularized bone tissue	[97]
Collagen	Natural collagen scaffolds freeze-dried and fixed into temporary shape; regain their original shape after absorbing water	Cartilage regeneration in a rabbit model of cartilage defects	[98]
Alginate	Alginate/PDA: shape change in minutes under laser light (808 nm)	4D biofabrication of artificial tissues and organs	[99]
	AA-MA/HA-MA: human EDTA competes with calcium ions in alginate; AA-MA tubes regain their original shape	Customized cell-filled shape-shifting scaffolds	[92]
SMA	NiTi SMA: SMA screws cooled and fixed into temporary shapes at 10–16°C; activated by heat when exposed to body temperature	Pedicle screw	[102]
	NiTi: C-bending of SMA NiTi rods at 34–47°C in an alternating magnetic field	EC-SMAR; treatment of rabbit scoliosis	[103]
SMC	BCP: ceramic sponge is wetted and compressed into a fixed shape; the compression is curled/folded and injected into the bone defect using a syringe; the BCP ceramic sponge reabsorbs and expands back to its original shape	Bone filler; GBR membranes	[104]

Abbreviations: EC-SMAR: Electromagnetically controlled shape-memory alloy rod; GelMA: Gelatin methacryloyl; SMA: Shape memory alloy; SMC: Shape memory ceramic.

Polycaprolactone (PCL) is a United States (US) Food and Drug Administration (FDA)-approved polymer. Due to its low price, biodegradability, and good biocompatibility, PCL has become one of the most widely used aliphatic polymers in the medical field in recent years and is a potential candidate for craniofacial repair. However, it was found that the mechanical properties of PCL materials are poor, and they degrade slowly.[76] Erndt-Marino et al.[79] created an SMP foam from PCL diacrylate (PCLDA) through photopolymerization that temporarily softens when treated with warm (60°C) saline. This facilitates adaptation to the bone defect boundary before shape fixation, and the material maintains its shape after cooling fixation. Additionally, hydroxyapatite deposition can be induced by applying a polydopamine (PD) layer to it. Taken together, PD-PCLDA reported higher osteoinductivity than uncoated materials. Buffington et al.[80] designed an SMP that is responsive to direct enzymatic activity, in which the shape-fixing component, PCL, is susceptible to enzymatic degradation, whereas the shape-memory component, Pellethane 5863-80A, is enzymatically stabilized. Temporal shapes were obtained after stretching PCL at melting temperature (T_m) and then cooling it, with PCL being compressed and Pellethane being stretched. Lipase is then added, and PCL is enzymatically degraded, causing Pellethane to shrink back to its previous state, creating a cell-compatible enzyme-responsive material that can be programmed to change shape.

Polylactic acid (PLA) is a biodegradable polymer consisting of lactic acid.[81] Although it has excellent biocompatibility, its degradation produces acidic products that can cause inflammation in the body, hindering the use of PLA in clinical applications. However, it can be modified and adapted to the various needs of tissue engineering scaffold materials. As most bones consist of dense bone and spongy cancellous bone, Langford et al.[82] designed a tubular PLA structure with an origami herringbone and water bomb mosaic design to replace dense bone. When deformation occurs, the center cavity grows larger, mimicking cancellous bone. This design

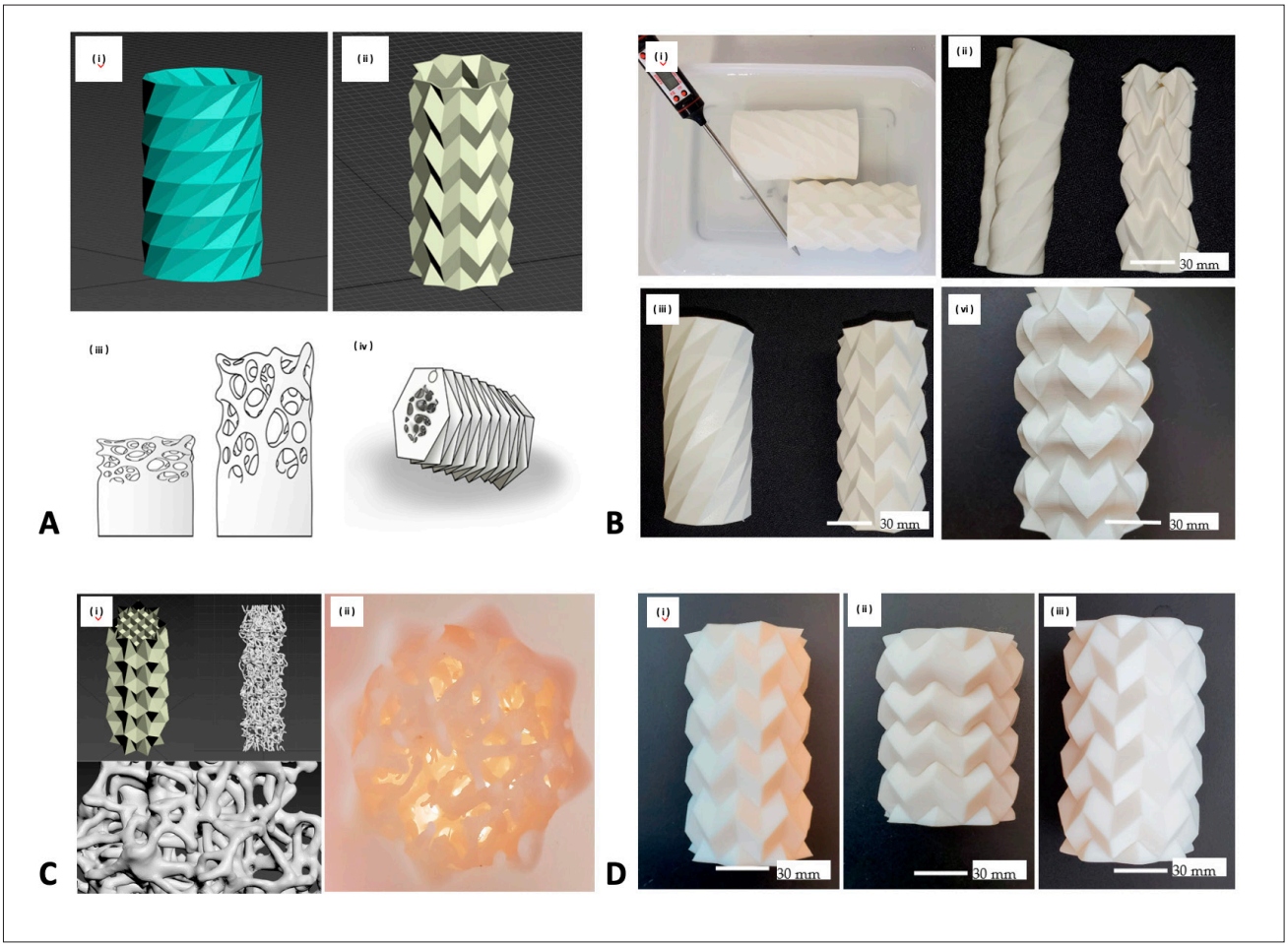

Figure 3. Schematic of PLA structure replace dense bone. (A) Computer-aided design (CAD) of (A, i) herringbone tessellation origami, (A, ii) waterbomb tessellation origami, (A, iii) natural cancellous bone, and (A, iv) combined tessellation origami and natural cancellous bone design. (B) The herringbone structure (B, i) at deformation in a 70°C water bath, (B, ii) right after deformation, (B, iii) after recovery, and (B, iv) after recovery from the fourth deformation. (C) Schematic of the central core and herringbone tessellation origami. Schematic of (C, i) design of the central core, and (C, ii) 3D-printed herringbone tessellation origami with substituting cancellous core. (D) As-printed herringbone tessellation origami with porous core. (D, i) As-printed herringbone tessellation origami with porous core (ii) after compression, and (iii) after recovery. Scale bars: 30mm. Adapted with permission from Langford et al.[82]

results in significantly different volumes in the temporary and original shapes, simulating the gap between bone trabeculae (Figure 3).

Polyurethanes (PUs) have microphase separation and shape-memory effects. They have been used in 4D printing due to their wide shape-memory temperature range and good biocompatibility.[83] Li et al.[84] created a novel kind of bifunctional PU that combines self-healing capabilities and near-body temperature shape memory ability in a polycarbonate (PC)-PU system. Conditioned by a chain extender, the system exhibited more than 96% shape fixation once deformed at the appropriate temperature, returning 100% to its original shape within 20 s when the transformation temperature approached the body temperature. Using a thermo-responsive 3D shape-memory PU (SMPU) structure, Hendrikson et al.[77] found that cell morphology changes with alterations in the mechanical environment due to deformation. However, the limited mechanical strength of PUs has restricted their use in bone tissue applications. To create shape-memory PUs with enhanced mechanical strength, Yang et al.[85] first synthesized hexamethylene diisocyanate and isosorbide (ISO) as long-chain diisocyanates, which were then used as a coupling agent to create novel linear SMPUs (ISO-PUs) from poly-D,L-lactide (PDLLA)-based macrodiol as the soft segment and ISO as the chain extender. A new linear SMPU (ISO-PU) was synthesized with improved mechanical properties and osteoblast-promoting properties. To create a temporary shape, the

ISO2-PU rectangular spline was first heated for 5 min at 60°C and then twisted 360°. After being refrigerated for 5 min at 4°C, the twisted spline was then placed in a 60°C environment to restore its original shape. The sample strip completely recovered within 600 s.[85] An innovative smart bone screw, containing SMPU, HA, and RGD, with high mechanical and shape-memory properties, was developed by Zhang et al.[86] for therapy. The screw was kept at 55°C for 10 min after compression to a small diameter and kept at room temperature for 10 min for fixation to a temporary shape. The screw finally restored its initial shape in water at 55°C for 20 s.[86]

Poly(glycerol dodecanoate) acrylate (PGDA) is an innovative SMP; synthesized from glycerol and dodecanedioic acid to create PGD, which is then modified by introducing acrylate groups, resulting in the photocured form PGDA. Its transformation temperature is between 20 and 37°C. The PGDA sample is cooled at 20°C for fixation in a temporary shape. It took the sample 8 s to return to its original shape after the transformation temperature is reached. PGDA was used to create vascular grafts for blood circulation in a rat aortic graft model, potentially improving bone tissue vascularization.[87]

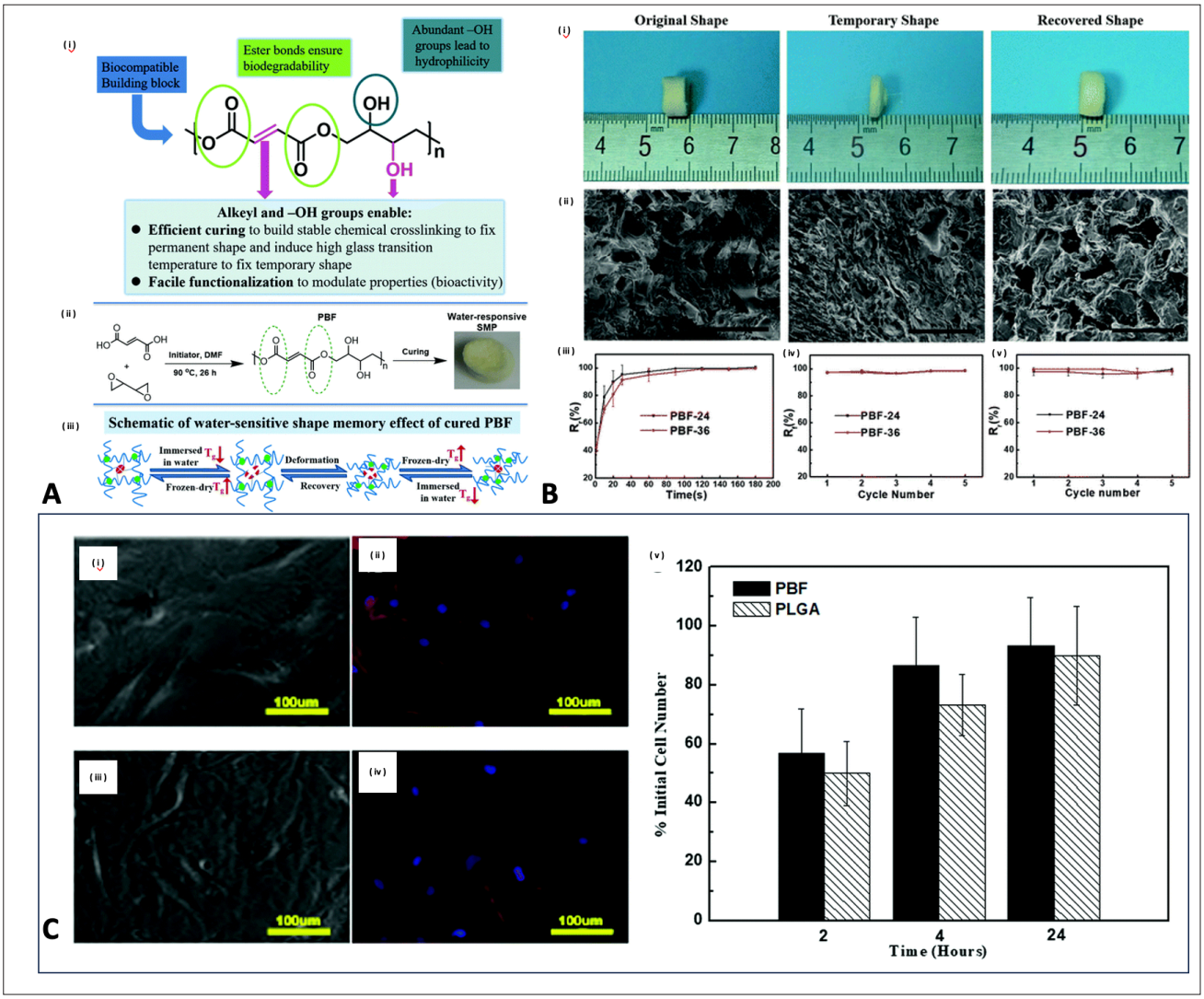

Figure 4. Schematic of water-responsive shape memory PBF polymer. (A) Structure (A, i), synthesis (A, ii), and working mechanism (A, iii) of poly(butanetetrol fumarate) (PBF)-based shape memory polymer. (B) Digital images (B, i), scanning electron microscopy (SEM) images (B, ii), and quantification of water-responsive shape-memory process of the PBF-24 scaffold (B, iii). (C) Cell attachment. Phase contrast images (i and ii) and fluorescence images of stained F-actin (ii and iv) of osteoblasts 24 h after seeding onto PBF (i and ii) and PLGA (iii and iv), (v) Osteoblast adhesion rates on PBF and PLGA. Scale bars: 100 μm. Adapted with permission from Guo et al.[38]

Poly(butanetetrol fumarate) (PBF), a humidity-responsive SMP designed by Kuo et al.[38] possesses good hydrophilicity. The PBF scaffolds were soaked in deionized water for 3 min to make them elastic, then squeezed into a temporary shape that solidified once dried. After re-immersion in deionized water, the PBF scaffold restored its elasticity and returned to its original form. It stimulates osteoblast attachment, proliferation, and ALP activity. PBF is also substantially functionalized, such as with BMP-2 via lateral hydroxyl groups for prolonged BMP-2 release (Figure 4).[38]

Poly(propylene fumarate) (PPF) is produced through successive polycondensation of diethyl fumarate and propylene glycol and has thermoresponsive properties.[88] Cemali et al.[89] investigated the effect of PPF on the bone structure using scanning electron microscopy (SEM) and mechanical testing systems (MTS), as well as the *in vitro* cellular interactions of heat-cured PPF/vinylphosphonic acid (VPA) and PPF/diethyl vinylphosphonate (VPES) scaffolds at different compositions. Their findings indicate good biocompatibility and support for osteogenesis as determined by von Kossa staining and both ALP and osteocalcin (OCN) activities.

In 2016, Miao et al.[13] used 4D bioprinting to create soybean oil epoxidized acrylate (SOEA) scaffolds inoculated with human MSCs by printing the scaffolds into strips and folding them 180° into a U-shape at 37°C for 10 min. The sample strips were maintained at −18°C for an additional 10 min before immediate immersion in phosphate-buffered saline (PBS) at 37°C to restore their original form (Figure 5).[13]

Shape-memory polymers (SMPs) are widely utilized for 4D printing of bone remodeling materials based on their reported advantages; lightweight, good shape-memory restoration, simple stimulation conditions, biodegradable, and low level of cytotoxicity. However, some common polymers (e.g., PCL) have limited degradation rates and mechanical properties. In contrast,

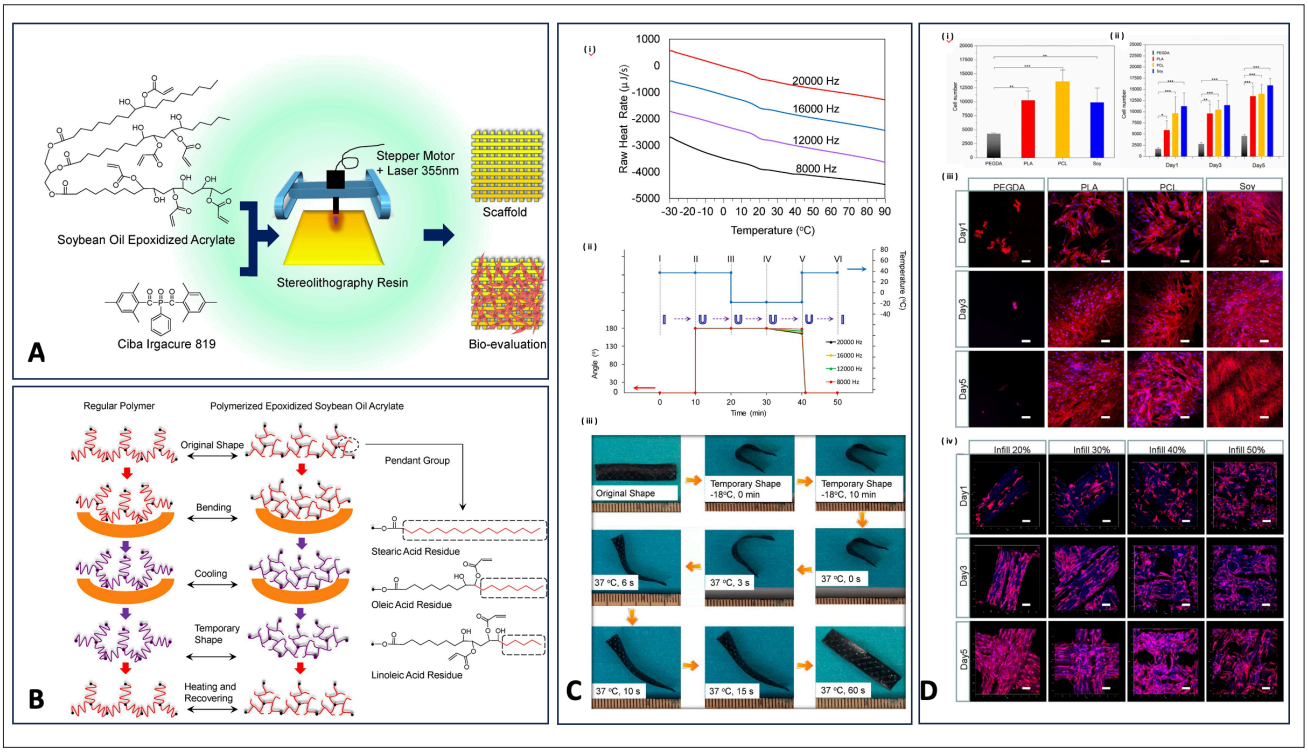

Figure 5. Schematic of 4D printing scaffold with novel SOEA. (A) Schematic of the soybean oil epoxidized acrylate (SOEA) fabrication process from raw material processing to resin fabrication and application. (B) Schematic of the difference in shape-memory mechanism between polymerized SOEA and regular polymer. (C) Shape memory performance. (C, i) Differential scanning calorimetry (DSC) curves of the polymerized SOEA printed with a speed of 10 mm/s at various laser frequencies. (C, ii) Shape-memory circle of fabricated scaffolds at various laser frequencies. (C, iii) Shape-memory circle demonstrated with a printed sample (laser frequency: 12,000 Hz; printing speed: 10 mm/s). (D) Cell attachment and proliferation. (D, i–ii) Human mesenchymal stem cell (hMSC) attachment (i) and proliferation (ii) on polyethylene glycol diacrylate (PEGDA), polylactic acid (PLA), polycaprolactone (PCL), and SOEA (Soy). (D, iii) Printed scaffolds from soybean oil epoxidized acrylate with different infill densities. (D, iv) Data are mean ± standard deviation, n = 6. *p < 0.05, **p < 0.01, ***p < 0.001. Scale bars are 100 μm. Adapted with permission from Miao et al.[13]

novel designs, such as PD-PCLDA and ISO-PU, exhibit enhanced osteoinductivity and mechanical properties due to their distinct structures or the incorporation of functional layers. These strategies address the limitations of traditional materials but may have challenges in complexity and cost. Therefore, the application of SMPs in bone repair necessitates comprehensive consideration and continuous research.

3.1.1.2. Smart-memory hydrogels

Although SMP scaffolds can be co-cultured with cells, it is now believed that SMPs cannot completely replace hydrogels due to their limited sustainability, cytocompatibility, material permeability, and mechanical properties in most environments. Therefore, gel materials with adequate mechanical strength and self-deforming gels have become popular bioinks.[90,91] There are two methods for using cell culture in the 4D printing of hydrogels: (i) cell-free biomaterial scaffold with cell inoculation afterward, and (ii) cell-containing bioscaffolds as replica analogues.[92] Natural biogels, such as cell membranes, connective tissues, cartilage, and insect wings, have intrinsic molecular arrangements in the form of organized aggregates. Recently, novel SMHs with anisotropic characteristics in several orientations were produced. These hydrogels are elastic, soft, and can expand in water, making them promising novel biomaterials.[93] Chitosan fibers exhibit reversible glass transition in the presence of moisture,[94] enabling them to function as scaffolds with shape memory functionality through hydration.

Gelatin can mimic the natural ECM due to its hydration properties, viscoelastic response, and ability to bind biologics (e.g., cells and GFs). However, its poor mechanical properties, over-swelling, and inconvenient diffusion of proteins, oxygen, nutrients, and waste products from encapsulated cells can lead to undesirable cellular behavior, often limiting their application in the field. Ying et al. developed nanofibrous gelatin scaffolds (NH-GS) by chemically modifying gelatin with heparin. The scaffolds were first moistened with distilled water, manually compressed into syringes, and then lyophilized to define their shape. They were injected into the culture using a syringe with a 2 mm diameter needle. To simulate intraoperative bleeding, 1 mL saline solution was pre-added to the culture dish. The scaffolds nearly restored their original structure and quickly regained their 3D shape, recovering over 90% of their initial volume. Heparin enhances the stability and regulated release of BMP-2, making it possible to create injectable, shape-memory, highly porous scaffolds suitable for maxillary sinus augmentation and bone regeneration.[95] Diba et al.[96] designed ultraviolet light (UV)-crosslinked gelatin samples that could form a temporary shape after freeze-drying and return to their original shape after immersion in PBS solution; non-UV-crosslinked gelatin samples failed to return to their original shape.

Methacrylated gelatin (GelMA) contains many arginine-glycine-aspartate (RGD) sequences, and the target sequence of a matrix metalloproteinase (MMP) is similar to that of natural ECM, thus promoting cell proliferation and spreading for enhanced cell survival. Yuan et al.[97] employed GelMA to create porous shape-memory cryogel microspheres (CMS), which effectively supported the regeneration of vascularized bone tissue in animal studies. Cryogels are porous, spongy hydrogels formed from hydrogel precursor solutions by freezing at subzero temperatures. The pore size and mechanical stability of the cryogel can be adjusted by the molecular weight/concentration of the polymer and the rate of cooling prior to freezing the gel; this was achieved by changing the duration of the gradient cooling from −20 to −196°C. In addition to having a porous network that protects the cells, the cryogel collapses, flows over the syringe needle, and recovers its initial shape and size outside the needle.[97]

Collagen (Col) has good biocompatibility and is fibrous, viscous, and durable as a natural adhesive. However, it lacks intrinsic rigidity, and its telopeptides may be antigenic. Jiang et al.[98] developed natural Col scaffolds from type I Col. These scaffolds can be freeze-dried to take on a transient shape before returning to their original shape when water is absorbed. Col scaffolds provide the benefits of genuine Col, such as enhanced chondrocyte adhesion, proliferation, and re-differentiation in rabbit models with cartilage defects. Alginate (Alg) is known for its high biocompatibility, low toxicity, and low cost, and can gel rapidly in the presence of Ca^{2+} ions. However, it has poor printability and restricted shape-morphing capabilities. As a result, Alg is frequently mixed with other polymers in 4D printing processes to create materials with adequate shape-shifting properties and printability. Luo et al.[99] used Alg/PD bioinks to print cell-laden structures. When exposed to 808 nm laser irradiation, the 4D-printed Alg/PDA scaffolds folded and changed shape within minutes. The long shape-change duration allowed for fine control of the scaffold's deformation angle by altering the laser power, irradiation period, and design pattern of the Alg/PDA pillar (Figure 6).[99]

Moreover, Alg and Ca^{2+} ions were crosslinked in methacrylated alginate (AA-MA) and methacrylated hyaluronic acid (HA-MA) memory-deformable hydrogels to create self-folding microtubules. Once EDTA is introduced to Alg to compete with the Ca^{2+} ions, the self-folding tubes expand and revert to their original

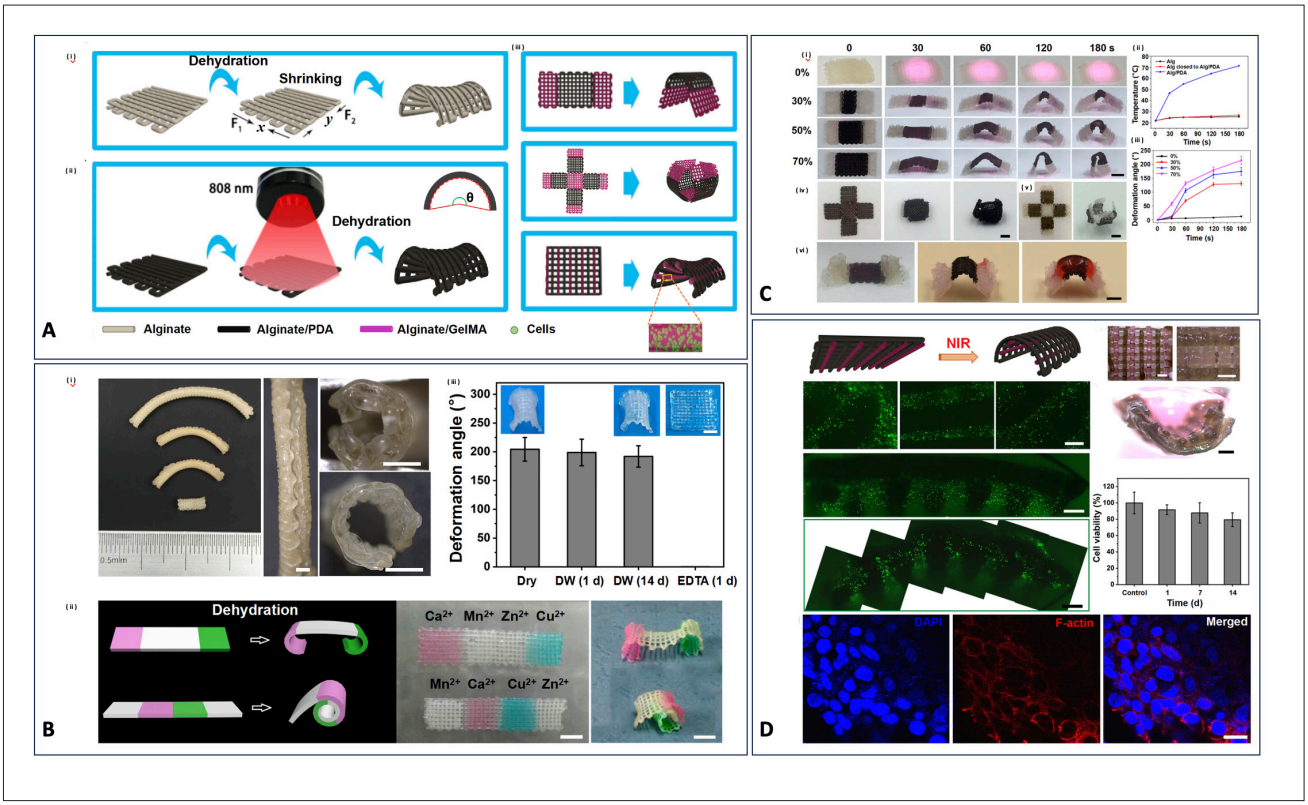

Figure 6. Schematic of near-infrared (NIR)-triggered 4D printing shape-morphing alginate/polydopamine. (A) A 3D-printed bi-layered alginate scaffold with NIR-driven shape-morphing behavior. (B) Shape memory properties. (B, i) 3D-printed alginate tubes of different sizes after dehydration-induced deformation. (B, ii) Programmed deformation of alginate constructs using different divalent cations for crosslinking. (B, iii) Shape recovery of deformed alginate scaffolds after incubation in deionized water (37°C) for 1 and 14 days, and in Ethylenediaminetetraacetic acid (EDTA) for 1 day, respectively. (C) NIR-induced shape change. (C, i–iii) Shape change (C, i), temperature (C, ii), and deformation angle (C, iii) of 3D-printed biphasic scaffolds consisting of alginate and alginate/polydopamine (PDA) struts with different area ratios under laser irradiation (0.5 W/cm^2; 808 nm) at different times. (C) Photographs show the shape change of 3D-printed alginate/PDA (iv) and biphasic (v) scaffolds in cross structures before and after laser irradiation. (vi) A 3D-printed biphasic scaffold with different heights in the alginate (ten layers) and alginate/PDA (two layers) parts undergoing NIR-induced shape change followed by printing alginate (staining with red ink) on the shape-changing area (alginate/PDA). (D) Schematic of the printed biphasic scaffolds consisting of alginate/PDA and cell-laden alginate/GelMA struts, and the shape change after NIR irradiation. (D, i–vii) Scale bars = 1 mm (B, i), 5 mm (B, ii) and 2 mm (B, iii), 1mm (D). Adapted with permission from Luo et al.[99]

dimensions. These tubes can differentiate into osteoblasts, chondrocytes, and adipocytes when they are filled with mouse bone marrow stromal cells.[92] SMH materials have shape-memory properties, allowing them to be introduced into a Petri dish or affected area via a syringe, which provides convenience in various medical applications. Their good biocompatibility, chemical modifications, and material combinations, based on specific functions and characteristics, have led to a gradual increase in the use of SMHs in the medical field. Likewise, the stability of SMH materials after injection needs to be enhanced due to poor mechanical strength.

3.1.1.3. Shape-memory alloys and ceramics

In order to create hyperelastic SMA bone implants, Ti6Al4V, and NiTi were combined.[100] β-phase 30 wt% Mg-Sc alloys exhibit both form memory and good mechanical characteristics. The compressive strain is 31 ± 3%, and the ultimate compressive strength is 603 ± 39 MPa. Animal investigations have demonstrated that these alloys have significant bone-healing properties.[101] Werner et al.[102] designed novel self-expanding SMA screws that were first pre-cooled using a coolant spray, followed by implantation of the screws. To activate at body temperature, each sample was momentarily submerged in isotonic saline. After implantation, seven SMA screws – four of which were unilaterally activated to increase the stability of traditional screw implantation – that were put into the vertebrae were correctly activated.[102] Hou et al.[103] employed an alternating magnetic field (AMF) to heat-treat NiTi rods made of SMA. This technique reached transition temperatures

(34–47°C), thereby facilitating C-shape bending. The rods deformed after implantation in the spinal region of rabbits by electromagnetic induction heating, and the deformation gradually increased over time, which could be applied to treat scoliosis in rabbits.[103] Zhang et al.[104] developed a biphasic calcium phosphate (BCP) ceramic sponge, which addressed the limitations of porous CaP ceramics, such as inherent brittleness and poor processability. The sponge can be compressed and curled or folded several times, injected into a bone defect using a syringe, and swelled to its original shape upon contact with water (Figure 7).[104]

Currently, SMCs are less frequently used in the field of bone repair. The hybrid application of SMAs yielded significant experimental findings regarding bone regeneration and demonstrated good mechanical and shape-memory capabilities. Self-expanding SMA screws were designed via spray pre-cooling and saline activation, which effectively improved the stability for implantation. However, adverse reactions due to their corrosive and frictional properties should also be considered, as well as the fact that some of these alloys may be limited to specific temperature ranges. BCP ceramic sponges address the limitations of porous CaP ceramics, such as brittleness and processability issues, and enable injection and autonomous shape restoration in bone defects. Nonetheless, SMC remains a brittle material, and the stress factor of multiple coiling or folding of ceramic sponges may have an impact on their structure. For both SMA and SMC materials, in-depth studies are warranted to address potential long-term performance and biocompatibility issues in practical bone repair applications.

3.1.2. Factors affecting smart material performance

Stimulus-responsive biomaterials that promote the osteogenic differentiation of stem cells are actively investigated for personalized bone repair. Analyzing these biocompatible materials can offer new insights for future research in 4D printing and bioprinting. These biomaterials can modify or adjust their functionalities in response to various environmental stimuli (Figure 8), including sound, light, pH, ions, water, temperature, electricity, biomolecules, cellular traction, magnetic fields, glucose, and enzymes, as well as their combinations (Table 2).[105]

3.1.2.1. Temperature

Thermo-responsive materials alter their physicochemical properties with temperature changes. Researchers had previously investigated stimulus-responsive biomaterials for *in vitro* bone tissue regeneration prior to the proposal of 4D bioprinting. For example, Dessi et al.[107] created a chitosan hydrogel with β-phosphoglycerol that responds to temperature. The physiological temperature of 37°C causes the hydrogel to change from a liquid to a gel. Its nanocrystalline shape promoted the attachment and proliferation of MG63 osteoblast-like cells by precisely imitating the chemical and physical structure of real bone tissue.[107] Since Poly(N-isopropylacrylamide) (PNIPAM)-based polymers have a low level of lower critical solution temperature (LCST) at 32°C, above which the gel morphology can be reversibly changed, they are the most frequently investigated thermo-responsive materials. Moreover, adding suitable components, such as polyethylene glycol (PEG) to PNIPAM and HEMA, can enhance mechanical properties and bioactivity.[108] Ozturk et al.[109] used Poly(N-isopropylacrylamide) (PNIPAAm) to design a tissue-engineered scaffold for investigating the effects of mechanical environment changes on cell proliferation and differentiation during structural deformation. The scaffold was chemically treated with thermo-responsive elastin-like polypeptides (ELP) to improve cell adherence. The study discovered that the temperature-induced expansion and contraction of the scaffold boosted cell growth. In order to minimize heat damage to healthy organization during photothermal treatment (used to treat a range of illnesses, including cancer), Wang et al.[110] developed a dual thermo-responsive polymer system. Two thermos-responsive polymers with different phase transition temperatures are present in this system. By screening different polymer combinations, they created complex structures with adjustable thermal properties.[110] Photothermal therapy is more precise and safer when using 4D-printed thermo-responsive polymer devices. These devices reduce the risk of damaging surrounding healthy tissues while improving treatment efficacy. Drug delivery systems consisting of 4D-printed hydrogels can release medications at controlled rates in response to certain temperatures, resulting in accurate delivery.[111] However, high temperatures can damage the cells within bioprinted structures, which can be avoided by incorporating small, non-volatile biomolecules or alternative copolymers to lower the glass-transition temperature (T_g) to 37°C.[61]

3.1.2.2. Magnetic field

Magnetically responsive material deformation is driven by a magnetic field, of which magnetic nanoparticles (MNPs) are the main component, including iron oxide (Fe_2O_3), iron tetraoxide (Fe_3O_4), platinum iron (FePt), and cobalt ferrite ($CoFe_2O_4$), which can be embedded in surfaces, suspended freely in suspension, or crosslinked with networks of polymers. MNPs can induce chemical and physical changes to polymer scaffolds in response to fluctuations in the magnetic field strength.[10,112,113] In 2014, Zhang et al. developed a 4D-printed MBG/PCL scaffold containing magnetic Fe_3O_4 nanoparticles.[114] This scaffold had compressive strength similar to natural bone. When

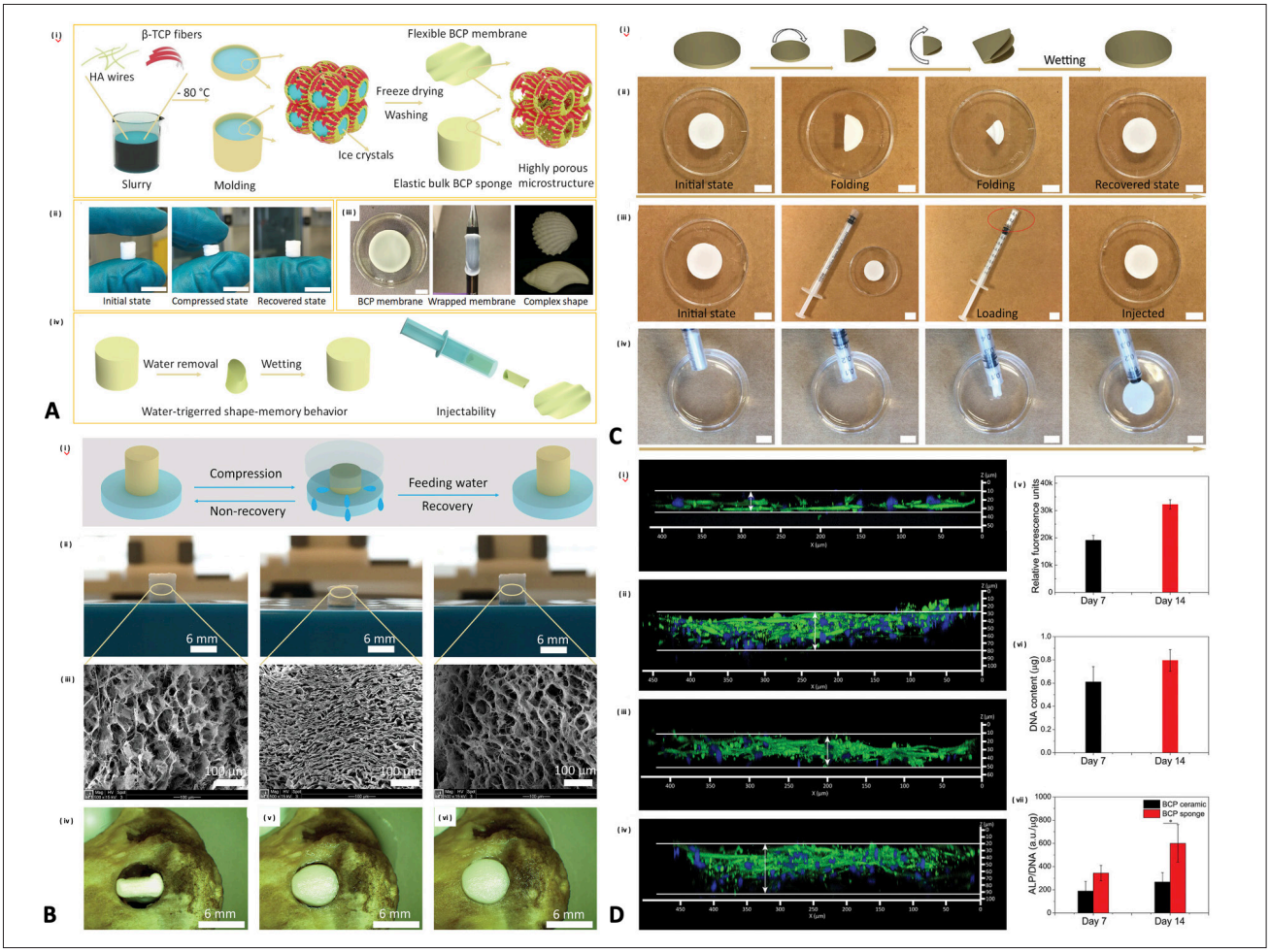

Figure 7. A biphasic calcium phosphate (BCP) sponge. (A) Schematic of BCP sponge. Scale bar: 1cm. (A, i) Schematic illustration of BCP ceramic sponge production. (A, ii) Images of the compression resistance capability of BCP ceramic sponge: initial state, compressed state by squeezing out of the free water, recovered state by absorbing water. (A, iii) As produced BCP sponges with complex shapes, BCP ceramic sponge membrane, and the membrane wrapped around a ballpoint pen. (A, iv) Concept of water-triggered shape-memory behavior and injectability. Scale bar: 1 cm. (B) Images of the compression resistance capability of BCP ceramic sponge. (B, i) Schematic representation of the shape-memory property of the BCP ceramic sponges (B, ii) Images of a BCP ceramic sponge in the original shape, compression-fixed shape, and recovered shape. (B, iii) SEM micrographs of a BCP ceramic sponge in the original shape, compression-fixed shape, and recovered shape. (B, iv–vi) Images of water-triggered, complete filling of a defect in chicken bone by using a precompressed BCP ceramic sponge. (C) Schematic representation of the process of folding, unfolding and syringe of BCP ceramic sponge membrane. Scale bar: 6mm. (C, i) Schematic representation of the process of folding and unfolding the BCP ceramic sponge membrane. (C, ii) Images of the BCP ceramic sponge membrane, syringe, BCP ceramic sponge membrane loaded in the syringe, and BCP membrane injected from the syringe. (C, iii) Images of BCP ceramic sponge membrane during different stages of injection. (D) Cell attachment and proliferation. Scale bar: 50μm. (D, i–iv) Cross-sectional view of 3D-reconstructed fluorescence images displaying human mesenchymal stem cell (hMSC) penetration on day 4 in (D, i) the conventional BCP ceramic and (D, ii) the BCP ceramic sponge; and on day 7 in (D, iii) the conventional BCP ceramic and (D, iv) the BCP ceramic sponge. (D, v) The viability of hMSCs cultured for up to 14 days on the BCP ceramic sponge. (D, vi) Proliferation of hMSCs cultured for up to 14 days on the BCP ceramic sponge. (D, vii) Normalized alkaline phosphatase (ALP) activity of hMSCs cultured for up to 14 days on the BCP ceramic sponge or the conventional BCP ceramic. Adapted with permission from Zhang et al.[104]

subjected to a magnetic field, the nanoparticles heated up, enhancing proliferation and differentiation, increasing ALP activity, promoting osteogenic gene expression, and stimulating apatite mineralization of h-BMSCs within the scaffold.[114] Meng et al.[115] determined that when pairs of nanoparticles bound to superparamagnetic nHA/PLA scaffolds, an external magnetic field promoted the proliferation of preosteoblasts and induced bone formation. The treatment of cartilage defects has been the focus of attention in bone tissue engineering therapies, and Col fibers placed in parallel were used by Betsch et al.[116] to create a magnetically sensitive 4D-bioprinted multilayered

Table 2. Classification of 4D printing material stimulation.

Stimulus classification	Material	Properties	Application	Ref.
Physical				
Temperature	Thermo-responsive chitosan hydrogel crosslinked with β-phosphoglycerol	Transforms from liquid to gel state at 37°C	Simulates natural bone tissue; bone hard tissue regeneration material	[107]
	Thermo-responsive elastin-like polypeptides (ELP)	Chemically modified with temperature-induced swelling and contraction	Promotes cell adhesion; mechanical changes increase cell proliferation on PNIPAAm scaffolds	[109]
	P(AAm-co-AN)-b- P(NIPAM-co-DMAa)-b-P(AAm-co-AN) ABA triblock copolymer	Exhibits UCST and LCST dual thermo-responsive phase behavior via RAFT polymerization synthesis	Reduces thermal damage to adjacent normal tissues; precision photothermal therapy	[110]
	UV-crosslinked PNIPAM hydrogel drug capsule shells	Changes in ambient temperature	Autonomous control of drug release behavior; controlled drug release	[111]
Electrical field	One-step cell printing/electrically stimulated gelatin hydrogel system	Electrical field induces orderly arrangement of C2C12 cells in bioink, deposits cell-filled GelMA fibers onto gelatin membrane for shape deformation; mimics muscle bundle membrane structure	*In vitro* modeling of cell-laden fiber bundles for drug testing	[122]
	CNT, BMP-2, and chemically crosslinked CMC hydrogel scaffolds	—	Non-invasive, continuous monitoring of osteogenic differentiation during bone regeneration (i.e., ALP electrochemical signaling, charge transfer, and resistivity)	[124]
	Macroporous graphene scaffolds	Conductive	Low-voltage controlled drug release from the scaffolds	[125]
Magnetic field	Pure type I collagen hydrogel	Iron NPs travel unidirectionally and collagen fibers are unidirectionally parallel under an external magnetic field	Accurately mimics the dynamics of natural cartilage; tissue engineering for treating cartilage defects	[116]
	Hydrogel scaffolds of HEMA, EGDMA, and SMA	Scaffold deformation upon application of an external magnetic field; inoculated hMSC alignment changes with the mechanical environment	Promotes cartilage formation	[117]
	Superparamagnetic NP/nHA/Polylactide (PLA) scaffolds	External magnetic field promotes preosteoblast proliferation	Induces bone formation	[115]
	Fe_3O_4@PCM/PEG/DOX system	AMF increases temperature above the T_m of PCM (42°C); DOX release below the T_m of PCM; PCM changes from liquid to solid phase; DOX and MNPs retain at the tumor	Targeted drug release in tumor therapy	[118]
	Porous Alg iron gel (AF)	Gel deforms under an external magnetic field; the amount of DOX released from the porous AF increases; iron oxide NPs regulate the sustained release of DOX from the gel	Drug release	[119]

(*Continued*)

Table 2. Continued...

Stimulus classification	Material	Properties	Application	Ref.
Acoustic field	Chitosan NB	Ultrasound-induced activity	Non-invasive, targeted DOX (drug) release	[134]
	Ultrasound/pH/GSH triple stimulation response biodegradable nanocapsules	DOX-containing PMAA shells covered with perfluorohexane crosslinked by disulfide bonds	Triple diagnostic and therapeutic drug release	[136]
Light	Cell-laden gradient hydrogels with pre-programmed deformation	Fabrication parameter alteration (UV absorber concentration, UV irradiation time, polymer concentration, hydrogel thickness) for pre-programmed hydrogel deformation	4D bone tissue engineering	[127]
	NIR light-responsive SMPU/Mg composite porous scaffolds	Original shape restoration under NIR light exposure; close bone contact; degradation of Mg particles and Mg^{2+} release promote osteogenesis	Bone tissue engineering	[129]
	3D-printed dual drug-carrying Col/SIM/nHAP-PGL stent	Rapid release of SIM; PGL release in response to NIR light; on-demand sequential release of both drugs	Controlled sequential release of different biomolecules in bone tissue engineering	[130]
Humidity	Humidity-responsive PEG-PCL-CNC nanocomposite	7°C water stimulation exhibits specific shape-memory effect	Drug delivery systems; TE stents; smart sutures; esophageal stents; vascular stents	[133]
Chemical				
pH	Chitosan/TPP scaffolds	Non-crosslinked primary amine content (CN) affects PH response to protein adsorption and release; CN affects the proliferation of BM-MSCs	Regenerative bone therapy	[139]
	PEG/DOX chitosan injectable	Hydrocoagulation capability	Hepatocellular carcinoma treatment	[140]
	L-arginine-grafted Alg hydrogel beads	Swells and delivers proteins at a specific pH	Oral delivery of proteins or drugs	[141]
Ionic strength	Bilayer DDR hydrogel	Composed of heat-treated layered structures; generates surface micropatterns for zinc-induced reversible shape memory behavior	Fabrication of programmable hydrogel surfaces	[142]
	Imidazole-zinc ion coordination shape-memory hydrogels	Imidazole-zinc ion coordination immobilizes the temporary shape of the hydrogel; complexing agent extracts zinc ions to restore the original shape; cell-laden hydrogel sheet folds into temporary tubular structure; L929 flat cells are grown and immobilized *in vitro* by small amounts of zinc ions	Implantable tissue engineering scaffolds	[143]
	Alg/MC hydrogels	Specific control of band spacing and angle of the pattern enables printing of 2D structures that respond to Ca^{2+} upon immersion in $CaCl_2$ solution; isotropic swelling and deformation forms simple or complex 3D structures	Biomedical engineering; fabrication of dynamic structures	[144]

(*Continued*)

doi: 10.36922/ijb.4450

Table 2. Continued...

Stimulus classification	Material	Properties	Application	Ref.
Biological				
Enzyme	MMP-sensitive HA hydrogel	Adjustable degradation rate; excellent MSC attachment and proliferation capacity	Tissue engineering; improved tissue defect regeneration and tissue remodeling	[146]
	HA/GS/MMT	HA, GS, and MMT bound in high roughness multi-layered membranes; gradual degradation in HAS solution or bacterial infection microenvironment releases GS	Long-term inhibition of biofilm formation	[145]
Multiple stimulus				
Temperature/pH	Thermo/pH-sensitive ABC copolymer triblock	Increasing pH at normal body temperature reduces the release rate (26%); increasing temperature to 46°C at the same pH reduces the release rate (42%).	Drug delivery	[149]
	PAA/pH-copolymerized hydrogel	Coagulates at pH 6–7 of infarcted heart at physiologic temperature; does not coagulate at pH 7.4 of blood at the same temperature	Cardiac tissue models	[150]
pH/Light	GNR/injectable NIR/pH-responsive poly(NIPAm-co-MPCD) hydrogels	—	Localized chemo-photothermal cancer therapy implants	[151]
Temperature/light	Poly(MEO2MA-co-OEgMA)	Surface copper sulfide NP photoactivation; formation of cleavable thermo-responsive nanocomposites; accommodation and release of bupivacaine anesthetics; temperature increase from 37 to 45°C increased drug release rate; stepwise irradiation of composite with 808 nm laser (1.89 W/cm^2) increases drug release rate	Anesthetic drug delivery	[152]
Magnetic field/light	Chitosan	Light-triggered drug delivery combined with magnetic micro-swimmers	Drug delivery	[153]

Abbreviations: CNT: Carbon nanotube; NP: Nanoparticle; MNP: Magnetic nanoparticle; NB: Nanobubble; PMAA: Polymethylmethacrylic acid; NIR: Near-infrared; SIM: Simvastatin; TPP: Tripolyphosphate; BM-MSCs: Bone marrow mesenchymal stem cells; Alg: Alginate; MC: Methylcellulose; MMP: Matrix metalloproteinase; HA: Hyaluronic acid; GS: Gentamicin; MMT: Montmorillonite; HAS: Hyaluronidase; GNR: Gold nanorod.

doi: 10.36922/ijb.4450

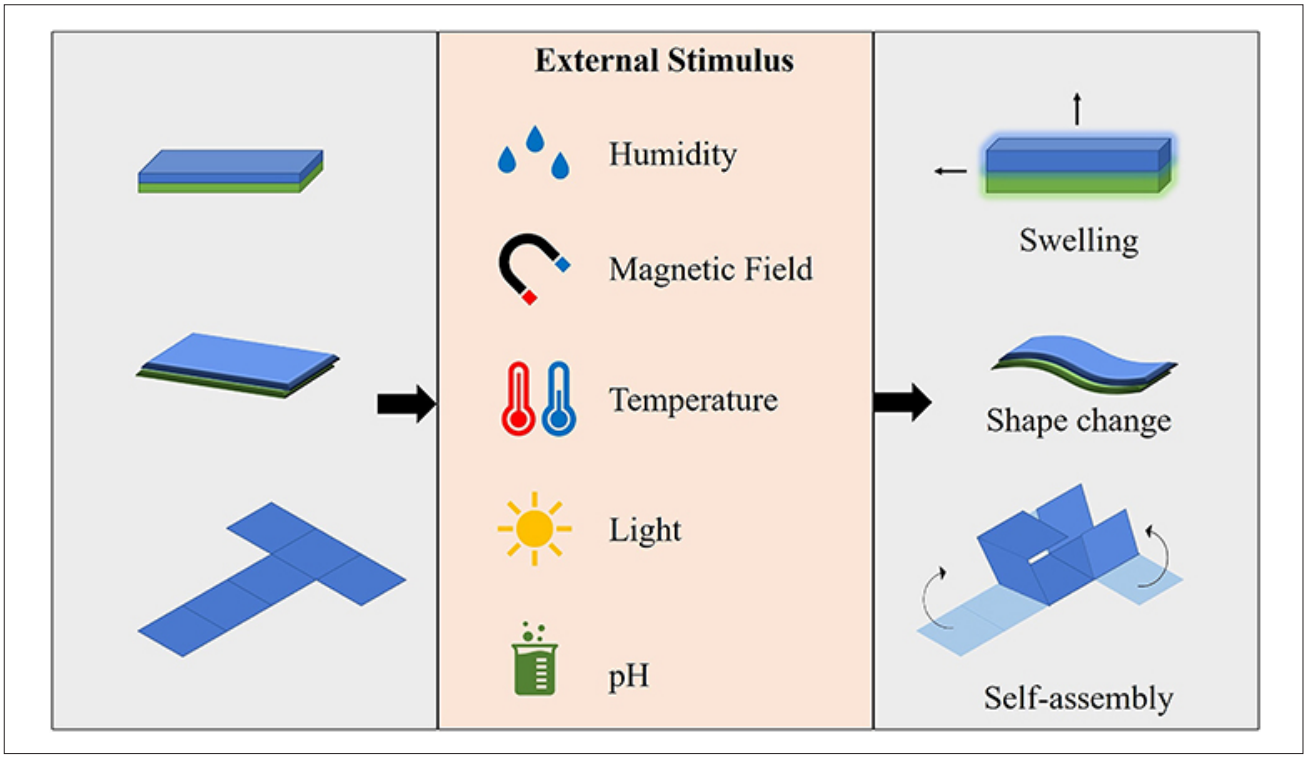

Figure 8. Responsiveness of smart materials in the presence of different external stimuli. Adapted from Tamay et al.[106]

structure. This alignment was accomplished through the unidirectional motion of iron nanoparticles in a printed hydrogel exposed to a magnetic field. Pure type I Col hydrogel outperformed the other samples in terms of Col fiber alignment. Furthermore, a blend of 0.2–0.5% agarose Col hydrogel had the strongest tendency for unidirectional fiber alignment during gelation in a magnetic field, closely resembling the dynamics of natural cartilage (Figure 9).[116]

Fuhrer et al. created a method for aligning Col fibers unidirectionally in a Col hydrogel by suspending nanomagnets in a gel combination. This process developed a hydrogel scaffold responsive to magnetic fields. When an external magnetic field is present, the scaffold deforms, altering the mechanical environment of the hMSCs and rearranging their arrangement to facilitate cartilage synthesis.[117]

Magnetic-responsive materials are exceedingly adaptable and can be utilized to deliver drugs precisely. Owing to their small size, MNPs can pass through biological membranes and cause issues like apoptosis, DNA damage, and inflammation. Therefore, they are typically mixed in polymeric materials (e.g., hydrogels) for tissue engineering and drug administration to provide controlled, sustained, and targeted drug release using magnetic signals.[112] Zhang et al.[118] created a Fe_3O_4@PCM/PEG/DOX system from Fe_3O_4 nanoparticles coupled with polyethylene glycol (PEG) 2000 and phase change material (PCM). It was discovered that doxorubicin (DOX) in the system was strapped in the solid 1-tetradecane at body temperature with almost no release of DOX; at the therapeutic threshold of 42°C or under the near-infrared (NIR) laser irradiation for approximately 4 h, almost 80% of the DOX could be released in 1.5 h. The Fe_3O_4@PCM/PEG/DOX system exhibited rapid release of DOX upon applying AMF. As a result, there is significant potential for the advancement of thermo-chemotherapy as a cancer treatment method.[118] Kim et al.[119] used gelatin, Alg, and iron oxide nanoparticles to make porous Alg iron gels (AF). When compared to non-magnetic stimulation, repeated application of a magnetic field at the gel's bottom greatly increased DOX release. The strength of the magnetic field and the duration of stimulation both increased DOX release. Sustained release of DOX using Alg hydrogel (AH) was facilitated by iron oxide nanoparticles, which also caused gel deformation in the magnetic field to speed up drug release.[119] As research on magnetically responsive materials grows, future advancements may enable more precise control in tissue engineering and drug delivery. Meanwhile, in-depth studies on the composite of MNPs with different polymer materials and their biocompatibility in organisms, as well

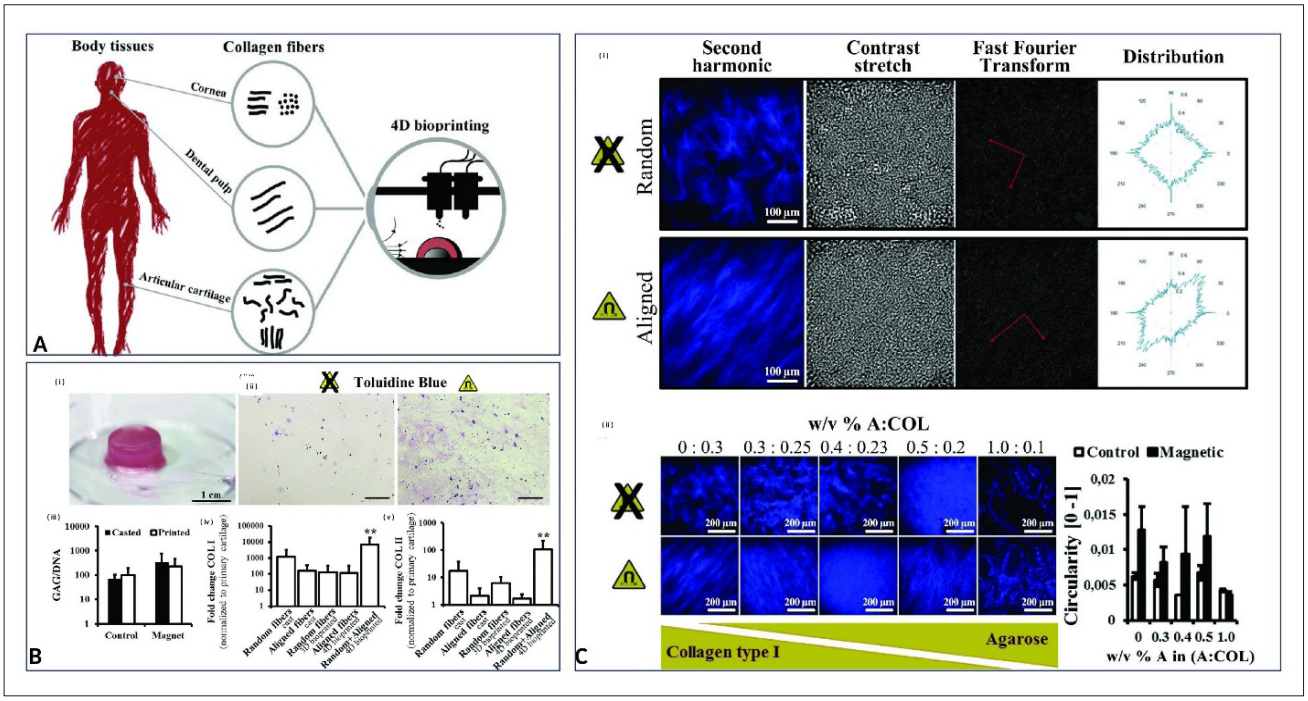

Figure 9. Schematic of bioprinted pure and magnetic cell-loaded hydrogels. (A) Incorporation of 4D bioprinting to imitate the architectural distribution of collagen fibers in multilayered complex tissues, such as articular cartilage, cornea, or dental pulp. (B) Histological (B, i–ii) and biochemical evaluation (B, iii–v) of 4D-bioprinted chondrocyte-loaded samples with and without aligned fibers. (C) Collagen fiber alignment in printable bioinks in the presence or absence of a magnetic field; (C, i) Second-harmonic generation pictures resulting from two-photon imaging of pure type I collagen hydrogels show randomly oriented fibers in the absence of a magnetic field, whereas unidirectionally aligned fibers are visible upon the use of a magnet that forces the motion of iron nanoparticles in one direction through the gel. Fast Fourier transform was applied to contrast stretch pictures in order to transform the imaging data into graphical information. (C, ii) Bioinks with varying agarose and type I collagen concentrations were compared in the presence (lower row) or absence (upper row) of a magnetic field. (B) Scale bar = 100 µm. Adapted with permission from Betsch et al.[116]

as the precision of intelligent programming control, are expected to promote 4D printing technology to achieve greater success in clinical applications.

3.1.2.3. Electrical field

Natural tissues (e.g., bone and cartilage) respond to electrical signals, using them for various functions. To boost tissue regeneration, researchers are developing smart, electrically responsive biomaterials that mimic natural repair mechanisms through electrical stimulation. In an electric field, these materials can change their form or function. They include both electrically responsive polymers and ceramics, such as Polyvinylidene fluoride (PVDF), Poly(3-Hydroxybutyrate-co-3-Hydroxyvalerate) (PHBV), polyamides, Poly-L-lactic acid (PLLA), Col, cellulose, BaTiO3, ZnO, and hexagonal boron nitride BN.[120] Under the influence of an electric field, the conductive material and the electrolyte solution transfer ions, causing the substance to change in size and shape. Increased conductive polymer concentrations can reduce electrical resistance, which minimizes the risk of cell damage due to overheating.[121] Yang et al.[122] used gelatin hydrogel and 4D bioprinting to produce a cell printing/electrical stimulation system. They used a 3D printer to extrude GelMA bioink with C2C12 cells and then aligned the cells using an electric field. GelMA fibers were placed on gelatin membranes, which distorted to resemble muscle bundles for drug testing and muscle repair or replacement (Figure 10).[122]

Carbon-based nanomaterials, such as graphene and carbon nanotubes (CNTs), have received attention lately for their ability to regulate stem cell proliferation and differentiation.[2] Lu et al.[123] coated CNTs with Veriflex to determine the effect of Veriflex-coated CNTs on polymer shape change. CNTs dramatically increased the polymer's electrical conductivity and responsiveness.[123] While the response of cells to changes in shape memory was not examined in this study, it offers theoretical guidelines for the use of CNTs in 4D-printed scaffolds for bone healing. Huang et al.[124] combined CNTs and BMP-2 with carboxymethyl cellulose (CMC) hydrogels to construct bioactive, electrochemically responsive scaffolds that stimulate bone formation and monitor osteogenic differentiation via ALP

signaling and charge transfer. This study features a novel approach for developing electrochemically responsive bioactive scaffolds for non-invasive and continuous monitoring of bone regeneration processes.[124] Servant et al.[125] created a graphene scaffold with good thermal and mechanical properties, demonstrating drug release control at low voltages. Current research is focused on creating smart, electrically responsive biomaterials that mimic tissue regeneration pathways by electrical stimulation, providing novel possibilities for tissue engineering and regenerative medicine. Future advances will improve our understanding of material-cell interactions and refine biomimetic designs for therapeutic use.

3.1.2.4. Light

Macromolecular substances, known as photosensitive polymers, alter their structural properties when exposed to particular wavelengths of light. The polymer chains within the 4D-bioprinted light-responsive materials undergo photodegradation when exposed to high spatial resolution light stimuli, resulting in shape deformation.[2] Light-responsive materials can produce changes in color, shape,

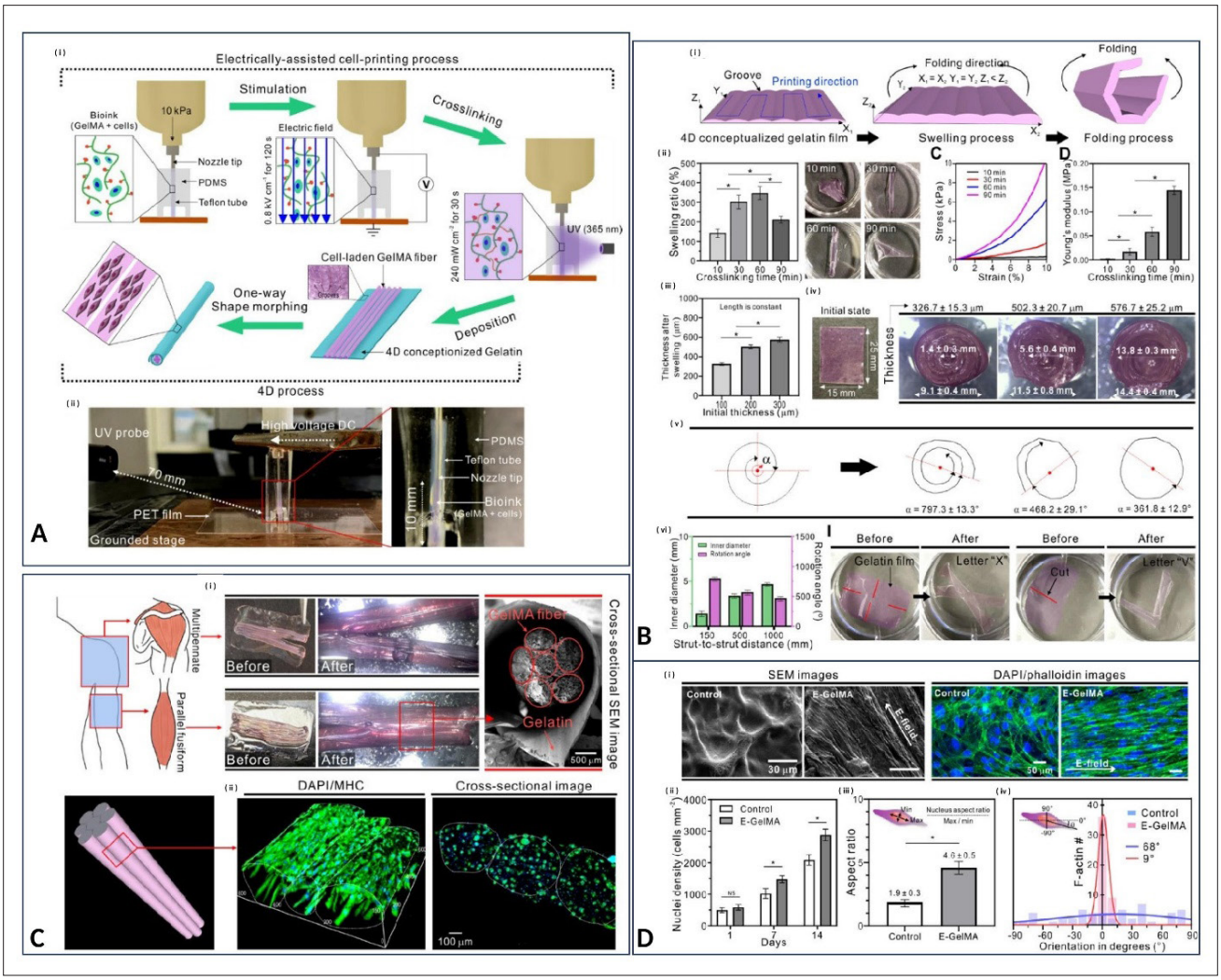

Figure 10. (A) Schematic of a cell-laden fibrous bundle mimicking the structure of the perimysium. (A, Schematic of shape memory function and electrically assisted cell-printing system.) Schematic of an electrically assisted cell-printing/crosslinking process and one-way shape morphing (4D) process for the fabrication of muscle fiber-like structures. (A, ii) Setup of an electrically assisted cell-printing system. (B) Shape morphing mechanism. Shape-morphing mechanism (B, i) and characterizations (B, i–ix) of the gelatin film. (C) The application of shape morphing and electrically assisted cell-printing system. (C, i) Application of cell-laden GelMA fibers with the shape morphing ability of gelatin film. (C, ii) 3D DAPI/MHC images of bundled GelMA fibers cultured for 21 days. (D) Cell culture. (D, i) SEM and fluorescence images of the control and E-GelMA (white arrows indicate electric field direction). (D, ii) Cell nuclei density counted after 1, 7, and 14 days of cell culture. (D, iii) Aspect ratio of cell nuclei. (D, iv) Orientation angle of F-actin. Abbreviations: Immunofluorescence for myosin heavy chain (MHC). Adapted with permission from Yang et al.[122]

or size as needed, such as shrinkage, bending, volume, and mechanical property changes. Furthermore, the shape-memory phenomenon in some hydrogels and polymers can be triggered by light.[126] Ding et al.[127] integrated UV absorbers into natural polymers to produce moldable and programmable hydrogels. They demonstrated the formation of shape gradients in hydrogel models using UV absorbance and explored applications in 4D biomedical devices. Various wavelengths, including UV and infrared (IR), can stimulate photo-responsive biomaterials. More UV radiation than IR radiation is absorbed by living tissues, which increases phototoxicity and decreases tissue permeability.[128] Since NIR radiation may enter tissues more deeply than UV light, it is recommended for biological applications. Furthermore, the lower energy of IR light enhances cell viability in cell-laden structures.[125] Zhang et al.[129] designed NIR light-responsive SMPU/Mg composite porous scaffolds. The programmed scaffold structure is restored under NIR light to achieve close bone contact. NIR radiation is favored over UV light for biological functions due to its deeper tissue penetration. Moreover, due to the thermo-responsive properties of SMPU and the excellent photothermal effect properties of Mg, the scaffolds were compressed above the transition temperature and fixed into a temporary shape after cooling. The compressed scaffolds were subjected to 808 nm NIR light (P = 1 W/cm^2). As NIR irradiation continued, the scaffold structure gradually returned to its original form. The compressed scaffolds can still recover their original shape after being immersed in water, and it is experimentally demonstrated that the shape recovery rate increases with increasing Mg particle concentration (Figure 11).[129]

Dong et al.[130] developed 3D-printed Col/SIM/nHAP-PGL scaffolds that can carry two medicines. These scaffolds are designed to administer the osteogenic drug Pageline (PGL) using NIR light-responsive PD-coated hydroxyapatite nanoparticles. A chemotactic small molecule drug called simvastatin (SIM) was directly mixed into the hydroxyapatite/Col bioinks utilized in 3D printing. The scaffolds enable the sequential release of both drugs: SIM is released promptly at the outset, while PGL is released in response to NIR light. This strategy provides a controlled way for different biomolecules to be delivered in turn in bone remodeling (Figure 12).[130]

Light-responsive biomaterials can be employed in 4D biomedical devices, including medical devices like vascular repair tubes, with better flexibility and repair properties. They achieve dynamic shape change through light stimulation. NIR light-responsive scaffolds for bone repair and controlled drug release have significant potential for clinical applications, and future research could be dedicated to further understanding the photosensitization mechanism of these materials and optimizing their design for improved performance.

3.1.2.5. Humidity

Water is ubiquitous in this world; thus, humidity-responsive polymers have been studied extensively. In tissue engineering, humidity-responsive scaffolds can deform to varying degrees through expansion and contraction as humidity changes.[131] Additionally, water diffusion is slow; thus, humidity-responsive materials have longer response times. PEG is one of the most widely utilized humidity-responsive polymers in 4D printing, which offers a fairly straightforward mechanism of transformation for structures packed with cells.[132] Liu et al. produced a water-stimulated deformation of PEG-PCL-CNC nanocomposites, which demonstrated a specific shape-memory effect when stimulated with 37°C water. Cytotoxicity tests confirmed the cytocompatibility of the nanocomposites, indicating their potential applications in tissue engineering scaffolds, drug delivery systems, smart sutures, vascular and esophageal stents, and smart sutures.[133] The combination of humidity-responsive materials with 3D printing technology constitutes a 4D printing design strategy, where controlled deformation of devices and structures through humidity changes. This approach holds significant clinical potential in the biomedical field, especially for tissue engineering and medical devices. It offers flexible fabrication methods and innovative material options for therapeutic and prosthetic applications.

3.1.2.6. Acoustic field

Numerous systems employ capsules or bubbles to generate cavitation and trigger an acoustic response. Zhou et al. studied the use of biocompatible chitosan nanobubbles (NB) for targeted administration of DOX via ultrasound. Their study demonstrated a significant increase in non-invasive DOX release after ultrasound activation. After 24 h, sonicated samples released much more DOX compared to those that were not sonicated.[134] Low-intensity focused ultrasound (LIFU) prompts the release of DOX and perfluoropentane, enhancing anticancer drug delivery. The results indicated that nanodroplets inhibited tumor growth more effectively than materials not exposed to LIFU, leading to improved animal survival.[135] Yang et al.[136] developed novel triple-stimulus-responsive (ultrasound/pH/glutathione) biodegradable nanocapsules. These nanocapsules had a perfluorohexane core covered by a DOX-containing polymethylmethacrylic acid (PMAA) shell, crosslinked with disulfide bonds for ultrasound-triggered drug release. Exposure to glutathione and acidic pH, combined with ultrasound stimulation, resulted in

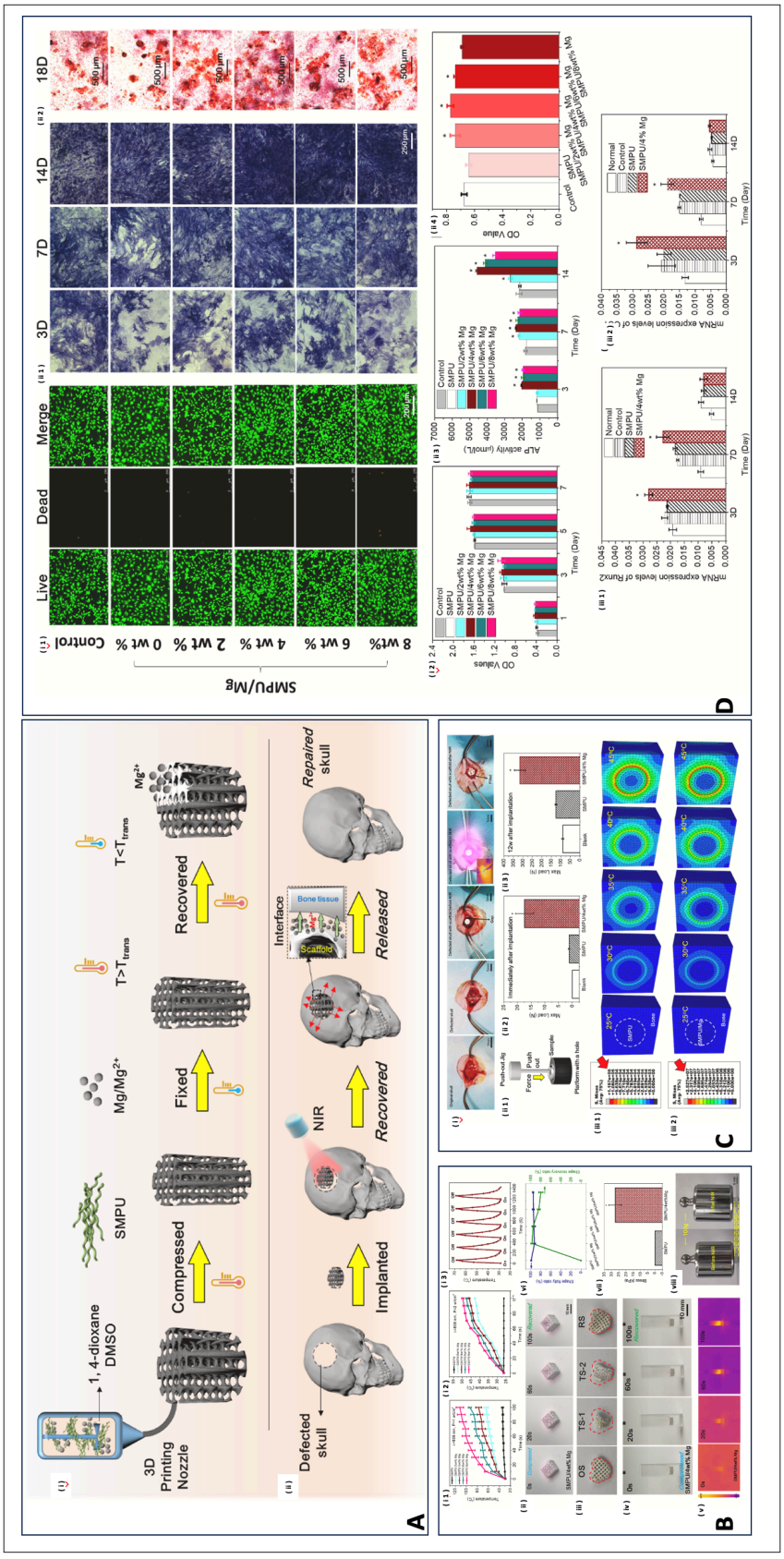

Figure 11. Schematic of NIR-responsive shape memory polyurethane/magnesium scaffolds. (A) Schematic illustration of (A, i) 3D-printed SMPU/Mg scaffold preparation and Mg^{2+} release; and the (A, ii) "3R" process. (B) Photothermal performances and shape-memory effect of 3D-printed scaffolds under NIR light. (C) Implantation of the 3D-printed scaffolds at the defective sites. (D) *In vitro* cell studies of the 3D-printed scaffolds. (D, i1) Fluorescence images of MC3T3-E1 cells after 3 days incubation, where the live cells are in green and dead cells are in red. (D, i2) Cell proliferation of MC3T3-E1 cells. Osteogenic differentiation: (D, ii1) ALP staining of BMSCs at 3, 7, and 14 days. (D, ii2) ARS staining of BMSCs at 18 days. (D, ii3) ALP activity. (D, ii4) Quantitative analysis of calcium nodules. (D, iii1–iii2) Expression levels of Runx2 (iii1) and OST (iii2) of rat BMSCs at 3, 7, and 14 days. Abbreviations: SMPU: Shape-memory polyurethane; NIR: Near-infrared. Adapted with permission from Zhang et al.129

enhanced drug release.[136] Nonetheless, ultrasound response faces challenges, including tissue penetration depth and ensuring targeted delivery before stimulation, which require further investigation. Li et al.[137] created 4D-printed building blocks from zinc-neutralized poly(ethylene-methacrylic acid) ionomer (Surlyn). These blocks enable active vibrational strip switching and manipulation of elastic waves in the 1000–4000 Hz range. This ionomer exhibits shape-memory behavior that can be rearranged into new shape patterns by applying thermal stimuli, thereby tuning the mechanical properties in the spatial and temporal dimensions.[137] Although some progress has been

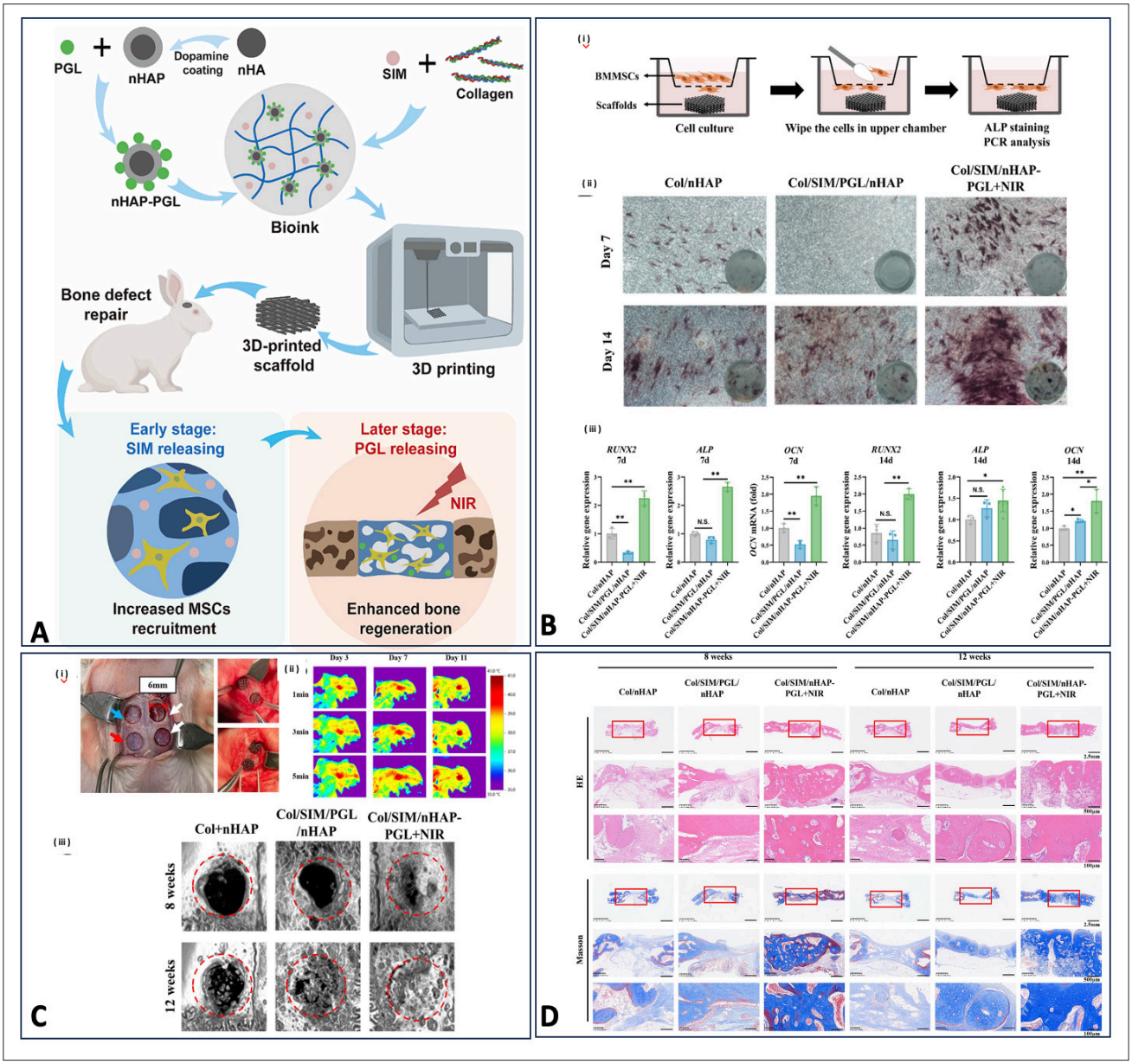

Figure 12. Schematic of near-infrared-light-responsive on-demand drug-delivery scaffold. (A) Schematic illustration for the fabrication of 3D-printed NIR light-responsive scaffolds with on-demand release, which increased MSC recruitment and enhanced bone regeneration. (B) Evaluation of *in vitro* osteoblastic capability of scaffolds with different releasing kinetics. (B, i) Schematic illustration of rabbit BMMSCs cultured with different scaffolds via the Transwell method. (B, ii) ALP staining and (B, iii) relative expression of osteogenic genes of BMSCs cultured with different scaffolds after 7 or 14 days of incubation. (C, i) Rabbits underwent cranial defect surgery and were implanted with scaffolds. (C, ii) Infrared thermal images at cranial defect sites implanted with Col/SIM/nHAP-PGL scaffold and treated with 808 nm NIR light irradiation (0.5 W/cm^2; 5 min). (C, iii) Representative micro-CT images of cranial bone defects implanted with different drug-loaded scaffolds 8 and 12 weeks after implantation. (C, iv) Quantitative comparison of the ratio of bone volume to tissue volume (BV/TV, %) and bone mineral density (BMD) between different groups. (D) H&E and Masson staining of histological sections at rabbit cranial defect areas at 8 and 12 weeks. Abbreviations: NIR: Near-infrared; MSC: Mesenchymal stem cell; H&E: Hematoxylin and eosin. Adapted with permission from Dong et al.[130]

made in the research of ultrasound-responsive materials in the field of drug delivery and the clinical application of acoustic-responsive materials, 4D printing technology is still in its early phases. Future development and application of acoustic-responsive 4D printing materials are projected to become a novel trend in biomedicine.

3.1.2.7. pH

Changes in pH can alter the properties of polymers or hydrogels. The human body's pH varies widely under normal and disease conditions. Acidic or basic groups in pH-responsive polymers either take in or release protons in response to pH variations. This mechanism enhances their self-assembly ability to react to pH fluctuations through ionized swelling and contraction.[138] Xu et al.[139] used injection molding to produce pH-responsive chitosan/tripolyphosphate hydrogels. Tumor extracellular matrices, including those in bone tumors, are typically acidic. Hence, pH-responsive drug delivery systems that change physically or chemically in acidic environments are highly valuable. Qu et al. studied injectable hydrogels made from PEG terminated with diphenylaldehyde and N-carboxyethyl chitosan, encapsulated with DOX, for treating hepatocellular carcinoma.[140] Beyond cancer treatment, smart delivery systems are being researched for issues like chronic gastric wounds, osteomyelitis, and diabetes. L-arginine-grafted Alg hydrogel beads were produced by Mohy Eldin et al.[141] At particular pH values, these beads expand and release proteins.[141] Since inflamed tissues, like tumors, are more acidic, pH-responsive delivery systems are useful for treating infections. However, pH-responsive materials have limitations. Implantation or drug delivery can alter the surrounding pH, potentially causing unintended activation of these materials. Additionally, fully replicating *in vivo* pH fluctuations remains a challenge, necessitating further research.

3.1.2.8. Ionic strength

Several studies have indicated that crosslinking cell-loaded biomaterial scaffolds with multivalent ions (such as Ca^{2+} and Zn^{2+}) are useful in bioprinting. For instance, Tao et al.[142] created a high-intensity cell-filled hydrogel with bidirectional reversible shape memory. This hydrogel utilizes CN-CN dipole-dipole interactions that reversibly respond to zinc ions. A bilayered DDR hydrogel consisting of a layered structure can be thermally treated to produce surface micropatterns, and the micropatterns can be subjected to zinc ions to drive a reversible shape-memory behavior, providing a simple method for fabricating programmable hydrogel gel surfaces.[142] Nan et al.[143] created another reversible shape-memory hydrogel using imidazole-zinc ion interaction. This reversible memory behavior enables the hydrogel to promote the proliferation of L929 cells and fold flat cell-filled hydrogel sheets into temporary tubular structures that can be stabilized *ex vivo* with few zinc ions, and the permanent shape can be restored by eliminating the zinc ions with a complexing agent, making them promising candidates for implantable tissue-engineered scaffolds.[143] Lai et al.[144] utilized synthetic hydrogels of Alg and methylcellulose (MC) that were 4D-printed into a series of patterned 2D structures, specifically controlling the spacing and angle θ of the patterned bands. The 2D structures responded to Ca^{2+} when immersed in a calcium chloride solution and deformed into simple or complex 3D morphologies through anisotropic swelling (Figure 13).[144]

3.1.2.9. Enzyme

Enzyme-responsive smart biomaterials can produce changes in the physicochemical structure of the material catalyzed by specific enzymes.[145] By acting as functional side groups or cross-linking the hydrogel, enzyme substrates have the ability to alter the form of hydrogels. MMP is an enzyme that induces swelling and degradation in certain hydrogels, and MMP levels are higher in some cancerous tissues. Kim et al.[146] produced MMP-responsive hyaluronic acid hydrogels that imitate the natural remodeling characteristics of the ECM. The MMP-sensitive properties of the scaffolds allowed for the localized activation of MMP by most cells during tissue remodeling and regeneration. These hydrogels have a tunable degradation rate and also exhibit good MSC attachment and proliferation.[146] The enzyme-responsive system prevents degradation of its payload, and at the same time can be selectively released to the target site.[147] Wang et al.[148] combined hyaluronic acid, gentamicin (GS), and montmorillonite (MMT) in multilayers. The fabricated high-roughness multilayers were progressively degraded in hyaluronidase (HAS) solution or bacterial infections in microenvironments to induce the responsive release of GS for the long-term inhibition of biofilm formation.[148] The main advantage of enzyme-responsive biomaterials in drug delivery is their selectivity, which helps protect healthy cells from harm.[145] The degradation rate of the materials is accelerated by the catalytic action of specific enzymes, leading to structural changes in the hydrogel. Although enzyme-responsive biomaterials can improve specificity and mitigate off-target effects in drug delivery, future research directions could focus on improving the selectivity and long-term effects of enzyme-responsive smart materials. Also, the intelligence and shape-memory function of enzyme-responsive smart materials should be thoroughly investigated, which is highly relevant to the field of 4D printing. Future research could focus on combining enzyme-responsive smart biomaterials with 4D printing technology to realize more complex and controllable structural changes.

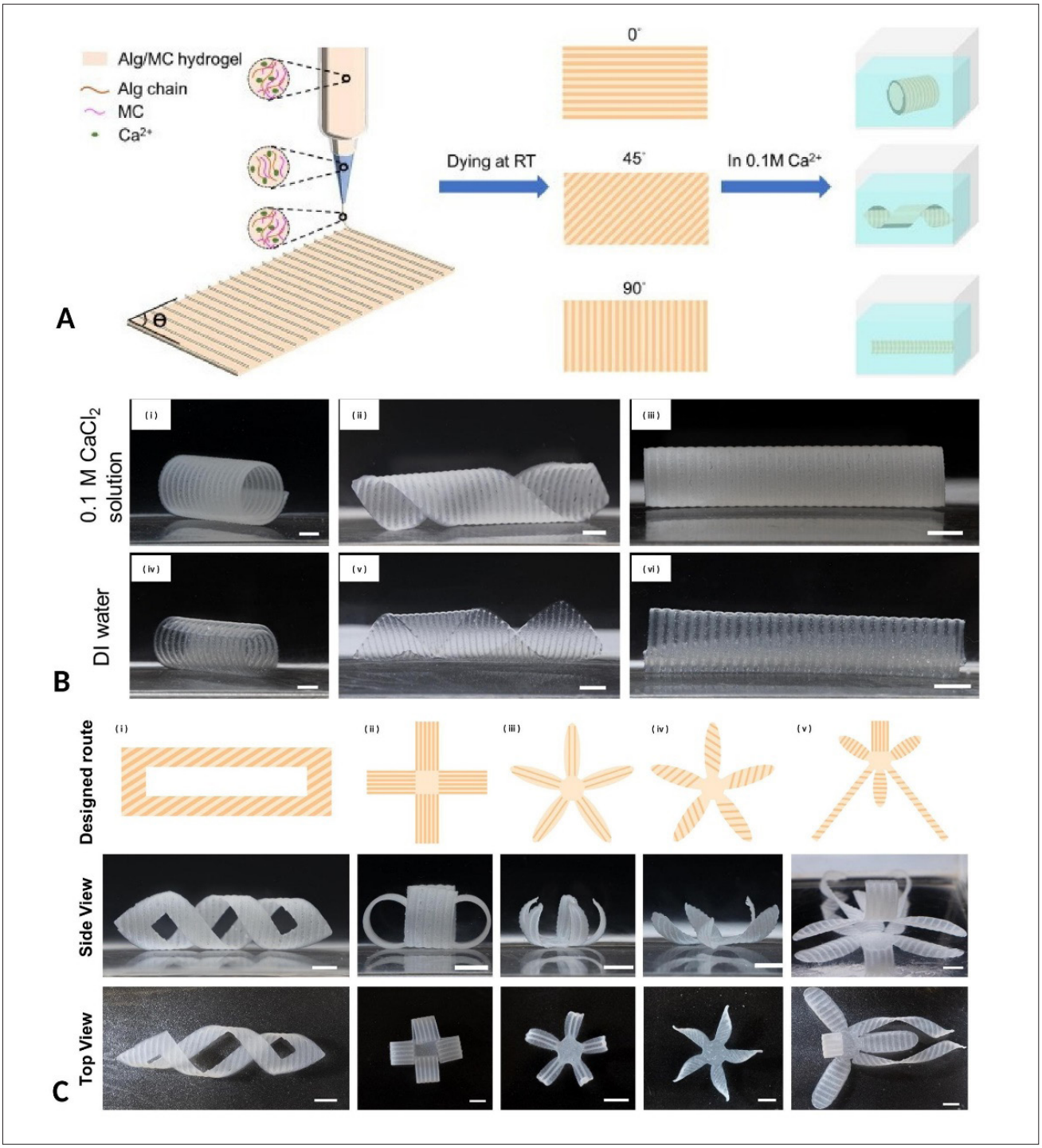

Figure 13. Schematic of 4D printing alginate (Alg)/methylcellulose (MC) hydrogels. (A) Schematic illustration of 4D printing patterned Alg/MC hydrogels and their 3D deformations on immersion in 0.1 M $CaCl_2$ solution. (B) 3D shape deformations of 4D-printed, simple patterned hydrogels with tube-curling structures. Angle = 0° (i, iv), 45° (ii, v), and 90° (iii, vi) correspondingly (Scale bar: 5 mm). (C) Designed routes of the 4D-printed patterned hydrogels and their corresponding complex 3D deformations from the side view and top view upon immersion in 0.1 M $CaCl_2$ solution: (C, i) a double helix with strip width of 1.4 mm and printing angle of 35°; (C, ii) an open cage structure with strip width of 1.43 mm and printing angles of 0, 90, 180, and 270°, respectively; (C, iii) a flower with each petal having strip width of 1.2 mm and printing angle of 0°; (C, iv) a flower with each petal having strip width of 1.2 mm and printing angle of 45°; (C, v) an orchid with a top rolling petal having strip width of 1.84 mm and angle of 0°, three bending petals having strip width of 2 mm and angle of 90°, and two twisting petals having strip width of 2 mm and angle of 45°. Scale bar: 5 mm). Abbreviations: Alg: Alginate; MC: Methylcellulose. Adapted with permission from Lai et al.[144]

3.1.2.10. Multiple stimuli

Combining multiple stimuli enhances the responsiveness of each stimulus and improves cell regulation. Common combinations include temperature-pH, temperature-magnetic field, light-temperature, light-magnetic field, pH-magnetic field, and enzyme-magnetic field. Addressing the challenges of stimulus-responsive systems involves integrating various responsive materials, offering a novel approach to overcoming these limitations. Multi-responsive biomaterials hold the potential to transform tissue engineering by reacting to multiple environmental stimuli, thereby creating structures that replicate natural tissue properties.

To improve DOX delivery, Daravan et al.[149] studied heat/pH-responsive ABC triblock copolymers. They found that the release rate increased in acidic environments and decreased as pH increased at normal body temperature. The release rate also dropped when the temperature was raised to 46°C across all pH levels.[149] For application in cardiac tissue models, Li et al.[150] created pH- and temperature-sensitive poly(acrylic acid) (PAA)-based hydrogels. Under the same temperature settings, these hydrogels remained liquid at blood pH (i.e., pH 7.4) but hardened at the acidic pH of an infarcted heart (pH 6–7).[150] For localized chemo-photothermal cancer therapy, injectable hydrogels composed of poly(NIPAm-co-MPCD)/gold nanorods (GNR) that respond to both pH and NIR are suitable.[151] A novel P(MEO2MA-co-OEgMA) nanocomposite containing light-responsive copper sulfide nanoparticles was presented by de Solorzano et al.[152] This substance combines to create a thermoresponsive, cleavable nanocomposite that can hold and release bupivacaine. As the temperature increased from 37 to 45°C, the release rate increased and was further improved by 808 nm laser irradiation.[152] Chitosan was used to produce biocompatible and biodegradable magnetic micro-swimmers through 4D bioprinting. This technique integrates micro-swimmer movement with controlled drug release, addressing limitations in therapeutic applications.[153] This research highlighted the effectiveness of integrating light-triggered drug delivery with magnetic micro-delivery systems, offering a promising approach for controlled drug delivery challenges.[154] However, the preparation of these materials is complex, and their response range may be limited.[155] Further research is required to understand these limitations and develop solutions.

3.1.3. 4D printing technologies for fabricating biomaterials

According to Momeni et al.,[68] 4D bioprinting is the process of printing stimulus-responsive smart materials using 3D bioprinting technology to change the size, form, or structural composition of an object material. These materials may or may not contain cells. Cell fusion and assembly are important aspects of 4D bioprinting that involve the formation and maturation of structures loaded with cells over time.[156] The primary difference between 3D and 4D bioprinting is in the materials and external stimuli employed, though the printing techniques employed are similar.[157] Conceptually, 3D printing is an additive manufacturing (AM) method.[158] 3D printing technology is the key to molding the biomaterial scaffolds. For bone tissue engineering, several AM technologies have been used, including material extrusion, powder bed fusion, vat photopolymerization, material jetting, binder jetting, directed energy deposition, and sheet lamination.[159]

Material extrusion processes involve the melting and deposition of material at high temperatures. Techniques include fused deposition molding (FDM), fused filament fabrication, screw-assisted AM, pneumatic or mechanical material extrusion, direct ink writing, and fused electrostatic spinning writing. The material is selectively extruded through nozzles or orifices to create complex 3D-printed parts in a layer-by-layer deposition.

Powder bed fusion includes selective laser melting (SLM), direct melt laser sintering (DMLS), selective laser sintering (SLS), and electron beam melting (EBM). By using 3D CAD in an inert environment with pre-set parameters, the powder bed fusion machine selectively applies thermal energy to specific areas of the powder bed (the granular material laid on the surface of the build platform) to fuse it into a solid shape, repeating the layer-by-layer operation until the print is complete.

Vat photopolymerization includes stereolithography (SLA) and digital light processing (DLP). In vat photopolymerization, a liquid photopolymer is placed in a container or drum, and the build platform is partially submerged near the liquid surface. Using 3D CAD pre-set parameters, a printer directs a light source to selectively cure the liquid photopolymer into a solid layer. The build platform is then resubmerged in the remaining resin and the process is repeated to complete the print.

Material jetting is similar to a 2D inkjet printer that uses a continuous or drop-on-demand (DOD) method to eject material from a nozzle onto a build platform. UV light is used to cure or harden the material layer. Since the material must be deposited in droplets, polymers, and waxes are the most commonly used materials.

Binder jetting involves the use of two materials: a powder-based material and an adhesive. The binder acts as an adhesive between the powder layers, usually in liquid form, while the build material is in powder form. To print,

the fresh powder material is laid down in a single layer, and the layers of build material and binder are deposited layer by layer to form the intended shape until the print is complete.

The directed energy deposition process begins with the creation of a 3D model using CAD software. In a controlled chamber with low oxygen levels, the molten material is deposited onto a specified surface and then solidifies, fusing the materials together to form a structure, similar to material extrusion, but with a nozzle that can move in multiple directions. For electron beam-based systems, the process takes place in a vacuum, whereas laser-based systems use a completely inert space in the processing of reactive metals.

Sheet lamination is the process of binding material sheets with a predefined shape/geometry together to form a 3D part. The layer thickness depends on the thickness of the material sheet, which determines the final quality of the printed part. Nonetheless, this approach is the least commonly used 3D printing technique.

4D printing relies on 3D printing technologies, particularly in the field of bone tissue engineering, and the technologies used to print responsive materials in 4D are compatible with AM processes. 4D printing is based on 3D printing technology, especially in the field of bone tissue engineering, and the technology used to print responsive materials for 4D printing is compatible with the AM process.[160,161]

Stereolithography (SLA) and SLS are laser-based printing technologies that are suitable for 4D printing. The ideal printing material for SLA should have a relatively low to medium viscosity and utilize polymer systems cured with smart photopolymers, such as those cured by UV light, enabling the printed structure to deform or change in response to an external light stimulus.[162] If a hydrogel is used as the material matrix, fillers such as iron-activated nanoparticles, CNTs, graphene, ceramics, metals, and enzymes or enzyme substrates can be doped into the material. This allows the material to respond to light and deform in response to external stimuli, such as magnetic fields, electric fields, temperature, or biological enzymes, thereby enhancing its mechanical properties. This combination allows the material to have programmable response properties in multiple environments.[163] While SLS is primarily preferred for printing thermoplastic materials, which tend to be semi-crystalline or amorphous with high melting points,[164] the polymers widely used in SLS technology are polyamides, polyurethanes, PEEK, and PCL.[165] These materials efficiently absorb specific wavelengths of laser energy during printing and can be sintered using laser layering with SMP, SMA, or SMC. Additionally, micrometer or nanoscale inorganic fillers can be added to enhance electrical and magnetic actuation.

Fused deposition molding (FDM) and DIW are extrusion-based printing technologies. FDM prints by extruding and depositing thermoplastic materials and is suitable for 4D printing. The process uses raw materials that are typically amorphous polymers, most commonly PLA and ABS. Other polymers are also used in FDM [e.g., polycarbonate (PC), PCL, Thermoplastic Polyurethane (TPU)] for printing SMPs (SMP, SMA, and SMC), where the SMP deforms in response to changes in heat or humidity, and is particularly suited to scaffold construction for bone tissue engineering.[166] Composites formed by the incorporation of metal or ceramic particles are widely studied for their applications. DIW enables the construction of dynamically responsive tissue structures using SMH and SMP with high precision, making them particularly suitable for soft tissues and vascular scaffolds.[61]

Inkjet bioprinting allows precise deposition of cells and biomaterials, suitable for building dynamic structures in 4D bioprinting. Using SMH (e.g., thermal hydrogels), cellular scaffolds and tissue structures can be fabricated that are able to deform according to environmental conditions.[167] It is also possible to combine SMA and SMP using a multi-actuator jetting system, which allows for the creation of 4D-printed junctions with different mechanical properties or responsiveness to stimuli.[164] However, it is only suitable for low- to medium-viscosity materials, as high-viscosity materials tend to clog the printhead during printing.

Digital light processing (DLP) is similar to SLA, except that it uses a digital light source for fast curing to print complex structures more rapidly. In addition to filler-free photopolymers, materials such as those containing ceramic or metal particles can be processed using DLP, streamlining the production of blends of polymers and inorganic phases. Electrically activated shape-memory composites consisting of photoresins and multi-walled CNTs (MWCNTs) have been produced by Mu et al.[168] Combined with smart materials, light control allows the printed tissue to deform under specific light conditions. This has great potential for applications in complex tissue engineering and drug delivery systems.[169]

Each of these technologies has its own advantages and can be flexibly selected for different application scenarios. The future will focus on designing and synthesizing more stimulus-responsive smart materials that can be precisely controlled, have good reproducibility recovery, high biocompatibility, and targeted homeostatic modulation of the disease microenvironment to meet diverse biomedical needs. Multifunctional 3D printing technologies continue to evolve, offering various options for printing with different

materials. The need for reversible and easy preparation techniques in the field of biomaterials has driven the research and application of 4D bioprinting technology.

3.2. Cells

Together with biomaterials, cells are among the most crucial components of effective bone regeneration. Several cell types are involved in the process of bone regeneration, which includes matrix creation, focused cell recruitment, proliferation, differentiation, and maturation of tissue function for transformation.[170] MSCs and osteoblasts are appropriate for 4D printing because they have immunomodulatory capabilities and secrete protective substances. MSCs, often known as "universal cells," are recommended for tissue regeneration due to their ability to self-renew and differentiate into a variety of cell types under certain conditions.[171,172] They can be produced from both embryonic and adult stem cells.[173]

According to research, MSCs derived from bone marrow, adipose tissue, and the periosteum play an important role in bone repair and have high osteogenic potential.[174,175] Bone marrow-derived progenitor cells can develop into osteoblasts *in vitro*, which is necessary for bone healing.[176] For example, Moncal et al.[177] demonstrated that after six weeks, rat BMSC-laden bioinks applied to craniomaxillofacial lesions resulted in 40% bone tissue development and 90% bone coverage. In contrast, untreated defects displayed 25% complete bone coverage and 10% new bone tissue.[177] Due to their versatility and capacity to grow into cells with immunomodulatory, osteoinductive, and anti-inflammatory properties, adipose-derived MSCs can facilitate bone regeneration and repair.[178] These MSCs have been tested in combination with scaffolds to enhance osteoinduction and remodeling in rodents.[179,180] Conejero et al.[181] demonstrated that rats with palatal bone defects can be repaired by these MSCs. MSCs and bone progenitor cells can also be found in the periosteum, a thin layer of vascular tissue that envelops the surfaces of bones. Research has demonstrated that the periosteum is a significant source of bone-forming cells during the healing of fractures.[182,183] Studies conducted *in vivo* have also revealed that progenitor cells from the periosteum provide better bone growth than cells produced from the bone marrow.[184] Despite the lack of specific markers for periosteal progenitor cells, they remain highly promising for tissue engineering research.[185]

In oral and maxillofacial surgery, there is ample potential as a cell repository due to the specificity of oral tissue structures and organs, including the apical papilla, pulp, deciduous papilla, periodontal membrane, and alveolar bone.[172] MSCs are quite specialized and classified into several types, including dental pulp stem cells (DPSCs), apical papilla stem cells (SCAPs), periodontal ligament stem cells (PDLSCs), odontoblasts (DFC), gingival fibroblasts (GF), human exfoliated deciduous dental stem cells (SHED), BMSCs, adipose-derived stem cells, and preosteoblasts (MC3T3E1 cells). These stem cells have been utilized in 4D printing applications.[154,186-199] The rich source of oral stem cells brings great applications and potential uses in oral tissue engineering.[172] DPSCs, SCAPs, and SHEDs are mostly used in 4D printing for tooth regeneration. MSCs with immunosuppressive characteristics are readily available from dental pulp.[200] Due to their great plasticity, ease of sourcing, and multipotency, DPSCs are a good fit for low-risk autologous therapies that target physical deficiencies.[201] GFs and other physiologically active substances can affect the differentiation of DPSCs.[202,203] According to Karbanova's research,[204] DPSCs exhibit multipotentiality, as evidenced by their ability to self-renew and expression of markers linked to vascular, neuronal, bone, and cartilage tissues.[204] Similarly, SCAPs exhibit strong mineralization and high levels of dentin salivary acid phosphoprotein, indicating odontogenic differentiation.[205] Restoring pulpal blood flow is an application of periodontal treatments that benefit from the enhanced biocompatibility of 3D-printed periodontal membrane cells.[206,207] *In vivo*, SHEDs encourage the growth of dentin and bones.[208] The dental germ is surrounded by dental follicular stem cells (DFSCs), which originate from the mesenchymal connective tissue. DFSCs can develop into osteoblast-like cells that generate mineralized matrix nodules and express osteoblast markers. They also have a stronger proliferation capacity than other stem cells.[193] Dental vesicles can also develop into periodontal membranes and serve as progenitors for other types of periodontal cells, such as osteoblasts and odontogenic osteocytes.[209,210] Diverse phenotypes of GFs present opportunities for regenerative therapy. Basic biomaterials with functionalities can promote GF differentiation and proliferation. Clinical studies have revealed that cultured GFs significantly reduce vertical pocket depth in the treatment of intraosseous periodontal defects when compared to β-tricalcium phosphate and Col membranes.[211] Human DPSCs (hDPSCs) have the potential to significantly grow and become colony-forming unit fibroblasts (CFU-F), making them promising for regenerative therapy.[212] Stromal stem cells from human dental pulp (SBP)-DPSCs, a pluripotent subpopulation of DPSCs, can synthesize 3D-woven bone tissue structures *in vitro* and differentiate into osteoblasts and endothelial cells. They work well with various scaffolds, have a long lifespan, and transform into mature bone tissue with proper vascularization and haversian tubes *in vivo*. Transplantation of SBP-DPSCs holds great promise for therapeutic use.[213] When exposed to a neurogenic medium,

SCAPs exhibit neurogenic markers such as nestin and neurofilament M. SCAPs are a unique and very efficient source of dental stem cells, despite the similarities between them and DPSCs. It is commonly known that SCAPs play a function in epigenesis and root development.[214]

The effects of biomaterials on stem cells are subject to further in-depth study due to the unstable relationship between their stimuli and stem cells. Some researchers have claimed that electrical stimulation has a significant effect on stem cells. For example, electrical stimulation was found to be extremely effective in the field of nerve and neurostimulation, but less effective in pluripotent stem cell differentiation.[215] Many studies have explored the use of external electric fields to influence stem cell behavior in cell cultures, utilizing capacitance or electromagnetic fields. This topic has been extensively reviewed.[216] However, more research is needed to understand the interaction between stimuli and cells in 4D printing. Previous investigations have examined the impact of low-density oscillatory ultrasound on osteogenic differentiation.[217] The use of biomaterials in scaffold design to control cell behavior through ultrasound stimulation is an emerging field. Magnetically responsive composites offer another approach to controlling cell fate. An external magnetic field provides a precise, targeted stimulus that can deeply penetrate tissues. Even in the lack of magnetically responsive materials, static magnetic fields (SMFs) and pulsed electromagnetic fields (PEMFs) are frequently utilized to promote cell proliferation and differentiation, particularly for bone tissue regeneration and repair. Studies reveal that PEMFs impact both cell proliferation and differentiation, while SMFs influence the differentiation of DPSCs and human adipose-derived MSCs (hADMSCs).[218,219] Therefore, magnetically responsive scaffolds in combination with magnetic fields can promote the response of stem cells to synergistic therapeutic tissue regeneration. In bone regeneration, the involvement of cells is crucial. These cells can differentiate into osteoblasts *in vitro* and play a key role in bone repair. Researchers have successfully used bioprinting technology to integrate BMSCs and adipose tissue-derived MSCs into scaffolds, achieving 3D printing of bone structures. This method demonstrated a considerable increase in bone coverage area and tissue development, opening new avenues for bone regeneration. The distinct anatomical features of dentistry and maxillofacial surgery present many opportunities for cell storage in the field of oral bone tissue engineering, with prospective uses in tooth regeneration and oral tissue engineering. In electrical stimulation and magnetic response composites, electrical stimulation has demonstrated promising results for nerve and neural stimulation, while magnetic response scaffolds combined with external magnetic fields are expected to facilitate stem cell response for synergistic therapeutic tissue regeneration. However, further in-depth studies are still needed in this area to understand the relationship between the stimulatory factors of biomaterials and stem cells. Overall, these studies provide strong support for bone regeneration and oral tissue engineering, offering great promise for future clinical applications and technology development. In the future, in-depth studies on the mechanisms of stimulus-responsive biomaterials, as well as optimizing the selection of cell types and combinations, will help to further advance the field.

3.3. Growth factors

Growth factors (GFs) are signaling molecules that are soluble and attach to the ECM, affecting distinct cellular responses such as growth, proliferation, and differentiation. For bone tissue, GFs at the defect site are essential for cell migration and healing. Functionalizing these GFs in tissue-engineered scaffolds can enhance bone regeneration. Osteoblast activity is regulated by GFs, such as IGF, PDGF, FGF, TGFβ, and BMPs, which act autocrinely and paracrinely through receptors on osteoblasts. For effective tissue-engineered scaffolds, precise timing in delivering these GFs and other bioactive molecules is essential to guide cellular responses and enhance regenerative potential.[220]

Bone formation, resorption, and remodeling are complex processes regulated by GFs. Therefore, cell development systems in bone tissue engineering need to be dynamic to support cells throughout the bone life cycle. Typically, soft tissue materials often focus on delivering BMPs for bone growth and VEGF for vascularization.[221] Ideal biomaterials regulate GF production and signaling by acting as a storage structure for GFs and mimicking the ECM.

Growth factors (GFs) have been attached to scaffolds via a variety of techniques in bone tissue engineering, such as covalent bonding, bioaffinity, and physical encapsulation.[222] Due to its profound impact on osteoblast metabolism, GFs are essential for bone repair. Bone mending and regeneration can be induced by BMPs. Moncal et al.[177] explored creating osteogenic bioinks by co-delivering plasmid DNA encoding BMP-2 and PDGF-B. Their bioinks, developed within six weeks, displayed higher bone tissue formation and coverage compared to control bioinks.[177] Mahmoudi et al.[223] created a hydrogel scaffold that was click-crosslinked using a BMP-2 mimetic peptide (BP). In human DPSCs, this structure successfully induced osteogenic differentiation and maintained BP for over a month. Bioink-created scaffolds supplemented with BMP-2 and TGF-β1 demonstrated improved bioactivity

and bone regeneration.[224] Furthermore, Freeman et al.[3] demonstrated that VEGF's spatial presentation influences *in vivo* angiogenesis, with implants exhibiting accelerated healing of large bone defects when VEGF gradients and BMP-2 were included. Chemical fixation, which provides controlled and sustained release, can overcome initial burst release seen with physical capture.[225,226] The use of growth hormones and cells in bioinks for bone regeneration is one recent development. Studies have demonstrated that SDF-1 controls cell migration and stimulates vascularization and bone regrowth.[227] Incorporating SDF-1 into hydrogels and PLA scaffolds enhances cell migration and osteogenesis.[228] Co-assembling hydrogel, SDF-1, and BMP-2 enable controlled release and periodontal bone tissue regeneration.[229] Although BMP-2 is effective in preclinical models, it has caused complications like ectopic bone formation and impaired healing in clinical settings.[230] In animal studies, BMP-7 supplementation enhanced bone formation and regeneration in PCL and β-TCP scaffolds.[229] Tan et al.[228] found that BMP-7 in PLA scaffolds enhanced bone regeneration and produced a porous bone structure. Other studies emphasize the importance of ECM protein motifs (like fibronectin and Col) in mimicking the ECM.[231] Current research also explores adenosine receptor activators and alternative GFs, such as FGF, TGF-β, PDGF, and IGF.[232] BMP-2 and these GFs have been reported to be highly osteoinductive in preclinical models within PCL, ceramic, and hydrogel scaffolds used for mandibular and cranial defects.[233,234] Unlike BMP-2's uncontrolled regeneration, bimatoprost-coated scaffolds improved bone regeneration in cranial and alveolar defects without complications.[233] Tanaka et al.[235] studied FGF-2 and carbonate apatite (CO3Ap) for periodontal regeneration, finding that their combination promoted new bone formation, scaffold replacement, and preserved adjacent bone integrity.

Systems that respond to stimuli have been developed to adjust GF release profiles in response to the needs of injured tissues. Microenvironmental signals like as pH, temperature, redox gradients, and enzymes can control drug release. The release of bioactive molecules can be further improved by external triggers like light, magnetic, and ultrasound. Smart biomaterials can respond to these triggers by altering their physical or chemical properties to control therapeutic release. These materials can minimize unintended off-target release and initiate controlled release by breaking down, expanding, contracting, transitioning from a sol to a gel, or changing their hydrophobicity.[236] Consequently, this approach helps in reducing severe side effects. Thus, the synergy between GFs and scaffolds enhances functionalization and better addresses the needs of natural tissues.

4. Recent research advances in 4D printing of implants in dentistry

Tissue engineering techniques for intraoral tissue defects are currently a major biomedical research hotspot. Bioprinting is used as a fabrication method that rapidly manufactures complex structures in combination with associated cells and scaffolds to enable extensive tissue regeneration. 3D printing strategies allow for bone regeneration,[177] *in vitro* modeling of alveolar bone,[237] regeneration of dental tissues,[238] studying periodontal membranes and periodontal ligaments,[206,239] regeneration of dentin and pulp,[240] and exploration of the scaffold applications in *in vitro* head and neck cancer models.[241] In addition to 3D bioprinting of scaffolds, scaffold-free methods utilize 3D cellular aggregate bioinks for periodontium[241] and bone regeneration[242,243] without a supporting hydrogel or matrix. Currently, half of the research on 3D bioprinting focuses on dental tissue engineering for alveolar bone regeneration.

However, 3D printing is considered static. With the dynamic changes exhibited in the course of oral tissue remodeling – such as the growth and movement of teeth, continuous skeletal repair of alveolar bone, expansion, and reconstruction of oral soft tissues, and restoration of periodontal membranes – the stability and accuracy of static 3D-printed implants do not meet the requirements of dynamic restoration. The "temporal" dimension of 4D printing technology can be pre-programmed through the morphology of the material function, combined with appropriate external stimuli, allowing oral scaffolds made of smart materials to adapt to changes in the morphology and function of oral tissues. This improves the predictability and stability of the restorative effect, bringing new therapeutic possibilities to dentistry.[9-11] 4D printing has two basic steps: processing and programming. Firstly, the model is processed into its original shape; it is then temporized into another shape and finally programmed to convert into another shape when exposed to certain stimuli.[244] Meanwhile, 4D printing enables the sustainable release of drugs, which can be applied in oral bone tissue defect repair and oral disease treatment to improve the therapeutic effect. Given that dental care is often precise and personalized, and that each patient's oral bone tissue is unique, 4D printing technology can be used to create a customized bone tissue engineering treatment plan. This includes prosthetic scaffolds and implants that are made to order, as they can better conform to the form and functional requirements of the patient's bone tissue. Based on each patient's needs, minimally invasive treatments are becoming more common. Additionally, the ability to fabricate intricate microstructures using 4D printing technology makes minimally invasive treatments more

practical for the dentistry industry. Micro-implants and micro-scaffolds can be positioned and implanted through tiny channels or orifices in the oral cavity, reducing surgical trauma and recovery time. The application and development of 4D printing technology are expected to promote technical innovation and treatment levels in the field of oral restoration.

In this regard, a summary of the literature on the potential applications of 3D printing in the oral cavity is provided. The material's ability to adapt to changes in oral stress and soft tissue elasticity, along with its ability to fit both hard and soft tissues due to its morphology memory function, make it suitable for use in implant dentures and removable dentures (Table 3).[244,245]

The most popular material for oral implants is titanium alloy. Despite its many advantages, titanium has been reported to cause allergies and surface degradation. One of the most recent advancements in implantology and maxillofacial surgery is the use of 4D printing for surgical guides, implants, and surgical scaffolds. SMP can transition from a deformed state to an original state, enabling dental implants to expand and fit tightly within the bone cavity for secure fixation.[246] Replacing titanium with SMPs enhances implant biocompatibility and osseointegration. Bone-shaped implants with shape-memory and root-fixing capabilities were developed by Akbarinia et al.[247] At −30°C, these implants – flexible closed-leg cylinders – snap snugly into bone sockets. When they warm up to body temperature and come into contact with the bone cavity, they return to their original bifurcated structure, providing stable attachment and inhibiting rotational movement. This initial stability can significantly reduce the conventional bone healing time.[247] Ying et al.[95] developed a humidity-responsive, injectable, shape-memory gelatin scaffold modified with heparin for bone regeneration in maxillary sinus lifts (Figure 14).

In contrast to metals, SMPs produce biocompatible degradation products and do not release metal ions that cause chronic diseases. The properties of SMPs far exceed those of other types of materials, demonstrating greater stability and higher biocompatibility in dentistry.[248] Pfau et al.[249] used thermo-responsive PCL-DA to treat craniomaxillofacial (CMF) bone defects and conducted an *in vivo* study with rabbit cranial bone. Findings revealed that SMP scaffolds have good biocompatibility and facilitate bone formation and peripheral inward growth.[249]

Successful bone augmentation in oral tissue reconstruction requires tension-free flap closure to avoid soft tissue dehiscence. Oral tissue reconstruction involves defects of various shapes and sizes, and 3D-printed hydrogel systems can facilitate soft tissue augmentation and expansion before bone reconstruction. Soft tissue expanders (STEs) have been used in reconstructive surgery to generate additional soft tissue before bone augmentation. Current STEs use a hydrogel-based self-expanding infiltration system (Figure 15).[250] STE-adjustable swelling properties are utilized to design customizable structures using 4D printing,[251,252] allowing for selective swelling of the structure after implantation to match the anatomical characteristics of the presented defect. Well-designed 4D-printed scaffolds enhance not only complex soft tissue regeneration but also other areas of regenerative dentistry by facilitating adaptive changes.

Recently, 4D-printed hydrogels have been developed[253] that can morphologically, physically, chemically, and functionally transform in response to specific stimuli in their environment. In periodontology, antimicrobial thermosensitive hydrogels that respond to highly specific stimuli (i.e., enzymes produced by bacteria that cause periodontitis) have been developed.[254] Another study explored the antimicrobial effects of thermoreversible polyisocyanide (PIC) hydrogels loaded with doxycycline and/or lipoxin A4. Although high polymer concentrations can be cytotoxic at local application sites, PIC can form hydrogels at lower concentrations in a thermoreversible manner, resulting in non-cytotoxic injectable solutions. *In vivo* studies in dogs with naturally occurring periodontitis demonstrated significant reductions in bacterial growth in the subgingival microbiota in groups treated with lipoxin A4 and doxycycline/lipoxin A4.[255] A polyethylene glycol diacrylate/short antimicrobial peptide smart hydrogel, containing CXCL12, which aids bone regeneration through endogenous stem cell recruitment, was developed specifically for periodontal disease.[256] This hydrogel mixes functional peptide modules with a hydrogel solution and undergoes gelation when stimulated at 37°C. The anchoring peptide is cleaved by gingival protease (an enzyme from *Porphyromonas gingivalis*), releasing the short antimicrobial peptide from the hydrogel. Unlike other groups without the smart peptide module, the enzyme-responsive hydrogels release antimicrobial peptides constantly and in a controlled manner over a period of 10 days. Within a rat model of periodontitis, the hydrogel promoted the migration and differentiation of periodontal stem cells *in vitro*, reduced the growth of *Porphyromonas gingivalis*, and exhibited osteogenic effects. This design enables specific treatment of certain disorders. Furthermore, a combination of an injectable thermosensitive chitosan hydrogel, PD nanoparticles, and an antimicrobial peptide (Nal-P-113) was utilized to treat periodontitis; the peptide and nanoparticles were released

Table 3. Recent research and applications of 4D printing implants in dentistry.

Research area	Materials	Applications	Features	Ref.
Oral implantology	SMA	Implant placement	At −30°C, these implants – flexible closed-leg cylinders – snap snugly into bone sockets; when warmed to body temperature and placed in contact with the bone cavity, they revert to their original bifurcated structure, providing stable fixation to prevent rotational movement	[247]
Oral and maxillofacial surgery	SMH	Maxillary sinus lift and dilation	The stent was moistened with distilled water and manually compressed into a syringe for freeze-drying to determine the shape; a syringe with a 2 mm diameter needle was injected into a Petri dish containing 1 mL of saline solution to simulate intra-operative bleeding; the stent almost regained its initial structure and immediately regained its 3D shape	[95]
	SMP	Treatment of CMF bone defects	Thermo-responsive PCL-DA scaffolds are biocompatible and favor bone formation and peripheral inward growth	[249]
	SMH	STE	The hydrogel-based self-expanding osmotic system promotes STE prior to skeletal reconstruction	[250]
	SMP	Bone defect repair	Integrated growth factors (GFs) in chemically crosslinked PCL shape-memory porous scaffolds; scaffolds gradually returned to their original shape in rabbit mandibular defects in response to body temperature while releasing GFs	[260]
Periodontology	SMH	Drug delivery for periodontal therapy	PEGPD@SDF-1 hydrogels, made from PEG-DA/DTT/FPM scaffolds, release an anchoring peptide SAMP when gingival protease is stimulated, effectively limiting the growth of *Porphyromonas gingivalis* and facilitate *in situ* periodontal tissue regeneration	[254]
	SMH	Specific periodontal therapy	Functional peptide modules are mixed with a hydrogel solution, followed by gelation when stimulated at 37°C; the anchoring peptide is cleaved by gingival protease (an enzyme from *Porphyromonas gingivalis*), releasing the short antimicrobial peptides from the hydrogel continuously and in a controlled manner over 10 days; the hydrogel demonstrated strong inhibition of *Porphyromonas gingivalis* growth, osteogenic effects in a rat periodontitis model, and enhanced migration and differentiation of periodontal stem cells *in vitro*; this design allows for specific treatment of certain diseases.	[256]
	SMH	Drug delivery for periodontal therapy	Thermo-reversible PIC hydrogels of low-concentration doxycycline and/or lipoxin A4 produce injectable solutions without cytotoxicity	[255]
	SMH	Drug delivery for periodontal disease treatment	Thermo-sensitive chitosan hydrogel coupled with polydopamine nanoparticles and antimicrobial peptide (Nal-P-113), which are released from the hydrogel within 13 days	[257]

Abbreviations: CMF: Craniomaxillofacial; STE: Soft tissue expander.

over a period of 13 days.[257] 4D-printed materials are expected to be used in periodontal implants in the future, especially for soft and hard tissue regeneration and less invasive therapies, owing to their remarkable morphologic memory deformation.

Better distribution to the target area was demonstrated by 4D-printed scaffolds made with organic materials like proteins, growth hormones, and stem cells, which initiated new tissue formation. It is anticipated that scaffolds created from the host's stem cells would mature into bone tissue that may be customized, opening up avenues for bone regeneration.[258] Various bone grafts have been used in recent research to increase the vertical and/or horizontal volume of the alveolar ridge to promote dental bone regeneration with satisfactory long-term outcomes. Further research into the interaction between 4D materials

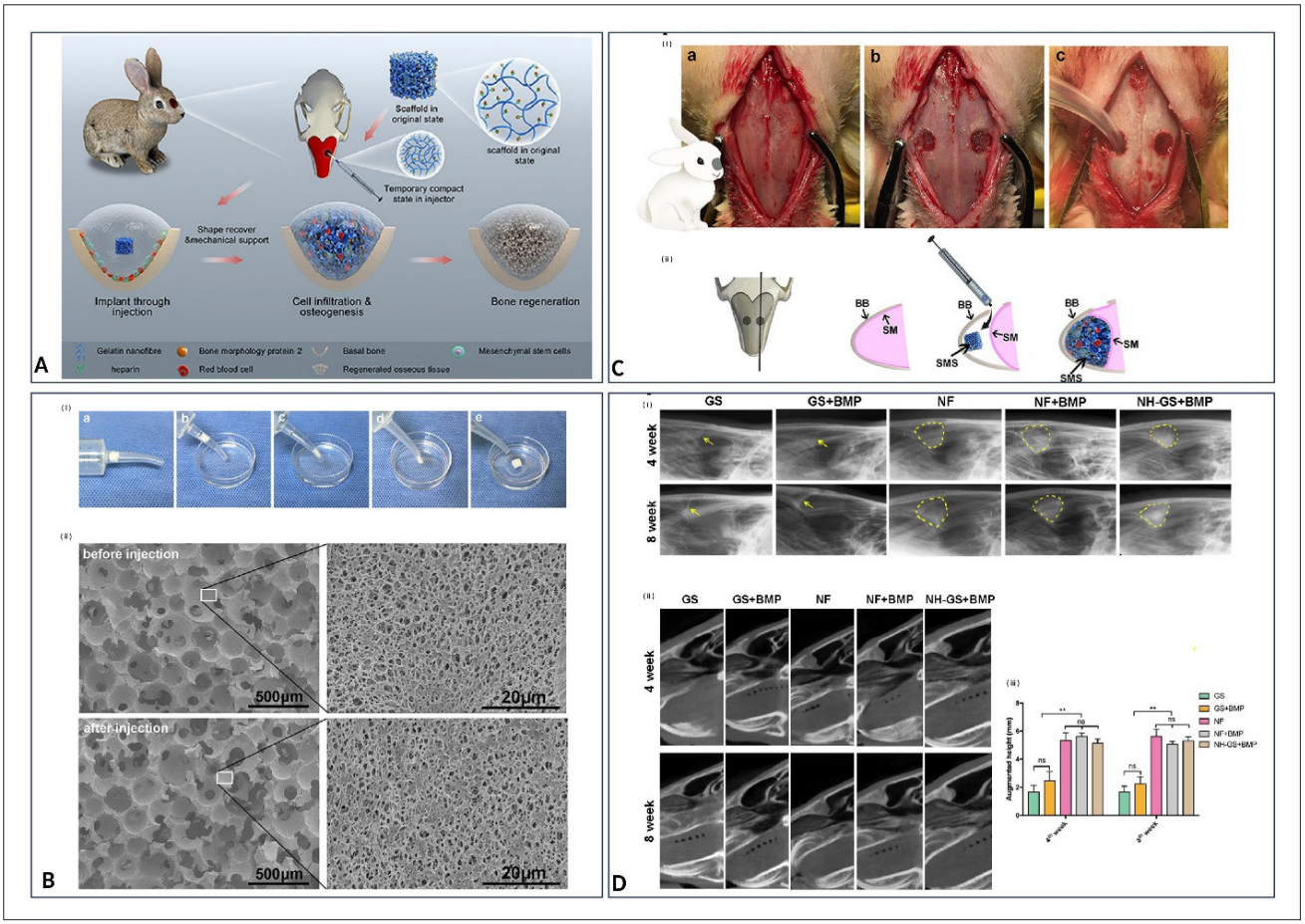

Figure 14. Schematic of ECM-mimicking heparin-modified nanofibrous Gelatin scaffold. (A) Schematic illustration for fabrication of shape-memory ECM-mimicking heparin-modified nanofibrous gelatin scaffold that increases bone regeneration in sinus augmentation. (B) Digital and SEM photographs of injectable NH-GS scaffold during injectability testing. (B, i) Syringe filled with NH-GS scaffold during injection (i–v). (B, ii) Representative SEM images of NH-GS structure before and after injection. (C) Maxillary sinus augmentation in rabbits (C, i) Photographs of the sinus augmentation surgery showing the implantation of NH-GS + BMP into the sinus cavity via injection. (C, ii) Schematic illustration of the sinus augmentation process. Abbreviations: BB: basal bone; SM: sinus membrane; SMS: shape-memory scaffold. (D) Bone regeneration in rabbit maxillary sinus augmentation model. (D, i) Representative dental films of sinus cavity at 4 and 8 weeks post-implantation. (D, ii) Representative CBCT images of augmented sinus at 4 and 8 weeks post-implantation, from sagittal view. (D, iii) Statistical analysis of augmented height in GS, GS + BMP, NF, NF + BMP, and NH-GS + BMP groups. Abbreviations: ECM: Extracellular matrix; SEM: Scanning electron microscopy. Adapted with permission from Ying et al.[95]

and dental tissues, as well as their degradation profiles in different bone types, suggests that SMP blended with ceramic biomaterials holds promise for dental applications due to their excellent printability, mechanical stability, and tissue integration. Son et al.[259] highlighted significant genetic differences between alveolar and long bones. Craniofacial bones typically form via intramembranous ossification, whereas long bones develop through endochondral ossification. Mouse alveolar bone-derived cells (mABDCs) express genes related to osteogenesis, neural crest (NC), and epithelial-mesenchymal interaction (EMI) differently from mouse long bone-derived cells (mLBDCs). During differentiation, BMP-4 significantly increased the expression of the osteogenic genes Msx2, Dlx5, and BMP-2. This impact was more pronounced in mABDCs than in mLBDCs, highlighting the crucial role BMP-4 plays in the creation of alveolar bone and the need for tissue-specific therapies.[259] Liu et al.[260] integrated GFs into chemically crosslinked PCL shape-memory porous scaffolds. These scaffolds gradually returned to their original shape in rabbit mandibular defects in response to body temperature while releasing GFs. Their research demonstrated the potential of shape-memory scaffolds for dynamic *in vivo* environments without significantly affecting drug delivery (Figure 16).[260]

Automated bioprinting techniques offer high precision in organizing cells and biological components, aiding in the customization of patient-specific scaffolds for bioscaffolding applications. Nevertheless, selecting suitable

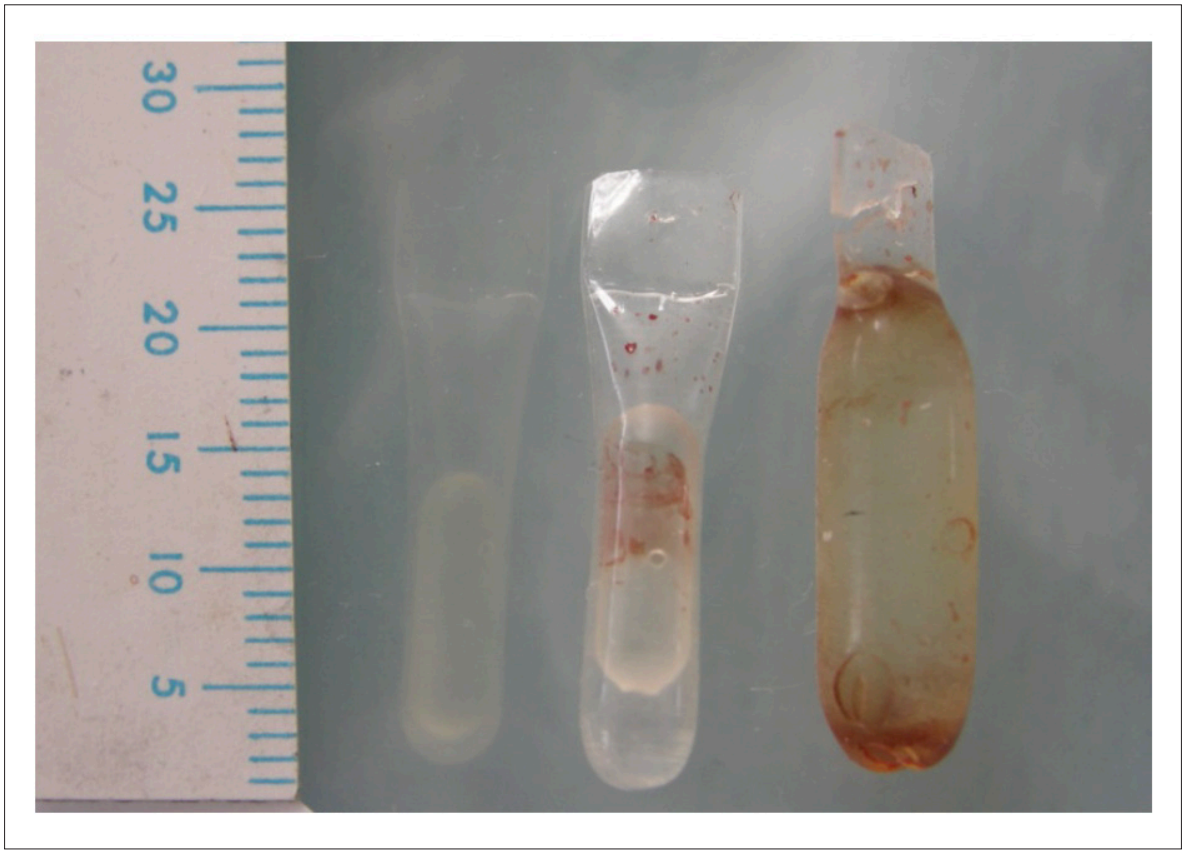

Figure 15. Osmed® Tissue Expander – Cylinder 0.7 mL: dimensions before (left) and after 1h (Middle) and 43 days (right). Adapted with permission from Uijlenbroek et al.[250]

biomaterials to encapsulate cells in bioinks tailored for alveolar bone tissue continues to be a formidable obstacle. The advancement of bioinks has enhanced our knowledge of how spatial organization and geometry affect cell behavior and function *in vitro*, potentially benefiting their application in *in vivo* models for regenerative dentistry.[261] Early bone regeneration requires neovascularization for delivering stem cells, nutrients, and oxygen.[262] Pre-vascularized scaffolds or cell aggregates have been the focus of recent studies due to the highly vascularized nature of bone tissue.[263-265] 4D printing techniques have been developed to generate multiscale tubular networks. For instance, shape transformations, like elongation, lumen expansion, bending, and clamping, can aid in tube formation by leveraging expansion mismatches and mechanical instabilities.[253,266] In hybrid 4D-printed designs, conductive biomaterials like graphene are used to provide chemical signals, physical guidance, and seamless integration for bone and nerve restoration, thereby allowing complex neural tissue regeneration.[2] To be effective, printed vascular structures must mimic both the structural complexity and biological functions of natural blood vessels.[267] Kirillova et al.[92] investigated 4D printing techniques for creating small-diameter functional blood vessels. They utilized two biopolymers, Alg, and hyaluronic acid, to develop a sophisticated deformable hydrogel with self-folding hollow tubes. Their findings indicate that 4D fabrication can be fine-tuned using printing and post-printing parameters.[92] Self-folding tubes can achieve inner diameters as small as 20 μm (similar to the tiniest blood vessels), while hydrogels offer physiological stimulation, maintaining high cell survival and promoting osteoblast differentiation.[91,268,269]

An ECM is a network of macromolecular structures that is released naturally by tissues to support cells and act as vital micro-scaffolds. Decellularized ECM hydrogel scaffolds can be created using 4D printing to promote the production of new tissue at defect areas.[270-273] Scaffolds made from decellularized natural tooth germ ECM are currently the best biomaterials for facilitating tooth regeneration, as they closely match the natural size of a tooth when derived from adult dental cells.[274] Significant research is required for complete tooth regeneration, including identifying appropriate cell sources that signal tooth growth and exploring the potential of induced pluripotent stem (iPS) cells. To direct adult cells in the

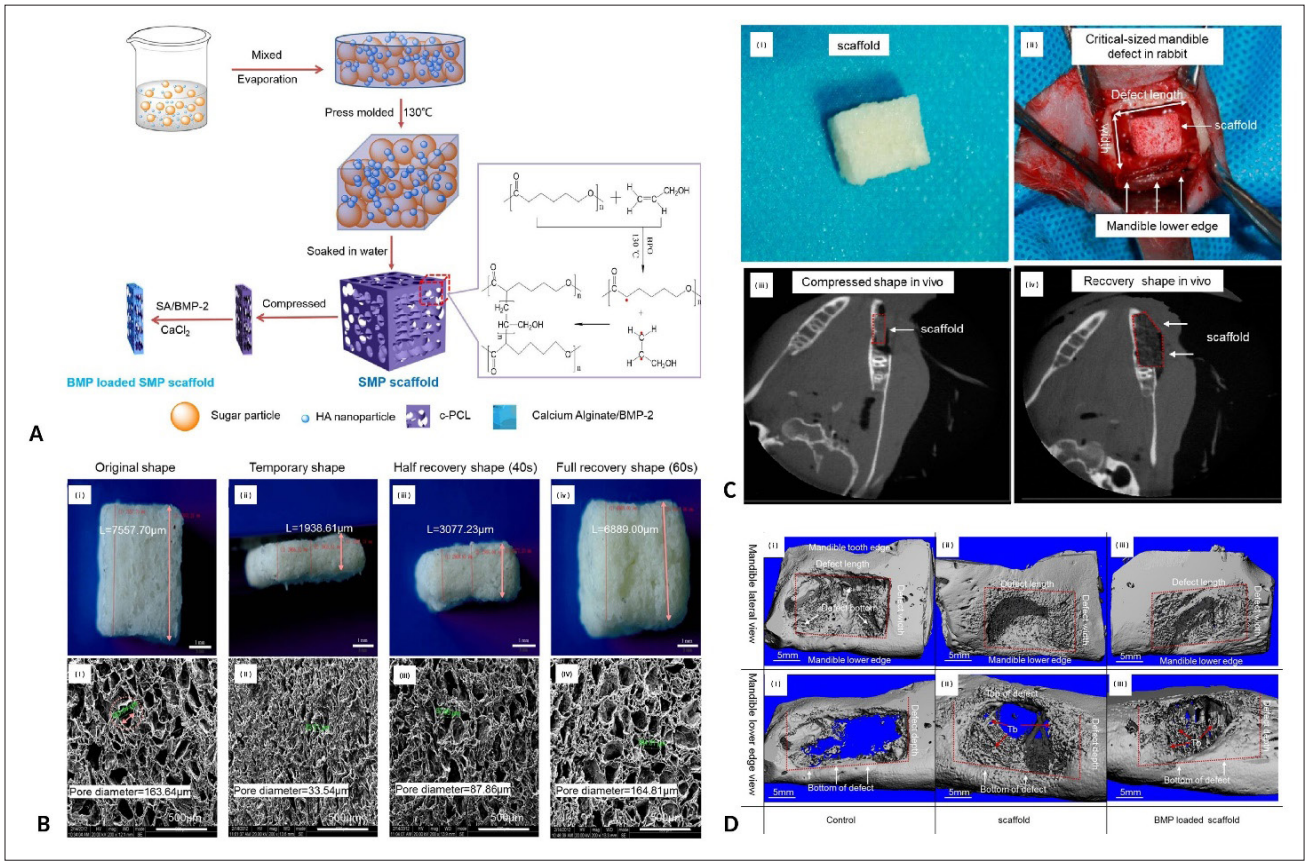

Figure 16. Schematic of Porous Nanocomposite Scaffold. (A) Schematic fabrication of shape-memory porous (SMP) nanocomposite scaffold with and without BMP-2. (B, i)–(B, iv) are the recovery process observed using an optical microscope, and images (B) The shape memory recovery process of the scaffold at 37 °C. Images (B, i)–(B, iv) are the recovery process observed using an optical microscope, and images(B, I)–(B, IV) correspond to the (B, i)–(B, iv) images, which show the recovery process of the interior pores of the scaffold observed using a scanning electron microscope(C) *In vivo* shape-memory recovery process of the BMP-2-loaded SMP scaffold observed using cone beam computed topography (CT). (C, i) Compressed scaffold and (C, ii) the scaffold implanted in the rabbit mandibular bone defect; the scaffold can recover from its temporary shape (C, iii) to the original shape (C, iv) *in vivo* after 10 min of implantation. (D) 3D micro-CT images of the bone defect area. (D, i)–(D, iii) images were viewed from the lateral side of the mandible and (D, i)–(D, iii) are viewed from the lower edge of the mandible. The red squares show the defect area and the white arrows show the defect bottom. Adapted with permission from Liu et al.[260]

creation of bioengineered tooth tissues and control important features of crown growth, size, and identity, it is imperative to comprehend the master genes involved in tooth induction and formation.[275] Furthermore, demineralized bone matrix in powder form is frequently utilized in orthopedic and periodontal regeneration.[276] In biomedical applications, decellularized ECM hydrogels with antimicrobial properties have been developed for various purposes: (i) skin regeneration by combining with thiolated chitosan,[277] (ii) bone regeneration by combining with chitosan,[246] and (iii) bone regeneration by drug loading.[278] This antimicrobial hydrogel is a promising candidate for dental tissue engineering. 4D printing can be used to create multilayer drug delivery systems with active ingredients.[245] The efficiency of antimicrobial dental hydrogels is enhanced by platforms for drug administration or stimulus-responsive biomaterials[279] sensitive to both intrinsic (pH, enzymes, reactive oxygen species [ROS], etc.) and extrinsic (temperature, light, ultrasound, mechanical forces, electric or magnetic fields, etc.) stimuli.[111,245,280] Given the complex relationships among alveolar bone tissues, multi-material and multicellular bioprinting is often essential.[281]

Despite recent advances in scaffold production and smart materials, the field of dentistry has not fully explored the potential of 4D-printed bone tissue creation. This is largely due to the complex and multilayered nature of oral tissue structure and development. The challenges include the lack of clinical relevance and translational potential of oral tissue engineering in predicting cell growth, differentiation, and maturation, difficulties in anticipating shape changes and precisely controlling 4D-printed implants, as well as ensuring implant mechanical stability,

along with regulatory and safety requirements. The oral cavity contains many types of tissues, such as dentin, enamel, pulp, periodontium, and mucosa, each with its own unique structure and physiological function, collectively forming a complex system. Oral tissues exhibit dynamic changes in different physiological processes, such as tooth growth, tooth movement, periodontal membrane repair, etc. These processes maintain the dynamic balance of oral tissues. Additionally, the differences between alveolar and craniofacial bones and long bones, as well as the complex neurovascular structure in the oral, contribute to the complexity and multilayered structure of oral tissues. This increases the mechanical instability of oral tissue engineering implants and complicates the precise prediction and control of accuracy and morphological changes in 4D printing, warranting further research to overcome these technical difficulties. Before clinical application, implants must undergo extensive testing of biological activity, as well as mechanical and chemical qualities, *in vitro* and *in vivo*. While *in vitro* models can characterize cellular functions, biological activity, toxicity, and immunogenicity, they do not replicate the complex oral environment. *In vivo*, rodent models also have limitations, including the small size of implants, lack of a Haversian canal system, minimal intracortical remodeling, low cancellous bone mass, physiological characteristics like tooth grinding, and different bone loading patterns.[37] The scientific uncertainties in applying 4D printing to oral bone tissue engineering, along with scalability, cost, and regulatory approvals, pose significant challenges that require robust quality management systems.

5. Conclusion

This review primarily focuses on the process and use of 4D printing in the healing of bone defects, with the aim of providing guidelines for the application of regenerative tissue engineering in orthopedics. It also elaborates on the latest research progress of 4D printing technology in dentistry, its advantages in dental bone tissue engineering repair, and the technical difficulties and future directions of 4D printing technology based on current research progress. Bone tissue engineering research continues to evolve toward modeling the complex structure of natural bone tissue.[3,282-284] Much remains to be learned about the hierarchical and anisotropic characteristics of bone, especially concerning vascularization and developmental physiology. Biomaterials for implantation currently focus on delivering cytokines or GFs. A comprehensive grasp of the different stages of bone healing and remodeling is crucial for effective intervention; otherwise, adverse effects such as an inflammatory response may disrupt the natural bone healing process. Concerns in the oral region include implant stability, bone regeneration capacity, adequate resorption rates, and soft tissue management. Mechanical stability and load-bearing capacity are especially important in the larger craniofacial area. 4D printing technologies enable the fabrication of smart biomaterials into form and functionally programmed structures through pre-programming and control, offering an excellent opportunity to address a variety of challenges in the field of dentistry. Additionally, they display promise for creating intricate multilayered tissue structures, likely influencing the applications of bone tissue engineering in dentistry and maxillofacial surgery, as well as future advancements.[245,285] Therefore, smart scaffolds formed through 4D printing are considered the fourth generation of bone repair devices.[286,287]

It remains challenging to develop biomaterials that are stimulus-responsive, printable, widely accessible, biocompatible, and economically friendly. Most *in vitro* studies have only demonstrated that 4D materials are responsive and restorative, but have not yet quantified these metrics, which are required to significantly improve the sensitivity and recovery of bone scaffolds. Neuromodulation and humoral processes are two major regulatory systems that maintain complex microenvironments *in vivo*. Thus, there is a great deal of promise for biomedical applications using 4D-printed materials that can self-deform in response to physiological signals. Given the complexity of the *in vivo* environment and the possibility of many stimuli, materials that can respond to multiple stimuli are essential. High temperatures and extreme pH should be avoided in biomedical applications, especially when living cells are involved. Although several existing biomaterials have been explored for biomanufacturing, with their cytocompatibility and efficacy in bone healing validated, further research is still warranted. Biomaterials used in bone tissue engineering demand high mechanical properties; however, the material's mechanical strength and the scaffold printing process can negatively impact cell viability. It has been previously demonstrated that mechanical loading can influence bone formation and defect remodeling.[288] Ideally, the mechanical properties of printed structures should closely resemble those of natural bone tissue. 4D printing of composite materials, such as multi-modular hybrid hydrogels, could enhance the mechanical and physicochemical characteristics of bone scaffolds. Despite efforts to enhance the mechanical properties of hydrogel-based materials, they still do not satisfy the required standards. Furthermore, incorporating composite elements and new multi-response capabilities can better mimic natural bone tissue, offering more precise control over bone regeneration, such as in nanomaterial composite scaffolds.[260] The design and pre-programming of

4D-printed structures with smart materials are particularly crucial to ensure functionality and shape adaptation.

However, while current smart material programs can manage simple stimuli and basic deformations like folding, twisting, and assembly, they have yet to replicate the complex microenvironment of skeletal tissues.[289] Stem cell bioprinting displays significant potential for bone tissue regeneration therapies. However, the high cell concentration standards required – 50 to 100 times higher than current levels – have hindered the progress of stem cell-based 4D printing in reaching commercial applications for regenerative orthopedics. Recent studies have also focused on developing scaffolds for osteogenic differentiation before gel encapsulation. Hydrogels have been utilized to create miniature tissues that mimic natural ones, such as aggregates, spheres, and organoids. Pursuing dynamic systems for regenerating tissues that are both anatomically and physiologically relevant is highly valuable. Novel biomaterials for tissue engineering are anticipated to be greatly aided by hydrogels that can adapt to the body's internal microenvironment. Furthermore, maintaining the durability of stimulus responsiveness during long-term use is essential. One notable shortcoming of 4D-printed bone structures is mechanical strength deterioration and poor recovery after repeated responses.[2] In addition to enhancing the accuracy of 4D printing artificial bone, it is also crucial to integrate other hardware devices and software algorithms into the fabrication process (Figure 17).[290,291] Machine learning (ML) algorithms have emerged as a transformative tool in AM, enabling the assimilation and analysis of vast datasets generated during the production process. These algorithms allow for real-time monitoring and control of printing parameters, thereby enhancing product quality and reducing manufacturing costs. ML methods can be classified into four categories: (i) supervised learning, where labeled datasets train the system to make predictions on new data; (ii) unsupervised learning, which identifies patterns in unlabeled datasets without human guidance; (iii) semi-supervised learning, a hybrid approach using both labeled and unlabeled data for more refined training; and (iv) reinforcement learning, an iterative process that refines parameters to achieve optimal outcomes.[292]

In the context of 4D printing, ML algorithms play a critical role by optimizing the printing process, predicting material properties, and anticipating morphological changes in printed parts. This is particularly important when working with smart materials, where ML can be employed to assess properties such as strength, conductivity, flexibility, and deformation behavior. By leveraging these insights, ML enables the design of optimized structures while minimizing experimental trials and material consumption. Additionally, key process parameters, such as temperature, print speed, and layer thickness, can be dynamically adjusted based on real-time data, allowing for seamless integration of smart materials and printing processes to improve overall efficiency and precision. For instance, a machine learning method was utilized to change the shapes of active composite structures based on demand.[293] A preliminary machine learning model was created to enhance the extrusion parameters of Pluronic F127 bioink for non-cellular applications.[294] The notion of 5D printing was announced in 2016, going beyond planar surfaces to curved layers. Research on 4D printing is still in its early phases, with many elements yet to be researched.[34]

The advantages of 4D bioprinting are often emphasized as a cutting-edge tissue engineering method with prospective benefits for medical and dental applications. This is because of the complexity of bone tissue development and structure in the oral cavity, the technical difficulties of oral tissue engineering techniques in predicting cell growth, differentiation, and maturation, which are mostly in the laboratory research stage, as well as the prediction of shape changes and precise control of 4D-printed implants. Hence, it is imperative to have a comprehensive understanding of the morphological alterations and procedures entailed in the repair and regeneration of bone tissue defects, along with the categorization of SMMs utilized in 4D printing for bone tissue engineering. Additionally, understanding the various factors, cells, and cytokines relevant to bone tissue engineering is critical for accurately predicting cell growth, differentiation, and maturation, as well as guiding changes in bone tissue morphology and function, particularly in oral bone tissues.

The precise control of shape deformation in 4D-printed bone tissue manufacturing techniques is dependent on the order and direction of the material's deformation movements. The deformation time under stimulated conditions is an additional crucial factor. Future research can thus closely monitor patients utilizing 4D-printed tissue engineering techniques, as treatment efficacy will depend on how quickly the material adopts its final shape and location, and how long it maintains its functionality based on that deformation time. Depending on the needs of treatment, some materials should not continue to deform over time, and their self-locking properties should be investigated in future studies to control the onset and pause of material deformation. As precision dentistry evolves, materials science is advancing towards greater customization. The emergence of SMPs offers significant customization possibilities and is a direct response to this trend. However, the application of SMPs in combination with 3D printing to develop 4D printing for oral and maxillofacial implants is still in its early stages. A lack of

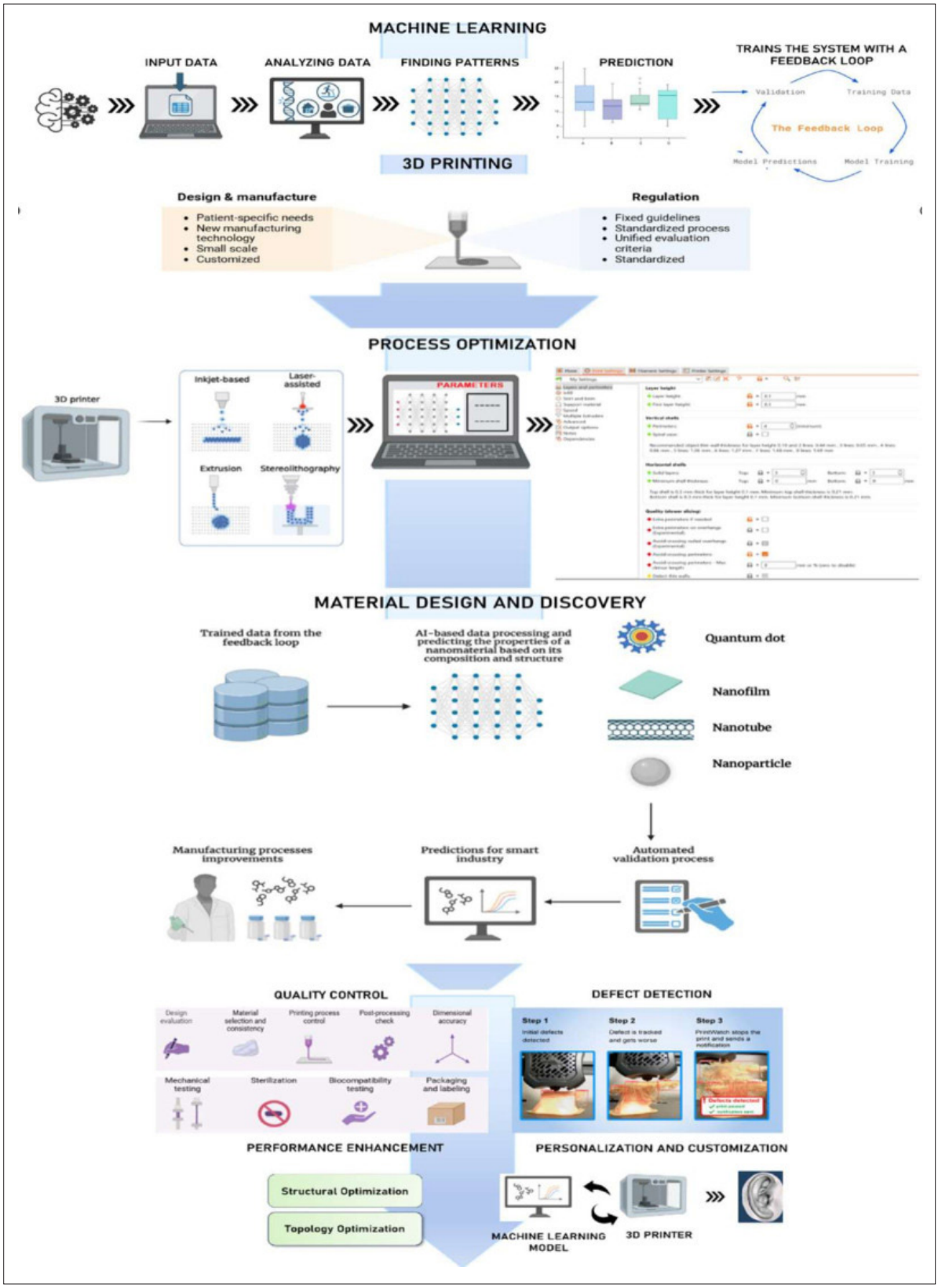

Figure 17. Machine learning combined with additive manufacturing. Adapted with permission from Agarwal et al.[292]

comprehensive preclinical and clinical research addressing the issues, drawbacks, and restrictions associated with 4D bioprinting in dentistry suggests great promise for this field. Strategies for regenerative engineering and alveolar bone tissue repair include the use of cells, growth hormones, biodegradable scaffolds, and nanomaterials. Nanomaterials possess remarkable physicochemical features and biomimetic qualities that can promote tissue regeneration and cell proliferation. One potential future treatment strategy is their use in oral tissue engineering. A thorough analysis of potential adverse effects is necessary before employing stem/progenitor cell transplantation in restorative dentistry.[295] Smart materials can be surgically inserted or injected to treat Temporomandibular Joint Syndrome (TMJ) problems and 4D-printed materials can replace cartilage while continuously moving to adjust for occlusion and joints. SMMs are used in 4D printing to create constructive, flexible, or environment-responsive products, opening up profitable opportunities for the target industry's growth. 4D printing can benefit dental practitioners and patients by personalizing dental components, medications, and equipment. Customized 4D implants, tools, and surgical supplies can speed up surgeries, shorten recuperation periods, and improve implant and surgical success rates.

Research on dental 4D printing is still in an early stage, with many aspects still to be investigated. In future clinical translation, there should also be a comprehensive and simultaneous consideration of the balance between the manufacturing process, structural design, material properties, morpho-functional transformation, and cost. Emerging assistive technologies like artificial intelligence can enhance simulation and forecasting, enabling precise control. In addition, regulatory issues are a key barrier to the adoption of 4D printing technology in the medical field. Due to the unique physical and chemical properties of 4D-printed smart materials, which may change in size and surface area upon stimulation, existing regulatory frameworks may not be adapted to these dynamic materials, resulting in a complex and time-consuming approval process. Currently, the approval process for 4D-printed biomedical devices typically involves multiple phases, including preclinical testing, clinical trials, and post-market surveillance.[296] This necessitates revising guidelines to address risk assessment testing protocols for smart materials. Secondly, biocompatibility is a critical concern, especially regarding the safety of long-term implants and their reactions within the body. Studies have demonstrated that smart materials, such as SMPs, have good biocompatibility, but further validation of their long-term stability and biodegradability in real-world clinical environments is still necessary. Since 4D printing is functional in the time dimension, 4D-printed materials need to maintain their dynamic deformability and continue to function over time during clinical use to support tissue regeneration and repair. To address these issues, future research efforts should focus on several areas. Firstly, more clinical trials on the biocompatibility and biodegradability of 4D-printed materials should be conducted to ensure their long-term safety and efficacy. Secondly, more targeted smart materials and designs should be developed to optimize their response and function in the human body. Finally, interdisciplinary collaboration, combining biomedical engineering, materials science, and clinical medicine, can accelerate the translation of 4D printing technology to clinical applications. Researchers and manufacturers will need to work closely with regulatory agencies to gain a clear understanding of the requirements and approval processes for 4D-printed biomedical devices. This includes ensuring that the materials used are biocompatible, that the manufacturing process meets quality standards, and that the device demonstrates safety and efficacy in preclinical and clinical testing. As more clinical trials and regulatory frameworks are optimized, the technology is expected to play an important role in the future of healthcare. It is also being analyzed prospectively to better understand the real possibilities and limitations of the technology in dental and maxillofacial-related applications. We believe this technology will offer great opportunities to address many dental challenges in the future.

Acknowledgments

None

Funding

This research was supported by the National Natural Science Foundation of China (32000964), the Guangdong Province Science and Technology Plan Project (2024A1515012265, 2020B1111560001, and 2022A1515140193), the Construction of Hainan Academician Innovation Centre of Guangdong Academy of Sciences (2022GDASZH-2022020402-01).

Conflict of interest

The authors declare no financial and personal relationships with other people or organizations that can inappropriately influence our work; there is no professional or other personal interest of any nature or kind in any product, service, and/or company that could be construed as influencing the position presented in, or the review of, the manuscript entitled.

Author contributions

Conceptualization: Wenlu Song, Weikang Xu, Xiangzhen Liu
Formal analysis: Wenlu Song, Chujie Xiao, Huinan Yin
Investigation: Wenlu Song, Junzhuo Qu
Methodology: Wenlu Song, Weihua Huang
Writing – original draft: Wenlu Song
Writing – review & editing: Weikang Xu, Xiangzhen Liu

Ethics approval and consent to participate

Not applicable.

Consent for publication

Not applicable.

Availability of data

Not applicable.

References

1. Florencio-Silva R, Sasso GRDS, Sasso-Cerri E, Simões MJ, Cerri PS. Biology of bone tissue: structure, function, and factors that influence bone cells. *BioMed Res Int.* 2015;2015:1-17. doi: 10.1155/2015/421746
2. Deng L, Yan Y. [Research status and progress of biomaterials for bone repair and reconstruction]. *Zhongguo Xiu Fu Chong Jian Wai Ke Za Zhi Zhongguo Xiufu Chongjian Waike Zazhi Chin J Reparative Reconstr Surg.* 2018;32(7):815-820. doi: 10.7507/1002-1892.201806028
3. Freeman FE, Pitacco P, Van Dommelen LHA, et al. 3D bioprinting spatiotemporally defined patterns of growth factors to tightly control tissue regeneration. *Sci Adv.* 2020;6(33):eabb5093. doi: 10.1126/sciadv.abb5093
4. Collins MN, Ren G, Young K, Pina S, Reis RL, Oliveira JM. Scaffold fabrication technologies and structure/function properties in bone tissue engineering. *Adv Funct Mater.* 2021;31(21):2010609. doi: 10.1002/adfm.202010609
5. Moroni L, Burdick JA, Highley C, et al. Biofabrication strategies for 3D *in vitro* models and regenerative medicine. *Nat Rev Mater.* 2018;3(5):21-37. doi: 10.1038/s41578-018-0006-y
6. Guo Y, Chi X, Wang Y, et al. Mitochondria transfer enhances proliferation, migration, and osteogenic differentiation of bone marrow mesenchymal stem cell and promotes bone defect healing. *Stem Cell Res Ther.* 2020;11(1):245. doi: 10.1186/s13287-020-01704-9
7. Kuang X, Roach DJ, Wu J, et al. Advances in 4D printing: materials and applications. *Adv Funct Mater.* 2019;29(2):1805290. doi: 10.1002/adfm.201805290
8. Wu JJ, Huang LM, Zhao Q, Xie T. 4D printing: history and recent progress. *Chin J Polym Sci.* 2018;36(5):563-575. doi: 10.1007/s10118-018-2089-8
9. Haleem A, Javaid M, Vaishya R. 4D printing and its applications in orthopaedics. *J Clin Orthop Trauma.* 2018;9(3):275-276. doi: 10.1016/j.jcot.2018.08.016
10. Gao B, Yang Q, Zhao X, Jin G, Ma Y, Xu F. 4D bioprinting for biomedical applications. *Trends Biotechnol.* 2016;34(9):746-756. doi: 10.1016/j.tibtech.2016.03.004
11. Zolfagharian A, Kaynak A, Bodaghi M, Kouzani AZ, Gharaie S, Nahavandi S. Control-based 4D printing: adaptive 4D-printed systems. *Appl Sci.* 2020;10(9):3020. doi: 10.3390/app10093020
12. Ge Q, Dunn CK, Qi HJ, Dunn ML. Active origami by 4D printing. *Smart Mater Struct.* 2014;23(9):094007. doi: 10.1088/0964-1726/23/9/094007
13. Miao S, Zhu W, Castro NJ, et al. 4D printing smart biomedical scaffolds with novel soybean oil epoxidized acrylate. *Sci Rep.* 2016;6(1):27226. doi: 10.1038/srep27226
14. Bodaghi M, Damanpack AR, Liao WH. Triple shape memory polymers by 4D printing. *Smart Mater Struct.* 2018;27(6):065010. doi: 10.1088/1361-665X/aabc2a
15. Zhang F, Wang L, Zheng Z, Liu Y, Leng J. Magnetic programming of 4D printed shape memory composite structures. *Compos Part Appl Sci Manuf.* 2019;125:105571. doi: 10.1016/j.compositesa.2019.105571
16. Nakielski P, Rybak D, Jezierska-Woźniak K, et al. Minimally invasive intradiscal delivery of BM-MSCs via fibrous microscaffold carriers. *ACS Appl Mater Interfaces.* 2023;15(50):58103-58118. doi: 10.1021/acsami.3c11710
17. Lin C, Liu L, Liu Y, Leng J. 4D printing of bioinspired absorbable left atrial appendage occluders: a proof-of-concept study. *ACS Appl Mater Interfaces.* 2021;13(11):12668-12678. doi: 10.1021/acsami.0c17192
18. Kitana W, Apsite I, Hazur J, Boccaccini AR, Ionov L. 4D biofabrication of T-shaped vascular bifurcation. *Adv Mater Technol.* 2023;8(1):2200429. doi: 10.1002/admt.202200429
19. del Barrio J, Sánchez-Somolinos C. Light to shape the future: from photolithography to 4D printing. *Adv Opt Mater.* 2019;7(16):1900598. doi: 10.1002/adom.201900598

20. Xie H, Yang KK, Wang YZ. Photo-cross-linking: a powerful and versatile strategy to develop shape-memory polymers. *Prog Polym Sci.* 2019;95:32-64. doi: 10.1016/j.progpolymsci.2019.05.001

21. Wan X, Luo L, Liu Y, Leng J. Direct ink writing based 4D printing of materials and their applications. *Adv Sci.* 2020;7(16):2001000. doi: 10.1002/advs.202001000

22. Castro NJ, Meinert C, Levett P, Hutmacher DW. Current developments in multifunctional smart materials for 3D/4D bioprinting. *Curr Opin Biomed Eng.* 2017;2:67-75. doi: 10.1016/j.cobme.2017.04.002

23. Li X, Shang J, Wang Z. Intelligent materials: a review of applications in 4D printing. *Assem Autom.* 2017;37(2):170-185. doi: 10.1108/AA-11-2015-093

24. Shin DG, Kim TH, Kim DE. Review of 4D printing materials and their properties. *Int J Precis Eng Manuf-Green Technol.* 2017;4(3):349-357. doi: 10.1007/s40684-017-0040-z

25. Ashammakhi N, Ahadian S, Zengjie F, et al. Advances and future perspectives in 4D bioprinting. *Biotechnol J.* 2018;13(12):e1800148. doi: 10.1002/biot.201800148

26. Liu T, Liu L, Zeng C, Liu Y, Leng J. 4D printed anisotropic structures with tailored mechanical behaviors and shape memory effects. *Compos Sci Technol.* 2020;186:107935. doi: 10.1016/j.compscitech.2019.107935

27. Weerasinghe DK, Hodge JM, Pasco JA, Samarasinghe RM, Azimi Manavi B, Williams LJ. Antipsychotic-induced bone loss: the role of dopamine, serotonin and adrenergic receptor signalling. *Front Cell Dev Biol.* 2023;11:1184550. doi: 10.3389/fcell.2023.1184550

28. Kenkre J, Bassett J. The bone remodelling cycle. *Ann Clin Biochem.* 2018;55(3):308-327. doi: 10.1177/0004563218759371

29. Langdahl B, Ferrari S, Dempster DW. Bone modeling and remodeling: potential as therapeutic targets for the treatment of osteoporosis. *Ther Adv Musculoskelet Dis.* 2016;8(6):225-235. doi: 10.1177/1759720X16670154

30. Shaheen MY, Basudan AM, de Vries RB, van den Beucken JJ, Jansen JA, Alghamdi H. S. Bone regeneration using antiosteoporotic drugs in adjunction with bone grafting: a meta-analysis. *Tissue Eng Part B Rev.* 2019;25(6): 500-509. doi: 10.1089/ten.teb.2019.0132

31. Gosset A, Pouillès, JM, Trémollieres F. Menopausal hormone therapy for the management of osteoporosis. *Best Pract Res Clin Endocrinol Metab.* 2021;35(6):101551. doi: 10.1016/j.beem.2021.101551

32. Fillingham Y, Jacobs J. Bone grafts and their substitutes. *Bone Jt J.* 2016;98-B(1_Supple_A):6-9. doi: 10.1302/0301-620X.98B.36350

33. Qasim M, Chae DS, Lee NY. Advancements and frontiers in nano-based 3D and 4D scaffolds for bone and cartilage tissue engineering. *Int J Nanomedicine.* 2019;14:4333-4351. doi: 10.2147/IJN.S209431

34. Haleem A, Javaid M, Vaishya R. 5D printing and its expected applications in orthopaedics. *J Clin Orthop Trauma.* 2019;10(4):809-810. doi: 10.1016/j.jcot.2018.11.014

35. Vijayavenkataraman S, Yan WC, Lu WF, Wang CH, Fuh JYH. 3D bioprinting of tissues and organs for regenerative medicine. *Adv Drug Deliv Rev.* 2018;132:296-332. doi: 10.1016/j.addr.2018.07.004

36. Wang W, Yeung KWK. Bone grafts and biomaterials substitutes for bone defect repair: a review. *Bioact Mater.* 2017;2(4):224-247. doi: 10.1016/j.bioactmat.2017.05.007

37. Henkel J, Woodruff MA, Epari DR, et al. Bone regeneration based on tissue engineering conceptions – a 21st century perspective. *Bone Res.* 2013;1(1):216-248. doi: 10.4248/BR201303002

38. Guo Y, Lv Z, Huo Y, et al. A biodegradable functional water-responsive shape memory polymer for biomedical applications. *J Mater Chem B.* 2019;7(1):123-132. doi: 10.1039/C8TB02462F

39. Christy PN, Basha SK, Kumari VS, et al. Biopolymeric nanocomposite scaffolds for bone tissue engineering applications – a review. *J Drug Deliv Sci Technol.* 2020;55:101452. doi: 10.1016/j.jddst.2019.101452

40. Lin X, Patil S, Gao YG, Qian A. The bone extracellular matrix in bone formation and regeneration. *Front Pharmacol.* 2020;11:757. doi: 10.3389/fphar.2020.00757

41. Fraile-Martínez O, García-Montero C, Coca A, et al. Applications of polymeric composites in bone tissue engineering and jawbone regeneration. *Polymers.* 2021;13(19):3429. doi: 10.3390/polym13193429

42. Gopal S, Multhaupt HAB, Couchman JR. Calcium in cell-extracellular matrix interactions. In: Islam MS, ed. *Calcium Signaling.* Cham: Springer International Publishing;2020:1079-1102. doi: 10.1007/978-3-030-12457-1_43

43. Ciosek Ż, Kot K, Kosik-Bogacka D, Łanocha-Arendarczyk N, Rotter I. The effects of calcium, magnesium, phosphorus, fluoride, and lead on bone tissue. *Biomolecules.* 2021;11(4):506. doi: 10.3390/biom11040506

44. Fakhry M, Hamade E, Badran B, Buchet R, Magne D. Molecular mechanisms of mesenchymal stem cell differentiation towards osteoblasts. *World J Stem Cells.* 2013;5(4):136-148.
doi: 10.4252/wjsc.v5.i4.136

45. Gu Q, Yang H, Shi Q. Macrophages and bone inflammation. *J Orthop Transl.* 2017;10:86-93.
doi: 10.1016/j.jot.2017.05.002

46. Wang JS, Mazur CM, Wein MN. Sclerostin and osteocalcin: candidate bone-produced hormones. *Front Endocrinol.* 2021;12:584147.
doi: 10.3389/fendo.2021.584147

47. Amarasekara DS, Kim S, Rho J. Regulation of osteoblast differentiation by cytokine networks. *Int J Mol Sci.* 2021;22(6):2851.
doi: 10.3390/ijms22062851

48. Hadjidakis DJ, Androulakis II. Bone remodeling. *Ann NY Acad Sci.* 2006;1092(1):385-396.
doi: 10.1196/annals.1365.035

49. Fuller K, Lawrence KM, Ross JL, et al. Cathepsin K inhibitors prevent matrix-derived growth factor degradation by human osteoclasts. *Bone.* 2008;42(1):200-211.
doi: 10.1016/j.bone.2007.09.044

50. Schemitsch EH. Size matters: defining critical in bone defect size!. *J Orthop Trauma.* 2017;31:S20.
doi: 10.1097/BOT.0000000000000978

51. Rowe P, Koller A, Sharma S. Physiology, bone remodeling. In: *StatPearls.* Treasure Island, FL:StatPearls Publishing;2024.

52. You D, Chen G, Liu C, et al. 4D printing of multi-responsive membrane for accelerated *in vivo* bone healing via remote regulation of stem cell fate. *Adv Funct Mater.* 2021;31(40):2103920.
doi: 10.1002/adfm.202103920

53. Fang Z, Song H, Zhang Y, et al. Modular 4D printing via interfacial welding of digital light-controllable dynamic covalent polymer networks. *Matter.* 2020;2(5):1187-1197.
doi: 10.1016/j.matt.2020.01.014

54. Özcan M, Hotza D, Fredel MC, Cruz A, Volpato CAM. Materials and manufacturing techniques for polymeric and ceramic scaffolds used in implant dentistry. *J Compos Sci.* 2021;5(3):78.
doi: 10.3390/jcs5030078

55. Leist SK, Zhou J. Current status of 4D printing technology and the potential of light-reactive smart materials as 4D printable materials. *Virtual Phys Prototyp.* 2016;11(4):249-262.
doi: 10.1080/17452759.2016.1198630

56. Sordi MB, Cruz A, Fredel MC, Magini R, Sharpe PT. Three-dimensional bioactive hydrogel-based scaffolds for bone regeneration in implant dentistry. *Mater Sci Eng C.* 2021;124:112055.
doi: 10.1016/j.msec.2021.112055

57. Lim HK, Hong SJ, Byeon SJ, et al. 3D-printed ceramic bone scaffolds with variable pore architectures. *Int J Mol Sci.* 2020;21(18):6942.
doi: 10.3390/ijms21186942

58. Huang J, Xia S, Li Z, Wu X, Ren J. Applications of four-dimensional printing in emerging directions: review and prospects. *J Mater Sci Technol.* 2021;91:105-120.
doi: 10.1016/j.jmst.2021.02.040

59. Mallakpour S, Tabesh F, Hussain CM. 3D and 4D printing: from innovation to evolution. *Adv Colloid Interface Sci.* 2021;294:102482.
doi: 10.1016/j.cis.2021.102482

60. Saska S, Pilatti L, Blay A, Shibli JA. Bioresorbable polymers: advanced materials and 4D printing for tissue engineering. *Polymers.* 2021;13(4):563.
doi: 10.3390/polym13040563

61. Li YC, Zhang YS, Akpek A, Shin SR, Khademhosseini A. 4D bioprinting: the next-generation technology for biofabrication enabled by stimuli-responsive materials. *Biofabrication.* 2016;9(1):012001.
doi: 10.1088/1758-5090/9/1/012001

62. Mandon CA, Blum LJ, Marquette CA. 3D–4D printed objects: new bioactive material opportunities. *Micromachines.* 2017;8(4):102.
doi: 10.3390/mi8040102

63. Zhang Z, Demir KG, Gu GX. Developments in 4D-printing: a review on current smart materials, technologies, and applications. *Int J Smart Nano Mater.* 2019;10(3):205-224.
doi: 10.1080/19475411.2019.1591541

64. Chu H, Yang W, Sun L, et al. 4D printing: a review on recent progresses. *Micromachines.* 2020;11(9):796.
doi: 10.3390/mi11090796

65. Melly SK, Liu L, Liu Y, Leng J. On 4D printing as a revolutionary fabrication technique for smart structures. *Smart Mater Struct.* 2020;29(8):083001.
doi: 10.1088/1361-665X/ab9989

66. Zhou W, Qiao Z, Nazarzadeh Zare E, et al. 4D-printed dynamic materials in biomedical applications: chemistry, challenges, and their future perspectives in the clinical sector. *J Med Chem.* 2020;63(15):8003-8024.
doi: 10.1021/acs.jmedchem.9b02115

67. Javaid M, Haleem A. Significant advancements of 4D printing in the field of orthopaedics. *J Clin Orthop Trauma.* 2020;11:S485-S490.
doi: 10.1016/j.jcot.2020.04.021

68. Momeni F, Mehdi Hassani MNS, Liu X, Ni J. A review of 4D printing. *Mater Des.* 2017;122:42-79.
doi: 10.1016/j.matdes.2017.02.068

69. Hoa SV, Cai X. Twisted composite structures made by 4D printing method. *Compos Struct.* 2020;238:111883.

doi: 10.1016/j.compstruct.2020.111883

70. Jeong HY, An SC, Lim Y, Jeong MJ, Kim N, Jun YC. 3D and 4D printing of multistable structures. *Appl Sci.* 2020;10(20):7254. doi: 10.3390/app10207254

71. Bodaghi M, Damanpack AR, Liao WH. Self-expanding/shrinking structures by 4D printing. *Smart Mater Struct.* 2016;25(10):105034. doi: 10.1088/0964-1726/25/10/105034

72. Bhanushali H, Amrutkar S, Mestry S, Mhaske ST. Shape memory polymer nanocomposite: a review on structure-property relationship. *Polym Bull.* 2022;79(6):3437-3493. doi: 10.1007/s00289-021-03686-x

73. Alshahrani HA. Review of 4D printing materials and reinforced composites: behaviors, applications and challenges. *J Sci Adv Mater Devices.* 2021;6(2):167-185. doi: 10.1016/j.jsamd.2021.03.006

74. Sobacchi C, Erreni M, Strina D, Palagano E, Villa A, Menale C. 3D bone biomimetic scaffolds for basic and translational studies with mesenchymal stem cells. *Int J Mol Sci.* 2018;19(10):3150. doi: 10.3390/ijms19103150

75. Park J, Park SY, Lee D, Song YS. Shape memory polymer composites embedded with hybrid ceramic microparticles. *Smart Mater Struct.* 2020;29(5):055037. doi: 10.1088/1361-665X/ab5e53

76. Subash A, Kandasubramanian B. 4D Printing of shape memory polymers. *Eur Polym J.* 2020;134:109771. doi: 10.1016/j.eurpolymj.2020.109771

77. Hendrikson WJ, Rouwkema J, Clementi F, Blitterswijk CA van, Farè S, Moroni L. Towards 4D printed scaffolds for tissue engineering: exploiting 3D shape memory polymers to deliver time-controlled stimulus on cultured cells. *Biofabrication.* 2017;9(3):031001. doi: 10.1088/1758-5090/aa8114

78. Stroganov V, Pant J, Stoychev G, et al. 4D biofabrication: 3D cell patterning using shape-changing films. *Adv Funct Mater.* 2018;28(11):1706248. doi: 10.1002/adfm.201706248

79. Erndt-Marino JD, Munoz-Pinto DJ, Samavedi S, et al. Evaluation of the osteoinductive capacity of polydopamine-coated poly(ε-caprolactone) diacrylate shape memory foams. *ACS Biomater Sci Eng.* 2015;1(12):1220-1230. doi: 10.1021/acsbiomaterials.5b00445

80. Buffington SL, Paul JE, Ali MM, Macios MM, Mather PT, Henderson JH. Enzymatically triggered shape memory polymers. *Acta Biomater.* 2019;84:88-97. doi: 10.1016/j.actbio.2018.11.031

81. Rajeshkumar G, Arvindh Seshadri S, Devnani GL, et al. Environment friendly, renewable and sustainable poly lactic acid (PLA) based natural fiber reinforced composites – a comprehensive review. *J Clean Prod.* 2021;310:127483. doi: 10.1016/j.jclepro.2021.127483

82. Langford T, Mohammed A, Essa K, Elshaer A, Hassanin H. 4D printing of origami structures for minimally invasive surgeries using functional scaffold. *Appl Sci.* 2021;11(1):332. doi: 10.3390/app11010332

83. Li Y, Zhang F, Liu Y, Leng J. 4D printed shape memory polymers and their structures for biomedical applications. *Sci China Technol Sci.* 2020;63(4):545-560. doi: 10.1007/s11431-019-1494-0

84. Shuai L, Jun Z, Jianjun C, Ming Y, Xuepeng L, Zhiguo J. Biodegradable body temperature-responsive shape memory polyurethanes with self-healing behavior. *Polym Eng Sci.* 2019;59(s2):E310-E316. doi: 10.1002/pen.25061

85. Yang W, Guan D, Liu J, Luo Y, Wang Y. Synthesis and characterization of biodegradable linear shape memory polyurethanes with high mechanical performance by incorporating novel long chain diisocyanates. *New J Chem.* 2020;44(8):3493-3503. doi: 10.1039/C9NJ06017K

86. Zhang Y, Hu J, Xie R, et al. A programmable, fast-fixing, osteo-regenerative, biomechanically robust bone screw. *Acta Biomater.* 2020;103:293-305. doi: 10.1016/j.actbio.2019.12.017

87. Zhang C, Cai D, Liao P, et al. 4D printing of shape-memory polymeric scaffolds for adaptive biomedical implantation. *Acta Biomater.* 2021;122:101-110. doi: 10.1016/j.actbio.2020.12.042

88. Le Fer G, Becker ML. 4D printing of resorbable complex shape-memory poly(propylene fumarate) star scaffolds. *ACS Appl Mater Interfaces.* 2020;12(20):22444-22452. doi: 10.1021/acsami.0c01444

89. Cemali G, Okutan B, Şafak EC, Köse GT. *In vitro* investigation of poly(propylene fumarate) cured with phosphonic acid based monomers as scaffolds for bone tissue engineering. *J Polym Res.* 2023;30(9):347. doi: 10.1007/s10965-023-03713-7

90. Joshi S, Rawat K, Karunakaran C, et al. 4D printing of materials for the future: opportunities and challenges. *Appl Mater Today.* 2020;18:100490. doi: 10.1016/j.apmt.2019.100490

91. Ahmed K, Shiblee MNI, Khosla A, Nagahara L, Thundat T, Furukawa H. Review – recent progresses in 4D printing of gel materials. *J Electrochem Soc.* 2020;167(3):037563. doi: 10.1149/1945-7111/ab6e60

92. Kirillova A, Maxson R, Stoychev G, Gomillion CT, Ionov L. 4D biofabrication using shape-morphing hydrogels. *Adv Mater.* 2017;29(46):1703443. doi: 10.1002/adma.201703443

93. Torbati AH, Mather PT. A hydrogel-forming liquid crystalline elastomer exhibiting soft shape memory. *J Polym Sci Part B Polym Phys.* 2016;54(1):38-52. doi: 10.1002/polb.23892

94. Zhang Y, Wang Q, Yi S, et al. 4D printing of magnetoactive soft materials for on-demand magnetic actuation transformation. *ACS Appl Mater Interfaces.* 2021;13(3):4174-4184. doi: 10.1021/acsami.0c19280

95. Ying Y, Li B, Liu C, Xiong Z, Bai W, Ma P. Shape-memory ECM-mimicking heparin-modified nanofibrous gelatin scaffold for enhanced bone regeneration in sinus augmentation. *ACS Biomater Sci Eng.* 2022;8(1):218-231. doi: 10.1021/acsbiomaterials.1c01365

96. Diba M, Koons GL, Bedell ML, Mikos AG. 3D printed colloidal biomaterials based on photo-reactive gelatin nanoparticles. *Biomaterials.* 2021;274:120871. doi: 10.1016/j.biomaterials.2021.120871

97. Yuan Z, Yuan X, Zhao Y, et al. Injectable GelMA cryogel microspheres for modularized cell delivery and potential vascularized bone regeneration. *Small.* 2021;17(11): 2006596. doi: 10.1002/smll.202006596

98. Jiang LB, Su DH, Liu P, Ma YQ, Shao ZZ, Dong J. Shape-memory collagen scaffold for enhanced cartilage regeneration: native collagen versus denatured collagen. *Osteoarthritis Cartilage.* 2018;26(10):1389-1399. doi: 10.1016/j.joca.2018.06.004

99. Luo Y, Lin X, Chen B, Wei X. Cell-laden four-dimensional bioprinting using near-infrared-triggered shape-morphing alginate/polydopamine bioinks. *Biofabrication.* 2019;11(4):045019. doi: 10.1088/1758-5090/ab39c5

100. Hamann I, Gebhardt F, Eisenhut M, et al. Investigation into the hybrid production of a superelastic shape memory alloy with additively manufactured structures for medical implants. *Materials.* 2021;14(11):3098. doi: 10.3390/ma14113098

101. Liu J, Lin Y, Bian D, et al. *In vitro* and *in vivo* studies of mg-30sc alloys with different phase structure for potential usage within bone. *Acta Biomater.* 2019;98:50-66. doi: 10.1016/j.actbio.2019.03.009

102. Werner M, Hammer N, Rotsch C, Berthold I, Leimert M. Experimental validation of adaptive pedicle screws – a novel implant concept using shape memory alloys. *Med Biol Eng Comput.* 2020;58(1):55-65. doi: 10.1007/s11517-019-02059-x

103. Hou Z, Liu Z, Zhu X, et al. Contactless treatment for scoliosis by electromagnetically controlled shape-memory alloy rods: a preliminary study in rabbits. *Eur Spine J.* 2020;29(5):1147-1158. doi: 10.1007/s00586-019-06207-7

104. Zhang Y, Li J, Soleimani M, et al. Biodegradable elastic sponge from nanofibrous biphasic calcium phosphate ceramic as an advanced material for regenerative medicine. *Adv Funct Mater.* 2021;31(40):2102911. doi: 10.1002/adfm.202102911

105. Holman H, Kavarana MN, Rajab TK. Smart materials in cardiovascular implants: shape memory alloys and shape memory polymers. *Artif Organs.* 2021;45(5):454-463. doi: 10.1111/aor.13851

106. Tamay DG, Dursun Usal T, Alagoz AS, Yucel D, Hasirci N, Hasirci V. 3D and 4D printing of polymers for tissue engineering applications. *Front Bioeng Biotechnol.* 2019;7:164. doi: 10.3389/fbioe.2019.00164

107. Dessì M, Borzacchiello A, Mohamed THA, Abdel-Fattah WI, Ambrosio L. Novel biomimetic thermosensitive β-tricalcium phosphate/chitosan-based hydrogels for bone tissue engineering. *J Biomed Mater Res A.* 2013;101(10):2984-2993. doi: 10.1002/jbm.a.34592

108. Wei H, Cheng SX, Zhang XZ, Zhuo RX. Thermo-sensitive polymeric micelles based on poly(*N*-isopropylacrylamide) as drug carriers. *Prog Polym Sci.* 2009;34(9):893-910. doi: 10.1016/j.progpolymsci.2009.05.002

109. Ozturk N, Girotti A, Kose GT, Rodríguez-Cabello JC, Hasirci V. Dynamic cell culturing and its application to micropatterned, elastin-like protein-modified poly(*N*-isopropylacrylamide) scaffolds. *Biomaterials.* 2009;30(29):5417-5426. doi: 10.1016/j.biomaterials.2009.06.044

110. Wang R, Wang X, Mu X, et al. Reducing thermal damage to adjacent normal tissue with dual thermo-responsive polymer via thermo-induced phase transition for precise photothermal theranosis. *Acta Biomater.* 2022;148:142-151. doi: 10.1016/j.actbio.2022.06.007

111. Zu S, Zhang Z, Liu Q, et al. 4D printing of core-shell hydrogel capsules for smart controlled drug release. *Bio-Des Manuf.* 2022;5(2):294-304. doi: 10.1007/s42242-021-00175-y

112. Adedoyin AA, Ekenseair AK. Biomedical applications of magneto-responsive scaffolds. *Nano Res.* 2018;11(10): 5049-5064. doi: 10.1007/s12274-018-2198-2

113. Lucarini S, Hossain M, Garcia-Gonzalez D. Recent advances in hard-magnetic soft composites: synthesis, characterisation, computational modelling, and applications. *Compos Struct.* 2022;279:114800. doi: 10.1016/j.compstruct.2021.114800

114. Zhang J, Zhao S, Zhu M, et al. 3D-printed magnetic Fe3O4/MBG/PCL composite scaffolds with multifunctionality of bone regeneration, local anticancer drug delivery and hyperthermia. *J Mater Chem B.* 2014;2(43): 7583-7595. doi: 10.1039/C4TB01063A

115. Meng J, Xiao B, Zhang Y, et al. Super-paramagnetic responsive nanofibrous scaffolds under static magnetic field enhance osteogenesis for bone repair *in vivo*. *Sci Rep.* 2013;3(1):2655. doi: 10.1038/srep02655

116. Betsch M, Cristian C, Lin YY, et al. Incorporating 4D into bioprinting: real-time magnetically directed collagen fiber alignment for generating complex multilayered tissues. *Adv Healthc Mater.* 2018;7(21):1800894. doi: 10.1002/adhm.201800894

117. Fuhrer R, Hofmann S, Hild N, et al. Pressureless mechanical induction of stem cell differentiation is dose and frequency dependent. *Plos One.* 2013;8(11):e81362. doi: 10.1371/journal.pone.0081362

118. Zhang Q, Liu J, Yuan K, Zhang Z, Zhang X, Fang X. A multi-controlled drug delivery system based on magnetic mesoporous Fe3O4 nanopaticles and a phase change material for cancer thermo-chemotherapy. *Nanotechnology.* 2017;28(40):405101. doi: 10.1088/1361-6528/aa883f

119. Kim C, Kim H, Park H, Lee KY. Controlling the porous structure of alginate ferrogel for anticancer drug delivery under magnetic stimulation. *Carbohydr Polym.* 2019;223:115045. doi: 10.1016/j.carbpol.2019.115045

120. Alam Ansari MA, Dash M, Camci-Unal G, et al. Engineered stimuli-responsive smart grafts for bone regeneration. *Curr Opin Biomed Eng.* 2023;28:100493. doi: 10.1016/j.cobme.2023.100493

121. Pourmasoumi P, Moghaddam A, Nemati Mahand S, et al. A review on the recent progress, opportunities, and challenges of 4D printing and bioprinting in regenerative medicine. *J Biomater Sci Polym Ed.* 2023;34(1):108-146. doi: 10.1080/09205063.2022.2110480

122. Yang GH, Kim W, Kim J, Kim G. A skeleton muscle model using GelMA-based cell-aligned bioink processed with an electric-field assisted 3D/4D bioprinting. *Theranostics.* 2021;11(1):48-63. doi: 10.7150/thno.50794

123. Lu H, Liu Y, Gou J, Leng J, Du S. Electrical properties and shape-memory behavior of self-assembled carbon nanofiber nanopaper incorporated with shape-memory polymer. *Smart Mater Struct.* 2010;19(7):075021. doi: 10.1088/0964-1726/19/7/075021

124. Huang Y, Zhang L, Ji Y, et al. A non-invasive smart scaffold for bone repair and monitoring. *Bioact Mater.* 2023;19:499-510. doi: 10.1016/j.bioactmat.2022.04.034

125. Municoy S, Álvarez Echazú MI, Antezana PE, et al. Stimuli-responsive materials for tissue engineering and drug delivery. *Int J Mol Sci.* 2020;21(13):4724. doi: 10.3390/ijms21134724

126. Bedell ML, Navara AM, Du Y, Zhang S, Mikos AG. Polymeric systems for bioprinting. *Chem Rev.* 2020;120(19):10744-10792. doi: 10.1021/acs.chemrev.9b00834

127. Ding A, Lee SJ, Ayyagari S, Tang R, Huynh CT, Alsberg E. 4D biofabrication via instantly generated graded hydrogel scaffolds. *Bioact Mater.* 2022;7:324-332. doi: 10.1016/j.bioactmat.2021.05.021

128. Bagheri A, Arandiyan H, Boyer C, Lim M. Lanthanide-doped upconversion nanoparticles: emerging intelligent light-activated drug delivery systems. *Adv Sci.* 2016;3(7):1500437. doi: 10.1002/advs.201500437

129. Zhang Y, Li C, Zhang W, et al. 3D-printed NIR-responsive shape memory polyurethane/magnesium scaffolds with tight-contact for robust bone regeneration. *Bioact Mater.* 2022;16:218-231. doi: 10.1016/j.bioactmat.2021.12.032

130. Dong Q, Wan Z, Li Q, et al. 3D-printed near-infrared-light-responsive on-demand drug-delivery scaffold for bone regeneration. 2023. doi: 10.21203/rs.3.rs-2702534/v1

131. Sydney Gladman A, Matsumoto EA, Nuzzo RG, Mahadevan L, Lewis JA. Biomimetic 4D printing. *Nat Mater.* 2016;15(4):413-418. doi: 10.1038/nmat4544

132. Morouço, P, Azimi B, Milazzo M, et al. Four-dimensional (bio-)printing: a review on stimuli-responsive mechanisms and their biomedical suitability. *Appl Sci.* 2020;10(24):9143. doi: 10.3390/app10249143

133. Liu Y, Li Y, Yang G, Zheng X, Zhou S. Multi-stimulus-responsive shape-memory polymer nanocomposite network cross-linked by cellulose nanocrystals. *ACS Appl Mater Interfaces.* 2015;7(7):4118-4126. doi: 10.1021/am5081056

134. Zhou X, Guo L, Shi D, Duan S, Li J. Biocompatible chitosan nanobubbles for ultrasound-mediated targeted delivery of doxorubicin. *Nanoscale Res Lett.* 2019;14(1):24. doi: 10.1186/s11671-019-2853-x

135. Cao Y, Chen Y, Yu T, et al. Drug release from phase-changeable nanodroplets triggered by low-intensity focused ultrasound. *Theranostics.* 2018;8(5):1327-1339. doi: 10.7150/thno.21492

136. Yang P, Li D, Jin S, et al. Stimuli-responsive biodegradable poly(methacrylic acid) based nanocapsules for ultrasound traced and triggered drug delivery system. *Biomaterials.* 2014;35(6):2079-2088. doi: 10.1016/j.biomaterials.2013.11.057

137. Li B, Zhang C, Peng F, Wang W, Vogt BD, Tan KT. 4D printed shape memory metamaterial for vibration bandgap switching and active elastic-wave guiding. *J Mater Chem C.* 2021;9(4):1164-1173. doi: 10.1039/D0TC04999A

138. Kocak G, Tuncer C, Bütün V. pH-responsive polymers. *Polym Chem.* 2017;8(1):144-176. doi: 10.1039/C6PY01872F

139. Xu Y, Han J, Chai Y, Yuan S, Lin H, Zhang X. Development of porous chitosan/tripolyphosphate scaffolds with tunable uncross-linking primary amine content for bone tissue engineering. *Mater Sci Eng C.* 2018;85:182-190. doi: 10.1016/j.msec.2017.12.032

140. Qu J, Zhao X, Ma PX, Guo B. pH-responsive self-healing injectable hydrogel based on *N*-carboxyethyl chitosan for hepatocellular carcinoma therapy. *Acta Biomater.* 2017;58:168-180.
doi: 10.1016/j.actbio.2017.06.001

141. Mohy Eldin MS, Kamoun EA, Sofan MA, Elbayomi SM. L-arginine grafted alginate hydrogel beads: a novel pH-sensitive system for specific protein delivery. *Arab J Chem.* 2015;8(3):355-365.
doi: 10.1016/j.arabjc.2014.01.007

142. Bai T, Han Y, Zhang P, Wang W, Liu W. Zinc ion-triggered two-way macro-/microscopic shape changing and memory effects in high strength hydrogels with pre-programmed unilateral patterned surfaces. *Soft Matter.* 2012;8(25):6846-6852.
doi: 10.1039/C2SM07364A

143. Nan W, Wang W, Gao H, Liu W. Fabrication of a shape memory hydrogel based on imidazole – zinc ion coordination for potential cell-encapsulating tubular scaffold application. *Soft Matter.* 2013;9(1):132-137.
doi: 10.1039/C2SM26918J

144. Lai J, Ye X, Liu J, et al. 4D printing of highly printable and shape morphing hydrogels composed of alginate and methylcellulose. *Mater Des.* 2021;205:109699.
doi: 10.1016/j.matdes.2021.109699

145. Wells CM, Harris M, Choi L, Murali VP, Guerra FD, Jennings JA. Stimuli-responsive drug release from smart polymers. *J Funct Biomater.* 2019;10(3):34.
doi: 10.3390/jfb10030034

146. Kim J, Park Y, Tae G, et al. Synthesis and characterization of matrix metalloprotease sensitive-low molecular weight hyaluronic acid based hydrogels. *J Mater Sci Mater Med.* 2008;19(11):3311-3318.
doi: 10.1007/s10856-008-3469-3

147. Zhang C, Pan D, Li J, et al. Enzyme-responsive peptide dendrimer-gemcitabine conjugate as a controlled-release drug delivery vehicle with enhanced antitumor efficacy. *Acta Biomater.* 2017;55:153-162.
doi: 10.1016/j.actbio.2017.02.047

148. Wang B, Liu H, Sun L, et al. Construction of high drug loading and enzymatic degradable multilayer films for self-defense drug release and long-term biofilm inhibition. *Biomacromolecules.* 2018;19(1):85-93.
doi: 10.1021/acs.biomac.7b01268

149. Davaran S, Ghamkhari A, Alizadeh E, Massoumi B, Jaymand M. Novel dual stimuli-responsive ABC triblock copolymer: RAFT synthesis, "Schizophrenic" micellization, and its performance as an anticancer drug delivery nanosystem. *J Colloid Interface Sci.* 2017;488:282-293.
doi: 10.1016/j.jcis.2016.11.002

150. Li Z, Fan Z, Xu Y, et al. pH-sensitive and thermosensitive hydrogels as stem-cell carriers for cardiac therapy. *ACS Appl Mater Interfaces.* 2016;8(17):10752-10760.
doi: 10.1021/acsami.6b01374

151. Xu X, Huang Z, Huang Z, et al. Injectable, NIR/pH-responsive nanocomposite hydrogel as long-acting implant for chemophotothermal synergistic cancer therapy. *ACS Appl Mater Interfaces.* 2017;9(24):20361-20375.
doi: 10.1021/acsami.7b02307

152. IO de Solorzano, T Alejo, M Abad, et al. Cleavable and thermo-responsive hybrid nanoparticles for on-demand drug delivery. *J Colloid Interface Sci.* 2019;533:171-181.
doi: 10.1016/j.jcis.2018.08.069

153. Bozuyuk U, Yasa O, Yasa IC, Ceylan H, Kizilel S, Sitti M. Light-triggered drug release from 3D-printed magnetic chitosan microswimmers. *ACS Nano.* 2018;12(9):9617-9625.
doi: 10.1021/acsnano.8b05997

154. Collado-González M, García-Bernal D, Oñate-Sánchez RE, et al. Cytotoxicity and bioactivity of various pulpotomy materials on stem cells from human exfoliated primary teeth. *Int Endod J.* 2017;50(S2):e19-e30.
doi: 10.1111/iej.12751

155. Leberfinger AN, Dinda S, Wu Y, et al. Bioprinting functional tissues. *Acta Biomater.* 2019;95:32-49.
doi: 10.1016/j.actbio.2019.01.009

156. Unagolla JM, Jayasuriya AC. Hydrogel-based 3D bioprinting: a comprehensive review on cell-laden hydrogels, bioink formulations, and future perspectives. *Appl Mater Today.* 2020;18:100479.
doi: 10.1016/j.apmt.2019.100479

157. Haleem A, Javaid M, Singh RP, Suman R. Significant roles of 4D printing using smart materials in the field of manufacturing. *Adv Ind Eng Polym Res.* 2021;4(4):301-311.
doi: 10.1016/j.aiepr.2021.05.001

158. Li J, Wu C, Chu P, Gelinsky M. 3D printing of hydrogels: rational design strategies and emerging biomedical applications. *Mater Sci Eng R Rep.* 2020;140:100543.
doi: 10.1016/j.mser.2020.100543

159. Ng WL, An J, Chua CK. Process, material, and regulatory considerations for 3D printed medical devices and tissue constructs. *Engineering.* 2024;36:146-166.
doi: 10.1016/j.eng.2024.01.028

160. Basak S. Is 4D printing at the forefront of transformations in tissue engineering and beyond? *Biomed Mater Devices.* 2024;2(2):587-600.
doi: 10.1007/s44174-024-00161-9

161. Ghosh S, Chaudhuri S, Roy P, Lahiri D. 4D printing in biomedical engineering: a state-of-the-art review of technologies, biomaterials, and application. *Regen Eng Transl Med.* 2023;9(3):339-365.
doi: 10.1007/s40883-022-00288-5

162. Miao S, Zhu W, Castro NJ, Leng J, Zhang LG. Four-dimensional printing hierarchy scaffolds with highly biocompatible smart

polymers for tissue engineering applications. *Tissue Eng Part C Methods.* 2016;22(10):952-963.
doi: 10.1089/ten.tec.2015.0542

163. Zhao T, Yu R, Li X, et al. 4D printing of shape memory polyurethane via stereolithography. *Eur Polym J.* 2018;101:120-126.
doi: 10.1016/j.eurpolymj.2018.02.021

164. González-Henríquez CM, Sarabia-Vallejos MA, Rodriguez-Hernandez J. Polymers for additive manufacturing and 4D-printing: materials, methodologies, and biomedical applications. *Prog Polym Sci.* 2019;94:57-116.
doi: 10.1016/j.progpolymsci.2019.03.001

165. Ali MH, Abilgaziyev A, Adair D. 4D printing: a critical review of current developments, and future prospects. *Int J Adv Manuf Technol.* 2019;105(1):701-717.
doi: 10.1007/s00170-019-04258-0

166. Senatov FS, Niaza KV, Zadorozhnyy MY, Maksimkin AV, Kaloshkin SD, Estrin YZ. Mechanical properties and shape memory effect of 3D-printed PLA-based porous scaffolds. *J Mech Behav Biomed Mater.* 2016;57:139-148.
doi: 10.1016/j.jmbbm.2015.11.036

167. Murphy SV, Atala A. 3D bioprinting of tissues and organs. *Nat Biotechnol.* 2014;32(8):773-785.
doi: 10.1038/nbt.2958

168. Mu Q, Wang L, Dunn CK, et al. Digital light processing 3D printing of conductive complex structures. *Addit Manuf.* 2017;18:74-83.
doi: 10.1016/j.addma.2017.08.011

169. Gou M, Qu X, Zhu W, et al. Bio-inspired detoxification using 3D-printed hydrogel nanocomposites. *Nat Commun.* 2014;5(1):3774.
doi: 10.1038/ncomms4774

170. DuRaine GD, Brown WE, Hu JC, Athanasiou KA. Emergence of scaffold-free approaches for tissue engineering musculoskeletal cartilages. *Ann Biomed Eng.* 2015;43(3):543-554.
doi: 10.1007/s10439-014-1161-y

171. Han Y, Li X, Zhang Y, Han Y, Chang F, Ding J. Mesenchymal stem cells for regenerative medicine. *Cells.* 2019;8(8):886.
doi: 10.3390/cells8080886

172. Zhai Q, Dong Z, Wang W, Li B, Jin Y. Dental stem cell and dental tissue regeneration. *Front Med.* 2019;13(2):152-159.
doi: 10.1007/s11684-018-0628-x

173. Hernández-Monjaraz B, Santiago-Osorio E, Monroy-García A, Ledesma-Martínez E, Mendoza-Núñez VM. Mesenchymal stem cells of dental origin for inducing tissue regeneration in periodontitis: a mini-review. *Int J Mol Sci.* 2018;19(4):944.
doi: 10.3390/ijms19040944

174. Ono N, Kronenberg HM. Bone repair and stem cells. *Curr Opin Genet Dev.* 2016;40:103-107.
doi: 10.1016/j.gde.2016.06.012

175. Shen C, Yang C, Xu S, Zhao H. Comparison of osteogenic differentiation capacity in mesenchymal stem cells derived from human amniotic membrane (AM), umbilical cord (UC), chorionic membrane (CM), and decidua (DC). *Cell Biosci.* 2019;9(1):17.
doi: 10.1186/s13578-019-0281-3

176. Friedenstein AJ, Chailakhyan RK, Gerasimov UV. Bone marrow osteogenic stem cells: *in vitro* cultivation and transplantation in diffusion chambers. *Cell Prolif.* 1987;20(3):263-272.
doi: 10.1111/j.1365-2184.1987.tb01309.x

177. Moncal KK, Tigli Aydın RS, Godzik KP, et al. Controlled co-delivery of pPDGF-B and pBMP-2 from intraoperatively bioprinted bone constructs improves the repair of calvarial defects in rats. *Biomaterials.* 2022;281:121333.
doi: 10.1016/j.biomaterials.2021.121333

178. Zhang Z, Yang X, Cao X, Qin A, Zhao J. Current applications of adipose-derived mesenchymal stem cells in bone repair and regeneration: a review of cell experiments, animal models, and clinical trials. *Front Bioeng Biotechnol.* 2022;10:942128.
doi: 10.3389/fbioe.2022.942128

179. Xu T, Yu X, Yang Q, Liu X, Fang J, Dai X. Autologous micro-fragmented adipose tissue as stem cell-based natural scaffold for cartilage defect repair. *Cell Transplant.* 2019;28(12):1709-1720.
doi: 10.1177/0963689719880527

180. Wang Z, Han L, Sun T, Wang W, Li X, Wu B. Osteogenic and angiogenic lineage differentiated adipose-derived stem cells for bone regeneration of calvarial defects in rabbits. *J Biomed Mater Res A.* 2021;109(4):538-550.
doi: 10.1002/jbm.a.37036

181. Conejero JA, Lee JA, Parrett BM, et al. Repair of palatal bone defects using osteogenically differentiated fat-derived stem cells. *Plast Reconstr Surg.* 2006; 117(3):857.
doi: 10.1097/01.prs.0000204566.13979.c1

182. Roberts SJ, van Gastel N, Carmeliet G, Luyten FP. Uncovering the periosteum for skeletal regeneration: the stem cell that lies beneath. *Bone.* 2015;70:10-18.
doi: 10.1016/j.bone.2014.08.007

183. Bahney CS, Zondervan RL, Allison P, et al. Cellular biology of fracture healing. *J Orthop Res.* 2019;37(1):35-50.
doi: 10.1002/jor.24170

184. Radtke CL, Nino-Fong R, Gonzalez BPE, Stryhn H, McDuffee LA. Characterization and osteogenic potential of equine muscle tissue- and periosteal tissue-derived mesenchymal stem cells in comparison with bone marrow- and adipose tissue-derived mesenchymal stem cells. *Am J Vet Res.* 2013;74(5):790-800.
doi: 10.2460/ajvr.74.5.790

185. Roberts SJ, Geris L, Kerckhofs G, Desmet E, Schrooten J, Luyten FP. The combined bone forming capacity of

human periosteal derived cells and calcium phosphates. *Biomaterials.* 2011;32(19):4393-4405.
doi: 10.1016/j.biomaterials.2011.02.047

186. Nuti N, Corallo C, Chan BMF, Ferrari M, Gerami-Naini B. Multipotent differentiation of human dental pulp stem cells: a literature review. *Stem Cell Rev Rep.* 2016;12(5): 511-523.
doi: 10.1007/s12015-016-9661-9

187. Nada OA, El Backly RM. Stem cells from the apical papilla (SCAP) as a tool for endogenous tissue regeneration. *Front Bioeng Biotechnol.* 2018;6:103.
doi: 10.3389/fbioe.2018.00103

188. Huang GTJ, Garcia-Godoy F. 13 – stem cells and dental tissue reconstruction. In: Spencer P, Misra A, eds. *Material-Tissue Interfacial Phenomena.* Sawston, Cambridge: Woodhead Publishing; 2017:325-353.
doi: 10.1016/B978-0-08-100330-5.00013-3

189. Kang J, Fan W, Deng Q, He H, Huang F. Stem cells from the apical papilla: a promising source for stem cell-based therapy. *BioMed Res Int.* 2019;2019:e6104738.
doi: 10.1155/2019/6104738

190. Kérourédan O, Bourget JM, Rémy M, et al. Micropatterning of endothelial cells to create a capillary-like network with defined architecture by laser-assisted bioprinting. *J Mater Sci Mater Med.* 2019;30(2):28.
doi: 10.1007/s10856-019-6230-1

191. Gao H, Li B, Zhao L, Jin Y. Influence of nanotopography on periodontal ligament stem cell functions and cell sheet based periodontal regeneration. *Int J Nanomedicine.* 2015;10:4009-4027.
doi: 10.2147/IJN.S83357

192. Salar Amoli M, EzEldeen M, Jacobs R, Bloemen V. Materials for dentoalveolar bioprinting: current state of the art. *Biomedicines.* 2022;10(1):71.
doi: 10.3390/biomedicines10010071

193. Zhou T, Pan J, Wu P, et al. Dental follicle cells: roles in development and beyond. *Stem Cells Int.* 2019;2019:e9159605.
doi: 10.1155/2019/9159605

194. Dave JR, Chandekar SS, Behera S, et al. Human gingival mesenchymal stem cells retain their growth and immunomodulatory characteristics independent of donor age. *Sci Adv.* 2022;8(25):eabm6504.
doi: 10.1126/sciadv.abm6504

195. Zhang Q, Nguyen PD, Shi S, Burrell JC, Cullen DK, Le AD. 3D bio-printed scaffold-free nerve constructs with human gingiva-derived mesenchymal stem cells promote rat facial nerve regeneration. *Sci Rep.* 2018;8(1):6634.
doi: 10.1038/s41598-018-24888-w

196. Pore-forming bioinks to enable spatio-temporally defined gene delivery in bioprinted tissues. *J Control Release.* 2019;301:13-27.
doi: 10.1016/j.jconrel.2019.03.006

197. Pizzicannella J, Diomede F, Gugliandolo A, et al. 3D printing PLA/gingival stem cells/EVs upregulate miR-2861 and -210 during osteoangiogenesis commitment. *Int J Mol Sci.* 2019;20(13):3256.
doi: 10.3390/ijms20133256

198. Attalla R, Puersten E, Jain N, Selvaganapathy PR. 3D bioprinting of heterogeneous bi- and tri-layered hollow channels within gel scaffolds using scalable multi-axial microfluidic extrusion nozzle. *Biofabrication.* 2018;11(1):015012.
doi: 10.1088/1758-5090/aaf7c7

199. Liu X, Gaihre B, George MN, et al. 3D bioprinting of oligo(poly[ethylene glycol] fumarate) for bone and nerve tissue engineering. *J Biomed Mater Res A.* 2021;109(1):6-17.
doi: 10.1002/jbm.a.37002

200. Pierdomenico L, Bonsi L, Calvitti M, et al. Multipotent mesenchymal stem cells with immunosuppressive activity can be easily isolated from dental pulp. *Transplantation.* 2005;80(6):836.
doi: 10.1097/01.tp.0000173794.72151.88

201. La Noce M, Paino F, Spina A, et al. Dental pulp stem cells: state of the art and suggestions for a true translation of research into therapy. *J Dent.* 2014;42(7):761-768.
doi: 10.1016/j.jdent.2014.02.018

202. Jin R, Song G, Chai J, Gou X, Yuan G, Chen Z. Effects of concentrated growth factor on proliferation, migration, and differentiation of human dental pulp stem cells *in vitro*. *J Tissue Eng.* 2018;9:2041731418817505.
doi: 10.1177/2041731418817505

203. Park JH, Gillispie GJ, Copus JS, et al. The effect of BMP-mimetic peptide tethering bioinks on the differentiation of dental pulp stem cells (DPSCs) in 3D bioprinted dental constructs. *Biofabrication.* 2020;12(3):035029.
doi: 10.1088/1758-5090/ab9492

204. Karbanová J, Soukup T, Suchánek J, Pytlík R, Corbeil D, Mokrý, J. Characterization of dental pulp stem cells from impacted third molars cultured in low serum-containing medium. *Cells Tissues Organs.* 2010;193(6):344-365.
doi: 10.1159/000321160

205. Comparative analysis of *in vitro* osteo/odontogenic differentiation potential of human dental pulp stem cells (DPSCs) and stem cells from the apical papilla (SCAP). *Arch Oral Biol.* 2011;56(7):709-721.
doi: 10.1016/j.archoralbio.2010.12.008

206. Thattaruparambil Raveendran N, Vaquette C, Meinert C, Samuel Ipe D, Ivanovski S. Optimization of 3D bioprinting of periodontal ligament cells. *Dent Mater.* 2019;35(12):1683-1694.
doi: 10.1016/j.dental.2019.08.114

207. Rombouts C, Giraud T, Jeanneau C, About I. Pulp vascularization during tooth development, regeneration, and therapy. *J Dent Res.* 2017;96(2):137-144.
doi: 10.1177/0022034516671688

208. Miura M, Gronthos S, Zhao M, et al. SHED: stem cells from human exfoliated deciduous teeth. *Proc Natl Acad Sci.* 2003;100(10):5807-5812.
doi: 10.1073/pnas.0937635100

209. Yao S, Pan F, Prpic V, Wise GE. Differentiation of stem cells in the dental follicle. *J Dent Res.* 2008;87(8):767-771.
doi: 10.1177/154405910808700801

210. Handa K, Saito M, Tsunoda A, et al. Progenitor cells from dental follicle are able to form cementum matrix *in vivo*. *Connect Tissue Res.* 2002;43(2-3):406-408.
doi: 10.1080/03008200290001023

211. Abdal-Wahab M, Abdel Ghaffar KA, Ezzatt OM, Hassan AAA, El Ansary MMS, Gamal AY. Regenerative potential of cultured gingival fibroblasts in treatment of periodontal intrabony defects (randomized clinical and biochemical trial). *J Periodontal Res.* 2020;55(3):441-452.
doi: 10.1111/jre.12728

212. Yasui T, Mabuchi Y, Toriumi H, et al. Purified human dental pulp stem cells promote osteogenic regeneration. *J Dent Res.* 2016;95(2):206-214.
doi: 10.1177/0022034515610748

213. d'Aquino R, Papaccio G, Laino G, Graziano A. Dental pulp stem cells: a promising tool for bone regeneration. *Stem Cell Rev.* 2008;4(1):21-26.
doi: 10.1007/s12015-008-9013-5

214. Sonoyama W, Liu Y, Yamaza T, et al. Characterization of the apical papilla and its residing stem cells from human immature permanent teeth: a pilot study. *J Endod.* 2008;34(2):166-171.
doi: 10.1016/j.joen.2007.11.021

215. Cheng H, Huang Y, Yue H, Fan Y. Electrical stimulation promotes stem cell neural differentiation in tissue engineering. *Stem Cells Int.* 2021;2021:e6697574.
doi: 10.1155/2021/6697574

216. Iwasa SN, Babona-Pilipos R, Morshead CM. Environmental factors that influence stem cell migration: an "Electric Field." *Stem Cells Int.* 2017;2017:e4276927.
doi: 10.1155/2017/4276927

217. Kusuyama J, Bandow K, Shamoto M, Kakimoto K, Ohnishi T, Matsuguchi T. Low intensity pulsed ultrasound (LIPUS) influences the multilineage differentiation of mesenchymal stem and progenitor cell lines through ROCK-Cot/Tpl2-MEK-ERK signaling pathway*. *J Biol Chem.* 2014;289(15):10330-10344.
doi: 10.1074/jbc.M113.546382

218. Lew WZ, Huang YC, Huang KY, Lin CT, Tsai MT, Huang HM. Static magnetic fields enhance dental pulp stem cell proliferation by activating the p38 mitogen-activated protein kinase pathway as its putative mechanism. *J Tissue Eng Regen Med.* 2018;12(1):19-29.
doi: 10.1002/term.2333

219. Galli C, Pedrazzi G, Mattioli-Belmonte M, Guizzardi S. The use of pulsed electromagnetic fields to promote bone responses to biomaterials *in vitro* and *in vivo*. *Int J Biomater.* 2018;2018:e8935750.
doi: 10.1155/2018/8935750

220. Hwang NS, Varghese S, Elisseeff J. Controlled differentiation of stem cells. *Adv Drug Deliv Rev.* 2008;60(2):199-214.
doi: 10.1016/j.addr.2007.08.036

221. Orciani M, Fini M, Di Primio R, Mattioli-Belmonte M. Biofabrication and bone tissue regeneration: cell source, approaches, and challenges. *Front Bioeng Biotechnol.* 2017;5:17.
doi: 10.3389/fbioe.2017.00017

222. Wang Z, Wang Z, Lu WW, Zhen W, Yang D, Peng S. Novel biomaterial strategies for controlled growth factor delivery for biomedical applications. *NPG Asia Mater.* 2017;9(10):e435.
doi: 10.1038/am.2017.171

223. Mahmoudi Z, Sedighi M, Jafari A, et al. *In situ* 3D bioprinting: a promising technique in advanced biofabrication strategies. *Bioprinting.* 2023;31:e00260.
doi: 10.1016/j.bprint.2023.e00260

224. Kim J, Choi HS, Kim YM, Song SC. Thermo-responsive nanocomposite bioink with growth-factor holding and its application to bone regeneration. *Small.* 2023;19(9):2203464.
doi: 10.1002/smll.202203464

225. Nyberg E, Holmes C, Witham T, Grayson WL. Growth factor-eluting technologies for bone tissue engineering. *Drug Deliv Transl Res.* 2016;6(2):184-194.
doi: 10.1007/s13346-015-0233-3

226. De Witte TM, Wagner AM, Fratila-Apachitei LE, Zadpoor AA, Peppas NA. Immobilization of nanocarriers within a porous chitosan scaffold for the sustained delivery of growth factors in bone tissue engineering applications. *J Biomed Mater Res A.* 2020;108(5):1122-1135.
doi: 10.1002/jbm.a.36887

227. Cheng M, Qin G. Chapter 11 – progenitor cell mobilization and recruitment: SDF-1, CXCR4, A4-Integrin, and c-Kit. In: Tang Y, ed. *Progress in Molecular Biology and Translational Science, Genetics of Stem Cells, Part A*. Cambridge, Massachusetts: Academic Press; 2012;111:243-264.
doi: 10.1016/B978-0-12-398459-3.00011-3

228. Lauer A, Wolf P, Mehler D, et al. Biofabrication of SDF-1 functionalized 3D-printed cell-free scaffolds for bone tissue regeneration. *Int J Mol Sci.* 2020;21(6):2175.
doi: 10.3390/ijms21062175

229. Tan J, Zhang M, Hai Z, et al. Sustained release of two bioactive factors from supramolecular hydrogel promotes periodontal bone regeneration. *ACS Nano.* 2019;13(5):5616-5622.
doi: 10.1021/acsnano.9b00788

230. Lopez CD, Diaz-Siso JR, Witek L, et al. Three dimensionally printed bioactive ceramic scaffold osseoconduction across critical-sized mandibular defects. *J Surg Res.* 2018;223:115-122.
doi: 10.1016/j.jss.2017.10.027

231. Dhavalikar P, Robinson A, Lan Z, et al. Review of integrin-targeting biomaterials in tissue engineering. *Adv Healthc Mater.* 2020;9(23):2000795. doi: 10.1002/adhm.202000795

232. Alvarez P, Hee CK, Solchaga L, et al. Growth factors and craniofacial surgery. *J Craniofac Surg.* 2012;23(1):20. doi: 10.1097/SCS.0b013e318240c6a8

233. Wang MM, Flores RL, Witek L, et al. Dipyridamole-loaded 3D-printed bioceramic scaffolds stimulate pediatric bone regeneration *in vivo* without disruption of craniofacial growth through facial maturity. *Sci Rep.* 2019;9(1):18439. doi: 10.1038/s41598-019-54726-6

234. Maliha SG, Lopez CD, Coelho PG, et al. Bone tissue engineering in the growing calvaria using dipyridamole-coated, three-dimensionally-printed bioceramic scaffolds: construct optimization and effects on cranial suture patency. *Plast Reconstr Surg.* 2020;145(2):337e. doi: 10.1097/PRS.0000000000006483

235. Nagayasu-Tanaka T, Anzai J, Takedachi M, Kitamura M, Harada T, Murakami S. Effects of combined application of fibroblast growth factor (FGF)-2 and carbonate apatite for tissue regeneration in a beagle dog model of one-wall periodontal defect. *Regen Ther.* 2023;23:84-93. doi: 10.1016/j.reth.2023.04.002

236. Qu M, Jiang X, Zhou X, et al. Stimuli-responsive delivery of growth factors for tissue engineering. *Adv Healthc Mater.* 2020;9(7):1901714. doi: 10.1002/adhm.201901714

237. Amler AK, Thomas A, Tüzüner S, et al. 3D bioprinting of tissue-specific osteoblasts and endothelial cells to model the human jawbone. *Sci Rep.* 2021;11(1):4876. doi: 10.1038/s41598-021-84483-4

238. Kim D, Lee H, Lee GH, Hoang TH, Kim HR, Kim GH. Fabrication of bone-derived decellularized extracellular matrix/ceramic-based biocomposites and their osteo/odontogenic differentiation ability for dentin regeneration. *Bioeng Transl Med.* 2022;7(3):e10317. doi: 10.1002/btm2.10317

239. Lee UL, Yun S, Cao HL, et al. Bioprinting on 3D printed titanium scaffolds for periodontal ligament regeneration. *Cells.* 2021;10(6):1337. doi: 10.3390/cells10061337

240. Lin YT, Hsu TT, Liu YW, Kao CT, Huang TH. Bidirectional differentiation of human-derived stem cells induced by biomimetic calcium silicate-reinforced gelatin methacrylate bioink for odontogenic regeneration. *Biomedicines.* 2021;9(8):929. doi: 10.3390/biomedicines9080929

241. Kort-Mascort J, Bao G, Elkashty O, et al. Decellularized extracellular matrix composite hydrogel bioinks for the development of 3D bioprinted head and neck *in vitro* tumor models. *ACS Biomater Sci Eng.* 2021;7(11):5288-5300. doi: 10.1021/acsbiomaterials.1c00812

242. Aguilar IN, Smith LJ, Olivos DJ, Chu TMG, Kacena MA, Wagner DR. Scaffold-free bioprinting of mesenchymal stem cells with the regenova printer: optimization of printing parameters. *Bioprinting.* 2019;15:e00048. doi: 10.1016/j.bprint.2019.e00048

243. Aguilar IN, Olivos DJ, Brinker A, et al. Scaffold-free bioprinting of mesenchymal stem cells using the regenova printer: spheroid characterization and osteogenic differentiation. *Bioprinting.* 2019;15:e00050. doi: 10.1016/j.bprint.2019.e00050

244. Hamza H. Dental 4D printing: an innovative approach. 2018;1(9):e17. doi: 10.30771/2018.4

245. Javaid M, Haleem A, Singh RP, Rab S, Suman R, Kumar L. Significance of 4D printing for dentistry: materials, process, and potentials. *J Oral Biol Craniofacial Res.* 2022;12(3):388-395. doi: 10.1016/j.jobcr.2022.05.002

246. Datta S, Rameshbabu AP, Bankoti K, et al. Decellularized bone matrix/oleoyl chitosan derived supramolecular injectable hydrogel promotes efficient bone integration. *Mater Sci Eng C.* 2021;119:111604. doi: 10.1016/j.msec.2020.111604

247. Akbarinia S, Sadrnezhaad SK, Hosseini SA. Porous shape memory dental implant by reactive sintering of TiH2-Ni-urea mixture. *Mater Sci Eng C.* 2020;107:110213. doi: 10.1016/j.msec.2019.110213

248. do Nascimento RO, Chirani N. 13 – shape-memory polymers for dental applications. In: Yahia L, ed. *Shape Memory Polymers for Biomedical Applications.* Woodhead Publishing Series in Biomaterials. Woodhead Publishing;2015:267-280. doi: 10.1016/B978-0-85709-698-2.00013-1

249. Pfau MR, Beltran FO, Woodard LN, et al. Evaluation of a self-fitting, shape memory polymer scaffold in a rabbit calvarial defect model. *Acta Biomater.* 2021;136:233-242. doi: 10.1016/j.actbio.2021.09.041

250. Uijlenbroek H, Liu Y, Wismeijer D. Soft tissue expansion: principles and inferred intraoral hydrogel tissue expanders. *Dent Oral Craniofacial Res.* 2016;1(6):178–185. doi: 10.15761/DOCR.1000140

251. Malekmohammadi S, Sedghi Aminabad N, Sabzi A, et al. Smart and biomimetic 3D and 4D printed composite hydrogels: opportunities for different biomedical applications. *Biomedicines.* 2021;9(11):1537. doi: 10.3390/biomedicines9111537

252. Naniz MA, Askari M, Zolfagharian A, Naniz MA, Bodaghi M. 4D printing: a cutting-edge platform for biomedical applications. *Biomed Mater.* 2022;17(6):062001. doi: 10.1088/1748-605X/ac8e42

253. Hwangbo H, Lee H, Roh EJ, et al. Bone tissue engineering via application of a collagen/hydroxyapatite 4D-printed biomimetic scaffold for spinal fusion. *Appl Phys Rev.* 2021;8(2):021403. doi: 10.1063/5.0035601

254. Liu S, Wang YN, Ma B, Shao J, Liu H, Ge S. Gingipain-responsive thermosensitive hydrogel loaded with SDF-1 facilitates in situ periodontal tissue regeneration. *ACS Appl Mater Interfaces.* 2021;13(31):36880-36893. doi: 10.1021/acsami.1c08855

255. Wang B, Booij-Vrieling HE, Bronkhorst EM, et al. Antimicrobial and anti-inflammatory thermo-reversible hydrogel for periodontal delivery. *Acta Biomater.* 2020;116:259-267. doi: 10.1016/j.actbio.2020.09.018

256. Wu D, Wang P, Wu Q, et al. Preparation and characterization of bomidin-loaded thermosensitive hydrogel for periodontal application. *J Mater Res.* 2022;37(18):3021-3032. doi: 10.1557/s43578-022-00706-y

257. Ma S, Lu X, Yu X, et al. An injectable multifunctional thermo-sensitive chitosan-based hydrogel for periodontitis therapy. *Biomater Adv.* 2022;142:213158. doi: 10.1016/j.bioadv.2022.213158

258. Irvine SA, Venkatraman SS. Bioprinting and differentiation of stem cells. *Molecules.* 2016;21(9):1188. doi: 10.3390/molecules21091188

259. Son C, Choi MS, Park JC. Different responsiveness of alveolar bone and long bone to epithelial mesenchymal interaction related factor. *JBMR Plus.* 2020;4(8):e10382. doi: 10.1002/jbm4.10382

260. Liu X, Zhao K, Gong T, et al. Delivery of growth factors using a smart porous nanocomposite scaffold to repair a mandibular bone defect. *Biomacromolecules.* 2014;15(3):1019-1030. doi: 10.1021/bm401911p

261. Mohd N, Razali M, Ghazali MJ, Abu Kasim NH. Current advances of three-dimensional bioprinting application in dentistry: a scoping review. *Materials.* 2022;15(18):6398. doi: 10.3390/ma15186398

262. Filipowska J, Tomaszewski KA, Niedźwiedzki Ł, Walocha JA, Niedźwiedzki T. The role of vasculature in bone development, regeneration and proper systemic functioning. *Angiogenesis.* 2017;20(3):291-302. doi: 10.1007/s10456-017-9541-1

263. Qu H, Fu H, Han Z, Sun Y. Biomaterials for bone tissue engineering scaffolds: a review. *RSC Adv.* 2019;9(45):26252-26262. doi: 10.1039/C9RA05214C

264. Burdis R, Kelly DJ. Biofabrication and bioprinting using cellular aggregates, microtissues and organoids for the engineering of musculoskeletal tissues. *Acta Biomater.* 2021;126:1-14. doi: 10.1016/j.actbio.2021.03.016

265. Miao Y, Chen Y, Luo J, et al. Black phosphorus nanosheets-enabled DNA hydrogel integrating 3D-printed scaffold for promoting vascularized bone regeneration. *Bioact Mater.* 2023;21:97-109. doi: 10.1016/j.bioactmat.2022.08.005

266. Zhao X, Xu Z, Xiao L, et al. Review on the vascularization of organoids and organoids-on-a-chip. *Front Bioeng Biotechnol.* 2021;9:637048. doi: 10.3389/fbioe.2021.637048

267. Miri AK, Khalilpour A, Cecen B, Maharjan S, Shin SR, Khademhosseini A. Multiscale bioprinting of vascularized models. *Biomaterials.* 2019;198:204-216. doi: 10.1016/j.biomaterials.2018.08.006

268. Dong Y, Wang S, Ke Y, et al. 4D printed hydrogels: fabrication, materials, and applications. *Adv Mater Technol.* 2020;5(6):2000034. doi: 10.1002/admt.202000034

269. Champeau M, Heinze DA, Viana TN, de Souza ER, Chinellato AC, Titotto S. 4D printing of hydrogels: a review. *Adv Funct Mater.* 2020;30(31):1910606. doi: 10.1002/adfm.201910606

270. Yang X, Ma Y, Wang X, et al. A 3D-bioprinted functional module based on decellularized extracellular matrix bioink for periodontal regeneration. *Adv Sci.* 2023;10(5): 2205041. doi: 10.1002/advs.202205041

271. Bousnaki M, Beketova A, Kontonasaki E. A review of *in vivo* and clinical studies applying scaffolds and cell sheet technology for periodontal ligament regeneration. *Biomolecules.* 2022;12(3):435. doi: 10.3390/biom12030435

272. Liang C, Liao L, Tian W. Advances focusing on the application of decellularized extracellular matrix in periodontal regeneration. *Biomolecules.* 2023;13(4):673. doi: 10.3390/biom13040673

273. Miao G, Liang L, Li W, et al. 3D bioprinting of a bioactive composite scaffold for cell delivery in periodontal tissue regeneration. *Biomolecules.* 2023;13(7):1062. doi: 10.3390/biom13071062

274. Zhang W, Vazquez B, Oreadi D, Yelick PC. Decellularized tooth bud scaffolds for tooth regeneration. *J Dent Res.* 2017;96(5):516-523. doi: 10.1177/0022034516689082

275. Aksel H, Sarkar D, Lin MH, Buck A, Huang GTJ. Cell-derived extracellular matrix proteins in colloidal microgel as a self-assembly hydrogel for regenerative endodontics. *J Endod.* 2022;48(4):527-534. doi: 10.1016/j.joen.2022.01.011

276. Ebrahimi Sadrabadi A, Baei P, Hosseini S, Baghaban Eslaminejad M. Decellularized extracellular matrix as a potent natural biomaterial for regenerative medicine. In: Turksen K, ed. *Cell Biology and Translational Medicine, Volume 13: Stem Cells in Development and Disease.* Cham: Springer International Publishing;2021:27-43. doi: 10.1007/5584_2020_504

277. Yu F, Khan AUR, Zheng H, et al. A photocrosslinking antibacterial decellularized matrix hydrogel with nanofiber

for cutaneous wound healing. *Colloids Surf B Biointerfaces.* 2022;217:112691.
doi: 10.1016/j.colsurfb.2022.112691

278. Fang B, Qiu P, Xia C, et al. Extracellular matrix scaffold crosslinked with vancomycin for multifunctional antibacterial bone infection therapy. *Biomaterials.* 2021;268:120603.
doi: 10.1016/j.biomaterials.2020.120603

279. Ribi Hans O. Plural element composite materials, methods for making and using the same. 20110140057. U.S. Patent. 2007. https://ppubs.uspto.gov/dirsearch-public/print/downloadPdf/20110140057 (accessed May 12, 2024).

280. Sheikh A, Abourehab MAS, Kesharwani P. The clinical significance of 4D printing. *Drug Discov Today.* 2023;28(1):103391.
doi: 10.1016/j.drudis.2022.103391

281. Ostrovidov S, Ramalingam M, Bae H, et al. Bioprinting and biomaterials for dental alveolar tissue regeneration. *Front Bioeng Biotechnol.* 2023;11:991821.
doi: 10.3389/fbioe.2023.991821

282. Zhou C, Wang Q, Zhang D, Cai L, Du W, Xie J. Compliant substratum modulates vinculin expression in focal adhesion plaques in skeletal cells. *Int J Oral Sci.* 2019;11(2):1-9.
doi: 10.1038/s41368-019-0052-3

283. Rifai A, Tran N, Leitch V, Booth MA, Williams R, Fox K. Osteoblast cell response on polycrystalline diamond-coated additively manufactured scaffolds. *ACS Appl Bio Mater.* 2021;4(10):7509-7516.
doi: 10.1021/acsabm.1c00757

284. Burdis R, Chariyev-Prinz F, Browe DC, et al. Spatial patterning of phenotypically distinct microtissues to engineer osteochondral grafts for biological joint resurfacing. *Biomaterials.* 2022;289:121750.
doi: 10.1016/j.biomaterials.2022.121750

285. Qu H. Additive manufacturing for bone tissue engineering scaffolds. *Mater Today Commun.* 2020;24:101024.
doi: 10.1016/j.mtcomm.2020.101024

286. Chang J, He J, Mao M, et al. Advanced material strategies for next-generation additive manufacturing. *Materials.* 2018;11(1):166.
doi: 10.3390/ma11010166

287. Clegg JR, Wagner AM, Shin SR, Hassan S, Khademhosseini A, Peppas NA. Modular fabrication of intelligent material-tissue interfaces for bioinspired and biomimetic devices. *Prog Mater Sci.* 2019;106:100589.
doi: 10.1016/j.pmatsci.2019.100589

288. Rees WM van, Matsumoto EA, Gladman AS, Lewis JA, Mahadevan L. Mechanics of biomimetic 4D printed structures. *Soft Matter.* 2018;14(43):8771-8779.
doi: 10.1039/C8SM00990B

289. Yang Q, Gao B, Xu F. Recent advances in 4D bioprinting. *Biotechnol J.* 2020;15(1):1900086.
doi: 10.1002/biot.201900086

290. Zhang W, Wang H, Wang H, et al. Structural multi-colour invisible inks with submicron 4D printing of shape memory polymers. *Nat Commun.* 2021;12(1):112.
doi: 10.1038/s41467-020-20300-2

291. Chung S, Song SE, Cho YT. Effective software solutions for 4D printing: a review and proposal. *Int J Precis Eng Manuf-Green Technol.* 2017;4(3):359-371.
doi: 10.1007/s40684-017-0041-y

292. Agarwal P, Mathur V, Kasturi M, Srinivasan V, Seetharam RN, S Vasanthan K. A futuristic development in 3D printing technique using nanomaterials with a step toward 4D printing. *ACS Omega.* 2024;9(36):37445-37458.
doi: 10.1021/acsomega.4c04123

293. Hamel CM, Roach DJ, Long KN, Demoly F, Dunn ML, Qi HJ. Machine-learning based design of active composite structures for 4D printing. *Smart Mater Struct.* 2019;28(6):065005.
doi: 10.1088/1361-665X/ab1439

294. Fu Z, Angeline V, Sun W. Evaluation of printing parameters on 3D extrusion printing of pluronic hydrogels and machine learning guided parameter recommendation. *Int J Bioprinting.* 2021;7(4):434.
doi: 10.18063/ijb.v7i4.434

295. Ahmed GM, Abouauf EA, AbuBakr N, Dörfer CE, El-Sayed KF. Tissue engineering approaches for enamel, dentin, and pulp regeneration: an update. *Stem Cells Int.* 2020;2020(1):5734539.
doi: 10.1155/2020/5734539

296. Ramezani M, Mohd Ripin Z. 4D printing in biomedical engineering: advancements, challenges, and future directions. *J Funct Biomater.* 2023;14(7):347.
doi: 10.3390/jfb14070347

ACCSCIENCE PUBLISHING

International Journal of Bioprinting

REVIEW ARTICLE

Application of three-dimensional printing in bacterial detection

Tingting Cui[1,2], Ziye Xu[1,2], and Ting Cao[1,2]*

[1]Department of Laboratory Medicine, the First Affiliated Hospital, Zhejiang University School of Medicine, Hangzhou, Zhejiang, China.

[2]Key Laboratory of Clinical *In Vitro* Diagnostic Techniques of Zhejiang Province, Hangzhou, Zhejiang, China.

Abstract

Diseases caused by bacterial infections, especially pathogen variations and drug-resistant bacteria, are a serious threat to human health globally. Accurate and rapid identification of bacterial pathogens is essential for early diagnosis of infections and timely treatment of disease. At present, the routine diagnostic methods for identifying bacterial pathogens in the clinic are bacterial culture, immunological detection, genetic analysis, etc. These methods are fundamental for bacterial detection and clinical diagnosis of pathogen infections in daily life. Notably, three-dimensional (3D) (bio)printing technology provides more options for bacterial detection due to its personalized design and manufacturing. Compared with traditional methods, 3D printing provides a more convenient, rapid, and accurate bacterial detection platform, thus meeting the urgent needs of clinical and scientific research. Here, we have summarized the research progress in 3D printing technology for bacterial detection, including bacterial detection sensors, microfluidic chips, bioprinting microarray technology, artificial intelligence, and spectroscopy, providing a scientific reference and addressing gaps in 3D printing-assistance bacterial detection. Additionally, technical advantages, challenges, and future development trends are also discussed in related healthcare fields.

Keywords: Three-dimensional (3D) printing; Bacterial detection; Bacterial infection

***Corresponding author:**
Ting Cao
(tingcao@zju.edu.cn)

Citation: Cui T, Xu Z, Cao T. Application of 3D printing in bacterial detection. *Int J Bioprint*. 2025;11(1):192-209. doi: 10.36922/ijb.4999

Received: September 30, 2024
Revised: November 4, 2024
Accepted: November 5, 2024
Published Online: November 5, 2024

Copyright: © 2024 Author(s). This is an Open Access article distributed under the terms of the Creative Commons Attribution License, permitting distribution, and reproduction in any medium, provided the original work is properly cited.

Publisher's Note: AccScience Publishing remains neutral with regard to jurisdictional claims in published maps and institutional affiliations.

1. Introduction

Bacterial detection, particularly early diagnosis of bacterial infection, is a global concern,[1] made more urgent by the increase in pathogen variations and drug-resistant bacteria.[2] Conventional bacterial detection methods in clinics consist of culture-based detection, immunological identification, and molecular biology technology, but still require further improvements in detection rate, sensitivity, specificity, and cost.[3] In recent years, three-dimensional (3D) (bio)printing technology has introduced new approaches to microorganism research,[4,5] as it is currently used in surgical and medical devices, drug delivery, and tissue engineering,[6,7] with the advantages of rapid prototyping, easy complex geometry fabrication, customization of heterogeneous component assembly, and cost-efficiency.[8] However, a comprehensive summary of (3D) printing in bacterial detection is lacking, which is crucial for advancing both 3D printing and clinical

bacterial diagnostics. Thus, this review aims to provide a comprehensive overview of 3D printing applications in bacterial detection. Concurrently, technical advantages, challenges, and future development trends are also discussed in related healthcare fields.

2. Current status of bacterial detection

Bacterial pathogens cause a variety of human diseases.[9] Given the increasing bacterial infection rates, simple, rapid, and low-cost detection strategies are urgently needed.[10] A series of technical methods are currently employed for bacterial detection in clinics, including traditional microbiological detection methods, immunological detection, and nucleic acid-based detection techniques.[11-15] Likewise, other analysis methods with 3D printing technology are being developed to enhance clinical bacterial detection, each with its intrinsic advantages and disadvantages.

Traditional microbial detection platforms based on morphology include smear microscopy and culture identification. Smear microscopy is one of the most basic methods for bacterial detection. It was widely used in the fields of medicine and biology soon after microscopy technology matured. By preparing and staining bacterial smears, the morphology, arrangement, and staining properties of bacteria can be observed under the microscope for preliminary identification and classification.[16] Bacterial culture is a classic method for bacterial detection. With the development of microbiology, researchers optimized media formulations and conditions to support the growth of various bacterial species.[17] By selecting appropriate media and environmental conditions, bacteria can proliferate *in vitro*; they can then be identified based on colony morphology and biochemical reactions. This method has high accuracy and can provide detailed biological information about bacteria, but it is time-consuming, usually taking days to weeks. Additionally, culturing fastidious bacteria and the complex operation also pose significant challenges that need to be addressed.[18]

Immunological detection is a detection method based on the specific recognition between antigen and antibody; its emergence and development are closely related to

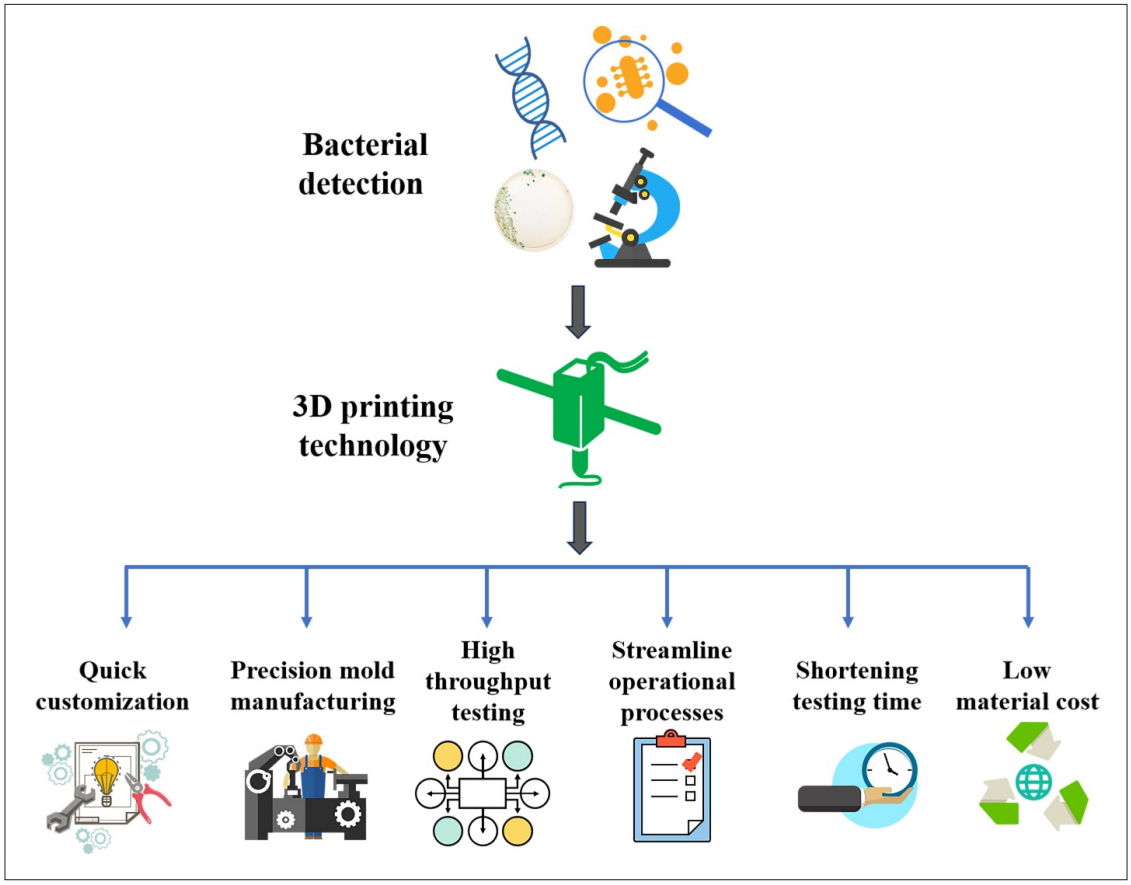

Figure 1. The advantages of 3D printing technology in bacterial detection.

advances in immunological research. Immunological detection targets pathogen proteins or metabolic substances, such as glycoproteins and polysaccharides,[19] to identify bacterial types mainly through specific antigens or antibodies during bacterial infections. This includes lateral flow devices, immunofluorescence, and enzyme-linked immune sorbent assay, among others.[20] This method has high sensitivity and good specificity; however, the detection results are affected by the quality of the antibody, with limited ability to detect new pathogens.

Molecular biological detection is a bacterial detection method that has emerged with the rapid development of molecular biology technology in recent decades. It uses unique gene sequences in bacteria for detection and is highly sensitive and specific. By extracting bacterial nucleic acid (DNA or RNA) from samples and using polymerase chain reaction (PCR) to amplify the target gene region, the rapid and accurate identification of bacteria can be achieved.[21] This method has high sensitivity and specificity, can be completed within a short time, and is widely used in the diagnosis and monitoring of infectious diseases. However, it is expensive, requires professional equipment and technicians, and may yield false positive/negative results.[22] Notably, isothermal nucleic acid amplification technology, an *in vitro* amplification method that uses enzymes with different functions and specific primers to rapidly amplify nucleic acids at constant temperature,[23] has been utilized for bacterial detection in recent years. This approach eliminates the thermal cycling step and simplifies the amplification process, providing a user-friendly operation condition.[24] Currently, the commonly used isothermal amplification methods include loop-mediated isothermal amplification (LAMP), nucleic acid sequence-based amplification (NASBA), recombinase polymerase amplification (RPA), rolling circle amplification (RCA), and hybridization chain reaction (HCR),[25] featuring advantages of simplicity, rapidity, and efficiency. However, aerosol contamination in the amplification process leads to false positive results; likewise, challenges in primer design and limitations in enzyme storage hinder its widespread practical application.[26] Capillary electrophoresis (CE) is a powerful tool for the identification and separation of charged compounds.[27] It is sometimes used in combination with various nucleic acid detection strategies to minimize the possibility of false/negative results. It has the advantages of high efficiency, small sample volume, and simple sample preparation, but along with shortcomings of time-consuming sample processing and high equipment cost.[28]

Next-generation sequencing (NGS), a representative of gene sequencing, has the advantages of high throughput and accuracy, displaying great potential for bacterial detection. By sequencing the whole genome or specific regions of bacteria (e.g., 16s rRNA region), accurate identification, typing, and drug resistance gene detection of bacteria can be achieved, particularly in complex samples.[29-31] However, it requires high data processing power for bioinformatics analysis and is relatively costly compared to other nucleic acid amplification methods, such as PCR.[32]

Gene chip technology uses nucleic acid hybridization to detect bacterial genes in samples. A large number of DNA or RNA fragments are hybridized on the surface of a solid carrier via base pairing; the hybridization signal is then detected using scanning equipment to obtain genetic information on the bacteria and achieve qualitative and quantitative detection.[33] Gene chips have high sensitivity and specificity and high-throughput capabilities, but there are challenges in terms of diagnostic speed, standardization, cost, and contamination risk.[34]

With advances in science and technology, chromatography and spectroscopy techniques based on bacterial proteins not only improve the accuracy, sensitivity, and speed of detection but also reveal a broader range of chemical and physical characteristics of bacteria. The primary principle of chromatographic detection of bacteria is using the distribution difference between the stationary phase and the mobile phase of bacteria or their metabolites through the chromatographic column and then analyzing separated components with the detector (i.e., usually mass spectrometry or other technical means) for qualitative analysis of separated constituents.[35,36] Chromatography has high separation efficiency, high sensitivity, and fast analysis speed for detecting bacteria, but it is challenged by complex sample pretreatment, high equipment cost, and technical requirements in operation. Spectrometry is used to qualitatively and quantitatively analyze bacteria by measuring the spectral signal produced by the interaction of bacteria or bacterial metabolites with light.[37,38] Its advantages—high sensitivity, high selectivity, non-destructiveness, rapidity, and efficiency—have demonstrated broad application prospects in bacterial detection. However, its disadvantages and limitations, such as high equipment cost, stringent sample requirements, and strong technical dependence, cannot be ignored.[39]

At present, the main challenges of bacterial detection are complex sample processing, long detection cycles, and the need for further improvements in sensitivity and specificity. Although traditional methods, such as Gram staining and PCR amplification, meet the needs of detection to a certain extent, they have limitations in dealing with rapidly mutating pathogens and improving detection throughput. A detailed comparison between various detection approaches is summarized in Table 1.

Table 1. Characteristics of different bacterial detection methods

Detection strategy	Method	Target pathogen	Principle	Detection accuracy	Detection speed	Advantages	Limitations	Ref.
Conventional	Culture-based identification	Bacteria, fungi, and viruses	According to bacterial shape, size, and staining; requires a nutrient medium	High accuracy	Slow (days to weeks)	Cost-effective simple	Low sensitivity; laborious testing	[96]
	Immunological detection	Bacteria, fungi, and viruses	Exploits affinity between microbial antigen and mono/polyclonal antibody	Frequent false positives	Fast (few hours)	High specificity; processes many samples simultaneously	Dependence on antigen-antibody interaction	[20]
	PCR	Bacteria, fungi, and viruses	Uses unique gene sequences in microorganisms for detection	Frequent false positives/negatives	Fast (few hours)	High sensitivity and specificity	Expensive; requires equipment and technicians	[22,97]
	Isothermal nucleic acid amplification	Bacteria, fungi, and viruses	Uses unique gene sequences in microorganisms for detection	Accuracy higher than PCR	Fast (few hours)	Amplification at constant temperature; high sensitivity	Aerosol contamination causes false positives; challenging primer design and enzyme storage	[25,26,96]
	Capillary electrophoresis	Bacteria, fungi, and viruses	Intracellular metabolites, extracellular metabolites, or cellular components of bacteria are determined	Reduced false positives/negatives	Fast (minutes to hours)	High efficiency; small sample volume; simple sample preparation	Sample processing is time-consuming; high equipment cost	[27,28]
	Next-generation sequencing	Bacteria, fungi, and viruses	Sequencing of whole genome or specific regions, such as the 16s rRNA region	High accuracy	-	High throughput and accuracy; suitable for all microorganisms	Relatively high cost; require strained personnel to operate	[20,29]
	Gene chip technology	Bacteria, fungi, and viruses	Uses nucleic acid hybridization to detect bacterial genes in samples	Frequent false positives in multiple testing	Fast	High specificity and sensitivity; detects multiple pathogens simultaneously; easy to operate	Expensive equipment; requires a high level of operational skill	[33]
	Chromatography	Bacteria	Analyze bacterial metabolites or components; often combined with other techniques (e.g., mass spectrometry)	-	Fast	High separation efficiency; high sensitivity	Complex sample pretreatment; high equipment costs; requires technical expertise	[35,36]

(Continued...)

Table 1. Continue...

Detection strategy	Method	Target pathogen	Principle	Detection accuracy	Detection speed	Advantages	Limitations	Ref.
Conventional	Spectroscopy	Bacteria	Spectral signals from bacteria interaction or metabolites	-	Fast	High sensitivity and selectivity; non-destructive; efficient	High equipment cost, sample requirements, and technical dependence	[37,39]
3D (bio) printing	Biological sensors	Bacteria	Establishment of the reactor; sample treatment and signal recognition	-	Fast	Simple operating device; improved applicability; low cost; high sensitivity and specificity; easy operation; fast response	3D-printed materials cannot fully satisfy the requirement (stability, sensitivity, durability etc.) of biosensors; different printing parameters for different scenarios limits large-scale production of biosensors	[81,83,84,85]
	Microfluidic chips	Bacteria	3D printing of microfluidic chips for signal recognition and transduction in bacterial detection	-	Fast	Enhanced detection limit; can culture and detect multiple pathogens simultaneously	Limited materials for 3D-printed microfluidic chips; 3D printing technology lacks uniform standards and specifications for chip production	[78,87,89]
	Bioprinting microarray technology	Bacteria	Biological probes (antibodies, DNA) can be precisely fixed on tiny matrices to form high-density microarray structures specific to bacterial targets	-	Fast	Easy to operate; rapid detection; potential for practical clinical application; enhanced bacterial capture efficiency	3D-printed microarray technology is not well-established; only applicable for specific bacteria or pathogens; limited detection range	[90,91]
	Combination of AI and spectral technology	Bacteria	3D bioprinting combined with AI and spectral analysis technology for bacterial detection	≥99%	Fast	High throughput testing; non-culture detection; non-destructive testing	High technical complexity; complex data processing; limited testing range; lack of uniform standards	[95]

Abbreviations: AI: Artificial intelligence; PCR: Polymerase chain reaction.

doi: 10.36922/ijb.4999

Therefore, exploring efficient and accurate bacterial detection technologies remains a key research focus.

3. Overview of 3D (bio)printing technology

3D printing technology is a bottom-up manufacturing method that builds 3D objects by stacking materials layer by layer.[40] The key principle of 3D printing is slicing and stacking. Through slicing a 3D model into many thin layers, specific printing equipment, such as a 3D printer, prints out powdered metal, plastic, or other materials layer by layer and stacks the layers to form a complete 3D entity.[41,42] This operation endows 3D printing with the ability of complex geometry fabrication that is usually difficult to achieve with traditional manufacturing techniques.[43] With advancements in material science, computer technology, and precision manufacturing, 3D printing has been widely used in medical, aerospace, automotive, construction, food, and other fields.[44-47] Notably, 3D printing significantly accelerates medical development with the printing of medical devices, implants, and prostheses.[48-50] In addition, it can also be applied in tissue engineering and regenerative medicine with the bioprinting of cells, tissues, organs, and microorganisms, which is also known as 3D bioprinting.[51,52] There are three main types of 3D bioprinting, namely extrusion-based, jetting-based, and vat photopolymerization-based bioprinting.

Extrusion bioprinting is a technique for fabricating 3D structures through continuous extrusion of bioink.[53] It has strong compatibility and can print various types of biomaterials, including high-viscosity bioinks (e.g., cell membranes) and hydrogels. Typically, extrusion bioprinting has a low cost, but its low resolution limits its application in the fabrication of complex structures. Moreover, it is prone to nozzle blockage, and shear stress generated during the extrusion process may damage the cells and reduce cell viability.[54]

Jetting-based bioprinting is a technology that accurately controls the spatial arrangement of bioinks by contactless, on-demand injection of droplets at specific locations. It mainly includes inkjet bioprinting, laser-assisted bioprinting, acoustic bioprinting, microvalve-based bioprinting, and electrohydrodynamic jet bioprinting.[55] Samples prepared by inkjet bioprinting have high resolution and cell viability. However, this technology cannot print biomaterials with high viscosity and high cell concentration.[56] The benefit of laser-assisted bioprinting is that it can use printable bioinks of different viscosities with high printing resolution. Since shear stress is avoided, high cell viability can be achieved, but the cost is relatively high.[57] Acoustic bioprinting supports multi-scale bioprinting, enabling precise printing of everything from larger cell aggregates to individual cells in cross-scale 3D. This nozzle-free bioprinting system avoids clogging problems and also reduces cell damage, but its system is relatively complex and expensive.[58] A typical microvalve-based bioprinting system consists of a three-axis mobile robot platform and multiple electromechanical microvalve print head arrays. Each microvalve print head is connected to a separate gas regulator; biomaterials and cells can be simultaneously ejected from different print heads. It precisely controls the deposition of multiple types of cells and biomaterials with high cell viability, high throughput, and moderate printing resolution. High printing pressure and small nozzle diameter lead to reduced cell viability.[59] Electrohydrodynamic jet bioprinting uses an electric field to pull a cell-loaded droplet from the tip of a nozzle and facilitates high-resolution printing, but there are challenges such as limited selection of printable inks, disordered fiber arrangement due to charge accumulation within the printed fibers, and fabrication of smaller 3D structures.[55]

Vat photopolymerization-based bioprinting is a technology that uses photosensitive resins to fabricate 3D structures layer-by-layer using light-curing technology, featuring stereolithography (SLA), digital light processing (DLP), continuous liquid interface production (CLIP), computed axial lithography (CAL), two-photon polymerization (TPP), or other light-curing technologies.[60] Vat photopolymerization-based bioprinting provides high-resolution-printed structures and good connectivity between the printed layers, with the ability to create complex structures. The disadvantage of this approach is exposure to UV light, which leads to cell damage and high cost.[61] This method can improve the printability and cell viability of bioink by photorheological measurements and bioink wavelength synchronization.[62]

In the process of bioprinting, cell damage may be due to various causes, such as shear stress, thermal stress, and radiation stress.[63] Due to the intrinsic characteristics of each bioprinting technique, the factor affecting cell viability varies for different bioprinting methods. The effect of extrusion bioprinting on cell viability mainly lies in shear stress and material crosslinking. Shear stress can negatively affect cell viability; nozzle diameter and bioink viscosity can affect the range of shear stress values.[64] The precursor hydrogel or polymer solution for bioprinting must be crosslinked to form a stable 3D structure with good shape fidelity. The type and concentration of the crosslinking agent, as well as the duration of crosslinking, may affect cellactivity.[65] Cell viability in jetting-based bioprinting is mainly affected by shear stress, thermal stress, droplet impact velocity, and droplet volume. During the printing process, the limited nozzle size requires low viscosity and low concentration of bioink to reduce shear

stress and protect cells from severe damage.[51] Cell damage in vat photopolymerization-based bioprinting results from the radiation stress of the light source and the cytotoxicity of the photoinitiator.[63] Although the cell damage caused by the ultraviolet laser is not significant for cell printing, it is lethal to bacteria. Under UV light, microbial DNA absorbs the radiation, leading to thymine base dimerization, which inactivates the bacteria.[66]

A key component of 3D bioprinting is bioink, which embeds cells or microorganisms in biocompatible and bioactive materials (e.g., collagen, hyaluronic acid, alginate, and other natural polymers).[67,68] By precisely controlling the printing process, 3D bioprinting can construct 3D biological structures with biological activity and specific functions, implying great potential in tissue engineering, drug screening, and disease modeling.[69-72] In addition, bioprinting also can be used in various fields beyond human tissues, such as the manufacture of cultured meat, the development of more sustainable bioinks, the integration of machine learning (ML) into the 3D bioprinting process, bioelectronics, and space bioprinting.[73] Bacterial detection is one such example.

In the process of pathogen detection, 3D printing mainly serves in the construction of functional devices for microorganism capture, isolation, culture, and detection, thereby improving the efficiency and accuracy of bacterial detection.[74,75] Benefiting from its intrinsic superiority, 3D printing allows researchers to design microbial detection devices with specific shapes, structures, and functions according to actual needs. 3D printing technology allows for rapid customization according to different industries and specific needs to accommodate different types of pathogen detection. Lee et al.[76] used SLA to create 3D spiral microchannels around a cylindrical chamber, which can detect *Escherichia coli* (*E. coli*) in real food matrices quickly and easily. Pahlow et al.[77] used inkjet printing to prepare a cartridge system for convenient and cost-effective isolation of pathogenic bacteria from sputum samples. Besides, microfluidic chips fabricated by 3D printing can achieve high-throughput detection. Feng et al.[78] used 3D printing to develop a novel chip with an aptamer-based nano-interferometer capable of identifying four different foodborne pathogens (*L. monocytogenes, E. coli, S. typhimurium*, and *S. aureus*) with high sensitivity, i.e., with a limit-of-detection of 10 colony-forming units (CFU)/mL. Moreover, 3D printing technology simplifies the operation process of bacterial detection and shortens the detection time. Malhotra et al.[79] developed a cost-effective and portable 3D-printed electrochemical biosensor that facilitated the rapid detection of certain *E. coli* species in 15 min using 500 µL samples and cost only $2.50 per test. The advantages of 3D printing in bacterial detection are presented in Figure 1. These devices are capable of providing a larger culture area, more efficient chemical exchange, and more sensitive signal reports, thus enabling rapid and accurate detection of bacteria. In addition, 3D printing supports the hybrid printing of multiple materials, which provides more possibilities for bacterial detection. For instance, researchers can print appropriate biomaterials into complex 3D structures to study the growth characteristics and reaction mechanisms of bacteria under different conditions.[80] Compared with traditional bacterial detection methods, 3D printing can provide a more convenient, rapid, and accurate bacterial detection platform, thus meeting the urgent needs of clinical and scientific research.

4. Research and application of 3D (bio) printing in bacterial detection

4.1. Biological sensors for bacterial detection

3D printing enables the fabrication of miniaturized and integrated sensors capable of detecting the presence, type, and number of bacteria, making bacterial detection more portable and rapid. In particular, the combination of 3D printing and nanotechnology for sensor construction enables the rapid identification and detection of specific pathogens, which is favorable for early clinical diagnosis and has significant potential for real-world applications.

The most common use of 3D printing in bacterial detection biosensors is the development of reactors. For example, Xu et al.[81] constructed a 3D-printed integrated handheld biosensor that can replace PCR instruments for nucleic acid amplification, simplifying the operating device and improving its applicability in practice. Likewise, it integrates recombinase polymerase amplification-clustered, regularly interspaced short palindromic repeats/Cas12a protein (RPA-CRISPR/Cas12a) and lateral chromatography strip analysis for visualization and rapid analysis. As displayed in Figure 2A, it can be used to detect *V. parahaemolyticus* easily and intuitively in the field. Angelopoulou et al.[82] used fused deposition modeling to fabricate an electrochemical immunosensor for rapid and ultrasensitive detection of *S. typhimurium* in poultry samples. The sensor uses cadmium/selenium-zinc salt quantum dots (QDs) as a marker and consists of three electrodes made of carbon black (CB)-polylactide filament and a scaffold (printed from the polylactide filament).The sensor used biotinylated anti-*S. typhimurium* antibodies and subsequently streptavidin labeling of Cd/Se ZnS QDs to determine *S. typhimurium* in fresh chicken meat by sandwich immunoassay and quantify bacteria by measuring Cd(II) released after the acidic dissolution of

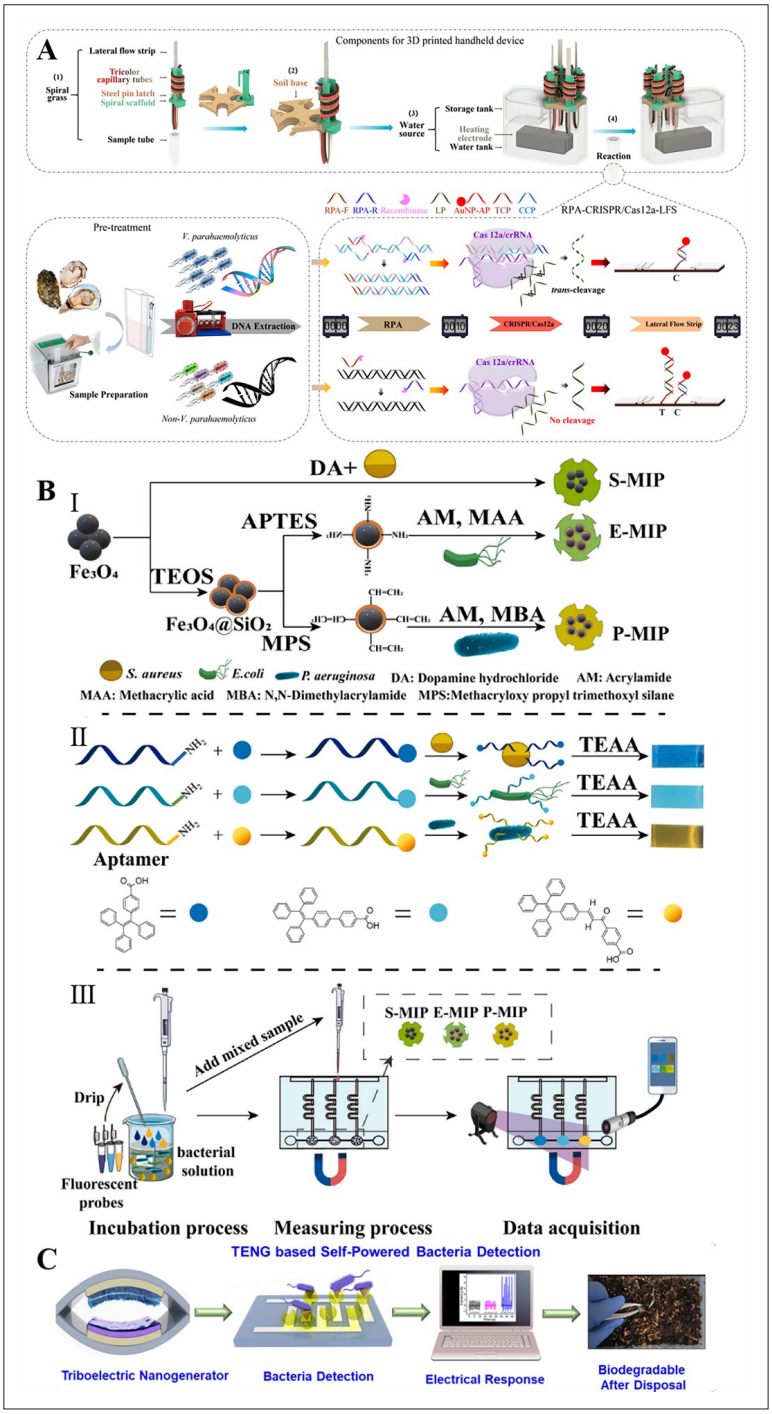

Figure 2. Biological sensors for bacterial detection. (A) Schematic diagram of *V. parahaemolyticus* detection with the integrated handheld biosensor. Adapted from ref.[81] (B) Illustration of the preparation of sensor device: (B, I) Synthesis of three magnetic molecularly imprinted materials; (B, II) Synthesis of fluorescent probes; (B, III) Schematic diagram of multiple detection of pathogenic bacteria. Adapted with permission from ref.[83] Copyright © 2023, Elsevier. (C) Schematic diagram of triboelectric nanogenerator (TENG)-based self-powered bacteria detection. Adapted from ref.[85] Abbreviations: RPA: recombinase polymerase amplification; LP: ligation probe; AP: AuNP-probe; TCP: test line capture probe; CCP: control line capture probe; CRISPR: clustered regularly interspaced short palindromic repeats; CRISPR/Cas: CRISPR-associated protein (Cas) system; LFS: lateral flow strip; crRNA: CRISPR RNA; TEOS: ethyl orthosilicate; DA: dopamine hydrochloride; APTES: aminopropyltriethoxysilane; MPS: methacryloxypropyl trimethoxyl silane. AM: acrylamide; MAA: methacrylic acid; MBA: N, N'-methylene diacrylamide; MIP: molecularly imprinted polymer; S-MIP: *S. aureus* imprinted material; E-MIP: *E. coli* molecularly imprinted material; P-MIP: *P. aeruginosa* molecularly imprinted material; TEAA: triethylammonium acetate; TENG: triboelectric nanogenerator. Miniaturized and integrated sensors made by 3D printing technology can be more portable and rapid to detect bacteria.

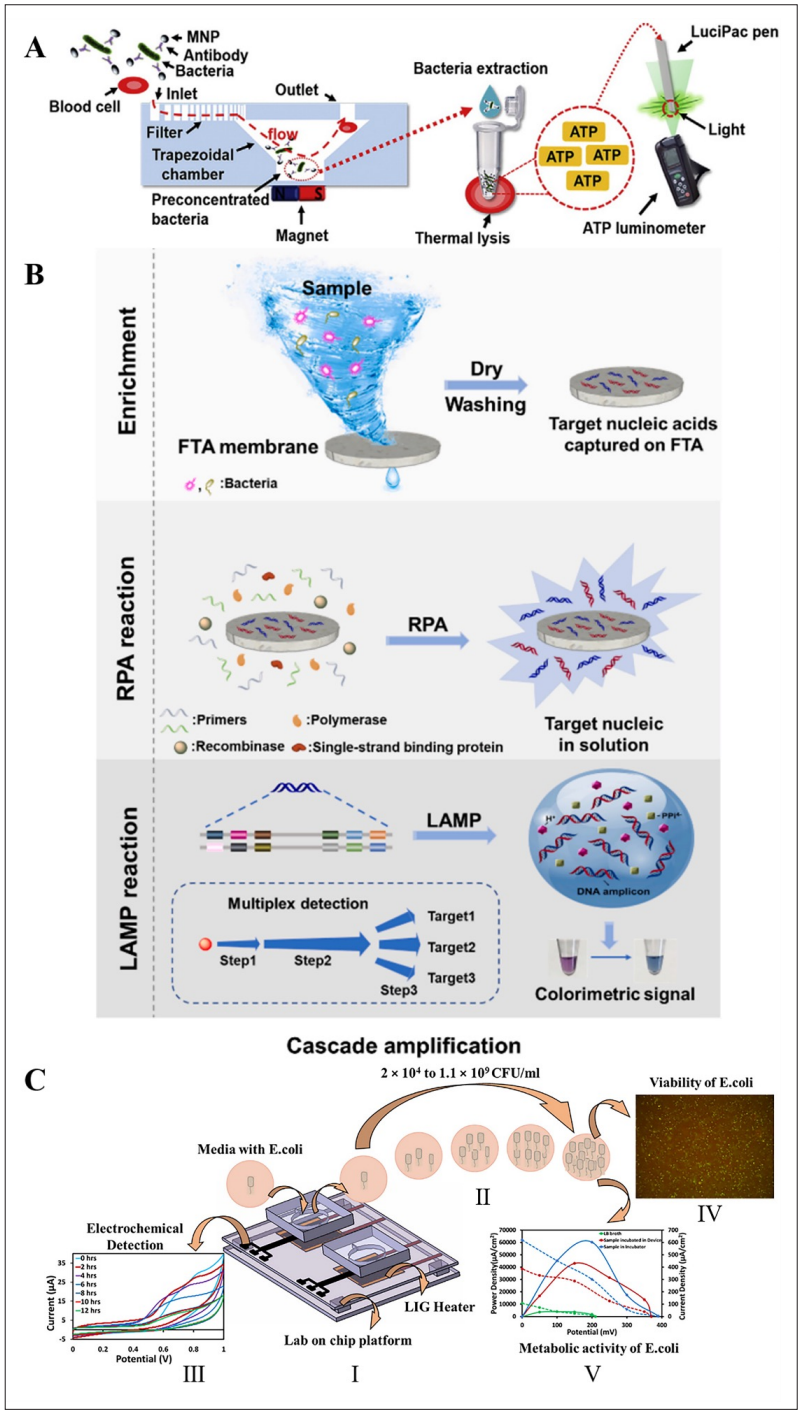

Figure 3. Microfluidic chips for bacterial detection. (A) Preconcentration of targeted bacterial cells in a 3D microfluidic magnetic preconcentrator (3DμFMP) with antibody-conjugated magnetic nanoparticles (Ab-MNPs). Adapted with permission from ref.[86] Copyright © 2016, Elsevier. (B) Design of flinders technology associates (FTA)-based multiplexed colorimetric assay for the detection of different pathogens. Adapted with permission from ref.[88] Copyright © 2021, Elsevier. (C) Schematic on the overview of the presented work: (C, I) microfluidics device integrated with screen-printed electrodes and laser-induced graphene (LIG) heater; (C, II) on-chip incubation of bacteria; (C, III) simultaneous electrochemical detection of bacteria; (C, IV) confirmation of viability through fluorescence imaging; (C, V) validation of metabolic activity by employing the cultured bacteria for a microbial fuel cell (graph represents the polarization curves). Adapted from ref.[89] Abbreviations: MNP: magnetic nanoparticle; ATP: adenosine triphosphate; FTA: flinders technology associates; RPA: recombinase polymerase amplification; LAMP: loop-mediated isothermal amplification; LIG: laser-induced graphene. 3D printing enables the multi-layer assembly of microfluidic chips in an automated manner, accelerating the development of complex sample processing for bacterial detection.

QDs by anodic stripping voltammetry (ASV). Yin et al.[83] developed a portable fluorescent sensor capable of rapid detection of various pathogenic bacteria (Figure 2B), using *E. coli, S. aureus*, and *P. aeruginosa* as target bacteria.. The transparent photosensitive resin was selected as the 3D printing material to prepare the microchannel device. The magnetic core-shell molecular imprinted polymer, using Fe_3O_4 and Fe_3O_4@SiO_2 as the matrix material, was fixed in the detection area by a magnetic field. It is then combined with a smartphone and an external lens to form a fluorescent sensor. This designed 3D model was used to enable the specific adsorption and detection of bacteria by magnetic core-shell molecular-imprinted polymers and fluorescent probes. Bacterial detection procedures, including incubation, enrichment, isolation, washing, and detection, were performed in the 3D model. The sensor has the advantages of low cost, high sensitivity, good specificity, easy operation, and fast response.

In addition, 3D printing technology also plays a role in sample treatment and signal recognition for bacterial biosensors. Zhang et al.[84] designed a quantitative sensing system based on 3D-printed Ag ion-selective electrodes for rapid and sensitive detection of bacteria in biological fluids that can be used for diagnosis such as urinary tract infections. This bacterial detector consists of three parts: a 3D-printed Ag-selective electrode (signal detection and transduction), a potentiometer (sensing and data processing), and a 3D-printed filter (sample preparation). Due to charge interactions, some of the extracellular Ag can bind directly to the bacterial cell wall; therefore, by detecting the loss of Ag added to the bacterial solution, the number of bacteria can be detected. Figure 2C features a biodegradable sensor system integrated with a triboelectric nanogenerator (TENG) for the detection of common pathogenic bacteria (*E. coli*) in the environment.[85] In this system, *E. coli* is detected by a simple carbohydrate-protein interaction mechanism using D-mannose functionalized 3D-printed polylactic acid (PLA) and brushed Agelectrodes. The adsorption capacity of D-mannose is usually altered by changing the concentration of *E. coli*, resulting in changes in electrical resistance. Therefore, the proposed biosensor can detect bacterial concentration by monitoring the output current.

4.2. Microfluidic chips

3D printing technology can accurately fabricate microfluidic chips with complex microchannel structures for bacterial detection, thereby simplifying the experimental process and improving detection efficiency. Microfluidic chips usually refer to miniaturized devices that engrave 10–100 μm microchannels in the chip, which can control the pattern of channels and the flow of fluids to achieve rapid and accurate detection of microorganisms. The tiny size concentrates chemicals in the chip, thus improving detection efficiency. The multilayer assembly of microfluidic chips, which can be realized with the assistance of automated 3D printing, accelerates the development of complex sample treatment for bacterial detection.

Park et al.[86] developed a bacterial reactor for sample processing displays by utilizing 3D printing to fabricate a 3D microfluidic magnetic preconcentrator (3DμFMP) with millimeter-scale features (Figure 3A); the all-in-one plastic device could selectively concentrate 100 mL of *E. coli* 700-fold in 1 h. Additionally, the device can withstand high temperatures and extreme pH values, and it can be recycled via chemical sterilization. Kim et al.[87] also reported a 3D-printed microfluidic platform that enabled bacterial preconcentration and purification of genomic DNA to improve the detection limit for molecular diagnostics of target pathogens in blood samples.

Besides sample processing, 3D-printed microfluidic chips can also be used for signal recognition and transduction in bacterial detection. Feng et al.[78] designed a microfluidic chip to detect multiple pathogens simultaneously using light. Their microfluidic chips are fabricated using 3D printing technology and can be modified for specific pathogens. The chip is divided into four sections, each dedicated to the detection of a specific pathogen. If the specific pathogen is present in the sample, it binds to the assay surface, the interaction of which transduces into an optical signal. The chip features an aptamer-based nano-interferometer that allows researchers to rapidly detect a variety of common bacteria at very low concentrations, such as *E. coli, S. typhimurium, L. monocytogenes,* and *S. aureus.* It has high sensitivity and specificity, with a detection limit of 10 CFU/mL, providing a cost-effective platform for distinguishing and screening different foodborne pathogens. Yin et al.[88] fabricated an integrated microfluidic chip using a clear methacrylate-based resin through 3D printing technology to rapidly detect SARS-CoV-2 and human intestinal pathogens in wastewater. It integrates nucleic acid extraction, two-stage isothermal amplification, and colorimetric detection on a chip (Figure 3B). The colorimetric signal during nucleic acid amplification is recorded in real time and analyzed by a programmed smartphone without the need for sophisticated equipment. Srikanth et al.[89] developed a simple, cost-effective, and miniaturized lab-on-a-chip platform to simultaneously culture and detect bacteria (Figure 3C). The temperature required for bacterial culture was provided by an optimized laser-induced graphene heater. A microfluidic chamber was integrated into a screen-printed electrode for electrochemical detection

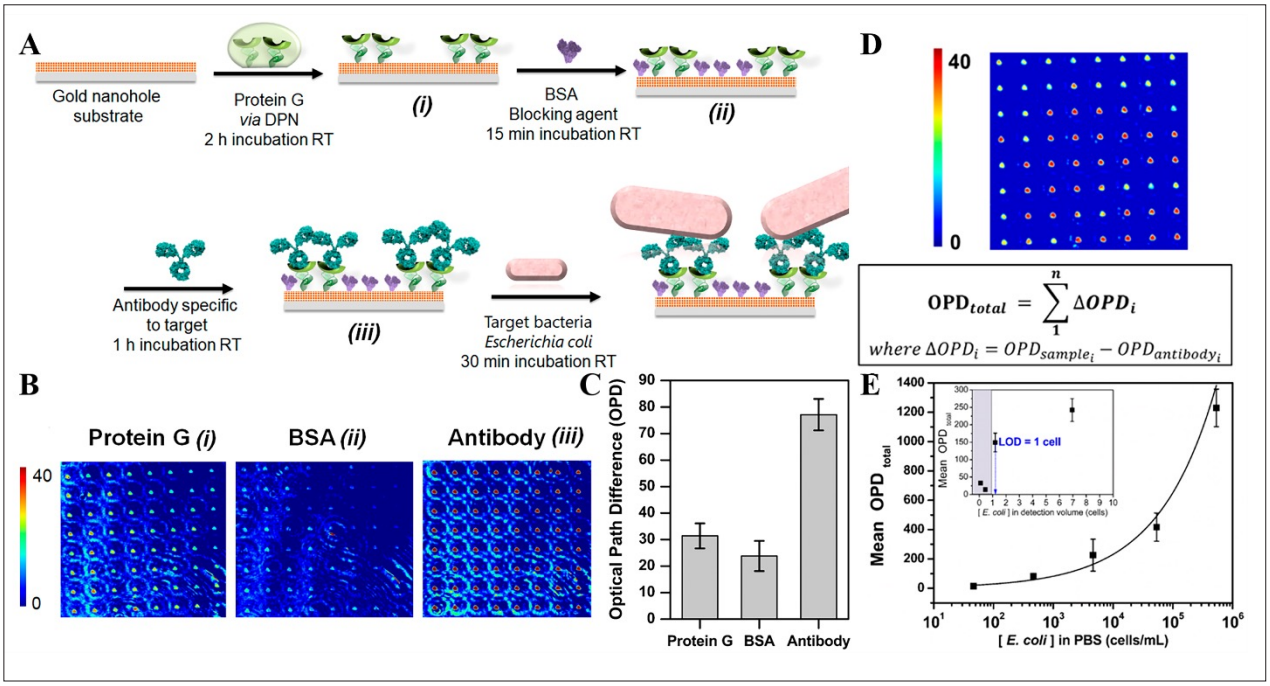

Figure 4. Bioprinting microarray technology for bacterial detection. (A) Biofunctionalization strategy (scheme not to scale). (B) Representative interferometric images for protein G spotting (B, i), BSA blocking (B, ii), and antibody immobilization, (B, iii) with the false color image indicative of the optical path difference (OPD) intensity. (C) Mean OPD signal (± standard deviation [SD]) obtained for inter-array (8 × 8, i.e., 64 microspots). (D) Interferometric image after *E. coli* incubation and the equation used to calculate the OPDtotal. (E) Calibration curve of E. coli in phosphate-buffered saline (PBS) without preconcentration (i.e., without bacteria enrichment) in a wide dynamic range of 10–106 cells/mL. (E, inset) Plot indicating the experimental limit of detection (LOD) in terms of cells in a constant detection volume of 150 µL. Adapted with permission from ref.[90] Copyright © 2019, American Chemical Society. 3D printing technology can precisely immobilize biological probes to form high-density microarray structures. These microarrays can specifically bind to target bacterial molecules to achieve rapid detection and identification of bacteria. Abbreviations: DPN: dip-pen nanolithography; RT: room temperature; BSA: bovine serum albumin; OPD: optical path difference; PBS: phosphate-buffered saline.

of bacteria. Through 3D packaging, a handheld device integrated with a portable potentiostat was realized, expanding practical applications.

4.3. Bioprinting microarray technology

By using 3D printing technology, biological probes (antibodies, DNA fragments, etc.) can be precisely fixed onto tiny matrices to form high-density microarray structures. These microarrays enable specific binding to target bacterial molecules to realize rapid detection and identification of bacteria.

Dey et al.[90] reported a portable point-of-care testing device based on lensless interference microscopy (LIM). Using high-performance nanoplasma technology and customized bioprinted microarrays, the device enables direct quantification of label-free bacteria (*E. coli*). The entire process from sample treatment to data processing was completed in only one operation within 40 min. As displayed in Figure 4A, protein G was first bioprinted onto a clean hydrophilic gold nanopore surface, using bovine serum albumin (BSA) as a blocking agent for non-specific absorption. The substrate was subsequently incubated with an *E. coli*-specific polyclonal antibody at a concentration of 500 µg/mL. After rinsing and drying the array, *E. coli* was incubated for quantification. Figure 4B and C indicates that the array generated after bioprinting protein G was visible, and an OPD value of about 30 was observed, confirming its binding to the substrate. Biomolecule height, surface density, and accumulated mass are reflected in the OPD signal. When BSA is anchored to the gold surface, the blocking step results in a decrease in the OPD signal, which effectively reduces the spot height, and finally a significant increase in the OPD value due to antibody attachment to protein G microspots. In this work, a high sensitivity of 1 bacterial cell was achieved by calculating the total OPD enhancement and testing the relationship between the concentration of *E. coli* in phosphate-buffered saline (PBS) and the average total OPD value (Figure 4D and E). The assay involves direct label-free quantification of *E. coli* without sample pretreatment, such as PCR, and/or the use of secondary antibodies or markers, providing quantification

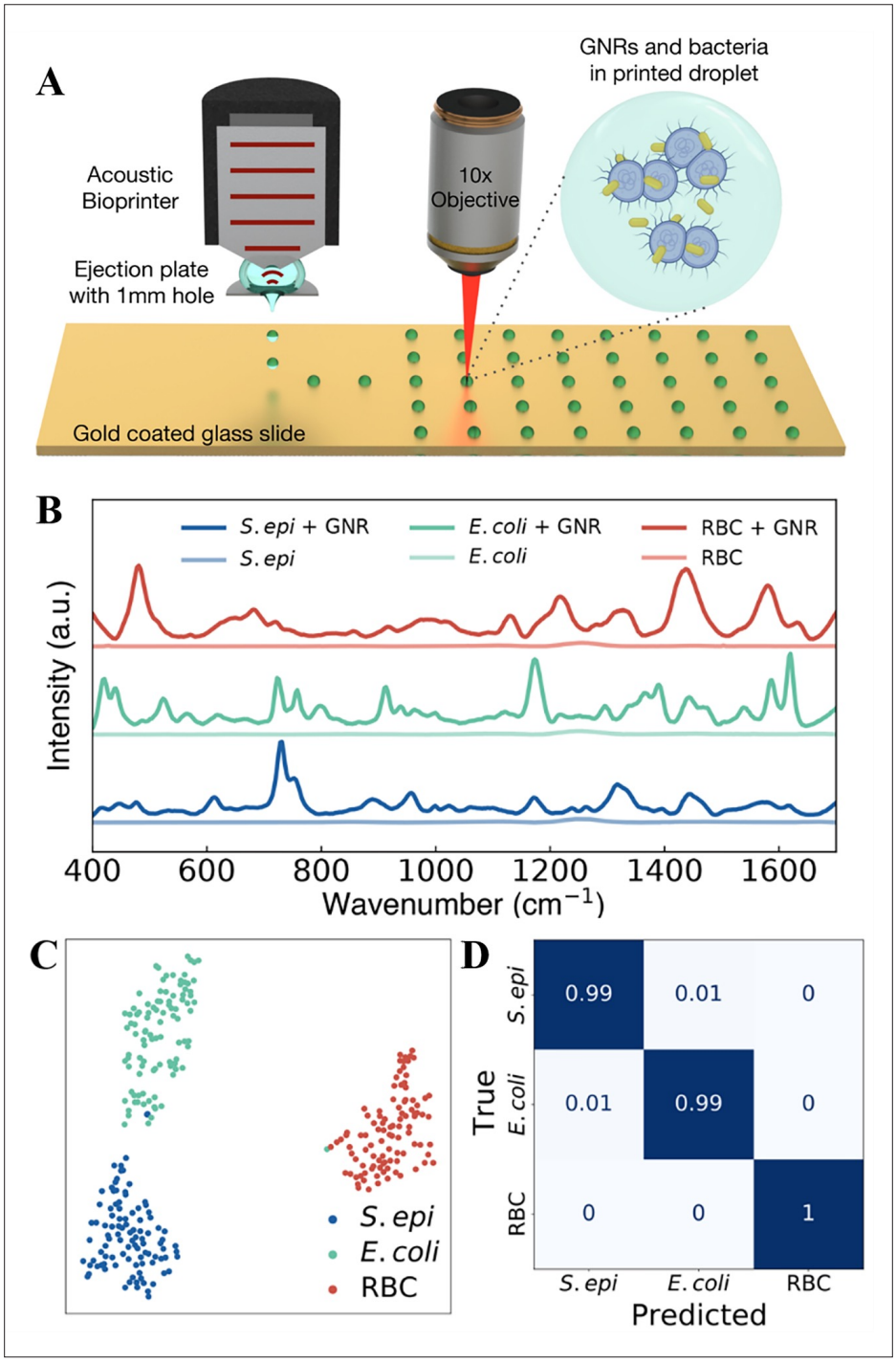

Figure 5. Combining AI and spectral technology for bacterial detection. (A) Schematic of acoustic printing platform and confocal Raman setup. (B) Mean surface-enhanced Raman spectroscopy (SERS) spectra of 100 measurements, each taken from single droplets printed from three cell lines (*S. epidermidis*, *E. coli*, and red blood cells [RBCs]) mixed with gold nanorods (GNRs). (C) A two-component t-distributed stochastic neighbor embedding (t-SNE) projection across all 300 Raman spectra acquired from droplets printed with GNRs. Data is plotted after performing a 24-component principal component analysis (PCA) for dimensionality reduction. (D) Normalized confusion matrix generated using a random forest classifier on the 300 spectra collected from single cell-line droplets of *S. epidermidis*, *E. coli*, and mouse RBCs mixed with GNRs. Adapted from ref.[95] Abbreviations: GNRs: gold nanorods; RBC: red blood cell; SERS: surface-enhanced Raman spectroscopy; t-SNE: t-distributed stochastic neighbor embedding; PCA: principal component analysis.

through a simple one-step process and demonstrating significant potential in practical applications.

Al-Taie et al.[91] used 3D printing to fabricate novel sampling matrices for the detection of respiratory pathogens in exhaled air. Fused deposition modeling was used to print polyvinyl alcohol (PVA) and create a multilayer matrix to trap bacteria and enhance bacterial capture efficiency. Quantitative assessment of bacterial recovery and detection of PVA sampling substrates was subsequently performed using quantitative PCR (qPCR), suggesting that the use of a PVA matrix could effectively recover mycobacteria. Compared with gelatin, PVA matrix is more environment-friendly due to its higher solubility in distilled water.

4.4. Combining artificial intelligence and spectral technology

The detection of bacteria by artificial intelligence (AI) is mainly based on ML, deep learning, and other algorithms. By training and learning with a large number of bacterial samples, the automatic identification and classification of bacteria can be realized based on extracted key information of bacteria.[92] For example, Nehal et al.[93] utilized a highly sensitive lab-on-a-chip with deep learning AI for the detection of bacteria in water. Cui et al.[94] developed an AI-assisted smartphone-based colorimetric biosensor for visual, rapid, and sensitive detection of pathogenic bacteria by measuring the hyaluronidase secreted by bacteria. The combination of 3D bioprinting technology with AI and spectral analysis technology can further improve the intelligent level of bacterial detection. AI algorithms can analyze complex biological signals and assist diagnostic decision-making, for which spectroscopic techniques, such as Raman spectroscopy and fluorescence spectroscopy, can provide bacterial molecular fingerprints and enhance the specificity and sensitivity of detection.

Safir et al.[95] developed an acoustic bioprinter, as shown in Figure 5A, which uses acoustic bioprinting technology in combination with Raman spectroscopy to achieve high-throughput identification of bacteria in blood. In this method, samples are digitized into single cells or a few cell droplets by acoustic bioprinting; each droplet is then rapidly detected using Raman spectroscopy, and the results are finally classified using ML to achieve the purpose of non-culture detection of pathogens in complex multicellular samples. As displayed in Figure 5B, the detection of *S. epidermidis*, *E. coli*, and mouse red blood cells indicated that almost no Raman signal was observed in droplets without gold nanorods (GNRs). Machine analysis was subsequently performed (Figure 5C); there were clear sample differences between each data set and cell type. Multiclass analysis of complex samples using a random forest classifier validated that the classification accuracy of all samples is ≥99% (Figure 5D).

In summation, 3D printing has great application potential in bacterial detection due to its outstanding intrinsic features. However, the limitations of the technique warrant further research in the field of 3D printing to advance its application in bacterial detection. When using 3D printing technology for bacterial detection, the materials involved should have a certain degree of biocompatibility and stability to ensure the activity and accuracy of bacteria in the detection process. In addition, the issue of equipment cost remains significant. Although the cost of 3D printing equipment is gradually decreasing, high-performance 3D printing equipment is still expensive. Compared with traditional biosensors, microfluidic chips, and other manufacturing technologies, 3D printing technology is still not sufficiently mature. The application of 3D printing technology to bacterial detection also requires certain professional knowledge and skills, including 3D modeling knowledge, material selection, printing parameter setting, and complex data processing ability.

5. Conclusion and future perspectives

3D printing technology, as an emerging manufacturing method in the biological field, has demonstrated great potential in life sciences and exhibited its unique advantages for bacterial detection. It can act as a sample treatment tool, signal recognition element, signal transporter, signal amplification pathway, and bioreaction carrier, all of which enable 3D printing technology to achieve more efficient, sensitive, and accurate bacterial detection. Personalized devices fabricated by 3D bioprinting can be customized according to specific detection needs, further accelerating bacterial detection in various scenarios.

However, several challenges remain. For example, optimizing printing parameters and material selection to improve the detection sensitivity and accuracy continues to be a long-standing challenge in bacterial detection. Additionally, the cost and time should also be considered, particularly the high cost of high-precision equipment and biomaterials, which limit large-scale production and widespread application of 3D printing. Moreover, the lack of standardized technical protocols and testing procedures can lead to discrepancies between laboratories or research institutions, affecting the accuracy and repeatability of results.

With the development of materials science, bioinformatics, AI, and other technologies, 3D printing technology has a broad application prospect in bacterial detection. Hence, we anticipate that 3D printing will adopt following enhancements for bacterial detection:

(i) Material innovation: More types of biomaterials and composites with higher performance will be developed to meet the specific needs of bacterial detection.

(ii) Combination of 3D printing and other advanced technologies: Advanced techniques (nanotechnology, gene editing technology, etc.) will be developed to obtain more efficient, accurate, automated, and integrated bacterial detection platforms.

(iii) Intelligent control and big data proceeding: The introduction of AI and ML can be further adapted to assist with bacterial detection.

(iv) Optimization: The standardization and normalization of 3D printing technology in the field of bacterial detection, along with establishing unified technical standards and operating procedures, would enhance the reliability and comparability of test results.

In conclusion, 3D printing technology is rapidly advancing in the field of bacterial detection. This review provides a comprehensive overview of 3D printing technology in bacterial detection, with the aim of offering a scientific reference and insight for bacteria-related studies. With advancements in technological development and interdisciplinary research, we believe that 3D printing technology will make significant contributions and breakthroughs in the field of bacterial detection in the future.

Acknowledgments

None.

Funding

This work was financially supported by the National Natural Science Foundation of China (Grant Number: 32400074) and Seed Funding of the First Affiliated Hospital, Zhejiang University School of Medicine (Grant Number: BQD2319).

Conflict of interest

The authors declare no conflicts of interest.

Author contributions

Conceptualization: All authors
Writing – original draft: Tingting Cui
Writing – review & editing: Ting Cao

Ethics approval and consent to participate

Not applicable.

Consent for publication

Not applicable.

Availability of data

Not applicable.

References

1. Varadi L, Luo JL, Hibbs DE, et al. Methods for the detection and identification of pathogenic bacteria: past, present, and future. *Chem Soc Rev.* 2017;46(16):4818-4832. doi: 10.1039/c6cs00693k

2. Huber F, Lang HP, Lang D, et al. Rapid and ultrasensitive detection of mutations and genes relevant to antimicrobial resistance in bacteria. *Glob Chall.* 2021;5(2):2000066. doi: 10.1002/gch2.202000066

3. Tang JW, Yuan Q, Wen XR, et al. Label-free surface-enhanced Raman spectroscopy coupled with machine learning algorithms in pathogenic microbial identification: current trends, challenges, and perspectives. *Interdiscip Med*. 2024;2(3):e20230060. doi: 10.1002/inmd.20230060

4. Santoni S, Gugliandolo SG, Sponchioni M, Moscatelli D, Colosimo BM. 3D bioprinting: current status and trends—a guide to the literature and industrial practice. *Bio-Des Manuf.* 2021;5(1):14-42. doi: 10.1007/s42242-021-00165-0

5. Md Fadilah NI, Khairul Nizam NAA, Fauzi MB. Antibacterial compounds-incorporated functional biomaterials for chronic wound healing application via 3D bioprinting: the mechanism of action. *Int J Bioprint.* 2024; 10(4):3372. doi: 10.36922/ijb.3372

6. Pramanik J, Brahma B, Pradhan S, et al. 3D printing application in biomedical—a review. *Mater Today Proc.* 2023. doi: 10.1016/j.matpr.2023.07.046

7. Ryoo M, Kim D, Noh J, Ih Ahn S. 3D-printed electronics for biomedical applications. *Int J Bioprint.* 2024. doi: 10.36922/ijb.4139

8. Liu Y, Sing S L. A review of advances in additive manufacturing and the integration of high-performance polymers, alloys, and their composites. *Mater Sci Addit Manuf.* 2023;2(3):1587. doi: 10.36922/msam.1587

9. Manos J. The human microbiome in disease and pathology. *APMIS*. 2022;130(12):690-705. doi: 10.1111/apm.13225

10. Ding X, Ma J, Fan T, et al. Inorganic nanoparticles-based strategies for the microbial detection in infectious diseases. *Interdiscip Med*. 2024;2(2):e20230045. doi: 10.1002/inmd.20230045

11. Sheikhzadeh E, Chamsaz M, Turner APF, Jager EWH, Beni V. Label-free impedimetric biosensor for *Salmonella* Typhimurium detection based on poly [pyrrole-co-3-carboxyl-pyrrole] copolymer supported aptamer. *Biosens Bioelectron.* 2016;80:194-200. doi: 10.1016/j.bios.2016.01.057

12. Nguyen TT, Trinh KTL, Yoon WJ, Lee NY, Ju H. Integration of a microfluidic polymerase chain reaction device and surface plasmon resonance fiber sensor into an inline all-in-one platform for pathogenic bacteria detection. *Sens Actuators B*. 2017;242:1-8. doi: 10.1016/j.snb.2016.10.137

13. Jackson N, Wu TZ, Adams-Sapper S, et al. A multiplexed, indirect enzyme-linked immunoassay for the detection and differentiation of *E. coli* from other Enterobacteriaceae and P. aeruginosa from other glucose non-fermenters. *J Microbiol Methods*. 2019;158(1):52-58. doi: 10.1016/j.mimet.2019.01.014

14. Ellington M J, Ekelund O, Aarestrup FM, et al. The role of whole genome sequencing in antimicrobial susceptibility testing of bacteria: report from the EUCAST Subcommittee. *Clin Microbiol Infect.* 2017;23(1):2-22. doi: 10.1016/j.cmi.2016.11.012

15. Shen W, Wang C, Zheng S, et al. Ultrasensitive multichannel immunochromatographic assay for rapid detection of foodborne bacteria based on two-dimensional film-like SERS labels. *J Hazard Mater.* 2022;437:129347. doi: 10.1016/j.jhazmat.2022.129347

16. Gopinath SC, Tang TH, Chen Y, Citartan M, Lakshmipriya T. Bacterial detection: from microscope to smartphone. *Biosens Bioelectron.* 2014;60:332-342. doi: 10.1016/j.bios.2014.04.014

17. Braga PAC, Tata A, Gonçalves dos Santos V, et al. Bacterial identification: from the agar plate to the mass spectrometer. *RSC Adv.* 2013;3(4):994-1008. doi: 10.1039/c2ra22063f

18. Yang M, Wang Z, Su M, et al. Smart nanozymes for diagnosis of bacterial infection: the next frontier from laboratory to bedside testing. *ACS Appl Mater Interfaces*. 2024;16(34) 44361-44375. doi: 10.1021/acsami.4c07043

19. Kabiraz MP, Majumdar PR, Mahmud MMC, Bhowmik S, Ali A. Conventional and advanced detection techniques of foodborne pathogens: a comprehensive review. *Heliyon*. 2023;9(4):e15482. doi: 10.1016/j.heliyon.2023.e15482

20. Aladhadh M. A review of modern methods for the detection of foodborne pathogens. *Microorganisms*. 2023;11(5):1111. doi: 10.3390/microorganisms11051111

21. Rodino Kyle G, Wolf Matthew J, Sheldon S, et al. Detection of tick-borne bacteria from whole blood using 16S ribosomal RNA gene PCR followed by next-generation sequencing. *J Clin Microbiol.* 2021;59(5):e03129-20. doi: 10.1128/JCM.03129-20

22. Yang Q, Zu J, Zhang S, et al. An overview of rapid detection methods for *Salmonella*. *Food Control*. 2025;167:110771. doi: 10.1016/j.foodcont.2024.110771

23. Cao X, Chen C, Zhu Q. Biosensors based on functional nucleic acids and isothermal amplification techniques. *Talanta*. 2023;253:123977. doi: 10.1016/j.talanta.2022.123977

24. Liu D, Zhu Y, Li N, et al. A portable microfluidic analyzer for integrated bacterial detection using visible loop-mediated amplification. *Sens Actuators B*. 2020; 310:127834. doi: 10.1016/j.snb.2020.127834

25. Lu Y, Zhang J, Lu X and Liu Q. Isothermal nucleic acid amplification based microfluidic "lab-on-a-chip" for the detection of pathogenic bacteria and viruses in agri-foods. *Trends Food Sci Technol.* 2024;148:104482. doi: 10.1016/j.tifs.2024.104482

26. Gao D, Guo X, Yang Y, et al. Microfluidic chip and isothermal amplification technologies for the detection of pathogenic nucleic acid. *J Biol Eng.* 2022;16(1):33. doi: 10.1186/s13036-022-00312-w

27. Kartsova LA, Makeeva DV, Kravchenko AV, Moskvichev D O. Polikarpova DA. Capillary electrophoresis as a powerful tool for the analyses of bacterial samples. *Trends Anal Chem.* 2021;134:116110. doi: 10.1016/j.trac.2020.116110

28. Lian DS, Zeng HS. Capillary electrophoresis based on nucleic acid detection as used in food analysis. *Compr Rev Food Sci Food Saf.* 2017;16(6):1281-1295. doi: 10.1111/1541-4337.12297

29. Okuda K I, Yoshii Y, Yamada S, et al. Detection of bacterial DNA from central venous catheter removed from patients by next generation sequencing: a preliminary clinical study. *Ann Clin Microbiol Antimicrob.* 2018;17(1):44. doi: 10.1186/s12941-018-0297-2

30. Song M, Han C, Liu L, et al. MIST: a microbial identification and source tracking system for next-generation sequencing data. *iMeta*. 2023;2(4):e146. doi: 10.1002/imt2.146

31. Xia H, Zhang Z, Luo C, et al. MultiPrime: a reliable and efficient tool for targeted next-generation sequencing. *iMeta*. 2023;2(4):e143. doi: 10.1002/imt2.143

32. Botan A, Campisciano G, Zerbato V, et al. Performance of 16S rRNA gene next-generation sequencing and the culture method in the detection of bacteria in clinical specimens. *Diagnostics*. 2024;14(13):1318. doi: 10.3390/diagnostics14131318

33. Zhang M, Wu J, Shi Z, et al. Molecular methods for identification and quantification of foodborne pathogens. *Molecules*. 2022;27(23):8262. doi: 10.3390/molecules27238262

34. Yin G, Bie S, Gu H, et al. Application of gene chip technology in the diagnostic and drug resistance detection of *Helicobacter pylori* in children. *J Gastroenterol Hepatol.* 2020;35(8):1331-1339.
doi: 10.1111/jgh.14980

35. Ding Q, Zhang W, Guo Y, et al. β-lactamase sensitive probe for rapid detection of antibiotic-resistant bacteria with gas chromatography-tandem mass spectrometry. *Anal Chem.* 2023;95(14):6098-6106.
doi: 10.1021/acs.analchem.3c00381

36. Olajide OE, Yi Y, Zheng J, Hamid AM. Strain-level discrimination of bacteria by liquid chromatography and paper spray ion mobility mass spectrometry. *J Am Soc Mass Spectrom.* 2023;34(6):1125-1135.
doi: 10.1021/jasms.3c00070

37. Boardman AK, Wong WS, Premasiri WR, et al. Rapid detection of bacteria from blood with surface-enhanced raman spectroscopy. *Anal Chem.* 2016;88(16): 8026-8035.
doi: 10.1021/acs.analchem.6b01273

38. Bullock A J, Garcia M, Shepherd J, Rehman I, Sheila M. Bacteria induced pH changes in tissue-engineered human skin detected non-invasively using Raman confocal spectroscopy. *Appl Spectrosc Rev.* 2019;55(2);158-171.
doi: 10.1080/05704928.2018.1558232

39. Usman M, Tang J W, Li F, et al. Recent advances in surface enhanced Raman spectroscopy for bacterial pathogen identifications. *J Adv Res.* 2023;51:91-107.
doi: 10.1016/j.jare.2022.11.010

40. Zhu J, Wu P, Chao Y, et al. Recent advances in 3D printing for catalytic applications. *Chem Eng J.* 2022;433:134341.
doi: 10.1016/j.cej.2021.134341

41. Liu N, Zhang X, Guo Q, Wu T, Wang Y. 3D bioprinted scaffolds for tissue repair and regeneration. *Front Mater.* 2022;9:925321.
doi: 10.3389/fmats.2022.925321

42. Aimar A, Palermo A, Innocenti B. The role of 3D printing in medical applications: a state of the art. *J Healthc Eng.* 2019;2019(10):5340616.
doi: 10.1155/2019/5340616

43. Cui M, Pan H, Su Y, et al. Opportunities and challenges of three-dimensional printing technology in pharmaceutical formulation development. *Acta Pharm Sin B.* 2021;11(8):2488-2504.
doi: 10.1016/j.apsb.2021.03.015

44. Nadagouda MN, Rastogi V, Ginn M. A review on 3D printing techniques for medical applications. *Curr Opin Chem Eng.* 2020;28:152-157.
doi: 10.1016/j.coche.2020.05.007

45. Alami A H, Ghani Olabi A, Alashkar A, et al. Additive manufacturing in the aerospace and automotive industries: recent trends and role in achieving sustainable development goals. *Ain Shams Eng J.* 2023;14(11):102516.
doi: 10.1016/j.asej.2023.102516

46. Bici A and Yunitsyna A. Analysis of 3D printing techniques for building construction: a review. *Constr Robot.* 2023;7(2):107-123.
doi: 10.1007/s41693-023-00108-4

47. Hussain S, Malakar S, Arora VK. Extrusion-based 3D food printing: technological approaches, material characteristics, printing stability, and post-processing. *Food Eng. Rev.* 2022;14(1):100-119.
doi: 10.1007/s12393-021-09293-w

48. Wang S, Zhao S, Yu J, Gu Z, Zhang Y. Advances in translational 3D printing for cartilage, bone, and osteochondral tissue engineering. *Small*. 2022;18(36):e2201869.
doi: 10.1002/smll.202201869

49. Cresswell-Boyes AJ, Davis GR, Krishnamoorthy M, Mills D, Barber AH. Composite 3D printing of biomimetic human teeth. *Sci Rep.* 2022;12(1):7830.
doi: 10.1038/s41598-022-11658-y

50. Vernon MJ, Mela P, Dilley RJ, et al. 3D printing of heart valves. *Trends Biotechnol*. 2024;42(5):612-630.
doi: 10.1016/j.tibtech.2023.11.001

51. Huang G, Zhao Y, Chen D, et al. Applications, advancements, and challenges of 3D bioprinting in organ transplantation. *Biomater Sci.* 2024;12(6):1425-1448.
doi: 10.1039/d3bm01934a

52. Herzog J, Franke L, Lai Y, et al. 3D bioprinting of microorganisms: principles and applications. *Bioprocess Biosyst Eng.* 2024;47(4):443-461.
doi: 10.1007/s00449-023-02965-3

53. Fu Z, Naghieh S, Xu C, et al. Printability in extrusion bioprinting. *Biofabrication*. 2021;13(3):033001.
doi: 10.1088/1758-5090/abe7ab

54. Bartolo P, Malshe A, Ferraris E, Koc B. 3D bioprinting: materials, processes, and applications. *CIRP Ann*. 2022;71(2):577-597.
doi: 10.1016/j.cirp.2022.06.001

55. Ng WL, Shkolnikov V. Jetting-based bioprinting: process, dispense physics, and applications. *Bio-Des Manuf.* 2024;7(5):771-799.
doi: 10.1007/s42242-024-00285-3

56. Choudary R, Saini N, Chopra DS, Singh D, Singh N. A comprehensive review of 3D bioprinting biomaterials: properties, strategies and wound healing application. *J Mater Res.* 2023;38(13):3264-3300.
doi: 10.1557/s43578-023-01078-7

57. McMillan A, McMillan N, Gupta N, Kanotra S P, Salem AK. 3D bioprinting in otolaryngology: a review. *Adv Healthcare Mater.* 2023;12(19):e2203268.
doi: 10.1002/adhm.202203268

58. Jentsch S, Nasehi R, Kuckelkorn C, et al. Multiscale 3D bioprinting by nozzle-free acoustic droplet ejection. *Small Methods*. 2021;5(6):e2000971. doi: 10.1002/smtd.202000971

59. Ng WL, Lee JM, Yeong WY, Win Naing M. Microvalve-based bioprinting - process, bio-inks and applications. *Biomater Sci*. 2017;5(4):632-647. doi: 10.1039/c6bm00861e

60. Li Y, Zhang X, Zhang X, Zhang Y, Hou D. Recent progress of the vat photopolymerization technique in tissue engineering: a brief review of mechanisms, methods, materials, and applications. *Polymers*. 2023;15(19):3940. doi: 10.3390/polym15193940

61. Frankowski J, Kurzatkowska M, Sobczak M, Piotrowska U. Utilization of 3D bioprinting technology in creating human tissue and organoid models for preclinical drug research—State-of-the-art. *Int J Pharm*. 2023;644(11):123313. doi: 10.1016/j.ijpharm.2023.123313

62. Seo JW, Kim GM, Choi Y, Cha JM, Bae H. Improving printability of digital-light-processing 3D bioprinting via photoabsorber pigment adjustment. *Int J Mol Sci*. 2022;23(10):5428. doi: 10.3390/ijms23105428

63. Xu HQ, Liu JC, Zhang ZY, Xu CX. A review on cell damage, viability, and functionality during 3D bioprinting. *Mil Med Res*. 2022;9(1):70. doi: 10.1186/s40779-022-00429-5

64. Lepowsky E, Muradoglu M, Tasoglu S. Towards preserving post-printing cell viability and improving the resolution: past, present, and future of 3D bioprinting theory. *Bioprinting*. 2018;11:e00034. doi: 10.1016/j.bprint.2018.e00034

65. Wang J, Cui Z, Maniruzzaman M. Bioprinting: a focus on improving bioink printability and cell performance based on different process parameters. *Int J Pharm*. 2023;640:123020. doi: 10.1016/j.ijpharm.2023.123020

66. Zhao T, Liu Y, Wu Y, Zhao M, Zhao Y. Controllable and biocompatible 3D bioprinting technology for microorganisms: fundamental, environmental applications and challenges. *Biotechnol Adv*. 2023;69(2):108243. doi: 10.1016/j.biotechadv.2023.108243

67. Prabhakaran P, Palaniyandi T, Kanagavalli B, et al. Prospect and retrospect of 3D bio-printing. *Acta Histochem*. 2022;124(7):151932. doi: 10.1016/j.acthis.2022.151932

68. Gungor-Ozkerim PS, Inci I, Zhang Y S, Khademhosseini A, Dokmeci MR. Bioinks for 3D bioprinting: an overview. *Biomater Sci*. 2018;6(5):915-946. doi: 10.1039/c7bm00765e

69. Jia W, Yang X, Liu Z, et al. Nasal cartilage tissue engineering materials based on 3D bioprinting: seed cells and dECM. *Appl Mater Today*. 2024;40(1):102364. doi: 10.1016/j.apmt.2024.102364

70. Sasikumar SC, Goswami U, Raichur AM. 3D bioprinting with visible light cross-linkable mucin-hyaluronic acid composite bioink for lung tissue engineering. *ACS Appl Bio Mater*. 2024;7(8):5411-5422. doi: 10.1021/acsabm.4c00579

71. Breathwaite E, Weaver J, Odanga J, Dela Pena-Ponce M, Lee JB. 3D bioprinted osteogenic tissue models for *in vitro* drug screening. *Molecules*. 2020;25(15):3442. doi: 10.3390/molecules25153442

72. Salles GR, Dall'Agnol Ferreira N, Pacheco-Soares C, Porcionatto MA. 3D bioprinted human neuron-like spheroids as an in vitro model for neurodegenerative diseases. *Alzheimers Dement*. 2023;19(S13):e075956. doi: 10.1002/alz.075956

73. Chua CK, An J, Fan S, et al. A perspective on transformative bioprinting. *Int J Bioprint*. 2024. doi: 10.36922/ijb.3525

74. Mori S, Ishiguro S, Miyazaki S, et al. Usefulness of a 3D-printing air sampler for capturing live airborne bacteria and exploring the environmental factors that can influence bacterial dynamics. *Res Microbiol*. 2021;172(6):103864. doi: 10.1016/j.resmic.2021.103864

75. Joskowiak A, Nogueira CL, Costa SP, et al. A magnetic nanoparticle-based microfluidic device fabricated using a 3D-printed mould for separation of *Escherichia coli* from blood. *Microchim Acta*. 2023;190(9):356. doi: 10.1007/s00604-023-05924-7

76. Lee W, Kwon D, Choi W, Jung GY, Jeon S. 3D-printed microfluidic device for the detection of pathogenic bacteria using size-based separation in helical channel with trapezoid cross-section. *Sci Rep*. 2015;5(1):7717. doi: 10.1038/srep07717

77. Pahlow S, Hentschel S, Horbert P, et al. Isolation of pathogenic bacteria from sputum samples using a 3D-printed cartridge system. *Anal Methods*. 2021;13(41):4884-4895. doi: 10.1039/d1ay00924a

78. Feng S, Mo K, Song X. 3D printed microfluidic chip integrated with nanointerferometer for multiplex detection of foodborne pathogens. *AIP Adv*. 2024;14(6):065033. doi: 10.1063/5.0208274

79. Malhotra S, Pham DS, Lau MPH, Nguyen AH, Cao H. A low-cost, 3D-printed biosensor for rapid detection of *Escherichia coli*. *Sensors*. 2022;22(6):2382. doi: 10.3390/s22062382

80. Aliyazdi S, Frisch S, Hidalgo A, et al. 3D bioprinting of *E. coli* MG1655 biofilms on human lung epithelial cells for building complexin vitroinfection models.*Biofabrication*. 2023;15(3):035019. doi: 10.1088/1758-5090/acd95e

81. Xu Y, Zhang Q, Li Y, Pang X, Cheng N. A 3D-printed integrated handheld biosensor for the detection of vibrio parahaemolyticus. *Foods*. 2024;13(11):1775. doi: 10.3390/foods13111775

82. Angelopoulou M, Kourti D, Mertiri M, et al. A 3D-printed electrochemical immunosensor employing Cd/Se ZnS QDs as labels for the rapid and ultrasensitive detection of *Salmonella typhimurium* in poultry samples. *Chemosensors*. 2023;11(9):475.
doi: 10.3390/chemosensors11090475

83. Yin P, Wang J, Li T, et al. A smartphone-based fluorescent sensor for rapid detection of multiple pathogenic bacteria. *Biosens Bioelectron*. 2023;242(3):115744.
doi: 10.1016/j.bios.2023.115744

84. Zhang T, Monia Kabandana GK, Ratajczak AM, Chen C. A quantitative sensing system based on a 3D-printed ion-selective electrode for rapid and sensitive detection of bacteria in biological fluid. *Talanta*. 2022;238(Pt 2):123040.
doi: 10.1016/j.talanta.2021.123040

85. Panda S, Hajra S, Kim HG, et al. Carbohydrate-protein interaction-based detection of pathogenic bacteria using a biodegradable self-powered biosensor. *J Mater Chem B*. 2023;11(42):10147-10157.
doi: 10.1039/d3tb01820b

86. Park C, Lee J, Kim Y, et al. 3D-printed microfluidic magnetic preconcentrator for the detection of bacterial pathogen using an ATP luminometer and antibody-conjugated magnetic nanoparticles. *J Microbiol Methods*. 2017;132:128-133.
doi: 10.1016/j.mimet.2016.12.001

87. Kim Y, Lee J, Park S. A 3D-printed millifluidic platform enabling bacterial preconcentration and DNA purification for molecular detection of pathogens in blood. *Micromachines*. 2018;9(9):472.
doi: 10.3390/mi9090472

88. Yin K, Ding X, Xu Z, et al. Multiplexed colorimetric detection of SARS-CoV-2 and other pathogens in wastewater on a 3D printed integrated microfluidic chip. *Sens Actuators B*. 2021;344:130242.
doi: 10.1016/j.snb.2021.130242

89. Srikanth S, Jayapiriya US, Dubey SK, Javed A, Goel S. A lab-on-chip platform for simultaneous culture and electrochemical detection of bacteria. *iScience*. 2022;25(11):105388.
doi: 10.1016/j.isci.2022.105388

90. Dey P, Fabri-Faja N, Calvo-Lozano O, et al. Label-free bacteria quantification in blood plasma by a bioprinted microarray based interferometric point-of-care device. *ACS Sens*. 2019;4(1):52-60.
doi: 10.1021/acssensors.8b00789

91. Al-Taie A, Han X, Williams CM, et al. 3-D printed polyvinyl alcohol matrix for detection of airborne pathogens in respiratory bacterial infections. *Microbiol Res*. 2020;241(20):126587.
doi: 10.1016/j.micres.2020.126587

92. Sharma A, Sharma A, Malhotra R, et al. An accurate artificial intelligence system for the detection of pulmonary and extra pulmonary Tuberculosis. *Tuberculosis*. 2021;131:102143.
doi: 10.1016/j.tube.2021.102143

93. Nehal SA, Roy D, Devi M, Srinivas T. Highly sensitive lab-on-chip with deep learning AI for detection of bacteria in water. *Int J Inf Technol*. 2019;12(2):495-501.
doi: 10.1007/s41870-019-00363-1

94. Cui R, Tang H, Huang Q, et al. AI-assisted smartphone-based colorimetric biosensor for visualized, rapid and sensitive detection of pathogenic bacteria. *Biosens Bioelectron*. 2024;259(8):116369.
doi: 10.1016/j.bios.2024.116369

95. Safir F, Vu N, Tadesse LF, et al. Combining acoustic bioprinting with AI-assisted Raman spectroscopy for high-throughput identification of bacteria in blood. *Nano Lett*. 2023;23(6):2065-2073.
doi: 10.1021/acs.nanolett.2c03015

96. Law JW-F, Ab Mutalib N-S, Chan K-G, Lee L-H. Rapid methods for the detection of foodborne bacterial pathogens: principles, applications, advantages and limitations. *Front Microbiol*. 2015;5(770):770.
doi: 10.3389/fmicb.2014.00770

97. Kim SO, Kim SS. Bacterial pathogen detection by conventional culture-based and recent alternative (polymerase chain reaction, isothermal amplification, enzyme linked immunosorbent assay, bacteriophage amplification, and gold nanoparticle aggregation) methods in food samples: a review. *J Food Saf*. 2020;41(1):e12870.
doi: 10.1111/jfs.12870

ACCSCIENCE PUBLISHING

International Journal of Bioprinting

REVIEW ARTICLE

Revolutionizing regenerative rehabilitation: 3D printing for musculoskeletal regeneration

Ai-Jia Guan[1,2†], Yong-Chao Zhao[3†], Xiao-Na Xiang[1,2†], Ma-Ling Gou[3*], and Hong-Chen He[1,2*]

[1]Rehabilitation Medicine Center and Institute of Rehabilitation Medicine, West China Hospital, Sichuan University, Chengdu, Sichuan, China

[2]Key Laboratory of Rehabilitation Medicine in Sichuan Province, West China Hospital, Sichuan University, Chengdu, Sichuan, China

[3]Department of Biotherapy, Cancer Center and State Key Laboratory of Biotherapy, West China Hospital, Sichuan University, Chengdu, Sichuan, China

Abstract

Musculoskeletal disorders, such as bone fractures, osteoarthritis, meniscus injuries, muscle diseases, and tendon injuries, are common disorders among individuals in need of rehabilitation. Trauma, sports-related injuries, and degeneration mainly cause these disorders. Regenerative rehabilitation medicine aims to enhance the regenerative capacity of musculoskeletal tissues and optimize functional recovery through the combination of regenerative medicine and rehabilitation medicine treatments. However, these treatments are insufficient for the complete restoration of damaged tissue structures. Three-dimensional (3D) printing technology, referred to as the additive manufacturing (AM) technique, can accelerate the rehabilitation process for musculoskeletal diseases, especially for developing regenerative rehabilitation and engineering rehabilitation. Recently, an increasing number of studies reported on the basic and clinical applications of 3D printing in assisting with the treatment of musculoskeletal disorders. Therefore, this review summarizes how 3D printing technologies are changing treatment and assessment methods, as well as improving therapeutic outcomes in regenerative rehabilitation for musculoskeletal diseases. Finally, this review discusses the current status of the clinical translation for 3D printing.

***Keywords*:** 3D printing; Regenerative rehabilitation; Musculoskeletal disorder; Medical devices; Tissue engineering

1. Introduction

Musculoskeletal disorders are complex and common, comprising more than 150 different disease conditions. They are characterized by impairments in the muscles, bones, cartilage, joints, and connective tissues, which can lead to temporary or lifelong limitations in functioning and participation.[1,2] Generally, the symptoms are pain (often persistent), loss of function, and limitations in mobility and dexterity, which reduce the individual's ability to work and participate in society.[1] Moreover, the global burden of musculoskeletal diseases is increasing. A recent analysis of the Global Burden of Disease

†These authors contributed equally to this work.

***Corresponding authors:**
Hong-Chen He
(hxkfhhc@126.com)

Ma-Ling Gou
(goumaling@scu.edu.cn)

Citation: Guan A-J, Zhao Y-C, Xiang X-N, Gou M-L, He H-C. Revolutionizing regenerative rehabilitation: 3D printing for musculoskeletal regeneration. *Int J Bioprint*. 2025;11(1):210-232. doi: 10.36922/ijb.4925

Received: September 24, 2024
1st revised: October 23, 2024
2nd revised: November 5, 2024
Accepted: November 7, 2024
Published Online: November 8, 2024

Copyright: © 2024 Author(s). This is an Open Access article distributed under the terms of the Creative Commons Attribution License, permitting distribution, and reproduction in any medium, provided the original work is properly cited.

Publisher's Note: AccScience Publishing remains neutral with regard to jurisdictional claims in published maps and institutional affiliations.

(GBD) reported that approximately 1.71 billion people globally live with musculoskeletal disorders, including bone fractures, osteoarthritis (OA), and other injuries.[3] Furthermore, musculoskeletal conditions are also the highest contributors to the global need for rehabilitation.[3] The current treatments of rehabilitation for these diseases include patient education, psychological interventions, physical therapy, exercise, use of assistive devices, and novel regenerative treatments, aiming to relieve symptoms, promote structural recovery, and improve function.[4–6]

Regenerative rehabilitation, first proposed by Ambrosio and Russell in 2010, "fuses" the characteristics of regenerative medicine and rehabilitation sciences.[7] The concept was further developed in 2018.[8] Regenerative rehabilitation integrates protocols, principles, and technologies of regenerative medicine and rehabilitation medicine. According to the International Classification of Functioning (ICF) model, rehabilitation focuses on the body's structure and function, activity, participation, and the relation between health conditions and contextual factors. From the perspective of the ICF model, regenerative therapy may accelerate tissue regeneration, repair, and functional reconstruction, ultimately improving the quality of life. With advances in tissue engineering and stem cell biology, regenerative rehabilitation can address broader challenges in biological sciences and healthcare.

Three-dimensional (3D) printing technology, referred to as an additive manufacturing (AM) technique, enables the fabrication of 3D constructs by the deposition of materials using computer-aided design and manufacturing techniques. Among them, 3D bioprinting (i.e., adding biomaterials to the inks) is the most popular branch of 3D printing. The field of rehabilitation has demonstrated advances when combined with engineering and organ regeneration. 3D printing technology involves precise fabrication from digital models that are built from individual data, offering tailored solutions that can significantly improve patient outcomes.[9] By precisely replicating the intricate structures of bones and tissues, 3D printing facilitates the development of individual-specific medical interventions. It has more incomparable advantages than other material-preparing methods, including the ability to fabricate complex products with a fast speed, high precision, high printing fidelity, controllable conditions, and cost-effectiveness.[10–12] Furthermore, it also can address the challenges associated with commercialization, stemming from insufficiency of standardization and industrialization in the preparation process.[13] Therefore, 3D printing technology has value in further research and applications in the field of regenerative rehabilitation for musculoskeletal disorders.

In this review, we introduce some standard material preparing methods and printing inks of 3D printing fabrication. We then discuss how 3D printing technologies are changing treatment and assessment methods, as well as improving therapeutic outcomes in regenerative rehabilitation for musculoskeletal diseases (Figure 1). Finally, this review assesses the current status of clinical translation for 3D printing.

2. Common 3D printing technologies for musculoskeletal regenerative rehabilitation

Generally, the core components of 3D printing technology are the printing equipment and printing inks. Herein, we summarize seven typical types of preparation methods for 3D fabrication and common printing inks.

2.1. Preparation methods of 3D printing technologies

3D printing technology, also known as rapid prototyping, is experiencing unprecedented growth and has become a versatile and advantageous platform for manufacturing various products in the medical field. The primary factors limiting its development are the printing materials and processes. After years of progress, 3D-printed biomaterials are now widely used in clinical medical practice. We summarize the key features of five major printing technologies, including inkjet printing (IP), stereolithography (SLA), extrusion-based printing, fused deposition modeling (FDM), and selective laser sintering (SLS), in the musculoskeletal repair field (Table 1).

In recent years, IP technology has gained popularity in various fields, such as drug delivery, tissue engineering, and disease modeling, due to its low cost, high efficiency, and precision. This technique allows for high-precision positioning of materials and cells[14] and single-cell printing[15] to create complex heterogeneous biomimetic structures. SLA can be subdivided into digital light processing (DLP), liquid crystal display, continuous liquid interface production, multi-jet printing, two-photon polymerization, and holographic 3D printing, based on the principles of pattern formation and printing technology.[16] Among these, DLP-3D printing is widely used in drug delivery, cell therapy, and tissue repair due to its high precision, achieving printing precision in the range of a few to tens of micrometers.[17] Extrusion-based printing is highly compatible with various rheological properties of materials and typically exhibits excellent mechanical performance and biocompatibility at room temperature. Extrusion-based printing can be used to manufacture a variety of products, such as medical devices, models, and biological scaffolds, but the filament formation process is

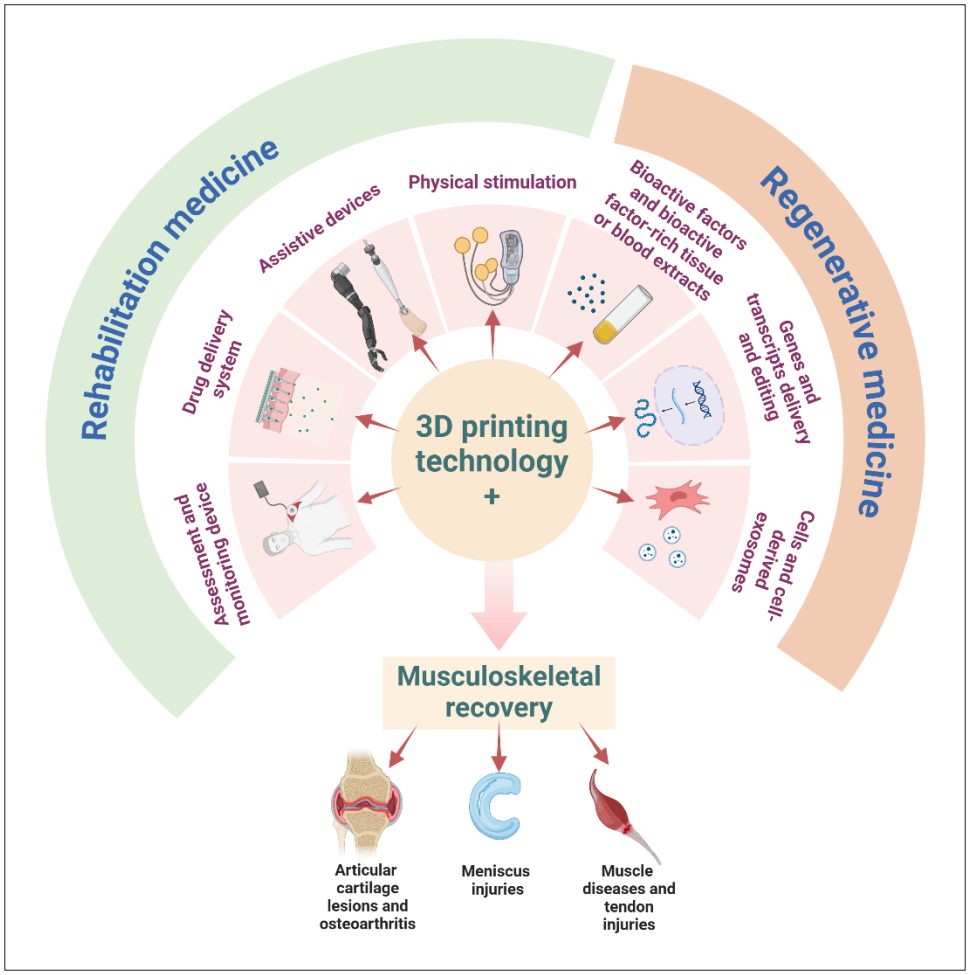

Figure 1. Schematic illustrations of 3D printing-based regenerative rehabilitation strategies. Created using BioRender (https://www.biorender.com/).

Table 1. Comparison of different 3D printing methods in the medical field.

Properties	Materials	Printing process	Resolution (μm)	Speed	Cell viability
Inkjet	Thermoplastic polymer	Serial (drop-by-drop)	50	Medium (mm/s)	> 85%
Light-based	Photosensitive polymer	Continuous plane (layer-by-layer)	1–6	Fast (mm^3/s)	85–95%
Extrusion	Thermoplastic polymer	Serial (line-by-line)	50	Slow (μm/s)	40–80%
FDM	Metals and alloys powder, ceramic, and polymer	Serial (line-by-line)	80	Slow (μm/s)	-
SLS	Metals and alloys powder, ceramic, and polymer	Serial (drop-by-drop)	80	Slow (μm/s)	-

Abbreviations: FDM, fused deposition modeling; SLS, selective laser sintering.

sensitive to temperature changes.[18] FDM enables flexible and complex designs, usually used in osteochondral tissue scaffolds and drug delivery systems.[19] The main drawbacks are the high temperatures required during printing, making it challenging to use materials and biologically active substances that are not resistant to high temperatures. SLS offers high precision, efficiency, and a wide range of material applicability, gaining increasing attention and application.[20] It can produce large quantities of products in a short time. Compared to other 3D printing technologies, it allows for mass production and rapid batch production of complex parts.[21] Each technology presents unique advantages and challenges essential for their application in biomedical fields.

2.2. Printing inks

The fundamental properties of a 3D-printed product can be determined by the material type and the assembly process. Common materials used for 3D printing include metallic materials (such as titanium alloys), inorganic materials (such as bioactive ceramics), organic materials (synthetic and natural polymer materials), and composite materials. In musculoskeletal applications, the common characteristics of materials used in 3D printing mainly include the following aspects:

(i) Printability: a crucial characteristic of these materials is their printability, which includes considerations of viscosity, flow properties, and the ability to maintain structural integrity during the printing process;

(ii) Biocompatibility: most materials, whether natural polymers, synthetic polymers, metals, or bioactive ceramics, must possess good biocompatibility to minimize adverse reactions when used *in vivo*;

(iii) Biodegradability: many materials (such as polylactic acid, polyesters, and natural polymers) demonstrate favorable biodegradability, allowing them to gradually break down within the body and reduce the risks associated with long-term implants;

(iv) Physical and mechanical properties: these materials are often engineered to exhibit specific mechanical strength and elasticity, dealing with different stress and tensile properties of tissues to support tissue regeneration and replacement;

(v) Modifiability: numerous polymers can be chemically modified to adjust their physical and chemical properties, such as altering crosslinking density or incorporating additional components to meet specific application needs;

(vi) Applicability in musculoskeletal regenerative rehabilitation: materials should have effects on the restoration of function and structure in damaged or diseased tissues.

2.2.1. 3D-printed materials for implants and scaffolds

Implants and scaffolds play a crucial role in the structural and functional reconstruction of the musculoskeletal system. They are often designed to exhibit bioactivity that promotes cell proliferation and differentiation and offers specific mechanical properties. They can provide mechanical support, fill defects in damaged areas, and serve as biodegradable scaffolds that facilitate tissue regeneration. 3D printing technology has significantly enhanced the development of personalized implants and scaffolds. This technique is characterized by its ability to support customized designs, ensure high reproducibility, maintain low production costs, and enable rapid prototyping. Additionally, it could fabricate scaffolds at micro and nano scales, thereby closely mimicking the natural structure and microenvironment of native tissues. Here, we introduce some commonly used materials in the fabrication of 3D-printed implants and scaffolds.

(i) Natural polymers: Natural polymers, extracted from natural materials, are compounds with low antigenicity, excellent biocompatibility, and biodegradability.[22] However, they have poor mechanical properties. Currently, commonly used natural polymers in 3D printing include collagen, gelatin, alginate, cellulose, chitosan, hyaluronic acid (HA), and decellularized extracellular matrix (dECM). While they have good biocompatibility and biodegradability, each material presents unique advantages and challenges (Table 2).

(ii) Synthetic polymers: Polyvinyl alcohol (PVA) is a water-soluble synthetic polymer known for its excellent biocompatibility, chemical stability, water absorption, non-toxicity, thermal stability, adjustable mechanical properties, and printability, making it a popular bioink in 3D printing.[23] Moreover, PVA exhibits strong hydrophilicity and hydrogen bonding properties due to its hydroxyl groups, forming gels with high physical stability. PVA hydrogels formed through crosslinking have various biomedical applications ranging from bone and cartilage regeneration to flexible sensors.[24–26] Polylactic acid (PLA), produced by ring-opening polymerization (ROP) of lactic acid, is one of the most consumed bioplastics globally. As a temporary extracellular matrix (ECM), PLA has good biodegradability, biocompatibility, and high ductility. However, pure PLA polymer has low mechanical strength. Thus, preparing PLA composites is needed to obtain better mechanical properties.[27] PLA is primarily used to manufacture degradable bone and cartilage tissue scaffolds. Polycaprolactone (PCL), a semi-crystalline polymer form of ε-caprolactone synthesized through ROP, is utilized in bone tissue engineering due to its biodegradability, non-toxicity, slow degradability, and high mechanical properties.[28] However, due to its poor hydrophilicity and low bioactivity, PCL used for tissue engineering scaffolds requires further combination with bioactive materials, such as tricalcium phosphate (TCP), hydroxyapatite (HA), Bio-Oss, or decellularized bone matrix to expand its application range.[29] Polyethylene glycol (PEG), a water-soluble polymer formed by polymerizing ethylene glycol, exhibits excellent biocompatibility and hydrophilicity. The stability

Table 2. The advantages and disadvantages of various natural polymers.

Type	Advantages	Disadvantages
Collagen	Excellent biocompatibility; low immunogenicity; abundant in the ECM	Limited mechanical strength
Gelatin and GelMA	Photopolymerizable to form hydrogels; controllable stiffness and porosity by adjusting parameters (e.g., hydrogel concentration, functionalization degree, and curing time); excellent biocompatibility and biodegradability	May require modification for improved stability
Alginate	Forms hydrogels under mild conditions; promotes bone healing and cartilage regeneration by regulating cell viability, osteogenic inductivity, and chondrogenic differentiation of MSCs; good biocompatibility, biodegradability, and non-antigenicity	May lack cell adhesion sites
Cellulose	Excellent mechanical properties; suitable for weight-bearing implants; degradable	Poor solubility (requires modification)
Chitosan	Mimics glycosaminoglycans in the ECM	Insufficient mechanical strength; unsatisfactory degradation rate
HA and MeHA	Non-toxic and non-immunogenic; good biocompatibility and biodegradability; improved physical properties (MeHA); extensively used in bone and cartilage tissue engineering	May require chemical modification for enhanced stability
dECM	Maintains various functional components that can support cell survival, growth, migration, and differentiation; mimics the native ECM structure to provide a more biomimetic environment for cells; good biocompatibility and low immunogenicity	Limited mechanical properties; potential for disease transmission; time-consuming and expensive production process; challenges in obtaining large quantities of tissue-specific dECM

Abbreviations: dECM, decellularized extracellular matrix; ECM, extracellular matrix; GelMA, methacrylate-based gelatin; HA, hyaluronic acid; MeHA, methacrylated hyaluronic acid; MSCs, mesenchymal stem cells.

and degradation rate of PEG hydrogels notably affects its applications. The ester bonding caused by acrylation slows the degradation rate of PEG. The biocompatibility and low immunogenicity of the acrylate-derivatives of PEG hydrogel make it a good choice for in-body applications.[30]

(iii) Metals: 3D-printed metals are primarily used in orthopedics for implants, as well as in soft robotics, sensor technology, and *in vitro* medical devices.[31,32] The type of metal material chosen depends on specific clinical needs. Most orthopedic implants are made of inert metals (cobalt–chromium alloys), some need to bond with host tissue (titanium alloys), and some require tissue growth to eventually replace the implant (magnesium alloys).[33] Current metal implants primarily use cobalt–chromium alloys and titanium alloys. Implantable metals must possess biocompatibility, corrosion resistance, high specific strength, high fatigue strength, high impact toughness, and low toxicity. One key issue with implants is stress shielding, which leads to bone loss due to the implant's inhibition of pressure on the bone. Stress shielding can be addressed by using materials with stiffness similar to cortical bone (e.g., magnesium) or by designing implants with porosity to reduce stiffness.[34]

(iv) Bioactive ceramics: Bioactive ceramics are a class of ceramic materials used for specific biological or physiological functions. They can be classified into three major categories: bioinert ceramics (alumina and zirconia), bioactive ceramics (bioactive glass and HA), and biodegradable ceramics (TCP). Each bioactive ceramic has its unique characteristics, such as the high hardness of alumina ceramics, the toughness of zirconia ceramics, and the chemical composition of HA, closely resembling the inorganic part of human bone. However, a common disadvantage of ceramics is their brittleness, leading to high costs and difficulty in forming complex shapes with traditional processing techniques.[35] 3D printing, an emerging manufacturing technology, offers advantages such as rapid prototyping, personalized production, and the formation of complex structures. The combination of 3D printing technology and bioactive ceramics meets the needs requirements for individualized treatment in the biomedical field.[36]

2.2.2. 3D-printed materials for rehabilitation assistive devices

3D-printed rehabilitation assistive devices mainly include prosthetics and orthotics, with the advantages of cost-effectiveness, lightweight, comfort, and breathability compared to traditional plaster or plastic devices. The

commonly used materials can be categorized into rigid and flexible materials. PLA and acrylonitrile butadiene styrene are the most widely used thermoplastic materials, commonly employed in FDM and SLS printing techniques.[37] Among flexible materials, thermoplastic polyurethane (TPU) is commonly used, often in FDM, SLS, and multi-jet fusion (MJF) printing techniques.[38] Additionally, composite materials have significantly enhanced stiffness, weight, and patient comfort. Recently, 3D-printed rehabilitation aids have evolved towards more complex and intelligent designs. For instance, Buchner et al. designed a tendon-driven hand capable of performing intricate actions such as grasping.[39] Moreover, 3D-printed braces can be integrated with monitoring systems to facilitate biomechanical analysis of joints, postoperative recovery monitoring, functional exercise assistance, and adjustments to rehabilitation programs.[40] Therefore, it is necessary to develop materials with higher strength and toughness and composite materials that support collaborative printing techniques, which enables the production of intricate, high-resolution, and precise devices while ensuring patient comfort and safety. Furthermore, it is essential to develop smart materials capable of responding to environmental changes, such as temperature, humidity, or force. These materials could adaptively adjust their properties during the rehabilitation process, providing personalized feedback and support tailored to the individual needs of patients. This integration of advanced materials and intelligent functionalities holds the potential to significantly enhance the efficacy and user experience of 3D-printed rehabilitation aids.

3. Impact of 3D printing technology on musculoskeletal regenerative rehabilitation methods

Functional recovery is a primary concern for patients with musculoskeletal system injury. Functional rehabilitation refers to the restoration of function in patients through rehabilitation strategies, which is critical for regaining physical function and enhancing quality of life. Physical factors, including light, sound, heat, force, and electrical and magnetic fields, play very important roles in rehabilitation medicine, aiming to minimize inflammation, relieve pain and swelling, and restore the function of damaged or aged tissues and organs. The beneficial effects of physical stimulation, such as mechanical, electrical, and magnetic stimuli, and therapeutic ultrasound, on cell viability and biological efficacy of different cells, including meniscal cells, fibroblasts, osteoblasts, chondrocytes, and mesenchymal stem cell-derived exosomes, have been investigated in previous studies.[41–44] In addition, physical factors can also regulate immune cell function and angiogenesis, as well as reducing inflammation and oxidative stress, thereby forming a microenvironment conducive to tissue repair.[45,46] The combination of physical stimulation and 3D printing technology enhances tissue repair.

The effective implementation of functional rehabilitation requires the coordination of rehabilitation assistive devices, which are defined as techniques designed to compensate for and enhance function.[47] With the increasing demand for customization, the 3D printed approach has found widespread application in the fabrication of personalized rehabilitation assistive devices tailored to the unique conditions of individual patients. 3D-printed assistive devices, including prostheses and orthoses, are well-fitting to patients' bodies and streamline procedures of recapitulation of patient-specific color, texture, stiffness, and shape. Moreover, they are more favorable in improving functional outcomes, such as reducing pain, improving comfort, preventing joint stiffness, and regaining range of motion.[48–51] For instance, a printed upper limb prosthesis for a child with traumatic amputation of the right wrist met the child's daily living needs, costing less than $20 and requiring less than 8 h for fabrication.[52] The fabrication of 3D-printed rehabilitation assistive devices has advantages in terms of time, cost-effectiveness, and environment-friendliness.[51–54] Therefore, 3D-printed rehabilitation assistive devices are an affordable, satisfying, and customizable alternative for patients with a variety of orthopedic conditions, including amputations, fractures, sprains, ligament tears, and tendinopathies.

Pharmacological interventions, such as corticosteroids and nonsteroidal anti-inflammatory drugs, are commonly applied to reduce inflammation and relieve pain, thus accelerating the repair of damaged tissues and reducing the time required for return to sports. However, systemic administration is usually associated with significant known risks.[55] Therefore, 3D-printed technology facilitates the development of precisely controlled drug delivery. For example, Majrashi et al. fabricated 3D-printed scaffolds capable of sustainably releasing dexamethasone locally, with dual capacities of anti-inflammation and pro-osteogenic differentiation. This highlights the potential of 3D printing technologies in developing precisely controlled drug delivery systems and reducing systemic side effects.[56]

The strategies of regenerative medicine to repair damaged and aged tissues and organs today rely on three types of biological components:

(i) Bioactive factors such as bioactive molecules (E7, R5, and Apt19s) and growth factors (transforming growth factor-beta [TGF-β] and platelet-derived growth factor-BB), and bioactive factor-rich tissue or blood extracts (platelet-rich plasma [PRP], platelet-

rich fibrin, bone marrow aspirate concentrate, autologous fat grafting, and stromal vascular fraction);

(ii) Genes and transcripts delivery and editing, in which tissue function is enhanced at the genetic level;

(iii) Cells and cell-derived exosomes, in which mesenchymal stem cells (MSCs), human umbilical vein endothelial cells, myoblasts, osteoblasts, and chondrocytes are commonly used in the treatment of musculoskeletal diseases.

In addition, tissue engineering and biomaterials combine principles from engineering, biology, and materials science to develop biological substitutes aimed at restoring, maintaining, or improving tissue function. They involve the use of biological components and biomaterial scaffolds to create functional tissue constructs that can be implanted or injected into the body to repair or replace diseased tissues. The integration of 3D printing technologies with tissue engineering and biomaterials has opened up new possibilities for creating more complex, functional, and personalized tissue constructs and implants, ultimately advancing the field of regenerative medicine and improving patient outcomes.

Regenerative rehabilitation, the fusion of regenerative and rehabilitation medicine, was first proposed by Ambrosio and Russell in 2010.[7] The concept was further elaborated by Rando and Ambrosio in 2018.[8] This emerging field aims to optimize the restoration of function through the integration of principles, protocols, and approaches of two similar fields. A recent network meta-analysis of 80 randomized controlled trials (RCTs) revealed that, compared to physical therapy alone or intra-articular injection of PRP or MSCs alone, the combination of physical therapy and regenerative therapy was more efficacious in reducing pain and enhancing walking capability for patients with knee OA.[57] A phase I/II clinical trial for patients with knee OA indicated that 1 year after implantation of a composite of culture-expanded allogeneic human umbilical cord blood-derived mesenchymal stem cells and HA (hUCB-MSCs-HA) hydrogel and postoperative exercises, regenerated cartilage with a smooth surface was observed at the defect sites. Besides, no significant adverse events were observed after 7 years of follow-up.[58] However, evidence from clinical studies is still limited for the efficacy and safety of cell transplantation and PRP injections. The impact of individual patient differences on efficacy cannot be ignored. Significant progress has been achieved in regenerative rehabilitation medicine through the advancements of 3D printing technology. The development of 3D printing technology has promoted the personalization, precision, and complexity of regenerative rehabilitation technology, resulting in more efficient tissue repair. Figure 2 summarizes the complete workflow for the 3D printing-based musculoskeletal regenerative rehabilitation process.

4. 3D-printed solutions in tissue regeneration for musculoskeletal disorders

4.1. Articular cartilage

Articular cartilage lesions commonly result from trauma induced by an external force or age-related degeneration.[59] Articular cartilage is a highly organized tissue with multilayer structures, including the hyaline cartilage layer and the underlying calcified cartilage layer, which provides a smooth joint surface and exhibits high elasticity, high toughness, high stiffness, and fast recovery.[13] Therefore, it can withstand a load of up to 100 MPa, can be less prone to fatigue, and can rapidly recover its deformation after unloading.[60] Progressive loss of articular cartilage induces joint inflammation, cartilage ECM remodeling, gradual tissue deterioration, and bone remodeling, ultimately resulting in the development of OA.[22,61–63] However, its ability of intrinsic repairment is poor due to low proliferative capacity and a lack of neurovascular components.[22] Besides, traditional therapies cannot fully restore the multilayered structure and complex interaction of cartilage. Thus, 3D printing-based cartilage tissue engineering is a potential choice.

3D-printed implants can facilitate tissue reconstruction due to their similar structure and biological function to normal cartilage. In addition, they can promote the growth and proliferation of chondrocytes by introducing beneficial cells, growth factors, and bioactive molecules. Selecting suitable materials is significant to the ideal function. Natural polymer materials have been widely explored as bioinks due to low antigenicity, biocompatibility, and degradability.[60] Li et al. fabricated a 3D-printed microenvironment-specific biomimetic hydrogel scaffold using GelMA, dopamine-grafted HA (HA-DA), and oxidized HA with the addition of the dECM derived from cartilage and bone encapsulated exosomes.[64] At 12 weeks after implantation in a rat model with osteochondral defect, the scaffold promoted the formation of hyaline cartilage, resembling the structure of normal tissue (Figure 3A). Moreover, 3D-printed PRP-laden GelMA hydrogel constructs remarkably facilitate superior cartilage and subchondral bone repair by promoting the migration and osteogenic and chondrogenic differentiation of bone marrow MSCs (BMSCs). Additionally, these constructs participate in the regulation of immune responses and mediate the transition of macrophages from the pro-inflammatory M1 phenotype to the anti-inflammatory and pro-regenerative M2 phenotype.[65] The 3D-printed scaffold could mimic the

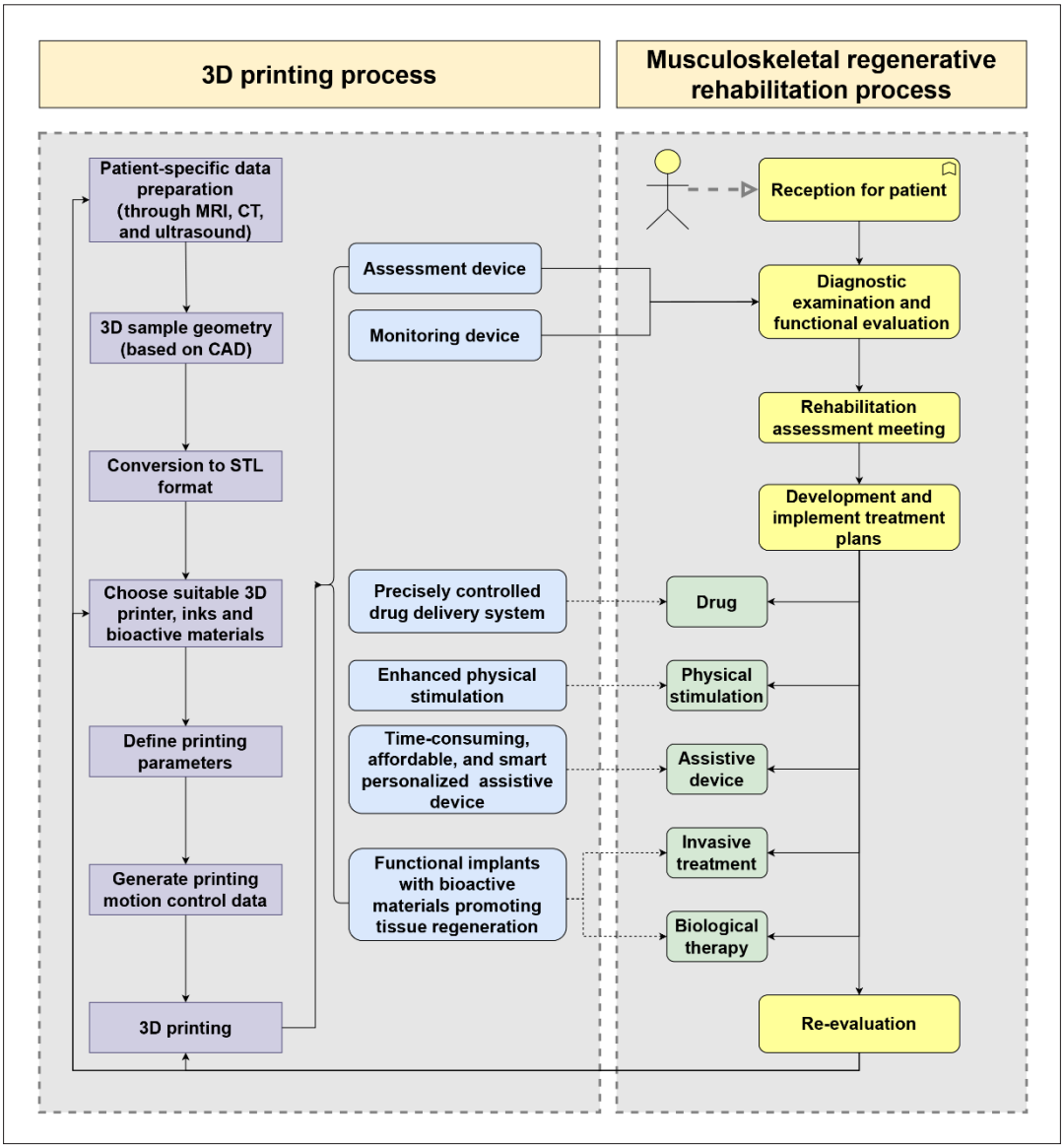

Figure 2. The 3D printing-based musculoskeletal regenerative rehabilitation process. Abbreviations: CAD, computer-aided design; CT, computed tomography; MRI, magnetic resonance imaging.

complex layers of normal articular cartilage. For example, Zhang et al. fabricated a multilayered nanohydroxyapatite (nHA)/hydrogel scaffold with a similar structure to that of osteochondral tissue, which possesses an increasing stiffness gradient from the cartilaginous layer to the subchondral bone layer. The scaffold exhibited remarkable mechanical properties, appropriate degradability, and high structural integrity for long periods of cell culture.[66]

Mechanical stimulation is a decisive factor for cartilage tissue formation. For example, a 12% compressive strain stimulated the generation of hyaline-like cartilage ECM, while a 24% compressive strain tended to produce fibrocartilage-like ECM.[67] However, there is no rigorous standard to identify the optimal parameters including type, intensity, volume, frequency, duration, timing, and progression of application. It is also unclear whether a traditional rehabilitation regimen is appropriate for patients receiving cartilage scaffold implantations. Inappropriate mechanical stimulation can cause substantial damage to the structure. A study indicated that mechanical compression for 5 days (3 h/day) could damage the hydrogel constructs, especially at 12% and 24% compressive strain conditions.[67] Hydrogel scaffolds with better mechanical properties may be able to withstand higher mechanical forces, effectively

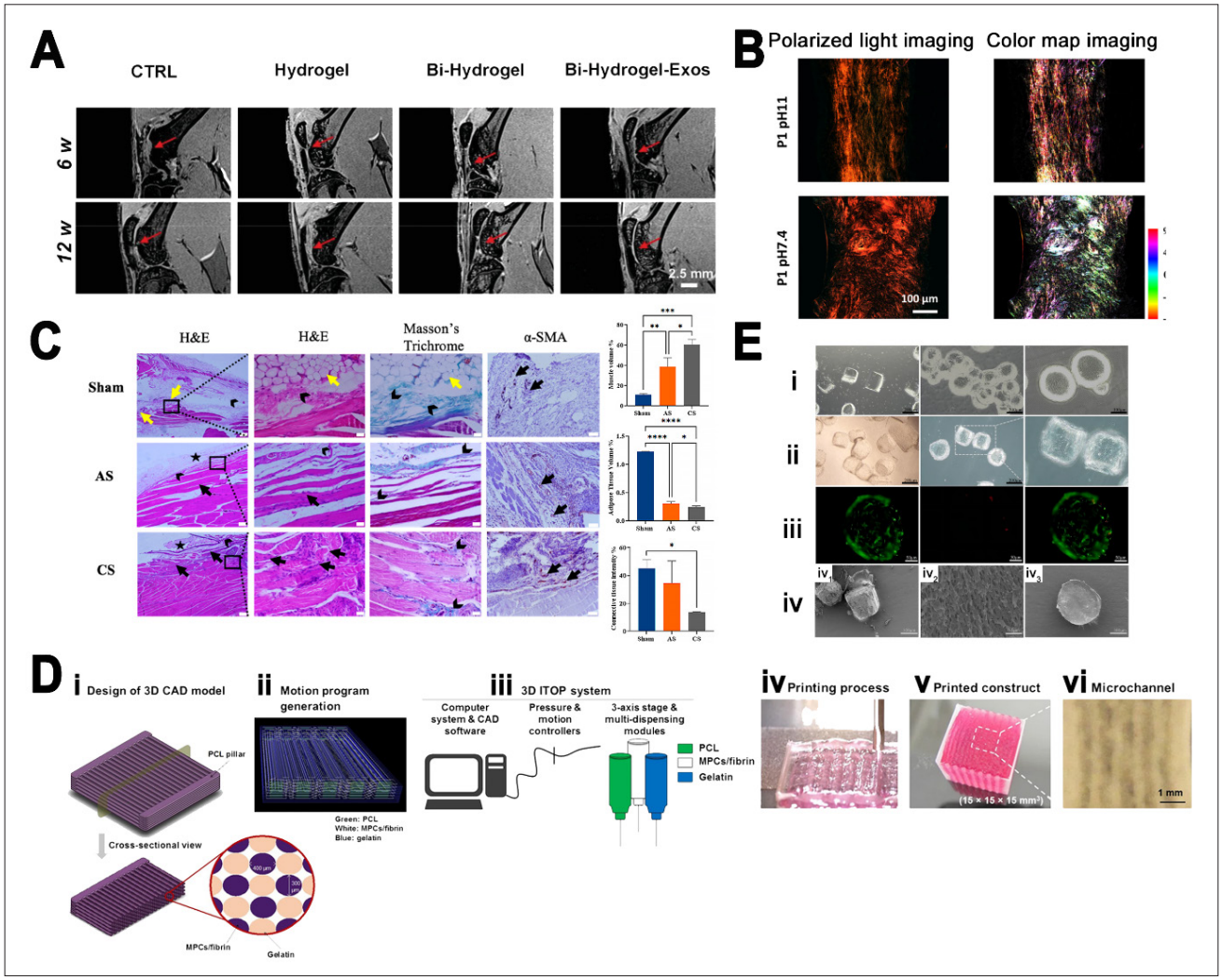

Figure 3. 3D printing-based treatment of musculoskeletal diseases. (A) MRI outcomes indicate that 3D-printed tissue-specific microenvironment biomimetic scaffolds promoted cartilage repair. Adapted with permission from Li et al.[64] Copyright © 2023 The Authors. Reprinted under the terms of the CC-BY license. (B) The direction of collagen fibers in printed ECM filaments with pH 11 compared to pH of 7.4. Adapted from Wang et al.[81] (C) Histopathological results of the defect region after four weeks implantation for the empty, AS, and CS groups in a rat tibialis anterior defect model. Adapted with permission from Gokyer et al.[101] Copyright © 2021 American Chemical Society. (D) 3D-printed skeletal muscle constructs: (D, i) design of the 3D model in CAD; (D, ii) motion program generation of the bioprinted muscle construct; (D, iii) schematic of the bioprinting process using the ITOP system; (D, iv) bioprinting process; (D, v) the bioprinted skeletal muscle constructs composed of multilayered myofiber bundles were fabricated up to 15 × 15 × 15 mm^3 in dimension; (D, vi) microchannels in the constructs created after the removal of the sacrificial patterns to maintain the viability of printed cells. Adapted with permission from Kim et al.[104] Copyright © 2018 The Author(s). Reprinted under the terms of the CC-BY license. (E) 3D printed GM co-cultured with TDSCs for tendon repair: (E, i) GelMA GM under an optical microscope; (E, ii) co-culture of TDSCs and GM; (E, iii) immunofluorescence staining of living (green) and dead (red) cells on GM; (E, iv_1) GM under SEM (×30000); (E, iv_2) surface morphology of GM under SEM (×30,000); (E, iv_3) Cross-section of GM under SEM (×30,000). Adapted from Li et al.[109] Abbreviations: AS, acellular scaffold; CAD, computer-aided design; CS, cell-laden scaffold; CTRL, blank control; ECM, extracellular matrix; GelMA, gelatin methacryloyl; GM, microparticles; ITOP, integrated tissue-organ printer; MPCs, muscle progenitor cells; MRI, magnetic resonance imaging; PCL, poly(ε-caprolactone); SEM, scanning electron microscope; TDSCs, tendon-derived stem cells.

enhancing their performance by adjusting manufacturing process parameters. Regulating the printing parameters (pressure,[68] moving speed,[68] and concentration of printing inks[69,70]) could change the mechanical properties of scaffolds. In addition, the introduction of silk fibroin and inorganic materials in the fabrication process is also a strategy to achieve desirable mechanical properties.[71,72] It should be noted that clinical trials are lacking to verify whether tissue-engineered cartilage can withstand long-term loads experienced by humans. However, this goal may not be necessary, as the majority of tissue-engineered cartilage constructs are typically designed to be biodegradable.

The ultimate objective is to enhance endogenous repair, rather than to depend on xenogenic scaffolds for structural support. In a phase I/II clinical trial, MRI scans of five participants with OA who received implantation of a composite of hUCB-MSCs and HA hydrogel, combined with postoperative rehabilitation (including muscle strength and joint mobility exercises, and non-weight-bearing ambulation), demonstrated regenerated cartilage comparable to that of healthy individuals.[58]

Physical factors are important for regenerative rehabilitation. Physical stimuli acting on mechanochemical transduction pathways may potentially reduce reliance on the mechanical properties of tissue-engineered cartilage. For example, low-intensity pulsed ultrasound (LIPUS) can modulate the integrin-FAK-PI3K/Akt pathway in OA chondrocytes, enhancing ECM production and reducing metalloproteinase levels.[73] Physical stimuli have been proven to promote cartilage regeneration and differentiation. 3D-printed flexible, conductive, and biodegradable scaffolds have the potential to control electrical stimulation in damaged cartilage areas.[74] Stimuli-responsive hydrogels (e.g., light, temperature, and magnetic) can be combined with physical therapies used in rehabilitation medicine (e.g., infrared light, magnetothermal therapy, and pulsed electromagnetic fields) to achieve precise treatment of damaged cartilage in patients. However, further development of bioinks suitable for clinical applications is necessary.

Rehabilitation medicine teams should collaborate with tissue engineering experts to develop regenerative rehabilitation strategies. This collaboration aims to optimize and enhance the repair performance of tissue-engineered cartilage in humans, thereby accelerating its clinical application.

4.2. Meniscus

The meniscus, a complex and crucial fibrocartilaginous tissue within the knee joint, assumes a semilunar wedge-shaped form that plays a pivotal role in ensuring the overall functionality of the joint.[75] Positioned between the femoral condyle and the tibial plateau, the meniscus undertakes the imperative functions of transferring and redistributing loads, providing cushioning, and absorbing shock, as well as joint lubrication and congruent stability.[76] Age-related degeneration and acute sports injuries are commonly acknowledged as two principal contributors to meniscal dysfunction.[77] Due to the inherent limited vascularity and suboptimal healing capacity of the meniscus,[78] the pursuit of desirable and sustained outcomes remains difficult. Meniscus injury and absence due to meniscectomy render the hyaline cartilage of the femur and tibia susceptible to excessive biomechanical forces, consequently accelerating the development of OA.[77,79,80] Given the unique anatomical structure and complex stress environment of the meniscus, meniscal regeneration remains to be a scientific and translational challenge. To this end, meniscal tissue engineering has emerged as a potential approach for treating meniscal defects.

Recently, appropriate biomimetic scaffolds have been constructed via 3D printing, imitating elaborate microstructure of the native meniscus with structural integrity and high-strength comprehensive mechanical properties. Wang et al. successfully used highly concentrated meniscus dECM inks at pH 11 to print artificial meniscus. These functional meniscal tissue equivalents had a compressive modulus comparable to that of a natural meniscus and could control the alignment of collagen fibrils (Figure 3B).[81] Characterized by a unique shape with high edges and a low center, the meniscus faces a complex stress environment, encompassing axial, hoop, and compressive mechanical stresses.[82] However, it is challenging to develop a meniscal replacement that recapitulates the anisotropic microarchitecture and modulus of the meniscus. To this end, Jian et al. developed a biomimetic meniscal scaffold using a multilayer strategy.[83] By employing a dual-nozzle and multi-temperature 3D bioprinting system, they integrated PCL with meniscal fibrocartilage chondrocyte-laden GelMA/meniscal ECM bioinks, achieving optimal biomimetic features in morphology and components. With a compression modulus of 12.63 MPa and a tensile modulus of 24.86 MPa in the radial direction, close to those of the human meniscus, this approach showcases promising advancements in creating functional meniscal replacements for potential applications in tissue engineering and regenerative medicine. However, the mechanical properties attained through this approach still exhibit a significant discrepancy when compared with the circumferential tensile modulus (78–120 MPa). To provide circumferential tensile supports, Zhang et al. 3D printed the radially and circumferentially oriented PCL fiber framework to imitate collagen fibers in the native meniscus.[84] Meanwhile, poly(N-acryloyl glycinamide) hydrogel was infused into the 3D-printed PCL framework, thus providing durable energy absorption and cushioning. The *in vivo* results demonstrated structural stability, efficient protection against cartilage wear, and an ameliorating effect on OA development. The 3D printing approach can handle complex requirements of mechanical properties of joints, presenting a fresh possibility for future meniscal regeneration strategies.

The meniscus exhibits a highly intricate microarchitecture characterized by the presence of diverse cellular types, ECM components, and organization in various regions, highlighting the heterogeneity of this

fibrocartilage.[76,85,86] The meniscal ECM comprises a densely woven and well-hydrated meshwork interlaced with circumferential collagen fibers and radial collagen fibers, interspersed with glycosaminoglycans (GAGs). Furthermore, the outer region, rich in fibroblast-like cells that exist within an ECM that mainly comprises type I collagen (Col I), confers resistance against tensile loads, while the inner region, rich in chondrocyte-like cells, which are embedded within an ECM that largely consists of type II collagen (Col II) and GAGs, contributes to resistance against compression. To promote anisotropic regeneration of meniscus-like tissue, Yan et al. developed a 3D-printed biomimetic meniscal scaffold loaded with intrinsic MSCs and growth factors, including TGF-β3 and connective tissue growth factor, known for their superior fibrochondrogenic capabilities.[87] The neomenisci exhibit an anisotropic matrix distribution, with the inner and middle zones abundant in Col II, aggrecan, and GAG, while the outer zone primarily contains Col I. Consequently, the anisotropic matrix distribution in the regenerated tissue enables shock absorption during knee joint motion, resembling the native menisci. In addition to matrix distribution, the distribution of cells in the meniscus is also anisotropic. Chae et al. printed a biomimetic meniscus construct using polyurethane (PU) and PCL polymers and cell-laden decellularized meniscal ECM (me-dECM) bioink.[88] The resulting neomeniscus displayed rounder chondrocyte-like cells and fewer fibroblast-like cells in the inner region of the neomeniscus at 8 weeks compared to 4 weeks, thus exhibiting favorable mechanical and biological properties similar to the native meniscus. Overall, 3D-printed scaffolds reconstruct anatomical structures and restore knee mobility and stability, making them promising options for regenerative meniscus repair.

Mechanical stimuli are significant for menisci to synthesize proteins and regulate cellular processes.[89] Ultrasound has been used to mechanically stimulate chondrocytes through integrin-mediated signaling pathways.[73,90] The combination of LIPUS and 3D hybrid scaffolds can promote chondrocyte migration, adhesion, proliferation, and viability, retain chondrocyte morphology, and increase the expression level of Col II and aggrecan.[91] Thus, mechanical stimuli through physical factors should be added to the 3D-printed tissue engineering to enhance tissue functions.

4.3. Muscle

Muscle diseases are conditions that affect the human muscular system, usually caused by injury, infection, aging, and hereditary factors, resulting in muscle wasting, loss of muscle mass, and decreased muscle strength.[92] Strength training and aerobic exercise programs are performed to improve muscle strength and muscle endurance.[93] Additionally, functional free muscle transfer procedures and the implementation of advanced orthotic bracing designs are adapted as therapeutic options for severe muscle diseases.[94] However, they fail to significantly improve functional outcomes and increase associated donor site morbidity.[95] In recent years, regenerative medicine and tissue engineering using 3D printing are emerging, aiming to more fully restore muscle form and function.

Volumetric muscle loss (VML) involves a severe loss of muscle tissue that transcends the inherent regenerative capabilities of skeletal muscles.[96] Traditionally, the gold standard for VML defect treatment is autologous muscle tissue implantation, yet these implants frequently exhibit poor efficacy and may lead to failure due to low regeneration efficiency stemming from the inadequate controllability of myofiber structural organization.[97] In response, tissue engineering structures employing synthetic or natural biomaterials tailored to artificial muscle tissues, coupled with live cells, have been developed to enhance muscle functions.[98] The bioprinting process provides controllable 3D spatial cell distribution in 3D frameworks with no effect on their activities.[99] In one example, Hwangbo et al. fabricated aligned muscle construct by using GelMA-based cell-laden structures, incorporating C2C12 or human adipose stem cells (hASCs), with an *in situ* UV crosslinking system for treating VML.[100] The study successfully developed GelMA structures with uniaxially aligned C2C12 cells, optimizing printing parameters to enhance cellular alignment and myotube heavy chain expression. *In vivo* experiments with hASC-laden muscle constructs demonstrated significant functional and volumetric restoration in VML-defective mice compared to conventionally crosslinked structures. Seyda et al. 3D printed biodegradable elastomeric TPU-based scaffolds seeded with autologous ASCs. After scaffold implantation in a rat tibialis anterior defect model, organized muscle regeneration significantly increased (Figure 3C).[101] The electrical activity and active force produced by the regenerated muscle were also increased, indicating that the scaffold enhanced the function of regenerative muscles.

The skeletal muscle is widely recognized for its high degree of vascularization, a crucial aspect for providing nutrients and oxygen and removing metabolic waste within the muscle tissue.[102] Despite its importance, the bioprinting of micro-vascularized skeletal muscle tissues presents ongoing challenges. Addressing this, Luo et al. employed the vertical 3D cryo-bioprinting technique to successfully fabricate the muscle-microvascular unit.[103] This innovative approach utilized C2C12 myoblasts and human umbilical vein endothelial cells, demonstrating a significant advancement in the development of micro-

vascularized skeletal muscle constructs. In another study, Kim et al. employed the integrated tissue-organ printer (ITOP) system to create a 10 × 7 × 3 mm^3 skeletal muscle construct with human muscle progenitor cells in a fibrin bioink with gelatin and PCL deposition (Figure 3D).[104] The construct, transplanted into the tibialis anterior (TA) muscle defect rat model, displayed enhanced tetanic force and TA muscle weight, with 82% muscle force restoration compared to normal TA muscle after 8 weeks. Moreover, it was well integrated with host vascular and neural networks. Thus, 3D bioprinting improves the accuracy and survival rate of muscle tissue constructs.

4.4. Tendon

Tendons are load-bearing structures that transmit forces from muscle to bone.[105] It is a type of connective tissue with minimal cellular presence and abundant collagen fibers organized in parallel alignment.[106] Tendon tears often occur due to strenuous exercise and age-related degeneration, accounting for over 30% of all musculoskeletal consultations.[107] Present therapeutic alternatives are limited, predominantly involving symptomatic interventions and surgeries. While surgical interventions may provide temporary relief for certain symptoms, the long-term effects, such as tendon adhesion, inferior mechanical properties, and the risk of re-injury, are unsatisfactory.[108] Owing to unsatisfactory outcomes of surgeries, engineered biomimetic tendon grafts that emulate the intrinsic properties of native tissues have been explored. Li et al. designed injectable GelMA microparticles (GM) laden with PRP and tendon-derived stem cells (TDSCs) to promote Achilles tendon regeneration and inhibit chronic inflammation by downregulating the PI3K-AKT pathway (Figure 3E).[109] In addition, Zhang et al. combined a small molecule culture system with 3D printing to create tendon grafts embedded with TSPCs, facilitating functional tendon repair and regeneration in both the ectopic and *in situ* tendon repair models.[106] Moreover, Kim et al. created a cell-laden construct for tendon tissue engineering, utilizing hASCs, and a dECM bioink derived from porcine tendon.[110] The resulting cell constructs exhibited controllable mechanical properties and significantly enhanced cellular activity. Notably, they showcased uniaxially aligned cell morphology and upregulated tendon gene expression, emphasizing the potential for advancing tendon tissue engineering.

3D printing is also applied to deal with the difficulties of repairing tendon–bone junctions. Rotator cuff tears, a common tendinopathy, resulting from acute trauma or chronic degenerative disorders, present challenges in restoration of the tendon–bone interface.[111,112] The native tendon-to-bone interface, comprising tendon, fibrocartilage, mineralized fibrocartilage, and bone, is intricate and challenging to restore owing to a lack of oxygen, growth factors, and other metabolically essential nutrients.[113] Current healing processes often lead to fibrovascular tissue formation instead of fibrocartilage regeneration, hindering biomechanical transduction, and causing dysfunction.[114] Consequently, the complex rotator cuff enthesis requires the exploration of biomimetic interfaces to improve surgical outcomes, offering potential alternatives and *ex vivo* living grafts. The evolving fields of tissue engineering and stem cell biology provide optimism for enhancing repaired tendon quality. For example, Cao *et al.* fabricated a biomimetic tendon-to-bone interface using a 3D-printed PCL–PCL/TCP–PCL/TCP multiphasic scaffold and a stratified cell-seeding method with GelMA.[115] Designed with three phases resembling the tendon, fibrocartilage, and bone, the scaffold facilitated the independent seeding of fibroblasts, BMSCs, and osteoblasts. This biomimetic approach offers potential applications in rotator cuff tendon-to-bone repair, serving as an alternative to biological fixation devices and providing an *ex vivo* living graft for damaged entheses.

In muscular tissue engineering, reconstructing the muscle–tendon unit (MTU) is a formidable challenge. The key part of MTU is the muscle–tendon junction, which transmits the mechanical forces of the muscle through the tendon to the skeletal system.[116] Luo et al. have developed an enabling vertical 3D cryo-bioprinting technique by combining extrusion bioprinting, directional freezing, and cryopreservation.[103] Applying this method to MTU fabrication using C2C12 myoblasts and NIH/3T3 fibroblasts, the resulting structures mimic the natural MTU. By strategically aligning cells and optimizing GelMA bioink formulations, this study advanced the precise control of bioprinting complex tissue structures.

5. Novel 3D-printed medical devices for musculoskeletal disorders

Medical devices play a crucial role in facilitating and augmenting regenerative and rehabilitative processes. A range of 3D-printed medical devices have been designed to support, monitor, assess, or enhance the delivery of regenerative treatments and rehabilitation interventions, contributing to the overall objective of improving patient outcomes.

Another challenge faced by researchers is the lack of sensors capable of non-invasively or implantably monitoring tissue responses to physical stimuli *in vivo*. 3D printing can be employed to manufacture assessment and monitoring devices to assess the progress of regenerative rehabilitation. Hou et al. developed a conductive ink

using the graphene nanoplate-carbon nanotube (GC) ink as the fusing agent (FA) for MJF printing to fabricate multilayered strain and humidity sensors, which can be used to monitor and predict human motions, monitor human breath, recognize five basic emergency hand signals, and indicate vital signs (Figure 4A).[117] It holds great potential for healthcare professionals to guide action-matched breathing, prevent patients from falling, and perform timely rescue measures. In addition, Paterson et al. developed a simple strategy for direct 3D printing of bioelectronic sensors on textiles using a very limited set of low-cost inks composed only of graphite flakes and silicone, thereby enabling accurate monitoring of hand functions involving records of simultaneous readings of pinch strength, thumb movement (flexion), and electromyography (EMG) of the abductor pollicis brevis muscle (Figure 4B).[118] 3D-printed devices provide objective, precise, and continuous data on the patient's function, movement patterns, and physiological responses, enabling healthcare professionals to accurately assess the progress of the patient's recovery. The development of such sensors will help in the development of personalized regenerative rehabilitation protocols.

Currently, the use of 3D printing for biomimetic fabrication seeks to recreate complex functions of natural organisms. Buchner et al. developed an inkjet-based multi-material deposition process termed vision-controlled jetting. This method uses contactless, continuous print adjustments to automatically create complex, functional systems and robots, offering a broader range of material families, elastic characteristics, high-resolution

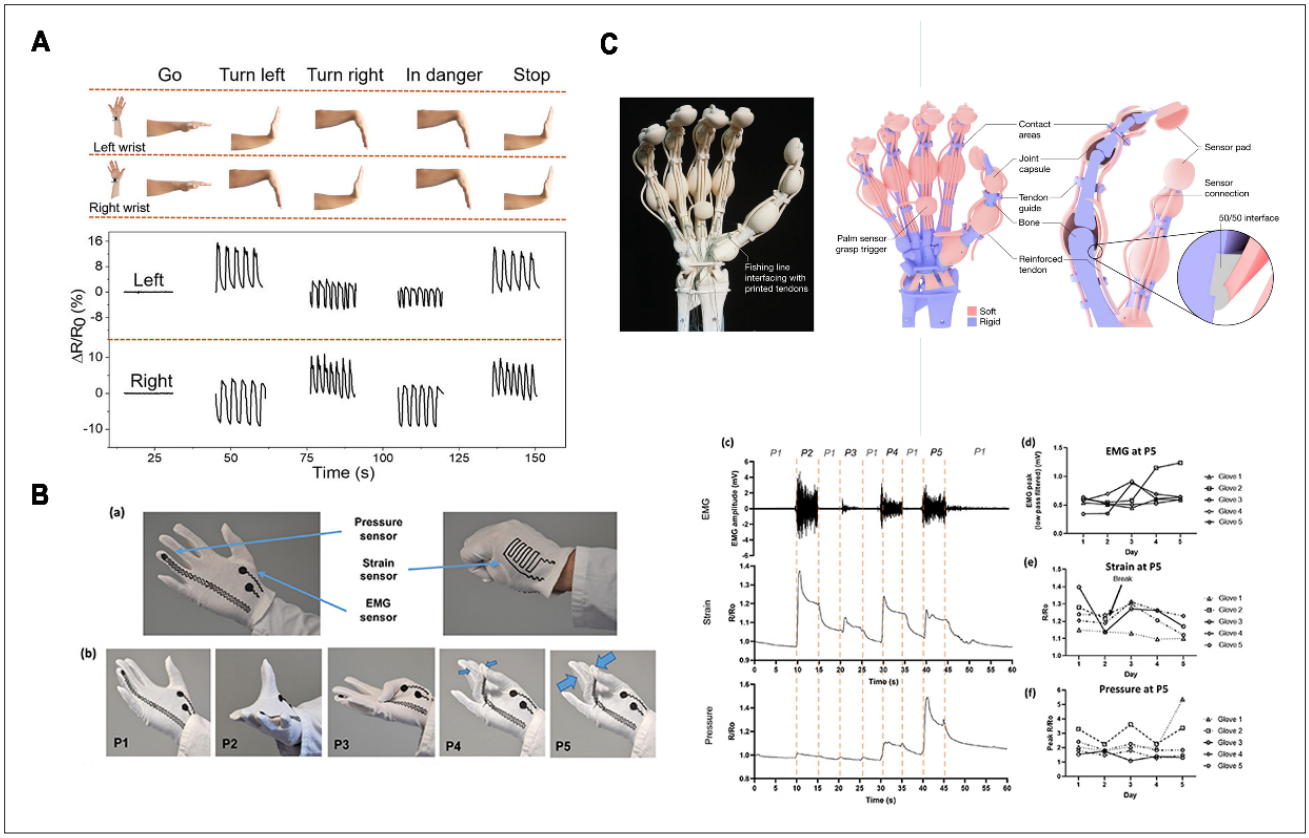

Figure 4. 3D-printed medical devices. (A) Discrimination of emergency signs based on two GC sensors worn on both wrists. Adapted with permission from Hou et al.[117] Copyright © 2023 The Authors. Reprinted under the terms of the CC-BY license. (B) 3D printed bioelectronic sensors for hand function monitoring. (B, a) Photographs of the fully printed gloves, displaying the placement and category of each sensor; (B, b) range of hand positions used during recording: P1, relaxed open hand; P2, thumb abduction; P3, thumb flexed across palm; P4, thumb and ring finger pinching with low force; P5, thumb and ring finger pinching with high force; (B, c) parallel sensor recordings of a typical glove, displaying the EMG of the abductor pollicis brevis and output of the strain and pressure sensors (vertical broken lines indicate the time when the hand assumes the indicated position); (B, d) peak of the low-pass filtered EMG burst; (B, e) peak resistance change of the strain sensor; (B, f) peak resistance change of the pressure sensor at P5 over the five sessions, with each glove individually tracked. Adapted with permission from Paterson et al.[118] Copyright © 2022 The Author(s). Reprinted under the terms of the CC-BY license. (C) A tendon-driven five-fingered soft-rigid hybrid gripper imitating a human hand printed in one process. Adapted with permission from Buchner et al.[39] Copyright © 2023 The Author(s). Reprinted under the terms of the CC-BY license. Abbreviations: EMG, Electromyography; GC, graphene nanoplate-carbon nanotube.

capabilities, and integrated actuation and sensing channels (Figure 4C).[39] This system was used to develop a multi-material tendon-driven hand, which is a fully functional print that is fitted with sensor pads and pneumatic signal lines. The tendon-driven hand can complete grasping actions autonomously, which may be beneficial for patients with physical disabilities to replace the fine motor function of hands. The potential of 3D printing technology holds significant promise for advancing the functional reconstruction of patients.

6. Clinical translation

Applying 3D printing technology in clinical practice still has some limitations. Firstly, health professionals should be educated and trained to improve acceptance and proficiency. Besides that, the absence of universally accepted testing standards poses a significant impediment to achieving consistent and uniform production of 3D-printed products. Notably, there is still a lack of clinical studies to verify the safety and efficacy of 3D-printed products in the clinical setting. Currently, clinical application research (data from www.ClinicalTrials.gov) demonstrates that the use of 3D-printed products for musculoskeletal diseases is mainly focused on orthoses and splints, with most of the studies concentrated in North America (Table 3; Figure 5). However, it is worth noting that clinical studies of 3D-printed scaffolds are still limited, despite the availability of commercially produced scaffolds using other methods in recent years.[13,119] Hence, greater emphasis should be placed on the clinical translation of 3D printing technology.

7. Conclusion

This review elucidated the transformative impact of 3D printing technologies on the workflow and therapeutic outcomes of musculoskeletal regenerative rehabilitation.

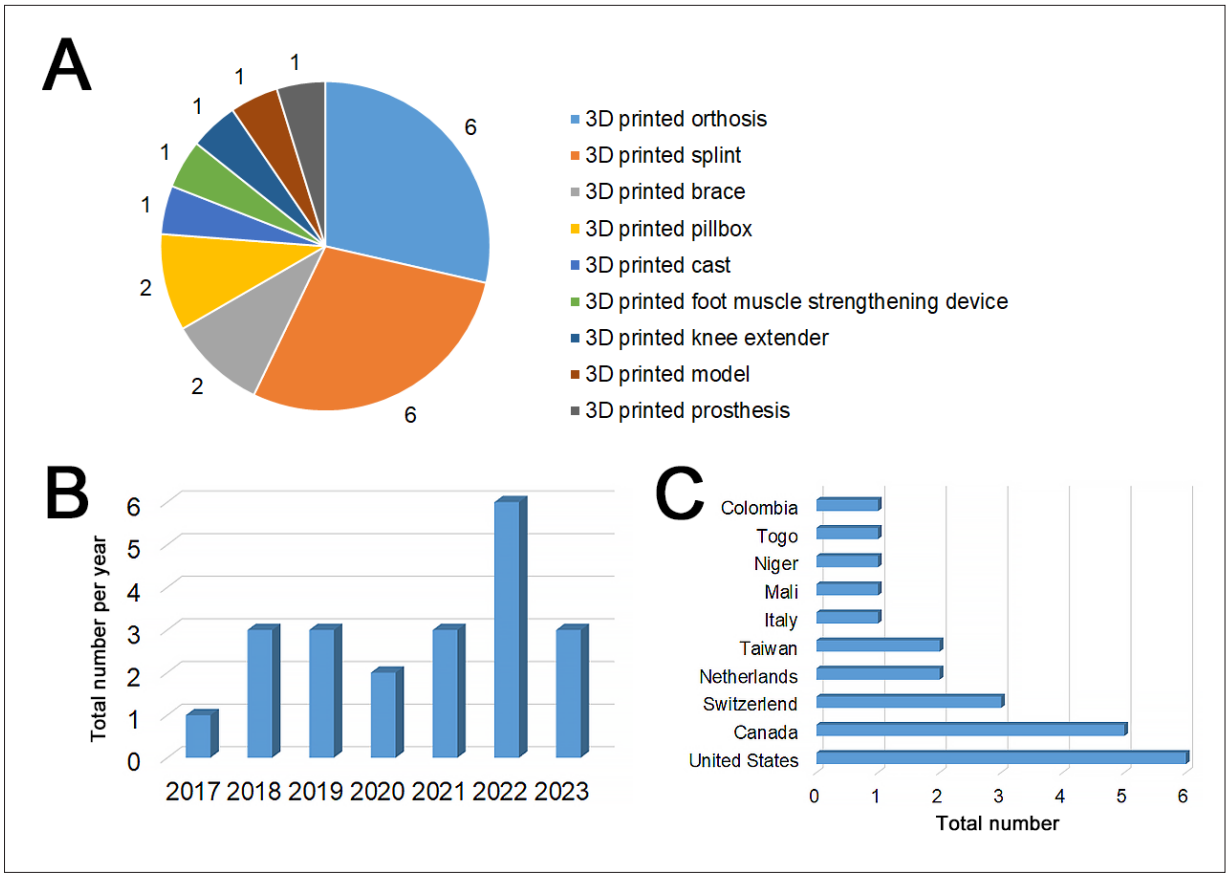

Figure 5. Statistics of the registered clinical trials of 3D-printed products for musculoskeletal diseases: (A) types of 3D-printed products for musculoskeletal diseases in registered clinical trials; (B) number of 3D-printed products for musculoskeletal diseases registered per year in the clinical trial registry system; and (C) the number of clinical trial registrations of 3D-printed products for musculoskeletal diseases around the world.

Table 3. Clinical application of 3D-printed products.

Application	Study title	Year	Type	Registration	Country	Design	Primary outcome
Scoliosis	A New Spinal Brace Design Concept for the Treatment of Adolescent Idiopathic Scoliosis	2018	3D-printed brace	NCT03365804	Canada	Single-blind RCT	Evaluated the in-brace Cobb angle on a radiograph
	Experimental Evaluation of Back Braces for the Treatment of Spinal Deformity Produced With 3D Printing Technology	2019	3D-printed brace	NCT04282408	Italy	Open-label, single-arm trial	Comfort and safety evaluation by using surveys
Distal radius fractures	Acceptability and Safety of 3D Printed Wrist-based Splints	2021	3D-printed splint	NCT05075135	Switzerland	Open-label RCT	Change in "Patient-Reported Splint Evaluation Questionnaire (PRSEQ)"
	A Clinical Comparison of Patient-Specific 3D Printed Splints Versus Conventional Splints in the Treatment of Distal Radius Fractures.	2023	3D-printed splint	NCT05902442	Netherlands	Open-label, single-arm trial	D-QUEST; CSD-OPUS; EQ-5D VAS; semi-structured interview
	Overnight and In-house 3D-printed Patient-specific Casts for Non-operative Treatment of Distal Radius Fractures	2020	3D-printed cast	NCT05346926	Switzerland	Open-label RCT	Score of modified patient satisfaction questionnaire; score of clinical effectiveness questionnaire
Sarcopenia	Foot Core Exercise Program on Balance Control and Walking in Aged Sarcopenia	2022	3D-printed foot muscle-strengthening device	NCT05750888	Taiwan	Quadruple-blind RCT	Sonographic imaging for the cross-sectional area of muscles; sonographic imaging for the width and thickness of muscles; balance test for standing posture for area of sway trajectory in CoP and CoM; balance test for standing posture for the velocity of sway trajectory in CoP and CoM; balance test for standing posture for the length of sway trajectory in CoP; functional walking test for spatiotemporal parameters; functional walking test for joint kinematics in the lower limb; functional walking test for joint kinetics in the lower limb; clinical questionnaires for assessment of physical capacity in the elderly; clinical questionnaires for assessment of functional capacity and falling condition in the elderly; clinical questionnaires for assessment of functional capacity and strength condition in the elderly

(Continued...)

Table 3. Continue...

Application	Study title	Year	Type	Registration	Country	Design	Primary outcome
ACL injury	Playmaker 3D Printed Knee Extender	2022	3D-printed knee extender	NCT05878652	United States	Triple-blind RCT	Knee extension range of motion; time to achieve full knee extension
Patient education	3D Printed Models in Mohs Micrographic Surgery	2018	3D-printed model	NCT03461965	United States	Open-label RCT	Percent of correct and incorrect Mohs quiz responses
Flat feet	Validation of Plantar Orthoses for Abnormal Plantar Arch Using a New Non-invasive Clinical Imaging System	2021	3D-printed orthosis	NCT05163418	Canada	Open-label, non-randomized trial	Change from baseline in the body's postural symmetry index at 2 months; change from baseline in the body's postural symmetry index at 6 months; change from baseline in the body's postural symmetry index at 12 months
Flexible flatfoot	The Effect of Customized Insoles on Biomechanics and Pain in Patients with Functional Flatfoot	2020	3D-printed orthosis	NCT04381039	Taiwan	Open-label, single-arm trial	F-scan system; visual analogue scale; foot function index
Hallux valgus	Dimensional Validation of the Hallux Valgus Orthosis	2021	3D-printed orthosis	NCT05163431	Canada	Open-label, single-arm trial	Change in big toe deviation angle during gait at 1 month; change in pain at 1 month; change in comfort at 1 month
Hand disease	New 3D Printed Wrist Orthosis	2022	3D-printed orthosis	NCT05597930	Canada	Open-label, randomized, crossover trial	Change in pain during treatment from baseline at day 14
Hand injuries and disorders	3D Printed Made to Measure Splints for Hand Patients	2019	3D-printed splint	NCT04306796	Switzerland	Open-label RCT	Change in patient comfort and satisfaction
	Three-dimensional Printed Hand Orthoses	2022	3D-printed orthosis	NCT05320211	Netherlands	Open-label, single-arm trial	Change from baseline in performance of ADL on the custom short form of the DF-PROMIS-UE at 4 months post-intervention
Orthopedic disorder	3D-printing and Access to Tele Rehabilitation	2018	3D-printed orthosis	NCT05947630	Mali; Niger; Togo	Open-label, randomized, crossover trial	10-m walk test; knee angle test; ankle angle test
Chronic disease	A 3D Printed Assistive Technology Intervention	2017	3D-printed pillbox	NCT03353038	United States	Open-label, single-arm trial	Incidence of treatment-emergent adverse events; QUEST2.0; ARMS
	Impact of Pillboxes on Medical Adherence	2019	3D-printed pillbox	NCT03861845	United States	Double-blind RCT	Medication adherence at 1 month; satisfaction with pillbox at 1 month; number of participants who completed the study

(Continued...)

Table 3. Continue...

Application	Study title	Year	Type	Registration	Country	Design	Primary outcome
Upper limb amputation below elbow	Redesign, Implementation, and Evaluation of the Effectiveness of the Aktio Myoelectric Prosthesis	2022	3D-printed prosthesis	NCT05510193	Colombia	Open-label, randomized, crossover trial	Functional status
Hand arthritis	Novel Splinting Technique Using 3D Models	2022	3D-printed splint	NCT05351060	United States	Open-label, single-arm trial	Change in range of motion of the hand (measured with a goniometer); change in range of motion of the hand (measured with a goniometer)
Hypermobility of interphalangeal joints	Splint Users' Satisfaction and Functional Status with Custom Finger Splints	2023	3D-printed splint	NCT05903391	United States	Single-blind, non-randomized controlled trial	Modified Orthotics and Prosthetics User Survey - Satisfaction with Device; Modified Orthotics and Prosthetics User Survey - Functional Status
Thumb osteoarthritis	3D-Printed Hand Orthosis Versus Thermoplastic Orthosis	2023	3D-printed splint	NCT05896410	Canada	Single-blind, randomized, crossover trial	Feasibility and general useability

Abbreviations: ACL, anterior cruciate ligament; ADL, activity of daily living; ARMS, adherence to refills and medications scale; CoM, center of mass; CoP, center of pressure; DF-PROMIS-UE, Dutch-Flemish Patient-Reported Outcomes Measurement Information System – Upper Extremity; QUEST2.0, Quebec User Evaluation of Satisfaction with Assistive Technology; RCT, randomized controlled trial.

Furthermore, we summarized the current landscape of clinical applications for 3D printing and discussed the clinical translation challenges of 3D printing. 3D printing technology can be seamlessly integrated with the protocols, principles, and technologies of both regenerative and rehabilitation medicine, driving a technological revolution in regenerative rehabilitation.

Looking ahead, the application of 3D printing in musculoskeletal disease treatment holds great promise for redefining regenerative rehabilitation interventions. Firstly, exploring the combination of 3D printing with novel physical therapies, such as pulsed electromagnetic fields (PEMFs), presents a holistic approach to systematic rehabilitation therapy. PEMFs are a bioelectromagnetic stimulation for bone and cartilage repair,[120–122] enhancing the growth and healing processes of the engineered cartilage.[123] Hence, 3D-printed products with novel physical properties can be formulated and utilized to enhance the overall rehabilitation effect in patients.[124] Furthermore, the integration of 3D printing with artificial intelligence (AI) can improve efficiency and accuracy. AI algorithms optimizing design processes, predicting material behaviors, and streamlining workflow showcase the potential to elevate 3D printing to new heights, fostering a seamless integration into routine clinical practice. In 4D printing, which incorporates "time" as the fourth dimension with 3D bioprinting, preprogramming smart materials enables the production of structures that dynamically react to external stimuli, adjusting their characteristics and functions for specific applications.[125,126] Moreover, AI has the potential to propel the transition from 4D printing to 5D printing, where AI will represent the fifth dimension.[125]

In summation, 3D printing is a rapidly advancing research field in regenerative rehabilitation for musculoskeletal disease treatment, demonstrating great potential for innovative approaches to evaluation, diagnosis, and treatment. With advances in new technologies and materials, we believe that 3D printing is crucial for accelerating the rehabilitation process and improving patients' quality of life.

Acknowledgments

None.

Funding

This work was supported by the National Natural Science Foundation of China (82302884), the Department of Science and Technology of Sichuan Province (2022JDKP0015), the Sichuan University Education Foundation (23JZH002), and the Sichuan University Postdoctoral Interdisciplinary Innovation Fund (JCXK2215).

Conflict of interest

Ma-Ling Gou is an Editorial Board Member of this journal but was not in any way involved in the editorial and peer-review process conducted for this paper, directly or indirectly. Separately, other authors declared that they have no known competing financial interests or personal relationships that could have influenced the work reported in this paper.

Author contributions

Conceptualization: All authors
Supervision: Hong-Chen He, Ma-Ling Gou
Writing – Original Draft: Ai-Jia Guan, Yong-Chao Zhao, Xiao-Na Xiang
Writing – Review & Editing: Ai-Jia Guan, Yong-Chao Zhao, Xiao-Na Xiang

Ethics approval and consent to participate

Not applicable.

Consent for publication

Not applicable.

Availability of data

Not applicable.

References

1. Briggs AM, Cross MJ, Hoy DG, et al. Musculoskeletal health conditions represent a global threat to healthy aging: a report for the 2015 World Health Organization World Report on Ageing and Health. *Gerontologist*. 2016;56:S243-S255. doi: 10.1093/geront/gnw002
2. Zheng YL, Song G, Guo JB. Interactions among lncRNA/circRNA, miRNA, and mRNA in musculoskeletal degenerative diseases. *Front Cell Dev Biol*. 2021;9:753931. doi: 10.3389/fcell.2021.753931
3. Cieza A, Causey K, Kamenov K, et al. Global estimates of the need for rehabilitation based on the Global Burden of Disease study 2019: a systematic analysis for the Global Burden of Disease Study 2019. *Lancet*. 2020;396(10267):2006-2017. doi: 10.1016/S0140-6736(20)32340-0
4. Collins NJ, Hart HF, Mills KAG. Osteoarthritis year in review 2018: rehabilitation and outcomes. *Osteoarthritis Cartilage*. 2019;27(3):378-391. doi: 10.1016/j.joca.2018.11.010
5. Zhu SY, Wang Z, Liang Q, et al. Chinese guidelines for the rehabilitation treatment of knee osteoarthritis: an CSPMR evidence-based practice guideline. *J Evid-Based Med*. 2023;16(3):376-393. doi: 10.1111/jebm.12555
6. Cavanaugh JT, Killian SE. Rehabilitation following meniscal repair. *Curr Rev Musculoskelet Med*. 2012; 5(1):46-58. doi: 10.1007/s12178-011-9110-y
7. Ambrosio F, Russell A. Regenerative rehabilitation: a call to action. *J Rehabil Res Dev*. 2010;47(3):Xi-Xv. doi: 10.1682/Jrrd.2010.03.0021
8. Rando TA, Ambrosio F. Regenerative rehabilitation: applied biophysics meets stem cell therapeutics. *Cell Stem Cell*. 2018;22(3):306-309. doi: 10.1016/j.stem.2018.02.003
9. Liaw CY, Guvendiren M. Current and emerging applications of 3D printing in medicine. *Biofabrication*. 2017; 9(2):024102. doi: 10.1088/1758-5090/aa7279
10. Zhang JM, Hu QP, Wang S, et al. Digital light processing based three-dimensional printing for medical applications. *Int J Bioprinting*. 2020;6(1):12-27. doi: 10.18063/ijb.v6i1.242
11. Murphy SV, Atala A. 3D bioprinting of tissues and organs. *Nat Biotechnol*. 2014;32(8):773-785. doi: 10.1038/nbt.2958
12. Trucco D, Sharma A, Manferdini C, et al. Modeling and fabrication of silk fibroin–gelatin-based constructs using extrusion-based three-dimensional bioprinting. *ACS Biomater Sci Eng*. 2021;7(7):3306-3320. doi: 10.1021/acsbiomaterials.1c00410
13. Zhou ZY, Cui J, Wu SL, et al. Silk fibroin-based biomaterials for cartilage/osteochondral repair. *Theranostics*. 2022;12(11):5103-5124. doi: 10.7150/thno.74548
14. Pinto RMR, Faraji M, Vinayakumar KB. A 3D-printed printhead: custom inkjet dispenser for medium viscosity fluids. *Adv Eng Mater*. 2024;26(12):14. doi: 10.1002/adem.202400205
15. Li XD, Liu BX, Pei B, et al. Inkjet bioprinting of biomaterials. *Chem Rev*. 2020;120(19):10596-10636. doi: 10.1021/acs.chemrev.0c00008
16. Rasaki SA, Xiong DY, Xiong SF, et al. Photopolymerization-based additive manufacturing of ceramics: a systematic review. *J Adv Ceram*. 2021;10(3):442-471. doi: 10.1007/s40145-021-0468-z
17. Zhang J, Hu Q, Wang S, et al. Digital light processing based three-dimensional printing for medical applications. *Int J Bioprint*. 2020;6(1):242. doi: 10.18063/ijb.v6i1.242
18. Zhang P, Gao Q, Yu KC, et al. Investigation on the temperature control accuracy of a print head for extrusion 3D printing and its improved design. *Biomedicines*. 2022; 10(6):13. doi: 10.3390/biomedicines10061233

19. Grivet-Brancot A, Boffito M, Ciardelli G. Use of polyesters in fused deposition modeling for biomedical applications. *Macromol Biosci*. 2022;22(10):29. doi: 10.1002/mabi.202200039

20. Tabriz AG, Kuofie H, Scoble J, et al. Selective laser sintering for printing pharmaceutical dosage forms. *J Drug Deliv Sci Technol*. 2023;86:13. doi: 10.1016/j.jddst.2023.104699

21. Han W, Kong LB, Xu M. Advances in selective laser sintering of polymers. *Int J Extreme Manuf*. 2022;4(4):37. doi: 10.1088/2631-7990/ac9096

22. Wu M, Zheng K, Li W, et al. Nature-inspired strategies for the treatment of osteoarthritis. *Adv Funct Mater*. 2023;34(4):2305603. doi: 10.1002/adfm.202305603

23. Baniasadi H, Madani Z, Ajdary R, et al. Ascorbic acid-loaded polyvinyl alcohol/cellulose nanofibril hydrogels as precursors for 3D printed materials. *Mater Sci Eng C-Mater Biol Appl*. 2021;130:12. doi: 10.1016/j.msec.2021.112424

24. Caprioli M, Roppolo I, Chiappone A, et al. 3D-printed self-healing hydrogels via digital light processing. *Nat Commun*. 2021;12(1):9. doi: 10.1038/s41467-021-22802-z

25. Kumar A, Han SS. PVA-based hydrogels for tissue engineering: a review. *Int J Polym Mater Polym Biomat*. 2017;66(4):159-182. doi: 10.1080/00914037.2016.1190930

26. Gu XC, Cheng HG, Lu XY, et al. Plant-based biomass/polyvinyl alcohol gels for flexible sensors. *Chem-Asian J*. 2023;18(18):18. doi: 10.1002/asia.202300483

27. Tümer EH, Erbil HY. Extrusion-based 3D printing applications of PLA composites: a review. *Coatings*. 2021;11(4):42. doi: 10.3390/coatings11040390

28. Murab S, Herold S, Hawk T, et al. Advances in additive manufacturing of polycaprolactone based scaffolds for bone regeneration. *J Mat Chem B*. 2023;11(31):7250-7279. doi: 10.1039/d2tb02052a

29. Yang XJ, Wang YT, Zhou Y, et al. The application of polycaprolactone in three-dimensional printing scaffolds for bone tissue engineering. *Polymers*. 2021;13(16):19. doi: 10.3390/polym13162754

30. Hamedi E, Vahedi N, Sigaroodi F, et al. Recent progress of bio-printed PEGDA-based bioinks for tissue regeneration. *Polym Adv Technol*. 2023;34(11):3505-3517. doi: 10.1002/pat.6164

31. Liang WQ, Zhou C, Zhang HW, et al. Recent advances in 3D printing of biodegradable metals for orthopaedic applications. *J Biol Eng*. 2023;17(1):24. doi: 10.1186/s13036-023-00371-7

32. Martinelli A, Nitti A, Po RC, et al. 3D printing of layered structures of metal-ionic polymers: recent progress, challenges and opportunities. *Materials*. 2023; 16(15):16. doi: 10.3390/ma16155327

33. Velásquez-García LF, Kornbluth Y. Biomedical applications of metal 3D printing. In: Yarmush ML, ed. Annual Review of Biomedical Engineering, vol. 23. Palo Alto: Annual Reviews 2021:307-338. doi: 10.1146/annurev-bioeng-082020-032402

34. Ni J, Ling H, Zhang S, et al. Three-dimensional printing of metals for biomedical applications. *Mater Today Bio*. 2019;3:18. doi: 10.1016/j.mtbio.2019.100024

35. Yuan XY, Xu YB, Lu TL, et al. Enhancing the bioactivity of hydroxyapatite bioceramic via encapsulating with silica-based bioactive glass sol. *J Mech Behav Biomed Mater*. 2022;128:9. doi: 10.1016/j.jmbbm.2022.105104

36. Liu MY, Wang YE, Liu XW, et al. Comprehensive review on fabricating bioactive ceramic bone scaffold using vat photopolymerization. *ACS Biomater Sci Eng*. 2023;9(6):3032-3057. doi: 10.1021/acsbiomaterials.3c00051

37. Vennam S, Vijayasankar KN, Pati F. 3D printed personalized assistive devices: a material, technique, and medical condition perspective. *Appl Mater Today*. 2024;40:15. doi: 10.1016/j.apmt.2024.102403

38. Li JQ, Chen SG, Shang X, et al. Research progress of rehabilitation orthoses based on 3D printing technology. *Adv Mater Sci Eng*. 2022;2022:16. doi: 10.1155/2022/5321570

39. Buchner TJK, Rogler S, Weirich S, et al. Vision-controlled jetting for composite systems and robots. *Nature*. 2023;623(7987):522-530. doi: 10.1038/s41586-023-06684-3

40. Wang B, Feng CW, Pan JY, et al. The effect of 3D printing metal materials on osteoporosis treatment. *Biomed Res Int*. 2021;2021:7. doi: 10.1155/2021/9972867

41. Wu D, Zhao XS, Xie JH, et al. Physical modulation of mesenchymal stem cell exosomes: a new perspective for regenerative medicine. *Cell Prolif*. 2024;57(8):16. doi: 10.1111/cpr.13630

42. Liu S, Zhang LG, Li Z, et al. Materials-mediated in situ physical cues for bone regeneration. *Adv Funct Mater*. 2024;34(1):32. doi: 10.1002/adfm.202306534

43. Shuai CJ, Yang WJ, Peng SP, et al. Physical stimulations and their osteogenesis-inducing mechanisms. *Int J Bioprinting*. 2018;4(2):20. doi: 10.18063/IJB.v4i2.138

44. Huang X, Das R, Patel A, et al. Physical Stimulations for Bone and Cartilage Regeneration. *Regen Eng Transl Med*. 2018;4(4):216-237. doi: 10.1007/s40883-018-0064-0

45. Liang WX, Liang BB, Yan KC, et al. Low-intensity pulsed ultrasound: a physical stimulus with immunomodulatory and anti-inflammatory potential. *Ann Biomed Eng*. 2024;52(8):1955-1981. doi: 10.1007/s10439-024-03523-y

46. Luo TY, Tan BW, Liao JF, et al. A review on external physical stimuli with biomaterials for bone repair. *Chem Eng J*. 2024;496:18. doi: 10.1016/j.cej.2024.153749

47. Axtell LA, Yasuda YL. Assistive devices and home modifications in geriatric rehabilitation. *Clin Geriatr Med*. 1993;9(4):803-821. doi: 10.1016/S0749-0690(18)30378-1

48. Nyberg EL, Farris AL, Hung B, et al. 3D-printing technologies for craniofacial rehabilitation, reconstruction, and regeneration. *Ann Biomed Eng*. 2017;45(1):45-57. doi: 10.1007/s10439-016-1668-5

49. Cuellar JS, Smit G, Breedveld P, et al. Functional evaluation of a non-assembly 3D-printed hand prosthesis. *P I Mech Eng H*. 2019;233(11):1122-1131. doi: 10.1177/0954411919874523

50. Rumfelt S, Mintz T, Brooks A. Rehabilitation and orthoses for adult hand fractures. In: Abzug JM, Gaston RG, Osterman AL, et al., eds. Pediatric and Adult Hand Fractures. Cham: Springer International Publishing; 2023: 389-413. doi: 10.1007/978-3-031-32072-9_22

51. Walker KJ, Przestrzelski BT, Kaluf B, et al. Novel 3D-printed foot orthoses with variable hardness: a comfort comparison to traditional orthoses. *Med Eng Phys*. 2023;115:103978. doi: 10.1016/j.medengphy.2023.103978

52. Xu GS, Gao L, Tao K, et al. Three-dimensional-printed upper limb prosthesis for a child with traumatic amputation of right wrist: a case report. *Medicine*. 2017;96(52):5. doi: 10.1097/md.0000000000009426

53. Dombroski CE, Balsdon MER, Froats A. The use of a low cost 3D scanning and printing tool in the manufacture of custom-made foot orthoses: a preliminary study. *BMC Res Notes*. 2014;7(1):443. doi: 10.1186/1756-0500-7-443

54. Silva K, Rand S, Cancel D, et al. Three-dimensional (3-D) printing: a cost-effective solution for improving global accessibility to prostheses. *Pm&R*. 2015;7(12):1312-1314. doi: 10.1016/j.pmrj.2015.06.438

55. Stout A, Friedly J, Standaert CJ. Systemic absorption and side effects of locally injected glucocorticoids. *Pm&R*. 2019;11(4):409-419. doi: 10.1002/pmrj.12042

56. Majrashi M, Kotowska A, Scurr D, et al. Sustained release of dexamethasone from 3D-printed scaffolds modulates macrophage activation and enhances osteogenic differentiation. *ACS Appl Mater Interfaces*. 2023;15(49):56623-56638. doi: 10.1021/acsami.3c09774

57. Liao CD, Chen HC, Huang MH, et al. Comparative efficacy of intra-articular injection, physical therapy, and combined treatments on pain, function, and sarcopenia indices in knee osteoarthritis: a network meta-analysis of randomized controlled trials. *Int J Mol Sci*. 2023;24(7):24. doi: 10.3390/ijms24076078

58. Park YB, Ha CW, Lee CH, et al. Cartilage regeneration in osteoarthritic patients by a composite of allogeneic umbilical cord blood-derived mesenchymal stem cells and hyaluronate hydrogel: results from a clinical trial for safety and proof-of-concept with 7 years of extended follow-up. *Stem Cells Transl Med*. 2017;6(2):613-621. doi: 10.5966/sctm.2016-0157

59. Rim YA, Nam Y, Ju JH. The role of chondrocyte hypertrophy and senescence in osteoarthritis initiation and progression. *Int J Mol Sci*. 2020;21(7):2358. doi: 10.3390/ijms21072358

60. Fu LL, Li L, Bian QY, et al. Cartilage-like protein hydrogels engineered via entanglement. *Nature*. 2023;618(7966):740-747. doi: 10.1038/s41586-023-06037-0

61. Cho Y, Jeong S, Kim H, et al. Disease-modifying therapeutic strategies in osteoarthritis: current status and future directions. *Exp Mol Med*. 2021;53(11):1689-1696. doi: 10.1038/s12276-021-00710-y

62. Grässel S, Aszodi A. Osteoarthritis and cartilage regeneration: focus on pathophysiology and molecular mechanisms. *Int J Mol Sci*. 2019;20(24):6156. doi: 10.3390/ijms20246156

63. Schroeppel JP, Crist JD, Anderson HC, et al. Molecular regulation of articular chondrocyte function and its significance in osteoarthritis. *Histol Histopathol*. 2011;26(3):377-394. doi: 10.14670/HH-26.377

64. Li Q, Yu H, Zhao F, et al. 3D printing of microenvironment-specific bioinspired and exosome-reinforced hydrogel scaffolds for efficient cartilage and subchondral bone regeneration. *Adv Sci*. 2023;10(26):2303650. doi: 10.1002/advs.202303650

65. Jiang GY, Li SH, Yu K, et al. A 3D-printed PRP-GelMA hydrogel promotes osteochondral regeneration through M2 macrophage polarization in a rabbit model. *Acta Biomater*. 2021;128:150-162. doi: 10.1016/j.actbio.2021.04.010

66. Zhang H, Huang H, Hao G, et al. 3D printing hydrogel scaffolds with nanohydroxyapatite gradient to effectively repair osteochondral defects in rats. *Adv Funct Mater*. 2020;31(1):2006697. doi: 10.1002/adfm.202006697

67. Sardroud HA, Chen XB, Eames BF. Applied compressive strain governs hyaline-like cartilage versus fibrocartilage-like ECM produced within hydrogel constructs. *Int J Mol Sci*. 2023;24(8):17.
doi: 10.3390/ijms24087410

68. Gong YP, Wang F, Al-Furjan MSH, et al. Experimental investigation and optimal 3d bioprinting parameters of SA-Gel porous cartilage scaffold. *Appl Sci-Basel*. 2020;10(3):768.
doi: 10.3390/app10030768

69. Shojarazavi N, Mashayekhan S, Pazooki H, et al. Alginate/cartilage extracellular matrix-based injectable interpenetrating polymer network hydrogel for cartilage tissue engineering. *J Biomater Appl*. 2021;36(5):803-817.
doi: 10.1177/08853282211024020

70. Ma FB, Ge YM, Liu N, et al. fabrication of a composite hydrogel with tunable mechanical properties for cartilage tissue engineering. *J Mat Chem B*. 2019;7(15):2463-2473.
doi: 10.1039/c8tb01331d

71. Deng CX, Yang J, He HT, et al. 3D bio-printed biphasic scaffolds with dual modification of silk fibroin for the integrated repair of osteochondral defects. *Biomater Sci*. 2021;9(14):4891-4903.
doi: 10.1039/d1bm00535a

72. Sadeghianmaryan A, Naghieh S, Yazdanpanah Z, et al. Fabrication of chitosan/alginate/hydroxyapatite hybrid scaffolds using 3D printing and impregnating techniques for potential cartilage regeneration. *Int J Biol Macromol*. 2022;204:62-75.
doi: 10.1016/j.ijbiomac.2022.01.201

73. Cheng K, Xia P, Lin Q, et al. Effects of low-intensity pulsed ultrasound on integrin-FAK-PI3K/Akt mechanochemical transduction in rabbit osteoarthritis chondrocytes. *Ultrasound Med Biol*. 2014;40(7):1609-1618.
doi: 10.1016/j.ultrasmedbio.2014.03.002

74. Prasopthum A, Deng ZX, Khan IM, et al. Three dimensional printed degradable and conductive polymer scaffolds promote chondrogenic differentiation of chondroprogenitor cells. *Biomater Sci*. 2020;8(15):4287-4298.
doi: 10.1039/d0bm00621a

75. Gee SM, Posner M. Meniscus anatomy and basic science. *Sports Med Arthrosc*. 2021;29(3):E18-E23.
doi: 10.1097/Jsa.0000000000000327

76. Makris EA, Hadidi P, Athanasiou KA. The knee meniscus: structure–function, pathophysiology, current repair techniques, and prospects for regeneration. *Biomaterials*. 2011;32(30):7411-7431.
doi: 10.1016/j.biomaterials.2011.06.037

77. Li L, Yang LF, Zhang KJ, et al. Three-dimensional finite-element analysis of aggravating medial meniscus tears on knee osteoarthritis. *J Orthop Transl.* 2020; 20:47-55.
doi: 10.1016/j.jot.2019.06.007

78. Tarafder S, Gulko J, Kim D, et al. Effect of dose and release rate of CTGF and TGFβ3 on avascular meniscus healing. *J Orthop Res*. 2019;37(7):1555-1562.
doi: 10.1002/jor.24287

79. Pauli C, Grogan SP, Patil S, et al. Macroscopic and histopathologic analysis of human knee menisci in aging and osteoarthritis. *Osteoarthritis Cartilage*. 2011;19(9):1132-1141.
doi: 10.1016/j.joca.2011.05.008

80. Murphy CA, Garg AK, Silva-Correia J, et al. The meniscus in normal and osteoarthritic tissues: facing the structure property challenges and current treatment trends. *Annu Rev Biomed Eng*. 2019;21(1):495-521.
doi: 10.1146/annurev-bioeng-060418-052547

81. Wang B, Barceló X, Von Euw S, et al. 3D printing of mechanically functional meniscal tissue equivalents using high concentration extracellular matrix inks. *Mater Today Bio*. 2023;20:12.
doi: 10.1016/j.mtbio.2023.100624

82. Gunja NJ, Huey DJ, James RA, et al. Effects of agarose mould compliance and surface roughness on self-assembled meniscus-shaped constructs. *J Tissue Eng Regen Med*. 2009;3(7):521-530.
doi: 10.1002/term.191

83. Jian Z, Zhuang T, Qinyu T. 3D bioprinting of a biomimetic meniscal scaffold for application in tissue engineering. *Bioact Mater*. 2021;6(6):1711-1726.
doi: 10.1016/j.bioactmat.2020.11.027

84. Zhang Q, Xu Z, Zhang X, et al. 3D printed high-strength supramolecular polymer hydrogel-cushioned radially and circumferentially oriented meniscus substitute. *Adv Funct Mater*. 2022;32(23):2200360.
doi: 10.1002/adfm.202200360

85. Chevrier A, Nelea M, Hurtig MB, et al. Meniscus structure in human, sheep, and rabbit for animal models of meniscus repair. *J Orthop Res*. 2009;27(9):1197-1203.
doi: 10.1002/jor.20869

86. Cheung HS. Distribution of Type-I, Type-Ii, Type-Iii, and Type-V in the pepsin solubilized collagens in bovine menisci. *Connect Tissue Res*. 1987;16(4):343-356.
doi: 10.3109/03008208709005619

87. Yan WQ, Maimaitimin M, Wu Y, et al. Meniscal fibrocartilage regeneration inspired by meniscal maturational and regenerative process. *Sci Adv.* 2023;9(45):eadg8138.
doi: 10.1126/sciadv.adg8138

88. Chae S, Lee S-S, Choi Y-J, et al. 3D cell-printing of biocompatible and functional meniscus constructs using meniscus-derived bioink. *Biomaterials*. 2021;267:120466.
doi: 10.1016/j.biomaterials.2020.120466

89. Grogan SP, Duffy SF, Pauli C, et al. Gene expression profiles of the meniscus avascular phenotype: a guide for meniscus tissue engineering. *J Orthop Res*. 2018;36(7):1947-1958.
doi: 10.1002/jor.23864

90. Whitney NP, Lamb AC, Louw TM, et al. Integrin-mediated mechanotransduction pathway of low-intensity continuous ultrasound in human chondrocytes. *Ultrasound Med Biol*. 2012;38(10):1734-1743. doi: 10.1016/j.ultrasmedbio.2012.06.002

91. Babaei M, Jamshidi N, Amiri F, et al. Effects of low-intensity pulsed ultrasound stimulation on cell seeded 3D hybrid scaffold as a novel strategy for meniscus regeneration: an in vitro study. *J Tissue Eng Regen Med*. 2022;16(9):812-824. doi: 10.1002/term.3331

92. Ebner N, Sliziuk V, Scherbakov N, et al. Muscle wasting in ageing and chronic illness. *ESC Heart Fail*. 2015;2(2): 58-68. doi: 10.1002/ehf2.12033

93. Voet NBM, van der Kooi EL, Riphagen II, et al. Strength training and aerobic exercise training for muscle disease. *Cochrane Database Syst Rev*. 2013;(7):CD003907. doi: 10.1002/14651858.CD003907.pub4

94. Grogan BF, Hsu JR, Consortium STR. Volumetric muscle loss. *J Am Acad Orthop Surg*. 2011;19:S35-S37. doi: 10.5435/00124635-201102001-00007

95. Basurto IM, Passipieri JA, Gardner GM, et al. Photoreactive hydrogel stiffness influences volumetric muscle loss repair. *Tissue Eng Part A*. 2022;28(7-8):312-329. doi: 10.1089/ten.tea.2021.0137

96. Shayan M, Huang NF. Pre-clinical cell therapeutic approaches for repair of volumetric muscle loss. *Bioeng Basel*. 2020;7(3):97. doi: 10.3390/bioengineering7030097

97. Nakayama KH, Quarta M, Paine P, et al. Treatment of volumetric muscle loss in mice using nanofibrillar scaffolds enhances vascular organization and integration. *Commun Biol*. 2019;2(1):170. doi: 10.1038/s42003-019-0416-4

98. Eugenis I, Wu D, Rando TA. Cells, scaffolds, and bioactive factors: engineering strategies for improving regeneration following volumetric muscle loss. *Biomaterials*. 2021;278:121173. doi: 10.1016/j.biomaterials.2021.121173

99. Shen S, Chen MX, Guo WM, et al. Three dimensional printing-based strategies for functional cartilage regeneration. *Tissue Eng Part B Rev*. 2019;25(3):187-201. doi: 10.1089/ten.teb.2018.0248

100. Hwangbo H, Lee H, Jin EJ, et al. Bio-printing of aligned GelMa-based cell-laden structure for muscle tissue regeneration. *Bioact Mater*. 2022;8:57-70. doi: 10.1016/j.bioactmat.2021.06.031

101. Gokyer S, Yilgor E, Yilgor I, et al. 3D printed biodegradable polyurethaneurea elastomer recapitulates skeletal muscle structure and function. *ACS Biomater Sci Eng*. 2021;7(11):5189-5205. doi: 10.1021/acsbiomaterials.1c00703

102. Latroche C, Gitiaux C, Chrétien F, et al. Skeletal muscle microvasculature: a highly dynamic lifeline. *Physiology*. 2015;30(6):417-427. doi: 10.1152/physiol.00026.2015

103. Luo ZY, Tang GS, Ravanbakhsh H, et al. Vertical extrusion cryo(bio)printing for anisotropic tissue manufacturing. *Adv Mater*. 2022;34(12):2108931. doi: 10.1002/adma.202108931

104. Kim JH, Seol YJ, Ko IK, et al. 3D bioprinted human skeletal muscle constructs for muscle function restoration. *Sci Rep*. 2018;8(1):12307. doi: 10.1038/s41598-018-29968-5

105. Andarawis-Puri N, Flatow EL, Soslowsky LJ. Tendon basic science: development, repair, regeneration, and healing. *J Orthop Res*. 2015;33(6):780-784. doi: 10.1002/jor.22869

106. Zhang YJ, Lei TY, Tang CQ, et al. 3D printing of chemical-empowered tendon stem/progenitor cells for functional tissue repair. *Biomaterials*. 2021;271:120722. doi: 10.1016/j.biomaterials.2021.120722

107. Mccormick A, Charlton J, Fleming D. Assessing health needs in primary-care - morbidity study from general-practice provides another source of information. *Br Med J*. 1995;310(6993):1534. doi: 10.1136/bmj.310.6993.1534d

108. Murray MM. Current status and potential of primary ACL repair. *Clin Sports Med*. 2009;28(1):51-61. doi: 10.1016/j.csm.2008.08.005

109. Li CS, Wang J, Yang WA, et al. 3D-printed hydrogel particles containing PRP laden with TDSCs promote tendon repair in a rat model of tendinopathy. *J Nanobiotechnol*. 2023;21(1):177. doi: 10.1186/s12951-023-01892-5

110. Kim D, Kim G. Bioprinted hASC-laden cell constructs with mechanically stable and cell alignment cue for tenogenic differentiation. *Biofabrication*. 2023;15(4):045006. doi: 10.1088/1758-5090/ace740

111. Patel M, Amini MH. Management of acute rotator cuff tears. *Orthop Clin North Am*. 2022;53(1):69-76. doi: 10.1016/j.ocl.2021.08.003

112. Keener JD, Patterson BM, Orvets N, et al. Degenerative rotator cuff tears: refining surgical indications based on natural history data. *J Am Acad Orthop Surg*. 2019;27(5):156-165. doi: 10.5435/Jaaos-D-17-00480

113. Huang Y, He B, Wang L, et al. Bone marrow mesenchymal stem cell-derived exosomes promote rotator cuff tendon-bone healing by promoting angiogenesis and regulating M1 macrophages in rats. *Stem Cell Res Ther*. 2020;11(1):496. doi: 10.1186/s13287-020-02005-x

114. Rothrauff BB, Tuan RS. Cellular therapy in bone-tendon interface regeneration. *Organogenesis*. 2014;10(1):13-28. doi: 10.4161/org.27404

115. Cao Y, Yang SB, Zhao DY, et al. Three-dimensional printed multiphasic scaffolds with stratified cell-laden gelatin methacrylate hydrogels for biomimetic tendon-to-bone interface engineering. *J Orthop Transl*. 2020;23:89-100. doi: 10.1016/j.jot.2020.01.004

116. Gaffney LS, Davis ZG, Mora-Navarro C, et al. Extracellular matrix hydrogels promote expression of muscle-tendon junction proteins. *Tissue Eng Part A*. 2022;28(5-6):270-282. doi: 10.1089/ten.tea.2021.0070

117. Hou YB, Gao M, Gao JW, et al. 3D printed conformal strain and humidity sensors for human motion prediction and health monitoring via machine learning. *Adv Sci*. 2023;10(36):e2304132. doi: 10.1002/advs.202304132

118. Paterson TE, Hagis N, Boufidis D, et al. Monitoring of hand function enabled by low complexity sensors printed on textile. *Flex Print Electron*. 2022;7(3):035003. doi: 10.1088/2058-8585/ac7dd1

119. Chen RY, Pye JS, Li JR, et al. Multiphasic scaffolds for the repair of osteochondral defects: outcomes of preclinical studies. *Bioact Mater*. 2023;27:505-545. doi: 10.1016/j.bioactmat.2023.04.016

120. Caliogna L, Bina V, Brancato AM, et al. The Role of PEMFs on Bone Healing: An In Vitro Study. *Int J Mol Sci*. 2022;23(22):17. doi: 10.3390/ijms232214298

121. Lang S, Ma J, Gong S, et al. Pulse electromagnetic field for treating postmenopausal osteoporosis: a systematic review and meta-analysis of randomized controlled trials. *Bioelectromagnetics*. 2022;43(6):381-393. doi: 10.1002/bem.22419

122. Tong J, Chen ZY, Sun GH, et al. The efficacy of pulsed electromagnetic fields on pain, stiffness, and physical function in osteoarthritis: a systematic review and meta-analysis. *Pain Res Manag*. 2022;2022:9939891. doi: 10.1155/2022/9939891

123. Stefani RM, Barbosa S, Tan ARR, et al. Pulsed electromagnetic fields promote repair of focal articular cartilage defects with engineered osteochondral constructs. *Biotechnol Bioeng*. 2020;117(5):1584-1596. doi: 10.1002/bit.27287

124. Liang Q, Ma Y, Yao X, et al. Advanced 3D-printing bioinks for articular cartilage repair. *Int J Bioprinting*. 2022;8(3):511. doi: 10.18063/ijb.v8i3.511

125. Pugliese R, Regondi S. Artificial intelligence-empowered 3d and 4d printing technologies toward smarter biomedical materials and approaches. *Polymers*. 2022;14(14):2794. doi: 10.3390/polym14142794

126. Gao B, Yang QZ, Zhao X, et al. 4D bioprinting for biomedical applications. *Trends Biotechnol*. 2016;34(9):746-756. doi: 10.1016/j.tibtech.2016.03.004

ACCSCIENCE PUBLISHING

International Journal of Bioprinting

RESEARCH ARTICLE

Patient-specific design and fabrication of a trapeziometacarpal joint orthosis using a computed tomography image-based finite element model

Chan Beom Park[1†], Ji Sup Hwang[2†], Hyun Sik Gong[3*], and Hyung-Soon Park[1*]

[1]Department of Mechanical Engineering, Korea Advanced Institute of Science and Technology, Daejeon, South Korea

[2]Department of Orthopedic Surgery, Seoul National University Hospital, Seoul, South Korea

[3]Department of Orthopedic Surgery, Seoul National University College of Medicine, Seoul National University Bundang Hospital, Seongnam-si, South Korea

Abstract

Osteoarthritis (OA) of the trapeziometacarpal joint (TMCJ) can be caused by biomechanical wear on the articular cartilage due to high joint contact pressure, leading to severe pain in the thumb. Static orthoses have been applied for treatment in the early stages of OA to immobilize the TMCJ in a comfortable posture, but they do not account for contact pressure at the TMCJ. This oversight results in a high failure rate in pain relief during splinting. To ensure successful treatment, it is desirable to immobilize the TMCJ in an optimal posture that minimizes biomechanical joint contact pressure. This paper presents a patient-specific TMCJ orthosis design for the optimal posture, based on joint contact pressure obtained from a computed tomography image-based finite element (FE) TMCJ model. The estimated pressure at the subject-specific optimal posture averaged 2.8E-3 MPa, which was lower compared to the average pressure of 3.2E-2 MPa at the non-optimal but comfortable posture. To maintain this subject-specific optimal TMCJ posture, the orthosis was designed based on individual hand geometries with three-dimensional (3D) printing technology. The 3D-printed orthosis was preliminarily evaluated by patients with moderate to severe OA, and all patients reported pain relief. The visual analog scale and disabilities of arm, shoulder, and hand scores improved by 1.8 ± 1.7 and 13.1 ± 5.4, respectively. For orthotic treatment in clinics, the FE model-based TMCJ orthosis design for the subject-specific optimal posture can relieve pain caused by OA.

Keywords: 3D printing; Computed tomography; Finite element model; Orthosis; Osteoarthritis; Patient-specific; Trapeziometacarpal joint

†These authors contributed equally to this work

***Corresponding authors:**
Hyun Sik Gong
(hsgong@snu.ac.kr)

Hyung-Soon Park
(hyungspark@kaist.ac.kr)

Citation: Park CB, Hwang JS, Gong HS, Park HS. Patient-specific design and fabrication of a trapeziometacarpal joint orthosis using a computed tomography image-based finite element model. *Int J Bioprint*. 2025;11(1):233-245. doi: 10.36922/ijb.4635

Received: August 23, 2024
Revised: September 22, 2024
Accepted: October 7, 2024
Published Online: October 8, 2024

Copyright: © 2024 Author(s). This is an Open Access article distributed under the terms of the Creative Commons Attribution License, permitting distribution, and reproduction in any medium, provided the original work is properly cited.

Publisher's Note: AccScience Publishing remains neutral with regard to jurisdictional claims in published maps and institutional affiliations.

1. Introduction

Osteoarthritis (OA) of the trapeziometacarpal joint (TMCJ), the most proximal joint comprising the thumb, is found in 33% of the population older than 50 years of age.[1] The pathogenesis of TMCJ OA is still not completely understood. One significant cause

is laxity in the TMCJ ligaments, which induces structural instability and results in abnormally increased joint contact pressure on the articular cartilage of the TMCJ during movements.[1] This high joint contact pressure causes cartilage degeneration by biomechanical wear, leading to OA with pain.[2–4]

In the early stages of OA, a static orthosis can be applied for pain relief. Considering that high joint contact pressure, which can be estimated using reconstructed finite element (FE) joint models,[5–8] is a primary biomechanical factor causing OA,[2–4] it is desirable to design the orthosis to immobilize the TMCJ in an optimal posture that minimizes joint contact pressure. This optimal TMCJ posture would vary for each individual due to differences in TMCJ geometries. Immobilizing the TMCJ in the individual optimal posture determined using an FE joint model may prevent further biomechanical cartilage wear due to the minimized contact pressure, thus alleviating pain at rest during splinting. For OA treatment, various static orthoses[9–18] have been developed.

Conventional orthoses have limited capability in achieving pain relief, as they typically immobilize the TMCJ in postures determined solely based on subjective comfort reported by patients. Despite reports indicating positive effects on pain relief and functional improvement during splinting,[9–11,13–15,17,18] orthoses designed based on subjective comfort during a brief hospital visit can lead to failure in pain relief at rest during splinting.[19–21] Non-optimal TMCJ postures with high joint contact pressure can be misperceived as comfortable and used for splinting because subjective comfort, significantly correlated with pain,[22] is influenced by emotional factors.[22,23] Therefore, a patient-specific orthosis design based on joint contact pressure using an FE model of the TMCJ is required to ensure that the TMCJ is maintained in the subject-specific optimal posture for minimal pressure. In this orthosis design process, three-dimensional (3D) printing technology[15,16,24–28] facilitates the fabrication of orthoses with varying geometries.

The main objective of this paper is to present a novel 3D printing design process for a patient-specific TMCJ orthosis by using an individual FE model-based joint contact pressure analysis to maintain the TMCJ in the subject-specific optimal posture that minimizes the pressure for successful pain relief, which was verified through pain assessment in a clinical setup. The FE method (FEM) was utilized to determine the individual optimal posture with an FE TMCJ model constructed from computed tomography (CT) images, and the orthosis was fabricated based on individual TMCJ geometries with the aid of 3D printing to maintain the optimal TMCJ posture during splinting. The capability of the proposed orthosis in relieving pain at rest was preliminarily evaluated in patients with TMCJ OA. The study includes an overview of the orthosis design process and evaluation method, followed by an assessment of its significance.

2. Materials and methods

2.1. Overall design process

The orthosis is primarily designed to ensure successful pain relief at rest during splinting by allowing patients to maintain the optimal TMCJ posture (Figure 1). The design steps for making the orthosis comprise (i) FE modeling of the individual TMCJ model, (ii) FE simulation for the optimal posture, and (iii) fabrication of the orthosis via 3D printing.

The individual FE TMCJ model is constructed using CT images of the thumb affected by OA. The constructed FE TMCJ model comprises the metacarpal, the trapezium, attached cartilages, and two fixed rotation axes[29,30] of the metacarpal. The cartilage of the metacarpal is set to move around the fixed cartilage of the trapezium via two rotation axes—flexion-extension (F/E) and abduction-adduction (A/A)—determined based on a reported geometric relationship with the trapezium[31] (details denoted in **Section 2.2**). Since opposition postures were considered undesirable due to the resulting high joint contact pressure,[32] pronation-supination movements required for opposition were excluded from the model. The cartilage movement results in varying contact pressure between the two cartilages.

The optimal TMCJ posture is determined by analyzing joint contact pressure on the cartilages using the constructed individual FE TMCJ model and FEM. As the cartilages glide, the TMCJ posture changes and the joint contact pressure is analyzed at various TMCJ postures using the FEM. Subsequently, the optimal TMCJ posture, which minimizes joint contact pressure, is determined among these postures for each individual.

A static TMCJ orthosis is custom-fabricated for each individual to immobilize the TMCJ in the optimal posture. Prior to modeling the orthosis, a 3D hand model posed in the optimal posture is constructed from CT images. The orthosis is then modeled to cover the 3D hand model, and the modeled orthosis is rigidly 3D-printed. This design ensures that individuals can maintain the optimal posture during splinting.

2.2. FE modeling of the individual TMCJ

An individual thumb affected by OA was scanned using a Brilliance iCT 256 CT scanner (Philips Medical Systems, the Netherlands) to construct the FE TMCJ model. Three different postures were scanned (Figure 2A): "neutral,"

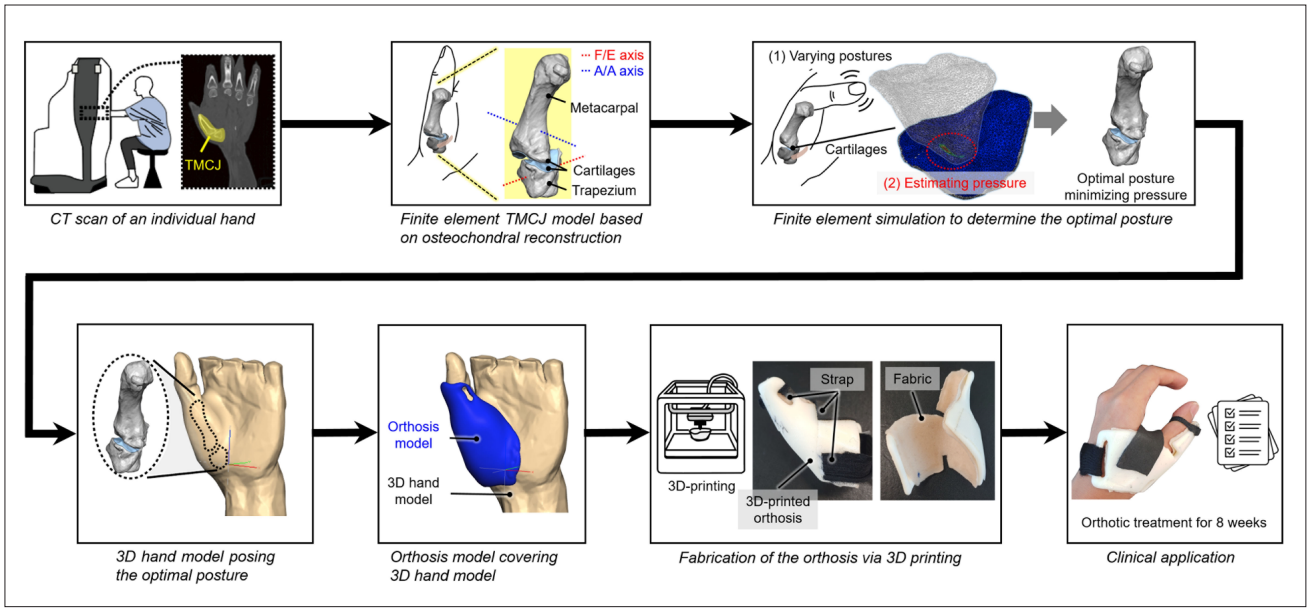

Figure 1. The design process used for the patient-specific TMCJ orthosis. The optimal posture that minimizes biomechanical joint contact pressure is determined for each individual using the FEM and an FE TMCJ model constructed from CT images. Subsequently, the orthosis is fabricated via 3D printing to enable patients to maintain the optimal posture during splinting. Abbreviations: A/A, abduction-adduction; CT, Computed tomography; F/E, Flexion-extension; FE, finite element; FEM, finite element method; TMCJ, trapeziometacarpal joint.

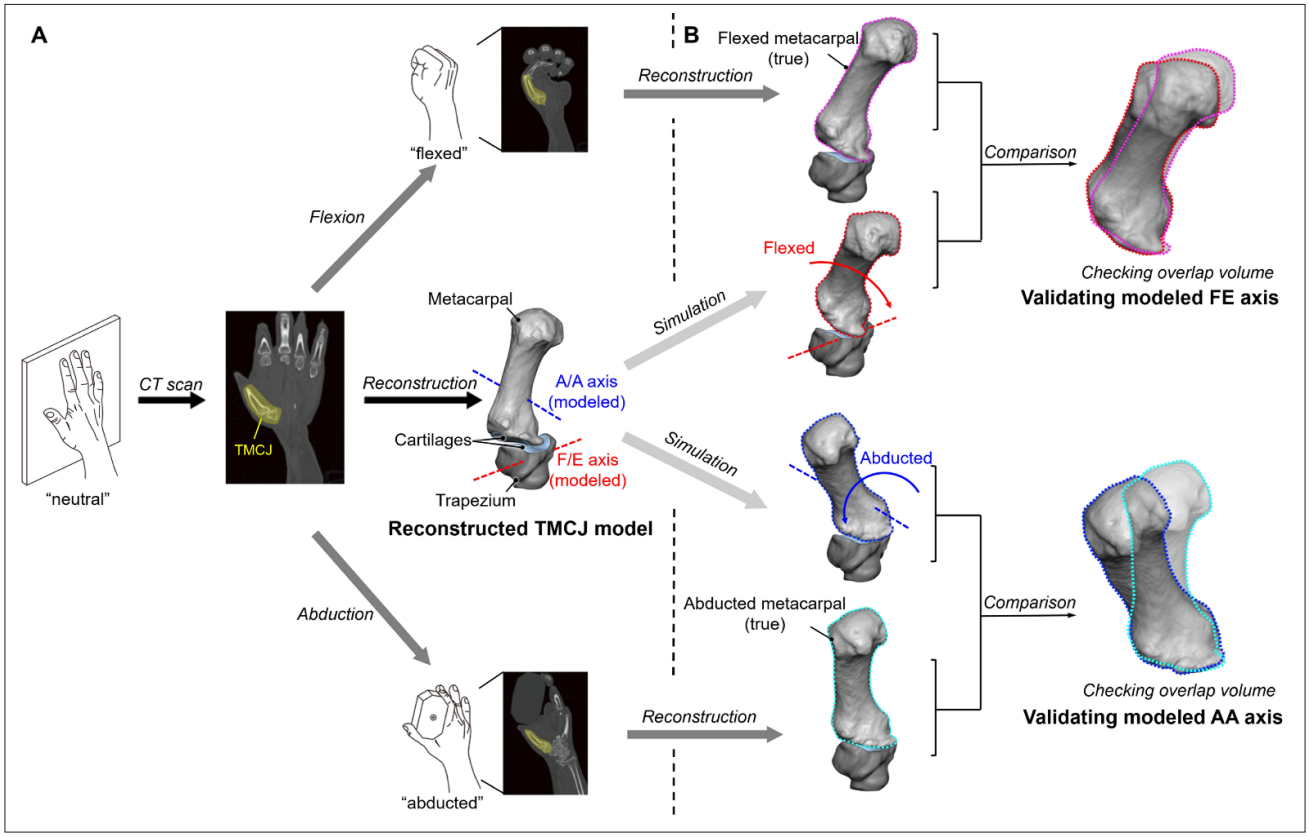

Figure 2. Construction of an individual FE TMCJ model. (A) The individual FE TMCJ model is constructed from CT images captured when the TMCJ is in the "neutral" posture. (B) The locations of determined rotation axes of the metacarpal are validated using the metacarpal reconstructed from CT images captured when the TMCJ is in the "flexed" and "abducted" postures. Abbreviations: A/A, abduction-adduction; CT, Computed tomography; F/E, Flexion-extension; FE, finite element; FEM, finite element method; TMCJ, trapeziometacarpal joint.

maintained in a fully extended posture by a flat object; "flexed," maintained in a thumb-in-fist position; and "abducted," maintained by holding a thick object. The following scanning protocol was used for the measurement: 120 kVp tube potential; 149 mAs tube current–time product; 128 × 0.625 mm section collimation; 0.5 ms rotation time; 0.4 pitch; 180 mm display field of view; pixel size of 0.3 × 0.3 mm; and 1-mm section thickness.

The individual FE TMCJ model was constructed using CT images. The metacarpal and the trapezium, along with their attached cartilages, were reconstructed from the CT images of the "neutral" posture using Mimics software (Materialise, Ltd, Belgium), obtaining articulating surface geometries of the cartilages. Due to the challenge in measuring the spatial thickness of thin cartilages using CT images,[33] the cartilages were reconstructed based on the surface geometries and the previously reported cartilage thickness from an *in vivo* study[2] using Geomagic Freeform software (3D Systems, Inc., United States of America [USA]). Note that these thickness values would not significantly affect FEM-based joint contact pressure analysis results, as joint contact pressure is estimated based on the indented distance from the measured articulating surfaces and their contact stiffness. The reconstructed metacarpal, trapezium, and cartilages were then imported into ABAQUS (version 6.14; Dassault Systèmes Simulia Corp., USA) software for FE analysis.

Locations of the rotation axes of the metacarpal were determined and fixed based on their geometric relationships with the trapezium.[29–31] To set the rotation axes, an origin of a global Cartesian coordinate was placed at the base of the trapezium with adjustment of its axes (+*x*, +*y*, and +*z*) respectively towards the palmar, radial, and distal directions.[31] The global Cartesian coordinate was then translated and rotated according to the reported Denavit–Hartenberg parameters,[31] and moved *z*-axes of the coordinates were respectively set as the F/E and A/A rotation axes.

The locations of rotation axes were validated using the reconstructed TMCJ from CT images of the "flexed" and "abducted" postures (Figure 2B). For the validation, it was confirmed whether the rotated metacarpal in the constructed FE TMCJ model overlapped with the metacarpal reconstructed from the CT images of the "flexed" and "abducted" postures. The overlap volume ratio was calculated as the volume of the overlap region divided by the volume of the reconstructed metacarpal from the "neutral" posture (**Equation I**). As it was reported that a structure reconstructed from CT images can have volume variation within ~8% of its volume,[34] it was calculated that a true rotation axis can result in a minimum overlap volume ratio of 85.2% by **Equation I**. Thus, the threshold for the overlap volume ratio was set as 80%, which was closed to the minimum of 85.2%. The global Cartesian coordinate located at the base of the trapezium was adjusted to ensure that the calculated overlap volume ratio exceeded the threshold. The rotation axes satisfying the threshold requirement were then used for the individual FE TMCJ model. Note that the rotation axes of the TMCJ were fixed based on the negligible translation of the metacarpal observed in CT images and reported on its kinematics with OA.[35,36]

$$Overlap\ volume\ ratio\ (\%) = \frac{Volume\ of\ the\ overlap\ region}{Volume\ of\ the\ metacarpal\ from\ "neutral"} \times 100 \quad (I)$$

2.3. FE simulation for the optimal posture

To obtain joint contact pressure at various TMCJ postures via FE simulation, it was necessary to define the material properties, boundary conditions, and contact properties of the cartilages. For the material properties, a Young's modulus of 1.12 MPa and a Poisson's ratio of 0.49 were used for the cartilages.[37] For the boundary conditions, assuming no deformation at the surfaces between the bones and the cartilages due to highly rigid bones compared to cartilages,[38] the distal aspect of the metacarpal cartilage was constrained by kinematic coupling to a reference point on the F/E rotation axis, with the proximal aspect of the trapezium cartilage fixed (Figure 3). For the contact properties between the cartilages, a friction coefficient of 0.002 and a contact stiffness of 250 kPa/mm were used,[39,40] with penalty friction formulation and linear pressure–overclosure relationship applied to define the tangential and normal contact behaviors, respectively. Note that a finite sliding formulation with a surface-to-surface discretization method was used to define contact interaction for FE analysis. Moreover, for the FE simulation, the free mesh algorithm in ABAQUS software was used to mesh the cartilages with 3D 10-node tetrahedral elements (C3D10H), resulting in an average of 37,884 elements and 60,148 nodes for each cartilage. The quality of this mesh was evaluated by aspect ratio, which was 1.83 ± 0.05 and considered acceptable as it was below 5.

The optimal TMCJ posture was determined by analyzing joint contact pressure in various TMCJ postures using the FEM with ABAQUS software. To enable users to perform daily activities after immobilizing the TMCJ, the optimal TMCJ posture was identified among postures that were abducted and flexed relative to the "neutral" posture. Therefore, the metacarpal cartilage in the FE TMCJ model was abducted and flexed via the determined A/A and F/E rotation axes under a static condition. Specifically,

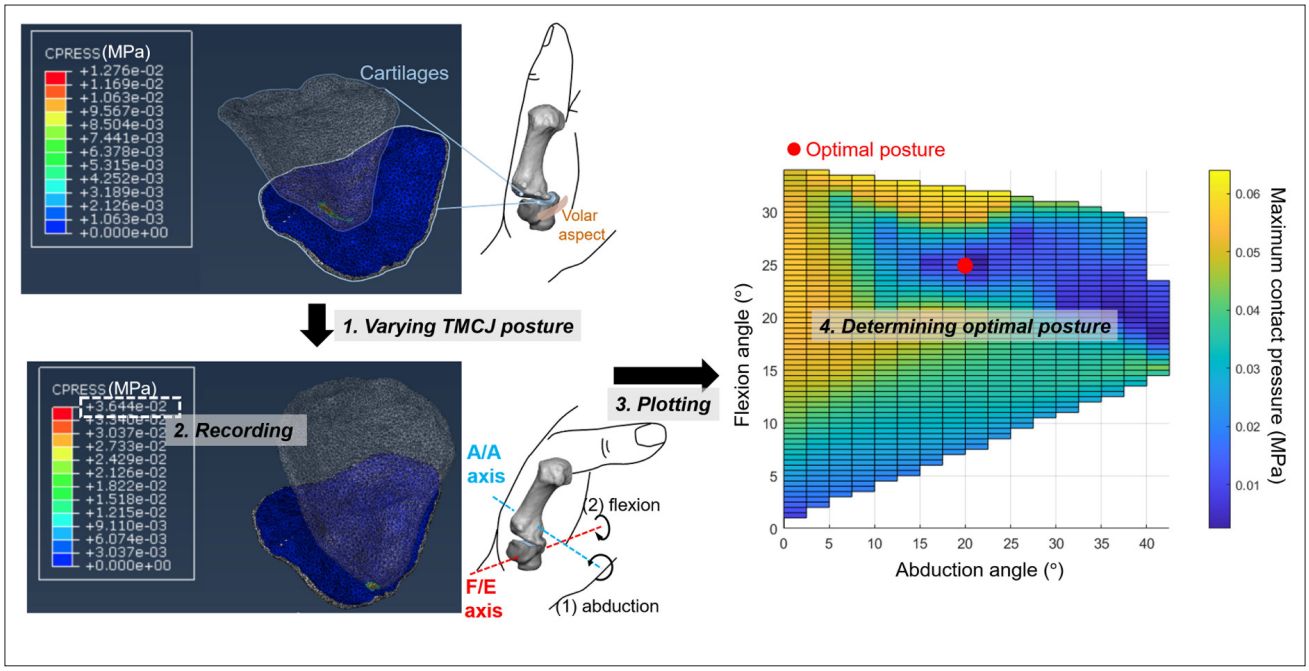

Figure 3. The FEM is applied to the constructed FE TMCJ model to determine the optimal posture that minimizes biomechanical joint contact pressure on the cartilage. Abbreviations: A/A, abduction-adduction; F/E, Flexion-extension; FE, finite element; FEM, finite element method; TMCJ: Trapeziometacarpal joint.

the metacarpal cartilage was first rotated around the A/A rotation axis for abduction before the FE simulation, and the abducted cartilage was then set to rotate around the F/E rotation axis by adjusting the kinematics of its coupled reference point for the simulation, while estimating joint contact pressure between the cartilages. The FEM-based maximum joint contact pressure was recorded for each TMCJ posture generated by the rotations. Subsequently, the optimal posture, which exhibited minimal joint contact pressure among various postures, was determined (Figure 3).

2.4. Fabrication of the orthosis via 3D printing

The orthosis was designed based on a 3D hand model posed in the optimal posture to immobilize the TMCJ in that posture during splinting. A 3D hand model posing the optimal posture was built prior to modeling the orthosis. Specifically, the overall hand geometry was reconstructed from CT images of the "neutral" posture. The thumb skin was then separated and rotated around the determined rotation axes to achieve the optimal posture. The orthosis was modeled to cover the built 3D hand model using Geomagic Freeform software (Figure 1). The modeled orthosis was then rigidly fabricated using a 3D printer (Cubicon Single; Hyvision System, Inc., South Korea) with a plastic material (ABS; Hyvision System, Inc., South Korea) and covered with fabric and straps.

2.5. Experimental evaluation

Orthoses fabricated using 3D printing were evaluated for their capability to maintain a targeted TMCJ posture and provide satisfactory wearing comfort during splinting (Figure 4). Two healthy subjects (healthy group [H1–2]; demographics listed in Table 1) were recruited for the evaluation. They were guided to fix the TMCJ in one of the flexion-abduction postures while maintaining the other fingers in a fully extended posture during 3D scanning using a 3D scanner (Sense2; 3D Systems Inc., USA). Subsequently, the orthosis was designed to cover the 3D hand model reconstructed from the 3D scanning data to maintain the scanned flexion-abduction posture as the targeted posture during splinting. After donning the 3D-printed orthosis, the TMCJ angles (i.e., θ_{sag} and θ_{cor}) were measured in the sagittal and coronal planes of the hand and compared to the angles measured from the printed 3D hand model. Note that the TMCJ angles were measured using a reflective marker-based motion capture system (Figure 4). Additionally, the subjects were asked to evaluate their satisfaction with wearing comfort by marking a 10-cm-long line.

Six patients (experimental [S1–4] and control [C1–2] groups; demographics listed in Table 1), diagnosed with TMCJ OA and consented to participate in this study, were recruited to evaluate the orthosis. Exclusion criteria were patients with inflammatory arthritis or neuromuscular

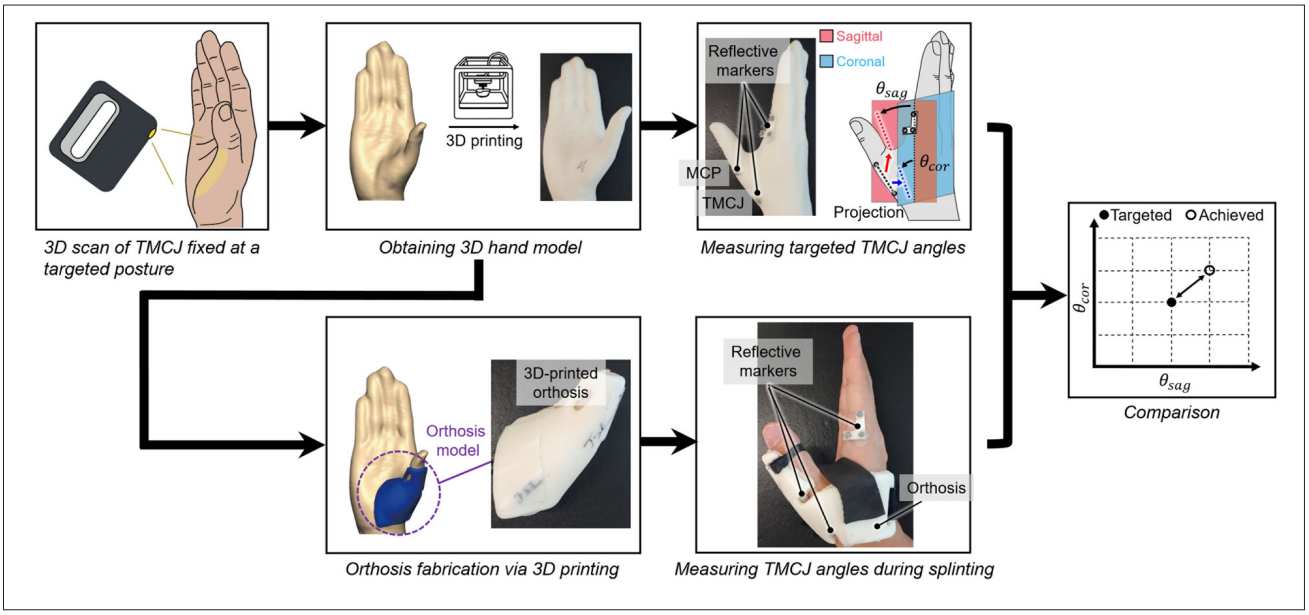

Figure 4. The experiment procedure used to evaluate the capability of the orthosis in maintaining the targeted TMCJ posture during splinting. Abbreviations: MCP, Metacarpophalangeal joint; TMCJ: trapeziometacarpal joint.

Table 1. Demographics of the enrolled subjects.

Participant number	Sex	Age (years)	Duration of pain (years)	Hand dominance	Involved hand	Eaton classification
H1	Male	26	-	Right	-	-
H2	Female	30	-	Right	-	-
S1	Female	51	1.2	Right	Right	3
S2	Female	78	1.5	Right	Left	3
S3	Female	51	0.8	Left	Left	3
S4	Female	58	5.0	Right	Left	3
C1	Female	53	1.0	Right	Left	2
C2	Female	73	2.1	Right	Left	4

disease. The orthosis for S1–4 was designed to fix the TMCJ to the optimal posture. All subjects were instructed to wear the orthosis as much as possible for 8 weeks. For comparison, C1–2 was provided with an orthosis that fixed the TMCJ in a non-optimal but comfortable posture, as conventional orthopedic treatment. Determining the most comfortable TMCJ posture was challenging due to the difficulty of distinguishing comfort levels among multiple comfortable postures based on subjective feelings. Therefore, splinting was performed using one of the postures that patients reported as comfortable and adopted in previous studies.[12] The research was approved by the Institutional Review Board of Seoul National University Bundang Hospital (No. B-2012-654-301), and written consent was obtained from each subject after the experiment was explained. The following criteria were measured for the evaluation:

(i) Disabilities of the arm, shoulder, and hand (DASH) and visual analog scale (VAS) scores: Before the application of the orthosis, all patients completed a DASH questionnaire. This self-administered questionnaire consists of 30 items and objectively measures the functional status and symptoms of patients with musculoskeletal disorders of the upper limb. The possible DASH score ranges from 0 (asymptomatic) to 100 (totally incapacitated).[41] At the follow-up visit 8 weeks after the application, the DASH questionnaire was re-administered. Conversely, VAS ranging from 0 to 10 was used to evaluate pain relief by the orthosis. Pain at rest (VAS_{rest}) and maximal pain (VAS_{max}) occurring

during daily activities that patients typically feel were measured at the initial and follow-up visits. Note that an decrease in the VAS score of 1 or more indicates an improvement in pain status.[42]

(ii) Pinch strength: Before the application of the orthosis, all patients were evaluated for their pinch strength using a pinch gauge (Asimow Engineering, USA). With their shoulder, elbow, forearm, and wrist in a neutral position, three consecutive attempts were made to measure pinch strength (kg), with a 1 min interval between each attempt.[43] The maximum value obtained was recorded. At the follow-up visit, the pinch strength was re-examined in the same manner.

(iii) Wearing comfort: The patients were asked to mark a 10-cm-long line to indicate their satisfaction with the orthosis in terms the wearing comfort.

3. Results

It was demonstrated by healthy subjects that orthoses fabricated via 3D printing can maintain the targeted TMCJ posture while providing satisfactory wearing comfort during splinting. The measured TMCJ angles during splinting and the targeted TMCJ angles are summarized in Figure 5. The TMCJ posture maintained by the orthosis was comparable to that of the 3D-scanned hand. The difference between the targeted and achieved TMCJ angles was 3.8° ± 0.4°. Moreover, the subjects scored 8.0 ± 1.4 for the wearing comfort of the 3D-printed orthosis.

The joint contact pressure analysis results and optimal TMCJ postures of patients are presented in Figure 6. Joint contact pressure was minimized at the optimal posture, while it increased as the postures deviated from the optimal posture. The joint contact pressure was considered valid, as the FEM-based pressure at a lateral pinch posture was comparable to the reported pressure measured in the lateral pinch posture at rest, which ranged from 6.0E-3 to 1.1E-2 MPa.[44] Additionally, the contact pattern during cartilage gliding matched the previous results.[45,46] Specifically, joint contact pressure areas move toward the volar aspect of cartilages as the flexion angle increases.

The optimal and immobilized postures were designed to coincide for S1–4, and these postures exhibited differences between individuals (Figure 6A). The flexion angle of the optimal posture was larger for S3 than for S1, S2, and S4, and the abduction angle varied between patients.

Differences were exhibited between the optimal and immobilized postures in the control group (Figure 6B). Joint contact pressures at the immobilized postures for C1 and C2 were similar, specifically 2.5E-2 and 3.9E-2 MPa, respectively. These pressures are only about half of the applied joint contact pressure (i.e., 7.8E-2 MPa) during lateral pinching with a grip force of 4.2 kg.[47]

Evaluation results of the orthoses are presented in Table 2. The orthosis for C1 was not assessed because C1 discontinued the orthotic treatment due to unrelieved pain at rest during splinting. Note that the Easton classification grade does not correlate with the VAS_{rest} score measured before splinting, as confirmed in previous research.[21,48]

3.1. DASH and VAS scores

The VAS_{rest} score improved for all S1–4, with a reduction of 1.8 ± 1.7. S1 and S2 reported no pain during splinting. The most significant decrease in the VAS_{rest} score was observed for S4, who exhibited minimal joint contact pressure among patients. Moreover, despite the immobilization of the TMCJ, the DASH score decreased by 13.1 ± 5.4 for S2–4, indicating

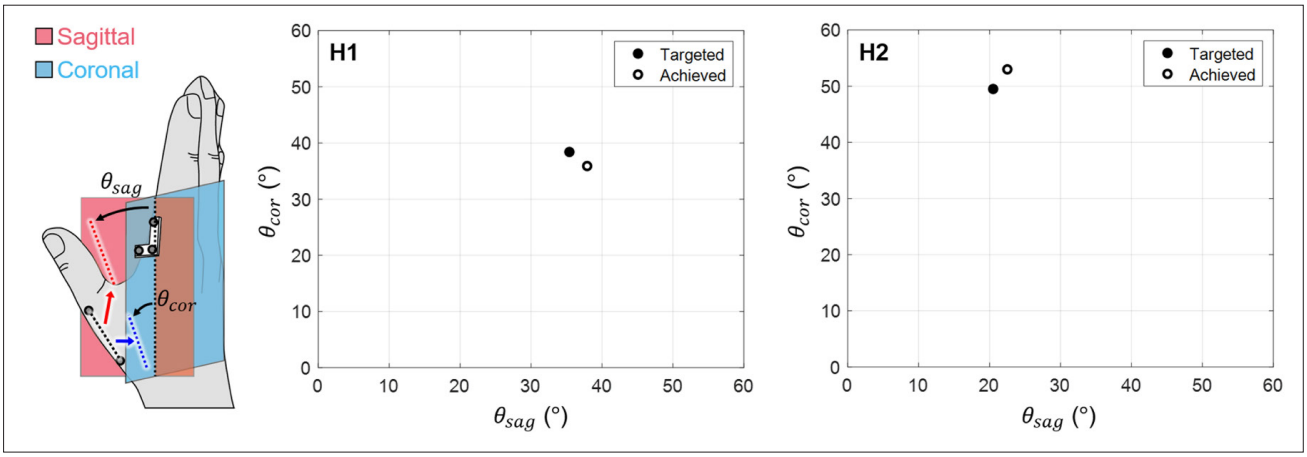

Figure 5. Measurement results of TMCJ angles for healthy subjects (H1 and H2) after donning the 3D-printed orthosis. The maintained TMCJ angles by the orthosis were comparable to the targeted TMCJ angles. Abbreviation: TMCJ, trapeziometacarpal joint.

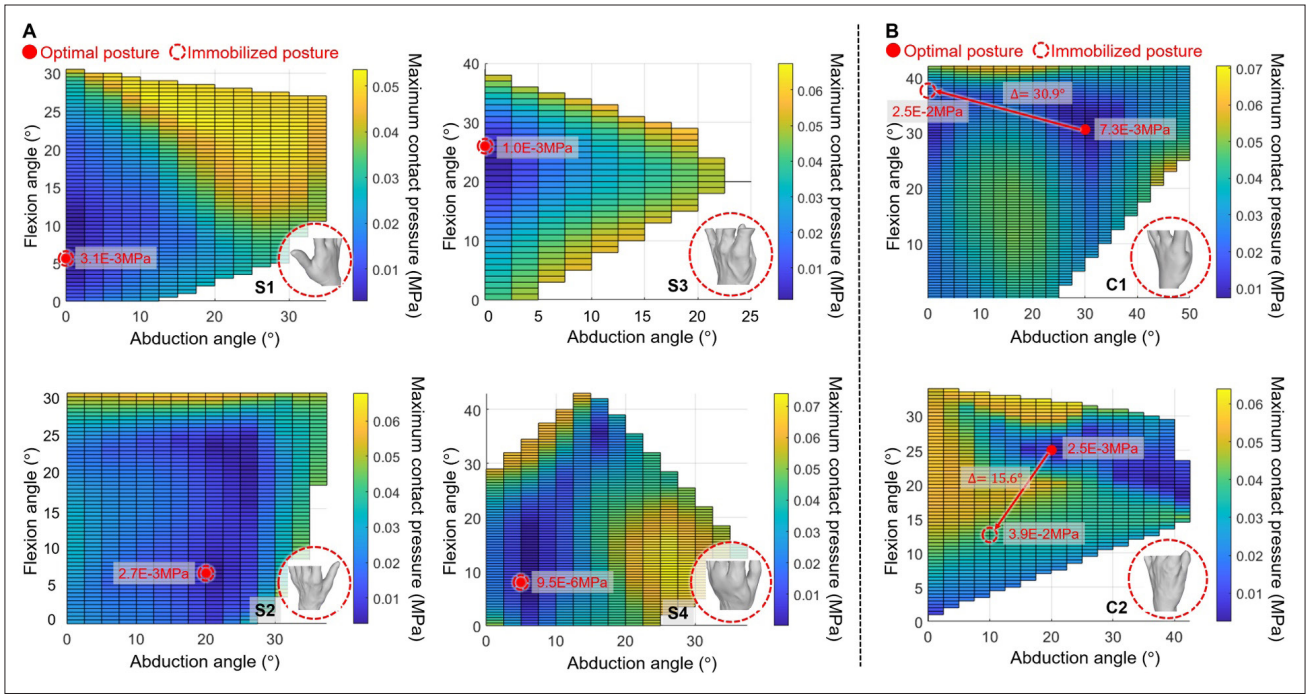

Figure 6. Analysis results of joint contact pressure for all patients. (A) The optimal and immobilized postures of the patients' orthosis in the experimental group. (B) The optimal and immobilized postures of the patients' orthosis in the control group.

Table 2. Evaluation results of the patients' orthosis.

Participant number	Before splinting				During splinting				
	VAS_{rest}	VAS_{max}	DASH	Pinch (kg)	VAS_{rest}	VAS_{max}	DASH	Pinch (kg)	Wearing comfort
S1	0	7	22.5	4.8	0	4	63.6	8.8	8
S2	1	4	50.0	5.3	0	3	43.1	5	8
S3	3	4	31.8	4.8	1	4	15.9	4.5	9
S4	6	8	41.5	5.4	2	5	25.0	5.4	10
C1	4	7	36.4	5.8	-	-	-	-	-
C2	1	4	15.9	5.3	0	4	11.4	5.1	9

Abbreviations: DASH, disabilities of arm, shoulder, and hand scores; VAS, visual analog scale.

an improvement in functional status possibly attributed to pain relief. Note that a TMCJ posture close to "neutral" would not be desirable for splinting due to the reported increase in the DASH score for S1, caused by difficulties in performing grasping with that posture. The VAS_{max} score for S1–2 and S4 also decreased during splinting.

For C2, VAS and DASH scores displayed improvement. The VAS_{rest} score decreased during splinting, while the VAS_{max} score did not change. The DASH score also improved, decreasing from 15.9 to 11.4.

3.2. Pinch strength

Pinch strength displayed no significant change; it decreased by a small amount, 0.2 ± 0.1 kg, for S2–4 and C2. Muscle weakness during splinting, possibly due to infrequent use, might have led to a decrease in pinch strength, even though pain was relieved.[49,50] However, there was an increase in pinch strength for S1, from 4.8 to 8.8 kg. As S1 was hindered in performing daily activities by the orthosis, the thumb flexors might have been frequently used to exert force against the orthosis to release from the immobilized posture, thus preventing muscle weakness. Therefore, S1 might have been capable of performing grasping more powerfully after experiencing pain relief.

3.3. Wearing comfort

All patients reported satisfaction with the wearing comfort of the orthosis during splinting. The orthosis was rated 8.8 ± 1.0 by S1–4 and 9 by C2.

4. Discussion

This study proposes a novel 3D printing design process for a TMCJ orthosis, based on joint contact pressure obtained using a CT image-based FE TMCJ model. The primary objective of the orthosis is to ensure successful pain relief at rest during splinting by enabling patients to maintain the subject-specific optimal TMCJ posture that minimizes biomechanical joint contact pressure. Before designing the orthosis, the optimal TMCJ posture was individually determined through joint contact pressure analysis using a FE TMCJ model. The orthosis was then designed to cover a 3D hand model posed in the optimal TMCJ posture, enabling the orthosis to maintain the optimal posture during splinting. The orthosis was preliminarily applied to patients with moderate to severe TMCJ OA, and they all achieved pain relief at rest.

Immobilizing the TMCJ at comfortable postures determined during a brief hospital visit cannot ensure the achievement of pain relief during long-term splinting. Immobilization can typically relieve biomechanical cartilage wear due to restricted joint mobilization. Therefore, immobilization has been utilized for OA treatment through static orthoses.[9–11,13–15,17,18] However, high joint contact pressure in immobilized postures may lead to localized wear at cartilage contact areas due to slight allowed movement,[51] resulting in inflammatory response and pain.[52] Postures with this high joint contact pressure can be misperceived as comfortable, as confirmed in the control group. This could be attributed to the improved pain tolerance typically observed in patients within a hospital environment by reduced anxiety due to the presence of professional clinicians.[22,23] Thus, the comfortable posture determined solely by patients may not guarantee the long-term comfort of the orthosis. As a result of the high joint contact pressure, pain relief at rest failed for one of two patients in the control group, while another patient reported pain relief despite their similar high joint contact pressure values. Patients with high VAS_{rest} scores of 3 or higher are reported to be vulnerable to experiencing increased pain during splinting,[48] and this vulnerability may result in the failure of pain relief for the patient with a high VAS_{rest} score. Therefore, it would be desirable to minimize joint contact pressure in the immobilized posture to achieve pain relief at rest for patients, regardless of their VAS_{rest} scores.

Immobilizing the TMCJ at the optimal posture may be beneficial in preventing the failure of pain relief. Reducing joint contact pressure is essential to minimize biomechanical wear on cartilages,[3,4] and this has been achieved in knee and hip joints by adjusting postures with the aid of FE joint models.[5–8] On the other hand, the TMCJ has been maintained in comfortable postures by orthoses without considering joint contact pressure, assuming that joint contact pressure is relieved with comfort.[9–11,13–15,17,18] However, TMCJ postures with high joint contact pressure can be misperceived as comfortable, as observed in patients in the control group. This may result in a high failure rate of pain relief, which ranges from 30% to 47%.[19–21] It would be desirable to avoid high joint contact pressure at the TMCJ by utilizing a CT-based individual FE model for TMCJ orthosis design. Thus, in this study, a CT image-based FE TMCJ model was applied to the orthosis design for minimum contact pressure. As a result, all four patients maintaining the optimal posture successfully achieved pain relief at rest during splinting, implying a reduction of joint contact pressure. Note that even patients with VAS_{rest} scores of 3 or higher before splinting achieved pain relief at rest through the optimal posture. Despite the limited room for improvement in the recruited patients of our study due to their relatively low pain scores in the baseline assessment compared to those in other studies,[9–11,13–15] the improvement in pain was comparable to that of conventional orthoses[9–11,13–15] that had displayed a positive effect on pain relief. Note that the VAS score at rest during splinting was only 0.75 ± 0.96 in this study. Thus, it was believed that there is potential for enhancing pain relief performance, as evidenced by the successful pain relief achieved by all four patients, in contrast to the high failure rate observed with conventional orthoses. Due to this pain relief, functional status in daily activities demonstrated improvement, with no significant change in grip strength possibly due to muscle weakness, which aligns with the results of previous studies on conventional orthoses.[9–11,15]

The distant location of the applied joint contact pressure from cartilage lesions may be beneficial in relieving maximal pain measured as VAS_{max} scores. Pain occurs when high pressure is applied to cartilage lesions, and the distribution of these cartilage lesions is reported to be varied for each patient.[53] In this study, cartilage lesions were expected to be located at the volar aspect for all patients, determined through the evaluation of subchondral sclerosis and bone spurs using CT images.[54] Moreover, it was anticipated that there would be more severe damage at cartilage areas closer to their volar edge.[2] Considering that joint contact pressure areas move towards the volar edge of cartilages as a flexion angle increases,[45,46] the optimal posture with a large flexion angle may result in high joint contact pressure applied to severely damaged cartilage areas during grasping, limiting the capability to relieve maximal pain for one patient in the experimental group. Both pain at rest and maximal pain may be alleviated with orthoses designed to apply minimal joint contact pressure to cartilage areas located far from lesions.

The compliance of TMCJ orthoses is important for users due to their long-term use. While soft materials can be used in the orthosis[17,18] to address the wearing discomfort experienced when using orthoses made from rigid materials, immobilizing the TMCJ posture may become challenging. Although the material used in the proposed orthosis was rigid, patients reported satisfaction with the wearing comfort after donning. The compliance of the orthosis was considered to be attributed to its design, which was based on individual hand geometry.[27,28] Additionally, thermoplastic pads commonly used in conventional orthoses can be utilized to fabricate the orthosis to maintain the optimal posture. The 3D hand model, posed in the optimal posture, can be 3D-printed and then covered with thermoplastic pads and fabric. These thermoplastic pads, covered with fabric, can also be employed to maintain the optimal posture during splinting.

The proposed orthosis design can be applied to static braces developed for the wrist OA. While the FEM has been utilized to analyze joint contact pressure at the wrist,[55,56] where OA commonly occurs, there are still limited studies on developing wrist OA braces designed based on a CT-based FE joint model for optimal postures.[57,58] The proposed orthosis design may aid in developing wrist OA braces for the optimal posture to achieve pain relief.

This study has limitations. The proposed orthosis was evaluated with a limited number of patients, and the evaluation was conducted only after 8 weeks of splinting. Nevertheless, we believe that the orthosis can reduce the failure rate of pain relief for patients with TMCJ OA, whether used for a shorter or longer period of splinting, due to its design, which reduces biomechanical joint contact pressure. Moreover, the locations of the rotation axes were fixed in the FE model, which may not be applicable to patients exhibiting significant translation of the metacarpal during movement due to severe structural instability.

5. Conclusion

This study presents a novel patient-specific design for a TMCJ orthosis aimed at achieving successful pain relief during splinting by using 3D printing technology. Despite the possibility of estimating joint contact pressure at the TMCJ using FE joint models, conventional TMCJ orthoses have been designed solely based on subjective comfort reported by patients without considering the contact pressure. To ensure pain relief during splinting, we introduce a TMCJ orthosis design using CT image-based FE TMCJ models to immobilize the TMCJ in the optimal posture that minimizes biomechanical joint contact pressure. The proposed 3D-printed TMCJ orthosis was applied to patients with OA and preliminarily demonstrated its capability in relieving pain for all patients, implying a reduction of joint contact pressure at the optimal posture.

By using 3D bioprinting technology and a subject-specific FE model, immobilization of the TMCJ in a subject-specific optimal posture that minimizes joint contact pressure is achieved for successful pain relief during splinting; otherwise, pain relief may fail due to high pressure. An orthosis designed solely based on subjective reports on comfort could not guarantee pain relief (i.e., one subject in the control group quit the study due to severe pain), which may be attributed to the high contact pressure. To reduce the failure rate of pain relief in clinical treatment, it would be desirable for the orthosis to be designed with the aid of a CT image-based FE model to maintain the TMCJ in the optimal posture. This optimal posture was found to vary between individuals, necessitating the patient-specific TMCJ orthosis design, which could be facilitated by 3D printing technology.

In future studies, the proposed orthosis will be evaluated on a sufficient number of patients over various splinting periods to demonstrate its capability to improve pain relief with strong statistical power compared to conventional TMCJ orthoses. Moreover, the material of the orthosis, which is ABS covered by fabrics in this study, will be improved for comfort after skin pressure distribution analysis with various 3D-printable materials, such as flexible thermoplastic polyurethane (TPU), further simplifying the fabrication process. Its capability to relieve pain even after doffing the orthosis worn for a longer period will be also assessed.

Acknowledgments

None.

Funding

This work was supported in part by the Korea Research Institute for defense Technology planning and advancedment(KRIT) grant funded by the Korea government (DAPA(Defense Acquisition Program Administration)) (No. 21-107-E00-009-02, “Realtime complex battlefield situation awareness technology”) and in part by the funding from the Korea government Ministry of Science and ICT (grant number RS-2023-00209251).

Conflict of interest

The authors declare they have no competing interests.

Author contributions

Conceptualization: All authors
Formal analysis: Chan Beom Park, Ji Sup Hwang
Investigation: Chan Beom Park, Ji Sup Hwang
Methodology: Chan Beom Park, Ji Sup Hwang
Supervision: Hyun Sik Gong, Hyung-Soon Park
Writing – original draft: Chan Beom Park, Ji Sup Hwang
Writing – review & editing: Hyun Sik Gong, Hyung-Soon Park

Ethics approval and consent to participate

The research was approved by the Institutional Review Board of Seoul National University Bundang Hospital (No. B-2012-654-301), and written consent was obtained from each subject after the experiment was explained.

Consent for publication

Written consent for publication was obtained.

Availability of data

The data that support the findings of this study are available from the corresponding authors upon reasonable request.

References

1. Gillis J, Calder K, Williams J. Review of thumb carpometacarpal arthritis classification, treatment and outcomes. *Can J Plast Surg.* 2011;19(4):134-138. doi: 10.1177/229255031101900409
2. Koff MF, Ugwonali OF, Strauch RJ, Rosenwasser MP, Ateshian GA, Mow VC. Sequential wear patterns of the articular cartilage of the thumb carpometacarpal joint in osteoarthritis. *J Hand Surg Am.* 2003;28(4):597-604. doi: 10.1016/S0363-5023(03)00145-X
3. Fontana L, Neel S, Claise J-M, Ughetto S, Catilina P. Osteoarthritis of the thumb carpometacarpal joint in women and occupational risk factors: a case–control study. *J Hand Surg Am*. 2007;32(4):459-465. doi: 10.1016/j.jhsa.2007.01.014
4. Fergusson CM. The aetiology of osteoarthritis. *Postgrad Med J.* 1987;63(740):439. doi: 10.1136/pgmj.63.740.439
5. Spierings J, Van Den Hengel M, Janssen RP, Van Rietbergen B, Ito K, Foolen J. Knee instability caused by altered graft mechanical properties after anterior cruciate ligament reconstruction: the early onset of osteoarthritis? *Front Bioeng Biotechnol*. 2023;11:1244954. doi: 10.3389/fbioe.2023.1244954
6. Wang Y, Fan Y, Zhang M. Comparison of stress on knee cartilage during kneeling and standing using finite element models. *Med Eng Phys.* 2014;36(4):439-447. doi: 10.1016/j.medengphy.2014.01.004
7. Esrafilian A, Stenroth L, Mononen M, Tanska P, Avela J, Korhonen R. EMG-assisted muscle force driven finite element model of the knee joint with fibril-reinforced poroelastic cartilages and menisci. *Sci Rep*. 2020;10(1):3026. doi: 10.1038/s41598-020-59602-2
8. Zhang Z, Sui D, Qin H, Li H, Zhang Z. Contact pressure distribution of the hip joint during closed reduction of developmental dysplasia of the hip: a patient-specific finite element analysis. *BMC Musculoskelet Disord.* 2020;21(600):1-12. doi: 10.1186/s12891-020-03602-w
9. Wajon A, Ada L. No difference between two splint and exercise regimens for people with osteoarthritis of the thumb: a randomised controlled trial. *Aust J Physiother.* 2005;51(4):245-249. doi: 10.1016/S0004-9514(05)70005-2
10. Carreira ACG, Jones A, Natour J. Assessment of the effectiveness of a functional splint for osteoarthritis of the trapeziometacarpal joint on the dominant hand: a randomized controlled study. *J Rehabil Med*. 2010; 42(5):469-474. doi: 10.2340/16501977-0542
11. Weiss S, Lastayo P, Mills A, Bramlet D. Prospective analysis of splinting the first carpometacarpal joint: an objective, subjective, and radiographic assessment. *J Hand Surg.* 2000;13(3):218-227. doi: 10.1016/S0894-1130(00)80005-8
12. Colditz JC. The biomechanics of a thumb carpometacarpal immobilization splint: design and fitting. *J Hand Ther.* 2000;13(3):228-235. doi: 10.1016/S0894-1130(00)80006-X
13. Cantero-Téllez R, Villafañe JH, Valdes K, Berjano P. Effect of immobilization of metacarpophalangeal joint in thumb carpometacarpal osteoarthritis on pain and function. A quasi-experimental trial. *J Hand Ther*. 2018;31(1):68-73. doi: 10.1016/j.jht.2016.11.005
14. Bani MA, Arazpour M, Kashani RV, Mousavi ME, Maleki M, Hutchins SW. The effect of custom-made splints in patients with the first carpometacarpal joint osteoarthritis. *Prosthet Orthot Int*. 2013;37(2):139-144. doi: 10.1177/0309364612454047
15. Eyiis E, Mathijssen NM, Kok P, Sluijter J, Kraan GA. Three-dimensional printed customized versus conventional plaster brace for trapeziometacarpal osteoarthritis: a randomized controlled crossover trial. *J Hand Surg Eur Vol* 2023;48(5):412-418. doi: 10.1177/17531934221146864
16. Chu C-H, Wang I-J, Sun J-R, Liu C-H. Customized designs of short thumb orthoses using 3D hand parametric models. *Assist Technol*. 2022;34(1):104-111. doi: 10.1080/10400435.2019.1709917

17. Hermann M, Nilsen T, Eriksen CS, Slatkowsky-Christensen B, Haugen IK, Kjeken I. Effects of a soft prefabricated thumb orthosis in carpometacarpal osteoarthritis. *Scand J Occup Ther*. 2014;21(1):31-39.
doi: 10.3109/11038128.2013.851735

18. Becker SJE, Bot AGJ, Curley SE, Jupiter JB, Ring D. A prospective randomized comparison of neoprene vs thermoplast hand-based thumb spica splinting for trapeziometacarpal arthrosis. *Osteoarthr Cartil Open*. 2013;21(5):668-675.
doi: 10.1016/j.joca.2013.02.006

19. Tsehaie J, Spekreijse KR, Wouters RM, et al. Predicting outcome after hand orthosis and hand therapy for thumb carpometacarpal osteoarthritis: a prospective study. *Arch Phys Med Rehabil*. 2019;100(5):844-850.
doi: 10.1016/j.apmr.2018.08.192

20. Berggren M, Joost-Davidsson A, Lindstrand J, Nylander G, Povlsen B. Reduction in the need for operation after conservative treatment of osteoarthritis of the first carpometacarpal joint: a seven year prospective study. *Scand J Plast Reconstr Surg Hand Surg*. 2001;35(4):415-417.
doi: 10.1080/028443101317149381

21. Suresh V, Frost CM, Lifchez SD. Selective thumb carpometacarpal joint denervation for painful arthritis: follow-up of long-term clinical outcomes. *J Hand Surg Glob Online*. 2023;5(1):108-111.
doi: 10.1016/j.jhsg.2022.02.005

22. Karacabay K, Savci A, Hergul FK. Investigating relationships between pain, comfort, anxiety and depression in surgical patients. *Cyprus J Med Sci*. 2022;7:40-47.
doi: 10.4274/cjms.2020.1758

23. Schloemann D, Hammert WC, Liu S, Bernstein DN, Calfee RP. Risk factors for failed nonsurgical treatment resulting in surgery on thumb carpometacarpal arthritis. *J Hand Surg*. 2021;46(6):471-477.
doi: 10.1016/j.jhsa.2021.02.009

24. Xiao YP, Xu HJ, Liao W, Li ZH. Clinical application of instant 3D printed cast versus polymer orthosis in the treatment of colles fracture: a randomized controlled trial. *BMC Musculoskelet Disord*. 2024;25(1):104.
doi: 10.1186/s12891-024-07212-8

25. Cho JE, Seo KJ, Ha S, Kim H. Effects of community ambulation training with 3D-printed ankle–foot orthosis on gait and functional improvements: a case series of three stroke survivors. *Front Neurol*. 2023;14:1138807.
doi: 10.3389/fneur.2023.1138807

26. Peng C, Tran P, Lalor S, Tirosh O, Rutz E. Tuning the mechanical responses of 3D-printed ankle-foot orthoses: a numerical study. *Int J Bioprint*. 2024; 10(3):3390.
doi: 10.36922/ijb.3390

27. Park CB, Park H-S. Portable 3D-printed hand orthosis with spatial stiffness distribution personalized for assisting grasping in daily living. *Front Bioeng Biotechnol*. 2023;11:895745.
doi: 10.3389/fbioe.2023.895745

28. Park CB, Hwang JS, Gong HS, Park H-S. A lightweight dynamic hand orthosis with sequential joint flexion movement for postoperative rehabilitation of flexor tendon repair surgery. *IEEE Trans Neural Syst Rehabil Eng*. 2024;32:994-1004.
doi: 10.1109/TNSRE.2024.3367990

29. Hollister A, Buford WL, Myers LM, Giurintano DJ, Novick A. The axes of rotation of the thumb carpometacarpal joint. *J Orthop Res*. 1992;10(3):454-460.
doi: 10.1002/jor.1100100319

30. D'Agostino P, Dourthe B, Kerkhof F, Stockmans F, Vereecke EE. In vivo kinematics of the thumb during flexion and adduction motion: evidence for a screw-home mechanism. *J. Orthop. Res*. 2017;35(7):1556-1564.
doi: 10.1002/jor.23421

31. Santos VJ, Valero-Cuevas FJ. Reported anatomical variability naturally leads to multimodal distributions of Denavit-Hartenberg parameters for the human thumb. *IEEE Trans Biomed Eng*. 2006;53(2):155-163.
doi: 10.1109/TBME.2005.862537

32. O'Brien VH, Giveans MR. Effects of a dynamic stability approach in conservative intervention of the carpometacarpal joint of the thumb: a retrospective study. *J Hand Ther*. 2013;26(1):44-52.
doi: 10.1016/j.jht.2012.10.005

33. Akiyama K, Sakai T, Koyanagi J, Murase T, Yoshikawa H, Sugamoto K. Three-dimensional distribution of articular cartilage thickness in the elderly cadaveric acetabulum: a new method using three-dimensional digitizer and CT. *Osteoarthr Cartil Open*. 2010;18(6):795-802.
doi: 10.1016/j.joca.2010.03.007

34. Prionas ND, Ray S, Boone JM. Volume assessment accuracy in computed tomography: a phantom study. *J Appl Clin Med Phys*. 2010;11(2):168-180.
doi: 10.1120/jacmp.v11i2.3037

35. Miura T, Ohe T, Masuko T. Comparative in vivo kinematic analysis of normal and osteoarthritic trapeziometacarpal joints. *J Hand Surg*. 2004;29(2):252-257.
doi: 10.1016/j.jhsa.2003.11.002

36. Hamann N, Heidemann J, Heinrich K, et al. Effect of carpometacarpal joint osteoarthritis, sex, and handedness on thumb in vivo kinematics. *J Hand Surg*. 2014; 39(11):2161-2167.
doi: 10.1016/j.jhsa.2014.08.012

37. Butz KD, Merrell G, Nauman EA. A three-dimensional finite element analysis of finger joint stresses in the MCP joint while performing common tasks. *Hand*. 2012;7(3): 341-345.
doi: 10.1007/s11552-012-9430-4

38. Peters AE, Akhatar R, Comerford EJ, Bates KT. The effect of ageing and osteoarthritis on the mechanical properties of cartilage and bone in the human knee joint. *Sci Rep.* 2018;8(1):5931.
doi: 10.1038/s41598-018-24258-6

39. Guilak F. The slippery slope of arthritis. *Arthritis Rheumatol.* 2005;52(6):1632-1633.
doi: 10.1002/art.21051

40. Yuh C, Laurent MP, Espinosa-Marzal RM, Chubinskaya S, Wimmer MA. Transient stiffening of cartilage during joint articulation: a microindentation study. *J Mech Behav Biomed Mater.* 2021;113:104113.
doi: 10.1016/j.jmbbm.2020.104113

41. Lee J-Y, Lim J-Y, Oh JH, Ko Y-M. Cross-cultural adaptation and clinical evaluation of a Korean version of the disabilities of arm, shoulder, and hand outcome questionnaire (K-DASH). *J Shoulder Elbow Surg.* 2008;17(4):570-574.
doi: 10.1016/j.jse.2007.12.005

42. Myles P, Myles D, Galagher W, et al. Measuring acute postoperative pain using the visual analog scale: the minimal clinically important difference and patient acceptable symptom state. *Br J Anaesth.* 2017;118(3):424-429.
doi: 10.1093/bja/aew466

43. Günther C, Bürger A, Rickert M, Schulz, C. Key pinch in healthy adults: normative values. *J Hand Surg Eur Vol.* 2008;33(2):144-148.
doi: 10.1177/1753193408087031

44. Cheema T, Salas C, Morrell N, Lansing L, Taha MMR, Mercer D. Opening wedge trapezial osteotomy as possible treatment for early trapeziometacarpal osteoarthritis: a biomechanical investigation of radial subluxation, contact area, and contact pressure. *J Hand Surg.* 2012; 37(4):699-705.
doi: 10.1016/j.jhsa.2012.01.013

45. Ateshian GA, Ark JW, Rosenwasser MP, Pawluk RJ, Soslowsky LJ, Mow VC. Contact areas in the thumb carpometacarpal joint. *J Orthop Res.* 1995; 13(3):450-458.
doi: 10.1002/jor.1100130320

46. Momose T, Nakatsuchi Y, Saitoh S. Contact area of the trapeziometacarpal joint. *J Hand Surg.* 1999;24(3): 491-495.
doi: 10.1053/jhsu.1999.0491

47. Hwang JS, Li Q, Kim J. A quantitative measurement of trapeziometacarpal joint pressure using a cadaveric model of lateral pinch. *J Orthop Res.* 2022;40(7):1523-1528.
doi: 10.1002/jor.25188

48. Nishimura K, Uehara K, Miura T, Ohe T, Tanaka S, Morizaki Y. Factors associated with surgical intervention for osteoarthritis of the thumb carpometacarpal joint. *J Hand Surg.* 2021;46(9):817-e1.
doi: 10.1016/j.jhsa.2021.01.009

49. Spaans AJ, Van Minnen LP, Kon M, Schuurman AH, Schreuders AT, Vermeulen GM. Conservative treatment of thumb base osteoarthritis: a systematic review. *J Hand Surg.* 2015;40(1):16-21.
doi: 10.1016/j.jhsa.2014.08.047

50. Suetta C, Hvid LG, Justesen L, et al. Effects of aging on human skeletal muscle after immobilization and retraining. *J Appl Physiol.* 2009;107(4):1172-1180.
doi: 10.1152/japplphysiol.00290.2009

51. Vanneste M, Stockmans F, Vereecke EE. The effect of orthoses on the kinematics of the trapeziometacarpal, scaphotrapeziotrapezoidal, and radioscaphoid joints. *J Orthop Res.* 2021;39(1):196-203.
doi: 10.1002/jor.24700

52. Estell EG, Silverstein AM, Stefani RM, et al. Cartilage wear particles induce an inflammatory response similar to cytokines in human fibroblast-Like Synoviocytes. *J Orthop Res.* 2019;37(9):1979-1987.
doi: 10.1002/jor.24340

53. Bae KJ, Jang HS, Gong HS, Kang Y, Kim J, Baek GH. Prevalence and distribution of MRI abnormalities in the articular cartilage and supporting ligaments in patients with early clinical stage first carpometacarpal joint osteoarthritis. *Skeletal Radiol.* 2020;49: 1089-1097.
doi: 10.1007/s00256-020-03383-2

54. Hwang JS, Lee HS, Gong HS. Three-dimensional analysis of the trapezium subchondral bone and its association with trapeziometacarpal joint osteoarthritis. *Calcif Tissue Int.* 2023;112(3):320-327.
doi: 10.1007/s00223-022-01040-5

55. Ledoux P, Lamblin D, Wuilbaut A, Schuind F. A finite-element analysis of Kienböck's disease. *J Hand Surg Eur Vol.* 2008;33(3):286-291.
doi: 10.1177/1753193408090757

56. Camus EJ, Aimar A, Van Overstraeten L, Schuind F, Innocenti B. Lunate loads following different osteotomies used to treat Kienböck's disease: a 3D finite element analysis. *Clin Biomech.* 2020;78:105090.
doi: 10.1016/j.clinbiomech.2020.105090

57. Van der Windt JW, Akkerman W, Hofstra M, Meussen P. Reduced pain and improved daily activities for individuals with hand osteoarthritis using a silicone wrist hand orthosis. *J Hand Ther.* 2023;36(3):669-677.
doi: 10.1016/j.jht.2022.09.003

58. Valdes K, Marik T. A systematic review of conservative interventions for osteoarthritis of the hand. *J Hand Ther.* 2010;23(4):334-351.
doi: 10.1016/j.jht.2010.05.001

ACCSCIENCE PUBLISHING

International Journal of Bioprinting

RESEARCH ARTICLE

3D-printed scaffolds with controlled-releasing compounds for ectopic activation of dormant ovarian follicles

Yali Yang[1†], Huashan Zhao[1†], Mingming Wu[2†], Lei Ge[1,3], Meiyue Wang[1], Feifei Du[1], Zhonglin Xiao[1,4], Li Xue[1,3], Pinpin Wang[2,3], Jie Chen[1], Tianxia Xiao[1], Pei-Gen Ren[1*], Changshun Ruan[2*], and Jian V. Zhang[1,5,6*]

[1]Shenzhen Key Laboratory of Metabolic Health, Center for Energy Metabolism and Reproduction, Shenzhen Institutes of Advanced Technology, Chinese Academy of Sciences, Shenzhen, Guangdong, China

[2]Center for Human Tissues and Organ Degeneration, Shenzhen Institutes of Advanced Technology, Chinese Academy of Sciences, Shenzhen, Guangdong, China

[3]University of Chinese Academy of Sciences, Beijing, China

[4]Faculty of Data Science, City University of Macau, Macau, China

[5]Faculty of Pharmaceutical Sciences, Shenzhen University of Advanced Technology, Shenzhen, Guangdong, China

[6]Sino-European Center of Biomedicine and Health, Shenzhen, Guangdong, China

[†]These authors contributed equally to this work.

***Corresponding authors:**
Pei-Gen Ren
(pg.ren@siat.ac.cn)

Changshun Ruan
(cs.ruan@siat.ac.cn)

Jian V. Zhang
(jian.zhang@siat.ac.cn)

Citation: Yang Y, Zhao H, Wu M, et al. 3D-printed scaffolds with controlled-releasing compounds for ectopic activation of dormant ovarian follicles. *Int J Bioprint*. 2025;11(1):246-258. doi: 10.36922/ijb.4941

Received: September 24, 2024
Revised: October 22, 2024
Accepted: October 30, 2024
Published Online: October 30, 2024

Copyright: © 2024 Author(s). This is an Open Access article distributed under the terms of the Creative Commons Attribution License, permitting distribution, and reproduction in any medium, provided the original work is properly cited.

Publisher's Note: AccScience Publishing remains neutral with regard to jurisdictional claims in published maps and institutional affiliations.

Abstract

Throughout a woman's reproductive life, hundreds of functioning follicles are activated for development, while thousands of dormant follicles remain in the ovaries. *In vitro* dormant follicle activation is an effective clinical strategy for women with fertility needs facing ovarian dysfunction. However, *in vivo* dormant follicle activation remains a challenge due to difficulties such as delivering stimulators to local sites. Here, we developed a compound-preloaded microporous scaffold by combining three-dimensional (3D) printing techniques with pharmacological activators to support and stimulate the activation and development of primordial follicles. The gelatin/alginate composite scaffolds exhibited exceptional mechanical properties and biological compatibility, effectively supporting the survival of ovarian granulosa cells for more than 7 days, which is essential for oocyte development. Furthermore, the ovarian tissue scaffold complex successfully survived after transplantation under the mouse kidney capsule, demonstrating its excellent biocompatibility. After pre-mixing widely used clinical activators into the bioink, the scaffold could gradually release the mixture of compounds, effectively activating primordial follicles. By transplanting the ovary–scaffold complex containing activators into the mouse abdominal subcutaneous pocket, dormant follicles could be activated subcutaneously and developed into growing follicles. The number of growing follicles is approximately three times higher compared to the group without activators. In conclusion, by integrating biomaterials, activators, and 3D printing technology, we have developed 3D-printed biological scaffolds that can ectopically support primordial follicle activation and development *in vivo*. This novel approach could provide a promising strategy for treating ovarian insufficiency and endocrine disorders in the clinic, without the need for *in situ* ovarian tissue grafting.

Keywords: 3D printing; Scaffold; Dormant ovarian follicles; Activation; Transplantation

1. Introduction

Ovarian dysfunction leads to female cycle disorders, menopause, and infertility.[1,2] To effectively address these issues, it is vital to have growing follicles available in the ovaries. Throughout a woman's reproductive years, only a limited number of primordial follicles are recruited and activated, leaving many dormant follicles in the ovaries. However, it remains a significant challenge to directly and effectively activate these dormant follicles *in vivo*.[3,4]

With the development of biomaterials and tissue engineering, using bioengineering to restore fertility has also gradually become a promising research avenue. Some research teams have used biocompatible materials and follicular cells to develop bioengineered ovaries.[5–9] It has been reported that ovarian tissues or oocytes wrapped in biocompatible materials can successfully produce healthy offspring,[10,11] suggesting that functional follicles can survive and grow in biocompatible material-printed grafts. The availability of functional follicles highly depends on the formation of a spherical structure composed of oocytes, surrounding granulosa cells, and theca cells, as well as indispensable angiogenesis, thereby establishing tissue-specific microenvironments.[12] However, biomaterials cannot provide sufficient space for the development of the follicles.

Since the invention of 3D printing by Chuck Hull in 1983, 3D printing technology has been widely used in the medical field, among which, 3D-bioprinted organs provide great convenience for clinical surgery, drug testing, and disease research. Meanwhile, 3D printing technology has been successfully applied to creating human organs such as liver, heart, and kidney.[13] However, its application in reproductive biology is still in its infancy, and restoring fertility through 3D-printed ovarian strategies is an exciting area of research.[14–19] Studies have demonstrated that mouse follicles can grow and ovulate successfully in 3D-printed porous scaffolds,[20] recover ovarian function *in vivo*, and even produce healthy offspring through natural mating.[17] However, these follicles are typically at advanced stages of development, such as preantral or antral follicles. For patients with undeveloped ovarian follicles, the scaffolds cannot help restore hormone levels or fertility. Therefore, a combination of the 3D-printed scaffold and primordial follicle activation, whether by activating follicles *in vitro* before transplantation, or by using the scaffold's slow-release properties for *in vivo* activation, holds significant research value for restoring hormone levels and fertility in patients with undeveloped follicles.

The selection of biomaterials for bioprinting is crucial to ensure the functionality of ovarian tissue. Gelatin is a water-soluble protein extracted from collagen, which is a main component of the extracellular matrix. Among various biomaterials, it is well-known for its excellent biocompatibility and biodegradability. After being chemically modified with methacryloyl, gelatin-methacryloyl (Gel-MA) can be easily solidified into a firm hydrogel under ultraviolet (UV) irradiation, making it a popular biomaterial as the printing ink.[21] Sodium alginate (Alg), a natural polysaccharide, is widely used in chemistry, biology, medicine, and food industries due to its film-forming, biodegradable, and biocompatible properties. These characteristics make it an ideal material for 3D bioprinting.[22]

In this study, we developed a 3D-printed porous scaffold using Alg and Gel-MA, leveraging their easy printing and molding characteristics, and incorporated stimulators to promote ectopic primordial follicle activation and growth. This Alg/Gel-based scaffold, featuring dual-crosslinking networks formed through ionic interactions between Alg and chemical crosslinking of Gel-MA, exhibits significantly improved mechanical properties. In addition, the activators were pre-mixed with the biomaterial, enabling the gradual release of the activators and the subsequent activation of primordial follicles after *in vivo* transplantation. Furthermore, our findings indicate that the 3D-printed scaffold containing activators can effectively support the ectopic activation of primordial follicles and subsequent development into growing follicles within the abdominal cavity of mice. This approach provides a promising direction for the clinical application of artificial ovaries and serves as a potential method for the clinical treatment of ovarian dysfunction and endocrine disorders.

2. Materials and methods

2.1. Materials

The main materials used in this study included gelatin from porcine skin (type A, reagent grade; Sigma-Aldrich, United States of America [USA]), MA (94%; Heowns Biochemical Technology Company, China), Alg (low viscosity; Sigma-Aldrich, USA), propranolol (PRO; BML-ST405-0005; Enzo Life Sciences, America), phosphatidic acid (PA; AvantiPolar Lipids, America), and a UV-light crosslinker (XL-1000 UV Crosslinker; Spectronics Corporation, USA).

2.2. Animals

All animal experiments were approved and performed in accordance with the guidelines of the Institutional

Animal Care and Use Committee of Shenzhen Institutes of Advanced Technology, Chinese Academy of Sciences. C57BL/6 mice were purchased from Beijing Vital River Laboratory Animal Technology Co., Ltd. (China) and maintained in our specific pathogen free-level animal facility. Green fluorescent protein (GFP)-reporting mice were purchased from the Nanjing Biomedical Research Institute of Nanjing University.

2.3. Bioink preparation and 3D printing

An appropriate amount (20 wt.%) of GelMA with 3 wt.% UV initiator 2-hydroxy-2-methylpropiophenone was dissolved in distilled water in a 60°C water bath. Thereafter, Alg was added to GelMA solution (the molar ratio of GelMA/Alg = 2:1) under atmospheric pressure and stirred in the dark for 20 min to form a homogeneous pre-hydrogel solution for 3D printing. The GelMA/Alg pre-hydrogel was transferred into a cylinder and installed into a 3D printer (Bioscaffolder 3.1; GeSiM, Germany). The printing parameters were 0.1–0.2 kPa for air pressure, 0.15 mm for fiber spacing and height, 10 mm/s for the printing speed, 50–60°C for the material barrel, and −20°C for the print platform. The angle between scaffold struts was 60°. The stimulators mixed into the material were 200 μM PA and 50 μM PRO. The 3D-printed scaffold was then put into the UV-light crosslinker for about 5 min and immersed in 1 mol/L of calcium chloride for further crosslinking and storage.[22,23]

2.4. Morphological examination with scanning electron microscopy

The appearance of the scaffolds, such as strands, pore size, and cross-section morphologies, was examined through a scanning electron microscope (SEM; ZEISS SUPRA®55; Carl Zeiss, Germany). Before SEM examination, the scaffolds were lyophilized in a freeze-dryer (BYK-025_TY3341; Beijing Boyikang Experimental Instrument Co. Ltd., China) for 24 h, and then coated with gold via a sputter coater.

2.5. Rheological testing

Rheological tests were performed with the ink on a rheometer (TA Instrument, Austria). The stage temperature was controlled between 15 and 40°C. The ink was loaded onto the stage, and mineral oil was used to prevent dehydration. The temperature sweep was carried out at 0.5°C/min and 1% strain.

2.6. Fourier-transform infrared spectroscopy

Fourier-transform infrared (FTIR) spectrometry (BRUKER VERTEX 70; Bruker, USA) was used to confirm the successful synthesis of the hydrogel.

2.7. Measurement of mechanical properties

The mechanical properties were evaluated via uniaxial compression test. After equilibration in deionized water, the scaffolds (14 × 14 × 3.5 mm) were measured on the tester (Instron 5697; Instron, USA). The crosshead speed was set at 10 mm/min.

2.8. Histological analyses

The tissues were collected and fixed in 4% paraformaldehyde for 24 h, dehydrated through graded ethanol, and embedded in paraffin. Thereafter, 5-μm-thick sections were stained with hematoxylin and eosin staining. For immunostaining, 3% peroxide was used to block endogenous peroxidase activity for 10 min at room temperature. Non-specific binding was blocked in phosphate-buffered saline (PBS) with 5% bovine serum albumin for 1 h at room temperature, followed by incubation with primary antibody (zona pellucida glycoprotein 3 [ZP3]) diluted in blocking solution (1:100) overnight at 4°C. After fully washing with PBS, the sections were incubated with the secondary antibody diluted in blocking solution for 1 h and detected with fresh diaminobenzidine solution; sections were counterstained with hematoxylin. Finally, the slides were photographed using an Olympus microscope (IX73P1F; Olympus, Japan).

2.9. PRO release assay

For the release assay, PRO was dissolved in the saline and PBS. The concentrations of the standard curve were 0, 3.125, 6.25, 12,5, 25, 50, and 100 μM, respectively. Scaffolds containing PRO were cut into 10 × 10 mm^2 and added into a 6-well plate with 5 mL saline and PBS, respectively. The drug release test was performed in a constant temperature shaker at 37°C with a rotational speed of 150 rpm. Approximately, 200 μL medium was removed at indicated time points, and the corresponding released medium of the same volume was added. The concentration of PRO in each sample was analyzed using a UV spectrophotometer (UV-8000, China) at 320 nm.[24] The cumulative drug release at different time points was calculated according to the standard curve.

2.10. Granulosa cell isolation and culture

The collection of ovarian granulosa cells was performed as described previously.[25] Briefly, 25-day-old female GFP mice were treated with pregnant mare serum gonadotropin (5 IU; ProSpec, Israel) for 48 h. Ovaries were removed and dissected from the oviducts and fat with a dissecting microscope. Granulosa cells were obtained from the ovarian tissue by follicular puncture and placed in PBS. The cell suspension was filtered with a 70 μm mesh sieve to remove oocytes and centrifuged at 1000 × *g* for 3 min.

Granulosa cells were cultured in DMEM/F12 medium complemented with 10% fetal bovine serum, 100 IU/mL penicillin, and 100 mg/mL streptomycin sulfate shortly for use. These granulosa cells were then seeded into the scaffold in 24-well plates for 7 days. The morphological change of the granulosa cells and scaffold was observed under a fluorescence microscope on days 1 and 7.

2.11. Transplantation

Ovaries from neonatal C57BL/6J mice were collected on day 3, as described above. The scaffolds were cut into proper size for implantation and rinsed with saline for 5 min. The recipient C57BL/6 mice (8–10 weeks) were weighed and anesthetized with avertin intraperitoneally. For kidney capsule transplantation, a longitudinal skin incision was made on the dorsum to expose the position of the kidney. A pair of forceps was used to hold the kidney out of the body; two small forceps were then used to split the capsule. Scaffolds with ovarian tissue were inserted into the capsule. For subcutaneous ectopic transplantation, the scaffolds containing ovarian tissue with or without stimulators were transplanted subcutaneously at the abdominal region of the recipient. Finally, sutures were used to close the incision. Due to the deficiency of growth hormone in ovariectomized recipient mice, the follicle stimulating hormone (FSH; 1 IU per day) was administrated through intraperitoneal injection to promote follicle growth. Three repeats of the experiment were carried out.

2.12. Statistical analysis

Data are presented as the mean ± Structural Equation Model (SEM). The statistical significance was assessed by a two-tailed Student's *t*-test. A p-value < 0.05 was considered statistically significant in this study.

3. Results

3.1. Preparation of scaffold materials and appearance of the 3D-printed porous scaffolds

Figure 1A illustrates the 3D printing process of the GelMA/Alg composite scaffold. The GelMA, containing unsaturated double bonds, can be efficiently crosslinked by UV light, while Alg can form an ionic crosslinking network through its strong interaction with divalent ions. This combination could enhance the construction of a high-strength GelMA/Alg composite hydrogel with double crosslinking networks. Moreover, the RGD motifs in the backbone of GelMA were beneficial for improving the biocompatibility of GelMA-based hydrogels; Alg's ability to adjust viscosity exhibits an outstanding adaptability for printing. Thus, the composite GelMA/Alg (2:1 in molar ratio) ink was ready for 3D printing; UV and ionic crosslinking were applied to solidify the 3D-printed GelMA/Alg hydrogel scaffolds. The printing process is displayed in Figure 1B and Video S1 (see Supplementary Information). The final shape of the printed scaffold after double crosslinking is featured in Figure 1C–F. The freeze-dried 3D scaffold microstructure displays a network of interconnected pores, and each pore size of the scaffold was 200 ± 50 μm (Figure 1G–I).

3.2. Gelatin/alginate-based scaffolds exhibit applicable mechanical properties

To meet the extrusion requirements of bioink, we generated a GelMA/Alg complex with optimized rheological properties to align with the pressure extrusion of a 3D printer (Figure 2A–D). The GelMA/Alg ink displays typical shear-thinning behaviors, and the viscosity can be adjusted by regulating the temperature in the range of 20–40°C, which is advantageous for extrusion printing. Characteristic absorption peaks at 819, 1031, and 1418 cm^{-1} for Alg, and 1242, 1336, and 1536 cm^{-1} for gelatin confirm the successful fabrication of hydrogel scaffold after double crosslinking (Figure 2E). At room temperature, 90% compression deformation was achieved for all wet-state supports. The scaffold exhibited good mechanical properties. The compression strength was about 3.3 MPa, with 400 kPa modulus, indicating that the scaffold was soft and elastic (Figure 2F).

3.3. Survival of ovarian granulosa cells *in vitro*

The process of isolating mice ovarian granulosa cells and cultivating them in a scaffold is illustrated in Figure 3A. To test the compatibility of the scaffold with ovarian cells, we chose granulosa cells dissected from GFP transgenic mice, which could be observed easily under a fluorescent microscope. It is demonstrated that the granulosa cells can adhere to the struts and maintain the basic cell morphology by day 1 (Figure 3B and D); an increase in interactions between the granulosa cells and the scaffold was observed after 7 days of culture (Figure 3C). Notable, the scaffold partially degraded over time, but the granulosa cells continued to grow in the struts, indicating that the scaffolds effectively support the survival of ovarian granulosa cells (Figure 3E).

3.4. Biocompatibility of the scaffolds for follicles under the kidney capsule

Although both gelatin and Alg are approved by the Food and Drug Administration (FDA, USA) and the National Medical Products Administration (NMPA, China) for clinical tissue engineering,[26,27] their biocompatibility for combined use for follicle development remains unclear.

The primordial follicle consists of a dormant oocyte and a single layer of pre-granulosa cells, which is at the initial stage of folliculogenesis and determines the duration of female reproduction.[28] In rodents, primordial follicles are

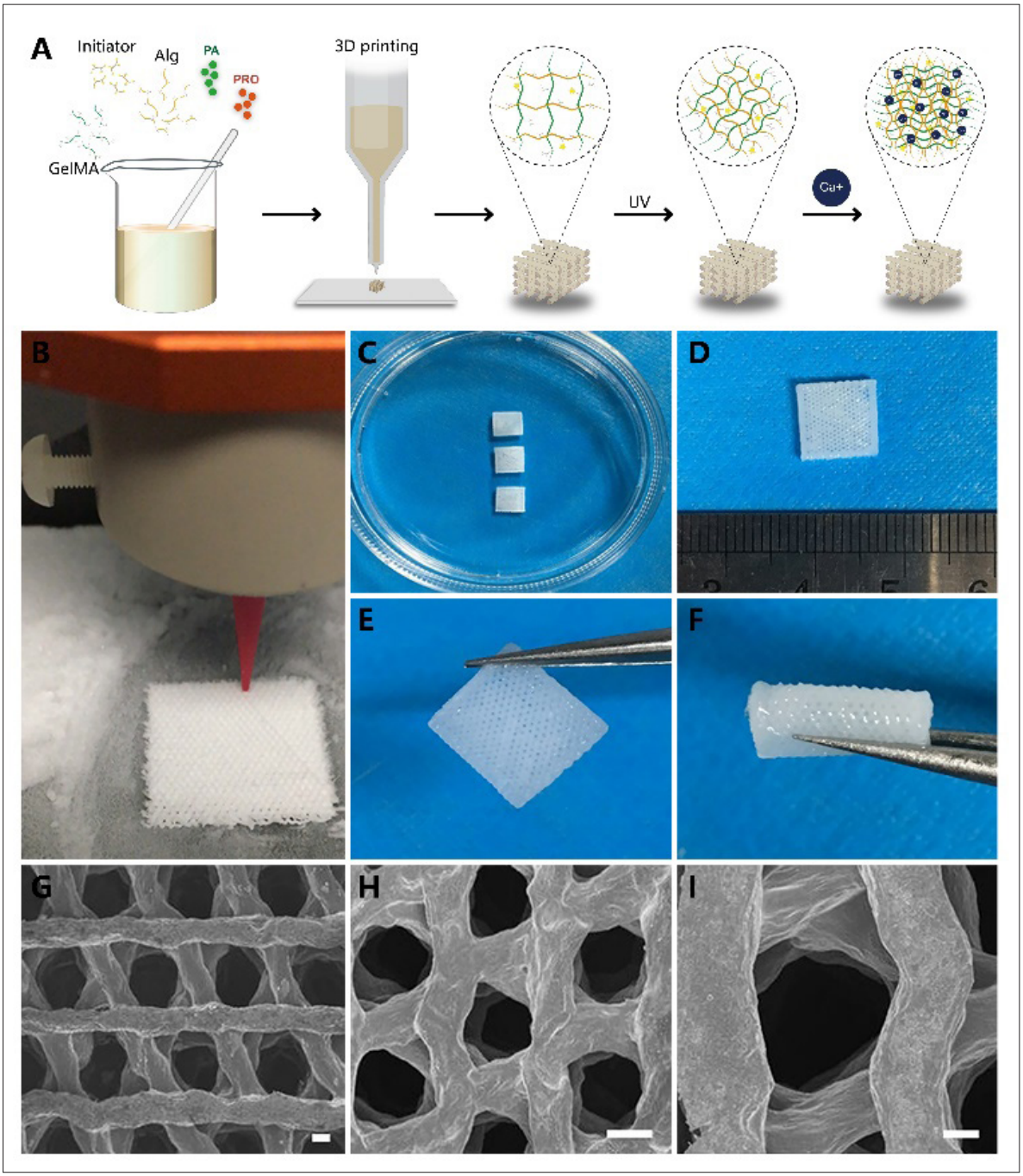

Figure 1. (A) Preparation of scaffold materials and the morphology of 3D-printed porous scaffolds. Te 3D printing process of the GelMA/Alg composite scaffold. (B) Te process of 3D printing on cryo-stage. (C–F) Appearance of scaffolds with proper elasticity. Appearance of the scaffolds (C), size of the scaffolds (D), side of the scaffolds (E), side of the scaffolds (F). (G–I) Observation of scaffold morphology via scanning electron microscopy is shown as magnification 40X (G), 50X (H), 100X (I), respectively. Scale bars: 100 μm (G, I), 200 μm (H). Abbreviations: Alg, alginate; GelMA, gelatin methacryloyl; UV, ultraviolet.

formed at about 19.5 days post coitum and re-assembled in the ovary until day 3 post parturition.[29] To validate the activation ability of PRO and PA, we selected the day 3 neonatal ovary as the model.

To validate scaffold biocompatibility for follicle development, the dissected day 3 ovarian tissue was placed in the scaffold and transplanted under the renal capsule of the adult female mouse with the ovary removed

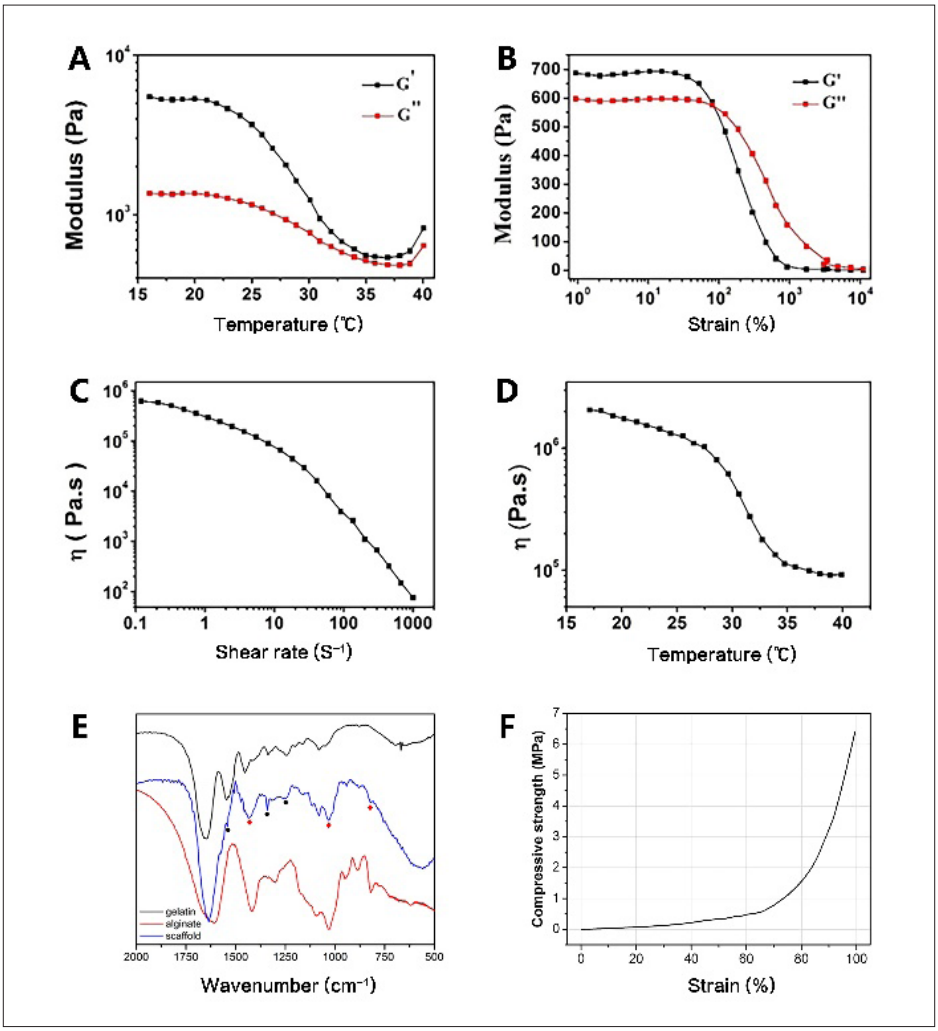

Figure 2. Mechanical properties of scaffolds. (A) Rheological properties of the scaffolds. (B) Tensile stress–strain and compressive stress–strain curves of the scaffolds. (C) Viscosity measurement of the scaffolds. (D) Result of temperature amplitude sweep test. (E) FTIR spectra. (F) Mechanical properties of the scaffolds. Abbreviations: FTIR, Fourier Transform Infrared Spectroscopy; G', elastic modulus; G'', damping modulus.

(Figure 4A–E). Results from Figure 4F and G suggested that follicle development within the scaffold proceeded normally after 1 week, with comparable morphology to the directly implanted day 3 ovarian tissue in the kidney capsule (Figure 4H and I).

3.5. Scaffold-induced sustained drug release

To activate the primordial follicles *in situ*, the ability of the scaffold to release activators locally is vital. PRO was chosen to evaluate the drug-release capabilities of the scaffold, and the concentrations of released PRO in saline and PBS were detected using a fluorescence spectrophotometer.

Standard curves of different PRO concentrations were initially plotted (Figure 5A and B). Then, at different time points, the supernatant collected from the two groups was evaluated to measure the PRO concentration. The results indicated that over time, the scaffold in saline rapidly released approximately 30% of PRO within the first hour, with a gradual increase to about 50% in 1–8 h, and then plateaued up to 96 h (Figure 5C). Similarly, the scaffolds in PBS also rapidly released 40% of the PRO in the first 4 h, slowly increasing to 50% in 4–24 h, and then also plateaued up to 96 h (Figure 5D). The scaffolds exhibited a consistent release profile in both saline and PBS, with a similar overall trend and sustained release efficiencies.

This characteristic has enabled us to develop a controlled system for realizing drug release. The PBS buffer was the primary compound of the tissue environment; the scaffold could be degraded slowly without extra stimulus, and the activators could be locally released, thereby minimizing systemic side effects.

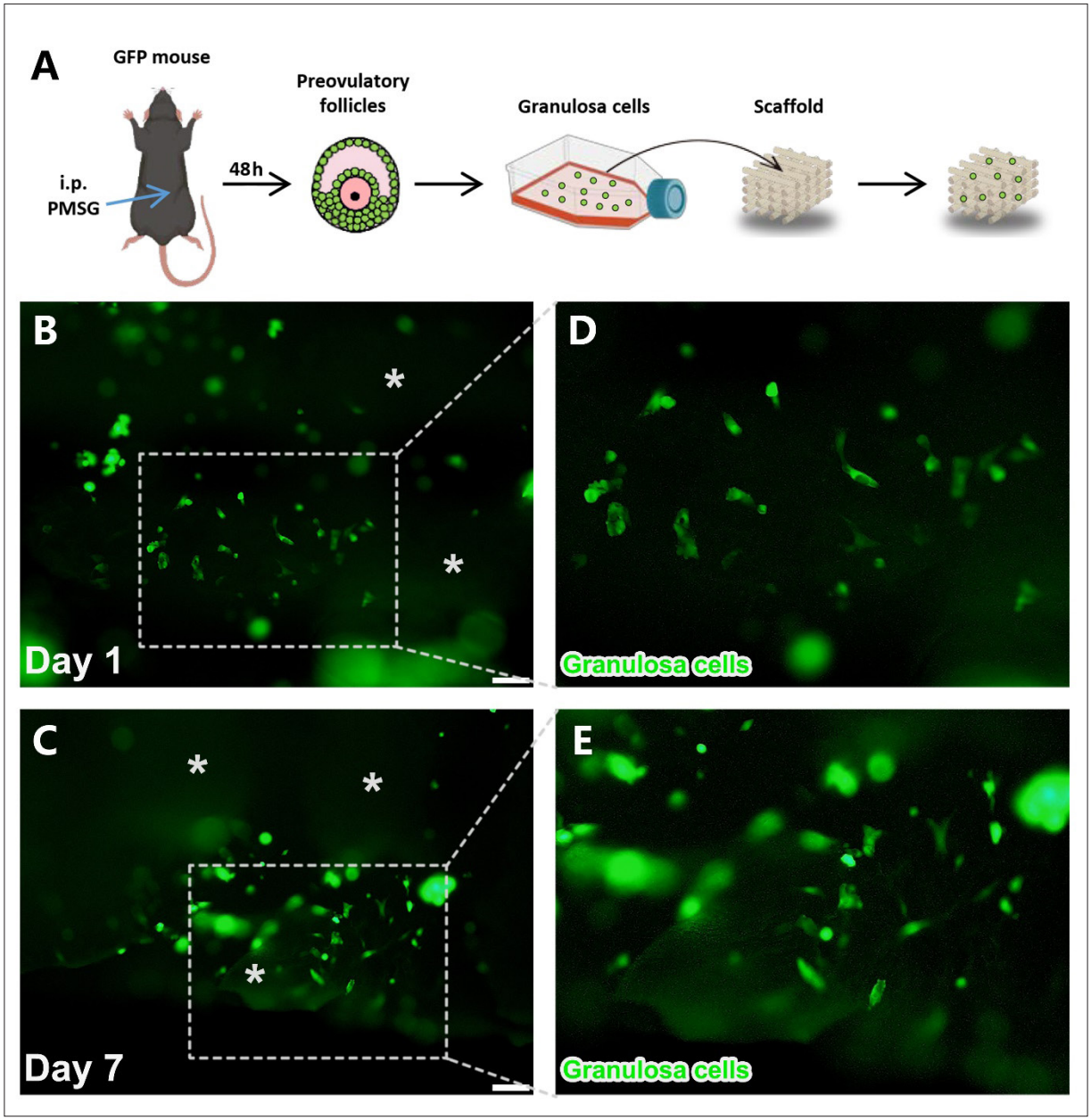

Figure 3. Ovarian granulosa cells survived in the scaffolds and interacted with struts *in vitro*. (A) The process of mouse ovarian granulosa cell isolation and implantation into the scaffold. (B and D) Fluorescence imaging of granulosa cells isolated from GFP transgenic mouse on the struts from day 1 of culture. (C and E) After 7 days of culture, the granulosa cells survived on the struts. * indicates the struts. Scale bar: 100 μm. Abbreviations: GFP, green fluorescent protein; i.p., intraperitoneal injection; PMSG, pregnant mare serum gonadotropin.

3.6. Dormant ovarian follicle activation and development in ectopic subcutaneous tissue

To ensure the practical use of an implanted artificial ovary, we tested if the scaffolds could support the activation and development of the primordial follicles when injected subcutaneously. We implanted the activated or inactivated ovary–scaffold complex into the abdominal subcutaneous pocket (Figure 6A). After FSH treatment in both activation and inactivation groups for 1 week, the primordial follicles in the activation group displayed obvious growing follicular morphological features, which were not observed in the inactivated group (Figure 6B). There is a significant increase in growing follicles in the activated group compared to the inactivated group (Figure 6C). Although few follicles could be observed in the inactivated group, there were no multiple layers of cuboidal granulosa cells,

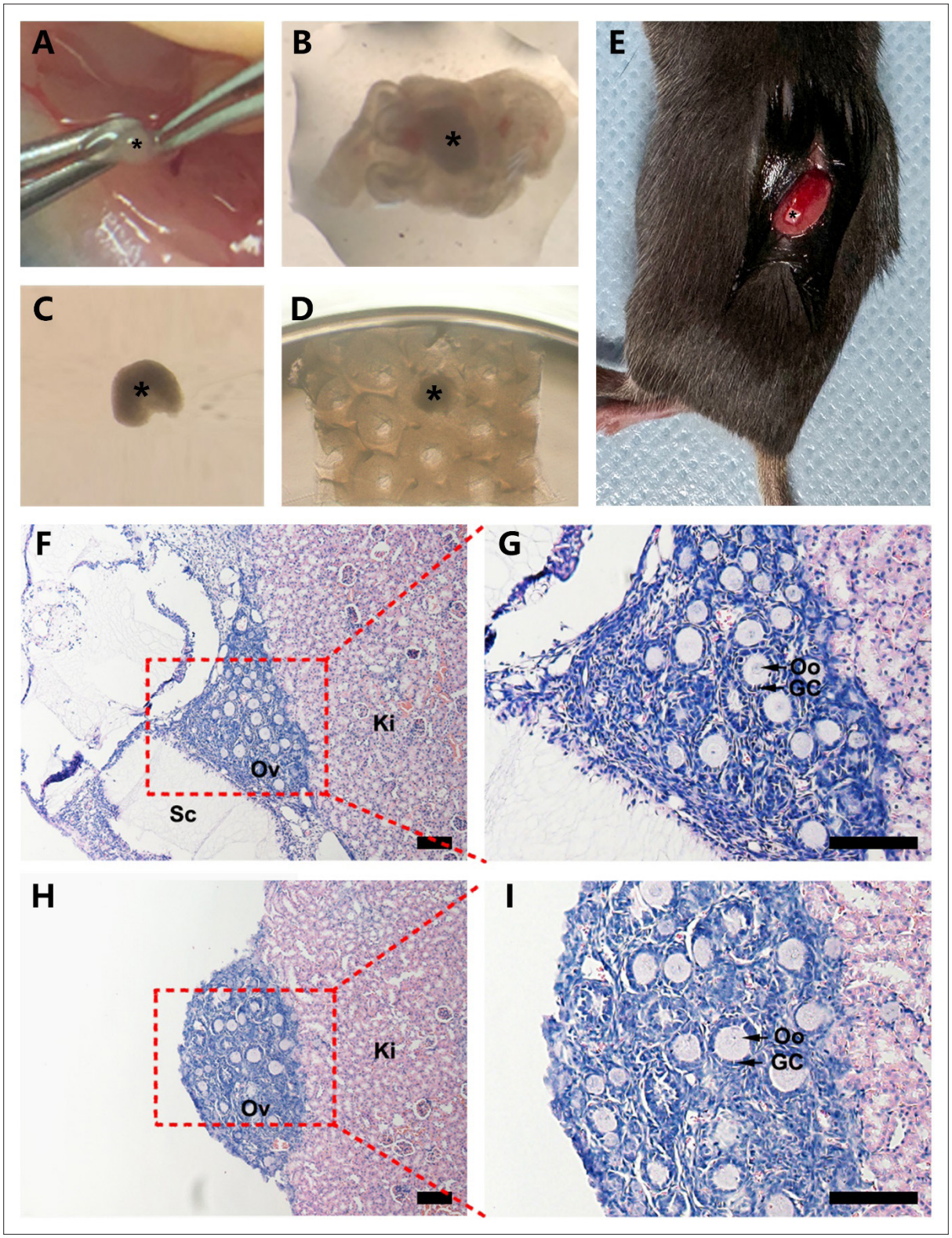

Figure 4. Biocompatibility test for the scaffolds under the kidney capsule. (A–E) Day 3 mouse ovary dissection, which was transferred to the scaffold, and then transplanted under the dorsal membrane of the kidney. (F and H) H&E section staining of kidney and ovary with scaffolds after transplantation for 1 week. (G and I) Enlarged morphology of ovary tissue grafted into the kidney capsule. Arrows indicated the ovary. Abbreviations: GC, granulosa cells; H&E, hematoxylin-eosin staining; Ki, kidney; Oo, oocyte; Ov, ovary; Sc, scaffold. Scale bars: 250 μm.

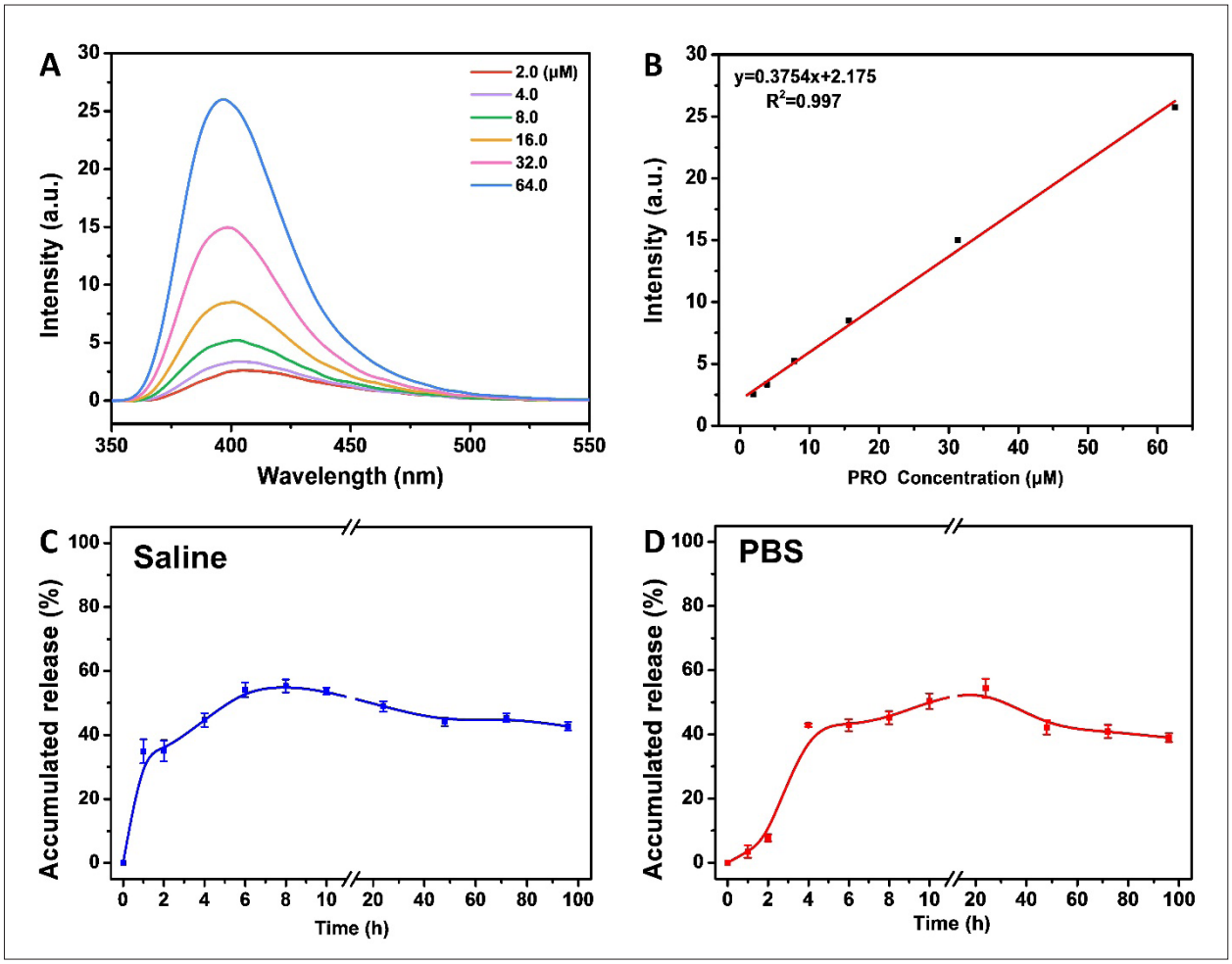

Figure 5. Sustained drug release in scaffolds. Propranolol (PRO) has a maximum emission spectrum at an excitation wavelength of 320 nm. (A) Fluorescence spectrum of different PRO concentrations. According to the maximum emission spectrum of different concentrations of PRO in Figure A, a (B) standard curve plotted based on (A). (C and D) Cumulative sustained release of the scaffold containing PRO in saline (C) and PBS (D), respectively ($n = 3$). The accumulated release refers to the amount of PRO in the scaffold. Abbreviation: PBS, phosphate-buffered saline.

which is essential during follicle development. These results were further confirmed by specific immunofluorescent staining of growing follicle biomarker ZP3. In addition, an abundance of growing follicles with zona pellucida shape and more granular cell layers were noticeable in the activated group, while the inactivated group lacked distinct ovarian and follicle morphological features (Figure 6D).

4. Discussion

Ovarian dysfunction would cause abnormalities in oogenesis, folliculogenesis, and ovulation, leading to infertility and endocrine disorders. Among them, primary ovarian insufficiency (POI) refers to the loss of ovarian functional follicles in women before the age of 40.[30] For patients with POI who have fertility needs, the most effective treatment is assisted reproductive technology. Clinical practice has found that the development potential of oocytes matured *in vitro* is poor, the abortion rate of embryo formation is relatively high, and there are no recognized effective improvement measures. Therefore, in this study, we introduced a strategy for the ectopic activation and development of primordial follicles *in vivo*, utilizing a well-designed scaffold printed from Alg and gelatin, integrated with activators.

Several materials have been utilized for printing 3D ovarian models, such as Alg, fibrin, and collagen.[14] In this study, we selected two widely used biomaterials in bioengineering that have excellent biocompatibility. Apart from materials, the crosslinking method is also critical to ensuring the function of the ovarian model. To date, the crosslinking methods for hydrogel include both chemical and physical methods.[31] Chemical methods refer to gels

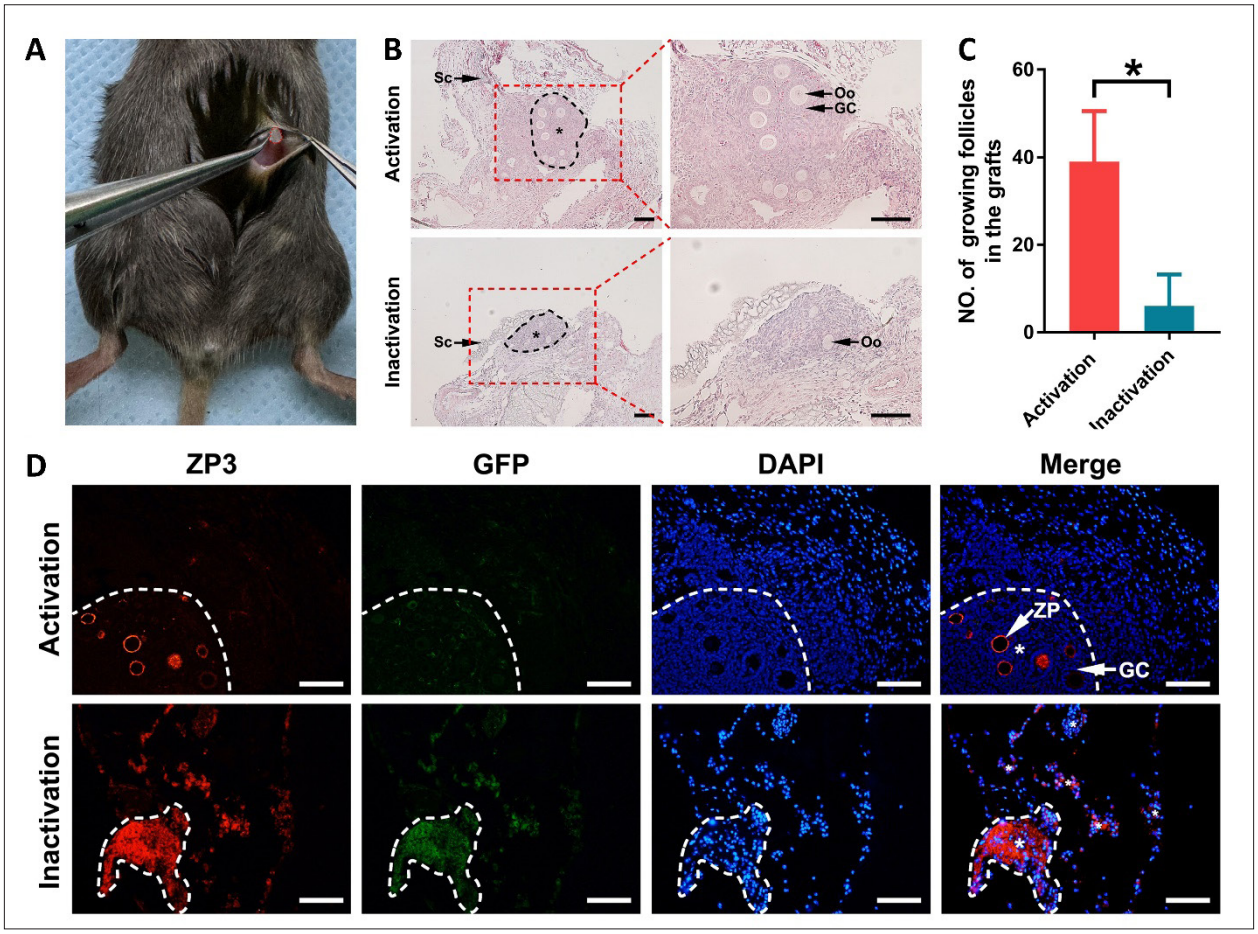

Figure 6. Dormant ovarian follicles were activated and developed within the ectopic subcutaneous tissue. (A) Schematic diagram of subcutaneous ectopic transplantation with scaffolds containing activators and day 3 ovary. (B) Morphological comparison of activated or inactivated primordial follicles. (C) Quantitative analysis was performed by counting the growing follicles in the grafts (n = 3). * indicates a significant difference (P=0.0137). (D) Immunofluorescent detection of growing follicle marker ZP3. The asterisk indicated the grafted ovary tissue. Abbreviations: GC, granulosa cells; Oo, Oocyte; Sc, scaffold; ZP, zona pellucida. Scale bars: 200 μm (B); 250 μm (D).

formed through the action of specific compounds or ions, such as Alg and DNA gel; physical methods are based on networks triggered by specific light wavelength or temperature changes, such as methylacrylamide-modified gelatin used in this study.[32] Therefore, in this study, by optimizing the ratio of gelatin to Alg, precisely controlling the 3D printer parameters, and combining the chemical and physical crosslinking methods, we have successfully obtained scaffolds with high porosity, uniform structure, and good mechanical stability. Furthermore, the results of co-culturing with granulosa cells and renal subcapsular transplantation indicate that the cells and ovarian tissues can survive and further develop in the scaffold, suggesting that the scaffold has good biocompatibility.

For primordial follicle activation, we selected a relatively mature activator combination, PA and PRO, which have been reported to activate the primordial follicle via the mTOR signaling pathway.[33] To date, studies related to primordial follicle activation have predominantly focused on signaling pathways. The use of the knockout mice model has revealed several signaling pathways in oocytes that contribute to the regulation of follicle activation. For example, the PI3K-PTEN-AKT-FOXO3 pathway is one of the most extensively studied.[34–36] Additionally, the downstream signal, mTOR, is regulated by the activation of AKT.[37,38] Currently, a variety of related activators and inhibitors have been used in clinical practice for the treatment of POI, such as the combination of mTOR and PI3K activators,[33] or mTOR and AKT activators.[39] Moreover, there are other alternative options for activating primordial follicles *in vitro*; further investigation is warranted to determine whether these options could still activate primordial follicles when incorporated into a scaffold.

The results of the release assay revealed that activators preloaded in the scaffolds could be gradually released in both PBS and saline, providing a more controlled system compared to the traditional in vitro activation process, which requires several hours of *in vitro* activation. This approach shortens patients' waiting time and reduces the adverse effects of prolonged exposure on follicles and oocytes when cultured *in vitro*. Furthermore, the ectopic activation model established here sheds light on future clinical applications and enables the growth of follicles through simple surgery and subcutaneous ectopic transplantation. Subcutaneous transplantation also simplifies the further handling of growing follicles, allowing for direct monitoring using ultrasonic techniques or the isolation of mature follicles for in vitro fertilization procedures.

By combining optimized biomaterials and 3D printing technology, along with the incorporation of primordial follicle activators, the future development of an artificial prosthetic ovary is on the horizon. This progress is expected to help alleviate endocrine disorders and even facilitate oocyte maturation.

5. Conclusion

We introduced a novel approach to developing a bioactive scaffold that could activate primordial ovarian follicles and facilitate their development into growing follicles in subcutaneous implantation sites. This study, for the first time, demonstrates the use of biostimulators released from biodegradable 3D scaffolds to more readily activate the primordial follicles ectopically. However, some technical challenges still need to be addressed. For example, it would be advantageous to implement *in vivo* imaging techniques for real-time monitoring of follicular development in the scaffold and develop a vascular system to supply nutrients to the scaffold.

Acknowledgments

None.

Funding

This study was supported by the National Natural Science Foundation of China (82301907), Guangdong Basic and Applied Basic Research Foundation (2024A1515010059 and 2024A1515030279), Shenzhen Medical Research Fund (B2404004), Shenzhen Science and Technology Program (JCYJ20220818101218040, JCYJ20220818103608017, JCYJ20220818103607015, JCYJ20220818102811025, JSGGKQTD20210831174330015), Shenzhen Key Laboratory of Metabolic Health (Grant No. ZDSYS20210427152400001), Sino-European Center of Biomedicine and Health.

Conflict of interest

The authors declare there is no conflict of interest.

Author contributions

Conceptualization: Jian V. Zhang, Changshun Ruan, Pei-Gen Ren
Data curation: Yali Yang, Mingming Wu
Formal analysis: Huashan Zhao, Zhonglin Xiao
Methodology: Yali Yang, Li Xue, Meiyue Wang, Jie Chen
Investigation: Jian V. Zhang, Tianxia Xiao
Writing – original draft: Yali Yang, Huashan Zhao
Writing – review & editing: Feifei Du, Li Ge, Pinpin Wang

Ethics approval and consent to participate

The animal experiments in this study were approved by the Institutional Animal Care and Use Committee of the Shenzhen Institutes of Advanced Technology, Chinese Academy of Sciences. All applicable guidelines and protocols for the care and use of animals were followed.

Consent for publication

Not applicable.

Availability of data

Data is available from the corresponding author upon reasonable request.

Supporting information

Video S1: The process of 3D printing on cryo-stage.

References

1. Liu CM, Ding LJ, Li JY, Dai JW, Sun HX. Advances in the study of ovarian dysfunction with aging. *Hereditas.* 2019;41(9):816-826.
doi: 10.16288/j.yczz.19-134

2. Harada M. Cellular senescence in the pathogenesis of ovarian dysfunction. *J Obstet Gynaecol Res.* 2024;50(5):800-808.
doi: 10.1111/jog.15918

3. Zhang T, He M, Zhang J, et al. Mechanisms of primordial follicle activation and new pregnancy opportunity for premature ovarian failure patients. *Front Physiol.* 2023;14:1113684.
doi: 10.3389/fphys.2023.1113684

4. Ford EA, Beckett EL, Roman SD, McLaughlin EA, Sutherland JM. Advances in human primordial follicle activation and premature ovarian insufficiency. *Reproduction.* 2020;159(1):R15-R29.
doi: 10.1530/rep-19-0201

5. Luyckx V, Dolmans MM, Vanacker J, et al. A new step toward the artificial ovary: survival and proliferation of isolated murine follicles after autologous transplantation in a fibrin scaffold. *Fertil Steril.* 2014;101(4):1149-1156. doi: 10.1016/j.fertnstert.2013.12.025

6. Vanacker J, Luyckx V, Dolmans MM, et al. Transplantation of an alginate-matrigel matrix containing isolated ovarian cells: first step in developing a biodegradable scaffold to transplant isolated preantral follicles and ovarian cells. *Biomaterials.* 2012;33(26):6079-6085. doi: 10.1016/j.biomaterials.2012.05.015

7. Shikanov A, Xu M, Woodruff TK, Shea LD. Interpenetrating fibrin-alginate matrices for in vitro ovarian follicle development. *Biomaterials.* 2009;30(29):5476-5485. doi: 10.1016/j.biomaterials.2009.06.054

8. Xu M, Fazleabas AT, Shikanov A, et al. In vitro oocyte maturation and preantral follicle culture from the luteal-phase baboon ovary produce mature oocytes. *Biol Reprod.* 2011;84(4):689-697. doi: 10.1095/biolreprod.110.088674

9. Kreeger PK, Deck JW, Woodruff TK, Shea LD. The in vitro regulation of ovarian follicle development using alginate-extracellular matrix gels. *Biomaterials.* 2006;27(5):714-723. doi: 10.1016/j.biomaterials.2005.06.016

10. Shikanov A, Zhang Z, Xu M, et al. Fibrin encapsulation and vascular endothelial growth factor delivery promotes ovarian graft survival in mice. *Tissue Eng Part A.* 2011;17(23-24):3095-3104. doi: 10.1089/ten.TEA.2011.0204

11. Kniazeva E, Hardy AN, Boukaidi SA, Woodruff TK, Jeruss JS, Shea LD. Primordial follicle transplantation within designer biomaterial grafts produce live births in a mouse infertility model. *Sci Rep.* 2015;5:17709. doi: 10.1038/srep17709

12. Henning NFC, Jakus AE, Laronda MM. Building organs using tissue-specific microenvironments: perspectives from a bioprosthetic ovary. *Trends Biotechnol.* 2021;39(8):824-837. doi: 10.1016/j.tibtech.2021.01.008

13. Jin Z, Li Y, Yu K, et al. 3D printing of physical organ models: recent developments and challenges. *Adv Sci.* 2021;8(17):e2101394. doi: 10.1002/advs.202101394

14. Nair R, Kasturi M, Mathur V, Seetharam RN, S Vasanthan K. Strategies for developing 3D printed ovarian model for restoring fertility. *Clin Transl Sci.* 2024;17(7):e13863. doi: 10.1111/cts.13863

15. Pennarossa G, Arcuri S, De Iorio T, Gandolfi F, Brevini TAL. Current advances in 3D tissue and organ reconstruction. *Int J Mol Sci.* 2021;22(2):830. doi: 10.3390/ijms22020830

16. Wu T, Gao YY, Su J, et al. Three-dimensional bioprinting of artificial ovaries by an extrusion-based method using gelatin-methacryloyl bioink. *Climacteric.* 2022;25(2): 170-178. doi: 10.1080/13697137.2021.1921726

17. Laronda MM, Rutz AL, Xiao S, et al. A bioprosthetic ovary created using 3D printed microporous scaffolds restores ovarian function in sterilized mice. *Nat Commun.* 2017;8:15261. doi: 10.1038/ncomms15261

18. Aydin S, Yaşlı M, Yildiz Ş, Urman B. Advancements in three-dimensional bioprinting for reproductive medicine: a systematic review. *Reprod Biomed Online.* 2024;49(4):104273. doi: 10.1016/j.rbmo.2024.104273

19. Gandolfi F, Ghiringhelli M, Brevini TAL. Bioengineering the ovary to preserve and reestablish female fertility. *Anim Reprod.* 2020;16(1):45-51. doi: 10.21451/1984-3143-ar2018-0099

20. Zivari-Ghader T, Dolati S, Mehdizadeh A, Davaran S, Rashidi MR, Yousefi M. Recent scaffold-based tissue engineering approaches in premature ovarian failure treatment. *J Tissue Eng Regen Med.* 2022;16(7):605-620. doi: 10.1002/term.3306

21. Gao F, Xu Z, Liang Q, et al. Osteochondral regeneration with 3D-printed biodegradable high-strength supramolecular polymer reinforced-gelatin hydrogel scaffolds. *Adv Sci.* 2019;6(15):1900867. doi: 10.1002/advs.201900867

22. Gao F, Xu ZY, Liang QF, et al. Direct 3D printing of high strength biohybrid gradient hydrogel scaffolds for efficient repair of osteochondral defect. *Adv Funct Mater.* 2018;28(13):1706644. doi: 10.1002/adfm.201706644

23. Zhai X, Ruan C, Ma Y, et al. 3D-bioprinted osteoblast-Laden nanocomposite hydrogel constructs with induced microenvironments promote cell viability, differentiation, and osteogenesis both in vitro and in vivo. *Adv Sci.* 2018;5(3):1700550. doi: 10.1002/advs.201700550

24. Sahoo J, Murthy PN, Biswal S, Sahoo SK, Mahapatra AK. Comparative study of propranolol hydrochloride release from matrix tablets with KollidonSR or hydroxy propyl methyl cellulose. *AAPS PharmSciTech.* 2008;9(2):577-582. doi: 10.1208/s12249-008-9092-2

25. Yang YL, Sun LF, Yu Y, et al. Deficiency of Gpr1 improves steroid hormone abnormality in hyperandrogenized mice. *Reprod Biol Endocrinol.* 2018;16(1):50. doi: 10.1186/s12958-018-0363-9

26. Sosnik A. Alginate particles as platform for drug delivery by the oral route: state-of-the-art. *ISRN Pharm.* 2014;2014:926157. doi: 10.1155/2014/926157

27. Jaipan P, Nguyen A, Narayan RJ. Gelatin-based hydrogels for biomedical applications. *MRS Commun.* 2017;7(3):416-426. doi: 10.1557/mrc.2017.92

28. Pepling ME. From primordial germ cell to primordial follicle: mammalian female germ cell development. *Genesis*. 2006;44(12):622-632.
doi: 10.1002/dvg.20258

29. O'Connell JM, Pepling ME. Primordial follicle formation – some assembly required. *Curr Opin Endocr Metab Res.* 2021;18;118-127.
doi: 10.1016/j.coemr.2021.03.005

30. Wesevich V, Kellen AN, Pal L. Recent advances in understanding primary ovarian insufficiency. *F1000Res*. 2020;9:F1000 Faculty Rev-1101.
doi: 10.12688/f1000research.26423.1

31. Gill EL, Li X, Birch MA, Huang YYS. Multi-length scale bioprinting towards simulating microenvironmental cues. *Biodes Manuf.* 2018;1(2):77-88.
doi: 10.1007/s42242-018-0014-1

32. Xu C. Freeform vertical and horizontal fabrication of alginate-based vascular-like tubular constructs using inkjetting. *J Manuf Sci Eng.* 2014;136(6):061020.

33. Sun X, Su Y, He Y, et al. New strategy for in vitro activation of primordial follicles with mTOR and PI3K stimulators. *Cell Cycle*. 2015;14(5):721-731.
doi: 10.1080/15384101.2014.995496

34. Castrillon DH, Miao L, Kollipara R, Horner JW, DePinho RA. Suppression of ovarian follicle activation in mice by the transcription factor Foxo3a. *Science.* 2003;301(5630):215-218.
doi: 10.1126/science.1086336

35. Liu L, Rajareddy S, Reddy P, et al. Infertility caused by retardation of follicular development in mice with oocyte-specific expression of Foxo3a. *Development.* 2007;134(1):199-209.
doi: 10.1242/dev.02667

36. Reddy P, Liu L, Adhikari D, et al. Oocyte-specific deletion of Pten causes premature activation of the primordial follicle pool. *Science.* 2008;319(5863):611-613.
doi: 10.1126/science.1152257

37. Adhikari D, Flohr G, Gorre N, et al. Disruption of Tsc2 in oocytes leads to overactivation of the entire pool of primordial follicles. *Mol Hum Reprod.* 2009;15(12):765-770.
doi: 10.1093/molehr/gap092

38. Adhikari D, Zheng W, Shen Y, et al. Tsc/mTORC1 signaling in oocytes governs the quiescence and activation of primordial follicles. *Hum Mol Genet.* 2010;19(3):397-410.
doi: 10.1093/hmg/ddp483

39. Cheng Y, Kim J, Li XX, Hsueh AJ. Promotion of ovarian follicle growth following mTOR activation: synergistic effects of AKT stimulators. *PLoS One.* 2015; 10(2):e0117769.
doi: 10.1371/journal.pone.0117769

ACCSCIENCE PUBLISHING

International Journal of Bioprinting

RESEARCH ARTICLE

Heterotopically differentiated PDLSCs-laden 3D-bioprinted scaffolds for concurrent oral hard and soft tissue regeneration

Huilin Zhu[1,2†], Ke Yi[1,2†], Zhihui Tang[1,2*],and Qing Li[1,2,3*]

[1] Second Clinical Division, Peking University School and Hospital of Stomatology, Beijing, China

[2] National Center for Stomatology and National Clinical Research Center for Oral Diseases and National Engineering Research Center of Oral Biomaterials and Digital Medical Devices, Beijing, China

[3] Center of Digital Dentistry, Peking University School and Hospital of Stomatology, Beijing, China

Abstract

Following dental extraction, the alveolar bone and gingival tissues could undergo varying degrees of resorption, which affects subsequent implant integration and aesthetic outcomes. Thus, having adequate volume of both hard and soft tissues for implantation or aesthetic restoration is essential for optimal results. Three-dimensional (3D) bioprinting technology offers the advantages of biomimicry, personalization, and precise spatial distribution, which are pivotal for enhancing the success and esthetics of dental restorations. In this study, we fabricated a construct with a natural transition and varying material concentrations by 3D bioprinting, comprising an upper layer of collagen/alginate/periodontal ligament stem cells (PDLSCs) and a lower layer of collagen/nano-hydroxyapatite (nHA)/alginate/PDLSCs. Characterization of the physicochemical properties revealed that the incorporation of nHA significantly enhanced the mechanical properties of both the bioink and the construct.Flow cytometry analysis confirmed the stemness of PDLSCs. Scanning electron microscopy (SEM) revealed that the construct possesses satisfactory pore density and a natural transition at the stratification point. The construct displayed good cell viability and proliferation, with the cellular movement observed at the stratification interface after bioprinting. Differentiation staining and quantitative reverse-transcription polymerase chain reaction (RT-qPCR) results demonstrated that PDLSCs within the 3D construct are capable of both osteogenic and fibroblastic differentiations. Ectopic transplantation in mice confirmed the biocompatibility of the construct. A rat tooth extraction model validated the construct's effectiveness in the integrated regeneration of both hard and soft tissues in alveolar ridge preservation. In conclusion, this personalized, concentration-varied 3D construct exhibits excellent biocompatibility and tissue preservation effects, holding significant potential for clinical application.

Keywords: 3D bioprinting; Heterotopic differentiation; Stem cells; Oral tissue engineering

†These authors have contributed equally to this work.

***Corresponding authors:**
Zhihui Tang (zhihui_tang@bjmu.edu.cn)

Qing Li (qingli@bjmu.edu.cn)

Citation: Zhu H, Yi K, Tang Z, Li Q. Heterotopically differentiated PDLSCs-laden 3D-bioprintedscaffolds for concurrent oral hard and soft tissue regeneration. *Int J Bioprint*. 2025;11(1):259-283. doi: 10.36922/ijb.4889

Received: September 19, 2024
1st revised: October 8, 2024
2nd revised: October 23, 2024
Accepted: October 24, 2024
Published Online: October 24, 2024

Copyright: © 2024 Author(s). This is an Open Access article distributed under the terms of the Creative Commons Attribution License, permitting distribution, and reproduction in any medium, provided the original work is properly cited.

Publisher's Note: AccScience Publishing remains neutral with regard to jurisdictional claims in published maps and institutional affiliations.

1. Introduction

The alveolar bone serves as the supportive structure for teeth, with the surface covered by gingival tissue. Following tooth extraction, both the alveolar bone and gingiva undergo a natural process of remodeling, generally resulting in a reduction in volume compared to the pre-extraction condition. Research suggested that within six months post-extraction, the extent of bone resorption is expected to range between 29% and 63% in width and 11% and 22% in height.[1] The resorption of hard and soft tissues may impede subsequent implant placement, particularly in the anterior region, where the deficiency in alveolar ridge dimensions may lead to suboptimal aesthetic outcomes.[2,3]

To mitigate the need for extensive bone and soft tissue augmentation procedures post-extraction, the concept of alveolar ridge preservation (ARP) has been introduced. The ARP technique involves the placement of bone substitutes in the alveolar socket, usually followed by a soft tissue graft.[4] The traditional ARP often employs graininess bone and autogenous soft tissues, involving complex procedures, extended clinical operation time, and a higher risk of postoperative complications. A review has highlighted that the combined use of bone and soft tissue substitutes in ARP is associated with increased treatment costs.[5] Three-dimensional (3D) bioprinting offers the potential to fabricate biomimetic, integrated hard and soft tissue structures to improve clinical outcomes. To enhance clinical efficiency and efficacy and to explore the effects of ARP, this article introduces a new integrated 3D-printed biomaterial.

Collagen has been extensively utilized in dental applications, such as membranes, bone institute materials, drug delivery systems, and hemostatic agents. It plays an important role in wound healing and angiogenesis, making it an ideal candidate for sealing wounds and closing extraction sites to facilitate healing.[6] Collagen-based membranes have been effective in periodontal and implant therapies, serving as barriers against epithelial migration.[7] A meta-analysis has demonstrated that crosslinked collagen membranes exhibit superior performance in restoring soft tissue thickness and height compared to other materials in ARP.[8] Nano-hydroxyapatite (nHA) serves as an ideal substitute for the inorganic component in natural bone minerals, boasting superior osteoinductive properties that render it advantageous for applications such as orthopedic implant coatings and bone substitute fillers.[9] The organic phase of bone tissue, predominantly composed of type I collagen, constitutes 90% of the bone composition, while the inorganic phase is primarily hydroxyapatite (HA).[10] The combination of HA and collagen is widely applied in the field of oral tissue regeneration. In clinical practice, ARP commonly involves the implantation of bone matrix materials, followed by the application of a collagen membrane over the top to facilitate the volumetric retention of both bone and soft tissues. Studies have demonstrated that the use of xenogeneic bone substitutes in conjunction with collagen membranes can effectively maintain bone structure following tooth extraction.[11,12] However, there remains a gap in the accessibility of an integrated material designed for the simultaneous regeneration of both hard and soft tissues in ARP.We integrated natural collagen with nHA to create a cohesive material, which is poised to facilitate future clinical applications.

The alveolar bone surface, characterized by compact bone, exhibits a gradual decrease in bone density with increasing depth.[13] The average content of HA in the trabecular bone is comparatively lower than that in the compact bone; therefore, 3D bioprinting technology can be used to mimic the variation in HA content within the alveolar bone by altering pore diameter density.[14] The gingival connective tissue is composed of a dense network of type I collagen fibers, providing rigidity to the gingiva and firmly attaching them to the alveolar bone.[15]

Periodontal ligament stem cells (PDLSCs) possess the multipotent ability to differentiate into cells of osteogenic and fibroblastic lineages.[16] In a pioneering study, Seo et al.[17] co-transplanted PDLSCs with HA scaffold into periodontal defects in mice, leading to the reconstruction of cementum and periodontal ligament-like structures. Previous studies on the construction of heterogeneous structures using 3D bioprinting have predominantly focused on the regeneration of articular cartilage and skin. Historically, layered structures in these studies have employed different types of cells, which were mixed with various materials to assess tissue regeneration outcomes.[18–21] Typically, when engineering tissues at different hierarchical levels, a blend of distinct cell types is employed. For instance, the construction of biomimetic tissues such as articular cartilage[21,22] and the muscle-tendon interface[23] demonstrates this approach. Therefore, the bidirectional differentiation of PDLSCs holds immense promise for applications in oral bone and soft tissue engineering. In previous studies, the differentiation capabilities of PDLSCs were primarily focused on osteogenic or fibroblastic applications,[24–26] with few researches having simultaneously leveraged the multi-lineage differentiation potential of these cells.[16] We have harnessed the multi-lineage differentiation advantages of PDLSCs, promoting their bidirectional differentiation within an integrated material, thereby proposing new possibilities for tissue regeneration and future clinical applications.

The extraction socket appears to be an excellent model for testing the integration of hard and soft tissue-printed

structures, offering the potential for further exploration into the simultaneous heterologous differentiation of stem cells and the biological effects of ARP. Consequently, the aim of this research is to design a macro and microporous structure that mimics the gradient variation of collagen/HA, and encapsulate heterotopically differentiated PDLSCs to manufacture a bioactive, integrated hard and soft tissue repair material for post-extraction sockets.

2. Materials and methods

2.1. Bioink preparation and characterization

2.1.1. Cell preparation

Healthy periodontal tissues were extracted from orthodontic teeth or impacted third molars removed from adults aged 18–25. PDLSCs were isolated using an enzymatic digestion method. The study was approved by the Ethics Committee of the Peking University School and Hospital of Stomatology (PKUSSIRB-201950166), and all patients provided informed consent for sample collection. The cell proliferation medium (PM) consisted of α-MEM (Gibco, USA) supplemented with 10% fetal bovine serum (NOVA Medical Science and Technology Co., Ltd., Shanghai, China) and 1% Penicillin-Streptomycin-Amphotericin B Solution (Analysis Quiz, Beijing, China). Cells were cultured in this medium at 37°C in a 5% CO_2 incubator, with the medium replaced every 2–3 days. Once 80% confluence was reached, the cells were subcultured using 0.25% trypsin-EDTA (Gibco, USA). The osteogenic differentiation medium (OM) for PDLSCs was freshly prepared immediately before use, containing 100 nM dexamethasone (Sigma–Aldrich Co., Germany), 50 mM L-ascorbic acid (Sigma–Aldrich Co., Germany), and 10 mM β-glycerophosphate (Sigma Aldrich Co., Germany). All PDLSCs were used within five passages post-isolation.

2.1.2. Bioink preparation

The bioinks were categorized into two groups: collagen/alginate (CA) and collagen/nHA/alginate (CHA). Type I bovine tendon collagen sponges (Collagen Biotechnology Co. Ltd., China) were dispersed at a concentration of 0.03g/mL in 0.05mol/L acetic acid to prepare the collagen ink. nHA particles, with an average size of 60–80 nm and a molecular weight of 502.31 (Macklin Biochemical Co. Ltd., Shanghai, China), were incorporated into the collagen gel and continuously stirred at 45 rpm at 4°C for 12 hours to obtain the collagen/nHA bioink. Both bioinks were uniformly mixed with 10% alginate (Cat no. 180947; Sigma Aldrich, Germany) for subsequent Ca^{2+}crosslinking in 3D constructs. A macroscopic photograph of the prepared bioinks is presented (Figure 1a). The PDLSC-laden bioinks were fabricated by gently mixing PDLSCs (1×10^6cells/mL) with the CA and CHA inks.

2.1.3. Rheological analysis

The rheological properties of various bioinks were evaluated using a rotational rheometer (Discovery HR2; TA Instruments, Inc., USA) to assess their storage modulus (G′), loss modulus (G″), and complex viscosity. After applying a 0.6 Pa pressure for one minute, the bioinks reached equilibrium. Liquid, acellular bioinks were loaded onto the Peltier stage for individual measurements, with each sample undergoing a single test before disposal. Oscillatory temperature sweeps from 4°C to 35°C at a rate of 1.5°C/min were performed, with a duration of 10 minutes, and stress sweeps from 0.1 to 1000 Pa were conducted at a frequency and strain of 1 Hz and 1%, respectively. Strain sweeps (from 0.01% to 1%) were carried out at a fixed frequency of 1 Hz, while frequency sweeps (from 0.1 to 100 Hz) were performed at a fixed strain of 1%. To determine whether the viscosity of the bioinks decreases over time under shear, steady-state shear measurements were conducted at shear rates ranging from 0.1 to 100 s^{-1}.

2.1.4. Attenuated total reflectance-Fourier transform infrared spectroscopyanalysis

Chemical compositions of the CA and CHA bioinks were analyzed using an attenuated total reflectance-Fourier transform infrared spectroscopy (ATR-FTIR) (Bruker, Germany), within the spectral range of 500 to 4000 cm^{-1} at a resolution of 4 cm^{-1}. Each sample was directly analyzed on the ATR accessory equipped with a diamond crystal. A total of 32 scans were performed for each sample.

2.1.5. Thermogravimetric analysis

The thermal stability of the samples was assessed using thermogravimetric analysis (TGA) performed on a Thermal Gravimetric Analyzer (TA Instruments, Newcastle, DE, USA). The temperature was ramped at a rate of 10°C per minute, starting from 0°C and reaching up to 300°C. Throughout the heating process, a continuous purge of nitrogen gas at a flow rate of 100 mL/min was maintained. The spectral data were collected using the Q600 software (TA Instruments).

2.1.6. Flow cytometric analysis

Flow cytometry was employed to assess the presence and abundance of surface markers in the extracted cells. The analysis aimed to detect the presence of mesenchymal markers CD29, CD90, and CD146, characteristic of PDLSCs, while also evaluating the absence of CD45 and STRO-1, which further confirms the stem cell phenotype. Following the second passage, when the cells reached approximately 80% confluence, they were treated with 0.25% trypsin/EDTA, enumerated, and then resuspended in a 1% bovine serum albumin (BSA) solution to prepare a cell suspension at a concentration of 1×10^6 cells/mL.

Fluorescent antibody dyes specific for human CD29, CD45, CD90, CD146, and STRO-1 (1:20 dilution; Proteintech, USA) were added to the cell suspension and incubated in the dark at 4°C for 30 minutes. Post-washing, the cells were resuspended in 1% BSA and analyzed using a flow cytometer (TY2021001557, NovoCyte, USA). The analysis included the collection of 10,000 fluorescently labeled cells to ensure sufficient data for statistical analysis.

2.2. Preparation for 3D-bioprinting constructs

2.2.1. 3D bioprinting

The fabrication of 3D-printed constructs was performed using an extrusion-based 3D bioprinter (BMP-C300-T300-IN3, Medprin, China). During the printing process, nozzles with an inner diameter of 160–210μm were utilized for the extrusion of CA and CHA bioinks. The hydrogel was successfully extruded into fine filaments under a pressure of 0.15 MPa (Figure 1b). The extrusion of hydrogel was hard with nozzles having an inner diameter less than 160μm, and when the nozzle diameter was too large, the hydrogel dropped, due to gravity, in droplet form. A 3D structure with varying densities was designed using SOLIDWORKS 2024 (Dassault Systems, USA) to create a continuous construct with a gradient of density from top to bottom. Prior to printing, the designed cuboid model was imported into the printer as a stereolithography file and converted into slices by the MP Bioprint-v41 software (Figure 1c). The construct consisted of 10 layers, with the upper 5 layers made of CA and the lower 10 layers made of CHA, whose upper 3 layers had a denser structure, while the lower 7 layers were more sparse, thus forming a density-varying printed structure that affects the distribution of nHA content. Both types of bioinks were loaded into two separate sterile 1 mL syringes and uniformly mixed with PDLSCs. The co-axial printing function was employed, with the syringe containing CA bioink printing the upper structure and the one with CHA bioink printing the lower structure (Figure 1d). The bioinks were extruded along the X-Y path of each layer and transitioned to the Z-axis at the end of each layer.

After multiple rounds of printing trials, the printing parameters were optimized (Table 1) to ensure the reproducibility of the printing process and to maximize cell viability. Once the construct was printed, it was crosslinked at room temperature using a 50 mM sterile calcium chloride ($CaCl_2$) solution for 10 minutes. Subsequently, it was rinsed with phosphate-buffered saline (PBS) to remove any residual $CaCl_2$ and then transferred to a PM for further cultivation.

2.2.2. Compressive modulus analysis

Given that the primary load-bearing mechanism for bone and soft tissues is compression[27] our study focused on the behavior of constructs under compressive loading. CA, CHA, and CA/CHA constructs of appropriate dimensions (10 mm × 10 mm × 5 mm) were fabricated, and their length, width, and thickness were manually verified using a vernier caliper. The compression tests were conducted using a universal testing machine (Instron Model 3342, Illinois Tool Works, Inc., MA, USA). Samples were placed between the load-bearing sensors of a circular metal plate and compressed at a rate of 0.5 mm/min to a deformation of 80%, with their compression displacement and the corresponding force values being recorded.

Table 1. The printing parameters of the extrusion-based 3D bioprinting

Group	Platform temperature (°C)	Pressure (MPa)	Speed (mm/s)	Needle gauge (G)
CA	4	0.15	8	30
CHA	4	0.15	8	27

Abbreviations: CA: Collagen/alginate; CHA: Collagen/nano-hydroxyapatite/alginate.

2.2.3. Scanning electron microscopy analysis

The microstructure of the constructs was examined using field-emission scanning electron microscopy (FESEM; Model S-4800; Hitachi High-Technologies Co., Tokyo, Japan). All samples were coated with a thin layer of platinum via sputtering to enhance the resolution of the micrographs. Subsequently, the gold-sputtered samples were observed under an acceleration voltage of 3 kV.

2.3. *In vitro* study

2.3.1. Cell viability assay

A live/dead cell staining kit (KeyGEN Biotech Co., Jiangsu, China) was employed to assess cell viability within the CA and CHA constructs on days 1, 4, and 7 post-printing. The constructs were incubated in a solution containing 8 μM propidium iodide and 2 μM calcein-AM for a period of 30–45 minutes. After incubation, the working solution was aspirated to terminate the staining process, and the samples were then examined using an inverted fluorescence microscope (Olympus, Japan).

2.3.2. Cell proliferation analysis

The Cell Counting Kit-8 (CCK-8; Analysis Quiz, Beijing, China) was utilized to assess cell proliferation within the CA and CHA constructs on days 1, 3, 5, and 7 post-printing. To mitigate the interference of the materials with the CCK-8 reagent, which could affect the experimental outcomes, healthy PDLSCs were cultured with the material extract. A 12-transwell plate was employed to co-culture the adherent cells with the material, with a fixed amount of material added to each well chamber and culture

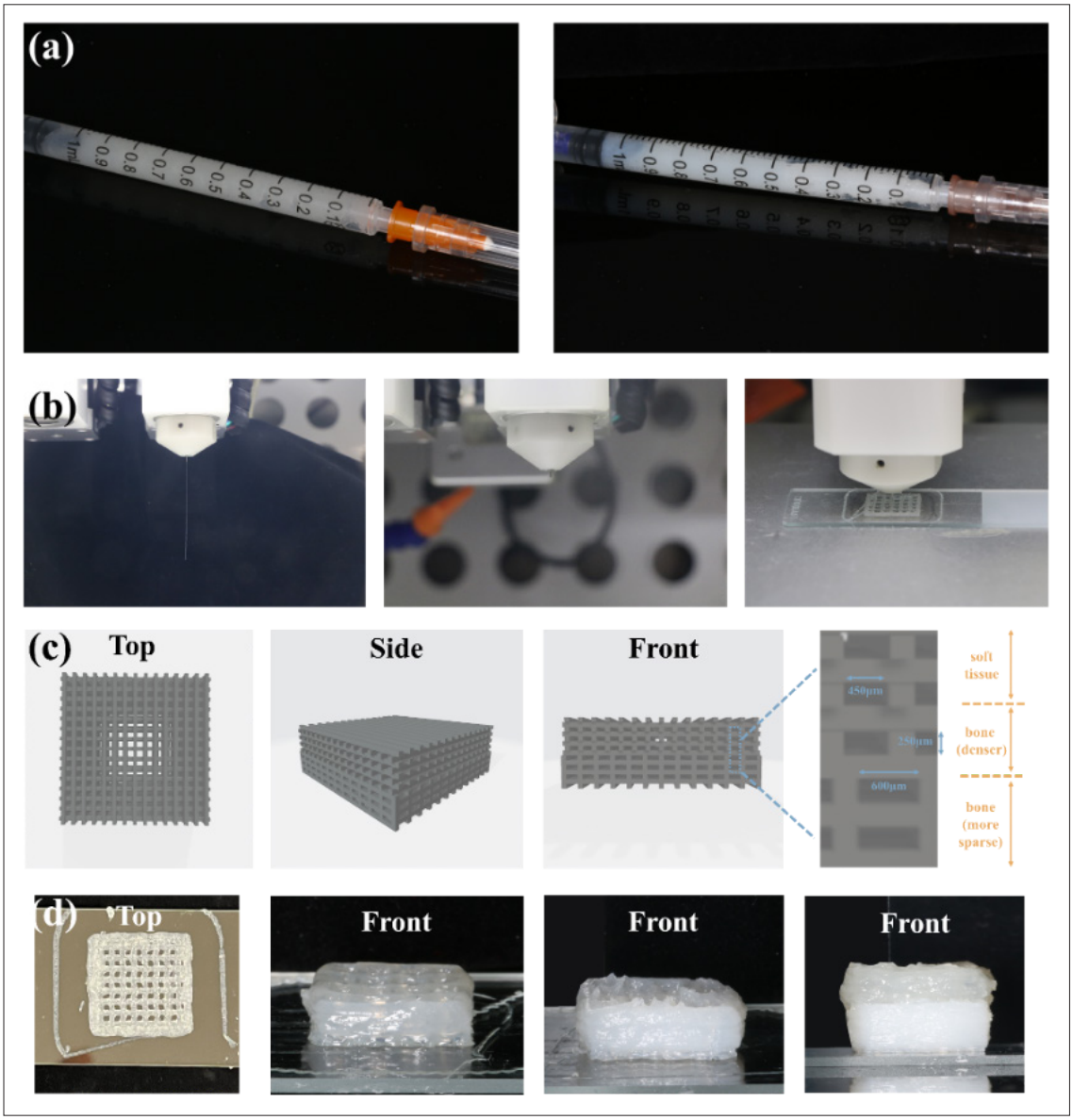

Figure 1. Macroscopic images of bioinks, bioprinting processes, and constructs. (a) The macroscopic appearance of the CA bioink (left) and the CHA bioink (right) within a 1 mL syringe. (b) The extrusion of fine filaments during printing (left), the inability to extrude the bioink when the nozzle diameter is too small (middle), and the ongoing printing process (right). (c) The designed 3D construct model with stratified layers, viewed from the top, side, and front. The upper layer of the lattice is designed with a pore size of 450 μm, and the lower layer, characterized by a more open structure, has lattice dimensions of 600 μm. The diameter of the filament employed is 250 μm. (d) Macroscopic photographs of the printed construct, viewed from the top and front. Abbreviations: CA: Collagen/alginate; CHA: Collagen/nano-hydroxyapatite/alginate.

medium added to submerge the material, with medium changes occurring every 48 hours. At the designated testing time, the CCK-8 reagent was added to the wells, and after a 2-hour incubation at 37°C, the supernatant was transferred to a 96-well plate. The optical density at 450 nm was measured using a microplate reader (BioTek ELX800, VT, USA). Cells without material stimulation served as the control group, with three replicates (n = 3).

2.3.3. Fluorescent staining of living cells

To determine whether cells at the transition between CA and CHA materials can migrate naturally, a live-cell fluorescence staining technique was employed to track cell locations. Cells were suspended in serum-free α-MEM medium at a concentration of 1×10^6 cells/mL and mixed with a live-cell fluorescent dye at a concentration of 5 μl/mL, then incubated at 37°C in the dark for 15 minutes. Cells intended for the CA bioink were stained with VybrantTM

DiO (Thermo Scientific, USA), while those for the CHA bioink were stained with VybrantTM DiD (Thermo Scientific, USA). As previously described, a construct with an upper layer of CA and a lower layer of CHA was printed using bioprinting technology and cultured in PM under dark conditions until day 7. The transition section of the material was then sectioned longitudinally and examined using a scanning electron microscope and an inverted fluorescence microscope to capture the cellular fluorescence imaging.

2.3.4. Alkaline phosphatase staining

An alkaline phosphatase (ALP) staining kit (Solarbio, Beijing, China) was employed to visualize ALP within cells based on the azo-coupling method, thereby assessing the osteogenic potential of PDLSCs within CHA constructs. Cells were cultured for 14 days using the CHA material extract stimulation method as described in Section 2.3.2. To validate the effectiveness of the custom-made OM, control groups were established with PDLSCs cultured in regular PM and OM without material stimulation. The experimental group was cultured with PDLSCs under material co-stimulation using the OM. To explore the osteogenic effect of the CHA material itself, an additional experimental group was included, where PDLSCs were cultured in regular medium under material co-stimulation. On the 7th and 14th days of culture, the medium was removed from the wells, and the cells were fixed for 1 minute with pre-cooled ALP fixative at 4°C. After rinsing with PBS, ALP incubation solution was added to cover the cells, followed by a 20-minute incubation at 37°C, and then rinsed with PBS. Finally, cells were counterstained with methyl green for 5 minutes, and the results were documented with photography.

2.3.5. Picro Sirius Redstaining

The fibroblastic differentiation of PDLSCs within CA constructs was evaluated using Picro Sirius Redstaining solution (Sigma–Aldrich Co., Germany). The experimental group design followed the same protocol as the ALP staining procedure. Cells in the well plates were fixed with 4% paraformaldehyde for 10 minutes, then rinsed with PBS. Afterward, the cells were submerged in Picro Sirius Reddye and incubated at room temperature for 60 minutes. The stain was aspirated, and the samples were rinsed twice with 0.5% acetic acid solution, followed by three rinses with anhydrous alcohol to dehydrate the samples. The final step involved photographing the results.

2.3.6. Quantitative reverse-transcription polymerase chain reaction

Quantitative reverse-transcription polymerase chain reaction (RT-qPCR) was employed to determine the transcriptional levels of specific genes in PDLSCs on the 7th and 14th days post-printing. Cells cultured with either CA or CHA material extract were collected from the well plates. Total RNA was extracted using the Trizol reagent (Invitrogen, USA) following the manufacturer's recommended protocol. Reverse transcription was performed using the PrimeScriptTM RT Reagent Kit (TaKaRa, Japan), and RT-qPCR was conducted with the FastStart Universal SYBR Green Master (Roche, Germany). Primer sequences are listed in Table 2. The expression levels of *COL1*, *ALP*, *RUNX2,* and *OPN* in PDLSCs stimulated by CHA material were assessed, as well as the expression levels of *COL1*, *PLAP1*, *FSP1,* and *ELASTIN* in PDLSCs stimulated by CA material. *GAPDH* served as an endogenous control, and the fold-difference was calculated using the $2^{-\Delta\Delta Ct}$ method, with triplicate samples ($n = 3$).

2.4. *In vivo* study

2.4.1. Biocompatibility analyses

In accordance with the ethical principles of the Laboratory Animal Research Ethics Committee of Peking University Health Science Center (Approval No.: DLASBD0054), constructs were implanted subcutaneously into 6- to 8-week-old male BALB/c nude mice (Charles River Laboratories, USA) to assess the biocompatibility of the 3D constructs. One week prior to the study, the animals were housed in two separate ventilated cages within an isolated specific pathogen-free (SPF) unit. The implants were categorized into two groups: acellular printed CHA and cellular printed CHA. Each animal was designated as an individual experimental unit. To ensure the reproducibility and reliability of the animal model data, six nude mice were selected for each group.

All instruments utilized in the procedure were sterilized using Cobalt-60 (Co-60) gamma radiation, ensuring aseptic conditions during surgery, which was conducted inside a laminar flow hood. Male BALB/c nude mice, aged 6–8 weeks and weighing approximately 20–25g ($n = 12$), were randomly assigned to two groups. Anesthesia was induced and maintained using isoflurane gas (RWD, China). A 10 cm longitudinal incision was made on the dorsal side of each mouse, and an implant (10 mm × 10 mm × 2 mm) was inserted subcutaneously. The incision was then closed with absorbable sutures. Following the procedure, the anesthesia was discontinued, and the mice were returned to their cages for further observation.

At the 2nd, 4th, and 8th weeks post-implantation, the nude mice were euthanized using an overdose of anesthesia. Macroscopic photographs of the subcutaneous constructs were taken to assess vascular ingrowth and the extent of *in vivo* absorption. The constructs were then

Table 2. Primers for *GAPDH*, *COL1*, *ALP*, *RUNX2*, *OPN*, *ELASTIN*, *FSP1*, and *PLAP1*.

Gene	Primer sequence (5' to 3')
GAPDH	Forward: GCACCGTCAAGGCTGAGAAC Reverse: ATGGTGGTGAAGACGCCAGT
COLI	Forward: CTGACCTTCCTGCGCCTGATGTCC Reverse: GTCTGGGGCACCAACGTCCAAGGG
ALP	Forward: TCAGAAGCTAACACCAACG Reverse: TTGTACGTCTTGGAGAGGGC
RUNX2	Forward: TCTGGCCTTCCACTCTCAGT Reverse: GACTGGCGGGGTGTAAGTAA
OPN	Forward: TCACCTGTGCCATACCAGTTAA Reverse: TGAGATGGGTCAGGGTTTAGC
ELASTIN	Forward: AAAGCAGCAGCAAAGTTCGG Reverse: ACCTGGGACAACTGGAATCC
FSP1	Forward: AGCTTCTTGGGGAAAAGGAC Reverse: CCCCAACCACATCAGAGG
PLAPI	Forward: CGATACAAAGAACTACAAAGGCTGG Reverse: GCATTTCCCAGTATTTCACCG

excised and fixed in a 4% paraformaldehyde solution for 24 hours, followed by dehydration and paraffin embedding. Sections were obtained by cutting perpendicular to the flap, and these were subjected to hematoxylin and eosin (HE) staining and Masson's trichrome staining for further histological evaluation.Following the implantation procedure, the number of capillaries within the material-embedded regions in the sections was counted under an optical microscope. Capillaries were defined as blood vessels with a diameter of less than 20 μm. Utilizing a microscope at a magnification of 20×, the number of capillaries was calculated for five random fields of view within the experimental area of each section in each group.

2.4.2. Evaluation of tissue regeneration effectiveness

In compliance with the ethical guidelines of the Laboratory Animal Research Ethics Committee of Peking University Health Science Center (Approval No.: DLASBD0054), constructs were implanted into the extraction sockets of the maxillary first molars (M1) in 6- to 8-week-old male nude rat to evaluate their efficacy in promoting hard and soft tissue regeneration at the extraction sites. Two weeks prior to the study, the animals were housed in two separate ventilated cages within an isolated SPF unit. The implants were categorized into three groups: acellular stratified printed CA/CHA, cellular printed CHA, and stratified cellular printed CA/CHA. Each mouse underwent extraction of the first molars on both the left and right maxillary sides, with each extraction site serving as an individual experimental unit. Each group's experiment was replicated three times. The control group consisted of extraction sites allowed to heal naturally without intervention.

All surgical instruments were sterilized using Co-60 gamma radiation to ensure aseptic conditions, and the surgical procedures were conducted within a laminar flow hood. Male nude mice, aged 6–8 weeks and weighing approximately 300–400 grams (n = 12), were randomly assigned to four groups.

Anesthesia was induced and maintained using isoflurane gas. After the complete extraction of the maxillary first molars on both the left and right sides, the implants were placed into the alveolar sockets and secured with absorbable sutures. Following the surgical intervention, the anesthesia was discontinued, and the mice were returned to their cages for subsequent observation and monitoring.

At weeks 4 and 8 post-surgery, the mice were euthanized by means of an overdose of anesthesia. The soft and hard tissue blocks at the extraction sites were excised and fixed in a 4% paraformaldehyde solution for 24 hours. Micro-computed tomography (micro-CT) scanning (SkyScan1276, Bruker, China) was performed to capture the sample structures, and the raw images obtained were processed and analyzed using CTAnalyser-CTvol and CTAnalyser-CTvox software (Bruker, China) to compare differences among the groups. The region of interest was defined using the CTAnalyser-CTAn software for 3D evaluation, which analyzed and measured the images based on grayscale to calculate the bone volume-to-tissue volume (BV/TV) ratio.[28]

Subsequently, the samples were dehydrated and embedded in paraffin. Sections were cut parallel to the longitudinal axis of the teeth to a thickness of 5 mm and stained with HE as well as Masson's trichrome stain for histological examination. Additionally, immunohistochemical (IHC) staining was performed on the samples using markers for CD31, BSP, OPN, COL-1, CTGF, and COL-3 to assess specific biological processes and tissue characteristics.

2.5. Statistical analysis

Data derived from triplicate experiments to ensure reproducibility are presented as mean ± standard deviation. The statistical analysis was conducted using SPSS software version 29.0 (IBM, USA). For comparisons between the two groups, a t-test was employed. A p-value of less than 0.05 was considered statistically significant.

3. Results

3.1. Preparation and characterization of bioinks

3.1.1. Rheological characterization

Investigating the rheological properties of bioinks is crucial for evaluating their printability. We assessed the storage modulus (G′) and loss modulus (G″) of CA and CHA bioinks at 4°C as a function of frequency (Figure 2a). Both G′ and G″ increased with increasing frequency. Throughout the entire frequency range, G′ consistently exceeded G″, indicating a gel-like behavior with a predominance of elastic characteristics. The CA bioink exhibited lower moduli, suggesting better flowability compared to the CHA bioink, which could account for the use of a smaller inner diameter nozzle for the CA bioink. At a given frequency, the incorporation of nHA particles increased the loss modulus and significantly enhanced the storage modulus, thereby improving the mechanical properties.

We further investigated the viscosity of the bioinks as a function of temperature and shear rate. Our findings indicated that the viscosity of the bioinks gradually decreases with the increase in temperature (Figure 2b). At a constant temperature, the incorporation of nHA was observed to enhance the viscosity of the bioinks. Beyond a critical temperature threshold of 45°C, the viscosity rapidly decreased. Within the initial temperature range of 4–25°C, the controlled rate of viscosity reduction was favorable for the execution of 3D printing. An increase in shear rate resulted in a significant reduction in viscosity, highlighting the pronounced shear-thinning behavior of both CA and CHA bioinks (Figure 2c). The viscosity of the CA and CHA bioinks was found to be quite similar, exhibiting closely matched shear-thinning characteristics. The addition of nHA, under the same shear rate conditions, was noted to augment the viscosity of the bioinks. Adjusting the shear rate to reduce the viscosity facilitates the extrusion of the bioinks, which is beneficial in protecting the cells from the detrimental effects of shear stress.[29]

3.1.2. ATR-FTIR analysis

Figure 2d presents the ATR-FTIR spectra of CA and CHA bioinks. The spectrum of CHA exhibited characteristic peaks of collagen and HA.[30] The amide I peak was located at 1633 cm^{-1}, corresponding to the carbonyl (C=O) stretching vibration, and the amide II peak was observed at 1529 cm^{-1}, indicative of the N-H bending vibration. The amide III peak was found in the vicinity of 1200 cm^{-1}, also associated with N-H bending vibrations. The presence of nHA was evidenced by the phosphate ($PO4^{3-}$) stretching bands within the range of 570–610 cm^{-1}. The results indicated

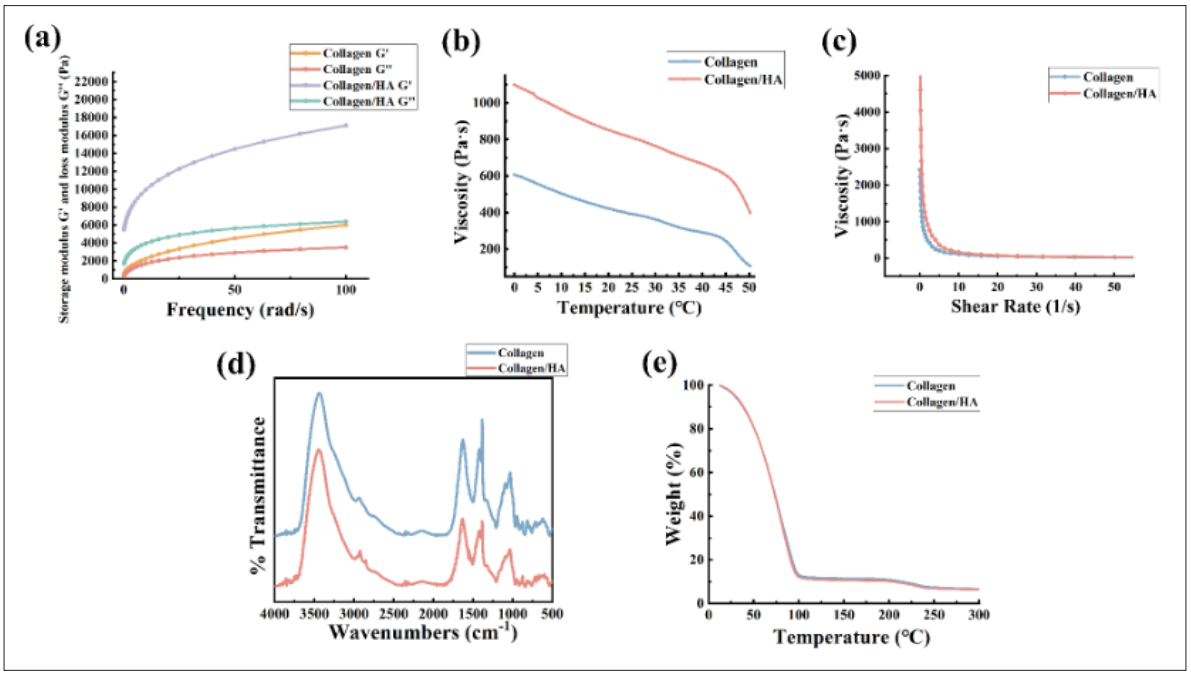

Figure 2. Characterization of physicochemical properties of the bioinks. (a) Rheological frequency sweep tests were conducted on both CA and CHA bioinks at 4°C, where G' denotes the storage modulus and G" represents the loss modulus. (b) The variation in viscosity of the two bioinks across different temperatures. (c) Illustration of the changes in viscosity of the bioinks under various shear rates. (d) The ATR-FTIR spectroscopic analysis of the bioinks reveals their chemical composition. (e) The TGA of the bioinks provides insights into their thermal stability. Abbreviations: ATR-FTIR: Attenuated total reflectance-Fourier transform infrared spectroscopy; HA: Hydroxyapatite; TGA: Thermogravimetric analysis.

that the incorporation of nHA did not affect the chemical structure of the collagen component.

3.1.3. TGA

TGA of the bioinks has confirmed that the weight loss of both bioinks is nearly synchronized under the influence of temperature (Figure 2e). Within the physiological temperature range of 37°C, the weight loss of the bioinks was minimal, which is advantageous for *in vivo* studies. The results indicated that due to thermal decomposition, the bioinks decomposed at temperatures exceeding 95°C. Consequently, all subsequent material sterilization was performed using gamma irradiation with a Co-60 source.

3.1.4. Flow cytometric analysis

Flow cytometry was employed to analyze the surface markers of PDLSCs, a critical step in characterizing their stem cell properties (Figure 3). The expression of CD29 and CD90, both positive, is indicative of mesenchymal stem cell (MSC) characteristics, and CD146 serves as a basis for identifying PDLSCs. Consistent with other MSCs, the majority of PDLSCs in culture exhibited negativity for CD45 (0.08% ± 0.02%) and STRO-1 (1.34% ± 0.09%). The analysis found that PDLSCs could express MSC-specific surface markers, including CD29 (99.86% ± 0.23%), CD90 (99.96% ± 0.05%), and CD146 (47.1% ± 0.36%). These findings suggested that the PDLSCs isolated from human teeth in this study possess the stemness of MSCs and were free from contamination by endothelial cells or hematopoietic stem cells.

3.2. Preparation and characterization of 3D constructs

3.2.1. Compressive modulus analysis

The stress-displacement curves (Figure 4a) and stress-strain curves (Figure 4b) of the 3D constructs demonstrated that the CHA/CA composite required a greater force to achieve the same degree of deformation compared to the CA construct, which exhibited the lowest compressive force required. This indicated that the incorporation of nHA enhanced the mechanical properties of the scaffold, and the layered CHA/CA scaffold's mechanical strength was conducive to subsequent *in vitro* and *in vivo* testing. The mechanical strength of the construct is also observable macroscopically in **Video S1** (see supplementary material).

3.2.2. Morphological analysis of 3D constructs

The microstructure of the construct's lattice framework was examined under SEM. Two distinct pore densities were

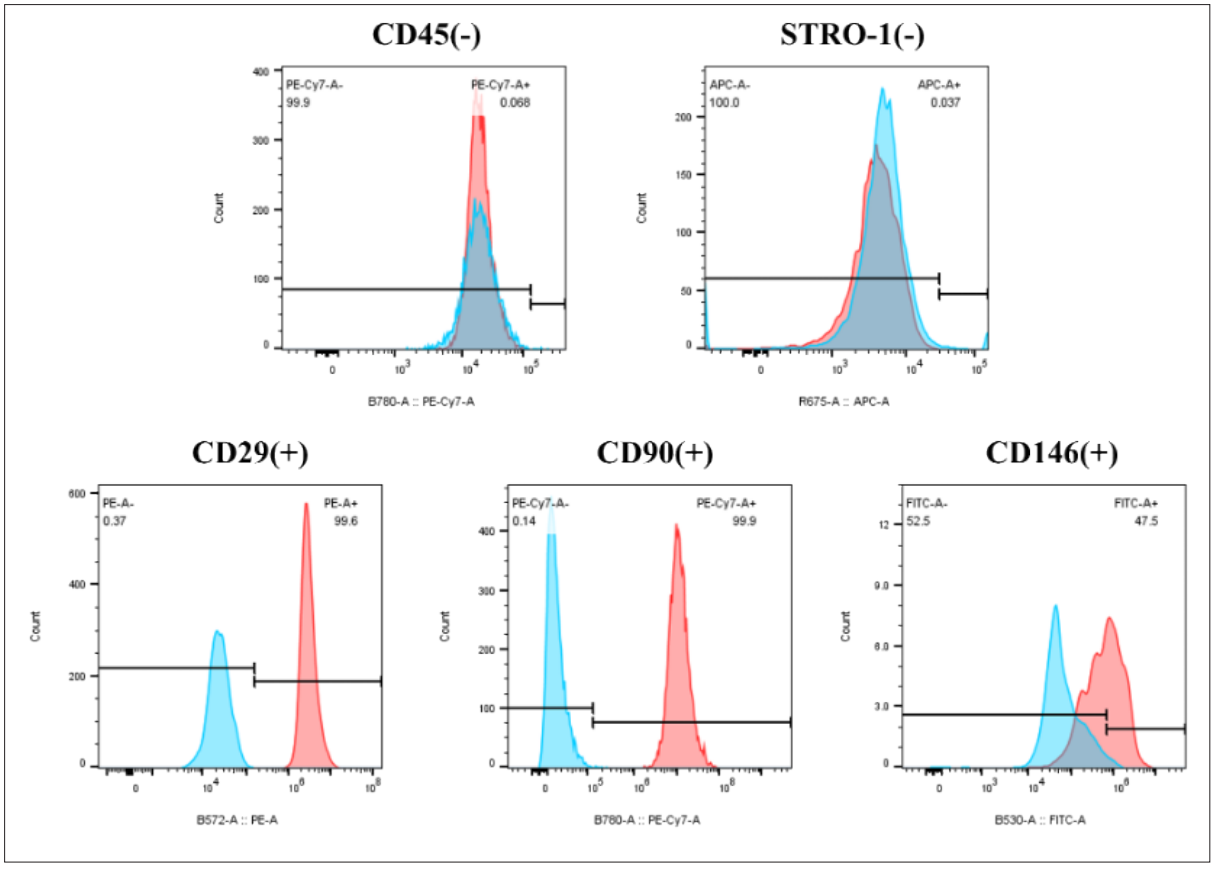

Figure 3. Flow cytometric analysis of PDLSCs based on characterization of stem cell markers: CD29 (+), CD90 (+), CD146 (+), CD45 (-), and STRO-1 (-).

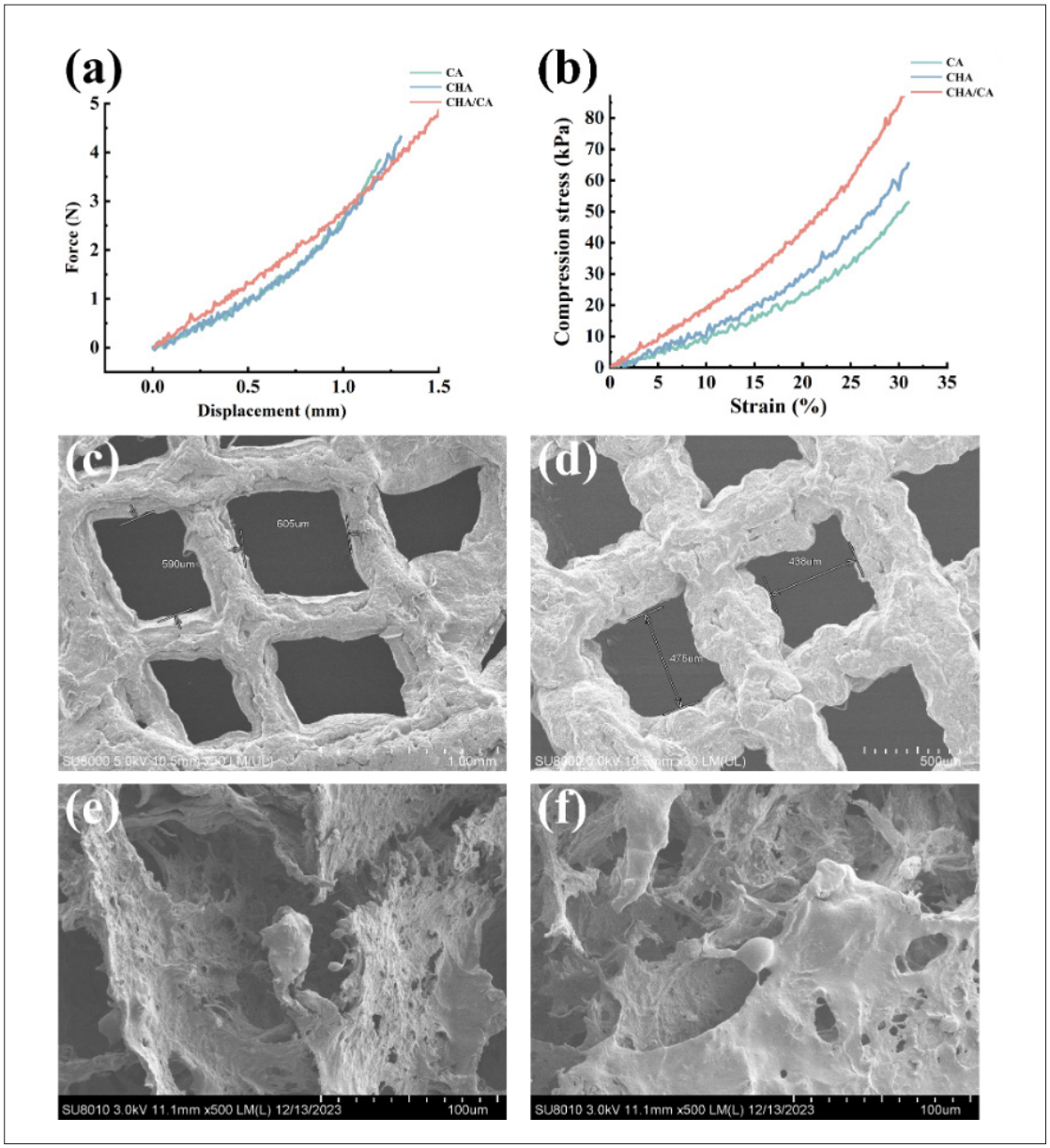

Figure 4. Mechanical properties and surface structure of the construct. (a) The force-displacement curves of the constructs. (b) The stress-strain curves of the constructs. (c) SEM image showinglarger pore sizes ofthe constructs near the bone tissue region, with macroscopic pore dimensions ranging from 550 to 600 μm. (d) SEM image showing smaller pore sizes ofthe constructs near the soft tissue region, with macroscopic pore dimensions ranging from 450 to 500 μm. (e) SEM image showing a micro-porous configuration in the microstructure of the construct near the bone tissue region. (f) SEM image showing a micro-porous configuration in the microstructure of the construct near the soft tissue region. Abbreviations: CA: Collagen/alginate; CHA: Collagen/nano-hydroxyapatite/alginate; SEM: Scanning electron microscopy.

designed for the construct to accommodate variations in the nHA content. The pore size in the region proximal to the bone tissue was tailored to be 550–600 μm (Figure 4c). In the region adjacent to the soft tissue, the pore size was reduced to 450–500 μm (Figure 4d). The microscopic findings confirmed that both types of constructs exhibited a porous structure, which is essential for enhanced cell infiltration and tissue integration (Figure 4e and 4f).

3.3. *In vitro* study

3.3.1. Cell viability

The cell viability within the constructs was assessed using a live/dead fluorescent staining method after 1, 4, and 7 days of *in vitro* culture, with the results depicted in Figure 5a. The 3D-printed constructs encapsulated the cells uniformly within the material, demonstrating high levels of cell viability sustained over the 7 days. Compared

to day 1, there was a significant increase in the density of live cells within the constructs.

3.3.2. Cell proliferation

Cell proliferation exhibited an upward trend throughout the culture period of 1, 3, 5, and 7 days, as shown in Figure 5b. At each measured time point, the optical density (OD) values for both the CHA and CA groups were higher than those of the control group, indicating enhanced cell growth in these groups. Notably, the proliferation rate of cells in the experimental groups peaked between days 5 and 7, suggesting an optimal period for cell expansion.

3.3.3. Fluorescent staining of living cells

To validate the natural transition between the two layers, we sectioned the transition zone longitudinally for both macroscopic and microscopic SEM observations. As illustrated in the previous macroscopic images of the materials, the upper construct composed of CA exhibited a translucent appearance, while the lower construct made of CHA appeared white (Figure 5c). SEM analysis revealed a seamless interface at the transition, indicating a tight connection between the two regions (Figure 5d). To verify the intermingling of PDLSCs carried by the two bioinks within the final construct, we utilized distinct red and green live-cell fluorescent dyes to label the cells within the bioinks for bioprinting. After one day of culture, the fluorescence images showed a clear stratification of red and green fluorescence in the upper and lower layers, respectively. By the 7th day of culture, the images displayed an intermingling of red and green fluorescence, demonstrating the natural migration of cells across the transition area (Figure 5e).

3.3.4. ALP staining

The ALP staining results at days 7 and 14 (Figure 6a) demonstrated that PDLSCs exhibited osteogenic potential when induced. Under the stimulation of CHA, the groups cultured in PM and OM showed a higher trend of purple nodules compared to the blank control group. Notably, CHA could also partially guide the differentiation of PDLSCs toward the osteogenic lineage in a PM environment due to the presence of nHA.

3.3.5. Picro Sirius Red staining

Figure 6b illustrates the Picro Sirius Red staining results of collagen fiber secretion by PDLSCs in the control and CA-induced differentiation groups on days 1, 7, and 14. Over

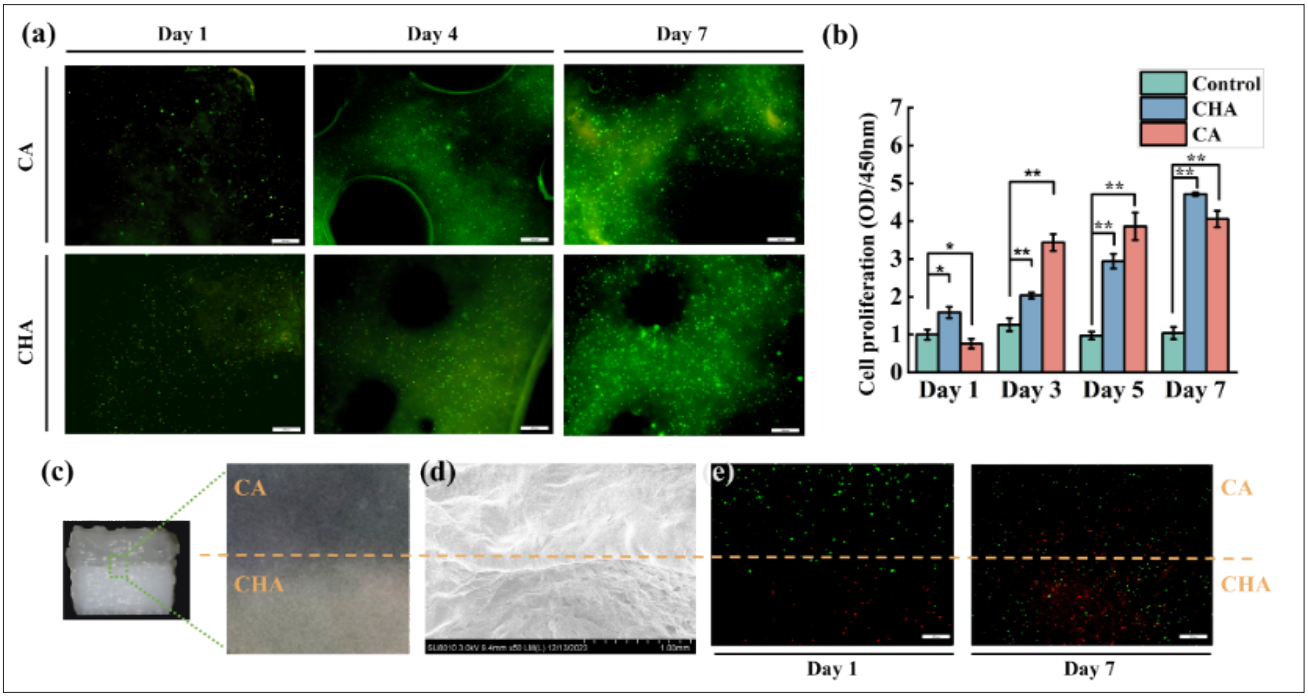

Figure 5. Cell viability and motility within the constructs. (a) Fluorescence images of live/dead staining of PDLSCs within the CA and CHA constructs at days 1, 4, and 7, with an initial cell seeding density of 1×10^6 cells/mL. (b) CCK-8 assay results for PDLSCs under the influence of CHA and CA at days 1, 3, 5, and 7 ($n = 5$). (c) Macroscopic image of the transitional structure showing an integrated and gradient variation. The upper transparent layer is composed of CA, while the lower white layer is made of CHA. (d) SEM images of the longitudinal section of the transitional structure showing an integrated result. (e) Fluorescence staining images of the longitudinal section of the transitional structure at days 1 and 7 showing the movement of cells from the upper and lower layers towards the interface over time. Cells within the bioinks of the upper and lower materials were stained with Vybrant™ DiO and Vybrant™ DiD fluorescent dyes (Thermo Scientific, USA), respectively. Scale bars: 200 μm (a, e). *$p < 0.05$; **$p < 0.01$. Abbreviations: CA: Collagen/alginate; CCK-8: Cell Counting Kit-8; CHA: Collagen/nano-hydroxyapatite/alginate; PDLSCs: Periodontal ligament stem cells; SEM: Scanning electron microscopy.

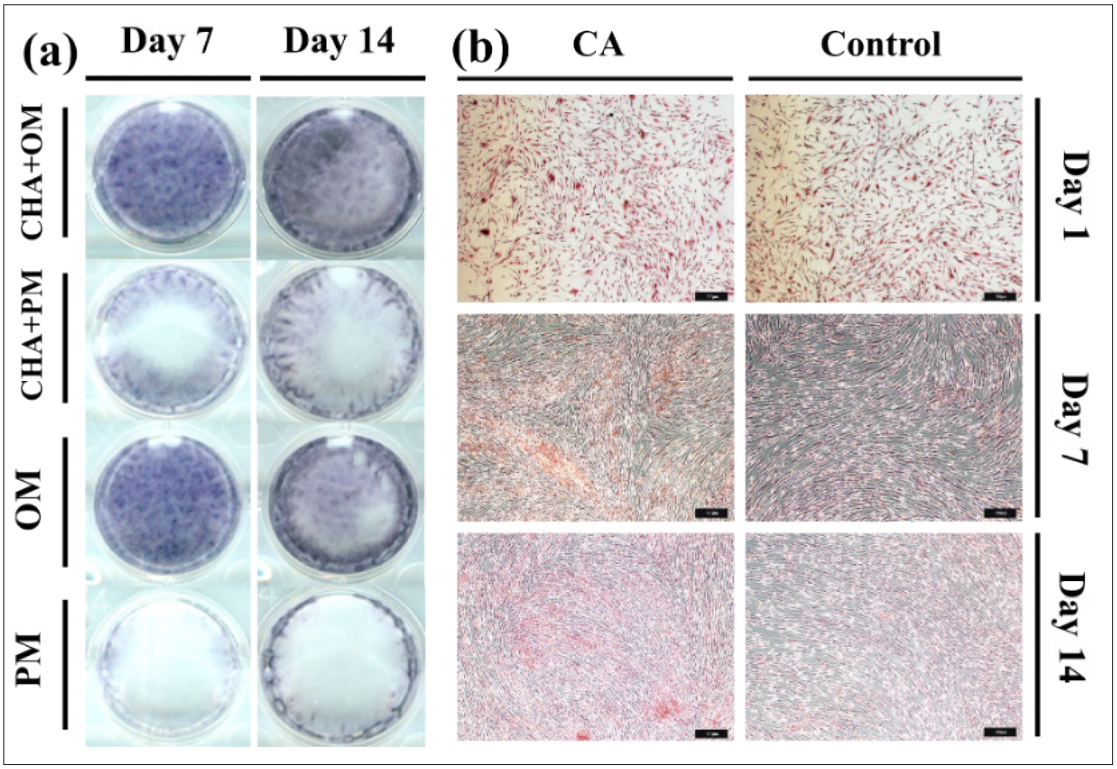

Figure 6. Differentiation staining results of PDLSCs under various material environments. (a) ALP staining results at days 7 and 14. The first row of images presents the experimental outcomes of OM cultivation under CHA material stimulation. The second row displays the results of PM cultivation under CHA material stimulation. The third row illustrates the outcomes of OM cultivation without material stimulation. The fourth row shows the results of PM cultivation without material stimulation. (b) Picro Sirius Redstaining results at days 1, 7, and 14. The images on the left column represent the experimental results under the stimulation of CA material, while the images on the right column depict the outcomes without any material stimulation. Scale bars: 500 μm. Abbreviations: CA: Collagen/alginate; CHA: Collagen/nano-hydroxyapatite/alginate; OM: osteogenic differentiation medium; PM: proliferation medium.

time, both groups displayed an increasing trend in the intensity of deep red staining, indicative of collagen fiber deposition. Comparatively, at each time point, the CA-induced differentiation group exhibited a higher amount of fibrils stained in deep red with a fuzzy appearance, while the control group demonstrated less staining and a milder effect.

3.3.6. Gene expression analysis

We employed RT-qPCR to evaluate the gene expression profiles of PDLSCs within constructs showing distinct osteogenic and fibrogenic potential, aiming to explore the influence of our fabricated constructs on the differentiation trajectory of stem cells (Figure 7). The findings indicated that under the stimulation of the CA construct, the expression levels of *COL1* and *PLAP1* were higher compared to the control group, with a slight decrease in expression over time. Additionally, the expression trends of the *FSP1* and *ELASTIN* genes exhibited an opposite trend. The *FSP1* gene expression showed an upward trend in the experimental group, while the expression of the *ELASTIN* gene progressively diminished. On day 7, when stimulated by the CHA construct, the expression level of *COL1* was higher than that of the control group; however, it declined over time. The expression of *ALP* and *RUNX2* in cells stimulated by CHA was significantly elevated compared to the control group. Furthermore, the *OPN* gene expression in cells stimulated by the CHA construct was lower and continued to decrease.

3.4. *In vivo* study

3.4.1. Histochemical analysis following ectopic transplantation in mice

Samples were harvested at weeks 2, 4, and 8 after implantation of the constructs into the dorsal region of mice. In the PDLSCs/CHA group, the remaining material's volume was significantly reduced compared to the initial volume (Figure 8c). The resorption of the material was accompanied by an increasingly evident distribution of surface blood vessels. Histological cross-sections of both constructs, stained with HE, revealed a porous meshwork, nHA nodes, and blood vessel distribution (Figure 8a and 8b). At week 2, blood vessels had infiltrated the interior of the construct. By weeks 4 and 8, the distribution of

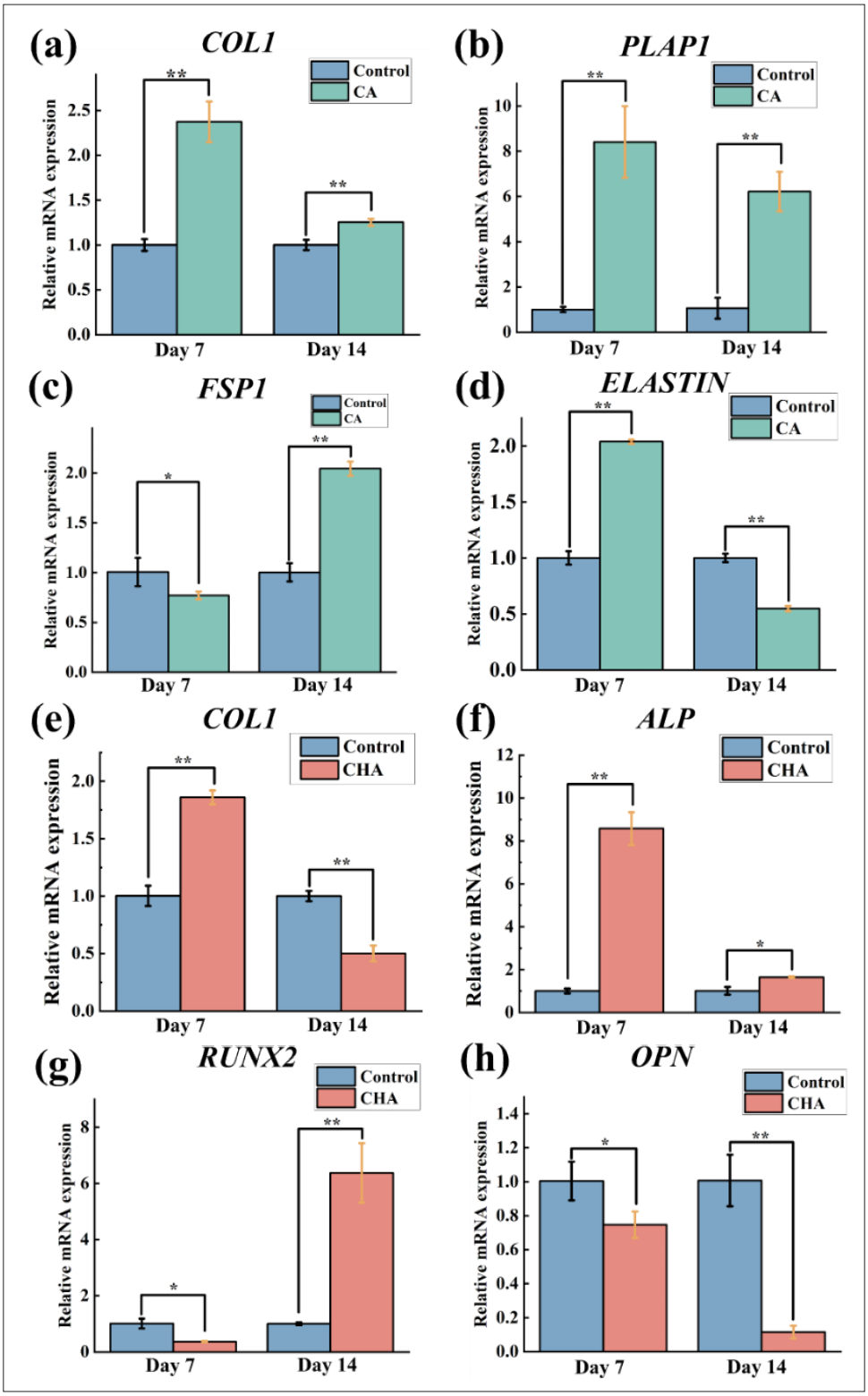

Figure 7. Gene expression in PDLSCs stimulated by different materials on days 7 and 14. (a–d) Gene expression levels of *COL1* (a), *PLAP1* (b), *FSP1* (c), and *ELASTIN* (d) in PDLSCs stimulated by CA material. (e–h) Gene expression levels of *COL1* (e), *ALP* (f), *RUNX2* (g), and *OPN* (h) in PDLSCs stimulated by CHA material. The control group represents normal PDLSCs without material stimulation. The Y-axis denotes the relative expression ratio of the target genes normalized to *GAPDH*. Data are presented as mean ± standard deviation, $n = 3$, $^{*}p < 0.05$, $^{**}p < 0.01$. Abbreviations: CA: Collagen/alginate; CHA: Collagen/nano-hydroxyapatite/alginate; PDLSCs: Periodontal ligament stem cells.

blood vessels became more profound with the increased degradation of the material. At week 8, the majority of the material had been degraded, corroborating the macroscopic findings. Compared to the cell-mixed constructs, the non-cell constructs exhibited accelerated structural degradation, while the cell-printed constructs maintained a more intact internal structure at the same time points. Masson's trichrome staining also demonstrated red-stained areas of the cell-printed constructs, suggesting the presence of mineralized extracellular matrix (ECM), whereas the non-cell constructs displayed a deep blue color, likely due to the lack of such mineralization. The semi-quantitative analysis of vascular count revealed that the number of vessels formed in the cellular constructs is consistently higher than that in the acellular constructs, and this vascular count increased over time (Figure 8d).

3.4.2. Histochemical analysis of rat tooth extraction wounds

A mouse tooth extraction model was developed to evaluate the soft tissue regenerative capacity, bone healing ability, and ARP effects of 3D constructs composed of CA/CHA, PDLSCs/CHA, and PDLSCs/CA/CHA. Micro-CT scanning was utilized to document and analyze the regenerative bone volume at the M1 extraction site. Figure 9a presents the reconstructed micro-CT images of the 4 groups (blank control, CA/CHA, PDLSCs/CHA, and PDLSCs/CA/CHA) at weeks 4 and 8 post-extraction, including 3D sagittal, 3D horizontal, and 2D frontal views of the murineM1 region. A micro-reconstruction of the central section of the extraction socket from the 3D CT images is depicted in Figure 9b, showing the healing process of the socket and the sparsity of newly formed trabecular bone (I) compared to the buccal and lingual bone plates (II). BV/TV ratio analysis was conducted according to published guidelines,[28] as shown in Figure 9c. The results indicated a significant increase in BV/TV in the material-implanted groups compared to the blank control group, with the PDLSCs/CHA/CA scaffold group showing the highest BV/TV ratio. At both weeks 4 and 8, the difference in the PDLSCs/CHA/CA scaffold group and the control group was extremely significant ($p < 0.01$). The acellular scaffold material group also demonstrated a positive trend in new bone formation compared to the control group, but the rate of bone volume increase was less than that of the cell-mixed material group.

The results suggested that the implantation of 3D constructs can effectively induce alveolar bone filling and protect the alveolar ridge post-extraction.

Histological examination of sections stained with HE and Masson's trichrome revealed that new bone formation was initiated from the apex and peripheral edges of the M1 extraction socket (Figure 10). At week 4, the absence of detectable scaffold material within the extraction socket, as indicated by the HE staining, suggested that the construct had largely degraded. In contrast to the control group without material placement, which exhibited the original morphology of the extraction socket and a small amount of woven bone, the experimental groups that received either cell-laden or non-laden layered biomaterials showed complete filling of the extraction sockets with thick trabecular bone. However, the extraction sockets implanted with non-layered material still exhibited some void structures.

To evaluate the angiogenic capacity of the tissue following the implantation of the material, we performed IHC staining for the endothelial cell marker CD31. At week 4 post-implantation, newly formed vessels were observed at the implantation sites. By week 8, the number of vessels had increased and were densely distributed within the implantation area. At week 4, the newly formed bone tissue in all groups showed strong BSP staining. By week 8, the bone tissue at both the control and implantation sites exhibited mild to moderate BSP staining. Positive expression of OPN was detected in osteoblasts and osteocytes surrounding and within the newly formed trabecular bone, with the most pronounced expression in the control group. The expression of OPN was significantly lower at week 8 compared to at week 4. COL-1 and COL-3 were uniformly expressed in both bone and soft tissues. The expression of CTGF showed an increasing trend with the progression of healing time.

Compared to the acellular material group, the material group containing PDLSCs exhibited significantly deeper staining of the osteogenic marker BSP at 4 weeks post-extraction, along with more intense staining of the vascular marker CD31. The same trend was observed in the IHC of soft tissue markers COL-1, CTGF, and COL-3. The PDLSCs/CA/CHA material group demonstrated higher expression levels of vascular, bone, and soft tissue markers early post-extraction, as evidenced by the IHC results when compared to the other material groups (Figure 11).

We employed a semi-quantitative approach to compare the expression levels of markers (Figure 12a–h). The CD31 expression in the implanted material group was higher than that in the control group. The experimental group exhibited a decreasing trend in BSP and OPN expression. Compared to the control group, the CTGF expression in the experimental group remained consistently higher. In both bone and superficial soft tissues, the expression of COL-1 in the experimental group was consistently higher than in the control group, while the content of COL-3 in the experimental group decreased over time compared to

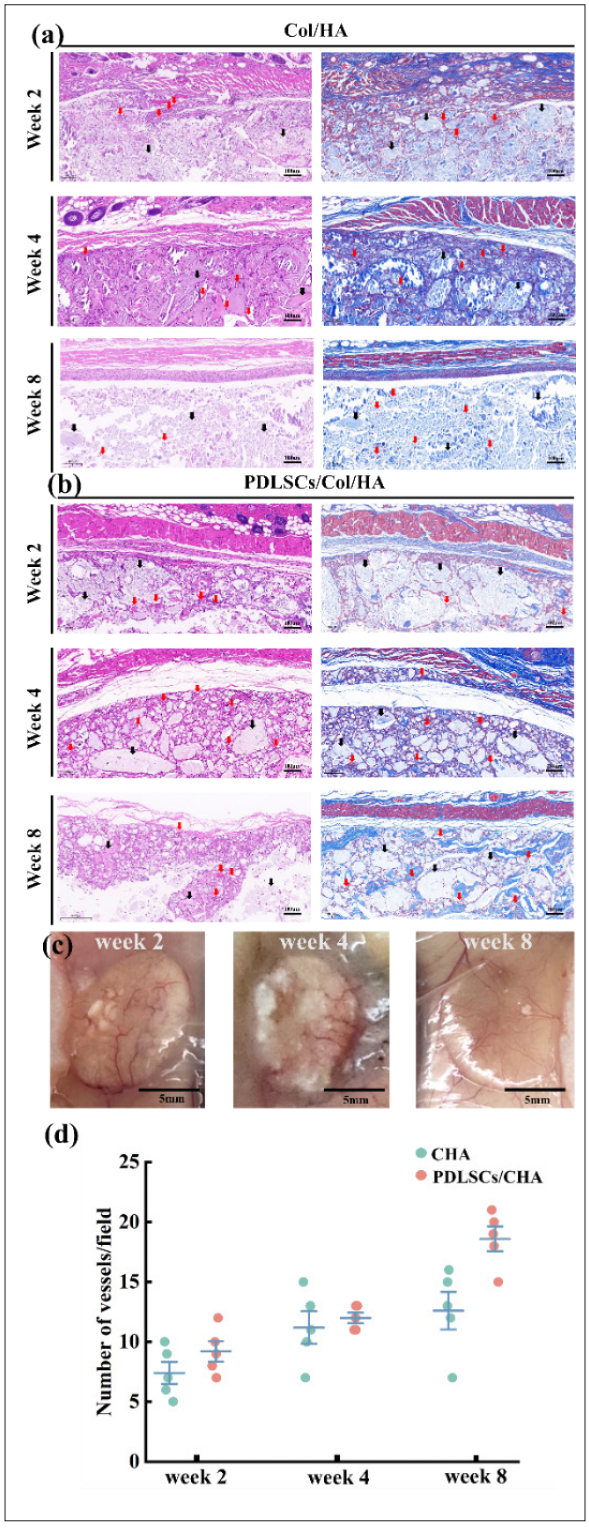

Figure 8. Ectopic implantation of acellular and cellular constructs on the dorsal region of mice followed by sample collection at weeks 2, 4, and 8 post-implantation. (a) Histological sections of acellular CHA constructs harvested at weeks 2, 4, and 8, stained with HE and Masson's trichrome. Scale bar: 100 μm. (b) Histological sections of cellular CHA constructs harvested at the same time points, stained with HE and Masson's trichrome. Scale bar: 100 μm. The red arrows indicate blood vessels and the blue arrows indicate the material. (c) Macroscopic photographs of the cellular CHA constructs at weeks 2, 4, and 8. Scale bar: 5 mm. (d) Semi-quantitative analysis of vascular density. $^{*}p < 0.05$, $^{**}p < 0.01$. Abbreviations: CA: Collagen/alginate; CHA: Collagen/nano-hydroxyapatite/alginate; Col: Collagen; HE: Hematoxylin and eosin; PDLSCs: Periodontal ligament stem cells.

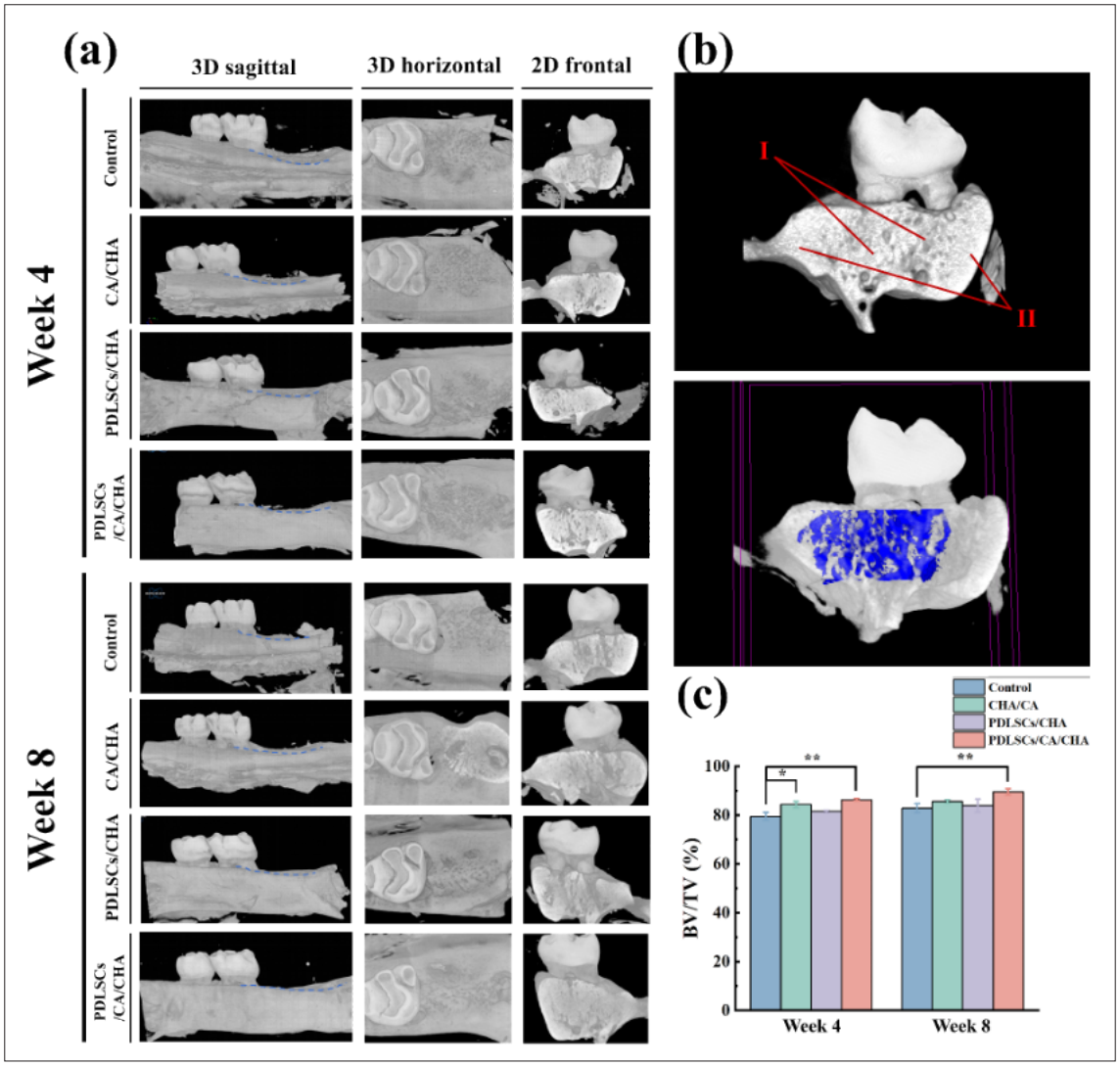

Figure 9. Bone tissue regeneration at the extraction site in rats. (a) The reconstructed micro-CT images of the M1 region in mice at 4 and 8 weeks post-extraction presented in 3D sagittal, 3D horizontal, and 2D frontal views. The blue dashed line delineates the resorption of buccal bone. At each time point (weeks 4 and 8), the first row of images shows the results of extraction sockets in the control group without any material implantation. The second row displays the outcomes of extraction sockets implanted with acellular CA/CHA materials. The third row presents the results of extraction sockets implanted with PDLSCs/CHA non-layered materials. The fourth row illustrates the outcomes of extraction sockets implanted with PDLSCs/CA/CHA materials. (b) Microscopic reconstruction process of the central portion of the rat extraction socket, with newly formed bone indicated by blue shading. The red arrow points to the newly formed bone (I) and the buccal and lingual bone plates (II). (c) Quantitative analysis of BV/TV within the murine extraction sockets. $^{*}p < 0.05$, $^{**}p < 0.01$. Abbreviations: BV/TV: Bone volume-to-tissue volume ratio; CA: Collagen/alginate; CHA: Collagen/nano-hydroxyapatite/alginate; micro-CT: Micro-computed tomography; PDLSCs: Periodontal ligament stem cells.

the control group. To investigate the quality of the formed soft tissue fibers, we calculated the ratio of COL-1 to COL-3 in soft tissue (Figure 12i). The results indicated that the ratio in the control group was significantly lower than in the implanted material group, with the stratified material group showing the highest ratio. To investigate the impact of the nHA content variation within the material on the formation of new bone, we also analyzed the difference in BSP expression between the denser bone areas on the surface and the internal trabecular bone regions. In the same sample, compared to the internal newly formed trabeculae, the surface denser newly formed bone material exhibited higher BSP expression. After implantation with the stratified material, the content of BSP in the bone was consistently higher than that in the non-stratified material implant. The trend of change over time was similar to that observed in the total newly formed bone as previously described (Figure 12g).

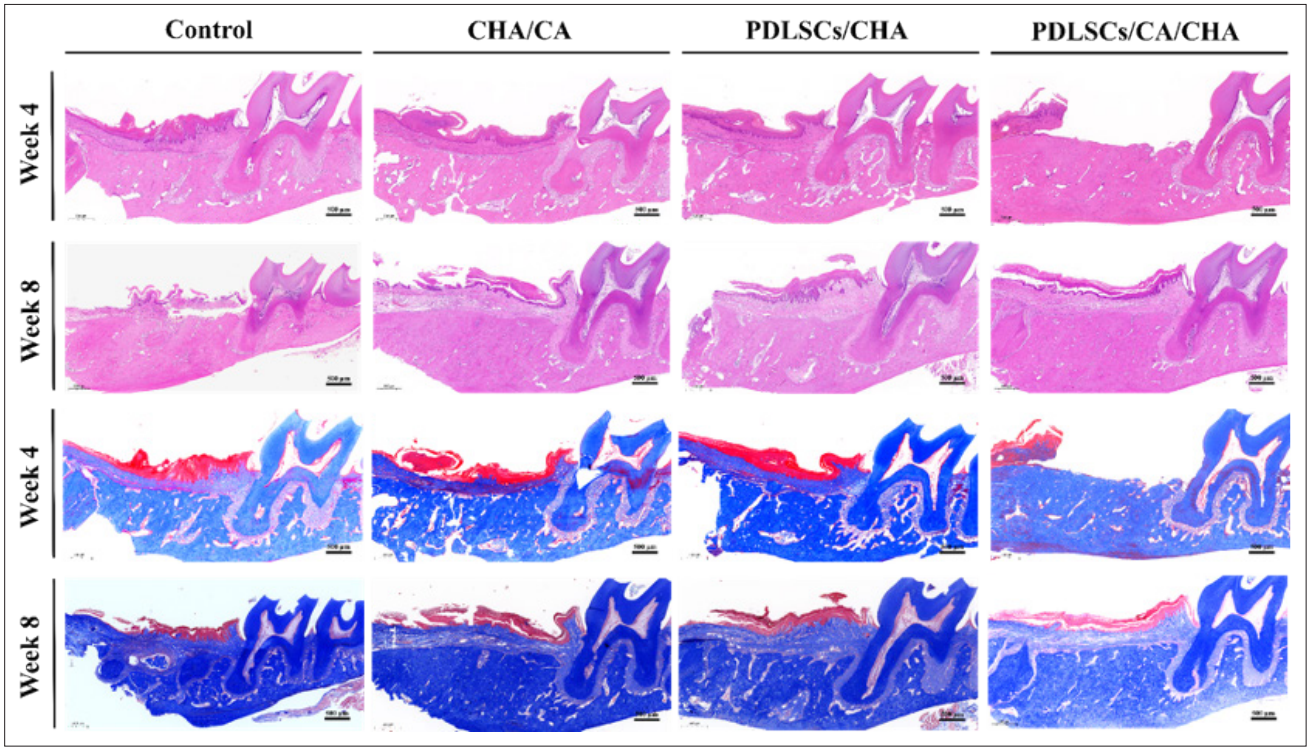

Figure 10. Histological sections of rat extraction sockets, obtained from longitudinal cuts, were stained with HE and Masson's trichrome. Scale bar: 500 μm. Abbreviations: CA: Collagen/alginate; CHA: Collagen/nano-hydroxyapatite/alginate; HE: Hematoxylin and eosin; PDLSCs: Periodontal ligament stem cells.

4. Discussion

In this research, we developed a 3D construct featuring a gradient in concentration, integration, and heterologous differentiation of one kind of stem cells, aimed at fostering the regeneration of both hard and soft tissues. This innovative approach to ARP has been validated through *in vitro* cellular assays and *in vivo* animal experiments, demonstrating its potential for further clinical investigation in the simultaneous regeneration of hard and soft tissues.

Hydrogel bioinks provide a 3D microenvironment for cells that closely mimics the ECM, exhibiting excellent biocompatibility. Collagen within the bioink offers attachment sites for cells, thereby promoting cell proliferation and differentiation.[31] However, the relatively low mechanical properties of collagen can limit its utility for subsequent *in vitro* and *in vivo* studies.[32] This study incorporated collagen with nHA to encapsulate stem cells within the hydrogel bioink and employed 3D bioprinting technology to construct scaffolds. The test results indicate that the hydrogel-based bioinks formulated with CA and CHA exhibit shear-thinning properties, which prevent excessive shear stress from affecting cell viability during the printing process.[33] Rheological frequency sweep measurements revealed that both ink solutions demonstrate gel-like characteristics, enabling them to be extruded from the nozzle. This suggests that gelation occurs uniformly and allows for more controlled ink deposition. Collagen provides tensile strength to the skeletal structure, while dispersed nHA crystals contribute to compressive strength.[34] Our physicochemical analysis of the bioink in this study corroborated these findings. The mechanical properties of the stratified CHA/CA construct aligned with the observed elasticity range of oral soft tissues, which, akin to natural skin, span from 10 to 100 kPa.[35]

3D bioprinting uses computer-aided design to engineer intricate structures, layering bioinks containing cells and biomaterials to create complex, 3D living constructs. This technology allows for the precise deposition of cell-laden biomaterials, facilitating the construction of complex 3D architectures. It has widespread application in the field of tissue regeneration.[36] During the printing process, the scaffold's material composition can be controlled by varying the porosity and geometric configuration of the structure.

As previously mentioned, to mimic the natural variation in human bone HA content, the scaffolds were designed with different pore sizes and densities in the upper and lower layers, thereby varying the nHA content.

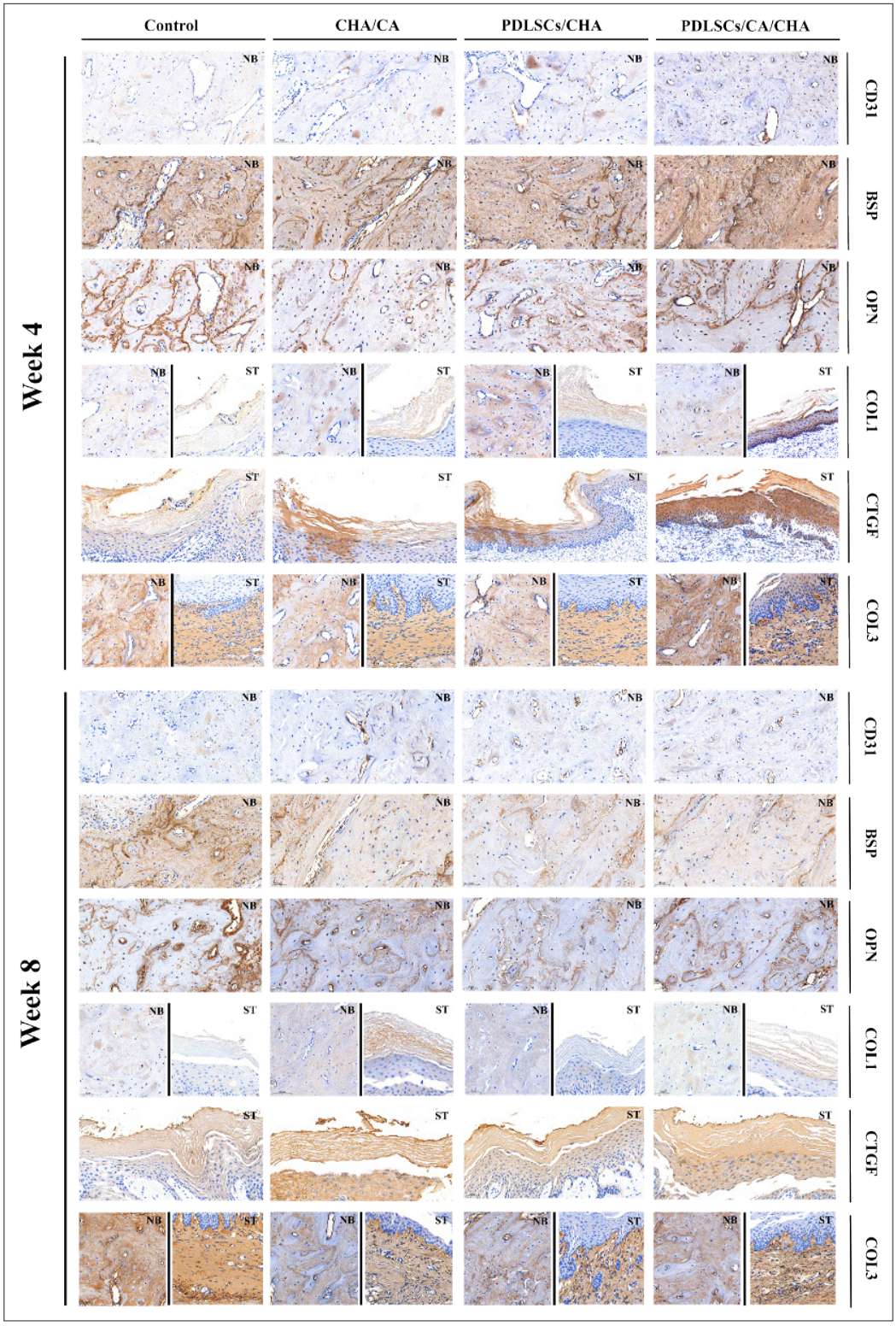

Figure 11. IHC results of longitudinal sections from murineextraction socket samples. The images from the first to the sixth rows depict the IHC results for CD31, BSP, OPN, COL-1, CTGF, and COL-3, respectively. The left four columns and the right four columns display the immunostaining results for each group at weeks 4 and 8, respectively. Scale bar: 50 μm. Abbreviations: CA: Collagen/alginate; CHA: Collagen/nano-hydroxyapatite/alginate; IHC: Immunohistochemistry; NB: New bone; PDLSCs: Periodontal ligament stem cells; ST: Soft tissue.

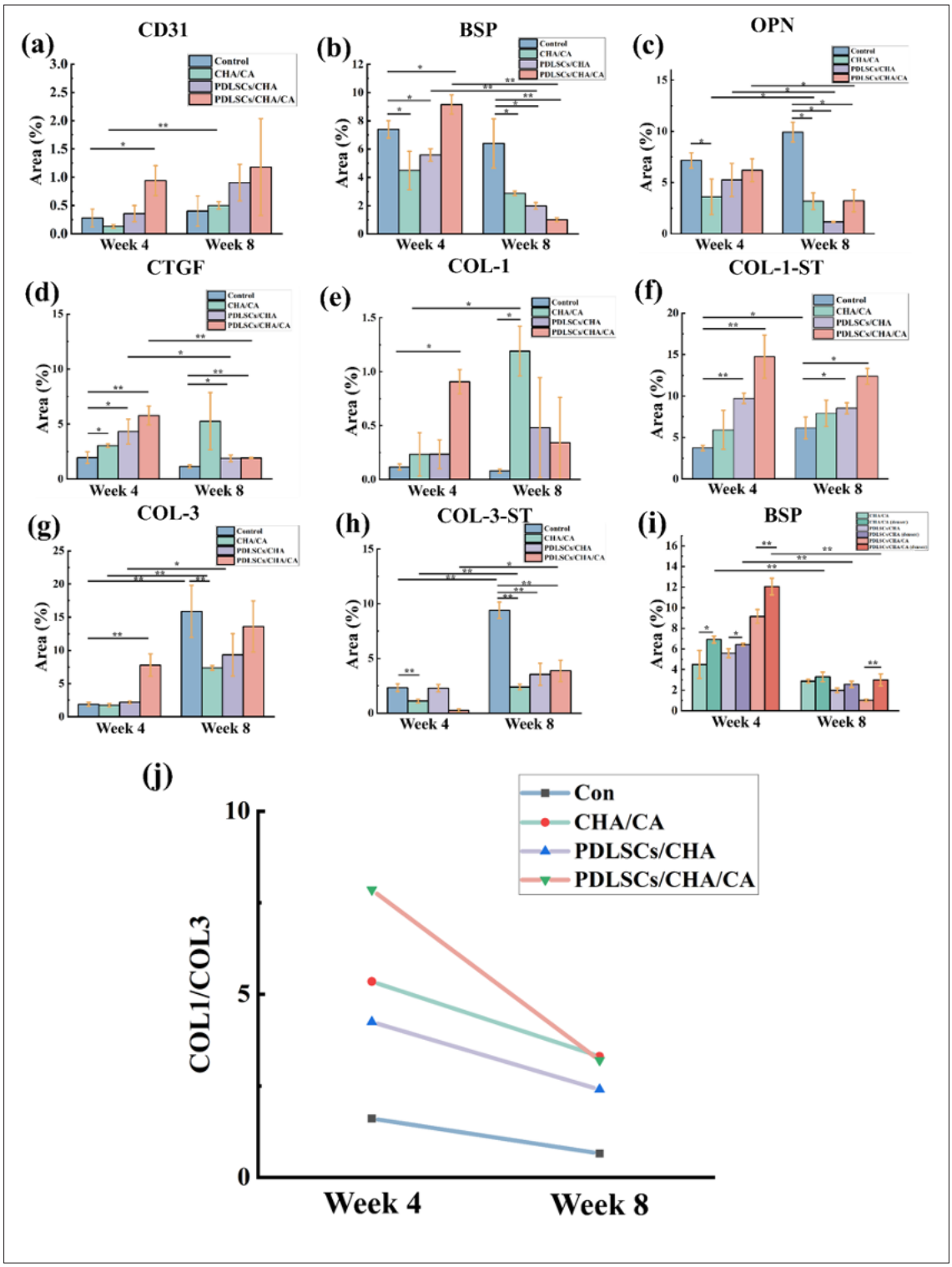

Figure 12. IHC expression level results. (a–h) IHC-based expression levels of markers in the longitudinal sections of murine tooth socket samples: CD31 (a), BSP (b), OPN (c), CTGF (d), COL-1 (e), COL-1-ST (f), COL-3 (g), and COL-3-ST (h). The results are presented as semi-quantitative data. (i) Semi-quantitative results of BSP expression in the internal bone and the denser superficial bone layer. (j) The ratio of COL-1 to COL-3. *$p < 0.05$, **$p < 0.01$. Abbreviations: CA: Collagen/alginate; CHA: Collagen/nano-hydroxyapatite/alginate; IHC: Immunohistochemistry; PDLSCs: Periodontal ligament stem cells; ST: Soft tissue.

The upper portion of the CHA component was designed with a denser internal lattice, while the lower portion had a sparser lattice, to control the nHA concentration. Thus, by designing the internal lattice space of the 3D construct, we created an integrated repair structure with gradient variations.

The SEM results showed that macro-lattice and micro-porosity within these scaffolds are considered crucial for tissue regeneration.[37] Research indicated that successful vascularization of engineered tissues *in vivo* requires space within the scaffold (>200 μm) to facilitate host cell infiltration and subsequent angiogenesis.[38] The porous structure of the material can promote cell infiltration, microvasculature formation, and enhance cell survival and differentiation potential.[39] Additionally, 150–700 μm porous biomaterials can enhance osteoconduction, facilitating the integration of the scaffold with host bone.[40] Researches also revealed that the porosity of the micropores (<10 μm) plays a significant role in enhancing the osteoinductive properties of the scaffold.[41,42] The presence of micropores enhances the permeability of the scaffold, thereby providing more sites for protein adsorption and facilitating its degradation.[43] This aligns with the structure of our material, which features a lattice of large pores (450–600 μm) and a surface with microporous structures, resembling those of scaffolds created by other researchers that exhibit osteoconductivity and good biocompatibility.

In this study, PDLSCs were subjected to flow cytometry to assess their phenotype. The results indicated that these cells exhibited characteristics of MSCs with multipotent differentiation capabilities. Research by Liu et al.[44] has demonstrated the trilineage differentiation potential of PDLSCs into osteoblasts, fibroblasts, and cementoblasts.[16] Studies have also shown that hydrogels composed of collagen and nHA enhance the osteogenic differentiation potential of MSCs. Togo et al.[45] discovered that embryonic stem cells can differentiate into fibroblast-like cells within 3D type I collagen gels,[46] and research suggested that the alignment of collagen matrices can influence the differentiation of fibroblasts. Consequently, this study encapsulated PDLSCs within hydrogels of varying compositions to guide their differentiation toward fibroblastic and osteogenic lineages, aiming to achieve simultaneous regeneration of hard and soft tissues.

Live/dead staining demonstrated that cell viability increased progressively with extended post-printing culture durations. The CCK-8 assay results indicated that material stimulation could promote cell proliferation. Within the initial 5 days post-printing, cells under CHA stimulation did not proliferate as extensively as those under CA stimulation. This observation may correlate with other studies reporting that an increase in amorphous calcium phosphate can potentially induce some cell apoptosis.[47]

PDLSCs cultured in a regular medium without osteogenic supplements showed no inclination toward osteogenic differentiation. However, upon the addition of CHA material stimulation, PDLSCs in regular culture conditions also exhibited a certain degree of osteogenic tendency. Additionally, the results demonstrated the potential of PDLSCs to differentiate into cells of both osteogenic and fibroblastic lineages under material stimulation during *in vitro* differentiation assays. Furthermore, the gene analysis test confirmed the differentiation trend of these cells. Under the stimulation of CA material, the expression levels of *COL1*, *PLAP1*, and *ELASTIN* in PDLSCs were significantly higher compared to the control group on day 7 ($p < 0.01$). Additionally, *FSP1* expression was double that of the control group on day 14. COL-1, a crucial component of the soft tissue collagen fibrils, contributes to the tensile strength of the ECM associated with tendons or ligaments.[48] In research by Takedachi et al.[49] *PLAP1* maintains the soft tissue characteristics of the periodontal tissue and plays a vital role in maintaining the homeostasis of periodontal tissue under mechanical stress. *FSP1* expression is a prominent indicator of fibroblastic differentiation.[50] Elastin, an essential ECM protein required for maintaining the elastic properties of skin, plays a significant role in the wound healing process.[51] Therefore, the gene expression results confirmed that CA material stimulation favored the differentiation of PDLSCs toward soft tissue lineage.

Concurrently, under CHA stimulation, PDLSCs differentiated toward the osteogenic lineage. On day 7, the expression levels of osteogenic factors *ALP*in the experimental group were higher than in the control group. *ALP* is a distinctive biochemical marker of the bone formation process[52] On day 14, the expression of *ALP* was 1.5 times higher than in the control group, indicating better osteogenic differentiation of PDLSCs in the experimental group ($p < 0.05$). The expression of *RUNX2* was slightly lower than in the control group on day 7, but by day 14, it showed a significant increase compared to the control group, further demonstrating the osteogenic induction capability of the material.

In this study, we employed murineheterotopic transplantation and tooth extraction wound healing experiments to validate the biocompatibility and the simultaneous regeneration capabilities of both hard and soft tissues of the material. Macroscopic observation of the tissue samples from the mouse back revealed the ingrowth of blood vessels and the degree of *in vivo* degradation of the material. Following the implantation of cell-printed

constructs, we observed more intact structures, which may be related to the encapsulation of cells within the constructs.[53,54]

The use of 3D porous scaffold materials for ARP remains an advanced tissue engineering technique. We innovatively introduced PDLSCs and promoted their bidirectional differentiation into bone and soft tissues within the scaffold material. At week 4 post-surgery, the extraction socket site in the control group still displayed empty socket structures, whereas new bone formation without residual scaffold material was observable in the histological sections of the experimental group's murine alveolar sockets. A previous study has indicated that rapid material degradation promotes the formation of new bone.[55] This conclusion is also supported by the 3D computed tomography (CT) images and BV/TV data of rats. It is noteworthy that the volume of BV in the stratified scaffold materials with or without cells was greater than that in the non-stratified implant materials. This may be attributed to the altered content of HA in the upper and lower layers of the CHA material.

Subsequently, we performed IHC staining for various markers to evaluate the specific changes in tissue at the implant site. Angiogenesis plays a crucial role in the wound healing process, providing oxygen and nutrients from the local vascular system to support tissue regeneration.[38] Through CD31 staining, we demonstrated that the implanted material did not hinder the normal process of blood clotting but instead increasedthevascular distribution over time, leading tomoreabundant and denser vascular networks. One study has demonstrated a successful attempt at seeding endothelial cells onto porous scaffolds prior to implantation to expedite vascular formation.[56] This could explain the significant increase in vascular distribution observed after the incorporation of stem cells, as indicated by staining results. BSP is a non-collagenous ECM protein associated with mineralized tissues and is related to the formation of alveolar bone and cementum. It is a marker protein for osteoblast differentiation.[57,58] The IHC results of this study showed stronger BSP staining in the newly formed bone during the early stages of healing, with staining intensity diminishing as the bone matures, consistent with other findings.[58] Additionally, Candeliere et al.[59] investigated the expression levels of BSP in the superficial and internal bones of the skull, revealing higher concentrations in the superficial areas. In our IHC semi-quantitative analysis, we validated the findings for the implanted material groups, observing similar results. We discovered that the superficial bone in the group implanted with stratified material exhibited higher BSP content compared to the non-stratified material group. This may be attributed to the stratified material's ability to facilitate a more natural gradient of bone regeneration, which is superior to that of the non-stratified material. In line with the results of the aforementioned PCR experiments, the staining results for OPN in the implanted material group were lighter than in the control group, and the expression of OPN in the sections at week 8 was lower than at week 4, indicating that the formed bone is maturing. This is similar to the findings of Chen et al.[60] Therefore, the staining results for bone matrix proteins suggested that the new bone matured more quickly after the implantation of the material, bringing the potential for the effectiveness of subsequent implant restoration. Type I collagen and type III collagen are the primary constituents of collagen fibers within the ECM. They exhibit distinct distribution patterns, with type I collagen showing a strong, diffused presence in both soft and hard tissue matrices of the control and material groups. Although type I collagen is generally recognized as more mature and possessing superior mechanical properties, type III collagen is typically observed earlier in the woundhealing phase. *In vitro* studies by Xin et al.[61] found a higher ratio of COL-1 to COL-3, signifying a better quality formation of collagen fibers and implying a more mature structure. Our *in vivo* experimental results demonstrated that, at week 8, the staining for COL-1 was weaker in the control group compared to the material group, while the staining for COL-3 was stronger in the control group than in the material group. This could indicate that the newly formed soft tissue at the implant site possesses superior mechanical properties due to the composition of the implanted materials, especially in the PDLSCs/CHA/CA experimental group. CTGF is considered to play a role in angiogenesis during wound healing after tooth extraction, with migrating and proliferating endothelial cells in granulation tissue expressing high levels of CTGF.[62] This suggests that CTGF may contribute to facilitating wound healing by initiating angiogenesis and granulation tissue formation. IHC results from our experiments showed a higher expression of CTGF in the material group compared to the control group. Collectively, these findings indicated that, as compared to the control group, the implanted stratified material effectively promoted the regeneration of both hard tissue in the alveolar socket and the overlying soft tissue following tooth extraction. Notably, the inclusion of mixed cells notably enhanced the tissue regenerative outcomes.

Preliminary findings of our research indicated that the integrated 3D constructs, which are characterized by variations in concentration, use of CA and CHA, and also integrated with PDLSCs, underscored the need to introduce innovative therapeutic strategies for the conservation of both oral soft and hard tissues. Previous studies have demonstrated that biomaterials utilized in

traditional ARP reduce the amount of newly formed bone and may impede the healing process of the alveolar socket.[63,64] In this research, we employed a murine model, which shows distinct healing patterns following tooth extraction compared to humans. To further substantiate the efficacy of the composite constructs and to confirm their capacity to facilitate rapid alveolar bone healing, subsequent experiments will be extended to large animal models, such as the beagle dogs. To surmount the clinical challenges faced in obtaining patient-derived stem cells for the present study, we intentionally included a cell-free group in the *in vivo* experiments. It is noteworthy that while the outcome did not match the performance of the groups incorporating stem cells, the cell-free constructs still managed to achieve commendable regenerative results in comparison to the control groups, indicating their potential utility in regenerative therapy.

5. Conclusion

Made of CA and CHA bioinks, a 3D layered construct featuring gradual variations in HA concentration was ingeniously engineered via bioprinting in this study for the integrated repair of tissues during ARP. This innovative process involves not only the incorporation of PDLSCs and the enhancement of scaffold's viability, but also the stimulation of their heterotopic differentiation ability. Applying this construct to all transplantation and post-tooth extraction in a murine model demonstrated its biocompatibility and its capacity to enhance the integrated regeneration of oral hard and soft tissues. This sophisticated construct may pave the way for practical use as customized integrated material following tooth extraction, showcasing the potential for clinical translation.

Acknowledgments

None.

Funding

This work was supported by the National Key Research and Development Program of China (2017YFA0701302, PKUSS20200113).

Conflict of interest

The authors declare they have no competing interests.

Author contributions

Conceptualization: Zhihui Tang, Qing Li
Formal analysis: Huilin Zhu, Ke Yi
Investigation: Huilin Zhu, Ke Yi
Methodology: Huilin Zhu
Writing–original draft: Huilin Zhu
Writing–review & editing: Zhihui Tang, Qing Li

Ethics approval and consent to participate

Isolation of primary human PDLSCs was approved by the Ethics Committee of the Peking University School and Hospital of Stomatology (PKUSSIRB-201950166), with informed consent obtained from all subjects or their legal guardians. Animal experiments of this study were approved by the Laboratory Animal Research Ethics Committee of Peking University Health Science Center (Approval No.: DLASBD0054).

Consent for publication

Not applicable.

Availability of data

Data is available from the corresponding author upon reasonable request.

Supplemental information

Video S1. Visual demonstration video of the mechanical properties of the construct.

References

1. Tan WL, Wong TLT, Wong MCM, Lang NP. A systematic review of post-extractional alveolar hard and soft tissue dimensional changes in humans. *Clin Oral Implants Res.* 2012;23(S5):1-21.
doi: 10.1111/j.1600-0501.2011.02375.x.

2. Khzam N, Arora H, Kim P, Fisher A, Mattheos N, Ivanovski S. Systematic review of soft tissue alterations and esthetic outcomes following immediate implant placement and restoration of single implants in the anterior maxilla. *J Periodontol.* 2015;86(12):1321-1330.
doi: 10.1902/jop.2015.150287.

3. Farmer M, Darby I. Ridge dimensional changes following single-tooth extraction in the aesthetic zone. *Clin Oral Implants Res*. 2014;25(2):272-277.
doi: 10.1111/clr.12108.

4. Aribau-Gumà C, Jorba-García A, Sánchez-Torres A, Sànchez-Garcés M. Alveolar ridge preservation: an overview of systematic reviews. *Int J Oral Maxillofac Surg.* 2022;51(2):234-242.
doi: 10.1016/j.ijom.2021.06.002.

5. Barootchi S, Tavelli L, Majzoub J, Stefanini M, Wang HL, Avila-Ortiz G. Alveolar ridge preservation: complications and cost-effectiveness. *Periodontol* 2000. 2023;92(1): 235-262.
doi: 10.1111/prd.12469.

6. Montazerian H, Davoodi E, Baidya A, Baghdasarian S, Sarikhani E, Meyer CE, Haghniaz R, Badv M, Annabi N, Khademhosseini A, Weiss PS. Engineered Hemostatic Biomaterials for Sealing Wounds. *Chem Rev* 2022;122(15):12864-12903. doi: 10.1021/acs.chemrev.1c01015.

7. Ayari H. The use of periodontal membranes in the field of periodontology: spotlight on collagen membranes. *J Appl Biomed* 2022;20(4):154-162. doi: 10.32725/jab.2022.020.

8. Canullo L, Pesce P, Antonacci D, Ravidà A, Galli M, Khijmatgar S, Tommasato G, Sculean A, Del Fabbro M. Soft tissue dimensional changes after alveolar ridge preservation using different sealing materials: a systematic review and network meta-analysis. *Clin Oral Investig*. 2022;26(1): 13-39. doi: 10.1007/s00784-021-04192-0.

9. Abere DV, Ojo SA, Oyatogun GM, Paredes-Epinosa MB, Niluxsshun MCD, Hakami A. Mechanical and morphological characterization of nano-hydroxyapatite (nHA) for bone regeneration: a mini review. *Biomed Eng Adv* 2022;4(3):100056. doi: 10.1016/j.bea.2022.100056.

10. Rosa N, Moura MFSF, Olhero S, Simoes R, Magalhães FD, Marques AT, Ferreira JPS, Reis AR, Carvalho M, Parente M. Bone: an outstanding composite material. *Appl Sci* 2022;12(7):1-16. doi: 10.3390/app12073381.

11. Han HS, Lee JT, Oh S, Cho YD, Kim S. Effectiveness of a collagen matrix seal and xenograft in alveolar ridge preservation: an experimental study in dogs. *Sci Rep* 2024;14(1):1-10. doi: 10.1038/s41598-023-50370-3.

12. Gabay E, Katorza A, Zigdon-Giladi H, Horwitz J, Machtei EE. Histological and dimensional changes of the alveolar ridge following tooth extraction when using collagen matrix and collagen-embedded xenogenic bone substitute: a randomized clinical trial. *Clin Implant Dent Relat Res.* 2022;24(3):382-390. doi: 10.1111/cid.13085.

13. Tonar Z, Khadang I, Fiala P, Nedorost L, Kochová P. Quantification of compact bone microporosities in the basal and alveolar portions of the human mandible using osteocyte lacunar density and area fraction of vascular canals. *Ann Anat*. 2011;193(3):211-219. doi: 10.1016/j.aanat.2011.02.001.

14. Reznikov N, Shahar R, Weiner S. Bone hierarchical structure in three dimensions. *Acta Biomater.* 2014;10(9):3815-3826. doi: 10.1016/j.actbio.2014.05.024.

15. Bartold PM. Connective tissues of the periodontium--preface. *Periodontol*. 2000. 2000;24(1):7-8. doi: 10.1034/j.1600-0757.2000.2240101.x.

16. Liu J, Zhao Z, Ruan J, Weir MD, Ma T, Ren K, Schneider A, Oates TW, Li A, Zhao L, Xu HHK. Stem cells in the periodontal ligament differentiated into osteogenic, fibrogenic and cementogenic lineages for the regeneration of the periodontal complex. *J Dent*. 2020;92:103259. doi: 10.1016/j.jdent.2019.103259.

17. Seo BM, Miura M, Gronthos S, Bartold PM, Batouli S, Brahim J, Young M, Robey PG, Wang CY, Shi S. Investigation of multipotent postnatal stem cells from human periodontal ligament. *Lancet*. 2004;364(9429):149-155. doi: 10.1016/S0140-6736(04)16627-0.

18. Li M, Sun L, Liu Z, Shen Z, Cao Y, Han L, Sang S, Wang J. 3D bioprinting of heterogeneous tissue-engineered skin containing human dermal fibroblasts and keratinocytes. *Biomater Sci*. 2023;11(7):2461-2477. doi: 10.1039/d2bm02092k.

19. Jian H, Li X, Dong Q, Tian S, Bai S. In vitro construction of liver organoids with biomimetic lobule structure by a multicellular 3D bioprinting strategy. *Cell Prolif.* 56(5):1-9. doi: 10.1111/cpr.13465.

20. Dai W, Zhang L, Yu Y, Yan W, Zhao F, Fan Y, Cao C, Cai Q, Hu X, Ao Y. 3D Bioprinting of heterogeneous constructs providing tissue-specific microenvironment based on host–guest modulated dynamic hydrogel bioink for osteochondral regeneration. *Adv Funct Mater*. 2022;32(23):1-12. doi: 10.1002/adfm.202200710.

21. Zhang Y, Li D, Liu Y, Peng L, Lu D, Wang P, Ke D, Yang H, Zhu X, Ruan C. 3D-bioprinted anisotropic bicellular living hydrogels boost osteochondral regeneration via reconstruction of cartilage–bone interface. *Innovation*. 2024;5(1):100542. doi: 10.1016/j.xinn.2023.100542.

22. Nguyen LH, Kudva AK, Guckert NL, Linse KD, Roy K. Unique biomaterial compositions direct bone marrow stem cells into specific chondrocytic phenotypes corresponding to the various zones of articular cartilage. *Biomaterials*. 2011;32(5):1327-1338. doi: 10.1016/j.biomaterials.2010.10.009.

23. Balestri W, Hickman GK, Morris RH, Hunt JA, Reinwald Y. Triphasic 3D in vitro model of bone-tendon-muscle interfaces to study their regeneration. *Cells*. 2023; 12(2):313. doi: 10.3390/cells12020313.

24. Panduwawala CP, Zhan X, Dissanayaka WL, Samaranayake LP, Jin L, Zhang C. In vivo periodontal tissue regeneration by periodontal ligament stem cells and endothelial cells in three-dimensional cell sheet constructs. *J Periodontal Res.* 2017;52(3):408-418. doi: 10.1111/jre.12405.

25. Zhu Y, Wang W, Chen Q, Ren T, Yang J, Li G, Qi Y, Yuan C, Wang P. Bioprinted PDLSCs with high-concentration GelMA hydrogels exhibit enhanced osteogenic differentiation in

vitro and promote bone regeneration in vivo. *Clin Oral Investig*. 2023;27(9):5153-5170.
doi: 10.1007/s00784-023-05135-7.

26. Adolpho LF, Lopes HB, Freitas GP, Weffort D, Campos Totoli GG, Loyola Barbosa AC, Freire Assis RI, Silverio Ruiz KG, Andia DC, Rosa AL, Beloti MM. Human periodontal ligament stem cells with distinct osteogenic potential induce bone formation in rat calvaria defects. *Regen Med*. 2022;17(6):341-353.
doi: 10.2217/rme-2021-0178.

27. Chen J, Ahmad R, Li W, Swain M, Li Q. Biomechanics of oral mucosa. *J R Soc Interface*. 2015;12(109):20150325.
doi: 10.1098/rsif.2015.0325.

28. Bouxsein ML, Boyd SK, Christiansen BA, Guldberg RE, Jepsen KJ, Müller R. Guidelines for assessment of bone microstructure in rodents using micro-computed tomography. *J Bone Miner Res*. 2010;25(7):1468-1486.
doi: 10.1002/jbmr.141.

29. Boularaoui S, Shanti A, Khan KA, Iacoponi S, Christoforou N, Stefanini C. Harnessing shear stress preconditioning to improve cell viability in 3D post-printed biostructures using extrusion bioprinting. *Bioprinting*. 2022;25(8):e00184.
doi: 10.1016/j.bprint.2021.e00184.

30. Popescu F, Titorencu I, Albu Kaya M, Miculescu F, Tutuianu R, Coman AE, Danila E, Marin MM, Ancuta DL, Coman C, Barbilian A. Development of innovative biocomposites with collagen, keratin and hydroxyapatite for bone tissue engineering. *Biomimetics*. 2024;9(7):428.
doi: 10.3390/biomimetics9070428.

31. Elango J, Hou C, Bao B, Wang S, Maté Sánchez de Val JE, Wenhui W. The molecular interaction of collagen with cell receptors for biological function. *Polymers (Basel)*. 2022;14(5):1-25.
doi: 10.3390/polym14050876.

32. Bose S, Li S, Mele E, Silberschmidt VV. Exploring the mechanical properties and performance of type-I collagen at various length scales: a progress report. *Materials (Basel)*. 2022;15(8):1-17.
doi: 10.3390/ma15082753.

33. Schwab A, Levato R, D'Este M, Piluso S, Eglin D, Malda J. Printability and shape fidelity of bioinks in 3D bioprinting. *Chem Rev*. 2020;120(19):11028-11055.
doi: 10.1021/acs.chemrev.0c00084.

34. Clarke B. Normal bone anatomy and physiology. *Clin J Am Soc Nephrol*. 2008;3(Suppl 3):S131-S139.
doi: 10.2215/CJN.04151206.

35. Joodaki H, Panzer MB, Skin mechanical properties and modeling: a review. *Proc Inst Mech Eng H*. 2018;232(4):323-343.
doi: 10.1177/0954411918759801.

36. P Jain, H Kathuria, N Dubey. Advances in 3D bioprinting of tissues/organs for regenerative medicine and in-vitro models. *Biomaterials*. 2022;287(8):121639.
doi: 10.1016/j.biomaterials.2022.121639.

37. Ghayor C, Bhattacharya I, Guerrero J, Ozcan M, Weber FE. 3D-printed HA-based scaffolds for bone regeneration: microporosity, osteoconduction and osteoclastic resorption. *Materials*. 2022;15(4):1433.
doi: 10.3390/ma15041433

38. Rouwkema J, Khademhosseini A. Vascularization and angiogenesis in tissue engineering: beyond creating static networks. *Trends Biotechnol*. 2016;34(9):733-745.
doi: 10.1016/j.tibtech.2016.03.002.

39. Carotenuto F, Politi S, Ul Haq A, De Matteis F, Tamburri E, Terranova ML, Teodori L, Pasquo A, Di Nardo P. From soft to hard biomimetic materials: tuning micro/nano-architecture of saffolds for tissue regeneration. *Micromachines*. 2022;13(5):1-25.
doi: 10.3390/mi13050780.

40. Zhang L, Yang G, Johnson BN, Jia X. Three-dimensional (3D) printed scaffold and material selection for bone repair. *Acta Biomater*. 2019;84(10):16-33.
doi: 10.1016/j.actbio.2018.11.039.

41. Li X, van Blitterswijk CA, Feng Q, Cui F, Watari F. The effect of calcium phosphate microstructure on bone-related cells in vitro. *Biomaterials*. 2008;29(23):3306-3316.
doi: 10.1016/j.biomaterials.2008.04.039.

42. Li X, Liu H, Niu X, Fan Y, Feng W, Cui FZ, F Watari F. Osteogenic differentiation of human adipose-derived stem cells induced by osteoinductive calcium phosphate ceramics. *J Biomed Mater Res B Appl Biomater*. 2011;97(1):10-19.
doi: 10.1002/jbm.b.31773.

43. Hernandez JL, Woodrow KA. Medical applications of porous biomaterials: features of porosity and tissue-specific implications for biocompatibility. *Adv Healthc Mater*. 2022;11(9):1-25.
doi: 10.1002/adhm.202102087.

44. Hayrapetyan A, Bongio M, Leeuwenburgh SCG, Jansen JA, van den Beucken JJJP. Effect of nano-HA/collagen composite hydrogels on osteogenic behavior of mesenchymal stromal cells. *Stem Cell Rev Rep*. 2016;12(3):352-364.
doi: 10.1007/s12015-016-9644-x.

45. Japudom J, Karaman S, Quartey BC, WMohamed WKE, Mahtani N, Garcia-Sabaté A, Teo J. Collagen fibril orientation instructs fibroblast differentiation via cell contractility. *Adv Sci*. 2023;10(22):1-14.
doi: 10.1002/advs.202301353.

46. Togo S, Sato T, Sugiura H, Wang X, Basma H, Nelson A, Liu X, Bargar TW, Sharp JG, Rennard SI. Differentiation of embryonic stem cells into fibroblast-like cells in three-dimensional type i collagen gel cultures. *Vitr Cell Dev Biol Anim*. 2011;47(2):114-124.
doi: 10.1007/s11626-010-9367-2.

47. Rivas M, Turon P, Alemán C, Puiggalí J, del Valle LJ. Incorporation of functionalized calcium phosphate nanoparticles in living cells. *J Clust Sci*. 33(1):2781-2795.
doi: 10.1007/s10876-021-02182-6.

48. Komatsu K. Mechanical strength and viscoelastic response of the periodontal ligament in relation to structure. *J Dent Biomech*. 2009;2010:502318. doi: 10.4061/2010/502318.

49. Takedachi M, Yamamoto S, Kawasaki K, Shimomura J, Murata M, Morimoto C, Hirai A, Kawakami K, Bhongsatiern P, Iwayama T, Sawada K, Yamada S, Murakami S. Reciprocal role of PLAP-1 in HIF-1α-mediated responses to hypoxia. *J Periodontal Res*. 2022:57(3):470-478. doi: 10.1111/jre.12976.

50. Knaup I, Symmank J, Bastian A, Neuss S, Pufe T, Jacobs C, Wolf M. Impact of FGF1 on human periodontal ligament fibroblast growth, osteogenic differentiation and inflammatory reaction in vitro. *J Orofac Orthop.* 2022;83(Suppl 1):42-55. doi: 10.1007/s00056-021-00363-6.

51. Gardeazabal L, Izeta A. Elastin and collagen fibres in cutaneous wound healing. *Exp Dermatol.* 2024;33(3):1-14. doi: 10.1111/exd.15052.

52. Schini M, Vilaca T, Gossiel F, Salam S, Eastell R. Bone turnover markers: basic biology to clinical applications. *Endocr Rev.* 2023;44(3):417-473. doi: 10.1210/endrev/bnac031.

53. Ogle ME, Segar CE, Sridhar S, Botchwey EA. Monocytes and macrophages in tissue repair: implications for immunoregenerative biomaterial design. *Exp Biol Med.* 2016;241(10):1084-1097. doi: 10.1177/1535370216650293.

54. Londono R, Dziki JL, Haljasmaa E, Turner NJ, Leifer, Badylak. The effect of cell debris within biologic scaffolds upon the macrophage response. *J Biomed Mater Res A*. 2017;105(8):2109-2118. doi: 10.1002/jbm.a.36055.

55. P Feng, R Zhao, W Tang, F Yang, H Tian, S Peng, H Pan, C Shuai. Structural and functional adaptive artificial bone: materials, fabrications, and properties. *Adv Funct Mater.* 2023;33(23):1-29. doi: 10.1002/adfm.202214726.

56. Levenberg S, Rouwkema J, Macdonald M, Garfein ES, Kohane DS, Darland DC, Marini R, Van Blitterswijk CA, Mulligan RC, D'Amore PA, Langer R. Engineering vascularized skeletal muscle tissue. *Nat Biotechnol.* 2005;23(7):879-884. doi: 10.1038/nbt1109.

57. Nagasaki K, Chavez MB, Nagasaki A, Taylor JM, Tan MH, Ma M, Ralston E, Thew ME, Kim DG, Somerman MJ, Foster L. The bone sialoprotein RGD domain modulates and maintains periodontal development. *J Dent Res.* 2022;101(10):1238-1247. doi: 10.1177/00220345221100794.

58. Chavez MB, Tan MH, Kolli TN, Zachariadou C, Farah F, Mohamed FF, Chu EY, Foster BL. Bone sialoprotein is critical for alveolar bone healing in mice. *J Dent Res.* 2023;102(2):187-196. doi: 10.1177/00220345221126716.

59. Candeliere GA, Liu F, Aubin JE. Individual osteoblasts in the developing calvaria express different gene repertoires. *Bone.* 2001;28(4):351-361. doi: 10.1016/S8756-3282(01)00410-0.

60. Chen J, Singh K, Mukherjee BB, Sodek J. Developmental expression of osteopontin (OPN) mRNA in rat tissues: evidence for a role for OPN in bone formation and resorption. *Matrix.* 1993;13(12):113-123. doi: 10.1016/s0934-8832(11)80070-3.

61. Xin Y, Xu P, Wang X, Chen Y, Zhang Z, Zhang Y. Human foreskin-derived dermal stem/progenitor cell-conditioned medium combined with hyaluronic acid promotes extracellular matrix regeneration in diabetic wounds. Stem Cell Res Ther. 2021;12(1):1-18. doi: 10.1186/s13287-020-02116-5.

62. Lee CH, Shah B, Moioli EK, Mao JJ. CTGF directs fibroblast differentiation from human mesenchymal stem/stromal cells and defines connective tissue healing in a rodent injury model. *J Clin Invest.* 2010;120(9):3340-3349. doi: 10.1172/JCI43230.

63. Becker W, Clokie C, Sennerby L, Urist MR, Becker BE, Histologic findings after implantation and evaluation of different grafting materials and titanium micro screws into extraction sockets: case reports. *J Periodontol.* 1998;69(4):414-421. doi: 10.1902/jop.1998.69.4.414.

64. Canellas JVDS, Ritto FG, C Figueredo CMDS, Fischer RG, de Oliveira GP, Thole AA, Medeiros PJD. Histomorphometric evaluation of different grafting materials used for alveolar ridge preservation: a systematic review and network meta-analysis. *Int J Oral Maxillofac Surg.* 2020;49(6);797-810. doi: 10.1016/j.ijom.2019.10.007.

ACCSCIENCE PUBLISHING

International Journal of Bioprinting

RESEARCH ARTICLE

Osteocytic PGE_2 receptors EP2/4 signaling create a physiological osteogenic microenvironment in polycaprolactone 3D modules

Jingjing Chen[1†], Qiuling Guo[1†], Jinling Zhang[1], Ying Zhang[1], Yangxi Liu[1], Pengtao Wang[1], Chengzhu Zhao[1], Linda F. Bonewald[2,3*], and Xiaolin Tu[1,3*]

[1] Laboratory of Skeletal Development and Regeneration, Key Laboratory of Clinical Laboratory Diagnostics (Ministry of Education), College of Laboratory Medicine, Chongqing Medical University, Chongqing, China

[2] Indiana Center for Musculoskeletal Health, Indiana University School of Medicine, Indianapolis, United States of America

[3] Department of Anatomy, Cell Biology, and Physiology, School of Medicine, Indiana University, Indianapolis, United States of America

(This article belongs to the Special Issue: *Made-to-order Organ*)

Abstract

3D bioprinting is a focused field in orthopedics, and its application with physiological osteogenic microenvironments (POMEs) is a prerequisite for authentic bone reconstruction. Mechanical stimulation produces prostaglandin E2 (PGE_2) in mechanosensory osteocytes, but it remains unclear whether osteocytic PGE_2 is a POME. PGE_2 is an inducer of osteogenesis by acting on bone marrow stromal cells through its receptors EP2/EP4 to initiate osteogenic differentiation and mineralization. Unfortunately, clinical trials of PGE_2 have reported side effects, including fever and drowsiness; targeting the PGE_2 receptor in specific tissues can avoid these side effects. Here, we demonstrate that osteocytic cell line MLO-Y4 from murine long bones treated with EP2/EP4 agonists for 24 h enhance osteogenic differentiation and mineralization, inhibit adipogenesis of the stromal cell line ST2, and induce tubule formation and angiogenic marker expression in human umbilical vein endothelial cells (HUVECs). Mechanistically, activation of the PGE_2 signaling pathway in osteocytes induces autocrine effects by upregulating the expression of EP2/EP4 receptors and COX-2 (*Ptgs2*), further amplifying PGE_2 signaling. PGE_2 produced by treated MLO-Y4 cells appears responsible for osteogenesis, alongside other unidentified factors. MLO-Y4 and ST2 cells, incorporated into POME 3D constructs, maintained over 95% viability over seven days. Treatment of osteocytes with a PGE_2 receptor agonist promotes ST2 cell proliferation and enhances osteoblast marker expression and mineralization. As 3D bioprinting closely models *in vivo* conditions, these data suggest that osteocytic PGE_2 receptor signaling is a safe and mild POME with great potential for translational applications.

Keywords: PGE_2; Physiological osteogenic microenvironment; 3D bioprinting; Osteogenic differentiation; Angiogenesis; Adipogenesis

†These authors contributed equally to this work.

***Corresponding authors:**
Linda F. Bonewald (lbonewal@iu.edu)

Xiaolin Tu (xtu@cqmu.edu.cn)

Citation: Chen J, Guo Q, Zhang J, et al. Osteocytic PGE_2 receptors EP2/4 signaling create a physiological osteogenic microenvironment in polycaprolactone 3D modules. *Int J Bioprint*. 2025;11(1):284-300. doi: 10.36922/ijb.3959

Received: June 17, 2024
Revised: August 4, 2024
Accepted: August 6, 2024
Published Online: August 8, 2024

Copyright: © 2024 Author(s). This is an Open Access article distributed under the terms of the Creative Commons Attribution License, permitting distribution, and reproduction in any medium, provided the original work is properly cited.

Publisher's Note: AccScience Publishing remains neutral with regard to jurisdictional claims in published maps and institutional affiliations.

1. Introduction

3D printing technology has traditionally been used for rapid prototyping of industrial materials such as metals and polymers. In recent years, it has been integrated with biotechnology (this combination is known as 3D bioprinting), displaying great potential in the biomedical field.[1] 3D bioprinting has several advantages, such as matching complex-shaped organs and precise control of manufacturing processes,[2] leading to research. However, 3D bioprinting faces a key challenge: developing a biologically active material that can achieve the function of original organs after implantation, and physiologically responding to internal and external stimuli to adapt to environmental changes.[3]

To address this issue, the concept of microenvironment has been introduced into the field of 3D bioprinting.[4] In a broad sense, microenvironment refers to the combination of physical, chemical, and biological factors present in cells and their surrounding areas. These factors collectively influence cell physiology and differentiation. In orthopedic 3D bioprinting, creating an osteogenic microenvironment that mimics physiological conditions is crucial for the reconstruction of authentic bone.[4]

Bone tissue is sensitive to mechanical stimulation, and enhanced mechanical stimulation has positive and anabolic effects on bone formation.[5] Osteocytes are the main mechanosensory cells in the skeleton, detecting changes in their microenvironment due to mechanical loading and converting them into biological responses by secreting prostaglandin E2 (PGE_2).[6] In a study on CX43 in murine osteocytes, a CX43-specific antibody inhibited the secretion of PGE_2, osteoblastic activity, and bone formation induced by mechanical loading. However, PGE_2 reversed this inhibition and restored the osteogenic response to mechanical loading.[7] Therefore, PGE_2 generation induced by mechanical loading is positively correlated with bone formation, leading us to question whether activating PGE_2 signaling in osteocytes could enhance bone formation. Osteocytes may be the ideal target for drug action as they account for more than 90% of the total number of cells in the skeleton. Additionally, osteocytes interact with each other through their dendrites to form a large regulatory network that facilitates drug action.

Moreover, PGE_2 also plays an active role in angiogenesis, which is responsible for the delivery of nutrients and oxygen in the body. Therefore, the formation of blood vessels is essential in bone regeneration and repair. *In vitro* and *in vivo* research data indicate that PGE_2 can promote the formation of blood vessels, primarily mediated by EP4 receptors and the downstream Protein Kinase A (PKA) signaling pathway.[8] However, due to its side effects, such as fever and drowsiness, PGE_2 is not acceptable as a bone-forming drug in clinical practice. Consequently, activating PGE_2 receptors is preferred to avoid these side effects.[9] EP2 and EP4 are the two PGE_2 receptors most associated with bone formation. In the cultivation of rat calvarial cells, PGE_2 not only promotes the expression of osteoblast markers and mineralization. Additionally, agonists of EP2 and EP4 further enhance these effects.[10] In humans, functional EP2 is lacking in osteoblasts or osteoclasts, leading to increased focus on EP4. In murine osteoblasts, the main downstream effect of EP4 signaling is the increased production of cAMP and COX-2.[11]

In our study, PGE2-treated osteocytic cell line MLO-Y4 promotes osteogenic differentiation of ST2 cells and mineralization. Moreover, EP4 and EP2 agonists CAY10580 (C10)- and Taprenepag isopropyl (Tap)-treated MLO-Y4 cells replicate the osteogenic effects of PGE_2. We found that MLO-Y4 cells treated with EP4 agonist C10 can promote osteogenic differentiation and mineralization of ST2 cells. As 3D scaffolds can rapidly simulate the *in vivo* microenvironment, in our established polycaprolactone (PCL)- and cell-integrated 3D bioprinting system (PCI3D),[12] the 7-day survival rate of cells can reach over 95% and support the osteogenic differentiation and mineralization of ST-2 cells. Meanwhile, the conditioned medium of osteocytes treated with EP2/4 agonists can induce the migration and angiogenesis of human umbilical vein endothelial cells (HUVECs), which is important for the regeneration and repair of bone tissue. In summary, osteocytic PGE_2 receptor signaling enhances osteogenesis and angiogenesis, inhibits adipogenesis, and promotes cell proliferation, osteogenic differentiation, and mineralization within simulated *in vivo* 3D scaffolds, suggesting a safe and mild physiological osteogenic microenvironments (POME). We built this POME using hard biomaterial as a bone developmental module through 3D bioprinting. This system allows cells to survive, grow, and develop for up to 28 days, effectively simulating physiological conditions for bone formation.

2. Materials and methods

2.1. Reagents and cells

PGE_2 and Tap were purchased from MedChemExpress (China); C10 was purchased from Chemegen (China); celecoxib was purchased from TargetMol (China); Matrigel was purchased from Corning (United States of America [USA]); Alizarin Red S was purchased from Solarbao Company (China); lyophilized gelatin methacryloyl (GelMA) and photo-cross-linking agent lithium phenyl-2,4,6-trimethylbenzoylphosphinate (LAP) were purchased from Sunp Biotech (China); and PCL was purchased from Aladdin (China).

MLO-Y4 was kindly provided by Dr. Lynda Bonewald of Indiana University School of Medicine, USA. ST2 cells were kindly provided by Dr. Steve Teitelbaum of Washington University in St. Louis, USA.

2.2. Assay kits

5-Bromo-4-chloro-3-indolyl phosphate p-toluidine salt (BCIP)/Nitrotetrazolium Blue chloride (NBT) alkaline phosphatase (AP) detection kit, AP activity detection kit, live/dead viability assay kit, cell counting kit-8 (CCK-8), and modified Oil Red O staining kit were purchased from Beyotime Biotechnology (China). The reverse transcription premix kit and Synergy Brands (SYBR) premix quantitative polymerase chain reaction (qPCR) kit were purchased from Accurate Biology (China).

2.3. Cell culture

Minimum Essential Medium α (α-MEM) and Dulbecco's Modified Eagle Medium (DMEM) were purchased from Gibco (USA); streptomycin and trypsin were purchased from Beyotime Biotechnology (China); fetal bovine serum (FBS) was purchased from Biological Industries (Israel); and HUVECs, Wnt3a-expressing cell line, and its control cell line were purchased from American Type Culture Collection (ATCC, USA).

Murine stromal and osteocytic cell lines ST2 and MLO-Y4 were cultured in α-MEM containing 10% FBS and 1% penicillin and streptomycin, as previously described.[13-15] Wnt3a-expressing, its control cell lines, and HUVECs were cultured in DMEM containing 10% FBS and 1% penicillin and streptomycin.[13-15] MLO-Y4 cells were seeded at 1×10^4/well in a 24-well plate and cultured overnight. The cells were then stimulated with PGE_2 (1, 2.5, and 7.5 μM), Tap (1, 5, and 20 μM), or C10 (10, 100, and 500 nM), respectively, for 24 h. Thereafter, the culture medium was removed, and ST2 cells were immediately added into each well to be co-cultured with the drug-treated osteocytes for three days before harvesting for assays.

2.4. Preparation of conditioned medium

MLO-Y4 cells were stimulated with 5 μM Tap or 500 nM C10 for 24 h, washed with serum-free medium, and further cultured with growth medium for another 24 h. The culture medium was collected as the conditioned medium and stored at −80°C until use. The control medium was collected in the same way in MLO-Y4 cells treated with dimethyl sulfoxide (DMSO) or ethanol. The Wnt3a medium was collected from the Wnt3a-expressing cell line treated with DMSO as described.[13-15]

2.5. RNA extraction and gene expression analysis

Total RNA extraction and qPCR were performed as reported.[16] To analyze gene expression, total RNA was extracted from the cells using Trizol. The cDNA was synthesized from total RNA using the reverse transcription premix kit and used as templates of qPCR to detect genes with specific primer sets (Table 1 and 2). The relative expression levels of mRNAs were normalized to the housekeeping gene glyceraldehyde-3-phosphate dehydrogenase (*Gapdh*) using the $2^{-\Delta Ct}$ method.

2.6. Polycaprolactone- and cell-integrated 3D Printing

As previously described,[15] lyophilized GelMA was thoroughly dissolved in α-MEM to prepare a 20% (w/v) GelMA solution containing 0.5% (w/v) of LAP that serves as an initiator of photo-crosslinking. The solution was sterilized through a filter (0.22 μm; Merck Millipore, Germany) and stored as a stock solution at 4°C until further use. The MLO-Y4 cells were first treated with DMSO/ethanol or Tap/C10 for 24 h. Following treatment,

Table 1. Sequences of primers (mouse) used for quantitative reverse transcription polymerase chain reaction (RT-qPCR).

Primer	Sequence	
	Forward	Reverse
Gapdh	GCACAGTCAAGGCCGAGAAT	GCCTTCTCCATGGTGGTGGTGAA
β-actin	AGAGGGAAATCGTGCGTGAC	CCATACCCAAGAAGGAAGGCT
Ptger2	TGCTTATCGTGGCTGTGCTC	GGAGAATGAGGTGGTCCGTC
Ptger4	ATGGTCATCTTACTCATCGCCAC	CTTTCACCACGTTTGGCTGAT
Ptgs2	CACAGCCTACCAAAACAGCCA	GCTCAGTTGAACGCCTTTTGA
Alpl	TTCGCTATCTGCCTTGCCTG	AGTCTGTGTCTTGCCTGCC
Runx2	CCGTGGCCTTCAAGGTTGT	TTCATAACAGCGGAGGCA
Col1α1	TCAACCCCGTCTACTTCCCT	TTCAACAGTCCAAGAACCCCAT
Ibsp	CAGAGGAGGCAAGCGTCACT	GCTGTCTGGGTGCCAACACT
Pparg	GCCAAGGTGCTCCAGAAGATGAC	GTGAAGGCTCATGTCTGTCTCTGTC
Cebpa	GCCAAACTGAGACTCTTC	TGGCATCTCTGTGTCAAC

Table 2. Sequences of primers (human) used for quantitative reverse transcription polymerase chain reaction (RT-qPCR).

Primer	Sequence	
	Forward	Reverse
Gapdh	GCACAGTCAAGGCCGAGAAT	GGCTGTTGTCATACTTCTCATGG
Hif-1	CCATTAGAAAGCAGTTCCGCAAGC	GTGGTAGTGGTGGCATTAGCAGTAG
Vegf	AGAGGGAAATCGTGCGTGAC	CCATACCCAAGAAGGAAGGCT
Angpt-1	ACTAGTAGTACAATGACAGTTTTCCTTTCC	AGATCTTCAAAAGTCCAAGGGCCGGATCAT
eNOS	TCACCTTCTTCCTGGACATCACTC	ACCACTTCCACTCCTCGTAGCG
VE-cad	TGCCTCCTATCCCAGTGTCGTATC	GCCTCGGTTCCCATATCTCATCTTG

2×10^5/mL of the treated cells were subsequently mixed with 8×10^5/mL ST2 cells in α-MEM, maintaining a concentration ratio of 1:4, which was previously reported as optimal for osteogenic differentiation.[12,15,17]An equal volume of GelMA solution was added to form a cell-laden solution, which was then placed into a syringe and refrigerated on ice. The cooled syringe was subsequently loaded into the cell-printing nozzle (ALPHA-IPT1; SunP Biotech, China), preparing it for 3D bioprinting.

Next, PCL was pre-melted at 95°C for 30 min before extrusion as beams (diameter: 400 μm; length: 15 mm) at a printing speed of 2 mm/s. At the end, the printing direction was adjusted to be perpendicular to the line just printed, continuing to print 1.1 mm, then the printing direction was adjusted again to turn back parallel to the first printing line, printing 15 mm long. A solution of GelMA loaded with cells was printed as hydrogel micelles (diameter: 300 μm; length 14 mm) between the PCL strips at 25°C at a printing speed of 5 mm/s length of 500 μm.[18] Once a layer was printed, the GelMA hydrogel was crosslinked under 405 nm blue light for 10 s before printing resumed vertically for the next layer. After printing four layers repeatedly, the 3D biological module is completed.

2.7. Cell viability assay

Cell viability in PCI3D modules was quantitated using a live/dead viability assay kit.[19] After 1, 4, and 7 days of cell culture, the cells were washed with phosphate-buffered saline (PBS) and incubated in the staining mixture, containing 1 μL calcein AM (Calcein acetoxymethyl ester) and 1 μL propidium iodide (PI) in 1 mL of assay buffer. Calcein AM was used to stain living cells, and PI was used to stain dead cells. The plates were incubated in an incubator for 0.5 h, and the samples were imaged immediately using an inverted fluorescence microscope (Leica, Germany). Cell viability was quantified using ImageJ software.

2.8. Cell proliferation assay

Cell proliferation assay was performed as previously reported.[13] Briefly, CCK-8 was used per the manufacturer's instructions to evaluate cell proliferation in the functional modules on days 1, 4, and 7 after culture. PCI3D modules were washed with PBS, cut into four pieces, and placed in a 96-well plate. A total of 10 μL CCK-8 solution in 100 μL PBS was added to each well, and the plate was then incubated for 2 h. Subsequently, the supernatant was pipetted into a new 96-well plate to measure the absorbance at 450 nm using a microplate reader.[20]

2.9. Osteogenic differentiation

After MLO-Y4 cells were treated with DMSO/ethanol or Tap/C10 at indicated concentrations for one day, the cells were co-cultured with ST2 cells at a ratio of 1:4 for three days. Osteogenesis was measured by AP staining, AP biochemical activity assay, qPCR for the expression of osteoblast marker genes, and mineralization assay.

2.9.1. Alkaline phosphatase staining

The culture medium was aspirated from each well. The cells were washed with PBS and fixed in 3.7% PBS-buffered formaldehyde for 5 min. AP staining was conducted according to a previously reported method.[14] Subsequently, the cells were washed three times with PBS and stained using the BCIP/NBT AP staining kit for 30 min.

For PCI3D modules, AP staining was performed on cells that were cultured in the PCI3D modules for 7 and 14 days. The staining process lasted for 4 h due to the slow differentiation of cells in the 3D scaffolds. The results were recorded using a digital camera.

2.9.2 Alkaline phosphatase biochemical activity assay

The biochemical activity of AP was determined in accordance with a previously reported method.[14] After adding 0.3 mL of 50 mM Tris/HCl (pH 7.4) to each well, the cells were scraped off, transferred from the plate to Eppendorf tubes, and sonicated for 30 s three times. This step was performed on ice. After centrifugation at 12,000 rpm/min for 3 min, the supernatant was immediately tested according to the instructions of the AP detection kit.

2.9.3. Matrix mineralization assay

After MLO-Y4 cells were stimulated with drugs for 24 h, they were cultured with ST2 cells at a ratio of 1:4 in an osteogenic medium containing 10 mM β-glycerophosphate and 50 μg/mL L-ascorbic acid, for 14 days to form mineralized nodules. The 3D module was first cultured in a complete medium for seven days and then cultured in the above osteogenic induction medium for 21 days. The cells were stained with 1% Alizarin Red S dye at 37°C for 30 min and photographed under a microscope. The samples were then washed with deionized water at room temperature and decolorized with 10% cetylpyridinium chloride for 1 h. Finally, the absorbance of the decolorized solution was measured at 562 nm to evaluate the mineralization status.

2.10. Angiogenesis assays

2.10.1. In vitro HUVEC tube formation assay

Tube formation was assessed as previously reported.[12] After receiving drug stimulation, MLO-Y4 cells were mixed with HUVECs at a ratio of 1:5 and seeded onto a 24-well plate pre-coated with 500 μL Matrigel. The cells were cultured in a 37°C, 5% CO_2 incubator for 4 h, photographed under a microscope, and quantitatively analyzed using ImageJ to evaluate the vascular network structure formed by HUVECs.

2.10.2. In vitro HUVEC cell migration assay

Transwell migration assay was performed as previously reported.[21] The polycarbonate membrane of the transwell chamber contains 8.0 μm small holes for the migration of cells. HUVECs were starved for 4 h and added with 700 μL DMEM containing 10% FBS and 300 μL conditioned medium. Approximately 5,000 HUVECs were added to the chamber and cultured at 37°C and 5% CO_2 for 24 h to facilitate cell migration onto the membrane. The migrated cells were stained with crystal violet for 5 min. Microscopic images were taken and quantitatively analyzed using ImageJ.

2.11. Adipogenesis assay

2.11.1. Adipogenic differentiation

Adipogenic differentiation assay was performed as previously reported.[22] Briefly, MLO-Y4 cells were stimulated with 500 nM C10 for 24 h, and the control group was treated with an equal volume of ethanol. The cells were then co-cultured with ST2 cells at a ratio of 1:4 in adipogenic medium (0.5 μM dexamethasone, 0.5 mM IBMX, 60 μM indomethacin, medium DMEM) for seven days. The lipid droplets formed in the ST2 cells were imaged under light microscopy and stained with Oil Red O.

2.11.2. Oil Red O staining

Oil Red O staining was performed as previously reported.[23] After adipogenic differentiation, the cells were washed twice with PBS and fixed with 4% formaldehyde for 5 min. The cells were washed three times with PBS and stained with a modified Oil Red O staining solution per the staining kit instructions. The stained cells were photographed under a microscope.

2.12. Statistical analysis

Statistical data analysis was performed using Graph Pad Prism 8.0.1 software, and all results were based on three independent replicates. Data is expressed as mean ± standard deviation (SD). One-way analysis of variance (ANOVA) was used to analyze differences between multiple groups, and two-way ANOVA was used to analyze differences between groups divided by two independent variables. The comparison between the two groups was performed using Student's *t*-tests, with p-values < 0.05 being considered statistically significant.

3. Results

3.1. PGE_2-treated osteocytes promote osteoblast differentiation of murine bone marrow stromal cells

We tested whether PGE_2-treated osteocytic cell line MLO-Y4 induces osteoblast differentiation. PGE_2 treatment of MLO-Y4 cells for 24 h increased the expression of PGE_2 receptors EP2 and EP4 in a dose-dependent manner Figure 1A, indicating a sufficient activation of PGE_2 signaling in osteocytes; however, other receptors EP1 and EP3 were not upregulated (data not included). CCK-8 assay results indicate that the tested concentrations of PGE_2 had little effect on the proliferation activity of MLO-Y4 cells within 24 h (Figure 1B). PGE_2-treated MLO-Y4 cells co-cultured with ST2 cells for three days displayed the highest increase in osteoblast differentiation at 2.5 μM PGE_2, observed from AP staining, the biochemical activity assay, and the expression of osteoblast marker genes (Figure 1C–E). Moreover, PGE_2-treated MLO-Y4 cells also promoted mineralization with increased mineralized bone nodules in the PGE_2-treated group (Figure 1F). PGE_2 treatment of MLO-Y4 cells did not increase the expression of osteoblast marker genes (Figure S1, Supplementary File), suggesting that activating PGE_2 signaling in osteocytes promotes osteoblast differentiation of ST2 cells.

3.2. Osteocytic PGE_2 receptor signaling promotes osteoblast differentiation

Subsequently, we examined whether PGE_2 receptor agonist-treated osteocytes may induce osteoblast differentiation by screening the concentrations of two agonists (Figure 2A). The EP2 agonist Tap at 1, 5, and 20 μM and the EP4 agonist C10 at 500 nM did not affect

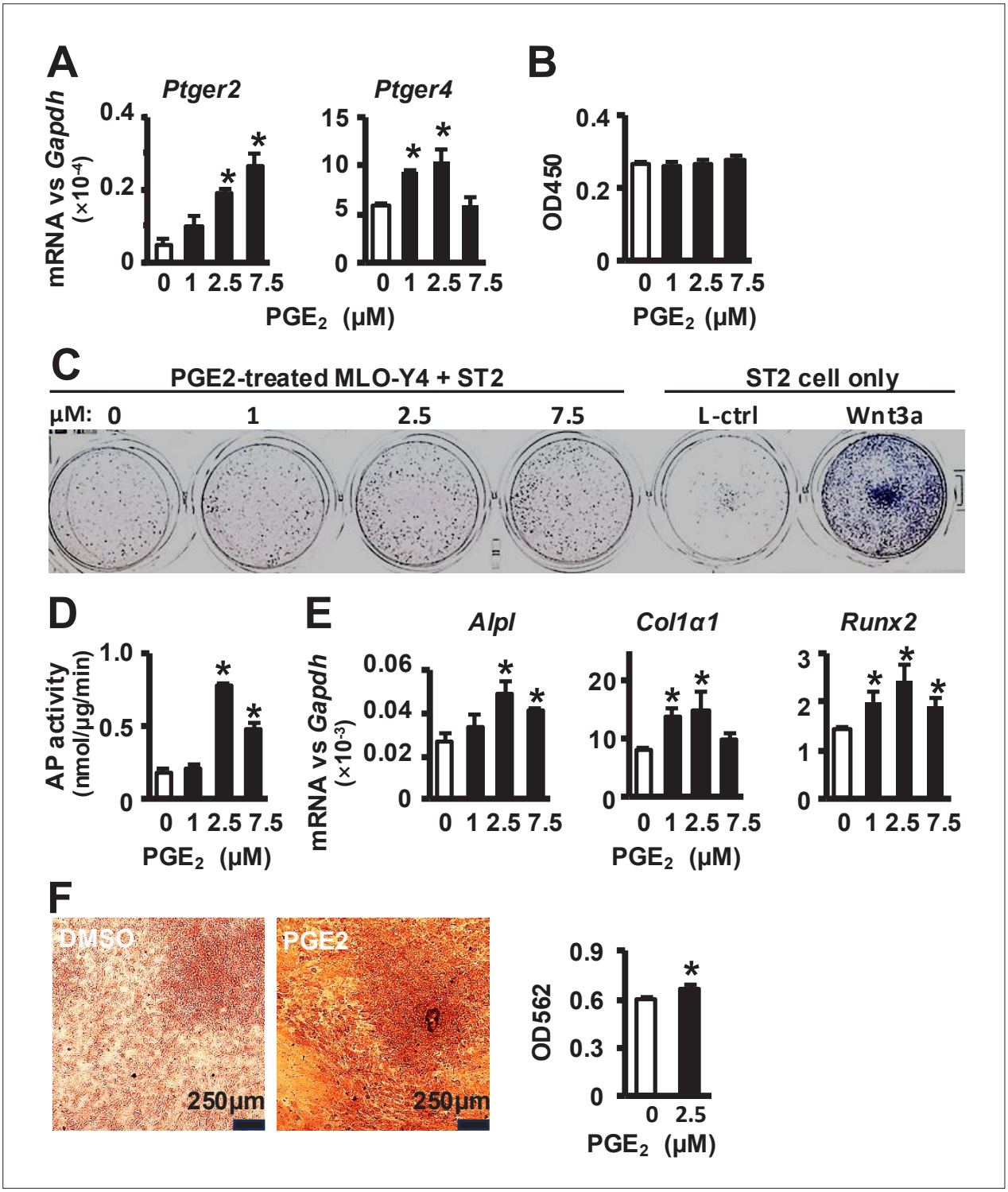

Figure 1. The effect of osteocytes treated with PGE_2 on osteogenesis in ST2 cells. (A) The expression of PGE_2 receptors EP2/EP4 (*Ptger2/Ptger4*) in MLO-Y4 cells treated PGE_2 for 24 h. (B) CCK8 assay for the proliferative activity of MLO-Y4 cells treated with PGE_2 for 24 h. (C–E) Osteoblast differentiation assay of the co-culture of MLO-Y4 and ST2. AP staining (C) and its biochemical activity assay (D), and qPCR for the expression of osteoblast marker genes (E) in the co-culture of PGE_2-treated MLO-Y4 cells and ST2 cells for three days. (F) Mineralization assay of bone nozzle formation by Alizarin Red S staining in the co-culture of PGE_2-treated MLO-Y4 cells and ST2 cells in osteogenic medium for 14 days. * $p < 0.05$ vs. DMSO by one-way ANOVA, $n = 3$ (A–D); * $p < 0.05$ vs. DMSO by Student's *t*-test, $n = 3$ (F). Scale bars: 250 μm. Abbreviations: ANOVA: Analysis of variance; AP: Alkaline phosphatase; DMSO: Dimethyl sulfoxide; CCK8: Cell counting kit 8; OD: Optical density; qPCR: Real-time polymerase chain reaction.

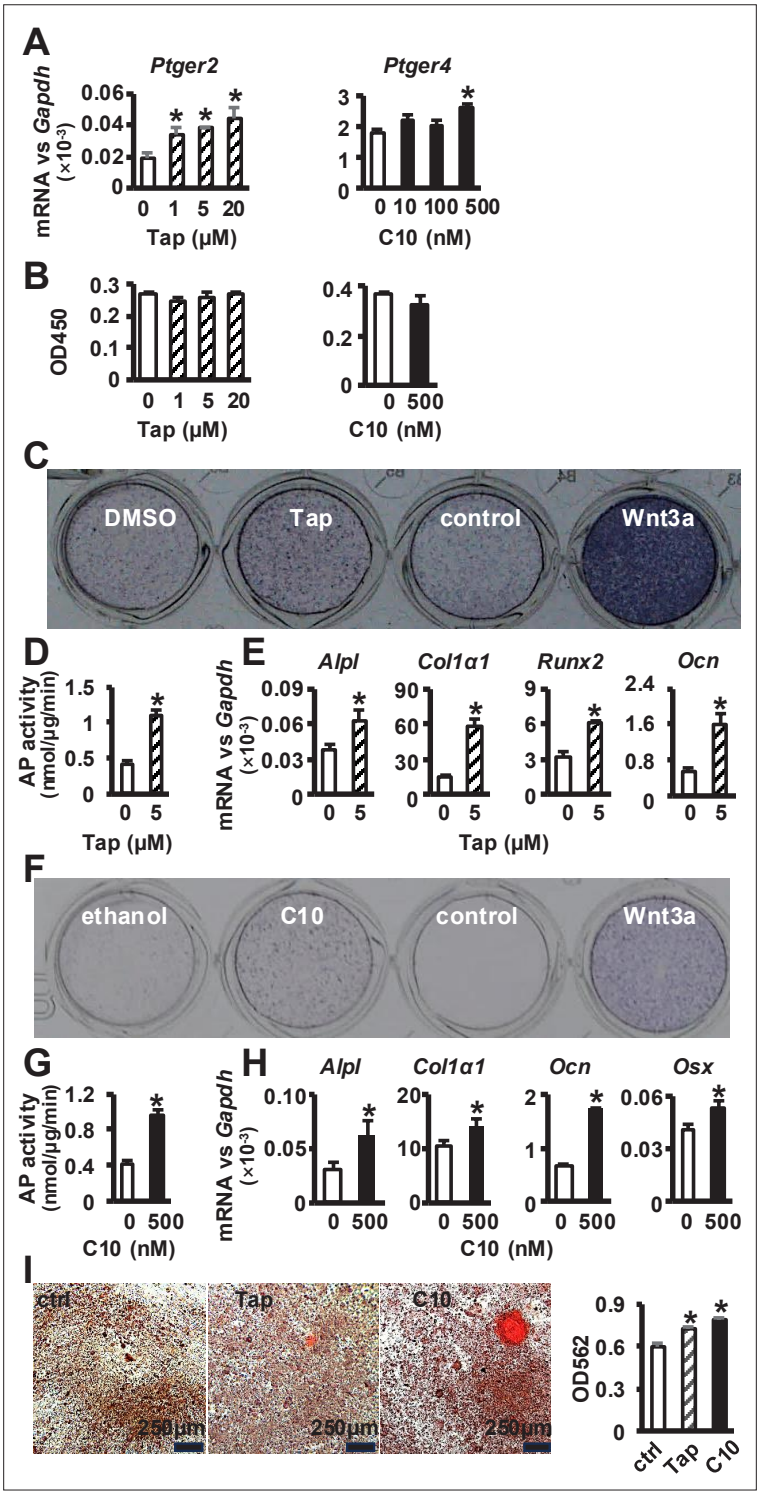

Figure 2. The effect of osteocytes treated with PGE_2 receptor agonist on osteogenesis in ST2 cells. (A) PGE_2 receptor agonist promotes the expression of PGE_2 receptor (*Ptger2/Ptger4*). (B) CCK8 assay for the proliferative activity of MLO-Y4 cells treated with EP2/4 agonists Tap or C10 for 24 h. (C–H) AP staining (C and F), its biochemical activity (D and G) assay, and qPCR to test the expression of osteoblast marker genes (E and H) in the co-culture of Tap/C10-treated MLO-Y4 cells and ST2 cells for three days. (I) Mineralization assay of bone nozzle formation by Alizarin Red S staining in the co-culture of Tap/C10-treated MLO-Y4 cells and ST2 cells in osteogenic medium for 14 days. *$p < 0.05$ vs. DMSO by one-way ANOVA, $n = 3$ (A, B, and I); *$p < 0.05$ vs. DMSO by Student's *t*-test, $n = 3$ (D, E, and H). Scale bars: 250 μm. Abbreviations: OD: Optical density; DMSO: Dimethyl sulfoxide; Ctrl: Control; AP: Alkaline phosphatase; CCK8: Cell counting kit 8; ANOVA: Analysis of variance.

the proliferation of MLO-Y4 cells after a 24 h treatment (Figure 2B). Similarly, these treated osteocytes were co-cultured with ST2 cells for three days. We observed that 5 μM Tap- and 500 nM C10-treated MLO-Y4 cells effectively induced osteoblast differentiation of ST2 cells from the AP staining (Figure 2C and F), biochemical activity assay (Figure 2D and G), and osteoblast marker gene expression assay (Figure 2E and H). Taken together, both agonist-treated osteocytes promoted osteoblast differentiation of ST2 cells; moreover, both PGE_2 receptor agonist-treated osteocytes increased the mineralization of ST2 cells (Figure 2I). Therefore, osteocytic PGE_2 receptor signaling promotes osteoblast differentiation of ST2 cells, consistent with the function of PGE_2-treated osteocytes.

3.3. Osteocytic EP4 inhibits the adipogenesis of ST2 Cells

The effect of C10-treated MLO-Y4 cells on adipogenesis was examined in ST2 cells. MLO-Y4 cells were treated with 500 nM C10 and its control with ethanol for 24 h, respectively, followed by co-culturing with ST2 cells in the adipogenesis medium. After seven days of adipogenic induction, the C10-treated osteocyte group displayed a reduction in lipid droplet formation, as visualized under light microscopy (Figure 3A) and after Oil Red O staining (Figure 3B). In addition, adipogenic gene expression was measured, and the results revealed that osteocytic EP4 inhibition markedly reduced the expression of *Pparg* and *Cebpa* (Figure 3C), indicating that osteocytic EP4 inhibits adipogenesis of ST-2 cells.

3.4. Osteocytic PGE_2 receptor signaling promotes the formation of vascular tubules in HUVECs

Angiogenesis is essential for transporting oxygen, nutrients, metabolites, etc. during bone regeneration. Next, we investigated whether osteocytic PGE_2 receptor signaling promotes angiogenesis in a HUVEC model for the formation of tubules. MLO-Y4 cells were co-cultured with HUVECs at a ratio of 1:5 for three days, and total RNA was extracted to detect pro-angiogenic factors. The expressions of *Vegf*, *Angpt-1*, *Hif-1*, and the vascular endothelial marker *VE-cad* were significantly upregulated in the C10 group compared to the ethanol-treated control group (Figure 4A). In the co-culture system, the formation of vascular tubules in the C10 group was significantly higher than in the ethanol-treated group (Figure 4B). Specifically, the number, total length, and branching nodes of the formed tubules increased by 2.8, 1.7, and 1.9 times, respectively, relative to the control group (Figure 4C). In addition, we measured the migration of HUVECs induced by the conditioned medium and observed that the conditioned medium of C10-treated MLO-Y4 promoted the migration of HUVECs with a 1.3-fold increase in migrated cell number and elevated *Vegf* expression compared to the ethanol-treated osteocyte group (Figure 4D and E). Likewise, we also observed similar results with Tap-treated MLO-Y4 cells (Figure S2, Supplementary File). Therefore, osteocytic PGE_2 receptor signaling promotes angiogenesis.

3.5. COX-2 inhibition of osteocytic EP4 markedly reduces osteoblast differentiation of ST2 cells

After 24 h treatment, the EP4 agonist C10 significantly increased the expression of COX-2 (*Ptgs2*) in MLO-Y4 cells (Figure 5A). Osteocytic EP4 signaling increased the osteoblast differentiation of ST2 cells, which was partially reversed by COX-2 inhibitor celecoxib as observed from the AP staining, biochemical activity assay, and expression of osteoblast marker genes (Figure 5B–D). Thus, activation of the PGE2 receptor signaling in osteocytes induces autocrine effects by promoting the expression of COX-2 (*Ptgs2*), further amplifying PGE_2 signaling.[24] PGE_2 produced by the treated MLO-Y4 cells appears to be responsible for osteogenesis, along with other unidentified factors.

3.6. Construction of POME PCI3D modules

We used the in-house-developed PCI3D[12] to bioprint C10-treated MLO-Y4 cells as a POME. Cells were embedded in a 10% GelMA hydrogel, which exhibits rheological behavior that varies between low and high temperatures.

MLO-Y4 cells treated with C10 for 24 h (POME) were mixed with ST2 cells in a ratio of 1:4 and then mixed with GelMA hydrogel. Next, the cell-laden hydrogel micelle was 3D-bioprinted onto the PCL beams, forming a layer of the PCI3D module. Subsequently, another layer was bioprinted perpendicular to the printing direction of the preceding printed layer. After continuously printing four layers, the printed construct becomes a POME PCI3D module (Figure 6A). The module is composed of repeatedly printed PCL bundles, cell-laden hydrogel micelles, and tunnels between adjacent cell-laden hydrogel micelles, with diameters of 400, 300, and 500 μm, respectively.

3.7. POME increases cell viability in PCI3D modules

Live/dead cell assay of the modules was performed on days 1, 4, and 7 of PCI3D module cultivation. The results indicate that both C10- and ethanol-treated groups exhibited similar survival rates of over 95% (Figure 6B and C). Next, we measured cell proliferation in the POME PCI3D modules, and the CCK-8 assay results indicate linear cell growth from days 1 to 7 of module cultivation. The C10-treated MLO-Y4 group exhibited a higher proliferative activity than the ethanol-treated osteocyte group on days 4 and 7 (Figure 6D). The above results indicate that cells grow well in the PCI3D modules, and the

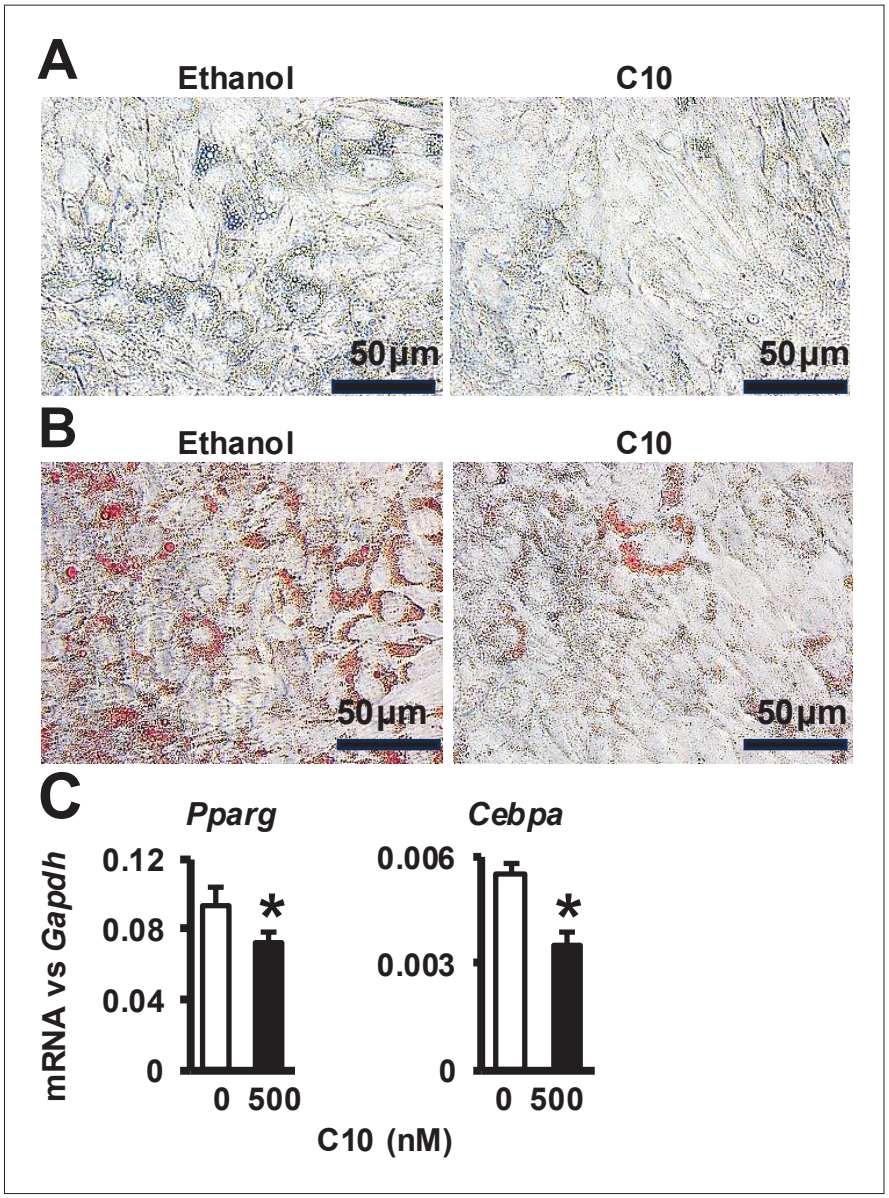

Figure 3. The effect of EP4 agonist-treated osteocytes on adipogenesis. (A–B) Inhibition of adipogenesis in the co-culture of EP4 agonist-treated osteocytes and ST2 cells in adipogenic medium for seven days without (A) or with (B) Oil Red O staining. (C) Expression of adipogenic transcription factors *Pparg* and *Cebpa* in the co-cultured cells. Scale bars: 50 µm. *$p < 0.05$ by Student's *t*-test, $n = 3$.

POME PCI3D modules can provide favorable conditions for ST2 survival, proliferation, and differentiation with C10-treated osteocytes.

3.8. POME promotes osteoblast differentiation in the POME PCI3D modules

The POME (C10-treated MLO-Y4) PCI3D modules were cultured in the growth medium for 7 and 14 days, respectively, and osteoblast differentiation in the modules was measured. The results from AP staining and the biochemical activity assay displayed an increase in osteoblast differentiation in the POME PCI3D modules compared to ethanol-treated MLO-Y4 PCI3D modules on days 7 and 14 of cultivation (Figure 7A and B). The AP activity of the POME PCI3D modules increased by 1.9 and 3.1 times that of ethanol-treated MLO-Y4 PCI3D modules on days 7 and 14, respectively. The expression of osteoblast markers, including *Alpl*, *Col1α1*, and *Runx2*, were significantly upregulated in the POME modules compared to the control (Figure 7C). Mineralization assay was performed with the modules cultivated in the growth medium for seven days, then in the osteogenic medium for 21 days, and finally stained with Alizarin

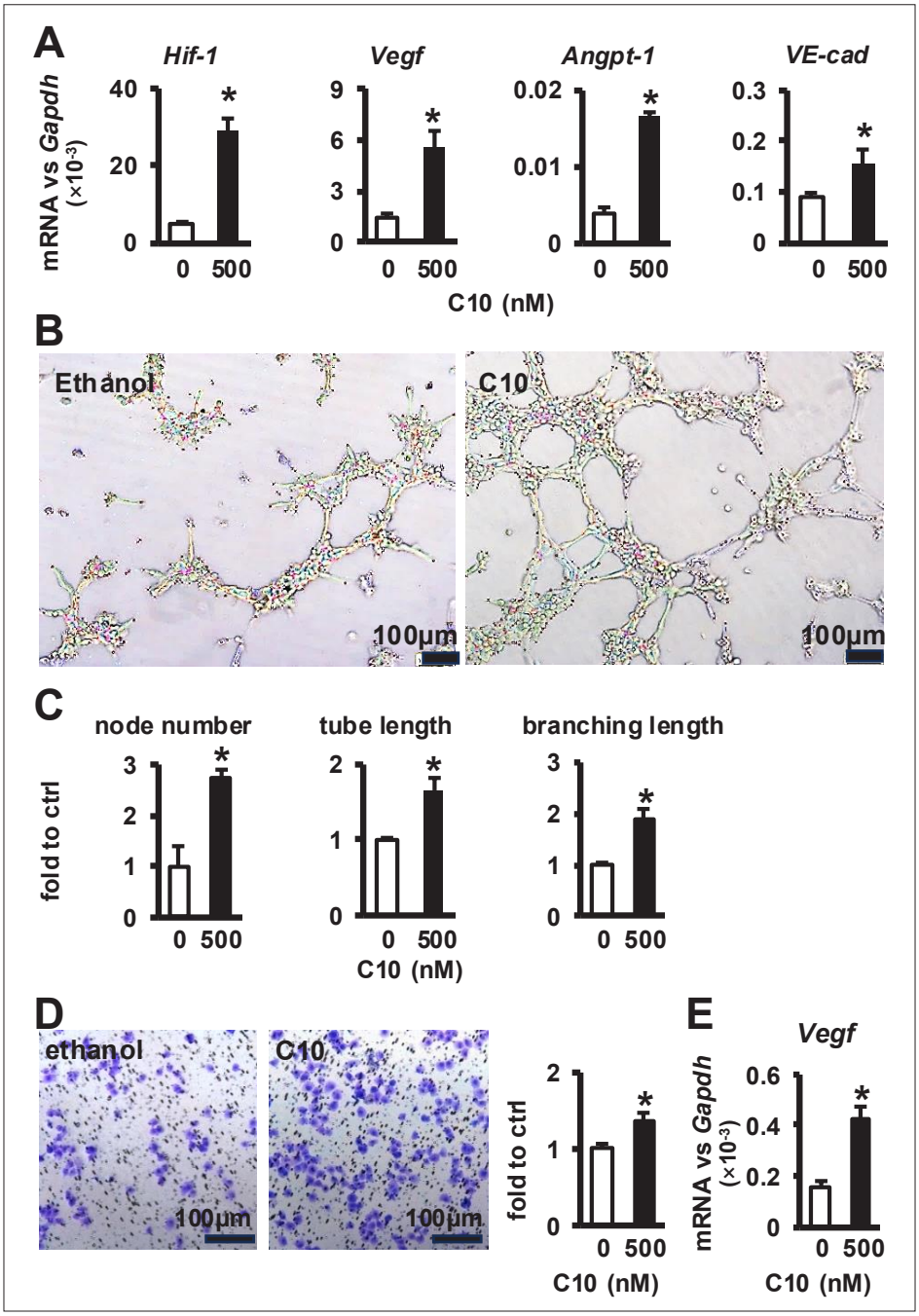

Figure 4. The effect of EP4 agonist-treated osteocytes on angiogenesis in HUVECs. (A) Angiogenic-related gene expression in the co-culture of C10-treated MLO-Y4 cells and HUVECs for three days. (B–C) Images (B) and calculation (C) of vascular tubule formation in the above co-culture for 4 h. (D) Migration of HUVECs cultured in 30% CM for one day. (E) Detection of *Vegf* expression in HUVECs cultured in 30% CM for one day. *$p < 0.05$ by Student's *t*-test, $n = 3$. Scale bars: 100 μm. Abbreviations: CM: Conditioned medium of C10-treated MLO-Y4 cells; HUVECs: Human umbilical vein endothelial cells; ctrl: Control.

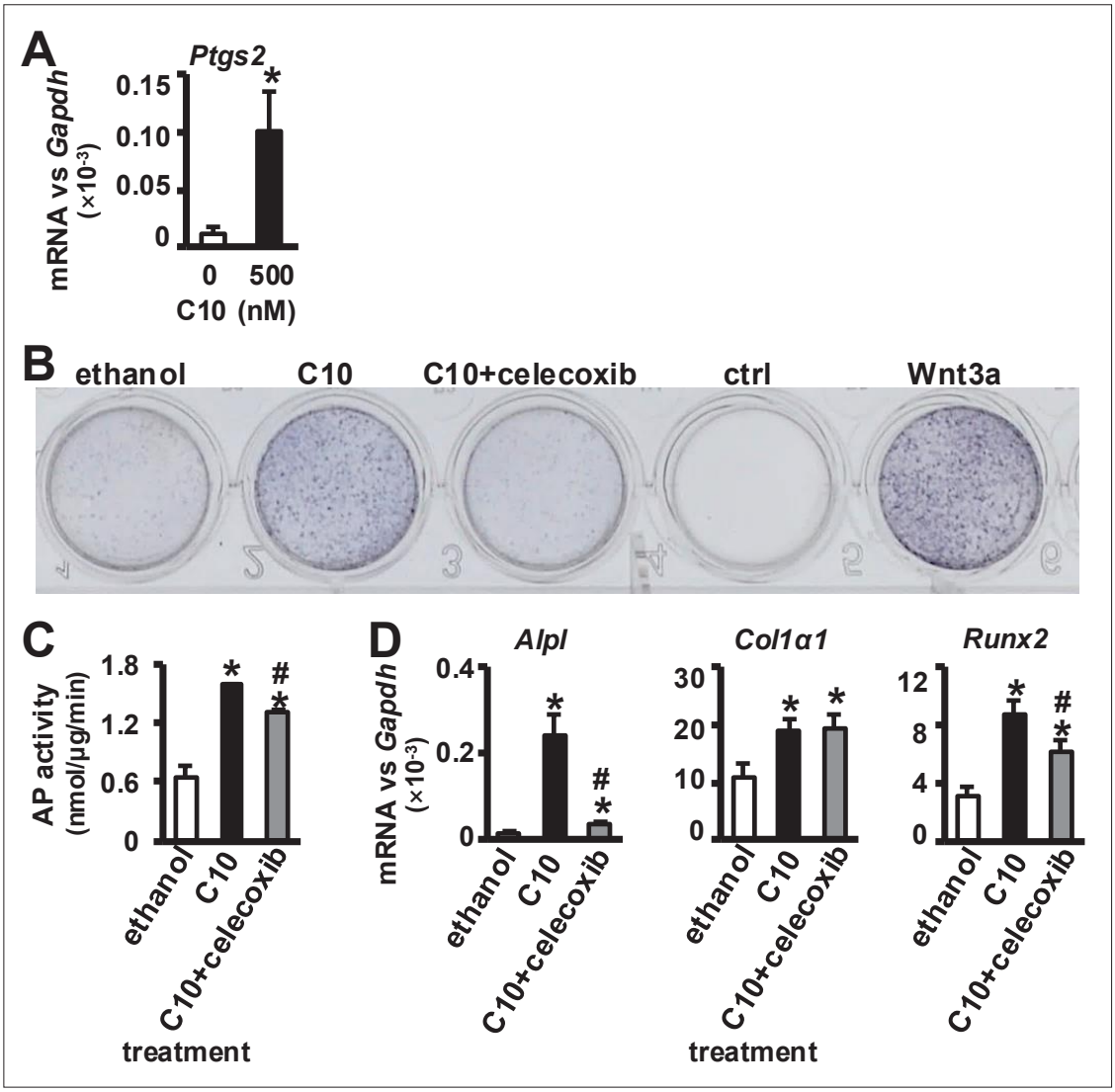

Figure 5. EP4 agonist-COX-2 (*Ptgs2*) axis in MLO-Y4 cells is responsible for its osteogenic function. (A) Upregulated expression of COX-2 (*Ptgs2*) in MLO-Y4 cells treated with C10 for 24 h. (B–D) The effect of COX-2 inhibitor on the osteogenic differentiation induced by C10-treated osteocytes: AP staining (B), its biochemical activity assay (C), and qPCR to test the expression of osteoblast marker genes (D). *$p < 0.05$ by one-way ANOVA, $n = 3$. Abbreviations: ANOVA: Analysis of variance; ctrl: Control; AP: Alkaline phosphatase.

Red S staining solution. The results demonstrated that more bone nozzles were formed in the POME PCI3D group than in the control group (Figure 7D), and the mineralization level was increased by 1.9 times relative to the control group. Likewise, we also observed similar results for the Tap-treated MLO-Y4 group (Figure S3, Supplementary File). Therefore, POMEs with EP2 and EP4 agonists promote osteogenesis in 3D-bioprinted modules, which could be developed as functional biomaterials for bone formation.

In addition, POME enhanced the expression of angiogenic factors *Hif1a* and *Angpt-1* (Figure 7E), suggesting a potential role for POME in angiogenesis.

4. Discussion

Researchers have been developing biomimetic bones, but artificially reconstructing authentic bones with both mechanical support and biological functionality remains a major challenge in orthopedic regenerative medicine. A tissue and organ 3D bioprinter reported in 2016 has produced constructs that support hard materials and stem cells, achieving cell survival, osteogenic differentiation, and vascularization,[25] opening a novel avenue in the field.[26,27] Later, it was discovered that POME in biomaterials is crucial for regulating osteoblast differentiation and enabling the production of authentic bone.[4] This study investigated the physiological function of PGE_2 produced

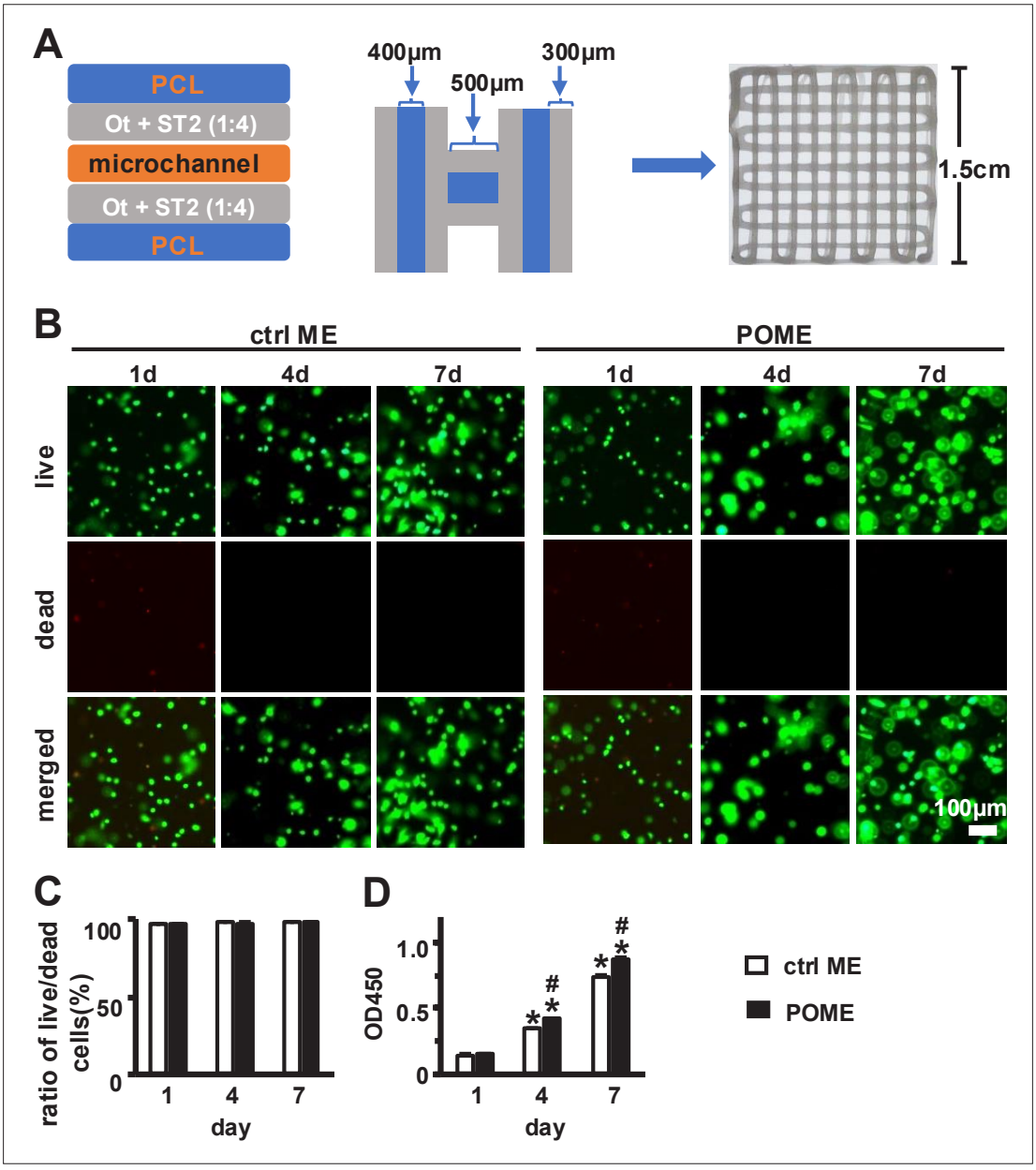

Figure 6. Reconstruction of polycaprolactone (PCL)- and cell-integrated 3D bioprinting system (PCI3D) modules with EP4 agonist-treated osteocytes to build a physiological osteogenic microenvironment (POME). (A) Schematic design (left) and image (right) of POME PCI3D module with hard biomaterial PCL bundles, cell-laden hydrogel bundles, and microchannels among these bundles. (B–D) Cell viability assay. Live/dead cell assay for the detection of cell survival rate (B and C) and cell proliferation by CCK8 (D) in the PCI3D modules cultured for the indicated day. *$p < 0.05$ vs. the value at day 1; #$p < 0.05$ vs ctrl-ME by two-way analysis of variance (ANOVA), $n = 3$. Scale bar: 100 μm. Abbreviations: POME: Physiological osteogenic microenvironment of the MLO-Y4 cells treated by EP4 agonist C10 for 1d; Ot: Osteocytic MLO-Y4 cells; ctrl-ME: Control microenvironment of the MLO-Y4 cells treated by ethanol for one day.

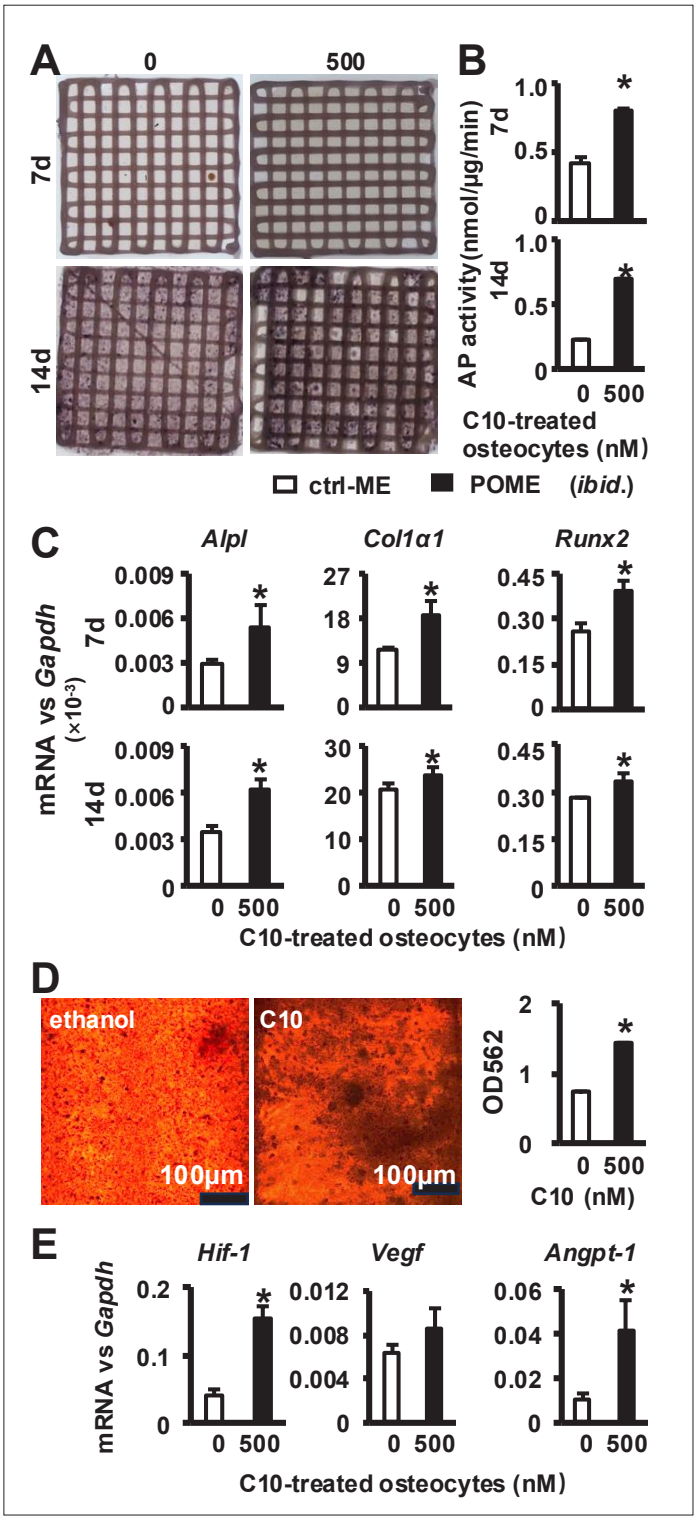

Figure 7. Effects of the POME of PCI3D modules on osteogenesis. (A–C) POME promotes osteoblast differentiation of ST2 cells in POME PCI3D modules. PCI3D modules were cultured for indicated days. AP staining (A), its biochemical activity assay (B), and qPCR for the detection of osteoblast marker gene expression (C). (D) Mineralization assay of bone nozzle formation by Alizarin Red S staining in the PCI3D modules cultured in growth medium for seven days and then in osteogenic medium for 21 days. (E) Angiogenesis-related gene expression after 14 days of culture in PCI3D modules. *$p < 0.05$ by Student's *t*-test, $n = 3$. Abbreviations: ctrl-ME: Control microenvironment of MLO-Y4 cells treated by ethanol for one day; POME: Physiological osteogenic microenvironment of the MLO-Y4 cells treated by EP4 agonist C10 for one day; AP: Alkaline phosphatase; qPCR: Quantitative polymerase chain reaction.

by mechanoreceptors, i.e., osteocytes. Our findings revealed that osteocytic PGE_2 and its receptor EP2/4 signaling axis promote osteogenic differentiation and angiogenesis of bone marrow stromal cells ST2 while inhibiting adipogenic differentiation. This function has been validated in a 3D-bioprinted module mimicking an *in vivo* environment.[28,29] Mechanistically, activation of the PGE_2 signaling pathway in osteocytes induces autocrine effects by promoting the expression of the EP2 and EP4 receptors and COX-2 (*Ptgs2*), further amplifying PGE_2 signaling. Thus, the POME PCI3D module is a safe and novel functional biomaterial reconstructed by 3D bioprinting, with significant potential applications.

One of our innovative discoveries is that osteocytic PGE_2 and the EP2/4 signaling axis form a POME. Although PGE_2 directly promotes osteoblast differentiation,[30] its effect on bone formation when acting on osteocytes has not been explored. Previously reported osteogenic differentiation induced by PGE_2 is attributed to its direct effects on bone marrow stromal cells,[31] calvarial primary osteoblasts,[31] mouse osteoblast cell line MC3T3-E1,[32] and ST2,[33] among others. In addition, studies have reported that the human prostate tumor cell line PC3 promotes osteoblast proliferation,[34] which plays an essential role in bone formation.[35] Collectively, these findings indicate a direct effect of PGE_2 on bone formation. PGE_2 produced by mechanical stimulation in osteocytes enhances the gap junction among osteocytes. After stress stimulation, PGE_2 appears in the MLO-Y4 culture medium in a time-dependent manner, activating the PKA signaling pathway. This induces the expression of COX-2, EP2, and CX43,[24] thereby enhancing the gap junction among osteocytes. However, its osteogenic effect has not yet been reported.

The osteocytic PGE_2 and its receptor signaling axis reportedly promote angiogenesis. In previous studies, EP4 specifically promoted the formation of vascular tubules in HUVECs and mice.[8] In our study, we observed that EP4 can promote the formation of vascular tubules in the HUVEC model, with assistance from EP2, suggesting that the POME PCI3D module promotes angiogenesis *in vivo*.

In addition, the POME PCI3D module reportedly inhibits adipogenesis. The role of the prostaglandin family in adipogenesis is unclear. PGE_2-EP4 can specifically and directly inhibit the expression of adipogenic transcription factor PPARγ to inhibit adipogenesis.[36] Mechanical loading promotes osteogenesis, whereas unloading increases sclerostin production, which inhibits Wnt signaling and osteogenesis while promoting fat formation.[37] Mechanical loading induces osteocytes to secrete PGE_2, which is a positive stress response factor.[38] Surprisingly, osteocytic PGE_2 receptor signaling not only promotes osteogenic differentiation but also inhibits adipogenic differentiation of bone marrow stromal cells, suggesting a possible mechanism of fat reduction with exercise.

Osteocytes are an ideal drug target due to their abundance in the skeleton, especially the lacuno-canalicular network. In mice, age-related bone loss is associated with a reduction in lacuno-canalicular network and osteocyte density.[39] Since PGE_2 enhances gap junctions among osteocytes, activating the osteocytic PGE_2 receptor signaling may be an effective strategy to prevent age-related bone loss. In our published work, we found that osteocytes treated with Wnt activator S24 expressed higher levels of EP4, which potentially promotes osteogenic differentiation and mineralization of bone marrow stromal cells. These osteocytes were successfully used to construct an osteogenic microenvironment[15] for authentic bone formation.[40] The above data suggest the possibility of activating the PGE_2 signaling pathway in osteocytes to construct a POME.

Under physiological conditions (e.g., mechanical stimulation, exercise), PGE_2 is secreted by osteocytes. Thus, activating PGE_2 receptor signaling in osteocytes is a safe and physiological approach, promoting bone formation in a relatively mild and stable manner. In contrast, sustained drug release may cause pathological changes or damage to surrounding tissues. The bioactive module constructed in this study, however, does not contain drugs. The constructed POME is safe and closely mimics the natural POME.[41] 3D-bioprinted models can closely simulate the *in vivo* microenvironment.[42] A review revealed that the 3D-bioprinted tumor organoid models can be used for personalized drug screening and precise treatments, achieving sensitivity, specificity, and accuracy of 63.3, 94.1, and 79.7% respectively for chemotherapy regimens.[43] This implies that the 3D module can simulate POME *in vivo* with characteristics closely mimicking the pathological microenvironment. Moreover, this suggests that the further development of 3D bioprinting will offer extensive possibilities for basic research and clinical applications, such as bioactive implants. Nonetheless, the functional module constructed by 3D printing in this study demonstrates that the osteocytic PGE_2-receptor signaling is a safe and effective POME with potential applications in treating bone-related diseases.

5. Conclusion

Mechanical stimulation induces the production of non-protein PGE_2 in osteocytes, which upregulates the expression of PGE_2 receptors. We found that osteocytic PGE_2 receptor signaling in osteocytes promotes osteoblast differentiation and angiogenesis, while also inhibiting

adipogenesis. As previously discovered, osteocytes promote osteoclast differentiation. Therefore, osteocytic PGE_2 receptor signaling constitutes POME with a cellular basis, potentially enabling the formation of metabolically active real bones, including bone formation and resorption. Based on this, we used a small molecule drug to transiently stimulate osteocytes for 24 h and prepared a safe (drug-free) and mild POME. We constructed the POME in hard biomaterials using 3D bioprinting, creating a skeletal development module where cells can survive, grow, and develop for up to 28 days, thus simulating the physiological conditions of bone formation.

Acknowledgments

The authors appreciate Bo Wang and Weimin Gong for their technical assistance.

Funding

This research was funded by the National Natural Science Foundation of China 82072450 (XL.T.), Chongqing Natural Science Foundation-Innovation and Development Joint Fund CSTB2022NSCQ-LZX0048 (XL.T.), and Young Scientists Fund of the National Natural Science Foundation of China 82202655 (C.Z.).

Conflict of interest

The authors declare that they have no competing interests.

Author contributions

Conceptualization: Jingjing Chen, Yangxi Liu, Pengtao Wang, Xiaolin Tu, Linda F. Bonewald

Formal analysis: Jingjing Chen, Qiuling Guo

Investigation: Jingjing Chen, Qiuling Guo, Jinling Zhang, Ying Zhang

Methodology: Jingjing Chen, Qiuling Guo, Yangxi Liu, Pengtao Wang

Writing – original draft: Jingjing Chen, Xiaolin Tu

Writing – review & editing: Chengzhu Zhao, Xiaolin Tu, Linda F. Bonewald

Ethics approval and consent to participate

Not applicable.

Consent for publication

Not applicable.

Availability of data

Data presented in this study are available on request from the corresponding authors.

Further disclosure

This study was orally presented by Jingjing Chen at the 15th Annual Congress of the Chinese Orthopedic Association on November 24, 2023.

References

1. Shapira A, Dvir T. 3D Tissue and organ printing-hope and reality. *Adv Sci (Weinh).* 2021;8(10):2003751. doi: 10.1002/advs.202003751

2. Ashammakhi N, Hasan A, Kaarela O, et al. Advancing frontiers in bone bioprinting. *Adv Healthc Mater.* 2019;8(7):e1801048. doi: 10.1002/adhm.201801048

3. Dey M, Ozbolat IT. 3D bioprinting of cells, tissues and organs. *Sci Rep.* 2020;10(1):14023. doi: 10.1038/s41598-020-70086-y

4. West-Livingston LN, Park J, Lee SJ, Atala A, Yoo JJ. The role of the microenvironment in controlling the fate of bioprinted stem cells. *Chem Rev.* 2020;120(19):11056-11092. doi: 10.1021/acs.chemrev.0c00126

5. Erlandson MC, Kontulainen SA, Chilibeck PD, Arnold CM, Faulkner RA, Baxter-Jones AD. Higher premenarcheal bone mass in elite gymnasts is maintained into young adulthood after long-term retirement from sport: a 14-year follow-up. *J Bone Miner Res.* 2012;27(1):104-110. doi: 10.1002/jbmr.514

6. Bonewald LF. The amazing osteocyte. *J Bone Miner Res.* 2011;26(2):229-238. doi: 10.1002/jbmr.320

7. Zhao D, Riquelme MA, Guda T, et al. Connexin hemichannels with prostaglandin release in anabolic function of bone to mechanical loading. *Elife.* 2022;11:e74365. doi: 10.7554/eLife.74365

8. Zhang Y, Daaka Y. PGE2 promotes angiogenesis through EP4 and PKA Cγ pathway. *Blood.* 2011;118(19):5355-5364. doi: 10.1182/blood-2011-04-350587

9. Graham S, Gamie Z, Polyzois I, et al. Prostaglandin EP2 and EP4 receptor agonists in bone formation and bone healing: *In vivo* and *in vitro* evidence. *Expert Opin Investig Drugs.* 2009;18(6):746-766. doi: 10.1517/13543780902893051

10. Cheng H, Huang H, Guo Z, Chang Y, Li Z. Role of prostaglandin E2 in tissue repair and regeneration. *Theranostics.* 2021;11(18):8836-8854. doi: 10.7150/thno.63396

11. Sakuma Y, Li Z, Pilbeam CC, et al. Stimulation of cAMP production and cyclooxygenase-2 by prostaglandin E(2) and selective prostaglandin receptor agonists in murine osteoblastic cells. *Bone.* 2004;34(5):827-834. doi: 10.1016/j.bone.2003.12.007

12. Wang P, Wang X, Wang B, et al. 3D printing of osteocytic Dll4 integrated with PCL for cell fate determination towards osteoblasts *in vitro*. *Bio-des. Manuf.* 2022;5(3):497-511. https://www.doi.org/10.1007/s42242-022-00196-1

13. Wang B, Khan S, Wang P, et al. A highly selective GSK-3β inhibitor CHIR99021 promotes osteogenesis by activating canonical and autophagy-mediated Wnt signaling. *Front Endocrinol (Lausanne).* 2022;13:926622. doi: 10.3389/fendo.2022.926622

14. Tu X, Joeng KS, Nakayama KI, et al. Noncanonical Wnt signaling through G protein-linked PKCdelta activation promotes bone formation. *Dev Cell.* 2007;12(1):113-127. doi: 10.1016/j.devcel.2006.11.003

15. Liu Y, Ruan X, Li J, et al. The osteocyte stimulated by Wnt agonist SKL2001 is a safe osteogenic niche improving bioactivities in a polycaprolactone and cell integrated 3D module. *Cells.* 2022;11(5):831. doi: 10.3390/cells11050831

16. Tu X, Delgado-Calle J, Condon KW, et al. Osteocytes mediate the anabolic actions of canonical Wnt/β-catenin signaling in bone. *Proc Natl Acad Sci USA.* 2015;112(5):E478-486. doi: 10.1073/pnas.1409857112

17. Zhang J, Zhang Y, Chen J, Gong W, Tu X. The osteocyte with SB216763-activated canonical Wnt signaling constructs a multifunctional 4D intelligent osteogenic module. *Biomolecules.* 2024;14(3):354. doi: 10.3390/biom14030354

18. Billiet T, Gevaert E, De Schryver T, Cornelissen M, Dubruel P. The 3D printing of gelatin methacrylamide cell-laden tissue-engineered constructs with high cell viability. *Biomaterials.* 2014;35(1):49-62. doi: 10.1016/j.biomaterials.2013.09.078

19. Zhang L, Xu M, Ren Q, et al. Human induced pluripotent stem cell-derived neural cells from Alzheimer's disease patients exhibited different susceptibility to oxidative stress. *Stem Cells Dev.* 2020;29(22):1444-1456. doi: 10.1089/scd.2020.0103

20. Zhang HY, Sun H. Up-regulation of Foxp3 inhibits cell proliferation, migration and invasion in epithelial ovarian cancer. *Cancer Lett.* 2010;287(1):91-97. doi: 10.1016/j.canlet.2009.06.001

21. Jia L, Zhou X, Huang X, et al. Maternal and umbilical cord serum-derived exosomes enhance endothelial cell proliferation and migration. *Faseb J.* 2018;32(8):4534-4543. doi: 10.1096/fj.201701337RR

22. Gong W, Li M, Zhao L, et al. Sustained release of a highly specific GSK3β inhibitor SB216763 in the PCL scaffold creates an osteogenic niche for osteogenesis, anti-adipogenesis, and potential angiogenesis. *Front Bioeng Biotechnol.* 2023;11:1215233. doi: 10.3389/fbioe.2023.1215233

23. Cai J, Huang J, Yang J, et al. The protective effect of selenoprotein M on non-alcoholic fatty liver disease: the role of the AMPKα1-MFN2 pathway and Parkin mitophagy. *Cell Mol Life Sci.* 2022;79(7):354. doi: 10.1007/s00018-022-04385-0

24. Cherian PP, Cheng B, Gu S, Sprague E, Bonewald LF, Jiang JX. Effects of mechanical strain on the function of Gap junctions in osteocytes are mediated through the prostaglandin EP2 receptor. *J Biol Chem.* 2003;278(44):43146-43156. doi: 10.1074/jbc.M302993200

25. Kang HW, Lee SJ, Ko IK, Kengla C, Yoo JJ, Atala A. A 3D bioprinting system to produce human-scale tissue constructs with structural integrity. *Nat Biotechnol.* 2016;34(3):312-319. doi: 10.1038/nbt.3413

26. Li J, Mooney DJ. Designing hydrogels for controlled drug delivery. *Nat Rev Mater.* 2016;1(12):16071. doi: 10.1038/natrevmats.2016.71

27. Pashuck ET, Stevens M. From clinical imaging to implantation of 3D printed tissues. *Nat Biotechnol.* 2016;34(3):295-296. doi: 10.1038/nbt.3503

28. Anthon SG, Valente KP. Vascularization strategies in 3D cell culture models: from scaffold-free models to 3D bioprinting. *Int J Mol Sci.* 2022;23(23):14582. doi: 10.3390/ijms232314582

29. Dellaquila A, Le Bao C, Letourneur D, Simon-Yarza T. *In vitro* strategies to vascularize 3D physiologically relevant models. *Adv Sci (Weinh).* 2021;8(19):e2100798. doi: 10.1002/advs.202100798

30. Blackwell KA, Raisz LG, Pilbeam CC. Prostaglandins in bone: bad cop, good cop? *Trends Endocrinol Metab.* 2010;21(5):294-301. doi: 10.1016/j.tem.2009.12.004

31. Choudhary S, Alander C, Zhan P, Gao Q, Pilbeam C, Raisz L. Effect of deletion of the prostaglandin EP2 receptor on the anabolic response to prostaglandin E2 and a selective EP2 receptor agonist. *Prostaglandins Other Lipid Mediat.* 2008;86(1-4):35-40. doi: 10.1016/j.prostaglandins.2008.02.001

32. Hakeda Y, Yoshino T, Natakani Y, Kurihara N, Maeda N, Kumegawa M. Prostaglandin E2 stimulates DNA synthesis by a cyclic AMP-independent pathway in osteoblastic clone MC3T3-E1 cells. *J Cell Physiol.* 1986;128(2):155-161. doi: 10.1002/jcp.1041280204

33. Koyama A, Otsuka E, Inoue A, Hirose S, Hagiwara H. Nitric oxide accelerates the ascorbic acid-induced osteoblastic differentiation of mouse stromal ST2 cells by stimulating the production of prostaglandin E(2). *Eur J Pharmacol.* 2000;391(3):225-231. doi: 10.1016/s0014-2999(00)00100-x

34. Perkel VS, Mohan S, Herring SJ, Baylink DJ, Linkhart TA. Human prostatic cancer cells, PC3, elaborate mitogenic activity which selectively stimulates human bone cells. *Cancer Res.* 1990;50(21):6902-6907.

35. Pradhan G, Samson SL, Sun Y. Ghrelin: much more than a hunger hormone. *Curr Opin Clin Nutr Metab Care.* 2013;16(6):619-624.
doi: 10.1097/MCO.0b013e328365b9be

36. Fujimori K. Prostaglandins as PPARγ modulators in adipogenesis. *PPAR Res.* 2012;2012:527607.
doi: 10.1155/2012/527607

37. Joiner DM, Tayim RJ, McElderry JD, Morris MD, Goldstein SA. Aged male rats regenerate cortical bone with reduced osteocyte density and reduced secretion of nitric oxide after mechanical stimulation. *Calcif Tissue Int.* 2014;94(5):484-494.
doi: 10.1007/s00223-013-9832-5

38. Kamel MA, Picconi JL, Lara-Castillo N, Johnson ML. Activation of β-catenin signaling in MLO-Y4 osteocytic cells versus 2T3 osteoblastic cells by fluid flow shear stress and PGE2: implications for the study of mechanosensation in bone. *Bone.* 2010;47(5):872-881.
doi: 10.1016/j.bone.2010.08.007

39. Tiede-Lewis LM, Xie Y, Hulbert MA, et al. Degeneration of the osteocyte network in the C57BL/6 mouse model of aging. *Aging (Albany NY).* 2017;9(10):2190-2208.
doi: 10.18632/aging.101308

40. Wang X, Ma Y, Chen J, et al. A novel decellularized matrix of Wnt signaling-activated osteocytes accelerates the repair of critical-sized parietal bone defects with osteoclastogenesis, angiogenesis, and neurogenesis. *Bioact Mater.* 2023;21:110-128.
doi: 10.1016/j.bioactmat.2022.07.017

41. Atala A, Bauer SB, Soker S, Yoo JJ, Retik AB. Tissue-engineered autologous bladders for patients needing cystoplasty. *Lancet.* 2006;367(9518):1241-1246.
doi: 10.1016/s0140-6736(06)68438-9

42. Zhou Z, Pang Y, Ji J, et al. Harnessing 3D *in vitro* systems to model immune responses to solid tumours: a step towards improving and creating personalized immunotherapies. *Nat Rev Immunol.* 2024;24(1):18-32.
doi: 10.1038/s41577-023-00896-4

43. Wang T, Pan W, Zheng H, et al. Accuracy of using a patient-derived tumor organoid culture model to predict the response to chemotherapy regimens in stage IV colorectal cancer: a blinded study. *Dis Colon Rectum.* 2021;64(7):833-850.
doi: 10.1097/dcr.0000000000001971

ACCSCIENCE PUBLISHING

International Journal of Bioprinting

RESEARCH ARTICLE

Design, fabrication, and evaluation of a novel 3D-printed temporomandibular joint prosthesis enhanced with elastic layers

Junqi Jiang[1], Zhiwei Jiao[2], Bingxue Cheng[3], Jianmin Han[4], Xiangliang Xu[1]*, and Chuanbin Guo[1]*

[1]Department of Oral and Maxillofacial Surgery, National Center of Stomatology and National Clinical Research Center for Oral Diseases and National Engineering Research Center of Oral Biomaterials and Digital Medical Devices and Beijing Key Laboratory of Digital Stomatology and Research Center of Engineering and Technology for Computerized Dentistry Ministry of Health and NMPA Key Laboratory for Dental Materials, Peking University School and Hospital of Stomatology, Beijing, China

[2]College of Mechanical and Electrical Engineering, Beijing University of Chemical Technology, Beijing, China

[3]State Key Laboratory of Tribology in Advanced Equipment, Tsinghua University, Beijing, China

[4]Tianjin Medical University School and Hospital of Stomatology & Tianjin Key Laboratory of Oral Soft and Hard Tissues Restoration and Regeneration Department, Tianjin, China

***Corresponding authors:**
XiangLiang Xu
(kqxxl@126.com)

Chuanbin Guo
(guodazuo@sina.com)

Citation: Jiang J, Jiao Z, Cheng B, Han J, Xu X, Guo C. Design, fabrication and evaluation of a novel 3D-printed temporomandibular joint prosthesis enhanced with elastic layers. *Int J Bioprint*. 2025;11(1):301-313. doi: 10.36922/ijb.4899

Received: September 20, 2024
1st revised: October 22, 2024
2nd revised: November 9, 2024
Accepted: November 20, 2024
Published Online: November 20, 2024

Copyright: © 2024 Author(s). This is an Open Access article distributed under the terms of the Creative Commons Attribution License, permitting distribution, and reproduction in any medium, provided the original work is properly cited.

Publisher's Note: AccScience Publishing remains neutral with regard to jurisdictional claims in published maps and institutional affiliations.

Abstract

Artificial temporomandibular joint (TMJ) replacement is a common intervention for the treatment of advanced TMJ diseases and ankylosis. The present study addresses the insufficient elasticity of existing artificial TMJs through the development of a composite material by incorporating high-density polyethylene into ultra-high-molecular-weight polyethylene. This was processed using fused deposition modeling 3D-printing technology to produce porous elastic layers with an elastic modulus similar to that of joint discs. An artificial TMJ prosthesis with physiological elasticity was successfully fabricated, applied to the surface of porous Ti–6Al–4V alloy, and validated through mechanical experiments. The results demonstrated that the elastic modulus of the synthetic cartilage exhibits a negative correlation with the number of staggered layers, while no significant relationship was observed between the elastic modulus and the alternating angle between the harnesses. The elastic modulus of the cartilage was measured to be 127.5 ± 16.1 MPa, while the maximum compressive strength was found to be 8.0 ± 1.3 MPa. Optimal performance was observed for a staggered layer count of five and a cross-angle of 90°. The bonding strength to the metal mandibular prosthesis was measured to be 2.62 ± 0.98 MPa, and the surface roughness was determined to be 1.6 μm. An elastic artificial TMJ process prosthesis in this study was successfully designed, fabricated, and validated through *in vitro* experiments, offering valuable insights for future advancements in artificial TMJ design.

Keywords: 3D printing; Artificial temporomandibular joint replacement; Elasticity; Porous elastic layers; Ultra-high-molecular-weight polyethylene; Ti–6Al–4V alloy

1. Introduction

Reconstruction of the temporomandibular joint (TMJ) typically involves autogenous bone grafting or the utilization of alloplastic TMJ implants. Compared with autogenous reconstruction, alloplastic TMJ replacement offers advantages in terms of reduced donor-site morbidity, shorter surgical duration, and the customizability to fit specific anatomical requirements.[1] Currently, the majority of TMJ prostheses consist of two components: an artificial fossa prosthesis constructed from ultra-high-molecular-weight polyethylene (UHMWPE) and an artificial condyle prosthesis composed of metal. There are two primary categories of TMJ prostheses available for clinical utilization: the stock Zimmer Biomet products and custom-made TMJ concepts products.[2] These artificial TMJ prostheses have been widely employed in clinical settings.[3] Nevertheless, it is important to note that current artificial TMJ prostheses systems do not feature biomimetic articular discs or articular cartilage structure, and this has significant implications related to their biomechanical differences from natural anatomical structures.[2] During mandibular movement, the discs exhibit a viscoelastic response to both static and dynamic loading, effectively absorbing stress.[4] Additionally, changes in loading patterns subsequent to reconstructive surgery can induce stress variations in the bilateral TMJ discs, which could potentially lead to calcification.[5] The disc functions as a vital cushioning element for the condylar prosthesis, and its absence may influence the resorption of healthy bone and the mobility of the healthy TMJ.

Elastic structures such as articular discs and cartilage are very important for the long-term functional movement of TMJs.[4,6] Accordingly, the lack of physiological elasticity during functional movement is a notable limitation of existing artificial TMJ prostheses. For instance, Xu et al.[7] compared the biomechanical behaviors of a custom-made mandibular condyle prosthesis and a total TMJ prosthesis using the finite element method. Their results showed that TMJ prosthesis materials with high Young's moduli affect the contralateral TMJ. Therefore, along with their morphology, the elasticity of TMJ prostheses should also be considered in the future.

Ti alloys and UHMWPE are commonly utilized materials in TMJ prostheses. Ti alloys are known for their high strength, low modulus of elasticity, and excellent biocompatibility. They are typically employed in the construction of the ramus of the condyle in U.S. Food and Drug Administration (FDA)-approved TMJ implants.[8] UHMWPE is a linear polyethylene with a high molecular weight that offers superior properties in terms of wear resistance, impact resistance, chemical resistance, and a low coefficient of friction.[9] This polymer is commonly used in the construction of the fossa of TMJ prostheses.

The utilization of additive manufacturing techniques has become prevalent in the fabrication of customized TMJ prostheses. Research has demonstrated the ability of selective laser melting to accurately construct the architecture of Ti alloys, while fused deposition modeling (FDM) has been employed to create objects from UHMWPE.[10,11] Thus, the application of these materials using these methods may present a novel approach to fabricating TMJ prostheses with enhanced comfort and longevity.

UHMWPE is a widely employed polymer with numerous excellent qualities. Since the 1960s, UHMWPE has been utilized in total joint replacements, including arthroplasty of the hip, knee, shoulder, and intervertebral discs.[12] Currently, UHMWPE-based materials are predominantly fabricated using subtractive methods such as turning or milling. In the context of additive manufacturing, the challenges posed by the high viscosity and poor fluidity of UHMWPE have been addressed by the blending of UHMWPE with other polymers such as polyethylene glycol or high-density polyethylene (HDPE). Ramli et al.[11] demonstrated that the incorporation of a 60% HDPE fraction improved the flowability and mechanical properties of UHMWPE for use in the FDM process. Additionally, Shokrgozar et al.'s research[13] confirmed the excellent biocompatibility of blended UHMWPE/HDPE composites *in vitro*.

However, the integration of such materials presents a significant engineering challenge due to their physical and chemical disparities.[14] Various techniques for combining dissimilar materials, particularly in polymer–metal hybrid structures, have emerged in recent years. Among these methods, "form fits" offer numerous advantages and significant potential for connections.[15] Wolf et al.[16,17,19] demonstrated that the incorporation of undercuts in joining structures can enhance adhesive joint strength through the introduction of mechanical interlocking, with the tensile adhesive strength of a 25°-undercut specimen surpassing those of specimens with other angles. Therefore, this method may be deemed appropriate for the development of an innovative TMJ prosthesis.

Currently, existing TMJ prostheses lack the incorporation of an articular disc and cartilage, which has significant biomechanical implications. As a result, there is a deficiency in physiological elasticity during the motion of TMJ prostheses, leading to an inability to fully meet the functional requirements of mandibular movement and potentially compromising long-term stability.

In the present study, we explored the use of biomimetic articular elastic layers composed of a UHMWPE/HDPE blend implemented in the condyle component to enhance the elasticity of TMJ prostheses. Ti–6Al–4V alloy was employed for biomimetic residual mandible prostheses, and UHMWPE was utilized for biomimetic articular elastic layers as a means to enhance the flexibility of TMJ condyle prostheses. The aim of this study was to establish hybrid structures comprising a UHMWPE/HDPE blend connected to a Ti alloy through form fits to replicate the interface between biomimetic articular elastic layers and the condyle component, and to assess their elasticity and adhesive strength.

2. Materials and methods

2.1. Materials and equipment

The UHMWPE used in this study was GUR 1020 (Ticona, Telford, UK) provided in powder form with a weight average molecular weight of 3.5×10^6 g/mol and a density of 0.93 g/cm^3. The HDPE used (PetroChina, Beijing, China) has a density of 0.954 g/m^3 and a weight average molecular weight of 1.2×10^5 g/mol. The material for the ramus of condyle prosthesis was Ti–6Al–4V alloy created using the Mlab Cusing 3D Metal Printing Machine (Concept Laser, Lichtenfels, Germany). The accuracy of the machine was approximately 40 μm.

UHMWPE with the addition of 60% HDPE was generated using a double-screw extruder. The resulting samples were formed into particles with an average diameter of 2 mm and subjected to preliminary print testing using a print-head nozzle with a diameter of 0.5 mm (Figure 1). We used our self-developed FDM 3D printer, which allows the manipulation of a large number of printing parameters: printing temperature (T), layer height (LH), printing speed (PS), printing acceleration (A), and flow rate (F).[18] After numerous printing runs, we determined the optimal printing parameters to be: T = 240°C, LH = 0.2 mm, PS = 350 mm/min, A = 0 mm/min^2, and F = 100%.

2.2. Design and mechanical testing of the articular elastic layer component

The porous model, designed using Simplify 3D software (Simplify3D, Ohio, America), featured a wire harness staggered structure aimed at reducing the material's elastic modulus to align with TMJ disc performance requirements. The porosity of the array was adjusted by manipulating parameters such as wire harness spacing and alternating angle. Specifically, wire harness spacings of 0.4, 1.0, and 1.6 mm were utilized. The alternating angle between the harnesses was set to 0°/30°, 0°/45°, 0°/60°, and 0°/90° (Figure 2). A standard 10 × 10 × 10 mm^3 cube structure was 3D-printed for each sample set to assess its compressive elastic modulus and maximum compressive strength using a universal testing machine (Figure 3). A total of six specimens were tested in each sample set.

2.3. Design and preparation of metal bone and elastic layers connection structure

First, the condyle component (Ti–6Al–4V alloy) was produced by selective laser melting. In this study, the condyle prosthesis was designed as a cube model (partner A) with geometrical dimensions of 30 × 10 × 10 mm^3 to facilitate the measurement of the joining strength. At the top of partner A, three rows with pin structures were located, consisting of three pins. In total, the joining

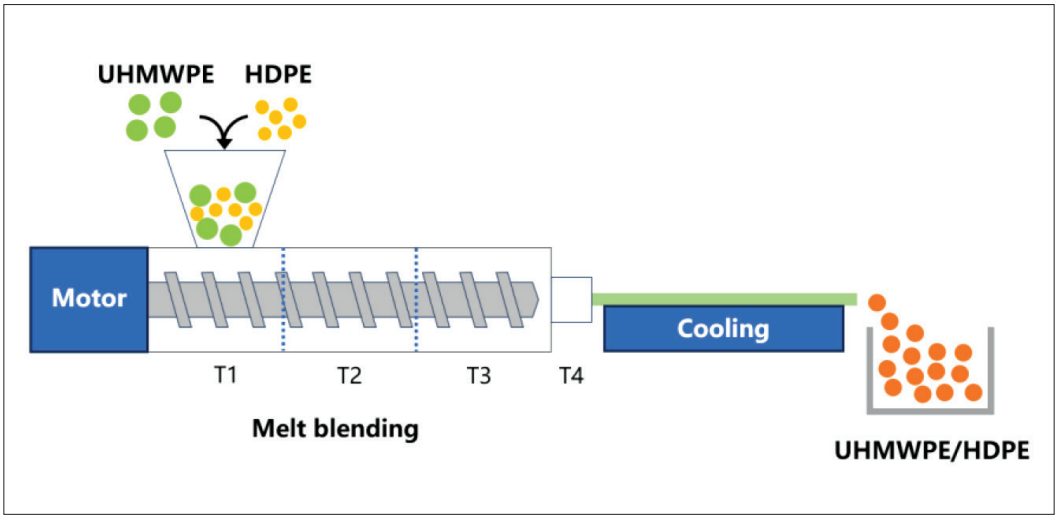

Figure 1. Preparation of UHMWPE with the addition of 60% HDPE using a double-screw extruder. Abbreviations: HDPE, high-density polyethylene; UHMWPE, ultra-high-molecular-weight polyethylene.

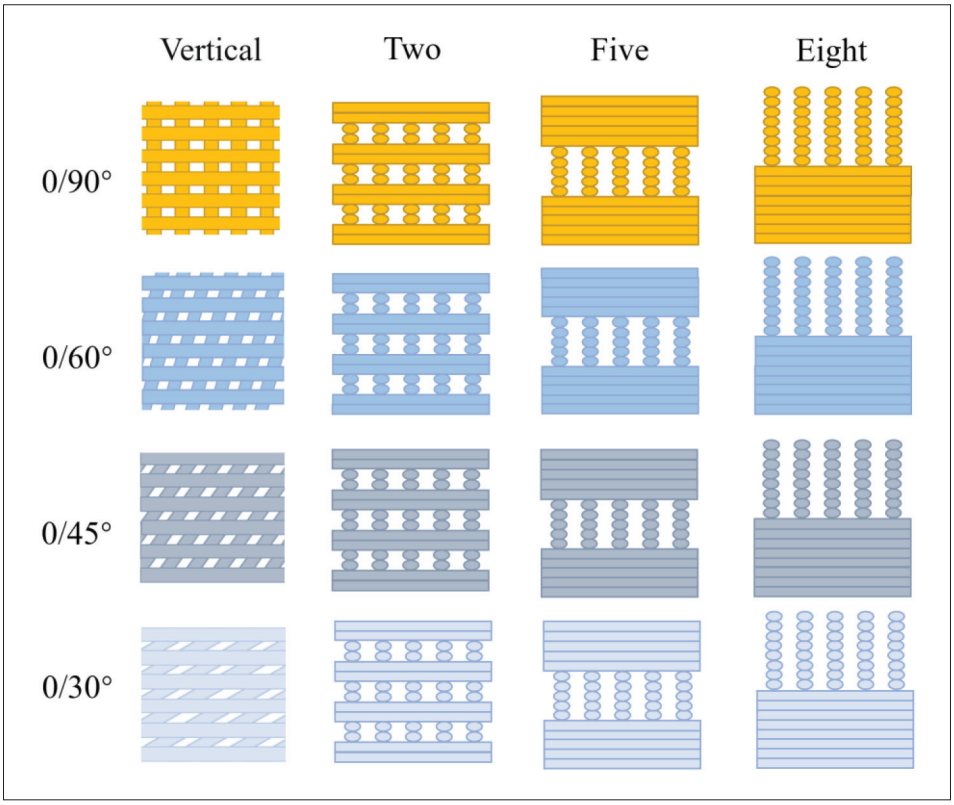

Figure 2. Schematics of porous scaffolds with distinct structural features having alternating angles of 0°/30°, 0°/45°, 0°/60°, and 0°/90°, and two, five, or eight crossing layers.

Figure 3. Universal testing machine.

surface had nine pins, which allowed for a doubled number of undercut structures (two undercut sections per pin). The section of the pin structure was trapezoid and defined by three parameters: the undercut angle, open width, and undercut depth. Their specific values are shown in Figure 4. We fabricated the undercut angle to 25° because this angle was found to significantly improve the tensile adhesive strength.[15] The material between the UHMWPE/HDPE condylar head and the titanium alloy riser was the UHMWPE/HDPE material.

Subsequently, a blend of UHMWPE with 60 wt% HDPE was utilized as the biomimetic material for articular elastic layers. This ratio has been determined to effectively enhance the processability of UHMWPE.[11] The composite material was heated to 180°C until it reached a molten state, and it was then extruded into the pin structure of the condyle component using a heated Al plate. It is crucial that the molten material completely covers the Ti alloys, serving as the base for the prepared biomimetic articular elastic layers. The scaffold structure of the printed elastic layer material is interconnected through welding with a welding plate temperature of 120°C. Biomimetic articular elastic layer specimens measuring 30 × 10 ×

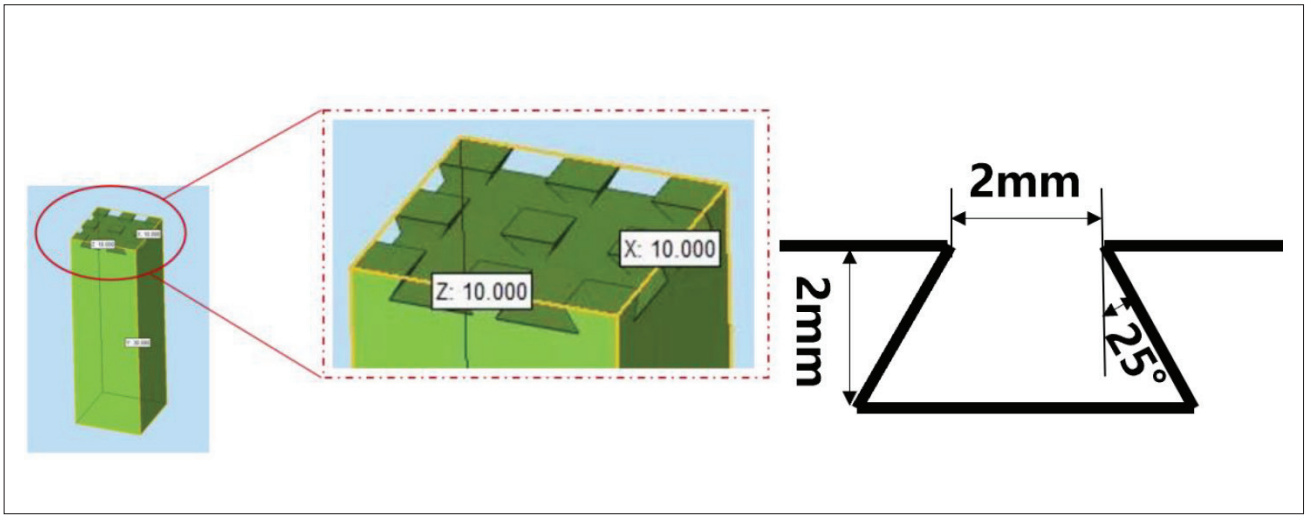

Figure 4. The joining surface. The joining surface with nine pin structures. The undercut angle was 25°. The open width and undercut depth were 2 mm.

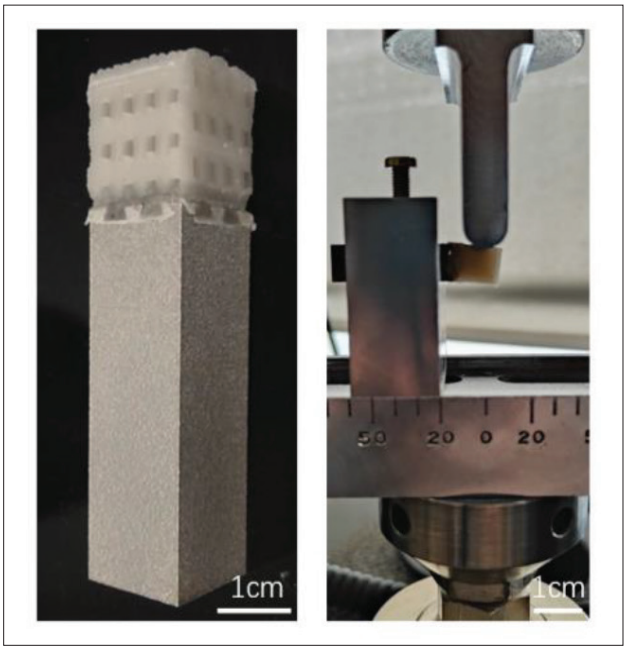

Figure 5. Shear strength measurements using the universal testing machine.

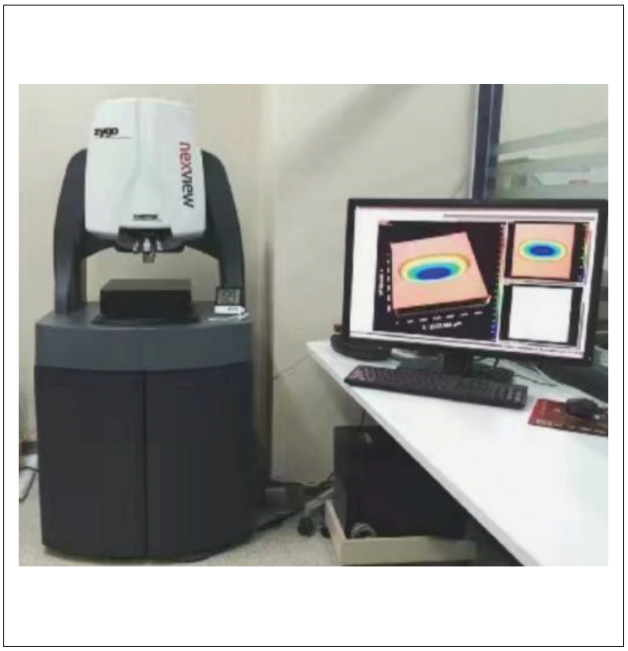

Figure 6. The white light interferometer used in this study.

10 mm^3 were produced using the FDM technique. The resulting specimen is depicted in Figure 5. Shear strength measurements were conducted using a universal testing machine equipped with a specialized membrane. The shear test was conducted using a specialized mold that applied vertical force on the superior material at 25°C, with a mold descending speed of 1 mm/min.

2.4. Polishing and surface-roughness measurement

The surface of the TMJ UHMWPE head must undergo polishing to mitigate the potential increase in wear degree and subsequent inflammatory response.[19] Ten samples resembling condylar heads were fabricated and subjected to polishing with sandpaper of varying mesh sizes (500, 800, 1000, 1200, and 1500). The average surface roughness

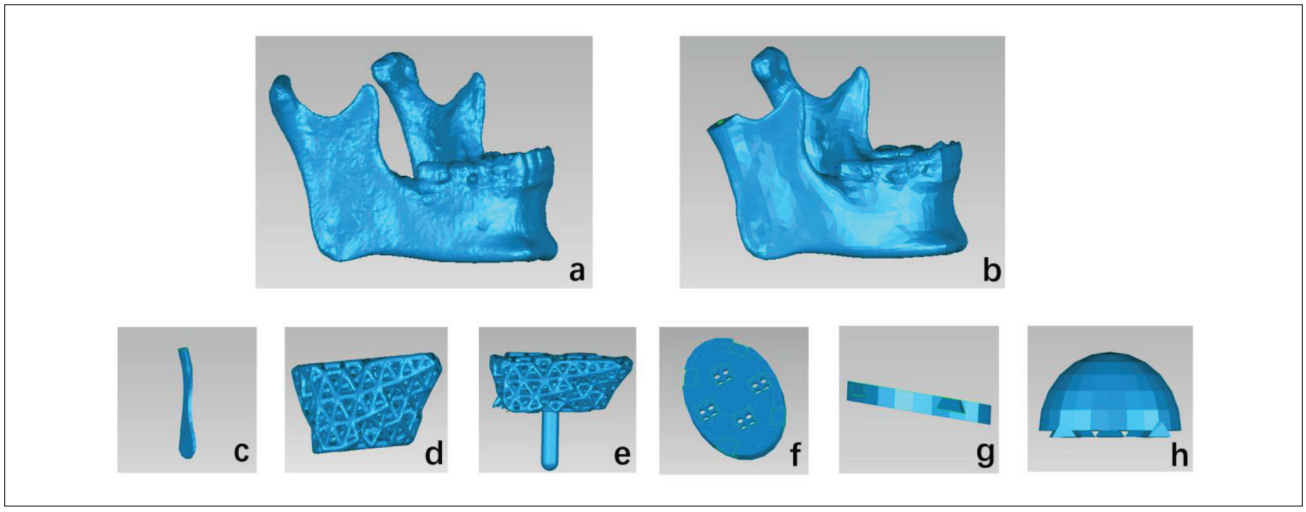

Figure 7. Design of the human condyle prosthesis**.** (a) 3D reconstruction of the subject's TMJ. (b) Simulated condylar defect. (c) Onlay plate. (d) Metal tetrahedral scaffolding structure. (e) Inlay rod. (f) Top view of the connecting structure. (g) Side view of the connection structure. (h) Bionic articular elastic layer structure. Abbreviation: TMJ, temporomandibular joint.

(Sa) of the joint head was measured with a white light interferometer (Figure 6). Three points were selected from the uppermost section of each sample to measure the surface roughness, and the average of these measurements was calculated to represent the roughness value.

2.5. Design and preparation of the human condyle prosthesis

We recruited one volunteer with healthy TMJ at the Department of Oral and Maxillofacial Surgery of Peking University School and Hospital of Stomatology, China (PKUSSIRB-201942015). Computed tomography (CT) images were acquired using 3D Accuitomo (Morita, Japan). Simulated arthrotomy was performed under the condylar neck. An 8-mm-high ellipsoidal bionic articular elastic layer was designed and the remaining space was filled with a metal tetrahedral scaffolding structure with a mean cell size of 2280 μm and a strut diameter of 570 μm. The primary significance of the porous structure lied in its ability to reduce the elastic modulus of the metal, which minimized stress shielding and reduced bone resorption around the prosthesis. This feature could promote muscle and bone integration, improving connectivity.[20] There were eight concave connection structures in the middle of the elastic layer and the metal with an additional concave connection structure positioned 2 mm apart. Sixteen 2 × 2 × 2 mm rejection holes were set above the metal to increase the connection strength. According to our previous research, a 1.5-mm-thick onlay

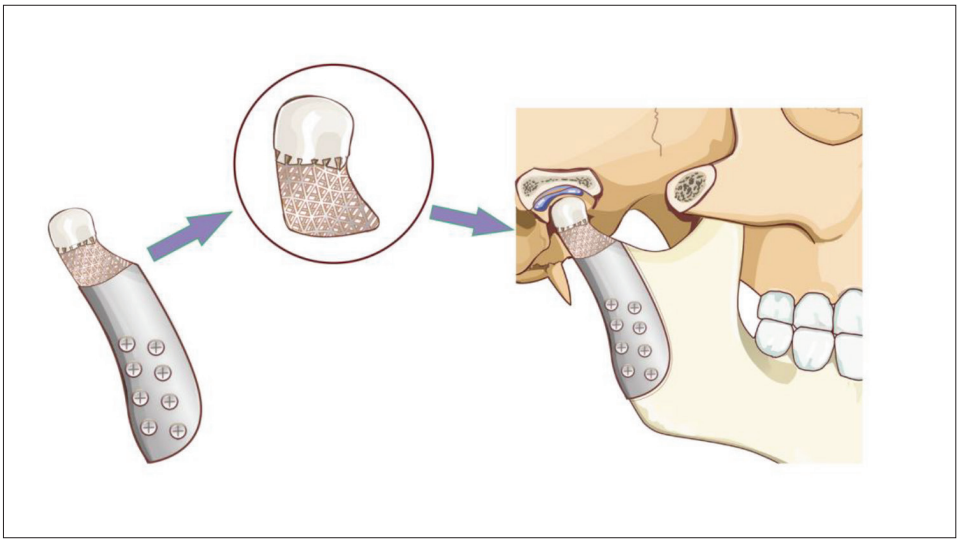

Figure 8. TMJ prosthesis design model. Abbreviation: TMJ, temporomandibular joint.

Figure 9. The head of the TMJ prosthesis. Abbreviation: TMJ, temporomandibular joint.

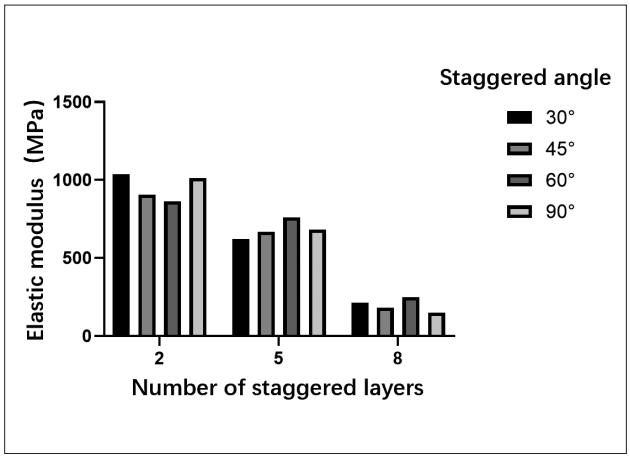

Figure 10. Elastic moduli of scaffold structures with varying staggered layers and angles.

plate was designed for the external side of the mandible, an inlay rod was designed for under the support structure, and transition smooth treatment was performed at the joint to enhance their connectivity with the bone (Figure 7).

The mandibular brancvh metal prosthesis was initially printed based on the design specifications, followed by printing of the bionic articular cartilage. Subsequently, the two components were interconnected through welding to finalize the preparation process (Figure 8).

2.6. Mechanical testing of the condyle prostheses *in vitro*

Due to the limitations of the universal testing machine, the onlay rod and inlay plate were removed for this part of the study to simulate the actual prosthetic head. A compression test was conducted for the 3D-printed condylar prostheses using the universal testing machine. A total of six physical models were used for the compression tests (Figure 9). The test temperature was 25°C, and the mold descending speed was 1 mm/min.

3. Results

3.1. Compressive elastic modulus and compressive strength of bionic articular elastic layer internal scaffold structure

Six samples were tested for each bracket structure type, and the average value was calculated for the final result. Figure 10 illustrates the elastic moduli of scaffold structures with varying staggered layers and angles. The findings suggest that an increase in the number of staggered layers results in a decrease in elastic modulus, while the elastic modulus is not influenced by the staggered angle. Liu et al.[21] reported that a 0°/90° cross-angle scaffold structure exhibits superior rigidity. Therefore, we finally decided upon a bracket structure with a staggered layer number of eight and a wiring harness interleaving angle of 90°. The elastic modulus of this structure was measured to be 127.5 ± 16.1 MPa with a maximum compressive strength of 8.0 ± 1.3 MPa shown in Figure 11.

3.2. Connection strength

A total of six samples were tested to assess the strength of the connection between UHMWPE and the metal joint, with shear strength calculated using the formula $p = 3F/2A$, where F is force, and A is cross-sectional area. The strength curves for the Ti-6Al-4V–UHMWPE connection are shown in Figure 12. The average strength is 2.62 ± 0.98 MPa.

3.3. Roughness

Ten polished samples were tested and the polished sample was shown in Figure 13. The surface roughnesses of the

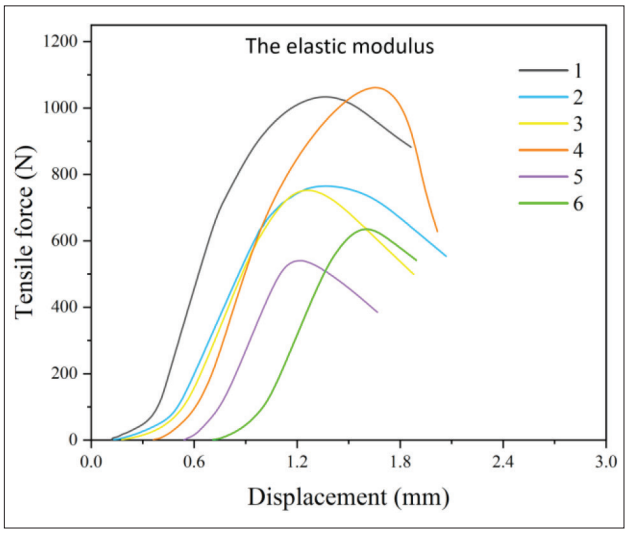

Figure 11. The elastic modulus of the structure with a staggered layer number of eight and a wiring harness interleaving angle of 90°.

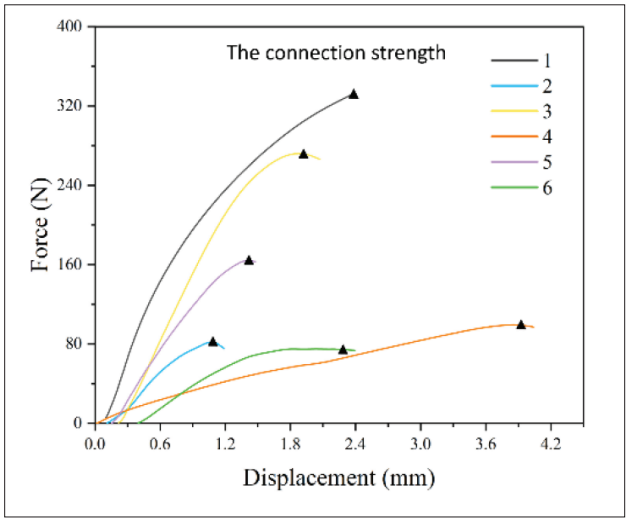

Figure 12. The connection strength of UHMWPE to the metal joint. Abbreviation: UHMWPE, ultra-high-molecular-weight polyethylene.

Figure 13. The polished samples. Comparison of polished and unpolished samples. The left sample was unpolished and the right one was polished.

condyle apexes after polishing were measured using a white light interferometer. Figure 14 shows the surface roughness after polishing (and after unfolding). The average roughness was 1.62 ± 0.13 μm.

3.4. Production and morphology analysis of TMJ prosthesis and elastic performance test of TMJ prosthesis

We effectively manufactured TMJ prostheses for healthy individuals in accordance with the procedures outlined in Section 2.5. Figure 15 shows the completed TMJ prostheses, which had already been polished. The elastic moduli of six prostheses were evaluated using a testing machine after removing the onlay plate and inlay rod. Figure 16 shows the elasticity modulus curves. An average modulus of 68 ± 0.32 MPa was recorded.

4. Discussion

The TMJ is the sole mobile joint in the oral and maxillofacial region and is the singular bilateral joint in the human body. It plays a crucial role in speech, mastication, deglutition, and other essential functions. TMJ tumors, joint ankylosis, trauma, and deformities can result in morphological abnormalities and functional impairment of the TMJ, impacting not only the esthetic aspect of patients' facial features but also causing physiological and psychological dysfunctions.[22] Artificial TMJ replacement is an effective approach for managing advanced stages of

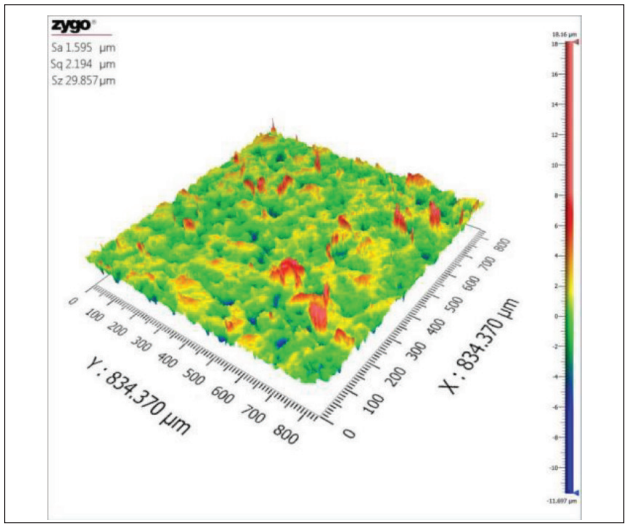

Figure 14. Surface roughness after polishing.

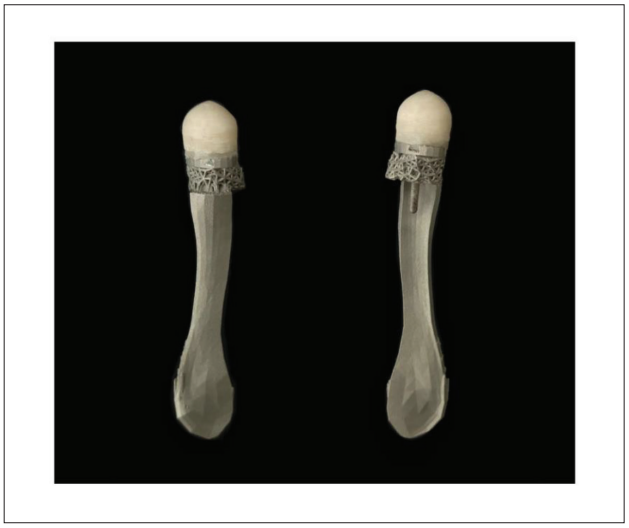

Figure 15. Completed TMJ prostheses.

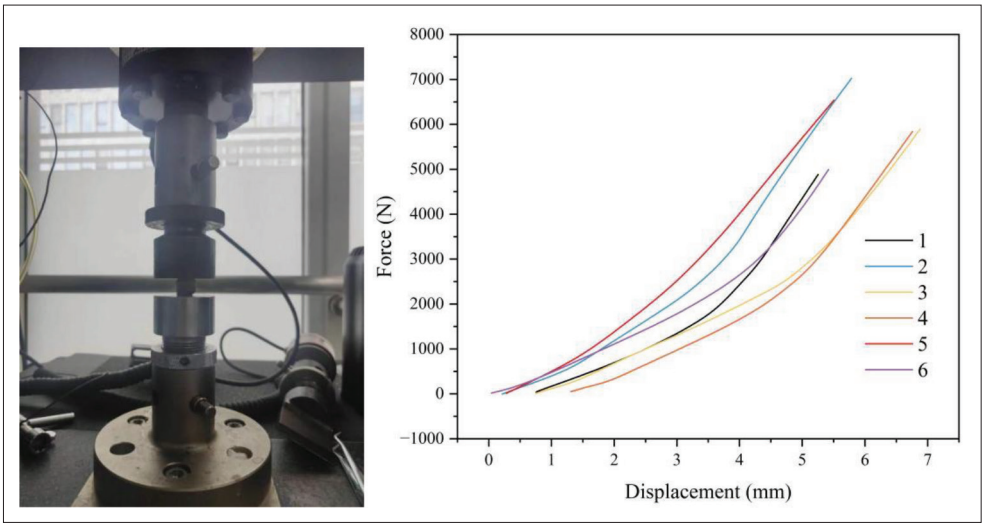

Figure 16. Compression experiment equipment and the resulting elasticity modulus curves.

TMJ disease.[23] Existing artificial joint prosthesis systems typically comprise a complete joint prosthesis consisting primarily of metal articular process prosthesis and a UHMWPE articular fossa prosthesis.[24] However, they lack the physiological elasticity of an actual articular disc, leading to constraints in functional movement and a barrier effect on stress distribution. Thus, the novel artificial joint prosthesis developed in this study utilized a hybrid UHMWPE/HDPE material for the bionic joint disc, resulting in an increased elasticity of the prosthesis. The elasticity of the new joint prosthesis was confirmed through mechanical testing.

The articular disc functions as a non-ossified structure within the TMJ, facilitating intricate movements and contributing significantly to jaw function by distributing stress, absorbing loads, and providing lubrication. The forces acting on the joint disc include compressive, tensile, and shear forces.[25] The articular disc is a kind of viscoelastic material. Barrientos et al.[6] reported that the behavior of the whole disc is primarily elastic, with some viscosity. Nickel et al.[6] demonstrated that the viscosity of a disc is augmented by a reduction in its elastic response, which is particularly evident under compressive loading conditions. Numerous investigations have evaluated the mechanical characteristics of joint discs from humans, sheep, and pigs, with their average compression modulus being a key parameter of interest. The average compression relaxation modulus and instantaneous compression modulus of a human joint disc at 20% strain are 37 and 1315 kPa, respectively.[26] Jiang et al.[27] analyzed the mechanical properties of 30 goat joint discs and found that the TMJ disc has certain compressive resistance (8.41 ± 2.12 MPa) and tensile resistance (9.54 ± 3.26 MPa). Yildirim et al.[28] used magnetic resonance imaging (MRI) to measure the elongation of the articular disc when the mouth is opened and closed, demonstrating its elastic properties. Hagandora et al.[29] reported that the elasticity of goat articular discs is better than that of the condylar cartilage. Many studies have demonstrated the importance of elasticity in joint discs, which is essential for the function of artificial joint prostheses.[6,27]

Currently, there are no materials that accurately replicate the properties of articular discs. Research in the field primarily centers on tissue engineering, material composition, and mechanical properties.[30–32] Some progress has recently been made in the field of 3D-printed scaffolds based on polycaprolactone (PCL) to simulate TMJ discs.[30] A novel synthetic TMJ disk was developed utilizing polyvinyl alcohol hydrogels and 3D-printed PCL, serving as an artificial joint disk reinforced through cyclic freeze-thawing crosslinking and PCL implantation.[31] Jiang et al.[32] developed a prosthesis construct with laser-drilled decellularized natural disc reinforced by PCL, which mimics the natural morphology, and structural, biomechanical, and biological property of the TMJ disc.

UHMWPE exhibits favorable properties such as wear resistance, impact resistance, self-lubricity, viscoelasticity, and corrosion resistance. The viscoelastic characteristics of UHMWPE are akin to those of the TMJ disc, which boasts exceptional compression and elastic properties.[25] In the field of orthopedics, 3D printing technology has found widespread application in the development of medical prostheses. This technology enables the modification of internal scaffold structures to lower a material's elastic modulus, allowing it to mimic the properties of human tissue.[6] UHMWPE is ill-suited to 3D printing due to its high viscosity and limited fluidity. In this study, HDPE was incorporated into UHMWPE using twin-screw blending

technology at a 6:4 ratio, and the resulting material was successfully utilized in FDM 3D printing, consistent with Ramli et al.'s study.[11] Thus, the challenge of 3D-printing UHMWPE was effectively addressed. The porous structures produced through 3D printing offer customizable pore size, shape, and porosity. The porous structure has the advantages of a low Young's modulus, high compressive strength, and abundant cell space for bone tissue engineering.[33] There is a stress barrier effect between the implant and the metal prosthesis, and the reduced stiffness of the implant will increase the shear stress between the implant and the surrounding bone.[34,35] There have been many attempts to make different metal scaffold structures with decreased elastic moduli that achieve the performance of bone. Wang et al.[36] produced Ti with a porosity of 32–47% that exhibited excellent Young's moduli in the range 23–62 GPa, and Barui et al.[37] designed a porous Ti-6Al-4V implant with an elastic modulus of 2.2–3.0 GPa. Li et al.[38] fabricated pure porous Ti with 50–70% porosity and different pore sizes by diffusion bonding. The Young's moduli of the materials were in the range of 1.0–7.5 GPa, and the yield stress was between 10 and 110 MPa. Thus, current developed materials have the Young's moduli of the GPa scale, presenting a notable disparity from that of the MPa scale of joint discs and articular cartilage, thereby posing challenges in achieving the desired elasticity for artificial joints.

This study utilized HDPE-modified UHMWPE and employed a rationally designed internal scaffold structure. The Young's modulus of 127.5 MPa obtained in this study aligns closely with the findings of Salimon et al.[39] regarding porous UHMWPE and the Young's moduli of the human joint discs. Additionally, the compressive strength of 8 MPa exceeds that of the human joint disc.[25] While maintaining adequate compressive strength, the prosthesis in this study had an elastic modulus that was significantly lower than that of current joint prostheses, including those with optimized internal pore structures.[40] This is a significant advancement. Currently, total joint replacement is complex and carries potential risks, including abnormal mandibular motor function and joint stiffness, which can impact movement in the healthy joint.[2,41] The enhanced flexibility of the joint head may allow for hemijoint replacement, a less invasive alternative that involves preserving the joint disc and only replacing the joint head, which is encompassed in a simpler operation with minimal impact on the healthy joint.

A variety of approaches have been recently proposed to join metals to polymers, including adhesive bonding, mechanical fasteners, joining processes, and direct assembly.[42] The study applied surface texture patterning to a Ti–6Al–4V alloy surface to better establish a connection with UHMWPE. A 25°-undercut-angle micropattern structure was utilized to achieve this connection, resulting in a shear strength of 2.62 MPa, which exceeds that experienced by articular discs.[43] This indicates that an integrated artificial Ti-6Al-4V–UHMWPE joint could meet the strength requirements of an artificial TMJ. Wear is the main factor in bone resorption and aseptic implant loosening of artificial TMJ replacement, contributing to long-term implant failure.[44,45] The rate of wear can be influenced by both material-related factors such as material choice, surface roughness, and factors related to the patient's jaw movement.[46] Even with the "gold-standard" biocompatibility of Co–Cr–Mo alloy and UHMWPE, wear debris can still appear.[2] In this research, the condyle head was modified to an elastic UHMWPE material to enhance the elasticity of the TMJ prosthesis and minimize wear, while the surface was polished to a roughness of 1.5 μm to better comply with artificial joint standards.[47] However, a wear test was not performed in this study as the prosthesis was customized, and there is currently no available equipment for customized TMJ fatigue testing. Based on the researches related to customized joint prostheses and movement of mandible, future studies could involve the development of a customized TMJ simulator to enable fatigue testing.

5. Conclusion

The current study has effectively implemented the design, fabrication, and modification of an artificial TMJ, whose elastic properties are superior to current joint prostheses. The new TMJ shows potential as a product for clinical application, introducing innovative concept of an elastic joint prosthesis, which could greatly enhance the performance of existing joint prostheses. Currently, only the elastic properties of the artificial TMJ have been evaluated. The overall elastic modulus was measured to be 68 MPa, indicating a slight reduction compared to simple biomimetic elastic layer material. Previous studies have established that the elastic modulus of two connected porous materials was influenced by the weakest segment.[48] This observed reduction in elastic modulus may be attributed to alterations in the shape structure. Since joint prosthesis implantation in animals was not performed in this study, we will carry out *in vivo* tests for further verification in subsequent studies.

Acknowledgments

None.

Funding

This work was supported by grants from Beijing Municipal Science & Technology Commission (Z201100005520055) and Clinical Research Foundation of Peking University School and Hospital of Stomatology (PKUSS-2023CRF205).

Conflict of interest

The authors declare they have no competing interests.

Author contributions

Conceptualization: Junqi Jiang, Xiangliang Xu, Chuanbin Guo
Formal analysis: Bingxue Cheng
Investigation: Junqi Jiang, Zhiwei Jiao, Jianmin Han, Bingxue Cheng
Methodology: Zhiwei Jiao, Jianmin Han
Writing – original draft: Junqi Jiang
Writing – review & editing: Xiangliang Xu, Chuanbin Guo

Ethics approval and consent to participate

The biomedical ethics committee of Peking University Hospital of Stomatology approved this study (PKUSSIRB-201942015). All procedures performed in studies involving human participants were in accordance with the ethical standards of the institutional and/or national research committee and with the 1964 Declaration of Helsinki and its later amendments or comparable ethical standards. Written informed consent was obtained from all participants.

Consent for publication

Informed consent was obtained from the participants for the publication of their data.

Availability of data

Data are available from the corresponding authors upon reasonable request.

References

1. Yoda T, Ogi N, Yoshitake H, et al. Clinical guidelines for total temporomandibular joint replacement. *Jpn Dent Sci Rev*. 2020,56(1):77-83. doi: 10.1016/j.jdsr.2020.03.001
2. Elledge R, Mercuri LG, Attard A, et al. Review of emerging temporomandibular joint total joint replacement systems. *Br J Oral Maxillofac Surg*. 2019,57(8):722-728. doi: 10.1016/j.bjoms.2019.08.009
3. De Meurechy N, Mommaerts MY. Alloplastic temporomandibular joint replacement systems: a systematic review of their history. *Int J Oral Maxillofac Surg*. 2018;47(6):743-754. doi: 10.1016/j.ijom.2018.01.014
4. Tanaka E, van Eijden T. Biomechanical behavior of the temporomandibular joint disc. *Crit Rev Oral Biol Med*. 2003;14(2):138-150. doi: 10.1177/154411130301400207
5. Jibiki M, Shimoda S, Nakagawa Y, et al. Calcifications of the disc of the temporomandibular joint. *J Oral Pathol Med*. 1999;28(9):413-419. doi: 10.1111/j.1600-0714
6. Barrientos E, Pelayo F, Tanaka E, et al. Dynamic and stress relaxation properties of the whole porcine temporomandibular joint disc under compression. *J Mech Behav Biomed Mater*. 2016;57:109-115. doi: 10.1016/j.jmbbm.2015.12.003
7. Xu X, Zhang J, Luo D, et al. Biomechanical comparison between the custom-made mandibular condyle prosthesis and total temporomandibular joint prosthesis in finite element analysis. *Acta Bioeng Biomech*. 2020;22(4):151-160. doi: 10.37190/ABB-01721-2020-03
8. Geetha M, Singh AK, Asokamani R, Gogia AK. Ti based biomaterials, the ultimate choice for orthopaedic implants-a review. *Prog Nat Sci Mater*. 2009;54(3):397-425. doi: 10.1016/j.pmatsci.2008.06.004
9. Kurtz S., ed. *UHMWPE Biomaterials Handbook–Ultra-high Molecular Weight Polyethylene in Total Joint Replacement and Medical Devices*, third ed. Amsterdam: Elsevier Inc.; 2016.
10. Ponader S, von Wilmowsky C, Widenmayer M, et al. In vivo performance of selective electron beam-melted Ti-6Al-4V structures. *J Biomed Mater Res A*. 2010;92:56-62. doi: 10.1002/jbm.a.32337
11. Ramli MS, Wahab MS, Ahmad M, and Bala AS. FDM preparation of bio-compatible UHMWPE polymer for artificial implant. *ARPN J Engd Appl Sci*. 2016;11(8). 5474-5480.
12. Musib MK. A review of the history and role of UHMWPE as a component in total joint replacements. *Int J Biol Sci*. 2012;1(1):6-10. doi: 10.5923/j.ijbe.20110101.02
13. Shokrgozar MA, Farokhi M, Rajaei F, etc. Biocompatibility evaluation of HDPE-UHMWPE reinforced β-TCP nanocomposites using highly purified human osteoblast cells. *J Biomed Mater Res A*. 2010;95(4):1074-1083. doi: 10.1002/jbm.a.32892
14. Amancio-Filho ST, Santos JFD. Joining of polymers and polymer-metal hybrid structures: recent developments and trends. *Polym Eng Sci*. 2009;49(8):1461-1476. doi: 10.1002/pen.21424
15. Wolf M, Kleffel T, Leisen C, Drummer D. Joining of incompatible polymer combinations by form fit using the vibration welding process. *Int J Polym Sci*. 2017; 2017:1-8. doi: 10.1155/2017/6809469
16. Wolf M, Hertle S, Drummer D. Influence of the thermomechanical properties on the joining of adhesion incompatible polymers by form-fit using the vibration welding process. eXPRESS Polym Lett. 2019,13(4):365-378. doi: 10.3144/expresspolymlett.2019.30

17. Matsuzaki R, Tsukamoto N, Taniguchi J. Mechanical interlocking by imprinting of undercut micropatterns for improving adhesive strength of polypropylene. *Int J Adhes Adhesiv*. 2016;68:124-132. doi: 10.1016/j.ijadhadh.2016.03.002

18. Barrios JM, Romero PE. Decision tree methods for predicting surface roughness in fused deposition modeling parts. *Materials (Basel)*. 2019;12(16):2574. doi: 10.3390/ma12162574

19. Jedenmalm A, Affatato S, Taddei P, et al. Effect of head surface roughness and sterilization on wear of UHMWPE acetabular cups. *J Biomed Mater Res A*. 2009;90(4):1032-1042. doi: 10.1002/jbm.a.32161

20. Xu X, Luo D, Guo C, Rong Q. A custom-made temporomandibular joint prosthesis for fabrication by selective laser melting: Finite element analysis. *Med Eng Phys*. 2017;46:1-11. doi: 10.1016/j.medengphy.2017.04.012

21. Liu H, Ahlinder A, Yassin MA, et al. Computational and experimental characterization of 3D-printed PCL structures toward the design of soft biological tissue scaffolds. *Mater Design*. 2020;188:11. doi: 10.1016/j.matdes.2020.108488

22. Vega LG, González-García R, Louis PJ. Reconstruction of acquired temporomandibular joint defects. *Oral Maxillofac Surg Clin North Am*. 2013;25(2):251-269. doi: 10.1016/j.coms.2013.02.008

23. Mercuri LG. Costochondral graft versus total alloplastic joint for temporomandibular joint reconstruction. *Oral Maxillofac Surg Clin North Am*. 2018;30(3):335-342. doi: 10.1016/j.coms.2018.05.003

24. Burgess M, Bowler M, Jones R, et al. Improved outcomes after alloplastic TMJ replacement: analysis of a multicenter study from Australia and New Zealand. *J Oral Maxil Surg*. 2014;72(7):1251-1257. doi: 10.1016/j.joms.2014.02.019

25. Stanković S, Vlajković S, Bošković M, et al. Morphological and biomechanical features of the temporomandibular joint disc: an overview of recent findings. *Arch Oral Biol*. 2013;58(10):1475-1482. doi: 10.1016/j.archoralbio.2013.06.014. Epub 2013 Jul 18. PMID: 23871384. doi: 10.1016/j.jmbbm.2015.12.003

26. Nickel JC, Iwasaki LR, Beatty MW, Marx DB. Laboratory stresses and tractional forces on the TMJ disc surface. *J Dent R*. 2004;83(8):650-654. doi: 10.1177/154405910408300813

27. Jiang N, Yang YT, Bi RY, et al. Comprehensive measurement and quantification of bio-mechanical properties of the temporomandibular joint disc. *Zhonghua Kou Qiang Yi Xue Za Zhi*. 2021;56(8):764-768. Chinese. doi: 10.3760/cma.j.cn112144-20210322-00133

28. Yildirim D, Dergin G, Tamam C, et al. Indirect measurement of the temporomandibular joint disc elasticity with magnetic resonance imaging. *Dentomaxillofac Radiol*. 2011;40(7):422-428. doi: 10.1259/dmfr/98030980

29. Hagandora CK, Chase TW, Almarza AJ. A comparison of the mechanical properties of the goat temporomandibular joint disc to the mandibular condylar cartilage in unconfined compression. *J Dent Biomech*. 2011;2011:212385. doi: 10.4061/2011/212385

30. Hu S, Yi Y, Ye C, et al. Advances in 3D printing techniques for cartilage regeneration of temporomandibular joint disc and mandibular condyle. *Int J Bioprint*. 2023;9(5):761. doi: 10.18063/ijb.761

31. Jiang N, Yang Y, Zhang L, et al. 3D-printed polycaprolactone reinforced hydrogel as an artificial TMJ disc. *J Dent Res*. 2021;100(8):839-846. doi: 10.1177/00220345211000629

32. Jiang N, Chen H, Zhang J, et al. Decellularized-disc based allograft and xenograft prosthesis for the long-term precise reconstruction of temporomandibular joint disc. *Acta Biomater*. 2023;159:173-187. doi: 10.1016/j.actbio.2023.01.042

33. Chen H, Han Q, Wang C, et al. Porous scaffold design for additive manufacturing in orthopedics: a review. *Front Bioeng Biotechnol*. 2020;8:609. doi: 10.3389/fbioe.2020.00609

34. Huiskes HWJ. Stress shielding and bone resorption in THA: clinical versus computer-simulation studies. *Acta Orthop Belg*. 1993; 59(Suppl 1):118-129.

35. Trebse R, Milosev I, Kovac S, et al. Poor results from the isoelastic total hip replacement. *Acta Orthop*. 2005;76(2): 169-176. doi: 10.1080/00016470510030535

36. Wang D, Li Q, Xu M, et al. A novel approach to fabrication of three-dimensional porous titanium with controllable structure. *Mater Sci Eng C Mater Biol Appl*. 2017;71:1046-1051. doi: 10.1016/j.msec.2016.11.119

37. Barui S, Chatterjee S, Mandal S, et al. Microstructure and compression properties of 3D powder printed T scaffolds with designed porosity: experimental and computational analysis. *Mater Sci Eng C Mater Biol Appl*. 2017;70(1):812-823. doi: 10.1016/j.msec.2016.09.040

38. Li F, Li J, Huang T, Kou H, Zhou L. Compression fatigue behavior and failure mechanism of porous titanium for biomedical applications. *J Mech Behav Biomed Mater*. 2017;65:814-823. doi: 10.1016/j.jmbbm.2016.09.035.

39. Salimon AI, Statnik ES, Zadorozhnyy MY, et al. Porous open-cell UHMWPE: experimental study of structure and mechanical properties. *Materials (Basel)*. 2019;12(13):2195. doi: 10.3390/ma12132195

40. Cheng KJ, Liu YF, Wang JH, et al. 3D-printed porous condylar prosthesis for temporomandibular joint replacement: design and biomechanical analysis. *Technol Health Care*. 2022;30(4):1017-1030.
doi: 10.3233/THC-213534

41. Bekcioglu B, Bulut E, Bas B. The effects of unilateral alloplastic temporomandibular joint replacement on the opposite-side natural joint: a finite-element analysis. *J Oral Maxillofac Surg*. 2017;75(11):2316-2322.
doi: 10.1016/j.joms.2017.05.017

42. Feistauer EE, Dos Santos JF, Amancio-Filho ST. A review on direct assembly of through-the-thickness reinforced metal-polymer composite hybrid structures. *Polym Eng Sci*. 2019;59(4):661-674.
doi: 10.1002/pen.25022

43. Lai W-FT, Bowley J, Burch JG. Evaluation of shear stress of the human temporomandibular joint disc. *J Orofac Pain*. 1998;12(2):153-159.
doi: 10.1016/S0278-2391(98)90138-0

44. Sagbas B, Durakbasa MN. Measurement of wear in orthopedic prosthesis. *Proc Int Cong Adv Appl Phys Mater Sci*. 2012;121(1):131-134.
doi: 10.12693/APhysPolA.121.131

45. Alonso A, Kaimal S, Look J, et al. A quantitative evaluation of inflammatory cells in human temporomandibular joint tissues from patients with and without implants. *J Oral Maxillofac Surg*. 2009; 67(4):788-796.
doi: 10.1016/j.joms.2008.09.010

46. Sinno H, Tahiri Y, Gilardino M, Bobyn D. Engineering alloplastic temporomandibular joint replacements. *McGill J Med*. 2010; 13(1):63.
doi: 10.26443/mjm.v13i1.252

47. De Meurechy N, Aktan MK, Boeckmans B, et al. Surface wear in a custom manufactured temporomandibular joint prosthesis. *J Biomed Mater Res B Appl Biomater*. 2022;110(6):1425-1438.
doi: 10.1002/jbm.b.35010

48. Bittner SM, Smith BT, Diaz-Gomez L, et al. Fabrication and mechanical characterization of 3D printed vertical uniform and gradient scaffolds for bone and osteochondral tissue engineering. *Acta Biomaterial.* 2019;90: 37-48.
doi: 10.1016/j.actbio.2019.03.041

ACCSCIENCE PUBLISHING

International Journal of Bioprinting

RESEARCH ARTICLE

3D bioprinting of biomimetic trachea with interspersed cartilage and vascularized connective tissue for prompt segmental tracheal reconstruction

Pengli Wang[1†], Ziming Wang[1†], Bohui Li[2], Lei Xie[3], Liang Guo[1], Yong Xu[1*], Dan Li[4*], Jiaoyu Yi[5*], and Bo Tao[1*]

[1]Department of Thoracic Surgery, Shanghai Pulmonary Hospital, School of Medicine, Tongji University, Shanghai, China

[2]Plastic Surgery Institute, Shandong Second Medical University, Weifang, Shandong, China

[3]Department of Thoracic Surgery, The Second Affiliated Hospital of Nanchang University, Nanchang, Jiangxi, China

[4]Department of Plastic and Reconstructive Surgery, Shanghai 9th People's Hospital, Shanghai Jiao Tong University School of Medicine, Shanghai, China.

[5]Department of Plastic Surgery, Renji Hospital, Shanghai Jiaotong University School of Medicine, Shanghai, China

(This article belongs to the *Special Issue: Bioprinting of Tissues and Organs: Materials, Technologies and Perspectives for Regenerative Medicine*)

Abstract

Segmental tracheal reconstruction remains a significant clinical challenge due to the lack of ideal tracheal substitutes. Three-dimensional (3D) bioprinting technique offers a promising avenue for the development of native-like tracheal substitutes. However, several challenges remain to be addressed, including deformation of 3D-printed C-shaped cell-laden hydrogels, fusion of regenerated C-shaped cartilage, and difficulty in regenerating vascularized connective tissue. Herein, we utilized 3D printing techniques to fabricate C-shaped chondrocyte-laden GelMA/PCL (CcGP) and S-shaped PCL chains (SPC). These were assembled into the SPC-CcGP construct, followed by mold casting (VEGF@GelMA) to establish tissue-engineered tracheal construct (TETC). *In vitro* experiments confirmed the stable chondrogenic potential of CcGP and the angiogenic capability of VEGF@GelMA. Subcutaneous implantation in nude mice and orthotopic transplantation in rabbit model further demonstrated that the TETC could achieve stable regeneration of cartilage and vascularized connective tissue. The engineered trachea could maintain luminal patency following prompt repair of rabbit tracheal defects. This study offers a promising approach for developing engineered tracheas with regenerated cartilage and vascularized connective tissue for prompt and effective segmental tracheal defect repair.

Keywords: 3D printing; Mold; Cartilage; Trachea reconstruction; Vascularized connective tissue

[†]These authors contributed equally to this work.

***Corresponding authors:**
Yong Xu (xuyong@tongji.edu.cn)
Dan Li (lidan2009best@163.com)
Jiaoyu Yi (yijiaoyu@renji.com)
Bo Tao (tbo0820@163.com)

Citation: Wang P, Wang Z, Li B, et al. 3D bioprinting of biomimetic trachea with interspersed cartilage and vascularized connective tissue for prompt segmental tracheal reconstruction. *Int J Bioprint*. 2025;11(1):314-326. doi: 10.36922/ijb.4955

Received: September 25, 2024
Revised: November 3, 2024
Accepted: November 19, 2024
Published Online: November 20, 2024

Copyright: © 2024 Author(s). This is an Open Access article distributed under the terms of the Creative Commons Attribution License, permitting distribution, and reproduction in any medium, provided the original work is properly cited.

Publisher's Note: AccScience Publishing remains neutral with regard to jurisdictional claims in published maps and institutional affiliations.

1. Introduction

Tissue engineered tracheal constructs (TETC) present a promising approach for the reconstruction of long-segment tracheal defects in which end-to-end anastomosis is not viable.[1] The trachea is a C-shaped cartilaginous tubular structure connecting the larynx superiorly and the main bronchi inferiorly. The C-shaped cartilage ring provides essential mechanical support for the trachea to maintain its patency. Vascularized connective tissue not only tightly bind the C-shaped tracheal cartilage but also supplies the necessary nutrients for both cartilage and epithelium.[2] Recently, numerous studies have reported that three-dimensional (3D) printing techniques have shown significant potential for fabricating scaffolds that accurately mimic the anatomical structure of the natural trachea while also restoring the biological function of TETC.[3]

In our previous study, we utilized 3D printing techniques to fabricate C-shaped chondrocyte-laden GelMA hydrogel rings, which were subsequently vascularized *in vivo*, facilitating the development of TETC.[4] However, several crucial challenges remain to be addressed: (1) difficulty for the C-shaped chondrocyte-laden gelatin methacrylate (GelMA) hydrogel to retain its biomimetic C-type structure, primarily due to insufficient mechanical strength; (2) fusion of the regenerated C-shaped cartilage rings at a later stage due to the lack of a supporting structure to maintain the spacing between the C-shaped chondrocyte-laden GelMA hydrogel segments; and (3) restricted formation of vascularized connective tissue within the spacing between the C-shaped chondrocyte-laden GelMA hydrogel segments due to the lack of a regenerative scaffold. Thus, we propose to first 3D-print C-shaped PCL scaffolds and S-shaped PCL chains, followed by the incorporation of chondrocyte-laden GelMA and VEGF@GelMA hydrogels.

Numerous studies have reported the fabrication of TETC using 3D-printed scaffold.[5,6] Hsieh et al.[7] fabricated 3D-printed tubular scaffolds with elasticity and sufficient mechanical properties to replace a portion of the rabbit trachea *in vivo* without collapse. However, the tubular structure is unable to replicate the relaxation and contraction functions of natural C-shaped tracheal cartilage, nor is it conducive to the flexibility required for cervical tracheal bending.[8,9] Some researchers have further proposed a ring-based strategy, in which engineered cartilage rings and fiber-hydrogel rings are alternately stacked to form a tubular structure.[10,11] This approach results in a TETC with enhanced flexibility and improved nutrient supply.[12,13] However, Gao et al.[14] reported a 30% mortality rate in rabbits following reconstructive surgery, with even poorer outcomes observed in a goat model. This was primarily due to the absence of C-shaped cartilage rings, which are essential for regulating airflow velocity through their relaxation and contraction, aiding in the clearance of mucus from the lumen.[15]

Thus, we employed 3D printing techniques to fabricate a C-shaped polycaprolactone (PCL) scaffold and then filled the gaps with a chondrocyte-laden GelMA hydrogel to fabricate C-shaped chondrocyte-laden GelMA/PCL (CcGP) construct. The 3D-printed C-shaped PCL scaffold provides adequate mechanical support for the chondrocyte-laden GelMA hydrogel, helping it withstand *in situ* stress on the trachea until the C-shaped regenerated cartilage matures, thereby preserving its biomimetic structure. To address the issue of fusion between regenerated C-shaped cartilage rings at later stages, we introduced 3D-printed S-shaped PCL chains (SPC) to fix the CcGP construct. The S-shaped PCL chains effectively regulate the spacing between the regenerated C-shaped cartilages, preventing fusion of the cartilage rings in the later stages. The S-shaped PCL chains-C-shaped chondrocyte-laden GelMA/PCL (SPC-CcGP) construct also provides a sufficient and stable regenerative environment to promote the ingrowth of vascularized connective tissue into the gaps between CcGP constructs.

Prompt vascularization is crucial for the long-term survival of regenerated cartilage tissue and the functional performance of TETC within the trachea.[16] Our preliminary research demonstrated that placing regenerative scaffolds between cartilage rings not only creates a favorable environment for the regeneration of vascularized connective tissue but also accelerates the integration of various components within the regenerated trachea.[17,18] Vascular endothelial growth factor (VEGF) is widely recognized as a key pro-angiogenic growth factor, with extensive and well-established research supporting its role in vascular development.[19] Therefore, we utilized a silicone tube as the internal support for the SPC-CcGP construct, placing the entire assembly into a mold. The VEGF-loaded GelMA hydrogel was then poured into the gaps within the SPC-CcGP construct to fabricate TETC.

In summary, the current study introduces a novel strategy for constructing TETC by 3D printing techniques. First, the mechanical strength of the 3D-printed C-shaped PCL scaffold was continuously optimized through mechanical testing. Finite element analysis (FEA) was employed to characterize the deformation and displacement fields of the C-shaped cartilage rings under external force. Next, *in vitro* experiments were conducted to assess the growth of chondrocytes and human umbilical vein endothelial cells (HUVECs), while the regeneration of C-shaped cartilage was further evaluated *in vivo* through subcutaneous implantation in nude mice. Subsequently, TETC were

fabricated through mold casting and applied to repair a rabbit long-segment tracheal defect model instantly, with the efficacy of this repair strategy thoroughly evaluated. This study is expected to address key challenges associated with the deformation of 3D-printed C-shaped cell-laden hydrogels, the tendency for regenerated C-shaped cartilage to fuse, and the difficulty in regenerating vascularized connective tissue.

2. Materials and methods

2.1. Materials

PCL (Mn 80,000 g/mol, Sigma–Aldrich), trypsin, type II collagenase, phosphate-buffered saline (PBS), and fetal bovine serum (FBS) were purchased from Macklin (Shanghai Macklin Biochemical Co., Ltd., China). GelMA and lithium phenyl-2,4,6-trimethylbenzoyl-phosphinate (LAP) was purchased from EFL (Shanghai, China).

2.2. Three-dimensional printing of C-shaped PCL scaffolds and S-shaped PCL chains

The properties of C-shaped and S-shaped PCL frameworks were designed using Materialise Magics 22.0 software (Materialise HQ, Belgium), and the frameworks were printed using 3D bioprinter system (Regenovo 3D Bio-Architect). In brief, PCL (Mn 80 000 g/mol, Sigma–Aldrich) were melted (at 100°C) in a printing chamber and then printed with the following parameters: printing temperature of 80°C, speed of 40 mm/s, and nozzle diameter of 0.3 mm. The distance of the internal line was set to 1, 1.5, and 2 mm to obtain 1.0, 1.5, 2.0 mm C-shaped PCL scaffold, respectively. All frameworks were sterilized using ethylene oxide before use.

2.3. Characterizations of C-shaped PCL and GelMA/PCL scaffolds

First, the mechanical properties of 1.0, 1.5, 2.0 mm C-shaped PCL scaffold (n = 3) were analyzed using a mechanical testing machine (Instron-5542; Canton, USA). The samples from all groups were subjected to compression at a rate of 1 mm/min until the depth of compression reached 30% of the initial height. We computed the elastic modulus using the initial 5–15% of the strain–stress curve. Additionally, compressive forces were applied in various directions to a single PCL (1.5 mm), GelMA/PCL (1.5 mm), and natural tracheal cartilage until a 50% compression was achieved, with the maximum pressure recorded. The mechanical properties of identical length SPC-CcGP structures and natural trachea were further evaluated using the same methodology. Then, the volume of the gaps of the C-shaped PCL scaffold were conducted by evaluating the volume of hydrogel dropping into the scaffold (n = 3).

Furthermore, the enzymatic degradation of GelMA/PCL and PCL scaffolds were evaluated by using an enzymatic solution (0.05% w/v collagenase) for 96 h *in vitro*. Briefly, the initial mass of scaffolds was measured and recorded as M_0, respectively. Subsequently, scaffolds were put into the enzymatic solution at 37°C for degradation. The degraded scaffolds were taken out at time points 0, 8, 16, 24, 48, and 96 h, and then washed with distilled water. The scaffolds were dried at 60°C, and the weight of the degraded sample were measured and recorded as M_t. The remaining ratio was calculated as $(M_0 - M_t)/M_0 \times 100\%$ (n = 3).

The release kinetics of VEGF@GelMA were assessed as previously described. Briefly, the VEGF@GelMA hydrogel was immersed in PBS for varying durations. At designated time points, 500 μL of the medium was withdrawn, and an equivalent volume of fresh PBS was added to maintain the total volume. The quantity of VEGF released into the medium was determined using an ELISA Kit (R&D Systems, Minneapolis, MN, USA) according to the manufacturers instructions. The release kinetics were calculated using the following formula:

$$mt = m1+m2+m3+\ldots+mx$$

where mx represents the amount released at time x, and mt denotes the cumulative amount of released VEGF protein.

2.4. Chondrocyte's preparation

As previously reported, chondrocytes were isolated from auricular cartilage of New Zealand white rabbits (aged 2 months), purchased from Shanghai Jiagan Experimental Animal Raising Farm (Shanghai, China). Isolated chondrocytes were cultured in Dulbecco's modified Eagle's medium (DMEM) medium (Gibco BRL, Grand Island, NY, United States) containing 10% fetal bovine serum (FBS; Gibco BRL) and 1% antibiotic-antimycotic (Gibco BRL). Chondrocytes in passage 2 were harvested for use.

2.5. Bioactivity of GelMA/PCL on chondrocytes

For pristine GelMA hydrogel precursors, we dissolved 10% w/v GelMA and 0.3% w/v LAP (a photoinitiator) in PBS. Then, 8.0×10^6 cells/mL chondrocytes were mixed with 10% w/v GelMA hydrogel precursors and injected into PCL scaffold. The mixture was then polymerized using ultraviolet light irradiation (365 nm, 20 mW/cm^2) for 30 s to obtain chondrocyte-loaded hydrogels. Subsequently, chondrocyte-loaded hydrogels were incubated at 37°C and 5% CO_2 for 5 days. The culture medium (DMEM supplemented with 10% FBS and 1% antibiotic-antimycotic) was changed every 2 days. The viability of chondrocytes in hydrogels was assessed using a Live/Dead Cell Viability Assay kit (Invitrogen, USA) according to the manufacturer's instructions. Additionally, the samples were examined using a confocal microscope (Leica, TCS

SP8 STED 3X) on days 1, 3, and 5. The live/dead staining images were analyzed using the ImageJ software (Wayne Rasband and contributors National Institutes of Health, USA) to quantify cell viability. To observe cell spreading in the hydrogels on days 1, 3, and 5, F-actin and nuclei were stained with phalloidin (Yeasen Biotechnology, China) and DAPI, respectively. Thereafter, the samples were observed and photographed using a confocal microscope (Leica, TCS SP8 STED 3X). Cell proliferation was assessed via Cell Counting Kit-8 (CCK-8; Beyotime Biotechnology, China) assay and DNA quantification on days 1, 3, and 5. CCK-8 assay was performed according to the manufacturer's instructions, and absorbance was measured at 450 nm using a spectrophotometer. DNA was quantified using the PicoGreen dsDNA assay kit (Invitrogen, USA) according to the manufacturer's instructions.

2.6. Bioactivity of VEGF@GelMA on HUVECs

VEGF and 10% w/v GelMA hydrogel precursors were mixed together and polymerized using ultraviolet light irradiation (365 nm, 20 mW/cm^2) for 30 s to fabricate the VEGF@GelMA hydrogel. To assess the effect of VEGF@GelMA on the migration ability of HUVECs, 5×10^5 cells/well were seeded into a 6-well plate. After incubation at 37°C for 24 h, a scratch was made using a 10 μL pipette tip. Floating or dead cells were washed away with PBS. Furthermore, 500 μL VEGF@GelMA hydrogel was injected into 6 well plates, 500 μL GelMA was utilized as the control group. The remaining cells were cultured with different hydrogels for an additional 24 h. Cell migration was analyzed using ImageJ software. The average migration rate was calculated using the following formula:

$$\text{Migration rate} = (R_0 - R_1)/R_0 \times 100\% \quad \text{(II)}$$

where R_0 is an initial scratch area and R_1 is the unhealed scratch area.

An *in vitro* vessel formation assay was also conducted using Matrigel-coated plates. HUVECs (5×10^4 cells/well) were co-cultured with 100 μL different hydrogels in a 48-well plate for 6 h. The formation of capillary-like tubes was observed under a microscope and quantified using the ImageJ software. Specifically, the Angiogenesis Analyzer plugin in ImageJ was used to measure the number of branch points and the total capillary length within the vascular network.

To assess the gene expression levels of endothelial nitric oxide synthase (eNOS; *NOS3*), fibroblast growth factor 2 (FGF2; *FGF2*), and hypoxia-inducible factor-1α (HIF-1α; *HIF1A*), real-time polymerase chain reaction (RT-PCR) was performed. Briefly, HUVECs (2×10^4 cells/well) were seeded in a 48-well plate for 24 h, followed by treatment with different hydrogels for 48 h. Total RNA was extracted using the MolPure Cell/Tissue miRNA Kit (Yeasen Biotechnology, China), and reverse transcription was conducted with Hifair II 1st Strand cDNA Synthesis SuperMix (Yeasen Biotechnology, China). RT-PCR was used to quantify mRNA levels of *NOS3*, *FGF2*, and *HIF1A*, normalized to *GAPDH*. Relative mRNA expression was calculated using the $2^{-\Delta\Delta Ct}$ method. Primer sequences are provided in **Table S1** (Supporting Information).

In addition, the protein expression levels of eNOS, FGF2, and HIF-1α were detected via Western blotting. Briefly, total protein extractions were prepared from samples using RIPA buffer (KeyGen, China). Protein samples were separated by sodium dodecyl sulfate-polyacrylamide gel electrophoresis (SDS-PAGE), transferred onto polyvinylidene fluoride (PVDF) membranes, and blocked with 5% bovine serum albumin. Subsequently, the PVDF membranes were covered with primary antibodies as probes against eNOS, FGF2, and HIF-1α (1:1000; Santa Cruz Biotechnology, Inc.) and **β-actin** antibodies (1:10,000; Abcam). After applying horseradish peroxidase (HRP)-conjugated goat anti-rabbit/mouse IgG antibody (1:10,000; Aspen Biotech, Shanghai, China), band visualization was performed with the aid of the ECL kit (Aspen Biotech, Shanghai, China), and their intensity was analyzed using Band-Scan software (DEVA Broadcast Ltd., Bulgaria)

2.7. *In vitro* and *in vivo* CcGP regeneration

To fabricate CcGP construct, we homogeneously mixed chondrocytes in the pristine GelMA hydrogel precursors at a concentration of 1×10^8 cells/mL. The chondrocyte-loaded hydrogels were then loaded into C-shaped PCL scaffold and crosslinked via photopolymerization (365 nm, 20 mW/cm^2) for 30 s. Subsequently, CcGP constructs were cultured in a chondrogenic medium composed of DMEM, 10 ng/mL of transforming growth factor beta 1 (TGF-β1; R&D Systems Inc, USA), 40 ng/mL of dexamethasone (Sigma, USA), 100 ng/mL of insulin-like growth factor (IGF-1; R&D Systems Inc, USA), and other supplements for 6 weeks as described in a previous study.[14] Concurrently, the chondrocyte-loaded hydrogels were implanted into anesthetized nude mice (4-week-old male mice). The cartilage rings were harvested after 3 and 6 weeks of implantation.

2.8. *In vivo* biomimetic tracheal regeneration

Two 3D-printed SPC were used to fix the CcGP construct to create the SPC-CcGP construct. The SPC-CcGP construct was then placed into a mold. VEGF@GelMA hydrogel was poured into the gaps of the SPC-CcGP construct to generate TETC and crosslinked via photopolymerization (365 nm, 20 mW/cm^2) for 30 s. Subsequently, the 1.5-cm-long native trachea in rabbits was resected, and the defect

was orthotopically reconstructed using TETC promptly with intermittent sutures (5-0 monofilament, COVIDIEN). A 2-cm-long silicone tube was utilized as an internal support. After confirming the absence of air leak or bleeding, muscles and subcutaneous tissues were sutured, and the incision was closed. Furthermore, subcutaneous emphysema in the neck of the rabbit was observed at 6 h post-surgery to assess the presence of any gaps between the graft and the native trachea. Penicillin (50000 U, QD; Huachu, China) and meloxicam (0.1 mg/kg, QD; Xinan, China) were administered for the next 5 days. The rabbits were sacrificed at 3, 4, and 6 weeks after reconstruction. The orthotopically transplanted tracheas with 0.5-cm-long adjacent native tracheas were harvested. Gross view and endoscopic images were obtained.

2.9. Histological and biochemical evaluation

The above-mentioned samples were fixed in 4% paraformaldehyde for 24 h, embedded in paraffin and sectioned. Hematoxylin-eosin (H&E) staining was performed to evaluate the histological structure of the cartilage rings. Safranin-O staininh and immunohistochemical staining of collagen II were performed to analyze glycosaminoglycan (GAG) and type II collagen deposition. Masson's trichrome staining was performed as previously described[10] to observe collagen fibers. After H&E staining, blood vessels were counted under a 200× magnification field, with at least three random fields counted.

Simultaneously, samples were digested in papain (Sigma, USA), and total GAGs were precipitated using guanidinium chloride (GnCl). The GAG precipitate was dissolved, and the optical density (OD) was determined at 595 nm. Subsequently, GAG content was calculated based on a standard curve established using chondroitin-4-sulfate. Total collagen content was quantified via a hydroxyproline-based assay. Briefly, the samples were dissolved in an alkaline hydrolysis solution, and free hydroxyproline hydrolysates were quantified using a previously described method.

2.10. Statistical analysis

The results are presented as the mean ± standard deviation. Statistical analysis was performed using GraphPad Prism 9.5.0 (GraphPad Software, Inc., San Diego, CA, USA). Non-parametric *t*-tests were used to compare two groups at each time point. Values with $p < 0.05$ were considered statistically significant.

3. Results

3.1. Characterizations of C-shaped PCL and GelMA/PCL scaffolds

Customized 3D models for a C-shaped ring and SPC was designed (see Figure S1, Supporting Information). To optimize the distance of internal line of C-shaped PCL scaffold, the distance of the internal line was set to 1.0, 1.5, and 2 mm to 3D-print 1.0, 1.5, and 2.0 mm C-shaped PCL scaffold. The printed C-shaped PCL scaffold could maintain their original shape (Figure 2A1–A3). Moreover, Figure 2A1–A3 demonstrates that the pore size of the C-shaped PCL scaffold increased as the spacing between the internal lines widened. The pictures of side view of C-shaped PCL scaffold (Figure 2A4), SPC-CcGP construct (Figure 2A5), and TETC (Figure 2A6) are shown. We further evaluated the compressive strength and elastic modulus of C-shaped PCL scaffolds with 1.0, 1.5, and 2.0 mm. Compression tests revealed that the 1.0 mm scaffold exhibited the highest resistance to compression, followed by the 1.5 and 2.0 mm scaffolds (Figure 2B). Additionally, the elastic modulus for the 1.0, 1.5, and 2.0 mm scaffolds was measured as 23.001 ± 1.776, 18.739 ± 1.467, and 14.549 ± 1.185 kPa, respectively (Figure 2C). Figure 2D shows the volume for the 1.0, 1.5, and 2.0 mm scaffolds was 134 ± 10, 170 ± 3, and 241 ± 4 μL. Considering that the 1.5 mm C-shaped PCL scaffold demonstrated a balance of favorable mechanical properties and sufficient gap volume, it was selected for subsequent experiments. Figure 2E and F indicates that the maximum stress of both the single PCL (1.5 mm) and GelMA/PCL (1.5 mm) groups was greater than that of the single natural tracheal cartilage; however, no statistical significance was observed between the single PCL (1.5 mm) and GelMA/PCL (1.5 mm) groups. Additionally, Figure 2G and H demonstrates that the maximum force exerted by the SPC-CcGP construct in various directions is superior to that of natural trachea of the same length. Figure 2I demonstrates that the biodegradation rate of the GelMA/PCL scaffold was higher than that of the pure PCL scaffold, likely due to the faster degradation of the GelMA component within the composite structure. As shown in Figure 2J, the cumulative release of VEGF from the VEGF@GelMA hydrogel reached approximately 58.8% at 96 h, indicating that sustained release of VEGF can be achieved with the VEGF@GelMA hydrogel over this duration.

3.2. Bioactivity of GelMA/PCL on chondrocytes

Live/dead staining revealed that chondrocytes in both the GelMA/PCL and GelMA groups exhibited high viability with minimal cell death. Notably, the increase in green fluorescent signals over time may be attributed to the proliferation of chondrocytes in the GelMA (Figure 3B). F-actin/DAPI staining showed no significant differences in cell spreading between the GelMA/PCL and GelMA groups on days 1, 3, and 5 (Figure 3B). These observations were further confirmed by quantitative analysis of cell viability (Figure 3C) and CCK8 (Figure 3D). The results of DNA quantification indicated that there was no statistically significant difference in cell proliferation between the GelMA/PCL and GelMA groups on days 1, 3, and 5 (Figure 3E).

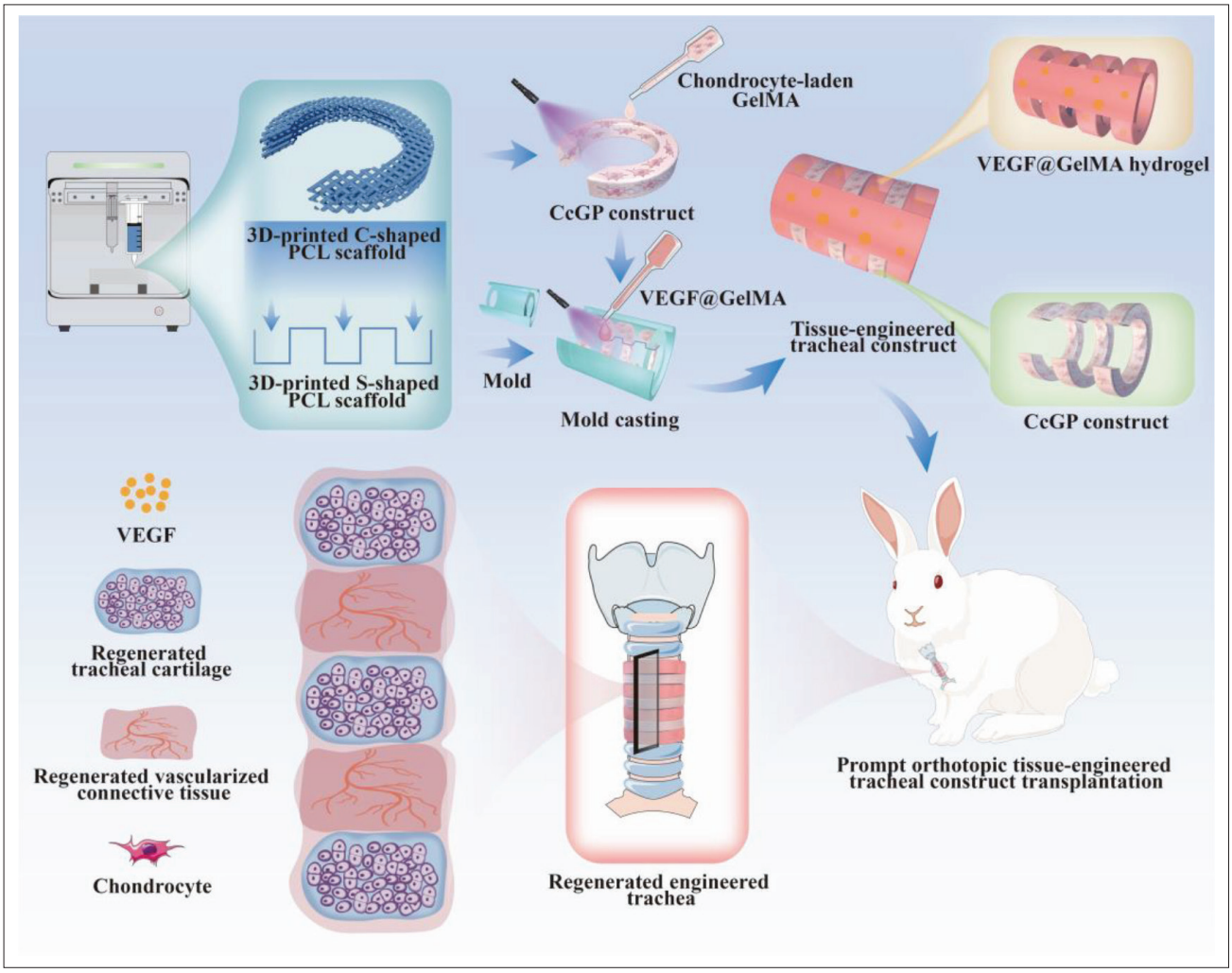

Figure 1. Schematic diagram of the overall experiments. First, C-shaped PCL scaffolds and S-shaped PCL chains were fabricated using 3D printing technology. Next, the chondrocyte-laden GelMA hydrogel was introduced into the gaps of the C-shaped PCL scaffold and crosslinked via photopolymerization to form the C-shaped chondrocyte-laden GelMA/PCL (CcGP) construct. The CcGP construct was then integrated into the S-shaped PCL chains (SPC) to create the SPC-CcGP construct. Subsequently, the SPC-CcGP construct was placed into a mold, and VEGF@GelMA hydrogel was poured into the gaps to generate the tissue-engineered tracheal construct (TETC). Finally, the TETC was used to regenerate biomimetic trachea in a rabbit model with a long-segment tracheal defect. Abbreviations: CcGP, C-shaped chondrocyte-laden GelMA/PCL; GelMA, gelatin methacrylate; PCL, polycaprolactone; VEGF, vascular endothelial growth factor.

3.3. Bioactivity of VEGF@GelMA hydrogel on HUVECs

Cell migration was assessed using a cell scratch assay. Results showed that the VEGF@GelMA group (75.44 ± 4.99%) exhibited enhanced cellular migration of HUVECs compared to GelMA group (40.60 ± 3.40%) (Figure 4A and B). Additionally, the tube formation assay demonstrated the same trend. Figure 4C revealed that the VEGF@GelMA group displayed a significantly higher number of tubes and increased tube length compared to GelMA group. The quantitative results presented consistent trends (Figure 4D and E). Compared with the GelMA group, the quantitative RT-PCR results for the VEGF@GelMA group showed higher expression of angiogenic genes, including *NOS3*, *FGF2*, and *HIF1A* (Figure 4F–H). In addition, Western blot results also showed higher protein expressions of eNOS, FGF2, and HIF-1α in VEGF@GelMA group compared with GelMA group (Figure S2, Supporting Information). These findings highlighted the enhanced angiogenic potential of VEGF@GelMA hydrogel, indicating its suitability for promoting angiogenesis and tissue regeneration applications.

3.4. Cartilage regeneration of CcGP construct *in vitro* and *in vivo*

To assess the cartilage regeneration ability of CcGP construct, C-shaped cartilage rings were regenerated and evaluated *in vitro* (Figure 5A). After 3 weeks of

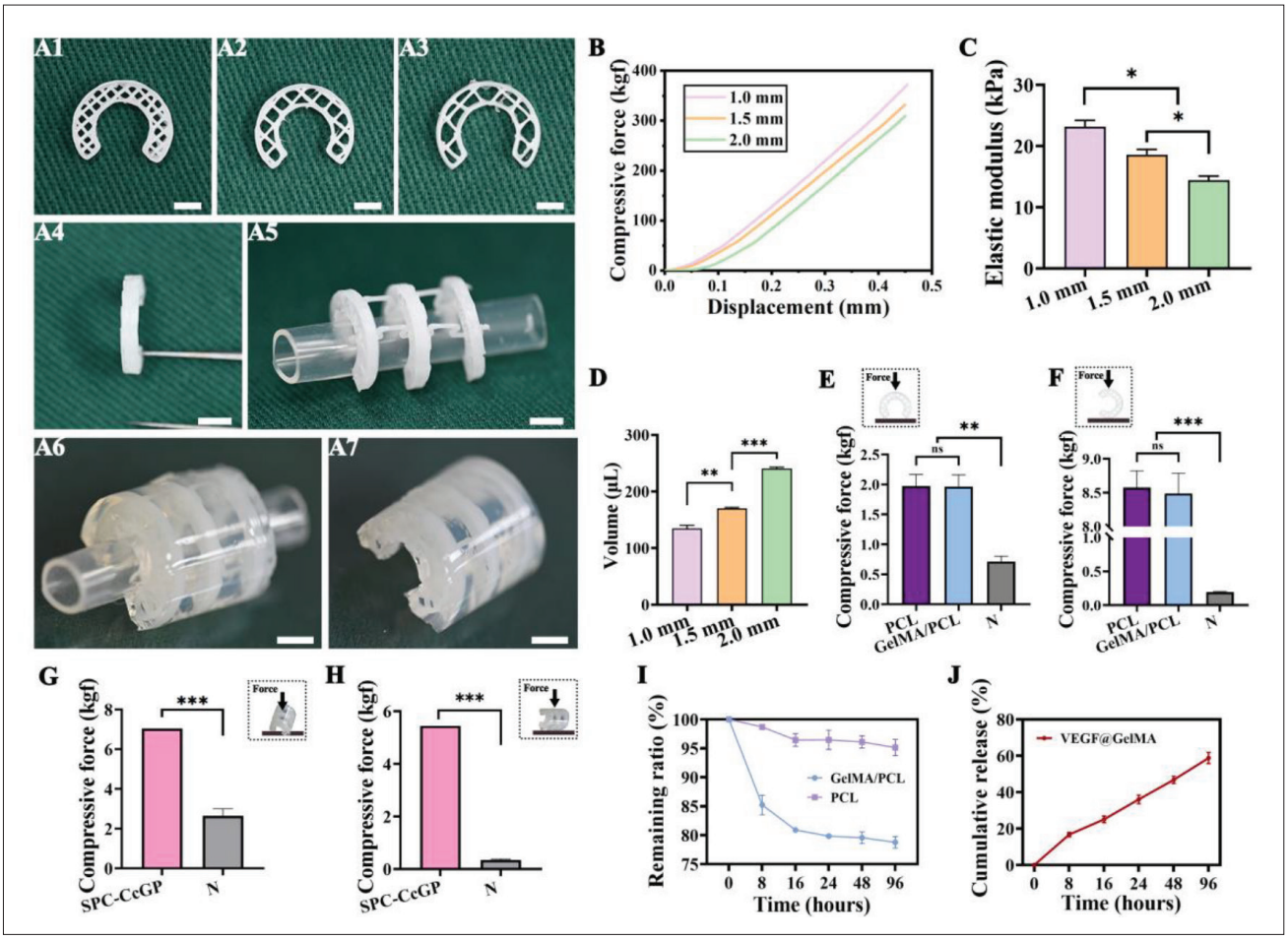

Figure 2. Characterizations of the 3D-printed C-shaped GelMA/PCL and PCL scaffolds. (A1–A3) 3D-printed 1.0 mm (A1), 1.5 mm (A2), and 2.0 mm (A3) PCL scaffolds in C shape. (A4) Side view of C-shaped PCL scaffold. (A5–A7) Fabrication of SPC-CcGP construct (A5) and TETC (A6, A7) with the assistance of a silicone tube. Scale bars: 3 mm. (B) Compressive force and (C) elastic modulus of 1.0, 1.5, and 2.0 mm C-shaped PCL scaffolds. (D) The volume of the gaps of the C-shaped PCL scaffold. (E, F) Compressive forces applied in various directions on the single PCL, GelMA/PCL, and natural tracheal cartilage (N). (G, H) Compressive forces applied in various directions on the SPC-CcGP construct and natural trachea (N). (I) *In vitro* biodegradability of GelMA/PCL and pure PCL scaffold. (J) Cumulative release kinetics of VEGF from the VEGF@GelMA hydrogel. $*p < 0.05$, $**p < 0.01$, $***p < 0.001$. Abbreviations: CcGP, C-shaped chondrocyte-laden GelMA/PCL; GelMA, Gelatin methacrylate; N, natural tracheal tissue/natural trachea; PCL, polycaprolactone; SPC, S-shaped PCL chains.

chondrogenic culture *in vitro*, H&E staining revealed that CcGP construct could form prominent cartilage-specific lacunae. The results of safranin-O, collagen II, and Masson's trichrome staining indicated that regenerated cartilage of CcGP construct had cartilage-specific extracellular matrix (ECM) deposition (Figure 5B). The cartilage-regenerating ability of CcGP construct was further evaluated in nude mice (Figure 5C). Figure 5D shows the intact C-shaped geometry of regenerated C-shaped cartilage rings. The H&E staining revealed that the regenerated cartilage of CcGP construct developed typical lacunae, and a homogeneous structure was observed at 3 weeks. The intense and homogeneous staining of safranin-O, collagen II, and Masson's trichrome indicated that cartilage-specific ECM deposition formed after 3 weeks cultivation in nude mice (Figure 5D). Furthermore, GAG content and total collagen content validated that the regenerated cartilage of CcGP construct matured with prolonged *in vitro* (Figure 5E and F) and *in vivo* (Figure 5G and H) incubation.

3.5. Regeneration of cartilage and vascularized connective tissue after prompt orthotopic transplantation of trachea

A long segmental tracheal defect in rabbit model was established (Figure S3A–B, Supporting Information), and the TETC was used to orthotopically reconstruct this tracheal defect (Figure S3C, Supporting Information). The gross and endoscopic images in Figure 6A demonstrate that the regenerated engineered tracheal tissue maintained an unobstructed lumen for 3 weeks, with no evidence of

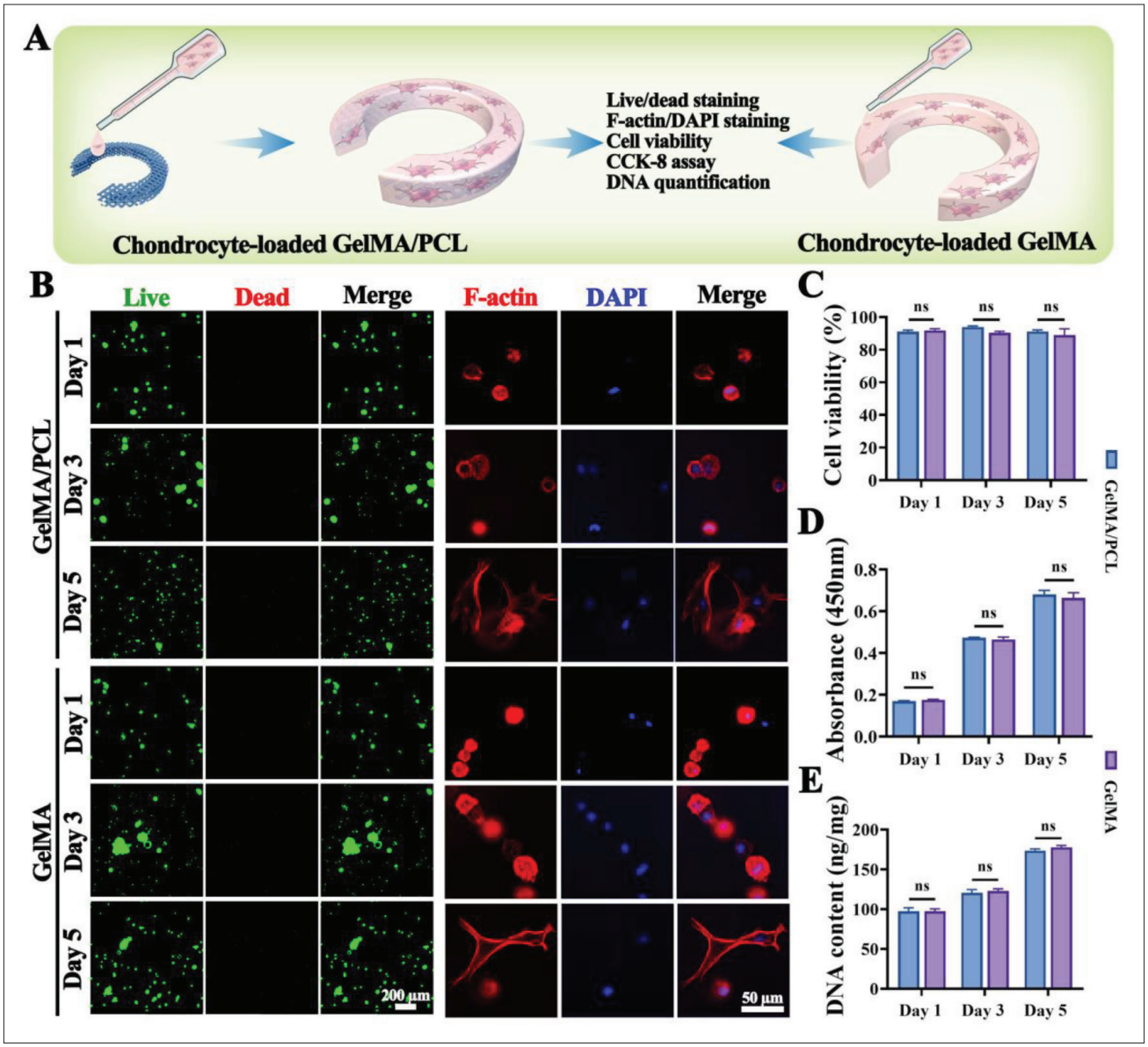

Figure 3. Bioactivity of GelMA/PCL and pure GelMA hydrogel on chondrocytes. (A) Schematic representation of chondrocyte-loaded GelMA/PCL and GelMA hydrogel. (B) Live/dead and F-actin/DAPI staining of chondrocytes in GelMA/PCL and pure GelMA. (C–E) Results on cell viability (C), cell proliferation based on CCK-8 assay (D) and DNA quantification (E) in chondrocyte-loaded GelMA/PCL and GelMA hydrogels on days 1, 3, and 5. Abbreviations: GelMA, gelatin methacrylate; ns, no statistical significance; PCL, polycaprolactone.

airway obstruction. The vertical and sectional views of the orthotopically regenerated engineered tracheal tissue after 4 and 6 weeks indicate the integration of tubular structure (Figure S4A–B, Supporting Information), suggesting that the mechanical strength of the engineered trachea is sufficient to preserve lumen patency. Besides, through repeated application of force to the implanted bioengineered trachea, we observed that the bioengineered trachea effectively maintained the shape of the lumen without causing obstruction (Video S1, Supporting Information). Furthermore, the experimental animals exhibited no signs of coughing, wheezing, or shortness of breath. Figure 6B shows schematic representation of the orthotopically regenerated engineered tracheal tissue. Compared to wide inner-diameter blood vessels of native trachea (Figure 6C), the regenerated engineered tracheal tissue exhibited a smaller lumen but a higher density of neovascularization (Figure 6D). Quantitative analysis showed that the VEGF/GelMA group promoted significantly more neovascularization compared to GelMA alone (Figure 6E).

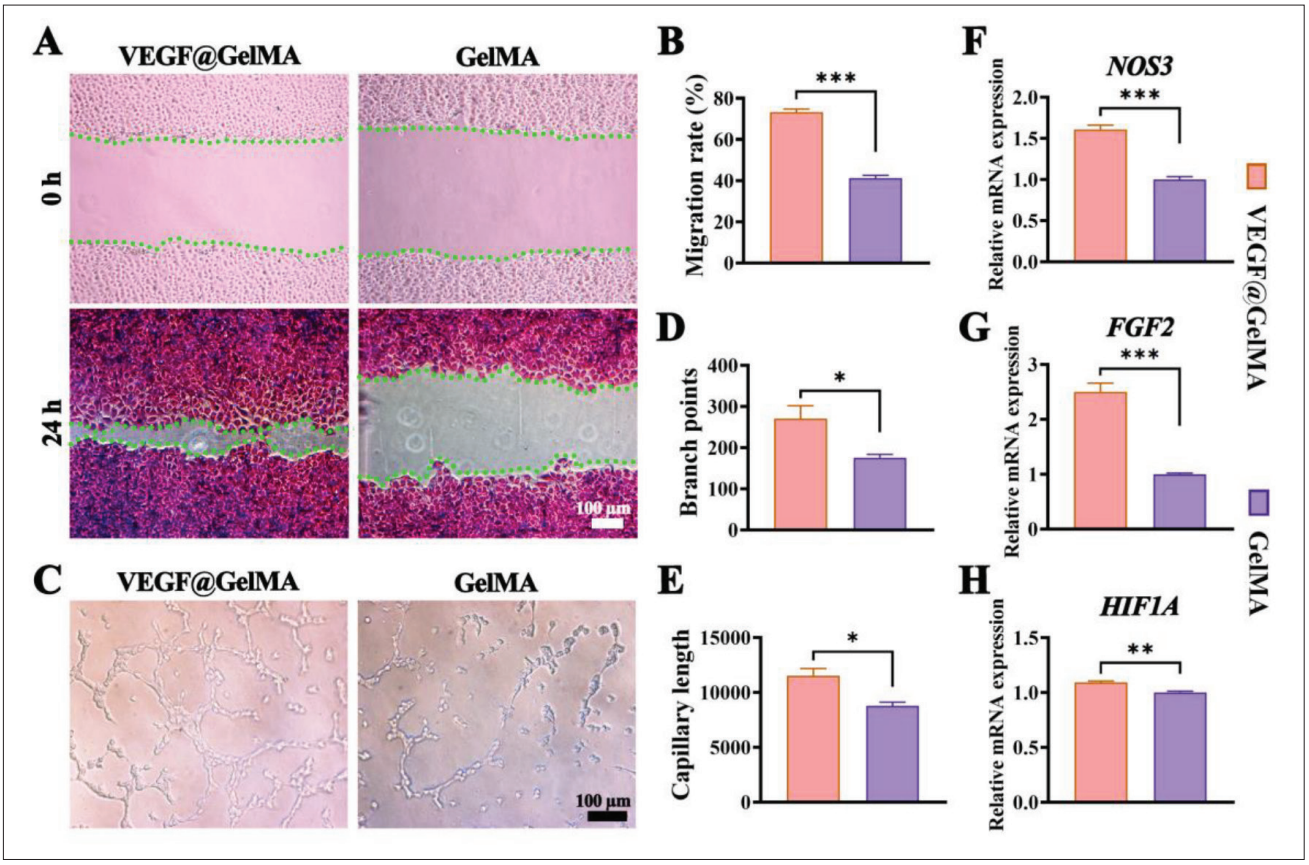

Figure 4. Angiogenic evaluation of VEGF@GelMA and pure GelMA hydrogel on HUVECs. (A, B) HUVEC migration ability as determined by cell scratch assay (A) and the corresponding quantitative outcomes (B). (C–E) Results of tube formation assay (C) and the quantitative outcomes regarding branch point number (D) and capillary length (E) of HUVECs. (F–H) Expression levels of key angiogenesis-related genes in HUVECs. *$p < 0.05$, **$p < 0.01$, ***$p < 0.001$. Abbreviations: GelMA, gelatin methacrylate; VEGF, vascular endothelial growth factor.

Masson's trichrome staining demonstrated that the regenerated C-shaped cartilage rings maintained their geometry 3 weeks after orthotopic transplantation. H&E staining revealed the formation of prominent cartilage-specific lacunae in the regenerated tracheal cartilage. Additionally, Safranin-O staining indicated the presence of cartilage-specific ECM deposition after 3 weeks (Figure 6F). Quantitative analysis further revealed that GAG content and total collagen content in the regenerated tracheal cartilage increased at 6 weeks compared to 3 weeks (Figure 6G and H). These findings confirmed that the TETC effectively repair tracheal defects, maintain lumen patency, and promote both neovascularization and cartilage regeneration.

4. Discussion

Currently, a strategy of direct excision and end-to-end anastomosis of the trachea is not feasible in adult patients, when more than half of the airway is affected.[20] Tracheal tissue engineering offers promising potential to address this clinical challenge. Several tracheal replacement strategies have been developed, including intact cartilaginous tubes and assembled constructs featuring either interrupted O-shaped or C-shaped cartilage rings.[21] However, these approaches faced challenges, such as the deformation of 3D-printed C-shaped cell-laden hydrogels, the tendency of regenerated C-shaped cartilage to fuse, and the difficulty in regenerating vascularized connective tissue.

Emerging 3D extrusion bioprinting strategies based on photocrosslinkable hydrogels have proven to be an attractive technology for the construction of heterogeneous tissue architectures.[22] Our preliminary research demonstrated that 3D printing of cell-laden photocrosslinked hydrogels allowed for precise shape control in order to mimic tracheal tissue. However, regenerating biomimetic tracheal tissue *in vivo* often resulted in deformation due to compression from surrounding tissues.[4] We hypothesized that this deformation was likely caused by the insufficient mechanical strength of the hydrogel, restraining immediate and effective tracheal reconstruction. Additionally, regenerating engineered trachea typically

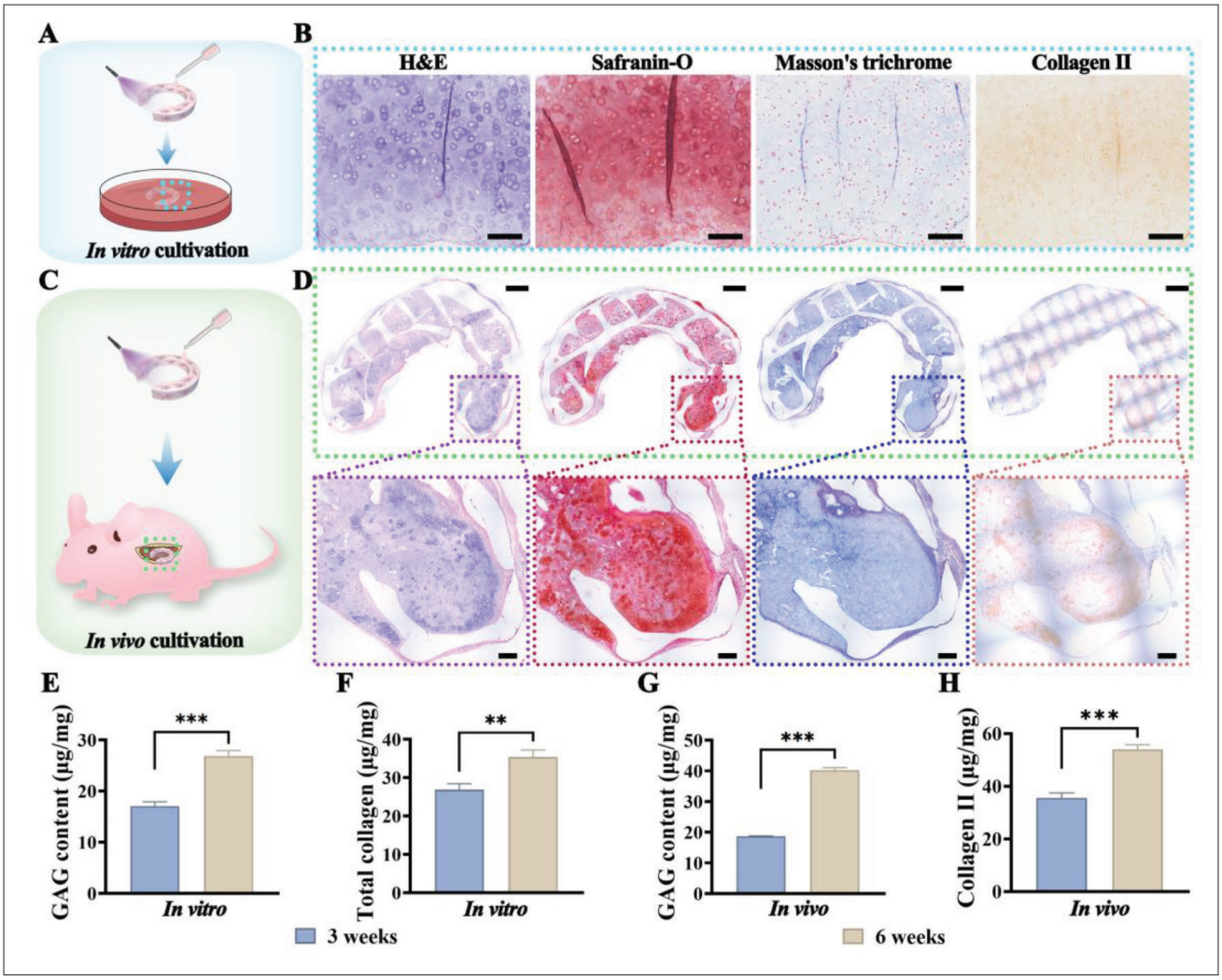

Figure 5. Cartilage regeneration of CcGP construct after *in vitro* and *in vivo* cultivation. (A) Schematic representation of *in vitro* regeneration of cartilage using chondrocyte-loaded GelMA hydrogel (blue dotted box indicates the regenerated cartilage *in vitro*). (B) Representative images of H&E, Safranin-O, Masson's trichrome, immunohistochemical collagen II staining of chondrocyte-loaded GelMA hydrogel after 3 weeks of *in vitro* chondrogenic culture. Scale bar: 200 μm. (C) Schematic representation of *in vivo* regeneration of C-shaped cartilage using CcGP construct (green-dotted box indicates the regenerated cartilage *in vivo*). (D) Representative images of H&E, Safranin-O, Masson's trichrome, immunohistochemical collagen II staining of chondrocyte-loaded GelMA hydrogel after 3 weeks in nude mice. Scale bar: 2 mm (main); 500 μm (inset). (E–H) Contents of GAG and collagen II, *in vitro* and *in vivo*, at 3 and 6 weeks. $^{**}p < 0.01$, $^{***}p < 0.001$. Abbreviations: CcGP, C-shaped chondrocyte-laden GelMA/PCL; GAG, Glycosaminoglycan; H&E, Hematoxylin-eosin.

requires a two-stage approach, involving intramuscular pre-implantation followed by end-to-end anastomosis through pedicled muscle transplantation, which is an intricate and time-consuming operation.[23] Researchers have explored the use of 3D bioprinted C-shaped TETCs for direct end-to-end anastomosis to repair segmental defects in the rabbit trachea, highlighting the potential of advanced 3D bioprinting for rapid and effective tracheal reconstruction.[5] Nevertheless, simply constructing TETCs with cell-laden hydrogels often lacks sufficient mechanical strength in the early stages of regeneration, necessitating internal support to maintain lumen patency.[5] Further, a "concrete-rebar structure" has been proposed as a strategy for tracheal tissue engineering. In this approach, bioengineered cartilage rings are fabricated by 3D-printing PCL combined with rabbit chondrocytes, while transmural angiogenesis is promoted by incorporating 3D printing PCL fibers and GelMA. Although this method offers early mechanical support for TETC, it involves an intricate and time-consuming operation to achieve full reconstruction.[13]

Here, we utilized a chondrocyte-laden GelMA and VEGF@GelMA hydrogel approach to simplify the

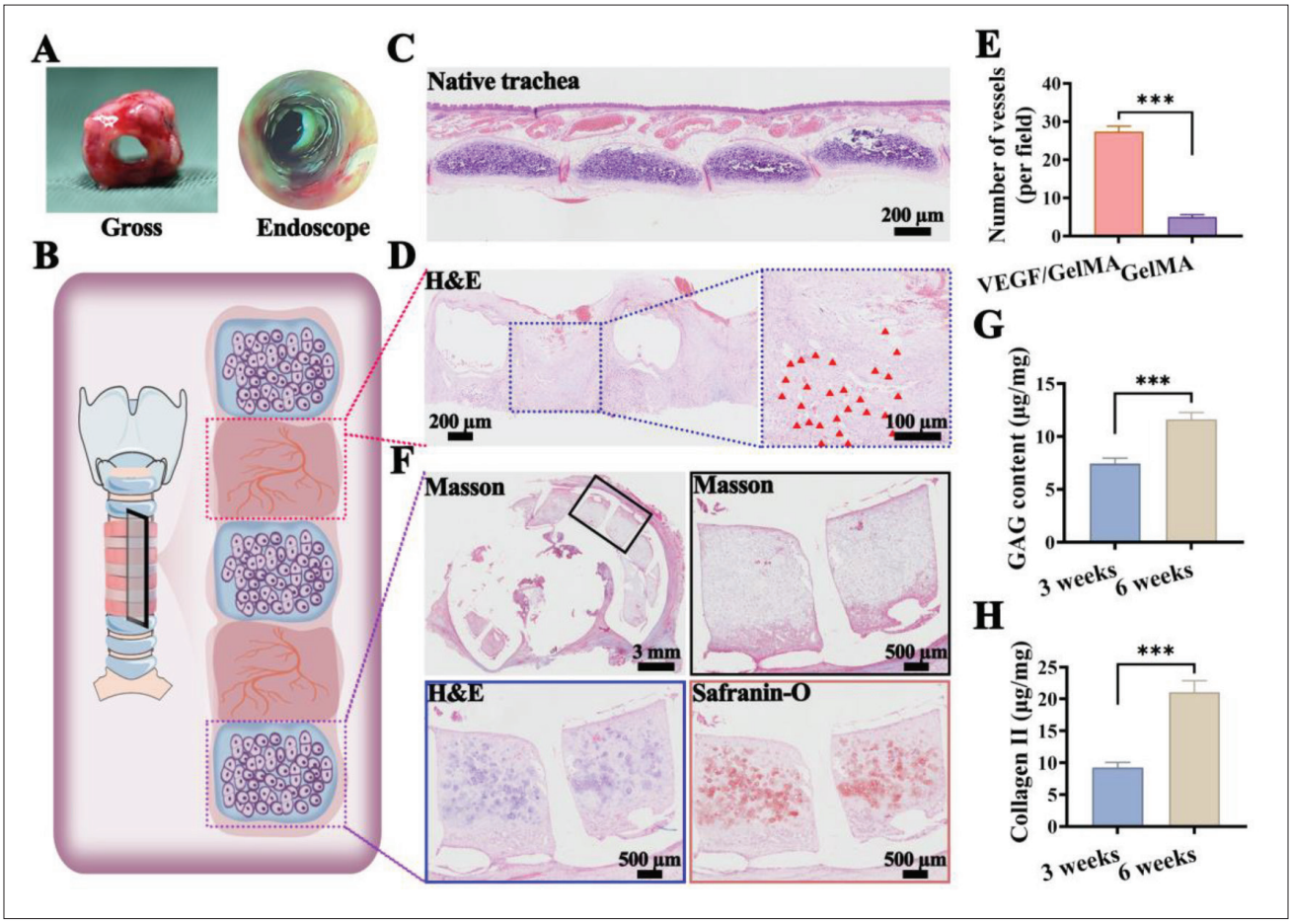

Figure 6. Prompt repair of tracheal defects using TETC in a rabbit model. (A) Gross view and endoscopic images at 3 weeks of regenerating engineered tracheal tissue. (B) Schematic representation of orthotopic regeneration of engineered tracheal tissue (red-dotted box indicates the regenerated vascularized connective tissue, whereas purple-dotted box indicates the regenerated cartilage). (C, D) H&E staining of native trachea (C) and regenerated vascularized connective tissue (D) after orthotopic tracheal transplantation at 3 weeks. (E) Number of vessels per field in VEGF/GelMA and GelMA hydrogels. (F) Masson's trichrome, H&E, safranin-O staining of regenerated tracheal tissue after orthotopic tracheal transplantation at 3 weeks. (G, H) GAG content (G) and collagen II content (H) at 3 and 6 weeks.***p <0.001. Abbreviations: GAG, glycosaminoglycan; GelMA, gelatin methacrylate; H&E, Hematoxylin-eosin; TETC, tissue-engineered tracheal construct; VEGF, vascular endothelial growth factor.

preparation process of TETC. The CcGP construct provided essential mechanical support to the engineered trachea, maintaining an unobstructed lumen and preventing cartilage deformation under compressive forces. The incorporation of SPC effectively maintained the spacing between the engineered tracheal cartilage, preventing fusion of the regenerated C-shaped cartilage and allowing space for the ingrowth of connective tissue. Blood vessels play a crucial role in wound healing and tissue regeneration, and vessel ingrowth from the host tissues into the TETC is vital for supplying adequate nutrients to the regenerated cartilage during tracheal defect reconstruction.[24,25] To facilitate this, we filled the gaps in the SPC-CcGP construct with VEGF@GelMA hydrogel to construct the TETC with sufficient mechanical strength and effective vascular regeneration for timely tracheal defect repair.

VEGF is a critical regulator of angiogenesis, the process of new blood vessel formation. It facilitates endothelial cell proliferation, migration, and differentiation, leading to capillary development and increased vascular permeability. This function is essential for providing an adequate supply of nutrients and oxygen to cartilage, particularly during regeneration.[26] Furthermore, VEGF has been demonstrated to enhance chondrocyte proliferation and promote the synthesis of cartilage-specific ECM components, such as collagen and proteoglycans.[27] The establishment of a vascular network is vital for meeting the metabolic demands of regenerating cartilage, thereby contributing to its structural integrity and overall functionality.

Our *in vitro* results demonstrated that the C-shaped PCL scaffold possesses sufficient mechanical properties

and biocompatibility, as evidenced by subcutaneous cartilage regeneration in nude mice. Additionally, *in vitro* experiments confirmed that VEGF@GelMA hydrogel effectively promotes angiogenesis. We selected PCL and GelMA for scaffold fabrication due to its excellent biodegradability and biocompatibility.[28,29] We speculated that the regenerated tracheal cartilage will progressively exhibit the mechanical support role of the C-shaped PCL scaffold with the degradation of PCL and GelMA. Furthermore, the formation of vascularized connective tissue will tightly bind the regenerated C-shaped tracheal cartilage, facilitating the successful regeneration of the engineered trachea.

Even though TETC can achieve stable regeneration of cartilage and vascularized connective tissue, as well as maintain luminal patency, it still has a certain limitation: a longer experimental period is needed to further verify the relationship between PCL degradation and the regeneration of cartilage tissue and vascularized connective tissue. Further evaluation of infection and inflammation indexes is necessary to assess their impact on TETC outcomes.

5. Conclusion

In this study, we initially utilized a 3D-printed C-shaped PCL scaffold to provide early mechanical support for the regenerated engineered trachea. Subsequently, mold casting was applied to construct TETC, which could effectively promote the regeneration of interspersed cartilage and vascularized connective tissue simultaneously. This strategy is expected to offer a promising strategy for prompt tracheal defect repair.

Acknowledgments

None.

Funding

The research was supported by the National Natural Science Foundation of China (82300068, 82102227, and 82302395), Young Elite Scientists Sponsorship Program by CAST (2023QNRC001), and the Natural Science Foundation of Shanghai (22YF1437400).

Conflict of interest

The authors declare that they have no conflicts of interest.

Author contributions

Conceptualization: Pengli Wang
Formal analysis: Lei Xie
Investigation: Ziming Wang
Methodology: Bohui Li
Writing–original draft: Liang Guo and Yong Xu
Writing–review & editing: Dan Li, Jiaoyu Yi and Tao Bo

Ethics approval and consent to participate

All animal experiments were performed in accordance with the Guide for the Care and Use of Laboratory Animals guidelines and were approved by the Shanghai Pulmonary Hospital Ethics Committee (K21-355Y).

Consent for publication

Not applicable.

Availability of data

The data that support the findings of this study are available from the corresponding author upon reasonable request.

References

1. Wei S, Zhang Y, Luo F, et al. Tissue-engineered tracheal implants: advancements, challenges, and clinical considerations. *Bioeng Transl Med*. 2024;9(4):e10671. doi: 10.1002/btm2.10671
2. Furlow PW, Mathisen DJ. Surgical anatomy of the trachea. *Ann Cardiothorac Surg*. 2018;7(2): 255-260. doi: 10.21037/acs.2018.03.01
3. Matai I, Kaur G, Seyedsalehi A, McClinton A, Laurencin CT. Progress in 3D bioprinting technology for tissue/organ regenerative engineering. *Biomaterials*. 2020;226:119536. doi: 10.1016/j.biomaterials.2019.119536
4. Wang P, Wang T, Xu Y, Song N, Zhang X. 3D-bioprinted cell-laden hydrogel with anti-inflammatory and anti-bacterial activities for tracheal cartilage regeneration and restoration. *IJB*. 2023;10(1):0146. doi: 10.36922/ijb.0146
5. Sun Y, Huo Y, Ran X, et al. Instant trachea reconstruction using 3D-bioprinted C-shape biomimetic trachea based on tissue-specific matrix hydrogels. *Bioact Mater*. 2024;32:52-65. doi: 10.1016/j.bioactmat.2023.09.011
6. Song X, Zhang P, Luo B, et al. Multi-tissue integrated tissue-engineered trachea regeneration based on 3D printed bioelastomer scaffolds. *Adv Sci*. 2024;11(39):e2405420. doi: 10.1002/advs.202405420
7. Hsieh C.-T., Liao C.-Y., Dai N.-T., et al. 3D printing of tubular scaffolds with elasticity and complex structure from multiple waterborne polyurethanes for tracheal tissue engineering. *Appl Mater Today*. 2018;12:330-341. doi: 10.1016/j.apmt.2018.06.004
8. Park JH, Ahn M, Park SH, et al. 3D bioprinting of a trachea-mimetic cellular construct of a clinically relevant size. *Biomaterials*. 2021;279:121246. doi: 10.1016/j.biomaterials.2021.121246

9. Park JH, Park JY, Nam I-C, et al. A rational tissue engineering strategy based on three-dimensional (3D) printing for extensive circumferential tracheal reconstruction. *Biomaterials*. 2018;185: 276-283. doi: 10.1016/j.biomaterials.2018.09.031

10. Xu Y, Guo Y, Li Y, et al. Biomimetic trachea regeneration using a modular ring strategy based on poly(sebacoyl diglyceride)/polycaprolactone for segmental trachea defect repair. *Adv Funct Mater*. 2020;30(42):2004276. doi: 10.1002/adfm.202004276

11. Xu Y, Dai J, Zhu X, et al. Biomimetic trachea engineering via a modular ring strategy based on bone-marrow stem cells and atelocollagen for use in extensive tracheal reconstruction. *Adv Mater*. 2022;34(6):2106755. doi: 10.1002/adma.202106755

12. Park JH, Hong JM, Ju YM, et al. A novel tissue-engineered trachea with a mechanical behavior similar to native trachea. *Biomaterials*. 2015;62:106-115. doi: 10.1016/j.biomaterials.2015.05.008.

13. Tang H, Sun W, Liu X, et al. A bioengineered trachea-like structure improves survival in a rabbit tracheal defect model. *Sci Transl Med*. 2023;15(714):eabo4272. doi: 10.1126/scitranslmed.abo4272

14. Gao E, Wang Y, Wang P, et al. C-shaped cartilage development using Wharton's Jelly-derived hydrogels to assemble a highly biomimetic neotrachea for use in circumferential tracheal reconstruction. *Adv Funct Mater*. 2023;33(14):2212830. doi: 10.1002/adfm.202212830

15. Luo X, Liu Y, Zhang Z, et al. Long-term functional reconstruction of segmental tracheal defect by pedicled tissue-engineered trachea in rabbits. *Biomaterials*. 2013; 34(13): 3336-3344. doi: 10.1016/j.biomaterials.2013.01.060

16. Li D, Yin Z, Liu Y, et al. Regeneration of trachea graft with cartilage support, vascularization, and epithelization. *Acta Biomater*. 2019;89: 206-216. doi: 10.1016/j.actbio.2019.03.003

17. Xu Y, Duan L, Li Y, et al. Nanofibrillar decellularized Wharton's Jelly matrix for segmental tracheal repair. *Adv Funct Mater*. 2020;30(14):1910067. doi: 10.1002/adfm.201910067

18. Gao E, Li G, Cao R, et al. Bionic tracheal tissue regeneration using a ring-shaped scaffold comprised of decellularized cartilaginous matrix and silk fibroin. *Compos B: Eng*. 2022;229:109470. doi: 10.1016/j.compositesb.2021.109470

19. Xu W, Wu Y, Lu H, et al. Sustained delivery of vascular endothelial growth factor mediated by bioactive methacrylic anhydride hydrogel accelerates peripheral nerve regeneration after crush injury. *Neural Regen Res*. 2022;17(9):2064-2071. doi: 10.4103/1673-5374.335166

20. Dikina AD, Alt DS, Herberg S, et al. A modular strategy to engineer complex tissues and organs. *Adv Sci (Weinh)*. 2018;5(5):1700402. doi: 10.1002/advs.201700402

21. Damiano G, Palumbo VD, Fazzotta S, et al. Current strategies for tracheal replacement: a review. *Life (Basel)*. 2021;11(7):618. doi: 10.3390/life11070618

22. Zhang YS, Haghiashtiani G, Hübscher T, et al. 3D extrusion bioprinting. *Nat Rev Methods Primers*. 2021;1(1):75. doi: 10.1038/s43586-021-00073-8

23. Xu Y, Li D, Yin Z, et al. Tissue-engineered trachea regeneration using decellularized trachea matrix treated with laser micropore technique. *Acta Biomater*. 2017;58:113-121. doi: 10.1016/j.actbio.2017.05.010

24. Crowley C, Klanrit P, Butler CR, et al. Surface modification of a POSS-nanocomposite material to enhance cellular integration of a synthetic bioscaffold. *Biomaterials*. 2016; 83:283-293. doi: 10.1016/j.biomaterials.2016.01.005

25. Eming SA, Martin P, Tomic-Canic M. Wound repair and regeneration: mechanisms, signaling, and translation. *Sci Transl Med*. 2014;6(265):265sr6. doi: 10.1126/scitranslmed.3009337

26. Hu K, Olsen BR. Vascular endothelial growth factor control mechanisms in skeletal growth and repair. *Dev Dyn*. 2017;246(4):227-234. doi: 10.1002/dvdy.24463

27. Li M, Yin H, Yan Z, et al. The immune microenvironment in cartilage injury and repair. *Acta Biomater*. 2022;140:23-42. doi: 10.1016/j.actbio.2021.12.006

28. Li X, Cho B, Martin R, et al. Nanofiber-hydrogel composite–mediated angiogenesis for soft tissue reconstruction. *Sci Transl Med*. 2019;11(490):eaau6210. doi: 10.1126/scitranslmed.aau6210

29. Liu Y, Zheng K, Meng Z, et al. A cell-free tissue-engineered tracheal substitute with sequential cytokine release maintained airway opening in a rabbit tracheal full circumferential defect model. *Biomaterials*. 2023;300:122208. doi: 10.1016/j.biomaterials.2023.122208

ACCSCIENCE PUBLISHING

International Journal of Bioprinting

RESEARCH ARTICLE

Sericin improves alginate-gelatin hydrogels' mechanical properties, porosity, durability, and viability of fibroblasts in cardiac spheroids

Martine Tarsitano[1,2], Clara Liu Chung Ming[1,3], Dana Idais[1,3], Hadi Mahmodi[4], Kaitlin Wyllie[5,6], Benedetta Isella[7], Thomas R. Cox[5,6], Irina Kabakova[4], Donatella Paolino[2,8], and Carmine Gentile[1,3]*

[1]School of Biomedical Engineering, Faculty of Engineering and IT, University of Technology Sydney, Ultimo, Sydney, NSW, Australia

[2]Department of Experimental and Clinical Medicine, School of Medicine and Surgery, University "Magna Graecia" of Catanzaro, Catanzaro, Italy

[3] Heart Research Institute, Newtown, Sydney, NSW, Australia

[4]School of Mathematical and Physical Sciences, Faculty of Science, University of Technology Sydney, Ultimo, NSW, Australia

[5]The Garvan Institute of Medical Research and The Kinghorn Cancer Centre, Darlinghurst, NSW, Australia

[6]School of Clinical Medicine, St Vincent's Healthcare Clinical Campus, UNSW Medicine and Health, Sydney, NSW, Australia

[7] Fibrothelium GmbH, Philipsstraße 8, Aachen, Germany

[8]Research Center "ProHealth Translational Hub", Department of Experimental and Clinical Medicine, "Magna Graecia" University of Catanzaro, Catanzaro, Italy

(This article belongs to the Special Issue: *3D Bioprinting DownUnder: Innovation, Advancements and Perspectives*)

***Corresponding author:**
Carmine Gentile
(carmine.gentile@uts.edu.au)

Citation: Tarsitano M, Ming CLC, Idais D, et al. Sericin improves alginate-gelatin hydrogels' mechanical properties, porosity, durability, and viability of fibroblasts in cardiac spheroids. *Int J Bioprint*. 2025;11(1):327-346. doi: 10.36922/ijb.5678

Received: October 29, 2024
Revised: November 21, 2024
Accepted: November 26, 2024
Published Online: November 27, 2024

Copyright: © 2024 Author(s). This is an Open Access article distributed under the terms of the Creative Commons Attribution License, permitting distribution, and reproduction in any medium, provided the original work is properly cited.

Publisher's Note: AccScience Publishing remains neutral with regard to jurisdictional claims in published maps and institutional affiliations.

Abstract

Biofabrication of cardiac patches is a challenging strategy proposed as an alternative to transplantation for end-stage heart failure patients. The optimization of the bioink used for this strategy can be limited by costs, properties, and biocompatibility of its building blocks. Lately, sericin has emerged within a wide range of natural proteins, thanks to its bioadhesive and biocompatibility potential. In this study, we assessed for the first time the effects of adding silk sericin on alginate-gelatin hydrogels, proposed for cardiac applications. To this aim, we first biofabricated sericin-containing hydrogels with increasing protein concentrations. Thus, we characterized hydrogels' mechanical behavior, porosity and structure through rheology, Brillouin microspectroscopy, and scanning electron microscopy. Then, we bioprinted the formulated hydrogels and evaluated their effects on human cardiac spheroids (CSs) *in vitro*. Our mechanical characterization demonstrated that adding sericin significantly enhanced the elasticity and the viscosity of alginate-gelatin hydrogels. Sericin also modified hydrogels' swelling behavior and their pore size, increasing by 20%, 62%, and 92% in Ser1%, Ser2%, and Ser3%, respectively. Although Ser1% did not exhibit significant effects on CSs, Ser2% and Ser3% enhanced cardiac cell viability for up to 14 days compared to the sericin-free hydrogel by acting on the fibroblast population. Sericin-based bioinks showed better printability and durability with +33% and +28% intact patches after 28 days of culture at 37°C compared to alginate-gelatin. Taken together, our results validated the use of sericin as a promising component for the optimization of bioink intended for cardiac applications.

Keywords: Sericin; Hydrogels; Cardiac spheroids; Myocardial infarction; Biomaterials; Alginate; Gelatin; 3D bioprinting

1. Introduction

Myocardial infarction (MI) remains a leading cause of morbidity and mortality worldwide.[1] By itself, an adult myocardium has low regenerative capacity compared to other tissues in the human body, especially when myocardial cells have been damaged after MI.[2] Instead of replacing the injured area with functional tissue, the physiological repairing response after MI results in the formation of fibrotic scar tissue, which thickens the heart wall and triggers left ventricular remodeling.[3] These events reduce the mechanical support to the organ, which is deprived of its full functionality to pump blood, due to the increased workload and oxygen demand, contributing to an increased risk of arrhythmias and the development of a failing heart.[4] The permanent remedy for patients with end-stage heart failure (HF) is heart transplantation.[5] However, heart transplantation is restricted by limited donors' availability and is associated with several post-surgery complications, such as graft rejection and immunosuppression-related problems.[5–7] In this scenario, cardiac bioengineering offers advanced and personalized approaches to transform MI treatment through innovative technologies, such as 3D bioprinting, as alternatives to whole-organ transplantation.[8,9] The epicardial application of 3D-bioprinted cardiac patches represents a pivotal technique aimed at repairing myocardial tissue after MI.[10–12] This approach allows to deliver cells with regenerative potential (such as stem cells) directly in the proximity of the injured myocardial area and provides mechanical support for the native myocardium, preventing its further deterioration after MI-related events.[13–16] Moreover, the evolution of the field enabled the possibility to create patient-tailored cardiac patches, by designing their shape and size to match the patient's specific infarcted region.[17] During the design of a cardiac patch, the selection of the bioink represents a fundamental step.[10,12] A suitable bioink should be able to both mimic the native extracellular matrix (ECM) and match mechanical properties standards to support the stress caused by cardiac mechanical forces.[18,19] Hydrogel-based bioinks, particularly those derived from natural polymers, have been widely used as biomaterials for these aims, thanks to their high biocompatibility, tunable mechanical properties, and ability to resemble the ECM organization.[11,20–23] Our team has previously proposed cardiac spheroids (CSs) as bioengineered cardiac tissues able to model the human cardiac pathophysiology *in vitro*.[24–27] We used CSs combined with a natural polymers-derived hydrogel, made of alginate and gelatin, to 3D-bioprint functional cardiac patches, which provided cardiac cells integration and viability *in vitro* and improved myocardial function in an *in vivo* model of MI.[25,28,29] Although these constructs were successfully transplanted during the testing on small animal modes, their mechanical properties, printability, and durability could be further improved to better match the requirements of the human cardiac tissue.[29,30]

Sericin is the globular protein that constitutes 25–30 wt% of the whole silk filament.[31] Sericin has the function of enveloping and binding the fibroin strands together, creating a layer which protects the cocoon from harmful microorganisms, such as bacteria and fungi.[32] The glue-like nature of sericin is crucial to ensure the cocoon's development and the maintenance of its structural integrity.[31] While silk fibroin has been widely used for biomedical applications due to its suitable elasticity, mechanical strength, and tunable degradation, silk sericin has been ignored and discarded as a byproduct of silk production in the textile industry, causing environmental pollution.[33] At present, intrinsic properties of sericin make it a promising candidate for biomedical applications, and its use provides a strong contribution to the "waste to resource" platform.[33,34] Sericin is rich in non-essential amino acids (e.g., serin, aspartic acid, glutamic acid, and glycine) and its intrinsic adhesive nature promotes cell growth and proliferation.[35,36] Compared to silk fibroin, sericin has reduced β-sheets structures, which results in difficult hydrogel formation, and this phenomenon justifies the often blending of sericin with other polymers, such as alginate.[37,38] When non-coupled with fibroin, sericin is low-immunogenic, and its anticancer, antioxidant, anticoagulation, anti-inflammatory, antibacterial, and wound healing properties have been documented in several drug delivery and tissue engineering studies.[39–43] This collected knowledge promises an interesting translation of sericin-based materials into cardiac tissue engineering. Although silk fibroin has been widely investigated in the preparation of both cardiac injectable hydrogels and 3D-bioprinted patches,[44] only a few studies have examined the role of sericin as a building block in biomaterials intended for the treatment of MI.[36,45]

In this study, we propose biofabricated alginate-gelatin hydrogels supplemented with sericin from silkworm (*Bombyx mori*). We hypothesize that, owing to its properties and structure, sericin may improve the mechanical characteristics of alginate-gelatin hydrogels, enhancing their elasticity without affecting the cardiac

cell viability of hydrogel-embedded CSs. The hypothesis was tested by biofabricating alginate-gelatin hydrogels with increasing sericin concentrations, which were first characterized in their mechanical properties by Brillouin microspectroscopy and classic rheology. The swelling and porosity properties were assessed by gravimetric and liquid displacement methods, while scanning electron microscopy (SEM) allowed us to evaluate the inner morphology of the biofabricated hydrogels and measure their pore sizes. All the prepared hydrogels were 3D-bioprinted to assess whether the addition of sericin affects the printability and durability of the biomaterials. Finally, CSs were generated *in vitro* and embedded in sericin-containing hydrogels to evaluate the toxicity ratio and cardiac cell distribution after incubation in the medium for up to 28 days.

2. Materials and methods

2.1. Materials

Alginic acid sodium salt from brown algae, gelatin from bovine skin, sericin *B. mori* (silkworm), calcium chloride, Dulbecco's phosphate-buffered saline (DPBS) with no calcium chloride or magnesium chloride, agarose, L-glutamine solution 200 mM, high-glucose Dulbecco's Modified Eagle's Medium (DMEM), Triton™ X-100, bovine serum albumin, and formalin solution were purchased from Sigma Adrich (Castle Hill, NSW, Australia). PureSilk® Sericin was kindly provided by Fibrothelium GmbH (Aachen, Germany) and used to perform comparative Brillouin microspectroscopy studies only. Penicillin-Streptomycin (Pen/Strep; Gibco) was obtained from Thermo Fisher Scientific Australia (Scoresby, VIC, Australia). Purified mouse anti-human CD31 was purchased from BD Life Sciences (Macquarie Park, NSW, Australia). Secondary donkey anti-mouse antibodies Alexa Fluor® 647-conjugated was purchased from Jackson ImmunoResearch Laboratories Inc. (West Grove, PA, USA). Troponin T-C Antibody (CT3) Alexa Fluor® 546-conjugated (cTNT) was obtained from Santa Cruz Biotechnology Inc. (Heidelberg, Germany). Alexa Fluor® 488 Anti-Vimentin antibody [V9] was purchased from Abcam (Melbourne, VIC, Australia). NucBlue™ Hoechst 33342 and LIVE/DEAD™ Viability/Cytotoxicity Kit (calcein-AM and ethidium homodimer-1) were purchased from Thermo Fisher Scientific Australia (Scoresby, VIC, Australia).

2.2. Preparation of hydrogels

Our previously established protocol was used during the preparation of alginate-gelatin hydrogels.[29,30] Briefly, alginic sodium salt (Alg, 4% w/v), gelatin (Gel, 8% w/v), and sericin (Ser, 0%, 1%, 2%, and 3% w/v) powders were first sterilized under UV light for 30 min. DMEM supplemented with 1% v/v Pen/Strep and 1% v/v L-glutamine 200 mM was heated at 50°C on Heating Plate Cimarec® (ThermoFisher Scientific) and the powders were slowly inserted under continuous stirring in a biosafety cabinet until they were completely solubilized in the media. The achieved hydrogel formulations (named henceforth as Ser0%, Ser1%, Ser2%, and Ser3%) were aliquoted and then sealed. All the aliquots were stored at 4°C for further analysis. The ionic cross-linking was performed with 2% w/v $CaCl_2$ solution promptly sterilized by filtration at 0.2 μm and added on top of gelated hydrogels.[30] Figure 1 provides a schematic representation of the biofabrication of sericin-containing hydrogels and the experimental plan.

2.3. Fourier transform infrared spectroscopy analysis

To identify any interactions occurring among sericin, alginate, and gelatin, a Fourier transform infrared spectroscopy (FTIR) study was carried out using a Nicolet™ iS™5 FT-IR Spectrometer (Thermo Fisher Scientific Inc., Waltham, MA, USA) equipped with an iD7 attenuated total reflectance (ATR) device. The vibrational spectra of single components' powders and freeze-dried crosslinked sericin-containing hydrogels were obtained at room temperature (25°C), using 64 scans and 4 cm^{-1} resolution, within the spectral region from 4000 to 400 cm^{-1} in transmission mode. OMNIC software (version 9.12.1019), Thermo Fisher Scientific, Waltham, MA, USA was used to automatically detect the peaks of the spectra.

2.4. Swelling test

The change in swelling properties of the hydrogels was evaluated by a gravimetric method as previously reported.[46] Briefly, freeze-dried sericin-containing hydrogels were immersed in PBS (pH 7.4) at 37°C. At specific time points (0, 0.5, 1, 2, 4, 6, and 24 h), hydrogels were withdrawn from PBS, wiped off excess buffer, and weighed. The swelling ratio (%) was calculated according to the following equation:

$$\text{Swelling ratio}(\%) = \frac{W_{wet} - W_{dry}}{W_{dry}} \times 100 \quad \text{(I)}$$

where W_{dry} is the weight of the freeze-dried hydrogel before the immersion in PBS, and W_{wet} is the weight of swollen hydrogel recorded at each time point.

2.5. Brillouin microspectroscopy and rheological characterization of hydrogels

Hydrogels were evaluated in their mechanical properties through rheology and Brillouin microspectroscopy. The rheological characterization of hydrogels before crosslinking involved the evaluation of dynamic moduli

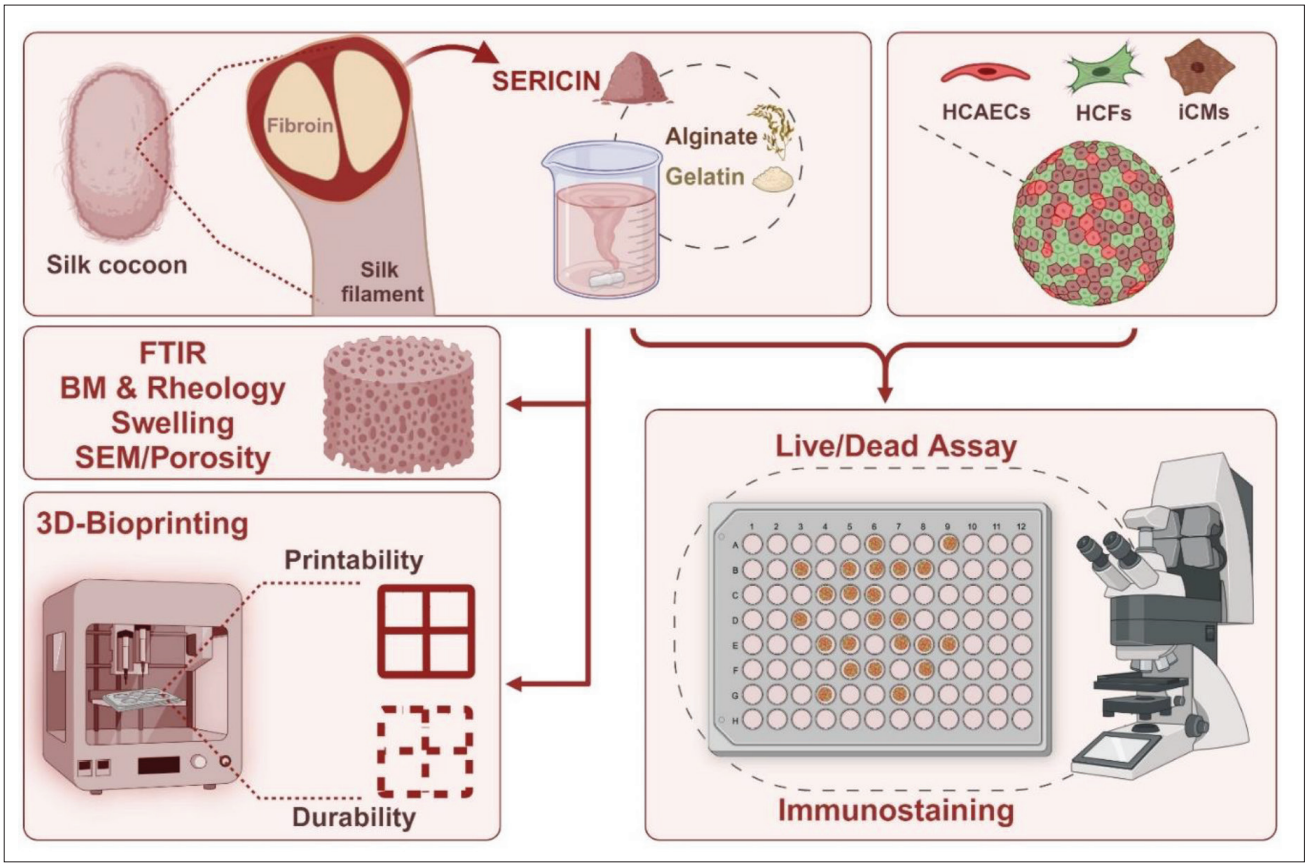

Figure 1. Schematic representation of the experimental plan. Silk sericin was used as an additive component in alginate-gelatin hydrogel biofabrication to obtain sericin-containing hydrogels at 1%, 2%, and 3% w/v sericin concentrations. We carried out FTIR studies on biofabricated hydrogels to assess their secondary structure and confirm the inclusion of sericin within the hydrogel network. Hydrogels were characterized by Brillouin microspectroscopy and rheology to assess their mechanical behavior and by SEM to observe the inner morphology. The gravimetric method on freeze-dried samples assessed the hydrogels' porosity as well as their swelling behaviors. All the biofabricated hydrogels were then 3D-bioprinted to evaluate their resolution after printing and durability after incubation at 37°C in the cell medium. CSs were generated by co-culturing HCAECs, HCFs, and iCMs, thus embedded in the biofabricated hydrogels to assess cardiac cell viability and distribution after 3, 14, and 28 days of incubation. Abbreviations: BM, Brillouin microspectroscopy; CSs, cardiac spheroids; FTIR, Fourier transform infrared spectroscopy; HCAECs, human coronary artery endothelial cells; HCFs, human cardiac fibroblasts; iCMs, iCell® cardiomyocytes; SEM, scanning electron microscopy.

(G', G'', and η^*) during oscillatory frequency sweep testing by using Kinexus® Pro rotational rheometer (Malvern Panalytical Ltd., Worcester, UK) equipped with a cone-plate geometry (diameter 40 mm, angle 2°). Each sample was gently put on lower geometry, previously heated and maintained at 25°C or 28°C by the connected Pelter unit (Malvern Panalytical Ltd., Worcester, UK). The sample was kept at rest for 5 minutes before starting the analysis, to dismiss any effect of sample loading on the rheological evaluation. The gap between geometries was fixed at 1 mm, and the operating frequency range was set at 0.1–10 Hz) with a constant shear stress of 1 Pa.[47] After crosslinking, the hydrogels were characterized by employing a dynamic hybrid rheometer (DHR-3, TA Instruments, New Castle, DE, USA) in an unconfined compression test. Each sample was molded using punch biopsies (8 mm diameter, KAI's Medical Products, Japan) and placed between the upper and lower geometries (8.0 mm parallel plate, Peltier plate Stainless steel, TA Instruments, New Castle, DE, United States). The unconfined compression test was performed at 25°C with a constant compression rate of 2 µm/s, by recording the axial force (N) and gap (µm) values as output data. The collected data were processed to obtain a stress–strain curve, and Young's modulus (kPa) was obtained from the linear region of the curve.[29]

Brillouin microspectroscopy apparatus involved a laser with approximately 200 mW continuous wave emission at 660 nm wavelength (Torus, Laser Quantum, Stockport, United Kingdom), integrated with a confocal microscope (CM1, The Table Stable Ltd., Mettmenstetten, Switzerland), a 3D scanning microscopy stage (SmarAct, Oldenburg, Germany), and a 6-pass scanning tandem Fabry-Perot interferometer (TFP1, The Table Stable Ltd.,

Mettmenstetten, Switzerland). This system was used to collect the spontaneous Brillouin scattering spectra, where the backscattered light was collected by an objective lens (20× Mitutoyo Plan Apo infinity corrected objective, NA = 0.42, WD = 20 mm) and subsequently redirected to the interferometer for analysis. The analysis was carried out on hydrogels before and after crosslinking and after incubation in DMEM (in the incubator at 37°C, 5% CO_2) to avoid hydrogel dehydration. Each sample was analyzed by recording the raw spectra of Stokes and Anti-Stokes Brillouin peaks at four arbitrary points within each hydrogel sample. The collected raw data were analyzed by fitting a Lorentzian model to every Stokes and Anti-Stokes Brillouin peak, produced as a result of optoacoustic interaction within the gel. The line fit was performed using Ghost Software ver. 7.00 (The Table Stable Ltd., Mettmenstetten, Switzerland) and the average value between Stokes and Anti-Stokes peaks was taken as the final Brillouin frequency shift (BFS; GHz, directly related to elasticity) or Brillouin linewidth (BLW; GHz, directly related to viscosity) to eliminate the influence of possible laser frequency drifting during the experiment. The hydrogels were analyzed before crosslinking, after crosslinking, and after incubation in DMEM (in an incubator at 37°C, 5% CO_2).[48]

2.6. Determination of pore size and porosity

The inner morphology of hydrogels was evaluated by means of SEM. The hydrogels (1 mL) were cast in 6-well plates and crosslinked after gelation. Squared cross-sections were cut from the center of each well to ensure a uniform surface, subsequently mounted on stubs covered with double adhesive carbon tabs and fully dried in a vacuum oven (100 kPa, Gallenkamp OVA031.XX1.5, Manchester, United Kingdom) for 24 h. Hereafter, a sputter coater machine (Leica EM ACE600, Leica Microsystems Pty Ltd, Macquarie Park, NSW, Australia) was employed to perform a 10 nm gold coating of samples, which were then imaged using the Zeiss EVO LS15 scanning electron microscope (Zeiss, Macquarie Park, NSW, Australia), furnished with a thermionic tungsten electron gun, by setting an acceleration voltage of 10 kV and a working distance of 10.5 mm. At least 15 images from random areas were acquired for each sample by Zeiss SmartSEM software and analyzed for pore size (area, μm^2) using ImageJ software by manually marking the perimeter borders of every single pore and using the measure tool of the software (Figure S1, Supporting Information), as previously reported.[29,49–51] The porosity of the biofabricated hydrogels was determined by the liquid displacement method as previously reported.[52,53] In detail, the freeze-dried hydrogels were submerged in a known volume (V_1) of PBS (pH 7.4) within a 10 mL graduated cylinder. After 2 h, the total volume was recorded (V_2), the swollen hydrogel removed, and the remaining liquid volume inside the cylinder was recorded (V_3). The porosity (%) was calculated according to the following equation:

$$\text{Porosity}(\%) = \frac{V_1 - V_3}{V_2 - V_3} \times 100 \quad \text{(II)}$$

2.7. 3D bioprinting, printability, and durability assessments

Sericin-containing hydrogels were 3D-bioprinted using the extrusion-based bioprinter BIO X6 (CELLINK, Gothenburg, Sweden) in simple squares with an internal cross to evaluate their printability and durability. The bioprinter chamber was sterilized with UV light and all the pre-printing stages were performed in a biosafety cabinet to ensure sterility conditions. At the moment of bioprinting, each hydrogel was warmed up to 30°C in a water bath and then transferred into a 3 mL cartridge by using a luer lock syringe and connector to avoid the formation of bubbles. The cartridge was then mounted with a 22G nozzle, with an inner diameter of 0.41 mm, and moved into a temperature-controlled printhead (with a control precision within 0.5 °C). The 3D model consisted of a 16 × 16 × 0.41 mm^3 (width × length × height) patch printed with two consecutive layers, and it was generated with DNA Studio 4 Software equipped with G-code Editor (CELLINK, Gothenburg, Sweden). To maintain the hydrogel in liquid state and allow rapid gelation during and after the printing, the printhead and the printbed temperatures were set at 28 and 10 °C, respectively. The printability of the bioprinted patches (n = 14) was assessed before crosslinking by measuring the inner width of the gelated hydrogel strands with ImageJ[50] and then comparing the value with the inner diameter of the nozzle according to the following equation:

$$\text{Printability ratio}(\text{AU}) = \frac{W_{pf}}{D_n} \quad \text{(III)}$$

where W_{pf} represents the width of the printed strand, and D_n is the inner diameter of the 22G nozzle.

The obtained 3D models were crosslinked with $CaCl_2$ solution and afterwards, they were submerged with DMEM and incubated (37°C, 5% CO_2 in air) for up to 28 days. The medium was withdrawn and replaced with fresh DMEM every 4 days, minimizing the movement during the procedure. To assess their durability in the cell culture medium, the patches were monitored for macroscopic disintegration by imaging them with EVOS

M7000 Imaging System (Thermo Fisher Scientific Inc., Scoresby, VIC, Australia) at fixed time points from the day of printing (day 0) and after 1, 3, 7, 14, 21, and 28 days of incubation. When any sign of the disintegration of the main structure occurred (such as dissolving or detachment of small hydrogel's fragments), the patch was considered "non survival."[30]

2.8. Cell culture and CS generation

Human cardiac fibroblasts (HCFs) and human coronary artery endothelial cells (HCAECs) were obtained from Cell Applications (San Diego, CA, USA), and they were cultured in Human Cardiac Fibroblast medium and MesoEndo growth medium (Cell Applications, Inc, San Diego, CA, USA), respectively. iCell® Cardiomyocytes (iCMs, cardiomyocytes differentiated from human-induced pluripotent stem cells) were obtained from FujiFilm Cellular Dynamics (Madison, WI, USA). According to the provider's instructions, iCMs were plated in iCell® Plating Medium and cultured in iCell® Maintenance Medium (Fujifilm Cellular Dynamics, Inc., Madison, WI, USA). The generation of human CSs was achieved by co-culturing HCFs, HCAECs, and iCMs at a ratio of 1:1:2, as reported in previous studies.[24,26,29] Non-adherent agarose microwells were formed by using 12–81 3D Petri Dish® cast silicone molds (Microtissues Inc., Providence RI, USA). Briefly, the autoclaved molds were filled with molten agarose (2% w/v in DPBS), once cooled at room temperature, the microwells were taken out from the mold and moved to 12-well plates submerged in DMEM and left in the incubator (37°C, 5% CO_2 in air) for 2 days to equilibrate while the medium was frequently refreshed. At the moment of CS generation, each cell type was spun and then combined by resuspending the pellets in CS medium (HCF medium, MesoEndo growth medium and iCell® maintenance medium at a 1:1:2 ratio).[26,29] The cellular suspension was seeded in the pre-equilibrated microwell chamber, and the constructs containing cells were incubated again. After a few hours, the cells started spontaneously to aggregate in the microwells, generating 81 CSs/agarose structure. The CS medium was refreshed until CSs were formed. For *in vitro* studies and imaging the CSs ($n \geq 3$) were plated in glass-bottom 96-well plates (Miltenyi Biotec, Macquarie Park, NSW, Australia) and the warm hydrogel (100 µL, 37°C) was added on top.[24]

2.9. Contractile activity and optical mapping measurements

To measure the contraction frequency (number of CS contractions per second) and the fractional shortening % (FS%), we recorded videos of contracting CSs in Ser0% and Ser3% hydrogels using the EVOS M7000 Imaging System (Thermo Fisher Scientific Inc., Scoresby, VIC, Australia) after 3, 14, and 28 days of incubation in normoxic conditions (37°C, 5% CO_2), as previously described.[54] To measure the conduction velocity (CV), CSs were plated in an 8-well chamber and incubated for 14 days at 37°C, 5% CO_2. CS-containing wells were loaded with 17.7 µM Rhod-2 AM (fluorescent Ca^{2+} indicator, Abcam, Melbourne, VIC, Australia), 0.02% Pluronic™ F127 (Thermo Fisher Scientific Inc., Scoresby, VIC, Australia), and 50 µM RH237 (Santa Cruz Biotechnology Inc., Heidelberg, Germany), and incubated for 2 h at 37°C, 5% CO_2. Each well was then washed with fresh culture medium three times and incubated for an additional 30 min with media prior to the individual transfer of CSs to 60 mm sterile cell culture plates (Corning). When ready for imaging, CSs were carefully moved to the OMS-PCIE-2002 optical mapping chamber (Mapping Lab Ltd, Manchester, UK) under an upright microscope equipped with high-speed CMOS cameras. Briefly, RH237 fluorescence as a function of the action potential was passed through a long-pass dichroic filter of 700 nm (FELH700, Thorlabs, Newton, NJ, USA), while Rhod-2 AM fluorescence as a function of Ca^{2+} was passed through a long-pass dichroic filter of 585 nm (FBH585, Thorlabs, Newton, NJ, USA). Both fluorescence signals were collected through a long-pass dichroic beamsplitter with a cutoff wavelength of 638 nm (DMLP638, Thorlabs, Newton, NJ, USA), then filtered by a 550 nm long-pass filter (FELH550, Thorlabs, Newton, NJ, USA) before voltage signals were imaged. A spatial resolution maximum of 512 × 512 pixels was utilized during acquisition, with a total mapping area of 64 × 64. Temporal resolution was set to 1000 frames/second at an exposure time of 0.9 ms over 10 s of recording time. Data were acquired in real-time using an 8-channel TTL analog-digital converter and OMapRecord 4.0 software (Mapping Lab Ltd, Manchester, UK), then processed using OMapScope 5.6.8 (Mapping Lab Ltd, Manchester, UK). Processing filters were applied to generate waveforms with low noise-to-signal ratios including a Gauss convolution of 9 × 9, a zero-phase filter window of 30, and theta smoothing intensity of 1.5. Waveform graphs were selected based on a selected region of interest (ROI) to display the lowest signal-to-noise ratio. A single peak representing a single contraction was used for calculating the CV values for action potential and calcium signals, per array, including temporal sequence recordings (slowed to 1/20th of the original speed) to display the propagation of signals at different regions of the CSs.

2.10. Live/Dead staining and immunostaining of CSs

To assess the cell viability of CSs embedded in sericin-containing hydrogels, the dead/live cells ratio was estimated over time at fixed time points, as previously described.[29,30] Briefly, CSs embedded in hydrogels were cultured in the incubator (37°C, 5% CO_2) for up to 28 days, by replacing the

medium every 2 days, and the viability was evaluated after 3, 14, and 28 days. LIVE/DEAD™ Viability/Cytotoxicity Kit and NucBlue™ were used to detect living cells, dead and total cells, by staining them with calcein-AM (1 µL/mL), ethidium homodimer-1 (EthD-1, 1 µL/mL), and Hoechst stain, respectively. The dyes were directly added to the medium on top of CSs-containing hydrogels and then incubated at 37°C (5% CO_2) for 3 h. After the incubation, the samples were washed three times with warm DPBS, according to the manufacturer's directions, and finally imaged with a STELLARIS 8 confocal microscope (Leica Microsystems Pty Ltd, Macquarie Park, NSW, Australia).

After 28 days of incubation, all cell types present in CSs embedded in hydrogels were identified by immunostaining. The samples were first fixed in 4% paraformaldehyde for 3 h at room temperature, washed in PBSA 0.01% (DPBS containing 0.01% sodium azide), permeabilized in 0.02% Triton-X/PBSA for 1 h, blocked with 3% BSA/PBSA, and then incubated with suitable primary and secondary antibodies at 4°C for 18 h.[26] HCAECs were labeled by primary mouse anti-human CD31 (6.25 µg/mL), revealed by a secondary donkey anti-mouse Alexa Fluor® 647-conjugated antibody (21 µg/mL). Troponin T-C Antibody (CT3) Alexa Fluor® 546-conjugated (10 µg/mL), Alexa Fluor® 488 Anti-Vimentin antibodies (2 µg/mL), and NucBlue™ (2 drops/mL) were used to stain iCMs, HCFs, and nuclei, respectively. All samples were imaged by STELLARIS 8 confocal microscope and the collected images were processed in ImageJ and Adobe Photoshop 25.3.1 (Adobe Systems, Inc., San Jose, CA, USA).[50] 3D-rendered images and videos were produced using Imaris visualization software (Oxford Instruments, Abingdon, Oxfordshire, UK).[28]

2.11. Statistical analysis

All the collected data were analyzed and plotted using GraphPad Prism version 8.4.2 for Windows (GraphPad Software, Boston, MA, USA). Swelling test results were analyzed using two-way analysis of variance (ANOVA) with Dunnett's multiple comparisons test. For all other experiments, we employed Brown–Forsythe and Welch ANOVA followed by Dunnett's multiple comparisons test. All results are expressed as mean ± standard error of mean (SE).

3. Results and discussion

3.1. The inclusion of sericin modulates the mechanical properties of alginate-gelatin hydrogels

To biofabricate sericin-containing alginate-gelatin hydrogels, we chose a range of sericin concentrations (1, 2, and 3% w/v) based on previous studies, which investigated the role of this protein in the formulation of functional hydrogels and scaffolds for biomedical purposes.[36,37,55] To characterize hydrogels' secondary structures, we first performed FTIR analyses on both freeze-dried hydrogels and single-component dry powders (Figure 2). Figure 2A shows the FTIR spectra of pure alginate, gelatin, and

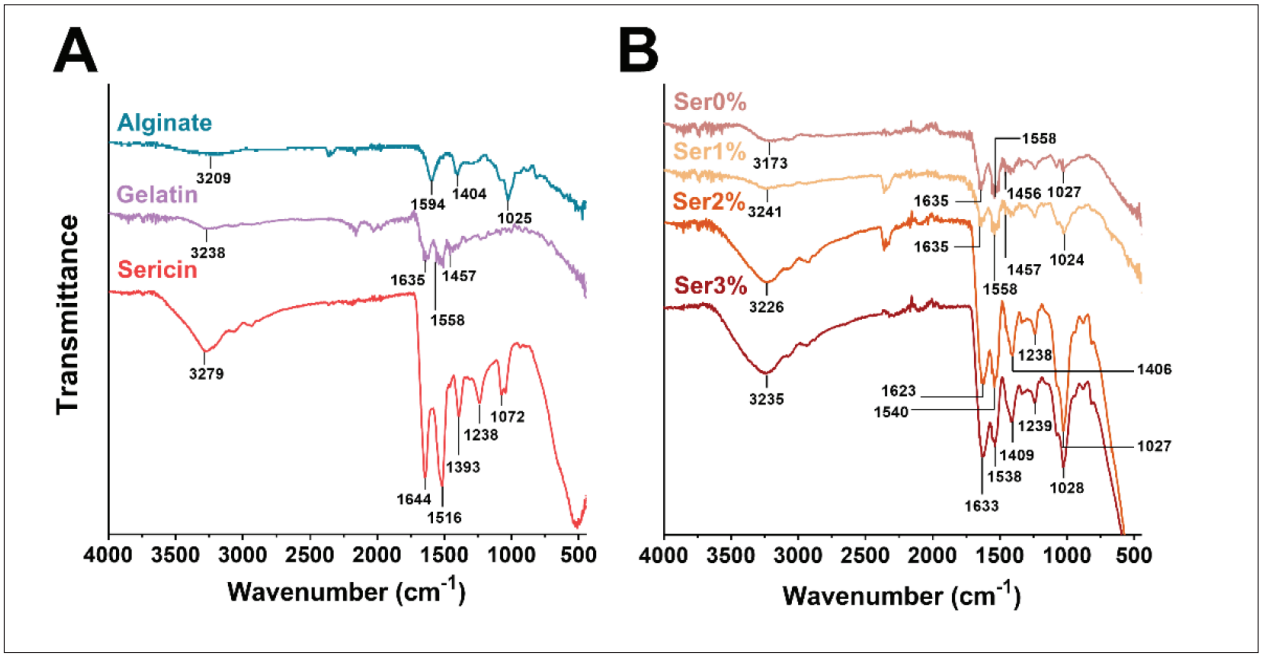

Figure 2. Secondary structure investigation by FTIR spectroscopy of sericin-containing alginate-gelatin hydrogels and their main components. FTIR spectra of alginate, gelatin, and sericin dry powders (A) and sericin-containing hydrogels freeze-dried after crosslinking (B). Abbreviation: FTIR, Fourier transform infrared spectroscopy.

sericin powders used in this study. The all components, in dry powder form, exhibited a broad peak at ~3200 cm^{-1} (hydroxyl group), related attributed to O—H stretching vibration, which was more pronounced in sericin's spectra due to the high content of serine amino acid.[56,57] The spectrum of alginic acid powder exhibits the typical peaks of the asymmetric and symmetric carboxyl group (—COOH stretching) of the polymeric backbone at 1594 and 1404 cm^{-1}, respectively.[58] In gelatin and sericin spectra, we identified peaks at 1635 and 1644 cm^{-1} (amide I), 1516 and 1558 cm^{-1} (amide II), and 1238 cm^{-1} (amide III), which were related to C=O stretching, N–H bending, and C–N stretching vibrations, respectively. All these peaks, together with sericin's footprint are visible in the spectra derived from all sericin-containing hydrogels (Figure 2B), confirming the incorporation of the silk protein within the polymeric network. Next, to evaluate the mechanical properties of the biofabricated hydrogels containing sericin, we performed a mechanical characterization through Brillouin microspectroscopy and classic rheology analyses. These methodologies provided complementary information on hydrogels'

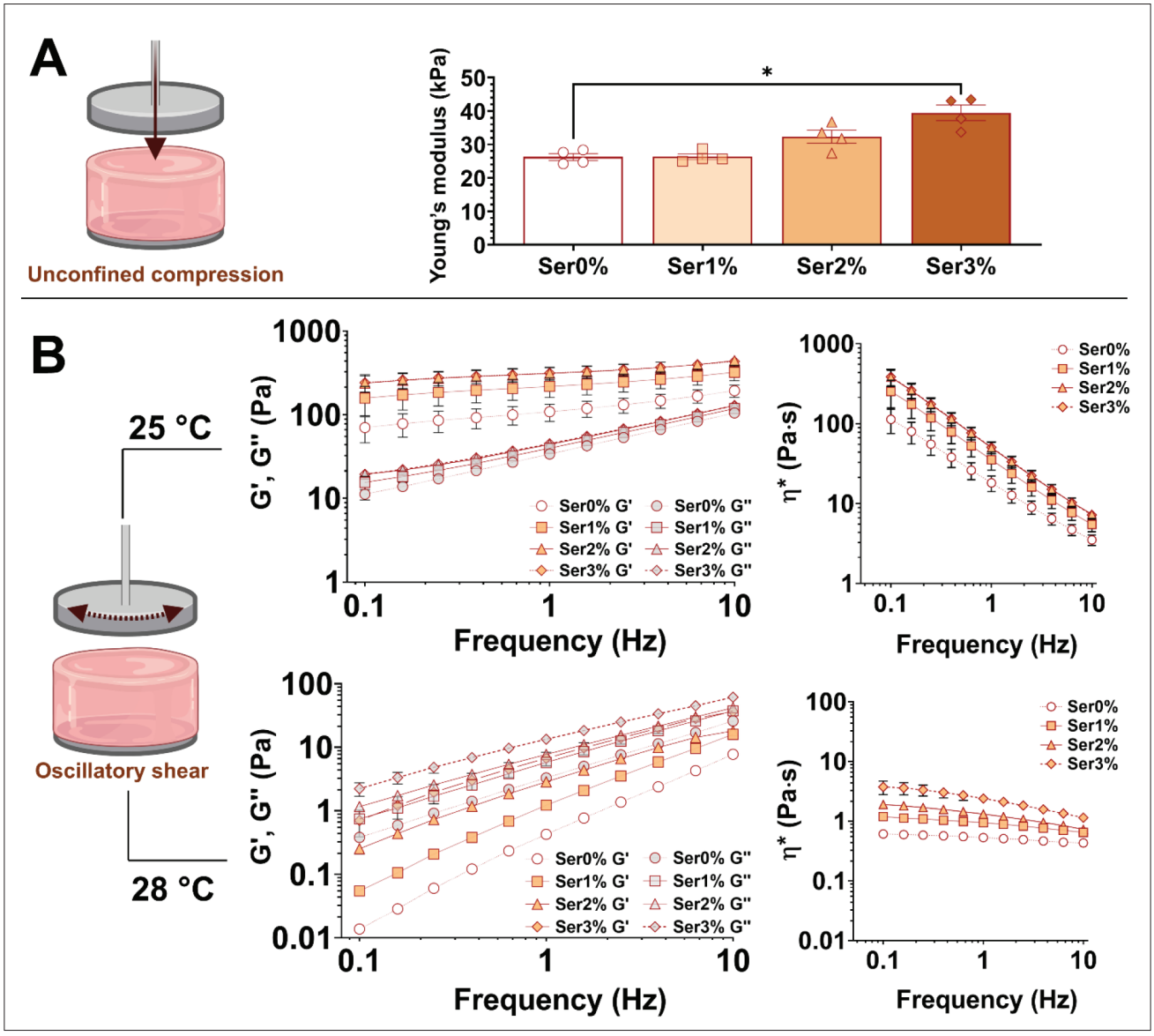

Figure 3. Rheology testing performed on sericin-containing hydrogels. (A) Young's moduli derived from an unconfined compression test. Brown–Forsythe and Welch ANOVA test was used to compare the groups (*$p < 0.05$). (B) Storage moduli (G'), loss moduli (G''), and complex viscosity (η^*) derived from frequency sweep measurements at 25°C (room temperature) and 28°C (printing temperature). Error bars represent the mean ± SE and are within the symbols if not visible ($n = 4$).

mechanical behavior and were previously successfully used by us to characterize the mechanical properties of hydrogels.[29,54,59] Indeed, with rheological analysis, we were able to provide fundamental insights into the materials, including their Young's moduli (Figure 3A) derived from an unconfined compression test, and dynamic moduli (storage modulus G' and loss modulus G'') and complex viscosity (η^*) under oscillatory amplitude sweep testing (Figure 3B). In detail, the addition of sericin to alginate-gelatin hydrogels increased their stiffness, as evidenced by Young's moduli recorded from the unconfined compression test. This effect was directly proportional to the concentration of sericin used and became significant ($p < 0.05$) for Ser3% formulation, which presented the greatest Young's modulus of 39.4 ± 4.7 kPa compared to 26.2 ± 6.4 kPa of Ser0% hydrogel (Figure 3A). Ser1%, Ser2%, and Ser3% improved the ability of Ser0% hydrogel to resist deformation under compressive stress by 4%, 21%, and 50%, respectively. This result was hence confirmed by the oscillatory amplitude sweeps test (Figure 3B). As expected, at a temperature of 25 °C, the storage modulus (G') was predominant on loss modulus (G'') for all biofabricated hydrogels, indicating a solid-like behavior. We detected an increase in the amplitude of the sericin-containing hydrogels' G', compared to Ser0%. This increase was directly proportional to the concentration of protein present, following the Young's moduli recorded (Figure 3A). Likewise, at the same temperature it was noted that as the concentration of sericin increased, the complex viscosity of the hydrogel also increased while preserving the shear thinning behavior of Ser0%. This result was consistent with the increase in BLW magnitude recorded by our Brillouin microspectroscopy analyses (Figure S2, Supporting Information). The same analysis was performed at 28°C to evaluate the hydrogels' mechanical properties during the bioprinting process. The temperature-dependent behavior of alginate-gelatin hydrogel is due to the presence of gelatin. This protein is well known for its thermal-reversible gelation properties, which make its derived mixtures change from *sol-to-gel* according to the temperature (24–30 °C).[60] However, this feature might be changed by the presence of additives, and it depends on the gelatin concentration, molecular weight, and source.[61] Under our experimental conditions, the *gel-to-sol* transition temperature of Ser0% is approximately 28 °C. Therefore, at 25 °C, the temperature is well below the gelation threshold, allowing the formation of a stable gel network and resulting in higher mechanical parameters. In contrast, at 28 °C, the system nears the gelation temperature, leading to partial solubilization and reduced viscoelastic properties. We detected that the gelatin's behavior was not altered by the presence of sericin within the hydrogel network, since at 28 °C, the G'' was larger than G' within the entire frequency range and the viscosity dropped as a function of the frequency amplitude. Despite all hydrogels showing a predominantly liquid-like behavior at 28 °C, for Ser 1%, Ser 2%, and Ser3% hydrogel formulations the proximity between G' and G'' curves is greater with the increase of sericin concentration. This result might indicate that sericin-containing hydrogels retain a greater degree of elasticity than Ser0% formulation. By itself, rheology lacks the micro-scale resolution that Brillouin microspectroscopy analysis provides, thus we further analyzed the biofabricated hydrogels through this contactless approach, based on the process of inelastic scattering that results from light's interaction with thermally excited acoustic phonons in GHz range within the hydrogel structure.[62] This technique allowed us to measure any change in frequency of the light scattered from the sample, known as Brillouin frequency shift (hereafter abbreviated in frequency shift), before and after the crosslinking, and after the incubation with cell culture medium for all formulated hydrogels. Due to the sensitivity of the method, we were able to detect small but significant differences in BFS and BLW magnitudes, which are related to the material's longitudinal elastic modulus and viscosity, respectively.[48,63,64]

Figure 4A demonstrates a significant increase in frequency shift for all sericin-containing hydrogels before crosslinking compared to Ser0% ($p < 0.001$). At this stage, the samples were analyzed after their gelation, and the modifications of frequency shift could be attributed to the change in hydrogels' solid fraction, due to the addition of sericin.[59] As the frequency shift relies both on the polymer concentration and the water content in the sample, we observed a slight reduction in frequency shift values after crosslinking (Figure 4B) and after the incubation with cell culture medium (Figure 4C) since the samples were hydrated by the presence of the crosslinking solution and the medium, respectively. The observed decrease in the frequency shift after crosslinking and incubation in DMEM is consistent with reports in the literature, which emphasize that the water content, rather than the intrinsic stiffness of the material, largely governs the mechanical behavior of hydrogels in physiological conditions.[65] Indeed, after crosslinking, the frequency shift values of both Ser2% and Ser3% hydrogel formulations were significantly changed ($p < 0.001$) compared to the Ser0% ones (Figure 4B), while the addition of sericin at 1% w/v did not alter this property ($p > 0.05$). After we incubated the samples with DMEM (37 °C, 5% CO_2), the increasing trend in frequency shift values with sericin concentration was maintained (Figure 4C), underlying the matrix stiffening effect. The Brillouin frequency shift results were consistent with the

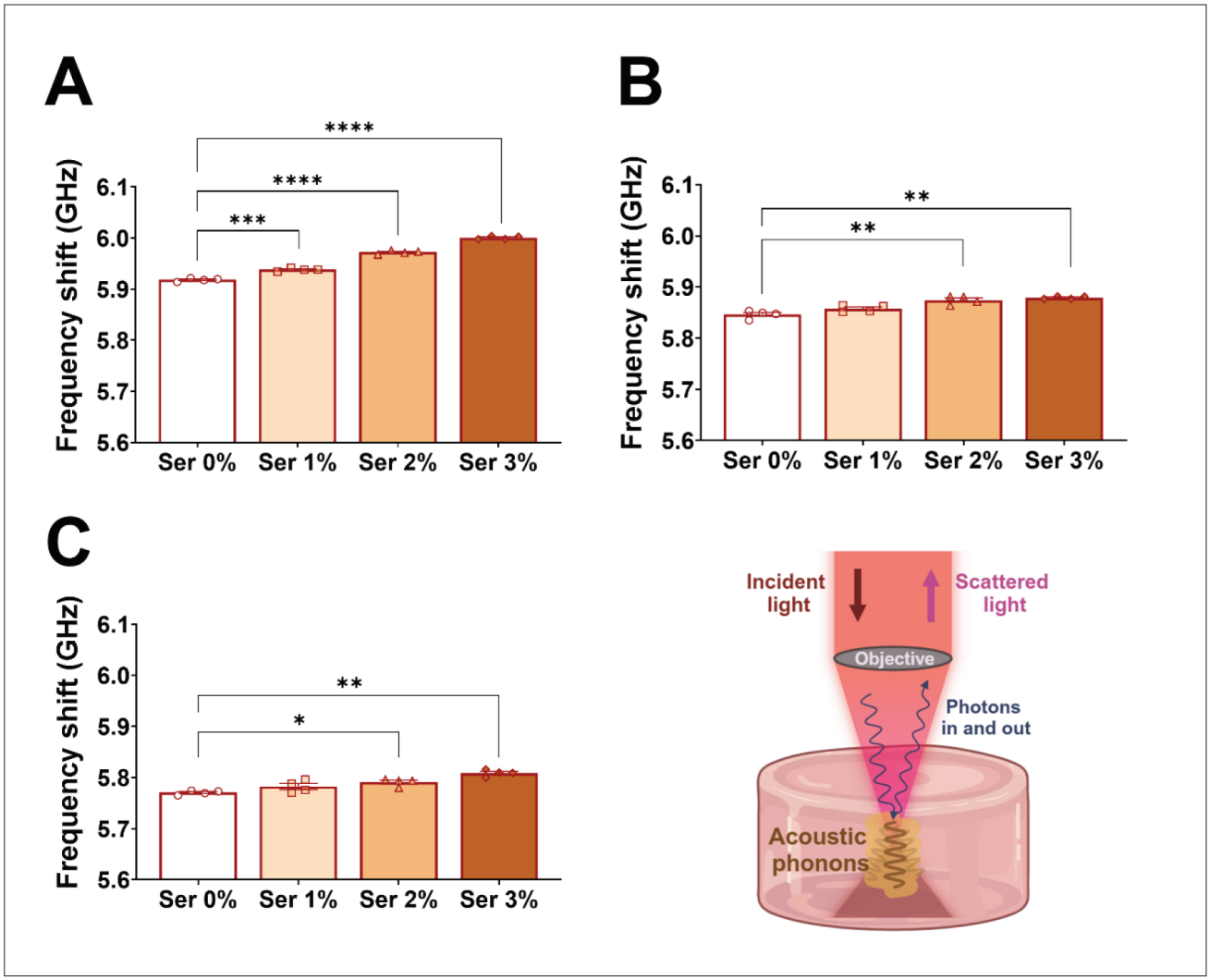

Figure 4. Brillouin microspectroscopy analysis on sericin-containing alginate-gelatin hydrogels. Frequency shift measurements of hydrogels' samples (A) before crosslinking, (B) after cross-linking, and (C) after incubation with the medium. Brown–Forsythe and Welch ANOVA test was used to compare the groups (*$p < 0.05$, **$p < 0.01$, ***$p < 0.001$, **** $p < 0.0001$). Error bars represent the mean ± SE and are within the symbols if not visible ($n = 4$).

ones generated when a different source of sericin was tested (Figure S3, Supporting Information).

Sericin's aminoacidic composition is rich in serine and other polar amino acids, resulting in more carboxyl (—COOH) and hydroxyl (—OH) groups, that may have participated in ionic crosslinking, most likely involving Ca^{2+} ions.[66] This could have facilitated the creation of interpenetrating network hydrogels with increased mechanical strength and therefore increased stiffness. These findings confirmed a greater sensitivity of Brillouin microspectroscopy than classic rheology in understanding mechanical behavior modifications on a microscale and highlighted the contribution of sericin in modulating the mechanical properties of alginate-gelatin hydrogels.

3.2. The addition of sericin increases alginate-gelatin hydrogel porosity

The porosity of a biomaterial plays a major role in biomedical applications since the exchange of nutrients, oxygen, and byproducts depends on the pore size and distribution within the polymeric network, and it is crucial to ensure cells' survival and function.[67] To establish the porosity of the formulated sericin-containing hydrogels, we performed SEM and pore size analysis, together with a gravimetric evaluation of swelling and porosity properties on freeze-dried hydrogel samples. The swelling test revealed an increased ability of sericin-containing hydrogels to absorb aqueous medium compared to the Ser0% formulation, and this effect was directly proportional to the

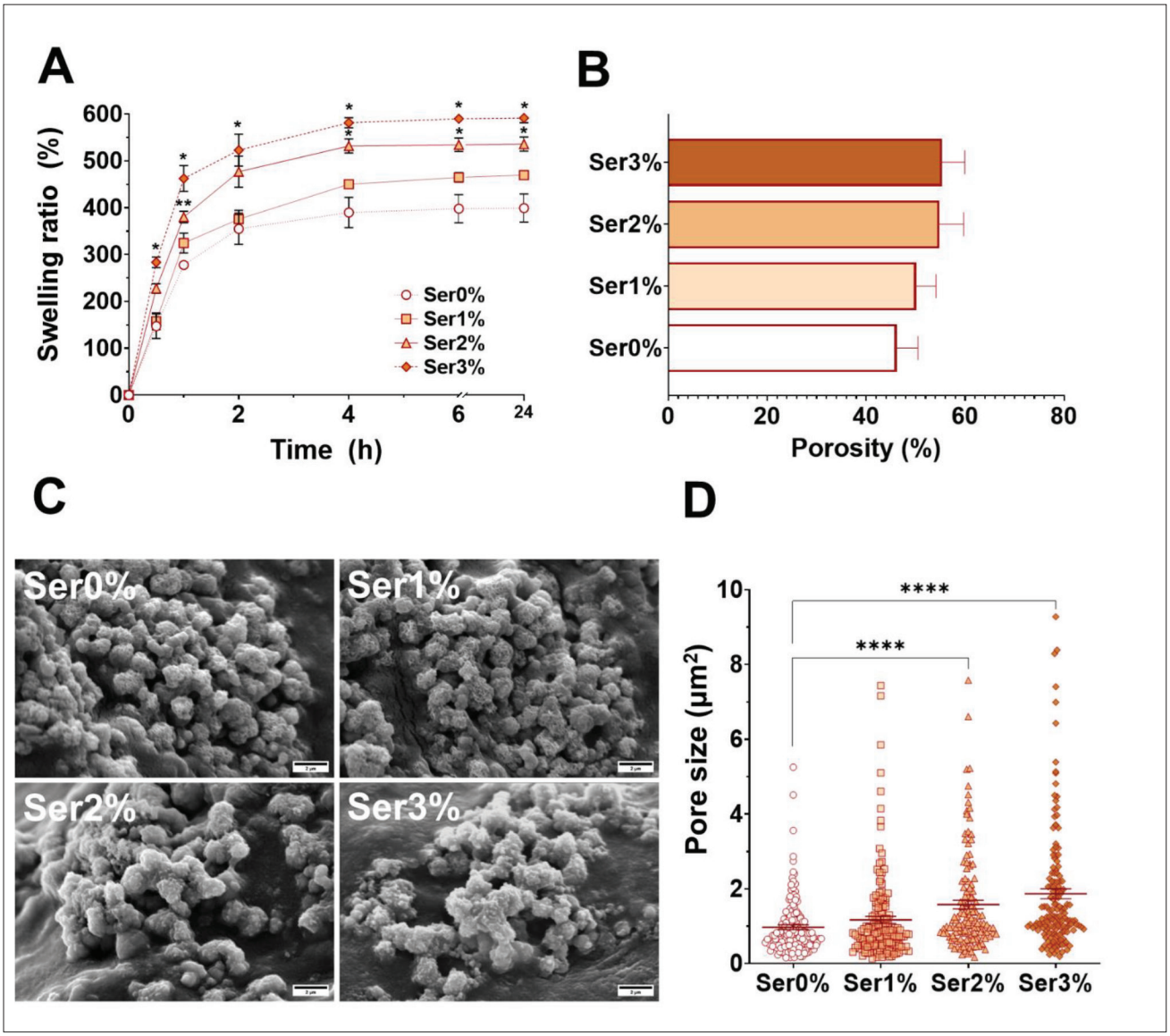

Figure 5. Swelling test, porosity test, and SEM analysis of sericin-containing alginate-gelatin hydrogels. (A) Swelling behavior of sericin-containing hydrogels with two-way ANOVA test with Dunnett's multiple comparisons test as statistical analysis to compare the groups with the control Ser0% (*p <0.05, **p < 0.01; n = 4). (B) Porosity percentages of formulated hydrogel samples after freeze-drying (n = 4). (C) Morphological examination of sericin-containing hydrogel through SEM. Scale bars: 2 μm. (D) Statistical analysis of pore size was performed using Brown–Forsythe and Welch ANOVA test to compare the groups (****p < 0.0001). Error bars represent the mean ± SE and are within the symbols if not visible (n ≥ 15). Abbreviation: SEM, scanning electron microscopy.

increase of sericin concentrations in hydrogels (Figure 5A). Particularly, when compared to the free-sericin hydrogel Ser0%, the swelling ratios were significantly enhanced in Ser2% and Ser3% formulations at almost all evaluated time points (p < 0.05 and p < 0.001, respectively). The maximum swelling equilibrium was reached after 4 h from the beginning of the immersion in PBS, after this time the swelling ratio percentage reached a plateau, independently from the presence of sericin protein within the samples. The presence of sericin could have improved the swelling behavior of alginate-gelatin hydrogels, by increasing the total hydrophilic groups' amount available to attract and interact with water molecules through hydrogen bonding and other polar interactions.[55] Moreover, the improvement of alginate-gelatin swelling properties can be attributed to the increase of the porosity in hydrogel samples with higher sericin concentration, as assessed by the liquid displacement method (Figure 5B). The higher the porosity of the hydrogel, the easier the contact of water molecules with the hydrophilic groups within the polymeric network.[68]

The inner morphology of biofabricated hydrogels was further evaluated by SEM (Figure 5C), and the pore size was measured by calculating the mean inner area of the pores. Based on our statistical analysis (Figure 5D), we found that the inclusion of sericin provided hydrogel networks with larger pores, as a function of the protein content in the hydrogel. In detail, the mean pore size of Ser1%, Ser2%, and Ser3% were increased by 20%, 62%, and 92% compared to the mean pore size of Ser0%. Once again, we recorded the most significant differences ($p < 0.0001$) for the hydrogels containing sericin at concentrations of 2% and 3% w/v. This effect is in positive agreement with previous studies, which reported the same situation for sericin-blends within a certain range of concentration of the protein (2–4% w/v).[67,68]

3.3. Hydrogels containing 3D-bioprinted sericin shows improved printability and durability features

To ascertain any effect related to the addition of sericin to alginate-gelatin hydrogels during the 3D bioprinting process, we carried out printability and durability studies. Once the mechanical and structural characterizations were completed, the biofabricated hydrogels containing increasing concentrations of sericin were bioprinted using the extrusion-based bioprinter BIOX6. We used the same operative parameters for all formulations to assess any difference in the bioprinting process of simple-shaped patches made of two consecutive layers. Although Brillouin microspectroscopy and rheology analyses have proved an increase in elasticity and viscosity as the sericin concentration in hydrogels was increased, all the tested formulations were printable at 28 °C and no occlusion of the nozzle occurred.

We bioprinted at least 12 constructs from each hydrogel formulation (with and without sericin) and assessed the width of each bioprinted strand, which was compared with the inner diameter of the printhead nozzle (0.41 mm) to obtain a ratio of printability. Then, we calculated a normalized printability ratio by comparing the sericin-

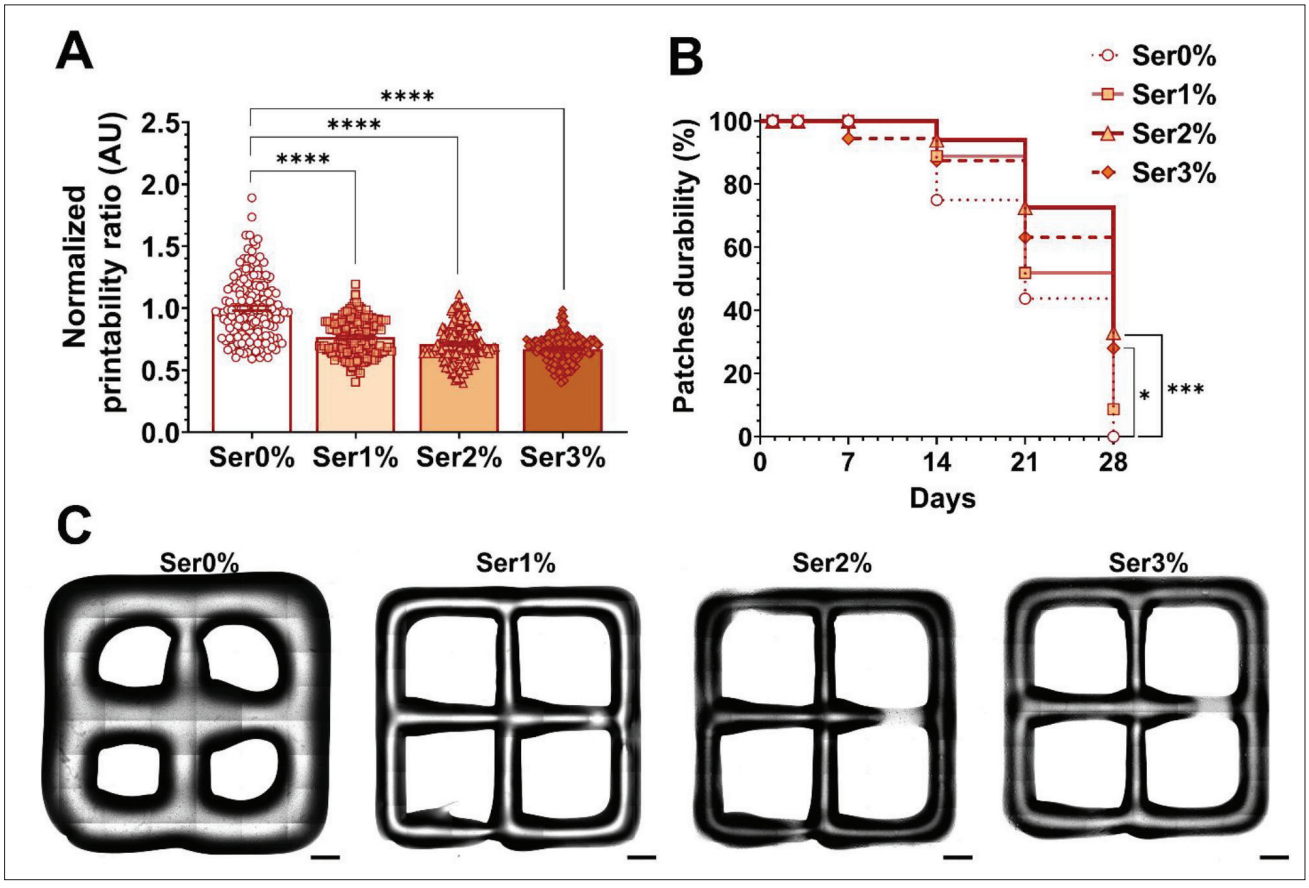

Figure 6. Printability and durability assessments of 3D-bioprinted sericin-containing hydrogels. (A) Statistical analysis of normalized printability ratio of Ser0%, Ser1%, Ser2%, and Ser3% was performed using Brown–Forsythe and Welch ANOVA test to compare the groups (****$p < 0.0001$). Error bars represent the mean ± SE and are within the symbols if not visible ($n = 14$). (B) Statistical analysis of 3D-bioprinted patches durability after crosslinking and incubation with cell culture medium for up to 28 days (37°C, 5% CO2 in air) by using log-rank (Mantel–Cox) test to compare the durability curves (*$p < 0.05$, ***$p < 0.001$, $n \geq 9$). (C) Representative images of 3D-bioprinted patch. Scale bars: 2 mm.

containing hydrogels with our control Ser0% hydrogel. Our statistical analysis showed that the resolution of the patches derived from Ser1%, Ser2%, and Ser3% was significantly improved ($p < 0.0001$) if compared with Ser0% (Figure 6A). This result demonstrated that the addition of sericin caused a reduction of the bioprinted strand widths, which were more similar to the diameter of the nozzle when sericin was included in the hydrogel formulation even at the lowest concentration of 1% w/v, as shown in Figure 6C. This result is in positive agreement with our rheological characterization of sericin-containing hydrogels, which at 28 °C showed greater viscosity values compared to Ser0% (Figure 3B). Previous studies have proved that in extrusion 3D bioprinting, the relationship between the strand diameter and bioink viscosity depends on the bioink shear-thinning or shear-thickening behaviour.[69,70] Our sericin-containing hydrogels all exhibited shear-thinning behaviors (Figure 3B), and in this case, their slightly greater viscosity could have determined a better resolution of the patches concerning the alginate-gelatin hydrogel, without hampering the process.[70]

To establish the durability of the bioprinted structures during a simulated cell culturing condition, we crosslinked the constructs and thus incubated them in the cell culture medium (37 °C, 5% CO_2) for up to 28 days. During this period, the patches were systematically observed through the EVOS M7000 Imaging System to detect any macroscopic and/or microscopic loss of fragments compared to the original structure (an example of the identification of disintegration signs is given in Figure S4, Supporting Infrmation) and to assess their durability, as reported in Figure 6B.

Three days after the beginning of the observation, all the structures maintained their original shape, and we did not record any strand detachment from the main structure, regardless of the presence of sericin. After 14 days, more than 80% of the bioprinted patches from sericin-containing hydrogels maintained their integrity and around 75% of Ser0%-derived patches survived undamaged from the incubation event. At day 28, the wholeness of patches bioprinted from Ser0% hydrogel was disintegrated, whereas the durability of Ser2% and Ser3% patches was statistically different with a 33% ($p < 0.001$) and 28% ($p < 0.05$) of intact structures recorded, respectively. The obtained durability results stated that the addition of sericin at concentrations of 2% and 3% w/v improved the durability of alginate-gelatin hydrogels, while Ser1% did not significantly affect this property (Figure 6B).

Effectively, this effect might be correlated with the increase of hydrogel's elasticity assessed by Brillouin microspectroscopy analysis, which reported a significant increase in the frequency shift for Ser2% and Ser3% compared to Ser0% (Figure 4), even after incubation with cell culture medium. The slight difference between the durability of Ser2%- and Ser3%-derived patches in cell medium could be justified by referring to their swelling behavior (Figure 5A). Indeed, owing to higher swelling rate, Ser3% might have caused slightly more rapid degradation of the bioprinted patches in PBS than Ser2%.[67]

3.4. The addition of sericin improves cardiac cell viability during the first 14 days in culture

To evaluate the effect on cardiac cell viability, we cultured CSs embedded in sericin-containing hydrogels for up to 28 days. CSs encompass the most representative cell types of adult human myocardial tissue, and they can recapitulate the complexity of the cardiac microenvironment.[24] At predetermined timepoints of 3, 14, and 28 days, we performed a live/dead assay. At each time point, the ratio between dead and live cells (henceforth toxicity ratio) was determined by evaluating the fluorescence of calcein-AM and EthD-1. As a cell-permeant dye, calcein-AM can freely diffuse into cells, but its acetoxymethyl ester structure can be cleaved only by intracellular esterase of live cells to produce the related green, fluorescent calcein. On the contrary, EthD-1 can only penetrate cells whose membranes have been damaged thus allowing the dye to bind nucleic acids of dead cells. Figure 7 summarizes the toxicity ratios measured at each time point together with the representative images derived from our confocal analysis. After 3 days, the toxicity ratios of CSs embedded in Ser2% and Ser3% formulations were significantly lower than Ser0% hydrogel. A reduction of 25% ($p < 0.01$) and 26% ($p < 0.001$) of the Ser0% toxicity ratio was recorded for Ser2% and Ser3%, respectively (Figure 7E). This result stated that the sericin concentrations used in hydrogels were not toxic for CSs. Quite the opposite, Ser2% and Ser3% supported the viability of cardiac cells, as stated by the reduction of the toxicity ratio as a result of an increased number of live cells. The observed trend was also confirmed after day 14 (Figure 7J) when we recorded a significant amelioration of the toxicity ratio for both formulations compared to Ser0%. However, after 28 days the toxicity ratio values of CSs embedded in all sericin-containing hydrogels were comparable to Ser0%, without any statistically significant difference (Figure 7O). We speculate that during the first 14 days of culturing in sericin-containing hydrogels, the cardiac cells were able to use the protein as a metabolic source before it was completely depleted, considering the spontaneous degradation of the hydrogel and the partial dissolution of sericin within the cell culture medium (regularly refreshed). This hypothesis is in accordance with

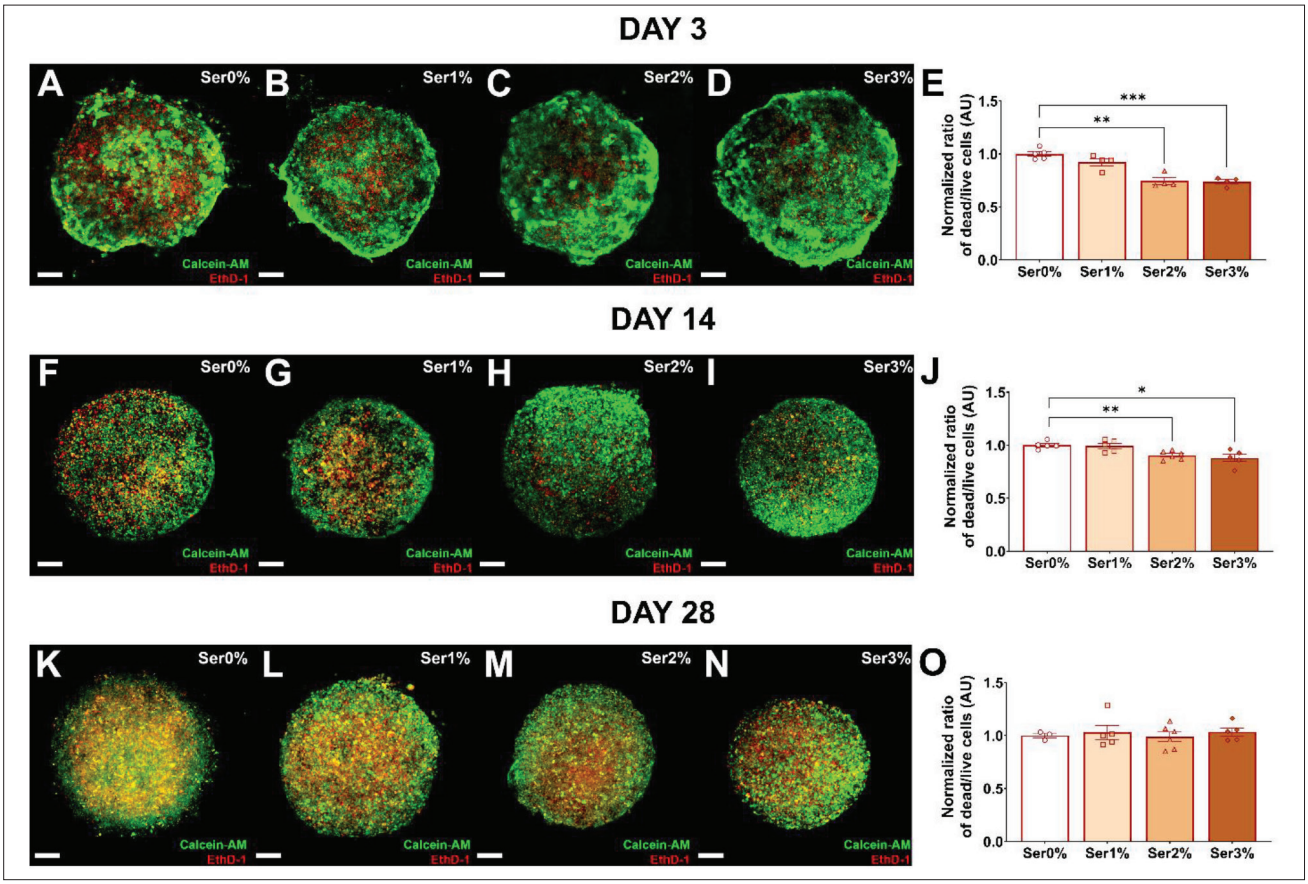

Figure 7. Representative confocal images of Live/Dead assay of CSs embedded in sericin-enriched hydrogels (A–D) after 3 days, (F–I) after 14 days, and (K–N) after 28 days of incubation (37°C, 5% CO2 in air). These images show the live (green, calcein-AM) and dead (red, EthD-1) staining of CSs. Statistical analysis of Dead/Live Cells Ratio of CSs (E) after 3 days, (J) after 14 days, and (O) after 28 days of incubation. Brown–Forsythe and Welch ANOVA test was used to compare the groups (*$p < 0.05$, **$p < 0.01$, ***$p < 0.001$). Error bars represent the mean ± SE and are within the symbols if not visible ($n \geq 3$). Scale bars: 100 μm. Abbreviations: CSs, cardiac spheroids; EthD-1: ethidium homodimer 1.

previous studies demonstrating that sericin enhances cellular energy metabolism and mitochondrial function and reduces apoptosis in cardiomyocytes and endothelial cells.[36,40,41] Sericin's capability to improve the viability and proliferation of certain cell types has been already documented in previous studies and explained as an effect of the protein's naturally cell-adhesive property and ability to affect cellular pathways. For example, the effect of sericin in promoting the viability and migration of human umbilical vessel endothelial cells, as well as antagonizing endothelial cells and cardiomyocytes apoptosis, has been attributed to sericin's intrinsic capability of promoting vascular endothelial growth factor alpha (VEGFα) expression.[36] We reckon that the improved viability of CSs embedded in sericin-containing hydrogels was certainly due to the intrinsic features of the protein, although a great contribution to this effect should be ascribed to the modifications that the protein had on hydrogel properties. Indeed, the reduction of toxicity ratio matched the increase of Ser2% and Ser3% hydrogels' porosity (Figure 5D), together with their improved mechanical properties (Figures 3A and 4C) and enhanced durability (Figure 6B). Moreover, the addition of sericin did not alter the CS contractile activity as demonstrated by the absence of statistically significant differences in both contraction frequency and fractional shortening % (FS%) of CSs embedded in Ser3% compared to the control Ser0% (Figure S5, Supporting Information).

3.5. Sericin-containing hydrogels increase the presence of cardiac fibroblasts in CSs

To evaluate if the addition of sericin could have affected the cell populations of CSs embedded in hydrogels, we performed an immunostaining.[25] Toward this end, after 28 days of culture in the cell medium, the CSs embedded in all formulated hydrogels were labeled to identify HCAECs, HCFs, and iCMs.[29] We thus measured the fluorescence derived from each labeled cell type during the confocal

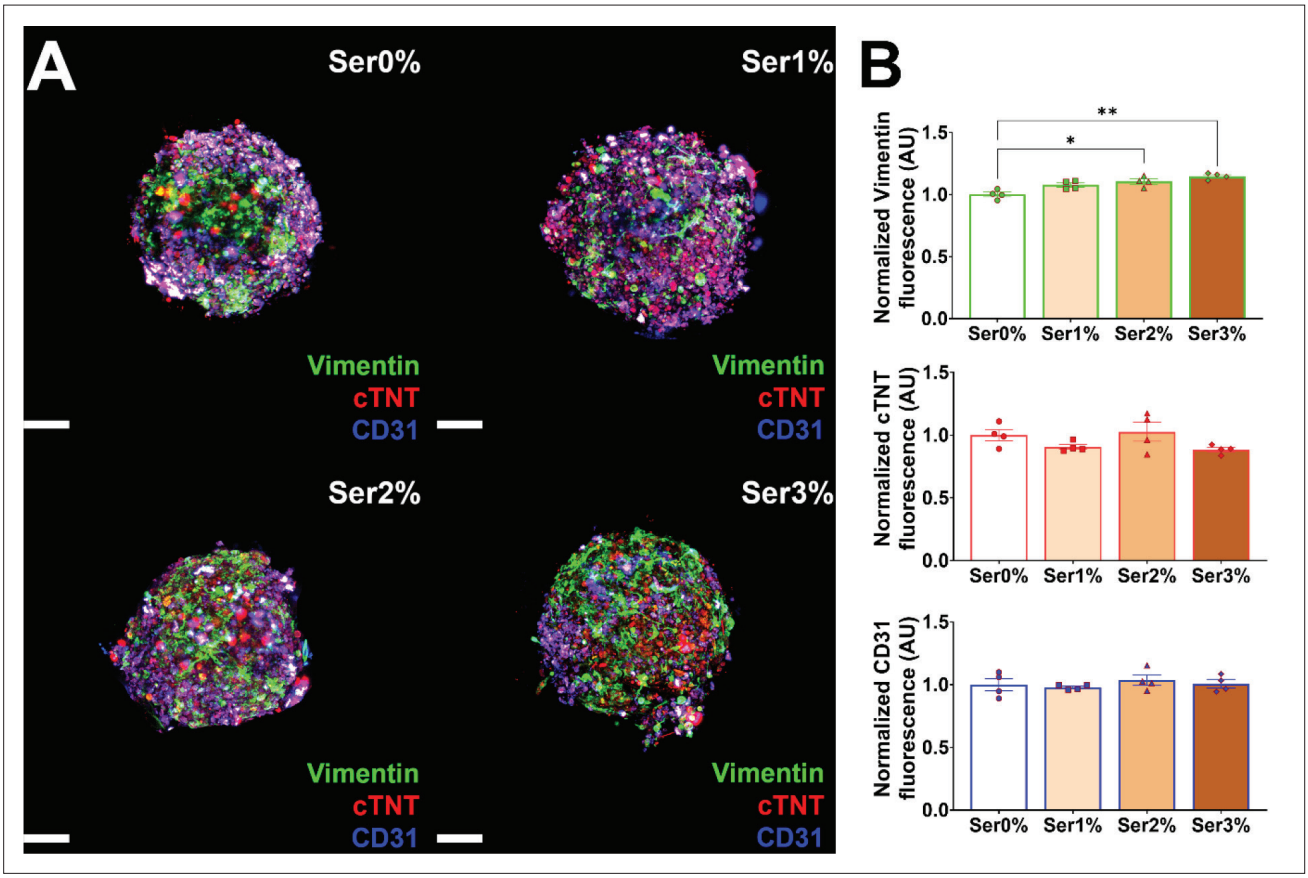

Figure 8. Collapsed z-stacks of confocal images of representative CSs after 28 days of incubation with sericin-containing hydrogels. (A) The CSs were stained with antibodies against vimentin (green) for HCFs, cTNT (red) for iCMs, and CD31 (blue) for HCAECs. Scale bars: 100 µm. (B) Statistical analyses of stained cells fluorescence were performed using Brown–Forsythe and Welch ANOVA test to compare the groups (*p < 0.05, **p < 0.01). Error bars represent the mean ± SE and are within the symbols if not visible (n = 4). Abbreviations: BM, brillouin microspectroscopy; CSs, cardiac spheroids; cTNT, Troponin T-C Antibody (CT3) Alexa Fluor® 546-conjugated; HCAECs, human coronary artery endothelial cells; HCFs, human cardiac fibroblasts; iCMs, iCell® cardiomyocytes.

microscope analysis of samples. Figure 8A shows the collapsed z-stacks of confocal images of representative CSs embedded in both Ser0% and hydrogels with increasing sericin content. Cardiac endothelial cells, fibroblasts, and cardiomyocytes stained with antibodies against CD31 (blue), vimentin (green), and cTNT (red), respectively, were present in all CSs derived from the long-term embedding in Ser1%, Ser2%, and Ser3% as in Ser0%. We did not record a statistically significant reduction of any cell-type fluorescence (Figure 8B). However, we documented an increase in the presence of cardiac fibroblast which was proportional to the protein concentration in hydrogels and became significant for Ser2% ($p < 0.05$) and Ser3% ($p < 0.01$) (Figure 8B). This result was confirmed by the 3D rendering of CSs obtained with Imaris software (Figure 9). The enhanced presence of cardiac fibroblasts after 28 days of embedding in sericin-containing hydrogels is likely related to the increased elasticity properties of Ser2% and Ser3%, justified by both our Brillouin microspectroscopy and rheology studies (Figures 3 and 4). Indeed, fibroblasts are sensitive to mechanical properties such as stiffness and elasticity, and they respond to changes in these parameters by modulating their motility and spreading.[69] For the first time, we documented this effect played on HCFs within CSs generated *in vitro*, since although this property of sericin is not new it has been reported before only for non-cardiac or non-human fibroblasts cell lines.[37,52,54,64,70]

4. Conclusion

In this study, we biofabricated for the first time alginate-gelatin hydrogels supplemented with increasing concentrations of sericin from silkworm *B. mori* and investigated their mechanical and structural properties, together with their potential application in 3D bioprinting as bioinks. Sericin-containing hydrogels exhibited improved

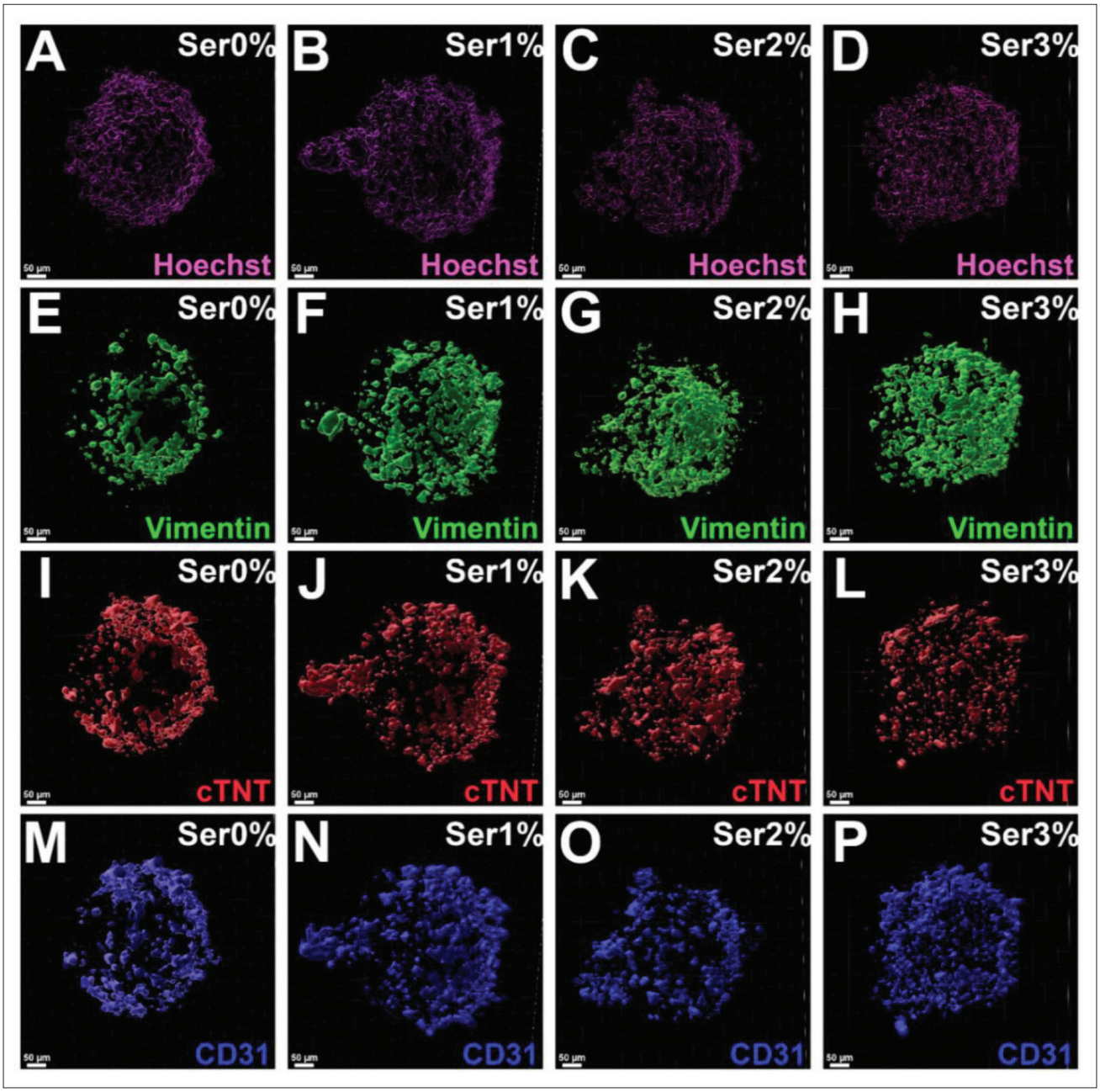

Figure 9. 3D rendering of immunostained CSs after 28 days of culturing in sericin-containing hydrogels. CSs nuclei were stained with (A–D) Hoechst (magenta) and labeled with antibodies against (E–H) vimentin (green, HCFs), (I–L) cTNT (red, iCMs), and (M–P) CD31 (blue, HCAECs). Scale bars: 50 µm. The full-length 3D-rendering videos of CSs are available as Videos S1–S4, Supporting Information..

mechanical properties in terms of elasticity, compression modulus, and viscosity, with higher swelling ratio and enhanced porosity than their counterpart sericin-free hydrogel. These properties ameliorated the performance of alginate-gelatin hydrogel bioink, improving the resolution of 3D-bioprinted patches, as well as their durability during simulated cell culture conditions for up to 28 days. The effects derived from the inclusion of sericin were directly related to its concentration within the polymeric hydrogel network. While Ser1% did not significantly affect alginate-gelatin properties, Ser2% and Ser3% formulations recorded the most significant differences in hydrogel mechanical, morphological, and durability features compared to Ser0%. Also, Ser2% and Ser3% improved CSs viability in hydrogels during the first 2 weeks of culture and Ser3% did not affect the contractile activity of CSs. More interestingly,

sericin-containing hydrogels played an effective role in modulating cardiac fibroblast distribution within CSs, but without altering cardiac endothelial and myocyte cellular populations. These results pave the way for further studies regarding the molecular and mechanotransduction mechanisms underlying these effects. Altogether, our findings support the use of sericin-containing hydrogels as advanced and improved bioinks for cardiac applications. To fully validate the therapeutic potential of these sericin-enriched hydrogels, it will be crucial to examine their adhesive performance and integration within dynamic *in vivo* cardiac environments. Future *in vivo* studies will focus on assessing the therapeutic efficacy, biocompatibility, and potential of sericin-enriched hydrogels in promoting cardiac tissue repair, reducing fibrosis, and enhancing functional recovery following MI.

Acknowledgments

The authors acknowledge the use of the Leica STELLARIS 8 confocal microscope in the Microbial Imaging Facility (MIF) in the Faculty of Science, University of Technology Sydney. They would like to thank Louise Cole and Amy Bottomley for their technical assistance. The authors acknowledge the training and the assistance for SEM analysis provided by Herbert Yuan, Professional Officer in the Microstructural Analysis Unit (MAU) in the Faculty of Science, the University of Technology Sydney.

Funding

Dr. Carmine Gentile was supported by a UTS Seed Funding, Heart Research Australia Grant, Perpetual IMPACT Grant, Catholic Archdiocese of Sydney Grant for Adult Stem Cell Research, and a Heart Research Institute Grant. Irina Kabakova and Hadi Mahmodi are supported by the Australian Research Council Centre of Excellence in Optical Microcombs for Breakthrough Science (CE230100006) and the Australian Research Council Centre of Excellence in Quantum Biotechnology (CE230100021). Thomas R. Cox is supported by the National Health and Medical Research Council (NHMRC). Kaitlin Wyllie is supported by the University Postgraduate Award (UPA) from the University of New South Wales (UNSW). Donatella Paolino was supported by grants from the Italian Ministry of Health (PSC SALUTE 2014–2020-POS4 "Cal-Hub-Ria"-T4-AN-09), and PNRR MAD-2022-12376814).

Conflict of interest

Carmine Gentile serves as the Guest Editor of the special issue: *3D Bioprinting DownUnder: Innovation, Advancements and Perspectives*, but did not in any way involve in the editorial and peer-review process conducted for this paper, directly or indirectly. Separately, other authors declare they have no competing interests.

Author contributions

Conceptualization: Carmine Gentile, Martine Tarsitano, Irina Kabakova, Thomas R. Cox, Donatella Paolino
Investigation: Martine Tarsitano, Clara Liu Chung Ming, Dana Idais, Hadi Mahmodi
Methodology: Martine Tarsitano, Carmine Gentile
Validation: Carmine Gentile, Irina Kabakova, Thomas R. Cox
Resources: Benedetta Isella, Carmine Gentile
Data Curation: Martine Tarsitano, Clara Liu Chung Ming, Kaitlin Wyllie
Visualization: Martine Tarsitano, Carmine Gentile
Supervision: Carmine Gentile, Donatella Paolino
Formal analysis: Carmine Gentile, Hadi Mahmodi
Writing – original draft: Martine Tarsitano
Writing – review & editing: Martine Tarsitano, Carmine Gentile, Irina Kabakova, Thomas R. Cox, Donatella Paolino
All authors have read and agreed to the published version of the manuscript.

Ethics approval and consent to participate

Not applicable.

Consent for publication

Not applicable.

Availability of data

Data is available from the corresponding author upon reasonable request.

Further disclosure

Part of or the entire set of findings have been presented in the 2024 Australian Bioprinting Workshop for Tissue Engineering and Regenerative Medicine (Sydney).

References

1. Tsao CW, Aday AW, Almarzooq ZI, et al. Heart disease and stroke statistics—2023 update: a report from the American Heart Association. *Circulation*. 2023;147(8):e93-e621. doi: 10.1161/CIR.0000000000001123

2. Cooke JP. Is cardiovascular regeneration possible? *Methodist Debakey Cardiovasc J*. 2023;19(5):1-4. doi: 10.14797/mdcvj.1307

3. Frantz S, Hundertmark MJ, Schulz-Menger J, Bengel FM, Bauersachs J. Left ventricular remodelling post-myocardial infarction: pathophysiology, imaging, and novel therapies. *Eur Heart J.* 2022;43(27):2549-2561. doi: 10.1093/eurheartj/ehac223

4. Schwinger RHG. Pathophysiology of heart failure. *Cardiovasc Diagn Ther.* 2021;11(1):263-276. doi: 10.21037/cdt-20-302

5. Awad MA, Shah A, Griffith BP. Current status and outcomes in heart transplantation: a narrative review. *Rev Cardiovasc Med.* 2022;23(1):11. doi: 10.31083/j.rcm2301011

6. Mantha A, Lee RO, Jr., Wolfson AM. Patient selection for heart transplant: balancing risk. *Curr Opin Organ Transplant.* 2022;27(1):36-44. doi: 10.1097/mot.0000000000000943

7. Benck L, Kransdorf EP, Emerson DA, et al. Recipient and surgical factors trigger severe primary graft dysfunction after heart transplant. *J Heart Lung Transplant.* 2021;40(9):970-980. doi: 10.1016/j.healun.2021.06.002

8. Huang K, Ozpinar EW, Su T, et al. An off-the-shelf artificial cardiac patch improves cardiac repair after myocardial infarction in rats and pigs. *Sci Transl Med.* 2020;12(538):eaat9683. doi: 10.1126/scitranslmed.aat9683

9. Wu CA, Zhu Y, Woo YJ. Advances in 3D bioprinting: techniques, applications, and future directions for cardiac tissue engineering. *Bioengineering (Basel).* 2023; 10(7):842. doi: 10.3390/bioengineering10070842

10. Das S, Nam H, Jang J. 3D bioprinting of stem cell-laden cardiac patch: a promising alternative for myocardial repair. *APL Bioeng.* 2021;5(3):031508. doi: 10.1063/5.0030353

11. Budharaju H, Sundaramurthi D, Sethuraman S. Efficient dual crosslinking of protein-in-polysaccharide bioink for biofabrication of cardiac tissue constructs. *Biomater Adv.* 2023;152:213486. doi: 10.1016/j.bioadv.2023.213486

12. Zheng Z, Tang W, Li Y, et al. Advancing cardiac regeneration through 3D bioprinting: methods, applications, and future directions. *Heart Fail Rev*. 2024;29(3):599-613. doi: 10.1007/s10741-023-10367-6

13. Yao Y, Li A, Wang S, et al. Multifunctional elastomer cardiac patches for preventing left ventricle remodeling after myocardial infarction in vivo. *Biomaterials*. 2022;282: 121382. doi: 10.1016/j.biomaterials.2022.121382

14. Garbern JC, Lee RT. Heart regeneration: 20 years of progress and renewed optimism. *Dev Cell.* 2022;57(4):424-439. doi: 10.1016/j.devcel.2022.01.012

15. Liu Chung Ming C, Ben-Sefer E, Gentile C. Stem cell-based 3D bioprinting for cardiovascular tissue regeneration. In: Zhang J, Serpooshan V, eds. *Advanced Technologies in Cardiovascular Bioengineering*. Springer International Publishing; 2022:281-312. doi: 10.1007/978-3-030-86140-7_13

16. Brazhkina O, Park JH, Park HJ, et al. Designing a 3D printing based auxetic cardiac patch with hiPSC-CMs for heart repair. *J Cardiovasc Dev Dis.* 2021;8(12):172. doi: 10.3390/jcdd8120172

17. Matthews N, Pandolfo B, Moses D, Gentile C. Taking it personally: 3D bioprinting a patient-specific cardiac patch for the treatment of heart failure. *Bioengineering.* 2022;9(3):93. doi: 10.3390/bioengineering9030093

18. Budharaju H, Subramanian A, Sethuraman S. Recent advancements in cardiovascular bioprinting and bioprinted cardiac constructs. *Biomater Sci.* 2021;9(6):1974-1994. doi: 10.1039/D0BM01428A

19. Lu TY, Xiang Y, Tang M, Chen S. 3D printing approaches to engineer cardiac tissue. *Curr Cardiol Rep.* 2023;25(6):505-514. doi: 10.1007/s11886-023-01881-y

20. Baheiraei N, Razavi M, Ghahremanzadeh R. Reduced graphene oxide coated alginate scaffolds: potential for cardiac patch application. *Biomater Res.* 2023; 27(1):109. doi: 10.1186/s40824-023-00449-9

21. Fischer B, Gwinner F, Gepp MM, et al. A highly versatile biopolymer-based platform for the maturation of human pluripotent stem cell-derived cardiomyocytes enables functional analysis in vitro and 3D printing of heart patches. *J Biomed Mater Res A.* 2023;111(10):1600-1615. doi: 10.1002/jbm.a.37558

22. Loureiro J, Miguel SP, Galván-Chacón V, et al. Three-dimensionally printed hydrogel cardiac patch for infarct regeneration based on natural polysaccharides. *Polymers.* 2023;15(13):2824. doi: 10.3390/polym15132824

23. Kazemi Asl S, Rahimzadegan M, Ostadrahimi R. The recent advancement in the chitosan hybrid-based scaffolds for cardiac regeneration after myocardial infarction. *Carbohydr Polym.* 2023;300:120266. doi: 10.1016/j.carbpol.2022.120266

24. Sharma P, Gentile C. Cardiac spheroids as in vitro bioengineered heart tissues to study human heart pathophysiology. *J Vis Exp.* 2021;167(167):33554972. doi: 10.3791/61962

25. Polonchuk L, Chabria M, Badi L, et al. Cardiac spheroids as promising in vitro models to study the human heart microenvironment. *Sci Rep*. 2017;7(1):7005. doi: 10.1038/s41598-017-06385-8

26. Sharma P, Liu Chung Ming C, Wang X, et al. Biofabrication of advanced in vitro 3D models to study ischaemic and doxorubicin-induced myocardial damage. *Biofabrication*. 2022;14(2):109-116.
doi: 10.1088/1758-5090/ac47d8

27. Sharma P, Wang X, Ming CLC, et al. Considerations for the bioengineering of advanced cardiac in vitro models of myocardial infarction. *Small*. 2021;17(15):e2003765.
doi: 10.1002/smll.202003765

28. Roche CD, Lin H, Huang Y, et al. 3D bioprinted alginate-gelatin hydrogel patches containing cardiac spheroids recover heart function in a mouse model of myocardial infarction. *Bioprinting*. 2023;30:e00263.
doi: 10.1016/j.bprint.2023.e00263

29. Polonchuk L, Surija L, Lee MH, et al. Towards engineering heart tissues from bioprinted cardiac spheroids. *Biofabrication*. 2021;13(4):34265755.
doi: 10.1088/1758-5090/ac14ca

30. Roche CD, Sharma P, Ashton AW, Jackson C, Xue M, Gentile C. Printability, durability, contractility and vascular network formation in 3D bioprinted cardiac endothelial cells using alginate-gelatin hydrogels. *Front Bioeng Biotechnol*. 2021;9:636257.
doi: 10.3389/fbioe.2021.636257

31. Saad M, El-Samad LM, Gomaa RA, Augustyniak M, Hassan MA. A comprehensive review of recent advances in silk sericin: extraction approaches, structure, biochemical characterization, and biomedical applications. *Int J Biol Macromol* 2023;250:126067.
doi: 10.1016/j.ijbiomac.2023.126067

32. Sahoo JK, Hasturk O, Falcucci T, Kaplan DL. Silk chemistry and biomedical material designs. *Nat Rev Chem*. 2023;7(5):302-318.
doi: 10.1038/s41570-023-00486-x

33. Liu J, Shi L, Deng Y, et al. Silk sericin-based materials for biomedical applications. *Biomaterials*. 2022;287:121638.
doi: 10.1016/j.biomaterials.2022.121638

34. Capar G, Pilevneli T. Cost-effective process development for sericin recovery from silk degumming wastewater. *Sustain Chem Pharm*. 2024;37:101405.
doi: 10.1016/j.scp.2023.101405

35. Silva AS, Costa EC, Reis S, et al. Silk sericin: a promising sustainable biomaterial for biomedical and pharmaceutical applications. *Polymers*. 2022;14(22):4931.
doi: 10.3390/polym14224931

36. Song Y, Zhang C, Zhang J, et al. An injectable silk sericin hydrogel promotes cardiac functional recovery after ischemic myocardial infarction. *Acta Biomater*. 2016;41:210-223.
doi: 10.1016/j.actbio.2016.05.039

37. Han L, Wang W, Chen Z, et al. Sericin-reinforced dual-crosslinked hydrogel for cartilage defect repair. *Colloids Surf B Biointerfaces*. 2023;222:113061.
doi: 10.1016/j.colsurfb.2022.113061

38. Zhang Y, Liu J, Huang L, Wang Z, Wang L. Design and performance of a sericin-alginate interpenetrating network hydrogel for cell and drug delivery. *Sci Rep*. 2015;5:12374.
doi: 10.1038/srep12374

39. Li Y, Wei Y, Zhang G, Zhang Y. Sericin from fibroin-deficient silkworms served as a promising resource for biomedicine. *Polymers*. 2023;15(13):2941.
doi: 10.3390/polym15132941

40. Rahimpour S, Jabbari H, Yousofi H, et al. Regulatory effect of sericin protein in inflammatory pathways; a comprehensive review. *Pathol Res Pract*. 2023;243:154369.
doi: 10.1016/j.prp.2023.154369

41. Rujimongkon K, Ampawong S, Isarangkul D, Reamtong O, Aramwit P. Sericin-mediated improvement of dysmorphic cardiac mitochondria from hypercholesterolaemia is associated with maintaining mitochondrial dynamics, energy production, and mitochondrial structure. *Pharm Biol*. 2022;60(1):708-721.
doi: 10.1080/13880209.2022.2055088

42. Zhu Y, Liu H, Qin S, et al. Antibacterial sericin cryogels promote hemostasis by facilitating the activation of coagulation pathway and platelets. *Adv Healthc Mater*. 2022;11(11):2102717.
doi: 10.1002/adhm.202102717

43. Mukherjee S, Krishnan A, Athira RK, Kasoju N, Sah MK. Chapter 13 - silk fibroin and silk sericin in skin tissue engineering and wound healing: retrospect and prospects. In: Sah MK, Kasoju N, Mano JF, eds. *Natural Polymers in Wound Healing and Repair*. Elsevier; 2022: 301-331.
doi: 10.1016/B978-0-323-90514-5.00005-5

44. Vettori L, Sharma P, Rnjak-Kovacina J, Gentile C. 3D bioprinting of cardiovascular tissues for in vivo and in vitro applications using hybrid hydrogels containing silk fibroin: state of the art and challenges. *Curr Tissue Microenviron Rep*. 2020;1(4):261-276.
doi: 10.1007/s43152-020-00026-5

45. Song Y, Wang H, Yue F, et al. Silk-based biomaterials for cardiac tissue engineering. *Adv Healthc Mater*. 2020;9(23):e2000735.
doi: 10.1002/adhm.202000735

46. Tarsitano M, Mancuso A, Cristiano MC, Paolino D, Fresta M. In situ swelling formulation of glycerol-monooleate-derived lyotropic liquid crystals proposed for local vaginal application. *Molecules*. 2022;27(19):6295.
doi: 10.3390/molecules27196295

47. Mancuso A, Cianflone E, Cristiano MC, et al. Lyotropic liquid crystals: a biocompatible and safe material for local cardiac application. *Pharmaceutics*. 2022;14(2):452.
doi: 10.3390/pharmaceutics14020452

48. Mahmodi H, Piloni A, Utama RH, Kabakova I. Mechanical mapping of bioprinted hydrogel models by brillouin microscopy. *Bioprinting*. 2021;23:e00151. doi: 10.1016/j.bprint.2021.e00151

49. Baptista M, Joukhdar H, Alcala-Orozco CR, et al. Silk fibroin photo-lyogels containing microchannels as a biomaterial platform for in situ tissue engineering. *Biomater Sci*. 2020;8(24):7093-7105. doi: 10.1039/d0bm01010c

50. Schneider CA, Rasband WS, Eliceiri KW. NIH Image to ImageJ: 25 years of image analysis. *Nat Methods*. 2012;9(7):671-675. doi: 10.1038/nmeth.2089

51. Tarsitano M, Liu Chung Ming C, Bennar L, et al. Chlorella-enriched hydrogels protect against myocardial damage and reactive oxygen species production in an in vitro ischemia/reperfusion model using cardiac spheroids. *Biofabrication*. 2025;17(1):015006. doi: 10.1088/1758-5090/ad8266

52. Zhang Y, Cao X, Zhang J, et al. A novel injectable sericin hydrogel with strong fluorescence for tracing. *Int J Biol Macromol*. 2024;258:129000. doi: 10.1016/j.ijbiomac.2023.129000

53. Li J-X, Zhao S-X, Zhang Y-Q. Silk protein composite bioinks and their 3D scaffolds and in vitro characterization. *Int J Mol Sci*. 2022;23(2):910. doi: 10.3390/ijms23020910

54. Vettori L, Tran HA, Mahmodi H, et al. Silk fibroin increases the elasticity of alginate-gelatin hydrogels and regulates cardiac cell contractile function in cardiac bioinks. *Biofabrication*. 2024;16(3):035025. doi: 10.1088/1758-5090/ad4f1b

55. Baptista-Silva S, Borges S, Costa-Pinto AR, et al. In situ forming silk sericin-based hydrogel: a novel wound healing biomaterial. *ACS Biomater Sci Eng*. 2021;7(4):1573-1586. doi: 10.1021/acsbiomaterials.0c01745

56. Chlapanidas T, Faragò S, Lucconi G, et al. Sericins exhibit ROS-scavenging, anti-tyrosinase, anti-elastase, and in vitro immunomodulatory activities. *Int J Biol Macromol*. 2013;58:47-56. doi: 10.1016/j.ijbiomac.2013.03.054

57. Rocha LK, Favaro LI, Rios AC, et al. Sericin from Bombyx mori cocoons. Part I: extraction and physicochemical-biological characterization for biopharmaceutical applications. *Process Biochem*. 2017;61:163-177. doi: 10.1016/j.procbio.2017.06.019

58. Sellimi S, Younes I, Ayed HB, et al. Structural, physicochemical and antioxidant properties of sodium alginate isolated from a Tunisian brown seaweed. *Int J Biol Macromol*. 2015;72:1358-1367. doi: 10.1016/j.ijbiomac.2014.10.016

59. Rad MA, Mahmodi H, Filipe EC, Cox TR, Kabakova I, Tipper JL. Micromechanical characterisation of 3D bioprinted neural cell models using Brillouin microspectroscopy. *Bioprinting*. 2022;25:e00179. doi: 10.1016/j.bprint.2021.e00179

60. Avallone PR, Romano M, Sarrica A, Delmonte M, Pasquino R, Grizzuti N. Effect of sugars on gelation kinetics of gelatin gels. *Fluids*. 2022;7(5):163. doi: 10.3390/fluids7050163

61. Ahmad MI, Li Y, Pan J, et al. Collagen and gelatin: structure, properties, and applications in food industry. *Int J Biol Macromol*. 2024;254:128037. doi: 10.1016/j.ijbiomac.2023.128037

62. Poon C, Chou J, Cortie M, Kabakova I. Brillouin imaging for studies of micromechanics in biology and biomedicine: from current state-of-the-art to future clinical translation. *J Phys Photonics*. 2021;3(1):012002. doi: 10.1088/2515-7647/abbf8c

63. Rioboó RJJ, Gontán N, Sanderson D, Desco M, Gómez-Gaviro MV. Brillouin spectroscopy: from biomedical research to new generation pathology diagnosis. *Int J Mol Sci*. 2021;22(15):8055. doi: 10.3390/ijms22158055

64. Kabakova I, Zhang J, Xiang Y, et al. Brillouin microscopy. *Nature Revs Methods Primers*. 2024;4(1):8. doi: 10.1038/s43586-023-00286-z

65. Wu P-J, Kabakova IV, Ruberti JW, et al. Water content, not stiffness, dominates Brillouin spectroscopy measurements in hydrated materials. *Nat Methods*. 2018;15(8):561-562. doi: 10.1038/s41592-018-0076-1

66. Tao G, Cai R, Wang Y, Zuo H, He H. Fabrication of antibacterial sericin based hydrogel as an injectable and mouldable wound dressing. *Mater Sci Eng C*. 2021;119:111597. doi: 10.1016/j.msec.2020.111597

67. Ekasurya W, Sebastian J, Puspitasari D, Asri PPP, Asri LATW. Synthesis and degradation properties of Sericin/PVA hydrogels. *Gels*. 2023;9(2):76. doi: 10.3390/gels9020076

68. Zhang Y, Chen H, Li Y, et al. A transparent sericin-polyacrylamide interpenetrating network hydrogel as visualized dressing material. *Polymer Test*. 2020;87:106517. doi: 10.1016/j.polymertesting.2020.106517

69. Miri AK, Mirzaee I, Hassan S, et al. Effective bioprinting resolution in tissue model fabrication. *Lab Chip*. 2019;19(11):2019-2037. doi: 10.1039/C8LC01037D

70. Schwartz R, Malpica M, Thompson GL, Miri AK. Cell encapsulation in gelatin bioink impairs 3D bioprinting resolution. *J Mech Behav Biomed Mater*. 2020;103:103524. doi: 10.1016/j.jmbbm.2019.103524

ACCSCIENCE PUBLISHING

International Journal of Bioprinting

RESEARCH ARTICLE

Parametric computational modeling of melt electrowritten scaffolds: Predicting the cellular micromechanical environment for gradient tissue engineering in rotator cuff repair

Sam E. Winston[1], Lynn M. Pezzanite[2], Steven Dow[2], and Kirk C. McGilvray[1]*

[1]Mechanical Engineering, Orthopaedic Bioengineering Research Laboratory, Colorado State University, Fort Collins, Colorado, United States of America

[2]Department of Clinical Sciences, Translational Medicine Institute, Colorado State University, Fort Collins, Colorado, United States of America

Abstract

Surgical interventions of the rotator cuff (RC) tendons are failing at unacceptably high rates. This is primarily due to clinical strategies failing to regenerate the biomechanical junction between bone and tendon (enthesis). Tissue engineering approaches for RC repair involve attempts at increasing the acute strength of the repair and directing the healing cascade to regenerate the enthesis. Advances in bioprinting, specifically melt electrowriting (MEW), allow precise fabrication of microarchitectures. Our group has utilized the functionality MEW offers to create a novel, single-material, gradient scaffold that approaches the mechanical gradients present in the RC. To characterize this novel geometry, high-throughput, parametric finite element analysis (FEA) models were generated: (1) to determine how tunable print parameters such as the radius of curvature of fibers, the fiber diameter, and the fiber spacing alter the gradient present in the scaffold's architecture; and (2) to predict, at the cellular level, what strain the scaffold generates regionally to ``instruct" the local cell milieu to produce healthy tissues (e.g., bone and tendon). FEA models predicted that mechanical gradients in the scaffold approached gradient levels seen in the RC (≈2 orders of magnitude), in which global strain gradients were driven by the radius of curvature of fibers. Additionally, our novel architecture significantly affected regional mechanics, which could be optimized for tenocyte and osteoblastic bioactivity. The data presented demonstrate a novel, tunable architecture capable of approaching biologically relevant gradients observed in the RC with potential to address the clinical problems associated with tendon–bone repairs in other regions of the body using only a single material.

Keywords: Melt electrowriting; Gradient tissue engineering scaffolds; Cellular microenvironment; Finite element analysis; Rotator cuff repair

***Corresponding author:**
Kirk McGilvray
(Kirk.McGilvray@colostate.edu)

Citation: Winston SE, Pezzanite L, Dow S, McGilvray KC. Parametric computational modeling of melt electrowritten scaffolds: Predicting the cellular micromechanical environment for gradient tissue engineering in rotator cuff repair. *Int J Bioprint*. 2025;11(1):347-362. doi: 10.36922/ijb.5125

Received: October 12, 2024
Revised: November 15, 2024
Accepted: November 18, 2024
Published Online: November 19, 2024

Copyright: © 2024 Author(s). This is an Open Access article distributed under the terms of the Creative Commons Attribution License, permitting distribution, and reproduction in any medium, provided the original work is properly cited.

Publisher's Note: AccScience Publishing remains neutral with regard to jurisdictional claims in published maps and institutional affiliations.

1. Introduction

In the United States, over 250,000 rotator cuff (RC) repair surgeries occur annually. These repairs are currently failing at unacceptable rates, around 20–94%.[1,2] Clinical approaches in RC repair generally employ "scaffolds" that attempt first to augment the acute strength of the repair to prevent tendon retraction from the bone and second to encourage the regeneration of the bone–tendon junction following healing.[3] However, examinations of repaired tissues that have re-failed indicate that the native biomechanical transition between bone and tendon, the enthesis, is not regenerated for many scaffold designs.[4] The enthesis repair site instead is replaced by unorganized, weaker scar tissue,[4] which retears due to the abnormal stress concentrations caused by the large disparities in mechanical properties formed across the bone–scar–tendon junction. The suboptimal clinical efficacy of existing scaffolds is partially attributable to their failure to deliver appropriate biomechanical and physiochemical cues to resident and infiltrating cell populations to regenerate enthesis tissues.[5,6]

These limitations have spawned interest in developing "instructive scaffolds," mainly through additive manufacturing (AM) techniques that attempt to replicate the native mechanical gradient of the enthesis. Additive manufacturing has given researchers the ability to develop complex scaffolds with tunable physical and mechanical properties (i.e., strength,[7] porosity, and surface roughness[8]), and has the potential to deliver clinicians the ability to implant patient specific implants.[9-11]

"Mechanically instructive" scaffolds are designed to provide mechanobiological cues to the relevant matrix-producing cell types (tenocytes, chondrocytes, and osteoblasts) to regenerate the native tissues and the extracellular matrix (ECM) characteristic of the enthesis, mitigating aberrant stress concentrations at the bone–tendon interface.[4] An "instructive" scaffold requires that it exposes each cell type to a mechanical microenvironment (encompassing aspects such as stiffness, pressure, strain, and shear) that mirrors the conditions of its corresponding healthy tissue, creating a pro-regenerative environment.

For example, tenocytes and osteoblasts differ largely in the mechanical stimuli they prefer. Osteoblast growth is typically optimized in rough,[12] low-strain environments,[13-18] and tenocyte growth is promoted in aligned,[12,19-21] higher-strain microenvironments.[22-24] Therefore, creating a scaffold to facilitate the successful regeneration of the enthesis requires spatially dependent biomechanical and biophysical properties. Thus, developing stiffness gradients for RC repair involves the use of multimaterial scaffolds (MMS)[25-27] with a limited number of single-material scaffolds (SMSs).[28-30]

However, most SMSs do not recreate the changes in mechanics observed across the bone-to-tendon interface, a change of ≈2 orders of magnitude in stiffness. In the attempt at reducing the stress concentrations observed in both MMSs and SMSs, our group has utilized melt electrowriting (MEW) to generate a novel functionally gradient material scaffold using a single material, which is dubbed Arc-S. The Arc-S uses offsetting arced paths (paths with a defined radius of curvature) to continuously change the fiber intersection angle across the length of the scaffold, generating continuous gradients of mechanical properties with an overall alignment of the fibers in the physiologic loading direction (Figure 1). To facilitate cell infiltration, the Arc-S would be embedded in a hydrogel allowing for the mechanical tailoring of the interstitial spaces.[31] The Arc-S scaffolds are generated with a single radius of curvature (R), which differs from previous gradient scaffolds developed using MEW by causing a tailorable mechanical gradient throughout the length of the scaffold rather than the more typical gradient through the layers (i.e., thickness) of the scaffold.[32-34]

Due to MEW's adaptability, the printing parameters that would contribute most to the Arc-S's graded mechanical properties remain uncharacterized. Computational models of scaffolds have been a valuable resource to model the mechanical behavior of scaffolds and to predict the cellular response to the mechanics of the scaffold.[18,35,36] Thus, previous computational models have aimed to predict how the scaffold mechanics affect the ECM production of cells to inform and optimize scaffold design for a single tissue type.[18,35]

To our knowledge, there are no studies that have developed multitissue finite element analysis (FEA) models to predict and optimize a scaffold for more than one tissue type (e.g., enthesis). Because of the amount of data that corroborates that different cell types respond positively to different stimuli, we aim to use published strain levels for osteoblasts and tenocytes that provide an anabolic response as a predictor of tissue healing. This will allow for the formation of a "tissue healing window" (THW) to quantify and later optimize how Arc-S might provide the correct mechanical loading stimulus to osteoblasts and tenocytes to regenerate the enthesis. Furthermore, due to the aligned nature of the tendon, we aim to investigate and quantify the principal strain distribution in the Arc-S's modeled unit cells to predict potential collagen fiber alignment of the naïve ECM that would be formed/embedded within the scaffold.

These works have three synergistic aims. First, we characterized the ARC-S's bulk gradient mechanical behavior as a function of MEW print geometries via modeling of the scaffold's fibers' regional mechanics. Next,

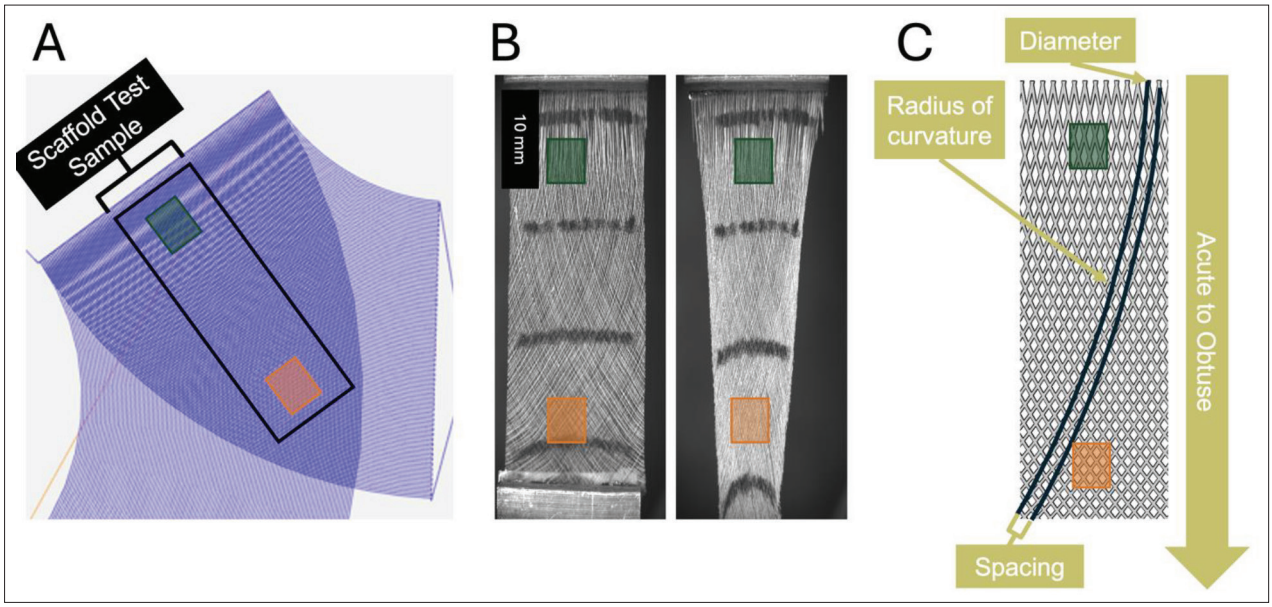

Figure 1. Schematic breakdown of scaffold from conceptualization to printing and modeling. (A) Rendering of Arc-S arced toolpaths with an outline of mechanical testing sample. (B) Scaffold in mechanical testing frame pre-loading and post-loading. The scaffold's acute (green) and obtuse (orange) sections are highlighted. (C) A representative image of the FEA model, with the MEW parameters of interest being highlighted. Abbreviations: FEA, finite element analysis; MEW, melt electrowriting.

we utilized the local displacement field generated from the bulk scaffold to predict how the scaffold's interstitial geometry's unit cell (UC) mechanical environments would facilitate potential bone and tendon healing, through parametric computational modeling. Finally, we aimed to determine how the scaffold geometry drives tissue alignment through eigenvector analysis of the UC models within the tendon healing regions of interest (ROIs).

Through these models, we hypothesize that we can generate an Arc-S that has the same gradient of mechanical properties present in bone and tendon across a length scale of a human enthesis to improve clinical outcomes of RC repair surgeries.

2. Materials and methods

2.1. Overview

MEW-printed scaffolds underwent uniaxial mechanical testing to validate the FEA models (Abaqus/CAE 2021, Dassault Systems, Vélizy-Villacoublay, France). The FEA models were split into two sections: a fibrous model of the scaffold and a representative UC that aimed to model the biomechanics in the interstitial spaces (Figure 2). The aim of the fibrous scaffold models was to create a structure that mimicked the global gradient seen in the RC's enthesis. UC models were developed to predict cellular behavior based on previously published THWs for specific cell types. These UC models will also provide data on functional collagen alignment based on the Arc-s' geometry.

2.2. Scaffold fabrication

Arced toolpath where the central radius of curvature (R) of the scaffold established the overall scaffold architecture (Figure 1A). A series of offsetting arcs were printed; then, a series of mirrored arcs were deposited directly on top of the previous layer, creating an angle-ply bilayer. This resulted in a gradient in fiber alignment across the length of the scaffold, in which two regions at the ends of the scaffold were selected to be analyzed, acute and obtuse, named after the angles formed in each ROI (Figure 1B).

Scaffolds (N = 5) were printed for model validation with a custom-built (MEW) printer using M_n = 45 kDa polycaprolactone (PCL; Polysciences, Inc., Warrington, PA, United States). MEW printer input settings were kept constant for all samples with an extrusion nozzle size of 20 g, pressure of 3.4 psi, 6.7 kV, collector distance of 3 mm, and a fiber spacing of 250 μm, while the radius was the print parameter altered with radius (R) = 50, 75, 100, 125, 150 mm. PCL was selected as it is a biocompatible polymer that prints well through MEW and has been used for both bone and tendon scaffolds.[37,38] After printing, fiber diameter (2 pixels/μm resolution) was measured by brightfield microscopy at 10× magnification (Nikon E800; Image-Pro Plus 10 [RRID:SCR_007369]).

2.3. Mechanical testing

MEW-printed scaffolds were trimmed with a surgical scalpel to a rectangular shape with a width of 15 mm and a length of 40 mm. Scaffolds were tested using a custom-built uniaxial tester, in which they were preloaded to 0.05 N and then loaded in tension to a 4% global strain at 0.1% strain per second (Figure 1B). Load data were collected at 100 Hz (Futek LCM300), and a digital camera (Grasshopper 3 Pt Gray) captured localized displacements at 200 fps. Images were used for digital image correlation and then synchronized with load data. Stress calculations were based on bulk area measurements taken with calipers (±0.1 mm) before testing. Moduli were calculated based on the slope in the linear region of the stress–strain curves. Regional moduli data were analyzed using paired *t*-tests to compare means of acute and obtuse moduli in the same scaffold radius group. Normality in groups was tested used the Shapiro-Wilk tests. Comparisons between acute and obtuse moduli, with *p*-values of <0.05, were considered statistically significant. Statistical tests were completed using GraphPad Prism 10.3.0 (GraphPad Software, Boston, MA, United States).

2.4. FEA fiber model generation

2.4.1. Geometric modeling

Through-thickness mechanics were deemed homogenous within the scaffold, and thus, scaffold geometry was simplified to a single bilayer, 2D wire model. Wire models have shown high predictive fidelity with sub-micro resolution for modeling microfibers previously and have the added advantage of limiting the computational burden of meshing with 3D elements.[39] Offsetting arcs were generated using a sweep path (Figure 2), and these arcs then underwent a duplication mirroring, which were merged with the original arc pattern. Perfect bonding between the two layers of the scaffold was applied. The part was then assigned a beam section with specific fiber diameters, recreating the 40 mm × 15 mm scaffold tested experimentally. These models were meshed using linear beam elements (B21) with a seed size of 0.15 mm. PCL was modeled as a linear elastic material with the properties E = 265 MPa and υ = 0.3.[40]

2.4.2. Boundary conditions

Nodes at the acute edge of the scaffold were fixed in all three degrees of freedom (U1 = U2 = UR3 = 0). Nodes at

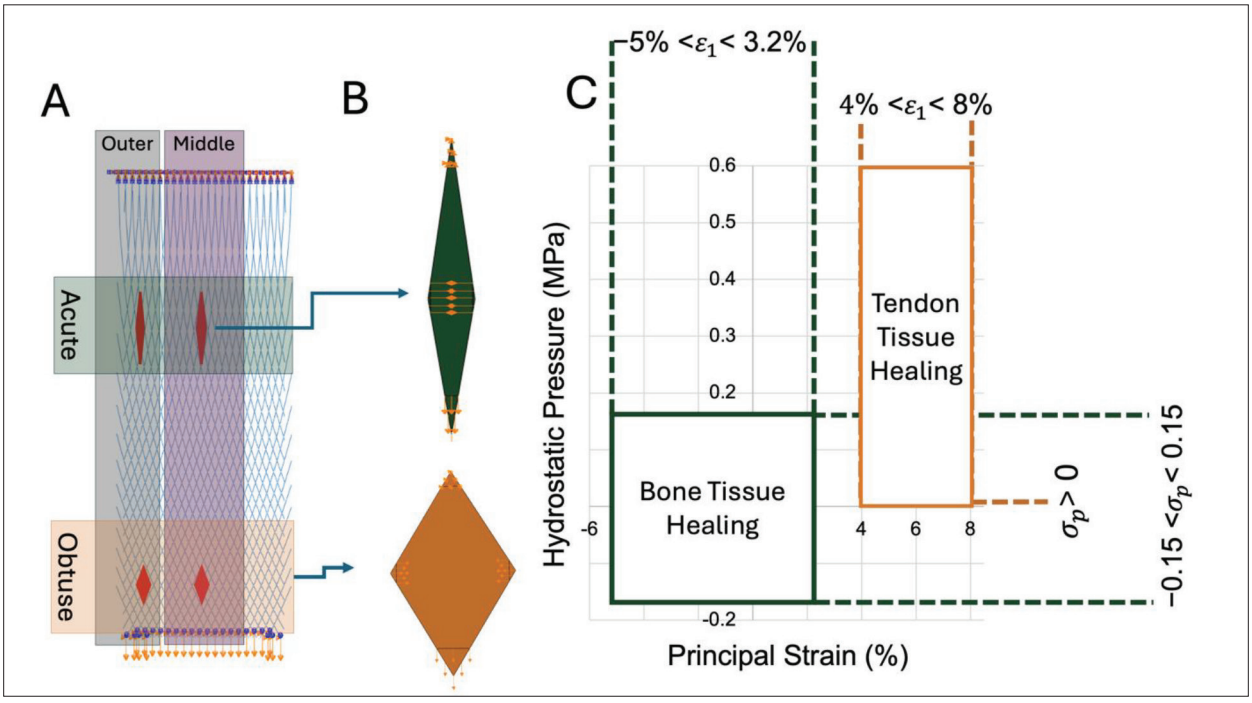

Figure 2. Breakdown of unit cell (UC) workflow and predictive modeling. (A) Graphical representative of unit cell (UC) generation, with middle/outer and acute/obtuse regions highlighted. (B) Part models of the representative acute and obtuse UCs are expanded to illustrate geometric differences and are bound by geometric differences and their respective boundary conditions. UC boundary conditions were matched by displacements found in the corresponding scaffold geometry. (C) Plot of tissue healing window (THW) for bone and tendon based on previously published data for optimization for bone and tendon healing. Bounds set for bone (osteoblasts) were −5% < ε1 < 3.2%, −0.15 MPa < σp < 0.15 MPa.. Bounds set for tendon (tenocytes) were 0 MPa < σp and 4% < ε1 < 8%.

the obtuse edge of the scaffold were loaded to 4% global strain along its primary axis while being constrained in all other directions (U2 = 1.6 mm, U1 = UR3 = 0).

2.4.3. Mesh convergence and validation

A mesh convergence was conducted by increasing the number of elements by 50% until the total strain energy of the model was reduced by less than 3%.[36,41] The FEA models were validated by comparing FEA prediction strains to strains measured in the mechanical testing experiments in both acute and obtuse regions of each specific scaffold geometry.

2.4.4. Parametric study design

To investigate how different print parameters alter the gradient properties of the scaffold, parametric FEA models were generated with varying fiber diameter (FD), fiber spacing (FS), and radius of curvature (*R*) (Figure 1C) for a total of 810 simulations. These parameters were selected because they are controllable during the MEW printing process and were deemed the architectural parameters most responsible for the graded mechanical effects in these scaffolds. Specifically, *R* = 38.5 mm was the smallest printable radius having enough fibers to fit the mechanical testing geometry, FD = 10 μm was the smallest diameter printable on our MEW machine, and 70 μm as an upper bound is well within MEW printability.[42] Smaller resolution increments were examined on the lower end of the diameter parametric table for two reasons: (1) it was predicted that smaller diameters would induce larger changes to the gradient behavior. Due to the curvature of the fibers, the obtuse region is placed in bending, allowing for the bending stiffness of the fibers to become more sensitive to loads as the diameter decreases. (2) Literature primarily focuses on printing MEW fibers on the lower parametric range since smaller fibers have been shown to be cellularly instructive for tissue healing.[21,43-45] An FS = 200 μm was chosen as a minimum fiber spacing to curb fiber bridging that could be present when moving forward with MEW prints of these scaffolds.[46] A known phenomenon where the accumulated charge in layer alignment of previously deposited fibers influences the placement of fibers that are being jetted (Table 1).

2.4.5. FEA analysis

Table 1. Parametric table for fibrous model of scaffold

Parameter	Start value	End value	Increment
Radius	38.5 mm	150 mm	12.5mm
Fiber diameter	10 μm	70 μm	5 μm from 10–30 μm 10 μm from 30–70μm
Fiber spacing	200 μm	600 μm	50 μm

For each scaffold geometry, displacement data was taken from a set of nodes down the middle and middle-outside length of the scaffold. These displacements were used to calculate finite strain using a numerical derivative (**Equation I**).

$$\varepsilon = \frac{\Delta u}{\Delta x}, \tag{I}$$

where ``*u*" represents displacement and ``*x*" denotes the nodes' initial position along the scaffold's length. The gradient effects of each scaffold geometry were calculated as a ratio of the acute and obtuse strains on the middle path, dubbed the strain gradient factor (SGF). This metric provided a nondimensional parameter to determine the magnitude of the stiffness gradient generated for each scaffold geometry, with larger SGFs being representative of a larger magnitude of change in mechanics across the length of the scaffold. Scaffolds with an SGF ≥50 could be deemed to recapitulate the expected mechanical gradient between bone and tendon observed in the RC.[47-49] Spearman's correlations were calculated to quantify each parameter's effect on the SGF.

2.5. Hydrogel model generation

2.5.1. Geometric modeling

To assess how the scaffold's geometry affected cellular response, four sub-regions of each scaffold geometry were taken and loaded with the displacements calculated from the corresponding whole scaffold ROI. The UCs generated were modeled as the resultant quadrilateral formed in the space between the MEW scaffold fibers. UCs representing each sub-region of one scaffold geometry were named after their respective positions within the scaffold: "outer acute," "middle acute," "outer obtuse," and "middle obtuse." Outer and inner UCs were analyzed to determine the effects that changes in the local strains subsequently drive differences in cellular behavior with respect to the cell's transverse position on the scaffold. The total number of simulations of the UC was 3240.

2.5.2. Meshing and materials

UCs were meshed at a seed size of 20 μm with 2D plane stress linear elements (CPS3). The interstitial hydrogel, modeled as GELMA, was assumed to be a linear elastic material with the following properties E = 50 kPa and ν = 0.3. The loading condition was displacement-controlled biaxial load with no unloading effects considered. Each UC vertex was subjected to the corresponding vertex's displacement calculated from the fibrous scaffold relative to the top vertex, such that the top vertex was fixed (Figure 2B).

2.5.3. Tissue healing window generation

To analyze how acute and obtuse regions of each scaffold would affect bone and tendon healing, a THW for osteoblast and tenocytes was developed. This window was created from published stress and strain data that showed anabolic responses to osteoblasts and tenocytes. Bounds for the bone and tendon healing window were $-5\% < \varepsilon_1 < 3.2\%$, -0.15 MPa $< \sigma_p < 0.15$ for osteoblast (bone) and 0 MPa $< \sigma_p$ and $4\% < \varepsilon_1 < 8\%$ (Figure 2C) with no hydrostatic pressure bounds for tenocytes (tendon).[13-18,21-23] It should be noted that the biomechanical bounds for tenocyte bioactivity are not as defined as that for osteoblasts, and thus, the tenocyte bounds herein represent a conservative THW.

The hydrostatic pressure and maximum principal strain were reported for each element within the UC and plotted against the THW. This enabled the calculation of the percentage (%) of elements within the THW for each scaffold geometry and ROI, giving insight into how the local mechanics of the scaffolds' gel-loaded interstitial spaces could potentially influence cell behavior. Obtuse and acute UCs were plotted against the tendon and bone THW, respectively (Figure 2C). Spearman's correlation coefficients were then calculated on each region to observe general trends in how print parameters affect predicted cellular activity. Optimal scaffold geometries were determined by taking the average between the middle and outer regions to identify the corresponding scaffold geometry with the maximum average percentage for each cell type.

2.5.4. Eigenvector analysis of obtuse regions to determine cell alignment

As a result of UC loading, a significant transverse compression was placed on the vertices of the UC, shifting in the principal alignment of the resultant eigenvector loads. This is of interest as cells are sensitive to eigenvector alignment, because they preferentially deposit ECM parallel to this axis *in vivo*.[50,51] To quantify potential shifts in the principal axis, distributions of elements' first eigenvectors were plotted in a histogram to visually examine the distribution of angles in the UC. Visual inspection of the data distribution revealed a non-uniform angular distribution, leading to the use of a von Mises distribution to quantify distribution coefficients, and using Maximum Likelihood Estimation (MLE) (Python, SciPy), where and represent a predictor of how well aligned the produced ECM would be and a validation that the location angle is in line with the loading direction, respectively.

3. Results

3.1. Mesh convergence and validation

Convergence was achieved at 24,000 elements. FEA predictions of regional strain fell within one standard deviation of 9 of 10 experimental scaffold groups (Figure 3A and B) with only the acute region of $R = 100$ mm group showing disagreement between experimental and FEA groups. At $R = 100$ mm, experimental data began to converge towards acute and obtuse regions having statistically the same modulus, indicating an inflection

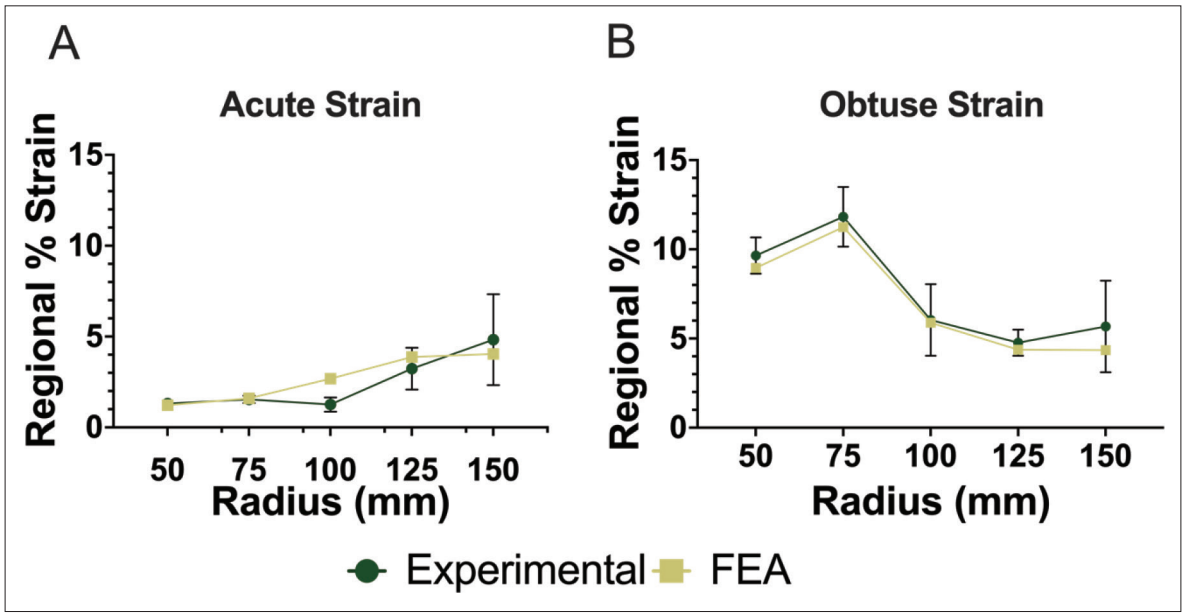

Figure 3. *Finite element model validation data.* (A) Strain measurements in acute region of scaffold for varying radii in experimental and FEA groups. Data of experimental group are plotted as mean ± SD. (B) Strain measurements in obtuse region of scaffold for varying radii in experimental and FEA groups. Data of experimental group are plotted as mean ± SD.

point in experimental results. The discrepancy in FEA and experimental data might be due to FEA predicting this inflection point early due to increased stiffness in the model that is persistently present in FEA modeling. This disparity was considered negligible since the behavior in the FEA models did agree with experimental results across the other groups, and it was assumed that the FEA models were successfully predicting experimental results, validating the models. Because the fibers were orders of magnitude stiffer than the hydrogel filler used for this study, it was assumed that since the fiber model was fully validated, mechanics of the hydrogel filler would be valid as the fibers would dominate the mechanical behavior of the construct.

3.2. Mechanical testing of fibrous scaffolds

Average regional moduli ranged from 206 ± 45.1 to 24.2 ± 3.4 kPa, 219 ± 117.7 to 22.4 ± 6.8 kPa, 250 ± 39.4 to 55.1 ± 12.1 kPa, 396 ± 150 to 208 ± 43.5 kPa, and 255 ± 84.7 to 207 ± 58 kPa, for R = 50, 75, 100, 125, and 150 mm, respectively (Figure 4). All sample groups passed the Shapiro-Wilk normality tests. Paired t-tests revealed statistical differences in scaffold groups, R = 50, 75, and

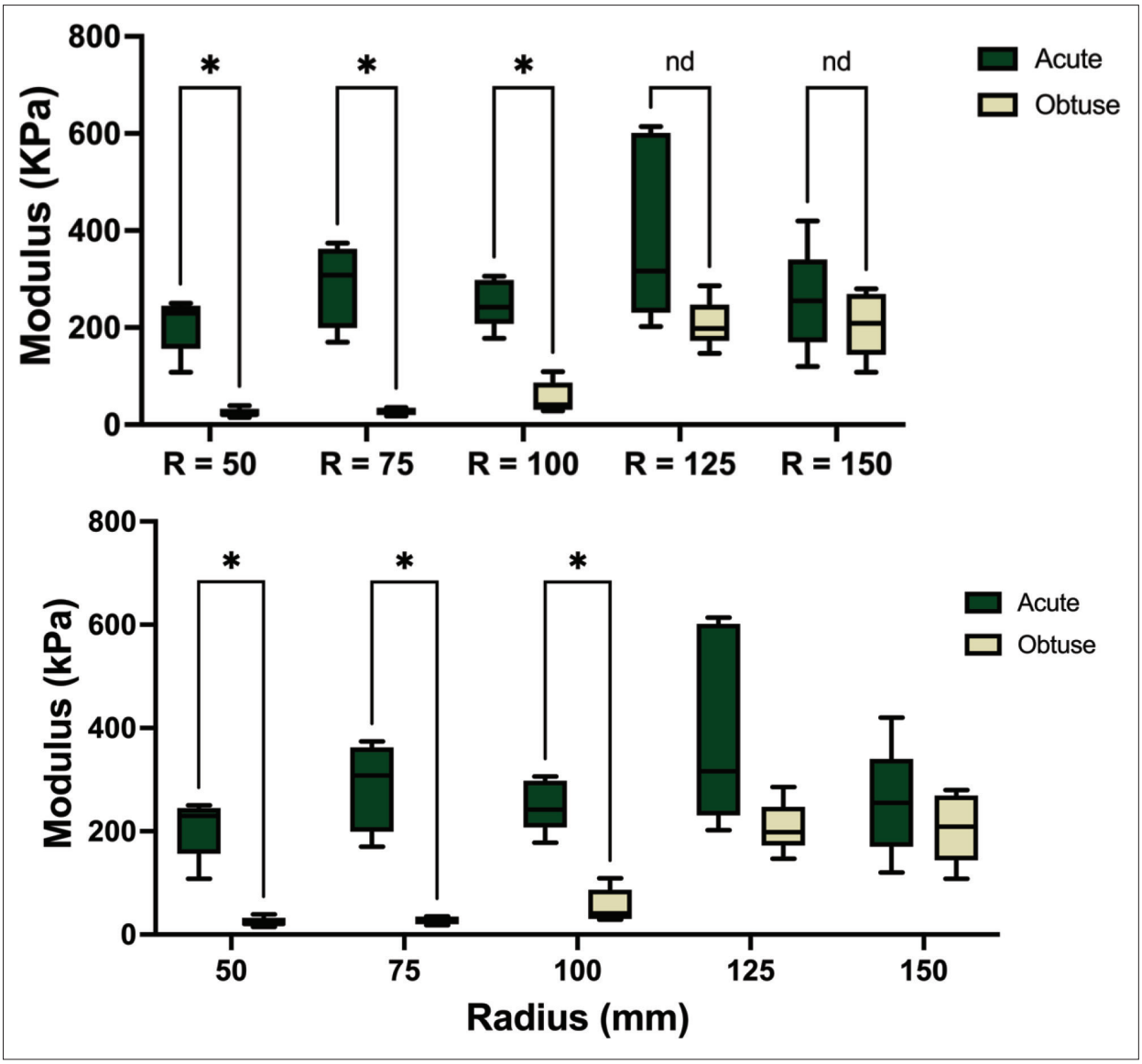

Figure 4. Box and whisker plots of regional moduli of different radii scaffolds with all other parameters being constant. p-values for R = 50, 75, and 100 mm were 0.0018, 0.009, and 0.0003, respectively. Average moduli for acute and obtuse regions were 206 ± 45.1 to 24.2 ± 3.4 kPa, 219 ± 117.7 to 22.4 ± 6.8 kPa, 250 ± 39.4 to 55.1 ± 12.1 kPa, 396 ± 150 to 208 ± 43.5 kPa, and 255 kPa ± 84.7 to 207 ± 58 kPa for R = 50, 75, 100, 125, and 150 mm. Significance set at $\alpha < 0.05$.

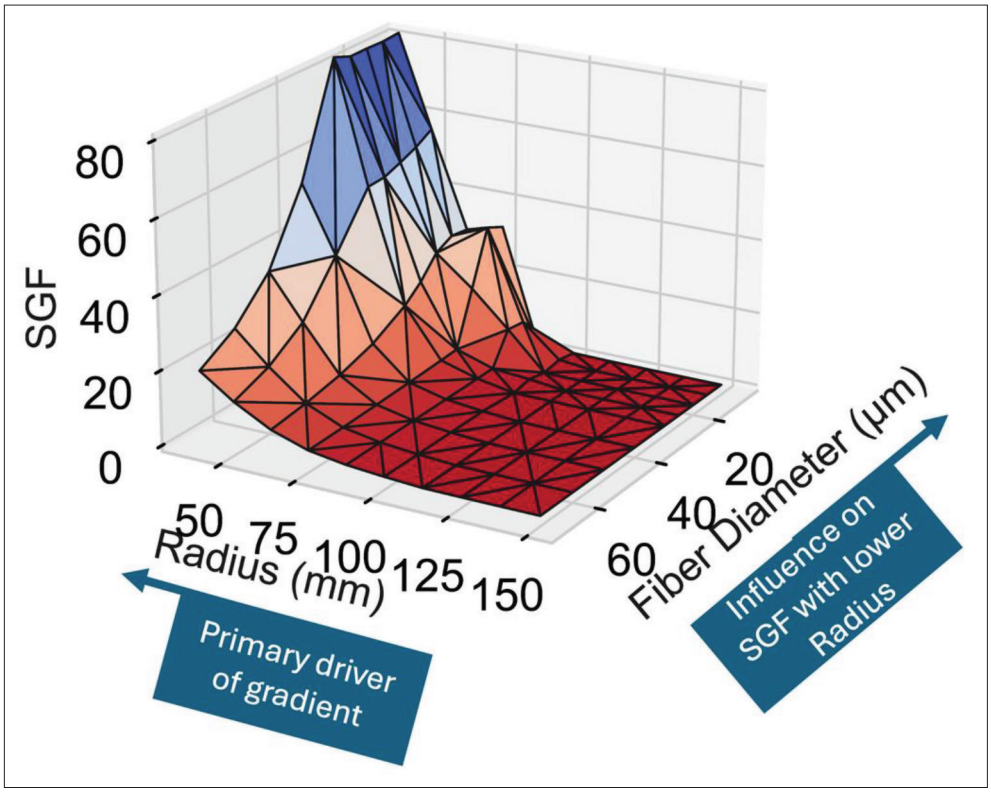

Figure 5. Representative 3D surface plot of FEA predictions ($N = 90$) with strain gradient factor (SGF) plotted against FD and R at the same fiber spacing (FS): 250 μm. Peak SGF = 83 was reached at $R = 38$ mm and FD = 30 μm, approaching the gradient present in human rotator cuff. Spearman's correlation coefficients for R, FD, and FS were −0.93, −0.068, and −0.048, respectively.

100 mm (p = 0.0018, 0.009, and 0.0003, respectively). Qualitatively, the convergence of obtuse and acute region moduli was noted as the radius of the scaffold increased. Scaffolds with a higher radius represent structures that have less curvature in the fibers. Less curvature reduces the difference in fiber angle between obtuse and acute regions, resulting in a homogeneous structure with little gradient in mechanical properties. No significant differences were found between the acute regional moduli of varying radii, suggesting that altering R only changes the obtuse moduli of the scaffold if FD and FS are held constant.

3.3. Parametric analysis of fibrous scaffold

SGF peaked at 83.5 with $R = 38.5$ mm, FD = 30 μm, and FS = 250 μm (Figure 5). SGF was minimized at 1 when $R = 125$ mm, FD = 10 μm, and FS = 60 μm. Out of the 810 simulated geometries, 41 parametric combinations demonstrated SGF > 50, indicating the potential appropriateness of mechanical behavior for enthesis repair. Of these scaffolds, $N = 31$ had $R = 38.5$ mm, $N = 9$ had $R = 50$ mm, and one had $R = 62.5$ mm. Scaffolds with $R >$ 112 mm had the SGFs constrained to around 2. Spearman's rank correlation coefficients of SFG with R, FD, and FS were calculated as −0.93, −0.068, and −0.048, respectively, indicating a strong negative correlation between SGF and R, and a minor correlation with FS and FD. These correlations make sense as low R scaffolds result in the largest change in fiber angle across the scaffold's length (19°–80° for R = 38 mm vs. 3°–29° for $R = 150$ mm), confirming previous findings in which fiber angle strongly affects mechanical properties regionally.[37,52] So, it does follow that because scaffolds with low R have scaffolds vary the fiber angle the most, they would have the largest change in mechanics compared to scaffolds with higher R. This phenomenon was also observed in the experimental data (Figure 4). On the contrary, higher-R scaffolds, with less variation in their fiber angles, do not alter regional mechanics and instead approach an SGF of 1. Complete analyses are shown in **Supplemental 1** (see Supplementary File).

3.4. Unit cell modeling to optimize tissue regeneration

3.4.1. *Acute unit cells–bone THW regions*

Much like the fiber models, the UC THW percentages in the acute region for bone had a clear inverse relationship with R, FD, and FS (Figure 6). Spearman coefficients for the middle acute region were −0.34, 0.21, and −0.44 for

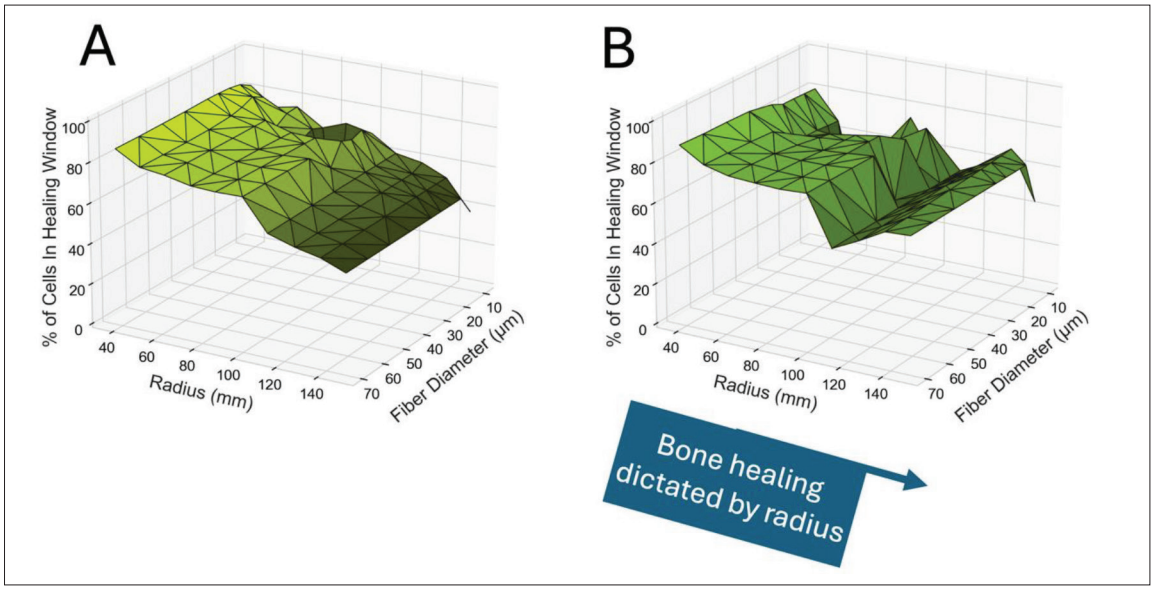

Figure 6. Representative plots of bone tissue healing window percentages in the outer acute region (A) and in the middle acute region (B) at a single fiber spacing (FS) = 250 μm. Both acute regions trended lower as radius (R) increased, with little difference in fiber diameter (FD). Spearman's correlation coefficients for all R, D, and FS in the outer acute region were −0.81, 0.081, and −0.31, respectively. Spearman's correlation coefficients for all R, D, and FS in the middle acute region were −0.34, 0.21, and −0.44, respectively.

R, FD, and FS, respectively. In the outer region, spearman coefficients were −0.81, 0.081, and −0.31 for *R*, FD, and FS, respectively. The maximum THW percentages were 87.5% and 97.9% in the middle and outer regions; these occurred in *R* = 38 mm and 50 mm, respectively. When averaging the middle and outer acute percentages in each scaffold, the scaffold with the highest THW percentage was *R* = 38 mm, FD = 70 μm, and FS = 250 μm, at 86% of the elements within the bone healing windows. When directly comparing the middle and outer acute regions against each other, there were very few differences in the percentages and trends for healing across scaffold geometries. Complete analyses are shown in **Supplemental 2, Supporting Information**.

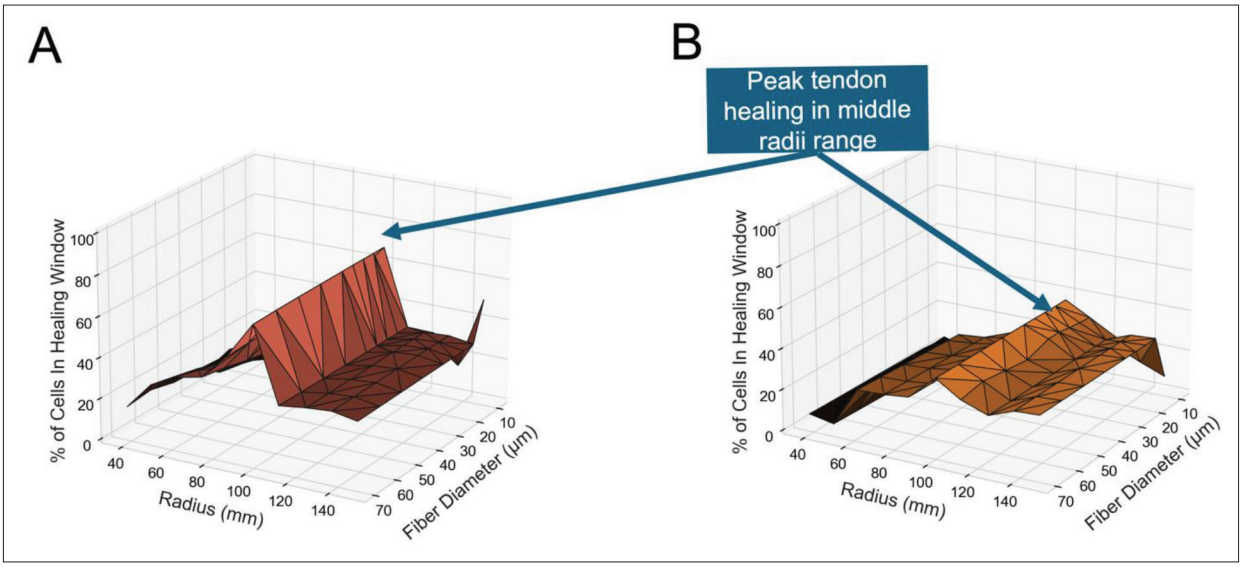

Figure 7. Representative plots of bone tissue healing window percentages in the outer obtuse region (A) and in the middle obtuse region (B) at a single fiber spacing (FS) = 300 μm. Both obtuse regions trended lower as radius (R) increased, with little difference in diameter (FD). Spearman's correlation coefficients for all R, D, and FS in the outer acute region were 0.2, 0.32, and −0.082, respectively. Spearman's correlation coefficients for all R, D, and FS in the middle obtuse region were 0.66, 0.12, and −0.017, respectively.

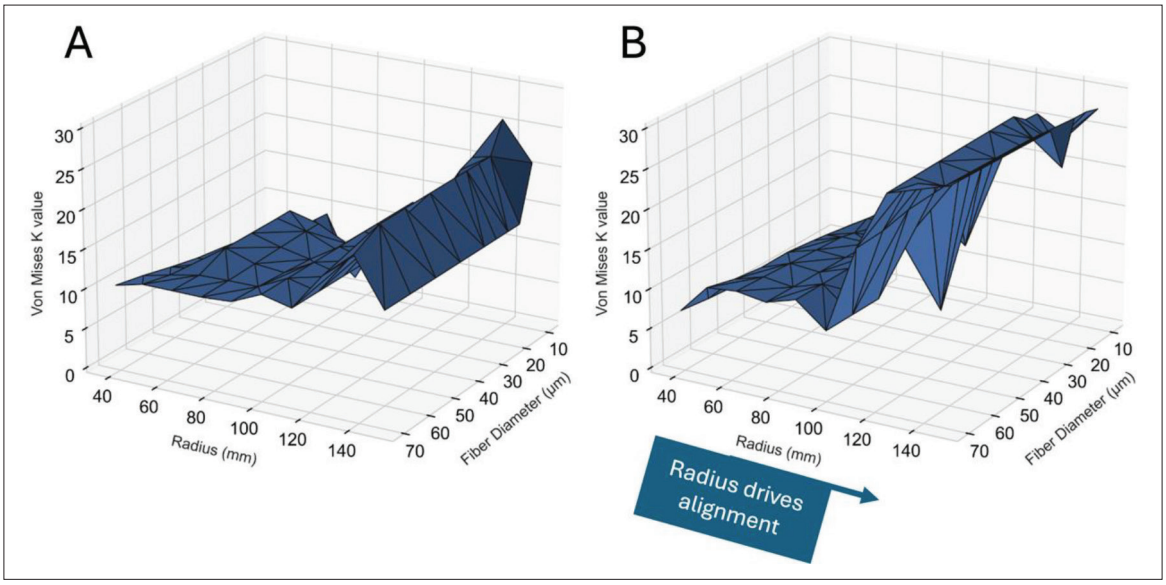

Figure 8. 3D plot of von Mises concentration coefficient (κ) and effects of scaffold parameters (radius [*R*] and fiber diameter [FD]) on κ for a single fiber spacing (FS) = 450 μm in the outer obtuse region (A) and middle obtuse region (B). Spearman's correlation coefficients for all *R*, FD, and FS input parameters were 0.86, −0.16, and −0.0073, respectively.

3.4.2. *Obtuse unit cells–tendon THW regions*

The THW UC percentages in the obtuse region for the tendon ROI demonstrated clear maximization and tapering off after the radius increased past *R* = 100 mm, indicating that scaffolds with *R* = 100 mm have the ideal geometry for tenocyte bioactivity and ECM production (Figure 7). Spearman coefficients for the middle obtuse region were 0.66, 0.12, and −0.017 for *R*, FD, and FS, respectively. In the outer region, coefficients were 0.2, 0.32, and −0.082 for *R*, FD, and FS, respectively. These data predict that radius and diameter are key factors in optimizing scaffold geometry for tendon regeneration by tenocytes. Meanwhile, the effects of FS are predicted to be negligible. Averaging the two region THW percentages found an optimal scaffold geometry at *R* = 100 mm, FS = 600 μm, FD = 40 μm, at an average of 52.5% of elements in the tenocyte THW. Complete analyses are shown in **Supplemental 2, Supporting Information**.

3.4.3. *Eigenvector assessment*

Visual inspection of eigenvector histograms revealed that the resultant primary axis angles followed the direction of loading and did not fall into a uniform distribution across ROIs. However, this distribution had very low variance, and from the 1620 UC simulations, only a single simulation (*R* = 100 mm, *D* = 25 μm, FS = 300 μm) fell outside 5% of the loading line. These data indicate that this specific scaffold geometry would not result in a preferred ECM production alignment during physiologic loading of the tendon following repairs. Comparing values against print parameters indicated that κ values were highest in high-radius scaffold (*R* >125 mm) (Figure 8) Spearman's correlation coefficients for *R*, FS, and FD were 0.86, −0.16, and −0.0073, respectively. This indicates again that *R* is the primary driver of the outcome parameter of this test. Mechanistically, this can be ascribed to the narrowing in the overall obtuse region shape as radius increases. This leads to a shape that, under load, has compliance in its obtuse region at the cost of transverse compression, which alters the concentration of the first eigenvector angle distribution. Complete analyses are shown in **Supplemental 3, Supporting Information**.

4. Discussion

Mechanical stimuli are critical for the cellular fate of repaired tissues.[45,53] The significant disparity of mechanics in interfacial tissues remains a significant challenge for tissue-engineering scaffolds. However, we have successfully generated a novel, single-material scaffold (SMS) with mechanical gradients, approaching the mechanical gradation levels in the RC's bulk properties.[54] With this elegant geometry, we have what we believe to be a more continuous mechanical gradient than those seen in other single-material gradients[27-29] or multimaterial gradients.[24] SMSs fabricated with electrospun nanofibers have demonstrated a stark contrast between "aligned" and "unaligned" regions when examining ECM production and cellular bioactivity.[27] These SMSs have shown benchtop success by displaying regional-specific elastic moduli, as well as demonstrating the ability to modulate the cellular response based on the region within the scaffold.[28] SMS's nanoscale fibers have also shown an

enhanced ability to instruct cells to produce more tendon-like matrix *in vitro*.[21,45] However, these scaffolds still result in stress concentrations with their stark transition regions, a shortcoming our scaffold can alleviate.

The manufacturability and translatability of the Arc-S's geometry also lend credence to further functionalization of biochemical gradients that have been shown to aid repair in preclinical models.[55,56] We believe the Arc-S's design can function as a "mechanical backbone" that can be improved with the addition of seeded cells,[56,57] drug functionalization,[58] or extracellular vesicles.[59] This geometry's elegance also gives translatability and tunability to other interfacial tissues found *in vivo* (aortic arch, ligaments, etc.) because the mechanical gradient can be tuned with one parameter (i.e., 80–1.1 with changes in *R*) to a high degree.

Additionally, we paired our bulk, tissue-engineering scaffold modeling with cellular-level predictions based on previously published *in vitro* data to optimize our scaffold for multitissue healing, screening candidate scaffolds for future work. Work in this field has been completed before, such as Page et al.[35] using FEA to model a UC of a fiber-embedded gel scaffold to determine which scaffold geometry best matches *in vitro* anabolic strain levels for intervertebral disc repair, or Claes and Heigele[18] pairing histology with finite element to generate the accepted hypothesis that stress and strain states lead toward specific tissue differentiation with the specific goal of defining the region that differentiate towards intramembranous ossification. To our knowledge, however, this is the first time multitissue behavior on one scaffold has been predicted *in silico*.

4.1. Parametric fibrous model

Fiber diameter did have a notable inverse correlation with SGF of scaffolds with a small *R* and a small FS. A lower *R* causes obtuse region fibers to be placed in bending rather than in tension. This shift causes a strong dependence on the bending stiffness, driven by FD's effect on moment of inertia, leading to lower R and lower FD to have synergistic increases on SGF.

This is of particular interest in MEW, in which variations in print speed can be optimized to change FD,[60] allowing control over FD and, thus, the SGF by varying the print speed across the scaffold's length for an individual fiber. Thus, creating a G-code with a continuously changing speed while the fiber is being jetted could produce a scaffold with thinner fibers in the obtuse region and thicker fibers in the acute region, resulting in another factor of continuous mechanical variation across the length of the scaffold, enabling greater SGFs potentially surpassing those seen in biological tissues. Though, challenges arise when printing high thickness scaffolds due to charge accumulation in the fibers, and with the nonuniform scaffold's height change, maintaining uniformity in the print across the layers would be challenging in the current state of MEW.[34]

Contrastingly, this MEW scaffold geometry does not follow the conventional pore morphologies of MEW bone and tendon scaffolds. MEW bone scaffolds are usually aligned with square pores, and tendon scaffolds are more aligned with lower fiber angles or even parallel fibers.[29,61] On this scaffold, the obtuse region's (tendon region) pore shape is closer to the typical bone scaffold than a tendon scaffold.

Generated from a single material with a continuous sweeping geometry, there is reduced risk to delamination, and high tunability in the gradient while only altering one input parameter, *R*. The gradient response of the scaffold novel geometry is material-independent, meaning that graded mechanics are preserved across different materials. This means that, while this analysis used PCL as the base material, it would be visible to implement this geometry in a spectrum of bioactive or natural biomaterials when MEW technology reaches that stage.[33] With the increase of material options in MEW and an introduction to filament-driven MEW systems,[62,63] there does exist the capacity for multimaterial MEW prints as well. For the Arc-S, this has broad implications for its implementation in surgery. Not only could the mechanical gradient be further enhanced by printing with a stiffer material on the acute side and a compliant material on the obtuse side (assuming solid bonding in the fibers), but the enthesis also has a stark material composition gradient,[64] and introducing a material gradient in addition to the mechanical gradients present in the Arc-S would further recapitulate the native enthesis. As an example, Abdal-hay et al.[65] has recently loaded a PCL scaffold printed through MEW with up to 40 wt% hydroxyapatite, a material well-known for its osteogenic behavior.[66] However, developing a multiphasic Arc-S would require efforts to refine a multimaterial filament feed system with high enough resolution.

In addition to its material independence, the ARC-S can be scaled, opening the door to patient-specific implants that are scaled to the patient's humerus and repaired tendon. Images from the patient's injured RC could later inform a patient-specific patch model built in FEA to then be simulated, validated *in silico*, and then implanted. Thus, creating a digital twin that would increase assurance of positive clinical outcomes in patients and clinicians alike.

4.2. Parametric unit cell model

Notably, in low-R scaffolds, there were differences between middle and outer obtuse regions for tendon healing response, but much less noted difference between middle and outer acute regions. All scaffolds underwent narrowing

in the obtuse region of the scaffold, inherent in the loading condition of the model, resulting in the translation towards the middle for the outer UCs and a compression for the middle UCs. Consequently, middle UCs had negative hydrostatic pressure, leading to lower percentages within the tendon THW in the middle region than in the outer region, which translated in the transverse direction. Acute region percentages were insensitive due to the definition of the bone THW, which allowed for hydrostatic compression. Scaffolds with lower R experienced this phenomenon because the bulk transverse compression of the obtuse region is higher than in scaffolds with higher R, making the percentage levels more uniform across the width of the scaffold.

For the UC assessments, it is worth noting that the scaffolds that were thought to demonstrate the largest SGF do not match the scaffolds with the best strain levels for bone and tendon ECM production. High-SGF scaffolds were in the low R, low diameter region of the parametric study. Contrastingly, the best scaffolds for tenocyte bioactivity were in the medium R domain with a clear maximum reached at around $R = 87$ and 100 mm. This does make sense based on the definition of the THWs with the difference between the bone and tendon region matching a SGF of ≈2×, rather than our target of 50× in the fiber models.

We are also constraining this cellular study to one bulk loading condition of 4% strain across the whole scaffold, when a distribution of strain levels would be present *in vivo*, especially during the stabilization period in clinical repair or during rehabilitation through physical therapy.[67] Assuming a linear proportion, altering the strain from 4% to somewhere near 1% would result in large shifts in the UC geometry that would be best for tendon regeneration.

Changes in mechanics due to changes in the elastic modulus of the UC were neglected due to the assumption that any hydrogel filler would be much more compliant than the MEW fibers, the dominating mechanical feature of the scaffold. This assumption also resulted in a displacement-controlled motion for the UC analyses, resulting in strain levels independent of the gel's stiffness. However, previous work suggests that MEW constructs stiffen during gel embedding.[68] This mechanism, though important, was outside the scope of the current study on this novel scaffold geometry. Another limitation in the UC study regarding the elastic modulus was the exclusion of temporal changes in mechanics due to ECM production in the UC altering strain levels near cells. As cells produce ECM in the hydrogel, spatial mechanics in the UC would alter and cause the initial strain map of the UC to change, inducing another change in the cellular response. The interplay between ECM production and the scaffold's change in mechanics would develop into a dynamic feedback loop, which would provide insights into enhancing long-term health of the repaired tissue. These models did not investigate this phenomenon; however, it should be considered for future work in the computational framework offered paired with benchtop validation studies to quantify and visualize the production of ECM in the enthesis for the enhancement of engineering scaffolds. Additional work would also aim to research how strains outside THWs would induce changes to the matrix production as the elements that are outside of this region have been neglected on this study. Taken together, these limitations indicate a need to generate a temporal computational model that takes strain data, maps to ECM deposition, and then stiffens or relaxes regions in the UC appropriately. Models like this have been developed for healing tendon, but, to our knowledge, this idea has not been adapted for predicting a scaffold's long-term efficacy.[69,70]

This work also only examined how normal stresses and strains predict tissue healing in our scaffold, neglecting shear. As one of the parameters of bone formation, fluid shear strain's effect has large implications for bone formation.[71] Tenocytes' response to shear, in contrast, is limited, and the normal strains experienced on tendon are given major emphasis because tendon primarily faces tensile loads.

4.3. Eigenvector assessment

Collagen alignment is a key marker of healthy tendons and manufacturing a scaffold that mimics the strain magnitude and the direction of the healthy tissue is vital to successful long-term tissue regeneration. For these reasons, most tendon scaffolds are highly aligned structures that allow the cells to reorient along the tendon's loading direction to produce aligned collagen.[21,44] This is because the maximum principal strain has been thought to dominate ECM production and cell alignment.[50,51] Therefore, when subjected to physiological strains, these aligned scaffolds produce a concentrated distribution of maximum principal strain angles, which facilitates improved deposition of aligned collagen, influenced by the scaffold geometry. Scaffolds with the highest radius had the largest κ values (smallest dispersity in angles). This means that with the three tissue healing outcome parameters (bone healing, tendon healing, and eigenvector assessment), a different scaffold is favorable for each outcome parameter. Displaying a need for balance in the appropriate parameters to optimize this scaffold's clinical performance in RC repair. Scaffold groups with the largest eigenvector correlation do morphologically match many fibrous, tendon scaffold geometries, and have data that suggest cells produce aligned collagen along the scaffold fibers, validating our findings that these would lead to the most aligned constructs.[21,44] However, due to the other factors in designing a scaffold for the enthesis, we do

not believe these scaffolds would be well-suited for clinical application, though their preliminary data necessitates further investigation outside of the computational realm. These scaffolds have limited graded effects, critical for acute stage repair, and the lowest bone strains in the UC, critical for long-term joining of the RC.

5. Conclusion

When combining the outcome parameters in these studies, there is a limit to the ability to weight all parameters and decide the best scaffold based on the metrics provided. Computational data successfully characterized a novel geometry for tissue-engineering scaffolds from print parameters and predicted tissue healing from multiple tissues on the same substrate. Future work will pair the UC FEA findings with *in vitro* stretching of scaffolds seeded with cells, as this work is currently devoid of benchtop analyses.

Our novel geometry can bridge the stiffness gap seen in the RC and has applications in other interfacial tissues and fields by virtue of its high degree of tunability characterized in our high-throughput, single-material models. The scaffold has the potential to be functionalized with material gradients as a postprocess to enhance its mimicry of the present complex gradient.

Acknowledgments

The authors would like to thank Jason Kuiper and Zachary Cartwright for the initial assembly of the melt electrowriting printer, as well as the other members of the Orthopaedic Bioengineering Research Laboratory for their guidance and mentorship.

Funding

This work was funded internally by the Orthopaedic Bioengineering Research Lab as well as the Walter Scott College of Engineering High Impact Research Award.

Conflict of interest

The authors declare they have no competing interests.

Author contributions

Conceptualization: Sam Winston, Kirk McGilvray
Formal analysis: Sam Winston
Investigation: Sam WInston
Methodology: Sam Winston, Kirk McGilvray
Supervision: Lynn Pezzanite, Steven Dow, Kirk McGilvray
Writing–original draft: Sam Winston
Writing–review & editing: Lynn Pezzanite, Steven Dow, Kirk McGilvray

Ethics approval and consent to participate

Not applicable.

Consent for publication

Not applicable.

Availability of data

Data is available from the corresponding author upon reasonable request

Further disclosure

Part of or the entire set of findings have been presented in a conference, academic meeting, congress. ASME SB3C Summer Bioengineering Conference, June 2024, Lake Geneva Wisconsin, USA: Results 3.1–3.3 with partial results from 3.4.1 and 3.4.2 were shown.

Tissue Engineering and Regenerative Medicine International Society World Congress, June 2024, Seattle Washington, USA: Results 3.1–3.3 with partial results from 3.4.1 and 3.4.2 were shown.

Computer Methods in Biomechanics and Biomedical Engineering Symposium, August 2024, Vancouver, BC, Canada: Results 3.1–3.4 with partial results from 3.4.3 were shown.

International Conference on Biofabrication, November 2024, Fukuoka, Japan: Complete Results were shown.

References

1. Colvin AC, Egorova N, Harrison AK, Moskowitz A, Flatow EL. National trends in rotator cuff repair. *J Bone Joint Surg Am*. 2012;94(3):227-233.
doi: 10.2106/JBJS.J.00739

2. Galatz LM, Ball CM, Teefey SA, Middleton WD, Yamaguchi K. The outcome and repair integrity of completely arthroscopically repaired large and massive rotator cuff tears. *JBJS*. 2004;86(2); 219-224.
doi: 10.2106/00004623-200402000-00002

3. Zhang X, Wang D, Wang Z, et al. Clinical perspectives for repairing rotator cuff injuries with multi-tissue regenerative approaches. *J Orthop Translat*. 2022;36:91-108.
doi: 10.1016/j.jot.2022.06.004

4. Zumstein MA, Lädermann A, Raniga S, Schär MO. The biology of rotator cuff healing. *Orthop Traumatol Surg Res*. 2017;103(1S):S1-S10.
doi: 10.1016/j.otsr.2016.11.003

5. Iannotti JP, Codsi MJ, Kwon YW, Derwin K, Ciccone J, Brems JJ. Porcine small intestine submucosa augmentation

of surgical repair of chronic two-tendon rotator cuff tears: a randomized, controlled trial. *JBJS*. 2006;88(6):1238-1244. doi: 10.2106/jbjs.E.00524

6. Malcarney HL, Bonar F, Murrell GAC. Early inflammatory reaction after rotator cuff repair with a porcine small intestine submucosal implant:a report of 4 cases. *Am J Sports Med*. 2005;33(6):907-911. doi: 10.1177/0363546504271500
7. Mobarak MH, Islam MA, Hossain N, et al. Recent advances of additive manufacturing in implant fabrication – a review. *Appl Surf Sci Adv*. 2023;18:100462. doi: 10.1016/j.apsadv.2023.100462
8. Yang Y, Wang G, Liang H, et al. Additive manufacturing of bone scaffolds. *IJB*. 2018;5(1):148. doi: 10.18063/ijb.v5i1.148
9. Wu Y, Liu J, Kang L, et al. An overview of 3D printed metal implants in orthopedic applications: present and future perspectives. *Heliyon*. 2023;9(7):e17718. doi: 10.1016/j.heliyon.2023.e17718
10. Kotrych D, Angelini A, Bohatyrewicz A, Ruggieri P. 3D printing for patient-specific implants in musculoskeletal oncology. *EFORT Open Rev*. 2023;8(5):331-339. doi: 10.1530/EOR-23-0066
11. Chen A, Su J, Li Y, et al. 3D/4D printed bio-piezoelectric smart scaffolds for next-generation bone tissue engineering. *Int J Extrem Manuf*. 2023;5(3):032007. doi: 10.1088/2631-7990/acd88f
12. Federici AS, Tornifoglio B, Lally C, Garcia O, Kelly DJ, Hoey DA. Melt electrowritten scaffold architectures to mimic tissue mechanics and guide neo-tissue orientation. *J Mech Behav Biomed Mater*. 2024;150:106292. doi: 10.1016/j.jmbbm.2023.106292
13. Kaspar D, Seidl W, Neidlinger-Wilke C, Claes L. *In vitro* effects of dynamic strain on the proliferative and metabolic activity of human osteoblasts. *J Musculoskelet Neuronal Interact*. 2000;1(2):161-164
14. Zhu J, Zhang X, Wang C, Peng X, Zhang X. Different magnitudes of tensile strain induce human osteoblasts differentiation associated with the activation of ERK1/2 phosphorylation. *Int J Mol Sci*. 2008;9(12):2322-2332. doi: 10.3390/ijms9122322
15. Yan Y-x, Gong Y-w, Guo Y, et al. Mechanical strain regulates osteoblast proliferation through integrin-mediated ERK activation. *PLOS ONE*. 2012;7(4):e35709. doi: 10.1371/journal.pone.0035709
16. Guo Y, Zhang C-q, Zeng Q-c, et al. Mechanical strain promotes osteoblast ECM formation and improves its osteoinductive potential. *BioMed Eng OnLine*. 2012;11(1):80. doi: 10.1186/1475-925X-11-80
17. Burger EH, Klein-Nulend J. Mechanotransduction in bone—role of the lacunocanalicular network. *FASEB J*. 1999;13(9001):S101-S112. doi: 10.1096/fasebj.13.9001.s101
18. Claes LE, Heigele CA. Magnitudes of local stress and strain along bony surfaces predict the course and type of fracture healing. *J Biomechan*. 1999;32(3):255-266. doi: 10.1016/S0021-9290(98)00153-5
19. Schoenenberger AD, Tempfer H, Lehner C, et al. Macromechanics and polycaprolactone fiber organization drive macrophage polarization and regulate inflammatory activation of tendon in vitro and in vivo. *Biomaterials*. 2020;249:120034. doi: 10.1016/j.biomaterials.2020.120034
20. Wu S, Peng H, Li X, Streubel PN, Liu Y, Duan B. Effect of scaffold morphology and cell co-culture on tenogenic differentiation of HADMSC on centrifugal melt electrospun poly (L-lactic acid) fibrous meshes. *Biofabrication*. 2017;9(4):044106-044106. doi: 10.1088/1758-5090/aa8fb8
21. El Khatib MA-O, Mauro AA-O, Di Mattia MA-O, et al. Electrospun PLGA fiber diameter and alignment of tendon biomimetic fleece potentiate tenogenic differentiation and immunomodulatory function of amniotic epithelial stem cells. *Cells*. 2020;9(5):1207. doi: 10.3390/cells9051207
22. Yang G, Im H-J, Wang JHC. Repetitive mechanical stretching modulates IL-1β induced COX-2, MMP-1 expression, and PGE2 production in human patellar tendon fibroblasts. *Gene*. 2005;363:166-172. doi: 10.1016/j.gene.2005.08.006
23. Wang T, Lin Z, Day RE, et al. Programmable mechanical stimulation influences tendon homeostasis in a bioreactor system. *Biotechnol Bioeng*. 2013;110(5):1495-1507. doi: 10.1002/bit.24809
24. Yang G, Crawford RC, Wang JHC. Proliferation and collagen production of human patellar tendon fibroblasts in response to cyclic uniaxial stretching in serum-free conditions. *J Biomech*. 2004;37(10):1543-1550. doi: 10.1016/j.jbiomech.2004.01.005
25. Chen Y, Hao M, Bousso I, Thomopoulos S, Xia Y. Reliable fabrication of mineral-graded scaffolds by spin-coating and laser machining for use in tendon-to-bone insertion repair. *Adv Healthc Mater*. 2024;13:e2402531. doi: 10.1002/adhm.202402531
26. Spalazzi JP, Dagher E, Doty SB, Guo XE, Rodeo SA, Lu HH. In vivo evaluation of a multiphased scaffold designed for orthopaedic interface tissue engineering and soft tissue-to-bone integration. *J Biomed Mater Res A*. 2008;86(1):1-12. doi: 10.1002/jbm.a.32073
27. Chen C, Shi Q, Li M, et al. Engineering an enthesis-like graft for rotator cuff repair: an approach to fabricate highly biomimetic scaffold capable of zone-specifically releasing stem cell differentiation inducers. *Bioact Mater*. 2022;16:451-471. doi: 10.1016/j.bioactmat.2021.12.021

28. Xie J, Li X, Lipner J, et al. "Aligned-to-random" nanofiber scaffolds for mimicking the structure of the tendon-to-bone insertion site. *Nanoscale*. 2010;2(6):923-926. doi: 10.1039/c0nr00192a

29. Tindell RK, Busselle LP, Holloway JL. Magnetic fields enable precise spatial control over electrospun fiber alignment for fabricating complex gradient materials. *J Biomed Mater Res A*. 2023;111(6):778-789. doi: 10.1002/jbm.a.37492

30. Xiong J, Wang H, Lan X, et al. Fabrication of bioinspired grid-crimp micropatterns by melt electrospinning writing for bone–ligament interface study. *Biofabrication*. 2022;14(2):025008. doi: 10.1088/1758-5090/ac4ac8

31. Jun I, Han H-S, Edwards JR, Jeon H. Electrospun fibrous scaffolds for tissue engineering: viewpoints on architecture and fabrication. *Int J Mol Sci*. 2018;19(3):745. doi: 10.3390/ijms19030745

32. Abbasi N, Abdal-hay A, Hamlet S, Graham E, Ivanovski S. Effects of gradient and offset architectures on the mechanical and biological properties of 3-d melt electrowritten (MEW) scaffolds. *ACS Biomater Sci Eng*. 2019;5(7):3448-3461. doi: 10.1021/acsbiomaterials.8b01456

33. Golafshan N, Castilho M, Daghrery A, et al. Composite graded melt electrowritten scaffolds for regeneration of the periodontal ligament-to-bone interface. *ACS Appl Mater Interfaces*. 2023;15(10):12735-12749. doi: 10.1021/acsami.2c21256

34. Saiz PG, Reizabal A, Vilas-Vilela JL, Dalton PD, Lanceros-Mendez S. Materials and strategies to enhance melt electrowriting potential. *Adv Mater*. 2024;36(24):2312084. doi: 10.1002/adma.202312084

35. Page MI, Linde PE, Puttlitz CM. High throughput computational evaluation of how scaffold architecture, material selection, and loading modality influence the cellular micromechanical environment in tissue engineering strategies. *JOR SPINE*. 2021;4(3):e1152. doi: 10.1002/jsp2.1152

36. Page M, Puttlitz C. Biaxial mechanics of 3D fiber deposited ply-laminate scaffolds for soft tissue engineering part II: finite element analyses. *J Mech Behav Biomed Mater*. 2019;100:103395. doi: 10.1016/j.jmbbm.2019.103395

37. Samavedi S, Olsen Horton C, Guelcher SA, Goldstein AS, Whittington AR. Fabrication of a model continuously graded co-electrospun mesh for regeneration of the ligament–bone interface. *Acta Biomater*. 2011;7(12):4131-4138. doi: 10.1016/j.actbio.2011.07.008

38. Dwivedi R, Kumar S, Pandey R, Mahajan A, Nandana D, Katti DS, Mehrotra D. Polycaprolactone as biomaterial for bone scaffolds: Review of literature. *J Oral Biol Craniofac Res*. 2020;10(1):381-388. doi: 10.1016/j.jobcr.2019.10.003

39. Polak-Krasna K, Mazgajczyk E, Heikkila P, Georgiadis A. Parametric finite element model and mechanical characterisation of electrospun materials for biomedical applications. *Materials (Basel)*. 2021;14(2):278. doi: 10.3390/ma14020278

40. Eshraghi S, Das S. Mechanical and microstructural properties of polycaprolactone scaffolds with one-dimensional, two-dimensional, and three-dimensional orthogonally oriented porous architectures produced by selective laser sintering. *Acta Biomater*. 2010;6(7):2467-2476. doi: 10.1016/j.actbio.2010.02.002

41. Wolynski JG, Ilić MM, Labus KM, Notaroš BM, Puttlitz CM, McGilvray KC. Direct electromagnetic coupling to determine diagnostic bone fracture stiffness. *Ann Transl Med*. 2022;10(9):510. doi: 10.21037/atm-21-5315

42. Tourlomousis F, Ding H, Kalyon DM, Chang RC. Melt electrospinning writing process guided by a "Printability Number". *J Manuf Sci Eng*. 2017;139(8):081004. doi: 10.1115/1.4036348

43. Eichholz KF, Hoey DA. Mediating human stem cell behaviour via defined fibrous architectures by melt electrospinning writing. *Acta Biomater*. 2018;75:140-151. doi: 10.1016/j.actbio.2018.05.048

44. Jenkins TL, Little D. Synthetic scaffolds for musculoskeletal tissue engineering: cellular responses to fiber parameters. *NPJ Regen Med*. 2019;4:15. doi: 10.1038/s41536-019-0076-5

45. Erisken C, Zhang X, Moffat KL, Levine WN, Lu HH. Scaffold fiber diameter regulates human tendon fibroblast growth and differentiation. *Tissue Eng Part A*. 2013;19(3-4):519-528. doi: 10.1089/ten.tea.2012.0072

46. Kim J, Bakirci E, O'Neill KL, Hrynevich A, Dalton PD. Fiber bridging during melt electrowriting of poly(ε-Caprolactone) and the influence of fiber diameter and wall height. *Macromol Mater Eng*. 2021;306(3):2000685. doi: 10.1002/mame.202000685

47. Morgan EF, Unnikrisnan GU, Hussein AI. Bone mechanical properties in healthy and diseased states. *Annu Rev Biomed Eng*. 2018;20:119-143. doi: 10.1146/annurev-bioeng-062117-121139

48. Fratzl P. *Collagen: Structure and Mechanics*; New York, NY: Springer; 2008:1-506.

49. Itoi E, Berglund LJ, Grabowski JJ, et al. Tensile properties of the supraspinatus tendon. *J Orthop Res*. 1995;13(4):578-584. doi: 10.1002/jor.1100130413

50. Kolel A, Ergaz B, Goren S, Tchaicheeyan O, Lesman A. Strain gradient programming in 3D fibrous hydrogels to direct graded cell alignment. *Small Methods*. 2023;7(1):2201070. doi: 10.1002/smtd.202201070

51. Vader D, Kabla A, Weitz D, Mahadevan L. Strain-induced alignment in collagen gels. *PLoS One*. 2009;4(6):e5902. doi: 10.1371/journal.pone.0005902

52. Cordin M, Bechtold T, Pham T. Effect of fibre orientation on the mechanical properties of polypropylene–lyocell composites. *Cellulose*. 2018;25(12):7197-7210. doi: 10.1007/s10570-018-2079-6

53. Engler AJ, Sen S, Sweeney HL, Discher DE. Matrix elasticity directs stem cell lineage specification. *Cell*. 2006;126(4):677-689. doi: 10.1016/j.cell.2006.06.044

54. Singh D, Rana A, Jhajhria SK, Garg B, Pandey PM, Kalyanasundaram D. Experimental assessment of biomechanical properties in human male elbow bone subjected to bending and compression loads. *J Appl Biomater Funct Mater*. 2019;17(2):2280800018793816. doi: 10.1177/2280800018793816

55. Chae S, Yong U, Park W, et al. 3D cell-printing of gradient multi-tissue interfaces for rotator cuff regeneration. *Bioact Mater*. 2023;19:611-625. doi: 10.1016/j.bioactmat.2022.05.004

56. Credille KT, Wang ZRC, Horner NS, et al. Biphasic interpositional allograft for rotator cuff repair augmentation is safe in an ovine model. *Arthroscopy*. 2023;39(9):1983-1997. doi: 10.1016/j.arthro.2023.03.018

57. Korpershoek JV, Ruijter M, Terhaard BF, et al. Potential of melt electrowritten scaffolds seeded with meniscus cells and mesenchymal stromal cells. *Int J Mol Sci*. 2021;22(20):11200. doi: 10.3390/ijms222011200

58. Xu T, Gu J, Meng J, Du L, Kumar A, Xu H. Melt electrowriting reinforced composite membrane for controlled drug release. *J Mech Behav Biomed Mater*. 2022;132:105277. doi: 10.1016/j.jmbbm.2022.105277

59. Nieuwoudt M, Woods I, Eichholz KF, et al. Functionalization of electrospun polycaprolactone scaffolds with matrix-binding osteocyte-derived extracellular vesicles promotes osteoblastic differentiation and mineralization. *Ann Biomed Eng*. 2021;49(12):3621-3635. doi: 10.1007/s10439-021-02872-2

60. Hrynevich A, Elçi BŞ, Haigh JN, et al. Dimension-based design of melt electrowritten scaffolds. *Small*. 2018;14(22): 1800232. doi: 10.1002/smll.201800232

61. Loewner S, Heene S, Baroth T, et al. Recent advances in melt electro writing for tissue engineering for 3D printing of microporous scaffolds for tissue engineering. *Front Bioeng Biotechnol*. 2022;10:896719. doi: 10.3389/fbioe.2022.896719

62. Mifsud T, Chatzistergos P, Maganaris C, et al. Supersonic shear wave elastography of human tendons is associated with in vivo tendon stiffness over small strains. *J Biomech*. 2023;152:111558. doi: 10.1016/j.jbiomech.2023.111558

63. Reizabal A, Kangur T, Saiz PG, et al. MEWron: an open-source melt electrowriting platform. *Additive Manuf*. 2023;71:103604. doi: 10.1016/j.addma.2023.103604

64. Apostolakos J, Durant TJ, Dwyer CR, et al. The enthesis: a review of the tendon-to-bone insertion. *Muscles Ligaments Tendons J*. 2014;4(3):333-342.

65. Abdal-hay A, Kocak-Oztug NA, Sheikh FA, et al. Fabrication of 3D bioactive melt electrowriting composite scaffold with high osteogenic potential. *Colloids Surf B: Biointerfaces*. 2025;245:114270. doi: 10.1016/j.colsurfb.2024.114270

66. Ielo I, Calabrese G, De Luca G, Conoci S. Recent advances in hydroxyapatite-based biocomposites for bone tissue regeneration in orthopedics. *Int J Mol Sci*. 2022;23(17): 9721. doi: 10.3390/ijms23179721

67. Sgroi TA, Cilenti M. Rotator cuff repair: post-operative rehabilitation concepts. *Curr Rev Musculoskelet Med*. 2018;11(1):86-91. doi: 10.1007/s12178-018-9462-7

68. Bas O, D'Angella D, Baldwin JG, et al. An integrated design, material, and fabrication platform for engineering biomechanically and biologically functional soft tissues. *ACS Appl Mater Interfaces*. 2017;9(35):29430-29437. doi: 10.1021/acsami.7b08617

69. Richardson WJ, Kegerreis B, Thomopoulos S, Holmes JW. Potential strain-dependent mechanisms defining matrix alignment in healing tendons. *Biomech Model Mechanobiol*. 2018;17(6):1569-1580. doi: 10.1007/s10237-018-1044-5

70. Chen K, Hu X, Blemker SS, Holmes JW. Multiscale computational model of Achilles tendon wound healing: Untangling the effects of repair and loading. *PLoS Comput Biol*. 2018;14(12):e1006652. doi: 10.1371/journal.pcbi.1006652

71. Wittkowske C, Reilly GC, Lacroix D, Perrault CM. In vitro bone cell models: impact of fluid shear stress on bone formation. *Front Bioeng Biotechnol*. 2016;4:87. doi: 10.3389/fbioe.2016.00087

ACCSCIENCE PUBLISHING

International Journal of Bioprinting

RESEARCH ARTICLE

Toward robust and reproducible pluripotent stem cell expansion in bioprinted GelMA constructs

Elizabeth R. Komosa[1,2], Wei-Han Lin[1,2] and Brenda M. Ogle[1,2,3,4,5,6,*]

[1]Department of Biomedical Engineering, College of Science and Engineering, University of Minnesota, Minneapolis, Minnesota, United States of America

[2]Stem Cell Institute, University of Minnesota, Minneapolis, Minnesota, United States of America

[3]Lillehei Heart Institute, University of Minnesota, Minneapolis, Minnesota, United States of America

[4]Department of Pediatrics, Medical School, University of Minnesota, Minneapolis, Minnesota, United States of America

[5]Institute for Engineering in Medicine, University of Minnesota, Minneapolis, Minnesota, United States of America

[6]Masonic Cancer Center, University of Minnesota, Minneapolis, MN, United States of America

(This article belongs to the Special Issue: *Bioprinting for Tissue Engineering and Modeling*)

Abstract

Combining the technologies of 3D bioprinting and human induced pluripotent stem cells (hiPSCs) has allowed for the creation of tissues with organ-level function in the lab, a promising technique for disease modeling and regenerative medicine. Expanding the stem cells in bioprinted tissues prior to differentiation allows for high cell density, which is important for the formation of cell-cell junctions necessary for macroscale function upon differentiation. Yet, stem cell expansion, critical to successful *in situ* differentiation, depends heavily on the composition of the bioprinted scaffold. Here, we demonstrate how a common bioink component, gelatin methacryloyl (GelMA), varies depending on the vendor and degree of functionalization. We found that the vendor/GelMA production technique played a greater role in dictating the mechanical properties of the bioprinted constructs than the degree of functionalization, emphasizing the importance of reporting detailed characterization of GelMA scaffolds. Furthermore, the ability of singularized hiPSCs to survive and expand in GelMA scaffolds greatly varied across batches from different vendors and degrees of functionalization, where expansion correlated with the mechanical properties of the scaffold. Yet, we found that using a commercial cloning supplement could restore the ability of single hiPSCs to survive and expand across GelMA types, thus compensating for the varied mechanical properties of the scaffolds. These findings provide a practical guide for the expansion of hiPSCs in GelMA constructs with various mechanical properties as required for successful *in situ* differentiation.

Keywords: Bioprinting; Scaffold characterization; GelMA; Human induced pluripotent stem cells; *In situ* expansion

***Corresponding author:**
Brenda Ogle (ogle@umn.edu)

Citation: Komosa ER, Lin WH, Ogle BM. Toward robust and reproducible pluripotent stem cell expansion in bioprinted GelMA constructs. *Int J Bioprint*. 2025;11(1):363-381. doi: 10.36922/ijb.4633

Received: August 22, 2024
1st revised: November 14, 2024
2nd revised: December 5, 2024
Accepted: December 9, 2024
Published Online: December 10, 2024

Copyright: © 2024 Author(s). This is an Open Access article distributed under the terms of the Creative Commons Attribution License, permitting distribution, and reproduction in any medium, provided the original work is properly cited.

Publisher's Note: AccScience Publishing remains neutral with regard to jurisdictional claims in published maps and institutional affiliations.

1. Introduction

The field of tissue engineering has rapidly grown with the advancement of both human induced pluripotent stem cells (hiPSCs) and three-dimensional (3D) bioprinting. The ability to create human-relevant disease models and to fabricate 3D tissues has opened the door for many applications, including basic biology studies of tissue- and organ-level function and disease mechanisms, as well as translational uses in drug screening and regenerative medicine. A recent field trend combines hiPSCs and 3D bioprinting, where stem cells are bioprinted,[1] expanded,[2–6] and then differentiated in the bioprinted tissue[7–12]—a process termed *in situ* expansion and differentiation (ISED). ISED in 3D tissues boasts many benefits, including enhanced biomimetic environments over two-dimensional (2D) culture and the formation of cell-cell and cell-matrix junctions, which are important for macroscale tissue function.[7,9–11,13–17] For instance, in bioprinted tissues, ISED enabled the fabrication of a 3D human cardiac chamber model capable of pump function.[10] A pump of this type allowed for first-time measurements of clinically relevant pressure-volume relationships and the inclusion of healthy and diseased human cell types. Similarly, the neural application of ISED led to spontaneous action potential recordings that were not seen in 2D cultures, as well as metabolic switching that demonstrated early and advanced maturation in the 3D cultures.[17] Importantly, robust and reproducible implementation of the ISED approach is dependent on the properties of the scaffold and the health of the printed stem cell population.

Gelatin methacryloyl (GelMA) is one of the most common base components of bioinks used in scaffold fabrication and bioprinting, including the ISED approach,[6,10–12,14,16] as its natural and synthetic components allow for tunable properties, cell binding motifs, and printability.[18] Tunable properties include matrix stiffness and pore size, altered by the source of raw gelatin, degree of gelatin functionalization (DoF), and GelMA concentration in the bioink. Further flexibility of GelMA bioinks has been demonstrated via supplementation with other potent factors for controlling stem cell activity.[10,14] However, the high batch-to-batch variability of GelMA makes reproducing results challenging and reduces the translatability of studies. Fabrication protocols vary among groups producing GelMA in-house and commercially. Even when the same fabrication conditions are utilized across groups, large variability in scaffold properties— may still happen—in a systematic review, DoF ranging from ~70% to ~99% was observed when the same approach was used by four different groups.[19] Scaffold properties (*e.g.*, DoF, swelling, and storage modulus) can diverge depending on synthesis conditions, including temperature, rate and amount of methacrylic anhydride addition, and stirring speed.[19] Further, several commercial products do not specify DoF, and vendors that do characterize DoF often use different testing parameters and methodologies, making it difficult to predict behavior for desired applications.

The use of human pluripotent stem cells (hPSCs) adds further complexity, as their pluripotent nature makes them particularly sensitive to local environments. For instance, hPSCs are highly susceptible to dissociation-induced cell death due to myosin hyperactivation, triggered by activation of Rho signaling upon singularization.[20,21] However, singularization of cells is common in extrusion bioprinting, currently the most common bioprinting modality, making hiPSCs difficult to employ in this context.. Inhibition of Rho-associated kinases (ROCK), via molecules such as Y-27632 and Fasudil, have helped to reduce cell death with singularization,[22] though high viability remains a challenge in 3D cultures. Moreover, substrate mechanics also impact both hPSC proliferation and differentiation.[23,24] For instance, Labouesse *et al.*[25] examined the impact of substrate stiffness on pluripotent stem cell gene expression, where principal component analysis on differentially expressed genes led to samples clustering by substrate stiffness rather than the density of tethered extracellular matrix proteins. While investigating the effect of substrate stiffness and mechanotransduction during early mesoderm induction Smith *et al.*[26] found that stiff substrates reduce β-catenin expression, a key component in many differentiation pathways, in early mesoderm induction, and discovered improved endothelial specification on compliant surfaces. These results demonstrate that the mechanical properties of a scaffold are likely to impact ISED outcomes.

Given the variability in GelMA characteristics and the impact of the microenvironment on stem cell culture, it is not surprising that inconsistencies in hiPSC expansion arise when switching between vendors and lots of GelMA. Variable expansion is a barrier to successful ISED, making it difficult to achieve consistent differentiation outcomes and therefore consistent tissue function. Here, we investigate two primary parameters that dictate the successful implementation of the ISED approach, namely GelMA material properties and hiPSC expansion capabilities. In this paper, we share some accessible means to monitor material properties and hiPSC expansion. Through the present study, we found that some GelMA products allow for improved hiPSC survival and expansion over others, a change in construct storage moduli accompanies cell expansion, and the addition of a cloning supplement post-print allows hiPSCs to survive and proliferate over a wider range of GelMA properties. These results will aid in future studies utilizing ISED for a range of applications.

2. Methods

2.1. Bioink preparation and bioprinting

Acellular bioink was made by dissolving 5, 7.5, or 10% w/v GelMA and 0.5% w/v lithium phenyl-2,4,6-trimethylbenzoylphosphinate (LAP; Allevi, USA) in a solution of 75% v/v mTeSR1 (cat#85850, STEMCELL Technologies, Canada) and 25% v/v acetic acid (20 mM) at 60°C. For cellular constructs, precursor ink was made with 10 or 20% w/v GelMA and 1% w/v LAP, which was mixed 1:1 with hiPSCs for a final concentration of 15 million cells/mL in 5% or 10% GelMA, respectively, and 0.5% LAP. Ink sources and lots are listed in Table 1. Three GelMA types were sourced from either a commercial supplier ("C") or an in-house facility ("H"), with two different DoFs (low 50% vs high >90%). Each GelMA type included 2–3 lots ("1," "2," or "3") for comparison. All GelMA products were derived from 300-bloom type A porcine gelatin to maintain consistency in the gelatin source, with only the production method and DoF varying across samples.

G-codes for the bioprinted constructs (10 × 10 mm^2, 1.2 mm thick) were generated in Slic3r, with 100% rectilinear infill. Multiple constructs were printed per g-code; constructs were deposited in a 30 mm dish containing a support bath. Support bath (FRESH v2.0)[27] was created using gum arabic and gelatin type B, as previously reported.[6] The diameters of support bath particles were quantified in ImageJ across 4 batches, 30 particles per batch. Bioprinting was done using an INKREDIBLE+ bioprinter (CELLINK, Sweden). To account for changes in viscosity among ink sources, the drop rate of ink from the needle was used to set the pressure,[10] where 3.1 ± 0.3 s between drops was found to give construct structures representative of the g-code. Viscous inks (10% inks from Advanced Biomatrix, USA) were printed at 32°C, and less viscous inks (5% inks from Advanced Biomatrix, USA; and _10%_ inks from Bioprinting Facility, University of Minnesota) were printed at 27°C. Upon completion of the g-code, the constructs were cross-linked with 405 nm blue light for 20 s each above and below the construct. The support bath was then melted by incubating at 37°C for 30 minutes. Constructs were rinsed three times with warm Dulbecco's PBS (DPBS; no calcium or magnesium, cat#14190144, Thermo Fisher Scientific, USA). Cast samples were made by pipetting 100 µL of 10% C-hi1 ink in circular 8 mm-diameter polydimethylsiloxane (PDMS) molds.

2.2. Swelling behavior

To assess the swelling behavior of the bioprinted constructs, the masses of acellular constructs were measured after 1 day of culture at 37°C in either mTeSR1 supplemented with 100 U/mL penicillin, 100 µg/mL streptomycin (pen-strep; Thermo Fisher Scientific, cat#15140122) or DPBS. Samples were then lyophilized in parafilm-lined dishes to prevent the wet gel from freezing into the dish. The mass swelling ratio (MSR) was calculated as the ratio of the wet mass (*Mw*) to the dry mass (*Md*) as expressed in **Equation I**:

$$MSR = \frac{Mw}{Md} \quad \text{(I)}$$

Per GelMA type, 2–4 ink batches were tested, with 2–3 constructs per batch.

2.3. Mechanical characterization

The storage and loss moduli of the constructs were measured on a Discovery HR-3 rheometer (TA Instruments) with 8 mm parallel plates. Acellular constructs were tested on the day of bioprinting; while cellular constructs were evaluated on days 0, 7, and 14 after bioprinting. Adhesive P60 grit sandpaper (cat# DUR 9D-VP-10, DuraGold, TCP Global, USA) was placed on the plates to minimize slippage of the constructs during testing. Biopsy punches (Acu-Punch, cat#0413, Acuderm, USA) were used to cut constructs

Table 1. GelMA sources and lot numbers.

Label	Source	Cat#	DoF (%)	Lot
C-lo1	Advanced Biomatrix	VL3500000502	50	9385
C-lo2	Advanced Biomatrix	VL3500000502	50	9521
C-lo3	Advanced Biomatrix	VL3500000502	50	9237
C-hi1	Advanced Biomatrix	5208	95	9272
C-hi2	Advanced Biomatrix	5208	95	8622
H-hi1	University of Minnesota Bioprinting Facility	G99	99	9
H-hi2	University of Minnesota Bioprinting Facility	G99	99	10

Note: Materials were used at 10% concentration, unless otherwise noted. Three GelMA types were sourced from either a commercial supplier ("C") or an in-house facility ("H"), with two different DoFs [(high (hi) and low (lo))]. Each GelMA type included 2–3 lots ("1," "2," or "3") for comparison.

Abbreviation: DoF: Degree of functionalization.

and sandpaper into 8 mm circles. Frequency sweeps were performed at 1% strain and 37°C, ranging from 0.1 to 2.5 rad/s. The reported values were measured at 0.1 rad/s. For acellular constructs, 2–4 ink batches per GelMA type were tested, with 3–4 constructs per batch. For cellular constructs, 1–2 constructs were tested for each replicate, with 3 ink batches used.

2.4. Cell culture

hiPSCs overexpressing cyclin D2 under the myosin heavy chain gene[28] (derived from a female donor; kindly provided by Dr Jianyi Zhang's lab at the University of Alabama at Birmingham were maintained in mTeSR1 media on Matrigel (cat#08-774-552, Corning, United States) and passaged with ReLeSR (cat#05872, STEMCELL Technologies, Canada). For cell singularization for bioprinting, hiPSCs were incubated with Accutase (cat#A6964, Millipore Sigma, Germany), rinsed twice with mTeSR1, and resuspended at 30 million cells/mL in mTeSR1 with 10 μM Y-27632 ROCK inhibitor (cat#S1049, Selleckchem, United States). Cells were combined with ink as described above. Bioprinted constructs were incubated in mTeSR1 with 5 μM Y-27632 and pen-strep for the first day of culture, followed by mTeSR1 only, and changed daily for the remainder of culture.

2.5. Monitoring glucose consumption in hiPSC cultures and expansion

Glucose levels of the media were measured every 24 hours (± 30 minutes) for 14 days. A drop of the media sample was placed on parafilm, combining media from the same conditions across replicates, and glucose levels were recorded using a Contour Next One Blood Glucose Monitoring System (Ascensia Diabetes Care, Switzerland). Glucose consumption was approximated by subtracting the measured glucose levels from the basal glucose levels of the media, which were recorded on day (d) 1 of the experiment or upon using a newly supplemented bottle of mTeSR1.

2.6. Histological preparation and immunostaining of constructs for cellular analysis

At the end of the 14-day culture period, constructs were fixed overnight at 4°C in 4% paraformaldehyde. Cells were prepared for cryosectioning as previously described.[6] Sections were stained with 5 μg/mL 4′,6-diamidino-2-phenylindole (DAPI; cat#D1306, Invitrogen, United States) for 10 minutes and mounted with a solution of DAPI/1,4-diazabicyclo[2,2,2]octane (DABCO; cat#D27802, Sigma-Aldrich, United States) in glycerol and PBS. Tile scan imaging was performed on a Leica Dmi8 fluorescence microscope, and DAPI colonies ≥ 2500 μm^2 were quantified and normalized to tissue area, as determined by brightfield images. Eight sections per construct were analyzed; four from the first 0–500 μm of the tissue and four from the 500–1000 μm of tissue depth, with 1–3 constructs per condition per print batch (n = 3).

For immunostaining, one construct per condition per print batch was stained for OCT3/4 and SP1 expression. Samples were permeabilized with 0.2% Triton X-100 (cat# T8787, Sigma-Aldrich, United States) for 1 hour and blocked with a solution of 5% bovine serum albumin, 1% glycine, 2% goat serum, and 0.1% Triton X-100 (BGST) for 2 hours. Mouse anti-OCT3/4 (1 μg/mL; cat#sc-5279, Santa Cruz Biotechnology, Country) and rabbit anti-SP1 (2.2 μg/mL; cat#PA5-29165, Invitrogen, United States) in BGST were incubated overnight at 4°C. Sections were then washed with 0.2% Tween-20 (cat#655204, Millipore, Germany) in PBS and incubated for 2 hours with secondary antibody (4 μg/mL AlexaFluor 488 goat anti-mouse [cat#A32723, Invitrogen, USA] and 4ug/mL—AlexaFluor 647 goat anti-rabbit [cat#A32733, Invitrogen, USA]). After washing with Tween-20, samples were stained with DAPI and mounted as described above. Tile scans were captured, and OCT3/4 expression was normalized to SP1 to determine the pluripotency of living cells. F-actin was visualized using a 30-minute incubation with ActinGreen 488 ReadyProbes Reagent (cat#R37110, Invitrogen, USA) on permeabilized slides.

2.7. Evaluation of hiPSC expansion using Y-27632 and CloneR2 treatments in bioprinted constructs

To determine potential improvements for hiPSC expansion in the bioprinted constructs, C-lo1 GelMA was used. Following bioprinting, constructs were first cultured in mTeSR1 supplemented with Y-27632 (5 μM) for 1 or 2 days or in mTeSR1 supplemented with CloneR2 (1:10; cat#100-0691, STEMCELL Technologies, Canada) for 2 days, and then the media was changed back to fresh mTeSR1 for the remainder of hiPSC expansion period. CloneR2-containing media was neutralized with 1 M NaOH to ensure consistent pH between the two media types. Following these treatments, constructs were cultured under either static or dynamic conditions. In the dynamic culture, constructs were rocked at 30 rpm on a Lab-Line 4630 3-D Rotator (Marshall Scientific, USA). Glucose levels were monitored daily, and constructs were fixed on day 7 post-print. The experiment was repeated using C-hi1 (5%) GelMA, with 1 day of Y-27632 treatment under static or dynamic conditions, as well as under dynamic conditions with CloneR2 treatment for 2 days.

2.8. Evaluation of hiPSC differentiation following Y-27632 and CloneR2 treatments in bioprinted constructs

The differentiation potential of CloneR2-treated samples was evaluated in C-lo1 constructs using established cardiac differentiation protocols.[10,29] Briefly, bioprinted constructs

were first treated with either CloneR2 for 2 days or Y-27632 for 1 day as described above, and then after the proliferation period (7 days for CloneR2-treated constructs and 14 days for Y-27632-treated controls), cardiac differentiation was initiated with 12 μM CHIR99021 (cat#SML1046, Sigma-Aldrich, USA) in RPMI (cat#11875-093, Gibco, USA) supplemented with 1× B27 without insulin (cat#A1895601, Gibco, USA). After 24 hours, this media was replenished with fresh RPMI/B27 without insulin. On day 3 of differentiation, half of the exhausted media was collected from each condition and combined with fresh RPMI/B27 without insulin and supplemented with 5 μM IWP2 (cat#3533, Tocris, United Kingdom). On day 5 of differentiation, media was replaced with RPMI supplemented with 1× B27 with insulin (cat#1504001, Gibco, USA). Media was changed again on day 7 of differentiation, and constructs were fixed on day 10. Constructs were stained whole-mount for cardiac troponin T (1 μg/mL; cat#MS295P1, Epredia, USA) on a rocker and imaged on a Nikon A1Rsi confocal microscope (Nikon, Japan). Nine z-stacks were taken from each construct, and maximum intensity projections were created. Each condition had 2–3 print batches, with 1–2 constructs per batch.

To verify differentiation ability in more complex tissues, human chambered muscle pump (hChaMP) models were bioprinted and differentiated as previously described,[10] with some modifications as follows: Rocking was performed at 3 rpm, and differentiation was initiated after 9 days of expansion. Videos demonstrating contractile function were recorded on a ZEISS Axiocam 208 microscope camera (ZEISS, Germany) on day 43 of differentiation.

2.9. Statistical analysis

Sample group comparisons were analyzed in JMP Pro 16.0 (JMP, USA). Normality was assessed with Shapiro–Wilk tests, and groups with normal distributions were compared using Student's *t*-tests or analysis of variance (ANOVA) tests and post-hoc Tukey–Kramer honestly significant difference (HSD) tests. For non-normal datasets, Mann–Whitney tests or Kruskal–Wallis tests with post-hoc Steel–Dwass tests were performed. For comparisons to a control value (modulus change with cell growth or study of culture conditions to improve hiPSC expansion), post-hoc analyses were performed with Dunnett's test (parametric) or Steel's test (nonparametric). P-values were calculated for a null hypothesis of unequal means (two-tailed) with a 95% confidence interval.

3. Results

3.1. Hydration medium and fabrication method impact construct material properties

We first evaluated the impact of hydration medium on the MSR of GelMA constructs. We found that constructs cultured in DPBS showed a significantly higher MSR compared to those cultured in mTeSR1 stem cell medium (Figure S1a, Supplementary File). This demonstrates the importance of performing studies in relevant media, as studies performed in DPBS may overestimate swelling and media uptake.

Next, we compared hydrogel material properties between cast constructs and extrusion-printed constructs in a support bath. Cast constructs exhibited a significant reduction in MSR, approximately half of what was observed in mTeSR1, and a more than 16-fold increase in storage modulus (G′) compared to printed constructs (Figure S1b, Supplementary File). Importantly, the variability in MSR and storage modulus was lower in cast samples compared to printed samples, both within single batches and across different ink batches (Figure S1a and S1b, Supplementary File).

To account for slight variations in bioink viscosities, we set the print pressure for pneumatic extrusion based on the drop rate of the ink from the needle. The variability observed in the printed constructs is likely attributed to differences in support bath properties or errors in setting pneumatic pressure, rather than issues with GelMA solubilization across batch. The microparticles of the support bath (12.98 ± 0.80 μm) and yield stress (75.6 ± 34.1 Pa) were consistent across batches (Figure S2, Supplementary File), suggesting that these parameters were not significant contributors to variability in construct properties.

In contrast, we observed a wide range of set pressures required for printing among different ink batches (Figure S1c, Supplementary File), identifying pneumatic pressure as a primary source of variability in construct properties. This is supported by the clustering of bioprinted samples by ink batch in Figure S1a (Supplementary File), while pipetted samples showed no batch-specific separation. Therefore, pneumatic printing is identified as a key source of variability in construct properties.

3.2. Increasing GelMA concentration yields scaffolds with increased stiffness and decreased swelling

We evaluated the effect of GelMA concentration on MSR and storage modulus, two key parameters for tuning GelMA scaffolds. Constructs were tested at 5, 7.5, and 10% GelMA concentrations (C-hi1) and we observed that required print pressures decreased significantly with decreasing GelMA concentration, despite lower print temperatures for the 5% and 7.5% formulations (Figure S3a, Supplementary File). The constructs followed expected trends, with increasing GelMA concentration leading to reduced MSR and increased stiffness. Specifically, constructs with higher GelMA concentrations exhibited

lower swelling and higher storage moduli (Figure S4, Supplementary File).

3.3. GelMA source and DoF significantly affect construct mechanical properties

We evaluated the impact of GelMA type and DOF on construct mechanical properties by evaluating three GelMA types (Table 1, Figure 1a). The GelMA types required a wide range of printing pressures (Figure S3b, Supplementary File), with source C inks needing over 90 kPa at 27°C. To standardize pressures, the print temperature for source C was raised to 32°C. The storage modulus (G′) and MSR were used to evaluate the mechanical properties of the GelMA constructs. A significant difference in MSR was observed between the C-hi and H-hi constructs, despite their similar DoF (Figure 1b). However, the MSR values of C-lo and C-hi constructs from source C were comparable. In terms of storage modulus, all three GelMA types demonstrated distinct values (Figure 1c). C-lo and C-hi constructs showed more similarity in G′ compared to the differences between C-hi and H-hi, indicating that the GelMA source and production method exerted a greater influence on construct stiffness than the DoF.

Interestingly, the differences in MSR and G′ among GelMA types were smaller than those caused by fabrication methods found in Figure S1a and S1b (Supplementary File). This suggests that the printing process plays a primary role in determining material properties of the construct, while the GelMA source is a secondary factor.

3.4. Lot-to-lot variability of GelMA depends on the manufacturing source

Breaking a given GelMA type down by a lot, we found some variability in MSR (Figure 1d) and G′ (Figure 1e). In general, the in-house-produced GelMA (H) exhibited greater lot-to-lot variability compared to the commercial products (C). No significant differences were found between the two C-hi lots, as MSR, G′, and set printing pressure were consistent (Figure S3c, Supplementary File). However, C-lo1 showed notable differences in MSR compared to C-lo2 and C-lo3, and in G′ compared to C-lo2. There was a non-significant increase in average printing pressure for C-lo2 relative to C-lo1 and C-lo3 (Figure S3c, Supplementary File). We also observed a large difference between MSR, stiffness, and print pressure H-hi1 vs. H-hi2, indicating significant lot variability that could affect downstream applications, such as hiPSC culture.

3.5. *In situ* expansion of hiPSCs is dictated by GelMA source and concentration

Given the variability observed in GelMA sources and lots, we next aimed to determine how these differences might affect hiPSC viability and expansion. hiPSCs were cultured in different lots of C-lo GelMA (C-lo1 and C-lo2), two concentrations of C-hi1 (10% and 5%), and H-hi1, which exhibited similar storage modulus (G′) but different MSR compared to C-hi1 (5%) (Figure 2a). When printing with cells, a slight increase in print pressures was noted compared to the corresponding acellular inks (Figure S3d, Supplementary File). While this increase was non-significant for most GelMA types (as confirmed by *t*-tests comparing acellular and cellular inks), a two-way ANOVA showed that the presence of cells significantly influenced print pressure across different GelMA types and temperatures ($p = 0.0026$).

3.6. Monitoring glucose consumption for assessing hiPSC growth and expansion in GelMA constructs over 14 days

We successfully monitored the growth and expansion of hiPSCs in GelMA over a 14-day period through daily measurements of glucose levels (Figure S5, Supplementary File) in the exhausted media, with glucose consumption approximated by subtracting the consistent baseline readings of 272.0 ± 5.0 mg/dL from fresh mTeSR1 media. By evaluating the glucose consumption curves for each GelMA type (Figure S5a, Supplementary File), we saw a similar value on day 1 for all GelMA types, suggesting consistency in cell numbers among the initial ink compositions. Surprisingly, there was also a consistent drop between d1 and d2, likely due to the death of hiPSCs cultured as sparse, single cells. Cells began to recover at different rates, dependent on the GelMA type. Comparison of consumption values at d3, d7, d10, and d14 of culture revealed the greatest difference among the GelMA types occurring at d7, where the C-lo constructs differed from H-hi1 and C-hi1 at both concentrations (Figure 2b). Interestingly, hiPSCs did not expand well at 10% concentration for C-hi1, with glucose levels decreasing by d7 of proliferation, so the culture of these constructs was terminated at this time point and C-hi1 (5%) was used for subsequent cell studies. Overall, hiPSCs grew best in C-lo1 and C-lo2, with significantly improved glucose consumption at d5–d7 compared to C-hi1 (5%) and H-hi1, with lower variability in consumption rates at each timepoint, and fairly reproducible outcomes between the two GelMA lots. Glucose consumption of the C-lo inks tended to plateau around d10, suggesting this GelMA type may not require 14 days of proliferation prior to inducing differentiation with the ISED approach.

3.7. Differential colony coverage and localization in GelMA constructs after 14 days of hiPSC proliferation

Tissue sections obtained at d14 of proliferation were stained with DAPI to determine cell coverage. We found

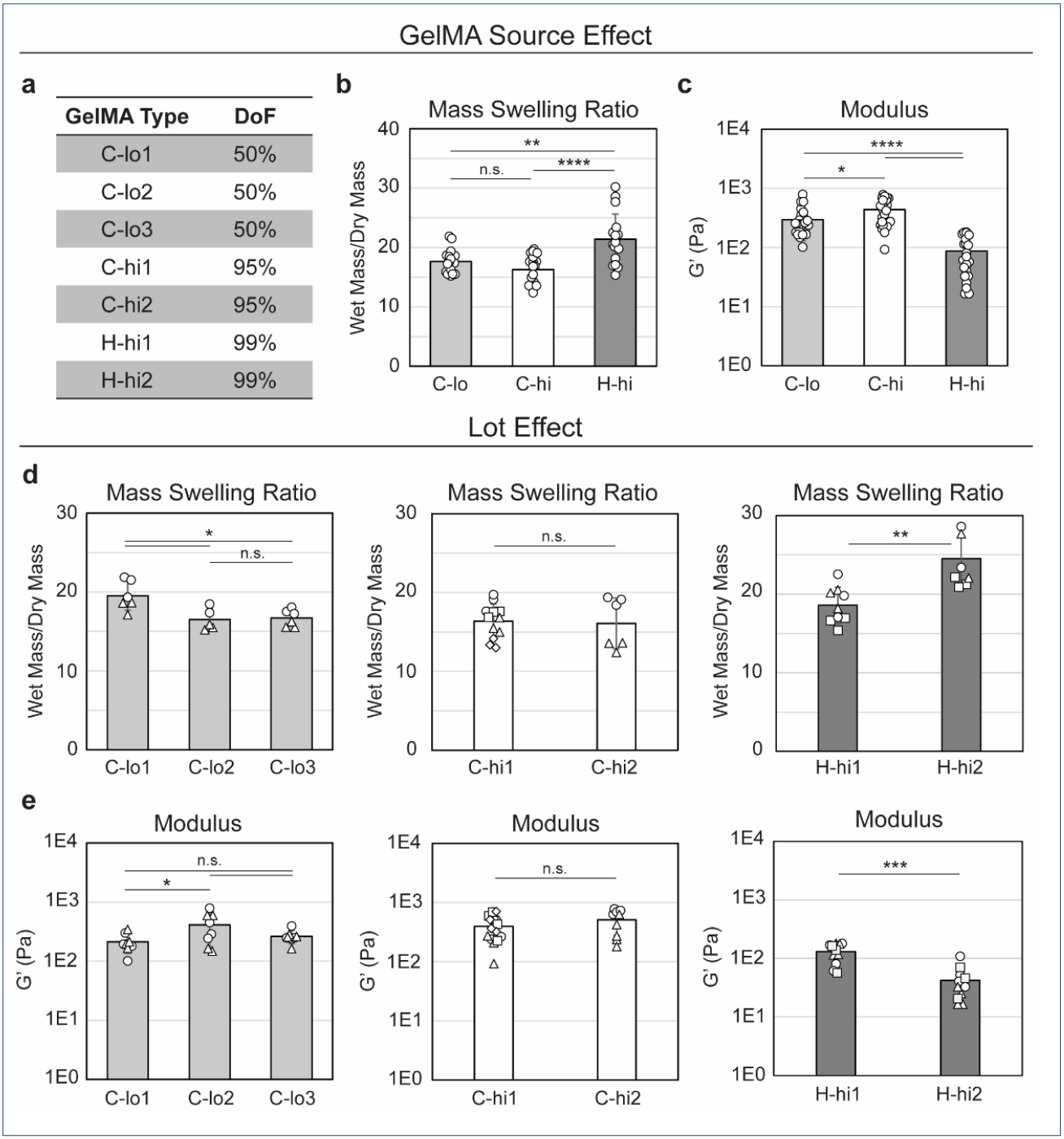

Figure 1. GelMA source and lot affect scaffold mass swelling and mechanical properties. (a) Summary of GelMA types. Labels are designated by source, DoF, and lot. Listed DoFs are obtained from product information. (b–c) Effect of GelMA type on MSR of acellular constructs after 1 day of culture in mTeSR1 (b) and G′ (c). Results show greater discrepancies between sources of GelMA than DoF. (d–e) Effect of GelMA lot on MSR (d) and G′ (e). Large variability was found between the two H-hi lots for both MSR and G′, and slight differences were seen among C-lo lots. (2–4 print batches per GelMA type, batches represented by the shape of data points on bar graphs, 2–3 constructs/batch for MSR, 3–4 constructs/batch for rheometry. *$p \leq 0.05$, **$p \leq 0.01$, ***$p \leq 0.001$, ****$p \leq 0.0001$, n.s. not significant.) Abbreviations: DOF: Degree of functionalization; GelMA: Gelatin methacryloyl; MSR: Mass swelling ratio.

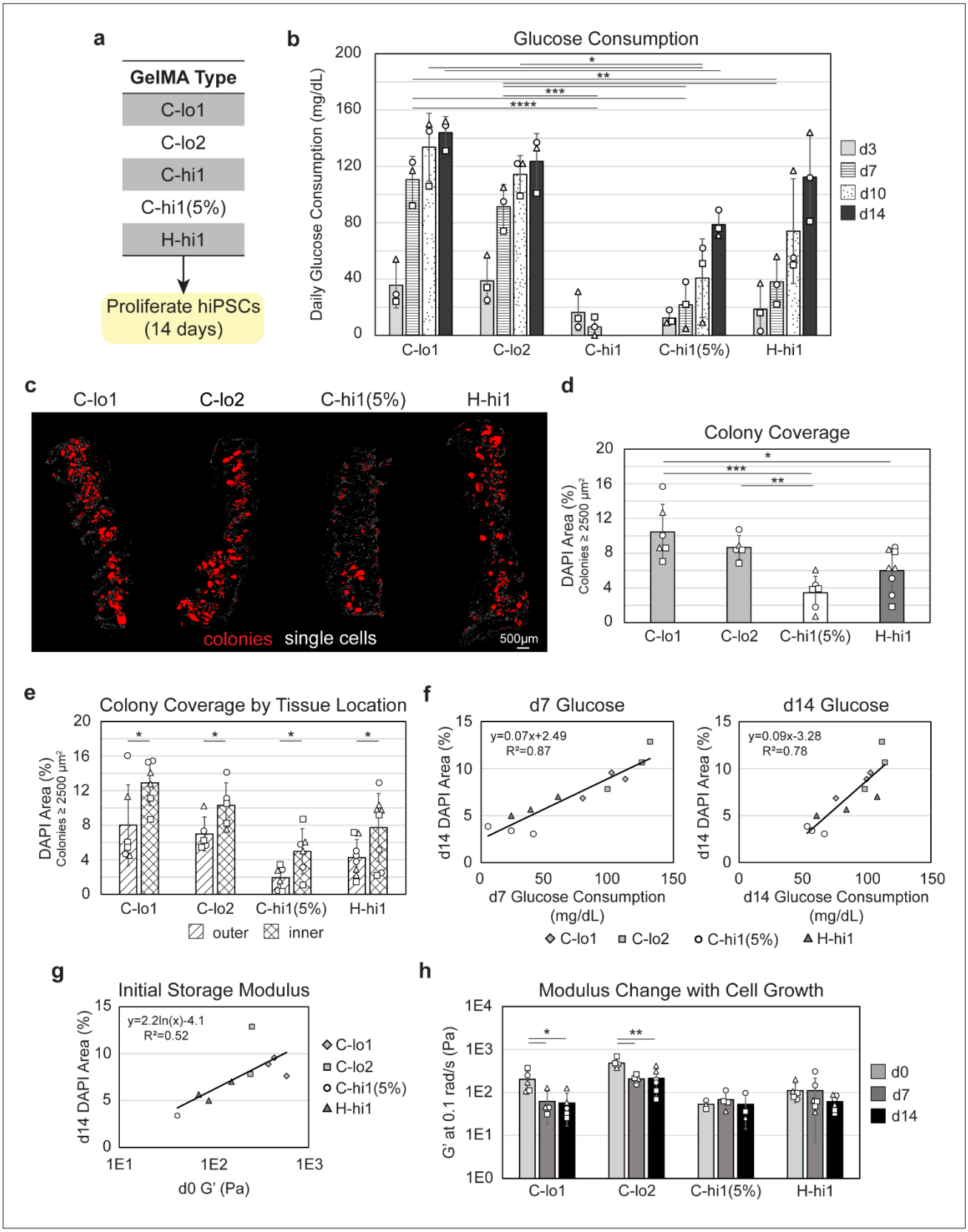
a
GelMA Type
C-lo1
C-lo2
C-hi1
C-hi1(5%)
H-hi1
Proliferate hiPSCs
(14 days)
b
Glucose Consumption
Daily Glucose Consumption (mg/dL)
200
160
120
80
40
0
*
**
***
****
C-lo1
C-lo2
C-hi1
C-hi1(5%)
H-hi1
d3
d7
d10
d14
c
C-lo1
C-lo2
C-hi1(5%)
H-hi1
colonies
single cells
500μm
d
Colony Coverage
DAPI Area (%)
Colonies ≥ 2500 μm²
20
16
12
8
4
0
*
***
**
C-lo1
C-lo2
C-hi1(5%)
H-hi1
e
Colony Coverage by Tissue Location
DAPI Area (%)
Colonies ≥ 2500 μm²
20
16
12
8
4
0
*
*
*
*
C-lo1
C-lo2
C-hi1(5%)
H-hi1
outer
inner
f
d7 Glucose
y=0.07x+2.49
R²=0.87
d14 DAPI Area (%)
15
10
5
0
0
50
100
150
d7 Glucose Consumption
(mg/dL)
d14 Glucose
y=0.09x-3.28
R²=0.78
d14 DAPI Area (%)
15
10
5
0
0
50
100
150
d14 Glucose Consumption
(mg/dL)
C-lo1
C-lo2
C-hi1(5%)
H-hi1
g
Initial Storage Modulus
y=2.2ln(x)-4.1
R²=0.52
d14 DAPI Area (%)
15
10
5
0
1E1
1E2
1E3
d0 G' (Pa)
C-lo1
C-lo2
C-hi1(5%)
H-hi1
h
Modulus Change with Cell Growth
G' at 0.1 rad/s (Pa)
1E4
1E3
1E2
1E1
1E0
*
**
C-lo1
C-lo2
C-hi1(5%)
H-hi1
d0
d7
d14

many singularized cells in all GelMA types (**Figure 2c**, *white* cells), and we suspected that since these cells had not formed colonies, they had likely died as a function of singularization in the printing process or due to lack of cell binding or nutrient access. Indeed, these singularized cells did not express F-actin or ubiquitous transcription factor SP1 (Figure S6, Supplementary File), confirming these cells had died early and remained trapped within the construct, similar to previous findings.[6] Thus, only colonies (Figure 2c, *red* regions) were quantified for each tissue. We found 3-fold greater colony coverage in C-lo1 relative to C-hi1 (5%) and 1.7-fold more than H-hi1 (Figure 2d). When examining the two lots of C-lo GelMA, we found that C-lo2 had a ~12% decrease in the area of hiPSC colonies, though this difference was not statistically significant. Colonies remained pluripotent in all GelMA types (Figure S7, Supplementary File).

Interestingly, when comparing colonies in cryosections taken from outer tissue (~0–500 μm from construct surface) vs. inner tissue (~500–1000 μm from construct surface), there were more colonies in the inner than the outer tissue (Figure 2e). This is similar to previous findings when examining colony localization across a 3D-bioprinted chamber model and is attributable to cell detachment with support bath removal and media changes.[6] Regardless, trends among colony coverage in the different GelMA types remained the same at both locations.

3.8. Correlation of glucose consumption and mechanical properties with hiPSC colony coverage in 3D-bioprinted GelMA constructs

We also examined the correlation between glucose consumption and final colony coverage, combining the values for all GelMA types to validate the utility of glucose consumption as an indicator of hiPSC expansion (Figure 2f**;** Figure S8, Supplementary File). The glucose consumption at d14 gave a high correlation to the colony coverage, as did consumption at d7 and d10. These data support the use of the glucose meter for easy quantification of cell growth in 3D. Using the earlier metrics to predict colony coverage at the end of the ISED proliferation period will be valuable to validating adequate expansion in a given GelMA type or lot and to standardizing the initiation of differentiation.

Another interesting trend we found by pooling all GelMA types was an increase in hiPSC colony coverage with increasing initial storage modulus (Figure 2g). As a relatively low range of G′ was used for these studies, we were surprised to see such a notable trend. This trend was also found with the initial loss modulus (G″; Figure S9a, Supplementary File). However, further study is needed to evaluate the effect of this phenomena, as there are several other variables relevant to the use of multiple GelMA types. For instance, there was a negative correlation between colony coverage and MSR, as well as between colony coverage and DoF (Figure S9b and S9c, Supplementary File). However, we did not see a trend between colony coverage and print pressure (Figure S9d, Supplementary File). Overall, the mechanical stiffness, affected by both DoF and MSR, appears to be a primary determinant of the viability and expansion of singularized hiPSCs.

3.9. Construct mechanical properties change with hiPSC expansion

During the 14-day hiPSC proliferation period, we monitored how cell growth impacted G′ and G″. Cellular constructs at d0 were comparable to the acellular constructs, showing the addition of cells to the ink did not initially affect construct properties. During *in situ* proliferation, the moduli of C-hi1(5%) and H-hi1 constructs did not change between d0 and d7, but both had slight, yet non-significant decreases between d7 and d14 (Figure 2h**;** Figure S10, Supplementary File). However, in C-lo1 and C-lo2 GelMA, we saw a drastic drop in both moduli by d7 of proliferation. Interestingly, there was no difference between the d7 and d14 moduli for these inks, during which time we found a less accelerated rate of glucose consumption compared to earlier days. Thus, these results correlate well with colony coverage and glucose consumption, suggesting that the cells reduce stiffness of the bulk tissue with volumetric expansion and likely cause some degree of remodeling.

Figure 2. Selection of GelMA type impacts hiPSC expansion. (a) Summary of GelMA types tested for 14-day hiPSC expansion. (b) Glucose consumption of hiPSCs in each GelMA type increases over the 14-day period except C-hi1, which was terminated at d7. Most statistical significance between groups was found at d7 of proliferation. (c) Images of cross-sections at the end of the proliferation time, with nuclei stained with DAPI. Colonies, shown in red, are found to be the viable cells in the constructs, whereas single cells (white) remaining at d14 are found to be non-viable. (d) Quantification of colonies in d14 cross-sections shows the highest growth in C-lo1 and C-lo2 and the lowest in C-hi1 (5%), in accordance with the glucose consumption results. (e) Examination of colony coverage in outer (0–500 μm) vs. inner (500–1000 μm) portions of the constructs show higher cell growth in the interior of the constructs compared to the exterior. Yet, trends seen in panel (d) remain the same in both regions of the construct. (f) Glucose consumption from d7 (left) and d14 (right) show a strong correlation with the final colony coverage at d14, suggesting an accurate technique for non-invasively measuring hiPSC growth in 3D prior to initiation of differentiation. (g) A notable correlation also exists between the initial storage modulus at d0 of proliferation and the final colony coverage, regardless of the GelMA type used. (h) Change in G′ with cell growth. G′ changes more in C-lo inks, which are the inks with the most hiPSC expansion. (3 print batches per GelMA type, batches represented by the shape of data points on bar graphs, 1–3 constructs/batch. $^{*}p \leq 0.05$, $^{**}p \leq 0.01$, $^{***}p \leq 0.001$, $^{****}p \leq 0.0001$.) Abbreviations: GelMA: Gelatin methacryloyl; hiPSC: Human induced pluripotent stem cell.

Examination of this impact is important for future studies of *in situ* differentiation, as substrate stiffness is an important regulator of cell morphology and can influence differentiation and maturation outcomes.

3.10. Use of CloneR2 improves hiPSC expansion in different GelMA types

After observing a significant decline in glucose consumption at d2 of proliferation, we hypothesized that this early cell death could be reduced by altering our standard 1-day treatment with ROCK inhibitor, Y-27632, as used for the studies in section 3.5 to 3.9. A reduction in initial cell death may lead to better colony coverage at an earlier time point. Thus, we tested several culture conditions with C-lo1, the GelMA type that is the most supportive of hiPSC expansion. We tested both static and dynamic (rocking) culture, with 1- or 2-day treatment of Y-27632, as well as 2-day treatment with a defined stem cell cloning supplement, CloneR2 (Figure 3a**;** Figure S11a and S11b, Supplementary File). We again monitored glucose levels and still saw a drop at day 2 for all Y-27632 conditions in both static and dynamic cultures (Figure S11a, Supplementary File). However, with CloneR2-treated samples (under both static and dynamic culture), there was an increase in consumption at d2, and glucose consumption continued to increase, whereas the consumption in Y-27632 conditions remained relatively unchanged until ~d4–5. The CloneR2 conditions at d3 were not found to be significantly different from the d14 consumption values found for C-lo1 in Figure 2b. Furthermore, all replicates from the CloneR2-treated groups surpassed the d14 control average within 4 or 6 days of culture for dynamic and static conditions, respectively (Figure 3b), indicating a significantly accelerated expansion of hiPSCs with CloneR2 treatment. After 7 days of culture, constructs were fixed and sectioned for histology. Colonies were again found to reflect the glucose consumption profiles, where the CloneR2-treated samples at d7 held similar colony coverage to the Y-27632-treated samples at d14 described in Figure 2d (Figure 3c–d). Fewer single (nonviable) cells appeared in CloneR2-treated samples, consistent with the increased glucose consumption on d2 of expansion. Relative to the d14 samples, CloneR2-treated samples had more colonies, which were generally smaller and more consistently sized, a possible advantage for differentiation outcomes.[48–50] The addition of CloneR2 and the corresponding increase in growth rate did not affect the pluripotency of the hiPSCs (Figure S12, Supplementary File). Statistical comparisons between the colony coverage of d14 control (1d-treated Y-27632) and d7 CloneR2-treated samples yielded a p-value of > 0.98, indicating similar growth in half the proliferation time. Interestingly, despite the lower average in colony coverage of the d7 1d-treated Y-27632 constructs relative to the d14 timepoint, the two were not found to be significantly different ($p = 0.068$), possibly due to the large variability at each timepoint. The remaining treatment groups were significantly lower than the d14 control. Interestingly, unlike the 14-day studies in Figure 2, we did not see a significant difference between the inner and outer regions of the constructs with any d7 constructs (Figure 3e). This suggests that either colonies continue expanding more within the interior of the tissues than the exterior in the following 7 days or the colonies near the exterior detach. Regardless, this further demonstrates the utility of CloneR2-treated tissues, as we can obtain a similar colony coverage in half the culture time, with improved consistency between regions of the tissue. This improved colony distribution is important for engineering tissues for any application.

In further studies with the less proliferative C-hi1 (5%) GelMA, we found that dynamic Y-27632 culture did not alter glucose consumption or colony coverage relative to its static control (Figure 3f and g**;** Figure S11c and S11d, Supplementary File), suggesting the poor growth in C-hi1 (5%) is not due to poor nutrient supply. However, dynamic CloneR2 was again found to accelerate glucose consumption, where d3 glucose consumption was equivalent to the d14 control (1-day Y-27632 C-hi1 (5%) samples described in Figure 2) (Figure 3f**;** Figure S11c, Supplementary File). Surprisingly, d7 glucose consumption of CloneR2-treated constructs was more than double the amount of the d14 samples and even exceeded that found at d14 in the best GelMA type, C-lo1. Colony coverage reflected these trends, with CloneR2-treated constructs matching the d14 C-lo1 values and far exceeding the d14 C-hi1 (5%) values (Figure 3g).

Figure 3. Early treatment with cloning supplement improves hiPSC expansion. (a) Summary of conditions tested with cells in C-lo1 GelMA. Cells were treated with Y-27632 for 1 or 2 days or with CloneR2 for 2 days, cultured for 7 days statically or dynamically on a rocker. (b) Glucose consumption of hiPSCs under each culture condition. d3 glucose consumption of CloneR2-treated samples do not differ from control samples at d14 (shown for reference). (c) Cross-sections showing colonies (red) after the 7-day proliferation, with nuclei stained with DAPI. Few single cells (white) remain in CloneR2-treated constructs. (d) Colony coverage after various culture condition treatments show similar growth in d7 CloneR2-treated samples relative to the d14 Y-27632-treated samples. (e) Colony coverage does not vary by region at d7 of culture in any culture condition. (f–g) Select conditions were tested with C-hi1 (5%) GelMA. Use of CloneR2 drastically improved hiPSC expansion, where d7 glucose measurements (f) and d7 colony coverage (g) far exceeded d14 C-hi1 (5%) values, even reaching values for d14 C-lo1 (shown for reference). (3 print batches per GelMA type, batches represented by shape of data points on bar graphs, 1–2 constructs/batch. Significance was found relative to d14 samples of the same ink type using Dunnett's test or Steel's test. $^{*}p \leq 0.05$, $^{**}p \leq 0.01$, n.s. not significant.) Abbreviations: GelMA: Gelatin methacryloyl; hiPSC: Human induced pluripotent stem cell.

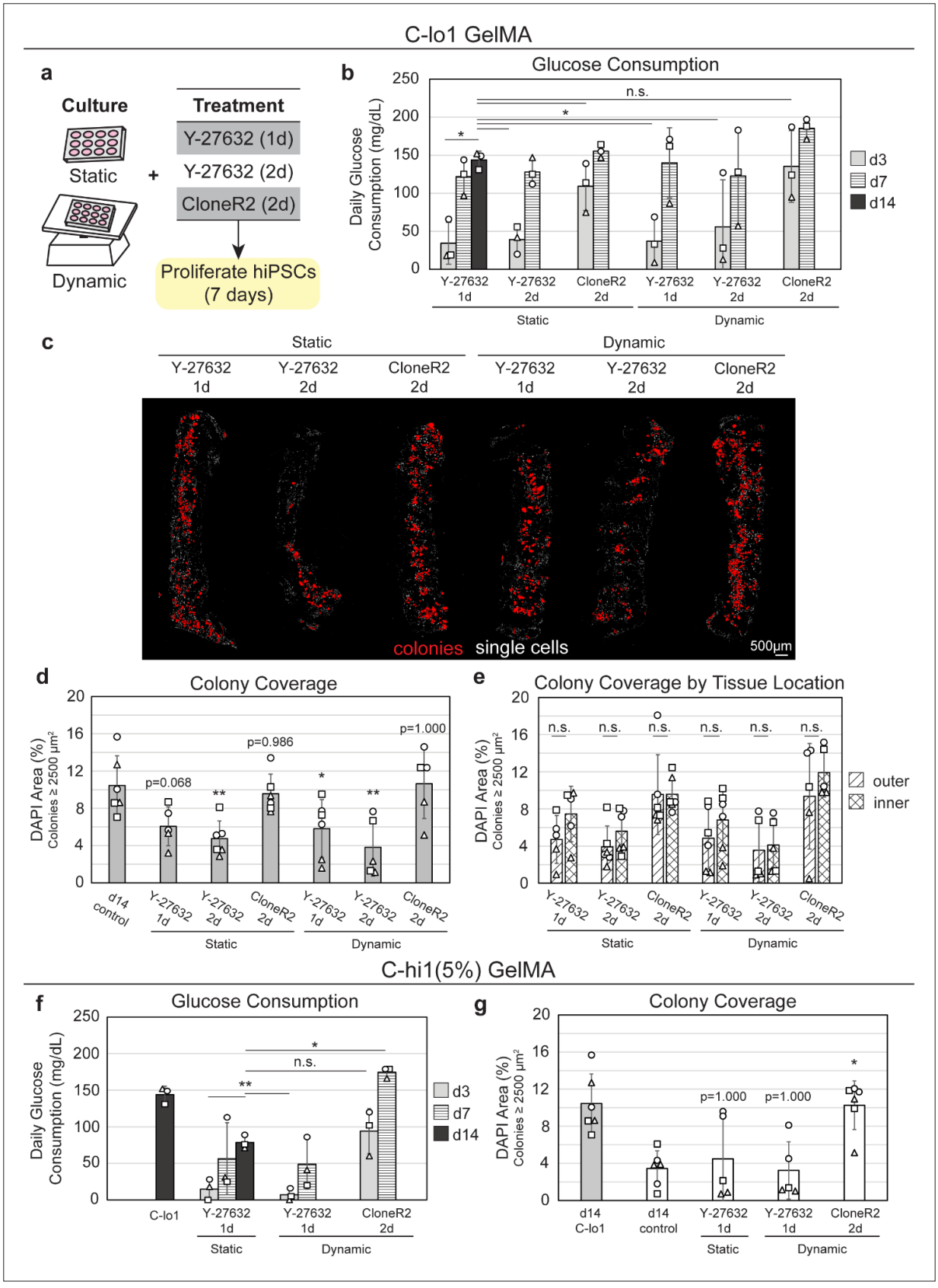
C-lo1 GelMA
a
Culture
Treatment
Static
+
Y-27632 (1d)
Y-27632 (2d)
CloneR2 (2d)
Dynamic
Proliferate hiPSCs
(7 days)
b
Glucose Consumption
Daily Glucose Consumption (mg/dL)
n.s.
*
d3
d7
d14
Y-27632 1d
Y-27632 2d
CloneR2 2d
Static
Dynamic
c
Static
Dynamic
colonies
single cells
500µm
d
Colony Coverage
DAPI Area (%)
Colonies ≥ 2500 µm²
p=0.068
p=0.986
p=1.000
d14 control
e
Colony Coverage by Tissue Location
outer
inner
C-hi1(5%) GelMA
f
Glucose Consumption
C-lo1
g
Colony Coverage
d14 C-lo1
d14 control

3.11. Cardiomyocyte differentiation and functional cardiac tissue formation following CloneR2-supported hiPSC expansion

After observing rapid hiPSC expansion with CloneR2, we next tested whether these highly proliferative cells could still differentiate into cardiomyocytes. After the 7-day proliferation phase with CloneR2 treatment, we induced differentiation of hiPSCs into cardiomyocytes in constructs made from C-lo1 GelMA (Figure 4a). After the following 10 days of cardiac differentiation, bioprinted constructs were stained for cardiac sarcomeric protein, cardiac troponin T (cTnT), to confirm differentiation outcomes. Both static and dynamic CloneR2 conditions yielded similar percentages of cTnT-positive cells compared to the Y-27632 control, indicating that CloneR2 did not negatively impact the differentiation process (Figure 4b and c). Of note, differentiation efficiency was low, likely due to the absence of additional extracellular matrix proteins known to improve differentiation outcomes, and the undifferentiated control expressed negligible cTnT (Figure S13, Supplementary File). We further tested CloneR2's effects using a complex 3D cardiac model, the hChaMP (Figure S14, Supplementary File). Following 9 days of CloneR2-supported hiPSC expansion, cardiomyocyte differentiation was induced. Both CloneR2- and Y-27632-treated hChaMP constructs exhibited synchronous and robust beating, confirming successful formation of functional cardiac tissue (Videos S1 and S2, Supplementary File). These results demonstrate the potential of CloneR2 to support hiPSC expansion and differentiation in advanced bioprinted tissue models.

4. Discussion

In this study, we identified several key parameters that can impact the ability of pluripotent stem cells to expand and differentiate in 3D-bioprinted constructs. Based on these results, we provide key recommendations for future work using the ISED approach and discuss limitations that remain unsolved.

4.1. Primary recommendations for improving *in situ* expansion of hiPSCs in GelMA-based scaffolds

4.1.1. Variability in GelMA properties emphasizes the need for reporting scaffold characterization beyond GelMA concentration

First, while GelMA is widely used for a variety of bioprinting applications, the properties of this material vary substantially among different manufacturers, despite similar DoF and gelatin starting material. Moreover, GelMA source, DoF, and concentration have a great influence on the ability of hiPSCs to expand in the constructs, which is problematic for achieving consistency in downstream differentiation applications.[40–43] To better understand the relationship between GelMA type and hiPSC growth, we employed MSR and rheometry as metrics to describe construct material properties.[30–36] MSR is a cheap and easy screening method to monitor differences in construct properties and can give an approximation of nutrient diffusion in a cell-laden construct.[30] Our studies revealed that concentration, media type, and scaffold preparation technique have a more profound impact on the MSR than GelMA type. On the contrary, GelMA type greatly influenced the storage modulus, where two GelMA types with similar DoFs from different manufacturers had quite different mechanical properties. Again, due to the sensitivity of hiPSCs, this inconsistency in mechanical properties may be critical to ensuring successful ISED.[44] These findings and a recent report by He *et al.*[51] underscore the need to thoroughly characterize scaffold properties, especially mechanical properties, for reproducibility. Currently, GelMA concentration is the only consistently reported parameter, but as we see, the mechanical properties of 10% GelMA can vary greatly depending on manufacturer, DoF, and lot number.

4.1.2. Pneumatic bioprinting and support bath characteristics influence construct material properties

Importantly, there are also several factors that can impact reproducibility in the bioprinting process itself. As bioprinted samples generated higher variability than cast samples for MSR and storage/loss moduli, even within the same ink batch, we see there is some degree of error introduced in bioprinting. While pneumatic printing offers a relatively easy-to-use biofabrication platform, it relies on a steady application of pressure with compressed gas and is easily affected by the viscosity of the bioink. Variability in viscosity among GelMA types and batches can impact the ability to generate consistent construct structures.[37–39] We aim to circumvent this issue by adjusting pressure to a consistent drop rate of ink from the needle,[10] but consistency of the applied pressure during printing is highly important. In many cases, setting the drop rate was not straightforward, as the drop rate could vary with the application of pressure within the same ink batch, suggesting pressure applied by the printer was not stable. This means printing outcomes are more prone to over extrusion or under extrusion, a likely cause of variability in the acellular and d0 rheometry data. As we observed a correlation between initial modulus and resulting cell growth, the lack of pneumatic stability can be a problem for achieving consistent hiPSC proliferation and differentiation. Use of a mechanical piston-driven extrusion printer may help circumvent some of these issues, as demonstrated in a recent study[39]; however, prior

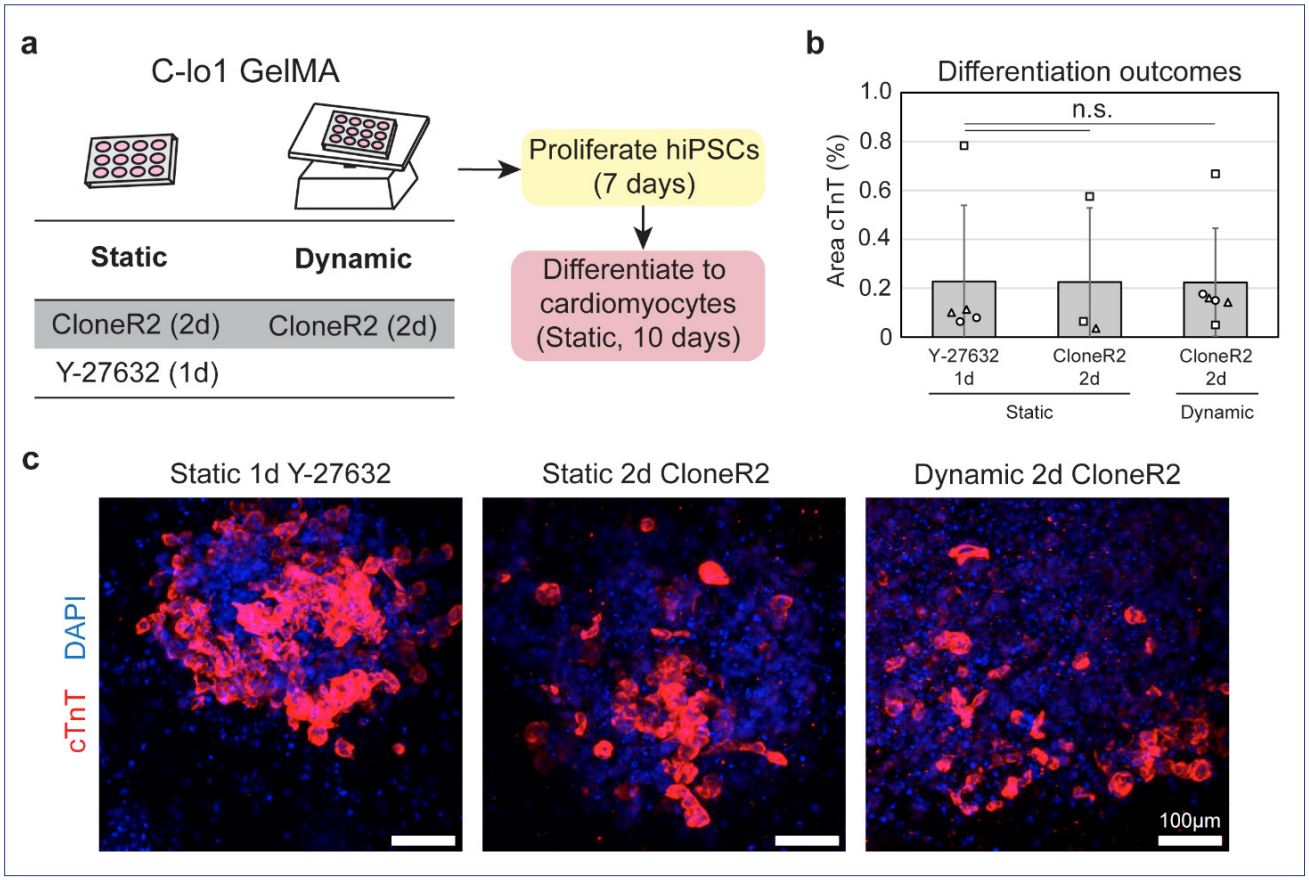

Figure 4. Treatment with CloneR2 does not inhibit the ability to differentiate hiPSCs from cardiomyocytes. (a) Schematic of expansion conditions tested prior to differentiation. Differentiation was initiated following 7 days of expansion. (b) The cTnT expression in differentiated tissues shows that hiPSCs in C-lo1 GelMA are able to differentiate to cardiomyocytes following treatment with static or dynamic CloneR2 culture. (c) Images of cTnT-expressing cardiomyocytes in each culture condition. (2–3 print batches per condition, batches represented by the shape of data points on bar graphs, 1–2 constructs/batch. Significance was found relative to control Y-27632 samples using Dunnett's test. n.s. not significant.) Abbreviations: cTnT: Cardiac troponin T; GelMA: Gelatin methacryloyl; hiPSC: Human induced pluripotent stem cell.

research of this printing modality is limited relative to pneumatic extrusion.[52]

Additionally, the use of a slurry-based support bath during printing dramatically increases porosity, as suggested by the large change in MSR between bioprinted and cast constructs. The use of a support bath is necessary for printing complex shapes with GelMA at low-viscosity concentrations that support cell growth; however, properties of the support bath, including viscosity, yield stress, and particle size, can certainly affect scaffold properties. While it has been shown that bulk hydrogels have many different properties than more porous scaffolds,[33] we were surprised to see the stark increase in stiffness and decrease in MSR in cast samples relative to bioprinted scaffolds, presumably due to the pores created by support bath particles. Also surprising was the greater impact of saline on the swelling of bioprinted samples relative to cast, again likely due to the increased porosity in the constructs. Thus, finding a balance between print resolution and porosity with a given GelMA type is necessary for cell survival. This again emphasizes the importance of reporting details of print parameters—support bath properties in parallel with bioink and scaffold properties.

4.1.3. hiPSC expansion can be quickly and non-invasively monitored via glucose consumption

When we investigated the impact of various GelMA types on hiPSC growth in bioprinted tissues, we found a strong correlation between hiPSC expansion and GelMA stiffness and DoF. We were able to easily monitor this growth with a handheld glucose meter. As cell growth can be variable (and exacerbated when switching between GelMA sources) and difficult to monitor via imaging in 3D culture (particularly with complex geometries), this tool allows us to quantify whether cells are expanding at an appropriate

rate in a given GelMA type or lot. This is important for knowing the adequate time to initiate differentiation, especially for protocols that require a certain cell density for efficient differentiation. Recently reported methods for assessing cell culture in 3D scaffolds, such as Raman spectroscopy[53] and optical coherence tomography,[54] can provide more information on cellular behavior, and will be interesting to study in future work. However, these methods are less accessible, quantitative, and require more extensive processing to obtain results. Thus, while glucose measurements are dependent on cellular metabolism, which can be variable between cell types and associated with varied cell behaviors of a single cell type, we found this method to be reliable for hiPSC expansion. We found a high correlation between glucose consumption at early time points (even at d7 of proliferation) and colony coverage at the end of the proliferation time. This result allows for early prediction of the resulting colony coverage at the end of the proliferation period (d14).

4.1.4. Substrate stiffness correlates with hiPSC expansion

We found that hiPSCs grew best in the C-lo inks, with good reproducibility between lots. However, much less expansion was seen in H-hi1 GelMA and in C-hi1 at concentrations of 5 or 10%. Thus, hiPSC growth may depend in part on DoF, with better expansion in GelMA with 50% DoF than with 95–99% DoF. Interestingly, there also appeared to be a correlation between initial G′ and final colony coverage. Few studies of 3D hiPSC culture have systematically examined the impact of substrate stiffness on hiPSC viability and expansion, despite the recent emphasis on the importance of 3D culture on biomimetic systems. Previous 2D studies seeding hPSCs on top of hydrogels have suggested an elastic modulus around 9–10 kPa was ideal for cell growth,[55,56] though in one of these studies, hPSCs had quickly detached from the surface of the softer substrates.[55] On the other hand, 3D studies have found high hPSC proliferation with storage modulus around 655–900 Pa.[44,57] These relatively soft hydrogels are beneficial in that they may allow for singularized hPSCs to proliferate and grow within the matrix and may elicit similar mechanosensitive pathways used by ROCK inhibitors, as suggested in one of these studies.[44] Here, we saw the highest expansion near a G′ of 400 ± 30 Pa, but as most hiPSCs did not survive on the highly functionalized C-hi1, which had a G′ in this range, further study is needed to evaluate the effects of other variables such as DoF, topography, or charge density[58] on hiPSC growth. Interestingly, prior work has shown substrate mechanics can affect hPSC colony morphology,[56,59,60] though the impact on single-cell viability has not been studied, and the effect of these changes in colony morphology on differentiation outcomes remains unclear.

During proliferation, we found a decrease in both G′ and G″ for the two C-lo inks. Matrix remodeling by stem cells has previously been shown to help maintain proliferative state, as well as pluripotency, via autocrine-induced JAK/Stat pathway.[61,62] Interestingly, we did not observe a large change in the high DoF inks, both of which had lower hiPSC expansion. DoF and concentration have previously been shown to be inversely correlated to degradability,[34,63] so the ability of hiPSCs to overturn the matrix in the lower DoF GelMA types and lower concentration of C-hi1 (5% relative to 10%) may have allowed for the improved expansion. This change in hydrogel mechanical properties is an important consideration for *in situ* expansion, as it may impact differentiation outcomes. Thus, identifying an optimal initial stiffness may be needed to achieve both high hiPSC expansion and high differentiation efficiency following matrix remodeling.

4.1.5. Cloning supplements can improve hiPSC expansion in constructs with mechanical properties suboptimal for hiPSC proliferation

We observed some variability in final colony coverage among constructs from the same GelMA type, even from within the same ink batch, with the same bioink and cell suspension mixtures. While some of these differences may be due to the printing process, hiPSCs can also be a source of variability, with spatial differences in cell growth and variable levels of cell death upon singularization. Moreover, from monitoring glucose consumption, we found hiPSCs in some GelMA types grew fast at the beginning before plateauing around d10, apparently caused by cell death or reduced proliferation from prolonged culture, whereas other GelMA types had slow initial growth, followed by more rapid expansion later. The GelMA types with faster initial proliferation had a higher colony coverage at the d14 endpoint than those that initially grew slower. This suggests a large impact of GelMA type on early hiPSC survival, likely exacerbated upon singularization of hiPSCs.

We therefore aimed to improve survival in the first days following printing with the use of dynamic culture or media supplementation. CloneR2 has previously been used to improve single-cell survivability in cloning and transfection applications[45–47] but has not been used for improving culture in bioprinting or culture of singularized hiPSCs in 3D scaffolds. With the use of this supplement, we found dramatic increases in glucose consumption and colony coverage in half the culture period for C-lo1 and achieved similar results with the less efficient construct, C-hi1 (5%). This demonstrates the potential

to improve the culture of hiPSCs on a desired scaffold type, regardless of whether it has optimal mechanical properties. The ability to recover hiPSC expansion in C-hi1 (5%) constructs by improving single-cell viability suggests that singularized hiPSCs are more sensitive than colonies to the scaffold properties. This is supported by the Y-27632-treated C-hi1 (5%) and H-hi1 samples that grew faster at later stages, only once colonies had begun to form. While it is well-known that singularized hiPSCs are prone to cell death, it is important to note that the impact of the scaffold on hiPSC culture appears to be an important driver in cell health as well. Perhaps with further development of methods to improve single-cell hiPSC viability, the impact of the scaffold on hiPSC culture will be less notable and variability will be further reduced. This will allow for greater options in scaffold mechanical properties that can be used for ISED applications.

4.2. Major limitations

In addition to the sources of variability described above, there are also many factors that create variability in the GelMA source, which are much harder for the user to control, and that exist concerning whether GelMA is made in-house or purchased commercially. These factors include the biophysical properties of the gelatin that affect macroscale properties,[64] batch-to-batch variabilities of the gelatin reactive groups available for functionalization,[65] and difficulties replicating the DoF. Moreover, the choice of gelatin source (animal source, type A vs type B, and bloom strength) used for producing GelMA can greatly impact scaffold properties.[40–43] Even quantification of DoF can give varying outputs depending on the assay used, which is problematic for studying the impact of DoF on cell viability. Regardless of method used for quantification (colorimetric, ^{1}H NMR, *etc.*), the choice of standard is crucial for accurate results, requiring the use of the original gelatin material to account for the inherent variability of gelatin.[65] This can make it difficult to compare products from various vendors, which either do not list the DoF or give a large range in their product details. Additionally, assays to detect functionalization with both methacrylate and methacrylamide groups are necessary for full characterization of the material.[63,66] Another limitation includes the shelf-life of GelMA, which is typically around 6–12 months for commercial products, making use of the same lot of GelMA for a given application difficult. Further, products are usually sold in discrete quantities, requiring solubilization of a large batch of ink at once, or aliquoting of the lyophilized product, which increases exposure risk to humidity and thereby impacts the shelf life.

Overall, these features emphasize the need for a consistent product, as well as more thorough characterization of GelMA scaffolds reported in the literature for improved reproducibility. Fortunately, some groups have reported improved methods for reducing batch-to-batch variability in GelMA production with the promise to overcome many of these limitations.[63,67] This is accomplished via a one-pot synthesis that raises the pH greatly above the isoelectric point of the gelatin for a complete reaction, with the addition of a buffer to maintain the pH throughout the reaction. This method has been demonstrated to lead to consistent DoF, as well as reproducible mechanical properties and cell viability, across 5 batches.[63]

Another relevant consideration on scaffold variability is current bioprinter technologies. Holding bioinks constant, a recent study examining the reproducibility of extrusion printing among 12 research groups demonstrated the immense variability that can occur due to user or bioprinter.[39] Researchers from each group were trained; labware, STL files, and bioink were identical; and analysis of resulting constructs was automated. Yet, inter- and intra-laboratory error in print fidelity existed, leaving room for future improvements in bioprinter development. For instance, use of flow meters on pneumatic printers may aid in controlling extrusion.[68]

In addition to the inherent limitations of GelMA and bioprinting, limitations remain in hiPSC culture as well. The results found here demonstrate that the effect of the scaffold on cell growth may be less pronounced with reduced death upon singularization. Thus, printing with colonies rather than singular hiPSCs may be beneficial. Generating consistent colony sizes would remain a challenge, although use of dextran sulfate has been shown to improve homogeneity of hPSC aggregate size,[69] and recent advances in bioreactor technology would allow for larger scale-up of these aggregates for printing.[70] For extrusion bioprinting, this would require a larger nozzle diameter, which will reduce print resolutions, and an increase in bioink viscosity to reduce colony dissociation.[11] Alternatively, printing could be performed via photolithography, though this is still an underdeveloped technology, with limitations including long printing times that may impact cell viability and challenges in multi-material printing.[71,72] However, as hiPSC applications develop, we will identify more methods of reducing variability in culture, both within a given cell line, and among different lines, especially key to effectively culturing patient-derived lines for translational applications.

5. Conclusion

In summary, our study evaluates several factors that can influence the growth of hiPSC in 3D environment, including scaffold mechanical properties, variability among GelMA samples, printing parameters, and the viability of singularized hiPSCs. We successfully employed a handheld glucose meter for rapid, quantitative, and non-invasive monitoring of cell growth. Our results indicate a strong dependence of hiPSC survival and expansion on the source of GelMA, with significant correlations to DoF and construct mechanical properties. Thus, we emphasize the importance of characterizing and reporting scaffold and printing parameters to enhance reproducibility across research groups. Importantly, we are able to recover some of the inhibitory effects of construct mechanical properties on hiPSC growth via the use of a cloning supplement that reduces the initial cell death of singularized cells. Overall, these insights are valuable for researchers developing hiPSC-laden 3D tissues for various *in situ* expansion and differentiation applications.

Acknowledgments

The authors thank the following University of Minnesota core facilities and their support staff involved in this research: University Imaging Centres, Polymer Characterization and Processing Facility, and Bioprinting Facility.

Funding

This work was supported by the EK, Grant 905669. National Institutes of Health, National Heart, Lung, and Blood Institute to BMO, R01 HL160779.

Conflict of interest

The authors declare they have no competing interests.

Author contributions

Conceptualization: Elizabeth R. Komosa, Brenda M. Ogle
Formal analysis: Elizabeth R. Komosa
Investigation: Elizabeth R. Komosa, Wei-Han Lin
Methodology: Elizabeth R. Komosa
Writing–original draft: Elizabeth R. Komosa
Writing–review & editing: All authors

Ethics approval and consent to participate

Not applicable.

Consent for publication

Not applicable.

Availability of data

All data that support the findings of this study are included within the article (and the supplementary files).

References

1. Ouyang L, Yao R, Zhao Y, Sun W. Effect of bioink properties on printability and cell viability for 3D bioplotting of embryonic stem cells. *Biofabrication*. 2016;8(3):035020. doi: 10.1088/1758-5090/8/3/035020
2. Faulkner-Jones A, Fyfe C, Cornelissen DJ, et al. Bioprinting of human pluripotent stem cells and their directed differentiation into hepatocyte-like cells for the generation of mini-livers in 3D. *Biofabrication*. 2015;7(4):044102. doi: 10.1088/1758-5090/7/4/044102
3. Ouyang L, Yao R, Mao S, Chen X, Na J, Sun W. Three-dimensional bioprinting of embryonic stem cells directs highly uniform embryoid body formation. *Biofabrication*. 2015;7(4):044101. doi: 10.1088/1758-5090/7/4/044101
4. Reid JA, Mollica PA, Johnson GD, Ogle RC, Bruno RD, Sachs PC. Accessible bioprinting: adaptation of a low-cost 3D-printer for precise cell placement and stem cell differentiation. *Biofabrication*. 2016;8(2):025017. doi: 10.1088/1758-5090/8/2/025017
5. Li Y, Jiang X, Li L, et al. 3D printing human induced pluripotent stem cells with novel hydroxypropyl chitin bioink: scalable expansion and uniform aggregation. *Biofabrication*. 2018;10(4):044101. doi: 10.1088/1758-5090/AACFC3
6. Komosa ER, Lin WH, Mahadik B, et al. A novel perfusion bioreactor promotes the expansion of pluripotent stem cells in a 3D-bioprinted tissue chamber. *Biofabrication*. 2024;16:014101. doi: 10.1088/1758-5090/ad084a
7. Gu Q, Tomaskovic-Crook E, Wallace GG, Crook JM. 3D bioprinting human induced pluripotent stem cell constructs for *in situ* cell proliferation and successive multilineage differentiation. *Adv Healthc Mater*. 2017;6(17): 1700175. doi: 10.1002/adhm.201700175
8. Nguyen D, Hagg DA, Forsman A, et al. Cartilage tissue engineering by the 3D bioprinting of iPS cells in a nanocellulose/alginate bioink. *Sci Rep*. 2017;7:658. doi: 10.1038/s41598-017-00690-y
9. Koch L, Deiwick A, Franke A, et al. Laser bioprinting of human induced pluripotent stem cells—the effect of printing and biomaterials on cell survival, pluripotency, and differentiation. *Biofabrication*. 2018;10(3):035005. doi: 10.1088/1758-5090/aab981
10. Kupfer ME, Lin WH, Ravikumar V, et al. *In situ* expansion, differentiation and electromechanical coupling of human

cardiac muscle in a 3D bioprinted, chambered organoid. *Circ Res*. 2020;127:207-224.
doi: 10.1161/circresaha.119.316155

11. Hamid OA, Eltaher HM, Sottile V, Yang J. 3D bioprinting of a stem cell-laden, multi-material tubular composite: an approach for spinal cord repair. *Mater Sci Eng C*. 2021;120:111707.
doi: 10.1016/J.MSEC.2020.111707

12. Lin WH, Zhu Z, Ravikumar V, et al. A bionic testbed for cardiac ablation tools. *Int J Mol Sci*. 2022;23(22):14444.
doi: 10.3390/ijms232214444

13. Gerecht S, Burdick JA, Ferreira LS, Townsend SA, Langer R, Vunjak-Novakovic G. Hyaluronic acid hydrogel for controlled self-renewal and differentiation of human embryonic stem cells. *Proc Natl Acad Sci USA*. 2007;104(27):11298-11303.
doi: 10.1073/pnas.0703723104

14. Kang H, Shih YRV, Hwang Y, et al. Mineralized gelatin methacrylate-based matrices induce osteogenic differentiation of human induced pluripotent stem cells. *Acta Biomater*. 2014;10(12):4961-4970.
doi: 10.1016/j.actbio.2014.08.010

15. Kerscher P, Turnbull IC, Hodge AJ, et al. Direct hydrogel encapsulation of pluripotent stem cells enables ontomimetic differentiation and growth of engineered human heart tissues. *Biomaterials*. 2016;83:383-395.
doi: 10.1016/J.BIOMATERIALS.2015.12.011

16. Kerscher P, Kaczmarek JA, Head SE, et al. Direct production of human cardiac tissues by pluripotent stem cell encapsulation in gelatin methacryloyl. *ACS Biomater Sci Eng*. 2017;3(8):1499-1509.
doi: 10.1021/acsbiomaterials.6b00226

17. Gilmozzi V, Gentile G, Riekschnitz DA, et al. Generation of hiPSC-derived functional dopaminergic neurons in alginate-based 3D culture. *Front Cell Dev Biol*. 2021;9:708389.
doi: 10.3389/FCELL.2021.708389

18. Rajabi N, Rezaei A, Kharaziha M, et al. Recent advances on bioprinted gelatin methacrylate-based hydrogels for tissue repair. *Tissue Eng Part A*. 2021;27(11-12):679-702.
doi: 10.1089/ten.TEA.2020.0350

19. Peyret C, Elkhoury K, Bouguet-Bonnet S, et al. Gelatin methacryloyl (GelMA) hydrogel scaffolds: Predicting physical properties using an experimental design approach. *Int J Mol Sci*. 2023;24(17):13359.
doi: 10.3390/ijms241713359

20. Ohgushi M, Matsumura M, Eiraku M, et al. Molecular pathway and cell state responsible for dissociation-induced apoptosis in human pluripotent stem cells. *Cell Stem Cell*. 2010;7(2):225-239.
doi: 10.1016/j.stem.2010.06.018

21. Chen G, Hou Z, Gulbranson DR, Thomson JA. Actin-myosin contractility is responsible for the reduced viability of dissociated human embryonic stem cells. *Cell Stem Cell*. 2010;7(2):240-248.
doi: 10.1016/j.stem.2010.06.017

22. Watanabe K, Ueno M, Kamiya D, et al. A ROCK inhibitor permits survival of dissociated human embryonic stem cells. *Nat Biotechnol*. 2007;25(6):681-686.
doi: 10.1038/nbt1310

23. Higuchi A, Ling Q-D, Kumar SS, et al. Physical cues of cell culture materials lead the direction of differentiation lineages of pluripotent stem cells. *J Mater Chem B*. 2015;3:8032-8058.
doi: 10.1039/C5TB01276G

24. Kaitsuka T, Hakim F. Response of pluripotent stem cells to environmental stress and its application for directed differentiation. *Biology (Basel)*. 2021;10(2):84.
doi: 10.3390/biology10020084

25. Labouesse C, Tan BX, Agley CC, et al. StemBond hydrogels control the mechanical microenvironment for pluripotent stem cells. *Nat Commun*. 2021;12:6132.
doi: 10.1038/s41467-021-26236-5

26. Smith Q, Chan XY, Carmo AM, Trempel M, Saunders M, Gerecht S. Compliant substratum guides endothelial commitment from human pluripotent stem cells. *Sci Adv*. 2017;3(5):e1602883.
doi: 10.1126/sciadv.1602883

27. Lee A, Hudson AR, Shiwarski DJ, et al. 3D bioprinting of collagen to rebuild components of the human heart. *Science*. 2019;365:482-487.
doi: 10.1126/science.aav9051

28. Zhu W, Zhao M, Mattapally S, Chen S, Zhang J. CCND2 overexpression enhances the regenerative potency of human induced pluripotent stem cell-derived cardiomyocytes: Remuscularization of injured ventricle. *Circ Res*. 2018;122(1):88-96.
doi: 10.1161/CIRCRESAHA.117.311504

29. Lian X, Hsiao C, Wilson G, et al. Robust cardiomyocyte differentiation from human pluripotent stem cells via temporal modulation of canonical Wnt signaling. *Proc Natl Acad Sci USA*. 2012;109(27):E1848-E1857.
doi: 10.1073/pnas.1200250109

30. Caliari SR, Burdick JA. A practical guide to hydrogels for cell culture. *Nat Methods*. 2016;13(5):405-414.
doi: 10.1038/nmeth.3839

31. Nichol JW, Koshy S, Bae H, Hwang CM, Yamanlar S, Khademhosseini A. Cell-laden microengineered gelatin methacrylate hydrogels. *Biomaterials*. 2010;31(21):5536-5544.
doi: 10.1016/j.biomaterials.2010.03.064

32. Xin Z, Lang Q, Yildirimer L, et al. Photocrosslinkable gelatin hydrogel for epidermal tissue engineering. Adv Healthc Mater. 2016;5(1):108-118.
doi: 10.1002/adhm.201500005

33. Yin H, Zhu M, Wang Y, Luo L, Ye Q, Lee BH. Physical properties and cellular responses of gelatin methacryloyl bulk hydrogels and highly ordered porous hydrogels. *Front Soft Matter*. 2022;2:1101680.
doi: 10.3389/frsfm.2022.1101680

34. Shie MY, Lee JJ, Ho CC, Yen SY, Ng HY, Chen YW. Effects of gelatin methacrylate bio-ink concentration on mechano-physical properties and human dermal fibroblast behavior. *Polymers (Basel)*. 2020;12(9):1930. doi: 10.3390/polym12091930

35. Vigata M, Meinert C, Bock N, Dargaville BL, Hutmacher DW. Deciphering the molecular mechanism of water interaction with gelatin methacryloyl hydrogels: role of ionic strength, pH, drug loading, and hydrogel network characteristics. *Biomedicines*. 2021;9(5):574. doi: 10.3390/biomedicines9050574

36. Hinton TJ, Jallerat Q, Palchesko RN, et al. Three-dimensional printing of complex biological structures by freeform reversible embedding of suspended hydrogels. *Sci Adv*. 2015;1(9):e1500758. doi: 10.1126/sciadv.1500758

37. Kesti M, Fisch P, Pensalfini M, Mazza E, Zenobi-Wang M. Guidelines for standardization of bioprinting: a systematic study of process parameters and their effect on bioprinted structures. *BioNanoMaterials*. 2016;17(3-4):193-204. doi: 10.1515/bnm-2016-0004

38. Strauß S, Schroth B, Hubbuch J. Evaluation of the reproducibility and robustness of extrusion-based bioprinting processes applying a flow sensor. *Front Bioeng Biotechnol*. 2022;10:831350. doi: 10.3389/fbioe.2022.831350

39. Grijalva Garces D, Strauß S, Gretzinger S, et al. On the reproducibility of extrusion-based bioprinting: round robin study on standardization in the field. *Biofabrication*. 2024;16: 015002. doi: 10.1088/1758-5090/acfe3b

40. Young AT, White OC, Daniele MA. Rheological properties of coordinated physical gelation and chemical crosslinking in gelatin methacryloyl (GelMA) hydrogels. *Macromol Biosci*. 2020;20(12):e2000183. doi: 10.1002/mabi.202000183

41. Sewald L, Claaben C, Gotz T, et al. Beyond the modification degree: impact of raw material on physicochemical properties of gelatin type A and type B methacryloyls. *Macromol Biosci*. 2018;18(12):e1800168. doi: 10.1002/mabi.201800168

42. Lee BH, Lum N, Seow LY, Lim PQ, Tan LP. Synthesis and characterization of types A and B gelatin methacryloyl for bioink applications. *Materials (Basel)*. 2016;9(10):797. doi: 10.3390/ma9100797

43. Zambuto SG, Kolluru SS, Ferchichi E, et al. Evaluation of gelatin bloom strength on gelatin methacryloyl hydrogel properties. *J Mech Behav Biomed Mater.* 2024;154:106509. doi: 10.1101/2023.11.13.566924

44. Lei Y, Schaffer DV. A fully defined and scalable 3D culture system for human pluripotent stem cell expansion and differentiation. *PNAS*. 2013;110(52):E5039-E5048. doi: 10.1073/pnas.1309408110

45. Ren X, Asami Takagi M, Shen Y. Efficient bi-allelic tagging in human induced pluripotent stem cells using CRISPR. *STAR Protoc*. 2023;4(1):102084. doi: 10.1016/j.xpro.2023.102084

46. Ludwik KA, Telugu N, Schommer S, Stachelscheid H, Diecke S. ASSURED-optimized CRISPR protocol for knockout/ SNP knockin in hiPSCs. *STAR Protoc*. 2023;4(3):102406. doi: 10.1016/j.xpro.2023.102406

47. Mojica-Perez SP, Stokes K, Jaklic DC, et al. Protocol for selecting single human pluripotent stem cells using a modified micropipetter. *STAR Protoc*. 2023;4(4):102629. doi: 10.1016/j.xpro.2023.102629

48. Bauwens CL, Peerani R, Niebruegge S, et al. Control of human embryonic stem cell colony and aggregate size heterogeneity influences differentiation trajectories. *Stem Cells*. 2009;26(9):2300-2310. doi: 10.1634/stemcells.2008-0183

49. Mohr JC, Zhang J, Azarin SM, et al. The microwell control of embryoid body size in order to regulate cardiac differentiation of human embryonic stem cells. *Biomaterials*. 2010;31(7):1885-1893. doi: 10.1016/j.biomaterials.2009.11.033

50. Rosowski KA, Mertz AF, Norcross S, Dufresne ER, Horsley V. Edges of human embryonic stem cell colonies display distinct mechanical properties and differentiation potential. *Sci Rep*. 2015;5:14218. doi: 10.1038/srep14218

51. He J, Sun Y, Gao Q, et al. Gelatin methacryloyl hydrogel, from standardization, performance, to biomedical application. *Adv Healthc Mater*. 2023;12(23):e2300395. doi: 10.1002/adhm.202300395

52. Tarassoli SP, Jessop ZM, Jovic T, Hawkins K, Whitaker IS. Candidate bioinks for extrusion 3D bioprinting – a systematic review of the literature. *Front Bioeng Biotechnol*. 2021;9:616753. doi: 10.3389/fbioe.2021.616753

53. Marzi J, Fuhrmann E, Brauchle E, et al. Non-invasive three-dimensional cell analysis in bioinks by Raman imaging. *ACS Appl Mater Interfaces*. 2022;14(27): 30455-30465. doi: 10.1021/acsami.1c24463

54. Babakhanova G, Agrawal A, Arora D, et al. Three-dimensional, label-free cell viability measurements in tissue engineering scaffolds using optical coherence tomography. *J Biomed Mater Res Part A*. 2023;111(8):1279-1291. doi: 10.1002/jbm.a.37528

55. Musah S, Morin SA, Wrighton PJ, Zwick DB, Jin S, Kiessling LL. Glycosaminoglycan-binding hydrogels enable mechanical control of human pluripotent stem cell self-renewal. *ACS Nano*. 2012;6(11):10168-10177. doi: 10.1021/nn3039148

56. Wang B, Tu X, Wei J, Wang L, Chen Y. Substrate elasticity dependent colony formation and cardiac differentiation

of human induced pluripotent stem cells. *Biofabrication*. 2018;11(1):015005.
doi: 10.1088/1758-5090/aae0a5

57. Liang Z, Liu C, Li L, et al. Double-network hydrogel with tunable mechanical performance and biocompatibility for the fabrication of stem cells-encapsulated fibers and 3D assemble. *Sci Rep*. 2016;6:33462.
doi: 10.1038/srep33462

58. Chen YM, Ogawa R, Kakugo A, Osada Y, Gong JP. Dynamic cell behavior on synthetic hydrogels with different charge densities. *Soft Matter*. 2009;5:1804-1811.
doi: 10.1039/B818586G

59. Keung AJ, Asuri P, Kumar S, Schaffer DV. Soft microenvironments promote the early neurogenic differentiation but not self-renewal of human pluripotent stem cells. *Integr Biol*. 2012;4(9):1049-1058.
doi: 10.1039/c2ib20083j

60. Arkenberg MR, Koehler K, Lin CC. Heparinized gelatin-based hydrogels for differentiation of induced pluripotent stem cells. *Biomacromolecules*. 2022;23(10):4141-4152.
doi: 10.1021/acs.biomac.2c00585

61. Przybyla LM, Voldman J. Attenuation of extrinsic signaling reveals the importance of matrix remodeling on maintenance of embryonic stem cell self-renewal. *PNAS*. 2012;109(3):835-840.
doi: 10.1073/pnas.1103100109

62. Przybyla LM, Theunissen TW, Jaenisch R, Voldman J. Matrix remodeling maintains embryonic stem cell self-renewal by activating Stat3. *Stem Cells*. 2013;31(6):1097-1106.
doi: 10.1002/stem.1360

63. Zhu M, Wang Y, Ferracci G, Zheng J, Cho NJ, Lee BH. Gelatin methacryloyl and its hydrogels with an exceptional degree of controllability and batch-to-batch consistency. *Sci Rep*. 2019;9(1):6863.
doi: 10.1038/s41598-019-42186-x

64. Richbourg NR, Wancura M, Gilchrist AE, et al. Precise control of synthetic hydrogel network structure via linear, independent synthesis-swelling relationships. *Sci Adv*. 2021;7(7):eabe3245.
doi: 10.1126/sciadv.abe3245

65. Zatorski JM, Montalbine AN, Ortiz-Cardenas JE, Pompano RR. Quantification of fractional and absolute functionalization of gelatin hydrogels by optimized ninhydrin assay and 1H NMR. *Anal Bioanal Chem*. 2020;412:6211-6220.
doi: 10.1007/s00216-020-02792-5

66. Yue K, Li X, Schrobback K, et al. Structural analysis of photocrosslinkable methacryloyl-modified protein derivatives. *Biomaterials*. 2017;139:163-171.
doi: 10.1016/j.biomaterials.2017.04.050

67. Shirahama H, Lee BH, Tan LP, Cho NJ. Precise tuning of facile one-pot gelatin methacryloyl (GelMA) synthesis. *Sci Rep*. 2016;6:31036.
doi: 10.1038/srep31036

68. Wenger L, Strauß S, Hubbuch J. Automated and dynamic extrusion pressure adjustment based on real-time flow rate measurements for precise ink dispensing in 3D bioprinting. *Bioprinting*. 2022;28:e00229
doi: 10.1016/j.bprint.2022.e00229

69. Lipsitz YY, Tonge PD, Zandstra PW. Chemically controlled aggregation of pluripotent stem cells. *Biotechnol Bioeng*. 2018;115(8):2061-2066.
doi: 10.1002/bit.26719

70. Nogueira DES, Rodrigues CAV, Carvalho MS, et al. Strategies for the expansion of human induced pluripotent stem cells as aggregates in single-use Vertical-Wheel™ bioreactors. *J Biol Eng*. 2019;13(1):74.
doi: 10.1186/s13036-019-0204-1

71. Zandrini T, Florczak S, Levato R, Ovsianikov A. Breaking the resolution limits of 3D bioprinting: future opportunities and present challenges. *Trends Biotechnol*. 2023;41(5):604-614.
doi: 10.1016/j.tibtech.2022.10.009

72. Elkhoury K, Zuazola J, Vijayavenkataraman S. Bioprinting the future using light: a review on photocrosslinking reactions, photoreactive groups, and photoinitiators. *SLAS Technol*. 2023;28(3):142-151.
doi: 10.1016/j.slast.2023.02.003

ACCSCIENCE PUBLISHING

International Journal of Bioprinting

RESEARCH ARTICLE

A 3D-bioprinted neuroinflammatory co-culture model for *in vitro* study of Parkinson's disease pathology

Hongliang Mao[1], Liangchen Yu[1], Yang Qiao[1], Menghui Liu[1], Xingliang Dai[1,2]*, and Hongwei Cheng[1]*

[1]Department of Neurosurgery, the First Affiliated Hospital of Anhui Medical University, Hefei, Anhui, China

[2]Department of Research and Development, East China Institute of Digital Medical Engineering, Shangrao, Jiangxi, China

Abstract

Parkinson's disease (PD), a common neurodegenerative disorder, is characterized by dopaminergic (DA) neuron apoptosis, mitochondrial dysfunction, and aggregation of α-synuclein (α-syn). In this study, we developed a three-dimensional (3D)-bioprinted neuroinflammatory co-culture model to simulate key pathological features of PD *in vitro*. Traditional 2D cell culture models fail to accurately replicate the complex microenvironment of PD, leading to the development of the 3D-bioprinted model. Utilizing a polyethylene glycol-hyaluronic acid methacryloyl hydrogel matrix, this model supports the co-culture of DA neurons and microglia, enabling a more accurate representation of PD pathology. Experimental results demonstrated that, under 6-hydroxydopamine induction, the 3D model successfully mimicked neuroinflammatory responses associated with PD, including M1 polarization of microglia and increased secretion of pro-inflammatory factors. Compared to traditional 2D models, DA neurons in the 3D model exhibited greater resistance to oxidative stress and neurotoxic challenges, with significantly slower rates of apoptosis. Additionally, the 3D model displayed key PD-specific pathological features, such as altered mitochondrial membrane potential, elevated reactive oxygen species levels, and overexpression of α-syn. This 3D-bioprinted PD model provides a closer-to-physiological platform for investigating the pathogenesis of PD and holds potential for use in drug screening. However, further optimization is required to enhance the model's complexity and long-term stability, including incorporating peripheral immune cells to better simulate the progression of chronic neuroinflammation.

***Keywords*:** 3D bioprinting; α-Synuclein aggregation; Dopaminergic neurons; Neuroinflammation; Parkinson's disease;

***Corresponding authors:**
Hongwei Cheng
(hongwei.cheng@ahmu.edu.cn)

Xingliang Dai
(daixingliang@ahmu.edu.cn)

Citation: Mao H, Yu L, Qiao Y, Liu M, Dai X, Cheng H. A 3D-bioprinted neuroinflammatory co-culture model for *in vitro* study of Parkinson's disease pathology. *Int J Bioprint*. 2025;11(1):382-399. doi: 10.36922/ijb.5717

Received: October 29, 2024
1st revised: December 2, 2024
2nd revised: December 16, 2024
Accepted: December 16, 2024
Published Online: December 16, 2024

Copyright: © 2024 Author(s). This is an Open Access article distributed under the terms of the Creative Commons Attribution License, permitting distribution, and reproduction in any medium, provided the original work is properly cited.

Publisher's Note: AccScience Publishing remains neutral with regard to jurisdictional claims in published maps and institutional affiliations.

1. Introduction

Parkinson's disease (PD) ranks as the second most common neurological disorder among middle-aged and elderly populations, primarily characterized by clinical symptoms, such as resting tremor, bradykinesia, rigidity, and impaired postural reflexes.[1,2] By the end of 2022, the annual incidence of PD in North America reached approximately 90,000 new

cases, marking a 50% increase from previous figures. As the population continues to age, projections indicate that the global PD patient count may rise to 12.9 million by 2040. In China, the prevalence of PD among individuals aged 65 and older stands at approximately 2.06%.[1] With the ongoing aging of the population in China, it is foreseeable that the prevalence of PD will continue to rise, placing a substantial burden on both society and affected families. Research has demonstrated that the pathology of PD is characterized by the apoptosis of dopaminergic (DA) neurons within the striatum and substantia nigra pars compacta (SNc) in the midbrain. Additionally, abnormal aggregation of α-synuclein (α-syn) occurs in the cytoplasm of neurons in the SNc, leading to the formation of Lewy bodies, a hallmark of the disease.[3] α-syn aggregation is a critical pathological hallmark of PD. Its accumulation is observed not only within neuritic projections, where it disrupts synaptic function but also within the cytoplasm, where it interferes with multiple intracellular pathways.[4] This interference results in nuclear and mitochondrial dysfunction, disruptions in intracellular trafficking, and blockage of the autophagy-lysosomal pathway. Collectively, these disruptions promote significant oxidative damage, which can ultimately lead to neuronal death.[5,6] A substantial body of evidence suggests that, in certain cases, α-syn-related pathology may represent an epiphenomenon, lacking a direct causal link to neuronal dysfunction and death.[7]

Current research indicates that neuroinflammation may serve as the initiating factor for the pathological features observed in PD patients.[8] Numerous PD animal studies have confirmed the presence of activated microglia in the SNc.[9,10] Microglia have been demonstrated to exhibit different phenotypes, such as M1 or M2, depending on specific stimulation patterns.[11] The neurotoxin 6-hydroxydopamine (6-OHDA), highly specific to catecholaminergic neurons and the dopamine transporter (DAT) in the brain, induces widespread and irreversible loss of midbrain DA neurons and is commonly used to create *in vitro* PD models.[9,10,12] Research demonstrates that 6-OHDA induces the M1 phenotype in microglia, promoting the expression of pro-inflammatory factors, such as TNF-α, IL-1β, and IL-6.[10,13,14] The accumulation of these cytokines ultimately damages adjacent DA neurons.[15] *In vitro* models reveal that 6-OHDA not only directly injures DA neurons but also prompts dying or dead neurons to release neurotoxic soluble factors, including α-syn and damage-associated molecular patterns (DAMPs). These factors perpetuate reactive microglial activation and proliferation, fueling neuroinflammatory cascades characteristic of neurodegenerative disease.[16,17] Activated microglia release pro-inflammatory factors that exacerbate damage to DA neurons, establishing a cycle of progressive neuron damage and death. Notably, most *in vitro* studies focus on 2D monolayer cultures of DA neurons under non-physiological adhesion conditions, often overlooking critical microenvironmental factors that influence disease progression. Thus, there is an urgent need to develop reliable *in vitro* models to study PD pathophysiology at the molecular level and enable high-throughput screening of PD-related pathogenic genes.

Advances in 3D cell culture technologies, particularly 3D bioprinting, have enabled the precise printing of multiple cell types within a 3D environment. This technology allows for the creation of complex, scaled, living tissues, and biomimetic structures of various animal and human models, significantly advancing biomedical research.[18,19,20] Such developments open new scientific possibilities for accurately investigating the microenvironmental interactions between DA neurons and microglia *in vitro*. In recent years, efforts to construct *in vitro* 3D models for neurodegenerative diseases, including Alzheimer's disease (AD) and PD, have steadily increased. Zhang et al.[21] proposed a 3D coaxial bioprinting approach to develop an *in vitro* AD model using human neural stem cells (NSCs). In this model, the printed core comprised NSCs with familial AD mutations, while the surrounding shell was composed of alginate. These structures allowed NSCs to self-assemble and self-aggregate, forming complex neural architectures beyond the limitations of conventional solid hydrogel matrices. The bioprinted AD model demonstrated amyloid-beta (Aβ) aggregation and elevated gene expression levels of Aβ and tau, surpassing those observed in 2D and traditional 3D control models. This innovative model offers a powerful tool for advancing neurodegeneration research within 3D *in vitro* AD models. Serna et al.[22] utilized a specific ratio of 2D-cultured human astrocytes and differentiated monocytes co-cultured with DA neurons to simulate neuroinflammatory responses, aiming to more accurately represent the neuroimmune microenvironment of PD *in vitro*. However, the study presents several limitations. Firstly, inflammation-related cells were cultured in a traditional 2D environment without constructing a 3D cell core. Secondly, microglia, essential participants in inflammatory processes, were absent—a limitation the authors themselves acknowledged as an area needing special attention. Midbrain organoid models offer particular promise for PD research, as they enable the simultaneous study of multicellular responses to PD-relevant stimuli within a tissue-mimetic structure.[23] Nevertheless, organoid models are costly, labor-intensive, time-consuming, and challenging to control precisely.[24]

To construct an *in vitro* 3D bioprinting model that replicates the microenvironment of DA neurons and

microglia, we employed 3D bioprinting technology using a polyethylene glycol-hyaluronic acid methacryloyl (PEG-HAMA) hydrogel system to simulate the extracellular matrix (ECM) components of DA neurons and microglia. Specifically, we utilized the mouse DA neuron line MN9D and the microglial cell line BV2, differentiating MN9D cells with n-butyrate, and co-culturing MN9D cores with BV2 cores. Additionally, 6-OHDA was applied to induce neuroinflammatory responses within the co-cultured immune cells, modeling pathologies associated with PD. This approach enabled a more precise investigation of the PD inflammatory environment *in vitro*. Utilizing animal cells in bioprinting provides a foundational step toward constructing human-based organ models, advancing the potential for reliable PD research in a controlled laboratory setting.

2. Materials and methods

2.1. Cell culture

The immortalized mouse midbrain-derived DA neuron cell line MN9D and microglial cell line BV2 were obtained from the Cell Bank of the Chinese Academy of Sciences (China). Cells were cultured in high-glucose Dulbecco's Modified Eagle Medium (DMEM) Complete Medium, supplemented with 10% fetal bovine serum, 1% GlutaMax, and 1% penicillin-streptomycin (Gibco, Life Technologies, United States of America [USA]) at 37 °C in a humidified atmosphere of 5% CO_2. The culture medium was refreshed every other day.

Differentiation of the MN9D cell line was conducted following the protocol established by Rick et al.[25] MN9D cells were seeded into Transwell inserts (Millipore), equivalent to 6-well plates, at a seeding density of 3×10^5 cells per well to adhere for 24 h. One day after plating, the medium was replaced with the complete medium plus 1 mM n-butyrate for 7 days. The medium was changed every 2–3 days throughout the experiment. Differentiation and maturation markers were assessed on Day 7. BV2 cells were seeded at 2×10^5 cells/well in 6-well plates and allowed to adhere for 24 h. To simulate the activated state of microglia in PD *in vivo*, mixed cultures of MN9D cells and BV2 cells were then treated with 50 μM 6-OHDA for 24 h. After stimulation, BV2 and MN9D cells and culture medium were collected for further analysis.

2.2. Material preparation and 3D bioprinting

Hyaluronic acid methacryloyl (HAMA), the photoinitiator lithium phenyl-2,4,6-trimethylbenzoylphosphonate (LAP), and PEG were purchased from EFL-Tech (China). LAP was dissolved in phosphate-buffered saline (PBS) at 37 °C to a final concentration of 0.25% (w/v). Once LAP was fully dissolved, HAMA was added and dissolved completely at 37 °C. PEG was then introduced to the HAMA/LAP solution to achieve the final concentrations outlined in Table 1. While the solution was still warm, it was transferred to a 15 mL centrifuge tube and mixed thoroughly. The mixture was then centrifuged at 1000 rpm for 3 min to remove any bubbles. To prevent light-induced crosslinking, the tube was wrapped in aluminum foil. The pre-gel solution was combined with centrifuged cells at a concentration of 1×10^7 cells/mL to prepare the bioink. The bioink was then injected into a custom mold, and printing parameters were adjusted. The temperature of both the printing platform and the reservoir was maintained at 37 °C. Crosslinking of the hydrogels was achieved by ultraviolet (UV) irradiation at a wavelength of 365 nm for 5 min (BP8601P; EFL-Tech, China).

2.3. Swelling rate

Immediately after printing and crosslinking, the 3D constructs were weighed and then incubated in DMEM at 37 °C with 5% CO_2. At different time points (0, 1, 2, 3, 4, 5, 6, and 7 days), the constructs were weighed again, with three constructs measured at each time point.

$$\text{Swelling rate} = (S_x - S_0)/S_0 \quad \text{(I)}$$

2.4. Rheological and mechanical characterization

Rheological testing was performed to evaluate the viscosity of the hydrogel formulations. The measurements were conducted using a rotational rheometer (MCR 302; Anton Paar, Austria) equipped with a parallel plate geometry (25 mm diameter; 1 mm gap). Hydrogel samples were prepared by mixing PEG and HAMA solutions with the photoinitiator, followed by centrifugation to remove air bubbles. Viscosity measurements were conducted at a constant shear rate of 10 s^{-1} across a temperature range of 10–40 °C to determine temperature-dependent viscosity profiles. Additionally, time-dependent viscosity changes were assessed at a constant temperature of 37 °C to simulate physiological conditions.

Table 1. Hydrogel formulation

Name	Concentration (%)	
	PEG	HAMA
P0H2	0	2
P1H2	1	2
P3H2	3	2
P5H2	5	2
P7H2	7	2
P10H2	10	2

Abbreviations: HAMA, hyaluronic acid methacryloyl; PEG, polyethylene glycol.

Mechanical testing was performed to evaluate the compressive modulus of the hydrogel scaffolds. Cylindrical hydrogel samples (10 mm diameter; 2 mm height) were prepared by crosslinking under UV irradiation (365 nm; 5 min) and subsequently hydrated in DMEM at 37 °C for 24 h. Compression tests were conducted using a universal testing machine (Instron 5944; Instron Corporation, USA) equipped with a 50 N load cell at a constant speed of 1 mm/min at room temperature. The compressive modulus was calculated from the linear region of the stress–strain curve (strain ≤ 10%) to assess the elasticity of the hydrogels. Comparisons were made between different hydrogel formulations to analyze the impact of PEG concentration on mechanical performance. All measurements were performed in triplicate.

2.5. Live/dead staining

Cell viability was assessed using a live/dead assay kit (Beyotime Biotech, China) following the manufacturer's protocol. In brief, 5 μL of propidium iodide (PI) and 5 μL of calcein-AM were added to 5 mL of assay buffer. The bioprinted constructs were incubated in this staining solution at room temperature for 30 min in the dark. Following gentle washing with 0.9% NaCl solution, live and dead cells were visualized using a fluorescence microscope (Eclipse Ti2; Nikon, Japan). The number of live cells (green) and dead cells (red) was counted in at least five random fields at 100× magnification, and cell viability (%) was calculated accordingly.

2.6. Alamar Blue assay

The tested cells and bioprinted structures were incubated in 96-well culture plates and treated with the complete medium containing 10 μL of Alamar Blue dye per well (Yeasen, Shanghai, China). After 4 h of incubation at 37 °C in the dark, fluorescence was measured using a fluorescence microplate reader (Thermo Fisher Scientific, Massachusetts, USA) at an excitation wavelength of 545 nm and an emission wavelength of 590 nm. The cell proliferation rate (%) was calculated as the ratio of fluorescence in each well relative to a control well without cells.

2.7. Scanning electron microscopy analysis

Surface observation of the shell and core structures was conducted using scanning electron microscopy (SEM). After 10 days of culture, the bioprinted constructs were washed with PBS, fixed in 2.5% glutaraldehyde for 1 h at room temperature, and then dehydrated through a graded ethanol series (70%, 80%, 90%, 95%, and 100%), with each step lasting 20 min. The samples were then frozen at –80 °C overnight and subsequently freeze-dried using a freeze dryer. Finally, they were observed and imaged using a ULTRA 55 scanning electron microscope (ZEISS, Germany).

2.8. Immunofluorescence analysis

To identify cellular biomarkers within the 3D structures, immunofluorescence analysis was conducted. The intact 3D-bioprinted structures were collected and fixed in 4% formaldehyde for 24 h. After dehydration, the samples were embedded in paraffin and sectioned into 5-micron slices. The sections were dewaxed and subjected to hematoxylin and eosin (H&E) staining according to standard protocols. Differentiation was performed using 1% acid-alcohol (1% HCl–70% ethanol) for a few seconds until the background became lighter, followed by washing in running water to achieve blue coloration. The sections were then immersed in eosin solution for 1 min. After dehydration and mounting, the sections were observed under a microscope. For immunofluorescence, sections were dewaxed, subjected to antigen retrieval, and incubated with primary antibodies overnight. The following day, sections were incubated with secondary antibodies for 1 h. Finally, the slides were mounted with a DAPI-containing mounting medium, and all immunofluorescent sections were imaged using a fluorescence microscope system (Eclipse Ti2; Nikon, Japan).

2.9. TUNEL staining

To assess apoptosis in MN9D cells, TUNEL staining was conducted using an *in situ* cell death detection kit (Beyotime, China) in accordance with the manufacturer's instructions. Briefly, cells were fixed in 4% paraformaldehyde (PFA), permeabilized with 0.5% Triton X-100, and incubated with a mixture of enzyme solution (TdT) and fluorescent labeling solution (1:9) at 37 °C for 1 h. Following this, cells were washed three times with PBS and stained with DAPI (Beyotime, China) for nuclear visualization. After immunostaining, cells were observed and analyzed under a fluorescence microscope (Eclipse Ti2; Nikon, Japan). For each section, at least five areas were analyzed. Apoptosis was quantified by calculating the ratio of TUNEL-positive cells to DAPI-positive cells in each field of view.

2.10. RNA isolation and quantitative reverse transcription polymerase chain reaction analysis

Total RNA was extracted using TRIzol, and RNA quantity and purity were assessed with a NanoDrop spectrophotometer (Thermo Scientific, Massachusetts, USA). RNA was then reverse-transcribed into complementary DNA (cDNA) following the protocol provided with the reverse transcription kit (Beyotime, China). For quantitative reverse transcription polymerase

chain reaction (qRT-PCR), amplification was carried out using SYBR Green qPCR SuperMix (C11733046; Invitrogen, USA) on an ABI PRISM® 7500 Sequence Detection System (Thermo Scientific, Massachusetts, USA) with the following program: 95 °C for 2 min; 95 °C for 15 s; 60 °C for 30 s; plate reading, 40 cycles. Each sample was analyzed in triplicate. Relative gene expression levels were calculated using the $2^{-\Delta\Delta Ct}$ method. The same procedure was applied to the 2D control group.

2.11. Western blotting

MN9D and BV2 cells were collected from both 2D and 3D culture conditions; cells were lysed using the Beyotime cell lysis kit (China), and protein concentration was quantified with the bicinchoninic acid (BCA) protein assay kit (Beyotime, China). Following concentration adjustment, 1/4 volume of 5× Loading Buffer (Beyotime, China) was added to each sample, and the mixtures were boiled in a 95°C water bath for 10 min. Protein concentrations were labeled on each tube, and samples were stored at –80 °C. After electrophoresis, proteins were transferred to polyvinylidene fluoride (PVDF) membranes (Merck KGaA, Germany), blocked with 5% skim milk for 1 h (Beyotime, China), and incubated with the appropriate primary and secondary antibodies (Proteintech, China). Thereafter, developing solutions A and B were mixed in a 1:1 ratio (Tanon™ High-sig ECL Western Blotting Substrate; Tanon Science & Technology, China), applied evenly to the strip, and then placed in the chemiluminescence imaging system for imaging (Tanon 5200; Tanon Science & Technology, China).

2.12. Intracellular reactive oxygen species (ROS) measurement

The DCFH-DA Cellular ROS Detection Kit (KeyGEN BioTECH, China) was used to quantify intracellular ROS levels in DA neurons within the evaluated PD models. For cells cultured under 2D conditions, the culture medium was discarded, added with 2 mL of trypsin (KeyGEN BioTECH, China), and incubated at 37 °C for 2 min. The cell suspension was transferred to a centrifuge tube, centrifuged at low speed for 3 min, and the supernatant was removed. For cells cultured under 3D conditions, the 3D constructs were thoroughly dissociated, transferred to a centrifuge tube, centrifuged at low speed for 3 min, and the supernatant was removed. The cells were then resuspended in 1 mL of DCFH-DA diluted in serum-free medium at a 1:1000 ratio and incubated at 37 °C for 20 min. The DCFH-DA solution was then removed by centrifugation at 1000 rpm for 3 min, and cells were washed three times with serum-free medium to eliminate any residual, non-internalized DCFH-DA. The ROS levels were measured using a fluorescence spectrophotometer.

2.13. Mitochondrial membrane potential measurement

JC-1 staining was employed to evaluate mitochondrial membrane potential. MN9D cells from 2D and 3D culture conditions were incubated with the JC-1 mitochondrial fluorescent probe (KeyGEN BioTECH, China). Specifically, the culture medium was discarded, and the cells were washed once with PBS. Thereafter, 1 mL of JC-1 working solution was added, ensuring the cells were evenly covered and incubated at 37 °C in a 5% CO_2 incubator for 20 min. After incubation, the supernatant was removed, and the cells were washed twice with 1× Incubation Buffer (KeyGEN BioTECH, China). Finally, 1 mL of cell culture medium was added for observation and analysis via a fluorescence microscope system (Eclipse Ti2; Nikon, Japan).

2.14. Statistical analysis

Data were analyzed using GraphPad PRISM 10.0 (GraphPad Software, USA) and presented as mean ± standard deviation. Differences between the two groups were assessed using Student's *t*-test, with statistical significance defined as two-tailed $p < 0.05$ ($^{*}p < 0.05$, $^{**}p < 0.01$, $^{***}p < 0.001$). Error bars indicate the standard deviation.

3. Results

3.1. Characterization of hydrogels

As a major component of the brain ECM, HA plays a crucial role in maintaining neural tissue homeostasis by influencing cell migration, proliferation, differentiation, and various cellular behaviors. Its biomechanical properties closely resemble those of brain tissue, and its strong water absorption capacity makes it an ideal hydrogel component.[26] However, limitations such as low strength, poor toughness, and susceptibility to degradation over prolonged culture hinder its applications and clinical translation. Previous studies have indicated that conventional water-soluble PEG can significantly enhance the crosslinking ability of hydrogels and notably reduce degradation rates.[27] Therefore, we tested several PEG-HAMA hydrogel systems at different concentrations before selecting the optimal composition for this study. Ultimately, we chose the P1H2 hydrogel system (1% PEG, 2% HAMA), which demonstrated optimal printability and facilitated neurosphere encapsulation, survival, and growth.

The inclusion of PEG facilitated rapid gelation of the structure during bioprinting at room temperature. Rheological analyses of the PEG-HAMA solution demonstrated a relatively consistent decrease in viscosity as the temperature increased from 10 to 40 °C

(Figure 2B and C). Notably, the ability to print at physiological temperature helps maintain cell viability by providing more conducive biological conditions. Additionally, using less viscous materials for printing can mitigate mechanical damage to cells generated by the printing process. Therefore, heating the solution to physiological temperature (37 °C) during printing can reduce the printing pressure and enhance the survival rate of cells within the bioink.

Figure 1B and C illustrates the morphology of the hydrogel solution before and after crosslinking, respectively. Code 1 (Figure 1F) represents the scaffold shape designed for long-term cell culture, featuring a cylindrical mesh structure with a diameter of 10 mm and a thickness of 1 mm, where the grid is a 1.25 mm square and a wall width of 375 μm; code 3 (Figure 1H) is intended for characterization purposes and consists of a solid cylindrical structure with a diameter of 10 mm and a thickness of 2 mm. The hydrogel swelling was subsequently examined (Figure 2A). Upon incubation in DMEM, the wet mass on Day 2 was approximately 1.7 times the dry mass recorded on Day 0, indicating significant absorption by the swelling medium. Starting from Day 2, the swelling rate gradually decreased and stabilized. Overall, the addition of PEG influenced the water absorption properties of HAMA, with the swelling capacity progressively diminishing as the PEG concentration increased.

We subsequently evaluated the mechanical strength of hydrogel compositions with varying components before and after crosslinking. Figure 2D and E illustrates the storage and loss modulus of hydrogels with different hydrogel materials, with the turning point of the curve indicating the onset of crosslinking. The data reveal that the mechanical strength of the hydrogel is significantly enhanced after the addition of PEG, and this improvement is directly proportional to the PEG content. Specifically, the incorporation of 1% PEG increased the mechanical strength by about 2.2-fold compared to pure HAMA (Figure 2E); increasing the PEG concentration significantly enhanced the crosslinking density and elasticity of the hydrogel.

3.2. 3D bioprinting of MN9D and BV2 cores *in vitro*

The P1H2 hydrogel solution was combined with a high-density cell suspension containing low-density matrix gel (1×10^7 cells/mL), and a 3D bioprinter was utilized to create a 3D grid scaffold structure filled with cells. Bioprinted constructs were cultured in fresh medium for 7–14 days, depending on the specific experiment, with the medium changed every 2–3 days. A parallel incubation procedure was conducted for the 2D control group, which was cultured in a traditional tiled format. To assess the impact of the bioprinting process on cell survival, cell viability was evaluated in the bioprinted MN9D and BV2 cells. Live/dead staining assays were conducted immediately after bioprinting, with live cells appearing green and dead cells red. The results indicated that most cells were green, with only a few red-stained cells observed in both the MN9D (Figure 3A–C) and BV2 (Figure 4A–C) cores. The survival rates of MN9D and BV2 cells in the bioprinting group were calculated to be 85.82% ± 0.93% and 88.41% ± 0.11%, respectively. In comparison, the survival rates in the 2D control group were 91.48% ± 2.04% and 90.36% ± 0.72%. Statistical analysis revealed no significant difference between the survival rates of the bioprinted cells ($p = 0.1785$) and those in the 2D control group ($p = 0.1501$). These findings indicate that the 3D printing process did not significantly impact cell viability (Figures 3D and 4D). Additionally, the Alamar Blue assay was utilized to evaluate the cell proliferation of MN9D and BV2 cells over 7 days of printing to further assess cell survival. The results demonstrated that the relative proliferation rate of the 3D construct exhibited sustained positive growth compared to Day 1, with BV2 cells exhibiting significantly stronger growth than MN9D cells. In contrast, the relative proliferation rates of the 2D and mix control groups were notably slower, with some instances of negative growth compared to Day 1, indicating significant limitations in their proliferation. These findings suggest that the 3D construct supports long-term cell survival and is suitable for extended *in vitro* culture (Figures 3K and 4K). Furthermore, we assessed the growth behavior of MN9D and BV2 cells within the 3D constructs through optical microscopy, SEM imaging, and H&E staining. Observations after 10 days of culture revealed that MN9D and BV2 cells within the 3D structure grew and aggregated freely, forming distinct cell clusters (Figures 3E and H and 4E and H). Under the light microscope, the proliferation rate of BV2 was significantly higher than that of MN9D cells, aligning with the results from the above Alamar Blue cell viability assessments. SEM imaging of the 3D structure illustrated the favorable growth of the P1H2 hydrogels and the core of the cell clusters (Figures 3G and J and 4G and J). The H&E staining results from the same period corroborated these findings (Figures 3F and I and 4F and I). On one hand, during the initial stages of printing, the bioink, prior to crosslinking, remains in a liquid, flowable state, which allows for a certain degree of cell aggregation due to intercellular interactions. Additionally, under physiological conditions, cells within a 3D microenvironment tend to form cell clusters or organoid structures through self-assembly and migration behaviors. This phenomenon is particularly pronounced in neurons and immune cells, which exhibit a strong tendency for intercellular adhesion. Therefore, we believe

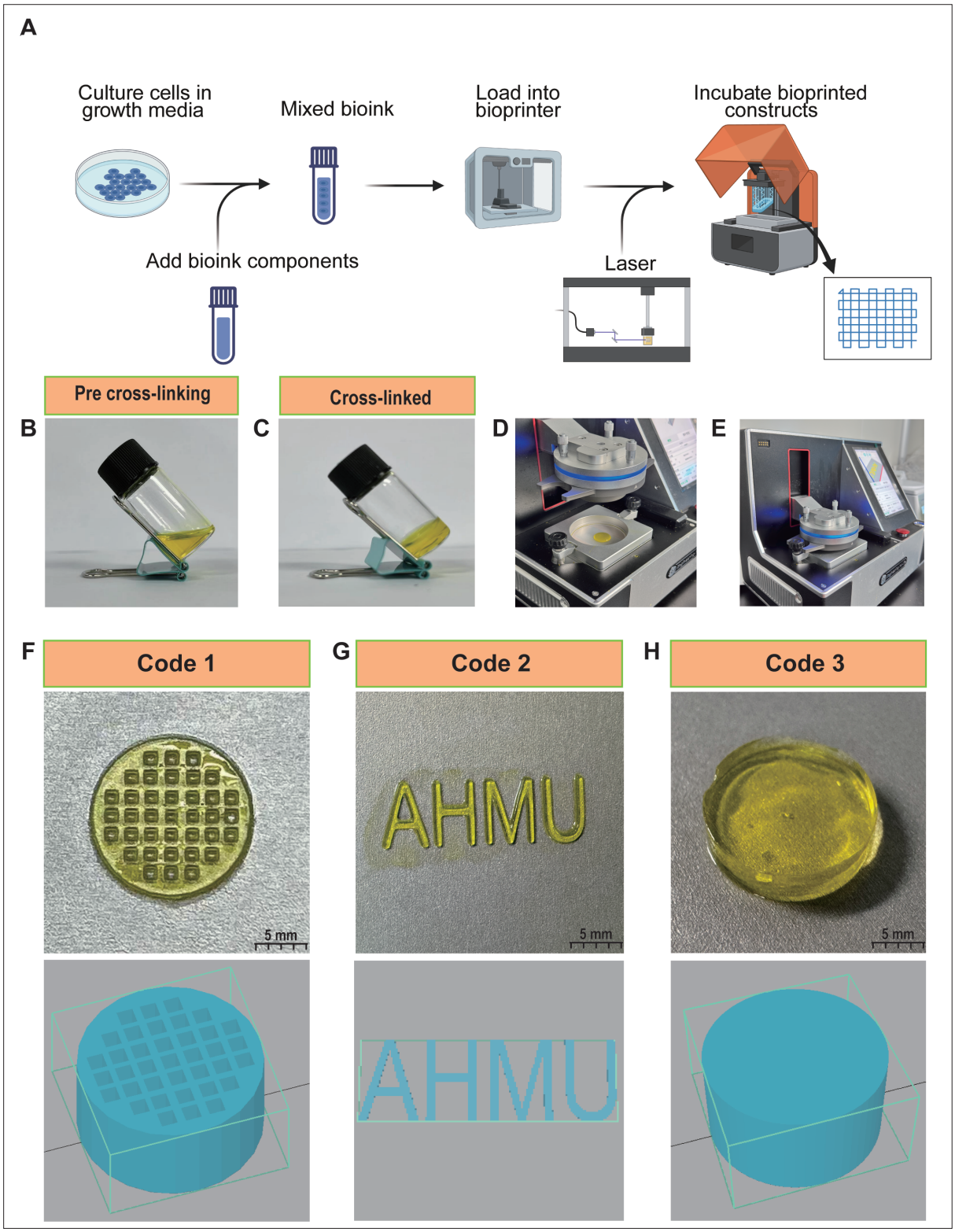

Figure 1. 3D bioprinting process and characterization of hydrogels. (A) Schematic diagram of the 3D-bioprinted *in vitro* model (Note: The illustrated bioprinter is a schematic diagram and may differ from the actual model; the schematic was created using BioRender [biorender.com]). (B and C) Macroscopic view of the hydrogel before (B) and after (C) crosslinking. (D and E) Working diagram of bioink solution in the printer cartridge before (D) and after (E) printing. (F and G) Models were predesigned and printed by engineers, displaying a circular grid model (Code 1; F), an "AHMU" text model (Code 2; G), and a cylindrical model (Code 3; H). Scale bars: 5 mm (F–H).

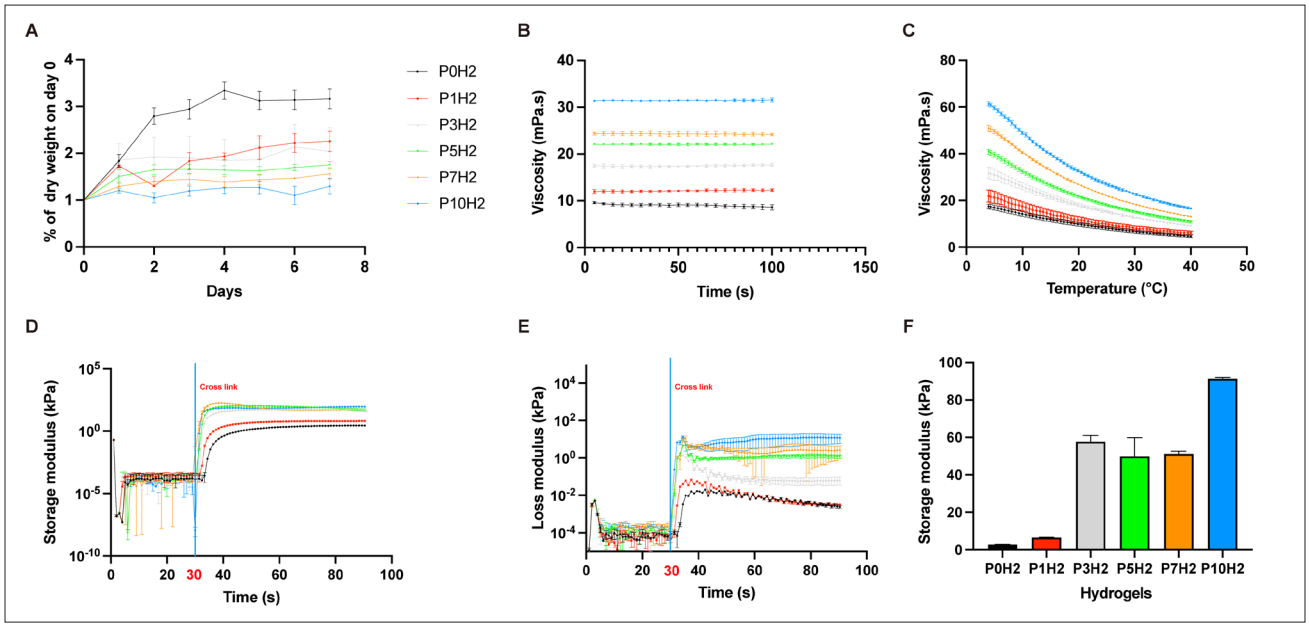

Figure 2. Characterization of hydrogels. (A) Swelling ratio of the crosslinked structure after immersion in DMEM for up to 7 days. (B) Viscosity–time curve for the crosslinked structure at a constant temperature. (C) Temperature–viscosity curve for the crosslinked structure. (D) Storage modulus–time curve of the different hydrogels. (E) Loss modulus–time curve of the different hydrogels. (F) Storage modulus of different hydrogels after full cross-linking. All samples were run in triplicate ($n = 3$).

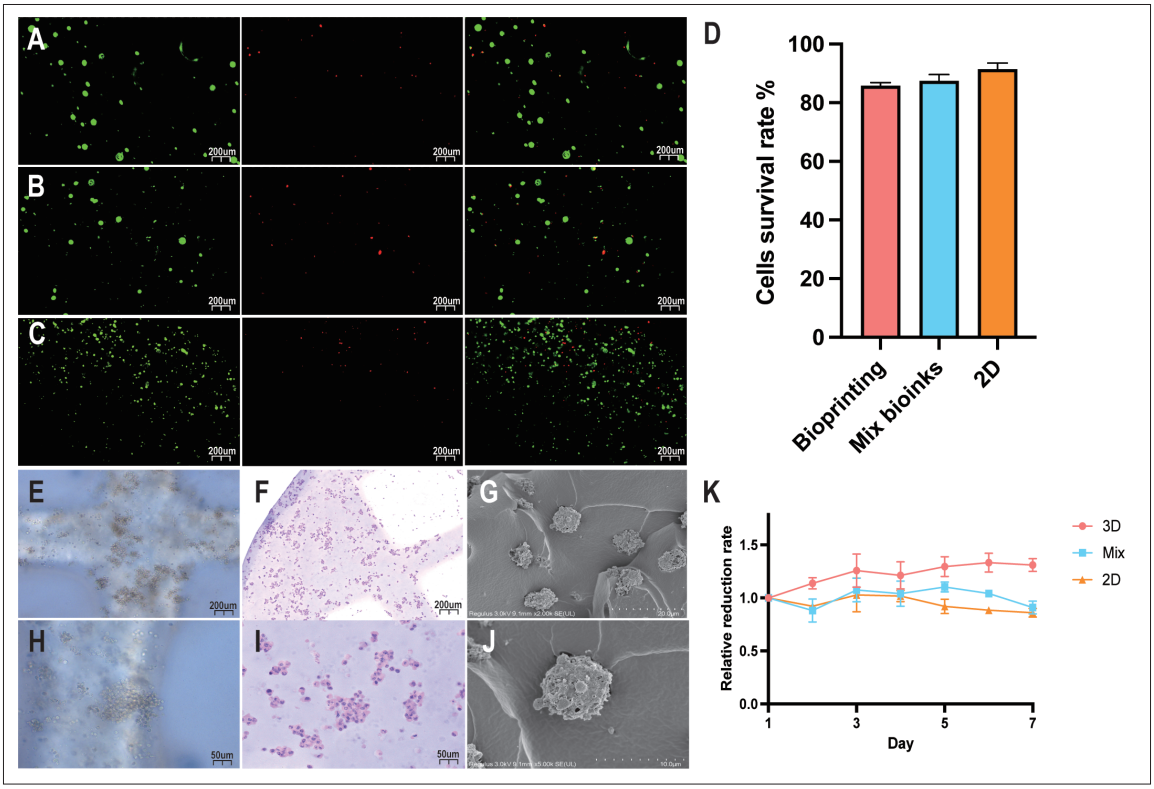

Figure 3. Cell proliferation capacity of the 3D-bioprinted MN9D *in vitro* model. (A–C) Live/dead staining of the 3D bioprinting (A), mix bioink (B), and 2D (C) groups, with live cells stained by calcein-AM (green) and dead cells stained by propidium iodide (PI; red). (D) Viability of MN9D cells after bioprinting. (E and H) The 10-day *in vitro* 3D culture of MN9D cells. (F and I) Hematoxylin and eosin (H&E) staining of MN9D cells after 10-day *in vitro* 3D culture. (G and J) Scanning electron microscopy (SEM) images of the P1H2 scaffold with MN9D cells. (K) Proliferation evaluation of 3D-bioprinted MN9D cells compared to cells from 2D and mixed bioink controls for 7 days. The error bars denote the standard deviation. Scale bars: A–C, E, F: 200 μm; H: 50 μm; H and I: G: 20 μm; J:10 μm.

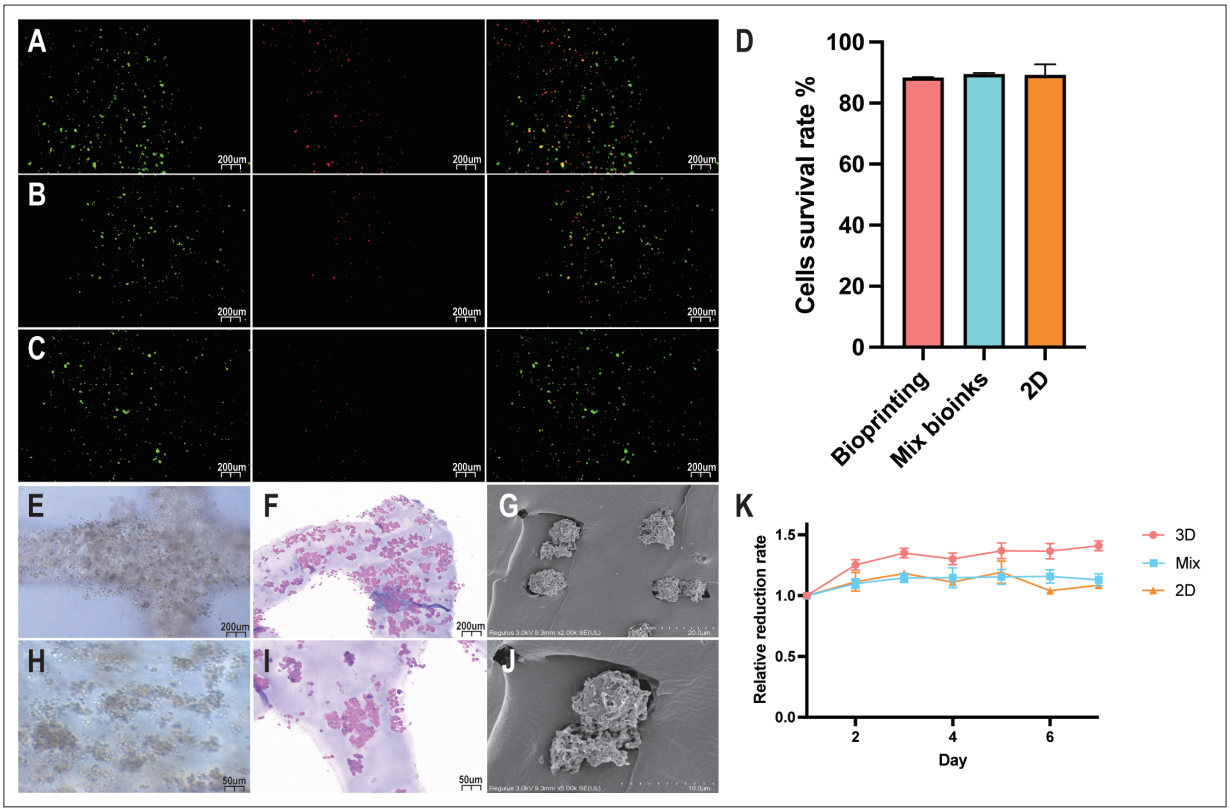

Figure 4. Cell proliferation capacity of the 3D-bioprinted BV2 *in vitro* model. (A–C) Live/dead staining of the 3D bioprinting (A), mix bioink (B), and 2D (C) groups, with live cells stained by calcein-AM (green) and dead cells stained by propidium iodide (PI; red). (D) Viability of BV2 cells after bioprinting. (E and H) The 10-day *in vitro* 3D culture of BV2 cells. (F and I) Hematoxylin and eosin (HE) staining of BV2 cells after 10-day *in vitro* 3D culture. (G and J) Scanning electron microscopy (SEM) images of the P1H2 scaffold with BV2 cells. (K) Proliferation evaluation of 3D-bioprinted BV2 cells compared to cells from 2D and mixed bioink controls for 7 days. The error bars denote the standard deviation. Scale bars: A–C and E, F: 200 μm; H and I: 20 μm; G: 20 μm; J: 10 μm.

that the clustering and aggregation of cells to some extent serve as compelling evidence of the successful biomimetic simulation of the 3D growth microenvironment for MN9D and BV2 cells within our bioprinting system.

3.3. N-butyrate induces 3D MN9D core differentiation *in vitro*

To construct functional DA cores *in vitro*, we replaced the culture medium with a complete medium containing 1 mM n-butyric acid after 1 week of MN9D core proliferation, facilitating their differentiation into DA neurons *in situ* within the 3D constructs. After 7 days of differentiation, the neuron-specific cytoskeleton marker Tuj1 expression was significantly upregulated in the 3D constructs compared to pre-differentiation levels, confirming the development of a more mature neuronal phenotype. Additionally, the DA neuron marker tyrosine hydroxylase (TH), the rate-limiting enzyme in dopamine synthesis,[28] was also upregulated, indicating effective differentiation of DA neurons (Figure 5A and B). At the protein level, the expressions of Tuj1, TH, and DAT were significantly elevated compared to pre-differentiation levels, with the 3D group demonstrating superior differentiation outcomes compared to the 2D group (Figure 5C–F). At the mRNA level, the expression levels of DAT, KCNJ6 (a marker for mature DA neurons[29]), TH, and Syn1 (a marker for synaptic activity[30]) were significantly upregulated compared to pre-differentiation levels, with the upregulation being more pronounced in the 3D group (Figure 5G–J). Overall, the *in situ* differentiation of DA neurons in the 3D group was superior to that of the traditional 2D group, demonstrating more mature differentiation and improved synaptic network connections.

3.4. Co-cultured 3D dopaminergic neuron and microglia cores exposed to the 6-hydroxydopamine model of neuroinflammation *in vitro*

To simulate paracrine secretion in the neuroinflammatory environment of PD, we placed the differentiated DA neuron core and the microglia core into a Transwell device for co-culture, subsequently using 6-OHDA to induce the secretion of inflammatory factors (Figure 6A). The proteins

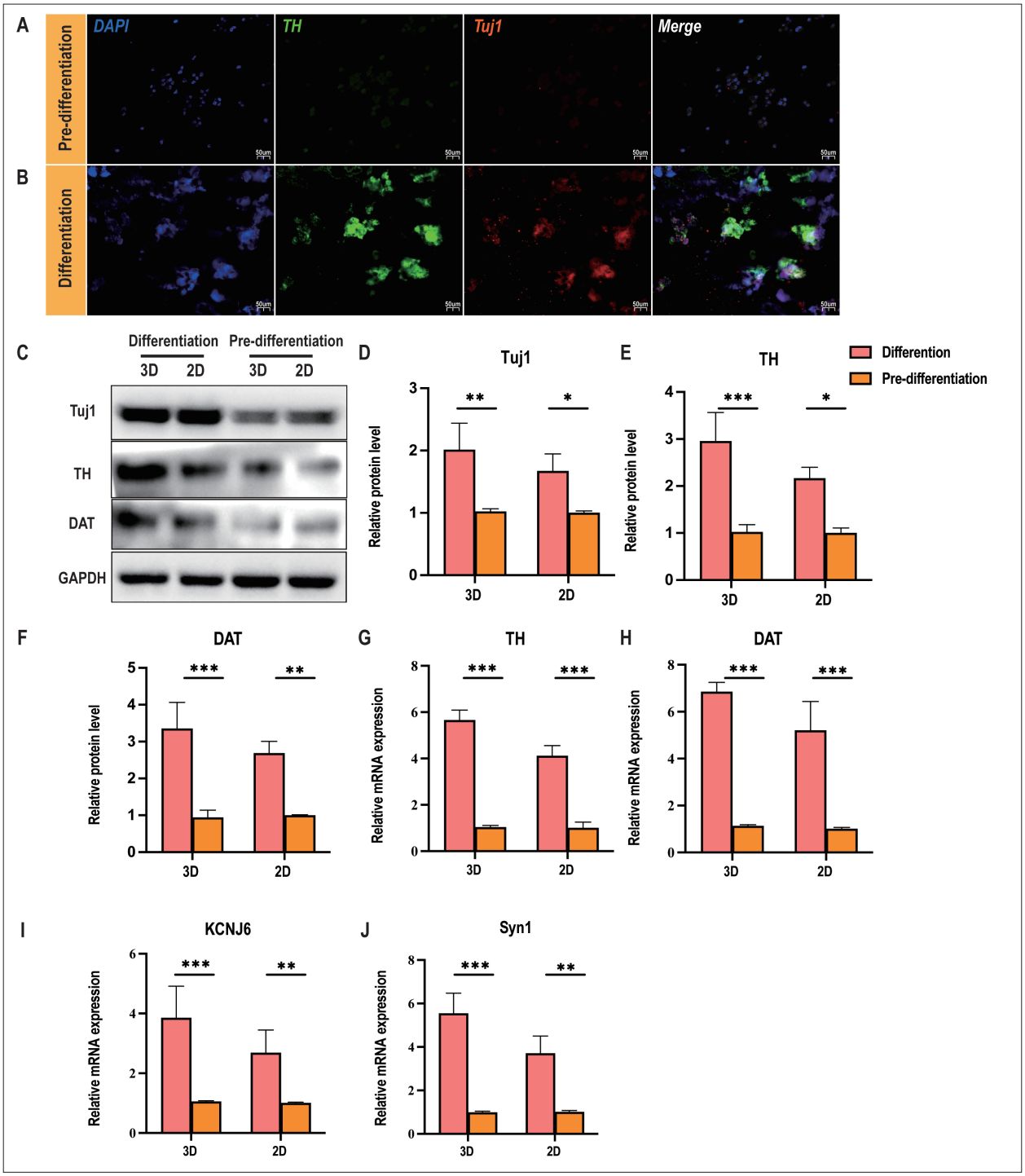

Figure 5. N-butyric acid differentiates dopaminergic (DA) neurons *in situ* and *in vitro* (A; before 3D neuron in situ differentiation and B; after 3D neuron in situ differentiation). Representative immunofluorescence images of tyrosine hydroxylase (TH; dopamine synthesis enzyme; green) and Tuj1 (neuronal cytoskeleton; red) staining before and after neuronal differentiation in 3D models. (C) Protein expression levels of Tuj1, TH, and DAT in 3D and 2D groups before and after differentiation. (D–F) Relative protein expression levels of Tuj1 (D), TH (E), and dopamine transporter (DAT; F). (G–J) Relative mRNA expression levels of TH (G), DAT (H), KCNJ6 (I), and Syn1 (J). $^{*}p < 0.05$; $^{**}p < 0.01$; $^{***}p < 0.001$. The error bars indicate the standard deviation. Scale bars: A and B; 50 μm.

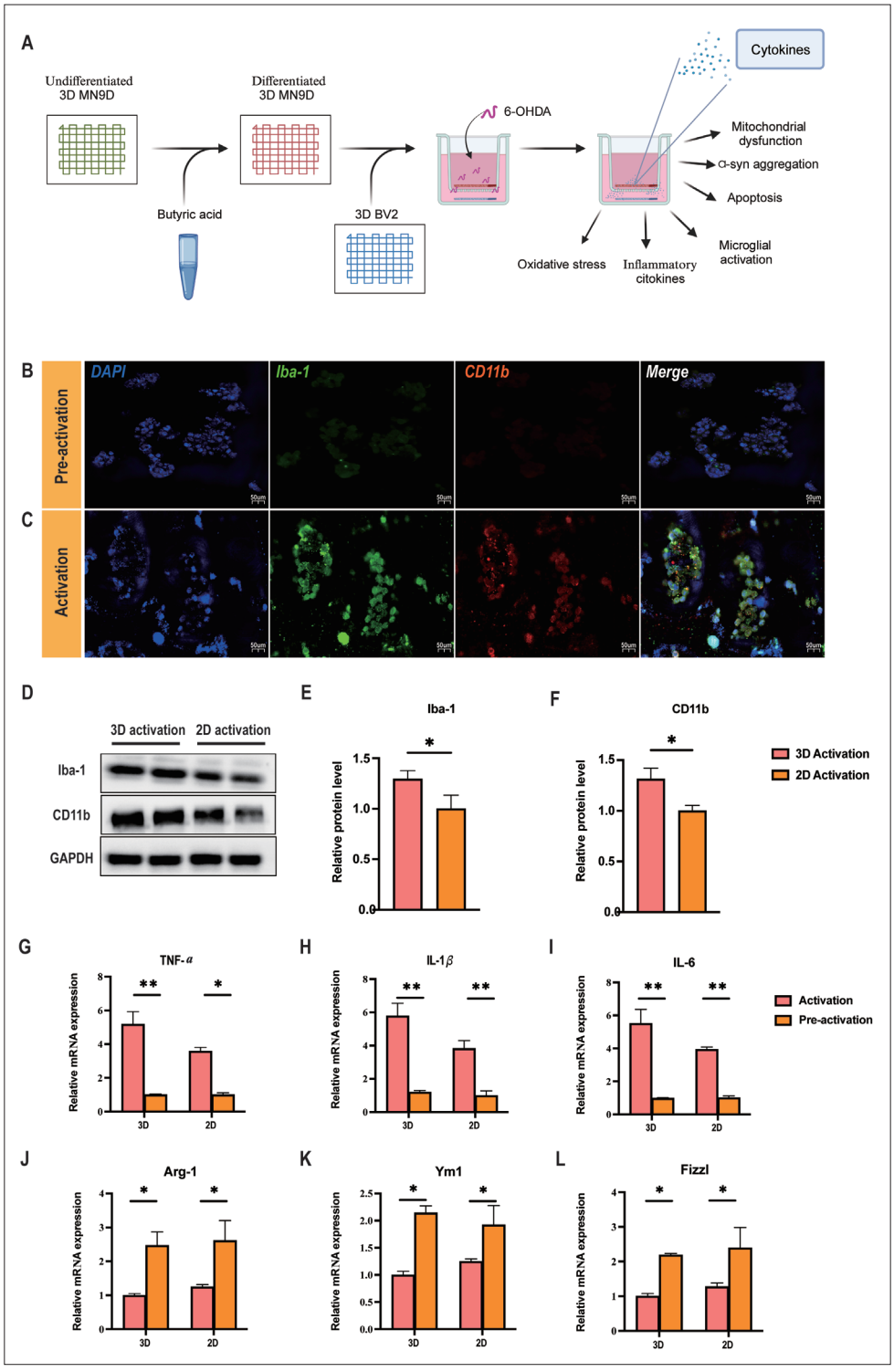

Figure 6. The 6-OHDA-stimulated 3D microglia recapitulated the neuroinflammatory environment. (A) Schematic diagram of the proposed stimulation protocol for inducing a neuroinflammatory environment and Parkinson's disease (PD)-like pathology in our co-culture system. The image was created using BioRender (BioRender.com). (B; 3D microglia pre-activation and C; means 3D microglia after activation). Representative immunofluorescence images displaying Iba-1 (green) and CD11b (red) staining before and after microglia activation in 3D models. (D) Protein expression levels of Iba-1 and CD11b in 3D and 2D groups before and after activation. (E and F) Relative protein expression levels of Iba-1 (E) and CD11b (F). (G–I) Relative mRNA expression levels of TNF-α (G), IL-1β (H), and IL-6 (I). (J–L) Relative mRNA expression levels of Arg-1 (J), Ym1 (K), and Fizz1 (L). $^{*}p < 0.05$; $^{**}p < 0.01$; $^{***}p < 0.001$. The error bars indicate the standard deviation. Scale bars: B and C; 50 μm. Abbreviation: 6-OHDA, 6-hydroxydopamine.

Iba-1 and CD11b are commonly utilized to assess microglial activation.[31] We observed that the expression levels of Iba-1 and CD11b in the 3D construct significantly increased 24 h after 6-OHDA treatment, confirming substantial microglial activation (Figure 6B and C). Additionally, the expression levels of Iba-1 and CD11b in the 3D microglial core were higher than those in the 2D microglial cultures (Figure 6D–F), indicating a greater degree of activation in the 3D group. To evaluate M1/M2 polarization, we further analyzed markers for M1 (TNF-α, IL-1β, and IL-6) and M2 polarization (Fizz1, Ym1, and Arg-1). The results indicated that the expressions of TNF-α, IL-1β, and IL-6 were significantly elevated following 6-OHDA treatment (Figure 6G–I), while the expression levels of Fizz1, Ym1, and Arg-1 were inhibited (Figure 6J–L). This indicates that microglia underwent M1 polarization, with 3D microglia exhibiting greater polarization than their 2D counterparts and having higher inflammatory factor expression levels. These data demonstrate that we successfully established an *in vitro* 3D neuroinflammatory environment.

3.5. The 6-hydroxydopamine-stimulated neuroinflammation co-culture system mimics Parkinson's disease-specific pathology

As described above, we induced PD-mimicking pathology within the 3D DA neuron cores by transferring the 3D-bioprinted differentiated DA neuron and microglia cores into a Transwell co-culture system, co-exposing them to soluble 6-OHDA. We investigated how this neuroinflammatory co-culture system recapitulates the microenvironment of PD by observing the development of key pathological features and comparing them with 2D DA neuron cultures exposed to 6-OHDA. 6-OHDA is known to trigger microglial activation, leading to various PD-related pathological changes.[10,14] The currently recognized pathological features of PD primarily include apoptosis of DA neurons, abnormal mitochondrial membrane potential, accumulation of intracellular ROS, and overexpression of intracellular α-syn.

In the 6-OHDA-stimulated 2D control group, more than 70% of DA neurons already demonstrated TUNEL(+) within the first 3 days of stimulation, indicating that apoptosis had occurred; by Day 5 of co-culture, almost all neurons had died (Figure 7E and F). In contrast, in our 3D co-culture system, only approximately 20% of stimulated DA neurons underwent apoptosis during the entire 5-day stimulation period (Figure 7D). Although the apoptosis rate of DA neurons was significantly reduced or the apoptotic events were significantly delayed in our 3D co-culture system, significant mitochondrial dysfunction was observed only 1 day after co-culture stimulation. We found that in the mitochondrial membrane, JC1 monomers gradually accumulate as the stimulation time is extended, and the accumulation effect of the 3D co-culture system is more obvious (Figure 7A–C). The accumulation of JC1 only occurs when the mitochondrial membrane potential decreases, which indicates that the input of neuroinflammatory mediators in the 3D culture state is more effective, leading to mitochondrial dysfunction. Further evaluation of intracellular ROS levels also confirmed this result. In our 6-OHDA-stimulated 3D co-culture model, intracellular ROS levels significantly increased, peaking just 1 day after stimulation. By the fifth day, ROS levels remained elevated (Figure 7G). This elevation can be attributed to multiple factors. Firstly, the introduction of neuroinflammatory mediators directly impacts ROS production by activating stress signaling pathways. Secondly, mitochondrial dysfunction contributes to the formation of an oxidative environment. The accumulation of ROS closely correlates with the disturbances in mitochondrial membrane potential. Over the following days, the oxidative response in the 3D co-culture model remained significantly higher than that observed in the 6-OHDA-stimulated 2D control group, confirming the sustained high levels of oxidative stress within the 3D co-culture environment.

The aggregation of α-syn in DA neurons is a critical pathological feature of PD. Within our co-culture system, the levels of intracellular α-syn in DA neurons changed significantly. Using western blot analysis, we found that, as the duration of co-culture stimulation increased, the expression of α-syn in the cells increased as well (Figure 8A and D). Further evaluation through RT-qPCR indicated that the expression levels of α-syn were significantly upregulated (Figure 8G), with this phenomenon being more pronounced in the 3D co-culture model. Notably, the accumulation of α-syn within the cells is closely associated with mitochondrial dysfunction and ROS accumulation, aligning with the enhanced mitochondrial dysfunction observed previously. These findings suggest that our 3D neuroinflammation co-culture system more effectively reproduces α-syn accumulation in DA neurons compared to the 2D control group. During the first 3 days of stimulation, DA neurons in our neuroinflammation co-culture model exhibited significant functional changes. The functional proteins TH, DAT, KCNJ6, and Syn1 demonstrated notable alterations (Figure 8A–C, E, F, H, and I). Notably, TH was significantly downregulated at both the gene expression and protein synthesis levels, indicating a substantial impairment in dopamine synthesis within DA neurons. Simultaneously, DAT and KCNJ6—transmembrane proteins critical for the release and recycling of dopamine—also demonstrated a significant decrease in expression levels. Furthermore, the downregulation of *Syn1* gene expression suggests that synapse formation in

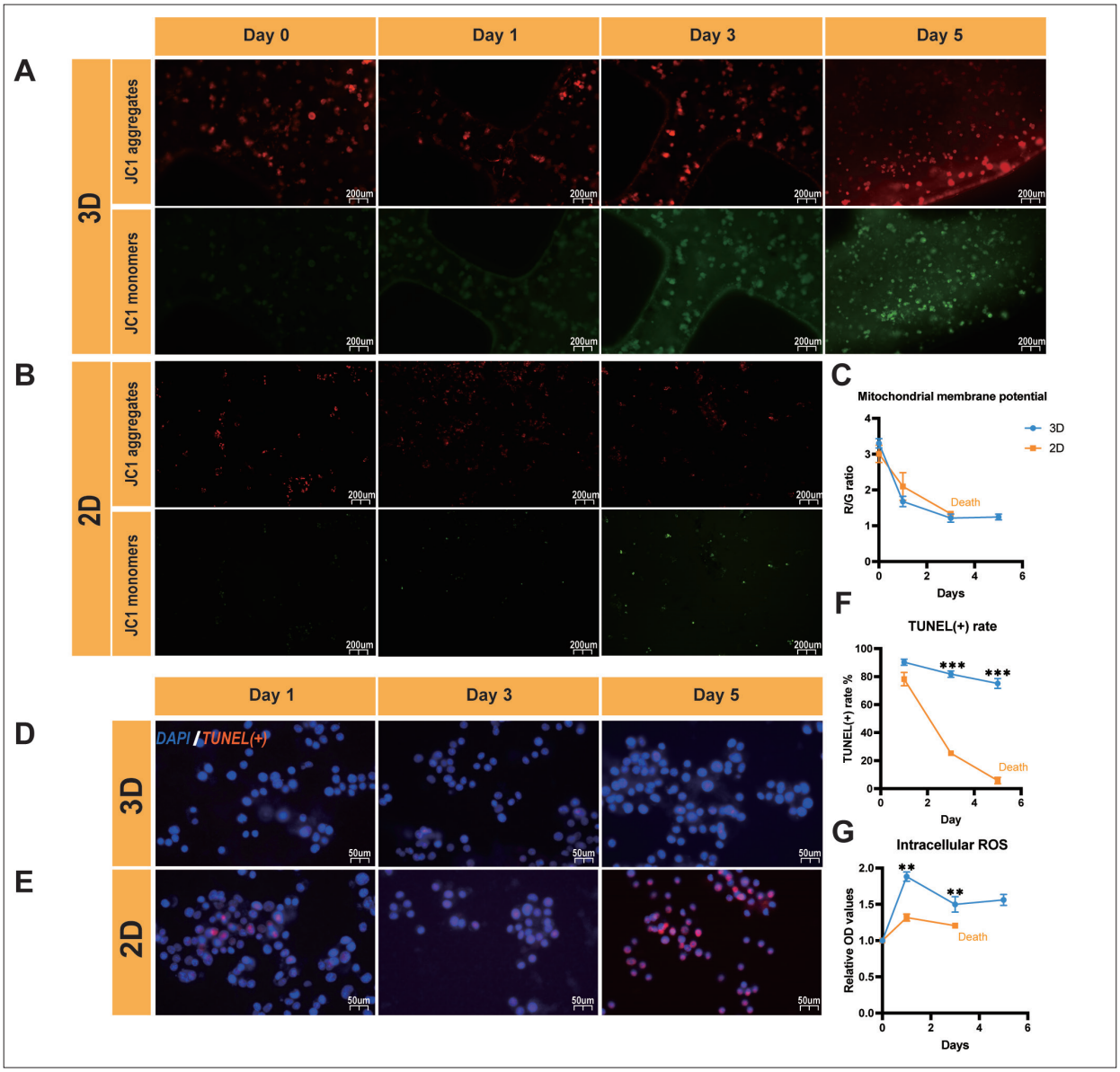

Figure 7. 6-hydroxydopamine (6-OHDA)-stimulated 3D neuroinflammatory co-culture model induces mitochondrial dysfunction and an oxidative environment, demonstrating a reduced cell apoptosis rate compared to the 2D co-culture model. (A and B) Immunofluorescence staining images of mitochondrial membrane potential in the 6-OHDA-stimulated 3D co-culture model at days 0, 1, 3, and 5, with JC1 monomers displayed in green and JC1 aggregates in red. (B) Immunofluorescence staining images of mitochondrial membrane potential in the 6-OHDA-stimulated 2D co-culture model at days 0, 1, and 3. (C) Red-to-green fluorescence (R/G) ratio for assessing mitochondrial membrane potential changes. (D and E) TUNEL staining images of 6-OHDA-stimulated 3D and 2D co-culture models at days 1, 3, and 5, with red indicating TUNEL (+). (F) The ratio of TUNEL(+) to DAPI over time. (G) Changes in intracellular reactive oxygen species (ROS) intensity (*$p < 0.05$; **$p < 0.01$; ***$p < 0.001$). The error bars indicate the standard deviation. Scale bars: A and B; 200 μm, D and E; 50 μm. Abbreviation: OD, optical density.

DA neurons is compromised, disrupting the connections within the neural network. Notably, we observed that these pathological changes were more pronounced in the 3D neuroinflammation co-culture group.

These results indicate that our P1H2 hydrogel 3D neuroinflammation co-culture model effectively mimics key pathological features of PD while displaying enhanced tolerance to neurotoxic insults. In contrast to the rapid cell death observed in 2D culture systems, this approach holds promise for establishing an *in vitro* chronic PD model over an extended period. This advancement will enable more precise and extensive studies on the onset and progression of the disease, and the model will be highly beneficial for the *in vitro* screening of drug candidates.

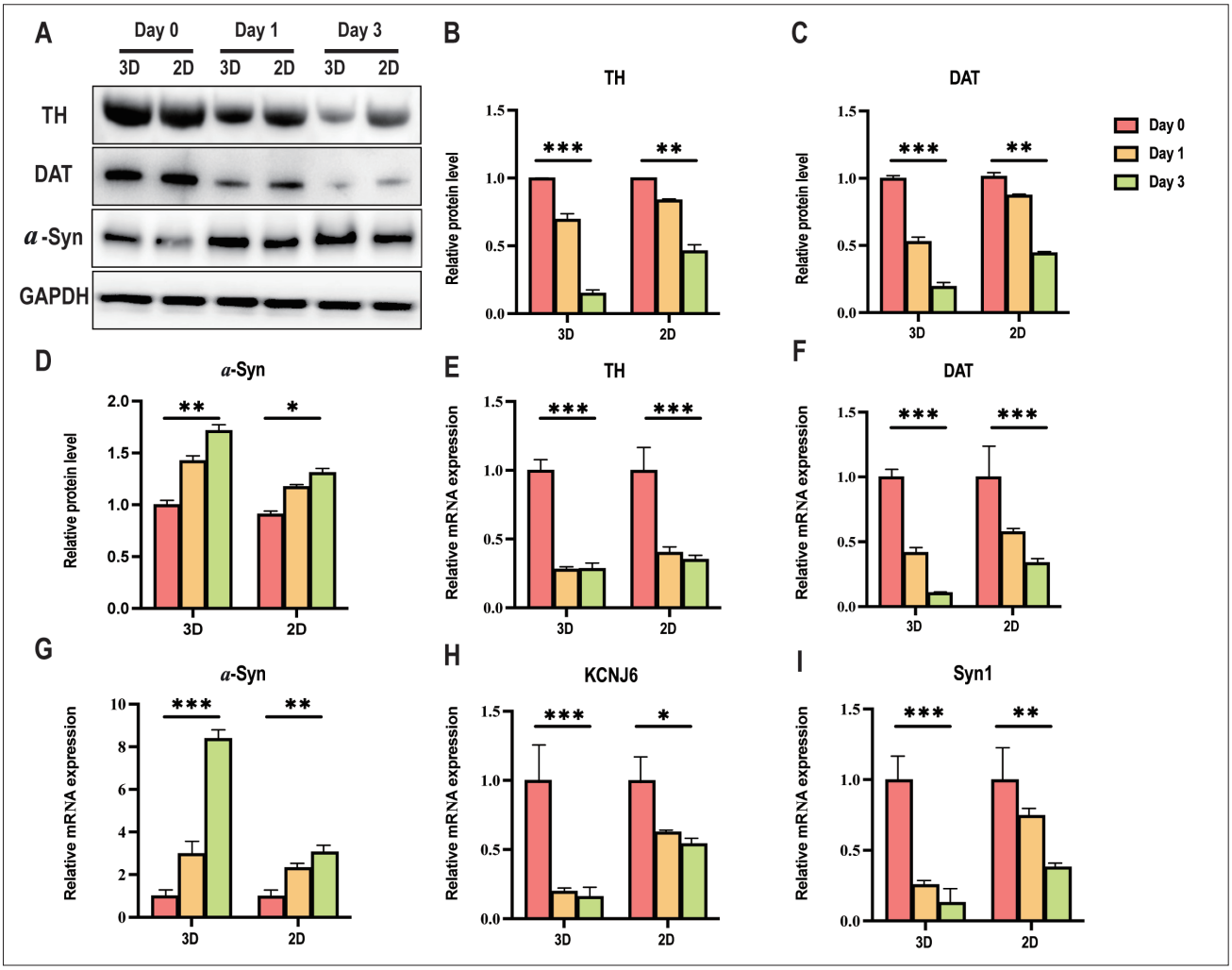

Figure 8. Intracellular α-syn accumulation, dopaminergic (DA), and synaptic dysfunction in the 6-hydroxydopamine (6-OHDA)-stimulated neuroinflammatory co-culture model. (A) Tyrosine hydroxylase (TH), dopamine transporter (DAT), and α-synuclein (α-syn) protein expression levels in 6-OHDA-stimulated 3D and 2D co-culture models at days 0, 1, and 3. (B–D) Relative protein expression levels of TH (B), DAT (C), and α-syn (D) protein. (E–I) Relative mRNA expression levels of TH (E), DAT (F), α-syn (G), KCNJ6 (H), and Syn1 (I). *$p < 0.05$; **$p < 0.01$; ***$p < 0.001$. The error bars indicate the standard deviation.

4. Discussion

Traditionally, 2D *in vitro* models have been inadequate in accurately reconstructing complex neuroinflammatory microenvironments. In contrast, 3D bioprinting offers a novel platform to simulate the interactions within the neuroinflammatory microenvironment between DA neurons and microglia. In our P1H2 hydrogel system, neurons and microglia cultured under 3D conditions proliferate, forming cell spheres, and producing inflammatory mediators, thereby inducing PD-related pathological characteristics in response to 6-OHDA. This study demonstrates that the bioprinted neuroinflammatory *in vitro* model more effectively simulated neuroinflammatory environmental conditions, providing a foundation for chronic *in vitro* model research.

The above analysis indicates that the PEG-HAMA hydrogel system exhibits printability at physiological temperature (Figure 2B and C). Additionally, the P1H2 hydrogel system demonstrates a favorable swelling rate (Figure 2A) and mechanical properties comparable to those of HAMA (Figure 2D–F). The printed uniform grid structure has a wall thickness of only 375 μm, ensuring sufficient hydrogel permeability and effective exchange with the culture medium, providing ample nutrients to the cells. Brain tissue exhibits distinct mechanical properties compared to other tissues, with Young's modulus of the brain ranging from approximately 0.1–1 kPa.[32] Wu et al.[33] investigated the culture of PC12 cells, a DA neuron model, on gelatin methacryloyl (GelMA)-based hydrogels with Young's modulus ranging from 3 to 180

kPa. Their findings revealed that the highest degree of cell attachment occurred on the softest GelMA hydrogels. However, the neurite length of PC12 cells exhibited a trend of initial increase followed by a decrease as the GelMA concentration increased, with the longest neurites observed on hydrogels with a Young's modulus of 34.9 kPa.[33] These results indicate that the optimal hydrogel stiffness for DA neuron growth is slightly higher than the average stiffness of normal brain tissue. HAMA hydrogels tend to degrade quickly, making it challenging to create a chronic *in vitro* neuroinflammatory microenvironment.[34] To address these limitations, we developed a P1H2 hydrogel system. The introduction of PEG significantly enhanced the mechanical properties of the hydrogel (approximately 6.6 kPa), and due to the crosslinking effects of PEG, the degradation rate was markedly reduced. The introduction of PEG increases the physical crosslinking points and network chain density, resulting in a more stable network structure. This network enhancement effect tends to flatten the degradation curve, reflecting an overall reduction in degradation rate. At lower PEG content, the degradation curve may exhibit a steeper decline. As the PEG content increases, the degradation curve becomes progressively smoother, demonstrating an extended material stability period and delayed degradation.[35] This modification preserved the favorable expansion of HAMA to a certain extent, enabling the construction of a more sustainable chronic neuroinflammatory model.

Since neuronal differentiation is accompanied by defects in cell proliferation and mechanical cell death is inevitable during the 3D bioprinting process, it is necessary to culture the cells under standard growth conditions for 7–10 days before implementing the differentiation protocol. After differentiation, 6-OHDA is applied for modeling. Therefore, n-butyrate or 6-OHDA cannot be mixed into the bioink during the printing stage. Building on this foundation, we demonstrate that 3D hydrogels facilitate the development of a more mature and interconnected DA neuron phenotype, primarily due to the favorable conditions for cell suspension growth. Additionally, the 3D microglial constructs, activated following 6-OHDA stimulation in the co-culture system, closely simulate an immune response reminiscent of the neuroinflammatory microenvironment. This activation promotes M1 polarization in microglia and leads to the secretion of numerous pro-inflammatory factors. Moreover, 6-OHDA acts as a mitochondrial stressor, exerting direct neurotoxic effects on DA neurons. These conditions trigger a series of PD-like pathologies within the 3D DA neuron network, including apoptosis of DA neurons, mitochondrial dysfunction, increased ROS accumulation, and α-syn aggregation. Notably, our findings indicate that the pathological impacts were more pronounced compared to the 2D neuroinflammation co-culture system. Importantly, neurons in the 3D model exhibited enhanced tolerance to these neurotoxic insults, resulting in a significantly slower rate of apoptosis. This represents a promising advantage over existing rotenone-based models, as the rapid cell death observed in 2D models limits our ability to study disease progression effectively. Indeed, several studies have demonstrated that neurons in 3D models exhibit enhanced tolerance to toxic damage. For instance, Serna et al.[22] used exogenous A53T α-syn to stimulate 3D neuronal constructs, co-culturing them with a 2D immune cell system. They observed that the apoptotic patterns in the 3D neuronal constructs were fewer and occurred later compared to those in the traditional rotenone-based 2D model. In contrast, our study employed a 3D co-culture system incorporating both DA neurons and microglia, providing a more realistic representation of the actual growth conditions and the physiological and pathological environments of the cells. This approach not only enhances the fidelity of the model but also allows for a more accurate investigation of neuronal responses to neurotoxic insults within a complex microenvironment.

In addition to the benefits of the 3D co-culture, our differentiation scheme is also relatively effective. The superior swelling rate of the hydrogel ensures that the 3D cells are in full contact with the differentiation-inducing agents, allowing for the establishment of a mature 3D DA neuron network within just 7 days of differentiation. This outcome contrasts sharply with the neuroepithelial stem cell organoid protocol developed by Monzel et al.,[36] which requires over 21 days to achieve similar DA neuron networks. The ability to maintain long-term 3D culture not only highlights the efficacy of our hydrogel system but also presents a significant challenge to the performance of both the hydrogels and the laboratory culture environment. This advancement facilitates more efficient studies in neurodevelopment and disease modeling. In contrast, short-term differentiation protocols are more controllable. Additionally, compared to previous 3D-bioprinted PD models,[37,38] our approach for *in vivo* DA neurons in 3D constructs employs an *in situ* differentiation protocol that is less invasive for the formation of neuronal networks. This is preferable to methods that involve embedding already differentiated DA neurons, which often require longer and less controllable periods to achieve axon regeneration. Furthermore, the regeneration efficiency of differentiated mature neurons tends to be low, frequently resulting in unsatisfactory neural network functionality. Moreover, traditional extrusion printing methods typically apply strong shear forces to the cells within the hydrogel, potentially leading to substantial cell death before differentiation can occur. In contrast, the hydrogel used in our study employs light-induced crosslinking, minimizing exposure to shear forces. This approach

significantly enhances the survival rate of neurons within the 3D construct, thereby promoting better outcomes for neuronal network development.

The neuroinflammatory process *in vivo* is highly complex, particularly in chronic neurodegenerative diseases. This study presents an extremely simplified *in vitro* model. Microglia, regarded as the innate immune cells of the central nervous system,[39] exhibit rapid activation during acute brain inflammation, prior to the intervention of peripheral immune responses.[40] However, as inflammation persists over time, chronic inflammation results in tissue degradation and disruption of the blood-brain barrier, permitting the infiltration of peripheral immune cells. During this phase, microglia produce ROS and release signaling molecules to recruit peripheral immune cells, thereby amplifying the inflammatory response.[41] Therefore, microglial activation is a crucial factor in the context of chronic neuroinflammation. To our knowledge, this study represents the first attempt to construct a 3D co-culture system comprising both DA neurons and microglia to simulate PD-related pathologies *in vitro*. This approach underscores that, alongside microglia, various other cell types contribute to the development of chronic neuroinflammation in the body, and the role of peripheral immune cells should not be overlooked. While some studies have begun to incorporate peripheral immune cells into 3D midbrain *in vitro* models to facilitate the formation of neuronal networks,[22,42] the precise effects of these peripheral immune cells on *in vitro* degenerative responses, as well as the specific roles of microglia within this context, remain to be thoroughly investigated. This highlights the need for further research to elucidate the complex interactions that underpin neuroinflammation in neurodegenerative diseases.

Despite the promising results of the 3D bioprinting technology for *in vitro* PD models, several limitations exist. First, while the 3D bioprinting system can partially replicate the neuroinflammation microenvironment, it cannot fully capture the complexity of the *in vivo* PD pathological environment. For example, peripheral immune cells, which play a crucial role in chronic neuroinflammation, are not included. Additionally, the model relies on mouse DA neurons and BV2 microglial cells, which, despite mimicking some aspects of human PD pathology, may limit the generalizability to clinical applications due to species differences. Although the 3D co-culture system demonstrated higher neuronal survival rates and better pathological reproduction compared to traditional 2D models, the biocompatibility and long-term stability of the model still require further investigation. Lastly, the choice of materials and mechanical properties presents challenges. While the inclusion of PEG improved the mechanical strength of the hydrogel, maintaining biocompatibility over extended culture periods remains an area that warrants further research.

5. Conclusion

This study demonstrates the potential of 3D bioprinting technology to create a more realistic *in vitro* model of PD by co-culturing DA neurons and microglia within a 3D hydrogel scaffold. The results indicate that this 3D model better simulates key pathological features of PD in the neuroinflammation microenvironment, such as oxidative stress and α-syn accumulation, compared to traditional 2D models. The P1H2 hydrogel system provided a favorable microenvironment for cell survival, differentiation, and long-term culture, allowing for a more detailed investigation of the neuroinflammatory microenvironment and its impact on PD progression. Although there are limitations, such as the exclusion of peripheral immune cells and reliance on mouse cells, this model offers significant advantages for studying chronic PD pathology and potential drug screening applications. Future research should focus on improving the complexity of the model by incorporating additional cell types and optimizing material properties for long-term stability. This 3D-bioprinted model represents a step forward in developing more accurate and reliable platforms for PD research *in vitro*.

Acknowledgments

The authors would like to acknowledge the contributions of our colleagues and research team members who have provided valuable input, discussions, and assistance at various stages of this study. Their collaboration and constructive feedback have enriched the research process and improved the quality of our findings.

Funding

This article was partially supported by: the National Natural Science Foundation of China (82473256); the Anhui Province Higher Education Scientific Research Project, China (2024AH050818); the Research Fund of Anhui Institute of Translational Medicine (2023zhyx-C19); the Health Research Program of Anhui (AHWJ2023A30007); the Anhui Provincial Natural Science Foundation (2208085MH251); the Anhui Provincial Quality Engineering Project for Higher Education (2022jyxm761); the Fundamental Research Funds for the Anhui Medical University (2021xkj131); the Jiangxi Provincial Natural Science Foundation (20242BAB25521); and the Ganpo Promising Talents Supporting Plan: Talent Development Project of Leading Academic and Technological Researchers in Key Disciplines (20243BCE51060).

Conflict of interest

The authors declare they have no competing interests.

Author contributions

Conceptualization: Hongwei Cheng, Xingliang Dai
Formal analysis: Hongliang Mao
Investigation: Hongliang Mao, Liangchen Yu, Menghui Liu
Methodology: Hongliang Mao, Yang Qiao, Liangchen Yu
Writing – original draft: Hongliang Mao
Writing – review & editing: Hongwei Cheng, Xingliang Dai

Ethics approval and consent to participate

Not applicable.

Consent for publication

Not applicable.

Availability of data

The data that support the findings of this study are available from the corresponding author upon reasonable request.

References

1. Dorsey ER, Bloem BR. The Parkinson pandemic-a call to action. *JAMA Neurol.* 2018;75(1):9-10. doi: 10.1001/jamaneurol.2017.3299
2. Barbosa AF, Voos MC, Chen J, et al. Cognitive or cognitive-motor executive function tasks? Evaluating verbal fluency measures in people with Parkinson's disease. *Biomed Res Int.* 2017;2017:7893975. doi: 10.1155/2017/7893975
3. Surmeier DJ, Obeso JA, Halliday GM. Selective neuronal vulnerability in Parkinson disease. *Nat Rev Neurosci.* 2017;18(2):101-113. doi: 10.1038/nrn.2016.178
4. Stefanis L. α-Synuclein in Parkinson's disease. *Cold Spring Harb Perspect Med.* 2012;2(2):a009399. doi: 10.1101/cshperspect.a009399
5. Luk KC. Oxidative stress and α-synuclein conspire in vulnerable neurons to promote Parkinson's disease progression. *J Clin Invest.* 2019;129(9):3530-3531. doi: 10.1172/jci130351
6. Wong YC, Krainc D. α-synuclein toxicity in neurodegeneration: mechanism and therapeutic strategies. *Nat Med.* 2017;23(2):1-13. doi: 10.1038/nm.4269
7. Polymeropoulos MH, Lavedan C, Leroy E, et al. Mutation in the alpha-synuclein gene identified in families with Parkinson's disease. *Science.* 1997;276(5321):2045-2047. doi: 10.1126/science.276.5321.2045
8. Pajares M, Rojo AI, Manda G, Manda G, Boscá L, Cuadrado A. Inflammation in Parkinson's disease: mechanisms and therapeutic implications. *Cells.* 2020;9(7):1687. doi: 10.3390/cells9071687
9. Yang R, Li DD, Li XX, Yang XX, Gao HM, Zhang F. Dihydroquercetin alleviates dopamine neuron loss via regulating TREM2 activation. *Int J Biol Macromol.* 2024;269(Pt 2):132179. doi: 10.1016/j.ijbiomac.2024.132179
10. Yu Z, Yang L, Yang Y, et al. Epothilone B benefits nigral dopaminergic neurons by attenuating microglia activation in the 6-hydroxydopamine lesion mouse model of Parkinson's disease. *Front Cell Neurosci.* 2018;12:324. doi: 10.3389/fncel.2018.00324
11. Jha MK, Lee WH, Suk K. Functional polarization of neuroglia: implications in neuroinflammation and neurological disorders. *Biochem Pharmacol.* 2016;103:1-16. doi: 10.1016/j.bcp.2015.11.003
12. Stępkowski TM, Wasyk I, Grzelak A, Kruszewski M. 6-OHDA-induced changes in Parkinson's disease-related gene expression are not affected by the overexpression of PGAM5 in in vitro differentiated embryonic mesencephalic cells. *Cell Mol Neurobiol.* 2015;35(8):1137-1147. doi: 10.1007/s10571-015-0207-5
13. Yan JQ, Sun JC, Zhai MM, Cheng LN, Bai XL, Feng CL. Lovastatin induces neuroprotection by inhibiting inflammatory cytokines in 6-hydroxydopamine treated microglia cells. *Int J Clin Exp Med.* 2015;8(6):9030-9037.
14. Zhang P, Li Y, Han X, Xing Q, Zhao L. Dexmedetomidine regulates 6-hydroxydopamine-induced microglial polarization. *Neurochem Res.* 2017;42(5):1524-1532. doi: 10.1007/s11064-017-2209-9
15. Kwon HS, Koh SH. Neuroinflammation in neurodegenerative disorders: the roles of microglia and astrocytes. *Transl Neurodegener.* 2020;9(1):42. doi: 10.1186/s40035-020-00221-2
16. da Silva DJ, Borges AF, Souza PO, et al. Decreased toll-like receptor 2 and toll-like receptor 7/8-induced cytokines in Parkinson's disease patients. *Neuroimmunomodulation* 2016;23(1):58-66. doi: 10.1159/000443238
17. Freeman L, Guo H, David CN, Brickey WJ, Jha S, Ting JP. NLR members NLRC4 and NLRP3 mediate sterile inflammasome activation in microglia and astrocytes. *J Exp Med.* 2017;214(5):1351-1370. doi: 10.1084/jem.20150237
18. Liu W, Zhong Z, Hu N, et al. Coaxial extrusion bioprinting of 3D microfibrous constructs with cell-favorable gelatin methacryloyl microenvironments. *Biofabrication.* 2018;10(2):024102. doi: 10.1088/1758-5090/aa9d44

19. Mota F, Braga L, Rocha L, Cabral B. 3D and 4D bioprinted human model patenting and the future of drug development. *Nat Biotechnol.* 2020;38(6):689-694. doi: 10.1038/s41587-020-0540-1

20. Kang HW, Lee SJ, Ko IK, Kengla C, Yoo JJ, Atala A. A 3D bioprinting system to produce human-scale tissue constructs with structural integrity. *Nat Biotechnol.* 2016; 34(3):312-319. doi: 10.1038/nbt.3413

21. Zhang Y, Chen H, Long X, Xu T. Three-dimensional-engineered bioprinted in vitro human neural stem cell self-assembling culture model constructs of Alzheimer's disease. *Bioact Mater.* 2022;11:192-205. doi: 10.1016/j.bioactmat.2021.09.023

22. Rueda-Gensini L, Serna JA, Rubio D, et al. Three-dimensional neuroimmune co-culture system for modeling Parkinson's disease microenvironmentsin vitro. *Biofabrication.* 2023;15(4). doi: 10.1088/1758-5090/ace21b

23. Chlebanowska P, Tejchman A, Sułkowski M, Skrzypek K, Majka M. Use of 3D organoids as a model to study idiopathic form of Parkinson's disease. *Int J Mol Sci.* 2020;21(3):694. doi: 10.3390/ijms21030694

24. Kim J, Koo BK, Knoblich JA. Human organoids: model systems for human biology and medicine. *Nat Rev Mol Cell Biol.* 2020;21(10):571-584. doi: 10.1038/s41580-020-0259-3

25. Rick CE, Ebert A, Virag T, Bohn MC, Surmeier DJ. Differentiated dopaminergic MN9D cells only partially recapitulate the electrophysiological properties of midbrain dopaminergic neurons. *Dev Neurosci.* 2006;28(6):528-537. doi: 10.1159/000095115

26. Jensen G, Holloway JL, Stabenfeldt SE. Hyaluronic acid biomaterials for central nervous system regenerative medicine. *Cells.* 2020;9(9):2113. doi: 10.3390/cells9092113

27. Bao B, Zeng Q, Li K, et al. Rapid fabrication of physically robust hydrogels. *Nat Mater.* 2023;22(10):1253-1260. doi: 10.1038/s41563-023-01648-4

28. Daubner SC, Le T, Wang S. Tyrosine hydroxylase and regulation of dopamine synthesis. *Arch Biochem Biophys.* 2011;508(1):1-12. doi: 10.1016/j.abb.2010.12.017

29. Simunovic F, Yi M, Wang Y, et al. Gene expression profiling of substantia nigra dopamine neurons: further insights into Parkinson's disease pathology. *Brain* 2009; 132(Pt 7):1795-1809. doi: 10.1093/brain/awn323

30. De Camilli P, Cameron R, Greengard P. Synapsin I (protein I), a nerve terminal-specific phosphoprotein. I. Its general distribution in synapses of the central and peripheral nervous system demonstrated by immunofluorescence in frozen and plastic sections. *J Cell Biol.* 1983;96(5):1337-1354. doi: 10.1083/jcb.96.5.1337

31. Hopperton KE, Mohammad D, Trépanier MO, Giuliano V, Bazinet RP. Markers of microglia in post-mortem brain samples from patients with Alzheimer's disease: a systematic review. *Mol Psychiatry* 2018;23(2):177-198. doi: 10.1038/mp.2017.246

32. Akolawala Q, Rovituso M, Versteeg HH, Rondon AMR, Accardo A. Evaluation of proton-induced DNA damage in 3D-engineered glioblastoma microenvironments. *ACS Appl Mater Interfaces.* 2022;14(18):20778-20789. doi: 10.1021/acsami.2c03706

33. Wu Y, Xiang Y, Fang J, et al. The influence of the stiffness of GelMA substrate on the outgrowth of PC12 cells. *Biosci Rep.* 2019;39(1):BSR20181748. doi: 10.1042/BSR20181748

34. Xia C, Chen P, Mei S, et al. Photo-crosslinked HAMA hydrogel with cordycepin encapsulated chitosan microspheres for osteoarthritis treatment. *Oncotarget.* 2017;8(2):2835-2849. doi: 10.18632/oncotarget.13748

35. Jin P, Pang A, Yang R, Guo X, He J, Zhai J. Study on mechanical properties of polyurethane cross-linked P(E-co-T)/PEG blended polyether elastomer. *Polymers (Basel).* 2022;14(24):5419. doi: 10.3390/polym14245419

36. Monzel AS, Smits LM, Hemmer K, et al. Derivation of human midbrain-specific organoids from neuroepithelial stem cells. *Stem Cell Rep.* 2017;8(5):1144-1154. doi: 10.1016/j.stemcr.2017.03.010

37. Abdelrahman S, Alsanie WF, Khan ZN, et al. A Parkinson's disease model composed of 3D bioprinted dopaminergic neurons within a biomimetic peptide scaffold. *Biofabrication.* 2022;14(4). doi: 10.1088/1758-5090/ac7eec

38. Fiore NJ, Ganat YM, Devkota K, et al. Bioengineered models of Parkinson's disease using patient-derived dopaminergic neurons exhibit distinct biological profiles in a 3D microenvironment. *Cell Mol Life Sci.* 2022;79(2):78. doi: 10.1007/s00018-021-04047-7

39. Gendelman HE. Neural immunity: friend or foe? *J Neurovirol.* 2002;8(6):474-479. doi: 10.1080/13550280290168631

40. Streit WJ, Mrak RE, Griffin WS. Microglia and neuroinflammation: a pathological perspective. *J Neuroinflammation.* 2004;1(1):14. doi: 10.1186/1742-2094-1-14

41. Garden GA. Epigenetics and the modulation of neuroinflammation. *Neurotherapeutics.* 2013;10(4):782-788. doi: 10.1007/s13311-013-0207-4

42. Kwak TH, Kang JH, Hali S, et al. Generation of homogeneous midbrain organoids with in vivo-like cellular composition facilitates neurotoxin-based Parkinson's disease modeling. *Stem Cells.* 2020;38(6),727-740. doi: 10.1002/stem.3163

ACCSCIENCE PUBLISHING

International Journal of Bioprinting

RESEARCH ARTICLE

Optimizing printability and mechanical properties of poly(3-hydroxybutyrate) biocomposite blends and their biological response to Saos-2 cells

Štěpán Krobot[1]*, Přemysl Menčík[1], Kateřina Chaloupková[1], Ján Bočkaj[2], Sára Vach Agócsová[2], Michala Klusáček Rampichová[3], Věra Hedvičáková[3], Pavol Alexy[2], Radek Přikryl[1], and Veronika Melčová[1]*

[1]Institute of Material Chemistry, Faculty of Chemistry, Brno University of Technology, Brno, Czech Republic

[2]Faculty of Chemical and Food Technology, Institute of Natural and Synthetic Polymers, Slovak University of Technology in Bratislava, Bratislava, Slovakia

[3]Institute of Experimental Medicine, Czech Academy of Sciences, Prague, Czech Republic

(This article belongs to the Special Issue: *3D Printing for Tissue Engineering and Regenerative Medicine-Series 2*)

Abstract

Bone tissue engineering requires scaffolds with three-dimensional (3D) structures that facilitate vascularization and new tissue growth. 3D printing, especially through fused deposition modeling (FDM), has emerged as an effective method for creating complex structures with high reproducibility. Early research in this area demonstrated the potential of poly(ε-caprolactone) (PCL) and poly(L-lactide) (PLLA) scaffolds for bone regeneration. Recently, polylactide (PLA) and polyhydroxyalkanoates (PHAs) have garnered attention for their biocompatibility and ability to support cell proliferation. Among PHAs, poly(3-hydroxybutyrate) (PHB) shows promise due to its intrinsic biocompatibility and resorbability, making it a candidate for FDM-based scaffold fabrication. In the presented study, we aim to develop and optimize a biocompatible PHB-based composite material for bone tissue engineering, incorporating PLA, hydroxyapatite, and the plasticizer Syncroflex 3114 to enhance mechanical properties and printability. This composite was processed into filaments for 3D printing and characterized through thermal, mechanical, and biological evaluations. Using a design of experiment approach, we investigated factors such as temperature performance, warping, degradation, and strength to determine the optimal composition for use in tissue engineering. Four optimal mixture compositions fulfilling the optimization criteria of having the most suitable properties for bone tissue engineering, namely the best printability and maximum mechanical properties, were obtained. The mixtures were optimized specifically for minimum warping coefficient (0.5); maximum flexural strength (66.9 MPa); maximum compression modulus (2.4 GPa); and maximum compression modulus (2.3 GPa) with a warping coefficient of no more than 1 at the same time. In conclusion, the study shows a new possible way to effectively develop and test 3D-printed PHB-based scaffolds with specifically optimized material properties.

Keywords: 3D printing; Design of experiment; Fused deposition modeling; Poly(3-hydroxybutyrate); Polylactide; Printability; Scaffold

***Corresponding authors:**
Štěpán Krobot
(Stepan.Krobot@vutbr.cz)

Veronika Melčová
(xcmelcova@fch.vut.cz)

Citation: Krobot S, Menčík P, Chaloupková K, et al. Optimizing printability and mechanical properties of poly(3-hydroxybutyrate) biocomposite blends and their biological response to Saos-2 cells. *Int J Bioprint*. 2025;11(1):400-417. doi: 10.36922/ijb.5175

Received: October 16, 2024
Revised: November 10, 2024
Accepted: December 3, 2024
Published Online: December 4, 2024

Copyright: © 2024 Author(s). This is an Open Access article distributed under the terms of the Creative Commons Attribution License, permitting distribution, and reproduction in any medium, provided the original work is properly cited.

Publisher's Note: AccScience Publishing remains neutral with regard to jurisdictional claims in published maps and institutional affiliations.

1. Introduction

Among the broad range of requirements for bone tissue engineering scaffolds, having a suitable three-dimensional (3D) structure allowing vascularization and growth of the new tissue stands as an important criterion.[1] This can be achieved by 3D printing, which offers effective production of complex structures with high reproducibility.[2–4] Nowadays, the most common 3D printing technique is fused deposition modeling (FDM), which can be exploited for biopolymers as well.[5–9]

The first FDM-printed scaffolds for bone tissue engineering emerged in 2001. Hutmacher et al.[10] 3D-printed poly(ε-caprolactone) (PCL) scaffolds with honeycomb and lay-down pattern structures featuring good adhesion and proliferation of human fibroblasts and osteoprogenitor cells and a compression stiffness of 42 MPa. Xiong et al.[11] fabricated poly(L-lactide) (PLLA) grid structures with a compression yield strength of 8 MPa. Further research in this field was focused on the thorough characterization of scaffold properties or performance tuning by (1) the addition of bioactive filler; (2) blending with other biopolymers; (3) change of internal 3D structure; or (4) surface modifications.

Regarding PCL, the mechanical properties of 3D-printed scaffolds with varying porosity and pore size have been described.[12–15] Also, a composite of PCL with bioactive glass was found to be printable and showed higher proliferation of human fibroblasts and increased compressive modulus than neat polymer.[16] Nevertheless, the most studied PCL-based material for FDM 3D printing is composite with tricalcium phosphate (TCP).[17–21] This material was subjected to tests *in vivo*, for example on rat critical-sized femoral defect model by Rai et al.[18] and on porcine mandibular defects by Konopnicki et al.[20] Currently, the material is approved for humans in the craniofacial region[22] and is commercially available.[23]

As for polylactide (PLA), the progress in the field of bone replacement prepared by all 3D printing techniques has been reviewed by Chen et al.[24] PLA scaffolds show biocompatibility and suitable viability and proliferation of osteosarcoma cells[25] and higher viability of human osteoblasts (hFOB) than titanium sample.[26] In terms of mechanical properties, the gyroid structure is currently in the spotlight.[27–29] First described in 1970 by Schoen,[30] it has an open porosity and high strength per weight. The possibility of printing PLA composites with bioactive inorganics, such as TCP,[31–33] bioactive glass,[34] and mostly hydroxyapatite (HA),[35–40] has also been reported. Matsuo et al.[35] observed better bone healing for a PLLA with 50 wt% HA in two patients with mandibular injuries than with titanium.

Another interesting group of materials often exploited for tissue engineering are polyhydroxyalkanoates (PHA).[41] PHA has been utilized in the field of FDM-printed scaffolds for bone replacement from the start and often acts as a secondary polymer in the blend with PCL[42] or PLA[43–49] nowadays. In the last years, successful attempts at FDM printing of materials with a PHA majority emerged. One such example is poly(3-hydroxybutyrate-co-3-hydroxyhexanoate) (PHBH). In 2020, a PHBH composite containing acetylated nanocellulose with improved thermomechanical properties[50] and PHBH scaffolds compatible with mouse 3T3 fibroblast cells and degradable in synthetic gastric juice[51] were reported. In 2022, Dong et al.[52] created and seeded PHBH structures with costal cartilage and tested for a nipple reconstruction *in vivo* with promising results. The mechanical properties of PHBH scaffolds were characterized as well.[53,54] Another example is poly(3-hydroxybutyrate-co-3-hydroxyvalerate) (PHBV) and 3D-printed scaffolds from its composite with bioglass, which are compatible with mouse preosteoblasts MC3T3-E1 cells.[55] Ye et al. demonstrated a PHA filled with up to 30 wt% of TCP featuring a compressive strength of 37 MPa, which showed improved response of MC3T3-E1 cells compared to non-filled PHA. However, the type of PHA used was not specified.[56]

Last but not least, poly(3-hydroxybutyrate) (PHB) biopolymer offers intrinsic biocompatibility and resorbability which also applies to its degradation products. Moreover, PHB stands out with the mechanical properties appropriate to the replacement of hard tissue.[57–60] Thermal instability and the complex processability of PHB pose a major challenge for FDM. Therefore, PHB was first printed by selective laser sintering (SLS) method by Pereira et al.[61] To our knowledge, FDM-printed blends with most PHB majority for tissue engineering are scarcely described in the literature, except for publications stemmig from our research group.[62,63] Kanabenja et al.[64] prepared a PHB/PLA 70/30 blend plasticized with polypropylene glycol (PPG) with different dosages of HA and characterized its thermomechanical properties, crystal structure, and flowability. Moroni et al. [65] verified the possibility of using PHB for 3D printing by direct powder extrusion one-step method. Moreover, PHB was loaded with a model drug up to 30 wt% and tested for a prolonged release for 20 days.

In this study, we aim to characterize the important thermal, mechanical, and biological properties of the plasticized material PHB/PLA filled with HA across a range of compositions applicable to FDM 3D printing. The novelty of this research is the use of an innovative

biocomposite material whose composition can be tailored to the desired properties. Using the design of the experiment method, we also aim to identify the composition of optimized material for tissue engineering of bones and predict its properties. The polymer matrix consisted of predominantly PHB, supplemented with a smaller proportion of PLA. PHB was chosen due to its inherent biocompatibility, biodegradability, suitable processability, and mixability with other biopolymers for improved properties.

2. Materials and methods

2.1. Materials

Polymer mixtures contained poly(3-hydroxybutyrate) (PHB) EDW 2394 from TianAn (Ningbo City, China) and amorphous poly(D,L-lactide) (PLA) Ingeo™ Biopolymer 4060D from NatureWorks (Minnetonka, MN, USA). The used plasticizer is Syncroflex™ 3114 (abbreviated as SN) from Croda (Rawcliff, UK). Bioactive ceramics hydroxyapatite/tricalcium phosphate blend (abbreviated as HA) from AppliChem (Darmstadt, Germany) with D_{50} = 2.8 μm was used for the blends of the design of experiments.

2.2. Design of experiment

In order to find the optimal proportions of the components of the PHB/PLA/SN/HA mixture, a 3-factor, 5-level Design of Experiment (DoE) test was conducted. The factors and their limits were set as follows:

- Factor 1; x_1 = PLA/PHB ranged from 5/95 to 50/50 so that most of the PHB content added is retained;
- Factor 2; x_2 = HA/(PHB+PLA) ranged from 5/95 to 30/70 due to expected limits in processability;
- Factor 3; x_3 = SN/(PHB+PLA+HA), the SN content in the whole mixture ranged from 5.6 to 12.4 wt%.

Factor 1 corresponds to the polymer matrix of the material which is the basis for the 3D-printed specimen. The ratio of PHB/PLA thus reflects the retainment of PHB in the mixture. Factor 2 corresponds to the addition of the bioactive filler to the matrix. In theory and under ideal conditions, an larger amount of filler added would lead to a better biological response. Factor 3 corresponds to the addition of the plasticizer to the matrix because a larger amount of plasticizer added is associated with better processability of the material and smoother process of 3D printing.

Real values and steps of the experiment for coded levels are listed in Table 1. The real limit values in coded levels −1.682 and 1.682 correspond with the borderline composition of the samples described above. The middle value of the factor is located on the coded coordinate 0. The confidence interval was 95%.

2.2.1. Sample composition

Subsequently, the mathematical matrix of samples with assigned coordinates in coded levels was created. The composition of individual mixtures (referred to as Mix 1–Mix 20) was calculated from the assigned coded levels using real values in Table 1. The actual composition of all prepared samples is given in Table 2. Mixtures 9–14 contain limit values of one of the factors while the rest of the factors are located at the middle value. In other words, on these mixtures, we can observe the effect of the maximum/minimum content of individual mixture components in the tested range on measured properties. The samples Mix 15–20 have all the factors in coded level 0, in the middle of the composition range. These samples are included to provide the statistical error of the measurement.

2.2.2. Results evaluation

Measured data were fitted with a 3D curve given by the following equation:

$$y = b_0 + b_1x_1 + b_2x_2 + b_3x_3 + b_{11}x_1^2 + b_{22}x_2^2 + b_{33}x_3^2 + b_{12}x_1x_2 + b_{13}x_1x_3 + b_{23}x_2x_3, \quad (1)$$

where x_{1-3} are factors of the experiment and b_{ij} are coefficients indexed with numbers 1–3 according to the DoE factor they relate to. The coefficients b_{1-3} indicate the degree of linear dependence of the measured parameter on the corresponding factor. The coefficients b_{11-33} give the degree of quadratic dependence of the measured

Table 1. Values of DoE in coded and real levels.

	Real values of the experiment					
Coded levels	**−1.682**	**−1**	**0**	**1**	**1.682**	**Step**
x_1 PLA/PHB	0.0526	0.2447	0.5263	0.8079	1.0000	0.2816
x_2 HA/(PHB+PLA)	0.0526	0.1288	0.2406	0.3524	0.4286	0.1118
x_3 SN/(PHB+PLA+HA)	0.0593	0.0760	0.1004	0.1249	0.1416	0.0244

Abbreviations: DoE, design of experiment; HA, hydroxyapatite; PHB, poly(3-hydroxybutyrate); PLA, polylactide; SN, Syncroflex™ 3114.

Table 2. Prepared samples with their composition in coded levels and respective weight fractions

	Factors in coded Levels			The actual composition			
Sample name	PLA/PHB	HA/ (PHB+PLA)	SN/ (PHB+PLA+HA)	PHB (wt%)	PLA (wt%)	SN (wt%)	HA (wt%)
Mix 1	−1	−1	−1	66	16	7	11
Mix 2	1	−1	−1	46	37	7	11
Mix 3	−1	1	−1	55	14	7	24
Mix 4	1	1	−1	38	31	7	24
Mix 5	−1	−1	1	63	15	11	10
Mix 6	1	−1	1	44	35	11	10
Mix 7	−1	1	1	53	13	11	23
Mix 8	1	1	1	36	29	11	23
Mix 9	−1.682	0	0	70	4	9	18
Mix 10	1.682	0	0	37	37	9	18
Mix 11	0	−1.682	0	57	30	9	5
Mix 12	0	1.682	0	42	22	9	27
Mix 13	0	0	−1.682	50	26	6	18
Mix 14	0	0	1.682	46	24	12	17
Mix 15–20	0	0	0	48	25	9	18

Abbreviations: HA, hydroxyapatite; PHB, poly(3-hydroxybutyrate); PLA, polylactide; SN, Syncroflex™ 3114.

parameter on the corresponding factor. Last but not least, the coefficients $b_{12/13/23}$ quantify the mutual effect of two factors. Statistical analysis of standard deviations of the results yields all coefficients together with their statistical relevance. Measured data are represented as 3D graphs, with two of the most statistically relevant factors on axes x and y. The third factor was fixed at a constant level.

2.3. Filament preparation

A total of 700 g of all mixtures was prepared. Compounding was performed with the corotating meshing twin screw extruder from Labtech Engineering Company (Samutprakarn, Thailand) with a screw diameter of 16 mm and length (L) diameter (D) ratio (L/D) of 40. The temperature setting from hopper to nozzle was: 60-120-180-190-190-190-170-160-160°C and the used rotations were 150 rpm. Granules were fed into a single screw extruder HAAKE Rheomex OS (Haake Technik GmbH, Vreden, Germany) with a screw diameter of 19 mm and an L/D of 30 and extruded into the form of 3D printing filaments. The temperature setting from hopper to nozzle was: 180-185-180-170°C for all samples except for Mix 5, 6 and 11, where the second heating zone setting was at 190°C. Rotations were set to 20 rpm. The filament diameter of 1.75 mm was controlled during the whole extrusion process.

2.4. Thermal properties

Basic thermal characterization was performed with differential scanning calorimetry (DSC) using DSC 2500 from TA Instrument (New Castle, DE, USA). The samples weighing 10–14 mg were hermetically sealed in aluminum pans and subjected to two heating cycles from −30 to 200°C with a 10°C·min^{-1} heating/cooling rate under a nitrogen atmosphere (50 mL·min^{-1}).

2.5. 3D printing

FDM 3D printer Original Prusa i3 MK3s (Prusa Research a.s., Prague, Czech Republic) was used with a nozzle with a standard diameter of 0.4 mm, controlled by the V3.9.0 firmware version manufactured by Prusa Research a.s. (Prague, Czech Republic). Another relevant setting of the printer is the printed layer height and width of 0.2 mm and 0.45 mm, respectively; the perimeter printing speed of 45 mm·s^{-1}; and the infill printing speed of 200 mm·s^{-1}. G-codes were prepared in PrusaSlicer, software version 1.41.2 (Prusa Research a.s., Prague, Czech Republic). PrusaSlicer is based on an open-source platform called Slic3r, which is licensed under the GNU Affero General Public License, version 3.

Firstly, optimal printing temperature was sought using a temperature tower test (TTT).[66] Each tower floor was printed with a different temperature. The geometrical elements present on each floor were visually evaluated and

compared as described in detail elsewhere.[66] Three towers were printed, covering temperature ranges of 220–195°C, 195–170°C and 170–150°C. The highest temperature of each aforementioned interval was recorded at the bottom of the corresponding tower, and each next floor was printed with a temperature which was 5°C lower.

Two temperatures identified by TTT were used for the warping test and fine-tuning of the printing conditions. During this test, the height of the specimen at the moment of its detachment from the printing bed was monitored, as described in our previous publications.[66] At least five testing specimens were measured.

2.6. Mechanical tests

2.6.1. Flexural test

Six standard test specimens for the three-point bending test with dimensions of 80 × 10 × 4 mm^3 were printed using optimized printing conditions for individual mixtures. Measurement was performed according to the ISO 178 standard method A using the universal testing device ZwickRoell Z010 (ZwickRoell GmbH & Co., Ulm, Germany) with a load indicator of maximum force 1 kN. The radius of the support and load was 5 mm, and the span was 64 mm. The flexural modulus was determined from the deformation range of 0.05–0.25%. The test speed was set to 2 $mm \cdot min^{-1}$ and the limit deformation to 10%.

2.6.2. Compression test

Optimized printing conditions were also used for the printing of the six standard test specimens for the compression test with dimensions of 10 × 4 × 10 mm^3. The standard ISO 604 was followed. ZwickRoell Z010 (ZwickRoell GmbH & Co., Ulm, Germany) with a load indicator of maximum force 10 kN was used. The compression modulus was determined from the deformation range of 1.25–1.50%. The test speed was 1 $mm \cdot min^{-1}$ and the limit deformation was 10%.

2.7. Biological tests

Planar testing specimens with 6 mm diameter and 1.5 mm height were printed with the surface composed of individual perimeters—the *top layer full* setting. At the same time, the granules of Mix 9, Mix 10, and Mix 15 were compression-molded to 1 mm thickness, and rounded specimens were cut out of the formed plates as a control to monitor the possible negative effect of 3D printing on the biocompatibility of the samples. All prepared scaffolds were sterilized in 70% ethanol for 30 min and then rinsed with phosphate-buffered saline (PBS) three times. Sterile scaffolds were placed into 96-well plates and 20 µL of differentiation culture medium containing 2 × 10^4 Saos-2 cells was added. The culture medium contained McCoy's medium (Sigma Aldrich) with 15% fetal bovine serum (FBS), 1% antibiotics (100 $\mu L \cdot mL^{-1}$ penicillin and 100 $\mu L \cdot mL^{-1}$ streptomycin; Sigma Aldrich), 10 nM dexamethasone (Medochemie), 2 mM β-glycerol phosphate (Sigma Aldrich) and 50 $\mu L \cdot mL^{-1}$ ascorbic acid-2-phosphate (Sigma Aldrich).

2.7.1. Metabolic activity assay

To determine the metabolic activity of the cells, metabolic activity assay (MTS) was conducted using CellTiter 96® AQueous One Solution Cell Proliferation Assay (Promega Corporation, WI, USA). The samples were transferred to clean wells and covered with 20 µL of MTS solution and 100 µL of fresh culture medium according to a standard procedure, which is already published.[62] In the control group, only the medium was aspirated and replaced with MTS solution and fresh medium. The samples were incubated in the solution for 2 h at 37°C. The absorbance was measured using an Infinite M200 PRO spectrophotometer (Tecan, Switzerland) at 490 and 690 nm wavelengths. The value measured on the sample incubated without cells was subtracted from the measured values. The value measured in the culture medium with MTS solution was subtracted from the cells on the culture plastic.

2.7.2. DNA quantification

Quantification of cellular DNA was performed using the Quant-iT™ dsDNA Assay Kit (Life Technologies). After MTS measurement, samples were placed in 200 µL lysis buffer (0.2% v/v Triton X-100, 10 mM Tris [pH 7.0], and 1 mM EDTA) and lysed in three freeze/thaw cycles, with thorough vortexing in between the cycles. During the analysis, 20 µL of cell lysate from each sample was added to 200 µL of reaction solution. The fluorescence signal intensity was measured using a fluorescence reader (Infinite M200 PRO, Tecan, Switzerland; λ_{ex} = 485 nm, λ_{em} = 523 nm). The results were evaluated using the calibration curve included in the kit.

2.7.3. Cell visualization

The distribution of cells and their shape was visualized using confocal microscopy. The samples were fixed with frozen methanol (−20°C) for 10 min. Subsequently, fluorescent probe 3,3′-diethyloxacarbocyanine iodide (DiOC6(3); 1 $\mu g \cdot mL^{-1}$ in PBS [pH 7.4]; Invitrogen) was added and incubated with the samples for 30 min at room temperature. Afterwards, propidium iodide (PI; 5 $\mu g \cdot mL^{-1}$ in PBS; Sigma Aldrich) was added for 5 min at room temperature. Subsequently, the samples were rinsed with PBS and visualized using a confocal microscope (Zeiss LSM 880 Airyscan, Oberkochen, Germany). The wavelengths used were λ_{ex} = 488 nm and λ_{em} = 520 nm for DiOC6(3) and λ_{ex} = 560 nm and λ_{em} = 580 nm for propidium iodide. Images obtained from confocal microscopy were further

used for depth cell penetration analysis. The individual images of different samples were color-coded based on their position along the Z axis. These colors correspond to the Z-axis scale in the Zeiss ZEN software, representing the position of the cells within the scaffold.

2.7.4. Alkaline phosphatase activity

Alkaline phosphatase (ALP) activity was measured as an indicator of osteogenic differentiation. The scaffolds were rinsed with PBS. Subsequently, 100 µL of ALP substrate (p-Nitrophenyl Phosphate Liquid Substrate System; Life Technologies) was added and the cells were incubated for 15 min in the dark at room temperature. After incubation, 66.6 µL of cell solution was pipetted into a new plate and 33.3 µL of 2 M NaOH solution was added to each well to stop the entire reaction. Formed ρ-nitrophenol was detected on a Synergy HT reader (BioTek Synergy HT, BioTek Instruments, Inc., USA) at a wavelength of 405 nm. The absorbance of the ALP substrate with cell carriers without cells was subtracted from the individual values.

2.7.5. Mineralization

Alizarin Red S Staining Quantification Assay kit (ARed-Q; ScienCell) was used to detect mineralization on scaffolds. Alizarin Red S forms a complex with calcium compounds in the chelation process resulting in a bright red product. After measuring ALP activity, the samples were firstly rinsed three times with PBS and then fixed in 3.6% formaldehyde (in PBS) for 15 min at room temperature. After removing the formaldehyde, the samples were rinsed three times in distilled water. The distilled water was removed and 0.1 mL of 40 mM ARS was added per well, followed by a 20-min incubation with gentle shaking. Subsequently, the samples were thoroughly rinsed in distilled water until the water was colored. Finally, the samples were photographed.

2.7.6. Statistical analysis

Six samples were used for all measurements, and at least four results were used for statistical analysis. Data were evaluated using GraphPad Prism 9.1.1. software (GraphPad Software, Boston, MA, USA). For data passing the normality test and the equality of variances test, pairwise analysis was performed using analysis of variance (ANOVA) and Tukey's comparison test for post hoc analysis. If the data were non-normally distributed, pairwise analysis was performed using Kruskal–Wallis test and Dunn's multiple comparison test for post hoc analysis. All results were considered statistically significant if $p < 0.05$.

3. Results and discussion

3.1. Thermal properties

The basic thermal properties of the prepared mixtures were characterized using DSC. The PLA used is amorphous, with a glass transition temperature of 52.2°C. Neat PHB exhibits mild T_g around 0.2°C and has a melting peak with a maximum of 172.4°C. The crystallinity of neat PHB is around 61%. In the mixtures, the glass transition of PHB was undetectable. T_g of PLA lies in the range 31–46°C and is driven by factor 3 (plasticizer content, SN/(PHB+PLA+HA)) as the only statistically significant coefficient from **Equation I** is linear (b_3). The coefficient is negative; therefore, the higher the plasticizer amount, the lower the glass transition temperature of PLA. The measured melting temperature of PHB lies between 161 and 171°C; however, no statistically significant dependency was proven. PHB crystallinity in the prepared composite mixtures was in the range of 52–64%. The statistically significant coefficient is quadratic b_{22}, which is connected to the factor 2 (HA/(PHB+PLA)). The coefficient has a negative value, thus there is a maximum of crystallinity at medium values of HA amount of the tested range.

3.2. Printability

During printing, it was verified that the edge limits of the experiment in PHB content (factor 1) and filler content (factor 2) are at the limit of the material's printability as well. The mixture with the highest amount of PHB (Mix 9) and HA (Mix 12) showed a profound brittleness and cracking during the unwinding of the filament, making them very user-unfriendly for FDM 3D printing. A suitable nozzle temperature for printing was identified by TTT and fine-tuned by warping measurement. It is important to note that this parameter combines the visual quality of the printed specimen (possible stringing, voids, or overhanging on some geometric elements) and the warping behavior; therefore, it includes both the rheology of the mixture during processing in 3D-printed extruder and the cooling behavior of the mixture. Figure 1 plots the dependence of the used printing temperature on factor 1 (PLA/PHA ratio) and factor 3 (plasticizer content), while factor 2 (HA amount) was fixed. Coefficients b_{12} and b_{23} combining the effect of filler addition with biopolymers ratio and plasticizer content, respectively, have the greatest influence on the printing temperature.

Factors 1 and 3 both have negative quadratic influences creating a dependency plane with a distinct maximum. Another significant contribution is the effects of linear coefficients related to the PLA/PHB ratio and the plasticizer content, which is evident in Figure 1B. The dependency of the printing temperature does not correlate with the PHB's melting temperature.

Generally, the primary cause of warpage during printing is thermal stresses in the printed specimen.[67] The cooling behavior and therefore the built-up residual stress of the specimen printed from amorphous and semi-

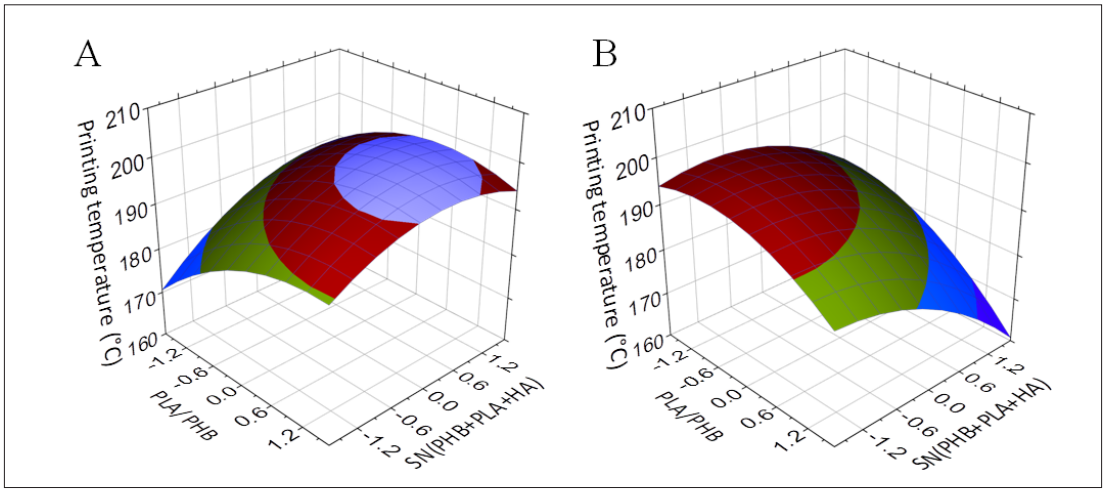

Figure 1. Printing temperature as a function of factor 1 (PHB/PLA) and factor 3 (SN/(PHB+PLA+HA)) with factor 2 (HA/(PHB+PLA)) set at the lowest amount of HA tested (A) and the highest amount of HA tested (B). Abbreviations: HA, hydroxyapatite; PHB, poly(3-hydroxybutyrate); PLA, polylactide; SN, Syncroflex™ 3114.

crystalline material differs profoundly.[68] Warping of studied mixtures can be mostly attributed to the crystallization of PHB during cooling. Therefore, it can be assumed that the higher the PHB content, the higher the warping coefficient. Indeed, the sample Mix 9 containing 70% PHB exhibited a warping coefficient of 10, meaning the testing specimen detached from the printing bed immediately upon start. Mix 7 also showed a profound warping during printing, and on the contrary, Mix 2 proved to be easy to process. Statistical evaluation supported that the PLA/PHB ratio has the major effect on warpage. A combination of linear and quadratic contribution is applied as can be seen from the graphs in Figure 2, where two plots of the dependence of the warping coefficient on factor 1 (PLA/PHA ratio) and factor 3 (plasticizer content) are shown, with a fixed value of factor 2 (HA amount). The addition of amorphous PLA content to the PHB/PLA blend reduces the warping coefficient. At the same time, due to the effect of the quadratic coefficient, there is a minimum in the dependence, which is desirable to reach. On the contrary, we can see a lower value of the warping coefficient at extreme values of the plasticizer factor, meaning around the minimum and maximum tested amount of the plasticizer. The addition of HA slightly increases the overall warping coefficient. For comparison, the warping coefficient value for commercially available PLA filament (Prusa Research, Prague, Czech Republic) is 2.9 ± 0.1. Apart from the composition of the blend, the warpage could be reduced by fine-tuning printing parameters, such as increasing the printing speed.[69]

3.3. Mechanical properties

For a successful replacement, it is important for the scaffold's mechanical properties to resemble those of the natural bone as much as possible. All materials were tested for mechanical properties under bending and compression, which simulate the stress naturally acting on a bone.

Flexural modulus and strength were evaluated, and their dependency on the most dominant composition-related factors is given in Figure 3. Flexural modulus lies in the region 2.3–3.7 GPa, the highest values were reached by Mix 4, 13, and 3, the mixtures with a high HA content and low plasticizer content. The lowest modulus was reached with Mix 5 and 6, which contain 10% of HA and 11% of the plasticizer. Statistically, all three factors significantly influence the modulus. The plasticizer content (factor 3) is the most important; the higher the SN content, the lower the modulus. On the other hand, the addition of PLA and HA has a positive effect on modulus, but the effect is 1–2 times weaker. In Figure 3A, there is the dependency of flexural modulus on factors 1 and 3 for the lowest tested amount of HA, and on the right is the dependency for the highest tested amount of HA. With the same amounts of SN and PLA/PHB ratio, only with an addition of HA, we achieve a 1 GPa modulus increase. Other statistically significant coefficients are b_{13} and b_{23} combining the influence of the plasticizer with the other two factors, which means that the plasticizer interacts not only with polymers but also with ceramic. Both are negative and reduce the flexural modulus.

The flexural strength of the measured samples is in the range of 36–59 MPa; the highest values were measured in Mix 2 and 13, followed by Mix 4. Similar to modulus, the flexural strength is mainly driven by the addition of plasticizer, which has a negative effect on this parameter, as depicted in Figure 3C and D. The second factor in

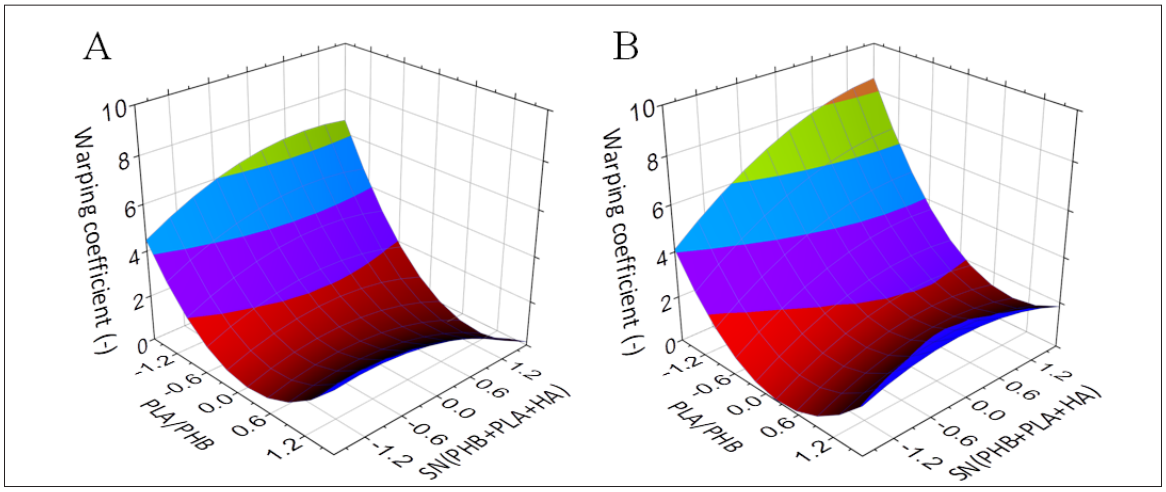

Figure 2. Warping coefficient as a function of factor 1 (PHB/PLA) and factor 3 (SN/(PHB+PLA+HA)) with factor 2 (HA/(PHB+PLA)) set at the lowest amount of HA tested (A) and the highest amount of HA tested (B). Abbreviations: HA, hydroxyapatite; PHB, poly(3-hydroxybutyrate); PLA, polylactide; SN, Syncroflex™ 3114.

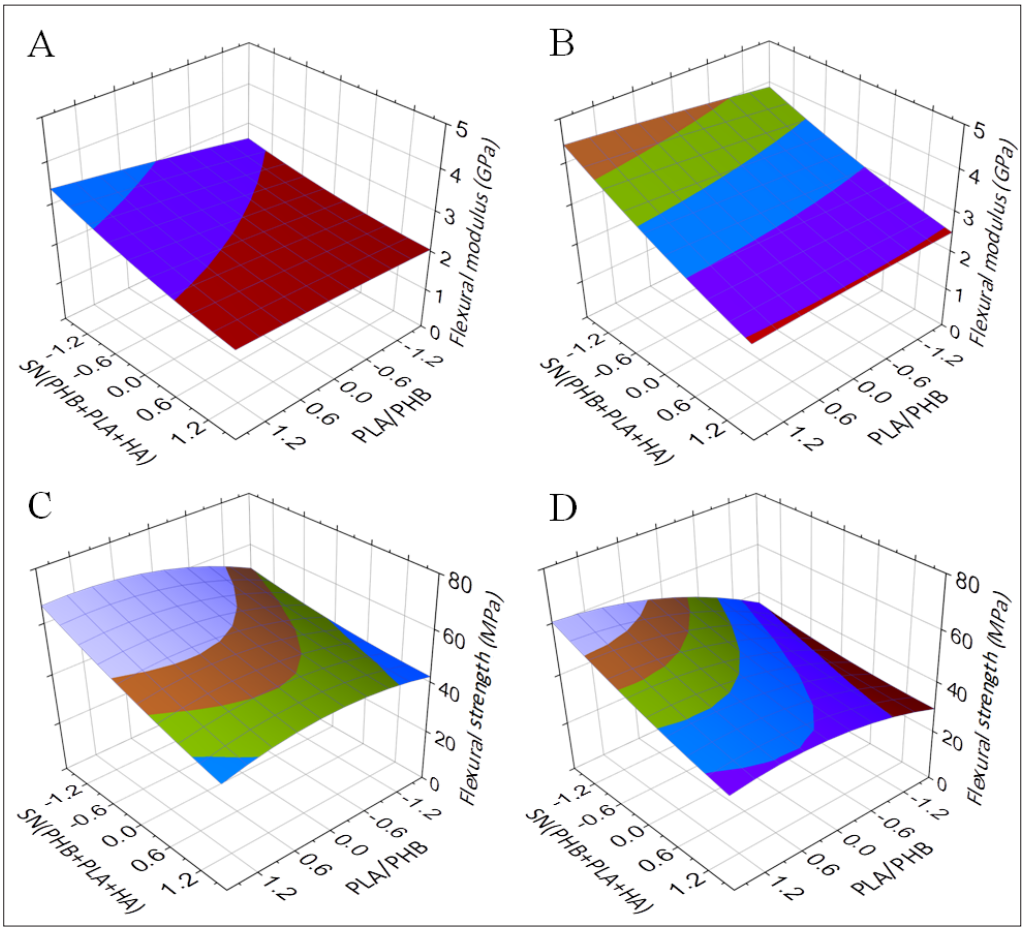

Figure 3. Flexural properties as a function of factor 3 (SN/(PHB+PLA+HA)) and factor 1 (PHB/PLA). Top panels: flexural modulus for factor 2 (HA/(PHB+PLA)) set at the lowest amount of HA tested (left) and the highest amount of HA tested (right). Bottom panels: flexural strength for factor 2 (HA/(PHB+PLA)) set at the lowest amount of HA tested (left) and the highest amount of HA tested (right). Abbreviations: HA, hydroxyapatite; PHB, poly(3-hydroxybutyrate); PLA, polylactide; SN, Syncroflex™ 3114.

relevance is the PLA/PHB ratio for which linear and quadratic coefficients are significant. Thus, the maximum flexural strength can be achieved with an intermediate PLA/PHB ratio of the tested range. The increase in HA content, although increasing the modulus, lowers the obtained flexural strength. In addition, coefficients b_{12} and b_{13} are statistically significant, therefore combining factor 1 with the two others. Practically, this means that the factors combine with each other and the effect of the addition of SN or HA differs depending on the PLA/PHB ratio.

Elastic modulus evaluated from a compression test is approximately two times lower than from a bending test, lying in the range of 0.9–1.8 GPa. The mixtures with the highest measured modulus and as well as the highest compression stress at 1% relative deformation are Mix 4 and 13. On the opposite side of the scale is Mix 6. The only two statistically significant coefficients from **Equation I** are b_2 and b_3, which relate to a linear contribution of factor 2 and factor 3, respectively. As can be also seen in Figure 4, the addition of plasticizer decreases the compression modulus while the addition of HA has a positive influence. The compressive strength of the PHA/20%β-TCP scaffold was 36.7 MPa, and 30% TCP had lower strength.[56] The compressive modulus of elasticity was recorded in the range of 0.8–1.2 GPa with a comparable trend to the compressive load capacity depending on the type of spongiosa and compaction fill. As already mentioned, the modulus of elasticity of the compact part of the bone is about 18 ± 4 GPa, while that of the porous bone in the femur region is 0.4 ± 0.3 GPa. The reported compressive strength of compact bone is 205 ± 17 MPa.[70] The considerable variance in spongiosa bone is due to the varying mineral content of the patient's bone, with a modulus variance of 50–600 MPa reported for the femoral neck.[71] Other papers also publish a mean value of the modulus of spongiosis in pressure around 100–600 MPa.[72,73] This may be due, as Gonzalez et al.[74] state, to the different temperature gradients of the printed body, which is subsequently reflected in its mechanical properties. Firstly, different crystallinity was observed in the lower and upper part of the printed body, secondly, this will also depend on the cohesion between the printed layers.[46] The presence of ceramic nanoparticles in a 3D-printed sample can lead to an improvement in its mechanical properties as long as there is no agglomeration of these nanoparticles.[75]

3.4. Biological response

Metabolic activity was measured using the MTS assay on days 1, 7, 14, and 21 of the experiment (**Figure 5**). The highest metabolic activity 24 h after placing the cells on the carriers was observed on the culture plastic (TCP), followed by the groups Mix 13 (the sample with the lowest amount of SN) and 12 (the highest amount of HA). The same applies on the 7th day of the experiment. On day 14, the metabolic activity of all 3D-printed samples was lower than for the TCP. On day 14 of the test, the values were comparable for all 3D-printed samples except for Mix 11 (the lowest amount of HA) and Mix 14 (the highest amount of SN), which exhibited the lowest metabolic activity. Although lower values were measured for Mix 15 (middle values of the composition) at the beginning of the experiment, on the 14th day, the metabolic activity was equal to that of the other groups. On day 21, the lowest metabolic activity was measured on Mix 11 and Mix 14. In

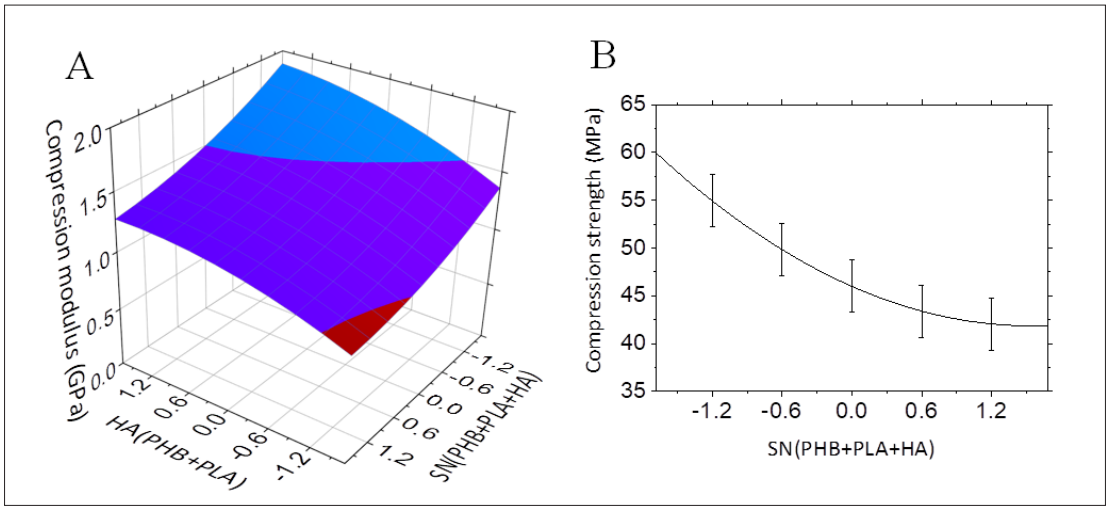

Figure 4. Compression modulus as a function of factor 3 (SN/(PHB+PLA+HA)) and factor 2 (HA/(PHB+PLA)) with factor 1 (PLA/PHB) set to an intermediate level (A), and compression strength as a function of factor 3 (B). Abbreviations: HA, hydroxyapatite; PHB, poly(3-hydroxybutyrate); PLA, Polylactide; SN, Syncroflex™ 3114.

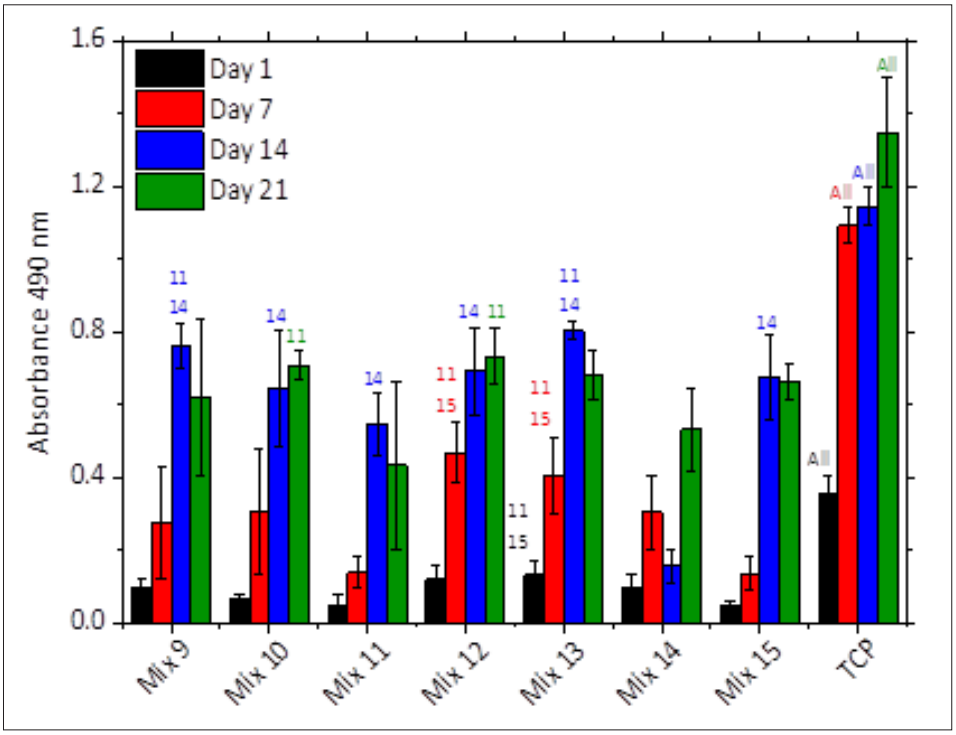

Figure 5. Metabolic activity of cells on 3D-printed supports measured by MTS. Saos-2 cells seeded on tissue culture plastic (TCP) were used as a control. A value above a column indicates that the corresponding group is significantly lower compared to the group represented by that column ($p < 0.05$, Tukey). Abbreviations: MTS, 3-(4,5-Dimethylthiazol-2-yl)-5-(3-carboxymethoxyphenyl)-2-(4-sulfophenyl)-2H-tetrazolium; TCP, tissue culture plastic.

the other groups, the absorbance was equal, but the values were lower than these measured on TCP.

Cell proliferation on 3D printed supports was measured using cellular DNA quantification (Figure 6). The highest amount of cells 24 h after deployment was observed on the culture plastic (TCP), the values were comparable on the other groups. On day 7, most cells were recorded on Mix 13, 10, and 12 scaffolds (see composition in Table 2). On the 14th day, there was a significant increase in the number of cells on Mix 13, even compared to the reference plastics. On the 21st day, there was no increase in the number of cells, and the largest amount of cells was observed on the TCP.

Cell distribution on the 3D-printed scaffolds was monitored by confocal microscopy on days 1, 7, 14, and 21 of the test (Figure 7). Cell nuclei were stained with propidium iodide (red color) and intracellular membranes by DiOC6(3) (green color). The distribution of cells was influenced by the method of cell seeding, through which the cells are seeded in a small drop of the culture medium to adhere to the scaffolds and not to be washed away from their surface. For this reason, the cell density was higher in the center of the carrier and decreased toward the sides. Therefore, it is not possible to deduct the number of cells from microscopy images. However, they reflect the results of the cell proliferation assay quite well. For example, in Mix 10 (PHB/PLA ratio 50/50), a fully confluent layer of cells was visible. On the other hand, the Mix 14 scaffold (the highest plasticizer amount) was evenly covered with cells, relatively sparsely though. On day 21, most samples were densely covered with cells. The fewest cells were observed in Mix 14. In some samples, it was evident that the cell layer had partially peeled off.

3.4.1. Osteogenic differentiation

ALP activity was measured as an indicator of osteogenic cell differentiation with results given in Figure 8. The highest ALP activity 24 h after deployment was observed on the TCP and then on the Mix 14 scaffold. On the 7th day, the highest value was measured for Mix 13 (the mixture with the lowest amount of plasticizer) and the lowest for Mix 14 (the highest amount of plasticizer). On the 14th day of the experiment, the ALP activity continued to increase for all the groups although to the least extent for Mix 14. On the 21st day, there was no further increase in ALP activity and the values were comparable among all samples.

Mineralization occurred in the late phase of cell incubation on the scaffolds as a bright red coloration, as detected on days 14 and 21 of the test (see Figure 9). It is

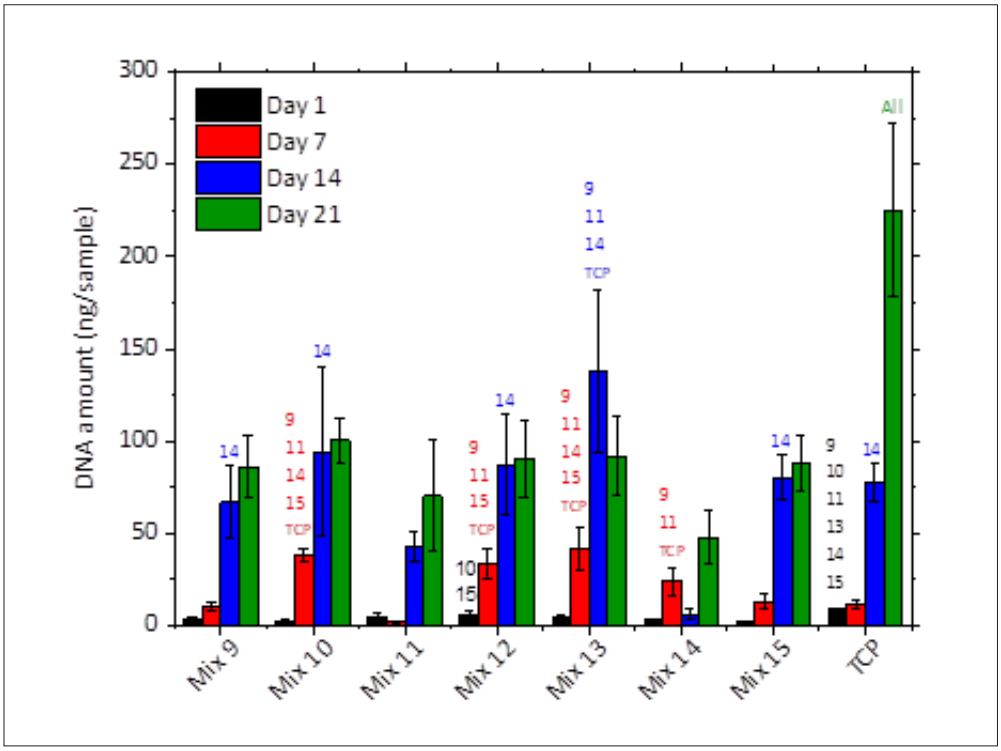

Figure 6. Cell proliferation measured by quantification of cellular DNA. Saos-2 cells seeded on culture plastic (TCP) were used as a control. A value above a column indicates that the corresponding group is significantly lower compared to the group represented by that column ($p < 0.05$, Tukey). Abbreviations: TCP, tissue culture plastic.

evident that the greatest degree of mineralization occurred on Mix 12. On the contrary, we observed a low level of staining on Mix 14. However, there was a large variability between individual samples. On the 21st day, there was an increase in mineralization indicated by more distinct staining, especially in Mix 10, 11, 12, 13, and 15 samples. The lowest mineralization level was observed in Mix 14, which corresponds to a smaller number of cells.

3.5. Optimized blend

From the results, it is possible to find the composition of the mixture within the tested range, which should have the most suitable properties for bone tissue engineering, namely the best printability and maximum mechanical properties. Four mixture compositions fulfilling the following optimization criteria were obtained: minimum warping coefficient; maximum flexural strength; maximum compression modulus; and maximum compression modulus with a warping coefficient of no more than one at the same time.

The fourth mixture is supposed to have an optimal ratio between the printability and mechanical properties and at the same time contains a high amount of bioactive filler, which is important for the biological response. The precise formula of this mixture is 35.2% PHB, 30.8% PLA, 28.3% HA, and 5.6% SN and was named an "optimized" mixture. The compressive strength of compact and trabecular bone is 205 ± 17 and 6.8 ± 4.8 MPa, respectively. The compression modulus of the compact part of the bone is around 18 ± 4 GPa, and for trabecular bone in the femur region, it is 0.4 ± 0.3 GPa.[70] Considerable variance in cancellous bone is due to the different mineral content in the patient's bone; for the femur neck, the modulus variance is from 50 to 600 MPa.[71] Other works have also reported the mean value of the modulus of elasticity in the compression of porous bone at around 100–600 MPa.[72,73,76] Wurm et al.[26] successfully employed FDM for the fabrication of PLA discs and the influence of processing technique upon the biocompatibility of printed parts was assessed. *In vitro* tests using human fetal osteoblasts showed no cytotoxic effects of PLA discs. Since FDM proved no negative influence on the biocompatibility of PLA, this 3D-printing technique could be further used in reconstructive surgery for the production of individual-shaped scaffolds or other implants.[26] PLA modulus encompasses over the range of 10–900 MPa, which spans the complete range of substrate moduli for trabecular bone (93–365 MPa) and the lower end of the range for cortical bone (87–500 MPa).[77] Osteogenic differentiation and mineralization increased as the substrate modulus increased from 10 to 900 MPa(Table 3).[78]

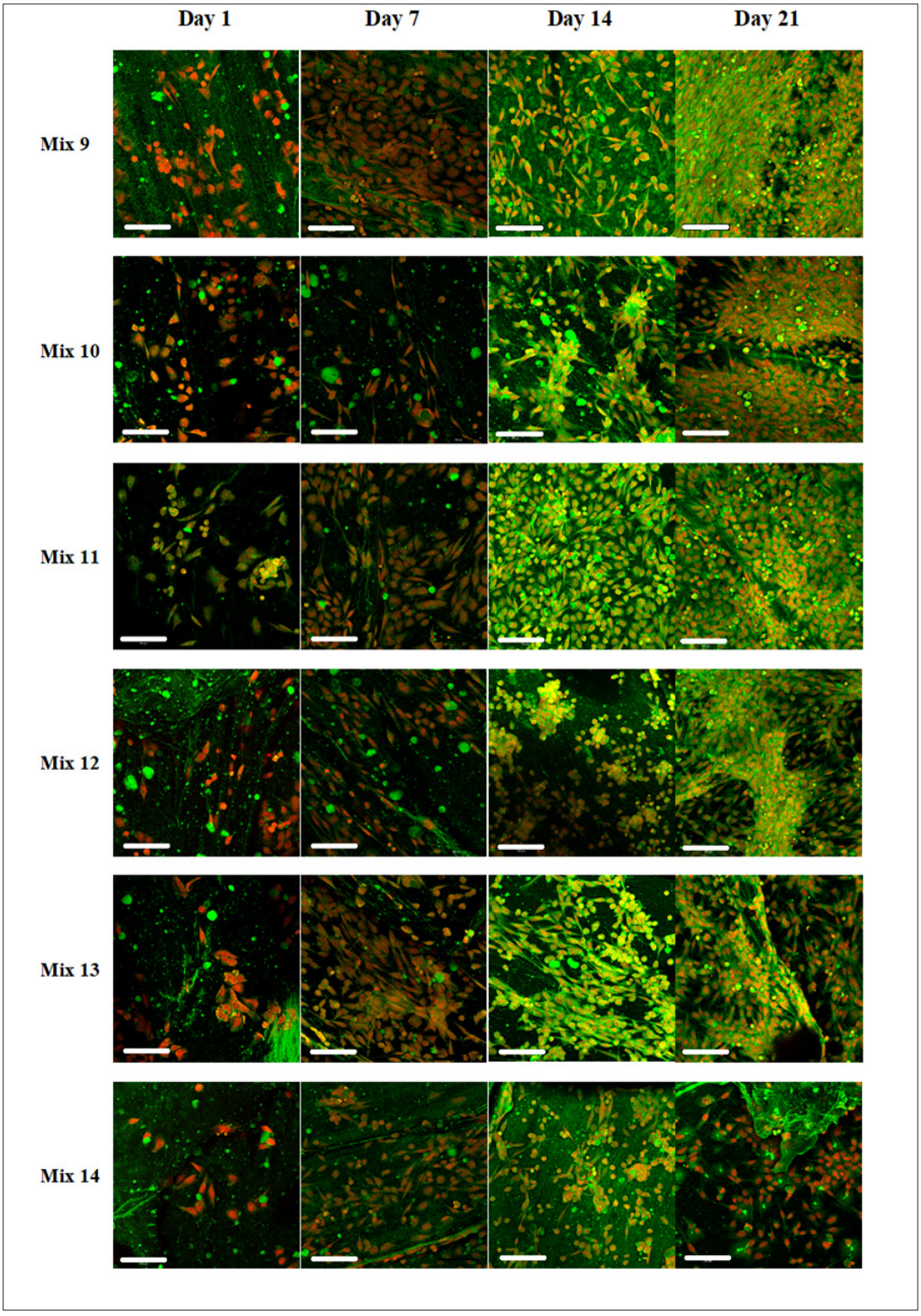

Figure 7. Cell adhesion and proliferation on the carriers on day 1, 7, 14, and 21. Cell nuclei were stained with propidium iodide (red), intracellular membranes with DiOC6(3) (green). Scale bar: 100 μm.

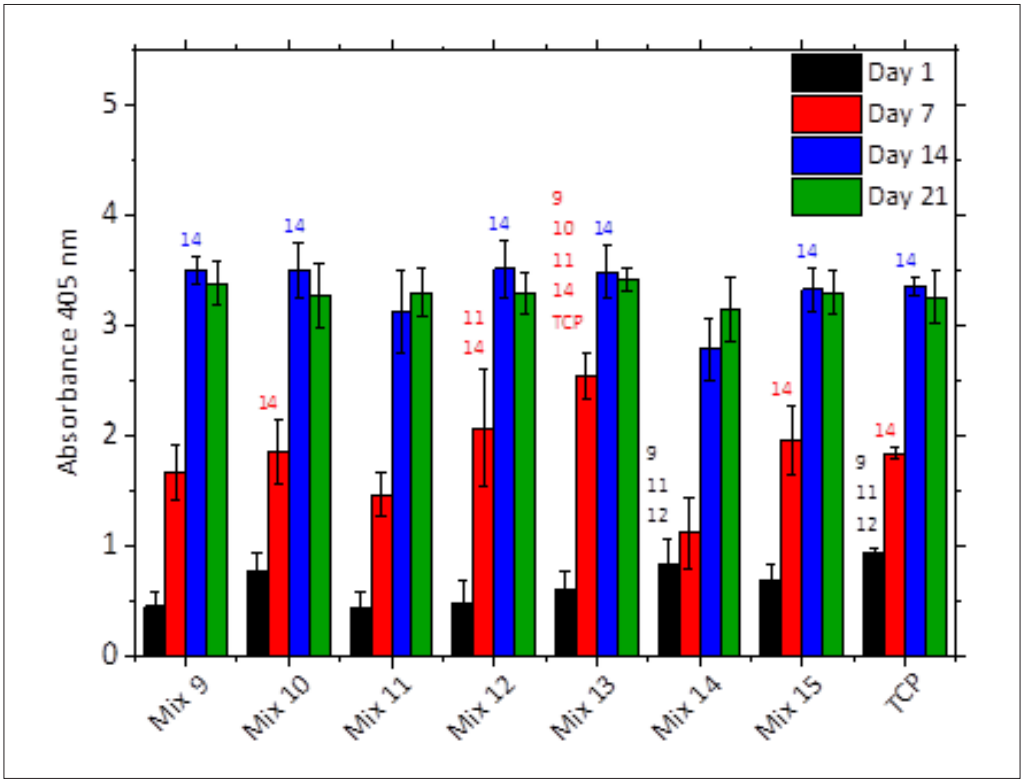

Figure 8. Alkaline phosphatase activity was measured as an indicator of osteogenic differentiation. Saos-2 cells seeded on culture plastic (TCP) were used as a control. A value above a column indicates that the corresponding group is significantly lower compared to the group represented by that column ($p < 0.05$, Tukey). Abbreviations: TCP, tissue culture plastic .

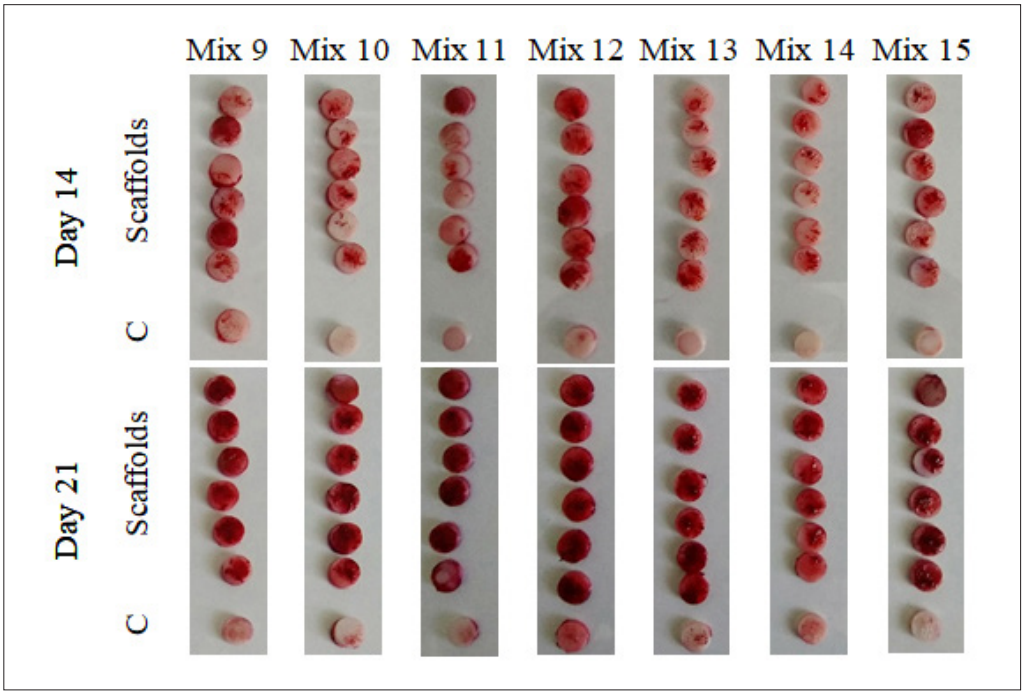

Figure 9. Mineralization on scaffolds detected with Alizarin Red S assay. Positive red staining indicates mineralization produced by the seeded Saos2 cells. Six samples were measured, and the samples in the last (7th) row are controls (C) without cells.

Table 3. The composition and theoretical properties of optimized blends.

	Composition (%)				Theoretical properties					
	PHB	PLA	HA	SN	Printing temperature (°C)	Warping coefficient (-)	Flexural modulus (GPa)	Flexural strength (MPa)	Compression modulus (GPa)	Stress at 1% deformation (MPa)
1	56	34	5	6	186.8	0.5[a]	3.1	64.9	1.4	6.3
2	48	42	5	6	189.4	1.7	3.3	66.9[a]	1.4	6.2
3	33	33	28	6	184.4	2.1	4.4	60.5	2.4[a]	15.2
4	35	31	28	6	188.2	1.0[a]	4.3	59.7	2.3[a]	14.1

[a] Optimized property.
Abbreviations: HA, hydroxyapatite; PHB, poly(3-hydroxybutyrate); PLA, polylactide; SN, Syncroflex™ 3114.

4. Conclusion

In conclusion, this study is aimed at the preparation and characterization of material properties of PHB-based composite blends, which are suitable for use in tissue engineering. The blends were processed into 3D-printing filaments and tested in terms of their printability, thermal and mechanical properties, and biological response. Biological properties were studied for 21 days on the mixtures with one of the four components in a limited amount within the scope of the experiment. All the 3D-printed scaffolds were biocompatible, and the cells adhered to the carriers had a good morphology. On day 21, there was no longer an increase in the number of cells, nor an increase in ALP activity. On the contrary, it was noticeable that there was an increase in mineralization. The highest metabolic activity, proliferation and rate of osteogenic differentiation were observed on the sample with the lowest amount of plasticizer (Mix 13) followed by the mixture containing the highest amount of bioactive hydroxyapatite (Mix 12). In contrast, the worst results were observed for the sample with the highest plasticizer content (Mix 14). Overall, our results show that PHB-based composite blends hold a great potential for tissue engineering applications. By adopting the design of experiment, we obtained four mixture compositions with minimum warping coefficient, maximum flexural strength, maximum compression modulus, and maximum compression modulus with a warping coefficient of no more than one at the same time.

Acknowledgments

None

Funding

Thee authors acknowledge the support from projects "New circular biotechnologies and biomedical applications" No. CZ.01.1.02/0.0/0.0/20_321/002 4676; "Excellence in regenerative medicine" No. CZ.02.01.01/00/22_008/0004562 and from Operational Program Integrated Infrastructure for the project "Center for Medical Bioadditive Research and Production (CEMBAM), code ITMS2014 +: 313011V358, co-financed by the European Regional Development Fund."

Conflict of interest

The authors declare they have no competing interests.

Author contributions

Conceptualization: Veronika Melčová, Radek Přikryl
Data curation: Veronika Melčová, Přemysl Menčík, Štěpán Krobot, Ján Bočkaj, Pavol Alexy
Formal analysis: Přemysl Menčík, Ján Bočkaj, Sára Vach Agócsová, Štěpán Krobot, Kateřina Chaloupková, Věra Hedvičáková
Funding acquisition: Radek Přikryl, Pavol Alexy, Michala Klusáček Rampichová
Investigation: Přemysl Menčík, Štěpán Krobot, Veronika Melčová, Kateřina Chaloupková, Věra Hedvičáková
Methodology: Veronika Melčová, Radek Přikryl, Michala Klusáček Rampichová
Project administration: Veronika Melčová
Supervision: Veronika Melčová, Radek Přikryl
Writing – original draft: Štěpán Krobot, Veronika Melčová
Writing – review & editing: Veronika Melčová, Štěpán Krobot, Michala Klusáček Rampichová

Ethics approval and consent to participate

Not applicable.

Consent for publication

Not applicable.

Availability of data

Data are available from the corresponding author upon reasonable request.

References

1. Abbasi N, Hamlet S, Love RM, Nguyen N.-T. Porous scaffolds for bone regeneration. *J Sci Adv Mater Devices.* 2020;5(1):1-9. doi: 10.1016/j.jsamd.2020.01.007
2. Ngo TD, Kashani A, Imbalzano G, Nguyen KTQ, Hui D. Additive manufacturing (3D printing): a review of materials, methods, applications and challenges. *Compos B Eng.* 2018;143:172-196. doi: 10.1016/j.compositesb.2018.02.012
3. Zhang Q, Zhou J, Zhi P, et al. 3D printing method for bone tissue engineering scaffold. *Med Nov Technol Devices.* 2023;17:100205. doi: 10.1016/j.medntd.2022.100205
4. Bose S, Vahabzadeh S, Bandyopadhyay A. Bone tissue engineering using 3D printing. *Mater Today*. 2013;16(12):496-504. doi: 10.1016/j.mattod.2013.11.017
5. Chiulan I, Frone AN, Brandabur C, Panaitescu DM. Recent advances in 3D printing of aliphatic polyesters. *Bioeng Basel Switz* 2017;5(1):E2. doi: 10.3390/bioengineering5010002
6. Shunmugasundaram M, Baig M, Madala A. A review of bio-degradable materials for fused deposition modeling machine. *Mater Today Proc.* 2020;27:1596-1600. doi: 10.1016/j.matpr.2020.03.267
7. Mehrpouya M, Vahabi H, Barletta M, Laheurte P, Langlois V. Additive manufacturing of polyhydroxyalkanoates (PHAs) biopolymers: materials, printing techniques, and applications. *Mater Sci Eng C Mater Biol Appl.* 2021;127:112216. doi: 10.1016/j.msec.2021.112216
8. Amrita, Manoj A, Panda RC. Biodegradable filament for 3D printing process: a review. *Eng Sci.* 2022;18(7):11-19. doi: 10.30919/es8d616
9. Rigotti D, Pegoretti A. Additive manufacturing with biodegradable polymers. In: *Biodegradable Polymers, Blends and Composites*. Woodhead Publishing; 2022:611-679. doi: 10.1016/B978-0-12-823791-5.00026-0.
10. Hutmacher DW, Schantz T, Zein I, Ng KW, Teoh SH, Tan KC. Mechanical properties and cell cultural response of polycaprolactone scaffolds designed and fabricated via fused deposition modeling. *J Biomed Mater Res.* 2001;*55*(2):203-216. doi: 10.1002/1097-4636(200105)55:2<203::AID-JBM1007>3.0.CO;2-7
11. Xiong Z, Yan Y, Zhang R, Sun L. Fabrication of porous poly(l-Lactic Acid) scaffolds for bone tissue engineering via precise extrusion. *Scr Mater.* 2001;45(7):773-779. doi: 10.1016/S1359-6462(01)01094-6.
12. Zein I, Hutmacher DW, Tan KC, Teoh SH. Fused deposition modeling of novel scaffold architectures for tissue engineering applications. *Biomaterials.* 2002;23(4):1169-1185. doi: 10.1016/S0142-9612(01)00232-0
13. Cao T, Ho K-H, Teoh S-H. Scaffold design and in vitro study of osteochondral coculture in a three-dimensional porous polycaprolactone scaffold fabricated by fused deposition modeling. *Tissue Eng.* 2003;9(Suppl 1):S103-S112. doi: 10.1089/10763270360697012
14. Park S, Kim G, Jeon YC, Koh Y, Kim W. 3D polycaprolactone scaffolds with controlled pore structure using a rapid prototyping system. *J Mater Sci Mater Med.* 2009;20(1):229-234. doi: 10.1007/s10856-008-3573-4
15. Domingos M, Chiellini F, Gloria A, Ambrosio L, Bartolo P, Chiellini E. Effect of process parameters on the morphological and mechanical properties of 3D bioextruded poly(E-caprolactone) scaffolds. *Rapid Prototyp J.* 2012;18(1): 56-67. doi: 10.1108/13552541211193502
16. Korpela J, Kokkari A, Korhonen H, Malin M, Närhi T, Seppälä J. Biodegradable and bioactive porous scaffold structures prepared using fused deposition modeling. *J Biomed Mater Res B Appl Biomater.* 2013;*101B*(4):610-619. doi: 10.1002/jbm.b.32863
17. Rai B, Teoh SH, Ho KH, et al. The effect of rhBMP-2 on canine osteoblasts seeded onto 3D bioactive polycaprolactone scaffolds. *Biomaterials.* 2004;25(24):5499-5506. doi: 10.1016/j.biomaterials.2004.01.007
18. Rai B, Lin JL, Lim ZXH, Guldberg RE, Hutmacher DW, Cool SM. Differences between in vitro viability and differentiation and in vivo bone-forming efficacy of human mesenchymal stem cells cultured on PCL–TCP scaffolds. *Biomaterials.* 2010;31(31):7960-7970. doi: 10.1016/j.biomaterials.2010.07.001
19. Teo EY, Ong S-Y, Chong MSK, et al. Polycaprolactone-based fused deposition modeled mesh for delivery of antibacterial agents to infected wounds. *Biomaterials.* 2011;32(1):279–287. doi: 10.1016/j.biomaterials.2010.08.089
20. Konopnicki S, Sharaf B, Resnick C., et al. Tissue-engineered bone with 3-dimensionally printed β-tricalcium phosphate and polycaprolactone scaffolds and early implantation: an in vivo pilot study in a porcine mandible model. *J Oral Maxillofac Surg.* 2015;73(5):1016.e1-1016.e11. doi: 10.1016/j.joms.2015.01.021
21. Dávila JL, Freitas MS, Inforçatti Neto P, Silveira ZC, Silva JVL, d'Ávila MA. Fabrication of PCL/β-TCP scaffolds by 3d mini-screw extrusion printing. *J Appl Polym Sci.* 2016;133(15):1-9. doi: 10.1002/app.43031
22. Sparks DS, Wiper J, Lloyd T, et al. Protocol for the BONE-RECON trial: a single-arm feasibility trial for critical sized lower limb BONE defect RECONstruction using the mPCL-TCP scaffold system with autologous vascularised corticoperiosteal tissue transfer. *BMJ Open.* 2023;13(5):e056440.

doi: 10.1136/bmjopen-2021-056440

23. *Next-level tissue regeneration*. Biomendex. https://biomendex.com/(accessed 2024-09-19).

24. Chen X, Chen G, Wang G, Zhu P, Gao C. Recent progress on 3D-printed polylactic acid and its applications in bone repair. *Adv Eng Mater.* 2020;22(4):1901065. doi: 10.1002/adem.201901065

25. Gregor A, Filová E, Novák M, et al. Designing of PLA scaffolds for bone tissue replacement fabricated by ordinary commercial 3D printer. *J Biol Eng.* 2017;11:31. doi: 10.1186/s13036-017-0074-3

26. Wurm MC, Möst T, Bergauer B, et al. In-vitro evaluation of polylactic acid (PLA) manufactured by fused deposition modeling. *J Biol Eng.* 2017;11(1):29. doi: 10.1186/s13036-017-0073-4

27. Germain L, Fuentes CA, van Vuure AW, Rieux Ad, Dupont-Gllain C. 3D-printed biodegradable gyroid scaffolds for tissue engineering applications. *Mater Des.* 2018;151:113-122. doi: 10.1016/j.matdes.2018.04.037

28. Alizadeh-Osgouei M, Li Y, Vahid A, Ataee A, Wen C. High strength porous PLA gyroid scaffolds manufactured via fused deposition modeling for tissue-engineering applications. *Smart Mater Med.* 2021;*2*:15-25. doi: 10.1016/j.smaim.2020.10.003

29. Eryildiz M. Fabrication of drug-loaded 3D-printed bone scaffolds with radial gradient porosity. *J Mater Eng Perform.* 2023;32(9):4249-4257. doi: 10.1007/s11665-022-07490-0

30. Schoen AH. *Infinite Periodic Minimal Surfaces Without Self-Intersections*. National Aeronautics and Space Administration; 1970.

31. Xiong Z, Yan Y, Wang S, Zhang R, Zhnag C. Fabrication of porous scaffolds for bone tissue engineering via low-temperature deposition. *Scr Mater.* 2002;46(11):771-776. doi: 10.1016/S1359-6462(02)00071-4

32. Drummer D, Cifuentes-Cuéllar S, Rietzel D. Suitability of PLA/TCP for fused deposition modeling. *Rapid Prototyp J.* 2012;18(6):500-507. doi: 10.1108/13552541211272045

33. Elhattab K, Bhaduri SB, Sikder P. Influence of fused deposition modelling nozzle temperature on the rheology and mechanical properties of 3D printed β-tricalcium phosphate (TCP)/polylactic acid (PLA) composite. *Polymers.* 2022;14(6):1222. doi: 10.3390/polym14061222

34. Distler T, Fournier N, Grünewald A, et al. Polymer-bioactive glass composite filaments for 3D scaffold manufacturing by fused deposition modeling: fabrication and characterization. *Front Bioeng Biotechnol.* 2020;8:552. doi: 10.3389/fbioe.2020.00552

35. Matsuo A, Chiba H, Takahashi H, Toyoda J, Abukawa H. Clinical application of a custom-made bioresorbable raw particulate hydroxyapatite/poly-l-lactide mesh tray for mandibular reconstruction. *Odontology.* 2010;98(1):85-88. doi: 10.1007/s10266-009-0111-x

36. Senatov FS, Niaza KV, Stepashkin AA, Kaloshkin SD. Low-cycle fatigue behavior of 3d-printed PLA-based porous scaffolds. *Compos Part B Eng.* 2016;97:193-200. doi: 10.1016/j.compositesb.2016.04.067

37. Esposito Corcione C, Gervaso F, Scalera F, Montagna F, Sannino A, Maffezzoli A. The feasibility of printing polylactic acid–nanohydroxyapatite composites using a low-cost fused deposition modeling 3D printer. *J Appl Polym Sci.* 2017;134(13);44656. doi: 10.1002/app.44656

38. Esposito Corcione C, Scalera F, Gervaso F, Montagna F, Sannino A, Maffezzoli A. One-step solvent-free process for the fabrication of high loaded PLA/HA composite filament for 3D printing. *J Therm Anal Calorim.* 2018;134(1):575-582. doi: 10.1007/s10973-018-7155-5

39. Esmaeili S, Akbari Aghdam H, Motififard M, et al. A porous polymeric–hydroxyapatite scaffold used for femur fractures treatment: fabrication, analysis, and simulation. *Eur J Orthop Surg Traumatol.* 2020;30(1):123-131. doi: 10.1007/s00590-019-02530-3

40. Dubinenko G, Zinoviev A, Bolbasov E, et al. Highly filled poly(l-lactic acid)/hydroxyapatite composite for 3D printing of personalized bone tissue engineering scaffolds. *J Appl Polym Sci.* 2021;138(2):49662. doi: 10.1002/app.49662

41. Alves AA, Siqueira EC, Barros MPS, Silva PEC, Houllou LM. Polyhydroxyalkanoates: a review of microbial production and technology application. *Int J Environ Sci Technol.* 2023;20(3):3409-3420. doi: 10.1007/s13762-022-04213-9

42. Kosorn W, Sakulsumbat M, Uppanan P, et al. PCL/PHBV blended three dimensional scaffolds fabricated by fused deposition modeling and responses of chondrocytes to the scaffolds. *J Biomed Mater Res B Appl Biomater.* 2017;105(5):1141-1150. doi: 10.1002/jbm.b.33658

43. Ausejo JG, Rydz J, Musiol M, et al. A comparative study of three-dimensional printing directions: the degradation and toxicological profile of a PLA/PHA blend. Polym Degrad Stab. 2018;152:191-207. doi: 10.1016/j.polymdegradstab.2018.04.024

44. Findrik Balogová A, Hudák R, Tóth T, et al. Determination of geometrical and viscoelastic properties of PLA/PHB samples made by additive manufacturing for urethral substitution. *J Biotechnol.* 2018;284:123-130. doi: 10.1016/j.jbiotec.2018.08.019

45. Ecker JV, Burzic I, Haider A, Hild S, Rennhofer H. Improving the impact strength of PLA and its blends with PHA in fused layer modelling. *Polym Test.* 2019;78:105929. doi: 10.1016/j.polymertesting.2019.105929

46. Rydz J, Włodarczyk J, Gonzalez Ausejo J, et al. Three-dimensional printed PLA and PLA/PHA dumbbell-shaped specimens: material defects and their impact on degradation behavior. *Materials.* 2020;13(8):2005. doi: 10.3390/ma13082005

47. Findrik Balogová A, Trebuňová M, Ižaríková G, et al. In vitro degradation of specimens produced from PLA/PHB by additive manufacturing in simulated conditions. *Polymers.* 2021;13(10):1542. doi: 10.3390/polym13101542

48. Gielisch M, Heimes D, Thiem DGE, et al. Steam-sterilized and degradable fused filament fabrication-printed polylactide/ polyhydroxyalkanoate surgical guides for dental implants: are they accurate enough for static navigation? *Int J Bioprint.* 2022;9(2):655. doi: 10.18063/ijb.v9i2.655

49. Kohan M, Lancoš S, Schnitzer M, Živčák J, Hudák R. Analysis of PLA/PHB biopolymer material with admixture of hydroxyapatite and tricalcium phosphate for clinical use. *Polymers.* 2022;14(24):5357. doi: 10.3390/polym14245357

50. Giubilini A, Siqueira G, Clemens FJ, et al. 3D-printing nanocellulose-poly(3-hydroxybutyrate-Co-3-hydroxyhexanoate) biodegradable composites by fused deposition modeling. *ACS Sustain Chem Eng.* 2020;8(27):10292-10302. doi: 10.1021/acssuschemeng.0c03385

51. Kovalcik A, Sangroniz L, Kalina M, et al. Properties of scaffolds prepared by fused deposition modeling of poly(hydroxyalkanoates). *Int J Biol Macromol.* 2020;161:364-376. doi: 10.1016/j.ijbiomac.2020.06.022

52. Dong X, Premaratne ID, Sariibrahimoglu K, Limem S, Scott J, Gadjiko M. 3D-printed poly-4-hydroxybutyrate bioabsorbable scaffolds for nipple reconstruction. *Acta Biomater.* 2022;143:333-343. doi: 10.1016/j.actbio.2022.02.040

53. Volpini V, Giubilini A, Corsi L, Nobili A, Bondioli F. Characterization of biocompatible scaffolds manufactured by fused filament fabrication of poly(3-Hydroxybutyrate-Co-3-Hydroxyhexanoate). R Soc Open Sci. 2022;9(4): 211485. doi: 10.1098/rsos.211485

54. Ivorra-Martinez J, Peydro MÁ, Gomez-Caturla J, Sanchez-Nacher L, Boronat T, Balart R. The effects of processing parameters on mechanical properties of 3D-printed polyhydroxyalkanoates parts. *Virtual Phys Prototyp.* 2023;18(1):e2164734. doi: 10.1080/17452759.2022.2164734

55. Aráoz B, Karakaya E, Wusener AG, et al. 3D printed poly(Hydroxybutyrate-Co-Hydroxyvalerate)—45S5 bioactive glass composite resorbable scaffolds suitable for bone regeneration. *J Mater Res.* 2021;36:4000-4012. doi: 10.1557/s43578-021-00272-9

56. Ye X, Zhang Y, Liu T, et al. Beta-tricalcium phosphate enhanced mechanical and biological properties of 3D-printed polyhydroxyalkanoates scaffold for bone tissue engineering. *Int J Biol Macromol.* 2022;209:1553-1561. doi: 10.1016/j.ijbiomac.2022.04.056

57. Chen G-Q, Wu Q. The application of polyhydroxyalkanoates as tissue engineering materials. *Biomaterials.* 2005;26(33):6565-6578. doi: 10.1016/j.biomaterials.2005.04.036

58. Lim J, You M, Li J, Li Z. Emerging bone tissue engineering via polyhydroxyalkanoate (PHA)-based scaffolds. *Mater Sci Eng C Mater Biol Appl.* 2017;79:917-929. doi: 10.1016/j.msec.2017.05.132

59. Butt FI, Muhammad N, Hamid A, Moniruzzaman M, Sharif F. Recent progress in the utilization of biosynthesized polyhydroxyalkanoates for biomedical applications - review. *Int J Biol Macromol.* 2018;120(Pt A): 1294-1305. doi: 10.1016/j.ijbiomac.2018.09.002

60. Gregory DA, Taylor CS, Fricker AT, et al. Polyhydroxyalkanoates and their advances for biomedical applications. *Trends Mol Med.* 2022;28(4):331-342. doi: 10.1016/j.molmed.2022.01.007

61. Pereira TF, Oliveira MF, Maia IA, et al. 3D printing of poly(3-Hydroxybutyrate) porous structures using selective laser sintering. *Macromol Symp.* 2012;319(1):64-73. doi: 10.1002/masy.201100237

62. Melčová V, Svoradová K, Menčík P, et al. FDM 3D printed composites for bone tissue engineering based on plasticized Poly(3-Hydroxybutyrate)/Poly(d,l-Lactide) Blends. *Polymers.* 2020;12(12):2806. doi: 10.3390/polym12122806

63. Krobot Š, Melčová V, Menčík P, et al. Poly(3-Hydroxybutyrate) (PHB) and polycaprolactone (PCL) based blends for tissue engineering and bone medical applications processed by FDM 3D printing. *Polymers.* 2023;15(10):2404. doi: 10.3390/polym15102404

64. Kanabenja W, Passarapark K, Subchokpool T, et al. 3D printing filaments from plasticized polyhydroxybutyrate/ polylactic acid blends reinforced with hydroxyapatite. *Addit Manuf.* 2022;59:103130. doi: 10.1016/j.addma.2022.103130

65. Moroni S, Khorshid S, Aluigi A, Tiboni M, Casettari L. Poly(3-Hydroxybutyrate): a potential biodegradable excipient for direct 3D printing of pharmaceuticals. *Int J Pharm.* 2022;623:121960. doi: 10.1016/j.ijpharm.2022.121960

66. Kontárová S, Přikryl R, Melčová V, et al. Printability, mechanical and thermal properties of poly(3-Hydroxybutyrate)-Poly(Lactic Acid)-plasticizer blends for three-dimensional (3D) printing. *Materials.* 2020;13(21):4736. doi: 10.3390/ma13214736

67. Armillotta A, Bellotti M, Cavallaro M. Warpage of FDM parts: experimental tests and analytic model. *Robot Comput-Integr Manuf.* **2018**;50:140-152. doi: 10.1016/j.rcim.2017.09.007

68. Antony Samy A, Golbang A, Harkin-Jones E, Archer E, Dahale M, McIlhagger A. Influence of ambient temperature on part distortion: a simulation study on amorphous and semi-crystalline polymer. *Polymers.* 2022;14(5):879. doi: 10.3390/polym14050879

69. Samy AA, Golbang A, Harkin-Jones E, Archer E, Tormey D, McIlhagger A. Finite element analysis of residual stress and warpage in a 3D printed semi-crystalline polymer: effect of ambient temperature and nozzle speed. *J Manuf Process.* 2021;70:389-399. doi: 10.1016/j.jmapro.2021.08.054

70. Wang X, Xu S, Zhou S, et al. Topological design and additive manufacturing of porous metals for bone scaffolds and orthopaedic implants: a review. *Biomaterials.* 2016;83:127-141. doi: 10.1016/j.biomaterials.2016.01.012

71. Haba Y, Skripitz R, Lindner T, et al. Bone mineral densities and mechanical properties of retrieved femoral bone samples in relation to bone mineral densities measured in the respective patients. *ScientificWorldJournal* 2012;2012:242403. doi: 10.1100/2012/242403

72. Rohlmann A, Zilch H, Bergmann G, Kolbel R. Material properties of femoral cancellous bone in axial loading. *Arch. Orthop Trauma Surg.* 1980;97(2); 95-102. doi: 10.1007/BF00450930

73. Uchiyama T, Tanizawa T, Muramatsu H, Endo N, Takahashi HE, Hara T. Three-dimensional microstructural analysis of human trabecular bone in relation to its mechanical properties. Bone. 1999;25(4):487-491. doi: 10.1016/S8756-3282(99)00188-X

74. Gonzalez Ausejo J, Rydz J, Musioł M, et al. Three-dimensional printing of PLA and PLA/PHA dumbbell-shaped specimens of crisscross and transverse patterns as promising materials in emerging application areas: prediction study. *Polym Degrad Stab.* 2018;156:100-110. doi: 10.1016/j.polymdegradstab.2018.08.008

75. Ayatollahi MR, Nemati Giv A, Razavi N, Khoramishad, H. Mechanical properties of adhesively single lap-bonded joints reinforced with multi-walled carbon nanotubes and silica nanoparticles. *J Adhes.* 2017; *93*(11): 896-913. doi: 10.1080/00218464.2016.1187069

76. Zilch H, Rohlmann A, Bergmann G, Kölbel R. Material properties of femoral cancellous bone in axial loading. Part II: time dependent properties. *Arch Orthop Trauma Surg (1978).* 1980;97(4):257-262. doi: 10.1007/BF00380706

77. Song Y, Li Y, Song W, Yee K, Lee K-Y, Tagarielli VL. Measurements of the mechanical response of unidirectional 3D-printed PLA. *Mater Des.* 2017;123:154-164. doi: 10.1016/j.matdes.2017.03.051

78. Guo R, Lu S, Page JM, et al. Fabrication of 3D scaffolds with precisely controlled substrate modulus and pore size by templated-fused deposition modeling to direct osteogenic differentiation. *Adv Healthc Mater.* 2015;4(12): 1826-1832. doi: 10.1002/adhm.201500099

ACCSCIENCE PUBLISHING

International Journal of Bioprinting

RESEARCH ARTICLE

Polydopamine-modified 3D-printed polycaprolactone scaffolds for promoting bone regeneration

Qian Zhong[1†], Shuai Huang[2†], Weihua Huang[2,3,4,5†], Hengpeng Wu[1], Yang Wang[2], Zhenyu Wen[1], Huinan Yin[2], Yixiao Wang[1], Weikang Xu[3,5*], and Qingde Wa[1*]

[1]Department of Orthopaedic Surgery, The Second Affiliated Hospital of ZunYi Medical University, Zunyi, Guizhou, China

[2]Department of Orthopaedic Surgery, The Second Affiliated Hospital of Guangzhou Medical University, Guangzhou, Guangdong, China

[3]Medical Materials and Engineering Research Laboratory, Institute of Biological and Medical Engineering, Guangdong Academy of Sciences, Guangzhou, Guangdong, China

[4]Department of Orthopaedic Surgery, The Affiliated Qingyuan Hospital (Qingyuan People's Hospital), Guangzhou Medical University, Qingyuan, Guangdong, China

[5]National Engineering Research Center for Healthcare Devices, Guangdong Key Lab of Medical Electronic Instruments and Polymer Material Products, Guangdong Institute of Medical Instruments, Guangdong Chinese Medicine Intelligent Diagnosis and Treatment Engineering Technology Research Center, Guangzhou, Guangdong, China

[†]These authors contributed equally to this work.

***Corresponding authors:**
Weikang Xu
(weikangxu1987@hotmail.com)

Qingde Wa
(wqd887zsy@126.com)

Citation: Zhong Q, Huang S, Huang W, et al. Polydopamine-modified 3D-printed polycaprolactone scaffolds for promoting bone regeneration. *Int J Bioprint*. 2025;11(1):418-438. doi: 10.36922/ijb.4995

Received: September 29, 2024
1st revised: November 6, 2024
2nd revised: December 16, 2024
Accepted: December 25, 2024
Published Online: December 26, 2024

Copyright: © 2024 Author(s). This is an Open Access article distributed under the terms of the Creative Commons Attribution License, permitting distribution, and reproduction in any medium, provided the original work is properly cited.

Publisher's Note: AccScience Publishing remains neutral with regard to jurisdictional claims in published maps and institutional affiliations.

Abstract

Polycaprolactone (PCL) is one of the most widely used three-dimensional (3D) printing materials with excellent biocompatibility and mechanical properties. However, its hydrophobic nature hinders cell adhesion and proliferation. Polydopamine (PDA) has been shown to promote proliferation and induce osteogenic differentiation of bone marrow mesenchymal stem cells (BMSCs) on polymer surfaces. Despite this, the impact of varying PDA coating thicknesses on the osteogenic differentiation of BMSCs has been minimally explored. In this paper, PCL scaffolds were fabricated using 3D printing technology, and PDA-coated PCL scaffolds (PDA-PCL-0, PDA-PCL-3, PDA-PCL-6, PDA-PCL-24) were prepared by immersing the scaffolds in an aqueous dopamine solution for fixed time points (0, 3, 6, 24 h) under constant shaking. The scaffolds were characterized and subjected to physicochemical performance tests to evaluate their effects on BMSC proliferation, adhesion, and osteogenic differentiation. The results showed that PDA-PCL-6 scaffolds exhibited significant immunomodulatory properties, promoting BMSC proliferation, adhesion, and osteogenic differentiation more effectively than the other groups. *In vivo* validation experiments, including micro-computed tomography, hematoxylin and eosin staining, Masson staining, and immunohistochemical analysis of bone morphologenetic protein 2 (BMP-2) and type I collagen (COL-I), confirmed that PDA-PCL-6 scaffolds significantly enhanced bone regeneration, histocompatibility, and hemocompatibility compared to uncoated scaffolds at 1, 2, and 3 months postoperation. In conclusion, our results indicate that a PDA coating obtained through 6-h immersion significantly enhances the biocompatibility and osteoinductive properties of PCL scaffolds, providing a promising strategy for bone defect repair.

Keywords: 3D printing; Bone regeneration; Polycaprolactone; Polydopamine

1. Introduction

The repair of bone defects resulting from trauma, infection, tumors, surgery, or other causes remains a significant challenge for orthopedic and plastic surgeons.[1] Bone defects larger than the critical size are beyond the organism's natural reparative capacity and require the intervention of bone graft substitutes.[2] Currently, autologous and allogeneic bone grafts are considered the gold standard for treating bone defects. However, their use is limited by disadvantages such as donor site hemorrhage, infection, pain, and the restricted availability of graft material.[3,4] Fortunately, in recent years, the rapid development of bone tissue engineering has led to the emergence of a wide variety of bone substitutes, offering promising materials for bone defect repair. Among these, 3D printing technology plays an important role in fabricating bone tissue engineering scaffolds. Its ability to control shape, structure, and porosity enables anatomical matching of bone defects, making it a valuable tool in bone defect treatment.[5]

Polycaprolactone (PCL), a hydrophobic aliphatic polyester, has been widely studied in biomedical applications due to its excellent biocompatibility, mechanical properties, low melting point (60 °C), and ease of processing.[6,7] However, PCL's hydrophobic nature, attributed to the multiple $-CH_2$ groups in its molecular structure, presents challenges for cell adhesion. This limitation hampers the attachment and growth of osteoblasts and neovascularization, both of which are critical for effective bone repair and regeneration. To address this issue, surface modification techniques have been proposed to augment the bioactivity of PCLscaffolds.[8] For example, Gharibshahian et al.[9] demonstrated that incorporating ceramic materials such as beta-tricalcium phosphate and hydroxyapatite, as well as magnesium oxide, improved the hydrophilicity, surface roughness, degradation rate, and osteoinductive properties of PCL scaffolds. Kikionis et al.[10] reported that PCL scaffolds combined with chlorella sulfated polysaccharide using a freeze-drying method promoted human bone marrow mesenchymal stem cell (BMSC) adhesion and osteogenic differentiation. Similarly, Wang et al.[11] showed that surface modification of PCL scaffolds with ZIF-8 and ZIF-8-mediated hydroxyapatite deposition increased surface roughness and significantly enhanced their *in vitro* and *in vivo* osteoinductivity and biocompatibility. Despite these promising results, the preparation processes for these surface-modified materials are often cumbersome.

Polydopamine (PDA) has emerged as a highly active coating material due to its molecular structure, which is rich in reactive functional groups such as –OH and $-NH_2$. These groups enable PDA to form strong bonds with the surfaces of various materials and cells, thereby facilitating cell–material adhesion and enhancing bioactivity. This interaction accelerates the healing of bone injuries.[12,13] By adjusting the reaction time between the PDA and the substrate material, the extent of surface functionalization can be meticulously controlled.[14]

Several studies have highlighted the osteogenic potential of PDA coatings. For instance, Teixeira et al.[15] demonstrated that PDA-coated polylactic acid scaffolds significantly enhanced alkaline phosphatase expression in mesenchymal stem cells, indicating improved bioactivity and osteogenic potential. Lin et al.[16] enhanced the hydrophilic and osteogenic properties of PCL scaffolds through PDA coating modification, though their study did not examine the effects of different PDA coating thicknesses or include *in vivo* data to support their findings. Xu et al.[17] observed that increasing PDA coating thickness promoted cell adhesion and proliferation, as well as improved osteogenesis. However, their study did not identify differences in the osteogenic effects of varying PDA coating thicknesses.

While these studies emphasize the excellent osteogenic properties of PDA coatings, they leave significant gaps in understanding the effects of different PDA coating thicknesses on immunomodulation and osteogenesis.

In this study, we prepared PCL scaffolds using a 3D printing technique with PCL as the raw material. The composite scaffold preparation process was designed to be simple and efficient by controlling the immersion time in dopamine aqueous solution to form PDA coatings of varying thicknesses on the scaffold surface. The performance of these PDA-coated scaffolds was then evaluated in terms of their ability to modulate macrophage polarization, promote cell proliferation and adhesion, enhance osteoinduction, and facilitate cranial bone defect repair.

2. Materials and methods

2.1. Materials

Polycaprolactone was purchased from Jinan Daigang Biotechnology Co. (China). Tris–HCl buffer (pH 8.5), dopamine hydrochloride (DA), $FeCl_3$, and $NH_3{\cdot}H_2O$ were obtained from McLean (XXX). Alkaline phosphatase assay kits and alizarin red staining kits were provided by Biyuntian Biotechnology Co (China). Ultrapure RNA kits, HiFi Script cDNA synthesis kits, and Ultra SYBR Mixture (Low ROX) were purchased from CWBIO (China). DMEM medium, fetal bovine serum, penicillin-streptomycin solution, phosphate buffer, trypsin, and CCK-8 kits were purchased from Gibco (China). Rat bone

marrow mesenchymal stem cells (BMSCs) were obtained from Shanghai Yansheng Industrial Co., Ltd. (China), and RAW264.7 cells was provided by Tongpai Biotechnology Co., Ltd. (China).

2.2. Preparation of polydopamine-polycaprolactone scaffolds

2.2.1. Printing of scaffolds

The scaffold model was designed using SolidWorks software, saved in STL format, and prepared for printing PCL. PCL particles were dried in a drying oven at 40 °C for 24 h and then added to the cartridge of a 3D printer (EFL-BP-6603, Suzhou Intelligent Manufacturing Research Institute, China). The preset model was loaded into the 3D printer system control software on the computer console, and the printing parameters were set as follows: needle inner diameter, 0.35 mm; holder diameter, 5 mm; aperture diameter, 300 μm; filament diameter, 350 μm; scaffold shape, porous cylinder; printing temperature, 60 °C; printing air pressure, 300 kPa; and printing speed, 10 mm/s. The printhead was activated to create the specified 3D porous cylindrical scaffolds. Scaffolds with a diameter of 10 mm and a height of 5 mm were reserved for mechanical strength tests, while the scaffolds with a diameter of 5 mm and a height of 1 mm were used for performance and cell experiments.

2.2.2. Polydopamine coating preparation

To prepare the DA solution, 50 mg of DA was dissolved in Tris–HCl buffer and stirred thoroughly to achieve a concentration of 2.5 mg/mL. The PCL scaffolds were immersed in the prepared DA solution and placed on a shaker for 0, 3, 6, and 24 h. After shaking, the samples were rinsed with deionized water to remove the unattached PDA and vacuum-dried for 24 h. The samples were categorized into four groups based on the immersion time as follows: PCL (control, also referred to as PDA-PCL-0), PDA-PCL-3, PDA-PCL-6, and PDA-PCL-24.

2.3. Physical and chemical properties of the scaffolds

2.3.1. Surface morphology and elemental composition of the scaffolds

Four groups of scaffolds were attached to the operating table using conductive adhesive, and their surfaces were sputter-coated with gold. The microscopic morphology and structure of the scaffolds were observed using a scanning electron microscope (SEM) (Phenom Prox, Merlin, the Netherlands) at an accelerating voltage of 10 kV. Our elemental analysis of the scaffolding was done using SEM (Phenom Prox, the Netherlands).

2.3.2. Fourier-transform infrared spectroscopy analysis

Scaffolds from each group were placed on the operating table of the Fourier-transform infrared (FTIR) spectrometer (Nicolet iS10, Thermo fisher, USA). The characteristic infrared absorption peaks of the scaffolds were analyzed in iso-ATR mode over a wave number range of 4000–400 cm^{-1}.

2.3.3. Porosity detection of the scaffolds

The porosity of the scaffolds was determined using a specific gravity flask 10ml (Shanghai Lugu Instrument Co., Ltd. China) method. The following measurements were recorded:

- M_0: The mass of the dried scaffold sample.
- M_1: The total mass of a specific gravity flask filled with anhydrous ethanol at room temperature.
- M_2: The total mass of the flask after placing the scaffold sample inside and ultrasonically treating it for 10 min to remove air bubbles.
- M_3: The residual mass of the scaffold after it was removed and weighed.

The porosity (P) was calculated using **Equation I**:

$$P = (M_2 - M_3 - M_0)/(M_1 - M_3) \quad \text{(I)}$$

2.3.4. Mechanical strength test of the scaffolds

The compressive modulus of the scaffolds was measured using a universal mechanical testing machine (345C-S, Instron, United States of America). At room temperature, the height of the scaffold was measured using a vernier caliper, and the scaffold was then placed on the test platform. The extrusion speed was set at 5 mm/min, and the test was terminated when the scaffold reached 80% compression deformation. During the compression plateau period, the pressure value was recorded as the compressive strength of the scaffold.

2.3.5. Dopamine release performance

Two steps were performed to assess dopamine release performance. These were following:

2.3.5.1. Step 1: Plotting the standard curve for DA release

A series of DA solutions with different concentration gradients (0, 1, 2.5, 5, 10, 15, 20, 25, and 50 μg/mL) were prepared. Into a 25 mL volumetric flask, 0.8 mL of $FeCl_3$ (1.992×10^{-2} mol/L) was pipetted, followed sequentially by 0.5 mL of DA solution and 0.5 mL of $NH_3{\cdot}H_2O$ (0.5 mol/L). The solution was diluted to the mark with water. Under alkaline conditions, $FeCl_3$ reacted with DA to

form a purplish-red compound. The absorbance was measured at 507 nm using an enzyme meter (United States of America), and a standard curve of DA concentration versus absorbance was generated.

2.3.5.2. Step 2: DA release testing

The scaffolds were placed in 48-well plates, and 1 mL of water was added to each well. The soaking solutions were collected on days 1, 3, 5, 7, and 14. The absorbance of each solution was measured using the method described above, and the DA release performance of each scaffold group was calculated based on the standard curve.

2.4. Cellular experiments

2.4.1. Cell culture and scaffold sterilization

Bone marrow-derived mesenchymal stem cells and RAW264.7 cells were cultured after resuscitation in a thermostatic cell culture incubator (MCO-18AIC, PHCbi, Japan) at 37 °C with 5% CO_2. The complete culture medium consisted of a high-glucose DMEM medium supplemented with 10% fetal bovine serum, 100 μg/mL penicillin, and 100 μg/mL streptomycin. The medium was replaced daily or every 2 days, depending on the cell condition. Cells were passaged upon reaching 70–80% confluence, and only cells at passages 3–5 were used for further experiments.

Scaffolds in each group were sterilized by soaking in 75% ethanol for 2 h, followed by three rinses with phosphate-buffered saline. The scaffolds were then placed overnight in a UV sterilizer (30–800 L, Shengzhiyuanhe Scientific and Educational Equipment Co., Ltd., China).

2.4.2. Cell adhesion evaluation

Bone marrow-derived mesenchymal stem cells from the third passage in the logarithmic growth phase were used. A cell suspension was prepared by digesting the cells with trypsin and resuspending them in a growth medium. The cells were seeded onto the surfaces of four groups of scaffolds at a density of 1×10^5 cells/cm^2 and cultivated in 48-well plates for 24 h.

After incubation, the culture medium was removed, and the scaffolds were transferred to new well plates using sterilized forceps. The cells on the scaffold surfaces were fixed with 2.5% glutaraldehyde buffer. The scaffolds were dehydrated using a graded ethanol series (30%, 50%, 70%, 80%, 90%, 95%) for 15 min at each concentration, followed by 20 min in anhydrous ethanol. The samples were air-dried naturally.

After dehydration, the scaffolds were mounted onto specimen holders and sputter-coated with gold. The surface morphology of the scaffolds after cell seeding, as well as the morphology and distribution of the BMSCs, was observed using SEM.

2.4.3. Cell proliferation evaluation

Bone marrow mesenchymal stem cells from the third passage, harvested during the logarithmic growth phase, were used in this study. A cell suspension was prepared by digesting the cells with trypsin and resuspending them in a growth medium. BMSCs were seeded onto the surfaces of the scaffolds at a density of 1×10^5 cells/cm^2 and cultured in 48-well plates. Following incubation for 1, 3, and 7 days, the medium was removed, and the scaffolds were transferred into new 48-well plates using forceps. Subsequently, a 10% cell counting Kit-8 (CCK-8) solution was added to each well, and the plate was incubated at 37 °C in a 5% CO_2 environment for 2 h. The absorbance at 450 nm was measured using a microplate reader to assess the proliferative capacity of the cells on the scaffolds.

2.4.4. Evaluation of macrophage polarization and osteogenic differentiation induced by the scaffolds

RAW264.7 macrophage cells were seeded onto the scaffolds in 48-well plates at a density of 5×10^4 cells per well. The complete medium was replaced every 2–3 days. On day 3, the expression levels of the M1 polarization marker geneinterleukin-1 beta (*Il1b*) and the M2 polarization marker gene *Cd206* were analyzed in the macrophage cells using polymerase chain reaction (PCR). Glyceraldehyde phosphate dehydrogenase (*Gapdh*) was used as the internal reference gene.

Bone marrow mesenchymal stem cells (1×10^5 cells per well) were seeded onto 48-well plates containing the scaffold samples. The osteogenic induction medium was prepared using a DMEM complete medium, supplemented with 0.39 mg dexamethasone, 1.76 mg vitamin C, and 306.11 mg sodium β-glycerophosphate per 100 mL. The BMSCs were cultured under osteogenic induction conditions for 14 days. At the end of the culture period, real-time fluorescence quantitative PCR (RT-PCR) was used to measure the expression of osteogenic marker genes, including alkaline phosphatase (*Alp*), Runt-related transcription factor 2 (*Runx2*), and collagen type I (*Col1*). *Gapdh* was used as the internal reference gene, the primer sequences used for real-time quantitative polymerase chain reaction of selected gene transcripts including Cd206 and Il1b are shown in Table 1. The data were analyzed using the $2^{-\Delta\Delta Ct}$ method, calculated as follows:

$$\Delta\Delta Ct = (Ct_{\text{target gene}} - Ct_{Gapdh})^{\text{experimental group}} - (Ct_{\text{target gene}} - Ct_{Gapdh})^{\text{control group}} \quad \text{(II)}$$

The relative expression (fold change) of each gene in the experimental group relative to the control group was calculated as $2^{-\Delta\Delta Ct}$.

Table 1. Primer sequences used for real-time quantitative polymerase chain reaction of selected gene transcripts

Gene transcript	Forward primer sequence (5'–3')	Reverse primer sequence (5'–3')
Gapdh	GCCATGAGGTCCACCACCCT	AAGGTCATCCCAGAGCTG
Alp	GGAGATGGTATGGGCGTCTC	GGACCTGAGCGTTGGTGTTA
Runx2	TCGGAGAGGTACCAGATGGG	AGGTGAAACTCTTGCCTCGT
Col1	TTCTCCTGGCAAAGACGGAC	CTCAAGGTCACGGTCACGAA
Cd206	ATGGATGTTGATGGCTACTGG	TTCTGACTCTGGACACTTGC
Il1b	TACAGGCTCCGAGATGAACA	AGGCCACAGGTATTTTGTCG

Alkaline phosphatase activity and calcium deposition were also evaluated to assess osteogenic differentiation. On day 7 of osteogenic induction, scaffolds were stained with an ALP staining kit. The bicinchoninic acid method was used for quantification of ALP enzyme activity. Briefly, cells in the well plates were lysed with lysis buffer according to the ALP assay kit instructions. The lysates were homogenized and centrifuged to extract the supernatant for the assay. The appropriate working solutions and samples were sequentially added to a 96-well plate. After incubation at 37°C for 30 min, the reaction was terminated, and absorbance was measured at 405 nm.

Calcium nodule staining and quantification of the scaffolds were performed on day 14 of osteogenic induction using the alizarin red staining kit. After staining, the scaffolds were photographed, and the alizarin red dye was extracted from the scaffolds using 10% cetylpyridinium chloride. The absorbance was measured at 562 nm to quantify calcium deposition.

2.5. *In vivo* evaluation of bone regeneration effect using a rat model for calvarial defects

A total of 27 male Sprague-Dawley (SD) rats, aged 8 weeks, were obtained from Zunyi Medical University (Guizhou, China) and housed in strict accordance with the recommendations in the Guide for Care and Use of Laboratory Animals of the National Institution of Health.

The rats were randomly assigned to three experimental groups of equal size (n = 9). Anesthesia was induced via intraperitoneal injection of a mixture containing 10% chloral hydrate and 25% urethane. Once anesthetized, the rats' scalps were shaved, and they were placed in a prone position on the operating table. The surgical site was disinfected with 1% iodine tincture and covered with a sterile drape. A midline incision (~2 cm) was made along the calvarium using a scalpel. Subcutaneous tissues were dissected using the blunt handle of the scalpel. The periosteum was gently incised along the sagittal suture of the skull, exposing the bilateral parietal bones, portions of the frontal bone, and portions of the occipital bone.

A 5-mm diameter full-thickness critical-sized bone defect was created bilaterally on the calvarium using a hollow trephine drill. The trephine bit was maintained perpendicular to the skull and operated at a low speed (1400–1500 rpm). As the drilling depth approached breakthrough, the applied force was reduced. At this point, relying solely on the weight of the trephine, the bit was tilted 20°–30° in the forward, backward, left, and right directions to gently complete the drilling. When only a small amount of bone remained connected, indicating that the drilling was almost complete, the looseness of the defect was tested with ophthalmic forceps, and the remaining bone around the circular defect was removed.

After the defect was created, the surgical site was rinsed with sterile saline. The bone defects were treated as follows (Figure 1): Group I received no scaffold (blank group), Group II received a PCL scaffold (control group), and Group III received a PDA-PCL scaffold (experimental group). Post-surgery, the rats were returned to their housing conditions, and penicillin (800,000 U/day) were administered intramuscularly for 3 consecutive days. The rats were sacrificed 4, 8, and 12 weeks post-implantation, after which the implants were dissected and prepared for micro-computed tomography (micro-CT) analysis and histological examination.

The histocompatibility test was performed by taking major organs such as heart, liver, spleen, lungs, and kidneys of rats and staining them with H&E sections.

2.6. Statistical analysis

Experimental data were expressed as mean ± standard deviation. Comparisons between groups were performed using one-way ANOVA in GraphPad Prism software. A p-value <0.05 indicated statistically significant differences, whereas p-values >0.05 indicated no significant differences between groups.

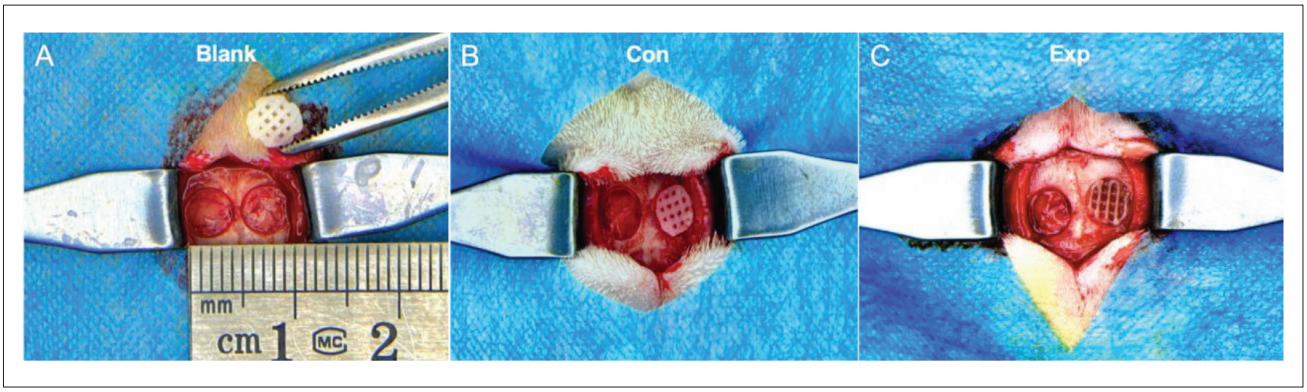

Figure 1. A rat cranial critical-sized defect of 5 mm was created. (A) Blank group (no scaffold). (B) Control group (pure PCL scaffold). (C) Experimental group (PDA-PCL scaffold).

3. Results

3.1. Characterization and physicochemical properties of scaffolds

The surface morphology of the four groups of scaffolds was observed using SEM at magnifications of 200×, 1000×, and 2000× (Figure 2A). The SEM analysis revealed that the fiber orientation of adjacent layers differed by 90°, with uniform coarseness and fineness. The scaffold surfaces exhibited a uniform pore distribution. In the PDA-modified groups (PDA-PCL-3, PDA-PCL-6, and PDA-PCL-24), grayish-black particles were observed on the scaffold surfaces. These particles resulted from the oxidative polymerization of DA on the surface of PCL, forming a PDA coating. The thickness of this coating increased with prolonged immersion times.[18]

Energy-dispersive X-ray spectroscopy analysis (Table 2) confirmed that no nitrogen atoms were detected in the PCL scaffolds. In contrast, nitrogen content increased in the PDA-modified scaffolds, measuring 5.99% in PDA-PCL-3, 6.82% in PDA-PCL-6, and 9.65% in PDA-PCL-24. This nitrogen content was attributed to the ethylamino group of PDA. Notably, the oxygen content rose to 32.11% in PDA-PCL-24 from 30.57% in the PCL group. In contrast, carbon and oxygen levels in the other PDA-coated scaffolds decreased compared to the PCL group. These variations likely resulted from the predominant contribution of the PCL substrate to the elemental composition and the limited depth of the energy spectral sweep.

Table 2. Elemental composition analysis of scaffolds of varying immersion duration in dopamine

Samples	Carbon (%)	Oxygen (%)	Nitrogen (%)
PCL	69.43	30.57	0
PDA-PCL-3	67.70	26.31	5.99
PDA-PCL-6	66.82	26.36	6.82
PDA-PCL-24	58.24	32.11	9.65

Further analysis revealed a gradual decrease in carbon content and a corresponding increase in oxygen content in the PDA-PCL-3, PDA-PCL-6, and PDA-PCL-24 groups with increasing immersion times. This trend aligned with the expected progression of DA oxidative polymerization. FTIR spectroscopy further confirmed the presence of PDA-specific reactive groups in the modified scaffolds. Peaks corresponding to O–H and N–H stretching vibrations were observed at 3000–3500 cm^{-1} (Figure 2B), with their intensity increasing with longer immersion times.

In the DA release experiments, based on the standard curve (Figure 2D), the PDA-PCL-24 scaffolds released approximately 40–72 nM of DA, PDA-PCL-6 released 33–44 nM, and PDA-PCL-3 released 5–7 nM (Figure 2E). Mechanical testing revealed that all scaffold groups exhibited a compressive strength of approximately 8 MPa (Figure 2C). Additionally, the porosity of all scaffolds was consistently around 75%, with no significant differences between groups. These findings indicate that the PDA coating did not change the original mechanical properties or porosity of the PCL scaffolds.

3.2. Effects of scaffolds on morphology and attachment of bone marrow mesenchymal stem cells

The extent of cell proliferation and adhesion to scaffolds is a critical factor in bone repair. To evaluate these parameters, we assessed the proliferative activity of BMSCs co-cultured with scaffolds using the CCK-8 assay on days 1, 3, and 7.

As shown in Figure 3B, the proliferative activity of cells on scaffolds with a PDA coating was significantly higher than that of the PCL group on days 1 and 3. By day 7, the

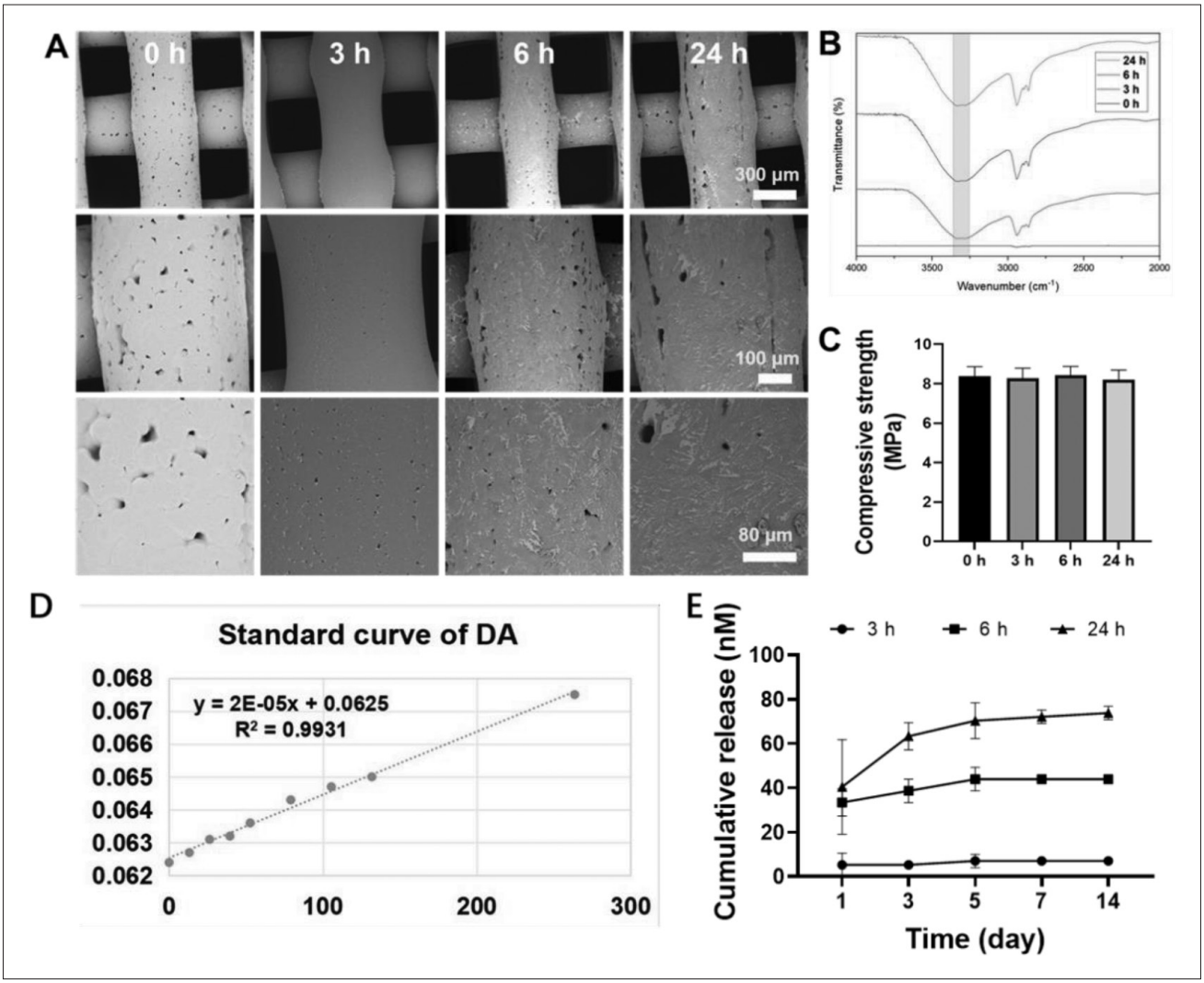

Figure 2. Material characterization and physicochemical property diagrams of the four groups of scaffolds. (A) Surface morphology. Scale bars: Top row: 300 μm; Middle row: 100 μm; Bottom row: 80 μm. Magnification: Top row: 200×; Middle row: 1000×; Bottom row: 2000×. (B) Fourier-transform infrared spectra. (C) Compression properties. (D) Standard curves for dopamine (DA) release. (E) DA release performance for each group. Notes: 0 h: The PCL group; 3 h: The PDA-PCL-3 group; 6 h: The PDA-PCL-6 group; 24 h: The PDA-PCL-24 group.

scaffolds in the PDA-PCL-6 group exhibited significantly enhanced pro-proliferative activity for BMSCs compared to the PCL group, whereas no significant differences were observed among the other groups.

Figure 3A displays SEM images of BMSCs adhering to the scaffolds after 1 day of culture. Numerous columnar and lamellar BMSCs were observed on the scaffold surfaces, with clear pseudopodia extending from the cells. These results were consistent with the cell proliferation findings. The PDA coating appeared to promote cell adhesion, with the PDA-PCL-6 group showing the most pronounced effect. In contrast, no significant differences in adhesion were noted between the PDA-PCL-3 and PDA-PCL-24 groups.

3.3. Evaluation of *in vitro* osteogenic and immunomodulatory properties of the scaffolds

To investigate the effects of PDA-coated scaffolds on the osteogenic differentiation of BMSCs, scaffolds were co-cultured with BMSCs. RT-PCR was used to analyze the expression of osteogenic genes, while ALP secretion and calcium nodule deposition were also evaluated.

As shown in Figure 4A and B, scaffolds with PDA coatings, particularly PDA-PCL-6, significantly enhanced ALP secretion compared to the other groups. Staining

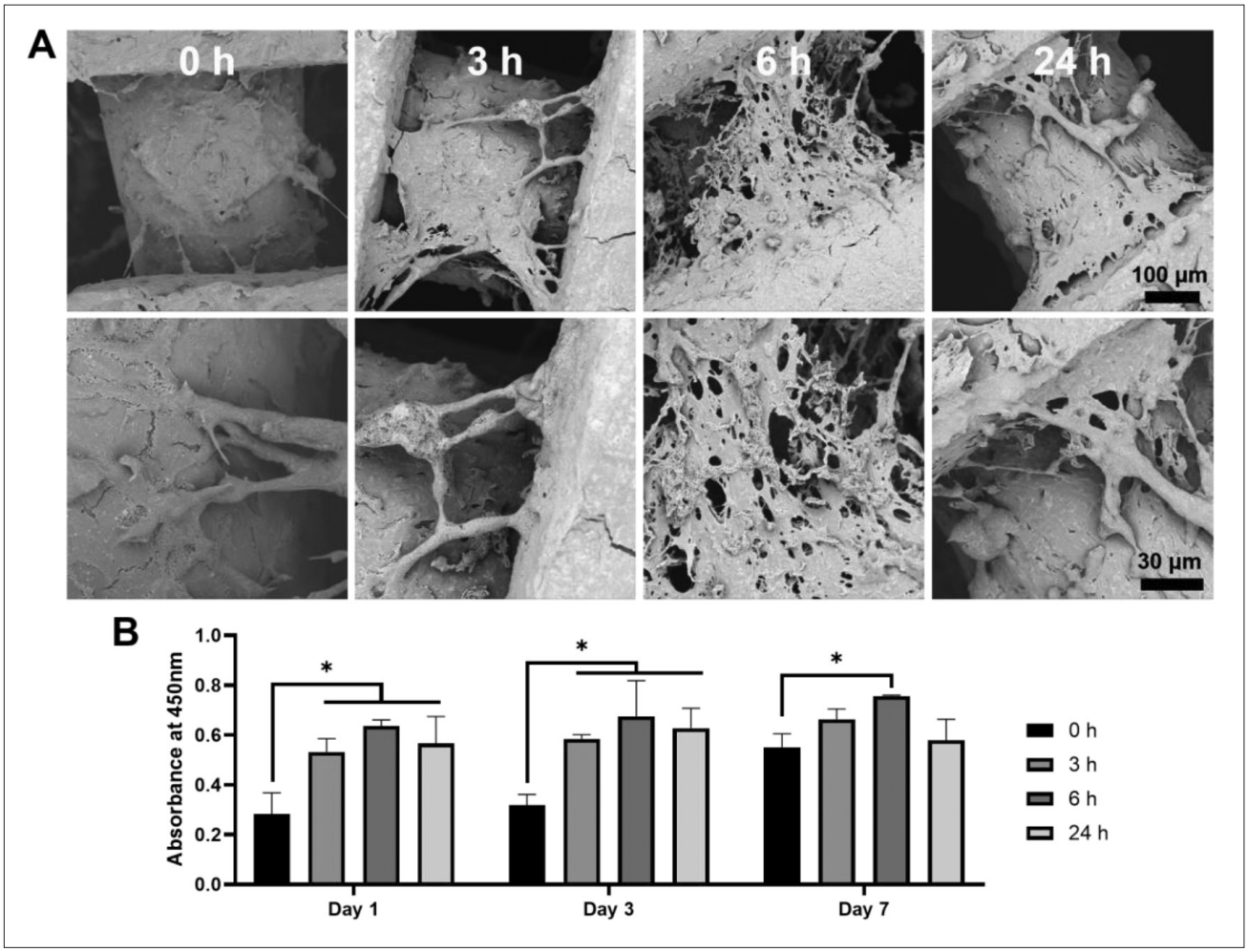

Figure 3. Enhanced bone marrow mesenchymal stem cell (BMSC) adhesion and proliferation on polydopamine-coated polycaprolactone scaffolds. (A) Scanning electron microscopic images showing BMSCs adhering to scaffolds after 24 h of culture. Scale bars: Top row: 100 μm; Bottom row: 30 μm. Magnification: Top row: 500×; Bottom row: 2000×. (B) Proliferation of BMSCs cultured on the four scaffold groups on days 1, 3, and 7. Notes: 0 h: The PCL group; 3 h: The PDA-PCL-3 group; 6 h: The PDA-PCL-6 group; 24 h: The PDA-PCL-24 group. *$p < 0.05$ indicates a significant difference against the PCL group.

and quantitative analysis of calcium nodules further demonstrated the superior performance of PDA-coated scaffolds. The PDA-PCL-6 group exhibited the highest calcium nodule content, while no significant differences were observed between the PDA-PCL-3 and PDA-PCL-24 groups (Figure 4C and D). These findings were in line with the trends observed in ALP secretion.

In terms of osteogenesis-related gene expression (*Runx2*, *Alp*, *Col1*) (Figure 4E), the PDA coating generally enhanced *Runx2* expression. The PDA-PCL-6 and PDA-PCL-24 groups showed similar expression levels, both of which were significantly higher than those in the PDA-PCL-3 group. *Alp* gene expression mirrored the ALP quantification results, with a significant increase observed in the PDA-PCL-6 group, while no significant differences were noted between the PDA-PCL-24 group and other groups. In terms of Col1 expression, compared with other groups, the PDA-PCL-6 group showed the highest expression level, and the PCL-3 group showed a higher expression level than the PCL group. There was no significant difference between the PDA-PCL-24, the PCL, and PCL-3 groups.

For immunomodulatory performance, PDA-coated scaffolds significantly upregulated the expression of *Cd206* and downregulated the expression of *Il1b* (Figure S2, Supporting Information). Among all groups, the PDA-PCL-6 group demonstrated the most pronounced ability to promote macrophage polarization from the M1 to

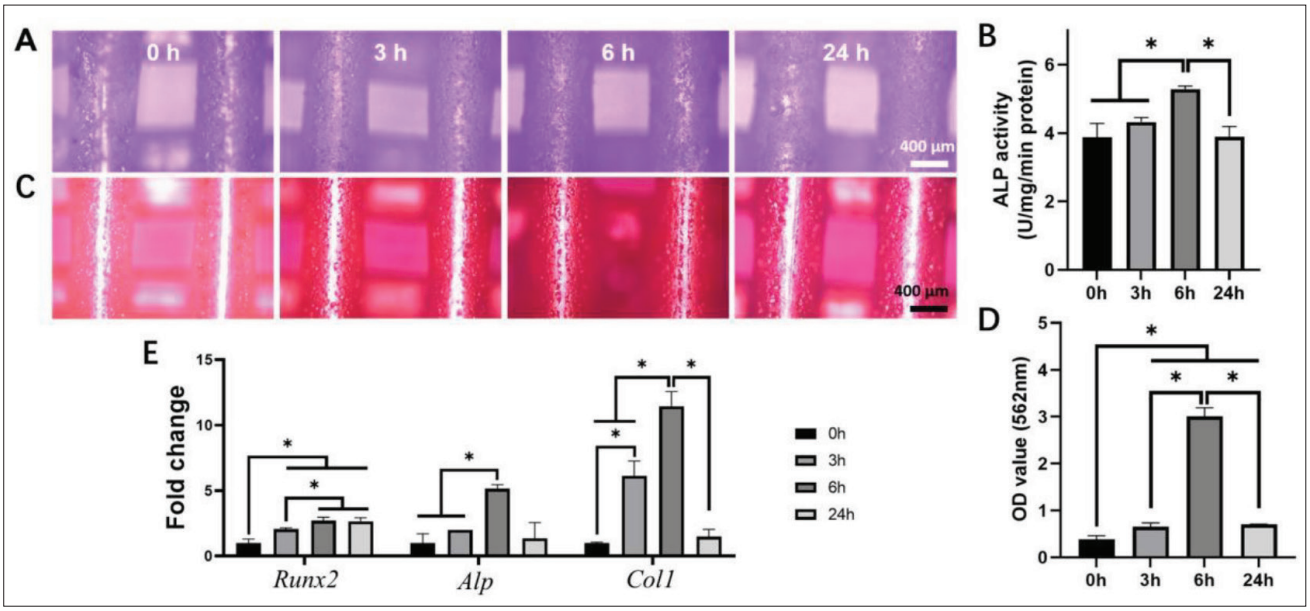

Figure 4. Evaluation of the enhanced *in vitro* osteogenic capacity of bone marrow mesenchymal stem cells (BMSCs) growing on the scaffolds. (A) Alkaline phosphatase (ALP) staining and (B) quantitative analysis of the scaffolds co-cultured with BMSCs on day 7. Scale bar: 400 μm. Magnification: 5×. (C) Calcium nodule staining and (D) quantitative plots of scaffolds co-cultured with BMSCs on day 14, respectively. Scale bars: 400 μm. Magnification: 5× (E) Expression of osteogenesis-related genes (*Runx2*, *Alp*, *Col1*) in BMSCs on day 14. Notes: 0 h: The PCL group; 3 h: The PDA-PCL-3 group; 6 h: The PDA-PCL-6 group; 24 h: The PDA-PCL-24 group. *$p < 0.05$ indicates a significant difference.

the M2 phenotype. This enhanced immunomodulatory performance is attributed to the oxidative free radical scavenging properties of PDA, which confer immunomodulatory activity to the scaffold, downregulate inflammatory cytokine expression, and stimulate the M2 macrophage phenotype.[19]

3.4. *In vivo* study of the scaffolds for bone regeneration

To evaluate the pro-regenerative properties of PDA-coated scaffolds *in vivo*, we selected PDA-PCL-6, which exhibited the highest bioactivity in the *in vitro* experiments, as the experimental group (Exp). A control group (Con; pure PCL) and a blank group (Blank) were also included. Micro-CT analysis was performed on the bone defect regions of three groups of SD rats at 4, 8, and 12 weeks postoperatively.

As depicted in Figure 5A, the blank group, which did not receive a scaffold implant, displayed minimal new bone formation within the defect area at both 4 and 8 weeks postoperatively. Even by 12 weeks, the increase in new bone tissue was negligible, suggesting a suboptimal bone repair process in the absence of a scaffold. In contrast, the PCL group, which was implanted with pure PCL scaffolds, showed some new bone formation at 4 weeks postoperatively. However, the increase in new bone tissue over the subsequent 8 and 12 weeks was insufficient to fully heal the substantial bone defect, highlighting the limited osteogenic potential of pure PCL scaffolds for bone repair.

The PDA-PCL group consistently demonstrated superior new bone formation compared to the PCL group at each time point. At 4 weeks, the growth of trabecular bone along the composite scaffold within the defect area was evident, and this growth progressively increased by 8 weeks. By 12 weeks, the defect area was nearly filled with trabecular and lamellar bone, indicating a significantly enhanced bone repair process.

Quantitative analysis of the bone volume fraction in the defect areas at 4, 8, and 12 weeks postoperatively, as presented in Figure 5B, confirmed that the PDA–PCL composite scaffolds provided superior bone repair efficacy. In comparison, the blank group exhibited the least favorable outcomes. Statistically significant differences were observed ($p < 0.05$), underscoring the enhanced osteoconductive properties of the PDA-modified scaffolds in promoting bone regeneration.

To further verify the *in vivo* bone defect repair effects of the three scaffold groups, rat skull specimens were collected at 4, 8, and 12 weeks postoperatively. Bone formation at the defect site was analyzed using hematoxylin and eosin (H&E) staining, Masson staining, and Movat staining.

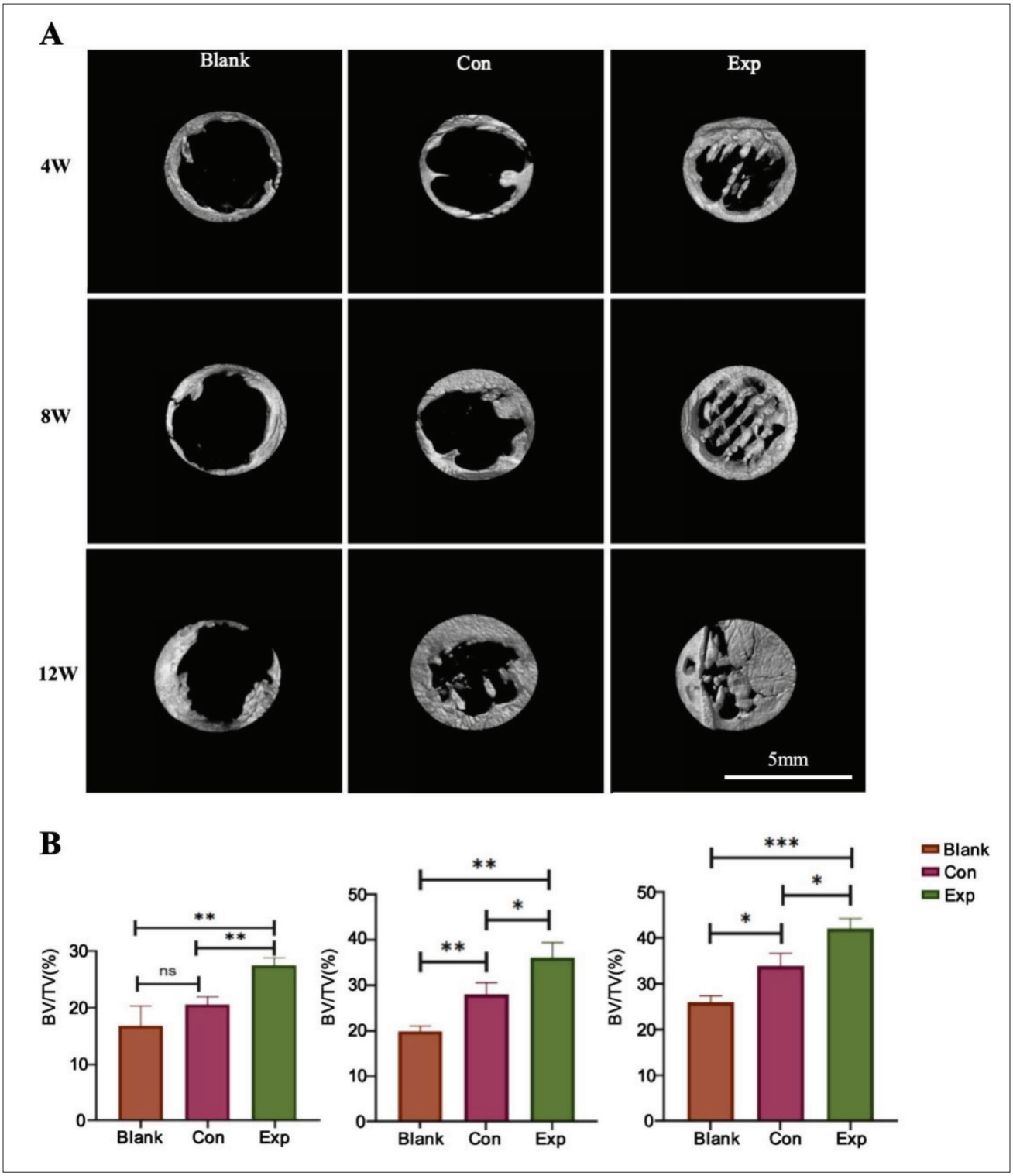

Figure 5. *In vivo* bone regeneration in a rat calvarial defect model. (A) Micro-computed tomography of rat calvarial defects at 4, 8, and 12 weeks postoperatively for each group. Scale bar: 5 mm. Magnification: 1.5×. (B) Quantitative analysis of bone volume fraction in the defect regions of rats at 4, 8, and 12 weeks (from left to right) for each group. Notes: Blank: No scaffold; Control: Treated with the PCL scaffold; Exp: Treated with the PDA-PCL scaffold. *$p < 0.05$ indicates a significant difference.

The H&E staining images at 4 weeks (Figure 6) revealed that the blank group exhibited a large amount of fibrous tissue and minimal new bone tissue in the bone defect area. In the PCL group, a small amount of new bone was observed within the defect area, whereas the PDA-PCL group showed significantly more new bone formation. At 8 weeks, the new bone tissue in the PDA-PCL group showed a wider distribution compared to the other two groups. Interconnected pores were filled with gradually forming new bone tissue, while osteoid tissue and small amounts of woven bone were observed at the material–bone interface and within the porous scaffold. By 12 weeks, as the PCL material degraded and the defect area further decreased, the new bone in the PDA-PCL group formed a continuous block. The new bone area in this group was significantly larger compared to the blank and PCL groups. Masson staining results (Figure 7) supported these findings. At 4 weeks, the PDA-PCL group showed more light blue collagen tissue and red muscle fiber tissue compared to the PCL group, with the least amount observed in the blank group. Over time, at 8 and 12 weeks, all groups exhibited further maturation of neoplastic bone tissue, with dark blue-stained mature collagen becoming prominent. This effect was most pronounced in the PDA-PCL group, followed by the PCL group.

Movat staining results (Figure 8) were in line with the trends observed in H&E and Masson staining. Movat staining identified collagen and reticulocyte fibers as yellow, proteoglycans as blue-green, and cellulose-like or fibrillar structures as dark red. In the PDA-PCL group, neoplastic bone tissue gradually replaced the scaffold, with a substantial presence of yellow-stained collagen fibers and reticular fibers forming more mature neoplastic bone and showing cortical bridging. In contrast, the blank group was dominated by muscle tissue with minimal neoplastic bone and insignificant cortical bridging. The PCL group demonstrated intermediate bone deposition and formation, falling between the other two groups.

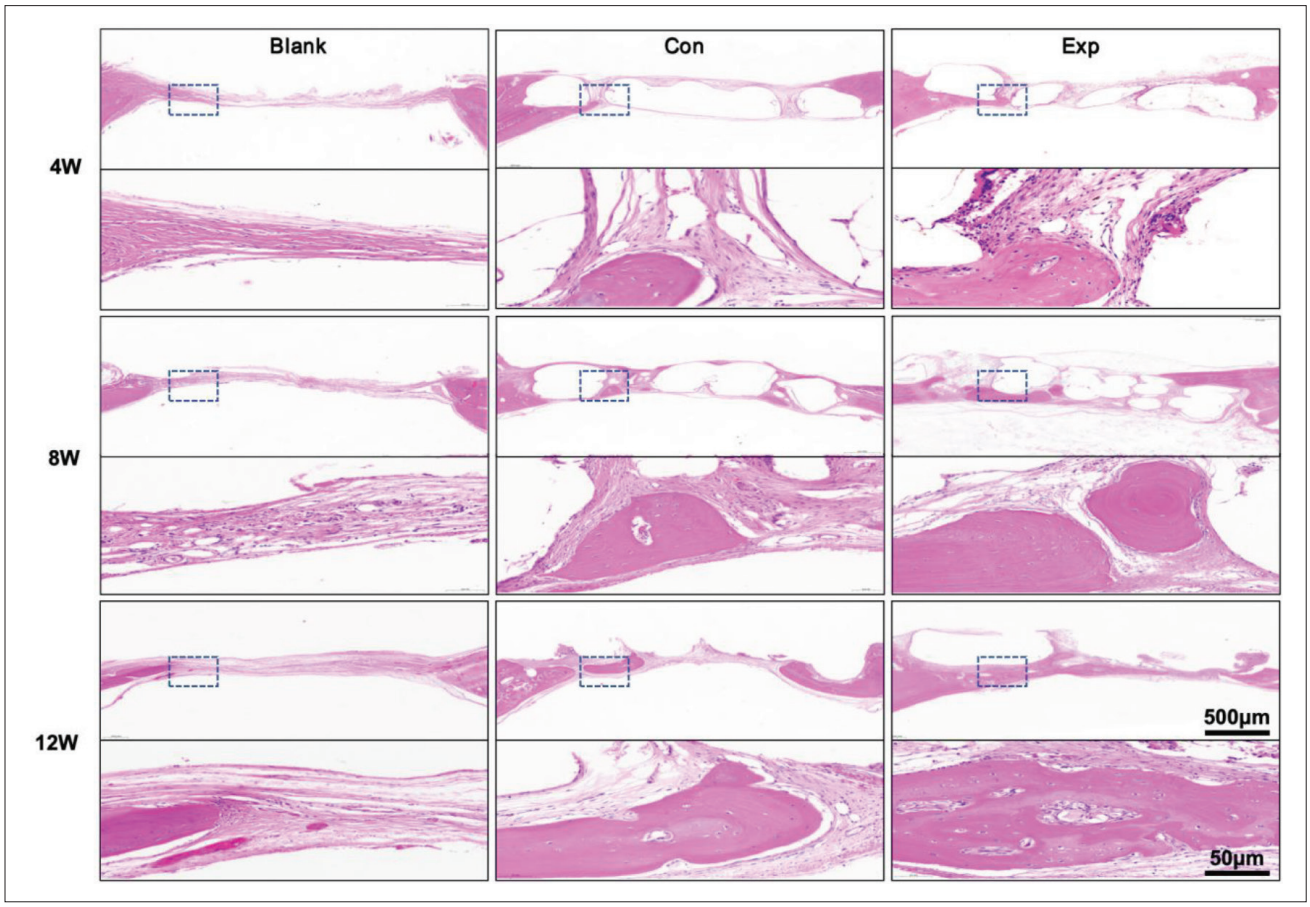

Figure 6. Hematoxylin and eosin staining of rat calvarial specimens at 4, 8, and 12 weeks postoperatively for each group. Scale bar: Top row of each time point: 500 μm; Bottom row of each time point: 50 μm. Magnification: Top row of each time point: 2×; Bottom row of each time point: 10×. Notes: Blank: No scaffold; Control: Treated with the PCL scaffold; Exp: Treated with the PDA-PCL scaffold.

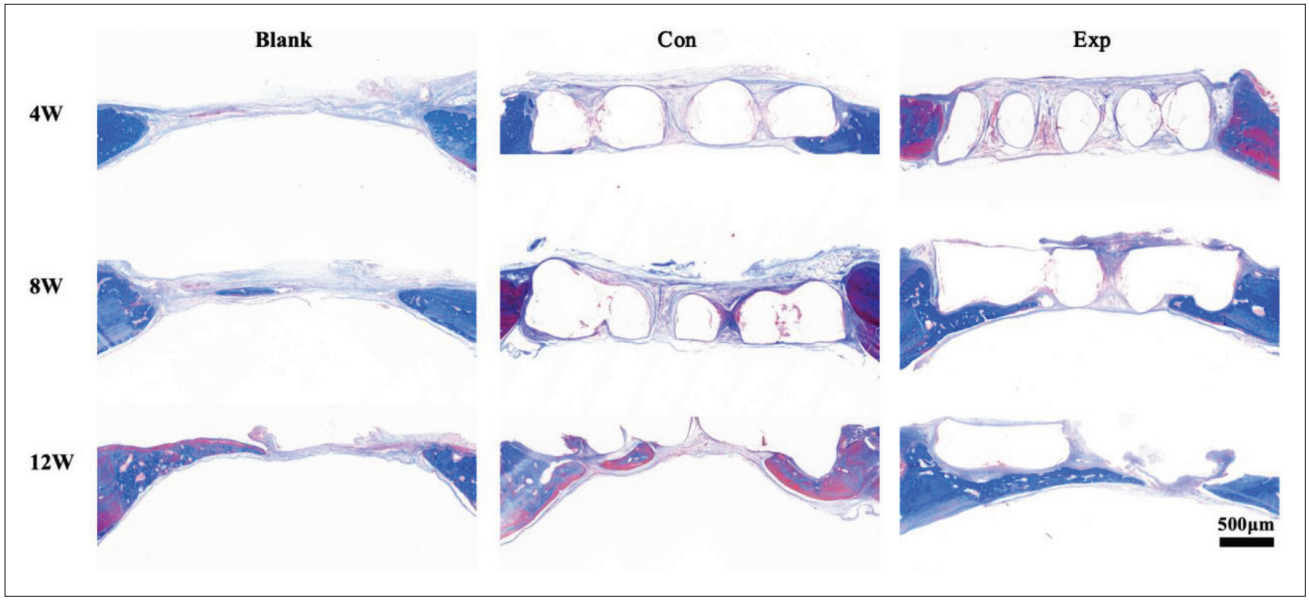

Figure 7. Masson staining of rat calvarial specimens at 4, 8, and 12 weeks postoperatively for each group. Scale bar: 500 μm. Magnification: 2×.

These results suggest that PDA-functionalized PCL scaffolds can effectively induce *in situ* bone regeneration without the need for exogenous seed cells or growth factors.

To further assess the osteoinductive potential of the scaffolds, immunohistochemical staining was performed to detect BMP-2 and COL-I expression in each group. As shown in Figures 9 and 10, at 4 weeks, distinct brown-yellow areas were observed around the newly formed tissue in the bone defect area of the PDA-PCL group, indicating positive expression of BMP-2 and COL-I. In contrast, the PCL group displayed only a few positive expression areas, while the blank group showed almost no detectable expression.

At 8 weeks, both the PDA-PCL and PCL groups showed discontinuous new bone formation. The PDA-PCL group exhibited deeper and more extensive brown-yellow positive expression areas around the new bone matrix for BMP-2 and COL-I, whereas the blank group showed only minimal BMP-2 and COL-I expression.

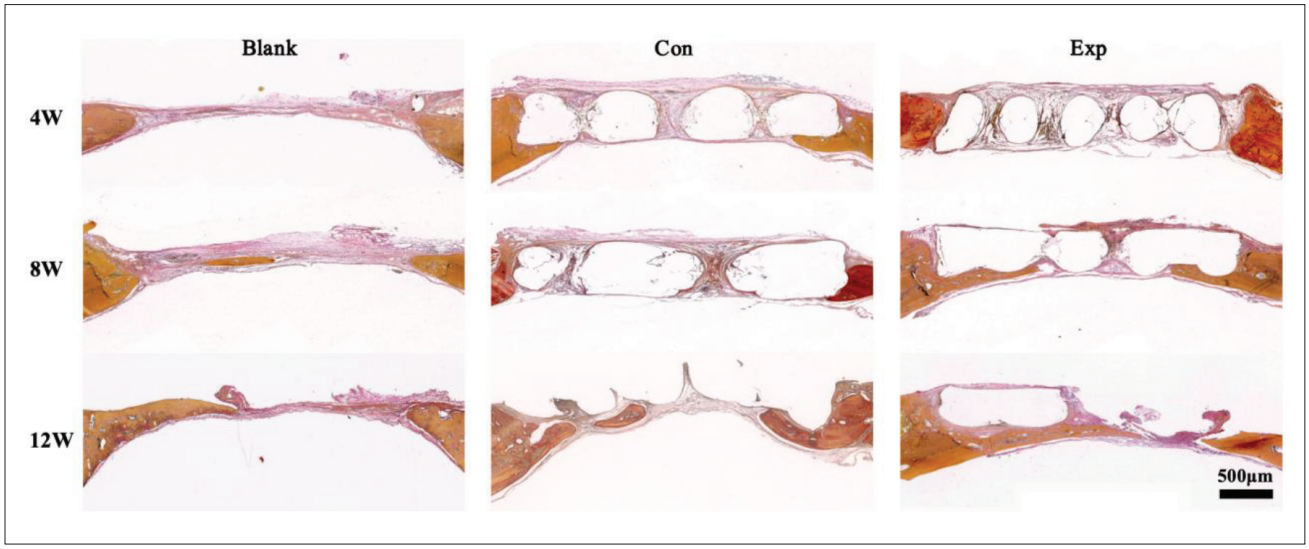

Figure 8. Movat staining of rat calvarial specimens at 4, 8, and 12 weeks postoperatively for each group. Scale bar: 500 μm. Magnification: 2×. Notes: Blank: No scaffold; Control: Treated with the PCL scaffold; Exp: Treated with the PDA-PCL scaffold.

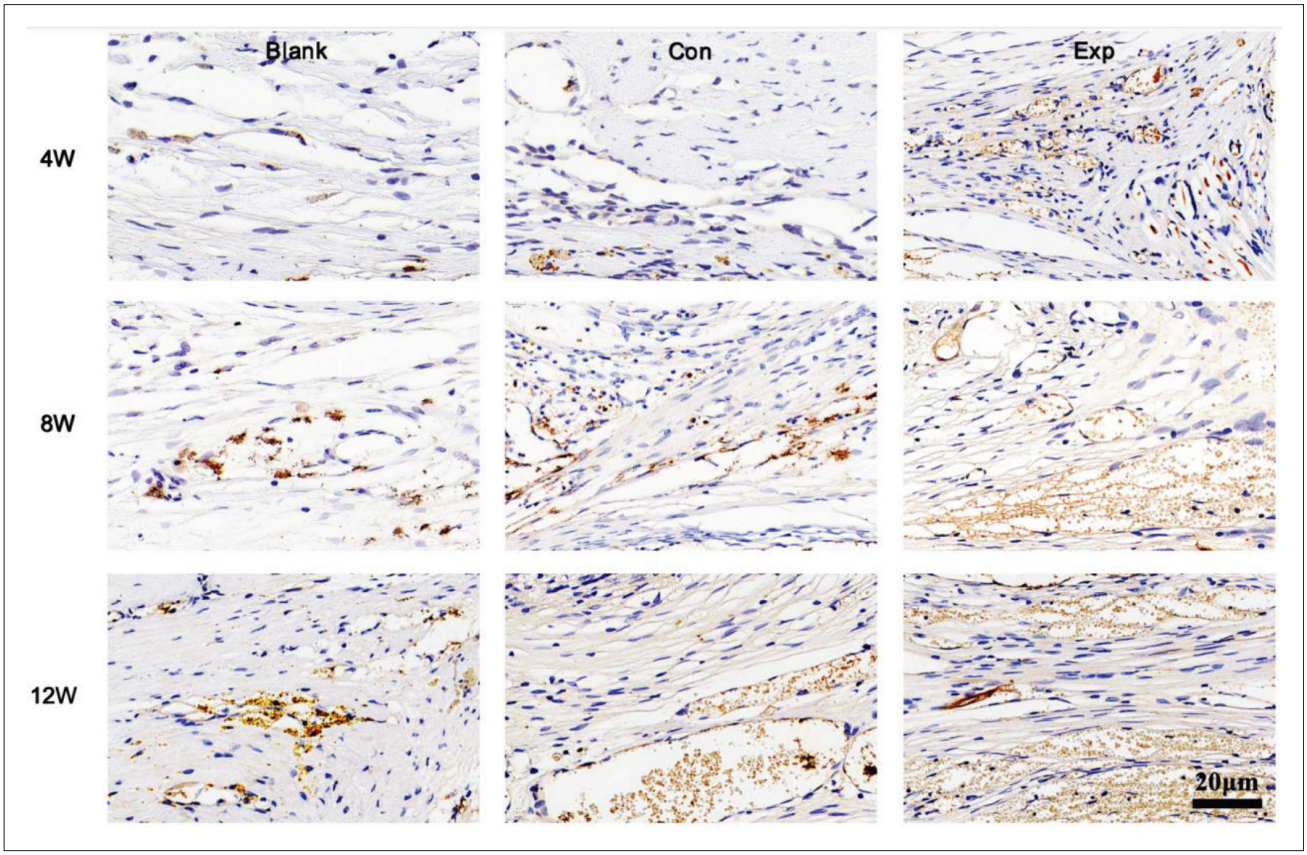

Figure 9. Immunohistochemical expression of BMP-2 in rat calvarial specimens at 4, 8, and 12 weeks postoperatively for each group. Scale bar: 20 μm. Magnification: 40×. Notes: Blank: No scaffold; Control: Treated with the PCL scaffold; Exp: Treated with the PDA-PCL scaffold.

By 12 weeks, BMP-2 and COL-I expression levels in the bone defect sites had increased across all groups compared to earlier time points. However, the PDA-PCL group demonstrated significantly greater positive expression than both the PCL and blank groups. These findings indicate that the PDA-functionalized coating significantly enhances the osteoinductive potential of PCL scaffolds and promotes the expression of bone tissue markers.

3.5. Histocompatibility of polydopamine-coated scaffolds *in vivo*

3.5.1. Blood indicator tests

The routine blood indices of rats from the three groups were measured at 4, 8, and 12 weeks postoperatively, as shown in Table 3. No statistically significant differences were observed among the blank group, PCL group, and PDA-PCL group in terms of white blood cell count, red blood cell count, hemoglobin, platelets, glutamate aminotransferase, glutamate aminotransferase, creatinine, and urea levels.

3.5.2. Hematoxylin and eosin staining of liver and kidney tissue

Liver and kidney specimens were collected from rats in each group, and histological sections were prepared and analyzed using H&E staining to identify pathological changes. As shown in Figure 11, liver structures such as the central vein, confluent areas, and hepatocytes were intact and well-defined across all groups, with normal size, morphology, and boundaries. No inflammatory cell infiltration was observed.

Similarly, kidney structures, including glomeruli, tubules, and mesangial cells, appeared normal in size, morphology, and boundaries across all groups, as shown in Figure 12. No signs of inflammatory cell infiltration were observed.

4. Discussion

Ideal bone repair materials should possess excellent biocompatibility, osteoinductivity, osteoconductivity, and osteointegration.[20] The biodegradable polymer

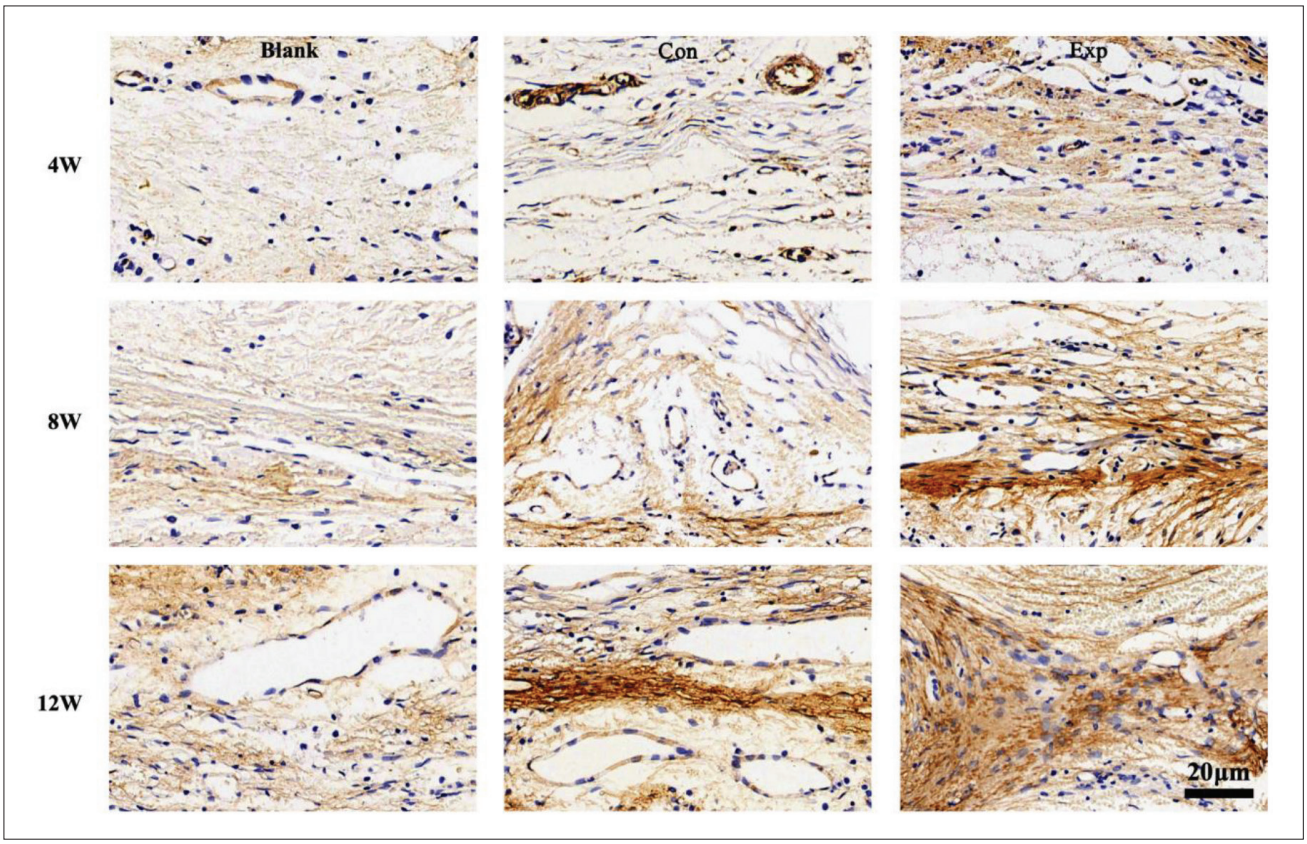

Figure 10. Immunohistochemical expression of COL-I in rat calvarial specimens at 4, 8, and 12 weeks postoperatively for each group. Scale bar: 20 μm. Magnification: 40×. Notes: Blank: No scaffold; Control: Treated with the PCL scaffold; Exp: Treated with the PDA-PCL scaffold.

PCL is widely used in bone tissue engineering due to its high plasticity and excellent biocompatibility. Upon degradation into water and carbon dioxide, PCL promotes bone defect repair while providing space for the ingrowth of new bone tissue and blood vessels, making it a suitable base material for bone tissue scaffolds.[21] However, PCL is inherently hydrophobic and lacks adequate sites for cell adhesion. Consequently, the single structure of PCL alone is insufficient to serve as an ideal bone scaffold material.[22]

Previous studies have shown that optimizing the 3D porous structure of scaffolds while maintaining mechanical strength and ensuring a highly interconnected internal pore network can significantly increase the surface area for cell attachment and enhance nutrient permeability.[23] For bone tissue engineering, scaffolds fabricated through 3D printing offer customizable geometric shapes and porosity, with micro-level interconnectivity that supports the ingrowth of bone tissue and blood vessels on the scaffold surface. These features facilitate nutrient delivery to cells and establish a strong connection with the host bone, showing good prospects for bone defect repair applications.[24] Previous research has shown that porous PCL scaffolds created using 3D printing significantly improved osteogenic effects in a pig condyle bone defect model.[25]

Numerous studies have highlighted the importance of surface characteristics and material–cell interactions in effective bone defect repair.[26] Functional modification of material surfaces can enhance hydrophilicity, adhesion, and interaction with cells and tissues, thereby improving biocompatibility.[27] PDA, a melanin-like substance, contains multiple active functional groups, such as catechol and hydrophilic amino groups. These groups enable PDA to strongly attach to material surfaces through covalent bonds, improving hydrophilicity, adhesion, and biocompatibility without eliciting an immune response in the human body.[28,29] Additionally, the catecholamine groups in PDA exhibit strong chelation with calcium ions, promoting calcium ion enrichment on scaffold surfaces and enhancing mineralization. This property further supports bone repair by increasing the scaffold's osteoinductive potential.[30]

In this study, 3D printing was used to fabricate PCL scaffolds, which were subsequently surface-modified with

Table 3. Blood indices of rats in each group at 4, 8, and 12 weeks postoperatively

Time point (week)	Clinical test indicators	Group			*p-value*
		Blank	Control	Experimental	
4	WBC (10^9/L)	11.15 ± 0.46	10.36 ± 0.86	11.68 ± 0.61	0.125
	RBC (10^{12}/L)	8.99 ± 0.61	8.12 ± 0.17	8.44 ± 0.58	0.655
	HB (g/L)	153.33 ± 4.73	162.00 ± 8.89	159.00 ± 7.81	0.399
	PLT (10^9 L)	936.67 ± 130.62	1005.00 ± 100.58	902.67 ± 140.76	0.619
	ALT (U/L)	53.00 ± 2.65	50.67 ± 3.06	53.33 ± 2.52	0.477
	AST (U/L)	113.67 ± 2.08	116.33 ± 4.16	118.33 ± 1.53	0.209
	Urea (mmol/L)	4.23 ± 0.15	4.83 ± 0.92	4.06 ± 0.27	0.281
	Cr (μmol/L)	37.33 ± 1.53	36.33 ± 5.69	31.33 ± 1.53	0.161
8	WBC (10^9/L)	9.89 ± 1.10	9.45 ± 1.35	9.44 ± 1.83	0.915
	RBC (10^{12}/L)	8.20 ± 0.28	8.74 ± 0.66	9.09 ± 0.84	0.304
	HB (g/L)	159.00 ± 8.72	157.67 ± 8.50	166.67 ± 6.03	0.378
	PLT (10^9/L)	897.33 ± 17.90	1000.00 ± 81.07	997.00 ± 207.65	0.572
	ALT (U/L)	41.67 ± 7.02	48.33 ± 3.79	45.00 ± 11.79	0.633
	AST (U/L)	122.00 ± 29.61	127.33 ± 22.03	134.67 ± 20.55	0.821
	Urea (mmol/L)	5.04 ± 0.68	4.73 ± 0.53	4.95 ± 0.23	0.764
	Cr (μmol/L)	36.67 ± 4.04	35.00 ± 3.61	34.33 ± 4.93	0.792
12	WBC (10^9/L)	10.49 ± 0.14	10.04 ± 0.23	10.27 ± 0.37	0.188
	RBC (10^{12}/L)	8.42 ± 0.40	8.90 ± 0.32	8.55 ± 0.38	0.315
	HB (g/L)	166.33 ± 3.79	168.00 ± 7.94	169.67 ± 3.51	0.766
	PLT (10^9/L)	945.33 ± 38.19	995.33 ± 25.42	991.33 ± 44.55	0.260
	ALT (U/L)	37.33 ± 3.79	35.00 ± 4.36	37.00 ± 1.73	0.690
	AST (U/L)	97.67 ± 5.03	96.67 ± 7.23	94.33 ± 4.16	0.767
	Urea (mmol/L)	4.96 ± 0.22	4.76 ± 0.43	4.76 ± 0.27	0.673
	Cr (μmol/L)	33.33 ± 3.06	36.33 ± 1.15	32.33 ± 2.52	0.182

Notes: Values are expressed as mean ± standard deviation. ALT, glutamate aminotransferase; AST, glutamate aminotransferase; Cr, creatinine; HB, hemoglobin; PLT, platelet; RBC, red blood cell count; WBC, white blood cell count.

PDA. The repair capacity of the PDA–PCL composite scaffolds was evaluated by comparing their physical properties, biocompatibility, *in vitro* osteoinductive potential on BMSCs, and *in vivo* osteoinductive potential on rat calvarial defect models. This approach provided a comprehensive assessment of the repair capabilities of PDA–PCL composite scaffolds in comparison to unmodified PCL scaffolds.

Polycaprolactone scaffolds were prepared using 3D printing technology, and PDA coating was applied via an immersion shaker method. The results (Figure 2) showed that the surface of the modified scaffolds became rougher due to the oxidative polymerization of DA, forming a PDA coating. PDA adheres to hydroxyl-containing PCL surfaces through chelation, hydrogen bonding, π-π stacking, and other non-covalent interactions.[31] This increased surface roughness significantly enhanced cell adhesion and proliferation.[32]

Elemental composition analysis and FTIR spectroscopy confirmed the presence of nitrogen on PDA-modified scaffolds, with nitrogen content and the characteristic PDA peak at 3000–3500 cm^{-1} increasing with immersion times. This increase was attributed to the introduction of surface amine groups from the PDA attachment, confirming the successful preparation of PDA-PCL scaffolds.[33] Although the compressive

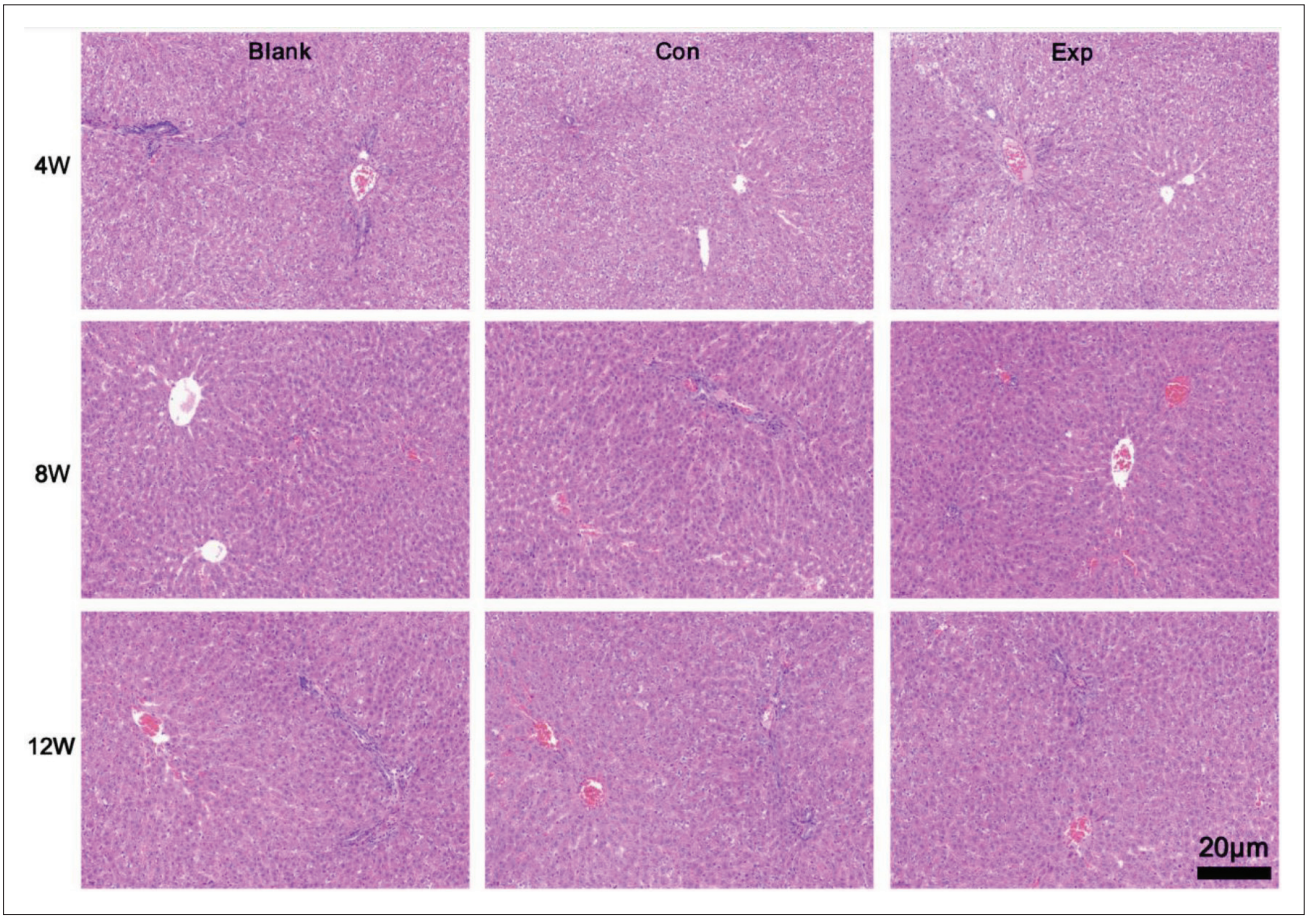

Figure 11. Hematoxylin and eosin staining of rat livers in each group at 4, 8, and 12 weeks postoperatively. Scale bar: 20 μm. Magnification: 40×. Notes: Blank: no scaffold; Control: treated with the PCL scaffold; Exp: treated with the PDA-PCL scaffold.

strength of human cortical bone ranges from 100 to 230 MPa and cancellous bone ranges from 2 to 12 MPa, the experimental results showed that the compressive strength of the PDA-PCL scaffolds was approximately 8 MPa. This value is sufficient for repairing bone defects in non-load-bearing areas.[34]

Before clinical application, tissue-engineered artificial bones must undergo biosafety testing, primarily focusing on the biocompatibility and cytotoxicity of the scaffolds.[35] To evaluate the biocompatibility of PDA–PCL composite scaffolds, BMSCs were seeded on PCL, PDA-PCL-3, PDA-PCL-6, and PDA-PCL-24 scaffolds. The results (Figure 3) showed that cell proliferation rates on modified scaffolds were higher than on plain PCL scaffolds, suggesting that PDA modification enhanced cell adhesion and proliferation. Importantly, PDA-coated PCL scaffolds did not exhibit cytotoxicity. Among the groups, scaffolds modified for 6 h (PDA-PCL-6) demonstrated the strongest ability to promote cell proliferation, with statistically significant differences.

Alkaline phosphatase is an early marker of osteoblast differentiation, and its activity is closely related to osteogenic potential, providing a preliminary assessment of the osteogenic performance of implanted materials.[36] Calcium nodule deposition, one of the hallmarks of advanced osteoblast maturation, further reflects the osteogenic capacity of scaffolds. In this study, PDA coating was shown to enhance the biological activity of PCL scaffolds, as demonstrated by ALP staining, alizarin red staining, and quantitative detection of calcium nodule deposition (Figure 4).

In terms of osteogenic gene expression, *Runx2*, a transcription factor in the bone morphogenetic protein (BMP) signaling pathway, is a major regulator of osteoblast development and bone formation. It is considered one of the earliest transcription factors to trigger osteogenic differentiation. ALP, widely recognized as a marker of osteoblast activity, represents an early phenotypic indicator of osteoblast and osteoclast differentiation. Additionally, COL-I is essential for bone tissue mineralization,

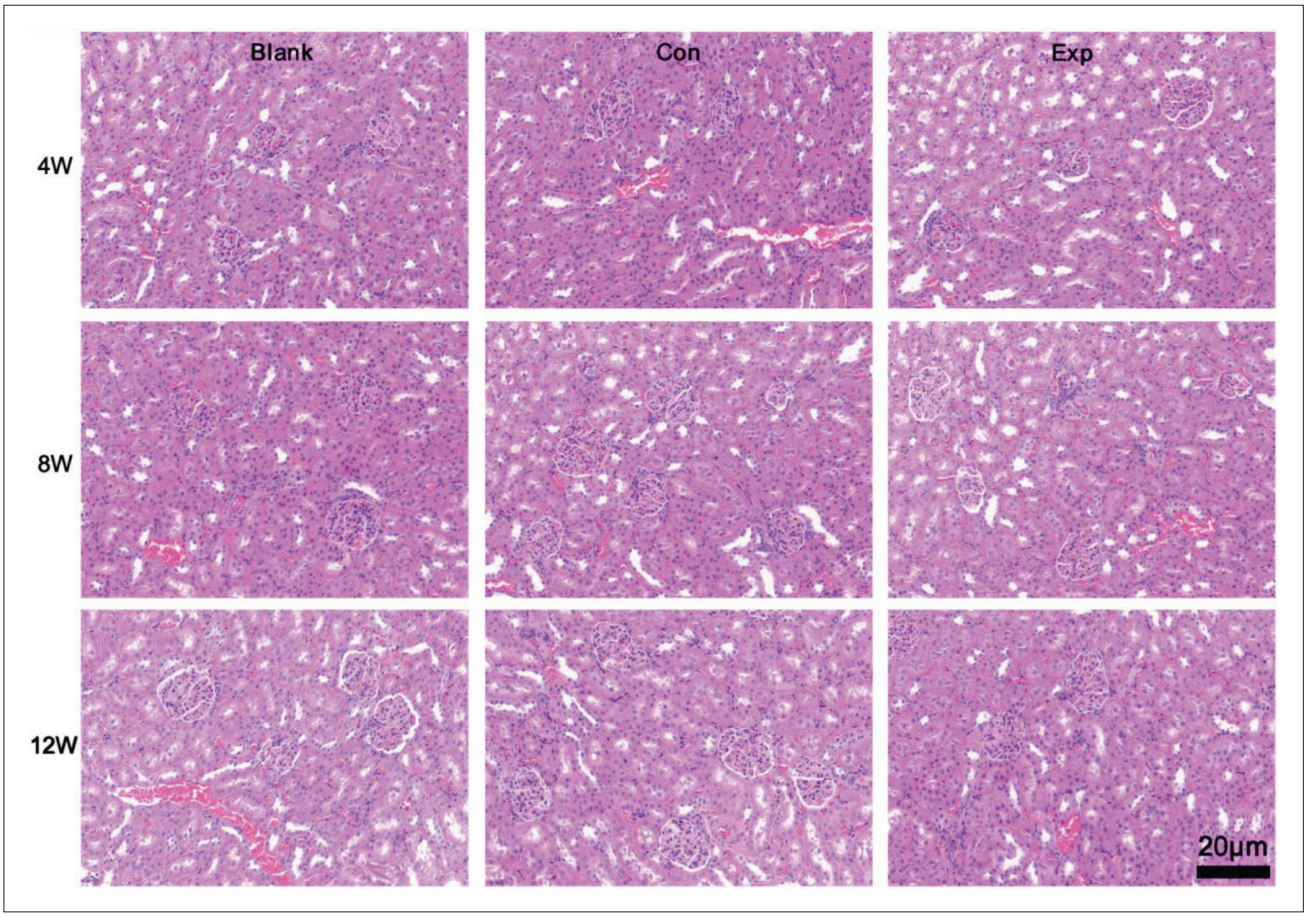

Figure 12. Hematoxylin and eosin staining of rat kidneys in each group at 4, 8, and 12 weeks postoperatively. Scale bar: 20 μm. Magnification: 40×. Notes: Blank: no scaffold; Control: treated with the PCL scaffold; Exp: treated with the PDA-PCL scaffold.

stimulating osteoblast adhesion and differentiation, and contributing to the formation of the organic matrix and structural integrity of cells.

In this study, the expression levels of *Runx2*, *Alp*, and *Col1* were measured using RT-PCR. Among the tested groups, the PDA-PCL-6 scaffolds exhibited the highest expression of these genes, followed by PDA-PCL-3. *Alp* expression levels in the PCL group were higher than in the PDA-PCL-24 group. No significant differences in *Col1* expression were observed between the PDA-PCL-0 and PDA-PCL-24 groups. These findings indicate that the PDA-PCL-6 group demonstrated the most significant osteogenic activity among the four groups.

Polydopamine degrades into a water-soluble compound in strongly alkaline solutions but remains essentially nondegradable in acidic and neutral environments, maintaining the original structure of DA during *in vitro* experiments.[37] DA activates DA receptors and induces ERK phosphorylation, thereby promoting osteogenic differentiation in BMSCs.[38,39] The appropriate PDA coating thickness plays a critical role in achieving superior cell adhesion and bone-enhancing properties, as excessively high DA concentrations may inhibit BMSC growth.

Sun et al.[40] demonstrated that a gradual increase in DA concentration (0.5–10 nM) favored osteogenic differentiation, while the DA-stimulated osteogenic performance diminished gradually at concentrations above 10 nM. Nonetheless, DA-mediated bone activity at 50 nM remained significantly higher than that at 5 nM. In this study, the DA concentration released by PDA-PCL-6 scaffolds ranged from 33–44 nM (Figure 2E), demonstrating exceptional osteoinductive performance. In addition, Pei et al.[41] found that DA concentrations below 2 mg/mL promoted macrophage polarization toward the M2 phenotype and reduced the secretion of inflammatory factors. All three groups of PDA-coated scaffolds in this study released DA below 2 mg/mL, confirming their excellent immunomodulatory properties. Unexpectedly, DA concentrations of 33–44 nM further enhanced macrophage polarization toward the M2 phenotype.

To evaluate the healing effects of PDA-coated scaffolds on cranial defects in rats, micro-CT imaging was performed on the cranial defect sites in each group. The new bone volume fraction was quantitatively analyzed and found to follow the trend: PDA-PCL group > PCL group > control group, with statistically significant differences between groups (Figure 5). Histological staining further corroborated these findings, revealing a progressive increase in new bone formation in the bone defect area of the PDA-PCL group over time. By week 12, as the implanted scaffold gradually degraded, the bone defect area in the experimental group (PDA-PCL group) was nearly filled with new bone tissue, followed by the control group (PCL group), while the blank group exhibited the least amount of new bone (Figures 6–8).

Immunohistochemical staining was utilized to further evaluate the repair of cranial bone defects in rats. The expressions of BMP-2 and COL-I, critical growth factors for bone tissue development, were analyzed. These factors play pivotal roles during new bone formation by inducing the differentiation of osteoblasts into osteogenic cells and promoting the reverse differentiation of fibroblasts, myoblasts, and bone marrow precursor cells into osteogenic cells.[42,43]

Immunohistochemical staining was performed on rat calvarial specimens from each group at 4, 8, and 12 weeks postoperatively. Results demonstrated that the expression of osteogenesis-related proteins in the PDA-PCL group was significantly higher than that in the blank and PCL groups across all time points. Additionally, blood indices and H&E-stained sections of the liver and kidney from rats in all groups showed no evident abnormalities, indicating that the PDA-functionalized PCL scaffolds exhibited excellent *in vivo* biocompatibility. These findings suggest that the PDA-functionalized coating significantly enhanced cell adhesion and conferred osteoinductive properties to the PCL scaffolds. In addition, the PDA–PCL composite scaffolds effectively promoted the repair of cranial bone defects in rats. However, this study only preliminarily investigated their effects on small cranial bone defects in rats. The potential of PDA-PCL scaffolds to repair segmental bone defects in other anatomical locations or larger volumes requires further in-depth studies.

5. Conclusion

This study successfully developed 3D-printed PCL composite scaffolds with a highly bioactive PDA coating. Compared with pure PCL scaffolds, the PDA-coated scaffolds, especially those in the PDA-PCL-6 group, demonstrated immunomodulatory properties and significantly enhanced the proliferation and adhesion of BMSCs as well as osteogenic differentiation. In addition, the PDA-coated scaffolds effectively facilitated the repair of cranial bone defects in rats while exhibiting excellent histocompatibility, offering a promising new approach to the treatment of bone defects. Nonetheless, further studies are necessary to evaluate the efficacy of these scaffolds in repairing larger or more extensive bone defects.

Acknowledgments

None.

Funding

This research was supported by the National Natural Science Foundation of China (32000964, 82160577), the Guangdong Province Science and Technology Plan Project (2024A1515012265, 2020B1111560001, and 2022A1515140193), the Program for Science and Technology Project of Guizhou Province, Qiankehe Platform Talents ([2021] 5613), the Key Program for Science and Technology Project of Guizhou Province (ZK [2021] 007), the GDAS' Project of Science and Technology Development (2022GDASZH-2022020402-01, 2022GDASZH-2022010110, 2020GDASZH-2022030604-01, and 2023GDASZH-2023010102).

Conflict of interest

We declare that we have no financial and personal relationships with other people or organizations that can inappropriately influence our work, and there is no professional or other personal interest of any nature or kind in any product, service and/or company that could be construed as influencing the position presented in, or the review of, the manuscript entitled.

Author contributions

Conceptualization: Qian Zhong, Shuai Huang, Weihua Huang, Weikang Xu, Qingde Wa

Data curation: Qian Zhong, Shuai Huang, Weihua Huang, Weikang Xu, Qingde Wa

Formal analysis: Qian Zhong, Shuai Huang, Weihua Huang

Funding acquisition: Weikang Xu, Qingde Wa

Investigation: Qian Zhong, Shuai Huang, Weihua Huang

Methodology: Qian Zhong, Shuai Huang, Weihua Huang

Project administration: Qian Zhong, Shuai Huang, Weihua Huang, Hengpeng Wu, Yang Wang, Zhenyu Wen, Huinan Yin, Yixiao Wang

Resources: Qian Zhong, Shuai Huang, Weihua Huang

Software: Qian Zhong, Shuai Huang, Weihua Huang

Validation: Weikang Xu, Qingde Wa
Visualization: Weikang Xu, Qingde Wa
Writing – original draft: Qian Zhong, Shuai Huang, Weihua Huang
Writing – review & editing: Weikang Xu, Qingde Wa

Ethics approval and consent to participate

All animal experiments were performed under the protocol approved by the Institutional Animal Care and Use Committee of Guangdong Quality Supervision and Testing Station for Medical and Health Care Appliances (Ethics approval number: 32000964).

Consent for publication

Not applicable.

Availability of data

Data are available from the corresponding author upon reasonable request.

References

1. Nauth A, McKee MD, Einhorn TA, Watson JT, Li R, Schemitsch EH. Managing bone defects. *J Orthop Trauma*. 2011;25(8):462-466.
doi: 10.1097/BOT.0b013e318224caf0

2. Schemitsch EH. Size matters: defining critical in bone defect size! *J Orthop Trauma*. 2017;31(Suppl 5):S20-S22.
doi: 10.1097/BOT.0000000000000978

3. Khodakaram-Tafti A, Mehrabani D, Shaterzadeh-Yazdi H, Zamiri B, Omidi M. Tissue engineering in maxillary bone defects. *World J Plast Surg*. 2018;7(1):3-11.

4. Dewey MJ, Milner DJ, Weisgerber D, et al. Repair of critical-size porcine craniofacial bone defects using a collagen-polycaprolactone composite biomaterial. *Biofabrication*. 2021;14(1):1-24.
doi: 10.1088/1758-5090/ac30d5

5. van der Heide D, Cidonio G, Stoddart MJ, D'Este M. 3D printing of inorganic-biopolymer composites for bone regeneration. *Biofabrication*. 2022;14(4):1-22.
doi: 10.1088/1758-5090/ac8cb2

6. Turnbull G, Clarke J, Picard F, et al. 3D bioactive composite scaffolds for bone tissue engineering. *Bioact Mater*. 2017;3(3):278-314.
doi: 10.1016/j.bioactmat.2017.10.001

7. Gharibshahian M, Salehi M, Beheshtizadeh N, et al. Recent advances on 3D-printed PCL-based composite scaffolds for bone tissue engineering. *Front Bioeng Biotechnol*. 2023;11:1168504.
doi: 10.3389/fbioe.2023.1168504

8. Nobles KP, Janorkar AV, Williamson RS. Surface modifications to enhance osseointegration-Resulting material properties and biological responses. *J Biomed Mater Res B Appl Biomater*. 2021;109(11):1909-1923.
doi: 10.1002/jbm.b.34835

9. Gharibshahian M, Salehi M, Kamalabadi-Farahani M, Alizadeh M. Magnesium-oxide-enhanced bone regeneration: 3D-printing of gelatin-coated composite scaffolds with sustained Rosuvastatin release. *Int J Biol Macromol*. 2024;266(Pt 1):130995.
doi: 10.1016/j.ijbiomac.2024.130995

10. Kikionis S, Ioannou E, Aggelidou E, et al. The marine polysaccharide ulvan confers potent osteoinductive capacity to PCL-based scaffolds for bone tissue engineering applications. *Int J Mol Sci*. 2021;22(6):3086.
doi: 10.3390/ijms22063086

11. Wang B, Zeng Y, Liu S, et al. ZIF-8 induced hydroxyapatite-like crystals enabled superior osteogenic ability of MEW printing PCL scaffolds. *J Nanobiotechnol*. 2023;21(1):264.
doi: 10.1186/s12951-023-02007-w

12. Ha YM, Kim YN, Jung YC. Rapid and local self-healing ability of polyurethane nanocomposites using photothermal polydopamine-coated graphene oxide triggered by near-infrared laser. *Polymers*. 2021;13(8):1274.
doi: 10.3390/polym13081274

13. Yan J, Wu R, Liao S, Jiang M, Qian Y. Applications of polydopamine-modified scaffolds in the peripheral nerve tissue engineering. *Front Bioeng Biotechnol*. 2020;8:590998.
doi: 10.3389/fbioe.2020.590998

14. Rezk AI, Ramachandra Kurup Sasikala A, Nejad AG, et al. Strategic design of a mussel-inspired in situ reduced Ag/Au-nanoparticle coated magnesium alloy for enhanced viability, antibacterial property and decelerated corrosion rates for degradable implant applications. *Sci Rep*. 2019;9(1):117.
doi: 10.1038/s41598-018-36545-3

15. Teixeira BN, Aprile P, Mendonça RH, Kelly DJ, Thiré RM da SM. Evaluation of bone marrow stem cell response to PLA scaffolds manufactured by 3D printing and coated with polydopamine and type I collagen. *J Biomed Mater Res B, Appl Biomater*. 2019;107(1):37-49.
doi: 10.1002/jbm.b.34093

16. Lin Y, Ou Y, Xu M, Chen J. Enhancing bone regeneration with bionic hydrolysis and biomimetic polydopamine coating on 3D-printed PCL scaffolds: a comparative study. *Mater Today Commun*. 2023;37:107262.
doi: 10.1016/j.mtcomm.2023.107262

17. Xu Z, Wang N, Liu P, et al. Poly(Dopamine) coating on 3D-printed poly-lactic-co-glycolic acid/β-tricalcium phosphate scaffolds for bone tissue engineering. *Molecules*. 2019;24(23):4397.
doi: 10.3390/molecules24234397

18. Lee H, Dellatore SM, Miller WM, Messersmith PB. Mussel-inspired surface chemistry for multifunctional coatings. *Science*. 2007;318(5849):426-430. doi: 10.1126/science.1147241

19. Li Y, Yang L, Hou Y, et al. Polydopamine-mediated graphene oxide and nanohydroxyapatite-incorporated conductive scaffold with an immunomodulatory ability accelerates periodontal bone regeneration in diabetes. *Bioact Mater*. 2022;18:213-227. doi: 10.1016/j.bioactmat.2022.03.021

20. Zhou S, Liu S, Wang Y, et al. Advances in the study of bionic mineralized collagen, PLGA, magnesium ionomer materials, and their composite scaffolds for bone defect treatment. *J Funct Biomater*. 2023;14(8):406. doi: 10.3390/jfb14080406

21. Guo R, Zhang R, Liu S, et al. Biomimetic, biodegradable and osteoinductive treated dentin matrix/α-calcium sulphate hemihydrate composite material for bone tissue engineering. *Regener Biomater*. 2023;10:rbad061. doi: 10.1093/rb/rbad061

22. Wang S, Gu R, Wang F, et al. 3D-Printed PCL/Zn scaffolds for bone regeneration with a dose-dependent effect on osteogenesis and osteoclastogenesis. *Mater Today Bio*. 2022;13:100202. doi: 10.1016/j.mtbio.2021.100202

23. Tang A, Ji J, Li J, et al. Nanocellulose/PEGDA aerogels with tunable poisson's ratio fabricated by stereolithography for mouse bone marrow mesenchymal stem cell culture. *Nanomaterials (Basel)*. 2021;11(3):603. doi: 10.3390/nano11030603

24. Wu Y, Liu J, Kang L, et al. An overview of 3D printed metal implants in orthopedic applications: present and future perspectives. *Heliyon*. 2023;9(7):e17718. doi: 10.1016/j.heliyon.2023.e17718

25. Dong J, Ding H, Wang Q, Wang L. A 3D-printed scaffold for repairing bone defects. *Polymers*. 2024;16(5):706. doi: 10.3390/polym16050706

26. Zhao Q, Gao S. Poly (butylene succinate)/silicon nitride nanocomposite with optimized physicochemical properties, biocompatibility, degradability, and osteogenesis for cranial bone repair. *J Funct Biomater*. 2022;13(4):231. doi: 10.3390/jfb13040231

27. Jia L, Han F, Wang H, et al. Polydopamine-assisted surface modification for orthopaedic implants. *J Orthop Transl*. 2019;17:82-95. doi: 10.1016/j.jot.2019.04.001

28. Xiao L, Li Y, Geng R, et al. Polymer composite microspheres loading 177Lu radionuclide for interventional radioembolization therapy and real-time SPECT imaging of hepatic cancer. *Biomater Res*. 2023;27(1):110. doi: 10.1186/s40824-023-00455-x

29. Mahnavi A, Shahriari-Khalaji M, Hosseinpour B, et al. Evaluation of cell adhesion and osteoconductivity in bone substitutes modified by polydopamine. *Front Bioeng Biotechnol*. 2022;10:1057699. doi: 10.3389/fbioe.2022.1057699

30. Du J, Zhou Y, Bao X, et al. Surface polydopamine modification of bone defect repair materials: Characteristics and applications. *Front Bioeng Biotechnol*. 2022; 10:974533. doi: 10.3389/fbioe.2022.974533

31. Caihong T, Fusheng M, Baoyong L, et al. Research status of the surface modification method based on polydopamine [in Chinese]. Chem Bull 2015;78: 983-990. doi: 10.14159/j.cnki.0441-3776.2015.11.003

32. Huang S, Liang N, Hu Y, Zhou X, Abidi N. Polydopamine-assisted surface modification for bone biosubstitutes. *BioMed Res Int*. 2016;2016:2389895. doi: 10.1155/2016/2389895

33. Li H, Zhao T, Cao F, et al. Integrated bioactive scaffold with aptamer-targeted stem cell recruitment and growth factor-induced pro-differentiation effects for anisotropic meniscal regeneration. *Bioeng Transl Med*. 2022; "7(3):e10302. doi: 10.1002/btm2.10302

34. Chang B, Liu X. Osteon: Structure, Turnover, and Regeneration. *Tissue Eng Part B Rev*. 2022;28(2):261-278. doi: 10.1089/ten.TEB.2020.0322

35. V K AD, Ray S, Arora U, Mitra S, Sionkowska A, Jaiswal AK. Dual drug delivery platforms for bone tissue engineering. *Front Bioeng Biotechnol*. 2022;10:969843. doi: 10.3389/fbioe.2022.969843

36. Ma YX, Jiao K, Wan QQ, et al. Silicified collagen scaffold induces semaphorin 3A secretion by sensory nerves to improve in-situ bone regeneration. *Bioact Mater*. 2022;9:475-490. doi: 10.1016/j.bioactmat.2021.07.016

37. Chen X, Yang W, Zhang J, Zhang L, Shen H, Shi D. Alkalinity triggered the degradation of polydopamine nanoparticles. *Polym Bull*. 2021;78(8):4439-4452. doi: 10.1007/s00289-020-03312-2

38. Wang CX, Ge XY, Wang MY, Ma T, Zhang Y, Lin Y. Dopamine D1 receptor-mediated activation of the ERK signaling pathway is involved in the osteogenic differentiation of bone mesenchymal stem cells. *Stem Cell Res Ther*. 2020;11(1):12. doi: 10.1186/s13287-019-1529-x

39. Xia S, Liu D, Jiang K, et al. Photothermal driven BMSCs osteogenesis and M2 macrophage polarization on polydopamine-coated Ti3C2 nanosheets/poly(vinylidene fluoride trifluoroethylene) nanocomposite coatings. *Mater Today Bio*. 2024;27:101156.

doi: 10.1016/j.mtbio.2024.101156

40. Sun H, Feng Y, Tu S, et al. Dopamine promotes osteogenic differentiation of PDLSCs by activating DRD1 and DRD2 during orthodontic tooth movement via ERK1/2 signaling pathway. *Regen Ther*. 2024;27:268-278. doi: 10.1016/j.reth.2024.03.025

41. Pei D, Zeng Z, Geng Z, et al. Modulation of macrophage polarization by secondary cross-linked hyaluronan-dopamine hydrogels. *Int J Biol Macromol*. 2024;270:132417. doi: 10.1016/j.ijbiomac.2024.132417

42. Donkiewicz P, Benz K, Kloss-Brandstätter A, Jackowski J. Survival rates of dental implants in autogenous and allogeneic bone blocks: a systematic review. *Medicina (Kaunas)*. 2021;57(12):1388. doi: 10.3390/medicina57121388

43. Li X, Zhou Q, Wu Y, et al. Enhanced bone regenerative properties of calcium phosphate ceramic granules in rabbit posterolateral spinal fusion through a reduction of grain size. *Bioact Mater*. 2022;11:90-106. doi: 10.1016/j.bioactmat.2021.10.006

ACCSCIENCE PUBLISHING

International Journal of Bioprinting

RESEARCH ARTICLE

Prevascularized cell sheets enhance therapeutic effect of extracellular matrix scaffolds in a one-stage skin grafting rat model

Fei Zhou[1,2†], Ning Liu[1,3†], Shuying Chen[1,2], Yahui Xiong[1,2], Zhaoqiang Zhang[4], Lei Chen[1,2*], and Yingbin Xu[1,2*]

[1]Department of Burn, Wound Repair & Reconstruction, The First Affiliated Hospital, Sun Yat-Sen University, Guangzhou, Guangdong, China

[2]Institute of Precision Medicine, The First Affiliated Hospital, Sun Yat-Sen University, Guangzhou, Guangdong, China

[3]Department of the Second Plastic and Aesthetic Surgery, The First People's Hospital of Foshan, Foshan, Guangdong, China

[4]Department of Oral and Maxillofacial Surgery, Stomatological Hospital, Southern Medical University, Guangzhou, Guangdong, China

Abstract

Dermal substitutes (DS) have been widely used in wound repair, but the low-survival rate of skin grafts with a DS remains an important challenge in regenerative medicine. This study aims to investigate the efficacy of combining prevascularized human mesenchymal stem cell sheets (PHCS) with DS in improving full-thickness wound healing. We used porcine dermis-derived decellularized extracellular matrix to construct an optimized 3D-printed DS, which exhibited the desired structure, good mechanical properties, and biocompatibility. Meanwhile, we constructed PHCS with a certain microstructure, which could enhance microvessel formation and maturation and upregulate the expression of angiogenic growth factors. An immunocompetent one-stage skin graft model *in vivo* demonstrated that the combination of PHCS and DS, along with split-thickness meshed skin autografting, could improve the repair effect of skin grafts, reduce graft fibrosis and later scar formation, and increase blood perfusion of skin grafts through early angiogenesis and rapid microvessel maturation. Our results suggest that the combination of PHCS and DS improves the repair effect of skin grafts through early angiogenesis for full-thickness skin defect repair.

Keywords: Angiogenesis; Decellularized extracellular matrix; Dermal substitutes; Prevascularized human mesenchymal stem cell sheets; Skin grafts.

†These authors contributed equally to this work.

***Corresponding authors:**
Yingbin Xu
(333xyb@163.com)

Lei Chen
(chenlei8@mail.sysu.edu.cn)

Citation: Zhou F, Liu N, Chen S, et al. Prevascularized cell sheets enhance therapeutic effect of extracellular matrix scaffolds in a one-stage skin grafting rat model. *Int J Bioprint*. 2025;11(1):439-452. doi: 10.36922/ijb.5659

Received: October 28, 2024
1st revised: November 26, 2024
2nd revised: December 17, 2024
Accepted: December 20, 2024
Published Online: December 20, 2024

Copyright: © 2024 Author(s). This is an Open Access article distributed under the terms of the Creative Commons Attribution License, permitting distribution, and reproduction in any medium, provided the original work is properly cited.

Publisher's Note: AccScience Publishing remains neutral with regard to jurisdictional claims in published maps and institutional affiliations.

1. Introduction

Skin defects can be caused by a variety of factors, adversely impacting the affected patients' health and posing a heavy burden on their families and the society. Cutaneous scars represent a common perennial complication of skin injury, with a prevalence rate of up to 70% following burn injury.[1] Despite the rapid growth of our understanding toward wound healing in the past decade, which leads to significant improvement of

treatments for various wound types, long-term cutaneous scars still present rather huge esthetic challenges due to its disfiguring nature and severe impact on the quality of life.[2] At present, both surgical and nonsurgical treatments for cutaneous scars are available as interventional measures. Although patients with scars could benefit from a combination of these approaches, their therapeutic efficacy is still far from perfect.[3]

Essentially, cutaneous scars are formed as a result of pathological repair following deep dermal injury. The key to preventing scar formation is to reduce pathological repair during the wound healing process.[4] In wound repair surgery, the thickness of the dermis contained in the skin graft has a definite correlation with the extent of subsequent contracture and cutaneous scars arising at the site transplanted with donated skin. Despite the better healing outcome from a full-thickness skin transplant, this procedure can result in a new donor site wound. Burke et al.[5] constructed a dermal substitute (DS) with bovine collagen and chondroitin sulfate (Integra) in the 1980s, combined with autologous split-thickness meshed skin autografting (STSG) in wound repair surgery, which could limit the damage to the donor site while reducing scarring in the recipient site. Unlike autografts, the angiogenesis of current DS takes a longer time due to the difference in ingredients and internal structure, as well as the absence of microvascular networks.[6] This disadvantage causes surgical complications, such as infection, tissue necrosis, delayed wound healing, and graft rejection. Therefore, accelerating the vascularization process of DS is a crucial issue in wound repair.

Three-dimensional (3D) printing plays a very important role in the preparation of biomaterial scaffolds. The current prevailing 3D bioprinting techniques include inkjet bioprinting, extrusion bioprinting, and light-assisted bioprinting in decellularized extracellular matrix (dECM) bioprinting. Extrusion-based bioprinting systems have been extensively developed in the field of tissue-engineered skin, which can be optimally designed in terms of structure and drug composition, enabling the creation of more flexible artificial substances that can be tailored for precise therapeutic purposes.[7,8] Extrusion-based printing is an optimal method for dECM printing, as it obviates the necessity for the addition of further chemicals.[9] Furthermore, extrusion-based printing aligns with our requirements because the dECM bioinks necessitate specific temperature conditions during the bioprinting process. In our previous research, we developed thermally gelled, nonrheologically modified dECM inks to construct a novel printed DS, which has a microporous structure with 100% connectivity. It has been confirmed that the combination of a printed DS and an STSG significantly promoted the repair of full-thickness skin defects.[10] Previous studies have mainly focused on prevascularization *in vitro* and loading with cytokines and stem cells in recent years. Stem cells are involved directly or indirectly in the angiogenesis cascade. They can secrete various growth factors to induce the migration and proliferation of endothelial cells at the wound site. Alternatively, they can differentiate into specific cells to form new blood vessels.[11] Cell sheet engineering techniques can improve the efficacy of delivering cells to the recipient site compared to classical cell delivery strategies, such as cell injection or spraying.[5] The engineering of cell sheets can preserve the extracellular matrix (ECM), cell–cell junctions, and cell–matrix links, thereby restricting the cells from entering the treated area.[12]

This study aimed to improve the early vascularization of the composite skin graft model and reduce scar formation after wound repair. Previous research by our group has demonstrated that the prevascularized cell sheet could effectively promote the degree of vascularization after the transplantation of STSG on the back of rat model.[13] In this study, we constructed a composite skin graft model and observed the effect of prevascularized human mesenchymal stem cell sheets (PHCS) on skin graft survival and scar formation to evaluate its potential as DS in clinical settings. We observed that the PHCS could effectively improve angiogenesis in the composite skin graft model and improve the local blood perfusion level. Meanwhile, the appearance of the skin graft was improved, and the scar contraction was significantly reduced.

2. Materials and methods

2.1. Development of dECM inks

Full-thickness skin was harvested from Large Yorkshire pigs (Jiangsu Unitrump Biomedical Technology Co. Ltd, China). The epidermis and hypodermis were isolated and decellularized in the same way as preparing the clinically used acellular dermal matrix.[14] The dECM powder used in this study was generously donated by Jiangsu Unitrump Biomedical Technology Co., Ltd. (China). The preparation process, including decellularization, lyophilization, and ultramicro-porphyrization, is proprietary and protected under their product patent. For transparency, we have included details of their preparation method, as described in their patent, in the Supplementary File. The dECM powder was dissolved in ultrapure water, then acidified to pH 3.0 by adding 0.1 M HCl to obtain 6%, 8%, and 10% w/v dECM solutions at room temperature. Next, the mixture was stirred for 1 h using a prewarmed (25°C) magnetic stirrer, after which the printable dECM inks were obtained.[10]

2.2. Rheological and tensile tests

Rheological measurements were performed using a Rheometer (HAAKE MARS III, Germany) equipped with 10.0 mm parallel plates. The temperature sweep experiments were performed from 4 to 37°C at a constant deformation of 0.5% in a frequency of 0.1/rads. The 8% w/v dECM solutions were placed in a 4 °C refrigerator and then immersed in glutaraldehyde solutions (0.1, 0.3, 0.6, or 0.9 wt%) for 24 h to allow hydrogel formation. The compression test of hydrogels was measured by a universal testing machine (BOSE, ElectroFroce®3220, USA) with a compression speed of 0.5 mm/s and a 60% strain level.

2.3. Preparation of printed dermal substitutes

The dECM powder was dissolved in ultrapure water to obtain 8% w/v solutions, which were then mixed with 0.1 M HCl to produce dECM bioinks. An in-house-developed single-head deposition system was used to print DS. The printing parameters were as follows: nozzle diameter, 0.4 mm; deposition speed, 50 mm/min; pneumatic pressure, 30–50 kPa; interior diameter of nozzle, 100 μm; nozzle temperature, 20°C; print bed temperature, 4°C; layer height, 250 μm; layer length, 2 cm; and layer width, 2 cm. The printing materials were immersed in glutaraldehyde solutions (0.3 wt%) for 24 h to obtain printed DS. The morphology of the printed DS was characterized by scanning electron microscopy (SEM; Quanta 400F, Thermo Fisher Scientific, USA).

2.4. Biocompatibility assay

Human bone-marrow mesenchymal stem cell (hBMSCs) were seeded at a density of 1×10^5 cells/cm^2 onto 96-well plates for 24 h. After discarding the culture medium, different concentrations of printed DS-conditioned medium (2 mL medium per 2 cm × 2 cm printed DS) were added. At the 24-h time point, CCK-8 (Dojindo Laboratories, Osaka, Japan) was applied to assess the cytotoxicity of DS according to the instructions. Then, the absorbance at 450 nm was measured using a microplate reader (Thermo Scientific).

The live/dead cell assays were performed using the Live/Dead Kit (Thermo Fisher Scientific, USA) according to the manufacturer's instructions. hBMSCs were cocultured with 50% and 100% DS-conditioned medium for 48 h at a cell density of 1×10^5/cm^2. Then, corresponding fluorescent images were taken under a confocal microscope (ZEISS, LSM880, Oberkochen, Germany). Live cells were stained with green fluorescence, whereas dead cells were with red fluorescence.

The adhesion of hBMSCs was observed through SEM and confocal microscope. After coculturing hBMSCs with DS for 3 days, the DS were washed with phosphate-buffered saline (PBS) to remove unattached cells and fixed in 2.5% glutaraldehyde at 4°C overnight. Then, the surface morphology of samples was examined by means of SEM (Quanta 400F, Thermo Fisher Scientific, USA) according to the standard procedures.

2.5. Culture of PHCS

The cell sheet cultivation method used was based on a previously described method with slight modifications.[15] At passages 3–5, the hBMSCs (Science Cell, USA) were seeded at a density of 2×10^4 cells/cm^2 on cover glasses coated with 20 μg/mL collagen I (BD Biosciences, USA). Then, hBMSCs were cultured for 2 weeks in a hypoxia chamber (BioSpherix, NY, USA) flushed with a gas mixture of the following composition: 2% O_2–5% CO_2–93% N_2 (v/v), incubated with α-MEM fortified with 20% fetal bovine serum, 1% L-glutamine, and 1% penicillin/streptomycin (Life Technologies, MD, USA). To produce PHCS, human umbilical vein endothelial cells (HUVECs; ScienCell, CA, USA) were seeded on top of hBMSC cell sheets at a density of 2×10^4 cell/cm^2 and cultured under normoxic conditions (20% O_2) for 2 weeks in endothelial cell medium (Science Cell, CA, USA). The medium was changed every other day.

2.6. Immunofluorescence staining of microvessels

Immunofluorescence analysis of PHCS was carried out using standard protocols. Cell sheets were washed twice using PBS, fixed in 4% paraformaldehyde, and blocked with 2% bovine serum albumin (Sigma, MO, USA) in 0.2% Triton X-100 (Sigma, MO, USA) for 30 min at room temperature. Rhodamine phalloidin (Thermo Fisher) was incubated for 30 min at room temperature for F-actin observation. For microvessel observation, the cells were incubated with mouse anti-CD31 (1:100, BBA7, R&D Systems, MN, USA) and anti-collagen IV (1:200, ab6586, Abcam, MA, USA) primary antibodies overnight at 4°C. Then, the cell sheets were incubated with anti-mouse IgG (H+L) AF488 (1:500, Cell Signaling Technology, MA, USA) and anti-rabbit IgG H&L AF555 (1:500; Cell Signaling Technology, MA, USA) for 1 h at room temperature. Nuclei were stained with a solution of 4,6-diamidino-2-phenylindole (DAPI, 1:1000, Thermo Fisher Scientific, Waltham, MA, USA). Images were acquired with a fluorescence microscope (Leica 6B, Leica, Wetzlar, Germany).

2.7. Permeability assay of microvessels

5% 70 kDa Texas Red-conjugated dextran (Thermo Fisher Scientific Life Sciences, Waltham, MA, USA) in PBS was incubated with PHCS at 37°C for 30 min, and excess dextran was removed by washing the PHCS in PBS.[16] This was followed by fixation, anti-CD31 staining, and confocal imaging (LSM880; Zeiss, Oberkochen, Germany) as described above.

2.8. Growth factor assay

After 14 days of coculturing with endothelial cell medium, the cell culture medium was collected. An assay using the human angiogenesis array (Ary007, R&D systems, Minneapolis, MN, USA) was performed according to the manufacturer's instructions. Quantitative analysis was carried out using GenePix Pro (San Jose, CA, USA).

2.9. *In vivo* evaluation

2.9.1. Immunocompetent one-stage skin graft model in vivo

All animals were kept in a pathogen-free environment and given access to food and water *ad libitum*. The procedures for care and use of animals were approved by the IEC (Independent Ethics Committee) for Clinical Research and Animal Trials of the First Affiliated Hospital of Sun Yat-Sen University ([2023]225) and all applicable institutional and governmental regulations concerning the ethical use of animals were followed. Male Sprague–Dawley rats, each weighing 200–220 g, were subjected to gas anesthesia (2% v/v isoflurane, 98% v/v O_2, administered at 2 L/min) before surgery. Full-thickness incisional wounds (including the panniculus carnosus) with a diameter of 2 cm were made symmetrically by scalpel excision on the dorsal and inguinal sides. The inguinal split-thickness skin graft was obtained as previously described.[17] Pelnac (single layer, Gunze, Japan), a swine-origin, standard implantable artificial dermis was applied as the positive control, which is a successful product for skin defects.[18] The rats were treated with different materials: STSG group (autologous, inguinal STSG), PL group (Pelnac + STSG), DS group (DS + STSG), and P-DS group (PHCS + DS + STSG). In the P-DS group, we placed the PHCS under the DS and transplanted the STSG onto the upper layer. The grafts were stitched to adjacent wound edges with discontinuous sutures. Then, they were bandaged and fixed by packing and compressing like how the procedures are performed on human patients. The external dressing was removed 7 days after the operation (except for the rats that needed to be sacrificed within 7 days). The skin grafts were observed 0, 4, 7, 14, and 28 days after the surgery. No immunosuppressive drugs were used throughout the animal experiments.

2.9.2. Evaluation of skin grafts

At 4, 7, 14, and 28 days post-surgery, images of dorsal skin grafts were photographed at the same spot using a digital camera. The border of the skin graft is traced with a transparent sheet, and the change in area is calculated by measuring the change in weight after trimming the transparent sheet.[17] The transplantation sites and boundaries were determined by scar lines and the absence of hair. The skin graft contraction was measured by the transparent sheet and expressed as a percentage of the remaining skin graft size to its original graft size using the following formula:

$$Skin\ graft\ size(\%) = \frac{Remaining\ skin\ graft\ size}{Original\ skin\ graft\ size} \times 100. \quad (I)$$

2.9.3. Histological analysis

The skin graft and surrounding tissues were harvested and divided into two parts along the centerline. Next, both parts of each sampled tissue were fixed with 4% paraformaldehyde for tissue histological staining and stored in liquid nitrogen (−196°C) for Western blotting experiments. Tissue sections (each 5 μm in thickness) were cut from paraffin blocks using a microtome (Shandon Finesse 325, Thermo Fisher Scientific Life Sciences, USA) and then deparaffinated and rehydrated before being used for staining. Hematoxylin and eosin (HE) staining and Masson's trichrome staining were performed following the manufacturers' standard protocols.[13] The collagen fiber accumulation level (expressed as the collagen index, CI) was computed for each pixel of the image according to the following formula:

$$CI = \frac{B+G}{2R+B+G}, \quad (II)$$

where R represents the red pixel values; B, the blue pixel values; and G, the green pixel values. The CI ranged from 0 for highly red objects to 1 for entirely blue-green objects.[19] The epidermal thickness, microvessels, and hair follicles were measured by using ImageJ software. Four stained sections per group at each time point were visualized using the Digital Slide Scanners (PANNORAMIC 1000, 3DHISTECH Ltd., Hungary). Three random fields/sections were selected for quantitative analysis.

2.9.4. Evaluation of blood perfusion

The amount of blood perfusion of the skin grafts was evaluated at each time point using a laser Doppler perfusion imager (LDPI) system (PeriScan PIM3, Perimed, Sweden). We placed the rats in a prone position, restrained their limbs and attached an anesthetic mask to their mouths and noses. The probe was used to scan the dorsal skin graft surface for at least 20 s, and the results were recorded as blood relative perfusion units (RPU). In addition, contrast images were converted to display a color-coded live flux image. During blood flow measurements, the temperature of the heating pad was kept constant at 37°C.

2.9.5. Immunofluorescence staining

The tissue sections were blocked with 2% bovine serum albumin in PBST for 1 h at room temperature and then

incubated overnight at 4°C with anti-rat CD31 antibody (1:50; AF3628, R&D systems, MN, USA) and anti-rat α-SMA antibody (1:100; AF1032, Affinity Biosciences, OH, USA), and then with anti-goat IgG H&L AF647 (1:250; L35458, Signalway Antibody, MD, USA), and anti-rabbit IgG H&L AF555 (1:500; 4413S, Cell Signaling Technology, MD, USA) for visualization for 1 h at room temperature. Procedures for nuclear staining and section images were performed as described above.

2.9.6. Cell tracking in vivo

PHCS was labeled with CM-Dil (Invitrogen, CA, USA) according to the manufacturer's instructions. HUVECs were labeled with carboxyfluorescein succinimidyl ester (CFSE; Molecular Probes, Leiden, the Netherlands) according to the manufacturer's instructions and then cocultured with PHCS for 2 weeks and then transplanted into a rat model for another 28 days. The samples were harvested and embedded in O.C.T. Finally, the frozen sections were stained with anti-rat CD31 and DAPI for observation.

2.10. Statistical analysis

The results are presented as mean ± standard deviation (SD). Statistical comparisons were analyzed with *t*-tests (between two groups) or one-way analysis of variance (ANOVA; among three or more groups). All statistical analyses were performed using GraphPad Prism v8 software, and differences were considered statistically significant when $p < 0.05$.

3. Results and discussion

3.1. Characterization of the printed dermal substitute

The white dECM powder was obtained through lyophilization and ultramicro-porphyrization (Figure 1A). The dECM solution exists as a liquid at 20°C and a semisolid at 4°C (Figure 1B). G' (storage modulus) and G'' (loss modulus) demonstrated that the hydrogel has strong temperature-sensitive properties (Figure 1C). Moreover, 8% w/v dECM solution had better printing performance at 20°C and could be quickly formed on the condensing plate after being extruded. Meanwhile, the best compressive properties were achieved with 0.3 wt% glutaraldehyde for the crosslinking process (Figure 1D). The appearance of the printed DS and the 3D printing process are shown in Figure 1E. The morphological features of the printed DS showed an accurate external 3D shape and good internal pore structure of the hydrogel (Figure 1F-a). The average pore diameter of the dermal substitute was 131.2 ± 96.8 μm, close to the pores of the human acellular dermal matrix,[20] which facilitated the sufficient exchange of oxygen, nutrients, and metabolic substances.

3.2. Biocompatibility of printed DS

The SEM images showed that hBMSCs adhered and grew well on the surface of the printed DS (Figure 1F-b), which demonstrated that the submicron structures of ECM-facilitated cell adhesion to the surfaces. By co-culturing and immunofluorescence staining, and using confocal microscopy for 3D reconstruction, we observed good adhere of the hBMSCs to the scaffold surface (Figure S1A, Supporting Information). Live/dead cell staining was used to visualize hBMSC viability. After culturing with printed DS-conditioned medium for 48 h, there was a large number of living cells and few dead cells (Figure S1B, Supporting Information), indicating that the printed DS had good cell viability. The CCK-8 results further demonstrated that the printed DS-conditioned medium showed no significant side effect on cell proliferation (Figure S1C, Supporting Information). Altogether, the crosslinked DS displayed good cytocompatibility with hBMSCs *in vitro*.

3.3. Characterization of the PHCS

The use of hBMSC-based tissue-engineered DS has become increasingly common, but there were no prospective studies to provide a reference on such use. On the one hand, hBMSCs are prone to age and may lose their original properties during *in vitro* amplification. On the other hand, hBMSCs mostly entered the DS in the form of suspension, the cell distribution in the obtained material was not easy to control, and the intercellular connection was weak. Without the protection of ECM, the cells easily caused cellular dysfunction and even apoptosis, which reduced the therapeutic effect of the material. After 2 weeks of stem cell culture under hypoxic conditions and coculture with HUVECs under normoxic conditions, we finally obtained PHCS. The PHCS had a certain thickness and strength, which could be completely removed from the culture plate and stacked.

The cytoskeleton morphology showed that PHCS had the characteristics of directional growth (Figure 2A). The images of CD31 staining indicated the formation of microvessels *in vitro* (Figure 2B). As shown in Figure 2C, the vessel percentage area, total number of junctions, total vessel length, and average vessel length for the PHCS were 14.30 ± 1.93%, 71.75 ± 23.96, 17.76 ± 3.40 mm, and 0.24 ± 0.06 mm, respectively. Therefore, these results showed that hypoxic condition is more conducive for blood vessel formation than the normoxic condition. After 2 weeks of coculture, HUVECs underwent a series of morphological changes and finally formed a unified and stable interlaced network structure. Figure 4D shows the maturation of the microvessels. After 14 days of coculture, a hollow tubular structure in the microvessels was seen through confocal 3D observation. The hollow pipe pile structure was

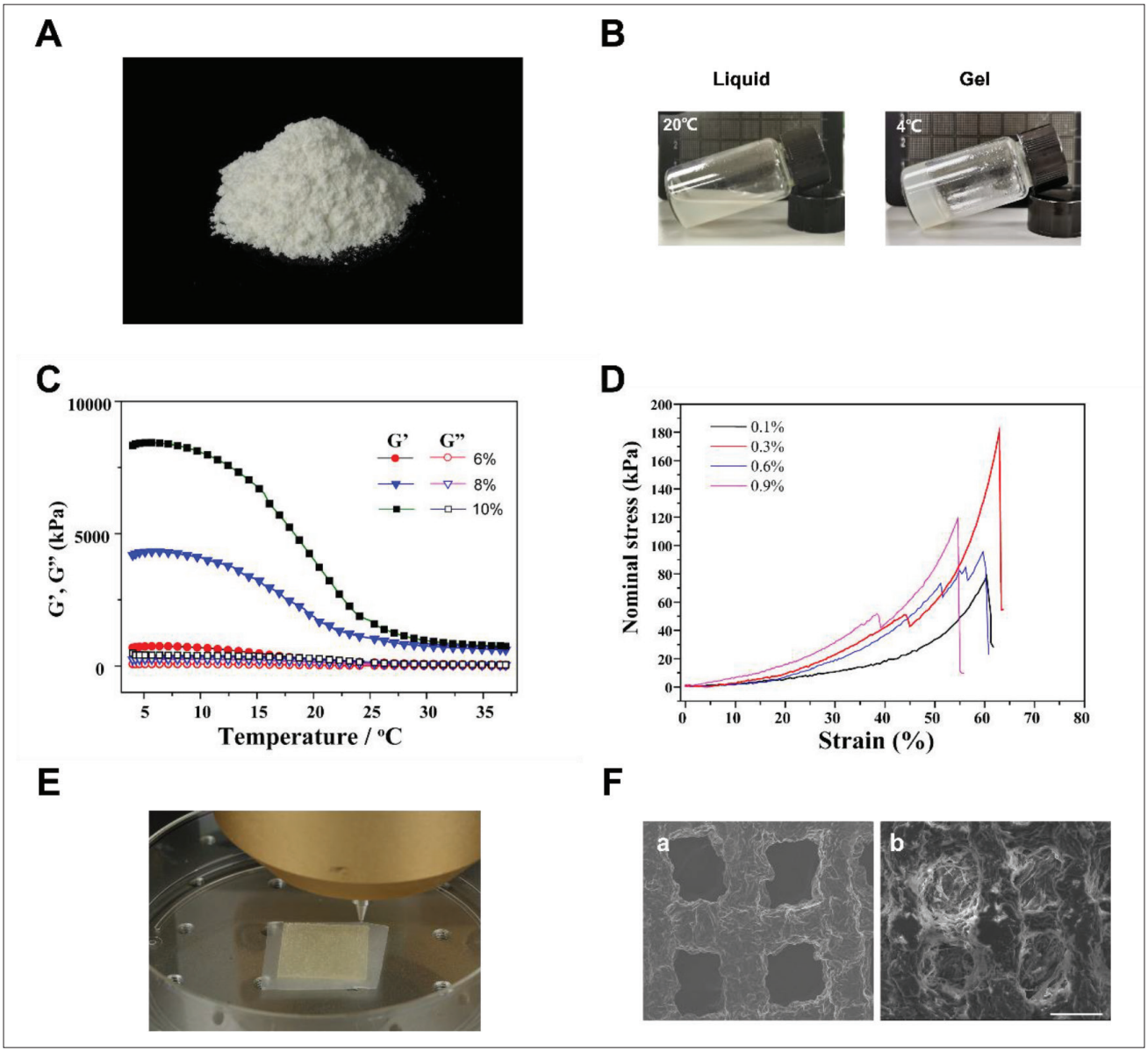

Figure 1. Characterization of the dECM bioink and printed dermal substitute. (A) The appearance of dermis-derived dECM powder. (B) The liquid and gel states of the bioinks at 20 and 4°C without crosslinking. (C) Rheological test of biological ink with different concentrations of dECM. (D) The nominal stress and strain relationship of the crosslinked dECM inks. (E) 3D Printing process of dECM inks. (F) SEM of a dermal substitute. Scale bar = 20 μm. Abbreviations: dECM, decellularized extracellular matrix; SEM, Scanning electron microscopy.

beneficial for the material to link with the blood vessels of the recipient wound bed, which could more quickly promote the early vascularization of the skin graft after implantation.[21] Collagen IV is one of the most important proteins in the microvessels,[22] and it mainly exists in the interstitium of cells and acts as a scaffold to support and protect cells. The images of collagen IV staining show a buildup of collagen IV around the microvessels, and its spatial relationship can be clarified with 3D imaging and Imaris software processing. In the permeability assay, the dextran tracer was uniformly distributed throughout the ECM, while the signal was significantly lower in the CD31-positive regions. Our results showed that the microvascular network had secure cell-cell junctions, which prevented dextran from freely diffusing into the lumina of microvessel (Figure 2E).

Growth factors play an essential role in the vascularization of ischemic tissue. The release of angiogenic growth factors from PHCS into the culture medium was evaluated through a human angiogenesis antibody array. Based on the intensity of the positive

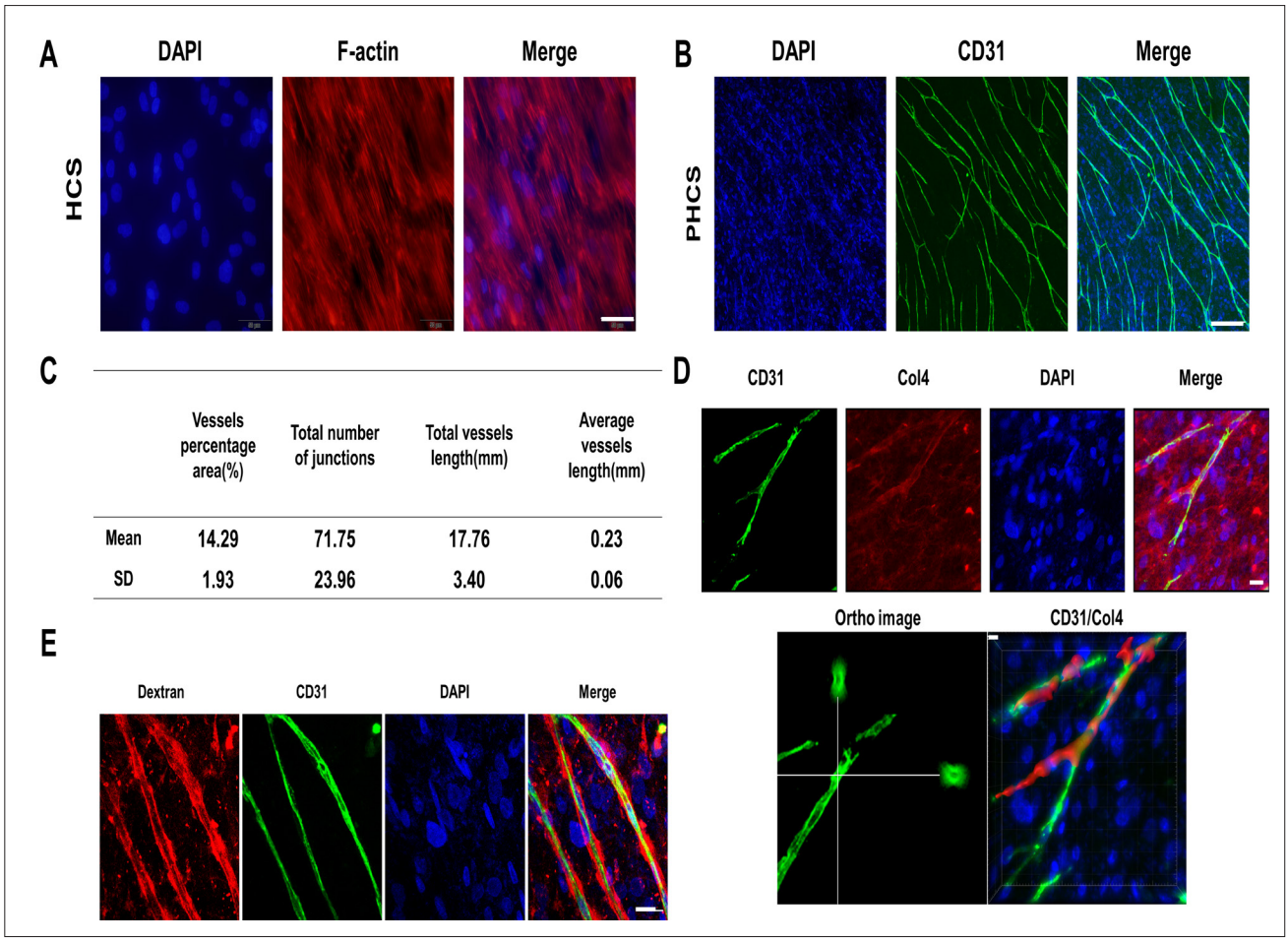

Figure 2. Characterization of PHCS. (A) F-actin immunofluorescence staining images of hBMSCs after 2 weeks of hypoxic culture. Scale bar = 50 μm. (B) CD31 immunofluorescence staining images of HUVEC after 2 weeks coculture with HCS. Scale bar = 100 μm. (C) Quantification analysis of microvascular structure. (D) CD31 and collagen IV immunofluorescence staining images of HUVEC after 2 weeks coculture with HCS. The orthoimage represents the profile structure, and the Imaris image represents the position relationship between collagen IV and HUVECs reconstructed by Imaris software. Scale bar = 50 μm. (E) Dextran permeability images. Scale bar = 50 μm. Abbreviations: HCS, human mesenchymal stem cell sheets; hBMSCs, human bone-marrow stem cells; HUVECs, human umbilical vein endothelial cells; PHCS, prevascularized human mesenchymal stem cell sheets.

dots, the most highly expressed growth factors mainly included epidermal growth factor (EGF), interleukin-8 (IL-8), vascular endothelial growth factor (VEGF), and tissue inhibitor of metalloproteinase 1 (Timp1) (Figure S2, Supporting Information). Moreover, EGF, IL-8, VEGF, and TIMP1 were highly expressed in the PHCS supernatant. EGF and VEGF can directly promote angiogenesis and proliferation of epidermal cells and fibroblasts after stem cell transplantation.[23] As a proinflammatory cytokine, IL-8 can be used as a biomarker for predicting the proangiogenic efficacy of hBMSCs.[24] TIMP1 can influence blood vessel formation by regulating ECM, evidenced by its ability in promoting angiogenesis at an early stage by inhibiting matrix metalloproteinase-9 activity.[25]

3.4. Morphological observation of skin grafts

This research used a rat inguinal skin graft model for animal experiments, mainly because the thickness of this model's skin is close to that of the rat STSG.[26] The impact of the skin thickness on wound repair has been discussed in a previous study.[17] Morphological changes and skin contraction are important indicators of skin graft surgery. We observed skin morphological changes in the STSG, DS, PL, and P-DS groups within 28 days postoperatively. Figure 3A shows the arrangement of the STSG, DS, and PHCS. On the fourth day after surgery, there was no significant difference in the skin graft area among the four groups (Figure 3B), mainly because suture binding and fixation limited the contraction of the skin. However, the grafted skin of the PL group was found to have

partial white changes, suggesting the possibility of tissue ischemia. Meanwhile, the surface of the graft skin in the P-DS group almost resembled that of the STSG group, indicating a satisfactory survival rate of the skin graft. On the seventh day after the operation, skin contraction in the STSG group (97.23 ± 13.49%) became more pronounced than in the P-DS group (93.74 ± 5.89%), but there was no significant difference compared with the DS group (94.60 ± 3.85%) (Figure 3C). On the 28th day after surgery, the skin area of the P-DS group (87.37 ± 4.04%) with fewer ulcers and eschar was significantly larger than that of the STSG group (60.16 ± 6.66%), PL group (67.86 ± 2.31%), and the DS group (74.05 ± 5.17%). All these results demonstrated that the P-DS group was the most effective in inhibiting the contraction of the skin grafts while ensuring their survival. Such an effect is attributable to the combination of the PHCS and the printed DS, which could increase the rate of vascularization and inhibit scarring-induced contraction of skin grafts.

3.5 Histological evaluation of skin grafts

To assess their therapeutic effect on the full-thickness wound, the skin appendages, dermal thickness, dermal collagen, and epidermal structure of the skin grafts were evaluated. As shown in Figure 3D and E, the STSG, PL, and DS groups showed thinned grafts and fewer follicle

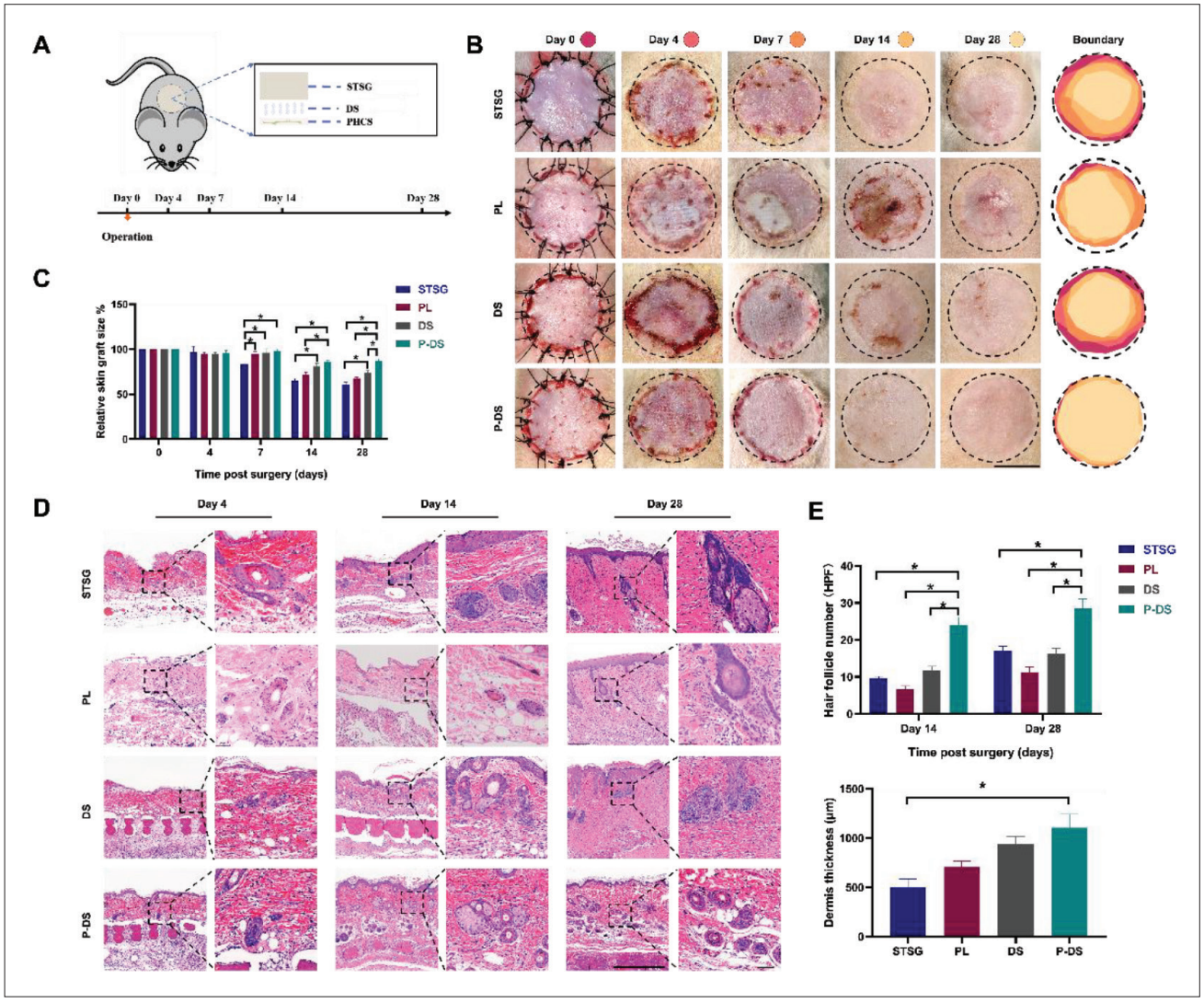

Figure 3. Morphological observation and pathological analysis of skin grafts. (A) Schematic diagram of the rat model of composite skin graft. (B) Morphological changes in skin across different experimental groups. Scale bar = 10 mm. (C) Quantification of the relative skin graft size. (D) HE staining of skin grafts at different time points. Scale bar = 1 mm for LPF; 50 μm for HPF. (E) Quantitative analysis of hair follicles and dermis thickness. All data are expressed as the mean ± SD (*$p < 0.05$). Group definitions are as follows: STSG group (autologous, inguinal STSG), PL group (Pelnac + STSG), DS group (DS + STSG), and P-DS group (PHCS + DS + STSG). Abbreviations: DS, dermal substitute; HE, Hematoxylin and eosin; HPF, high power field; LPF, low power field; PHCS, prevascularized human mesenchymal stem cell sheets; STSG, split-thickness meshed skin autografting.

and sebaceous glands on the fourth day. The P-DS group exhibited more hair follicle structures and typical epidermal structures in the early stage of the grafted skin. These pathological changes are generally caused by surgical operations and insufficient local blood perfusion.[27] On the 28th day after surgery, the number of hair follicles in the P-DS group was significantly higher than that in other treatment groups, suggesting a better therapeutic effect (STSG: 17.0 ± 2.58 vs. PL: 11.25 ± 2.99 vs. DS: 10.5 ± 2.08 vs. P-DS: 28.5 ± 5.07). In addition, due to the implantation of the DS, the thickness of the dermis in the composite skin graft group (P-DS group) increased significantly, which could maintain general morphology during the observation time (day 28, STSG: 503.40 ± 82.89 vs. PL: 706.60 ± 57.62 vs. DS: 943.00 ± 73.015 vs. P-DS: 1105.20 ± 136.93 μm). In the early postoperative days, host tissues could grow along with the pores of the scaffold in the P-DS group, and there was no apparent inflammatory cell aggregation in the tissues around the scaffold. Noticeably, the degradation of the DS and the growth of host tissues could be observed at 28 days postoperatively in the P-DS group, suggesting that the DS had attained the expected biocompatibility.

The morphological findings of the dermis and epidermis are shown in Figure 4. The collagen volume index and the epidermal thickness at 28 days postoperatively was significantly different among the groups. Masson's trichrome staining was used to analyze the morphology of the dermis, in which the blue-shaded areas represent

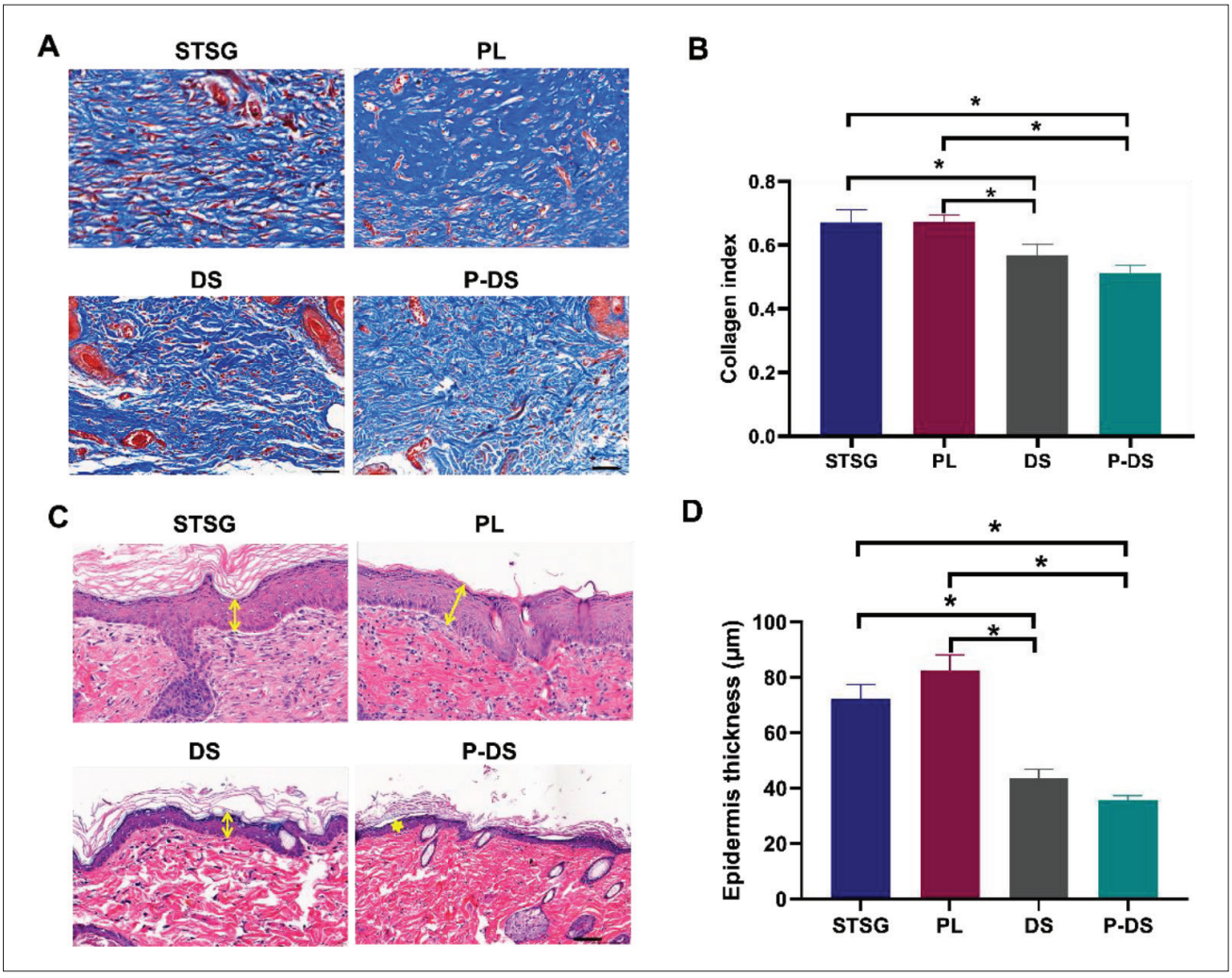

Figure 4. Dermis and epidermis histology analysis. (A) Representative Masson's trichrome staining images of the dermis at 28 days after surgery. Scale bar = 50 μm. (B) Quantitative analysis of the collagen index. (C) HE staining of the epidermis at 28 days after surgery. Scale bar = 50 μm. (D) Quantitative analysis of epidermis thickness at 28 days after surgery. All data are expressed as the mean ± SD (*$p < 0.05$). Group definitions are as follows: STSG group (autologous, inguinal STSG), PL group (Pelnac + STSG), DS group (DS + STSG), and P-DS group (PHCS + DS + STSG). Abbreviations: DS, dermal substitute; HE, Hematoxylin and eosin; PHCS, prevascularized human mesenchymal stem cell sheets; STSG, split-thickness meshed skin autografting.

the collagen fibers (Figure 4A). The STSG group exhibited immature collagen (light blue) surrounding the fibroblasts on day 28, whereas collagen fibers were still in an admixed naïve state in the PL group. Conversely, mature collagen (bright blue) fibers were present in the DS and the P-DS groups on day 28. As shown in Figure 4B, significantly less collagen deposition was observed in the P-DS group (CI: 0.514 ± 0.023). Notably, the CI in the DS group (0.569 ± 0.034) was very close to that in the P-DS group. The dermis was mainly composed of collagen, elastin, and fibrin. Additionally, an earlier study has proven that DS has a large number of ECM molecules of the skin tissue, which can effectively improve the effect of skin graft repair.[28] The combination of PHCS and DS could further improve the repair effect of skin grafts and reduce graft fibrosis and the subsequent scar formation. As shown in Figure 4C and D, the STSG group and PL group had significantly thicker epidermises than the P-DS group (35.76 ± 3.48 μm), and the DS group (43.54 ± 7.47 μm) had an epidermal thickness closest to that of the P-DS group.

3.6. Blood perfusion assay

Figure 5A shows a schematic diagram of performing blood perfusion monitoring on a rat. On the 4th, 7th, 14th, and 28th days after surgery, we used LDPI to analyze the local blood perfusion changes of the skin graft. As shown in Figure 5B, the P-DS group had a higher average RPU in the early stage of skin grafting, which suggested that the skin graft could quickly restore local microcirculation in the early postoperative period, ensuring adequate supply of oxygen and nutrients. Due to the destruction of the original microvascular structure in the early stage of skin grafting, rapid angiogenesis was needed to regain blood perfusion for the grafted skin,[29] which was an important factor in composite skin grafting combined with DS. On the one hand, PHCS could effectively improve the survival of the skin graft; on the other hand, it could significantly reduce pathological repair after injury.[30] On day 28, the blood perfusion in the P-DS group was lower than that in the PL group, indicating that the P-DS group had entered the tissue remodeling phase, while the PL group was still in the proliferative phase.

As shown in Figure 5C, the average value of RPU of DS skin grafts was significantly lower than that of the STSG group and P-DS group on the fourth day after surgery (STSG: 128.97 ± 8.75 vs. PL: 92.33 ± 7.56 vs. DS: 1127.67 ± 11.24 vs. P-DS: 133.33 ± 8.02). There was a similar trend on the 7th and 14th days after surgery. However, at 28 days postoperatively, the local perfusion in the P-DS group and STSG group was significantly decreased, while the local

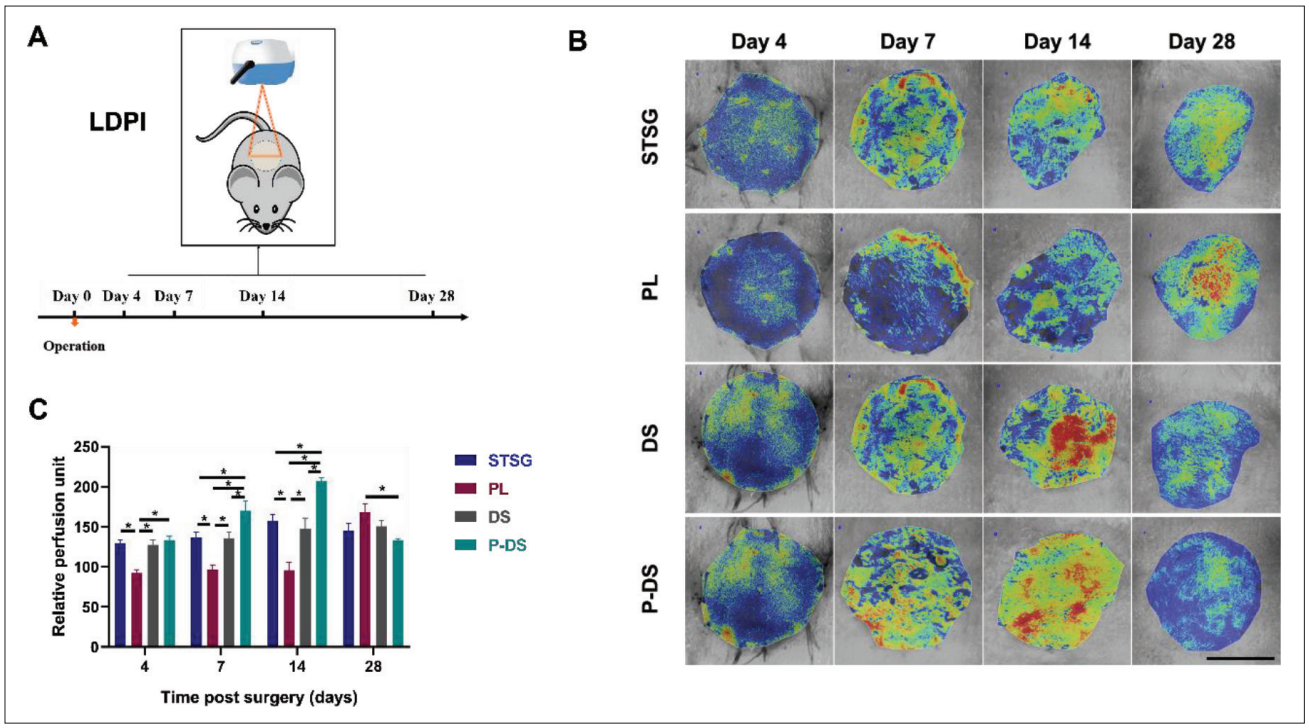

Figure 5. Blood perfusion of skin graft. (A) Schematic diagram of blood perfusion evaluation. (B) Images of blood perfusion in the different experimental groups. (C) Quantitative blood perfusion of the grafted skin. All data are expressed as mean ± SD (*$p < 0.05$). Group definitions are as follows: STSG group (autologous, inguinal STSG), PL group (Pelnac + STSG), DS group (DS + STSG), and P-DS group (PHCS + DS + STSG). Abbreviations: DS, dermal substitute; PHCS, prevascularized human mesenchymal stem cell sheets; STSG, split-thickness meshed skin autografting.

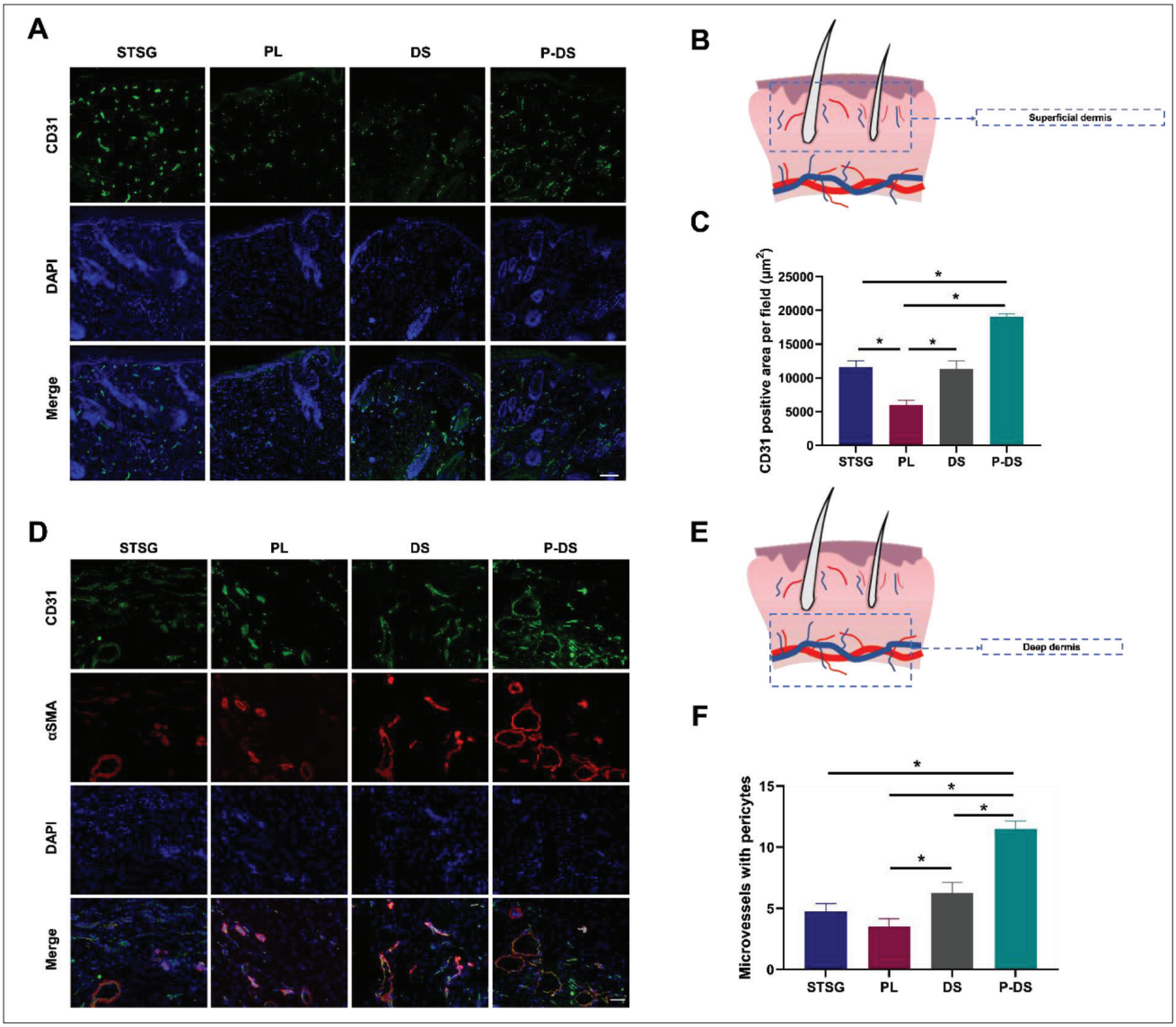

Figure 6. Microvessels formation of skin graft. (A) Representative immunofluorescence images of CD31 in the superficial dermis 7 days after surgery. Scale bar = 100 μm. (B) Schematic diagram of the superficial dermis. (C) Quantitative analysis of the CD31-positive area in the superficial dermis. (D) Representative immunofluorescence images of CD31 and α-SMA in the deep dermis at 28 days after surgery. Scale bar = 100 μm. (E) Schematic diagram of the deep dermis. (F) Quantitative analysis of mature blood vessels in the deep dermis. All data are expressed as mean ± SD (*$p < 0.05$). Group definitions are as follows: STSG group (autologous, inguinal STSG), PL group (Pelnac + STSG), DS group (DS + STSG), and P-DS group (PHCS + DS + STSG). Abbreviations: DS, dermal substitute; PHCS, prevascularized human mesenchymal stem cell sheets; STSG, split-thickness meshed skin autografting.

perfusion in the DS group was significantly increased (STSG: 145.05 ± 16.67 vs. PL: 168.21 ± 17.51 vs. DS: 150.63 ± 12.64 vs. P-DS: 132.65 ± 3.53). All results suggested that P-DS could improve the early postoperative perfusion of skin grafts, and the local perfusion could be restored to near-normal levels 28 days after surgery. However, the PL group and DS group still experienced significant perfusion enhancement 28 days after surgery. Earlier studies have proven that stem cells can effectively promote the vascularization process of DS.[31]

3.7. Microvascular changes of skin graft

Angiogenesis is a crucial step for the survival of skin grafts, especially composite skin grafts.[32] The formation of new capillaries is necessary for the nutrient supply of the transplanted tissue and the excretion of metabolites. Due to the lack of microvascular structure in the DS and the simultaneous increase in the overall thickness of the graft, it is crucial to promote early vascularization after transplantation. Figure 6B and E shows the schematic diagrams of the superficial dermis and deep dermis,

respectively. Immunofluorescence of CD31 and αSMA was used to confirm the therapeutic effect by promoting vascularization. As shown in Figure 6, the P-DS group had better vascularization performance in the early stage of the skin than the other treatment groups (Figure 6A and C), and the number of mature blood vessels in the late stage of the wound was also significantly higher than that of the other treatment groups (Figure 6D and F). Improved angiogenesis was observed in the P-DS group, as compared with the other groups, in the superficial dermis on day 7. On day 28, the P-DS group showed the highest number of microvessels with pericytes in the deep dermis, which was significantly increased compared to the other groups. Furthermore, forming mature blood vessels (CD31+SMA+) in the later stage can avoid pathological repair and fibrosis of the graft and effectively reduce scar formation.[33] Combined with the pathological changes of microvessels, we speculated that there are two possible reasons why PHCS could improve the repair effect of composite skin grafts. The first reason is that early angiogenesis reduces tissue ischemic damage, and the other reason is that the formation of mature microvessels accelerates the physiological repair process of the graft.

3.8. Cell tracking *in vivo*

With the cell-labeling method, we can track living PHCS cells *in vivo*. Stem cells have various functions after implantation, among which differentiation into pericytes is of great significance for the function of new microvessels.[34] As shown in Figure S3, Supporting Information, the CM-Dil signal around endothelial cells has microvascular morphology, suggesting that hBMSCs may act as pericytes *in vivo* to promote blood vessel formation. Moreover, more endothelial cell aggregates in the transplanted cells are found, suggesting that the transplanted cells can improve the local microenvironment and promote angiogenesis.

4. Conclusion

The purpose of this work is to construct printed DS and PHCS for the treatment of full-thickness wounds. The 3D-printed DS showed appropriate pore sizes, good mechanical properties, and biocompatibility. The PHSC showed higher expression of CD31 and collagen IV, which could upregulate the secretion of EGF, IL-8, VEGF, and TIMP1. In addition, the P-DS group (PHCS + DS + STSG) inhibited the contraction of the skin grafts while ensuring the survival of the grafts and reducing graft fibrosis and the subsequent scar formation. Overall, our results suggest that the combination of PHCS and DS holds great potential for treating full-thickness skin defects. In future studies, we will explore the potential mechanisms of other interactions between PHCS and DS in immunomodulation, extracellular matrix synthesis and degradation, and skin appendage regeneration to provide new insights into further improving the quality of full-thickness skin defect repair.

Acknowledgments

Thank you to the Institute of Precision Medicine of the First Affiliated Hospital of Sun Yat-sen University for providing the experimental site.

Funding

This study was supported by the Natural Science Foundation of Guangdong Province (2020A1515110694).

Conflict of interest

The authors declare they have no competing interests.

Author contributions

Conceptualization: Fei Zhou, Ning Liu
Data curation: Shuying Chen, Yahui Xiong
Formal analysis: Yahui Xiong, Zhaoqiang Zhang
Investigation: Fei Zhou, Ning Liu
Methodology: Shuying Chen, Yahui Xiong
Project administration: Fei Zhou, Ning Liu
Resources: Yahui Xiong
Software: Yahui Xiong
Supervision: Yingbin Xu, Zhaoqiang Zhang
Validation: Zhaoqiang Zhang, Lei Chen
Writing–original draft: Fei Zhou, Ning Liu
Writing–review & editing: Zhaoqiang Zhang, Lei Chen, Yingbin Xu

Ethics approval and consent to participate

The procedures for care and use of animals were approved by the IEC (Independent Ethics Committee) for Clinical Research and Animal Trials of the First Affiliated Hospital of Sun Yat-Sen University ([2023]225) and all applicable institutional and governmental regulations concerning the ethical use of animals were followed.

Consent for publication

Not applicable.

Availability of data

Data is available from the corresponding author upon reasonable request.

References

1. Jeschke MG, van Baar ME, Choudhry MA, Chung KK, Gibran NS, Logsetty S. Burn injury. *Nat Rev Dis Primers*. 2020;6(1):1-25.
doi: 10.1038/s41572-020-0145-5

2. Limandjaja GC, Belien JM, Scheper RJ, Niessen FB, Gibbs S. Hypertrophic and keloid scars fail to progress from the CD34- /α-smooth muscle actin (α-SMA)+ immature scar phenotype and show gradient differences in α-SMA and p16 expression. *Br J Dermatol*. 2020;182(4):974-986.
doi: 10.1111/bjd.18219

3. Finnerty CC, Jeschke MG, Branski LK, Barret JP, Dziewulski P, Herndon DN. Hypertrophic scarring: the greatest unmet challenge after burn injury. *Lancet*. 2016;388(10052): 1427-1436.
doi: 10.1016/S0140-6736(16)31406-4

4. Mascharak S, desJardins-Park HE, Davitt MF, et al. Preventing Engrailed-1 activation in fibroblasts yields wound regeneration without scarring. *Science*. 2021;372(6540):eaba2374.
doi: 10.1126/science.aba2374

5. Burke JF, Yannas IV, Quinby WC, Bondoc CC, Jung WK. Successful use of a physiologically acceptable artificial skin in the treatment of extensive burn injury. *Ann Surg*. 1981;194(4):413-428.
doi: 10.1097/00000658-198110000-00005

6. Zhou F, Hong Y, Liang R, et al. Rapid printing of bio-inspired 3D tissue constructs for skin regeneration. *Biomaterials*. 2020;258:120287.
doi: 10.1016/j.biomaterials.2020.120287

7. Tan SH, Ngo ZH, Sci DB, Leavesley D, Liang K. Recent advances in the design of three-dimensional and bioprinted scaffolds for full-thickness wound healing. *Tissue Eng Part B Rev*. 2022;28(1):160-181.
doi: 10.1089/ten.TEB.2020.0339

8. Zhang J, Wehrle E, Rubert M, Müller R. 3D bioprinting of human tissues: biofabrication, bioinks, and bioreactors. *Int J Mol Sci*. 2021;22(8):3971.
doi: 10.3390/ijms22083971

9. Elomaa L, Almalla A, Keshi E, Hillebrandt KH, Sauer IM, Weinhart M. Rise of tissue- and species-specific 3D bioprinting based on decellularized extracellular matrix-derived bioinks and bioresins. *Biomater Biosyst*. 2023;12:100084.
doi: 10.1016/j.bbiosy.2023.100084

10. Chen L, Li Z, Zheng Y, et al. 3D-printed dermis-specific extracellular matrix mitigates scar contraction via inducing early angiogenesis and macrophage M2 polarization. *Bioact Mater*. 2021;10:236-246.
doi: 10.1016/j.bioactmat.2021.09.008

11. Melchiorri AJ, Nguyen BNB, Fisher JP. Mesenchymal stem cells: roles and relationships in vascularization. *Tissue Eng Part B Rev*. 2014;20(3):218-228.
doi: 10.1089/ten.TEB.2013.0541

12. Kirby GTS, Michelmore A, Smith LE, Whittle JD, Short RD. Cell sheets in cell therapies. *Cytotherapy*. 2018;20(2): 169-180.
doi: 10.1016/j.jcyt.2017.11.004

13. Chen L, Xing Q, Zhai Q, et al. Pre-vascularization enhances therapeutic effects of human mesenchymal stem cell sheets in full thickness skin wound repair. *Theranostics*. 2017;7(1):117-131.
doi: 10.7150/thno.17031

14. Lei X, Yang Y, Shan G, Pan Y, Cheng B. Preparation of ADM/PRP freeze-dried dressing and effect of mice full-thickness skin defect model. *Biomed Mater*. 2019;14(3):035004.
doi: 10.1088/1748-605X/ab0060

15. Zhou F, Zhang L, Chen L, et al. Prevascularized mesenchymal stem cell-sheets increase survival of random skin flaps in a nude mouse model. *Am J Transl Res*. 2019;11(3): 1403-1416.
https://pmc.ncbi.nlm.nih.gov/articles/PMC6456548/

16. Zhang L, Qian Z, Tahtinen M, Qi S, Zhao F. Prevascularization of natural nanofibrous extracellular matrix for engineering completely biological three-dimensional prevascularized tissues for diverse applications. *J Tissue Eng Regen Med*. 2018;12(3):e1325–e1336.
doi: 10.1002/term.2512

17. Zhai Q, Zhou F, Ibrahim MM, et al. An immune-competent rat split thickness skin graft model: useful tools to develop new therapies to improve skin graft survival. *Am J Transl Res*. 2018;10(6):1600-1610.
https://pmc.ncbi.nlm.nih.gov/articles/PMC6038090/

18. Lou X, Xue H, Li G, et al. One-stage pelnac reconstruction in full-thickness skin defects with bone or tendon exposure. *Plast Reconstr Surg Glob Open*. 2018;6(3):e1709.
doi: 10.1097/GOX.0000000000001709

19. Ibrahim MM, Bond J, Bergeron A, et al. A novel immune competent murine hypertrophic scar contracture model: A tool to elucidate disease mechanism and develop new therapies. *Wound Repair Regen*. 2014;22(6):755-764.
doi: 10.1111/wrr.12238

20. Wang Y, Xu R, He W, et al. Three-dimensional histological structures of the human dermis. *Tissue Eng Part C Methods*. 2015;21(9):932-944.
doi: 10.1089/ten.TEC.2014.0578

21. Amirsadeghi A, Jafari A, Eggermont LJ, Hashemi SS, Bencherif SA, Khorram M. Vascularization strategies for skin tissue engineering. *Biomater Sci*. 2020;8(15): 4073-4094.
doi: 10.1039/d0bm00266f

22. Sorushanova A, Delgado LM, Wu Z, et al. The collagen suprafamily: from biosynthesis to advanced biomaterial development. *Adv Mater*. 2019;31(1):1801651. doi: 10.1002/adma.201801651

23. Yang M, Li Q, Sheng L, Li H, Weng R, Zan T. Bone marrow-derived mesenchymal stem cells transplantation accelerates tissue expansion by promoting skin regeneration during expansion. Ann Surg. 2011;253(1):202-209. doi: 10.1097/SLA.0b013e3181f9ba1ah

24. Kim HK, Lee SG, Lee SW, et al. A subset of paracrine factors as efficient biomarkers for predicting vascular regenerative efficacy of mesenchymal stromal/stem cells. *Stem Cells*. 2019;37(1):77-88. doi: 10.1002/stem.2920

25. Liu H, Chen B, Lilly B. Fibroblasts potentiate blood vessel formation partially through secreted factor TIMP-1. *Angiogenesis*. 2008;11(3):223-234. doi: 10.1007/s10456-008-9102-8

26. Haifei S, Xingang W, Shoucheng W, Zhengwei M, Chuangang Y, Chunmao H. The effect of collagen–chitosan porous scaffold thickness on dermal regeneration in a one-stage grafting procedure. *J Mech Behav Biomed Mater.* 2014;29:114-125. doi: 10.1016/j.jmbbm.2013.08.031

27. Glotzbach JP, Levi B, Wong VW, Longaker MT, Gurtner GC. The basic science of vascular biology: implications for the practicing surgeon. *Plast Reconstr Surg*. 2010;126(5):1528-1538. doi: 10.1097/PRS.0b013e3181ef8ccf

28. Piperigkou Z, Götte M, Theocharis AD, Karamanos NK. Insights into the key roles of epigenetics in matrix macromolecules-associated wound healing. *Adv Drug Deliv Rev*. 2018;129:16-36. doi: 10.1016/j.addr.2017.10.008

29. Cai Z, Saiding Q, Cheng L, et al. Capturing dynamic biological signals via bio-mimicking hydrogel for precise remodeling of soft tissue. *Bioact Mater*. 2021;6(12):4506-4516. doi: 10.1016/j.bioactmat.2021.04.039

30. Lorden ER, Miller KJ, Bashirov L, et al. Mitigation of hypertrophic scar contraction via an elastomeric biodegradable scaffold. *Biomaterials*. 2015;43:61-70. doi: 10.1016/j.biomaterials.2014.12.003

31. Klar AS, Güven S, Biedermann T, et al. Tissue-engineered dermo-epidermal skin grafts prevascularized with adipose-derived cells. *Biomaterials*. 2014;35(19): 5065-5078. doi: 10.1016/j.biomaterials.2014.02.049

32. Frueh FS, Später T, Körbel C, et al. Prevascularization of dermal substitutes with adipose tissue-derived microvascular fragments enhances early skin grafting. *Sci Rep*. 2018;8(1):10977. doi: 10.1038/s41598-018-29252-6

33. DiPietro LA. Angiogenesis and wound repair: when enough is enough. *J Leukoc Biol*. 2016;100(5):979-984. doi: 10.1189/jlb.4MR0316-102R

34. Hu W, Zhu S, Fanai ML, Wang J, Cai J, Feng J. 3D co-culture model of endothelial colony-forming cells (ECFCs) reverses late passage adipose-derived stem cell senescence for wound healing. *Stem Cell Res Ther*. 2020; 11(1):355. doi: 10.1186/s13287-020-01838-w

ACCSCIENCE PUBLISHING

International Journal of Bioprinting

RESEARCH ARTICLE

Collagen-sodium alginate-silk fibroin 3D-printed scaffold loaded with polydatin promotes cartilage regeneration by improving lipid metabolism and cell apoptosis

Weibin Du[1,2†*], Wenxiang Zeng[1,2†], Zhenwei Wang[1,2†], Huahui Hu[1,2], Yanghua Tang[1,2], Wei Zhuang[1,2], Guoping Cao[1,2] and Gang Qu[1,2*]

[1]Research Institute of Orthopedics, Jiangnan Hospital Affiliated to Zhejiang Chinese Medical University, Hangzhou, Zhejiang, China

[2]Hangzhou Xiaoshan Hospital of Traditional Chinese Medicine, Hangzhou, Zhejiang, China

(This article belongs to the *Special Issue: Bioprinting of Nanomaterials for Biomedical Applications*)

Abstract

Cartilage defects negatively impact the quality of life of over 500 million people worldwide. 3D-printed scaffolds loaded with polydatin (PD) have shown significant potential in cartilage defect repair. This study aims to investigate their reparative effects and analyze the associated metabolic changes using lipidomics techniques, providing new strategies for treating cartilage defects. Biocompatible 3D-printed scaffolds containing PD were prepared and 30 New Zealand rabbits were divided into three groups (10 rabbits per group) that underwent either sham surgery (Normal group) or surgical creation of a cartilage defect without scaffold filling (Model group) or with the developed scaffold filling (Scaffold group). After three months of intervention, the repair of cartilage defects was evaluated through macroscopic observation, micro-CT, hematoxylin and eosin (H&E) staining, and Safranin O/fast green (SFO/FG) staining. The expression of vascular endothelial growth factor A vascular endothelial growth factor A (VEGFA), Col2a1, and biglycan was detected by immunofluorescence while lipid metabolic profiling analysis was conducted on newly formed cartilage tissue to comprehensively evaluate the scaffold's mechanism of action. Macroscopic observation, micro-CT, H&E staining, and SFO/FG staining indicated that the repair of cartilage defects in the Scaffold group was significantly better than in the Model group, closely resembling the Normal group. Lipidomics revealed that the Scaffold group modulated 36 metabolites, with a recovery rate of 69.23%, including ceramides (Cers), glycerophospholipids (GPs), and sphingomyelins (SMs). Immunofluorescence analysis showed increased expression of cartilage cell markers Sox9, Col2a1, biglycan, and VEGFA, along with a reduction in cell apoptosis (all $p < 0.05$) after scaffold implantation. These findings collectively suggest that the PD-loaded 3D-printed scaffold promotes cartilage repair by restoring lipid metabolites in cartilage tissue, inhibiting chondrocyte apoptosis, enhancing vascular-related protein expression, and accelerating cartilage collagen matrix remodeling.

Keywords: 3D printing; Cartilage regeneration; Lipid metabolism; Cell apoptosis; Polydatin

[†]These authors contributed equally to this work.

***Corresponding authors:**
Gang Qu
(122653595@qq.com)

Weibin Du
(dwbbdm@163.com)

Citation: Du W, Zeng W, Wang Z, et al. Collagen-sodium alginate-silk fibroin 3D-printed scaffold loaded with polydatin promotes cartilage regeneration by improving lipid metabolism and cell apoptosis. *Int J Bioprint*. 2025;11(1):453-469. doi: 10.36922/ijb.6548

Received: November 23, 2024
1st revised: December 22, 2024
2nd revised: December 23, 2024
Accepted: December 24, 2024
Published Online: December 24, 2024

Copyright: © 2024 Author(s). This is an Open Access article distributed under the terms of the Creative Commons Attribution License, permitting distribution, and reproduction in any medium, provided the original work is properly cited.

Publisher's Note: AccScience Publishing remains neutral with regard to jurisdictional claims in published maps and institutional affiliations.

1. Introduction

Cartilage defects are often caused by osteoarthritis, injuries, or other factors, and have become a widespread condition globally, placing a heavy economic burden on healthcare systems and patients.[1,2] Cartilage defects negatively impact the quality of life for over 500 million people worldwide, and effective treatments have remained a significant challenge in clinical practice for nearly a decade.[3] Current treatment methods for cartilage defects, such as microfracture repair, high-density grafting, autologous and allogenic cartilage regeneration, and chondrocyte regeneration, can alleviate pain and enhance joint function.[4-7] However, the long-term clinical success rate beyond five years is poor, often necessitating total knee arthroplasty or revision surgeries for patients.[8,9] To overcome these challenges, osteochondral tissue engineering is a potentially promising solution. Through tissue engineering approaches, improved osteochondral regeneration protocols can be developed, effectively facilitating drug delivery.[10,11]

3D printing is a method for fabricating cartilage scaffolds that can be personalized, allowing for precise control of target structures.[12,13] Additionally, 3D printing technology can facilitate the delivery of cells, growth factors, or nanoparticles to injury sites, promoting cartilage regeneration for therapeutic purposes.[14,15] In our previous research, 3D printing technology has been repeatedly applied to achieve traumatic skin repair and drug delivery.[16,17] In this study, bioactive matrices were incorporated into the existing framework to enhance bioactivity, improve adhesion to growth plate chondrocytes, and support their growth while better aligning with the growth rate of tissue cells.

Polydatin (PD) is the active component of *Polygonum cuspidatum* and a glycoside derivative of resveratrol.[18] PD has demonstrated various biological benefits, with studies indicating its roles in bone metabolism regulation, anti-inflammatory effects, antioxidant properties, apoptosis regulation, and autophagy modulation.[19-21] Furthermore, research shows that PD can alleviate chondrocyte damage induced by inflammatory factors, and inhibit osteoclast formation and bone resorption, while also providing protection and repair for cartilage and subchondral bone.[19,22] However, there have been no studies applying PD to cartilage tissue engineering thus far.

Based on our group's pre-experiments and a review of relevant literature, we found that cartilage defect repair in rabbit knee joints reaches a critical stage at three months. At this time point, the overall condition of cartilage repair exhibits a notable contrast, leading most studies to select three months as the baseline for assessment and comparison. This period consistently demonstrates a more accurate reflection of the effects of cartilage repair compared to earlier time points.[23-25] Observations conducted either shorter or longer than three months may encounter incomplete or fully recovered cartilage repair, thereby diminishing the significance of inter-group comparisons.[26,27] Consequently, to enable a direct and meaningful comparison of the extent of cartilage repair, we established three months as the intervention time point to thoroughly investigate the mechanism by which the scaffold contributes to the cartilage repair process.

In this study, we developed a collagen-sodium alginate-silk fibroin 3D-printed scaffold loaded with PD to facilitate cartilage defect regeneration. We evaluated its compatibility with cartilage *in vitro* and assessed its efficacy in treating osteochondral defects in rabbits. Histopathological and lipidomic approaches were used to elucidate the mechanism of action underlying cartilage repair.

2. Methods

2.1. Experimental animals

Thirty male New Zealand white rabbits (2–3 kg) were grouped and acclimatized for one week at the Animal Experiment Center of Zhejiang Chinese Medical University before the experiment. The purchase and breeding of the New Zealand white rabbits, and other animal procedures followed the animal research guidelines set by the National Institutes of Health and the Animal Research Committee. Approval was obtained from the Animal Ethics Committee of Zhejiang Chinese Medical University (No. IACUC-20231030-14).

2.2 Preparation of 3D-printed scaffold loaded with PD

2.2.1. Preparation and sterilization of printing materials

While stirring, sodium alginate (Sigma, USA) and silk fibroin (Hefei Bomei Biotechnology Co., LTD, China), 0.8 g each, were dissolved in 8 L sterile phosphate-buffered saline (PBS) to make the printing material in solution state. The materials were loaded into a sealed container and subjected to intermittent sterilization at 70°C for 30 minutes each time, with a 24-hour interval between each session, for a total of three times. After these treatments, the materials were stored at 4°C for future use. Following these procedures, they were prepared as the 3D-printing substrate material.

2.2.2. Printing of scaffolds

Sodium alginate and silk fibroin were continuously printed and extruded into a flat dish using 3D bioprinting

technology (BioScaffolder, GeSiM, Germany) under the control of a computer-aided design (CAD) and a pneumatic pressure system. Immediately after printing, 5% calcium chloride was added to the scaffolds, and the scaffolds were instantly cross-linked and cured within the cross-linking solution. After curing, the scaffolds were washed with PBS and then transferred to petri dishes. The above steps were done in aseptic conditions. The printing parameters include a needle diameter of 0.41 mm, an extrusion air pressure of 120 kPa, a stent diameter of 6 mm, and a layer height of 2.4 mm. Each stent consisted of six layers, with each layer comprising six strips, printed at a 90° angle. The material was maintained at a heating temperature of 37°C throughout the process. Then, a mixture of 0.2% type I collagen (Hangzhou Xinyou Biotechnology Co., LTD, China) and 50 μM PD (Beijing Huawei Ruike Chemical Co., LTD, China) was added dropwise to the scaffolds. The petri dishes were then put into the incubator at 37°C for 2 hours to allow the collagen to change from liquid to gel. We arranged the above experimental steps and prepared a total of 20 scaffolds for backup.

2.3. Model preparation and grouping

Under inhalation anesthesia with isoflurane (Shanghai Yuyan Scientific Instrument Co., Ltd., China) at a rate of 0.4 mL/min, an incision was made along the inner edge of the patella, followed by careful separation of the subcutaneous tissue and incision of the medial joint capsule. The patella was dislocated laterally, and a hole was drilled at the center of the femoral trochlea in the rabbit knee joint using an electric drill, with a diameter of 5 mm and a depth of 3 mm, to create a cartilage defect model. The incision was then sutured layer by layer.

Using a random number table, 30 New Zealand rabbits were randomly divided into three groups, with ten rabbits in each group. The specific groupings were as follows: Normal group (sham surgery, no cartilage damage); Model group (surgical creation of cartilage defect model, no scaffold filling); Scaffold group (surgical creation of cartilage defect, filled with a 3D-printed scaffold containing PD, with scaffold preparation following the protocol established by our research group previously[16]). The distal femur was collected for analysis after three months. The experimental scheme is shown in Figure 2a.

2.4. Cell viability test

Cell viability was evaluated using the Cell Counting Kit-8 (CCK-8) method. To evaluate the optimal concentration of PD, chondrocytes were first evenly plated in a 96-well plate at a density of 1×10^4 cells per well and cultured for 24 hours. Different concentrations (10, 20, 50, 100, and 200 μM) of PD were added, and after 24 hours, 10 μL of CCK-8 solution (Hangzhou Nuoyang Bio-Technology Co., LTD, China) was added to each well. The plate was then incubated at 37°C in a 5% CO_2 incubator for 2 hours. The optical density (OD) value of absorbance was measured at a wavelength of 450 nm using a microplate reader (Bio-Rad, USA).

To evaluate the effect of PD scaffolds on cell viability, 1×10^4 chondrocytes were cultured on empty plates (blank), non-PD scaffolds (control group), and scaffolds containing PD (experimental group). Then 10 μL CCK-8 solution was added at 12, 24, 36, 48, 60, 72, and 84 hours. The plates were then incubated and the OD value of absorbance was measured as described above. Finally, the cell viability value was calculated according to the following formula: Cell viability (%) = [(OD value of experimental group − OD value of blank)/(OD value of control group − OD value of blank)] × 100%.

2.5. Measurement of scaffold water absorption and expansion rate

Three lyophilized scaffolds were each added to 1 mL of physiological saline and placed on a shaker at 37°C and 135 rpm/min. The scaffolds were removed every 30 minutes, surface moisture was dried, and the mass of the scaffolds after water absorption was measured, with observations continuing for 3 hours. The water absorption expansion rate was calculated using the following formula: Water absorption expansion rate (%) = [(mass of the scaffold after absorption − dry mass of the scaffold)/dry mass of the scaffold] × 100%.

2.6. TUNEL detection

A scaffold was placed in a 24-well plate, and 1×10^4 cells were seeded onto the scaffold. After 48 hours, the scaffold was removed and observed under a microscope for imaging. The scaffold was then fixed in 4% paraformaldehyde (Wuhan Servicebio Technology CO., LTD, China) for 20 minutes and permeabilized with 0.5% Triton X-100 (Wuhan Servicebio Technology CO., LTD, China) for 10 minutes. Subsequently, the TUNEL apoptotic assay (Wuhan Servicebio Technology CO., LTD, China) was performed according to the manufacturer's instructions, followed by 4', 6-diamidino-2-phenylindole (DAPI) nuclear staining. Finally, stereoscopic images were captured under laser confocal microscopy (Nikon, Japan). The distal femoral tissue of rabbits was fixed in 4% paraformaldehyde, decalcified in 10% Ethylene Diamine Tetraacetic Acid (EDTA), dehydrated through a graded alcohol series, embedded in paraffin, and sectioned at 5 μm. The sections were permeabilized with 0.5% Triton X-100 for 10 minutes, followed by TUNEL apoptotic assay (Wuhan Servicebio Technology CO., LTD, China) and DAPI staining. Imaging was performed under a fluorescence microscope.

2.7. Scanning electron microscopy observation

The 3D-printed scaffold containing PD was fixed overnight at 4°C in a 2.5% glutaraldehyde solution (Hangzhou Nuoyang Biotechnology Co., LTD, China). After fixation with 1% osmium tetroxide (Hangzhou Nuoyang Biotechnology Co., LTD, China), the samples underwent dehydration through graded concentrations of ethanol (30, 50, 70, 80, 90, and 100%). They were then treated with a mixture of ethanol and isopropyl acetate, followed by critical point drying and platinum sputtering, and subsequently observed under a scanning electron microscope.

2.8. Histopathological examination

The distal femoral tissue of rabbits was fixed in 4% paraformaldehyde, decalcified in 10% EDTA, dehydrated through a graded alcohol series, and embedded in paraffin. Sections (5 μm) were stained with hematoxylin and eosin (H&E) and Safranin O/fast green (SFO/FG), and observed under a microscope after being mounted with neutral resin.

2.9. Micro-CT detection

The rabbit femur was obtained, and the distal soft tissue was removed. After fixation in paraformaldehyde for 48 hours, it was preserved in a 75% ethanol solution. Micro-CT scans (Skyscan1176, Bruker micro-CT N.V., Kontich, Belgium) were performed on the distal femur to create 3D images, allowing for the observation of microstructural changes in the modeling area.

2.10. UHPLC-QTOF/MS pre-treatment of cartilage tissue

Rabbit cartilage tissue was crushed in liquid nitrogen and 30 mg was added to ten times its volume of isopropanol and vortexed for 1 minute. After ice bath sonication for 30 minutes, the sample was vortexed again for 1 minute and left overnight at −20°C. The following day, the centrifuge was pre-cooled to 4°C and centrifuged at 13,000 rpm for 15 minutes. The supernatant (200 μL) containing cartilage tissue was nitrogen-blown to dryness, reconstituted in 100 μL of isopropanol, and centrifuged at 13,000 rpm for 15 minutes, with 80 μL of supernatant placed in an injection vial for analysis. An equal amount was homogenized, centrifuged, nitrogen-dried, and reconstituted to prepare quality control (QC) samples.

2.11. Liquid chromatography and mass spectrometry

The following conditions were used for liquid chromatography and mass spectrometry: Column: Waters Acquity BEH C18 column (2.1 × 100 mm, 1.7 μm); Column temperature: 55°C; Mobile phase A: water-acetonitrile (40:60, containing 0.1% formic acid and 5 mM ammonium formate); Mobile phase B: isopropanol-acetonitrile (90:10, containing 0.1% formic acid and 5 mM ammonium formate); Flow rate: 0.3 mL/min; Injection volume: 2 μL. The samples were analyzed using a SCIEX Exion LC coupled with an X500B QTOF mass spectrometer (AB Sciex, Foster City, CA, USA). Electrospray ionization (ESI) was used in positive and negative ion scanning modes, with a scanning range of m/z 150–1050.

2.12. Data preprocessing

The raw data was filtered using MarkerView 1.3.1 software (AB Sciex, Foster City, CA, USA), and a data matrix transformation was performed, primarily including information on the mass-to-charge ratio (m/z), retention time (Rt), and peak area (intensity). After normalizing all data using the total peak area, an Excel table was generated for subsequent lipidomics analysis. To reduce signal interference from random errors, variables in QC with relative standard deviation RSD ≥40% were initially removed in Excel. The Excel file was then imported into SIMCA 14.1 (Umetrics, Umeå, Sweden) for multivariate statistical analysis. Finally, partial least squares discriminant analysis (PLS-DA) was conducted on all groups to observe the overall metabolic profile changes of all samples, with permutation tests used to validate model overfitting.

2.13. Differential metabolite analysis

Orthogonal partial least squares discriminant analysis (OPLS-DA) was further used to screen for differential variables between Normal and Model groups. The screening criteria were: Variable Importance in Projection VIP ≥1 and |pcorr| ≥0.4. The selected variables were subjected to significance testing using the Mann-Whitney test, with a p-value ≤0.05 indicating significant differential variables. Fold change (FC) was calculated, with FC (Model / Normal) plotted on the x-axis and p-value as the y-axis to create a volcano plot. Variables farther from the origin indicate greater differential contribution, with red indicating significant upregulation post-modeling (FC >1.5), blue indicating significant downregulation (FC < 0.67), and gray indicating no difference.

2.14. Immunofluorescence detection

Femoral tissue was fixed in 4% paraformaldehyde, decalcified in 10% EDTA, and then embedded in paraffin before slicing (5 μm). After dewaxing and rehydrating, antigen retrieval was performed, followed by permeabilization with 0.5% Triton X-100 for 10 minutes. Primary antibodies of SRY-box transcription factor 9 (Sox9) (1:500), vascular endothelial growth factor A (VEGFA) (1:500), (Collagen Type II Alpha 1) Col2 (1:500), and biglycan (1:500) (Beijing, Boaoson Biotechnology Co., Ltd, China) were prepared. The primary antibodies were incubated together with the fluorescent secondary antibodies, followed by mounting with a DAPI-containing

mounting medium. Images were captured using a fluorescence microscope.

2.15. Statistical analysis

All experimental results were expressed as mean ± SD (standard deviation). All statistical analyses were performed using SPSS 21.0 software (IBM, China). A p-value of less than 0.05 was considered statistically significant.

3. Results

3.1. PD-collagen-sodium alginate-silk fibroin 3D-printed scaffold is compatible with chondrocyte

To screen for the most suitable PD concentration for chondrocyte growth, we identified 50 μM as the optimal concentration through the CCK-8 assay (Figure 1a). The 3D-printed scaffold containing PD is transparent and exhibits good formability, uniform pore size, consistent spacing, and even thickness, as well as good water absorption and swelling properties (Figures 1b and c). In addition, we used CCK-8 to screen the effects of different scaffolds on cell proliferation and found that scaffolds containing PD components had a significant impact on chondrocyte proliferation (Figure 1d). When chondrocytes were seeded onto the scaffold, we observed that the cells adhered and grew around the voids. In TUNEL assays, only a small number of cells seeded onto the scaffold were found to be apoptotic (Figure 1e). Scanning electron microscopy revealed numerous protrusions around the scaffold pores, which are beneficial for cell adhesion (Figure 1f). After cell implantation, we found that the cells were able to adhere and grow stably on the scaffold (Figure 1g). These results indicate that the PD-collagen-sodium alginate-silk fibroin 3D-printed scaffold has good cell compatibility, facilitating cell adhesion and growth.

3.2. Implantation of PD-collagen-sodium alginate-silk fibroin 3D-printed scaffold in defected rabbit cartilage promotes cartilage repair

To verify the scaffold's effects on cartilage *in vivo*, we established a distal femoral cartilage defect model in rabbits and implanted the scaffold at the defect site (Figure 2b). Three months post-implantation, we harvested the distal femur of the rabbits and found that the cartilage defect was better repaired under the scaffold's influence compared to the Model group (Figure 2c). Subsequently, histopathological examinations showed that good cartilage repair was evident under H&E and SFO/FG staining after scaffold implantation (Figures 2d and e). Additionally, micro-CT analysis of the harvested femur indicated that the cartilage defect area post-implantation was closer to that of the Normal group compared to the Model group (Figure 2f). Collectively, these results show that the implantation of the scaffold improved the repair of the cartilage defect in the distal femur of rabbits.

3.3. Repeatability and stability of the UHPLC-QTOF/MS method

Figures 3a and b present the overlaid QC plots under positive and negative ion modes. The spectra are almost entirely overlapping, indicating that the data obtained is stable and reliable. The principal component analysis (PCA) plots for all samples under negative and positive ion modes are shown in Figures 3c and d, respectively. The QC samples cluster tightly, suggesting good stability and repeatability of the experiment. Moreover, the Normal, Model, and Scaffold groups are distinctly separated, with the Scaffold group positioned in between, indicating significant changes in the lipid profile of the Model group post-modeling, and that treatment can partially revert these changes. Further analysis using PLS-DA for all groups is illustrated in Figures 3e–h, where clear distinctions among the three groups are observed; the Scaffold group is positioned between the Normal and Model groups, suggesting that the lipid profile in the Scaffold group is shifting toward recovery.

3.4. Differential metabolite analysis results

Figures 4a–d show the OPLS-DA results for the Normal group versus the Model group, indicating a difference between the two groups and confirming the validity of the model. Figure 4e presents a volcano plot for both models, where variables further from the origin indicate greater differential contributions, with red signifying significant upregulation post-modeling, blue indicating significant downregulation, and gray showing no differences. Subsequently, differential variables were filtered and annotated, as seen in Table 1. A total of 52 differential metabolites were identified, primarily consisting of ceramides (Cers), glycerophospholipids (GPs), sphingomyelins (SMs), and triglycerides (TGs). The scaffold group showed a recovery of 36 metabolites, with a recovery rate of 69.23%. The Venn diagram illustrating the differential metabolites identified in all three groups is shown in Figure 4f. The heatmap of the 52 differential metabolites is illustrated in Figure 4g, where red indicates high response and blue indicates low response. Differences between Normal and Model groups are evident, with some recovery in the Scaffold group—particularly notable in the Cers. The fold changes ($\log_2$) of the 36 recovered metabolites in the Model (compared to Normal group) and Scaffold (compared to the Model group) groups are presented in Figure 4h, showing that these metabolites, mainly Cers, GPs, and SMs, were generally decreased in the Model group but significantly increased after treatment.

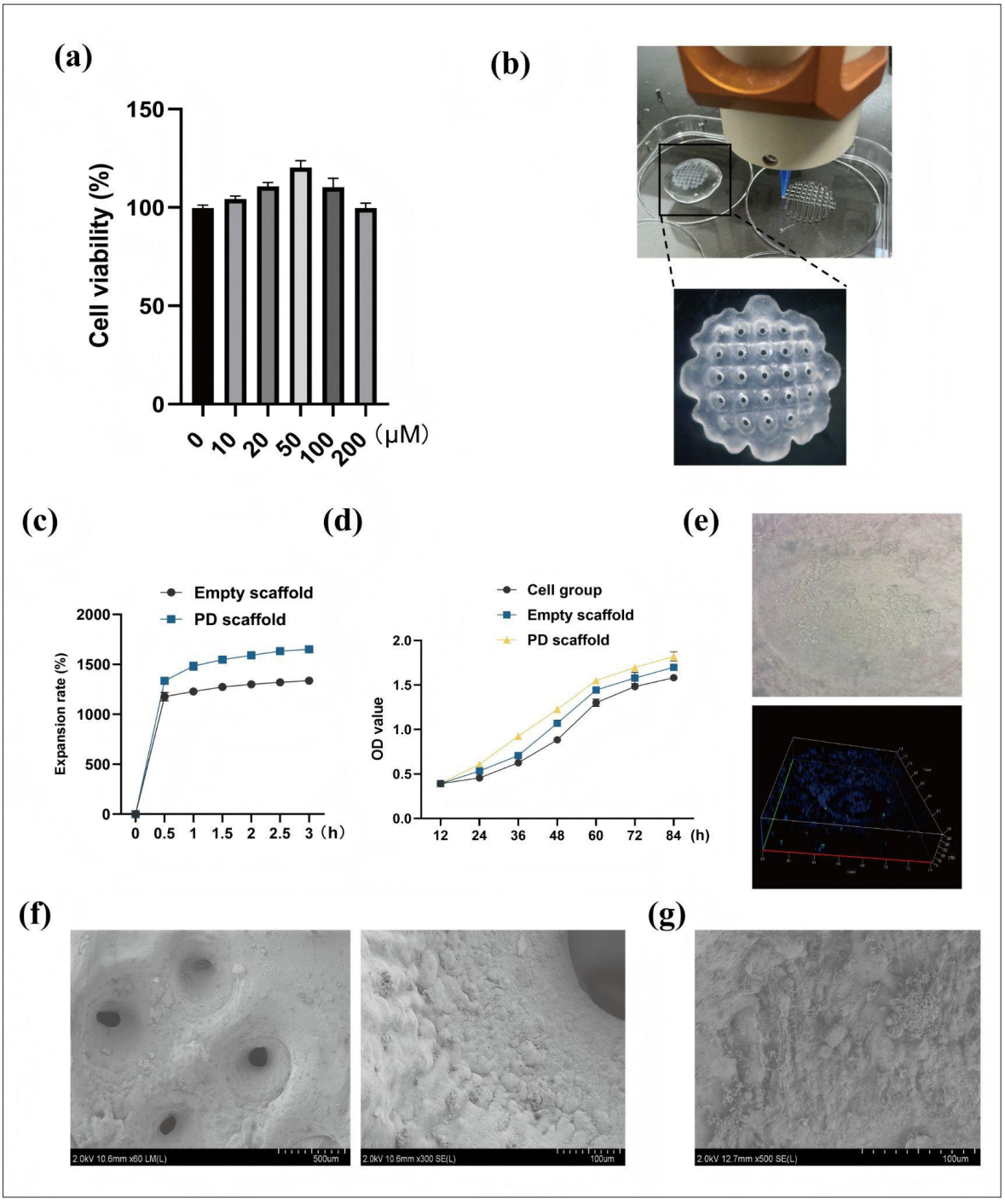

Figure 1. Preparation and evaluation of PD-collagen-sodium alginate-silk fibroin 3D-printed scaffold and its chondrocyte compatibility. (a) CCK-8 assay screening for optimal concentration of PD for chondrocyte growth; (b) Images of the 3D printing procedure and the resulting scaffold structure; (c) Water absorption and swelling rates of the scaffold; (d) CCK-8 assay comparing the effects of different scaffolds on cell proliferation; (e) Microscopic images showing chondrocytes growing around the scaffold pore size (magnification ×50), with TUNEL staining showing blue for cell nuclei and green for apoptotic (TUNEL positive) cells (magnification ×10); (f) Scanning electron microscopy images of the scaffold surface (magnification ×60 and ×300); and (g) Visualization of cells growing on the scaffold (magnification ×500). Abbreviations: CCK-8: Cell Counting Kit-8; PD: Polydatin; OD: Optical density.

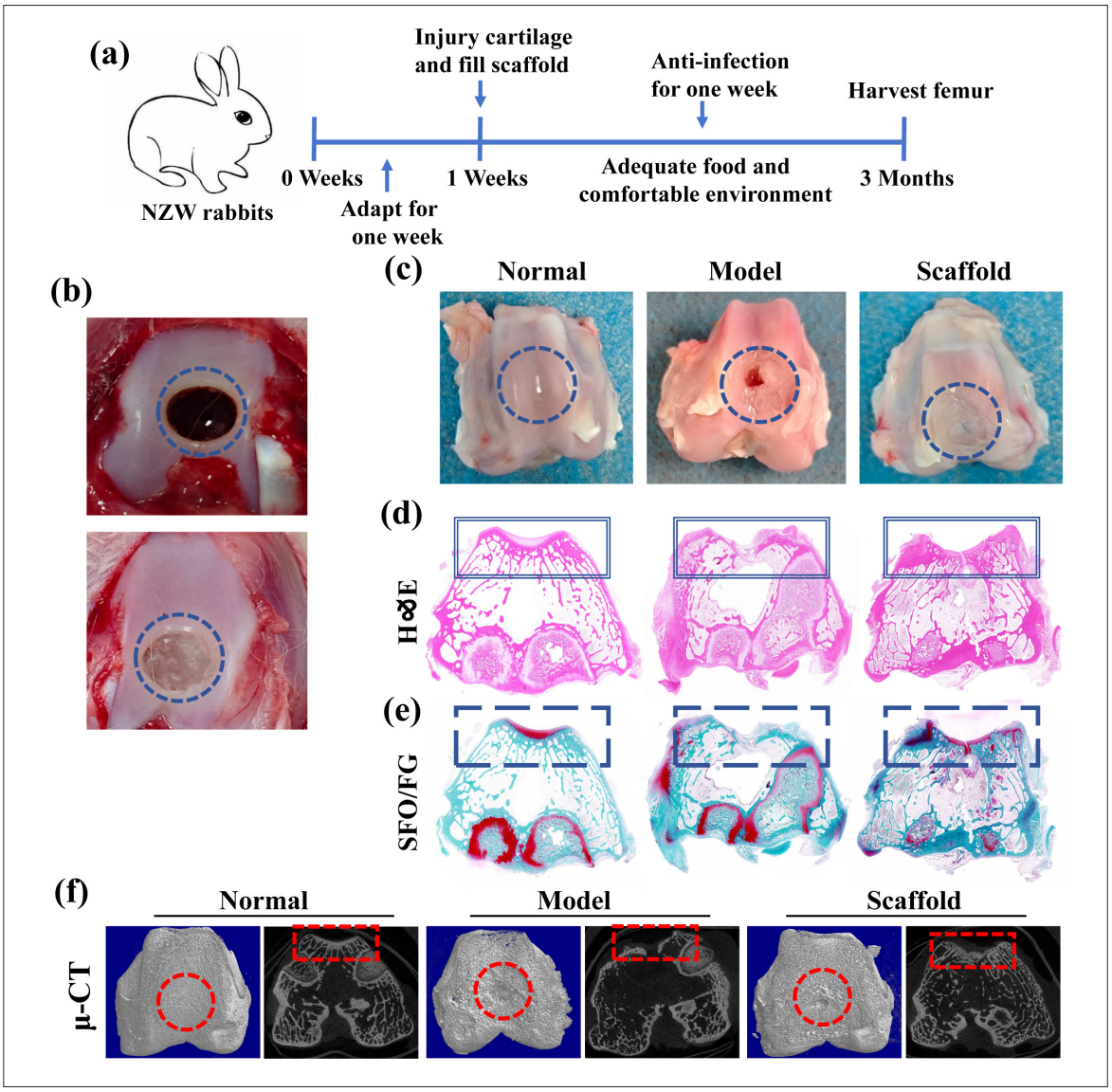

Figure 2. Scaffold implantation in rabbit cartilage defects facilitates cartilage repair. (a) Experimental workflow for animal study; (b) Images of cartilage defects before and after scaffold implantation; (c) Macroscopic appearance of the distal femur after three months post-implantation, with circles indicating defect sites (magnification × 1); (d) H&E staining of the distal femur, with rectangles indicating defect sites (magnification × 1); (e) SFO/FG staining of the distal femur, with rectangles indicating defect sites (magnification × 1); and (f) Micro-CT imaging of the distal femur, with circles indicating 3D defect sites and rectangles indicating 2D defect sites (magnification × 1). Abbreviations: H&E: Hematoxylin and eosin; NZW: New Zealand; SFO/FG: Safranin O/fast green.

The TG compounds were elevated in the Model group but were not regulated by the treatment group.

3.5. Implantation of scaffolds promotes the proliferation of chondrocytes, angiogenesis, and collagen matrix remodeling

TUNEL and immunofluorescence assays were performed on tissues from the distal femur modeling area across the three groups. After scaffold implantation, the number of apoptotic cells significantly decreased compared to the model group (Figures 5a and b). Additionally, immunofluorescence results indicated that, after scaffold implantation, the expression of Sox9, VEGFA, Col2a1, and biglycan in the damaged local area significantly reverted, becoming closer to the normal group (Figures 5c–g). These results suggest that scaffold implantation is beneficial for chondrocyte proliferation, angiogenesis, and collagen matrix remodeling. Finally,

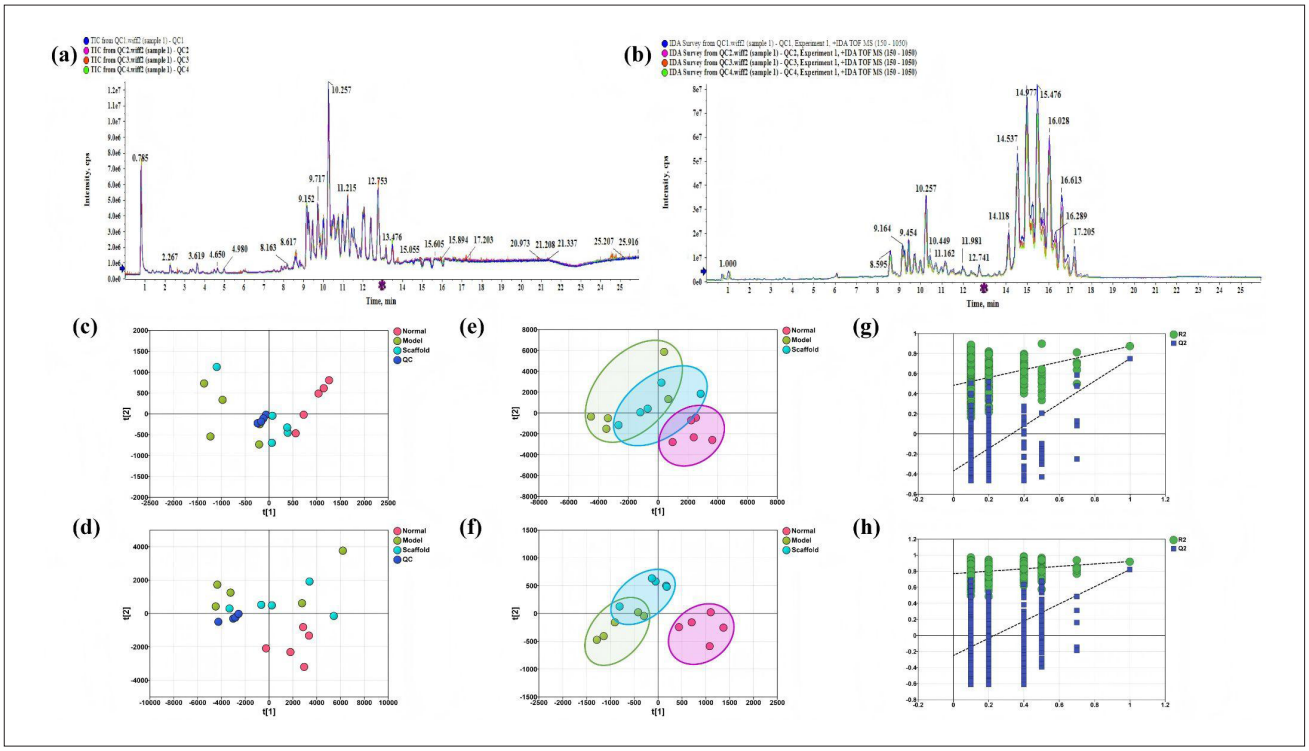

Figure 3. QC sample BPC overlay and data quality assessment in negative and positive ion modes. (a) Negative ion mode; (b) Positive ion mode. Data quality assessment: (c) PCA scatter plot for negative ion mode (R^2X = 0.846, Q^2 = 0.663); (d) PCA scatter plot for positive ion mode (R^2X = 0.916, Q^2 = 0.803); (e) PLS-DA scatter plot for negative ion mode (R^2X = 0.873, R^2Y = 0.940, Q^2 = 0.710); (f) PLS-DA scatter plot for positive ion mode (R^2X = 0.914, R^2Y = 0.858, Q^2 = 0.537); (g) PLS-DA negative ion permutation test; and (h) PLS-DA positive ion permutation test. Abbreviations: BPC: Base peak chromatogram; QC: Quality control; PCA: Principal component analysis; PLS-DA: Partial least squares discriminant analysis.

based on lipidomics techniques and immunofluorescence results, along with Kyoto Encyclopedia of Genes and Genomes (KEGG) pathway analysis and literature reviews, a schematic diagram (Figure 6) was created to explore the potential mechanism of action of the PD-collagen-sodium alginate-silk fibroin 3D-printed scaffold in rabbit cartilage defect repair.

4. Discussion

Due to the poor self-repair capability of natural cartilage, effective treatment options for cartilage repair are limited. Tissue engineering offers a promising alternative for tissue replacement, particularly through the development of scaffolds that can provide localized delivery, are tissue-compatible, and effectively promote tissue regeneration. To achieve these characteristics, we prepared a collagen-sodium alginate-silk fibroin 3D-printed scaffold loaded with PD to promote cartilage regeneration. Collagen is the most abundant protein in the human body and a component of the extracellular matrix (ECM), possessing unique strength and toughness suitable for the regeneration of various tissues, including bone, cartilage, and skin.[28] Silk fibroin is a natural protein containing essential amino acids, known for its good biocompatibility, unique mechanical properties, excellent processability, and degradability.[29] Sodium alginate, a natural polysaccharide extracted from brown algae, is commonly used in tissue engineering materials and enhances the drug release and rapid solidification capabilities of scaffolds.[30,31] The incorporation of silk fibroin and sodium alginate into collagen effectively improves the degradation rate and enhances its adhesion to growth plate chondrocytes, supporting cell growth and better matching the growth rate of tissue cells.

Our group has been investigating these matrix materials for an extended period, and preliminary studies have indicated that these materials exhibit favorable biocompatibility *in vivo*, without significant immune rejection or inflammatory responses.[17] In this study, after 3D printing, we prepared a porous scaffold with good water absorption and swelling properties. Chondrocytes were seeded onto the scaffold, demonstrating good cell compatibility and promoting cell adhesion and growth. Subsequently, the scaffolds were implanted into rabbit cartilage defects, resulting in satisfactory repair of the defect area. Lipidomics analysis revealed that 36 metabolites were restored in the scaffold group, achieving a recovery rate

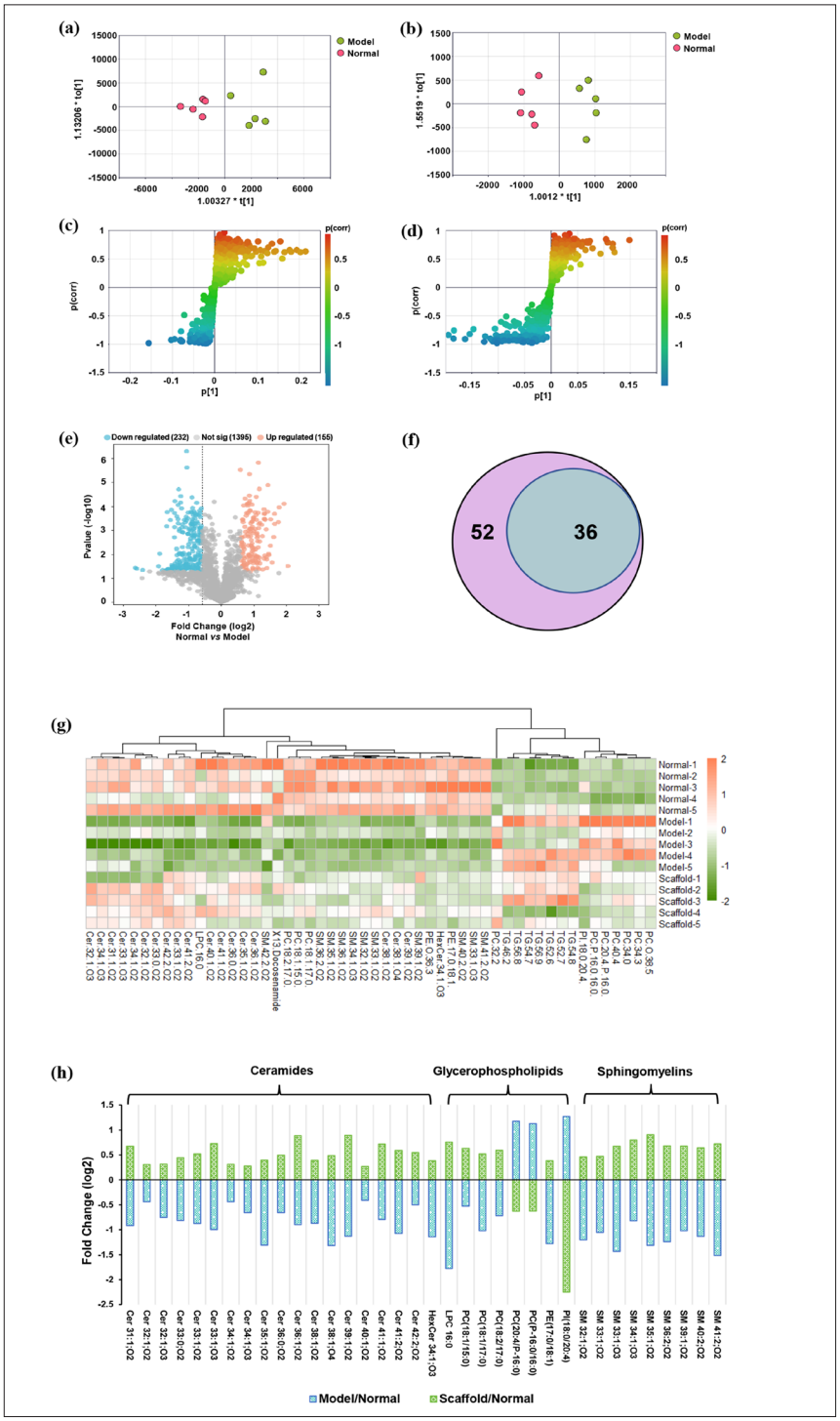

Figure 4. Analysis of differential metabolites. (a) OPLS-DA scatter plot for Model vs. Normal in negative ion mode (R^2X 0.668, R^2Y 0.951, Q^2 0.765); (b) Negative ion S-plot; (c) OPLS-DA scatter plot for Model vs. Normal in positive ion mode (R^2X 0.824, R^2Y 0.866, Q^2 0.779); (d) Positive ion S-plot; R^2X and R^2Y display the fraction of the sum of squares for the selected component, i.e. what percentage of the information in the original data is explained by the model through principal components. Q^2: The fraction of the total variation of X or Y that can be predicted by a component, as estimated by cross-validation. (e) Volcano plot highlighting metabolites with p-value ≤0.05 and fold change (Model/Normal) >1.5 (upregulated; red dots) or <0.67 (downregulated; blue dots); (f) Venn diagram showing overlap among differential metabolites; (g) Heatmap of 52 differential metabolites; and (h) Log_2 fold change of 36 everted metabolites, indicating recovery trends in the Scaffold group. Abbreviations: OPLS-DA: Orthogonal partial least squares discriminant analysis.

Table 1. Differential metabolites across groups

No.	Metabolites	Formula	rt	Ion mode	m/z	VIP	p(corr)	p	p	FC	FC	Regulated
								M vs N	S vs M	M/N	S/M	
1	LPC 16:0	$C_{24}H_{50}NO_7P$	2.29	M+H	496.3400	1.05	−0.79	0.0283	0.0283	0.74	1.24	√
2	13-Docosenamide	$C_{22}H_{43}NO$	6.12	M+H	338.3411	2.16	−0.77	0.0472	0.1172	0.48	1.31	—
3	SM 32:1;O2	$C_{37}H_{75}N_2O_6P$	7.95	M+H	675.5424	1.01	−0.97	0.0090	0.0283	0.42	1.60	√
4	SM 33:1;O3	$C_{38}H_{77}N_2O_7P$	8.20	M+H	705.5539	1.38	−0.94	0.0090	0.0090	0.35	1.65	√
5	PC 32:2	$C_{40}H_{76}NO_8P$	8.54	M+H	730.5432	1.06	0.74	0.0090	0.7540	1.28	0.94	—
6	Cer 31:1;O2	$C_{31}H_{61}NO_3$	8.55	M+FA−H	540.4607	1.04	−0.82	0.0090	0.0472	0.50	1.65	√
7	PC 34:3	$C_{42}H_{78}NO_8P$	8.60	M+H	756.5506	1.27	0.73	0.0283	0.1745	1.64	0.78	—
8	SM 33:1;O2	$C_{38}H_{77}N_2O_6P$	8.61	M+H	689.5573	4.23	−0.98	0.0090	0.0163	0.48	1.51	√
9	Cer 32:1;O3	$C_{32}H_{63}NO_4$	8.71	M+FA−H	570.4739	1.12	−0.75	0.0163	0.0472	0.58	1.65	√
10	SM 34:1;O3	$C_{39}H_{79}N_2O_7P$	8.79	M+H	719.5689	2.21	−0.93	0.0090	0.0090	0.55	1.31	√
11	Cer 32:1;O2	$C_{32}H_{63}NO_3$	9.17	M+FA−H	554.4784	1.82	−0.63	0.0472	0.0472	0.71	1.46	√
12	HexCer 34:1;O3	$C_{40}H_{77}NO_9$	9.22	M+FA−H	760.5595	1.31	−0.90	0.0090	0.0472	0.43	1.37	√
13	PI(18:0/20:4)	$C_{47}H_{83}O_{13}P$	9.24	M−H	885.5501	2.02	0.69	0.0472	0.0163	2.41	0.21	√
14	Cer 33:1;O3	$C_{33}H_{65}NO_4$	9.27	M+FA−H	584.4906	2.45	−0.87	0.0090	0.0472	0.49	1.59	√
15	SM 36:2;O2	$C_{41}H_{81}N_2O_6P$	9.27	M+FA−H	773.5767	1.25	−0.90	0.0090	0.0472	0.41	1.30	√
16	PC(20:4/P-16:0)	$C_{44}H_{80}NO_7P$	9.67	M+FA−H	810.5662	1.77	0.78	0.0090	0.0283	2.26	0.65	√
17	Cer 33:1;O2	$C_{33}H_{65}NO_3$	9.73	M+H	524.5035	1.39	−0.88	0.0090	0.0090	0.54	1.85	√
18	PC(18:1/15:0)/ PC(16:0/17:1)	$C_{41}H_{80}NO_8P$	9.75	M+FA−H	790.5570	2.66	−0.94	0.0090	0.0472	0.63	1.21	√
19	SM 35:1;O2	$C_{40}H_{81}N_2O_6P$	9.77	M+H	717.5884	2.15	−0.94	0.0090	0.0283	0.40	1.40	√
20	PC(18:2/17:0)	$C_{43}H_{82}NO_8P$	9.8	M+FA−H	816.5747	1.15	−0.93	0.0090	0.0472	0.59	1.25	√
21	Cer 34:1;O3	$C_{34}H_{67}NO_4$	9.84	M+FA−H	598.5049	2.66	−0.86	0.0090	0.0472	0.63	1.41	√
22	PC O-38:5	$C_{46}H_{84}NO_7P$	9.85	M+H	794.6033	1.12	0.76	0.0283	0.2506	2.01	0.68	—
23	Cer 33:0;O2	$C_{33}H_{67}NO_3$	10.07	M+FA−H	570.5101	1.07	−0.79	0.0163	0.0472	0.57	1.74	√
24	Cer 34:1;O2	$C_{34}H_{67}NO_3$	10.25	M+FA−H	582.5100	5.06	−0.76	0.0163	0.0472	0.74	1.24	√
25	SM 36:1;O2	$C_{41}H_{83}N_2O_6P$	10.31	M+H	731.6068	2.79	−0.92	0.0090	0.0758	0.47	1.32	—
26	PC(P-16:0/16:0)	$C_{40}H_{80}NO_7P$	10.66	M+FA−H	762.5645	1.24	0.83	0.0090	0.0472	2.19	0.65	√
27	PC(18:1/17:0)	$C_{43}H_{84}NO_8P$	10.73	M+FA−H	818.5912	2.53	−0.98	0.0090	0.0163	0.48	1.39	√

(Continued ...)

Table 1. (*Continued ...*)

No.	Metabolites	Formula	rt	Ion mode	m/z	VIP	p(corr)	p	p	FC	FC	Regulated
								M vs N	S vs M	M/N	S/M	
28	Cer 35:1;O2	$C_{35}H_{69}NO_3$	10.76	M+H	552.5343	1.27	−0.96	0.0090	0.0090	0.40	1.87	√
29	PC 40:4	$C_{48}H_{88}NO_8P$	10.88	M+H	838.6280	1.00	0.83	0.0283	0.1172	2.32	0.65	—
30	PE(17:0/18:1)	$C_{40}H_{78}NO_8P$	10.96	M−H	730.5408	1.36	−0.96	0.0090	0.0472	0.40	1.32	√
31	PE O-36:3	$C_{41}H_{78}NO_7P$	11.05	M+H	728.5584	1.54	−0.91	0.0090	0.9168	0.65	1.03	—
32	PC 34:0	$C_{42}H_{84}NO_8P$	11.11	M+H	762.5997	1.66	0.78	0.0283	0.1745	2.57	0.60	—
33	SM 40:2;O2	$C_{45}H_{89}N_2O_6P$	11.15	M+H	785.6518	1.43	−0.92	0.0090	0.0472	0.45	1.30	√
34	Cer 36:1;O2	$C_{36}H_{71}NO_3$	11.24	M+H	566.5495	1.57	−0.89	0.0090	0.0163	0.53	1.59	√
35	Cer 36:0;O2	$C_{36}H_{73}NO_3$	11.54	M+FA−H	612.5558	1.16	−0.82	0.0090	0.0090	0.61	1.51	√
36	SM 41:2;O2	$C_{46}H_{91}N_2O_6P$	11.58	M+H	799.6646	2.09	−0.95	0.0090	0.0163	0.29	1.69	√
37	SM 39:1;O2	$C_{44}H_{89}N_2O_6P$	11.62	M+FA−H	817.6432	1.38	−0.93	0.0090	0.0090	0.49	1.44	√
38	Cer 38:1;O4	$C_{38}H_{75}NO_5$	11.65	M+FA−H	624.5559	2.57	−0.93	0.0090	0.0472	0.37	1.59	√
39	SM 42:2;O2	$C_{47}H_{93}N_2O_6P$	12.01	M+H	813.6844	1.41	−0.64	0.0472	0.7540	0.74	0.98	—
40	Cer 38:1;O2	$C_{38}H_{75}NO_3$	12.07	M+FA−H	638.5713	2.89	−0.92	0.0090	0.0090	0.55	1.43	√
41	Cer 41:2;O2	$C_{41}H_{79}NO_3$	12.38	M+H	634.6130	1.60	−0.95	0.0090	0.0090	0.46	1.86	√
42	Cer 39:1;O2	$C_{39}H_{77}NO_3$	12.45	M+FA−H	652.5879	2.51	−0.92	0.0090	0.0163	0.46	1.56	√
43	Cer 42:2;O2	$C_{42}H_{81}NO_3$	12.73	M+H	648.6278	1.56	−0.83	0.0163	0.0090	0.69	1.55	√
44	Cer 40:1;O2	$C_{40}H_{79}NO_3$	12.80	M+FA−H	666.6035	2.18	−0.80	0.0090	0.0090	0.75	1.20	√
45	Cer 41:1;O2	$C_{41}H_{81}NO_3$	13.15	M+FA−H	680.6168	2.36	−0.86	0.0090	0.0090	0.57	1.36	√
46	TG 56:8	$C_{59}H_{98}O_6$	14.35	M+NH4	920.7663	1.60	0.69	0.0472	0.6015	3.42	0.74	—
47	TG 46:2	$C_{49}H_{90}O_6$	14.39	M+NH4	792.7043	1.49	0.70	0.0472	0.4647	2.71	0.67	—
48	TG 52:7	$C_{55}H_{92}O_6$	14.41	M+H	849.6933	1.03	0.84	0.0283	0.6015	1.57	0.96	—
49	TG 56:9	$C_{59}H_{96}O_6$	14.54	M+H	901.7253	1.78	0.70	0.0472	0.4647	1.51	0.94	—
50	TG 54:8	$C_{57}H_{94}O_6$	14.58	M+H	875.7112	1.72	0.81	0.0283	0.7540	1.50	0.97	—
51	TG 54:7	$C_{57}H_{96}O_6$	15.02	M+H	877.7256	1.60	0.78	0.0283	0.3472	1.32	0.96	—
52	TG 52:6	$C_{55}H_{94}O_6$	15.16	M+H	851.7134	1.00	0.71	0.0472	0.6015	1.29	0.91	—

Abbreviations: Cer: Ceramide; Col2a1: Collagen Type II Alpha 1; CDP: Cytidine-diphosphate; ECM: Extracellular matrix; LPC: Lysophosphatidylcholine; M vs N: Model versus Normal; S vs M: Scaffold versus Model; m/z: Mass-to-charge ratio, m is the standard proton mass and z is the charged particle; PE: Phosphatidyl ethanolamine; PC: Phosphatidylcholine; p(corr): Correlation coefficient, the correlation coefficient between the sample score and the variable; Sox9: SRY-box transcription factor 9; FA: Fatty acid; FC: Fold change; SM: Sphingomyelins; SMS: SM synthase; Rt: Retention time; TG: Triglycerides; VIP: Variable importance in projection.

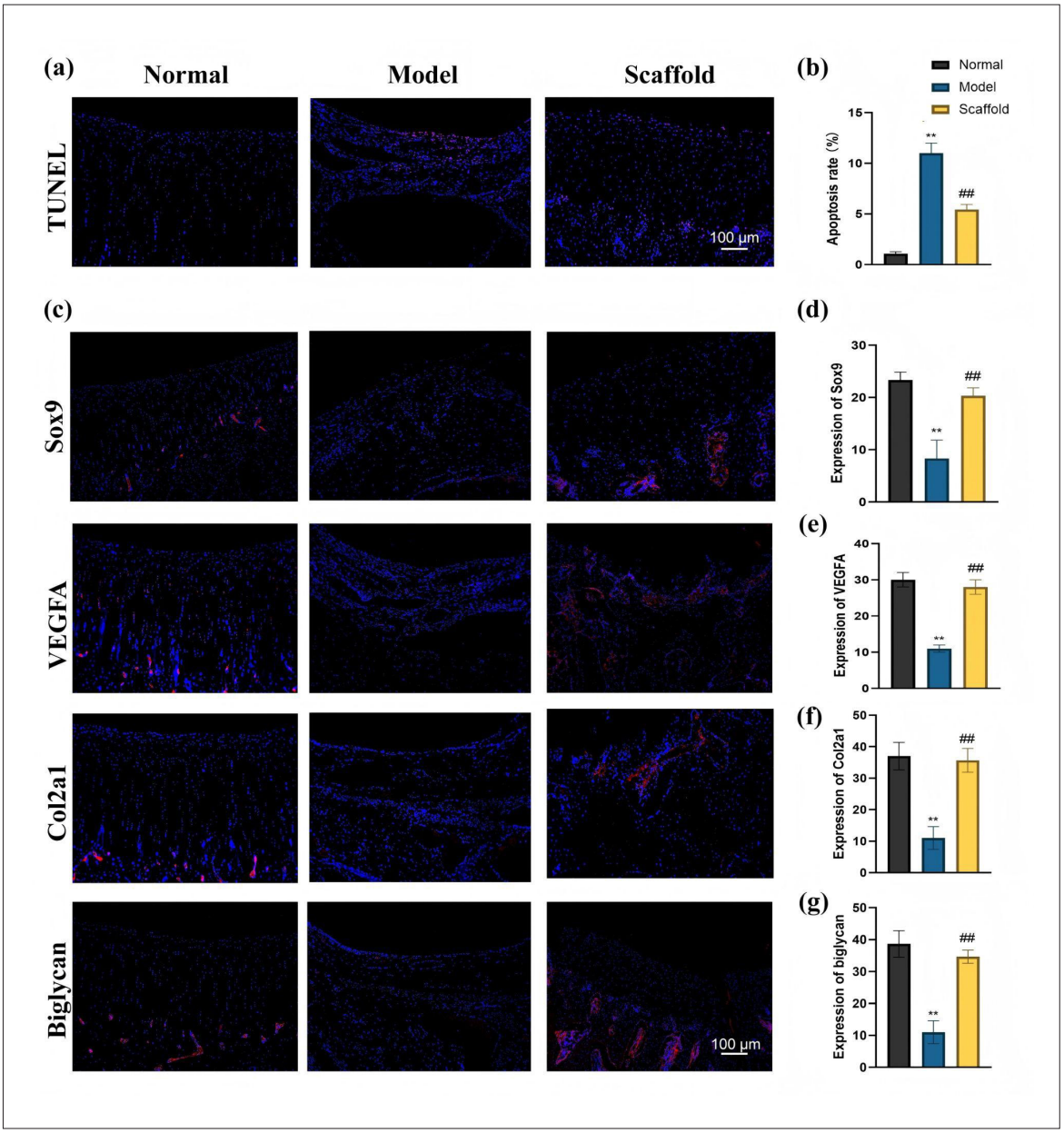

Figure 5. Scaffold implantation promotes chondrocyte proliferation, angiogenesis, and matrix stabilization. (a) TUNEL detection in rabbit distal femur, with blue indicating cell nuclei and green indicating TUNEL-positive cells; (b) Quantitative statistics of TUNEL-positive cells in different groups; (c) Immunofluorescence detection of Sox9, VEGFA, Col2a1, and biglycan expression, with blue indicating cell nucleus and red indicating positive expression sites; and (d–g) Quantitative statistics of Sox9, VEGFA, Col2a1, and biglycan expression based on immunofluorescence data. Data are expressed as mean ± SD. ns, no statistical significance; *p <0.05, **p <0.01 compared to Normal group; # p <0.05, ## p <0.01 compared to Model group, n = 5 per group. Abbreviations: Col2a1: Collagen Type II Alpha 1; Sox9: SRY-box transcription factor 9; SD: Standard deviation; VEGFA: Vascular endothelial growth factor A.

of 69.23%. The main metabolites recovered were Cers, GPs, and SMs. Furthermore, after scaffold implantation, immunofluorescence showed increased expression of Sox9, Col2a1, biglycan, and VEGFA in chondrocytes, along with a reduction in cell apoptosis.

Cer is a class of lipid molecules present in cell membranes that play a crucial role in regulating cellular functions and signal transduction.[32] Cer is involved in processes such as apoptosis (programmed cell death), inflammatory responses, and cellular stress. They also play

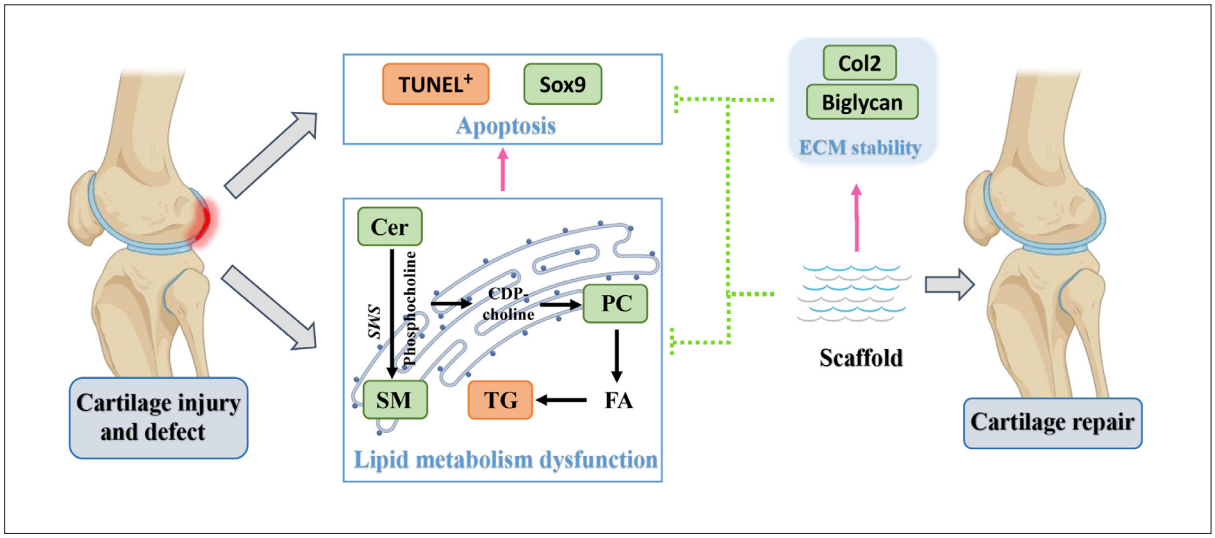

Figure 6. Diagram of cartilage injury and repair mechanisms. The green box indicates metabolites decreased after cartilage injury, while the orange box indicates metabolites increased. Green text indicates biochemical markers that decrease after cartilage injury, while orange text indicates those that increase. Red arrows indicate stimulation and green arrows indicate inhibition. Abbreviations: Cer: Ceramide; Col2a1: Collagen Type II Alpha 1; CDP: Cytidine-diphosphate; ECM: Extracellular matrix; PC: Phosphatidylcholine; Sox9: SRY-box transcription factor 9; FA: Fatty acid; SM: Sphingomyelins; SMS: SM synthase; TG: Triglycerides.

a key role in regulating membrane fluidity, signaling, and metabolism.[33] In apoptosis and inflammatory response research, Ye et al.[21] found that PD could improve the pathological injury of rat knee cartilage tissue and inhibit apoptosis in knee osteoarthritis. This mechanism of action may be through the regulation of autophagy mediated by the Adenosine Monophosphate-Activated Protein Kinase/Mammalian Target of Rapamycin (AMPK/mTOR) signaling pathway. Another study pointed out that PD could have a protective effect on knee cartilage by inhibiting nuclear factor kappa B (NF-κB) and Wnt/β-catenin signaling pathways and reducing the occurrence of inflammation.[34] These research results were a key factor in our research group selecting PD as the intervention method and may also represent one of the mechanisms of PD's action in this study. Both apoptosis and inflammatory reactions are closely related to the fluctuation of Cer levels. Most studies focus on the relationship between increased Cer levels and cartilage damage, indicating that elevated Cer is associated with inflammation, apoptosis, and the progression of osteoarthritis.[35,36] However, Cer can have a protective role in certain contexts, and a decrease in Cer levels may reflect membrane damage or dysfunction in cellular functions.[37,38] Damaged chondrocytes cannot effectively synthesize or maintain normal levels of Cer. Conversely, when cartilage is injured by external stress, the body attempts to promote the repair of the damaged cartilage tissue by modulating inflammatory responses and cellular protective mechanisms, and the reduction in Cer levels is a manifestation of the body's response to injury.[39] In this study, after damage to chondrocytes, local Cer levels decreased in rabbit cartilage defects, leading to membrane damage or dysfunction that failed to trigger protective mechanisms for cartilage repair. Following scaffold implantation, Cer levels rebounded, enhancing the stability of damaged local chondrocytes and aiding in the repair process.

SMs are synthesized from Cer and phosphatidylcholine via SM synthase (SMS), and the decrease in Cer levels is accompanied by a reduction in SMs.[40] Sox9 is a transcription factor that plays a critical role in cartilage formation and development.[41] As a member of the SRY-box transcription factor (SOX) family, it promotes normal chondrocyte function and development by regulating the expression of cartilage-related genes such as Col2 and biglycan.[42,43] Research shows that SM may influence the role of Sox9 in chondrocytes by regulating the phosphorylation state of transcription factors or intracellular signaling pathways.[44] Conversely, Sox9 may also affect the expression of genes associated with SMS, indirectly regulating the levels of SM.[45,46] Furthermore, during cartilage development, Sox9 maintains the balance of cartilage by regulating cellular growth and apoptosis. Sox9 promotes the survival of chondrocytes and can inhibit excessive apoptosis.[42] Col2 is the main component of the cartilage matrix, and its degradation products are commonly used as biomarkers for cartilage injury and diseases like osteoarthritis.[47] Col2 interacts with integrins, influencing cellular signaling pathways. Changes in membrane sphingolipids can affect integrin dynamics, thereby impacting cell adhesion and

migration.[48] The expression of Sox9 is crucial for the synthesis of Col2 during cartilage development. Sox9 promotes transcription by directly binding to the promoter region of the Col2.[49,50] A lack of Sox9 leads to reduced expression of Col2, affecting the normal formation and function of cartilage.[51] Our findings demonstrated that scaffold implantation inhibited apoptosis of chondrocytes, promoted Sox9 expression, and enhanced ECM repair; additionally, it restored disrupted lipid metabolism in cartilage tissue to homeostasis, thereby accelerating cartilage repair.

Despite some limitations, including the need for further experimental studies to verify the mechanism of action of the 3D-printed scaffold containing polydatin on lipidomics and apoptosis in cartilage damage, as well as the lack of clinical trials to validate its efficacy, our findings provide new insights into cartilage injury repair. These results serve as foundational experimental evidence for future clinical trials.

5. Conclusion

This study developed a 3D-printed scaffold composed of collagen, sodium alginate, and silk fibroin, loaded with PD, designed to aid chondrocyte adhesion and growth. Upon implantation into rabbit cartilage defects, the scaffold facilitated the restoration of disrupted lipid metabolism to homeostasis, decreased chondrocyte apoptosis, promoted the expression of vascular-related proteins, and supported cartilage collagen matrix remodeling, thereby accelerating cartilage repair.

Acknowledgments

The authors acknowledge the guidance of Professor Yadong Yang from the School of Laboratory Medicine and Bioengineering, Hangzhou Medical College (Hangzhou, China) in the field of 3D printing.

Funding

This research was supported by multiple funds from the following: the National Natural Science Foundation of China (No. 81904053); Zhejiang Provincial Natural Science Foundation of China (No. LTGY24H290006); Zhejiang Province Medical and Health Science and Technology Project (No. 2025KY191); Special Research Project of the Affiliated Hospital of Zhejiang Chinese Medical University (No. 2021FSYYZY43); Hangzhou Science and Technology Planning Project (No. 20220919Y084); Zhejiang Province Traditional Chinese Medicine Science and Technology Project (No. 2023ZR046); and Hangzhou Bio-Medicine and Health Industry Development Support Science and Technology Project (Nos. 2023WJC243 and 2023WJC249).

Conflict of interest

All the authors declare that they have no conflicts of interest.

Author contributions

Conceptualization: Weibin Du, Wenxiang Zeng
Data curation: Weibin Du, Wenxiang Zeng
Formal analysis: Wenxiang Zeng, Zhenwei Wang, Huahui Hu, Yanghua Tang, Wei Zhuang
Funding acquisition: Weibin Du
Methodology: Weibin Du, Zhenwei Wang, Huahui Hu, Yanghua Tang, Gang Qu
Project administration: Gang Qu
Supervision: Guoping Cao, Gang Qu
Validation: Zhenwei Wang, Huahui Hu, Yanghua Tang
Writing–original draft: Weibin Du, Wenxiang Zeng
Writing–review & editing: Guoping Cao, Gang Qu

Ethics approval and consent to participate

The purchase, feeding, and other animal procedures followed the animal research guidelines of the National Institute of Health and the Animal Research Committee. All animal experiments were approved by the Experimental Animal Ethics Committee of Zhejiang Chinese Medical University (No. IACUC-20231030-14).

Consent for publication

Not applicable.

Availability of data

All data generated and/or analyzed during this study are included in this published article.

References

1. Paul S, Schrobback K, Tran PA, et al. GelMA-glycol chitosan hydrogels for cartilage regeneration: the role of uniaxial mechanical stimulation in enhancing mechanical, adhesive, and biochemical properties. *APL Bioeng*. 2023;7(3):036114. doi: 10.1063/5.0160472

2. Wei W, Ma Y, Yao X, et al. Advanced hydrogels for the repair of cartilage defects and regeneration. *Bioact Mater*. 2020;6(4):998-1011. doi: 10.1016/j.bioactmat.2020.09.030

3. Liu YY, Intini C, Dobricic M, O'Brien FJ, LLorca J, Echeverry-Rendon M. Collagen-based 3D printed poly (glycerol sebacate) composite scaffold with biomimicking

mechanical properties for enhanced cartilage defect repair. *Int J Biol Macromol*. 2024;280(Pt 2):135827.
doi: 10.1016/j.ijbiomac.2024.135827

4. Peng L, Li H, Deng H, et al. Combination of a human articular cartilage-derived extracellular matrix scaffold and microfracture techniques for cartilage regeneration: a proof of concept in a sheep model. *J Orthop Translat*. 2023;44: 72-87.
doi: 10.1016/j.jot.2023.09.004

5. Li H, He Z, Li W, et al. Exploring the mechanism of microfracture in the treatment of porcine full-thickness cartilage defect. *Am J Sports Med*. 2023;51(4):1033-1046.
doi: 10.1177/03635465231153630

6. Huang Z, Liu C, Zheng G, et al. Articular cartilage regeneration via induced chondrocyte autophagy by sustained release of leptin inhibitor from thermo-sensitive hydrogel through STAT3/REDD1/mTORC1 cascade. *Adv Healthc Mater*. 2023;12(30):e2302181.
doi: 10.1002/adhm.202302181

7. Lee KW, Chung K, Nam DH, Jung M, Kim SH, Kim HG. Decellularized allogeneic cartilage paste with human costal cartilage and crosslinked hyaluronic acid-carboxymethyl cellulose carrier augments microfracture for improved articular cartilage repair. *Acta Biomater*. 2023;172: 297-308.
doi: 10.1016/j.actbio.2023.10.008

8. Migliorini F, Maffulli N, Baroncini A, et al. Allograft versus autograft osteochondral transplant for chondral defects of the talus: systematic review and meta-analysis. *Am J Sports Med*. 2022;50(12):3447-3455.
doi: 10.1177/03635465211037349

9. Wang AS, Nagelli CV, Lamba A, Saris DBF, Krych AJ, Hevesi M. Minimum 10-year outcomes of matrix-induced autologous chondrocyte implantation in the knee: a systematic review. *Am J Sports Med*. 2024;52(9):2407-2414.
doi: 10.1177/03635465231205309

10. Chen R, Pye JS, Li J, Little CB, Li JJ. Multiphasic scaffolds for the repair of osteochondral defects: Outcomes of preclinical studies. *Bioact Mater*. 2023;27:505-545.
doi: 10.1016/j.bioactmat.2023.04.016

11. Shaygani H, Mofrad YM, Demneh SMR, Hafezi S, Almasi-Jaf A, Shamloo A. Cartilage and bone injectable hydrogels: a review of injectability methods and treatment strategies for repair in tissue engineering. *Int J Biol Macromol*. 2024; 282(Pt 2):136689.
doi: 10.1016/j.ijbiomac.2024.136689

12. Cheah CM, Chua CK, Leong KF, Chua SW. Development of a tissue engineering scaffold structure library for rapid prototyping. Part 1: investigation and classification. *Int J Adv Manuf Technol*. 2003;21:291-301.
doi: 10.1007/s001700300034

13. Cheah CM, Chua CK, Leong KF, Chua SW. Development of a tissue engineering scaffold structure library for rapid prototyping. Part 2: parametric library and assembly program. *Int J Adv Manuf Technol*. 2003;21: 302-312.
doi: 10.1007/s001700300035

14. Du J, Zhu Z, Liu J, et al. 3D-printed gradient scaffolds for osteochondral defects: current status and perspectives. *Int J Bioprint*. 2023;9(4):724.
doi: 10.18063/ijb.724

15. O'Shea DG, Hodgkinson T, Curtin CM, O'Brien FJ. An injectable and 3D printable pro-chondrogenic hyaluronic acid and collagen type II composite hydrogel for the repair of articular cartilage defects. *Biofabrication*. 2023;16(1): 015007.
doi: 10.1088/1758-5090/ad047a

16. Du W, Wang Z, Han M, et al. Astragalus polysaccharide-containing 3D-printed scaffold for traumatized skin repair and proteomic study. *J Cell Mol Med*. 2024;28(16):e70023.
doi: 10.1111/jcmm.70023

17. Du W, Hu J, Huang X, et al. Feasibility of repairing skin defects by VEGF(165) gene-modified iPS-HFSCs seeded on a 3D printed scaffold containing astragalus polysaccharide. *J Cell Mol Med*. 2023;27(15):2136-2149.
doi: 10.1111/jcmm.17800

18. Gong W, Zhang N, Sun X, et al. Cardioprotective effects of polydatin against myocardial injury in HFD/stz and high glucose-induced diabetes via a Caveolin 1-dependent mechanism. *Phytomedicine*. 2024;135:156055.
doi: 10.1016/j.phymed.2024.156055

19. Zhang Z, Sun Z, Jia R, et al. Protective effects of polydatin against bone and joint disorders: the *in vitro* and *in vivo* evidence so far. *Nutr Res Rev*. 2024;37(1):96-107.
doi: 10.1017/S0954422423000082.

20. Bagheri Bavandpouri FS, Azizi A, Abbaszadeh F, et al. Polydatin attenuated neuropathic pain and motor dysfunction following spinal cord injury in rats by employing its anti-inflammatory and antioxidant effects. *Front Pharmacol*. 2024;15:1452989.
doi: 10.3389/fphar.2024.1452989

21. Ye Z, Lin J, He C, et al. Polydatin protects against articular cartilage degeneration by regulating autophagy mediated by the AMPK/mTOR signaling pathway. *Histol Histopathol*. 2024;39(11):1505-1515.
doi: 10.14670/HH-18-739

22. Tang S, Tang Q, Jin J, et al. Polydatin inhibits the IL-1beta-induced inflammatory response in human osteoarthritic chondrocytes by activating the Nrf2 signaling pathway and ameliorates murine osteoarthritis. *Food Funct*. 2018;9(3):1701-1712.
doi: 10.1039/c7fo01555k

23. Zhao Z, Wang Y, Yin B, et al. Defect-adaptive stem-cell-microcarrier construct promotes tissue repair in rabbits with knee cartilage defects. *Stem Cell Rev Rep*. 2023;19(1):201-212. doi: 10.1007/s12015-022-10421-0

24. Ye C, Chen J, Qu Y, et al. Naringin in the repair of knee cartilage injury via the TGF-beta/ALK5/Smad2/3 signal transduction pathway combined with an acellular dermal matrix. *J Orthop Translat*. 2021;32:1-11. doi: 10.1016/j.jot.2021.06.004

25. Liu H, Liu H, Yang Q, Fan Z. LncRNA SNHG1 enhances cartilage regeneration by modulating chondrogenic differentiation and angiogenesis potentials of JBMMSCs via mitochondrial function regulation. *Stem Cell Res Ther*. 2024;15(1):177. doi: 10.1186/s13287-024-03793-2

26. Yang Z, Li H, Tian Y, et al. Biofunctionalized structure and ingredient mimicking scaffolds achieving recruitment and chondrogenesis for staged cartilage regeneration. *Front Cell Dev Biol*. 2021;9:655440. doi: 10.3389/fcell.2021.655440

27. Hu G, Liang Z, Fan Z, et al. Construction of 3D-bioprinted cartilage-mimicking substitute based on photo-crosslinkable Wharton's jelly bioinks for full-thickness articular cartilage defect repair. *Mater Today Bio*. 2023;21:100695. doi: 10.1016/j.mtbio.2023.100695

28. Kim YB, Lee H, Kim GH. Strategy to achieve highly porous/biocompatible macroscale cell blocks, using a collagen/genipin-bioink and an optimal 3D printing process. *ACS Appl Mater Interfaces*. 2016;8(47):32230-32240. doi: 10.1021/acsami.6b11669

29. Zhou Z, Cui J, Wu S, Geng Z, Su J. Silk fibroin-based biomaterials for cartilage/osteochondral repair. *Theranostics*. 2022;12(11):5103-5124. doi: 10.7150/thno.74548

30. Fang Z, Liu G, Wang B, et al. An injectable self-healing alginate hydrogel with desirable mechanical and degradation properties for enhancing osteochondral regeneration. *Carbohydr Polym*. 2024;343:122424. doi: 10.1016/j.carbpol.2024.122424

31. Fang K, Li P, Zhang B, et al. Insights on updates in sodium alginate/MXenes composites as the designer matrix for various applications: a review. *Int J Biol Macromol*. 2024;269:132032. doi: 10.1016/j.ijbiomac.2024.132032

32. Sanchez-Ballester NM, Bataille B, Soulairol I. Sodium alginate and alginic acid as pharmaceutical excipients for tablet formulation: structure-function relationship. *Carbohydr Polym*. 2021;270:118399. doi: 10.1016/j.carbpol.2021.118399

33. Chaurasia B, Summers SA. Ceramides in metabolism: key lipotoxic players. *Annu Rev Physiol*. 2021;83:303-330. doi: 10.1146/annurev-physiol-031620-093815

34. Hu L, Luo D, Zhang H, He L. Polydatin inhibits IL-1β-mediated chondrocyte inflammation and ameliorates cartilage degradation: involvement of the NF-κB and Wnt/β-catenin pathways. *Tissue Cell*. 2022;78:101865. doi: 10.1016/j.tice.2022.101865

35. Alizadeh J, da Silva Rosa SC, Weng X, et al. Ceramides and ceramide synthases in cancer: focus on apoptosis and autophagy. *Eur J Cell Biol*. 2023;102(3):151337. doi: 10.1016/j.ejcb.2023.151337

36. Armistead J, Höpfl S, Goldhausen P, et al. A sphingolipid rheostat controls apoptosis versus apical cell extrusion as alternative tumour-suppressive mechanisms. *Cell Death Dis*. 2024;15(10):746. doi: 10.1038/s41419-024-07134-2

37. Peche VS, Pietka TA, Jacome-Sosa M, et al. Endothelial cell CD36 regulates membrane ceramide formation, exosome fatty acid transfer and circulating fatty acid levels. *Nat Commun*. 2023;14(1):4029. doi: 10.1038/s41467-023-39752-3

38. Bao HN, Yin J, Wang LY, et al. Aberrant accumulation of ceramides in mitochondria triggers cell death by inducing autophagy in Arabidopsis. *J Exp Bot*. 2024;75(5):1314-1330. doi: 10.1093/jxb/erad456

39. Tu H, YL Li. Inflammation balance in skeletal muscle damage and repair. *Front Immunol*. 2023;14:1133355. doi: 10.3389/fimmu.2023.1133355

40. Adada M, Luberto C, Canals D. Inhibitors of the sphingomyelin cycle: sphingomyelin synthases and sphingomyelinases. *Chem Phys Lipids*. 2016;197:45-59. doi: 10.1016/j.chemphyslip.2015.07.008

41. Haseeb A, Kc R, Angelozzi M, et al. SOX9 keeps growth plates and articular cartilage healthy by inhibiting chondrocyte dedifferentiation/osteoblastic redifferentiation. *Proc Natl Acad Sci USA*. 2021;118(8):e2019152118. doi: 10.1073/pnas.2019152118

42. Lefebvre V, Angelozzi M, Haseeb A. SOX9 in cartilage development and disease. *Curr Opin Cell Biol*. 2019;61:39-47. doi: 10.1016/j.ceb.2019.07.008

43. Song H, Park K. Regulation and function of SOX9 during cartilage development and regeneration. *Semin Cancer Biol*. 2020;67(Pt 1):12-23. doi: 10.1016/j.semcancer.2020.04.008

44. Gilbert SJ, Blain EJ, Duance VC, Mason DJ. Sphingomyelinase decreases type II collagen expression in bovine articular cartilage chondrocytes via the ERK signaling pathway. *Arthritis Rheum*. 2008;58(1):209-220. doi: 10.1002/art.23172

45. Piacentino ML, Fasse AJ, Camacho-Avila A, Grabylnikov I, Bronner ME. SMPD3 expression is spatially regulated in

the developing embryo by SOXE factors. *Dev Biol*. 2024; 506:31-41.
doi: 10.1016/j.ydbio.2023.11.011

46. Lucki NC and MB Sewer. Nuclear sphingolipid metabolism. *Annu Rev Physiol*. 2012;74:131-51.
doi: 10.1146/annurev-physiol-020911-153321

47. Xu Z, Xu B, Lundström SL, et al. A subset of type-II collagen-binding antibodies prevents experimental arthritis by inhibiting FCGR3 signaling in neutrophils. *Nat Commun*. 2023;14(1):5949.
doi: 10.1038/s41467-023-41561-7

48. Zeltz C, Gullberg D. The integrin-collagen connection – a glue for tissue repair? *J Cell Sci*. 2016;129(4):653-664.
doi: 10.1242/jcs.180992

49. Lauer JC, Selig M, Hart ML, Kurz B, Rolauffs B. Articular chondrocyte phenotype regulation through the cytoskeleton and the signaling processes that originate from or converge on the cytoskeleton: towards a novel understanding of the intersection between actin dynamics and chondrogenic function. *Int J Mol Sci*. 2021;22(6):3279.
doi: 10.3390/ijms22063279

50. Renard E, Porée B, Chadjichristos C, et al. Sox9/Sox6 and Sp1 are involved in the insulin-like growth factor-I-mediated upregulation of human type II collagen gene expression in articular chondrocytes. *J Mol Med (Berl)*. 2012;90(6):649-666.
doi: 10.1007/s00109-011-0842-3

51. Simental-Mendía M, Lara-Arias J, Álvarez-Lozano E, et al. Cotransfected human chondrocytes: over-expression of IGF-I and SOX9 enhances the synthesis of cartilage matrix components collagen-II and glycosaminoglycans. *Braz J Med Biol Res*. 2015;48(12):1063-1070.
doi: 10.1590/1414-431X20154732

ACCSCIENCE PUBLISHING

International Journal of Bioprinting

RESEARCH ARTICLE

Replication of an intervertebral disc using an in-house bioprinter: A proof-of-concept study

Emmaëlle Carrot[1], Perrine de Villemagne[2], Paul Humbert[1], Sébastien Grastilleur[1], Benoit Rosa[2], Boris Halgand[1], Yoan Le Guennec[1], Johann Clouet[1], Vianney Delplace[1], Pierre Weiss[1], Franck Halary[3], Jean-Yves Hascoët[2], Marion Fusellier[1], Luciano Vidal[2,4], Jérôme Guicheux[1]*, and Catherine Le Visage[1]*

[1]Nantes Université, Oniris, INSERM, CHU Nantes, Regenerative Medicine and Skeleton, RMeS, UMR 1229, Nantes, Pays de la Loire, France

[2]CNRS UMR 6183, Nantes Université, École Centrale Nantes, Rapid Manufacturing Platform, Institut de Recherche en Génie Civil et Mécanique (GeM), Nantes, Pays de la Loire, France

[3]3Nantes Université, INSERM, Center for Research in Transplantation and Translational Immunology, UMR 1064, Nantes, Pays de la Loire, France

[4]Department of Plastic and Reconstructive Surgery, Clinique Bretéché - ELSAN, Nantes, Pays de la Loire, France

(This article belongs to the Special Issue: *Advances in Bioprinting and Organ-on-a-chip and Applications for Precision Medicine*)

Abstract

The intervertebral disc, a fibro-cartilaginous structure, contains a gelatinous core (*nucleus pulposus*) surrounded by collagen fiber lamellae (*annulus fibrosus*). Intervertebral disc degeneration leads to a debilitating disorder, and new treatments are currently being developed. Unfortunately, conventional monolayer *in vitro* models fail to predict the clinical efficacy of novel therapies accurately. Here, we report a bioprinted construct that mimics the macroscopic and microscopic architecture of the intervertebral disc. First, a 3D model was created from a histological section of a sheep lumbar intervertebral disc. The printability of the ink, gelatin (7% w/v), alginate (0.6% w/v), and hyaluronic acid (0.2% w/v) was optimized by varying the printing pressure (70–110 kPa), printing speed (2–10 mm/s), and nozzle type (needle or tip). *Nucleus pulposus* and *annulus fibrosus* cells, harvested from 4-month-old lambs, were bioprinted (5×10^5 cells/mL) using an in-house extrusion bioprinter. Cell viability (live/dead assay), shape (actin immunostaining), distribution (confocal microscopy), and matrix synthesis (immunostaining) were evaluated after 21 days of culture. We used a parametric study to quantify and optimize the factors (pressure, printing speed, nozzle type) influencing the filament width. The 3D construct exhibited fidelity to the initial design and maintained stability in length, width, and height for 21 days. Fluorescent labeling confirmed the distribution of *nucleus pulposus* and *annulus fibrosus* cells in each tissue, replicating the native intervertebral disc structure. We also evidenced cell viability and collagen type 1 synthesis. This bioprinted construct offers a promising alternative to current *in vitro* models, potentially enabling more relevant preclinical evaluations.

Keywords: 3D bioprinting; Alginate; Hydrogel; In-house extrusion bioprinter; *In vitro* 3D model; Gelatin; Hyaluronic acid

***Corresponding authors:**
Catherine Le Visage (catherine.levisage@inserm.fr)

Jérôme Guicheux (jerome.guicheux@univ-nantes.fr)

Citation: Carrot E, de Villemagne P, Humbert P, et al. Replication of an intervertebral disc using an in-house bioprinter: A proof-of-concept study. *Int J Bioprint.* 2025;11(1):470-484. doi: 10.36922/ijb.5021

Received: October 10, 2024
1st revised: November 12, 2024
2nd revised: December 1, 2024
3rd revised: December 6, 2024
Accepted: December 9, 2024
Published Online: December 9, 2024

Copyright: © 2024 Author(s). This is an Open Access article distributed under the terms of the Creative Commons Attribution License, permitting distribution, and reproduction in any medium, provided the original work is properly cited.

Publisher's Note: AccScience Publishing remains neutral with regard to jurisdictional claims in published maps and institutional affiliations.

1. Introduction

The intervertebral disc (IVD) is a fibro-cartilaginous structure essential for maintaining the mobility and stability of the human spine and absorbing and distributing shocks.[1,2] It consists of three primary tissues: a central gelatinous core (*nucleus pulposus* [NP]), an outer network of collagen fibers (*annulus fibrosus* [AF]), and two cartilaginous endplates on either side, which connect to the vertebral bodies.[3,4] The NP is a highly hydrated tissue comprising 70%–90% of water[5] bound by sulfate proteoglycans[6,7] and randomly organized type II collagen fibers,[8,9] with a viscoelastic behavior.[10–12] The young and healthy NP contains two cell types: large notochordal cells, whose number decreases with age,[13] marking the onset of disc degeneration,[14] and nucleopulpocytes or NP cells, resembling articular chondrocytes.[15,16] The total cell density in the NP is about 4200 cells/mm^3[3,17] and both cells are responsible for maintaining homeostasis by synthesizing the extracellular matrix (ECM).[18] The NP is surrounded by the AF, which consists of 15–25 concentric fibrocartilaginous lamellar bands of type I collagen fibers.[19,20] The AF structure is highly resistant, retaining the NP during spinal movements.[21,22] The AF cells, located between the lamellae and aligned with the collagen fibers, are fibroblast-like cells with an elongated shape and produce their surrounding ECM.[23] In young and healthy AF, cells are found at a density of about 12,000 cells/mm^3, and this number tends to decrease with age.[24]

Due to the high frequency of movement, IVD is frequently disrupted, causing degenerative changes.[25] This degeneration is responsible for 40% of low back pain cases,[26] which affects 80% of the global population at least once in their lifetime.[27] The etiology of IVD degeneration remains poorly understood, and existing treatments, such as spinal fusion or IVD replacement, fail to maintain the IVD tissue integrity or halt its decline.[28] In the long term, these surgical interventions may even accelerate the process of IVD degeneration. Presently, novel therapies are being developed to address the etiological cause of degeneration. These new treatments include gene therapy[29] and cell therapy,[30] often combined with the injection of a biomaterial.[31] Each of these therapies acts on one or several aspects of the degeneration. An ECM-mimicking biomaterial can directly restore mechanical properties,[32] and injection of growth factors[33] or gene therapy[34] can stimulate ECM synthesis, relieve inflammation,[35,36] and delay disease progression. The evaluation of these therapies mainly relies on 2D *in vitro* models before progressing to *in vivo* models.[37] Despite the widespread use of 2D *in vitro* culture models, their lack of morphological complexity and cell–ECM interactions significantly oversimplifies the cellular environment. 3D *in vitro* culture systems, such as pellet configuration[38] or encapsulation in alginate hydrogel,[39] have been explored to maintain IVD cell phenotype as seen in native conditions. Although these 3D models are more relevant as they replicate the 3D IVD structure, they are limited to one tissue, AF or NP, and lack repeatability and reproducibility.[40] Only a few complete models replicating the 3D structure of the disc, along with its particular tissues, have been documented.[41] These artificial IVD models were developed for total disc replacement and demonstrated a partial restoration of the spine biomechanics.[42,43] However, the design of these models was not intended to evaluate biological treatments, as the maturation of the model occurs *in vivo* to reproduce a healthy IVD.

Therefore, in this study, we aim to develop a 3D construct that mimics an ovine IVD from a macroscopic and microscopic point of view, with *in vitro* maturation, so that this model could be used to evaluate new therapeutic strategies. The ovine spine is primarily used as a preclinical model because of its biomechanical and cellular similarities with the human one.[44] A bioprinting technique was used to reproduce the specific shape of the IVD and deposit the cells constituting the model. We specially designed an in-house 3D extrusion bioprinter for this project. The bioprinting path was adapted from the histological section of sheep lumbar IVD to be as close to native tissue as possible. Cells extracted from young lumbar ovine IVDs were encapsulated into a gelatin/alginate/hyaluronic acid (HA) ink. This ink was designed to provide the cells with a favorable 3D environment, enabling them to secrete *de novo* ECM, which, after maturation, will form an IVD-like tissue.[45] After optimizing the bioprinting parameters, constructs were obtained and evaluated for up to 21 days of culture. We demonstrated that cells were well homogeneously distributed into the IVD construct and remained viable for up to 21 days of culture. Moreover, both cells in the IVD exhibited a round shape and synthesized collagen, a major component of the IVD ECM.

2. Materials and methods

2.1. Bioprinter

For the development of the bioprinter, a set of specifications was considered based on the type of bioinks to be used and the type of structure to be printed. Temperature control at the level of the printing head and the printing plate was conceived. Separate control of both was designed, with a temperature range between -25 and 100°C. A laser control system was mounted on the deposition plate to position and control the printing head on the printer plate and its different axes. Three linear axes were composed by an encoder resolution of 0.01 µm, ±0.4 µm of bidirectional repeatability, and ±2.5 µm positional accuracy. A post-

processing system was meticulously developed to correct and control the printer's trajectories, ensuring the high quality of the printed objects designed and conceived using computer-aided design (CAD) (Figure 1).

2.2. Optimization of the ink formulation

Different concentrations (w/v) of alginate from brown algae (A2033; Sigma Aldrich, USA), gelatin from bovine skin (G9391; Sigma Aldrich, USA), and HA from *Streptococcus* (53747; Sigma Aldrich, USA) were tested (Table 1). Formulations 1–3 contain 0.6%, 1.2%, or 1.8% of alginate, respectively, 8% of gelatin, and no HA. In formulations 4–9, gelatin was set to 7%, and alginate was set at 0.6% or 1.2% for formulations 4–6 and 7–9, respectively. HA concentration was set at 0% for formulations 4 and 6, 0.2% for formulations 5–8, and 0.3% for formulations 6 and 9.

The powders were mixed in warm water (30–50°C) to solubilize the gelatin. The desired ink volume was transferred into a 10 mL syringe (7012112; Nordson, USA). A plunger sealed the syringe (7012178; Nordson, USA). Air bubbles were removed by centrifugation at 260 × *g* for 3 min. The ink was then equilibrated at 22°C to induce a pre-gelation step, making it printable. Inks were placed into the bioprinter developed by Ecole Centrale Nantes (France) and extruded through different needle diameters (0.20 and 0.25 mm) at 20 kPa and with a printing speed of 10 mm/s to form a square of 1 × 1 cm on 10 layers. Parameters based on the ink aspect (granular or homogeneous), the extrusion process (continuous or not), and the filament uniformity (ranging from + [irregular] to +++ [uniform]) were visually assessed to validate the ink formulation.

2.3. Optimization of printing parameters

After selecting the ink formulation, the printing parameters were defined. The influence of the nozzle type, the extrusion pressure, and the printing speed were assessed to optimize the printing resolution. Two nozzle types were tested: a 0.20 or 0.25 mm internal diameter stainless steel needle and a 0.20 or 0.25 mm internal diameter polyethylene tip. The printing speed was set at 4, 8, or 10 mm/s, and the extrusion pressure was set at 70, 90, or 110 kPa. For each condition, two 2-cm-long filaments were extruded and photographed, and four measurements of the filament thickness were performed. The cordon width was measured using ImageJ® software (1.54j; National Institutes of Health, United States of America [USA]). The optimal printing parameters were selected to obtain the finest filament for greater printing precision (n = 3 independent experiments).

2.4. Cell isolation and culture

Two 4-month-old lambs from Ecole Nationale Vétérinaire de Nantes (ONIRIS) were used to collect NP and AF cells.

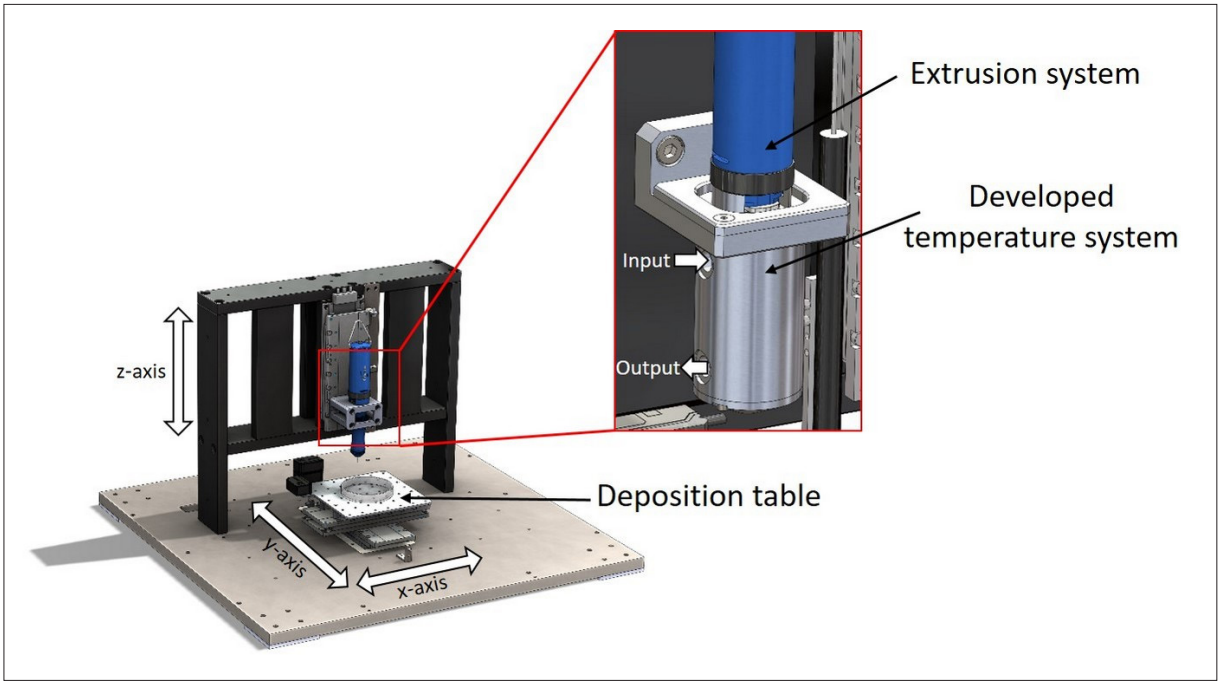

Figure 1. Custom-made bioprinter. The bioprinter is based on three linear axes (x, y, and z) with a micrometer resolution. The extrusion-based machine is under pneumatic control. The bioprinter integrates two temperature systems (head of the syringe and deposition table) composed of an input and output flow, which enables viscosity control of the bioink. The tempered liquid is driven through a hollow circuit set to the desired temperature.

Table 1. List of primers for gene expression analysis

Name	Forward primer (5'–3')	Reverse primer (5'–3')
GAPDH	TCCTGCCCCACCTCCACCAC	GGGCTCCCTAAGCCCCTCCC
COL1A1	CGTGACGCACGGCCAAGAGG	AGATCTGGCAGGGCACGGGT
COL2A1	CTGCTCATCCAGGGCTCAAA	CTTACCGGTGTGTTTCGTGC

The lambs were euthanized, and IVDs were surgically isolated. The AF and NP tissues were cut into ~ 0.5 × 1 cm fragments and rinsed with phosphate-buffered saline (PBS) containing 2% penicillin/streptomycin solution (P/S; 15070-063; Gibco, USA) at room temperature. The tissue fragments were subjected to three consecutive digestions of 0.05% hyaluronidase (H4272; Sigma Aldrich, USA) in Hanks' Balanced Salt Solution (L0606; Biowest, France) for 15 min at 37°C, 0.2% trypsin (T9935; Sigma Aldrich, USA) in Hanks' Balanced Salt Solution for 30 min at 37°C, and 0.25% collagenase (C5138; Sigma Aldrich, USA) in Dulbecco's Modified Eagle culture medium (DMEM containing glucose [GlutaMAX™] and pyruvate; 31966-021; Gibco, USA), supplemented with 10% fetal bovine serum (FBS; S1810; Dominique Deutscher, France), 1% P/S, and 1% amphotericin B (15290; Gibco, USA) for 15 h at 37°C. The cells were filtered through a 70 µm sieve, centrifuged, and resuspended in culture medium before being plated and incubated at 37°C under 5% CO_2. Cells were amplified in DMEM/10% FBS/1% P/S, passaged at 80%–90% confluence, and re-seeded at around 7000 cells/cm².

2.5. Cell phenotype

The differential expression of collagen type I and II in ovine AF and NP cells was assessed by quantitative reverse transcription polymerase chain reaction (RT-qPCR) and immunohistofluorescence (IF).

For RT-qPCR, AF and NP cells at passage 1 were cultivated to confluence in 6-well plates, and RNA was isolated with a Nucleospin RNA XS kit (740902; Macherey-Nagel, Germany). RT was carried out with a Verso cDNA synthesis kit (AB1453A; Thermo Fisher Scientific, USA) with a 1:3 mix of Anchored Oligo(dT) and Random Hexamers. qPCR was performed with SYBR™ Select Master Mix (4472908; Thermo Fisher Scientific, USA) on a thermocycler CFX96 (Bio-Rad, USA) with the primers. The primer sequences are displayed in Table 1 (n = 3 independent experiments), with GAPDH as the internal control in this study. The expression levels of relative genes were normalized to GAPDH, and the results were calculated as fold changes using the $2^{-\Delta\Delta CT}$ formula.

For immunofluorescence, AF and NP cells at passage 4 were cultivated to confluence in 48-well plates, and the cell layers were fixed with 4% (w/v) paraformaldehyde for 20 min. Cells were permeabilized with 0.5% (v/v) Triton X-100 in PBS for 10 min and incubated for 30 min in blocking solution (1% [w/v] bovine serum albumin and 2% [v/v] normal donkey serum in PBS). Primary antibodies for collagen I (ab138492; Abcam, UK) and collagen II (ab34712; Abcam, UK) were diluted at 3.5 and 4.12 µg/mL in blocking solution, respectively, and incubated on the cells for 1 h. Cells were then incubated with the fluorescent secondary antibody (donkey anti-rabbit Alexa Fluor 488; A32790; Thermo Fisher Scientific, USA) diluted at 4 µg/mL in PBS for 1 h, followed by 30 min incubation with Alexa Fluor-568 Phalloidin (A12380; Thermo Fisher Scientific, USA) diluted at 2.5 µg/mL in PBS of and 10 min incubation with DAPI (D1306; Thermo Fisher Scientific, USA) diluted at 2.5 µg/mL in PBS. Image acquisition was performed with a microscope Axio Zoom.V16 (Zeiss, Germany).

2.6. Fluorescent labeling of disc cells

Confluent NP and AF were rinsed with PBS before labeling their cell membrane with fluorochromes. The AF cells were incubated in PBS solution containing 2 µg/mL of 3,3'-dioctadecyl-5,5'-di(4-sulfo-phenyl)oxacarbocyanine, sodium salt (D7778; Sigma Aldrich, USA). NP cells were incubated in a PBS solution containing 2 µg/mL of Vybrant™ CM-DiI Cell-Labeling Solution (V22888; Sigma Aldrich, USA). Both cell types were incubated for 15 min at 37 °C under 5% CO_2, followed by 15 min at 4 °C. A confocal fluorescence microscope (Eclipse Ti2; Nikon, Japan) was used to confirm the fluorescent cell labeling before trypsinizing and mixing cells with the ink.

2.7. Extrusion process

The selected ink composed of 7% (w/v) gelatin, 0.6% (w/v) of alginate, and 0.2% (w/v) of HA was mixed with 2×10^5 cells/mL of either AF cells or NP cells. Syringes were loaded as described above and placed in a nozzle connected to a cooling system set at 22°C. The extrusion was performed through a 0.25 mm diameter needle (7018333; Nordson, USA) into a 100 mm diameter culture dish (430167; Corning, USA). The model was designed based on collagen I histological staining of the lumbar IVD of sheep, and its dimensions were 20 (length [L]) × 16 (width [W]) × 2 mm (height [h]). The resulting IVD construct was crosslinked for 15 min at room temperature

with sterile 100 mmol/L $CaCl_2$ (C7902; Sigma Aldrich, USA) in water. The IVD construct was then transferred to a 35 mm diameter culture dish (83.3900; Sarttedt, Germany) containing culture medium supplemented with 10% FBS, 1% P/S, 1% amphotericin B, and 0.17 mmol/L 2-phospho-L-ascorbic acid (49752; Sigma Aldrich, USA). The construct was incubated at 37°C under 5% CO_2. The culture medium was changed twice a week for up to 21 days. IVD constructs were observed before and after crosslinking and after 21 days of culture using a Dino-Lite microscope (AF4515ZTL; Dino-Lite Microscope, Taiwan). The sample's length, width, and height were measured using ImageJ® software (n = 3 independent experiments).

2.8. Cell visualization, density, and distribution

Cell visualization in the bioprinted construct was performed using fluorescently labeled cells. After 21 days of culture, labeled cells were identified in the IVD construct using a confocal fluorescence microscope. Z-stack acquisition (2.0 mm height; 68 stacks) was performed in six Region Of Interest (ROIs), and Z-projection was used to qualitatively analyze global IVD cell distribution on the x- and y-axis. For cell distribution quantification on the z-axis, cells on Z-stack images corresponding to 0.5, 1.0, 1.5, and 2.0 mm height were counted using the analyze-particle plugin for ImageJ® software (n = 3 experimental replicates). Cell density and distribution were then assessed on non-fluorescently labeled IVD constructs using a Live/Dead™ viability/cytotoxicity kit (L3224; Invitrogen, USA) after 1, 7, 14, and 21 days of culture. The culture medium was removed, and the constructs were rinsed with 2 mmol/L $CaCl_2$ diluted in distilled water. The constructs were then incubated in the dark for 1 h at 37°C with 2 µg/mL of calcein-AM, 4 µg/mL of EthD-1, and 2 µg/mL of Hoechst 33342 trihydrochloride (H3569, λ_{ex} = 352 nm and λ_{em} = 461 nm; Life Technologies, USA), all diluted in culture medium. Constructs were rinsed three times with 2 mmol/L $CaCl_2$ diluted in distilled water and added back to the culture medium. Z-stack acquisition (2.0 mm height) was performed using a confocal fluorescence microscope. Cell density was quantified by counting the number of cells positive to calcein in the entire Z-stack acquisition using the 3D objects counter in ImageJ® software (n = 3 experimental replicates).

2.9. Histological analysis

The IVD constructs were gently removed from the culture dish using a spatula, and excess liquid was removed with a paper towel to limit crystal formation during freezing. The bottom of a freezing cassette (03075; Surgipath, USA) was covered with an Optimal Cutting Temperature (OCT) cryogenic embedding medium (LAMB/OCT; Thermo Fisher Scientific, USA). The constructs were deposited in the center of the cassette and covered with OCT before being immersed for 30 s in isopentane (24872.298; VWR, USA), previously cooled in liquid nitrogen. Once frozen, the samples were sectioned at -20°C into 10 µm slices using a cryostat (CryoStar NX70®; Thermo Fisher Scientific, USA). The slices were then placed on polysine-coated slides (10219280; Thermo Fisher Scientific, USA), and the slides were dried at room temperature for 20 min. Before staining, the samples were post-fixed for 10 min in 4% (w/v) paraformaldehyde to promote the adhesion of the sections onto the slides. Sections were stained following standard protocols with hematoxylin-eosin-saffron (HES; 01562E; Diapath, ITALY) or Alcian blue (AB; 361186; VWR, USA).

2.10. Immunohistochemistry

Enzyme unmasking was performed on post-fixed sections with 0.1% trypsin (T9935; Sigma, USA) in PBS at 37°C for 1 h. Sections were rinsed with PBS and incubated with a 3% solution of H_2O_2 (H1009; Sigma, USA) in PBS at room temperature for 20 min to reduce the non-specific background due to the endogenous peroxidase. Sections were washed with PBS and incubated with 4% bovine serum albumin (A9647; Sigma, USA) and 10% goat serum (G9023; Sigma, USA) in PBS at room temperature for 20 min. The sample sections were then incubated with primary collagen type I antibody (Ab138492; Abcam, UK) diluted at 3.5 µg/mL in antibody diluent (S3022; DAKO, Denmark) overnight at 4°C; negative controls were incubated with only antibody diluent. After a rinsing step with PBS, the sections were incubated for 30 min at room temperature with an anti-rabbit IgG (ImmPRESS HRP Reagent Kit, MP7401; Vector Laboratories, USA). After a rinsing step in PBS, a freshly prepared chromogen 3,3'-diaminobenzidine (SK-4105; ImmPACT, Vector Laboratories, USA) solution was added to the sections. The sections were counterstained with Mayer's hematoxylin and mounted using a permanent aqueous mounting medium (Scy Tek Laboratories, USA); sections were scanned using a microscope slide scanner (NanoZoomer S360; Leica, Germany).

2.11. Statistical analysis

All quantitative data are expressed as the mean ± standard deviation (SD). The statistical analysis comprised paired t-test (gene expression); two-way analysis of variance (ANOVA), followed by Tukey multiple comparisons (parameters for printing conditions, measure of IVD construct size, and z-axis cell distribution); and Shapiro-Wilk test for validating their normality, followed by Tukey comparison test. The analysis was performed using GraphPad Prism version 10.0.0 for Windows (GraphPad Software, USA). A p-value < 0.05 was considered significant.

3. Results

3.1. Optimizing the ink formulation

The first step of the study was to define the concentrations of alginate, gelatin, and HA that would compose the ink (Table 2). First, we selected a gelatin concentration of 8% (w/v) in all inks. We used alginate at 0.6% (w/v) in formulation 1, 1.2% (w/v) in formulation 2, and 1.8% (w/v) in formulation 3. For these three formulations, the ink was granular, and the extruded filaments were not continuous or uniform (Figure S1, Supporting Information). We then added HA to the gelatin/alginate composition to create formulations 4–9, reducing the gelatin concentration to 7% [w/v] to achieve a homogeneous ink and enhance the extrusion process. We noticed that with 0.3% (w/v) of HA, the extruded filaments were continuous but not uniform (formulations 6 and 9). By decreasing the percentage of HA to 0.2% (w/v), the drawn filaments were more uniform (formulations 5 and 8). The formulation that formed a smooth and extrusion-compatible ink with uniform filaments contained 7% (w/v) of gelatin, 0.6% (w/v) of alginate, and 0.2% (w/v) of HA (formulation 5). This formulation was then selected for all subsequent experiments.

3.3. Optimizing the printing conditions

We tested several parameters known to influence the bioprinting process. Different extrusion pressures (70, 90, and 110 kPa), printing speeds (4, 8, and 10 mm/s), and nozzles (stainless steel needle and polyethylene cone of 0.20 and 0.25 mm diameter) were evaluated (Figure 2). Overall, the width of the filament obtained with a 0.20-mm diameter nozzle was significantly lower than that obtained with a 0.25-mm diameter nozzle. For both nozzle types, the filament width was the highest for the highest pressure (110 kPa) or the slowest printing speed (4 mm/s). The filament width increased for a given printing speed and increasing pressure; this increase was more significant with the nozzle of 0.25 mm diameter ($p < 0.01$). In contrast, for a given pressure and increasing printing speed, the filament width decreased for both nozzle modes. Similarly, this decrease was more significant for a nozzle of 0.2 mm ($p < 0.0001$). These differences indicated that the printing speed and pressure affected the bioprinting process. Based on these results, all subsequent experiments were performed using a 0.25-mm diameter needle, a pressure of 70 kPa, and a printing speed of 10 mm/s, which produced filaments with a width of 0.64 ± 0.11 mm.

3.4. Workflow from histological section to bioprinted intervertebral disc construct

After determining the optimal printing parameters, we designed the model to replicate an IVD from a sheep as accurately as possible. First, the phenotype of cells extracted from ovine IVDs was characterized. We used RT-qPCR to confirm that cells isolated from the AF and the NP exhibited distinct gene expression profiles (Figure S2A, Supporting Information). AF cells preferentially expressed COL1A1, while NP cells preferentially expressed COL2A1, as confirmed by immunofluorescence (Figures S2B and S2C, Supporting Information). We then used an IVD of a healthy sheep for the design (Figure 3A). The histological section of the IVD (Figure 3B) was used to generate a virtual 3D model (Figure 3C). We sliced and translated the IVD CAD into G-code instructions (Figure 3D) for further bioprinting using the optimized extrusion parameters (Figure 3E). We then bioprinted

Table 2. Optimization of the ink formulation

Formulation	Concentration (% [w/v])			Ink observation	Extrusion	Filament uniformity
	Alginate	Gelatin	Hyaluronic acid			
F1	0.6	8	-	Granular	Not continuous	N.A.
F2	1.2	8	-	Granular	Not continuous	N.A.
F3	1.8	8	-	Granular	Not continuous	N.A.
F4	0.6	7	-	Homogeneous	Continuous	++
F5	0.6	7	0.2	Homogeneous	Continuous	+++
F6	0.6	7	0.3	Homogeneous	Continuous	+
F7	1.2	7	-	Homogeneous	Continuous	++
F8	1.2	7	0.2	Homogeneous	Continuous	++
F9	1.2	7	0.3	Homogeneous	Continuous	+

Note: Nine formulations of different concentrations (w/v) of alginate, gelatin, and hyaluronic acid were extruded through different needle diameters (0.20 and 0.25 mm) at 20 kPa and with a printing speed of 10 mm/s. The ink aspect (granular or homogeneous), the extrusion process (continuous or not), and the filament uniformity (ranging from + [irregular] to +++ [uniform]) were visually assessed to validate the ink formulation. Abbreviation: N.A., not applicable.

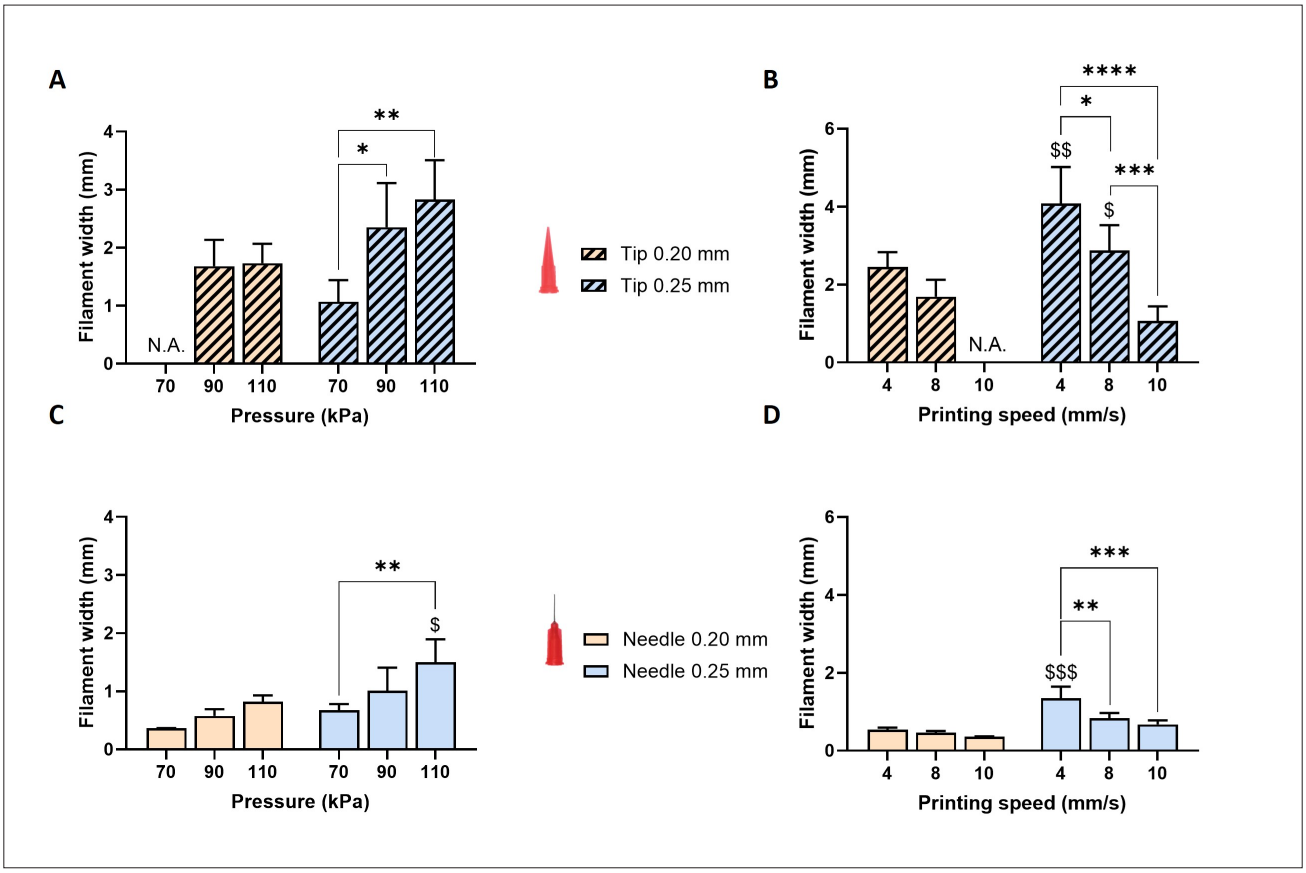

Figure 2. Optimization of printing conditions. (A) Filament width as a function of pressure (printing speed = 10 mm/s) for a tip with different internal diameters (0.20 mm or 0.25 mm). (B) Filament width as a function of printing speed (pressure = 70 kPa) for a tip with different internal diameters (0.20 mm or 0.25 mm). (C) Filament width as a function of pressure (printing speed = 10 mm/s) for a needle with different internal diameters (0.20 mm or 0.25 mm). (D) Filament width as a function of printing speed (pressure = 70 kPa) for a needle with different internal diameters (0.20 mm or 0.25 mm). Bioink comprises 0.6% alginate, 7% gelatin, and 0.2% hyaluronic acid and is extruded at 22°C. Results are expressed as the mean ± standard deviation (n = 3 independent experiments). \$ ($p < 0.05$), \$\$ ($p < 0.01$), \$\$\$ ($p < 0.001$), and \$\$\$\$ ($p < 0.0001$) indicate a significant difference with the 0.20 mm needle or tip at the same pressure or printing speed. *$p < 0.05$; **$p < 0.01$; ***$p < 0.001$; ****$p < 0.0001$ indicate a significant difference. Abbreviation: N.A., not applicable.

the AF section as a multi-lamellar circle, followed by bioprinting of the NP in its center. We crosslinked the resulting IVD construct for 15 min at room temperature with sterile 100 mmol/L $CaCl_2$ in water. We measured the dimensions of the bioprinted constructs immediately after printing, before the crosslinking step, after the crosslinking step, and after 21 days of culture (Figure 3G). The expected dimensions of the construct were 20 (L) × 16 (W) × 2 mm (h). Immediately after printing, the measured dimensions were 21.76 (L) × 17.86 (W) × 2.5 mm (h) and were significantly different from the expected values ($p < 0.05$). After crosslinking, the measured dimensions were 22.65 (L) × 18.45 (W) × 2.53 mm (h). Size measurements were not significantly different from the size before crosslinking, but they were significantly different from the expected values ($p < 0.01$ for the width; $p < 0.001$ for the length). However, after 21 days of culture, we noticed that the construct dimensions decreased to 20.39 (L) × 17.1 (W) × 1.53 mm (h). Even if the length significantly differed after crosslinking ($p < 0.01$), the size was similar to the expected values. The bioprinted structure retained its shape, demonstrating the fidelity of its layout.

3.5. Cell distribution and density

Disc cells (NP and AF cells) were labeled with fluorochromes (Figure 4A) before their incorporation into the ink for bioprinting. Cell distribution in the x-, y-, and z-axes were monitored over 21 days of culture. At day 21, cell membrane labeling was maintained, and NP and AF cells retained their initial distribution within the construct in the x- and y-axis (Figure 4B). The NP (red) and AF (green) cells were observed in the periphery and the center of the construct, respectively.

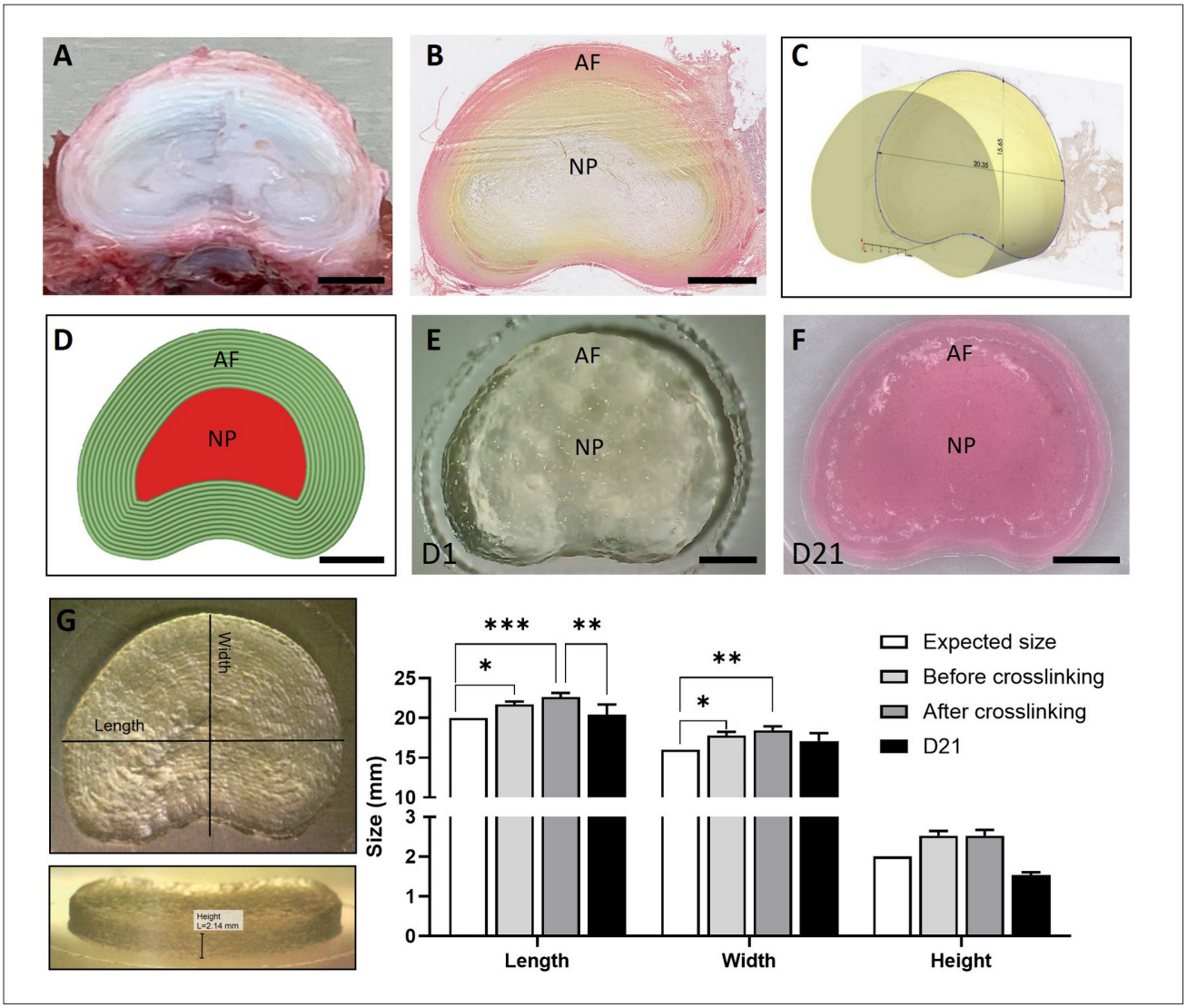

Figure 3. From histological section to bioprinted intervertebral disc (IVD) constructs. (A) The morphological aspect of a lumbar ovine IVD. (B) Collagen I histological staining of an ovine IVD. (C) Virtual 3D model. (D) Slicing 3D IVD model. (E and F) 3D-bioprinted IVD construct after bioprinting (E) and after 21 days of culture (F). (G) Image of the construct and dimensions (length, width, and height) before and after crosslinking and after 21 days at 37°C. The results are expressed as the mean ± standard deviation ($n = 3$ independent experiments). *$p > 0.05$, **$p < 0.01$; ***$p < 0.001$. Scale bars: 5 mm. Abbreviations: AF, annulus fibrosus; NP, *nucleus pulposus*.

Cell distribution on the *z*-axis was also quantified as a function of time (Figures 4C and D and S3, Supporting Information). After 1 day of culture, the NP and AF cells appeared homogenously distributed across the construct height. No differences in the cell number at different heights were observed. In any section of the construct, there were 17–24% NP cells and 19–26% AF cells. After 21 days of culture, the vertical distribution of cells appeared slightly different. The height of the construct decreased from day 1 to day 21. Cells were evident on the top of the constructs at both time points, i.e., 2 mm for day 1 and 1.5 mm for day 21. In contrast, in the lower part of the disk, the percentage of cells increased by 35.6% for NP cells and 33.1% for AF cells at day 21, which is significantly different from day 1 ($p < 0.001$ for NP cells; $p < 0.01$ for AF cells). The final cell density was assessed in the bioprinted IVD construct (Figure 5). Initially, the construct incorporated 1.5×10^5 NP and 1×10^5 AF cells per mL of ink. The AF cell density remained stable for the culture duration, while the NP cell density slightly decreased to 1×10^5 cells/mL after 7 days, then dropped to 2.99×10^4 cells/mL after 21 days of culture.

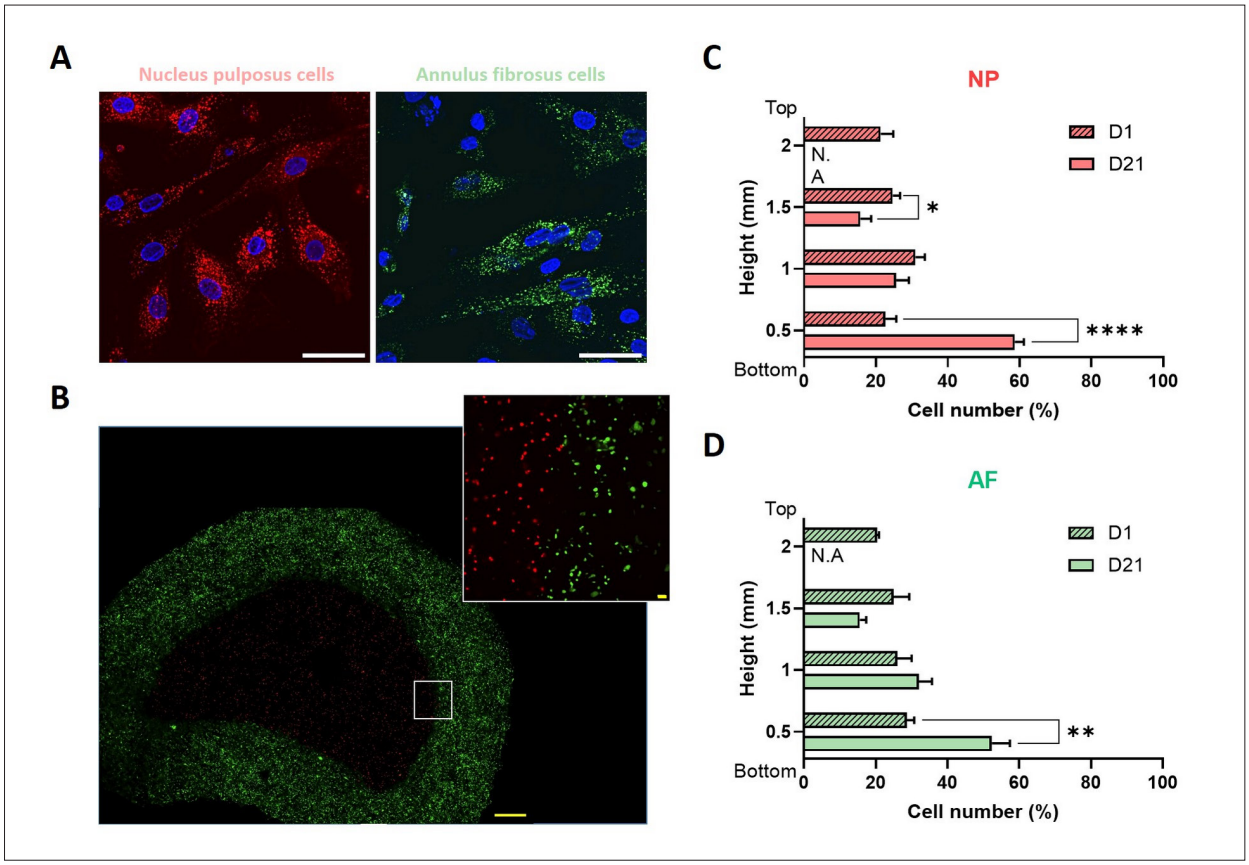

Figure 4. Visualization of fluorescent *nucleus pulposus* (NP) and *annulus fibrosus* (AF) cells and distribution in a bioprinted intervertebral disc (IVD) construct. (A) Representative images of 2D NP cells labeled with Vybrant™ CM-DiI Cell-Labeling Solution (A, left) and 2D AF cells labeled with SP-DiOC18(3) (A, right). (B) IVD fluorescent cells in the IVD construct after 21 days of culture and corresponding zoom-in (B, inset). (C and D) Distribution of NP cells (C) and AF cells (D) in the height of the 3D construct as a function of time (days 1 [D1] and 21 [D21]). Z-stack acquisition (2.0 mm height) was performed in six regions of interest (ROIs). Results are expressed as the mean ± standard deviation (n = 3 experimental replicates). $^{**}p < 0.01$; $^{***}p < 0.001$. Scale bars: 50 µm (A; B, inset); 1 mm (B).

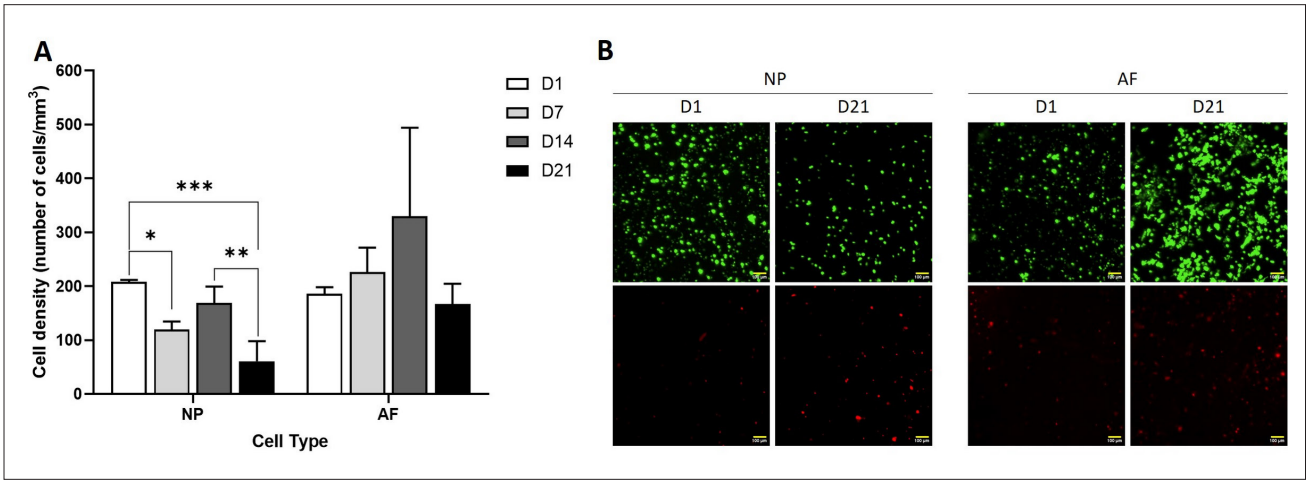

Figure 5. *Nucleus pulposus* (NP) and *annulus fibrosus* (AF) cell density in intervertebral disc (IVD) constructs bioprinted from days 1, 7, 14, and 21 of culture. (A) Cell density (number of cells/mm^3) of both NP and AF parts as a function of time. Results are expressed as the mean ± standard deviation (n = 3 experimental replicates). $^{*}p < 0.05$; $^{**}p < 0.01$; $^{***}p < 0.001$. (B) Representative Z-projection images of cells stained with calcein-AM (green) and ethidium homodimer-1 (red) in the IVD constructs on days 1 and 21. Scale bars: 100 µm.

3.6. Extracellular matrix synthesis and cell morphology

Histological sectioning, staining (HES and AB), and immunohistochemistry (collagen type 1) were performed after 21 days of culture to determine whether the cells printed and cultured in the bioinks synthesized ECM. Sections of a native sheep IVD were also used. AB staining, which highlights the presence of negatively charged molecules, such as polysaccharides, confirmed that after 21 days of culture, the construct was positively stained with AB, highlighting the presence of alginate and HA (Figure 6, top row). Similarly, HES staining indicated the presence of homogenous light pink staining in the AF and NP parts, highlighting the presence of gelatin (Figure 6, middle row). NP and AF cells were identified in the NP and AF sections, respectively. Most cells appeared to be condensed or rounded, and all were positive for intracellular collagen type 1, indicating that the cells were still synthesizing collagen after 21 days of culture (Figures 6, bottom row, and S4, Supporting Information). Sections of a native sheep IVD were also used (Figure S5, Supporting Information).

4. Discussion

Preclinical evaluation of novel biological therapies relies predominantly on studying their efficacy using 2D *in vitro* models. While these models have their uses, particularly in initial studies of cellular toxicity and preliminary proof-of-concept validation, their inability to directly translate results to the *in vivo* environment is a significant constraint. This limitation underscores the urgent need for new *in vitro* models that more accurately represent *in vivo* tissue, thereby improving the translatability of preclinical results to clinical situations. This study, therefore, investigates the possibility of developing a 3D IVD construct containing ovine AF and NP cells, as sheep are widely used as models for disc degeneration. The potential of this new construct to mimic the macroscopic and microscopic organization of the native lumbar ovine IVD promises a more effective approach to preclinical research.

We developed an in-house 3D bioprinter, which we presented here for the first time. It was designed to precisely control the temperature of both the ink used and the printed construct. Owing to the high printing resolution of our printer, the IVD constructs obtained closely matched theoretical models, ensuring high fidelity and precision in their reproduction.

The choice of ink also plays a role in the bioprinting resolution.[46] The selected ink comprises 7% gelatin, 0.6% alginate, and 0.2% HA. It was designed to provide cells with a favorable 3D environment for *de novo* ECM secretion, which, after maturation, forms an IVD-like tissue. Gelatin contributes to the bioink's printability.[47,48] At room temperature, the bioink exhibits the characteristics of an extrudable gel that retains its shape after extrusion when the gelatin concentration is at least 3% (w/v). Furthermore, from a biological point of view, gelatin is obtained by hydrolysis of collagen, which is found in significant quantities in native IVD.[49] Alginate is a

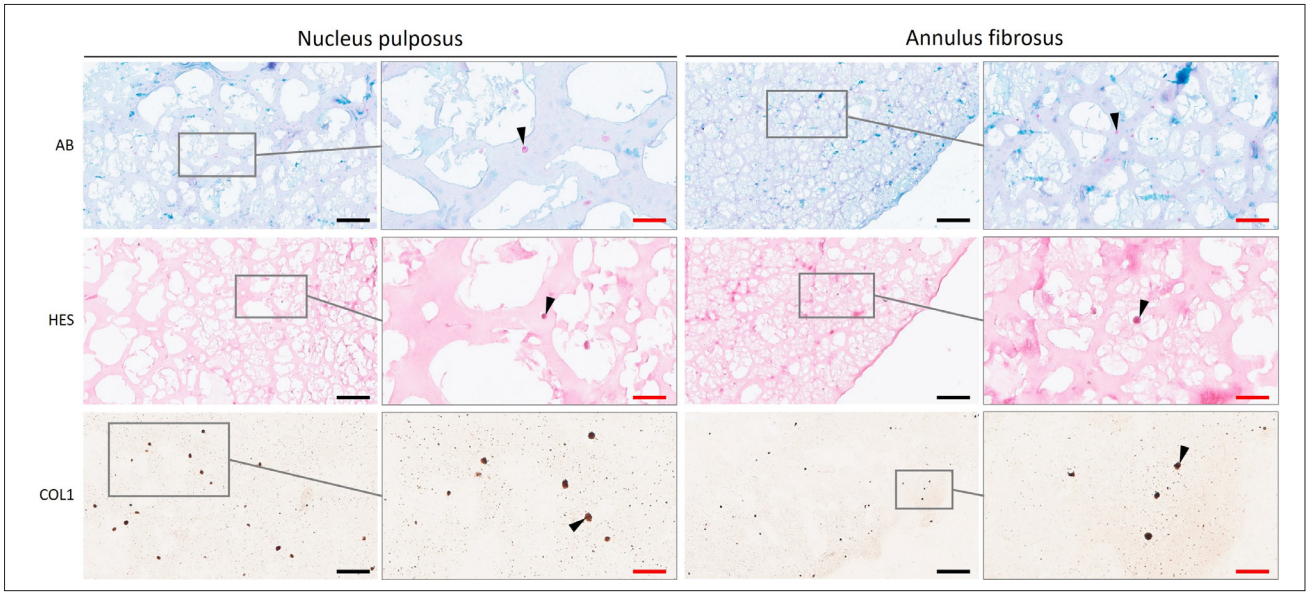

Figure 6. Histological analysis of intervertebral disc (IVD) constructs cultured for 21 days. Representative images of Alcian blue (AB; top row), hematoxylin-eosin-saffron (HES; middle row), and collagen type 1 (COL1; bottom row) staining of *nucleus pulposus* and *annulus fibrosus* parts of the IVD construct after 21 days of culture. Black arrows indicate cells. Scale bars: 200 μm (black); 50 μm (red).

polymer widely used to encapsulate IVD cells and has been reported to promote their specific phenotype.[50,51] After crosslinking with $CaCl_2$, the model was incubated at 37°C. At this temperature, the gelatin liquefies, while the crosslinked alginate retains the 3D structure of the tissue. Finally, HA, a glycosaminoglycan highly present in the NP, is essential in retaining water in the gelatinous body and enhancing the bioink's ability to mimic the IVD. The development of this bioink has also demonstrated that the incorporation of HA enhances its fluidity, thereby facilitating the creation of a deposit filament with superior resolution.[52] The printing conditions of this bioink were then optimized to ensure the highest resolutions. The effect of various parameters, such as nozzle type, pressure, and printing speed on filament size was studied. As expected, the filament is thinner when printing speed increases and pressure decreases. Extrusion pressure has a direct effect on flow and filament thickness. For identical printing speeds, lower pressure reduces the force required to extrude the ink through the nozzle, reducing flow, and filament diameter.[53] Nozzle diameter and geometry also influence filament thickness. Smaller diameter nozzles require higher pressure to maintain the same flow rate as larger diameter nozzles. Consequently, reducing pressure with a smaller nozzle results in a thinner filament due to the lower velocity.[54] Finally, shear stresses are distributed more gradually in tips than in needles, where the transition is rougher. This can lead to thicker filaments with tips, as the bioink undergoes less constriction and shear stress than with needles. Computational fluid dynamics have demonstrated that changes in the design of the nozzle, like the convergence angle and the length of the nozzle, affect the flow rate and shear stress, consequently changing the thickness of the filament.[54,55] The needle was selected in this work because it produces finer filaments compared to the tip. Although the 0.20 mm needle produced finer filaments than the 0.25 mm needle, we did not select it because small diameters increase shear stress, which can damage the cells and reduce their viability and pressure.[55] To minimize the impact of the bioprinting process on the cells, we selected the 0.25 mm needle, the lowest pressure of 70 kPa, and the printing speed of 10 mm/s, which enabled us to obtain the finest filament.

The bioprinted IVD construct was cellularized with cells extracted from a sheep IVD. The sheep model is an *in vivo* model commonly used to study the development of new therapies to treat disc degeneration because of its physiological and anatomical similarities with humans.[56,57] Cell viability was well-maintained in the construct, given the biocompatibility of the ink components. Previous studies using similar inks based on alginate, HA, and gelatin have demonstrated their ability to maintain cell density and viability.[58–60] However, cell density decreased after 21 days in this study, particularly in the NP, further deviating from the *in vivo* cell density of the model. This decrease can be attributed to limited diffusion of the culture medium in the large construct, leading to nutrient and oxygen deficiency in the central regions. This phenomenon of limited diffusion is widely described in the literature, and mathematical models of nutrient diffusion, cell proliferation, and cell death have been investigated.[61] They emphasize a risk for oxygen and glucose depletion within bioprinted constructs, particularly in large ones. In native tissues, a vascular network in the cartilage endplates enables nutrient supply to non-vascularized NP tissues.

The microscopic organization of the IVD was well-reproduced, with the NP cells in the center and the AF cells arranged around them. This organization was maintained throughout the 21-day culture. However, one of the limitations of this work is that this difference between NP and AF was well-marked, whereas, in native IVD, a cellular gradient is observed.[23,62] Indeed, NP cells are more densely populated in the center, and AF cells exhibit a gradual transition in composition and concentration towards the periphery. Incorporating a gradient into the construct could undoubtedly improve the biomimicry of the model by positively influencing cell–cell interactions, thus leading to biological responses closer to those observed in native IVD tissues. Moreover, histological results demonstrated that AF cells, which are elongated *in vivo*, maintained a circular phenotype, as expected in a non-degradable alginate gel. In the bioink, gelatin and HA can support cell adhesion and growth. However, these polymers are soluble because they are not cross-linked, and their persistence over time in the model is uncertain. As a result, the 3D environment is mainly based on alginate, which has no binding sites to which cells can adhere.[63] To improve cell adhesion, the bioink could be enhanced by incorporating a modified alginate with an RGD peptide sequence.[50,51] This sequence serves as a recognition site, allowing AF cells to anchor and acquire a fibroblastic phenotype close to that *in vivo*. Moreover, AF cells did not exhibit any specific organization in the construct. *In vivo*, these cells are aligned along the collagen fibers they produce, which is not the case here. Thus, incorporating a fibrous mesh in the construct also offers significant potential to improve this organization and the model's biomechanical functions.[66–68]

Finally, collagen deposition was not observed, even though the cells expressed the gene associated with collagen production, and intracellular collagen synthesis was demonstrated before and after cell encapsulation. The culture duration might have been too short to allow visible collagen accumulation. Alternatively, the porosity and composition of the microenvironment

could have favored the diffusion of the secreted collagen toward the culture medium, preventing its localized deposition. A longer culture duration might be necessary to allow significant collagen deposition; modifications to the ink composition could also be considered to trap macromolecules synthesized by the cells. Moreover, AF cells are mechanosensitive, meaning they can detect and convert mechanical signals into biochemical signals, such as ECM synthesis. Thus, applying mechanical load to the 3D construct in the future could enhance ECM deposition. Mordechai et al.[69] designed AF laminates made of silk fibers reinforced with alginate hydrogel to replicate native AF mechanical behavior, without the need for collagen synthesis. Moxon et al.[70] reported another approach to mimic the structural properties of an IVD. They printed collagen filaments to stimulate the formation of elongated, mature fibers by the AF cells.[70]

Future studies are warranted to address the shortcomings of this work. Besides incorporating a fibrous mesh to improve the AF organization, using a pre-crosslinked alginate with better stress relaxation properties might favor the deposition of collagen and other ECM molecules, thus enhancing the formation of an IVD-like microenvironment. The next step of this study, which will be crucial to demonstrate the relevance of our work, will be to implement a validation of a therapy's efficacy in the 3D-bioprinted model and in a relevant and well-established preclinical model, such as the sheep, where spontaneous disc degeneration occurs. Once the relevance of this type of bioprinted model has been validated, the incorporation of primary human NP and AF cells, although scarcely available, could be implemented to demonstrate the ability of a bioprinted IVD model in accurately predicting the success of bioinspired therapies for IVD degeneration.

5. Conclusion

In this study, we demonstrated the potential of bioprinting technology to fabricate a 3D model that mimics the architecture of a native IVD. Using an in-house extrusion bioprinter, we optimized bioprinting parameters (filament width, pressure, printing speed, and nozzle type) and the 3D cellular organization. We displayed the structural similarity and the excellent integration of both AF and NP tissues, thereby highlighting the promising potential of this IVD construct in the development of relevant *in vitro* models.

Acknowledgments

The authors acknowledge the SC3M platform from the INSERM/NU/ONIRIS UMR1229 RMeS Laboratory (SFR Bonamy, BioCore, Inserm UMS 016, CNRS UAR 3556, Nantes, France) and the IBISA MicroPICell facility (Biogenouest, France), a member of the national infrastructure France-Bioimaging, supported by the French National Research Agency (ANR-10-INBS-04). The authors thank Hilel Moussi for their assistance. The graphical abstract was created using BioRender.

Funding

This study was supported by the RFI Bioregate program of Pays de la Loire Region within the framework of the 4D-BIODIV project, the European Commission's Horizon 2020 funding program for the iPSpine project (grant number: 825925), the EXCELLDISC project (ANR-19-CE18-0020-01), and the INDEED project (ANR-19-CE06-0028-02).

Conflict of interest

The authors declare they have no competing interests.

Author contributions

Conceptualization: J.Y. Hascoët, J. Guicheux, C. Le Visage, J. Clouet, M. Fusellier, V. Delplace, P. Weiss, F. Halary
Formal analysis: E. Carrot, P. de Villemagne, L. Vidal
Funding acquisition: J.Y. Hascoët, J. Guicheux, C. Le Visage
Investigation: E. Carrot, P. de Villemagne, P. Humbert, S. Grastilleur, B. Rosa, B. Halgand, Y. Le Guennec
Methodology: E. Carrot, P. Humbert, S. Grastilleur
Writing–original draft: E. Carrot, C. Le Visage
Writing–review & editing: All authors

Ethics approval and consent to participate

Not applicable.

Consent for publication

Not applicable.

Availability of data

Data used in this work are available from the corresponding author upon reasonable request.

References

1. Wilke HJ, Galbusera F. Biomechanics of the healthy and diseased spine. In: Biological Approaches to Spinal Disc Repair and Regeneration for Clinicians (1st ed.). Stuttgart, Germany: Georg Thieme Verlag KG; 2017:30-36. doi: 10.1055/b-0037-145106

2. Amin DB, Lawless IM, Sommerfeld D, Stanley RM, Ding B, Costi JJ. The effect of six degree of freedom loading sequence

on the in-vitro compressive properties of human lumbar spine segments. *J Biomech*. 2016;49(14):3407-3414. doi: 10.1016/j.jbiomech.2016.09.009

3. Gravel JT, Abduljabbar FH, Ouellet J, Haglund L. The human spinal disc: relevant anatomy and physiology. In: Biological Approaches to Spinal Disc Repair and Regeneration for Clinicians (1st ed.). Stuttgart, Germany: Georg Thieme Verlag KG; 2017:2-10. doi: 10.1055/b-0037-145103
4. Lavignolle B. The intervertebral disc. In: Vital JM, Cawley DT, eds. *Spinal Anatomy : Modern Concepts*. Springer International Publishing; 2020:207-216. doi: 10.1007/978-3-030-20925-4_14
5. Al-Abbasi M, Al-Rubai AJF, Assi MH. Quantification of the water content of human intervertebral discs in various regions and conditions. *Al-Rafidain J Med Sci*. 2024;6(2):43-47. doi: 10.54133/ajms.v6i2.715
6. Johnstone B, Bayliss MT. The large proteoglycans of the human intervertebral disc. Changes in their biosynthesis and structure with age, topography, and pathology. *Spine*. 1995;20(6):674-684. doi: 10.1097/00007632-199503150-00008
7. Pattappa G, Li Z, Peroglio M, Wismer N, Alini M, Grad S. Diversity of intervertebral disc cells: phenotype and function: diversity of intervertebral disc cells. *J Anat*. 2012;221(6):480-496. doi: 10.1111/j.1469-7580.2012.01521.x
8. Sivan SS, Hayes AJ, Wachtel E, et al. Biochemical composition and turnover of the extracellular matrix of the normal and degenerate intervertebral disc. *Eur Spine J*. 2014;23 (Suppl. 3):S344-S353. doi: 10.1007/s00586-013-2767-8
9. Zhang S, Liu W, Chen S, et al. Extracellular matrix in intervertebral disc: basic and translational implications. *Cell Tissue Res*. 2022;390(1):1-22. doi: 10.1007/s00441-022-03662-5
10. Vogel A, Pioletti DP. Damping properties of the nucleus pulposus. *Clin Biomech*. 2012;27(9):861-865. doi: 10.1016/j.clinbiomech.2012.06.005
11. Krull C, Lutton A, Olesik J, Walter B. A method for measuring intra-tissue swelling pressure using a needle micro-osmometer. *Eur Cell Mater*. 2020;40:146-159. doi: 10.22203/eCM.v040a09
12. Urban JPG, McMullin JF. Swelling pressure of the inervertebral disc: influence of proteoglycan and collagen contents. *Biorheology*. 1985;22(2):145-157. doi: 10.3233/BIR-1985-22205
13. Pazzaglia UE, Salisbury JR, Byers PD. Development and involution of the Notochord in the human spine. *J R Soc Med*. 1989;82(7):413-415. doi: 10.1177/014107688908200714
14. Tan Z, Chen P, Dong X, et al. Progenitor-like cells contributing to cellular heterogeneity in the nucleus pulposus are lost in intervertebral disc degeneration. *Cell Rep*. 2024;43(6):114342. doi: 10.1016/j.celrep.2024.114342
15. Risbud MV, Schoepflin ZR, Mwale F, et al. Defining the phenotype of young healthy nucleus pulposus cells: recommendations of the Spine Research Interest Group at the 2014 annual ORS meeting. *J Orthop Res*. 2015;33(3):283-293. doi: 10.1002/jor.22789
16. Mwale F, Roughley P, Antoniou J. Distinction between the extracellular matrix of the nucleus pulposus and hyaline cartilage: a requisite for tissue engineering of intervertebral disc. *Eur Cells A¨nd Mater*. 2004;8:58-64. doi: 10.22203/eCM.v008a06
17. Tomaszewski KA, Walocha JA, Mizia E, Gładysz T, Głowacki R, Tomaszewska R. Age- and degeneration-related variations in cell density and glycosaminoglycan content in the human cervical intervertebral disc and its endplates. *Pol J Pathol*. 2015;66(3):296-300. doi: 10.5114/pjp.2015.54964
18. Urban JPG, Roberts S, Ralphs JR. The nucleus of the intervertebral disc from development to degeneration. *Am Zool*. 2000;40(1):53-061. doi: 10.1093/icb/40.1.53
19. Marchand F, Ahmed AM. Investigation of the laminate structure of lumbar disc anulus fibrosus. *Spine*. 1990;15(5):402-410. doi: 10.1097/00007632-199005000-00011
20. Liang H, Luo R, Li G, Zhang W, Song Y, Yang C. The proteolysis of ECM in intervertebral disc degeneration. *Int J Mol Sci*. 2022;23(3):1715. doi: 10.3390/ijms23031715
21. Costi JJ, Stokes IA, Gardner-Morse M, Laible JP, Scoffone HM, Iatridis JC. Direct measurement of intervertebral disc maximum shear strain in six degrees of freedom: motions that place disc tissue at risk of injury. *J Biomech*. 2007;40(11):2457-2466. doi: 10.1016/j.jbiomech.2006.11.006
22. Guerin HAL, Elliott DM. Structure and properties of soft tissues in the spine. In: *Spine Technology Handbook*. Academic Press; 2006:35-62. doi: 10.1016/B978-012369390-7/50004-6
23. Torre OM, Mroz V, Bartelstein MK, Huang AH, Iatridis JC. Annulus fibrosus cell phenotypes in homeostasis and injury: implications for regenerative strategies. *Ann N Y Acad Sci*. 2019;1442(1):61-78. doi: 10.1111/nyas.13964
24. Liebscher T, Haefeli M, Wuertz K, Nerlich AG, Boos N. Age-related variation in cell density of human lumbar intervertebral disc. *Spine*. 2011;36(2):153-159. doi: 10.1097/brs.0b013e3181cd588c
25. Samanta A, Lufkin T, Kraus P. Intervertebral disc degeneration—current therapeutic options and challenges. *Front Public Health*. 2023;11:1156749.

doi: 10.3389/fpubh.2023.1156749

26. Casiano VE, Sarwan G, Dydyk AM, Varacallo M. Back pain. In: *StatPearls*. StatPearls Publishing; 2023. Accessed March 29, 2023. http://www.ncbi.nlm.nih.gov/books/NBK538173/

27. Hay SI, Abajobir AA, Abate KH, et al. Global, regional, and national disability-adjusted life-years (DALYs) for 333 diseases and injuries and healthy life expectancy (HALE) for 195 countries and territories, 1990–2016: a systematic analysis for the Global Burden of Disease Study 2016. *Lancet*. 2017;390(10100):1260-1344. doi: 10.1016/S0140-6736(17)32130-X

28. Meddeba M, Hatirab F, Habboubia K, Mestiria. Biomechanical Study of the Behavior of the Intervertebral Disc: Intact Lumbar Spine Versus Arthrodesis. *J Orthop Bone Disord*. 2024;8(2):1-4. doi: 10.23880/jobd-16000265

29. Sampara P, Banala RR, Vemuri SK, Av GR, Gpv S. Understanding the molecular biology of intervertebral disc degeneration and potential gene therapy strategies for regeneration: a review. *Gene Ther*. 2018;25(2):67-82. doi: 10.1038/s41434-018-0004-0

30. Tamagawa S, Schol J, Sakai D. Cell therapy for intervertebral disc regeneration: progress and hurdles in clinical translation. *Indian Spine J*. 2024;7(2):131-141. doi: 10.4103/isj.isj_17_24

31. Liu Y, Zhao Z, Guo C, et al. Application and development of hydrogel biomaterials for the treatment of intervertebral disc degeneration: a literature review. *Front Cell Dev Biol*. 2023;11:1286223. doi: 10.3389/fcell.2023.1286223

32. Doench I, Tran TA, David L, et al. Cellulose nanofiber-reinforced chitosan hydrogel composites for intervertebral disc tissue repair. *Biomimetics (Basel)*. 2019;4(1):19. doi: 10.3390/biomimetics4010019

33. Hingert D, Barreto Henriksson H, Baranto A, Brisby H. BMP-3 promotes matrix production in co-cultured stem cells and disc cells from low back pain patients. *Tissue Eng Part A*. 2020;26(1-2):47-56. doi: 10.1089/ten.tea.2019.0125

34. Tang SN, Salazar-Puerta AI, Heimann MK, et al. Engineered extracellular vesicle-based gene therapy for the treatment of discogenic back pain. *Biomaterials*. 2024;308:122562. doi: 10.1016/j.biomaterials.2024.122562

35. Barcellona MN, Ní Néill T, O'Brien FJ, Dixon JE, Curtin CM, Buckley CT. Modulation of inflammation and regeneration in the intervertebral disc using enhanced cell-penetrating peptides for MicroRNA delivery. *Adv NanoBiomed Res*. 2024;4(7):2300112. doi: 10.1002/anbr.202300112

36. Yuan B, Rudeen K, Li J, et al. Biodegradable microspheres and hydrogel drug delivery system of tumor necrosis factor (TNF) inhibitor and growth differentiation factor 5 (GDF5) reduces disk inflammation in the rabbit model. *Spine (Phila Pa 1976)*. 2023;48(15):E257-E265. doi: 10.1097/BRS.0000000000004686

37. Rivera Tapia ED, Meakin JR, Holsgrove TP. In-vitro models of disc degeneration – a review of methods and clinical relevance. *J Biomech*. 2022;142:111260. doi: 10.1016/j.jbiomech.2022.111260

38. Yung Lee J, Hall R, Pelinkovic D, et al. New use of a three-dimensional pellet culture system for human intervertebral disc cells: initial characterization and potential use for tissue engineering. *Spine* (Phila Pa 1976). 2001;26(21):2316-2322. doi: 10.1097/00007632-200111010-00005

39. Le Maitre CL, Freemont AJ, Hoyland JA. The role of interleukin-1 in the pathogenesis of human intervertebral disc degeneration. *Arthritis Res Ther*. 2005;7(4):R732. doi: 10.1186/ar1732

40. McDonnell EE, Buckley CT. Two- and three-dimensional in vitro nucleus pulposus cultures: an in silico analysis of local nutrient microenvironments. *JOR Spine*. 2022;5(3):e1222. doi: 10.1002/jsp2.1222

41. Zhang A, Cheng Z, Chen Y, Shi P, Gan W, Zhang Y. Emerging tissue engineering strategies for annulus fibrosus therapy. *Acta Biomater*. 2023;167:1-15. doi: 10.1016/j.actbio.2023.06.012

42. Liu Y, Peng L, Li L, et al. 3D-bioprinted BMSC-laden biomimetic multiphasic scaffolds for efficient repair of osteochondral defects in an osteoarthritic rat model. *Biomaterials*. 2021;279:121216. doi: 10.1016/j.biomaterials.2021.121216

43. Yuan D, Chen Z, Xiang X, et al. The establishment and biological assessment of a whole tissue-engineered intervertebral disc with PBST fibers and a chitosan hydrogel in vitro and in vivo. *J Biomed Mater Res B Appl Biomater*. 2019;107(7):2305-2316. doi: 10.1002/jbm.b.34323

44. Fusellier M, Clouet J, Gauthier O, Tryfonidou M, Le Visage C, Guicheux J. Degenerative lumbar disc disease: in vivo data support the rationale for the selection of appropriate animal models. *Eur Cell Mater*. 2020;39:17-48. doi: 10.22203/eCM.v039a02

45. Pourchet LJ, Thepot A, Albouy M, et al. Human skin 3D bioprinting using scaffold-free approach. *Adv Healthc Mater*. 2017;6(4):1601101. doi: 10.1002/adhm.201601101

46. Wang J, Cui Z, Maniruzzaman M. Bioprinting: a focus on improving bioink printability and cell performance based on different process parameters. *Int J Pharm*. 2023;640:123020. doi: 10.1016/j.ijpharm.2023.123020

47. Abedi K, Keshvari H, Solati-Hashjin M. Extrusion-based bioprinting: considerations toward gelatin-alginate bioink. *Rapid Prototyp J*. 2024;30(6):1094-1104. doi: 10.1108/RPJ-06-2023-0207

48. Seok JM, Ahn M, Kim D, et al. Decellularized matrix bioink with gelatin methacrylate for simultaneous improvements

in printability and biofunctionality. *Int J Biol Macromol*. 2024;262:130194.
doi: 10.1016/j.ijbiomac.2024.130194

49. Rajasekaran S, Soundararajan DCR, Nayagam SM, et al. Novel biomarkers of health and degeneration in human intervertebral discs: in-depth proteomic analysis of collagen framework of fetal, healthy, scoliotic, degenerate, and herniated discs. *Asian Spine J*. 2023;17(1):17-29.
doi: 10.31616/asj.2021.0535

50. Melrose J, Smith S, Ghosh P, Taylor TKF. Differential expression of proteoglycan epitopes and growth characteristics of intervertebral disc cells grown in alginate bead culture. *Cells Tissues Organs*. 2001;168(3):137-146.
doi: 10.1159/000047829

51. Thonar E, An H, Masuda K. Compartmentalization of the matrix formed by nucleus pulposus and annulus fibrosus cells in alginate gel. *Biochem Soc Trans*. 2002;30(6):874-878.
doi: 10.1042/bst0300874

52. Ouyang L, Yao R, Zhao Y, Sun W. Effect of bioink properties on printability and cell viability for 3D bioplotting of embryonic stem cells. *Biofabrication*. 2016;8(3):035020.
doi: 10.1088/1758-5090/8/3/035020

53. Habib MA, Khoda B. Rheological analysis of bio-ink for 3D bio-printing processes. *J Manuf Process*. 2022;76:708-718.
doi: 10.1016/j.jmapro.2022.02.048

54. Magalhães IP, Oliveira PMD, Dernowsek J, Casas EBL, Casas MSL. Investigation of the effect of nozzle design on rheological bioprinting properties using computational fluid dynamics. *Matéria (Rio J.)* 2019;24(3):e12401.
doi: 10.1590/s1517-707620190003.0714

55. Chand R, Muhire BS, Vijayavenkataraman S. Computational fluid dynamics assessment of the effect of bioprinting parameters in extrusion bioprinting. *Int J Bioprint*. 2022; 8(2):545.
doi: 10.18063/ijb.v8i2.545

56. Reitmaier S, Schmidt H. Review article on spine kinematics of quadrupeds and bipeds during walking. *J Biomech*. 2020;102:109631.
doi: 10.1016/j.jbiomech.2020.109631

57. Yoshizato H, Morimoto T, Nonaka T, et al. Animal model for anterior lumbar interbody fusion: a literature review. *Spine Surg Relat Res*. 2024;8(4):373-382.
doi: 10.22603/ssrr.2023-0262

58. Duan B, Hockaday LA, Kang KH, Butcher JT. 3D bioprinting of heterogeneous aortic valve conduits with alginate/gelatin hydrogels. *J Biomed Mater Res A*. 2013;101A(5):1255-1264.
doi: 10.1002/jbm.a.34420

59. Fedorovich NE, De Wijn JR, Verbout AJ, Alblas J, Dhert WJA. Three-dimensional fiber deposition of cell-laden, viable, patterned constructs for bone tissue printing. *Tissue Eng Part A*. 2008;14(1):127-133.
doi: 10.1089/ten.a.2007.0158

60. Wang X, Yan Y, Pan Y, et al. Generation of three-dimensional hepatocyte/gelatin structures with rapid prototyping system. *Tissue Eng*. 2006;12(1):83-90.
doi: 10.1089/ten.2006.12.83

61. Gironi P, Petraro L, Santoni S, Dedé L, Colosimo BM. A computational model of cell viability and proliferation of extrusion-based 3D-bioprinted constructs during tissue maturation process. *Int J Bioprinting*. 2023;9(4):741.
doi: 10.18063/ijb.741

62. Bruehlmann SB, Rattner JB, Matyas JR, Duncan NA. Regional variations in the cellular matrix of the annulus fibrosus of the intervertebral disc. *J Anat*. 2002;201(2):159-171.
doi: 10.1046/j.1469-7580.2002.00080.x.

63. Rastogi P, Kandasubramanian B. Review of alginate-based hydrogel bioprinting for application in tissue engineering. *Biofabrication*. 2019;11(4):042001.
doi: 10.1088/1758-5090/ab331e

64. Li QQ, Xu D, Dong QW, Song XJ, Chen YB, Cui YL. Biomedical potentials of alginate via physical, chemical, and biological modifications. *Int J Biol Macromol*. 2024; 277:134409.
doi: 10.1016/j.ijbiomac.2024.134409

65. Sandvig I, Karstensen K, Rokstad AM, et al. RGD-peptide modified alginate by a chemoenzymatic strategy for tissue engineering applications. *J Biomed Mater Res A*. 2015; 103(3):896-906.
doi: 10.1002/jbm.a.35230

66. Yang J, Yang X, Wang L, et al. Biomimetic nanofibers can construct effective tissue-engineered intervertebral discs for therapeutic implantation. *Nanoscale*. 2017;9(35):13095-13103.
doi: 10.1039/c7nr03944a

67. Zhou P, Chu G, Yuan Z, et al. Regulation of differentiation of annulus fibrosus-derived stem cells using heterogeneous electrospun fibrous scaffolds. *J Orthop Transl*. 2021;26: 171-180.
doi: 10.1016/j.jot.2020.02.003

68. Gluais M, Clouet J, Fusellier M, et al. In vitro and in vivo evaluation of an electrospun-aligned microfibrous implant for Annulus fibrosus repair. *Biomaterials*. 2019;205:81-93.
doi: 10.1016/j.biomaterials.2019.03.010

69. Mordechai HS, Aharonov A, Sharon SE, et al. Toward a mechanically biocompatible intervertebral disc: engineering of combined biomimetic annulus fibrosus and nucleus pulposus analogs. *J Biomed Mater Res A*. 2023;111(5):618-633.
doi: 10.1002/jbm.a.37519

70. Moxon SR, McMurran Z, Kibble MJ, Domingos M, Gough JE, Richardson SM. 3D bioprinting of an intervertebral disc tissue analogue with a highly aligned annulus fibrosus via suspended layer additive manufacture. *Biofabrication*. 2024;17(1):015005.
doi: 10.1088/1758-5090/ad8379

ACCSCIENCE PUBLISHING

International Journal of Bioprinting

RESEARCH ARTICLE

3D-printed biomimetic liposomal hydrogels for localized and targeted treatment of drug-resistant *Candida albicans* vaginitis

Lina Dong[1†], Wenyan Wang[2†], Bixing Fang[3†], Meixuan Liu[1], Miao Pan[1], Xiaoqi Li[1], Aobuliaximu Yakupu[1], Chunmao Han[1], Qiong Li[1]*, and Xingang Wang[1]*

[1]Department of Burns and Wound Care Center, The Second Affiliated Hospital, Zhejiang University School of Medicine, Hangzhou, Zhejiang, China

[2]School of Pharmaceutical Sciences (Shenzhen), Sun Yat-sen University, Shenzhen, Guangdong, China

[3]Department of Otolaryngology, The Second Affiliated Hospital, Zhejiang University School of Medicine, Hangzhou, Zhejiang, China

Abstract

The excessive use of antibiotics has precipitated the emergence of drug-resistant bacterial strains, underscoring the critical need for developing novel, targeted antimicrobial agents. Among the burgeoning class of nanomaterials, silver clusters have attracted considerable attention due to their broad-spectrum and enduring antimicrobial properties, coupled with the crucial advantage of not eliciting resistance. These features render them exceptionally promising in the landscape of antimicrobial therapy. Nevertheless, the constraints associated with the topical application of silver clusters and the adverse effects linked to high-dose shock therapy pose significant challenges that require resolution. To surmount these obstacles, we engineered a sophisticated nanodrug delivery system capable of specific bacterial recognition and synergistic interaction with antimicrobial agents to accomplish precise antibacterial efficacy. Through the interaction between bacterial recognition receptor proteins (TLR2 and TLR4) on macrophage membranes and pathogen-specific molecular patterns on bacteria, we observed that cultivating macrophages in the presence of specific bacteria markedly upregulated the expression of these receptors. We subsequently isolated these specialized membrane proteins, integrated them into liposomes, and loaded silver clusters to formulate composite biomimetic liposomes (Lip@MOMP$_2$@AgNCs). These liposomes can be effectively administered to sites of vaginal infection via intravenous injection, facilitating specific bacterial recognition, and precise targeting. Moreover, we devised a 3D-printed hydrogel mesh scaffold incorporating Lip@MOMP$_2$@AgNCs, which amalgamates the injectable liposomal formulation with the 3D-printed hydrogel scaffold to realize sustained and localized drug release. This investigation not only advances a specific and promising therapeutic strategy for combating drug-resistant *Candida albicans* vaginitis but also forges new pathways in addressing the formidable challenge of antibiotic resistance.

Keywords: 3D printing; Hydrogel; Liposomes; Silver nanoclusters; Vaginitis

†These authors contributed equally to this work

***Corresponding authors:**
Qiong Li
(liqiongzessk@zju.edu.cn)

Xingang Wang
(wangxingang8157@zju.edu.cn)

Citation: Dong L, Wang W, Fang B, et al. 3D-printed biomimetic liposomal hydrogels for localized and targeted treatment of drug-resistant *Candida albicans* vaginitis. *Int J Bioprint*. 2025;11(1):485-500. doi: 10.36922/ijb.5851

Received: November 11, 2024
Revised: December 23, 2024
Accepted: January 3, 2025
Published Online: January 3, 2025

Copyright: © 2025 Author(s). This is an Open Access article distributed under the terms of the Creative Commons Attribution License, permitting distribution, and reproduction in any medium, provided the original work is properly cited.

Publisher's Note: AccScience Publishing remains neutral with regard to jurisdictional claims in published maps and institutional affiliations.

1. Introduction

Vulvovaginal candidiasis (VVC) represents a pervasive and complex clinical condition, afflicting approximately 75% of women with at least one episode during their lifetime, with 50% experiencing recurrent infections.[1] A striking 80% of these cases are ascribed to the most pathogenic species of *Candida*, notably *Candida albicans*.[2] The prevailing treatment modalities, which encompass the application of 2–3% sodium bicarbonate solutions for vaginal irrigation or sitz baths, frequently yield suboptimal outcomes, extending the therapeutic process and occasionally culminating in disease recurrence.

As delineated by the Centers for Disease Control and Prevention (CDC) guidelines established in 1998, the prescribed oral medication for recurrent VVC is fluconazole, administered at a dosage of 150 mg weekly over 6 months.[3,4] Nonetheless, this therapeutic regimen not only necessitates a protracted duration to attain efficacy but also falters in the complete eradication of hyphae and spores. Furthermore, the protracted use of fluconazole may foster resistance development in *C. albicans*.[5] Recent investigations have unveiled that 14.6% of *C. albicans* strains manifest significantly diminished sensitivity to fluconazole.[6] Thus, there exists a pressing imperative to devise an effective antimicrobial agent with a reduced propensity for resistance to treat resistant *Candida vaginitis*.

In this milieu, silver nanoparticles (AgNPs) have garnered substantial interest due to their exceptional antibacterial attributes, demonstrating considerable promise for clinical applications.[7–9] However, the nanoscale dimensions of silver nanoparticles elicit concerns regarding cytotoxicity to normal tissue cells, thereby constraining their clinical utility.[10–12] Overcoming the limitations of silver nanoparticles and alleviating the deleterious effects of systemic accumulation within the body emerge as critical challenges.

To this end, we propose the development of an efficacious drug delivery system exhibiting outstanding biocompatibility. To mitigate the cytotoxic repercussions of silver nanoparticles on human tissues, we have opted for glutathione-modified silver nanoclusters (AgNCs) as our antimicrobial agents. These nanoclusters, characterized by their diminutive size,[13] enable effective renal clearance and manifest substantial activity against resistant strains while upholding commendable biocompatibility.[14] To further diminish direct contact between AgNCs and normal tissues and to prolong the duration of drug release *in vivo*, we encapsulated AgNCs within liposomes.

Moreover, inspired by the pioneering research of Wang et al.[15] on the precise treatment of bacterial infections, we adorned the liposomes with specific receptor proteins extracted from pretreated macrophage membranes. TLR2 and TLR4, located on bacterial membranes, play a pivotal role in recognizing bacterial membrane components,[16,17] thereby endowing the liposomes with the capability to specifically target bacteria.

To achieve sustained and localized drug delivery, we integrated injectable liposomal formulations with 3D-printed hydrogel scaffolds. Recent advances in 3D bioprinting technology have demonstrated its potential for the precise fabrication of hydrogel scaffolds with tailored structural and mechanical properties.[18–20] Various bioprinting techniques, including extrusion-based, jetting-based,[21] and vat photopolymerization-based methods,[22] have been developed for hydrogel deposition, each with unique advantages and limitations. Extrusion-based bioprinting, widely recognized for its compatibility with high-viscosity bioinks and ability to create complex structures,[23] was selected for this study due to its superior printability and ease of use in fabricating stable hydrogel scaffolds suitable for drug delivery applications. This approach ensures precise deposition and structural integrity while accommodating the rheological properties of the hydrogel precursors.

In conclusion, we have engineered a biomimetic liposome system constructed from a phospholipid bilayer, incorporating specific membrane proteins from macrophages to facilitate selective bacterial recognition, and loaded with AgNCs to achieve precise and effective treatment of resistant *C. albicans* infections. Furthermore, the incorporation of extrusion-based 3D bioprinting technology into our platform enhances the controlled release and localized delivery of the therapeutic agents (Scheme 1), offering a more effective treatment option for clinical application.

2. Materials and methods

2.1. Materials

Hyaluronic acid (HA; molecular weight 100–200 kDa) was acquired from Lifecore Biomedical (United States of America [USA]). Methacrylic anhydride (MA), Irgacure 2959, Carbomer 940, and phospholipids (i.e., dipalmitoylphosphatidylcholine [DPPC], distearoylphosphatidylcholine [DSPC], and dioleoylphosphatidylcholine [DOPC]), were procured from Sigma–Aldrich (USA). Cholesterol and estradiol benzoate were sourced from Macklin (China). Monoclonal antibodies, that is, CD282 (TLR2), CD284 (TLR4), and

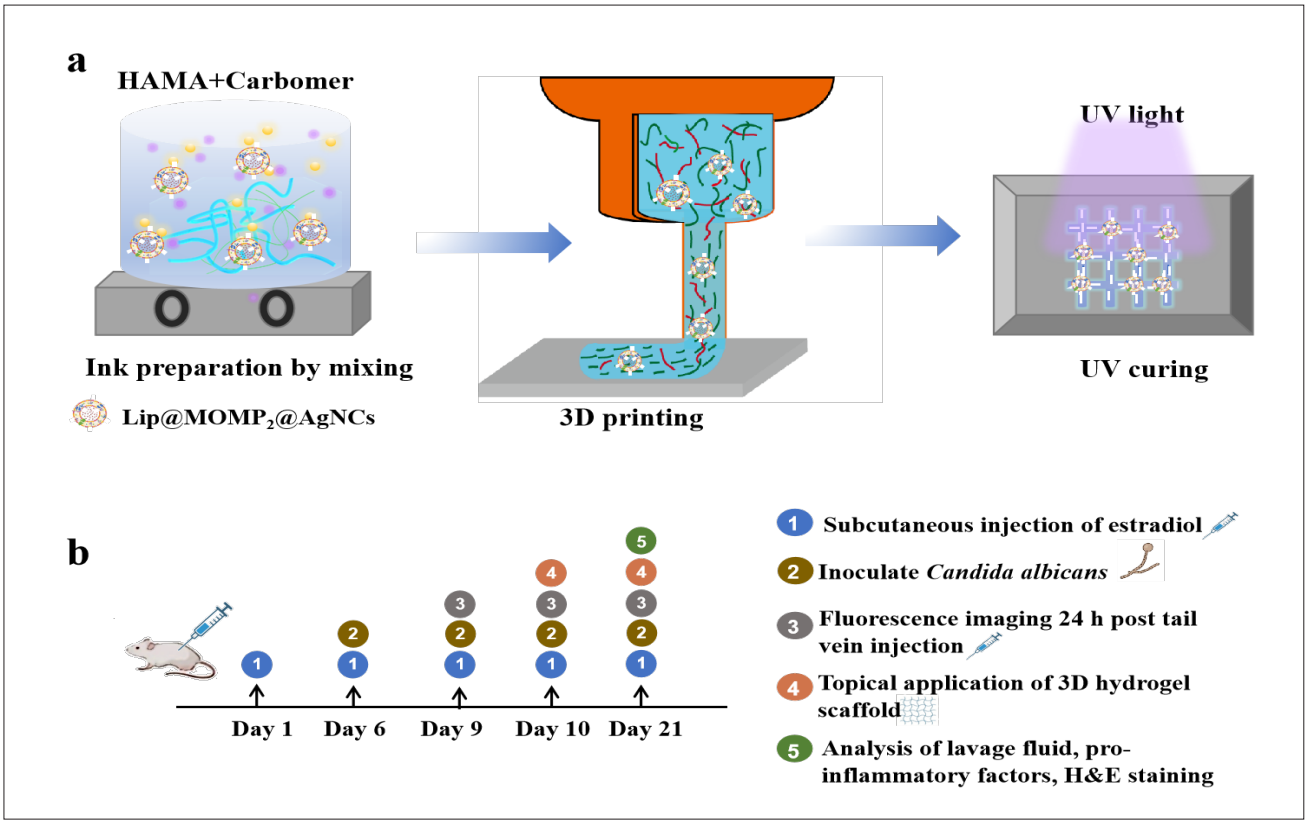

Scheme 1. Preparation and application of Lip@MOMP$_2$@AgNCs hydrogel *in vivo study.* (a) Lip@MOMP$_2$@AgNCs hydrogel printing process. (b) Animal study process, illustrating the administration of the hydrogel formulation *in vivo* in a mouse model. Abbreviations: HAMA, hyaluronic acid; H&E, Hematoxylin and Eosin Staining; UV, ultraviolet.

CD45, were obtained from Thermo Fisher Scientific (USA). Fourier transform infrared spectroscopy (FT-IR, Nicolet iS50, USA) was employed to analyze the lyophilized hydrogel samples within the spectral range of 4000–400 cm^{-1}. The AgNCs particle size distribution of the samples was measured using a Zetasizer Nano-ZS, which can detect sizes from 0.3 to 10,000 nm.

2.2. Preparation of AgNCs

In accordance with the methodology[14] previously delineated by our research group, aqueous solutions of $AgNO_3$ (1.25 mL, 20 mM) and glutathione (GSH; 1.5 mL, 50 mM) were initially amalgamated in 50 mL of distilled water. Under vigorous agitation, 0.5 mL of a $NaBH_4$ (112 mM) solution was introduced to the mixture. Within 5 min, a wine-red solution materialized, which was subsequently allowed to incubate at ambient temperature for 3 h, transitioning to a colorless state. Thereafter, an additional 0.5 mL of the $NaBH_4$ solution was incrementally added, followed by intensive stirring for 30 min and an aging period of 6 h, culminating in the formation of a red AgNCs solution. The synthesized AgNCs were then subjected to purification via ultrafiltration (3000 Da) and stored at 4 °C for subsequent utilization.

2.3. Extraction of macrophage membrane proteins MOMP$_1$ and MOMP$_2$

Macrophage membrane proteins were meticulously extracted using a membrane protein extraction kit from untreated J774.A1 cells, resulting in the isolation of MOMP$_1$ post-purification. In parallel, MOMP$_2$ was obtained from the membrane proteins of J774.A1 cells that had been exposed to *C. albicans*. The concentrations of these proteins were quantitatively measured using a BCA protein assay kit. Subsequently, equivalent amounts of both membrane proteins were subjected to Western blot analysis to evaluate the expression levels of TLR2, TLR4, and CD45.

2.4. Synthesis of Lip@MOMP$_2$

Lip@MOMP$_2$ was synthesized through the thin-film dispersion technique. A concoction of DPPC, DSPC, DOPC, and cholesterol was dissolved in a chloroform–methanol solution (3:1 v/v) at a precise molar ratio of

5:1:3:1. The solvent was meticulously removed using a rotary evaporator, thus creating a thin lipid film. $MOMP_2$, with a membrane protein to lipid weight ratio of 1:300, was subsequently dispersed in phosphate-buffered saline (PBS). This mixture was subjected to three cycles of vigorous vortexing at 45 °C, each lasting 3 min, to ensure proper hydration of the lipid film. The resultant Lip@$MOMP_2$ suspension was then extruded 10 times through a cellulose acetate membrane with a 200 nm pore size at 45 °C to obtain unilamellar vesicles. Finally, these vesicles were dialyzed overnight using a 1000 kDa membrane to effectively remove any residual solvents and unbound $MOMP_2$.

2.5. Assembly of Lip@$MOMP_2$@AgNCs

Lip@$MOMP_2$, AgNCs (50 μg/mL), and 2% $NaHCO_3$ were mixed in a ratio of 2:1:2 and incubated at 45 °C for 30 min. The mixture was then dialyzed for 3 h using a 1000 kDa membrane to obtain Lip@$MOMP_2$@AgNCs.

2.6. Release kinetics of Lip@$MOMP_2$@AgNCs

Drug release experiments were meticulously conducted using 200 mL of PBS (pH 4.2) and vaginal simulation fluid (pH 6.8) as the release media, both maintained at a constant temperature of 37 °C with continuous agitation at 60 rpm. The release of the encapsulated Lip@$MOMP_2$@AgNCs was monitored over a defined temporal course. At predetermined intervals—specifically 10, 20, 30, 60 min, 1, 1.5, 2, 3, 4, 5, 6, 9, 12, 18, and 24 h—1 mL aliquots of the release medium were carefully withdrawn and immediately replenished with an equivalent volume of fresh medium to maintain equilibrium. The ultraviolet (UV) absorbance of the aliquots was measured, facilitating the calculation of drug concentration via a standard curve.

2.7. Synthesis of the Lip@$MOMP_2$@AgNCs hydrogel

Hyaluronic acid methacrylate (HAMA) was synthesized in accordance with a previously established protocol.[24] Following this, 2% carbopol was incorporated into the HAMA solution in varying mass ratios of HAMA to Carbopol, specifically 1:2, 3:2, and 5:2, yielding distinct hydrogel precursors. To these mixtures, Lip@$MOMP_2$@AgNCs were introduced at varying concentrations—250, 500, 750, and 1000 μg/mL—and were meticulously dispersed throughout the HAMA-carbopol solutions. This process resulted in the formation of the Lip@$MOMP_2$@AgNCs hydrogel precursor.

2.8. 3D printing of the Lip@$MOMP_2$@AgNCs hydrogel

The Lip@$MOMP_2$@AgNCs hydrogel precursors were loaded into a 5 mL syringe, and the printing model was designed using Biomaker software. The hydrogels were then 3D-printed using a SunP CPD1/Biomaker printer with I2959 as the photoinitiator. Post-printing, the entire structure was cured under 10 mW/cm² UV light at 365 nm for 5 min to ensure structural integrity. The printing parameters included a speed of 10 mm/s, an extrusion rate of 0.9 mm^3/s, and a 25 G needle.

2.9. Antimicrobial evaluation of the Lip@$MOMP_2$@AgNCs hydrogel

The Lip@$MOMP_2$@AgNCs were co-cultured with a concentration of 10^5 CFU/mL of *Escherichia coli* and *C. albicans* for 6 h. Following the co-cultivation period, the microbial cells underwent a washing process with PBS twice and were subsequently immersed in a 2.5% glutaraldehyde solution at 4 °C for 2 h to ensure proper fixation. Post-fixation, the samples were subjected to centrifugation at 3000 rpm for 10 min, followed by two additional washes with PBS. The cells then underwent a dehydration protocol, utilizing a graded series of ethanol solutions—30%, 50%, 70%, and 90%—and culminating in absolute ethanol. After centrifugation to remove the supernatant, the samples were transferred into a mixture of ethanol and tert-butanol in a 1:1 ratio, with subsequent removal of the supernatant. The exchange was completed with two washes using pure tert-butanol. Finally, a 10 μL aliquot of the homogenized bacterial-tert-butanol suspension was carefully deposited onto a silicon wafer and vacuum-dried overnight. After sputter-coating with gold, the samples were subjected to scanning electron microscopy (SEM) analysis.[25]

2.10. *In vitro* antimicrobial testing

In vitro antimicrobial assays were performed against the clinically relevant pathogenic bacteria, *C. albicans* and *E. coli*.[26] The antimicrobial activity of the samples was evaluated by calculating the inhibition rate. Briefly, the aforementioned bacteria were co-cultured at a concentration of 10^7 CFU/mL with various concentrations of AgNCs and Lip@$MOMP_2$@AgNCs in a shaking incubator set at 37 °C and 150 rpm for 6 h. The resulting bacterial suspension was diluted 10^5 times with PBS and evenly spread on Luria–Bertani (LB) agar plates. A blank agar plate was used as a control under the same conditions. After incubation at 37 °C for 12 h, the plates were photographed, and the number of colonies was counted.

2.11. Assessment of cytotoxicity via live/dead cell staining

L929 and HSF cells, at a concentration of 5×10^4 cells/mL, were carefully seeded into 12-well plates and incubated for 24 h at 37 °C under a humidified atmosphere containing 5% CO_2. Subsequently, each well was supplemented with 1 mL of culture medium, which included varying concentrations of AgNCs and composite liposomes, and the plates were returned to the incubator for an additional 24-h period. Following this incubation, 500 μL of a live/

dead cell staining solution was introduced into each well, followed by further incubation for 15 min. The viability of the cells was then meticulously evaluated using an inverted fluorescence microscope, providing insights into the cytotoxic effects of the treatments.

2.12. Hemolysis assay

Initially, 3 mL of human blood was collected and subjected to washing with physiological saline by means of centrifugation at 1500 rpm. The obtained red blood cells were subsequently diluted in physiological saline to prepare a 2% red blood cell suspension. Thereafter, 100 μL of this suspension was combined with 1 mL of varying concentrations of Lip@$MOMP_2$@AgNCs solution. For the negative control group, 100 μL of the red blood cell suspension was mixed with 1 mL of physiological saline, while the positive control group consisted of 100 μL of the suspension added to 1 mL of deionized water. These samples were incubated in a water bath at 37°C for 1 h, followed by centrifugation at 3000 rpm for 15 min. Subsequently, 100 μL of the supernatant was carefully transferred to a 96-well plate, and the optical density (OD) at 540 nm was determined using a microplate reader. The hemolysis rate was then calculated following a specific formula[27,28]:

$$\text{Hemolysis rate}\,(\%) = \frac{OD_{positive} - OD_{negative}}{OD_{sample} - OD_{negative}} \times 100\% \quad (I)$$

2.13. Cell seeding on hydrogel scaffolds

The Lip@$MOMP_2$@AgNCs hydrogel scaffolds were initially submerged in a culture medium and stored at 4 °C overnight to ensure thorough saturation. L929 cells were cultured in RPMI-1640 medium, enriched with 10% fetal bovine serum (FBS), at 37 °C in a 5% CO_2 environment to maintain optimal growth conditions. A cell suspension, containing L929 cells at a concentration of 5×10^6 cells/mL, was meticulously seeded onto the prepared scaffolds. To support cell viability and proliferation, the culture medium was refreshed every two days.

2.14. Study of vaginitis treatment in mice

Seven-week-old female BALB/c mice (20–21 g) were allocated into six distinct groups and allowed a 1-week acclimation period prior to commencing the experiment. The mice were administered subcutaneous injections of estradiol benzoate oil (0.05 mL; 0.2 mg/0.1 mL) on alternate days, totaling three doses. On the sixth day, each mouse was intravaginally inoculated with 5×10^4 spores of *C. albicans* for 3 consecutive days to establish infection. Following this, sterilized samples (physiological saline, Lip@AgNCs, Lip@$MOMP_1$@AgNCs, Lip@$MOMP_2$@AgNCs, and fluconazole) were administered via tail vein injection (100 μL each), and fluorescence imaging was conducted 24 h post-injection to evaluate the biodistribution of Lip@AgNCs and Lip@MOMP@AgNCs across various organs. These injections were repeated at 2-day intervals, for a total of three administrations. In addition, hydrogels containing Lip@AgNCs, Lip@$MOMP_1$@AgNCs, and Lip@$MOMP_2$@AgNCs were applied topically to the vulvar region. A cohort of uninfected mice served as the blank control group ($n = 5$).

Vaginal lavage samples were collected on days 1, 7, 9, 11, 13, 15, 17, 19, and 21. The lavage fluids underwent vortex mixing for 3 min, followed by serial dilution at a 1:1000 ratio. These diluted samples were subsequently plated on agar for further analysis. After a 12-h incubation period, photographs were captured, and colony counts were meticulously conducted to assess fungal growth.

2.15. Statistical analysis

All data were expressed as at least three independent experiments. All the data were analyzed using one-way analysis of variance (ANOVA). Significant differences are indicated at $^*p < 0.05$, $^{**}p < 0.01$, and $^{***}p < 0.001$.

3. Results and discussion

3.1. Preparation and characterization of Lip@$MOMP_2$@AgNCs

In recent years, the escalating prevalence of antibiotic-resistant pathogens has posed profound challenges to public health, necessitating the invention of innovative therapeutic strategies. In response to this medical exigency, we initiated the present study, focusing on the extraction and purification of membrane proteins from J774.A1 macrophage cells, to enhance targeted antibacterial interventions. Specifically, a membrane protein extraction kit was employed to isolate $MOMP_1$ from untreated J774.A1 cells, while $MOMP_2$ was obtained from J774.A1 cells exposed to *C. albicans*. By extracting key receptor proteins, chiefly TLR2 and TLR4, from the membranes of the *Candida*-treated macrophages, we engineered biomimetic vesicles adorned with these proteins (Lip@$MOMP_2$), endowing them with the capability for specific bacterial recognition (Figure 1a). Furthermore, these vesicles were seamlessly integrated with minuscule AgNCs, culminating in Lip@$MOMP_2$@AgNCs (Figure 1b). This avant-garde approach aims to achieve precise targeting and effective treatment of diseases associated with drug-resistant *Candida* species.

SEM images revealed that conventional liposomes (Lip) possess a smooth surface with an average diameter of approximately 151 nm (Figure 1c). In stark contrast, the biomimetic liposomes (Lip@$MOMP_2$) displayed distinct

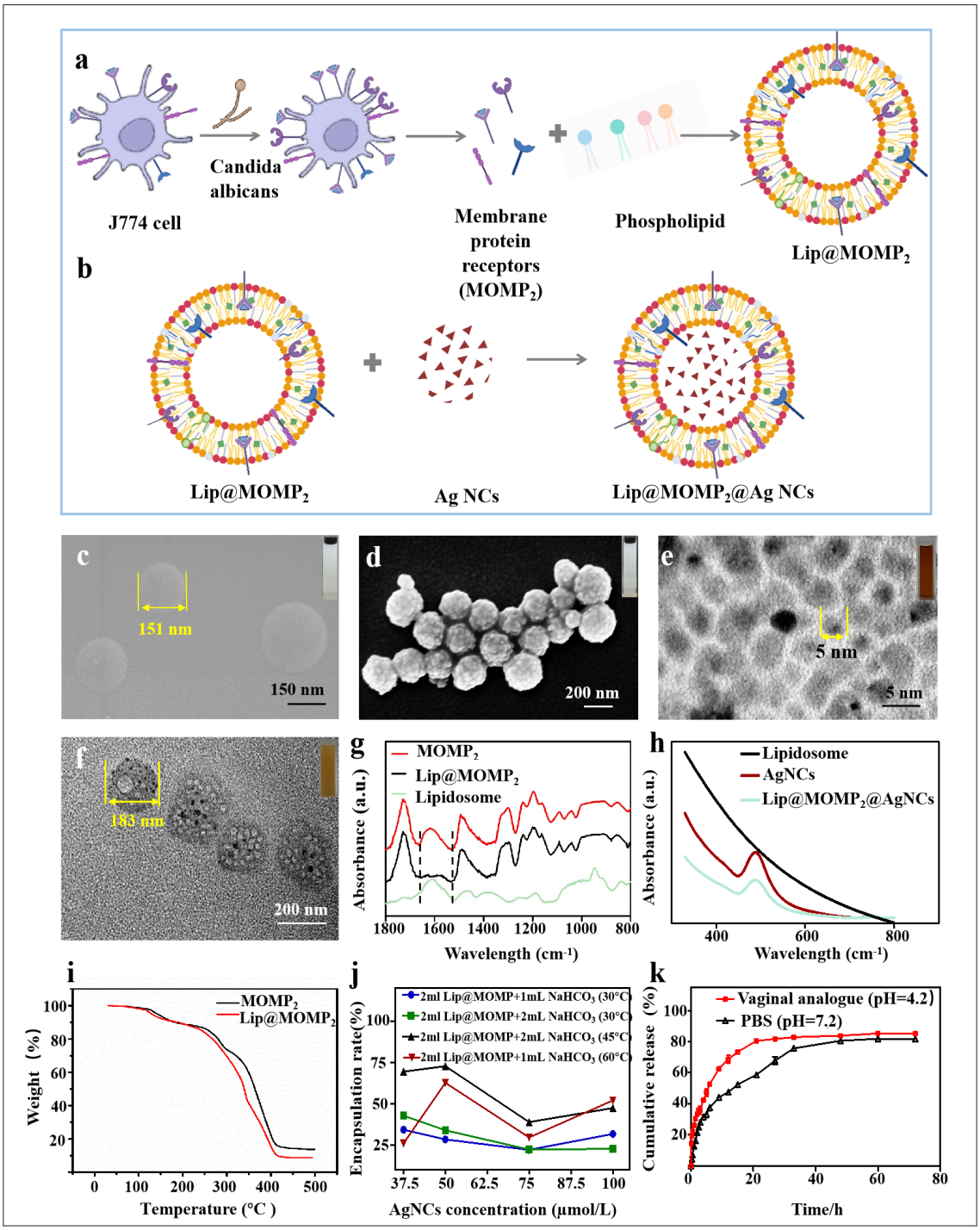

Figure 1. Images of Lip@$MOMP_2$@AgNCs solution. (a) Schematic representation of the synthesis of biomimetic liposomes (Lip@$MOMP_2$). (b) Schematic representation of the synthesis of Lip@$MOMP_2$@AgNCs. (c–e) Scanning electron microscopy (SEM) images of conventional liposomes (Lip; c), biomimetic liposomes (Lip@$MOMP_2$; d), and AgNCs (e). The solutions of Lip, Lip@MOMP2, and AgNCs. (c–e, inset). (f) Transmission electron microscopy (TEM) image of Lip@$MOMP_2$@AgNCs. The solutions of Lip@MOMP2@AgNCs. (f, inset). (g) Fourier-transform infrared spectroscopy (FTIR) spectra of Lip@$MOMP_2$ (red), Lip (black), and $MOMP_2$ (green). The amide region peaks (dashed lines) represent the characteristic absorption region of peptide bonds in proteins. (h) Ultraviolet (UV) spectra of Lip@$MOMP_2$ (black), AgNCs (red), and Lip@$MOMP_2$@AgNCs (green). (i) Thermogravimetric analysis (TGA). (j) Encapsulation efficiency of Lip@$MOMP_2$@AgNCs under varying concentrations of AgNCs, different temperatures, and different amounts of $NaHCO_3$. (k) Cumulative release profiles of Lip@$MOMP_2$@AgNCs in vaginal simulated fluid (pH = 4.2) and phosphate-buffered saline (PBS; pH = 7.2) (n = 3). Scale bars: 150 nm (c); 200 nm (d and f); 5 nm (e). Abbreviation: AgNCs, silver nanoclusters.

surface protrusions (Figure 1d), which we preliminarily identified as the specific receptor proteins ($MOMP_2$) derived from J774.A1 macrophage cell membranes. Dynamic light scattering (DLS) analysis indicated that Lip@$MOMP_2$ predominantly exhibited particle sizes ranging from 100 to 200 nm (Figure S1b, Supporting Information), with a zeta potential of -20.17 mV. According to pertinent studies, negatively charged nanoliposomes within the 100–200 nm size bracket, when delivered via tail vein injection in mice, have around 60% of the injected dose circulating in the bloodstream. This attribute diminishes hepatic accumulation and enhances clearance, thereby significantly mitigating the biotoxicity of Lip@$MOMP_2$. Additionally, the average size of AgNCs was approximately 5 nm (Figures 1e and S1, Supporting Information). Nanoparticles smaller than 6 nm are readily excreted via the renal pathway,[29,30] rendering the synthesized AgNCs a safe antimicrobial candidate for clinical applications. The zeta potential of AgNCs was measured at 3.1 mV (Figure S1, Supporting Information), which facilitates their interaction with the negatively charged Lip@$MOMP_2$. Transmission electron microscopy (TEM) and elemental distribution images of Lip@$MOMP_2$@AgNCs (Figures 1f and S2, Supporting Information) reveal the presence of black dots, confirming the successful encapsulation of AgNCs within Lip@$MOMP_2$.

To further substantiate the successful assembly of Lip and $MOMP_2$, Fourier-transform infrared spectroscopy (FTIR) was employed to analyze Lip, $MOMP_2$, and Lip@$MOMP_2$ (Figure 1g). The amide I (1600–1690 cm^{-1}) and amide II (1480–1575 cm^{-1}) regions correspond to the C=O stretching and N–H bonding of $MOMP_2$, respectively. Notably, distinctive absorption peaks in the amide region were observed in the $MOMP_2$ and Lip@$MOMP_2$ samples, while no such peaks were detected in the Lip group, indicating the successful synthesis of Lip@$MOMP_2$. UV spectroscopy analysis was employed to validate the encapsulation of AgNCs within Lip@$MOMP_2$ (Figure 1h). The results revealed characteristic absorption peaks at 485 nm for both AgNCs and Lip@$MOMP_2$@AgNCs, whereas no absorption peak was present for Lip@$MOMP_2$ at this wavelength, confirming the successful loading of AgNCs into Lip@$MOMP_2$. In summary, Lip@$MOMP_2$@AgNCs have been successfully prepared, and Lip@$MOMP_2$ exhibits favorable thermal stability (Figure 1i).

To refine the encapsulation strategy for Lip@$MOMP_2$, we meticulously explored various parameters, including drug loading temperature, AgNCs concentration, and the amount of 5% $NaHCO_3$. Based on the phase transition temperature of Lip@$MOMP_2$, we established experimental conditions at 30, 45, and 60 °C. Ultimately, it was discerned that at 45 °C, with an AgNCs concentration of 50 μg/mL, in conjunction with 2 mL of biomimetic lipid vesicles and 2 mL of $NaHCO_3$, the encapsulation efficiency attained a pinnacle of 72.76% (Figure 1j). Consequently, the maximal drug loading capacity of Lip@$MOMP_2$@AgNCs was computed to be 11.9%. The drug release profile of Lip@$MOMP_2$@AgNCs is illustrated in Figure 1k. In the vaginal simulation medium, the cumulative release of AgNCs reached 78.4% after 24 h, whereas in PBS at pH 7.2, the cumulative release was 58.2%. After 36 h, the release rates of AgNCs in both media began to stabilize. Overall, Lip@$MOMP_2$@AgNCs exhibited a more rapid release rate of AgNCs in the vaginal simulation medium compared to PBS at pH 7.2, with the release profiles also indicating the sustained-release characteristics of Lip@$MOMP_2$@AgNCs.

3.2. Printability of the Lip@$MOMP_2$@AgNCs hydrogel

In clinical practice, the management of vulvovaginal candidiasis encompasses an initial focus on targeting inflammation at the affected sites, eradicating *C. albicans*, and ensuring optimal ventilation while managing secretions as pivotal elements of supportive therapy. We have equipped Lip@$MOMP_2$@AgNCs with both targeted bacterial recognition capabilities and anti-inflammatory properties. To augment therapeutic efficacy, we engineered a 3D-printed hydrogel scaffold embedded with Lip@$MOMP_2$@AgNCs for localized application in the vulvar region. Through a synergistic approach combining injection and topical application, Lip@$MOMP_2$@AgNCs can precisely identify inflamed sites within the bloodstream. The mesh-like hydrogel scaffold not only conforms intimately to the vulvar anatomical structure, permitting adequate air circulation and facilitating secretion expulsion but also enables the *in situ* release of Lip@$MOMP_2$@AgNCs. Consequently, the integration of injection and topical application of Lip@$MOMP_2$@AgNCs achieves a synergistic enhancement of antimicrobial efficacy.

To facilitate *in situ* release of Lip@$MOMP_2$@AgNCs for antibacterial and anti-inflammatory effects, Lip@$MOMP_2$@AgNCs hydrogels were prepared at varied concentration ratios of HAMA:carbopol (1:2, 3:2, and 5:2). SEM images disclosed the internal porous architectures of these hydrogels, with the 1:2 and 3:2 ratios displaying well-defined network structures (Figure 2a–c). Additionally, the precursor hydrogels of Lip@$MOMP_2$@AgNCs exhibited shear-thinning behavior at elevated shear rates, as demonstrated by the viscosity–shear rate curves. This property underscores their suitability for 3D printing applications under similar shear conditions. The Lip@$MOMP_2$@AgNCs hydrogel exhibits elastic properties, as evidenced by the temporal evolution of the storage modulus

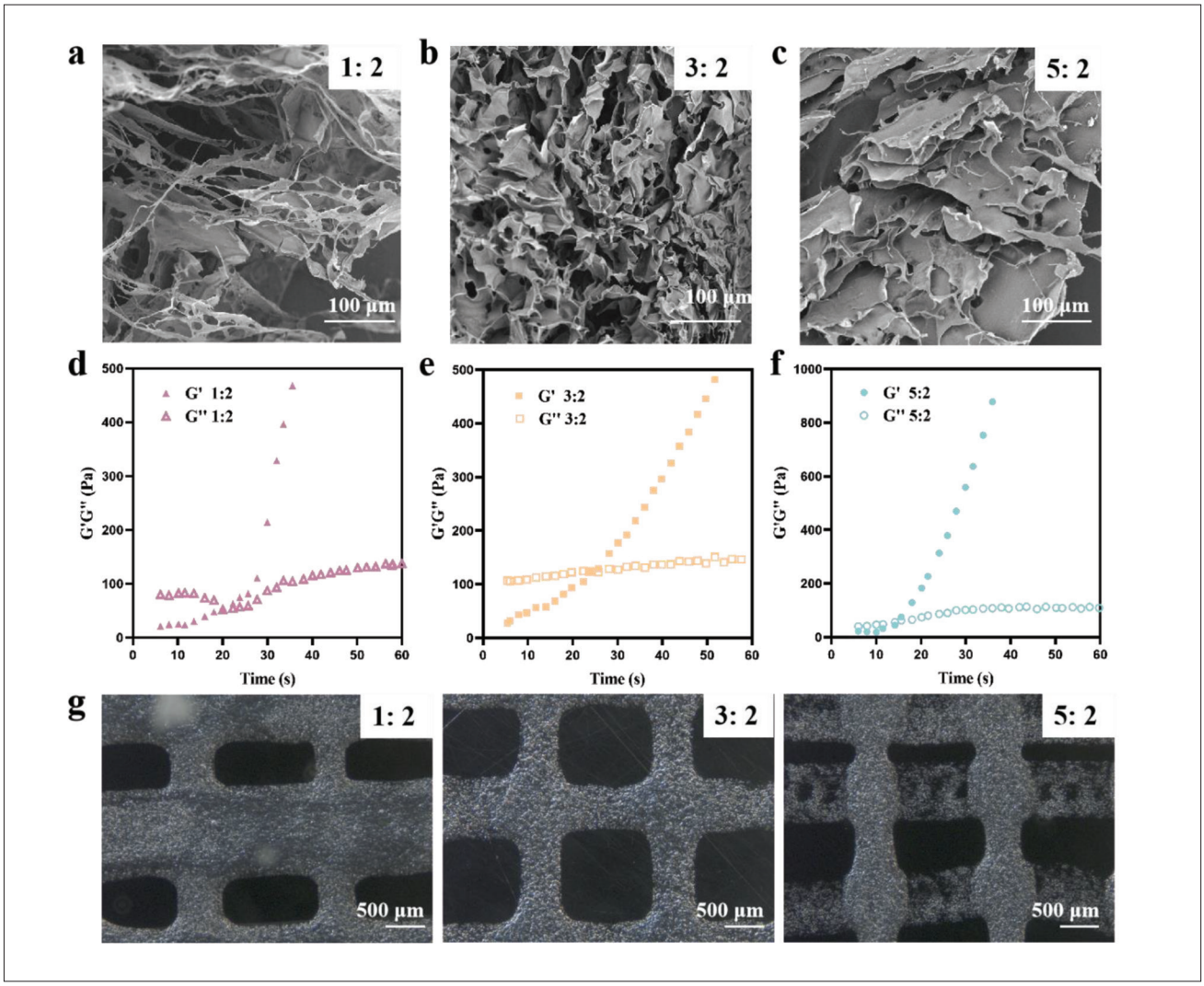

Figure 2. Preparation and characterization of Lip@MOMP$_2$@AgNCs hydrogel. (a–c) Scanning electron microscopy (SEM) images of the cross-section of Lip@MOMP$_2$@AgNCs hydrogel at different ratios of HAMA:Carbopol: 1:2 (a), 3:2 (b), and 5:2 (c). (d–f) Temporal evolution of the storage modulus (*G'*) and loss modulus (*G"*) of hydrogel precursors at different ratios of HAMA:carbopol during ultraviolet (UV) irradiation: 1:2 (d), 3:2 (e), and 5:2 (f). (g) The 3D printing structure of Lip@MOMP$_2$@AgNCs hydrogel at different ratios of HAMA:Carbopol: 1:2, 3:2, and 5:2. Scale bars: 100 μm (a–c); 500 μm (g). Abbreviations: AgNCs, silver nanoclusters; HAMA, hyaluronic acid methacrylate.

(*G'*) and loss modulus (*G"*). As displayed in Figure 2d–f, the storage modulus (*G'*) increases over time and surpasses the loss modulus (*G"*), indicating the transition of the hydrogel into a solid-like state. Moreover, the yield stress results further corroborate the mechanical performance of the hydrogel. The yield stress values for hydrogels with different component ratios (1:2, 3:2, and 5:2) were determined, with calculated values of approximately 71.45, 150.4, and 607.1 Pa, respectively (Figure S3, Supporting Information). These findings demonstrate that the hydrogel's mechanical properties, including elasticity and yield stress, are well-suited to ensuring structural integrity during the 3D printing process. In addition, Figure S4, Supporting Information, demonstrates the swelling and degradation behavior of hydrogels with different ratios of Lip@MOMP$_2$@AgNCs. To evaluate the printability of hydrogels with varying ratios, different formulations were tested. It was determined that the 3:2 ratio of Lip@MOMP$_2$@AgNCs hydrogels yielded the most stable grid structure with the most uniform lines. Consequently, this concentration ratio was selected for subsequent experiments (Figure 2g).

3.3. Biosafety of the Lip@MOMP$_2$@AgNCs hydrogel

To evaluate the biocompatibility of the Lip@MOMP$_2$@AgNCs hydrogel, we conducted co-culture experiments with varying concentrations of AgNCs and Lip@MOMP$_2$@AgNCs in L-929 cells and human umbilical vein endothelial

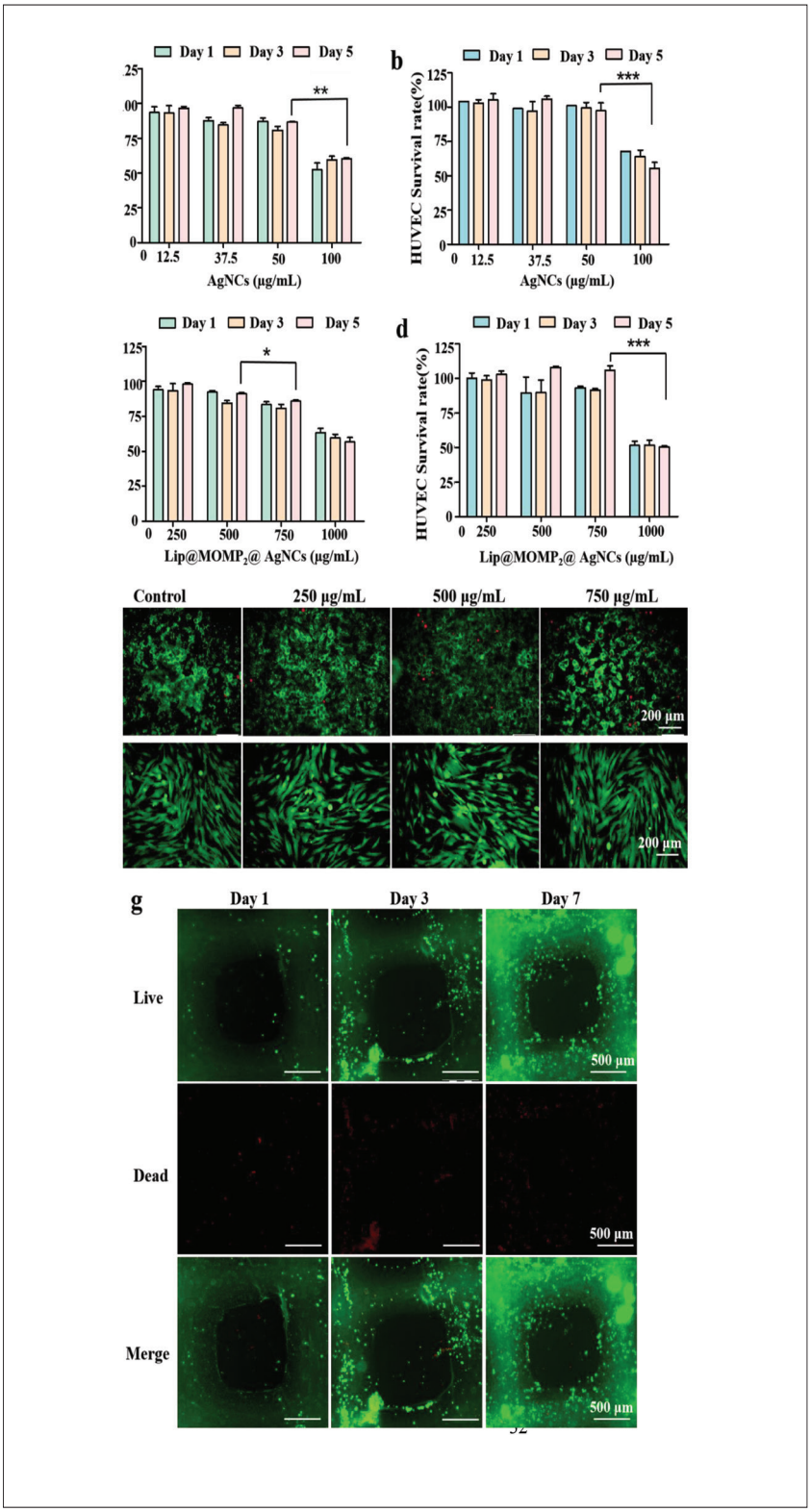

Figure 3. The biocompatibility of the Lip@MOMP$_2$@AgNCs hydrogel. (a–d) Cytotoxicity of different concentrations of AgNCs and Lip@MOMP$_2$@AgNCs hydrogel on L-929 cells (a and c) and human umbilical vein endothelial cells (HUVECs; b and d). *$p < 0.05$; **$p < 0.01$; ***$p < 0.001$. (e and f) Live/dead staining images of L-929 cells (e) and human skin fibroblasts (HSF; f) co-cultured with different concentrations of Lip@MOMP$_2$@AgNCs hydrogel. (g) L-929 cells cultured on Lip@MOMP$_2$@AgNCs hydrogel scaffolds. Scale bars: 200 μm (e and f); 500 μm (g). Abbreviation: AgNCs, silver nanoclusters.

cells (HUVECs) over 1, 3, and 5-day periods. The findings revealed that at concentrations up to 50 μg/mL, cell viability for both L-929 and HUVECs exceeded 85% by day 5 (Figure 3a and b). At a concentration of 750 μg/mL, the viability of L-929 and HUVECs on day 5 was 71.6% and 74.7%, respectively. However, at 500 μg/mL, both cell types exhibited viabilities exceeding 90% (Figure 3c and d). Further corroborating the biocompatibility of the Lip@MOMP$_2$@AgNCs hydrogel, live/dead staining assays conducted on L-929 and human skin fibroblasts (HSFs) aligned with the observed cell viability results (Figure 3e and f). Additionally, L-929 cells cultured on 3D-printed Lip@MOMP$_2$@AgNCs hydrogel scaffolds exhibited robust viability at days 1, 3, and 7, suggesting that the scaffold is conducive to cell growth and demonstrates excellent biocompatibility (Figure 3g).

To further ascertain the safety profile of Lip@MOMP$_2$@AgNCs, hemolysis assays were performed using a 2% red blood cell suspension across various formulations, including AgNPs, AgNCs, Lip@AgNCs, Lip@MOMP$_1$@AgNCs, and Lip@MOMP$_2$@AgNCs. The hemolysis rate for AgNPs was determined to be 12.4%, whereas AgNCs, Lip@AgNCs, and Lip@MOMP$_1$@AgNCs exhibited hemolysis rates below 5%. Notably, the hemolysis rate for Lip@MOMP$_2$@AgNCs was measured at 2.8%, which remains below the 5% threshold, indicating excellent blood compatibility (Figure S5, Supporting Information).

3.4. Antibacterial properties of the Lip@MOMP$_2$@AgNCs hydrogel

Upon confirming the biocompatibility of the AgNCs and Lip@MOMP$_2$@AgNCs hydrogel system, we advanced our investigation to examine its *in vitro* antibacterial efficacy against *E. coli* and drug-resistant *C. albicans*. To elucidate the underlying mechanism, SEM was employed to observe morphological alterations in the microorganisms post-treatment with varying concentrations of Lip@MOMP$_2$@AgNCs hydrogel solutions.

The SEM analysis revealed that both *E. coli* and drug-resistant *C. albicans* experienced notable wrinkling and compromised membrane integrity when exposed to 250 μg/mL Lip@MOMP$_2$@AgNCs hydrogel (Figure 4a and b). At elevated concentrations (500 and 750 μg/mL), complete disruption of the bacterial membranes was observed, leading to cellular shrinkage. Plate count methodology further demonstrated that AgNCs at a concentration of 37.5 μg/mL possessed considerable antibacterial effects against both organisms, with concentrations exceeding 50 μg/mL achieving antibacterial rates surpassing 95% (Figure 4c and d). Remarkably, the antibacterial effect was particularly pronounced at a Lip@MOMP$_2$@AgNCs hydrogel concentration of 500 μg/mL (Figure 4e and f). Given the differential cytotoxicity between the 500 and 750 μg/mL hydrogel concentrations, we ultimately identified 500 μg/mL as the optimal therapeutic concentration for Lip@MOMP$_2$@AgNCs hydrogel.

In exploring the impact of bacteria on immune responses, the pivotal role of Toll-like receptors (TLRs)—pattern recognition receptors located on cell membranes that are integral to the immune system—must be considered. The recognition of microbial pathogens by these receptors is essential for initiating the host's immune response to extracellular pathogens.[31–33] Among the various pattern recognition receptors (PRRs), TLRs were the first to be identified and remain the most extensively studied, known for recognizing a broad spectrum of pathogen-associated molecular patterns (PAMPs).[34] TLR2 and TLR4 stand out as significant receptors, primarily recognizing distinct pathogen components; TLR2 interacts with bacterial peptidoglycan, while TLR4 focuses on bacterial lipopolysaccharides.

In our study, the targeting capability of Lip@MOMP$_2$@AgNCs liposomes was enhanced by incorporating specific receptor proteins, primarily TLR2 and TLR4, extracted from pre-treated macrophage membranes. These receptors are crucial for recognizing bacterial components,[35,36] with TLR2 binding bacterial peptidoglycan and TLR4 recognizing lipopolysaccharides. By incorporating TLR2 and TLR4, Lip@MOMP$_2$@AgNCs liposomes gain enhanced specificity for targeting bacteria.

To assess immune activation and the targeting effect of Lip@MOMP$_2$@AgNCs, we co-cultured J774.A1 cells with *C. albicans* and performed flow cytometry to measure the expression of TLR2, TLR4, and CD45. Notably, after infection, both TLR2 and TLR4 expressions were significantly upregulated. Specifically, the percentage of TLR2-positive cells in the treatment group increased to 94.12%, compared to 84.17% in the control group (Figure S6, Supporting Information). Similarly, TLR4 expression rose to 99.71% in the treatment group, while the control group reported 84.17%. These results suggest that Lip@MOMP$_2$@AgNCs liposomes enhance immune responses by facilitating pathogen recognition through TLR signaling pathways.

In Figure S7, Supporting Information, Western blot analysis confirmed the upregulation of TLR2 and TLR4 in J774.A1 cells co-cultured with *C. albicans*, reinforcing the flow cytometry findings. In contrast, CD45 expression, a marker for leukocytes, displayed a smaller increase (83.22% in the treatment group vs. 81.62% in the control group) (Figure S6, Supporting Information), indicating that the

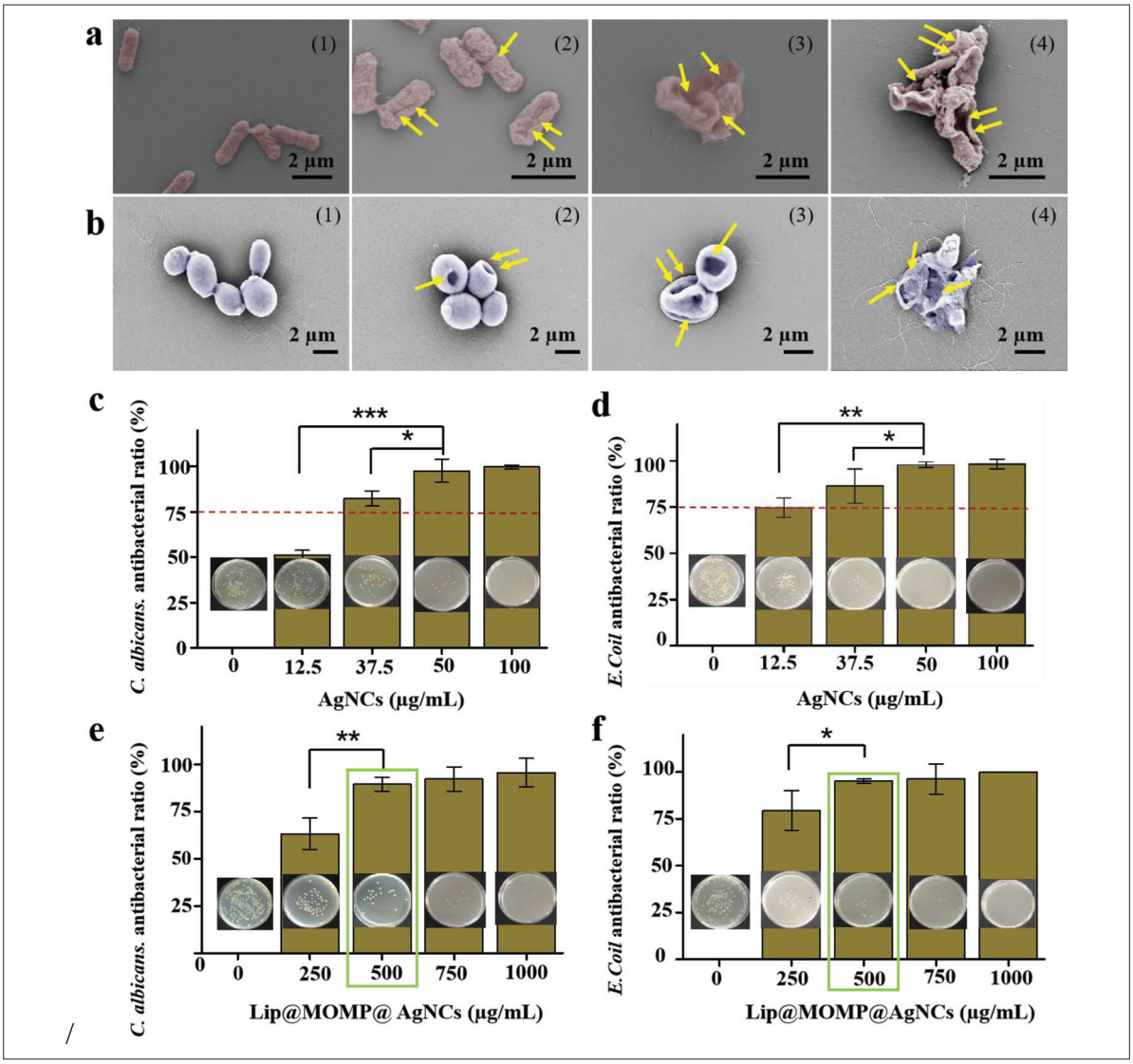

Figure 4. The yellow arrows indicate the locations of bacterial shrinkage. (a and b) Scanning electron microscopy (SEM) images of *Escherichia coli* and *Candida albicans* treated with different concentrations of Lip@MOMP$_2$@AgNCs hydrogel solutions: (1) blank control; (2) 250 μg/mL; (3) 500 μg/mL; and (4) 750 μg/mL. Yellow arrows indicate the locations of bacterial shrinkage. (c and d) Antimicrobial rates of different concentrations of AgNCs against drug-resistant *C. albicans* (c) and *E. coli* (d). The red dashed line represents an antibacterial rate of 75% (e and f). Antimicrobial rates of different concentrations of Lip@MOMP$_2$@AgNCs hydrogel solutions against drug-resistant *C. albicans* (e) and *E. coli* (f). The green boxes denote the Lip@MOMP$_2$@AgNCs hydrogel concentrations selected for subsequent experiments. n =5 (The experiment was conducted with five independent replicates under the same experimental conditions.). *$p < 0.05$; **$p < 0.01$; and ***$p < 0.001$. Scale bars: 2 μm (a and b). Abbreviation: AgNCs, silver nanoclusters.

treatment had a lesser effect on immune cell recruitment. These findings confirm that *C. albicans* infection activates TLR-mediated immune responses and that the incorporation of TLR2 and TLR4 in Lip@MOMP$_2$@AgNCs liposomes can enhance bacterial pathogen recognition. This provides a theoretical foundation for utilizing these liposomes in targeted bacterial therapy,[37–39] with the potential to improve therapeutic outcomes against resistant pathogens.

3.5. Therapeutic efficacy of Lip@MOMP2@AgNCs on *C. albicans* vaginitis *in vivo*

To further substantiate the therapeutic efficacy and targeting precision of the Lip@MOMP$_2$@AgNCs hydrogel system, we developed a murine model of vaginal inflammation for treatment assessment, as depicted in the timeline illustrated in Figure 5a. Histological examination via Hematoxylin/eosin (HE) staining (H&E) staining on day 9 revealed pronounced infiltration of inflammatory cells within the vaginal tissues of the control group, along

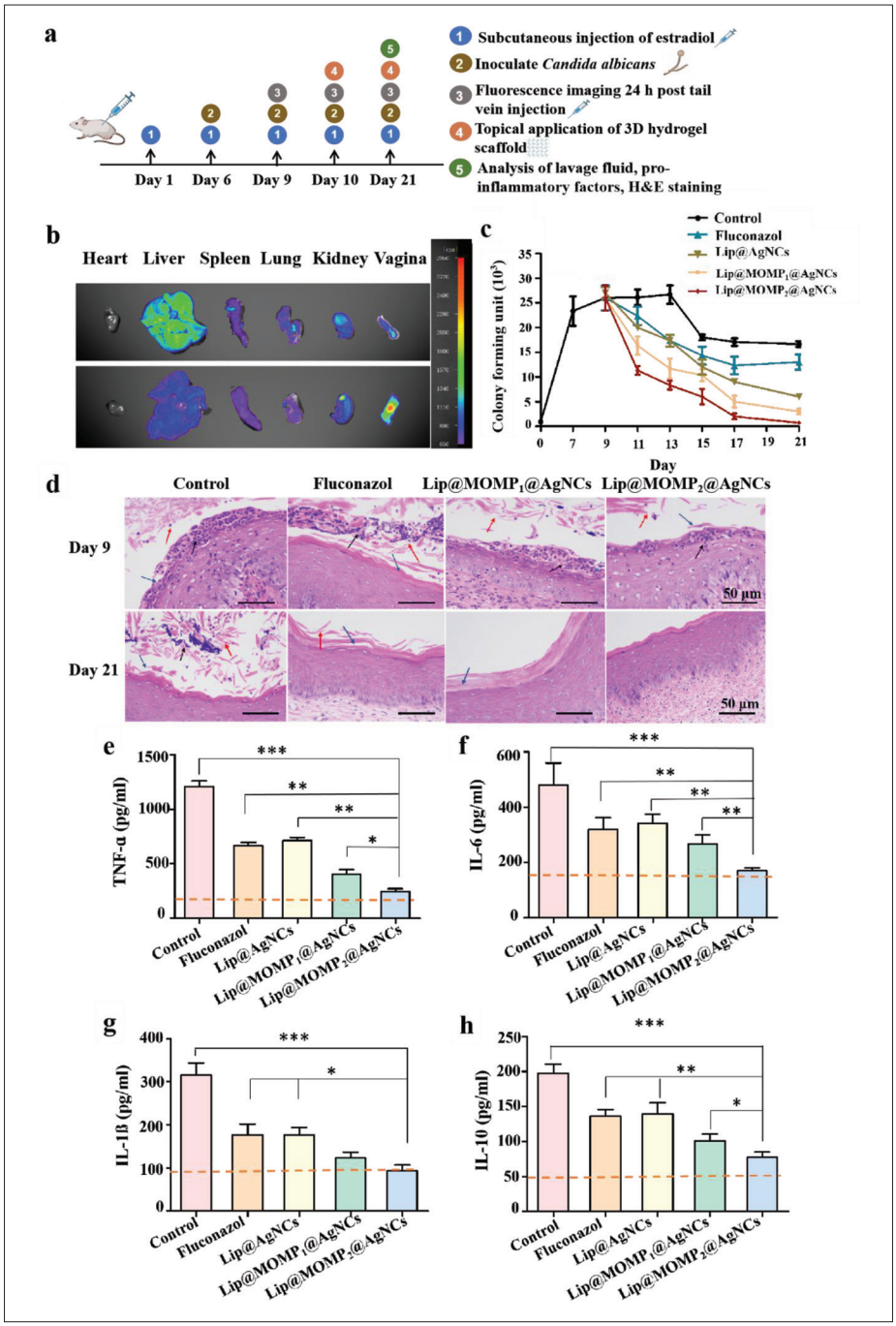

Figure 5. Animal study of Lip@MOMP@AgNCs hydrogel for vginitis treatment. (a) Schematic representation of the establishment and treatment of vaginal inflammation in the mice model. (b) After intravenous injection of Lip@AgNCs or Lip@MOMP@AgNCs, fluorescence imaging displays the distribution of Lip@AgNCs or Lip@MOMP@AgNCs in various organs of the mice 24 h post-injection. (c) Bacterial counts in vaginal lavage fluid collected from the model groups at baseline (day 0) and on days 7, 9, 11, 13, 15, 17, and 21, following a dilution of 10^3 and plating. (d) H&E staining of vaginal tissue from the control group (saline), fluconazole group, Lip@$MOMP_1$@AgNCs hydrogel group, and Lip@$MOMP_2$@AgNCs hydrogel group on days 9 and 21 (post-treatment). Black arrows: abundant neutrophils; red arrows: shed vaginal epithelial cells; blue arrows: damaged vaginal epithelial cells. (e–h) Expression levels of TNF-α, IL-6, IL-1β, and IL-10 in vaginal tissue from the control group, fluconazole group, Lip@AgNCs group, Lip@$MOMP_1$@AgNCs group, and Lip@$MOMP_2$@AgNCs group ($n = 3$; $^*p < 0.05$; $^{**}p < 0.01$; $^{***}p < 0.001$). The dashed orange line represents the expression levels of pro-inflammatory factors in the blood of normal mice. Abbreviations: AgNCs, silver nanoclusters; H&E, hematoxylin and eosin.

with evident cellular damage. This was accompanied by a significant upregulation of pro-inflammatory cytokines TNF-α, IL-6, IL-1β, and IL-10 in the bloodstream, highlighting a marked disparity in pro-inflammatory factor expression between the model and normal mice. This confirms the successful establishment of a mouse model of drug-resistant *C. albicans* vaginitis, providing a robust platform for further investigations.

To verify the targeting capacity of the $MOMP_2$ protein-decorated liposomes, we administered either Lip@AgNCs or Lip@$MOMP_2$@AgNCs via tail vein injection on Day 9. Fluorescent imaging performed 24 h post-injection demonstrated that Lip@AgNCs primarily accumulated in the hepatic region, whereas Lip@$MOMP_2$@AgNCs predominantly localized within the vaginal tissues (Figure 5b). This finding corroborates the targeting capability of the $MOMP_2$ protein, informing the design of subsequent therapeutic strategies.

To amplify the therapeutic effect, a 3D-printed hydrogel mesh scaffold containing Lip@$MOMP_2$@AgNCs was applied locally to the vulvar region, facilitating the *in situ* release of the therapeutic agent. This strategy, combining systemic injection with topical application, achieved a synergistic antimicrobial effect. Bacterial load assessments in the vaginal wash of the inflammatory model mice on Day 9 revealed counts of 2.5×10^4, compared to only 8×10^2 in normal mice, indicating a substantial increase. This prompted an examination of bacterial count changes in vaginal tissues (Figure 5c). The antibacterial efficacy of Lip@$MOMP_2$@AgNCs hydrogel was recorded as 64.1%, 78.3%, and 92.1% on days 11, 15, and 21, respectively, compared to 21.7%, 59.8%, and 63.9% for Lip@AgNCs, and 41.7%, 56.5%, and 78.3% for Lip@MOMP1@AgNCs. In contrast, fluconazole only achieved a 44.3% antibacterial rate by Day 21, markedly lower than that of the Lip@$MOMP_2$@AgNCs group.

As depicted in Figures 5d and S8, Supporting Information, by Day 21 of treatment, the fluconazole group still exhibited significant inflammatory cell presence and epithelial damage in vaginal tissues. The Lip@$MOMP_1$@AgNCs hydrogel group exhibited only slight epithelial damage, while the Lip@$MOMP_2$@AgNCs hydrogel group exhibited no substantial tissue damage, underscoring the differential efficacy of the treatments. Moreover, histopathological analysis revealed no significant histological alterations in major organs (heart, liver, spleen, lungs, and kidneys) between the Lip@$MOMP_2$@AgNCs group and the control group of normal mice (Figure S9, **Supporting Information**), indicating low systemic toxicity and supporting the potential for clinical application.

Data in Figures 5e–h demonstrate that fluconazole modestly reduced TNF-α, IL-6, IL-1β, and IL-10 levels by 40.2%, 63.6%, 49.4%, and 34.7%, respectively. The Lip@AgNCs group exhibited reductions of 38.9%, 56.1%, 46.3%, and 32.8%. Lip@$MOMP_1$@AgNCs treatment decreased inflammatory secretion by 61.2%, 52.9%, 59.4%, and 34.7%. In comparison, Lip@$MOMP_2$@AgNCs achieved substantial downregulation of TNF-α, IL-6, IL-1β, and IL-10 by 72%, 61.3%, 64.7%, and 62.5%, respectively. While the fluconazole group displayed some downregulation of inflammatory markers, it was significantly less pronounced than in the Lip@$MOMP_2$@AgNCs group. Post-treatment, pro-inflammatory factor expression levels in the Lip@$MOMP_2$@AgNCs hydrogel group approached normalcy. In summary, the therapeutic efficacy of Lip@$MOMP_2$@AgNCs against drug-resistant *C. albicans* vaginitis surpassed that of both Lip@$MOMP_1$@AgNCs and fluconazole, with the effectiveness hierarchy being Lip@$MOMP_2$@AgNCs > Lip@$MOMP_1$@AgNCs > fluconazole.

4. Conclusion

In this study, we successfully engineered a sophisticated nanoparticle drug delivery system designed to enhance the antibacterial efficacy against resistant *C. albicans* by ingeniously integrating specific receptor proteins derived from macrophage membranes with diminutive AgNCs. The resultant composite biomimetic liposome, Lip@$MOMP_2$@AgNCs, exhibits an impressive capacity to accurately target infection sites via intravenous administration, demonstrating precise bacterial recognition and specificity. This is coupled with excellent biocompatibility and therapeutic efficacy.

Furthermore, the strategic incorporation of a 3D-printed hydrogel scaffold embedded with Lip@$MOMP_2$@AgNCs allows for sustained and localized drug release, thereby amplifying the antibacterial effect and concurrently minimizing potential adverse side effects. The findings indicate that Lip@$MOMP_2$@AgNCs offers substantial advantages in treating drug-resistant *C. albicans* vaginitis, evidenced by superior antibacterial rates and more effective modulation of inflammatory markers compared to conventional fluconazole therapy. This innovative therapeutic strategy provides a highly effective solution for managing resistant bacterial infections and offers novel insights for optimizing clinical treatment protocols.

Overall, our research presents a groundbreaking approach for the treatment of resistant *C. albicans* vaginitis and paves the way for potential future directions in antibacterial drug development. This work showcases

promising clinical application prospects and holds significant scientific value.

Acknowledgments

None.

Funding

This work was financially supported by the National Key Research and Development Project (2022YFC2403100; 2022YFC2403104), the National Natural Science Foundation of China (81772069, 81801911), and the Medical and Health Science and Technology Project of the Zhejiang Province (2020KY786).

Conflict of interest

The authors declare they have no competing interests.

Author contributions

Conceptualization: Wenyan Wang, Lina Dong, Bixing Fang
Data curation: Wenyan Wang, Lina Dong
Formal analysis: Bixing Fang, Aobuliaximu Yakupu
Funding acquisition: Xingang Wang, Chunmao Han
Investigation: Meixuan Liu, Miao Pan, Xiaoqi Li
Project administration: Xingang Wang
Supervision: Xingang Wang, Qiong Li
Writing – original draft: Wenyan Wang, Lina Dong
Writing – review & editing: Lina Dong, Xingang Wang

Ethics approval and consent to participate

All procedures were performed with the approval of the Animal Ethics Committee of Tsinghua Shenzhen International Graduate School, Tsinghua University (202246).

Consent for publication

Not applicable.

Availability of data

Data is available from the corresponding author upon reasonable request.

References

1. Rodero CF, Fioramonti Calixto GM, Dos Santos KC, et al. Curcumin-loaded liquid crystalline systems for controlled drug release and improved treatment of vulvovaginal candidiasis. *Mol Pharm*. 2018;15(10):4491-4504. doi: 10.1021/acs.molpharmaceut.8b00507
2. Sheary B, Dayan L. Recurrent vulvovaginal candidiasis. *Austral Fam Phys*. 2005;34(3):147-150. doi: 10.1016/j.ajog.2015.06.067
3. Story K, Sobel R. Fluconazole prophylaxis in prevention of symptomatic *candida* vaginitis. *Curr Infect Dis Rep.* 2020;22(1):2. doi: 10.1007/s11908-020-0712-7
4. Tietz H-J. Fluconazole for recurrent vulvovaginal candidiasis. *Medizinische Monatsschrift fur Pharmazeuten* 2009;32(6):227. doi: 10.1055/s-0029-155292
5. Khan Z, Ahmad S, Asadzadeh M. A pilot study showing fluconazole and flucytosine activities against candida glabrata are affected by low ph: implications for the treatment of recurrent vulvovaginal candidiasis. *Clin Exp Obstet Gynecol.* 2024;51(2):39. doi: 10.31083/j.ceog5102039
6. Ying Y, Zhang J, Huang SB, et al. Fluconazole susceptibility of 3,056 clinical isolates of candida species from 2005 to 2009 in a tertiary-care hospital. *Indian J Med Microbiol.* 2015;33(3):413-415. doi: 10.4103/0255-0857.158569
7. Martins Maciel AA, Cunha FA, Freire TM, et al. Development and evaluation of an anti-candida cream based on silver nanoparticles, *3 Biotech.* 2023;13(11):352. doi: 10.1007/s13205-023-03776-9
8. Zhang C, Yang X, Yu L, et al. Electrospun polyasparthydrazide nanofibrous hydrogel loading with in-situ synthesized silver nanoparticles for full-thickness skin wound healing application. *Mater Design.* 2024;239:112818. doi: 10.1016/j.matdes.2024.112818
9. Zhang H, Zhang Y, Li Y, et al. A novel silver nanoparticles-decorated metal-organic framework with rapid and sustained antimicrobial activity against drug-resistant *candida albicans* through synergistic chemodynamic and sonodynamic therapy. *Adv Ther.* 2023;6(8):2300074. doi: 10.1002/adtp.202300074
10. Akter M, Sikder MT, Rahman MM, et al. A systematic review on silver nanoparticles-induced cytotoxicity: physicochemical properties and perspectives. *J Adv Res.* 2017;9:1-16. doi: 10.1016/j.jare.2017.10.008
11. Nasim I, Kumar SR, Vishnupriya V, et al. Cytotoxicity and anti-microbial analysis of silver and graphene oxide bio nanoparticles. *Bioinformation*. 2020;16(11):831-836. doi: 10.1016/j.jare.2017.10.008
12. Wolff N, Bialas N, Loza K, et al. Increased cytotoxicity of bimetallic ultrasmall silver-platinum nanoparticles (2 nm) on cells and bacteria in comparison to silver nanoparticles of the same size. *Materials (Basel)*. 2024;17(15):3702. doi: 10.3390/ma17153702
13. Yuan X, Setyawati MI, Tan AS, et al. Highly luminescent silver nanoclusters with tunable emissions: cyclic reduction-decomposition synthesis and antimicrobial properties, *NPG Asia Mater.* 2013;5:e39. doi: 1038/am.2013.3

14. Ai F, Liu T, Liu Y, et al. A 3d printed wound cooling system incorporated with injectable, adsorbable, swellable and broad spectrum antibacterial scaffolds for rapid hematischesis processing. *J Mater Chem B*. 2018;6(37):5940-5948. doi: 10.1039/c8tb01625a

15. Wang C, Wang Y, Zhang L, et al. Pretreated macrophage-membrane-coated gold nanocages for precise drug delivery for treatment of bacterial infections. *Adv Mater.* 2018;30(46):e1804023. doi: 10.1002/adma.201804023

16. Taylor PR, Martinez-Pomares L, Stacey M, Lin HH, Brown GD, Gordon S. Macrophage receptors and immune recognition. *Annu Rev Immunol*. 2005;23:901-944. doi: 10.1146/annurev.immunol.23.021704.115816

17. Yu L, Pan J, Du L, et al. Novel roles of tlr2and tlr4in innate immunity against virus infections. *Chin J Virol.* 2018;34(4):570-578. doi: 10.1016/j.bjid.2015.10.011

18. Gao Q, Lee J-S, Kim BS, et al. Three-dimensional printing of smart constructs using stimuli-responsive biomaterials: a future direction of precision medicine. *Int J Bioprint.* 2023;9(1):230-257. doi: 10.18063/ijb.v9i1.638

19. Li Z, Zheng A, Mao Z, et al. Silk fibroin-gelatin photo-crosslinked 3D-bioprinted hydrogel with MOF-methylene blue nanoparticles for infected wound healing. *Int J Bioprint.* 2023;9(5):459-473. doi: 10.18063/ijb.773

20. Chen H, Zhang X, Shang L, et al. Programmable anisotropic hydrogels with localized photothermal/magnetic responsive properties. *Adv Sci*. 2022;9(26): 2202173-2202182. doi: 10.1002/advs.202202173

21. Chen XB, Anvari-Yazdi AF, Duan X, et al. Biomaterials/bioinks and extrusion bioprinting. *Bioact Mater.* 2023;28:511-536. doi: 10.1016/j.bioactmat.2023.06.006

22. Ng WL, Shkolnikov V. Jetting-based bioprinting: process, dispense physics, and applications. *Bio-Design Manuf.* 2024;7(2):771-799. doi: 10.1007/s42242-024-00285-3

23. Li Y, Zhang X, Zhang X, et al. Recent progress of the vat photopolymerization technique in tissue engineering: a brief review of mechanisms, methods, materials, and applications. *Polymers*. 2023;15(19):3940-3975. doi: 10.3390/polym15193940

24. Guo Z, Mi S, Sun W. A facile strategy for preparing tough, self-healing double-network hyaluronic acid hydrogels inspired by mussel cuticles. *Macromol Mater Eng.* 2019;304(4):1800715. doi: 10.1002/mame.201800715

25. Ouyang J, Liu R-Y, Chen W, et al. A black phosphorus based synergistic antibacterial platform against drug resistant bacteria. *J Mater Chem B*. 2018;6(39):6302-6310. doi: 10.1039/c8tb01669k

26. Munshi R, Talele G, Shah R. *In-vitro* evaluation of antimicrobial activities of *Escherichia coli*, *Klebsiella pneumoniae*, *Salmonella typhi*, *Neisseria gonorrhoeae*, and *Candida albicans* nosodes. *Homeopathy*. 2022;111(01):42-48. doi: 10.1055/s-0041-1727149

27. Henkelman S, Rakhorst G, Blanton J, et al. Standardization of incubation conditions for hemolysis testing of biomaterials. *Mater Sci Eng C*. 2009;29(5):1650-1654. doi: 10.1016/j.msec.2009.01.002

28. Teng Z, Wang S, Su X, et al. Facile synthesis of yolk-shell structured inorganic-organic hybrid spheres with ordered radial mesochannels. *Adv Mater.* 2014;26(22):3741-3747. doi: 10.1002/adma.201400136

29. Liang G, Jin X, Zhang S, et al. RGD peptide-modified fluorescent gold nanoclusters as highly efficient tumor-targeted radiotherapy sensitizers. *Biomaterials*. 2017;144:95-104. doi: 10.1016/j.biomaterials.2017.08.017

30. Qi Y, Xu M, Lu H, et al. Hepatic biotransformation of renal clearable gold nanoparticles for noninvasive detection of liver glutathione level via urinalysis. *Angew Chem Int Ed Engl*. 2024;63(36):e202409477. doi: 10.1002/anie.202409477

31. Yin W, Yu J, Lv F, et al. Functionalized nano-mos with peroxidase catalytic and near-infrared photothermal activities for safe and synergetic wound antibacterial applications. *ACS Nano*. 2016;10(12):11000-11011. doi: 10.1021/acsnano.6b05810

32. Netea MG, Van Der Meer JWM, Kullberg BJ. Toll-like receptors as an escape mechanism from the host defense. *Trends Microbiol.* 2004;12(11):484-488. doi: 10.1016/j.tim.2004.09.004

33. Sasai M, Yamamoto M. Pathogen recognition receptors: ligands and signaling pathways by toll-like receptors. *Int Rev Immunol.* 2013;32(2):116-133. doi: 10.3109/08830185.2013.774391

34. Quesniaux V, Fremond C, Jacobs M, et al. Toll-like receptor pathways in the immune responses to mycobacteria. *Microbes Infect*. 2004;6(10):946-959. doi: 10.1016/j.micinf.2004.04.016

35. Simpson ME, Petri WA, Jr. TLR2 as a therapeutic target in bacterial infection. *Trends Mol Med*. 2020;26(8):715-717. doi: 10.1016/j.molmed.2020.05.006

36. Udgata A, Dolasia K, Ghosh S, Mukhopadhyay S. Dribbling through the host defence: targeting the TLRs by pathogens. *Crit Rev Microbiol*. 2019;45(3):354-368. doi: 10.1080/1040841X.2019.1608904

37. Choudhury QJ, Ambati S, Link CD, Lin X, Lewis ZA, Meagher RB. Dectin-3-targeted antifungal liposomes efficiently bind and kill diverse fungal pathogens. *Mol Microbiol*. 2023;120(5):723-739. doi: 10.1111/mmi.15174

38. Jani K, Mehta S, Patel R, Prajapati B, Patel G. Focused insights into liposomal nanotherapeutics for antimicrobial treatment. *Curr Med Chem*. 2024.
doi: 10.2174/0109298673322058241003073312

39. Singh I, Kumar S, Singh S, Wani MY. Overcoming resistance: chitosan-modified liposomes as targeted drug carriers in the fight against multidrug resistant bacteria-a review. *Int J Biol Macromol*. 2024;278(Pt 4):135022.
doi: 10.1016/j.ijbiomac.2024.135022

ACCSCIENCE PUBLISHING

International Journal of Bioprinting

RESEARCH ARTICLE

Gradient hydroxyapatite nanoparticles with spatial distribution facilitate the healing of tendon-to-bone interface

Lei Wang[1,2†], Liguo Sun[1,3†], Zhennan Qiu[4,5†], Zhao Zhang[1], Yubo Shi[1,6], Jingyi Dang[1], Weidong Tao[1], Jiankang He[4,5], and Hongbin Fan[1*]

[1]Department of Orthopedic Surgery, Xijing Hospital, the Air Force Military Medical University, Xi'an, Shaanxi, China

[2]Department of Orthopaedic Trauma, Zhongshan Hospital Affiliated to Xiamen University, Xiamen, Fujian, China

[3]Department of Medical Management, Shaanxi Provincial Hospital of Chinese Medicine, Xi'an, Shaanxi, China

[4]State Key Laboratory for Manufacturing Systems Engineering, Xi'an Jiaotong University, Xi'an, Shaanxi, China

[5]Rapid Manufacturing Research Center of Shaanxi Province, Xi'an Jiaotong University, Xi'an, Shaanxi, China

[6]Department of Orthopedic Surgery, Xiangyang No.1 People's Hospital, Hubei University of Medicine, Xiangyang, Hubei, China

[†]These authors contributed equally to this work.

***Corresponding author:**
Hongbin Fan
(fanhb@fmmu.edu.cn)

Citation: Wang L, Sun L, Qiu Z, et al. Gradient hydroxyapatite nanoparticles with spatial distribution facilitate the healing of tendon-to-bone interface. *Int J Bioprint*. 2025;11(1):501-516. doi: 10.36922/ijb.6181

Received: November 17, 2024
Revised: December 19, 2024
Accepted: December 31, 2024
Published Online: January 2, 2025

Copyright: © 2025 Author(s). This is an Open Access article distributed under the terms of the Creative Commons Attribution License, permitting distribution, and reproduction in any medium, provided the original work is properly cited.

Publisher's Note: AccScience Publishing remains neutral with regard to jurisdictional claims in published maps and institutional affiliations.

Abstract

Tendon-to-bone interface (TBI) injuries have become increasingly common due to the growing competition in sports. Electrohydrodynamic (EHD) three-dimensional (3D) printing is a promising strategy for controllably fabricating biomimetic micro/nanoscale architecture in musculoskeletal tissue engineering. This study aims to fabricate a novel biomimetic EHD-printed poly(ε-caprolactone) (PCL) with gradient hydroxyapatite (HA) nanoparticles utilizing modified dopamine self-polymerization reaction and assess the biocompatibility and efficacy of osteogenic differentiation and interface regeneration *in vivo*. The fabricated scaffold PCL-PDA-HA (PPH) has a diameter of 190.35 ± 41.96 nm in areas with lower HA concentration and 446.54 ± 125.42 nm in areas with higher HA concentration; the scaffold was demonstrated to profoundly facilitate osteogenic differentiation of tendon stem/progenitor cells (TSPCs), enhancing the expression of RUNX2 and ALP. On day 14, the expression of osteogenic genes, including *Bmp2* (~3.12-fold, $p < 0.001$) and *Runx2* (~3.24-fold, $p < 0.001$), was significantly elevated compared to those of PCL groups. New fibrocartilage formation and TBI healing were observed in the PPH group *in vivo*. Therefore, our work demonstrated a facile green synthesis avenue for enhancing TBI healing via TSPCs' osteogenic differentiation, which supplied a novel approach to augment the therapeutic effects of ligament graft in TBI reconstruction.

Keywords: Gradient; Hydroxyapatite; Tendon-to-bone interface; Tendon stem/progenitor cells

1. Introduction

The tendon-to-bone interface (TBI; also known as enthesis) is a complex connecting tendon and bone. It ensures tissue stability and functional activity by mechanically transferring the load between these two distinctly different tissues. The intricateness of the enthesis allows for normal musculoskeletal activity but also presents huge challenges for its repair.[1] Unfortunately, the most common causes of TBI injuries are acute or mild trauma and aging of the tendon during regular activities.[2] Nevertheless, regenerated TBIs typically exhibit fibrovascular scars instead of the four distinct transition zones (tendon, uncalcified fibrocartilage, calcified fibrocartilage, and bone). As a result, tissue toughness is rarely restored, increasing the risk of re-injury, and further deterioration of repaired TBIs.[2–5] An unrestored gradient interface structure leads to unfavorable consequences following surgical procedures, more likely, contributing to prolonged pain, high rates of re-injury, and instability of repaired TBIs.[6]

The intricate nature of the native interface, coupled with its limited healing capacity, often renders surgery for a torn rotator cuff unsuccessful, resulting in disorganized fibrovascular scar tissue.[7] This scar tissue exhibits poor biomechanical quality, leading to a post-surgical re-rupture rate of 25–75%.[8] Previous studies have indicated that the tensile strength of the regenerated TBI is primarily influenced by osteointegration with the graft and fibrocartilage formation.[9,10] Consequently, various treatments have been developed to expedite the healing process of TBI by accelerating the formation of bone and/or fibrocartilage. Jiang et al.[11] demonstrated that hydroxyapatite (HA)/type I collagen paste could facilitate TBI healing by providing an osteogenic scaffold and microenvironment, thereby enhancing the biomechanical strength of the repaired TBI. Furthermore, Shi et al.[10] confirmed that the bone microarchitecture and biomechanical properties were improved during the healing process of a canine TBI model through the local administration of metformin. Additionally, an earlier study indicated that the transplantation of stem cell sheets could enhance the biomechanical robustness of the autograft used in anterior cruciate ligament (ACL) reconstruction.[12]

The bionic TBI repair technique has been widely utilized in animal models, demonstrating promising applications in enhancing post-injury TBI repair.[13] Given that the mineral content of the enthesis increases from tendon to bone, it is feasible to design hierarchical scaffolds that mimic the natural TBI structure.[14,15] Numerous studies have demonstrated that hierarchically structured scaffolds effectively promote the regeneration and remodeling of injured TBI.[16] Polydopamine (PDA) coating has been confirmed to create thin, surface-adherent films, and secondary modifications on various inorganic and organic materials under alkaline pH and oxygen conditions.[17,18] Furthermore, the oxygen-dependent PDA gradient on material surfaces presents a direct and adaptable approach for fabricating hierarchical structures or chemical gradient scaffolds for biomedical applications.[19–21] This PDA gradient surface can modulate the arrangement of secondary biomolecules, such as HA.[19] Green synthesis of HA has reported favorable biocompatibility for the polymerized structure and the ability to induce osteogenic differentiation and osseointegration of artificial ligaments.[22–25] In the current study, it is hypothesized that the gradient HA-modified scaffold (PCL-PDA-HA, PPH) can facilitate the healing of the TBI.

To verify the hypothesis, biomimetic gradient HA nanoparticles with a spatial distribution were successfully incorporated into electrohydrodynamic (EHD)-printed poly(ε-caprolactone) (PCL) scaffolds. *In vitro* research was then performed to evaluate osteogenic differentiation and osseointegration capacity of tendon stem/progenitor cells (TSPCs) on the scaffold. Furthermore, the TSPCs/scaffold was implanted in a TBI model to explore their role in promoting TBI healing.

2. Materials and methods

2.1. Fabrication and modification of the scaffold

A commercial EHD printing platform (BioPioneer-1; Shaanxi Bioprintissue Medical Technologies Co., Ltd, China) was utilized to fabricate the PCL scaffolds. In order to obtain a homogenous solution, tiny PCL pellets were put into a metal cartridge and melted at 90°C. According to a prior study,[7] the main parameters of extrusion pressure, applied voltage, nozzle-to-collector distance, and stage moving speed for melt EHD printing were at 150 mBar, 4.0 kV, 3 mm, and 25 mm/s, respectively. The entire procedure was completed at 35% humidity and 23°C (room temperature).

PDA nanoparticles on the scaffold were synthesized using a traditional facile approach, with slight modifications to the method previously reported.[20] To create PDA gradients (PCL-PDA [PP] scaffolds), the scaffolds were affixed to a plastic square dish (Scheme 1). Subsequently, these square dishes were positioned atop a polydimethylsiloxane triangular block, which was inclined at an angle of 30°. The PCL scaffold was then submerged in a solution of dopamine (2 mg/mL) combined with Tris–HCl buffer (10 mM, pH 8.5) (Sigma Aldrich, USA) at ambient temperature for 4 h. Deionized water (DW) was

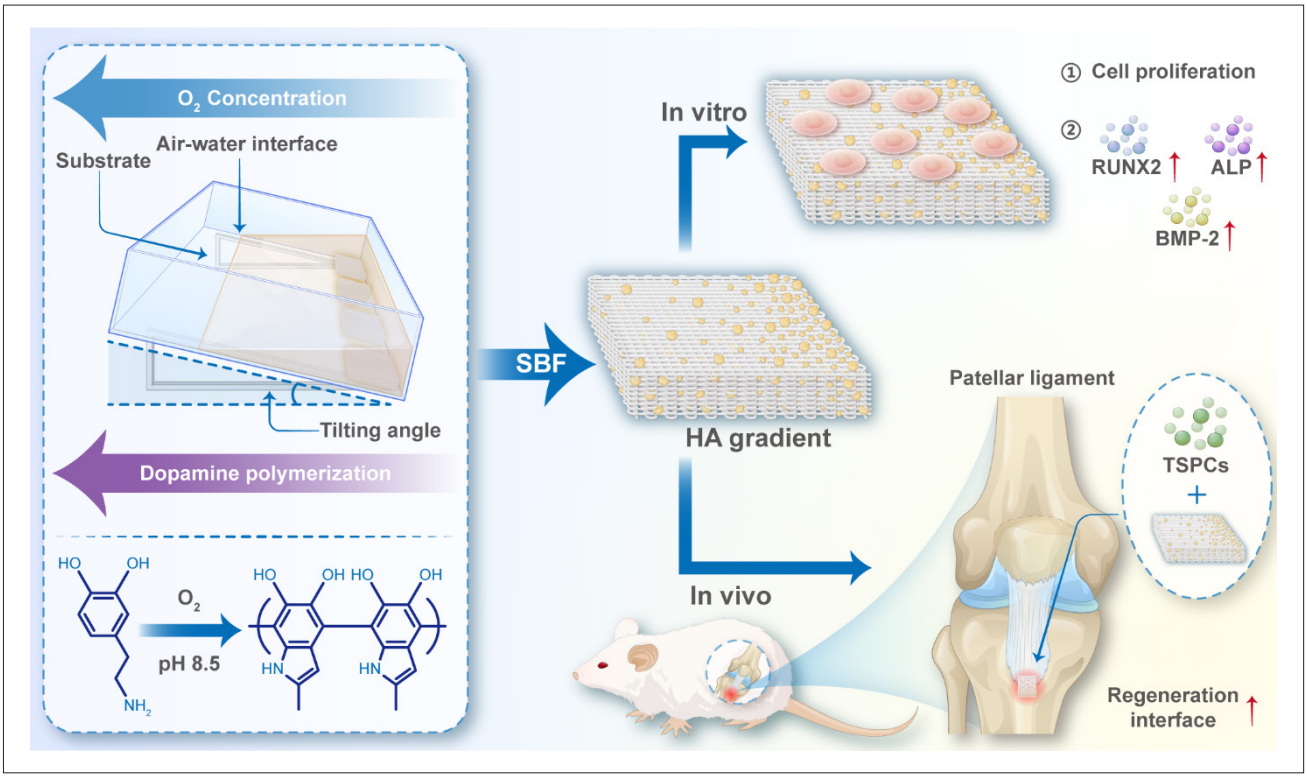

Scheme 1. Schematic illustration of fabricating an HA gradient with spatial distribution scaffold for potential application in TBI regeneration. Abbreviations: HA, hydroxyapatite; SBF, simulated body fluid; TSPCs, tendon stem/progenitor cells.

used to cleanse the excess PDA, accompanied by gentle shaking. The HA coating procedure involved immersing the PP scaffolds in 1.5 × simulated body fluid (SBF) and incubating them at 36.5 °C for 5 days.[26] After immersion, the PPH scaffolds were rinsed with DW and dried using nitrogen gas.

2.2. Morphology of the scaffold

Scanning electron microscopy (SEM; Thermoscientific, United States of America [USA]) fitted with a field-emission gun (5.0 kV) was used to evaluate the morphology of the fibrous scaffold. To reduce the effect of charging, gold coating was performed for 1 min. Components of the PCL scaffold were assessed using electron dispersive spectroscopy (EDS).

2.3. Surface roughness evaluation

Atomic force microscopy (AFM; Agilent Technologies Inc. USA) was used to measure the roughness of a single fiber in a scaffold in non-contact mode. The scaffold was fastened to a flat metal platform, and four random locations were scanned at 10 × 10 μm^2 each. The absolute size distribution of the nanoparticles was calculated using Image J and Origin.

2.4. Hydrophilicity of the scaffold

The hydrophilicity of the scaffold was assessed by conducting a water contact angle (WCA) measurement, with G10 angle measurements taken both before and after modification. A droplet of DW (2 μL) was expelled from a micro-syringe, and the angle was determined using a telescopic goniometer. Five repetitions were conducted for each sample.

2.5. Surface chemical element analysis

X-ray photoelectron spectroscopy (XPS; ESCALAB Xi+; Thermo Fisher, USA) was employed to qualitatively examine the surface chemistry of the samples in an ultrahigh vacuum. The recorded elements included carbon (C1s), oxygen (O1s), nitrogen (N1s), phosphorus (P2p), and calcium (Ca2p), which were detected in the 278–298, 524–546, 390–410, 124–144, and 340–360 eV regions, respectively. The area surveyed was 500–500 μm, with a duration of 30 min. Avantage software was utilized to analyze the recorded survey spectrum.

2.6. Isolation and culture of tendon stem/progenitor cells

As previously established,[27] TSPCs were isolated from 3-week-old Sprague-Dawley rats. Briefly, the tendon and the adjacent paratenon were removed from the bilateral Achilles tendon, minced, and subjected to digestion

using type I collagenase (3 mg/mL; OriCell, China) for approximately 2.5 h at 37°C. Following phosphate-buffered saline (PBS; OriCell, China) washing, the acquired single-cell suspensions were subjected to incubation in a complete medium supplemented with 10% fetal bovine serum (FBS; Gibco, USA), 2 mM L-glutamine (Oricell, China), and 1% penicillin-streptomycin (PS; Oricell, China) at 37 °C with 5% CO_2. The medium was altered at regular intervals of 2–3 days, and cells from passages 3–5 were used for subsequent experiments.

2.7. Proliferation and viability of tendon stem/progenitor cells on the scaffold

TSPCs were seeded onto scaffolds (PCL, PP, and PPH) at a density of 2 × 10^5/well in 12-well culture plates. Each scaffold sample was trimmed to 15 × 15 mm^2 and sterilized with 75% ethanol and 6-h ultraviolet irradiation. Cell proliferation was assessed using the Cell Count Kit-8 (CCK-8; Beyotime, China) on days 1, 4, and 7. Specifically, TSPCs were supplemented with 100 μL of CCK-8 solution, transferred to a new 24-well culture plate, and incubated for 30 min in a 5% CO_2 atmosphere at 37 °C. The optical density (OD) value was then measured at 450 nm using a microplate reader.

TSPCs on scaffolds were stained using the Live/Dead Cell Kit (Thermo Fisher Scientific, USA) to assess cell viability. After incubation periods of 1, 4, and 7 days, TSPCs were stained with the Live/Dead Kit for 30 min. Subsequently, observations were conducted using a confocal laser scanning microscope (CLSM; A1+; Nikon, Japan). Viable cells exhibited a green tint, while dead cells displayed a red tint.

2.8. Cell adhesion evaluation

Following incubation of TSPCs on scaffolds for 1, 3, and 7 days, the samples were fixed in 4% paraformaldehyde (PFA) for 15 min. Subsequently, the cells underwent three PBS washes, followed by Triton-X100 permeabilization for 30 min at ambient temperature. Rhodamine phalloidin (Yeasen Biotech Co., Ltd, China) and DAPI (Solaribio, China) were used to stain the cytoskeleton and cell nuclei, respectively. Finally, the images were captured with CLSM.

Cell sheets incubated for 3 days were preserved in glutaraldehyde solution, dehydrated using gradient ethanol, sputtered with gold under vacuum, and scanned using SEM at a high-power field to observe the TSPCs inside the scaffold.

2.9. Western blot analysis

Proteins derived from TSPCs, cultured for either 7 or 14 days, were extracted using a mixture of Radio Immunoprecipitation Assay (RIPA) lysis buffer and a protease inhibitor cocktail. The proteins from each group were transferred onto Polyvinylidene fluoride membranes that had been immersed in methyl alcohol for 1 min. The membranes were then incubated in 5% non-fat milk for 1 h. All antibodies, including those for GADPH, Scleraxis, TNMD, COL2A1, SOX9, ALP, and RUNX2 proteins (Proteintech, China), were allowed to incubate at 4 °C overnight. The membranes were then washed three times with TBST, with each wash lasting 5 min, before incubation at room temperature for 1 h with the respective secondary antibodies. Finally, images of the membranes were captured using the Amersham Imager.

2.10. Quantitative reverse transcription polymerase chain reaction

The TSPCs on scaffolds were broken down by trypsin after incubation at various intervals. The cells were supplemented with a Trizol reagent (Invitrogen, USA) to extract the total RNA. Subsequently, 1 μg RNA was employed for cDNA synthesis with the PrimeScript™ RT Master Mix (Takara, Japan). Polymerase chain reaction (PCR) amplification was carried out using TB Green® Premix Ex Taq™ II (Takara, Japan) as per the instructions provided by the manufacturer. The design and procurement of each primer (Table S1, Supporting Information) were performed by Tsingke Biotechnology Co., Ltd (China). The $2^{-\Delta\Delta Ct}$ method was employed to determine the relative gene expression level, which was then compared to the normalized control housekeeping gene GAPDH (n = 3).

2.11. Animal experiments

2.11.1. Surgical procedure

The Air Force Military Medical University Animal Ethics Committee approved all animal experiments, which were conducted in accordance with the Guidelines for the Care and Use of Laboratory Animals (IACUC-20241499). The *in vivo* evaluation of PPH scaffolds involved 96 male Sprague-Dawley rats (280–320 g) that were randomly divided into four groups (24 per group): the sham group (without graft implantation), the PCL group (PCL loaded with TSPCs), the PP group (PDA-modified PCL loaded with TSPCs), and the PPH group (gradient nano-HA [nHA]-modified PP scaffold loaded with TSPCs). Two authors (W.T. and J.D.) conducted all animal experiments but did not participate in the subsequent result collection. All scaffolds with TSPCs were cultured in the medium for 14 days. The surgical interventions were carried out in accordance with previously outlined procedures.[8] After a midline sternotomy was performed in the knee joint, the patellar tendon (PT) was meticulously dissected. The lower part of the ligament (approximately 3 × 7 mm^2 defect), including the TBI, was cut off to expose the remnant tendon and its insertion at the tibial tuberosity. Following that, the inserted PT at the tibial tuberosity was detached and

ground with a tiny wheel saw until the osseous interface was unveiled. Then, the scaffolds loaded with TSPCs were implanted in the proximal area, which was stitched with the remnant tendinous part with Ethicon 6-0 suture, and the distal area, which was secured with the osseous part. In the sham group, the interface was completely severed without any intervention. After closing the surgical incision, the knee joint was fastened in the resting position for 1 week to protect the reattachment.

2.11.2. Micro-computed tomography analysis

The samples (n = 4 per group) were harvested at 1, 2, and 3 months post-surgery and fixed in 4% PFA for 24 h. The samples were then scanned utilizing a micro-computed tomography (CT) scanner (SkyScan1276; Bruker, Germany). The scanned images were processed using NRecon, DataViewer, Ctvox, and CTAn. The 3D-reconstructed datasets were analyzed to obtain the bone mineral density (BMD) and the trabecular bone volume fraction (BV/TV) within the region of interest. Additionally, the mid-sagittal image of each sample was obtained for visualization comparison.

2.11.3. Biomechanical analysis

The PT–bone complexes (n = 4 per group) were harvested at 1, 2, and 3 months post-surgery for subsequent analysis. All redundant soft tissue in the knee joint, except for the PT, was removed to minimize interferences. The proximal end of the PT and the shaft of the tibia were immobilized securely using clamps specifically designed for both extremities, allowing for tensile loading in the mechanical testing machine and precise alignment to ensure a vertical force application. The examination was conducted consistently at a speed of 5 mm/min, with the instantaneous loads at failure documented. The load–deformation curve was employed to calculate the failure load, and the slope of the linear portion of the curve was analyzed to determine stiffness. All tensile evaluations were performed at room temperature, with the samples kept moist using PBS throughout the entire process.

2.11.4. Histology and gross observation

All rats were sacrificed at 1, 2, and 3 months postoperatively through intravenous administration of a pentobarbital overdose (100 mg/kg). Subsequently, all samples were photographed for gross observation. Following micro-CT and biomechanical analysis, the PT–bone complexes from each group underwent decalcification and paraffin embedding, followed by sectioning using a saw microtome to a thickness of 6 μm, parallel to the longitudinal axis of the tibia. The microstructure of the new bone, the TBI, and the alignment of the fibrocartilage cells were assessed through Hematoxylin and eosin (H&E) staining. The relative width of the PT–bone interface was calculated as part of the histomorphometric analysis. The continuity and orientation of collagen at the repaired interface were evaluated using modified Masson trichrome staining. The fibrocartilage area, which was meticulously outlined and measured with ImageJ software, was analyzed using Safranin O/fast green (S&F) staining. The histological score was quantified based on three criteria (fibrocartilage formation, new bone formation, and graft bonding to adjacent tissues), with a maximum score of nine points indicating optimal results.[28]

2.12. Statistical analysis

GraphPad Prism 10 software (GraphPad Co., USA) was employed to compute all statistical data. The findings were presented as the mean ± standard deviation. One-way or two-way analysis of variance (ANOVA) was utilized to compare three or four groups of datasets. Statistical differences were considered significant for all outcomes when the p-value was <0.05.

3. Results

3.1. Characterization of scaffolds

The SEM analysis of the PPH scaffold revealed a gradient image with spatial distribution (Figure 1A). Following the application of PDA and the subsequent reaction, distinct nanoparticles resembling the adhesive plaque of mussels were deposited onto the scaffold. These nanoparticles aggregated on the surface, varying in size from the nano- to micro-scale (Figure 1B). After treatment with SBF, it was observed that with an increase in oxygen density due to the elevation of base inclination, HA nanoparticles exhibited an almost spherical shape, with a diameter of 190.35 ± 41.96 nm in areas with lower HA concentration and 446.54 ± 125.42 nm in areas with higher HA concentration (Figure 1B). The predominant size distribution of nanoparticles in the lower HA concentration area was 140–240 nm (approximately 75%), while in the higher HA concentration area, it was 300–600 nm (approximately 81%) (Figure 1B). This variation in nanoparticle size indirectly indicated a gradient spatial distribution. Non-contact AFM demonstrated that the topography of all HA particles was relatively consistent and homogeneous across the modified EHD-printed fiber surface (Figure 1C). EDS was conducted to confirm the presence of the corresponding elements, indicating successful immobilization of calcium (Ca) and phosphorus (P) onto the scaffold surface, with a Ca/P ratio of 7.06% (Figure 1D). Additionally, XPS analysis was performed to further validate the surface elemental spectrum. The binding energy positions were as follows: C1s (284.8 eV) corresponding to C-C and C-H, O1s (531.5 eV) indicating C-O or C=O, N1s (399 eV) from PDA, P2p (132.2 eV) representing P=O, and Ca2p (346 eV) from potential Ca^{2+} (Figure 1E). Finally, following PDA

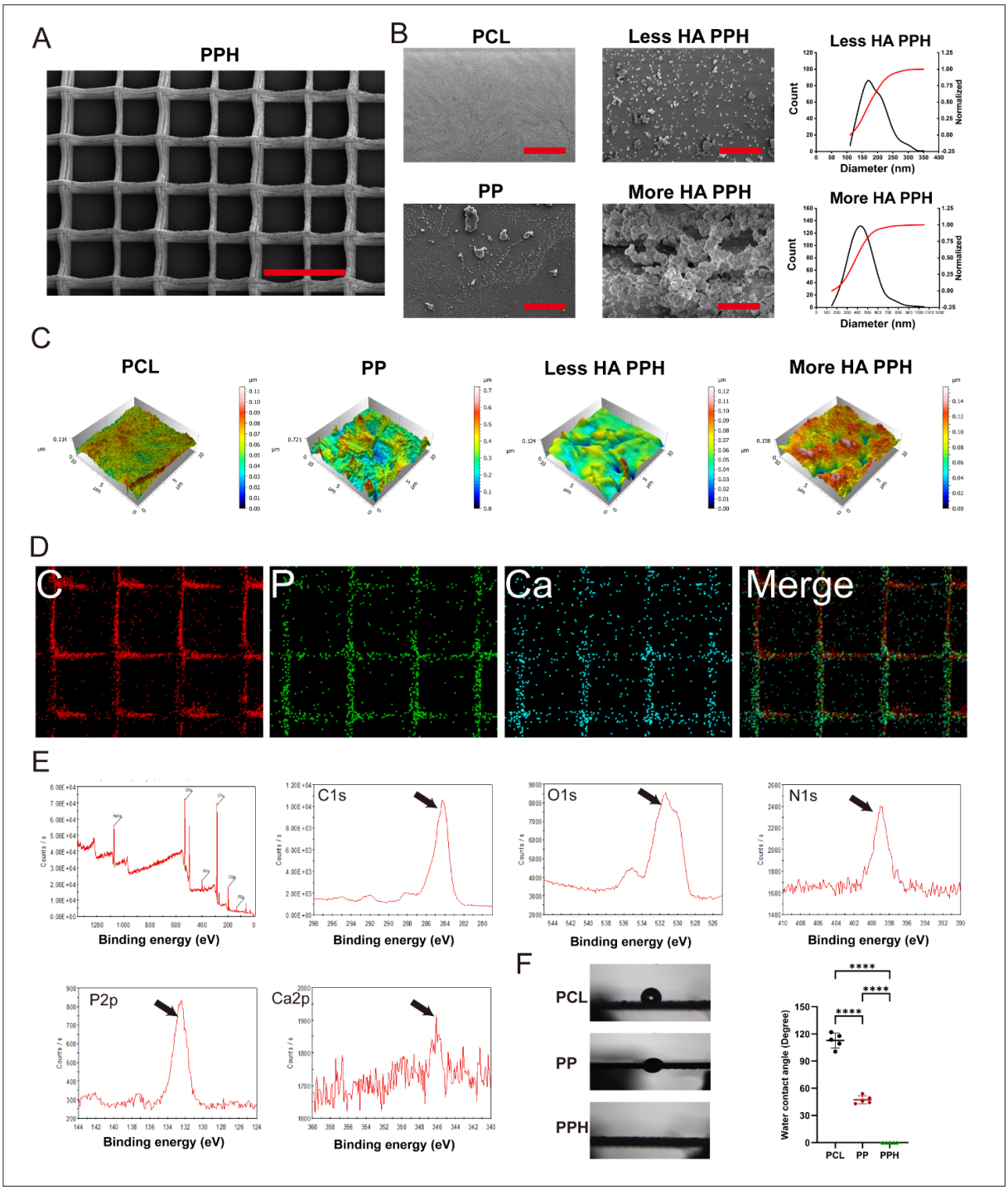

Figure 1. Surface characteristics of the EHD-printed scaffolds. (A) Representative SEM image of PPH scaffold at low magnification (×100). (B) SEM of PCL and PP scaffolds at high magnification (×10,000) and particle distribution of PPH scaffold fiber surface with low and high nHA concentrations. (C) Scanning of scaffold surfaces using non-contact AFM reveals varied distributions. (D) EDS elemental mapping for C, P, and Ca. (E) XPS spectra of the survey scan, C1s, O1s, N1s, P2p, and Ca2p of the PPH scaffold. For E, the arrow denote the corresponding elements binding energy peak. (F) The WCA of scaffolds and corresponding quantitative analysis. ****$p < 0.0001$. Scale bars: 500 μm (A); 5 μm (B). Abbreviations: AFM, atomic force microscopy; EDS, electron dispersive spectroscopy; EHD, electrohydrodynamic; HA, hydroxyapatite; PCL, poly(ε-caprolactone); PPH, PCL-PDA-HA; PP, PCL-PDA; SEM, scanning electron microscopy; WCA, water contact angle; XPS, X-ray photoelectron spectroscopy.

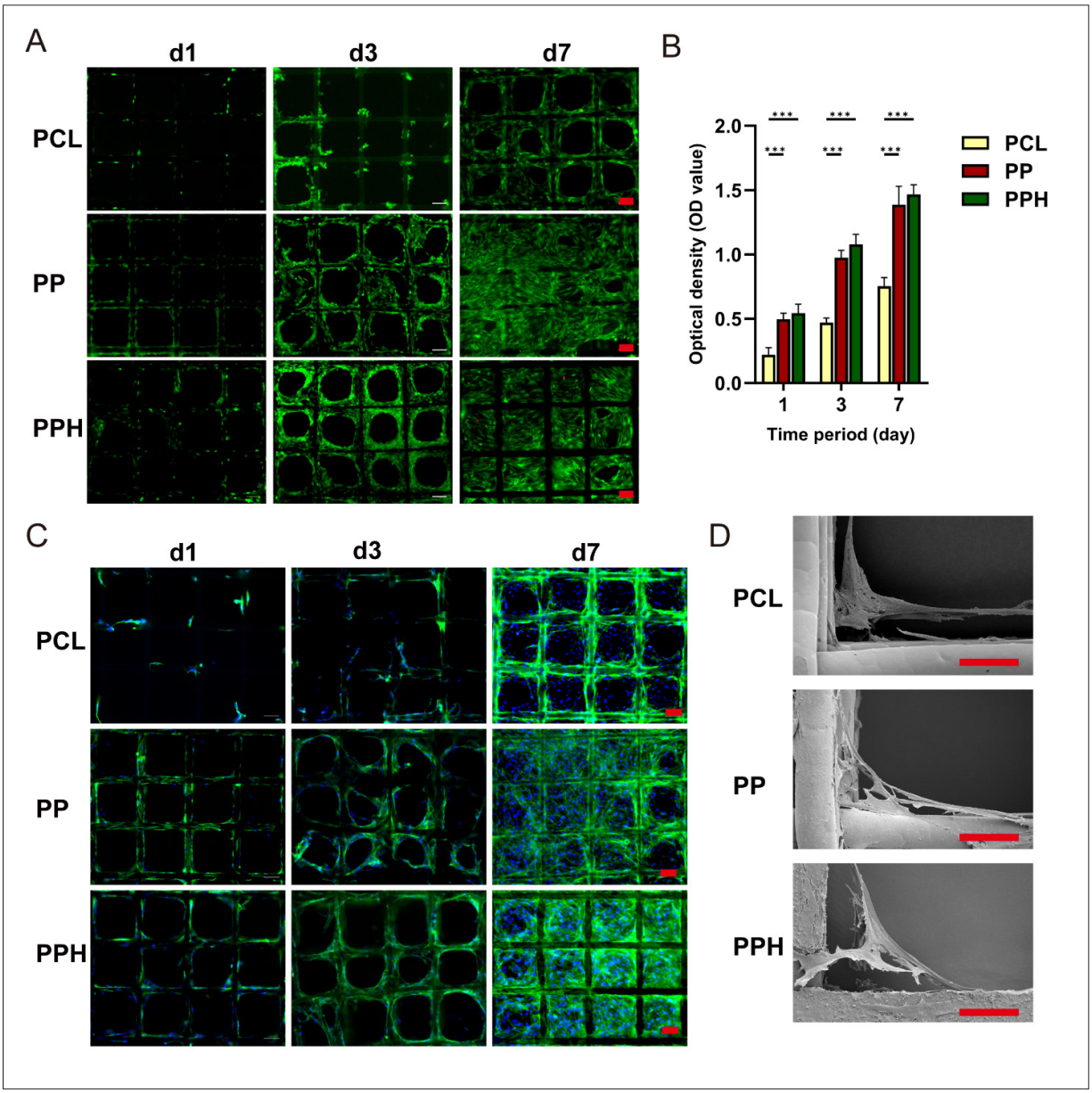

Figure 2. Biocompatibility of PCL, PP, and PPH scaffolds. (A) Live/dead staining of TSPCs on each scaffold after 1, 3, and 7 days of culture. (B) TSPCs proliferation on scaffolds was evaluated by CCK-8 assay. ***$p < 0.001$. Scale bars: 100μm (A) and (C), 50 μm (D). (C) Images of cell cytoskeleton (green) and nuclei (blue) of TSPCs exhibiting the effects of three scaffolds on TSPCs morphology at days 1, 3, and 7. (D) SEM images of TSPCs seeded on PCL, PP, and PPH substrates on day 1. Abbreviations: PCL, poly(ε-caprolactone); PP, PCL-PDA; PPH, PCL-PDA-HA; SEM, scanning electron microscopy; TSPCs, tendon stem/progenitor cells.

coating, the hydrophilicity of the scaffolds was significantly enhanced, as evidenced by a decrease in WCA (Figure 1F). Notably, the PPH scaffold, exhibiting a zero-degree WCA, demonstrated super-hydrophilicity (Figure 1F).

3.2. *In vitro* tendon stem/progenitor cell culture

3.2.1. Cell viability, proliferation, and morphology

The proliferation of TSPCs on EHD-printed scaffolds was investigated to evaluate their compatibility. Given the strong adhesion capacity of TSPCs and their infiltration into the scaffolds, CLSM was utilized to assess live/dead

staining. As illustrated in Figure 2A, only a limited number of TSPCs adhered to the surface of the pure PCL scaffold on day 1 post-seeding, primarily due to its hydrophobicity. In contrast, TSPCs were more concentrated on each individual scaffold fiber, suggesting that the modified surface materials are more conducive to cell adhesion and dissemination. Initially, TSPCs expanded from the peripheral fibers toward the core, ultimately saturating all fibers in the scaffolds. The CCK-8 assay results indicated that TSPCs exhibited a higher growth rate on the PP and PPH scaffolds between days 1 and 7. The absorbance values for TSPCs seeded on the PP and PPH scaffolds were significantly greater than those on the PCL scaffold by day 7, indicating that the enhanced hydrophilicity of the materials also promoted proliferation (Figure 2B). The initial spreading and adherence of TSPCs to the scaffold fibers were more pronounced on the PP and PPH scaffolds compared to the PCL scaffold on day 1 (Figure 2C). After 7 days, a comprehensive and widely distributed cell morphology was observed, filling the entire scaffold fibers and the intermediate pores (Figure 2C). SEM images of the cell morphology corroborated the findings from the cytoskeleton staining (Figure 2D).

3.2.2. Related gene and protein expression

The expression of tenogenic, chondrogenic, and osteogenic genes was assessed to determine the differentiation among three groups *in vitro*. At the genetic level, all related genes were expressed without statistical differences at day 7 of co-culture (Figure 3A–C). By day 14, the expression of tenogenic and chondrogenic genes in the PPH group increased slightly compared to other groups, indicating that PDA and HA did not inhibit gene expression (Figure 3A and B). However, as expected, on day 14, the expression of osteogenic genes, including *Bmp2* (~3.12-fold, $p < 0.001$) and *Runx2* (~3.24-fold, $p < 0.001$), was significantly elevated compared to those of the PCL group (Figure 3C). Simultaneously, the western blot (WB) analysis demonstrated that nHA did not inhibit or promote tenogenic and chondrogenic expression at the protein level (Figure 3D and E). Consistent with the expression of certain osteogenic genes, PPH scaffolds significantly facilitated the expression of RUNX2 and ALP at the protein level on day 14, as indicated by the WB results (Figure 3F).

3.3. *In vivo* animal study

3.3.1. Macroscopic observation

No wound infections or fatalities were observed during the entire follow-up. Following the anesthetization and exposure of rat knee joints, all grafts remained intact and exhibited comparable texture and color between groups (Figure 4A).

3.3.2. Micro-computed tomography evaluation

The micro-CT scan was utilized to assess the newly regenerated bone in the TBI of the knee joint, and the findings were presented in Figure 4B–D. The value of BV/TV and BMD in all groups exhibited an increased trend from 1 to 3 months. Micro-architectural parameters calculation indicated that the PPH group had significantly higher BV/TV (Figure 4B) and BMD (Figure 4D) compared with other groups in 1, 2, and 3 months postoperatively. The 3D reconstructions of the interface tissue directly revealed that more trabecular bone formation was found in the PPH group at 2 and 3 months after surgery (Figure 4C). These findings demonstrated that PPH scaffolds significantly facilitated osteointegration between the graft and the interface of the bone tissue.

3.3.3. Biomechanical assessment

From 1 to 3 months post-surgery, the failure load (FL) and stiffness were measured and calculated at different time points (Figure 4E). The FL in all scaffold groups was significantly higher than in the control group. Meanwhile, regarding FL, no significant differences were found between the PCL and PP groups, and the FL value in the PPH group was much higher (Figure 4F). The stiffness in each group displayed a similar trend with the FL value, with greater biomechanical strength in the PPH group (Figure 4G).

3.3.4. Histological analysis

Histological analysis of the TBI was conducted to evaluate the healing efficacy at various phases following surgery. The width of the TBI structure negatively impacted the quality of healing.[29] According to H&E staining results, fibrous fibrovascular interface formation was observed in all groups at the TBI site (Figure 5A). Notably, the PPH group exhibited the least pronounced fibrous interface at the TBI compared to the other groups, as evidenced by the semi-quantitative measurement of interface width at 1, 2, and 3 months post-surgery (Figure 5B). During the follow-up period after the operation, S&F staining was performed to assess the newly formed fibrocartilage layers within the TBI tissue. In the sham group, minimal cartilage was detected throughout the entire follow-up period post-surgery. Among the four groups, the PPH scaffold demonstrated the highest degree of fibrocartilage formation at the junction compared to the other groups (Figure 5C). Furthermore, semi-quantitative analysis revealed that the PPH group had the largest fibrocartilage area at 1, 2, and 3 months (Figure 5D). At the TBI site, Sharpey-like collagen fibers were most prominent in the PPH group compared to the other three groups at each postoperative time point (Figure 5E). Additionally, by 3 months post-surgery, it was evident that the material scaffolds had integrated with the bone area of the TBI in the PCL, PP, and PPH groups (Figure 5E).

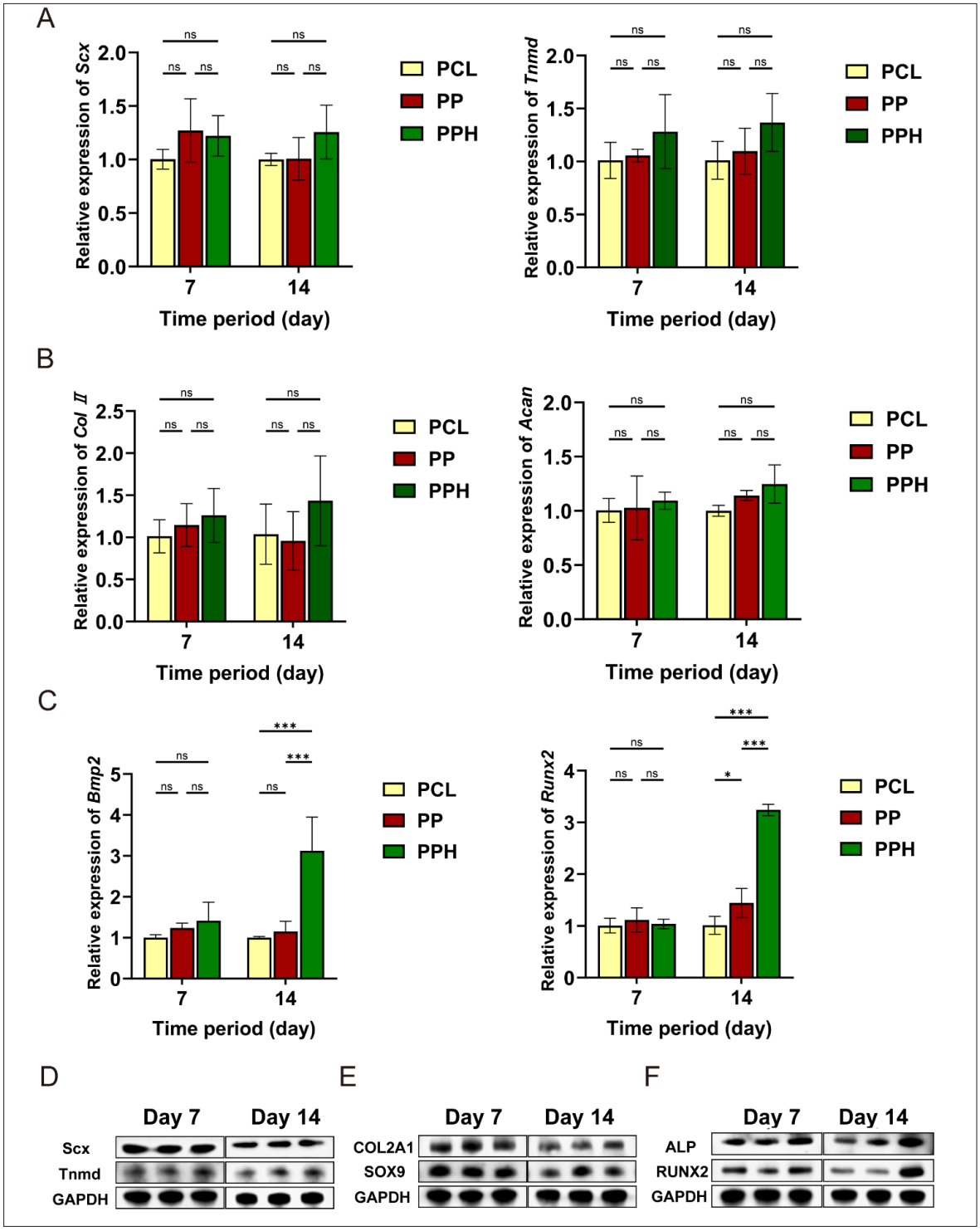

Figure 3. Quantitative qRT-PCR and WB indicated that only osteogenesis of TSPCs was enhanced by the PPH scaffold. (A) The expression of tendon-related genes level, including *Scx* and *Tnmd*. (B) The expression of cartilage-related genes level, including *Col II* and *Acan*. (C) The expression of bone-related genes in the PPH group, including *Bmp2* and *Runx2*, was significantly upregulated compared with the other two groups. (D) WB of tenogenic (Tnmd and Scx) protein levels of TSPCs cultured on PCL, PP, and PPH substrates after 7 and 14 days. (E) WB of chondrogenic (SOX9 and COL2A1) protein levels of TSPCs cultured on PCL, PP, and PPH substrates after 7 and 14 days. (F) WB of osteogenic (ALP and RUNX2) protein levels of TSPCs cultured on PCL, PP, and PPH substrates after 7 and 14 days. *$p < 0.05$; ***$p < 0.001$; ns: not significant. Abbreviations: PCL, poly(ε-caprolactone); PPH, PCL-PDA-HA; PP, PCL-PDA; qRT-PCR, quantitative reverse transcription polymerase chain reaction; TSPCs, tendon stem/progenitor cells; WB, Western Blot.

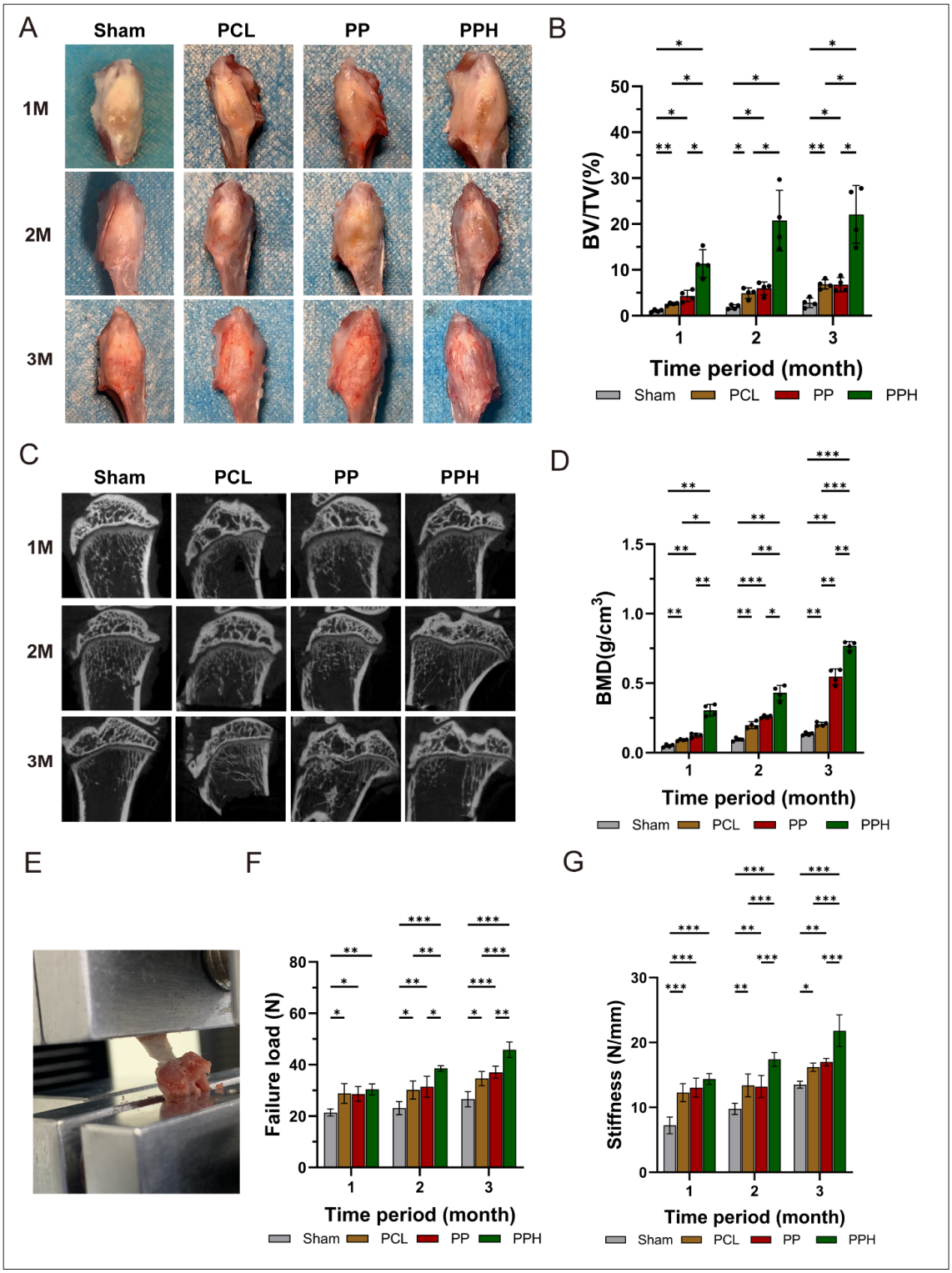

Figure 4. Biomechanical and micro-CT analyses of samples. (A) Macroscopic view of the specimen at 1, 2, and 3 months (M). (B) The bone volume fraction (BV/TV) of all groups at 1, 2, and 3 months (n = 4). (C) Representative images of the tibial tuberosity at 1, 2, and 3 months postoperatively. (D) Bone mineral density (BMD) values of the repaired TBI at 1, 2, and 3 months postoperatively. (E) Appearance of the biomechanical test specimen. (F and G) The failure load (F) and stiffness (G) of test specimens from each group (n = 4). *p < 0.05; **p < 0.01; ***p < 0.001. Abbreviations: PCL, poly(ε-caprolactone); PP, PCL-PDA; PPH, PCL-PDA-HA.

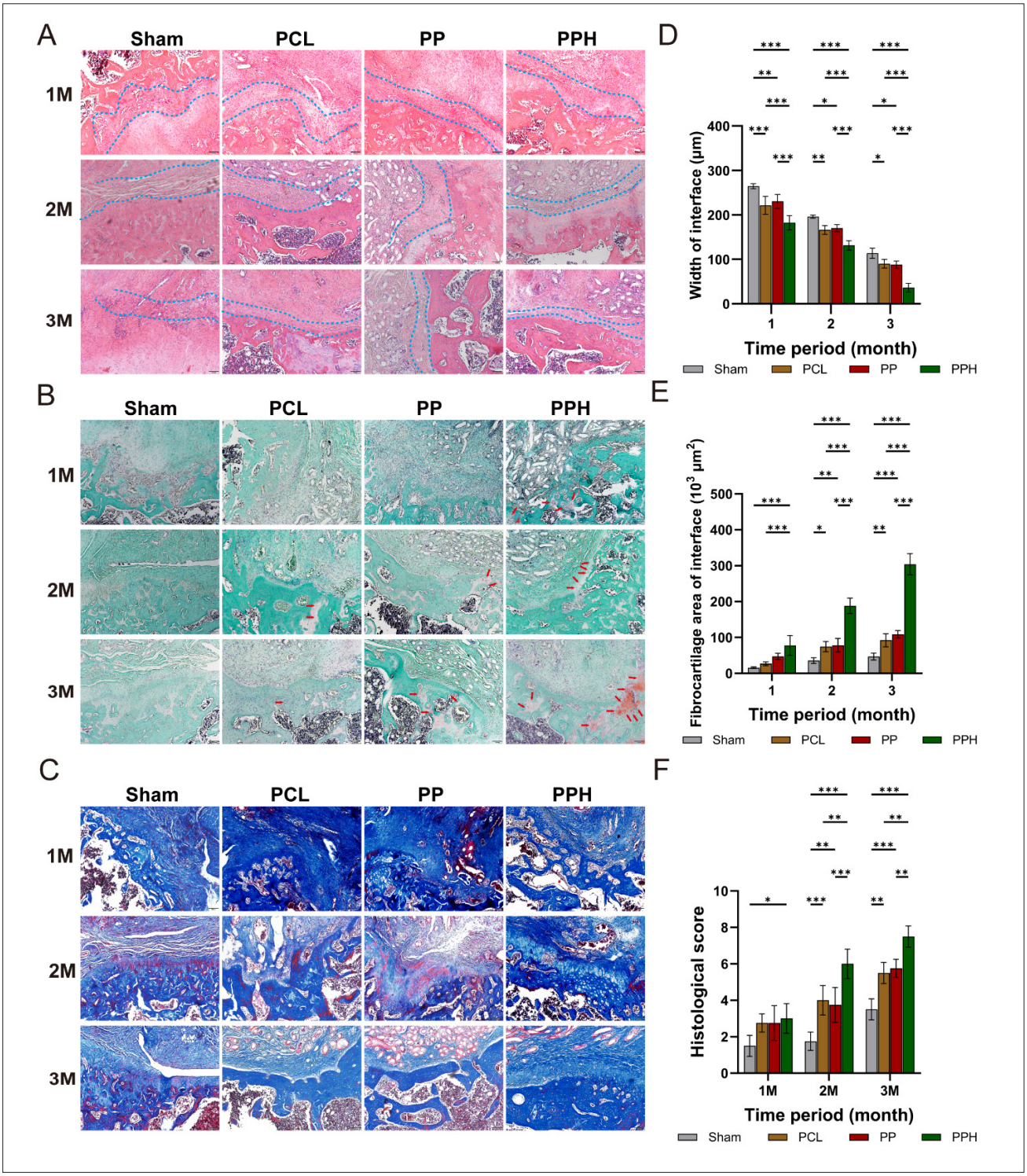

Figure 5. Histopathological analysis of samples of scaffolds in Sprague-Dawley rats PT defect models. (A) Representative image of H&E staining of the TBI at 1, 2, and 3 months postoperatively. Irregular blue lines depict the interface. (B) Quantitative analysis of the relative width of the TBI (n = 4). Yellow arrows indicate the presence of fibrocartilage tissues. (C) Representative images of S&F staining of the TBI at 1, 2, and 3 months postoperatively. (D) Quantitative analysis of the fibrocartilage area of the TBI (n = 4). (E) Representative image of Masson staining of the TBI at 1, 2, and 3 months postoperatively. (F) Mean histological scores (mean ± standard deviation) of the TBI of all groups at 1, 2, and 3 months postoperatively (n = 4). *p < 0.05; **p < 0.01; ***p < 0.001. Abbreviations: H&E, Hematoxylin and eosin; PCL, poly(ε-caprolactone); PP, PCL-PDA; PPH, PCL-PDA-HA; PT, patellar tendon; S&F, Safranin O/fast green; TBI, tendon-to-bone interface.

At 1 month post-surgery, no significant difference was observed in histological scores between the PCL, PP, and PPH scaffolds; however, a statistical difference was noted only between the PPH and sham groups (Figure 5F). Regarding the scores at 2 and 3 months post-surgery, the results indicated that all scaffold groups performed better than the sham group, with the PPH group demonstrating the most favorable outcomes. No significant differences were found between the PCL and PP groups (Figure 5F).

4. Discussion

In this study, we employed a modified facile method to fabricate PDA gradients through the oxygen diffusion phenomenon, resulting in thickness gradients of HA nanoparticles on an EHD-printed scaffold. The results demonstrated that this gradient scaffold, loaded with TSPCs, significantly enhanced the healing of TBI injuries. Characterization tests confirmed the successful fabrication of gradient nanoparticles on the scaffold surface. Biocompatibility assessments, along with quantitative reverse transcription polymerase chain reaction and WB results, indicated that the osteogenic capability of TSPCs was promoted by HA *in vitro*. Histological analyses, micro-CT imaging, and biomechanical tests collectively support the potential of the modified EHD-printed scaffold in restoring TBI function.

Numerous reports have sought to implement various gradient synthesis strategies to promote healing in TBI injury. To create a biomimetic scaffold that facilitates TBI regeneration, Qiu et al.[30] employed a direct method involving the swelling of a composite film made from PCL and hyaluronic acid, thereby achieving a gradient in HA density at the interface. Stanton et al.[31] developed aligned gelatin micro-ribbon hydrogel scaffolds featuring an HA gradient to simulate TBI, utilizing a single cell source (human mesenchymal stem cells) to induce zonal-specific differentiation, which represents a promising approach. Su et al.[32] fabricated gradient PCL/calcium phosphate silicate composite films using a tape casting procedure. The resulting scaffold demonstrated superior capacity for TBI regeneration, characterized by improved collagen alignment, gradient mineralized distribution, and increased tissue cellularity. These studies primarily focused on a monophasic method for fabricating the interface, rather than employing a multiphasic scaffold, yet achieved satisfactory efficacy. Bai et al.[33] assessed microfibrous dual-triphase scaffolds (composed of nHA, nano-magnesium-oxide, and kartogenin) to demonstrate their biological advantages in enthesis healing. This scaffold could enhance cellular differentiation, biomechanical properties, and biochemical environment for TBI repair. In our study, we used a scaffold size of 250 μm for scaffold preparation because it represents the minimum distance required to maintain a neat structure with the highest fiber density structure while ensuring structural consistency. The results by Liu et al.[34] indicated that 3D-printed PCL scaffolds with 200 μm spacing could inhibit chondrocyte dedifferentiation. In the current study, the scaffolds with 250 μm were more appropriate. The deviations arise from the differences in scaffold materials and seed cells. Additionally, previous research has indicated that the hierarchical structure of scaffolds can further enhance TBI healing.[35–37] In a recent study, Zhang et al.[16] compared the healing efficacy of TBI using both monophasic and hierarchical grafts. They concluded that these two graft designs could achieve comparable healing results for TBI repair, as evidenced by histological and biomechanical outcomes. Hierarchical biomaterials have been validated as effective in facilitating *in situ* TBI regeneration and remodeling in both *in vivo* and *in vitro* studies; however, the complexity of their design and construction may limit their practical application. Therefore, we employed a more feasible and straightforward method, utilizing a biomaterial loaded with osteogenic elements to achieve comparable efficacy.

Osteogenesis, driven by osteogenic components, is a critical process in TBI regeneration by regulating new bone formation and remodeling. Previous studies have suggested that this process may serve as a therapeutic target for TBI healing.[10,38,39] In our research, we investigated the efficacy of gradient HA in facilitating TBI healing via osteogenesis. HA has been demonstrated to promote the osteogenesis of stem cells and enhance osteoinduction at the interface.[23,25,40] Micro-CT, BMD, BV/TV, H&E staining, and biomechanical assessments indicated that the PPH scaffold demonstrated superior new bone formation and bone remodeling compared to the PCL and PP scaffolds, corroborating findings from previous studies.[11,31,41] However, the specific mechanisms by which gradient minerals facilitate interface healing, as well as the potential pivotal role of gradient thickness, require further investigation.

Exogenous stem cells have been identified as significant contributors to the construction of TBI models in the existing literature, with many studies focusing on their potential to regenerate injured TBI tissues. Matsumoto et al.[12] demonstrated that adipose-derived stem cell sheets facilitated TBI healing and graft mid-substance recovery in an *in vivo* rabbit model. Liu et al.[42] engineered a composite of bone marrow-derived mesenchymal stem cell (BMSC) sheets, finding that this approach enhanced rotator cuff healing in a canine non-weight-bearing model. Zuo

et al.[43] established that costal cartilage stem cells exhibited superior survival, proliferation, and *in situ* regeneration capabilities of TBI tissues following transplantation, compared to BMSCs. Furthermore, TSPCs, which possess enhanced tenogenic and osteogenic properties, as well as a stronger spontaneous chondrogenic potential, warrant greater attention in the context of TBI healing.[1] However, to the best of our knowledge, there are few studies addressing the role of exogenous TSPCs in TBI regeneration. Tarafder et al.[44] employed scaffolds embedded with tenogenic, chondrogenic, and osteogenic growth factors to facilitate their release *in vivo*. These scaffolds could effectively recruit endogenous TSPCs and promote the integrative healing of TBI through the regeneration of a robust fibrocartilaginous interface. However, it remains unclear whether exogenous TSPCs transplantation can recruit endogenous TSPCs or support their spontaneous differentiation.

In the current study, we designed the mineralization gradation using a modified dopamine self-polymerization reaction tailored to oxygen diffusion gradients, thereby forming gradient HA nanoparticles. Moreover, to the best of our knowledge, we are the first to transplant TSPCs into the TBI region as seed cells. Previous literature has reported various methods to achieve compositional gradation, including regulation of immersion time in SBF,[15,45] manipulation of bioactive macromolecule deposition,[46] modulation of electrospray deposition with a physical moving mask,[47] and gravity-induced sedimentation and diffusion.[48] In our study, the inclined PDA nanoparticles serve as a bioactive and biocompatible template for the formation of a green HA gradient structure, which creates a biomimetic microenvironment conducive to the healing of TBI injury. This straightforward and efficient strategy leverages extensive catechol chemistry and nanoparticles to achieve the desired gradient structure, promoting osteogenesis while also scavenging excessive reactive oxygen species (ROS).[49] Elevated levels of ROS in the microenvironment can disrupt osteoblast function, increasing the likelihood of implant osseointegration failure.[50,51] Scaffolds with functional gradation can effectively mimic the distinct characteristics of transitional tissue, such as those found in TBI.[52] Therefore, the combination of our method with EHD-printed scaffolds can enhance biomineral gradients, thereby improving their capacity to facilitate TBI repair.

We first achieved a gradient of oxygen concentration by changing the tilt of the substrate to complete the gradient of dopamine, thereby further achieving the gradient of biomineralization. This simple modification imitated the gradient structure of the interface area, which is more conducive to the regeneration of TBI.

5. Conclusion

Our study focused on utilizing an inclined PDA strategy to fabricate a graded HA structure for facilitating TBI healing. This modification enhanced the surface hydrophilicity and roughness, making the scaffolds conducive to cell proliferation and adhesion. Meanwhile, gradient HA nanoparticles could promote the TSPCs towards osteogenesis *in vitro*, and we demonstrated the effectiveness of TSPCs in promoting TBI regeneration *in vivo* through a PT repair model. The findings suggest that the graded topographical HA may support interface regeneration. In summary, this study has established a user-friendly and beneficial bioactive framework to enhance the capacity of TSPCs in TBI restoration, indicating promising prospects for future translational applications.

Acknowledgments

The authors would like to thank the statistical professors from the Medical Statistics Teaching and Research Office at Air Force Medical University for their assistance in applying the appropriate statistical analyses to obtain the pertinent outcomes.

Funding

This work was supported by the National Natural Science Foundation of China (No. 31971272); the International Science and Technology Cooperation Key Program project of Shaanxi Province (No.2023-GHZD-25); and the Rapid Response Project of the Air Force Military Medical University (2023KXKT081).

Conflict of interest

Jiankang He serves as the Editorial Board Member of the journal but was not involved in the editorial and peer-review process conducted for this paper, directly or indirectly. Other authors declare they have no competing interests.

Author contributions

Conceptualization: Lei Wang, Hongbin Fan
Investigation: Jingyi Dang, Zhao Zhang, Weidong Tao, Liguo Sun
Methodology: Yubo Shi, Lei Wang, Zhennan Qiu
Formal analysis: Jiankang He, Zhennan Qiu, Hongbin Fan
Writing – original draft: Lei Wang, Liguo Sun, Zhennan Qiu
Writing – review & editing: Lei Wang, Hongbin Fan

Ethics approval and consent to participate

All animal experiments were approved by the Air Force Military Medical University Animal Ethics Committee and

were implemented complying with the Guidelines for the Care and Use of Laboratory Animals.

Consent for publication

Not applicable.

Availability of data

The data that support the findings of this study are available from the corresponding author upon reasonable request.

References

1. Shengnan Q, Bennett S, Wen W, et al. The role of tendon derived stem/progenitor cells and extracellular matrix components in the bone tendon junction repair. *Bone*. 2021;153:116172.
doi: 10.1016/j.bone.2021.116172

2. Derwin KA, Galatz LM, Ratcliffe A, et al. Enthesis repair: challenges and opportunities for effective tendon-to-bone healing. *J Bone Joint Surg Am*. 2018;100:e109.
doi: 10.2106/JBJS.18.00200

3. Bonnevie ED, Mauck RL. Physiology and engineering of the graded interfaces of musculoskeletal junctions. *Annu Rev Biomed Eng*. 2018;20:403-429.
doi: 10.1146/annurev-bioeng-062117-121113

4. Rossetti L, Kuntz LA, Kunold E, et al. The microstructure and micromechanics of the tendon-bone insertion. *Nat Mater*. 2017;16:664-670.
doi: 10.1038/nmat4863

5. Genin GM, Thomopoulos S. The tendon-to-bone attachment: unification through disarray. *Nat Mater*. 2017;16:607-608.
doi: 10.1038/nmat4906

6. Lu HH, Thomopoulos S. Functional attachment of soft tissues to bone: development, healing, and tissue engineering. *Annu Rev Biomed Eng*. 2013;15:201-226.
doi: 10.1146/annurev-bioeng-071910-124656

7. Yin Z, Chen X, Zhu T, et al. The effect of decellularized matrices on human tendon stem/progenitor cell differentiation and tendon repair. *Acta Biomater*. 2013;9:9317-9329.
doi: 10.1016/j.actbio.2013.07.022

8. Galatz LM, Ball CM, Teefey SA, et al. The outcome and repair integrity of completely arthroscopically repaired large and massive rotator cuff tears. *J Bone Joint Surg Am*. 2024;86:219-224.
doi: 10.2106/00004623-200402000-00002

9. Lu H, Chen C, Qu J, et al. Initiation timing of low-intensity pulsed ultrasound stimulation for tendon-bone healing in a rabbit model. *Am J Sports Med*. 2016;44:2706-2715.
doi: 10.1177/0363546516651863

10. Shi Q, Zhang T, Chen Y, et al. Local administration of metformin improves bone microarchitecture and biomechanical properties during ruptured canine achilles tendon-calcaneus interface healing. *Am J Sports Med*. 2022;50:2145-2154.
doi: 10.1177/03635465221098144

11. Jiang Q, Wang L, Liu Z, et al. Canine ACL reconstruction with an injectable hydroxyapatite/collagen paste for accelerated healing of tendon-bone interface. *Bioact Mater*. 2023;20:1-15.
doi: 10.1016/j.bioactmat.2022.05.003

12. Matsumoto T, Sato Y, Kobayashi T, et al. Adipose-derived stem cell sheets improve early biomechanical graft strength in rabbits after anterior cruciate ligament reconstruction. *Am J Sports Med*. 2021;49:3508-3518.
doi: 10.1177/03635465211041582

13. Lei T, Zhang T, Ju W, et al. Biomimetic strategies for tendon/ligament-to-bone interface regeneration. *Bioact Mater*. 2021;6:2491-2510.
doi: 10.1016/j.bioactmat.2021.01.022

14. He SK, Ning LJ, Yao X, et al. Hierarchically demineralized cortical bone combined with stem cell-derived extracellular matrix for regeneration of the tendon-bone interface. *Am J Sports Med*. 2021;49:1323-1332.
doi: 10.1177/0363546521994511

15. Liu W, Lipner J, Xie J, et al. Nanofiber scaffolds with gradients in mineral content for spatial control of osteogenesis. *ACS Appl Mater Interfaces*. 2014;6:2842-2849.
doi: 10.1021/am405418g

16. Zhang X, Han K, Fang Z, et al. Enhancement of tendon-to-bone healing: choose a monophasic or hierarchical scaffold? *Am J Sports Med*. 2023;51:2688-2700.
doi: 10.1177/03635465231182976

17. Lee H, Dellatore SM, Miller WM, et al. Mussel-inspired surface chemistry for multifunctional coatings. *Science*. 2007;318:426-430.
doi: 10.1126/science.1147241

18. Lee H, Rho J, Messersmith PB. Facile conjugation of biomolecules onto surfaces via mussel adhesive protein inspired coatings. *Adv Mater*. 2009;21:431-434.
doi: 10.1002/adma.200801222

19. Perikamana S, Shin YM, Lee JK, et al. Graded functionalization of biomaterial surfaces using mussel-inspired adhesive coating of polydopamine. *Colloids Surf B Biointerfaces*. 2017;159:546-556.
doi: 10.1016/j.colsurfb.2017.08.022

20. Madhurakkat PS, Lee J, Ahmad T, et al. Harnessing biochemical and structural cues for tenogenic differentiation of adipose derived stem cells (ADSCs) and development of an in vitro tissue interface mimicking tendon-bone insertion graft. *Biomaterials*. 2018;165:79-93.
doi: 10.1016/j.biomaterials.2018.02.046

21. Yang HC, Wu QY, Wan LS, et al. Polydopamine gradients by oxygen diffusion controlled autoxidation. *Chem Commun (Camb)*. 2013;49:10522-10524.
doi: 10.1039/c3cc46127k

22. Ghorbani F, Zamanian A, Behnamghader A, et al. A facile method to synthesize mussel-inspired polydopamine nanospheres as an active template for in situ formation of biomimetic hydroxyapatite. *Mater Sci Eng C Mater Biol Appl*. 2019;94:729-739.
doi: 10.1016/j.msec.2018.10.010

23. Liu F, Wang X, Chen T, et al. Hydroxyapatite/silver electrospun fibers for anti-infection and osteoinduction. *J Adv Res*. 2020;21:91-102.
doi: 10.1016/j.jare.2019.10.002

24. Cai J, Wan F, Dong Q, et al. Silk fibroin and hydroxyapatite segmented coating enhances graft ligamentization and osseointegration processes of the polyethylene terephthalate artificial ligament in vitro and in vivo. *J Mater Chem B*. 2018;6:5738-5749.
doi: 10.1039/c8tb01310a

25. El-Habashy SE, Eltaher HM, Gaballah A, et al. Hybrid bioactive hydroxyapatite/polycaprolactone nanoparticles for enhanced osteogenesis. *Mater Sci Eng C Mater Biol Appl*. 2021;119:111599.
doi: 10.1016/j.msec.2020.111599

26. Kokubo T, Takadama H. How useful is SBF in predicting in vivo bone bioactivity? *Biomaterials*. 2006;27:2907-2915.
doi: 10.1016/j.biomaterials.2006.01.017

27. Bi Y, Ehirchiou D, Kilts TM, et al. Identification of tendon stem/progenitor cells and the role of the extracellular matrix in their niche. *Nat Med*. 2007;13(10):1219-1227.
doi: 10.1038/nm1630

28. Cheng P, Han P, Zhao C, et al. High-purity magnesium interference screws promote fibrocartilaginous entheses regeneration in the anterior cruciate ligament reconstruction rabbit model via accumulation of BMP-2 and VEGF. *Biomaterials*. 2016;81:14-26.
doi: 10.1016/j.biomaterials.2015.12.005

29. Hays PL, Kawamura S, Deng XH, et al. The role of macrophages in early healing of a tendon graft in a bone tunnel. *J Bone Joint Surg Am*. 2008;90:565-579.
doi: 10.2106/JBJS.F.00531

30. Qiu J, Ahn J, Qin D, et al. Biomimetic scaffolds with a mineral gradient and funnel-shaped channels for spatially controllable osteogenesis. *Adv Healthc Mater*. 2022;11:e2100828.
doi: 10.1002/adhm.202100828

31. Stanton AE, Tong X, Jing SL, et al. Aligned gelatin microribbon scaffolds with hydroxyapatite gradient for engineering the bone-tendon interface. *Tissue Eng Part A*. 2022;28:712-723.
doi: 10.1089/ten.TEA.2021.0099

32. Su W, Guo J, Xu J, et al. Gradient composite film with calcium phosphate silicate for improved tendon -to-bone intergration. *Chem Eng J*. 2021;404:126473.
doi: 10.1016/j.cej.2020.126473

33. Bai L, Kasimu A, Wang S, et al. Electrohydrodynamic-printed dual-triphase microfibrous scaffolds reshaping the lipidomic profile for enthesis healing in a rat rotator cuff repair model. Small. 2024;2024:e2406069.
doi: 10.1002/smll.202406069

34. Liu X, Zhang Z, Shi Y, et al. Effect of electrohydrodynamic printing scaffold with different spacing on chondrocyte dedifferentiation. *Ann Transl Med*. 2022;10:743.
doi: 10.21037/atm-22-2796

35. Zhang X, Song W, Han K, et al. Three-dimensional bioprinting of a structure-, composition-, and mechanics-graded biomimetic scaffold coated with specific decellularized extracellular matrix to improve the tendon-to-bone healing. *ACS Appl Mater Interfaces*. 2023;15:28964-28980.
doi: 10.1021/acsami.3c03793

36. Bai L, Han Q, Meng Z, et al. Bioprinted living tissue constructs with layer-specific, growth factor-loaded microspheres for improved enthesis healing of a rotator cuff. *Acta Biomater*. 2022;154:275-289.
doi: 10.1016/j.actbio.2022.10.058

37. Chae S, Sun Y, Choi YJ, et al. 3D cell-printing of tendon-bone interface using tissue-derived extracellular matrix bioinks for chronic rotator cuff repair. *Biofabrication*. 2021;13(3): 035005.
doi: 10.1088/1758-5090/abd159

38. Zheng C, Lu H, Tang Y, et al. Autologous freeze-dried, platelet-rich plasma carrying icariin enhances bone-tendon healing in a rabbit model. *Am J Sports Med*. 2019;47:1964-1974.
doi: 10.1177/0363546519849657

39. Wang J, Xu J, Wang X, et al. Magnesium-pretreated periosteum for promoting bone-tendon healing after anterior cruciate ligament reconstruction. *Biomaterials*. 2021;268:120576.
doi: 10.1016/j.biomaterials.2020.120576

40. Chien CY, Tsai WB. Poly(dopamine)-assisted immobilization of Arg-Gly-Asp peptides, hydroxyapatite, and bone morphogenic protein-2 on titanium to improve the osteogenesis of bone marrow stem cells. *ACS Appl Mater Interfaces*. 2013;5:6975-6983.
doi: 10.1021/am401071f

41. Han F, Li T, Li M, et al. Nano-calcium silicate mineralized fish scale scaffolds for enhancing tendon-bone healing. *Bioact Mater*. 2023;20:29-40.
doi: 10.1016/j.bioactmat.2022.04.030

42. Liu Q, Yu Y, Reisdorf RL, et al. Engineered tendon-fibrocartilage-bone composite and bone marrow-derived mesenchymal stem cell sheet augmentation promotes rotator cuff healing in a non-weight-bearing canine model. *Biomaterials*. 2019;192:189-198.
doi: 10.1016/j.biomaterials.2018.10.037

43. Zuo R, Liu J, Zhang Y, et al. In situ regeneration of bone-to-tendon structures: Comparisons between costal-cartilage

derived stem cells and BMSCs in the rat model. *Acta Biomater*. 2022;145:62-76.
doi: 10.1016/j.actbio.2022.03.056

44. Tarafder S, Brito JA, Minhas S, et al. In situ tissue engineering of the tendon-to-bone interface by endogenous stem/progenitor cells. *Biofabrication*. 2019;12(1):15008.
doi: 10.1088/1758-5090/ab48ca

45. Li X, Xie J, Lipner J, et al. Nanofiber scaffolds with gradations in mineral content for mimicking the tendon-to-bone insertion site. *Nano Lett*. 2009;9:2763-2768.
doi: 10.1021/nl901582f

46. Tanes ML, Xue J, Xia Y. A general strategy for generating gradients of bioactive proteins on electrospun nanofiber mats by masking with bovine serum albumin. *J Mater Chem B*. 2017;5:5580-5587.
doi: 10.1039/C7TB00974G

47. Xue J, Wu T, Qiu J, et al. Promoting cell migration and neurite extension along uniaxially aligned nanofibers with biomacromolecular particles in a density gradient. *Adv Funct Mater*. 2020;30:2002031.
doi: 10.1002/adfm.202002031

48. Zhu C, Pongkitwitoon S, Qiu J, et al. Design and fabrication of a hierarchically structured scaffold for tendon-to-bone repair *Adv Mater*. 2018;30:e1707306.
doi: 10.1002/adma.201707306

49. Yu Y, Li X, Li J, et al., 2021, Dopamine-assisted co-deposition of hydroxyapatite-functionalised nanoparticles of polydopamine on implant surfaces to promote osteogenesis in environments with high ROS levels. *Mater Sci Eng C Mater Biol Appl.* 2021;131:112473.
doi: 10.1016/j.msec.2021.112473

50. Bolduc JA, Collins JA, Loeser RF. Reactive oxygen species, aging and articular cartilage homeostasis. *Free Radic Biol Med*. 2019;132:73-82. doi: 10.1016/j.freeradbiomed.2018.08.038

51. Tothova L, Celec P. Oxidative stress and antioxidants in the diagnosis and therapy of periodontitis. *Front Physiol*. 2017 8:1055.
doi: 10.3389/fphys.2017.01055

52. Zhu C, Qiu J, Thomopoulos S, et al. Augmenting tendon-to-bone repair with functionally graded scaffolds. *Adv Healthc Mater*. 2021;10:e2002269.
doi: 10.1002/adhm.202002269

ACCSCIENCE PUBLISHING

International Journal of Bioprinting

RESEARCH ARTICLE

Improved osseointegration and segmental stability of 3D-printed porous tantalum cages with micro-scale structures for spinal fusion

Hang Liang[1], Jingyao Tu[2], Bingjin Wang[1], Kun Wang[1], Xiaobo Feng[1], Wenbin Hua[1], Shuai Li[1], Xinyi Chen[2], Lei Tan[1]*, and Cao Yang[1]*

[1]Department of Orthopedics, Union Hospital, Tongji Medical College, Huazhong University of Science and Technology, Wuhan, Hubei, China

[2]Department of Oncology, Tongji Hospital, Tongji Medical College, Huazhong University of Science and Technology, Wuhan, Hubei, China

(This article belongs to the Special Issue: *Novel Materials and Processing for Medical 3D Printing and Bioprinting-Series 2*)

Abstract

Spinal fusion surgery is an effective therapy for patients with disc herniation and degenerative disc disease. In this procedure, the intervertebral cage plays a key role in reconstructing stability and achieving fusion, though its clinical efficacy is limited by inadequate osseointegration. In this study, we developed a tantalum (Ta) cage, featuring micro-scale roughness and a porous microstructure, using advanced three-dimensional (3D) printing techniques. The aim of the study was to investigate its osteogenic potential *in vitro* and intervertebral fusion capability *in vivo*. Compared with conventional polyetheretherketone cages, *in vitro* biological experiments demonstrated that the 3D-printed porous Ta (3D-pTa) cages significantly enhanced osteoblast adhesion, proliferation, and differentiation. *In vivo* spinal fusion studies in a sheep model demonstrated significant increases in bone-implant contact and bone volume to total volume ratios ($p < 0.05$) with the 3D-pTa cages, indicating marked bone ingrowth and effective spinal fusion. Additionally, mechanical tests revealed that the 3D-pTa cages provided consistent stability and stiffness, significantly reducing the range of motion at various time points ($p < 0.05$). Our findings indicate that the 3D-pTa cage effectively facilitates bone fusion and possesses reliable biosafety, highlighting its potential for future clinical application in spinal surgery.

Keywords: 3D printing; Interbody fusion cage; Osseointegration; Porous Ta; Spine surgery

***Corresponding authors:**
Cao Yang
(caoyangunion@hust.edu.cn)

Lei Tan
(tanlei_union@hust.edu.cn)

Citation: Liang H, Tu J, Wang B, et al. Improved osseointegration and segmental stability of 3D-printed porous tantalum cages with micro-scale structures for spinal fusion. *Int J Bioprint*. 2025;11(1):517-531. doi: 10.36922/ijb.4811

Received: September 10, 2024
1st revised: October 27, 2024
2nd revised: November 11, 2024
Accepted: November 21, 2024
Published Online: November 22, 2024

Copyright: © 2024 Author(s). This is an Open Access article distributed under the terms of the Creative Commons Attribution License, permitting distribution, and reproduction in any medium, provided the original work is properly cited.

Publisher's Note: AccScience Publishing remains neutral with regard to jurisdictional claims in published maps and institutional affiliations.

1. Introduction

Interbody fusion surgery is an effective treatment for unstable spinal segments, aimed at preserving neurological function and restoring spinal stability.[1] The procedure involves implanting an intervertebral cage within the disc space to maintain segmental stability and promote bony fusion between adjacent vertebrae.[2] Among the various materials used for intervertebral cages, polyetheretherketone (PEEK) has gained popularity due to its favorable biocompatibility and moderate elastic modulus, which mitigate the risks

of load redistribution and unintended bone remodeling.[3,4] Additionally, the radiolucency of PEEK allows for precise radiographic evaluation of fusion.[5,6] However, the biological inertness of PEEK poses challenges for osseointegration in clinical applications.[7] This limitation can lead to fibrous tissue encapsulation, isolating the implant from the host bone, and increasing the risk of pseudarthrosis.[8,9] Given these concerns, improving the osteogenic properties of cages remains a significant focus in the field of spinal fusion, highlighting the ongoing need for innovative materials that enhance osteointegration.

In clinical practice, the ideal bone implant must exhibit osteoinductive properties in physiological environments and mechanical characteristics that prevent stress shielding and subsidence.[10–12] Compared to titanium (Ti) and cobalt–chromium–molybdenum (CoCrMo) alloys, tantalum (Ta) offers superior mechanical properties and osteogenic activity, making it a preferred material in orthopedic applications.[13] However, the challenging fabrication process, high elastic modulus, and density of Ta limit its broader application in orthopedics.[14] Recently, porous Ta (pTa) has been increasingly preferred for load-bearing applications, owing to its excellent mechanical properties, bioactivity, and biosafety.[15] Notably, pTa has a lower elastic modulus than bulk Ta and does not release harmful ions, which is often a concern with conventional Ti alloys.[16] On one hand, Ta microparticles facilitate bone ingrowth, while the bioactive Ta pentoxide layer surpasses conventional bioactive fillers in promoting bone ingrowth and enhancing both early and long-term implant stability. On the other hand, the porous structure of pTa provides spaces conducive to bone ingrowth, facilitating early-stage osseointegration effectively.[17,18] The elastic modulus of engineered pTa can be tailored to closely align with that of human bone, thereby reducing stress shielding and offering long-term stability in load-bearing regions.[19] As a result, pTa has increasingly attracted attention as a preferred material for cages in recent years.

Commercial porous Ta (pTa) implants (Zimmer, United States of America [USA]), produced using chemical vapor deposition (CVD) technology, have gained significant market share and have been successfully used in various medical applications including spine fusion.[13] However, this traditional manufacturing approach comes with certain challenges, such as high costs, long production times, and inefficiency. Moreover, the CVD process limits customization and results in less flexible pore structures.[20] In contrast, additive manufacturing (AM), commonly known as 3D printing, offers a modern alternative by overcoming these issues.[21] 3D printing provides enhanced design flexibility and precision, enabling the production of porous metal scaffolds with complex architectures tailored to specific requirements.[22,23] These capabilities are particularly advantageous in medical contexts, where patient-specific solutions are increasingly needed.[24] Recent studies on pTa scaffolds fabricated using selective laser melting (SLM) technology indicate that optimizing the pore structure of Ta scaffolds can enhance cell infiltration, growth, and differentiation, thereby leading to superior *in vitro* and *in vivo* outcomes with higher rates of bone ingrowth and bone contact.[25] Similarly, research on pTa scaffolds prepared by SLM with varying porosities has demonstrated that higher porosity levels, particularly around 70%, facilitate better osteogenic proliferation, differentiation, and osseointegration, suggesting an optimal design for future clinical applications.[26] In addition to its biological benefits, recent studies have demonstrated that 3D-printed porous Ta scaffolds possess excellent mechanical strength and fatigue resistance that are advantageous for load-bearing applications. Wauthle et al.[27] produced a highly porous (80%) pure Ta implant by SLM, achieving a yield strength of 12.7 MPa, an elastic modulus of 1.22 GPa, and a fatigue limit of 7.35 MPa, indicating its relatively high resistance to cyclic loading. In another study, reducing the porosity from 85% to 65% led to a substantial increase in compressive yield strength, from 11.9 to 35.7 MPa, along with an increase in elastic modulus, from 1.1 to 3.0 GPa values that are within the range observed in human cancellous bone.[28] A comprehensive study on porous Ta scaffolds with varying pore sizes confirmed that the compressive strength of Ta was 25–30 MPa for a pore size of 450 μm and 10–12 MPa for a pore size of 650 μm, both comparable to the mechanical properties of natural trabecular bone.[29] Additionally, Chen et al.[30] demonstrated that lattice Ta structures exhibit excellent mechanical strength, with the Y-gradient structure achieving the highest plateau stress of 27.3 ± 0.9 MPa and a compressive modulus of 2.0 ± 0.1 GPa, demonstrating their suitability for load-bearing applications. These mechanical properties of 3D-printed porous Ta, combined with its biocompatibility, make it a promising material for spinal implants, where both mechanical support and biological integration are essential.

In this study, porous Ta cages were fabricated using SLM technology. *In vitro* studies were performed to assess the biocompatibility and osteogenic potential of the 3D-printed pTa cages, while *in vivo* osseointegration performance and biosafety were assessed and compared with conventional PEEK cages using the sheep cervical fusion model. Additionally, non-destructive range of motion (ROM) tests were employed to measure the mechanical stability. In summary, this work presents an effective strategy for manufacturing 3D-pTa cages with significant potential for clinical translation and application.

2. Methods

2.1. Fabrication and characterization of 3D-pTa cages

The 3D-pTa cages used in this study were manufactured by Huanan Farsoon High Technology Co., Ltd. (China). The 3D models of the samples were designed using Unigraphics NX (Siemens PLM Software, USA) based on computed tomography (CT) data of sheep cervical vertebrae. The cages were 3D printed using a Farsoon FS121M (China) laser printer with medical-grade pure Ta powder (average particle size: 15–53 μm). The porous structure was designed to achieve a pore size of 500–600 μm and a porosity of 68–78%, aiming to balance mechanical strength and biological performance. Customized PEEK scaffolds with identical shapes and dimensions were also fabricated (Shandong Weigao Orthopedic Device Co., Ltd., China). All samples underwent ultrasonic cleaning in acetone, anhydrous ethanol, and distilled water for 15 min each.

The pore characteristics and surface morphology of 3D-pTa cages were analyzed by scanning electron microscopy (Zeiss, Germany). The elemental composition of 3D-pTa cages was analyzed by energy dispersive spectroscopy (EDS; Zeiss, Germany). Atomic force microscopy (AFM, Bruker) was used to study the microscopic features of the 3D-pTa cages. Mechanical properties of the 3D-pTa cages were performed according to ISO-13314 standards. Uniaxial compression tests were conducted using a universal testing machine (Instron 3369, USA) at a crosshead speed of 0.5 mm/min until failure. The compressive strength and elastic modulus were calculated from the stress–strain curves.

2.2. *In vitro* cytocompatibility assessment

2.2.1. Cell culture

Mouse embryo osteoblast precursor (MC3T3-E1) cells were obtained from the China Center for Type Culture Collection. The MC3T3-E1 cells were cultured in minimum essential medium-α (MEM-α, Gibco, USA) containing 10% fetal bovine serum and 1% antibiotic-antimycotic solution at 37 °C in a humidified atmosphere with 5% CO_2. Cells were passaged using 0.25% trypsin-EDTA after reaching 90% confluence.

2.2.2. Cell adhesion and proliferation

MC3T3-E1 cells were seeded onto various cages at a concentration of 5×10^4 cells/mL. Cell adhesion and proliferation were measured using the Cell Counting Kit-8 (CCK-8) assay at predefined time points (6, 12, and 24 h; 1, 3, and 7 days). At each time point, the culture medium was replaced with 500 μL of 10% CCK-8 solution in each well. The absorbance at 450 nm was recorded by a microplate reader. The adhesion rate was calculated using the formula:

$$\text{Adhesion rate} = \frac{\text{ODtest} - \text{ODblank}}{\text{ODcontrol} - \text{ODblank}} \times 100\% \quad \text{(I)}$$

2.2.3. Cytoskeletal and live/dead staining

MC3T3-E1 cells were seeded onto different cages at a density of 5×10^4 cells/mL and incubated for 3 and 7 days at 37 °C with 5% CO_2. The samples were fixed in 4% paraformaldehyde for 10 min and subsequently permeabilized with 0.1% Triton X-100 for 15 min. The samples were then gently washed with phosphate-buffered saline (PBS; pH 7.4) and stained with DAPI (4',6-diamidino-2-phenylindole) solution (5 μg/mL) for 10 min to label the nuclei. Phalloidin-FITC was used to stain the cytoskeleton for 30 min, followed by observation under a confocal laser scanning microscope (CLSM; Olympus, Japan). For live/dead staining, MC3T3-E1 cells were cultured in different cages for 3 and 7 days. Cell viability was assessed using the live/dead staining kit according to the manufacturer's protocol. Fluorescence images were captured using a CLSM (Olympus, Japan).

2.2.4. Scanning electron microscopy observation of cell morphology

MC3T3-E1 cells were cultured on different scaffolds for 3 and 7 days. The cages were washed with PBS three times, followed by overnight fixation at 4 °C in 2.5% glutaraldehyde. After washing three times with deionized water, the cages were dehydrated through a sequential ethanol gradient (30%, 50%, 70%, 80%, 90%, and 100%) for 10 min each. Once dried and gold sputter-coated, the cages were visualized using scanning electron microscopy (SEM; Zeiss, Germany).

2.3. *In vitro* osteogenic response assessment

Alkaline phosphatase (ALP) activity, ALP staining, alizarin red S (ARS) staining, and quantitative polymerase chain reaction (qPCR) were employed to assess the osteogenic differentiation of MC3T3-E1 cells. After 3 days of culture on the different scaffolds, cells were trypsinized and reseeded in 24-well plates at a density of 2×10^4 cells/mL. Cells directly seeded in 24-well plates were used as the control group. ALP activity was examined on days 7 and 14 using p-nitrophenyl phosphate (pNPP) (BioDee, China), with absorbance quantified at 405 nm. ALP staining was conducted on days 7 and 14, while ARS staining was conducted on days 14 and 21. In brief, the cells were fixed with 4% paraformaldehyde and stained using ALP and ARS staining kits (Servicebio, China), then imaged using a microscope (Olympus, Japan). Quantitative analysis of calcium deposition was also performed. Runt-related

transcription factor 2 (Runx2), osteocalcin (OCN), osteopontin (OPN), and collagen I (COL I) were analyzed as osteogenic differentiation markers by qPCR on days 7 and 14. TRIzol reagent (Invitrogen, USA) was used to extract total RNA, followed by reverse transcription into complementary DNA (cDNA) with the PrimeScript RT reagent kit (Takara, Japan). Real-time PCR was carried out with SYBR Green Master Mix (Roche Applied Science, Germany), and GAPDH was used to normalize relative mRNA expression levels.

2.4. *In vivo* experiments

2.4.1. Animal model and surgical procedures

This study utilized a sheep cervical interbody fusion model, conducted following the ethical guidelines established by the Animal Care and Use Committee of Tongji Medical College, Huazhong University of Science and Technology. Twelve adult female sheep (24 months old; 45–55 kg) were randomly divided into two groups: 3D-pTa cages and PEEK cages. Under anesthesia, the sheep were positioned supine, and the surgical site was sterilized and draped. A standard Smith-Robinson anterior approach was used to expose the anterior surfaces of the C3-5 vertebrae. The annulus fibrosus at the C3-4 and C4-5 intervertebral spaces was incised, and the nucleus pulposus was removed. The endplates were prepared using a bone rasp to ensure the complete removal of non-osseous tissues while preserving the integrity of the posterior longitudinal ligament. The experimental group received two 3D-pTa cages per animal, while the control group received two PEEK cages, followed by anterior cervical plating. Postoperatively, ceftiofur sodium (3–5 mg/kg) was administered intramuscularly for three continuous days.

2.4.2. X-ray analysis

At postoperative weeks 0, 12, and 24, the sheep were euthanized and X-ray imaging (Faxitron, USA) was performed. The average disc space height (DSH) was evaluated using lateral radiographs based on the anterior and posterior DSH values:

$$\text{Average DSH} = \frac{\text{Anterior DSH} + \text{Posterior DSH}}{2} \quad \text{(II)}$$

2.4.3. Ex vivo non-destructive range-of-motion testing

At postoperative weeks 12 and 24, the sheep were euthanized, and the spinal segments containing the cages were carefully excised. The specimens were encased in saline-soaked gauze and preserved at -20 °C. Before testing, the spinal segments were gradually defrosted overnight at 4 °C, and the fixation plates and screws were removed. The specimens were clamped at both ends and placed in a spinal 3D motion testing machine (MTS858 Mini Bionix, USA). The system exerted pure moments to imitate flexion-extension (FE), lateral bending (LB), and axial rotation (AR). Continuous torque (6 Nm) was applied in three loading/unloading cycles non-destructively across all six motion modes. A digital image correlation (DIC) system (high-resolution stereo DIC, China) captured the segmental motion between vertebrae. ROM was recorded based on the degree of displacement under maximum load, while stiffness was determined by the slope of the moment–ROM curve.

2.4.4. Histological analysis

After non-destructive biomechanical testing, the cervical spine segments were dehydrated using a sequential ethanol gradient (70–100% v/v) and infiltrated with methyl methacrylate. The segments were sliced into 150 μm sections with a microtome (Leica Microsystems, Germany) and polished to a target thickness (50 μm). Histological sections were stained with hematoxylin-eosin (HE) and methylene blue-acid fuchsin to observe the mineralized tissue within and surrounding the cages. Histological images were acquired with a polarized optical microscope (Olympus, Japan). The bone volume to total volume (BV/TV) ratio was estimated by calculating the ratio of bone area and total scaffold area. The bone-implant contact (BIC) was defined as the percentage of the implant perimeter showing direct bone-to-implant contact without any intervening soft-tissue layers. In this study, BIC was quantified by calculating the ratio of the length of bone tissue directly contacting the inner surface of the implant window to the total perimeter length of the implant window of the cage. BIC is calculated using the following equation:

$$\text{BIC} = \frac{\text{Bone} - \text{implant contact length in the implant window}}{\text{Total perimeter of the implant window}} \times 100\% \quad \text{(III)}$$

2.4.5. In vivo biosafety assessment

The health status of the sheep was monitored daily postoperatively. Cerebrospinal fluid biochemical parameters, including total protein (TP), albumin (ALB), glucose (GLU), sodium (Na), and chloride (Cl), as well as hematological parameters, including white blood cells (WBC), neutrophils (NEU), neutrophil percentage (NEU%), red blood cells (RBC), hemoglobin (HB), and platelets (PLT), were measured preoperatively and at postoperative weeks 12 and 24. Spinal cord specimens were collected at 24 weeks post-surgery and stained with HE to assess potential pathological changes.

2.5. Statistical analysis

Statistical evaluation was carried out using SPSS version 20.0, with results presented as mean ± standard deviation. Data were collected from at least three independent experiments and evaluated using the Student's *t*-test for two-group comparisons and one-way analysis of variance (ANOVA) for multi-group analyses. Statistical significance was determined at $^{*}p < 0.05$, $^{**}p < 0.01$, and $^{***}p < 0.001$.

3. Results

3.1. Characterization of the 3D-pTa cage

Figure 1A and B illustrates the fabrication process and external appearance of the 3D-pTa cage, respectively. Macroscopically, the cage surface is smooth and uniform, featuring a consistent porous structure. The SEM images further revealed the microstructure of the 3D-pTa cage (Figure 1D), displaying uniform strut diameters with a micro-scale rough surface. The surface micromorphology and roughness of PEEK scaffolds were further detected by AFM (Figure S1, Supporting Information). The observed pore sizes at the micro-level corresponded well with the macroscopic design. Additionally, EDS analysis confirmed that the 3D-pTa cage consisted solely of Ta and oxygen elements (Figure 1C and E). These findings validate the successful fabrication of a porous pure Ta cage using 3D printing. The measured pore size, porosity, and mechanical strength of the 3D-pTa cages are listed in Table S1,

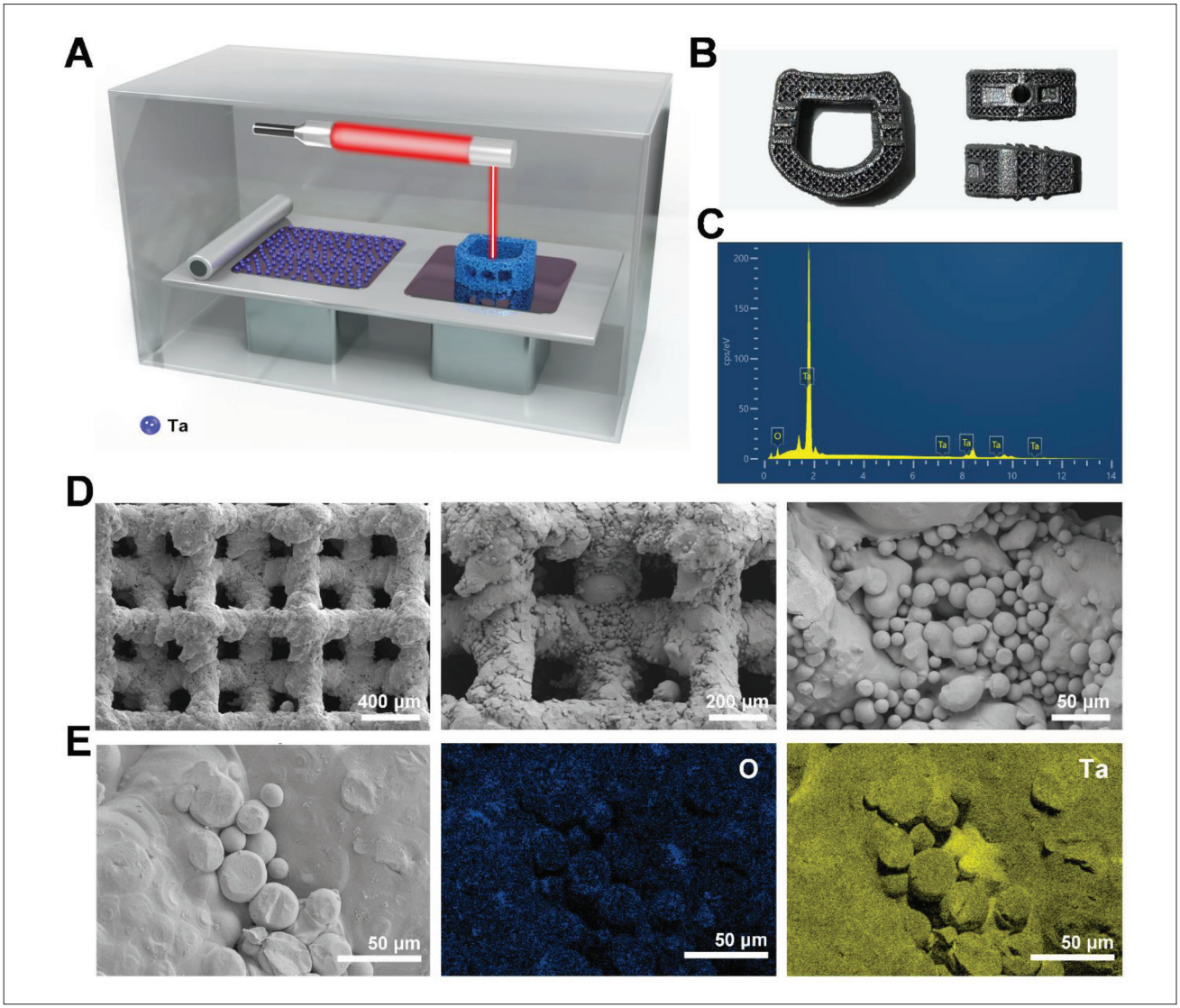

Figure 1. Characterization of the 3D-pTa cage. (A) Schematic illustration for the fabrication of the 3D-pTa cage. (B) Photographs of the actual 3D-pTa cage. (C) EDS analysis of the 3D-pTa cage. (D) SEM micrographs of the 3D-pTa cage. (E) EDS mapping of the 3D-pTa cage. Scale bars: 400 μm (D, left); 200 μm (D, middle); 50 μm (D, right; E). Abbreviations: EDS, energy dispersive spectroscopy; SEM, scanning electron microscopy.

Supporting Information. The compressive strength of the 3D-pTa cages was found to be 75.28 MPa, and the elastic modulus was approximately 1.92 GPa. These values are within the range of human cancellous bone and indicate that the cages possess sufficient mechanical strength for load-bearing applications in spinal fusion.

3.2. *In vitro* cytocompatibility evaluation of the 3D-pTa cage

Given that cell adhesion is a primary biological response when interacting with biomaterials, MC3T3-E1 cell adhesion was assessed at 6, 12, and 24 h. As displayed in Figure 2A, at all measured time points, the adhered cell count in the 3D-pTa cage group was markedly higher than in the PEEK and control groups ($p < 0.05$). Cell proliferation activity was further assessed after culturing for 1, 3, and 7 days. The results indicated time-dependent cell proliferation across all groups, with optical density (OD) values in the 3D-pTa group consistently higher compared to the PEEK and control groups, suggesting enhanced cell adhesion and proliferation in the 3D-pTa cages (Figure 2B).

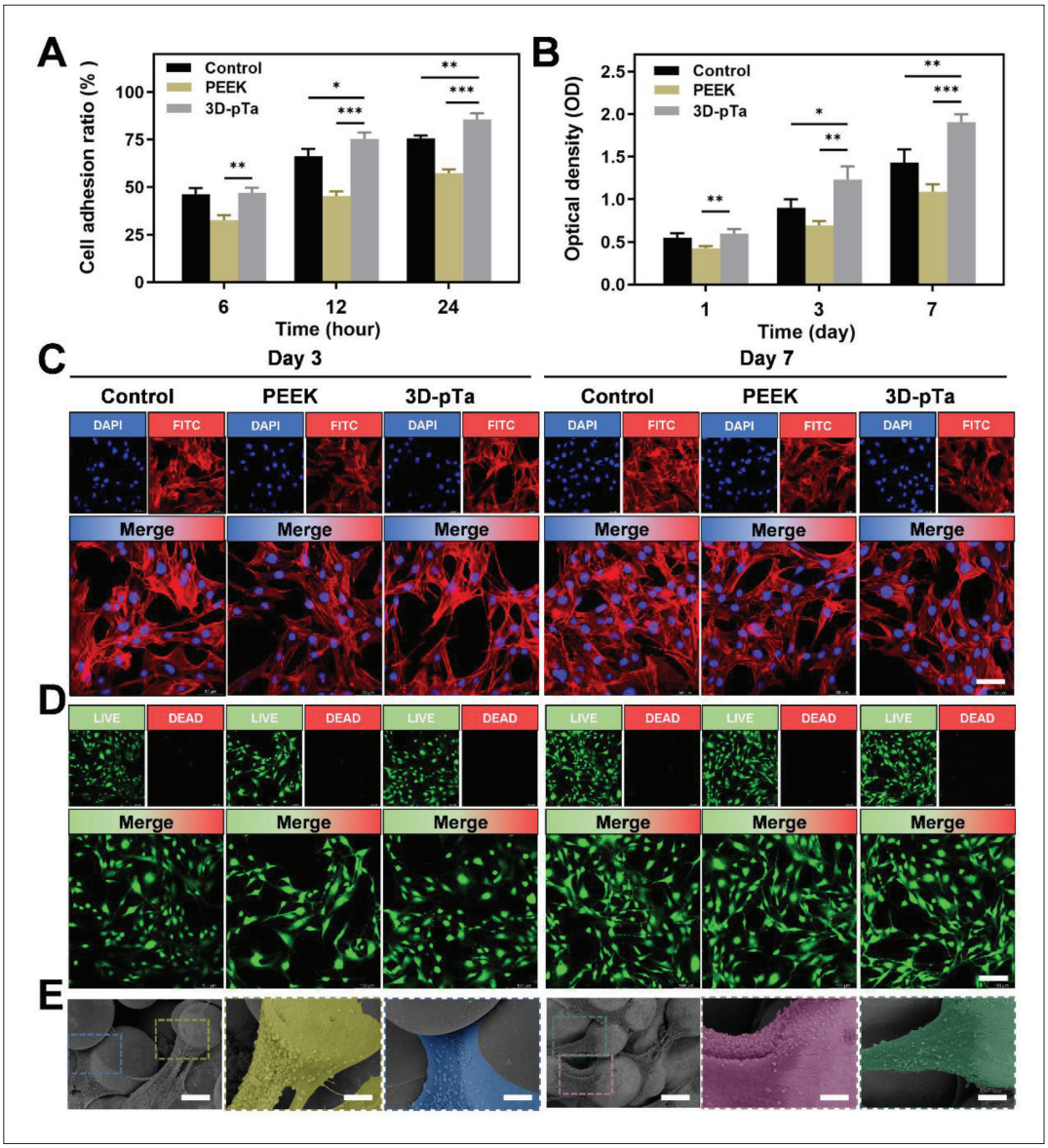

Figure 2. *In vitro* viability of MC3T3-E1 cells cultured on different samples. (A) Cell adhesion ratio at 6, 12, and 24 h. (B) Cell proliferation on days 1, 3, and 7. (C) Immunofluorescence staining at days 3 and 7 (red: cytoskeleton; blue: nuclear). (D) Live/dead staining fluorescence images at days 3 and 7. (E) Morphology of cells adhering to the surface of the scaffolds determined by SEM at 3 and 7 days. $n = 3$; *$p < 0.05$; **$p < 0.01$; ***$p < 0.001$. Scale bars: 50 μm (C); 100 μm (D); 10 μm (E, left); 5 μm (E, middle and right). Abbreviations: PEEK, polyetheretherketone; SEM, scanning electron microscopy.

Figure 2C displays the cytoskeletal morphology of MC3T3-E1 cells cultured on the cages, with cytoskeletons stained red using FITC-Phalloidin and nuclei stained blue with DAPI. After 3 and 7 days of culture, MC3T3-E1 cells on the 3D-pTa cages exhibited well-spread morphologies. Live/dead staining images demonstrated high cell viability in both the 3D-pTa and PEEK cage groups (Figure 2D). SEM observations of MC3T3-E1 cell adhesion on the 3D-pTa cage after days 3 and 7 revealed that cells were fully spread, displaying prominent filopodia and abundant microfilaments (Figure 2E).

3.3. *In vitro* osteogenic effect of the 3D-pTa cage

ALP staining and quantitative analysis were performed after 7 and 14 days of incubation to evaluate the osteogenic differentiation of MC3T3-E1 cells (Figure 3A). The 3D-pTa group exhibited the highest staining intensity. ALP activity measurements further confirmed that the 3D-pTa cage group exhibited significantly higher ALP activity compared to the PEEK and control groups. Mineralization of MC3T3-E1 cells was assessed using ARS staining (Figure 3B). After 14 and 21 days of culture, the 3D-pTa group displayed the most pronounced increase in calcium nodules compared to the control and PEEK groups. Quantitative analysis of ARS revealed that the number of mineralized nodules in the 3D-pTa group was approximately twice that of the other two groups. Furthermore, the expression levels of osteogenic markers Runx2, OCN, OPN, and COL I in MC3T3-E1 cells were quantified using qPCR after 7 and 14 days of incubation. The results indicate that compared to the control and PEEK groups, the 3D-pTa group exhibited significantly elevated expression levels of all tested markers (Figure 3C). These findings indicate that the 3D-pTa cage exhibits enhanced osteopromotive effects.

3.4. Postoperative imaging results

As displayed in Figure 4A, lateral cervical X-rays were taken immediately postoperatively, as well as at 12 and 24 weeks. The results demonstrated that both the 3D-pTa and PEEK cages remained stable over time with no significant displacement or subsidence (Figure 4A). Additionally, no significant difference was observed in the average DSH between the 3D-pTa and PEEK groups throughout the follow-up period (Figure 4B), indicating that the 3D-pTa cage possesses compressive strength comparable to that of the PEEK cage.

3.5. Osseointegration by histomorphometric analysis

Histological analysis revealed that, in the PEEK cage group, new bone formation was limited, and significant fibrotic reactions were observed surrounding the cages, leading to inadequate integration with the host bone. In contrast, after 6 months, the 3D-pTa cage group exhibited more substantial new bone formation, with abundant trabecular bone present at the interface between the cage and bone. Notably, neither cage group displayed any signs of osteolysis (Figure 5A and B). Figure 5C and D presents the quantitative evaluation of BIC and BV/TV at 12 and 24 weeks postoperatively. The results indicate that both BIC and BV/TV were greater in the 3D-pTa group than in the PEEK group at both time points. These findings suggest that the 3D-pTa cage achieved superior bone integration and intervertebral fusion compared to the PEEK cage.

3.6. Biomechanical testing

ROM testing was conducted on the operated vertebrae to evaluate the mechanical stability of the interbody fusion. Compared to the PEEK group, the 3D-pTa group demonstrated significantly lower ROM values across the six loading axes (two axes per loading mode) at 12 and 24 weeks, indicating better early interbody fusion and enhanced mechanical stability (Figure 6A–C). Stiffness analysis of the intervertebral fusion segments using the kinematic system further confirmed these findings, indicating that the mechanical stiffness in the 3D-pTa group exceeded that in the PEEK group (Figure 6D–F).

3.7. *In vivo* biosafety results

Gross anatomical analysis at 24 weeks postoperatively revealed no subcutaneous fluid accumulation or inflammatory changes at the surgical sites in either group. Extensive bone growth was observed around the implants, with tight integration between the implants and the surrounding bone, and no evidence of loosening (Figure 7A). Histological analysis of the spinal cord specimens revealed no significant pathological changes in the 3D-pTa group (Figure 7B). Cerebrospinal fluid biochemical parameters, including TP, ALB, GLU, Na, and Cl, as well as complete blood count results, such as WBC, NEU, NEU%, RBC, HB, and PLT, were all within normal reference ranges for both groups, with no significant differences in statistics found between them (Figure 7C and D). These findings indicate that the 3D-pTa cage demonstrates good *in vivo* biosafety.

4. Discussion

Ta scaffolds, recognized for their strong mechanical properties, can be employed as permanent implants, facilitating rapid postoperative recovery of movement and activity.[31] Although Ta has demonstrated excellent osseointegration, its application as a cage material for spinal fusion remains relatively underexplored. With the swift progress in AM, porous Ta implants are now designed not

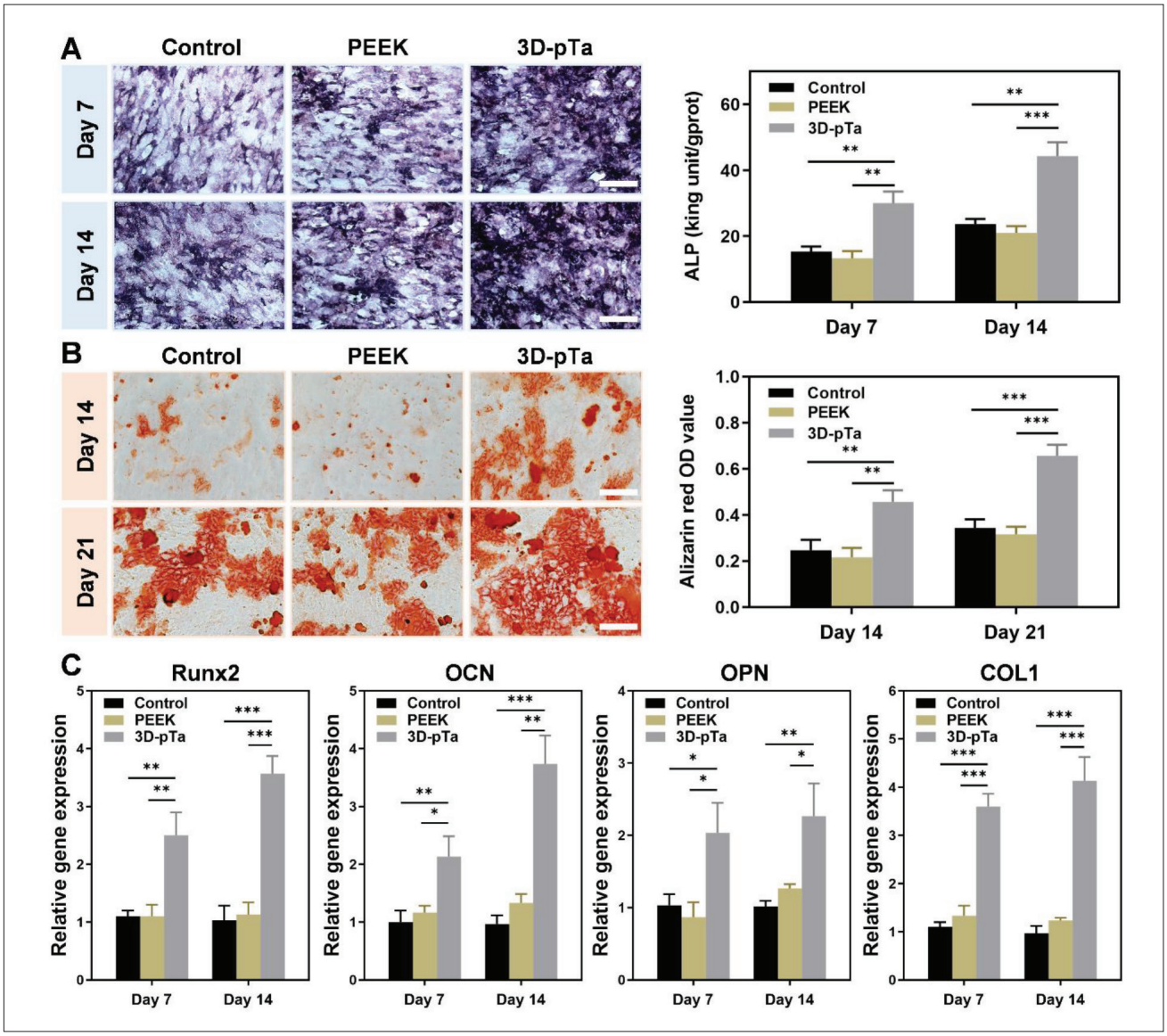

Figure 3. *In vitro* osteogenic performances of MC3T3-E1 cells cultured on different samples. (A) Staining images and quantitative results of ALP activity on days 7 and 14. (B) Staining images and quantitative results of ARS on days 14 and 21. (C) Osteogenesis-related gene expression, including Runx2, OCN, OPN, and COL1 on days 7 and 14. $n = 3$; *$p < 0.05$; **$p < 0.01$; ***$p < 0.001$. Scale bars: 100 μm (A and B). Abbreviations: ALP, alkaline phosphatase; ARS, Alizarin red S; COL1, Collagen I; OCN, osteocalcin; OD, optical density; OPN: osteopontin; PEEK, polyetheretherketone; Runx2, runt-related transcription factor 2.

only to ensure optimal mechanical performance but also to achieve optimized porous structures.[32,33] This is particularly beneficial for spinal fusion, as this technology significantly reduces the elastic modulus of Ta to match that of human cancellous bone, while optimizing pore configurations to enhance surface properties, cellular behavior, and intervertebral bone integration. In this study, we utilized SLM technology to produce a pTa cage and combined *in vitro* cellular experiments with *in vivo* spinal fusion tests to evaluate the potential of 3D-pTa as an interbody fusion cage material.

The balance between providing sufficient initial mechanical support and preventing stress shielding is crucial for the long-term success of spinal fusion implants.[34] The porous architecture of the 3D-pTa cage reduces the overall elastic modulus of the implant to better match that of cancellous bone. This reduction in stiffness minimizes stress shielding effects, allowing for a more natural

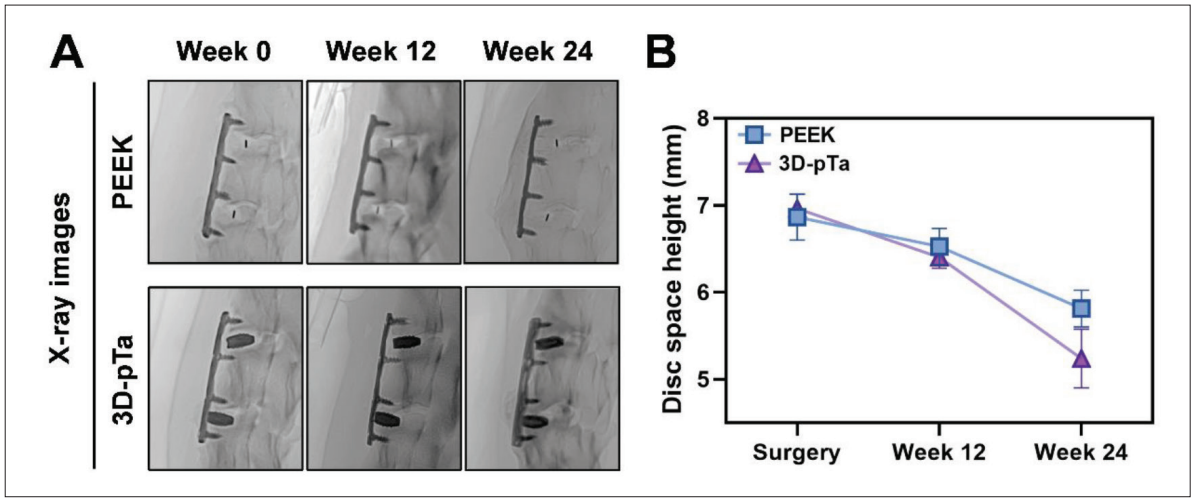

Figure 4. Postoperative imaging results. (A) Representative lateral cervical radiographs at postoperative weeks 0, 12, and 24. (B) DSH analysis at postoperative weeks 0 ($n = 6$), 12 ($n = 6$), and 24 ($n = 6$). Abbreviations: DSH, disc space height; PEEK, polyetheretherketone.

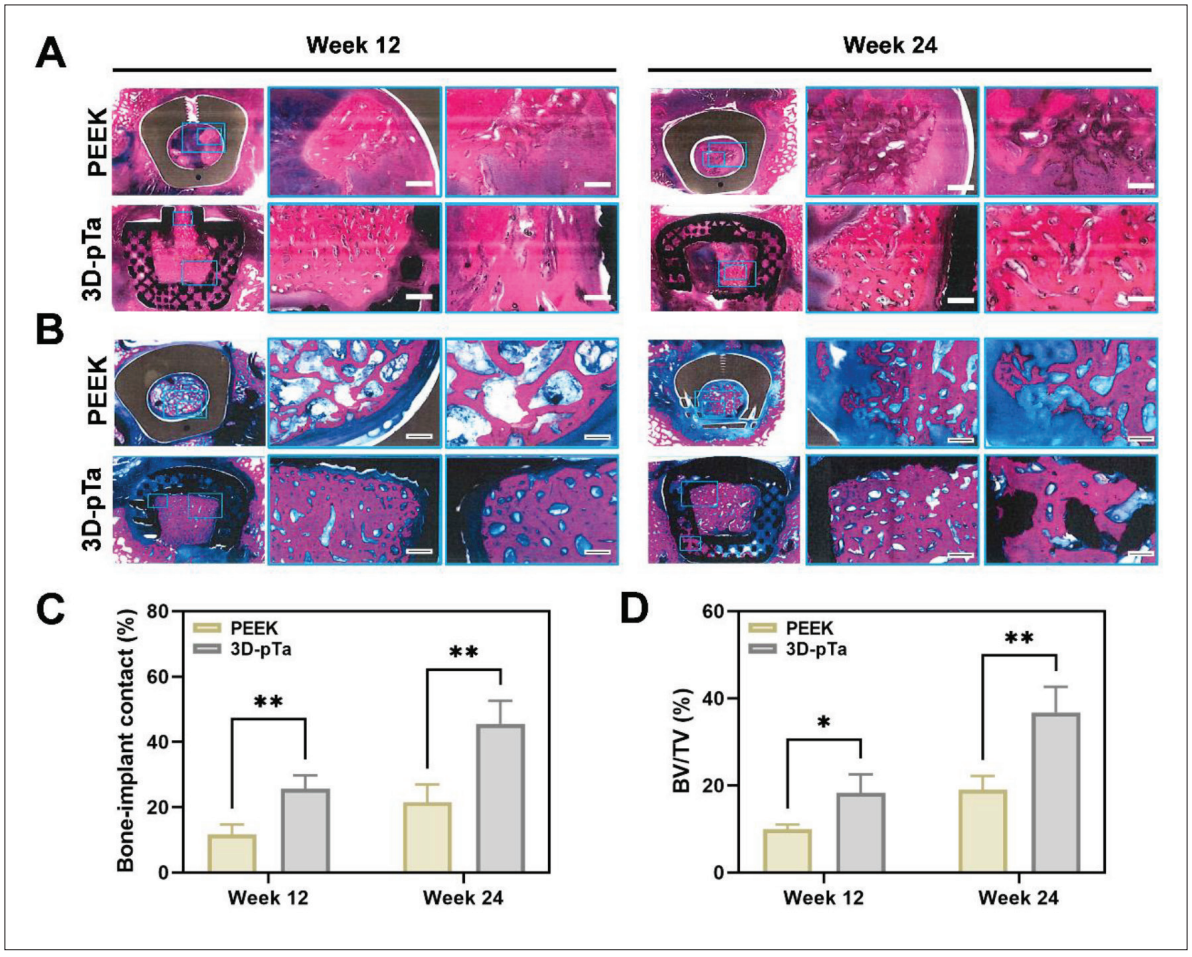

Figure 5. *In vivo* osseointegration evaluation in sheep cervical fusion model at weeks 12 and 24. (A) H&E staining and (B) methylene blue-acid fuchsin staining of different cages. Scale bars: 100 μm. (C) Bone-implant contact and (D) bone volume to total volume were calculated and statistically analyzed. $n = 3$; $^{*}p < 0.05$; $^{**}p < 0.01$. Abbreviations: BV/TV, bone volume to total volume; H&E, hematoxylin-eosin; PEEK, polyetheretherketone.

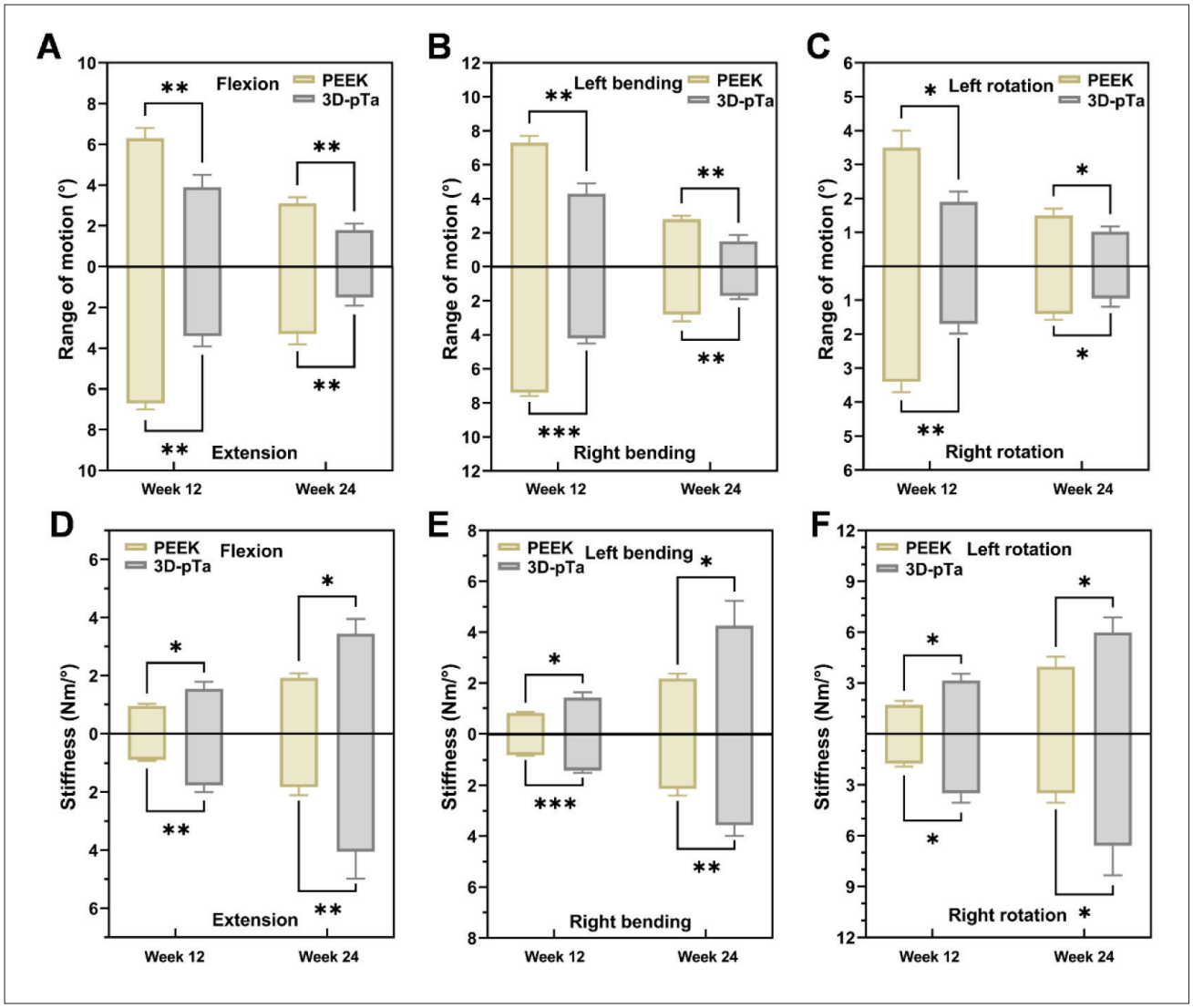

Figure 6. Analysis of mechanical stability and loading stiffness at weeks 12 and 24. (A–C) Results of mechanical stability evaluated by the range of motion: (A) flexion/extension; (B) left/right bending; and (C) left/right rotation. (D–F) Results of stiffness analysis in all loading modes: (D) flexion/extension; (E) left/right bending; and (F) left/right rotation. $n = 3$; $^{*}p < 0.05$; $^{**}p < 0.01$; $^{***}p < 0.001$. Abbreviation: PEEK, polyetheretherketone.

load distribution, and promoting bone remodeling and regeneration.[29] Additionally, the interconnected porous network facilitates bone ingrowth and vascularization, enhancing the biological fixation of the implant over time. The micro-scale pore sizes have been demonstrated to promote vascularization and bone tissue ingrowth by facilitating nutrient and oxygen diffusion. The 3D architecture facilitates the formation of new blood vessels, which is crucial for sustaining osteogenesis and enhancing the rate of bone ingrowth.[35] As new bone forms within and around the porous structure, the mechanical load is gradually transferred from the implant to the newly formed bone, ensuring sustained mechanical stability during the healing process. This gradual load transfer is essential to prevent stress shielding and to stimulate continuous bone remodeling, ultimately leading to successful spinal fusion.[36]

Cell adhesion is the initial and critical step in the interaction between cells and materials, serving as a prerequisite for cell spreading and proliferation on implant surfaces, which is essential for effective bone regeneration.[37] The assessments of cell adhesion and proliferation revealed that osteoblast proliferation on the 3D-pTa scaffold was significantly higher than on the PEEK scaffold on days 1, 3, and 7 (Figure 2A and B). Further SEM analysis revealed that osteoblasts on the 3D-pTa scaffold were fully extended,

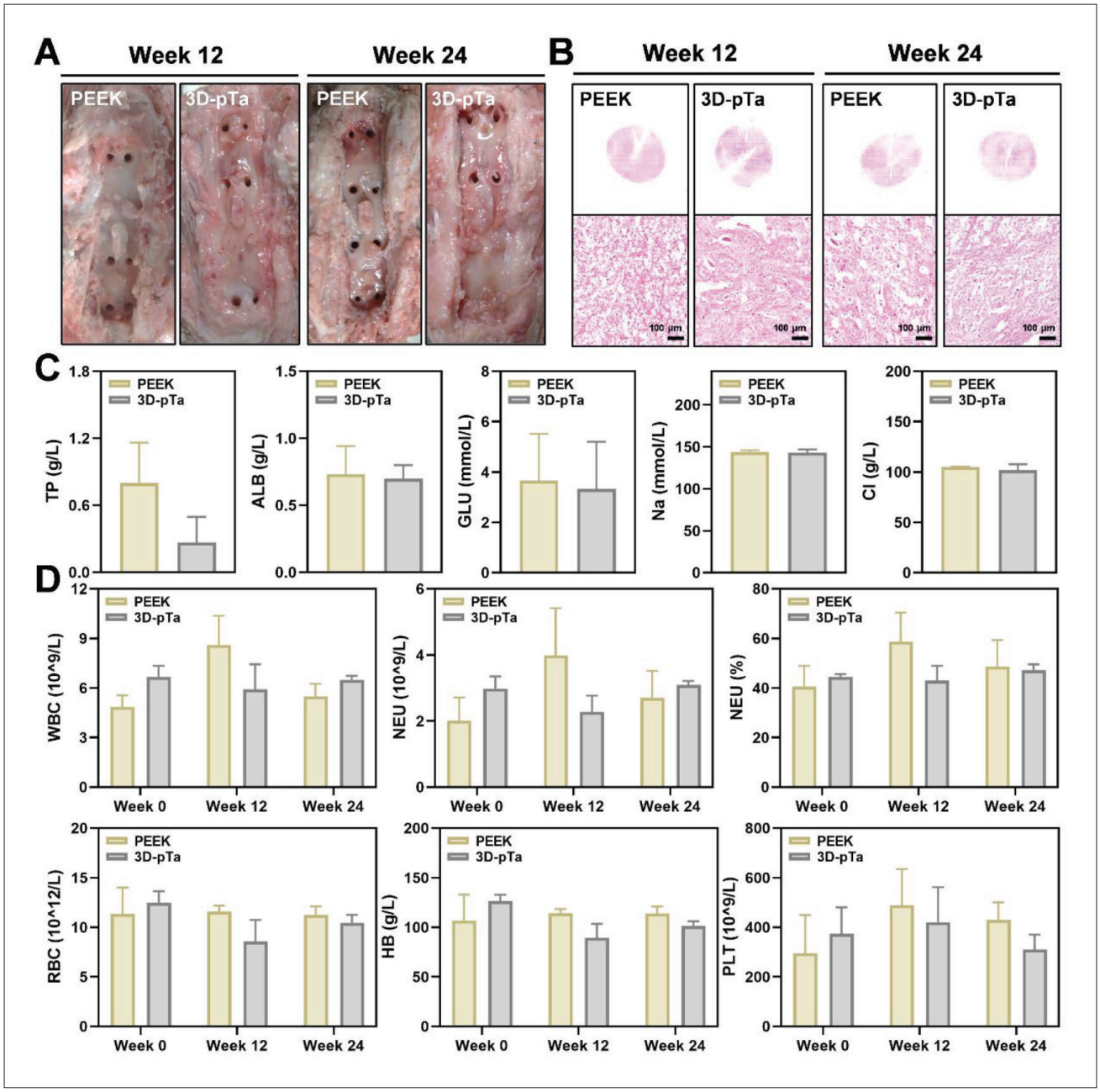

Figure 7. *In vivo* biosafety evaluation at postoperative weeks 0, 12, and 24. (A) Gross anatomical photos of the surgical site. (B) Histopathological observations of the spinal cord. (C) Cerebrospinal fluid biochemical tests. (D) Hematological examinations. Scale bars: 100 μm (B). Abbreviations: ALB, albumin; Cl, chloride; GLU, glucose; HB, hemoglobin; Na, sodium; NEU, neutrophils; PEEK, polyetheretherketone; PLT, platelets; RBC, red blood cells; TP, total protein; WBC, white blood cells.

exhibiting numerous filopodia and lamellipodia, indicating that the material effectively supports cell attachment and extension (Figure 2E). The enhanced proliferation may be attributed to the inherent high wettability and surface energy of Ta, as well as the rough micro-scale surface structure formed during the 3D printing process, which collectively promotes cell adhesion and proliferation.[38,39] Surface roughness at the micro-scale enhances protein adsorption, which facilitates cell adhesion by providing more anchoring sites for integrin binding.[40] Additionally, studies comparing the culture of human mesenchymal stem cells (hMSCs) on 3D porous scaffolds with 2D scaffolds have reported significantly higher hMSC counts and elevated alkaline phosphatase levels on the 3D porous

scaffolds.[41] The pore size and geometry of the Ta scaffold affect cell morphology by guiding cytoskeletal organization and focal adhesion formation, which are essential for subsequent cell proliferation and differentiation.[42] These findings suggest that the inherent properties of the 3D-pTa cage create an osteoinductive environment that facilitates early and robust bone ingrowth.

The successful clinical outcome of bone implants hinges on the effective osteointegration of biomaterials with regenerating bone tissue, making osteogenic activity a fundamental characteristic of implants. Ta has been reported to enhance osteoblast function and maturation [19]. To directly evaluate the impact of 3D-pTa on osteogenesis, we assessed ALP activity, ARS staining, and the expression of osteogenesis-related genes (*Runx2*, *OCN*, *OPN*, *COL1*).[43–45] We found that the 3D-pTa cage significantly enhances osteogenic capability compared to the PEEK cage. Previous studies have reported that Ta is capable of increasing bone mass by enhancing stem cell renewal, stimulating osteoblast differentiation, and suppressing osteoblast apoptosis.[46,47] Additionally, the 3D biomimetic porous structure provides a biological microenvironment that facilitates nutrient and waste transport, thereby promoting ALP activity and triggering osteogenic gene expression.[48,49]

In vivo animal implantation models are essential for examining the efficacy of interbody fusion applications. The anatomy of the sheep's cervical spine closely resembles that of humans, with similar vertebral dimensions and biomechanical properties, making sheep a commonly used model for spinal fusion studies.[50] Research has demonstrated that sheep cervical vertebrae and intervertebral discs have anatomical parameters similar to those of human cervical spines.[51,52] Therefore, we selected the sheep cervical spine as the interbody fusion model to evaluate the performance of the novel 3D-pTa cage. A slight decrease in DSH was observed from 1 to 6 months post-implantation in both groups. This decrease can be attributed to physiological remodeling processes and the settling of the cages into the vertebral endplates under continuous loading conditions.[53] Importantly, the decrease in DSH remained within clinically acceptable limits, and no significant subsidence or implant displacement was observed, indicating the stability and efficacy of the 3D-pTa cages in maintaining spinal segment integrity. Due to the radiolucency of Ta, micro-CT, and X-ray imaging could not visualize the internal bone structure of the 3D-pTa cage. To assess bone integration, we performed histological staining of undecalcified bone sections to determine BV/TV and BIC in the fusion area. Histological images revealed that the 3D-pTa cage exhibited substantial bone filling within the previously porous implant windows, whereas the PEEK cage displayed poor bone integration and loose bone fragments. The early interaction between the implant and bone observed with the 3D-pTa cage likely enhances stability and reduces micromotion in a shorter timeframe, thereby promoting early fusion and stability. Further quantitative analysis demonstrated that new bone formation was more extensive in the 3D-pTa cage than in the PEEK cage. Additionally, the contact between the newly formed bone and the 3D-pTa cage surface was more intimate, indicating better bone integration. Good BIC results are crucial for stable anchoring between the scaffold and vertebrae. In this study, the BIC of the 3D-pTa cage at 12 and 24 weeks was markedly greater than that of the PEEK cage. The absence of material in the implant windows of the 3D-pTa cage allowed for a clearer observation of the bone integration effect. Our results suggest that even without allografts or osteoinductive substances, the intrinsic bioactivity of the 3D-pTa cage promotes bone ingrowth and integration. Therefore, the osseointegration properties of the 3D-pTa implant make it a clinically effective and cost-efficient option.

Biocompatibility assessment is a critical step in the clinical translation of any new medical implant.[54,55] Although some studies have demonstrated the favorable cellular compatibility of porous Ta, few have assessed the possible systemic toxicity of 3D-pTa. In this study, multiple parameters, including health status monitoring, hematological analysis, cerebrospinal fluid biochemical tests of cerebrospinal fluid, and spinal cord pathological assessments, were employed to assess the biocompatibility of the 3D-pTa cage. These findings revealed no significant differences in biocompatibility between the 3D-pTa and PEEK groups.

5. Conclusion

We developed an optimized porous Ta interbody fusion cage using AM. The 3D-pTa cage displayed promising biological performance *in vitro*, with improved cell adhesion, proliferation, and osteogenic differentiation. In a sheep spinal fusion model, the 3D-pTa cage demonstrated accelerated bone ingrowth, with BV/TV ratios significantly higher than those of the PEEK cage ($p < 0.05$), and superior integration that led to a marked reduction in ROM ($p < 0.05$), indicating stable fusion outcomes. Moreover, the 3D-pTa cage demonstrated dependable biocompatibility and biosafety. These findings suggest that the 3D-pTa cage could be a valuable option for clinical use in spinal fusion procedures.

Acknowledgments

The authors would like to thank the Hunan Huaxiang Medical Technology Co., Ltd. for providing the materials and equipment.

Funding

The work was supported by the National Natural Science Foundation of China (NSFC; No. 82130072 and No. 82302669).

Conflict of interest

The authors declare that they have no known competing financial interests or personal relationships that could have appeared to influence the work reported in this paper.

Author contributions

Conceptualization: Cao Yang
Formal analysis: Hang Liang, Jingyao Tu, Xinyi Chen
Investigation: Hang Liang, Bingjin Wang, Kun Wang, Xiaobo Feng, Wenbin Hua
Methodology: Hang Liang, Jingyao Tu, Bingjin Wang
Writing – original draft: Hang Liang
Writing – review & editing: Lei Tan, Shuai Li

Ethics approval and consent to participate

The animal surgical procedures involved in this study were approved by the Institutional Animal Care and Use Committee (IACUC) of Shenzhen Advanced Animal Study Service Centre (Approval No. F2409006S).

Consent for publication

Not applicable.

Availability of data

Data are available from the corresponding authors upon reasonable request.

References

1. Buser Z, Brodke DS, Youssef JA, et al. Synthetic bone graft versus autograft or allograft for spinal fusion: a systematic review. J Neurosurg Spine. 2016;25:509-516. doi: 10.3171/2016.1.Spine151005
2. Hirvonen T, Siironen J, Marjamaa J, Niemela M, Koski-Palken A. Anterior cervical discectomy and fusion in young adults leads to favorable outcome in long-term follow-up. Spine J. 2020;20:1073-1084. doi: 10.1016/j.spinee.2020.03.016
3. Gu X, Sun X, Sun Y, et al. Bioinspired modifications of PEEK implants for bone tissue engineering. Front Bioeng Biotechnol. 2020;8:631616. doi: 10.3389/fbioe.2020.631616
4. Feng X, Yu H, Liu H, et al. Three-dimensionally-printed polyether-ether-ketone implant with a cross-linked structure and acid-etched microporous surface promotes integration with soft tissue. Int J Mol Sci. 2019;20:3811. doi: 10.3390/ijms20153811
5. Buck E, Li H, Cerruti M. Surface modification strategies to improve the osseointegration of poly(etheretherketone) and its composites. Macromol Biosci. 2020;20:e1900271. doi: 10.1002/mabi.201900271
6. Panayotov IV, Orti V, Cuisinier F, Yachouh J. Polyetheretherketone (PEEK) for medical applications. J Mater Sci Mater Med. 2016;27:1-11. doi: 10.1007/s10856-016-5731-4
7. Kurtz SM, Devine JN. PEEK biomaterials in trauma, orthopedic, and spinal implants. Biomaterials. 2007;28:4845-4869. doi: 10.1016/j.biomaterials.2007.07.013
8. Toth JM, Wang M, Estes BT, Scifert JL, Seim HB, Turner AS. Polyetheretherketone as a biomaterial for spinal applications. Biomaterials. 2006;27:324-334. doi: 10.1016/j.biomaterials.2005.07.011
9. Zhang W, Liu L, Zhou H, et al. Surface bisphosphonation of polyetheretherketone to manipulate immune response for advanced osseointegration. Mater Design. 2023; 232:112151. doi: 10.1016/j.matdes.2023.112151
10. Al-Tamimi AA, Fernandes PRA, Peach C, Cooper G, Diver C, Bartolo PJ. Metallic bone fixation implants: a novel design approach for reducing the stress shielding phenomenon. Virtual Phys Prototy. 2017;12:141-151. doi: 10.1080/17452759.2017.1307769
11. Pobloth AM, Checa S, Razi H, et al. Mechanobiologically optimized 3D titanium-mesh scaffolds enhance bone regeneration in critical segmental defects in sheep. Sci Transl Med. 2018;10:eaam8828. doi: 10.1126/scitranslmed.aam8828
12. Turnbull G, Clarke J, Picard F, et al. 3D bioactive composite scaffolds for bone tissue engineering. Bioact Mater. 2018;3:278-314. doi: 10.1016/j.bioactmat.2017.10.001
13. Levine BR, Sporer S, Poggie RA, Della Valle CJ, Jacobs JJ. Experimental and clinical performance of porous tantalum in orthopedic surgery. Biomaterials. 2006;27:4671-4681. doi: 10.1016/j.biomaterials.2006.04.041
14. Sumner DR. Long-term implant fixation and stress-shielding in total hip replacement. J Biomech. 2015;48:797-800. doi: 10.1016/j.jbiomech.2014.12.021
15. Tang Z, Xie YT, Yang F, et al. Porous tantalum coatings prepared by vacuum plasma spraying enhance BMSCs osteogenic differentiation and bone regeneration. PLoS One. 2013;8:e66263. doi: 10.1371/journal.pone.0066263
16. Alipal J, Pu'ad NASM, Nayan NHM, et al. An updated review on surface functionalisation of titanium and its

alloys for implants applications. Mater Today Proc. 2021; 42:270-282.
doi: 10.1016/j.matpr.2021.01.499

17. Han Q, Wang CY, Chen H, Zhao X, Wang JC. Porous Tantalum and titanium in orthopedics: a review. ACS Biomater Sci Eng. 2019;5:5798-5824.
doi: 10.1021/acsbiomaterials.9b00493

18. Sagomonyants KB, Hakim-Zargar M, Jhaveri A, Aronow MS, Gronowicz G. Porous tantalum stimulates the proliferation and osteogenesis of osteoblasts from elderly female patients. J Orthop Res. 2011;29:609-616.
doi: 10.1002/jor.21251

19. Huang G, Pan ST, Qiu JX. The clinical application of porous tantalum and its new development for bone tissue engineering. Materials. 2021;14:2647.
doi: 10.3390/ma14102647

20. Balla VK, Banerjee S, Bose S, Bandyopadhyay A. Direct laser processing of a tantalum coating on titanium for bone replacement structures. Acta Biomater. 2010; 6: 2329-2334.
doi: 10.1016/j.actbio.2009.11.021

21. Guo Y, Xie K, Jiang WB, et al. In vitro and in vivo study of 3D-printed porous tantalum scaffolds for repairing bone defects. ACS Biomater Sci Eng. 2019;5:1123-1133.
doi: 10.1021/acsbiomaterials.8b01094

22. Wang LN, Yuan B, Chen F, et al. Ability of a novel biomimetic titanium alloy cage in avoiding subsidence and promoting fusion: a goat spine model study. Mater Design. 2022;213:110361.
doi: 10.1016/j.matdes.2021.110361

23. Pei X, Wang LN, Wu LN, et al. In-situ synthesized hydroxyapatite whiskers on 3D printed titanium cages enhanced osteointegration in a goat spinal fusion model. Mater Design. 2023; 233: 112270.
doi: 10.1016/j.matdes.2023.112270

24. Laratta JL, Vivace BJ, Lopez-Pena M, et al. 3D-printed titanium cages without bone graft outperform PEEK cages with autograft in an animal model. Spine J. 2022; 22:1016-1027.
doi: 10.1016/j.spinee.2021.12.004

25. Wang XY, Zhang DC, Peng HT, Yang JZ, Li Y, Xu JX. Optimize the pore size-pore distribution-pore geometry-porosity of 3D-printed porous tantalum to obtain optimal critical bone defect repair capability. Biomater Adv. 2023;154:213638.
doi: 10.1016/j.bioadv.2023.213638

26. Jiao JY, Hong QM, Zhang DC, et al. Influence of porosity on osteogenesis, bone growth and osteointegration in trabecular tantalum scaffolds fabricated by additive manufacturing. Front Bioeng Biotech. 2023;11:1117954.
doi: 10.3389/fbioe.2023.1117954

27. Wauthle R, van der Stok J, Amin Yavari S, et al. Additively manufactured porous tantalum implants. Acta Biomater. 2015;14:217-225.
doi: 10.1016/j.actbio.2014.12.003

28. Yang J, Gao H, Zhang D, et al. Static compressive behavior and material failure mechanism of trabecular tantalum scaffolds fabricated by laser powder bed fusion-based additive manufacturing. Int J Bioprint. 2022; 8: 438.
doi: 10.18063/ijb.v8i1.438

29. Jin J, Wang D, Qian H, et al. Precision pore structure optimization of additive manufacturing porous tantalum scaffolds for bone regeneration: a proof-of-concept study. Biomaterials. 2025;313:122756.
doi: 10.1016/j.biomaterials.2024.122756

30. Chen W, Yang J, Kong H, et al. Fatigue behaviour and biocompatibility of additively manufactured bioactive tantalum graded lattice structures for load-bearing orthopaedic applications. Mater Sci Eng C Mater Biol Appl. 2021;130:112461.
doi: 10.1016/j.msec.2021.112461

31. Yuan K, Zhang K, Yang YQ, et al. Evaluation of interbody fusion efficacy and biocompatibility of a polyetheretherketone/calcium silicate/porous tantalum cage in a goat model. J Orthop Transl. 2022;36:109-119.
doi: 10.1016/j.jot.2022.06.006

32. Zhang CX, Zhou ZW, Liu N, et al. Osteogenic differentiation of 3D-printed porous tantalum with nano-topographic modification for repairing craniofacial bone defects. Front Bioeng Biotech. 2023;11:1258030.
doi: 10.3389/fbioe.2023.1258030

33. Fan HQ, Deng S, Tang WT, et al. Highly porous 3D printed tantalum scaffolds have better biomechanical and microstructural properties than titanium scaffolds. Biomed Res Int. 2021;2021:2899043.
doi: 10.1155/2021/2899043

34. Cheers GM, Weimer LP, Neuerburg C, et al. Advances in implants and bone graft types for lumbar spinal fusion surgery. Biomater Sci. 2024;12:4875-4902.
doi: 10.1039/d4bm00848k

35. de Silva L, Bernal PN, Rosenberg A, Malda J, Levato R, Gawlitta D. Biofabricating the vascular tree in engineered bone tissue. Acta Biomater. 2023;156:250-268.
doi: 10.1016/j.actbio.2022.08.051

36. Loenen ACY, Peters MJM, Bevers RTJ, et al. Early bone ingrowth and segmental stability of a trussed titanium cage versus a polyether ether ketone cage in an ovine lumbar interbody fusion model. Spine J. 2022;22:174-182.
doi: 10.1016/j.spinee.2021.07.011

37. Li MM, Yin SH, Lin MZ, et al. Current status and prospects of metal-organic frameworks for bone therapy and bone repair. J Mater Chem B. 2022;10:5105-528.
doi: 10.1039/d2tb00742h

38. Huang G, Pan ST, Qiu JX. The osteogenic effects of porous Tantalum and Titanium alloy scaffolds with different unit cell structure. Colloid Surface B. 2022;210:112229.

doi: 10.1016/j.colsurfb.2021.112229

39. Babuska V, Kasi PB, Chocholata P, et al. Nanomaterials in bone regeneration. Appl Sci Basel. 2022;12:6793. doi: 10.3390/app12136793

40. Barberi J, Spriano S. Titanium and protein adsorption: an overview of mechanisms and effects of surface features. Materials (Basel). 2021;14:1590. doi: 10.3390/ma14071590

41. Ji S, Guvendiren M. 3D printed wavy scaffolds enhance mesenchymal stem cell osteogenesis. Micromachines (Basel). 2019;11:31. doi: 10.3390/mi11010031

42. Wang X, Liu W, Yu X, et al. Advances in surface modification of tantalum and porous tantalum for rapid osseointegration: a thematic review. Front Bioeng Biotechnol. 2022; 10:983695. doi: 10.3389/fbioe.2022.983695

43. McGilvray KC, Easley J, Seim HB, et al. Bony ingrowth potential of 3D-printed porous titanium alloy: a direct comparison of interbody cage materials in an in vivo ovine lumbar fusion model. Spine J. 2018;18:1250-1260. doi: 10.1016/j.spinee.2018.02.018

44. Xu CC, Wu FH, Yang J, et al. 3D printed long-term structurally stable bioceramic dome scaffolds with controllable biodegradation favorable for guided bone regeneration. Chem Eng J. 2022; 450:138003. doi: 10.1016/j.cej.2022.138003

45. Wei XH, Zhou WH, Tang Z, et al. Magnesium surface-activated 3D printed porous PEEK scaffolds for osseointegration by promoting angiogenesis and osteogenesis. Bioact Mater. 2023;20:16-28. doi: 10.1016/j.bioactmat.2022.05.011

46. Qian H, Lei T, Hua L, et al. Fabrication, bacteriostasis and osteointegration properties researches of the additively-manufactured porous tantalum scaffolds loading vancomycin. Bioact Mater. 2023;24:450-462. doi: 10.1016/j.bioactmat.2022.12.013

47. Liguori A, Gino ME, Panzavolta S, et al. Tantalum nanoparticles enhance the osteoinductivity of multiscale composites based on poly(lactide-co-glycolide) electrospun fibers embedded in a gelatin hydrogel. Mater Today Chem. 2022;24:100804. doi: 10.1016/j.mtchem.2022.100804

48. Jia CQ, Zhang Z, Cao SQ, et al. A biomimetic gradient porous cage with a micro-structure for enhancing mechanical properties and accelerating osseointegration in spinal fusion. Bioact Mater. 2023;23:234-246. doi: 10.1016/j.bioactmat.2022.11.003

49. Feng XB, Ma L, Liang H, et al. Osteointegration of 3D-printed fully porous polyetheretherketone scaffolds with different pore sizes. ACS Omega. 2020;5:26655-26666. doi: 10.1021/acsomega.0c03489

50. Shen YW, Yang Y, Liu H, et al. Preliminary results in anterior cervical discectomy and fusion with the uncovertebral joint fusion cage in a goat model. BMC Musculoskel Dis. 2021;22:1-10. doi: 10.1186/s12891-021-04412-4

51. Sheng SR, Wang XY, Xu HZ, Zhu GQ, Zhou YF. Anatomy of large animal spines and its comparison to the human spine: a systematic review. Eur Spine J. 2010;19:46-56. doi: 10.1007/s00586-009-1192-5

52. Kandziora F, Pflugmacher R, Scholz M, et al. Comparison between sheep and human cervical spines: an anatomic, radiographic, bone mineral density, and biomechanical study. Spine (Phila Pa 1976). 2001;26:1028-1037. doi: 10.1097/00007632-200105010-00008

53. Godlewski B, Bebenek A, Dominiak M, Karpinski G, Cieslik P, Pawelczyk T. Subsidence following cervical discectomy and implant-to-bone ratio. BMC Musculoskelet Disord. 2022;23:750. doi: 10.1186/s12891-022-05698-8

54. Mathieu L, Marie-Solenne F, Cécile B, et al. Biocompatibility of four common orthopedic biomaterials following neuroelectromyostimulation: an study. J Biomed Mater Res B. 2018;106:1156-1164. doi: 10.1002/jbm.b.33927

55. Bernard M, Jubeli E, Pungente MD, Yagoubi N. Biocompatibility of polymer-based biomaterials and medical devices - regulations, screening and risk-management. Biomater Sci Uk 2018;6:2025-2053. doi: 10.1039/c8bm00518d

ACCSCIENCE PUBLISHING

International Journal of Bioprinting

RESEARCH ARTICLE

3D-printed cardiac patch coated with human extracellular matrix hydrogel: Significant improvement of cell adhesion and immune reaction

Marjan Enayati[1,2]*, Christopher Riedmüller[1,2], Sabrina Rohringer[1,2], Lukas Weber[1], Felix Pointner[1], Luis Pichelkastner[1], Marta Bonora[2,3], Ana Isabel Antunes Goncalves[1], Francesco Moscato[2,3,4], Ewald Unger[3], Emir Benca[5], Marvin Dötzlhofer[1], Bruno K. Podesser[1,2], Karl H. Schneider[1,2,4] and Helga Bergmeister[1,2]

[1]Center for Biomedical Research and Translational Surgery, Medical University Vienna, Austria

[2]Ludwig Boltzmann Institute for Cardiovascular Research, Vienna, Austria

[3]Center for Medical Physics and Biomedical Engineering, Medical University Vienna, Austria

[4]Austrian Cluster for Tissue Regeneration, Vienna, Austria

[5]Department of Orthopedics and Trauma Surgery, Medical University Vienna, Austria

Abstract

Constructing a cell-inductive scaffold that promotes the proliferation of cardiac-specific host cells for effective myocardium repair is a great challenge in the realm of cardiac tissue engineering. Three-dimensional (3D) printing allows for the precise fabrication of intricate structures like cardiac patches but produces large pores (sub-macron), reducing surface area for cell attachment and tissue regeneration. Moreover, the hydrophobic nature of most polyesters used in 3D printing further complicates cell adhesion and integration. In this study, human chorion placenta extracellular matrix (hpcECM) hydrogel with highly preserved ECM components, such as glycosaminoglycans (GAG), elastin, and collagen, was coated on a hydrophobic 3D-printed poly-ε-caprolactone (PCL) patch. The presence of hpcECM on the 3D-printed PCL patches could significantly induce higher levels of cell attachment, proliferation, and activation of cells such as human umbilical vein endothelial cells (HUVECs), endothelial progenitor cells (EPCs), H9c2 undifferentiated/differentiated cardiomyoblasts and fibroblasts. Fibronectin-coated samples served as controls in the experiment. Coating efficiency, hpcECM modulus of elasticity (in nanoscale), surface profile roughness, and contact angle measurements were performed and confirmed the significant potential of hpcECM as a stable, soft, hydrophilic coating matrix with low modulus of elasticity for 3D-printed synthetic constructs. Furthermore, hpcECM could modulate the high expression of inflammatory genes (CCR7 and IL-1α, expressed after 72 hours) via high expression of IL-10 in macrophages after one week. Expression of adhesion molecules (ICAM, VCAM-1, and PECAM-1) and hemolysis rate did not show statistically significant changes. All these findings highlight hpcECM as a promising immunomodulatory matrix supporting tissue-specific cell attachment and activation; particularly, hydrophobic 3D-printed constructs would outperform equivalents like fibronectin-coated constructs.

***Corresponding author:**
Marjan Enayati
(marjan.enayati@meduniwien.ac.at)

Citation: Enayati M, Riedmüller C, Rohringer S, et al. 3D-printed cardiac patch coated with human extracellular matrix hydrogel: Significant improvement of cell adhesion and immune reaction. *Int J Bioprint*. 2025;11(1):532-555. doi: 10.36922/ijb.6383

Received: November 21, 2024
Revised: December 23, 2024
Accepted: January 2, 2025
Published Online: January 2, 2025

Copyright: © 2025 Author(s). This is an Open Access article distributed under the terms of the Creative Commons Attribution License, permitting distribution, and reproduction in any medium, provided the original work is properly cited.

Publisher's Note: AccScience Publishing remains neutral with regard to jurisdictional claims in published maps and institutional affiliations.

Keywords: 3D printing; Human placenta chorion ECM; Induced hydrophilicity; Cell adhesion; Immunomodulation

1. Introduction

Heart diseases such as myocardial infarction (MI) remain major causes of death and hospitalization worldwide.[1] Following MI, ventricular wall remodeling in the infarcted area reduces cardiac output and leads to scar tissue, fibrosis, or thinning.[2,3] Cardiac tissue engineering offers a promising approach for heart tissue repair. One prominent example of a product stemming from cardiac tissue engineering is a cardiac patch, which is a thin construct fixed on the patient's tissue to provide mechanical and regenerative support in order to preserve and amend the local microenvironment. The cardiac tissue engineering approach involves an accurate combination of cardiac cells and biomaterials that imitate the complexity of the native heart. Facilitating cell adhesion on biomaterials is crucial for promoting adequate cardiac cell proliferation. At present, both synthetic and natural biomaterials are used in cardiac tissue regeneration. Synthetic biomaterials, particularly aliphatic polyesters, are valued for their ease of customization, simple fabrication, good mechanical properties, and degradability.[4] However, their hydrophobic surfaces and absence of specific cell recognition sites can restrict their applications, necessitating strategies to improve cell affinity to these polymers. There are various methods appropriate to enhance the hydrophilicity and cell affinity of a hydrophobic biopolymer. These include chemical modifications (*e.g.*, introducing polar functional groups such as hydroxyl groups),[5] blending with hydrophilic counterparts like chitosan or agarose,[6] incorporation of hydrophilic additives (such as nanomaterials like hydroxyapatite [HA])[7] or surface modifications (via plasma treatment or coating).[8] Each method has its own advantages and disadvantages. Among these methods, surface coating is a straightforward method compatible with common techniques such as dip-coating or spray-coating, making it accessible for large-scale production. One ideal approach is coating with natural biomaterials and creating an extracellular matrix (ECM)-like environment that enhances early cell attachment and migration while preserving the polymer backbone's integrity.[9] Collagen, gelatin, fibrin- and ECM-based hydrogels are major natural biomaterials due to their biocompatibility, ease of handling, and natural degradability.[4,10,11] Pei et al.[12] showed that a hierarchical poly-ε–caprolactone (PCL)-HA construct could induce osteogenesis in human adipose stem cells (hASCs) in the presence of type I collagen coating and plasma surface treatment. Furthermore, gelatin-coating could enhance the adhesion of human mesenchymal stem cells and cellular bioactivity in graphene oxide-incorporated electrospun PCL constructs.[13]

However, there are still disadvantages associated with each available biomaterial in the coating approach. Collagen, derived from animals, humans, or recombinant systems, shows poor mechanical stability, immunogenicity, and rapid enzymatic degradation.[14] Gelatin, a biocompatible denatured collagen, lacks thermostability and suitable pore size, limiting its clinical use.[15] Fibronectin supports cell adhesion but may promote atherosclerotic plaque formation, warranting caution in cardiovascular applications.[16] As an example, mesenchymal stem cell-seeded fibronectin-modified PCL patches could promote neovascularization and reduce inappropriate left ventricle remodeling in an MI rat model. Despite their advantages in applications, fibronectin-immobilized PCL fibrous patch is not considered a significant stride achieved in the realm of cardiac tissue engineering.[17] Extracellular matrix from decellularized tissue (or decellularized extracellular matrix, dECM) is an optimal natural biomaterial for cell interaction, capable of mimicking native tissue environments. Nevertheless, these natural biomaterials are not without shortcomings, such as their detrimental immunogenicity against mammalian antigens (such as α-gal epitope) and their demanding production and sterilization process.[18]

In this study, the potential of a self-developed human chorion placental ECM hydrogel to increase cell adhesion and proliferation on synthetic polymer scaffolds was investigated. PCL is a polymer approved by the U.S. Food and Drug Administration (FDA), equipped with excellent biocompatibility, suitable biodegradability, and tunable mechanical properties, which are promising characteristics to withstand the challenging requirements of the cardiac environment.[19] The human placenta and its components (such as the amniotic and chorionic membrane, and the umbilical cord) are considered sources of abundant biological materials and have been applied as membranes or hydrogels in a broad range of therapies.[20] For example, decellularized placenta allograft membranes (PAM) including amnion and chorion promote faster and more organized healing in ocular tissues[21] and enable advanced wound care applications.[22] It has been reported that the application of bioengineered cardiac patches consisting of the decellularized placenta and human-induced pluripotent stem cells in an MI rodent model could significantly improve cell retention and neovascularization and reduce infarct size.[23]

Recently, there has been a strong interest in using placenta-based ECM hydrogels for the repair of ischemic myocardial tissue[24] or as a component of bioinks in 3D bioprinting technology.[25,26] However, the majority of the studies utilized the ECM of the placenta as a whole, instead of using the individual components. For example, placenta ECM bioink mixed with silk fibroin and alginate has been utilized to create scaffolds for full-thickness skin repair. The placenta ECM could enhance angiogenesis, re-epithelialization, and formation of granulation tissue in the mice wound healing model after 21 days.[27] The potential of amnion ECM as a biomaterial has been intensively investigated,[28] whereas the chorion-derived ECM is relatively unexplored. Amnion ECM hydrogels are already commercialized for wound healing applications,[29] and decellularized amnion membrane approaches have been widely used in bone regeneration applications,[30,31] where they induce an inflammatory reduction after transplantation.[32] Regarding chorion-based hydrogels, McQuilling et al.[31,33] found that native chorion membranes contain more growth factors (pg/cm^2) compared to amnion. However, after dehydration, the content was significantly lowered. All these findings emphasize the necessity of modifying tissue processing. Furthermore, other studies showed a higher potential of chorion in osteogenic applications[31,33] and inflammatory reduction (in the form of exosomes derived from human chorion membrane extracts)[31] compared to amnion. Our group has successfully established a method for the decellularization of chorion, a technique already applied in the creation of ECM hydrogels and small-diameter vascular grafts.[34,35].

To the best of our knowledge, there is no published literature describing the usage of human chorion placenta extracellular matrix (hpcECM) hydrogel as a component, nor as a coating agent for a 3D-printed cardiac patch. 3D printing provides precise control over the deposition of materials to form intricate structures. Nonetheless, the resolution of the pores in these constructs tends to be relatively large (with sub-macron pores), compared to other methods such as electrospinning, where sub-micron pores are created.[36] Therefore, the coating efficiency of a hydrophobic construct with large pores might be challenging, especially in the case of using less concentrated hydrogels as a coating agent. In this study, PCL patches with relatively large pores were precisely fabricated via a 3D-Bioplotter. Subsequently, patches were coated with an hpcECM hydrogel of two different concentrations (0.02% hpcECM-PCL and 0.2% hpcECM-PCL). First, the surface characteristics and efficiency of coating in terms of morphology, pore size, porosity, roughness, wettability, and mechanical properties (unidirectional tensile strain measurements and nanoindentation) were studied. Afterward, the influence of hpcECM on attachment/proliferation/activation of cardiac cells (such as endothelial progenitor cells (EPCs), endothelial cells (ECs), H9c2 differentiated/undifferentiated cardiomyoblasts, and fibroblasts), expression of adhesion molecule such as intercellular adhesion molecule 1 (ICAM-1) and vascular cell adhesion molecule 1 (VCAM-1), immunomodulatory behavior (M1 and M2 macrophages and cytokine gene expression makers), and hemocompatibility were studied. Uncoated printed PCL with and without pores and fibronectin-coated PCL patches served as controls. In this study, it was shown that the hpcECM hydrogel provided a cell-inductive environment with an excellent potential to improve the proliferation of cardiac-specific host cells as a coating interface on synthetic 3D-printed scaffolds compared to its equivalents such as fibronectin-coated constructs.

2. Materials and methods

2.1. Production and characterization of hpcECM gel

The production of hpcECM gels from the human placenta has been described previously by our group.[35] All the procedures were approved by the institutional ethics committee of Medical University of Vienna (EK-Nr.: 1602/2018), and consent was obtained from the mothers prior to tissue use. Briefly, the donated placentas were obtained from cesarean sections performed at the Department of Obstetrics and Gynecology at the Medical University of Vienna (Austria). Chorion was isolated from the basal tissue, amnion and umbilical cord. The decellularization process was conducted using 2% Triton X-100 (Sigma-Aldrich GmbH, Vienna, Austria) and 0.02% ethylenediaminetetraacetic acid (EDTA, Sigma-Aldrich GmbH, Vienna Austria) for 3 days with 3 phosphate-buffered saline (1× PBS) washing steps in between. 0.4% DNase (Roche AG, Basel, Switzerland) treatment was subsequently applied for DNA removal. Afterwards, decellularized tissues were stored in 0.18% peracetic acid in 4.8% ethanol (Sigma-Aldrich GmbH, Vienna, Austria) for 2.5 hours for sterilization. Samples were frozen at −20°C, lyophilized, and cryo-milled with a Freezer Mill 6770 (SPEX Sample Prep LLC, Metuchen, NJ, USA). Porcine gastric mucosa pepsin (Roche AG, Basel Switzerland) was used for solubilization of the chorionic powder by enzymatic digestion under acidic conditions (0.1 M HCl; Merck, Darmstadt, Germany). pH neutralization of the resulting gel using 1 M NaOH (Merck, Darmstadt, Germany) and adjusting the salt concentration to 1× were performed. The final product was stored at −80°C.

Hematoxylin and eosin (H&E) staining was conducted to validate complete cell removal from the tissue. To do so,

the tissues were paraformaldehyde-fixed, dehydrated and embedded with Tissue-Plus™ OCT Compound (Clear Cryostat Embedding Medicum; Scigen Scientific Inc., Gardena, CA, USA). Afterward, the samples were sectioned (each 20 µm) and placed on the slide for H&E staining, according to the manufacturer's protocol (Morphisto, Offenbach, Germany). To control the quality of the product, each batch of the produced hpcECM powder in the form of pre-gel solutions was examined for further biochemical quantification methods such as assessing the residual DNA, elastin, glycosaminoglycan (GAG), and collagen content. Briefly, DNA Extraction Mini Kit (Favorgen, Taipei, Taiwan) and AccuBlue® High Sensitivity dsDNA Quantitation Kit (Biotium, Fremont, CA, USA) were used for DNA extraction and quantification. Collagen content was assessed by measuring the hydroxyproline content of neutralized samples following hydrolysis in 6 M HCl at 110°C for 20 hours. 1,9-dimethyl-methylene blue (DMB; Sigma-Aldrich GmbH, Vienna, Austria) staining of the pre-gel samples was conducted to identify the sulfated GAG content. Fastin™ Elastin Assay (Biocolor, Carrickfergus, UK) was utilized to assess the elastin content.

2.2. 3D printing of the scaffolds and morphological studies

The EnvisionTEC 3D-Bioplotter (EnvisionTEC GmbH, Gladbeck, Germany), a 3D printing tool based on a pneumatic extrusion system was used to fabricate PCL (Mn 45000 kDa; Sigma-Aldrich, St. Louis, MO, USA) based porous thin patches. These patches were designed using Magics EnvisionTEC (V13; Materialise, Leuven, Belgium), Bioplotter RP V2.9, and VisualMachines BP V2.2 (both EnvisionTEC GmbH, Gladbeck, Germany) software. For printing, pure PCL pellets were heated up to 90°C, followed by dispersion through the nozzle with a diameter of 400 µm and with a printing pressure of 9 bar (Table 1).

Thin patches were printed in two layers. The first one was a continuous line pattern with an additional wave-pair pattern on top (Figure 1a and 1b), printed with specific printing parameters. The utilized pneumatic extrusion technique provides high reproducibility and precise control over the pore size and shape.

Table 1. Printing parameters.

Parameter	Value
Printhead temperature	90°C
Platform temperature	40°C
Printing pressure	9 bar
Nozzle diameter	400 µm
Pre-flow	0.08 s
Post-flow	–0.12 s
Wait time between layers	120 s

2.3. Structural analysis, coating visualization, roughness and surface profile

The morphology and size of the pores were investigated utilizing scanning electron microscopy (SEM) images. To investigate pore size, five samples (1 × 0.5 cm) from each group (0.02% hpcECM-PCL, 0.2% hpcECM-PCL, and uncoated PCL) were prepared. Subsequently, five random positions from each sample have been selected and analyzed using ImageJ (version 2.14.0/1.54f). For each group, the surface area of 100 pores was measured and compared. Further, the porosity of the coated and uncoated samples was calculated by a gravimetric method from the known mass and the measured dimensions of the 3D-printed patches as earlier described (n = 5).[37] Immunofluorescence staining against fibronectin was performed to detect the coating layer as hpcECM contains various basal lamina proteins, fibronectin, laminin, and collagen.[35] Polymer samples were cut into 1 × 0.5 cm pieces and placed into 24-well plates. Coating with 0.02% hpcECM-gel (0.2 mg/mL), 0.2% hpcECM-gel (2 mg/mL), 0.02 % fibronectin (0.2 mg/mL), and 0.1% (1 mg/mL) was performed for 2 and 72 hours at 37°C. Previously, it was shown that the higher concentration of fibronectin (at 2 mg/mL) did not result in significant differences in terms of cell adhesion or coating efficiency (data not shown) compared to lower concentration of fibronectin (1 mg/mL). Uncoated samples were incubated in Phosphate-buffered saline (PBS). The specimens were fixed in 4% paraformaldehyde overnight at 4°C. Primary mouse anti-human fibronectin antibody (clone 3F12, 1:200 dilution in PBS/1% bovine serum albumin (BSA); Thermo Fisher Scientific, Vienna, Austria) and secondary goat anti-mouse 647 (Abcam, Cambridge, UK) were used. Fluorescence mounting medium (Agilent Technologies, Santa Clara, CA, USA) including 1 µM DAPI (Sigma-Aldrich GmbH, Vienna, Austria) was used prior to confocal microscopy (Zeiss LSM700, Anna Spiegel Image Facility, Austria).

Roughness and the surface profile of the patches were analyzed using a VR-5200 wide-area 3D optical microscanner/profilometer (Keyence, Keyence International, Mechelen, Belgium). High-resolution, single-shot 3D microscopic measurements were taken with a precision of 0.1 µm. The instrument recorded data from 800,000 points within four seconds at a working distance of 75 mm, while maintaining the same 0.1 µm resolution. The analysis followed the roughness standard outlined in ISO 25178-2:2012.

2.4. Mechanical characterizations

Mechanical characteristics of the coated and uncoated samples (0.02% hpcECM-PCL, 0.2% hpcECM-PCL, and uncoated PCL) were assessed in both macro and micro

scales via unidirectional tensile strain and nanoindentation measurements, respectively. To assess the bulk macro mechanical properties of the constructs, an Anton Paar MCR301 rheometer (Anton Paar GmbH, Graz, Austria) with a clamp system was utilized. Force-displacement data were recorded to determine ultimate tensile strength (UTS), strain at failure (SAF), and modulus of elasticity (E) ($n = 5$ per group). Tests were performed at a strain rate of 1 mm/min, with measurements taken up to the failure point of the material. UTS was calculated by normalizing the force measurements to the effective cross-sectional area. Herein, the mass of PCL was measured (1.2 mg/mm^3), and the effective cross-sectional area was calculated using sample dimensions (24 × 12 × 0.4 mm) and weight.

Nanoindentation was performed using the Nanoindenter ZHN (ZwickRoell GmbH & Co. KG, Ulm, Germany). Samples were attached to microscope slides using a thin two-sided adhesive tape to avoid bulking. The slides were then fixed using a clamp-type sample holder (ZwickRoell GmbH & Co. KG, Ulm, Germany). Sixteen positions were measured from each group (2 samples per group, 8 positions per sample). Each measuring point was positioned in a way to avoid interference with neighboring indents (a minimal distance of 30 μm between the points). The material's Poisson's ratio was assumed at 0.25. Indentation was performed using a Berkovich indenter with a 15 μm nominal radius. Before testing, the indenter was position-calibrated and the contact force was set at 17 μN. The measurement sequence, included a linear force slope of 1 mN/s until 10 mN maximum force was reached. The maximum force was held for 5 s before unloading to 0 mN for 4 s. The unloading curve was fitted by default between 97% and 39% of the maximum load. Before data analysis, an automatic zero-point correction was applied. No thermal drift correction was applied as the material was considered viscoelastic. Mechanical properties were calculated with the manufacturer's software (InspectorX V5.5.4; ZwickRoell GmbH & Co. KG, Ulm, Germany) for each measuring point. The position of the measuring points was controlled, following the experiments, and in case the indents were in sites of curved local surfaces, the corresponding measuring point data were excluded from the analysis. Reported data include the indentation hardness H_{IT} (force divided by contact area under load) and the indentation modulus E_{IT}. Under ideal circumstances (no material pile-up or sink-in), the E_{IT} is equal to the modulus of E.

2.5. Wettability and hydrophilicity characterization

Water contact angle (WCA) and free surface energy (FSE) measurements were investigated (PCL patches coated with 0.02% and 0.2% hpcECM vs uncoated samples and flat non-porous printed PCL samples). A goniometer equipped with a camera (KRÜSS DSA25, KRÜSS GmbH, Hamburg, Germany) and post-process software (ADVANCE, KRÜSS GmbH, Hamburg, Germany; and Angle Meter 360 application, AK APP Develop, Russian Federation) were employed for the WCA measurements. WCA measurement on the surfaces was performed using a 5 μL droplet of deionized water gently dispensed on the surface by a motorized syringe. WCA data on three porous and three non-porous patch samples were collected (5 WCA measurements/patch). FSE of the solid area was performed by employing the model of Owens–Wendt–Rabel & Kaelble (OWRK).[38] In the OWRK methods, contact angles of two liquids (2 μL droplets, deionized water, and diiodo-methane) with different polarities were acquired to calculate the FSE. Due to the rapid absorption of liquid through the patch (owing to the high porosity), a video of the drop deposition was recorded and the frame with a stable drop was used for the WCA calculation with the Angle Meter 360. Furthermore, to investigate the influence of the topography and exclusively study the repellent properties of the coating, PCL flat, non-porous samples with the same dimensions were printed, coated, and examined for WCA measurements.

2.6. Biocompatibility and cell proliferation assessments

Biocompatibility of the patches including the influence of the hpcECM coating on cell proliferation and cell viability were studied and compared utilizing human umbilical vein endothelial cells (HUVECs; Lonza Group AG, Basel, Switzerland) and human foreskin fibroblasts (HFFs; ATCC, Manassas, VA, USA). Pooled donor HUVECS were cultured in Endothelial Growth Medium 2 (EGM-2; Lonza, Wakesville, MD, USA) and HFFs were cultivated in Fibroblast Growth Medium 3 (FGM-3; Lonza, Wakesville, MD, USA). Both media were supplemented with 10% fetal bovine serum (FBS; Sigma-Aldrich GmbH, Vienna, Austria) and 1% penicillin/streptomycin (Gibco, OK, USA). After harvesting the cells at 80% confluency, HUVECs and HFFs (each at a density of 2 × 10^4 cells/cm^2) were seeded on the 0.02% hpcECM-PCL, 0.2% hpcECM-PCL and uncoated sterile PCL patches (0.5 × 1 cm) in 24-well plates. After 24, 48, and 72 hours of cell cultivation, the viability of HUVECs and HFFs was quantified using a colorimetric methoxynitrosulfophenyl-tetrazolium carboxanilide (XTT) assay cell viability method utilizing 2,3-Bis(2-methoxy-4-nitro-5-sulfophenyl)-2H-tetrazolium-5-carboxanilide inner salt (XTT; Santa Cruz Biotechnology, Dallas, TX, USA) and a Spark® Multimode Microplate Reader (TECAN, TECAN Austria GmbH, Gröding, Austria).

Furthermore, live/dead assay was also applied to the H9c2 (undifferentiated and differentiated) and fibroblasts after 24 and 72 hours to determine the amount of

viable and dead cells via calcein AM (for live cells) and propidium iodide (PI; for dead cells) staining. To do so, $2 \times 1\ 0^5$ HFFs were cultured on 0.5 × 1 cm piece patches. Subsequently, cells were stained with 2.5 µg/mL PI (Sigma-Aldrich, Austria) and 1 µg/mL calcein AM Biotium, Fremont, CA, USA) for 30 min. After three washing steps and paraformaldehyde (Sigma-Aldrich GmbH, Vienna, Austria) fixation (overnight at 4°C), coated and uncoated patches were mounted using a fluorescence mounting medium and were imaged using an LSM700 confocal microscope (Zeiss, Munich, Germany).

2.7. Hemocompatibility assays

Blood clotting and hemolysis assays were performed. For the blood clotting assay, patches were coated with 0.02% or 0.2% hpcECM and weighed accordingly. Glass coverslips were used as positive controls. Freshly donated human blood from non-anti-coagulated volunteers was collected in EDTA tubes and recalcified (ethical committee approval number: EK Nr: 2321/2020, 10 mM $CaCl_2$; Sigma-Aldrich GmbH, Vienna, Austria). The coated patches were incubated for 1 hour at 37°C in the recalcified blood and then weighed again. The mass gained after the incubation was considered a sign of thrombus formation on the surface.

Furthermore, the hemolytic behavior of the coated patch was assessed. 0.02% and 0.2% hpcECM-coated and uncoated patches were incubated with diluted blood (1:5 dilution with 0.9% NaCl) for 1 hour at 37°C. Subsequently, samples were centrifuged (3000 rpm, 5 min) and absorbance of the supernatants was measured at 541 nm wavelength with a Spark® Multimode Microplate Reader (TECAN, TECAN Austria GmbH, Gröding, Austria). Blood diluted with distilled water (1:5 dilution) served as a positive control, whereas 0.9% NaCl (1:5 dilution) served as a negative control accordingly. Control groups did not include any constructs.

The hemolysis ratio was determined using the following formula:

$$\text{Hemolysis ratio}\,(\%) = \frac{\text{Abs}_S - \text{Abs}_{NC}}{\text{Abs}_{PC} - \text{Abs}_{NC}} \times 100 \qquad \text{(I)}$$

where Abs_S is the absorbance of sample; Abs_{NC} is the absorbance of negative control; and Abs_{PC} is the absorbance of positive control.

2.8. Isolation and attachment of EPCs

EPCs were isolated from 45 mL of donated human blood (collected from healthy male and female volunteers; approved by the ethics committee: EK-NR.: 2321/2020) via density centrifugation using Ficoll Paque Plus (Cytiva, Marlborough, MA, USA). The peripheral blood mononuclear cell (PBMC) portion was isolated and washed with PBS followed by centrifugation steps. Cells were resuspended in EGM-2 medium. Polymer samples were cut into 0.5 × 1 cm pieces and placed into 24-well plates. Coating with 0.02%, 0.2% hpcECM, and 0.02% fibronectin was performed for 2 hours at 37°C. Uncoated samples were incubated in Dulbecco's phosphate-buffered saline (1× DPBS (−/−), Sigma-Aldrich GmbH, Vienna, Austria). Fibronectin-coated samples served as control. One million freshly isolated cells were seeded per PCL construct and incubated in EGM-2 medium for one week with medium changes every second day. The specimens were fixed in 4% paraformaldehyde and stained with primary mouse anti-human Prom-1 antibody (clone 2F8C5, 1:200 dilution in PBS/1% BSA; Thermo Fisher Scientific, Vienna, Austria) for 1 hour at room temperature subsequently. Goat anti-mouse 647 (Abcam, Cambridge, UK) was used as the secondary antibody. After three washing steps, samples were mounted with a mounting medium containing 1 µM DAPI (both Sigma-Aldrich GmbH, Vienna, Austria). Samples were analyzed utilizing a confocal microscope (Zeiss, LSM700).

2.9. Differentiated and undifferentiated H9c2 cardiomyoblast activation and proliferation

H9c2 undifferentiated cells (rat myocardial cell line) and differentiated cells (via retinoic acid [RA]) were cultured on the 0.02 % or 0.2% hpcECM-coated and uncoated samples (2×10^4 cells/cm^2). XTT and live/dead assays were performed to identify cell proliferation and the amount of viable and dead cells as mentioned before (**Section 2.6**) after 24, 48, and 72 hours. Differentiation of the H9c2 cells was induced using RA. Briefly, H9c2 undifferentiated cells were cultured in DMEM with 4.5 g/L glucose, 10% FBS (Gibco, OK, USA), and 1% penicillin/streptomycin (Gibco, OK, USA) until reaching 60% confluence. Subsequently, a reduced serum concentration, at 1% FBS, was used, and 1 µg/mL of RA (Merck, Darmstadt, Germany) was added to the medium. The medium was refreshed every 24 hours for the next 5 days. On day 5, the cells were ready for further procedures. Additionally, the activation of H9c2 differentiated cells and the influence of hpcECM on the activation of H9c2 cells were studied via troponin T staining. To do so, differentiated cells were seeded into a plate (8×10^5 cells/mL) for 24 hours. The cells were fixed in 4% paraformaldehyde (PFA) in PBS for 20 min followed by a 15-min incubation in 100 mM glycine. The cell permeabilization was performed using 0.1% Triton X-100 for 5 min. Unspecific binding sites were blocked with 4% BSA in PBS for 1 hour. The primary antibodies used were rabbit cardiac troponin T (1:200; ProteinTech, 15513-1-AP), and isolectin GS-IB4

from Griffonia simplicifolia, Alexa Fluor™ 488 Conjugate (1:200; Thermo Fisher, I21411). Secondary antibody was goat anti-rabbit IgG antibody (H+L), Texas Red (1:200; Abcam, TI-1000). Vectashield antifade mounting medium with DAPI (H-1200-10) was used to mount the coverslip on the glass slide. Samples were analyzed utilizing a Zeiss LSM700 confocal microscope (Carl Zeiss Microscopy GmbH, Germany, oberkochen).

2.10. Quantitation of adhesion molecule expression via RT-qPCR

Polymer samples were cut into 0.5 cm pieces and placed into 24-well plates. Coating with 0.02% or 0.2% hpcECM or 0.02% fibronectin was performed for 2 hours at 37°C. Uncoated samples were incubated in PBS (−/−). The coating solutions were then removed and HUVECs (P5-P7) were seeded to the constructs (2×10^5 cells/specimen) for 72 hours. Cells were detached with Accutase (Sigma-Aldrich GmbH, Vienna, Austria) and spun down, and subsequently, RNA was isolated using a Favorprep™ Tissue Total RNA Purification Mini Kit (Favorgen, Taipei, Taiwan). The synthesis of the complementary DNA (cDNA) was performed with a QuantiTect Reverse Transcription Kit (QIAGEN Inc., Valencia, CA, USA). Gene expression levels of *ICAM1*, *VCAM1,* and platelet endothelial cell adhesion molecule 1 (*PECAM1*) were evaluated with a 7500 real-time PCR system (Thermo Fisher Scientific, Vienna, Austria). The sequences of all primers are shown in Table 2.

2.11. Evaluation of inflammatory behavior utilizing primary macrophage cells

The influence of hpcECM coating on the expression of pan-, pro- and anti-inflammatory macrophages (CD68, CCR7, CD80, CD163, and CD206) and cytokines (IL-1α, TNF-α, and IL-10) was studied using qPCR. To do so, human PBMCs were isolated from three donors and differentiated into macrophages.[39] Subsequently, the macrophages were seeded on the uncoated, 0.02% and 0.2% hpcECM-coated PCL patches (5×10^5 cells/well) in 24-well plates ($n = 6$, derived from 3 donors) for 1, 3, and 7 days. Total cellular RNA was isolated using the RNeasy Mini Kit via the QIAcube system (both from Qiagen, Valencia, CA, USA). Reverse transcription was performed using the Go–ScriptTM Reverse Transcription System (Promega GmbH, Vienna, Austria). Finally, the real-time PCR was performed with a Roche light cycler 480 (Roche AG, Basel, Switzerland). Briefly, the Ficoll separation method was used for the isolation of PBMCs (same protocol as described in **Section 2.8**).

Isolated PBMCs were re-suspended in RPMI 1640 with 10% FBS (Millipore, Darmstadt, Germany) and seeded on tissue culture plates. Macrophage colony-stimulating factor (M-CSF) was added to the PBMCs for 5 days till they were differentiated into macrophages. Non-adherent cells were removed by washing the plates with PBS after 2 hours. Uncoated PCL constructs served as controls. All of the primers used in this study are shown in Table 2.

2.12. Statistical analysis

All data are expressed as mean ± standard deviation (SD). Statistical analyses were performed using GraphPad Prism software (Version 9.5.1, GraphPad Software Inc., CA, USA). The normal distribution of data was tested with the Shapiro–Wilk test. Based on the distribution of the data, unpaired *t*-test, one-way analysis of variance (ANOVA), or two-way (ANOVA) were applied. In detail, post hoc tests were conducted as multiple comparisons using either Sidak's or Tukey's test according to the distribution of the data. The Kruskal–Wallis test one-way analysis of variance (ANOVA) was employed to assess differences between the

Table 2. Primer sequences.

Gene	Forward (5' to 3')	Reverse (5' to 3')
CCR7	GCTGGTCTGAGCATTTGAGT	CCAGAAACTGTTCCCACCTG
CD68	CCTGGGTTGCTAACCATCTCC	CCAGTGCTCTCTGTAACCGT
CD80	CGGGAAACACTGCTAGTACC	AAAGCCTTTAGAGCCAGCCC
CD163	CTCCTTACTCTCCTGATGCCAA	TGAAGACTCTGGATCTGCTGGT
CD206	CTTAGTTCCGCCCTCCTGTC	TGCCTCAGAGCAGACTTACC
GAPDH	GGAAGGAAATGAATGGGCAG	CCCAATACGACCAAATCAGAG
ICAM1	ATGCCCAGACATCTGTGTCC	GGGGTCTCTATGCCCAACAA
IL1A	CAGTGGTCTCATGGTTGTCA	CTTGAGCCAGTAATTGGTCCG
IL10	CTCAGCACTGCTCTGTTGCCT	AGCTGTTCTCAGACTGGGTGC
PECAM1	GCAACACAGTCCAGATATCG	GAC CTC AAA CTG GGC ATC AT
TNFA	TCGGGCCGACTATCTCGACT	CGTCCTCCTCACAGGGCAAT
VCAM1	GGGAAGATGGTCGTGATCCTT	TCTGGGGTGGTCTCGATTTTA

three coating groups. In the case of a significant Kruskal–Wallis test, Dunn's test with Bonferroni correction was performed pairwise between specific pooled groups. Also, statistical significance was set at $p < 0.05$ for all statistical tests.

3. Results and discussion

3.1. 3D printing process and characterization of hpcECM

Material selection, architecture, and mechanical characteristics of the patch are prerequisites for sufficient integration of the patch into the anatomy of the heart for providing adequate mechanical and regenerative support. At the macro scale, the geometry and morphology of the patch are important parameters, whereas, at the microscale, the complex 3D architecture of the scaffold determines the prerequisites for cell migration and proliferation, vascularization, and nutrient, metabolite, and oxygen diffusion.[40,41] The biodegradable PCL patches were printed in three steps with a 3D-Bioplotter through a pneumatic extrusion technique. The first layer provided vertical lines (strand width of 266.136 ± 3.461 µm, printing speed: 16 mm/s), covered by a second layer consisting of oval-shaped pores with various ellipsis aspect ratios (major axis/minor axis of the oval, strand width 423.178 ± 17.760 µm) (Figure 1a–c and 1e). The surface of the strands represented micro-pores (Figure 1d). The printing parameters such as printing temperature, speed, pressure, and platform temperature were precisely optimized (Table 1). In this study, the major focus was to enhance cardiac-specific cell adhesion and proliferation on an extremely hydrophobic thin patch, which typically has limited available surface for cell attachment. The geometry of the studied patch had large pores with relatively thin strand width, representing a suitable model with restricted available surface for cell attachment.

3D-printed patches were subsequently coated with human placenta chorion ECM. The decellularization process of the chorion membrane and the quality of the produced hpcECM hydrogel were examined for each batch. H&E staining of the decellularized samples showed the structural integrity of the ECM protein network[42] and revealed complete cell component removal (Figure 1f and 1g). DNA content was reduced significantly (99.99975%) with average DNA residues of 4064.50 ± 44.56 ng/mg dry weight for native and 1.00 ± 0.03 ng/mg dry weight for decellularized samples (DNA removal efficiency: 99.99975%). Since this residual amount is less than 50 ng double-stranded DNA (dsDNA) per mg dry weight, this product is considered a safe hydrogel in terms of causing an immune reaction after application.[43] The macromolecule composition of the ECM proteins is substantial for cell adhesion, differentiation, and migration.[44] Therefore, the post-decellularization content of ECM proteins was evaluated. The collagen content of native (157.11 ± 17.97 µg/mg) and decellularized tissue (243.06 ± 26.22 µg/mg dry weight) was preserved considerably. The increase in collagen content is due to normalization of values to the dry weight of the samples, this reflects the loss of cell mass and soluble proteins in the tissue.[34,45] Elastin content showed no significant reduction (native: 1.43 ± 0.09 µg/mg dry weight; decellularized: 1.36 ± 0.14 µg/mg dry weight). GAG quantification showed 75% preservation of GAG content (native: 1.15 ± 0.05 µg/mg dry weight, decellularized: 0.87 ± 0.04 µg/mg dry weight) The protein composition analyses confirmed a successful decellularization process, with the preservation of protein structure (Figure 1h–k).

3.2. Surface and mechanical characterizations

Mechanical stiffness and topographical characteristics of the cellular 3D environment have a tremendous influence on the fate of cells in terms of adhesion, migration, proliferation, and even differentiation. Cells actively examine and adopt their pericellular space to fit their requirements. This is a bi-directional interchange between the characteristics of the 3D extracellular environment and their own secreted pericellular medium.[46] For instance, cells are capable of sensing and probing the micro stiffness of the surrounding and degrading the ECM matrix to regulate their fate in a dynamic manner.[47] In regard to the dynamic nature of the biological process, biodegradable polymers, and hydrogels in *in vitro* settings can be contemplated as initial examples of dynamic procedures, where the integrity and stiffness progressively decline with time via hydrolysis or enzymatic degradation.[48]

The influence of hpcECM coating on the surface and mechanical characteristics of the biodegradable patch were assessed via pore size, porosity, nanoindentation, unidirectional tensile strain, wettability, surface topography and roughness studies. However, the first critical step was to confirm the successful coating process and validate the method of the coating in 0.02% and 0.2% hpcECM hydrogel-coated samples. Initially, SEM was utilized to visualize the coating. SEM images of the 0.02% hpcECM-PCL, 0.2% hpcECM-PCL, and uncoated PCL samples are shown in Figure 2a and 2b. The coating could not be detected via SEM imaging due to the very low concentration of the utilized hydrogel and therefore possible creation of an extremely thin layer of ECM on the surface. Next, the immunofluorescence staining method was utilized to visualize the coating. It was previously shown that laminin and fibronectin were successfully preserved in the hpcECM gel after the decellularization process.[35] Therefore, coating visualization was examined via immunofluorescence staining of fibronectin. Samples

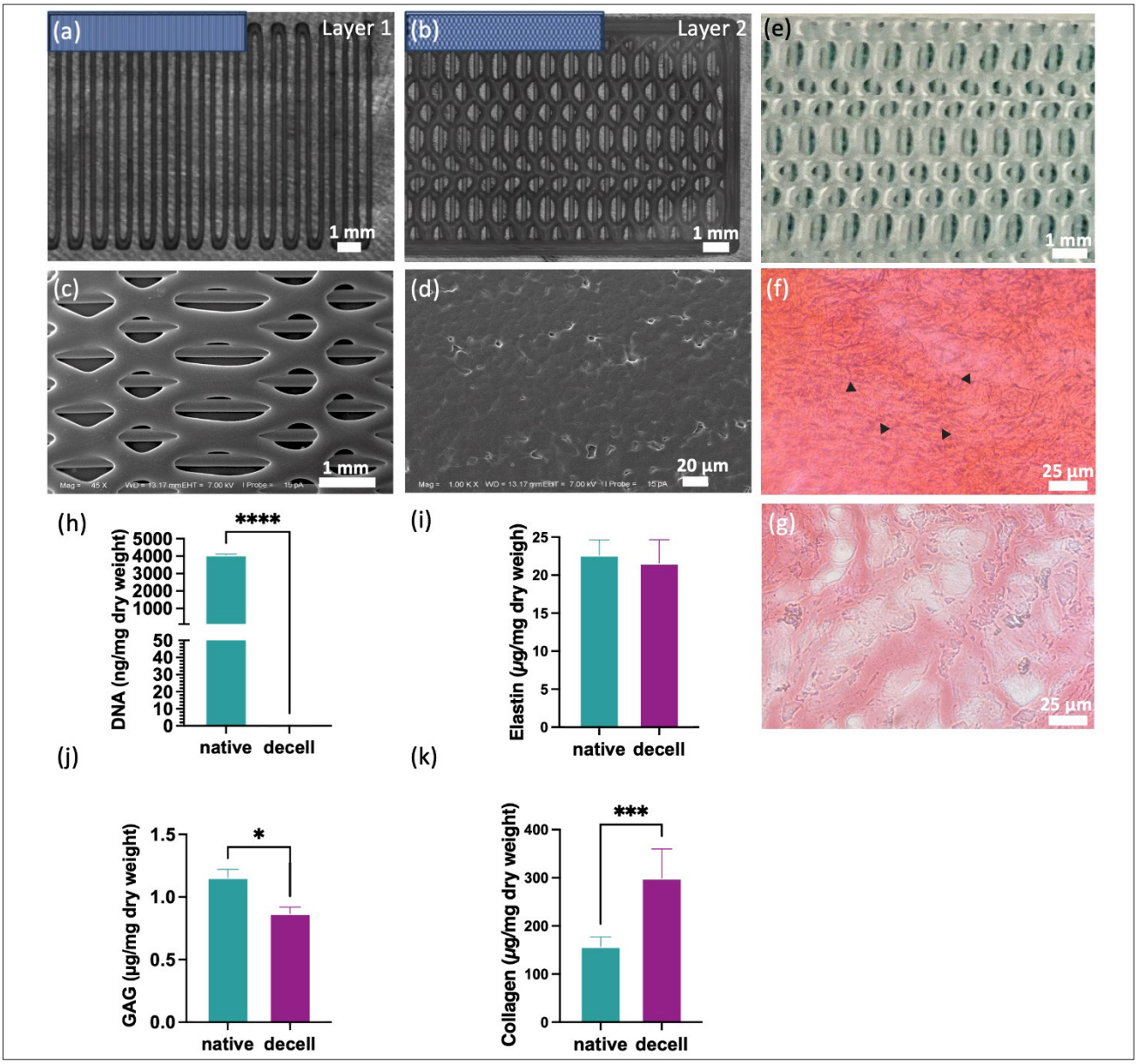

Figure 1. 3D printing fabrication process and material development via decellularization. The utilization of 3D printing provided an accurate control of PCL deposition for the fabrication of a patch with large pores. (a, b) structure of the 3D-printed layers. (c–e) SEM micrographs of the patch: (c) macrostructure, (d) microstructure (surface topography), and (e) prototype printed patch. Characterization of ECM hydrogel confirmed a successful decellularization and production of human placenta chorion ECM hydrogel. (f, g) H&E stained images confirmed the absence of cells after decellularization: (f) native chorion, and (g) decellularized chorion (arrows show the native cells in the native tissue). (h) DNA content was significantly reduced in the decellularized tissues compared to the native tissues (****$p < 0.0001$, 99.9997%). (i–k) The amount of (i) elastin, (j) GAG, and (k) collagen preserved in the decellularized tissue ($n = 4$). Abbreviations: GAG: Glycosaminoglycans; H&E: Hematoxylin and eosin; hpcECM: Human chorion placenta extracellular matrix; PCL: Poly-ε-caprolactone; SEM: Scanning electron microscopy.

coated with 0.02% (2 mg/mL) and 0.1% (1 mg/mL) fibronectin served as controls. Fibronectin has previously shown great potential in supporting re-endothelialization of polymeric grafts as a coating agent and reducing fibrosis with low immunogenicity leading to cardiac repair as a cardiac patch.[17,49] In terms of optimization of the method, samples incubated for 2 hours in coating solution were compared with samples incubated for 72 hours. Uncoated samples showed no signal, proofing the lack of background signals. A thin layer of positive staining was present in all coated samples (Figure 2e). In general, increasing the incubation time from 2 to 72 hours slightly increased the

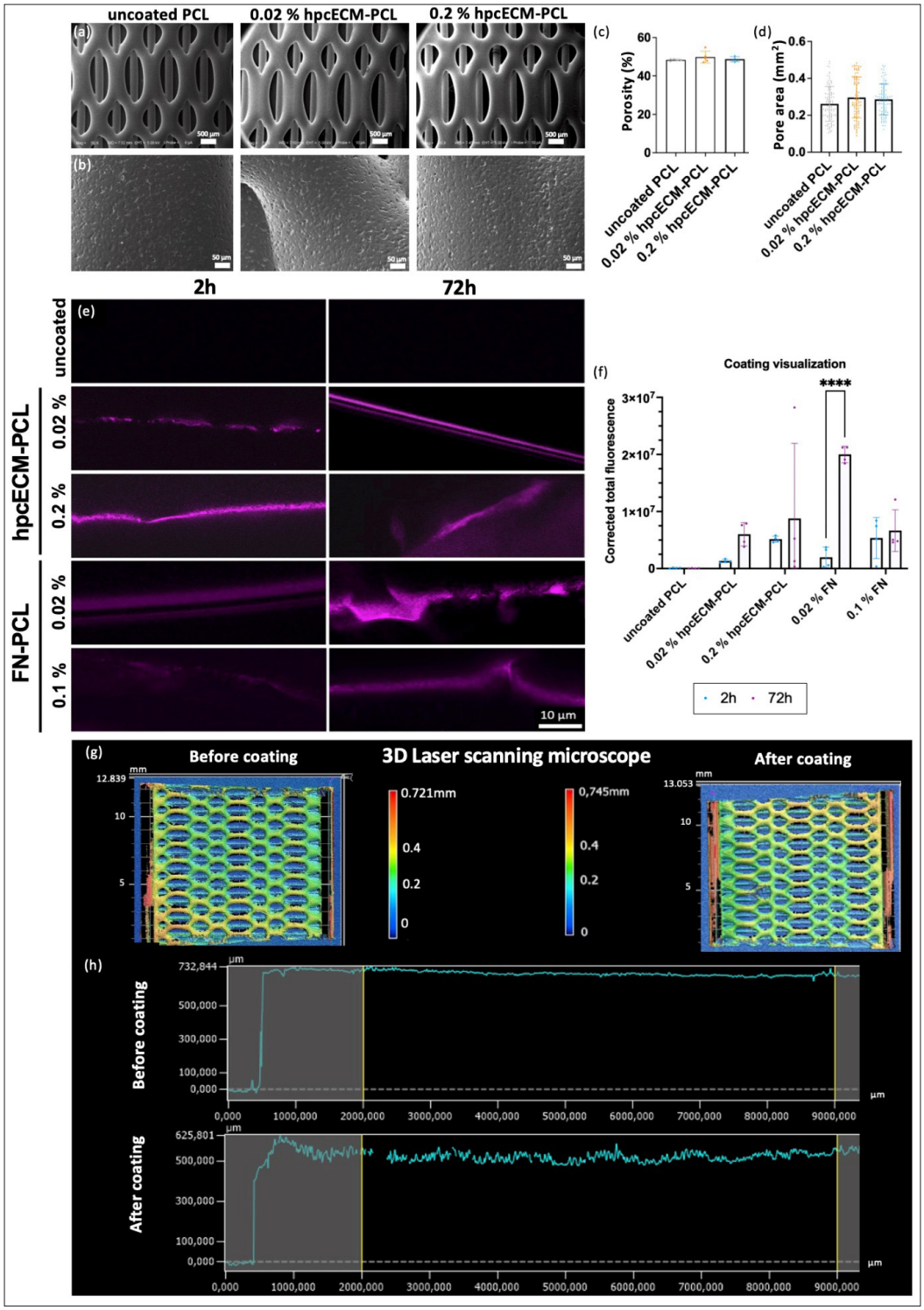

Figure 2. Scanning electron microscopy, porosity, pore size, coating visualization, 3D optical microscanner/profilometer results. (a, b) SEM images of coated and uncoated samples in two different magnifications: _50_× in (a); _500_× in (b). (c) Porosity, (d) pore size, (e) fibronectin immunofluorescence staining of the samples, with the fibronectin signal detected in both hpcECM- and fibronectin-coated samples. (f) Quantification of coating efficiency and influence of incubation time on coating; no significant differences were observed between the groups (except for samples coated with less concentration of fibronectin) (****$p < 0.0001$). (g, h) Results from 3D optical profilometer: (g) surface height profile, and (h) roughness profile and quantifications measured by VR-5200 wide-area 3D optical profilometer. The presence of hpcECM caused a smoother surface inducing a decline in surface roughness. Abbreviations: FN: Fibronectin; hpcECM: Human chorion placenta extracellular matrix; PCL: Poly-ε-caprolactone; SEM: Scanning electron microscopy.

efficiency of coating (Figure 2f). However, this was only significant in 0.02% of fibronectin-coated samples. The coating efficiency with lower fibronectin concentration increases with incubation time.

Furthermore, pore size and porosity were studied (Figure 2c and 2d). The mean pore size distribution of the uncoated PCL samples, 0.02% hpcECM-PCL, and 0.2% hpcECM-PCL was 0.26 ± 0.09, 0.31 ± 0.12, and 0.29 ± 0.09 mm^2, respectively. The large standard deviation is attributed to the existence of two different pore size categories (large and small ones) in the patch design. The porosity of the uncoated PCL samples, 0.02% hpcECM-PCL, and 0.2% hpcECM-PCL was 48.34 ± 0.01%, 48.74% ± 0.01%, and 49.79 ± 0.03%, respectively. In general, coating did not show any significant effect on the pore size distribution and porosity. The pneumatic extrusion technique provided high reproducibility and precise control over the pore size, shape, and pore size distribution.

The surface profile and the roughness of the patches before and after coating were further studied via a 3D optical microscanner/profilometer. An example of the surface profile of a sample coated with 0.02% hpcECM hydrogel is shown in Figure 2g. The surface color coding and height of the patches before and after coating changed slightly. This indicates the presence and distribution of the hpcECM coating on the porous material. Further quantifications were applied to measure the surface roughness, a factor that also influences cell attachment. Increased surface roughness has been shown to increase cell adhesion on polymers.[50] 3D-printed patches had micropores on the surface providing a relatively rough surface; however, the addition of a thin hpcECM hydrogel layer led to a smoother surface and the average roughness decreased from 13.9 µm to 5.9 µm in 0.02% hpcECM-PCL (57% decrease) and from 15.0 µm to 5.3 µm in 0.2% hpcECM-PCL (64.6% decrease) (Table 3, Figure 2h). This could translate to less potential in cell adhesion; however, it should be noted that surface wettability is another critical factor that could compensate for the low surface roughness.

Contact angle measurements and FSE measurements could give us an insight to the degree of hydrophobicity of the uncoated PCL and hpcECM-coated samples (Figure 3a–d). In this study, porous 3D-printed samples were compared with an identical 3D-printed flat nonporous PCL structure, in order to additionally investigate the role of porosity in the coating process.

Both flat and porous samples showed a very significant reduction in contact angles between coated and uncoated groups ($p < 0.0001$), confirming the role of hpcECM in inducing surface hydrophilicity to the hydrophobic biopolymer. In contrast to the flat samples, there were no significant differences between the samples coated with 0.2% and 0.02% hpcECM in porous samples. This could be due to the fast absorption of the droplet on the porous samples causing challenges in contact angle measurements and leading to a higher SD (Figure 3b and 3c). Furthermore, FSE data showed that the more concentrated hpcECM could provide high surface energy, suggesting the higher hydrophilicity (0.2% hpcECM-PCL: 58 mN/m, 0.02% hpcECM-PCL: 41 mN/m, uncoated PCL: 31 mN/m) (Figure 3d). Additionally, clear differences regarding the shape of the droplet on the surface of the samples were apparent (Figure 3a). In aliphatic polyesters such as PCL, the presence of hydrocarbon backbones induces low hydrophilicity, which limits cell spreading and therefore ECM formation.[51] However, in our study, the hpcECM hydrogel coating could provide a hydrophilic layer consisting of fundamental constituents of the ECM. This thin layer of ECM hydrogel could support a range of biomimetic systems leading to a higher moiety and induced interaction between cells and biomaterials. Furthermore, the mechanical characteristics of the 0.02% hpcECM-PCL, 0.2% hpcECM-PCL and uncoated PCL patches were analyzed via unidirectional tensile strain measurements (Figure 3e–h). The ultimate tensile strength (UTS), strain at failure (SAF), and modulus of E of the uncoated patch were 3.59 ± 0.4 Mpa, 11.84% ± 2.8% MPa, and 31.78 ± 7.3 Mpa, respectively. No significant differences were

Table 3. Roughness profile and quantifications measured by 3D optical profilometer.

Sample	Ra Avg. (µm)	Ra Max. (µm)	Ra Min. (µm)	SD (µm)
Uncoated PCL_1	13.99	28.24	6.87	6.80
0.02 % hpcECM-PCL_1	5.93	14.97	1.80	4.35
Uncoated PCL_2	15.03	39.30	2.64	11.78
0.2 % hpcECM-PCL_2	5.37	11.99	2.32	3.31

Notes: PCL_1: PCL patch group one, Samples in group one were coated with 0.02% hpcECM-PCL; PCL_2: PCL patch group two, Samples in group two were coated with 0.2% hpcECM-PCL.

Abbreviations: hpcECM: Human chorion placenta extracellular matrix; PCL: Poly-ε-caprolactone; Ra Avg.: Average roughness; Ra Max.: Maximum roughness; Ra Min.: Minimum roughness; SD: Standard deviation.

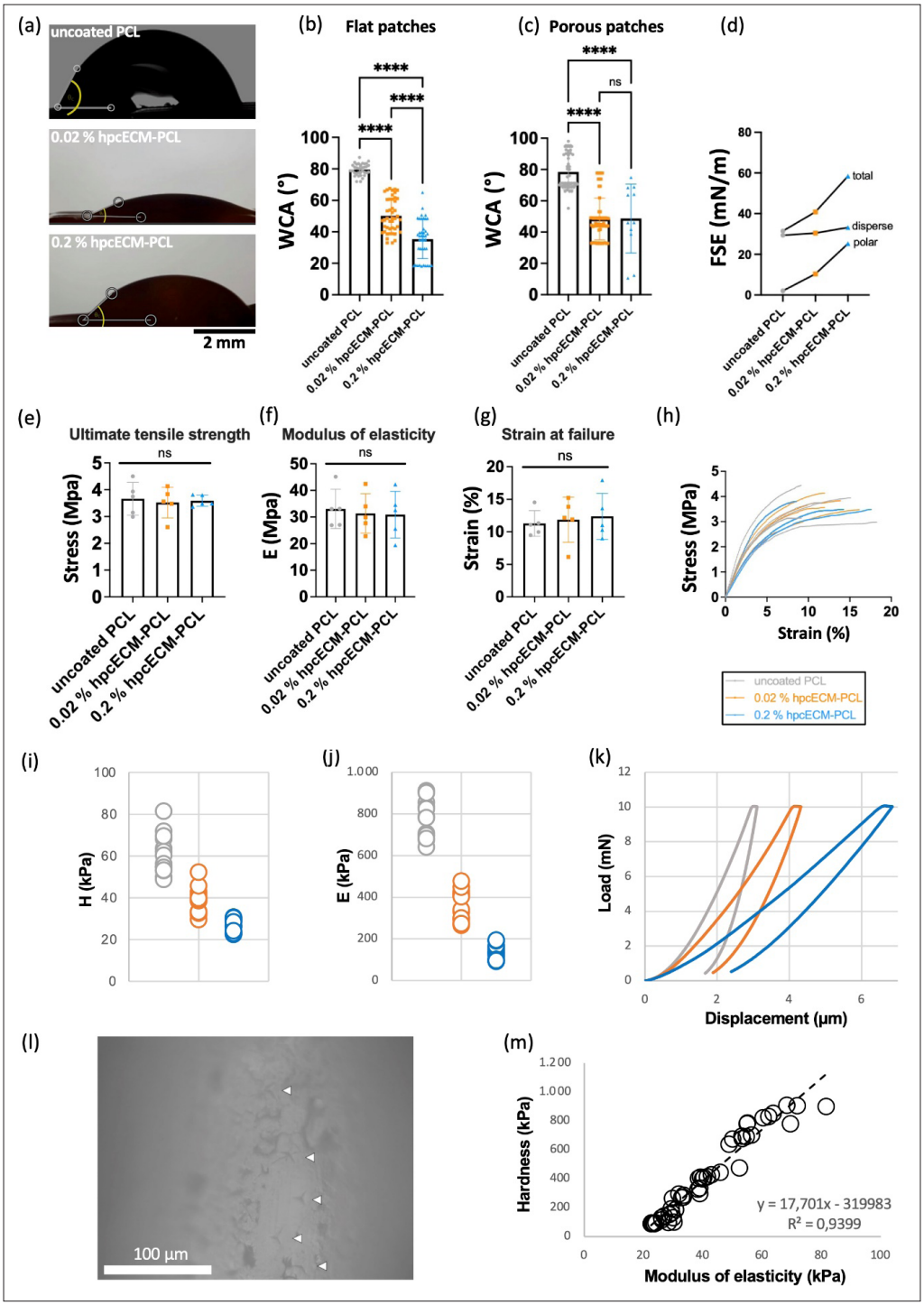

Figure 3. Wettability analysis, mechanical characterization via unidirectional tensile strain, and nano-indentation measurements. (a–c) Wettability and contact angle measurements of flat vs porous samples. (d) Free surface energy (FSE) characterization; polar, dispersed, and total FSE based on different hpcECM concentrations. A higher FSE indicates a more hydrophilic surface. Increased hydrophilic properties with increasing hpcECM concentration were observed. (e–h) Unidirectional tensile strain measurements: (e) ultimate tensile strength (UTS), (f) modulus of elasticity (E), (g) strain at failure (SAF), and (h) stress-strain curve. (i–l) Results pertaining to nanoindentation: (i) indentation hardness; (j) indentation modulus of elasticity; (k) typical load-displacement curves from nanoindentations, showing that hpcECM provided a softer and more elastic environment at the cellular level; (l) image showing indentation positions on the surface (indicated by white arrows). (m) Correlation between indentation hardness and indentation modulus confirmed the high accuracy of the gel mechanical characterization method at the nanoscale level. Abbreviations: hpcECM: Human chorion placenta extracellular matrix; PCL: Poly-ε-caprolactone.

Table 4. Mechanical characteristics via nanoindentation and unidirectional tensile strain measurements.

Sample	H_{IT} (MPa)	E_{IT} (MPa)	UTS (MPa)	SAF (%)	E (MPa)
Uncoated PCL	0.06 ± 0.08	0.77 ± 0.08	3.66 ± 0.61	11.29 ± 1.96	33.07 ± 7.40
0.02% hpcECM-PCL	0.03 ± 0.05	0.35 ± 0.07	3.59 ± 0.20	12.38 ± 3.53	30.9 ± 8.73
0.2% hpcECM-PCL	0.02 ± 0.01	0.12 ± 0.03	3.52 ± 0.57	11.86 ± 3.47	31.37 ± 7.38

Abbreviations: E: Modulus of elasticity; E_{IT}: Indentation modulus; H_{IT}: Indentation hardness; hpcECM: Human chorion placenta extracellular matrix; PCL: Poly-ε-caprolactone; SFA: Strain at failure; UTS: Ultimate tensile strength.

observed in the stress-strain response between the coated and uncoated groups at the macroscopic level (Figure 3h). The mechanical characteristics of cardiac tissues vary between systolic and diastolic phases, with infarcted tissue exhibiting even significantly greater stiffness. For instance, the modulus of elasticity of human cardiac tissue differs from 0.02 to 0.50 MPa. Furthermore, the UTS and the SAF are in the ranges of 3–15 kPa and 22–90%, respectively. This wide range highlights the challenge of defining optimal mechanical properties for related applications.[40,52] In general, the hpcECM-PCL patch was stiffer compared to the cardiac tissue and the bulk modulus of elasticity of the patches was significantly higher than that reported for the native human cardiac tissue. However, it has been shown previously that even much stiffer cardiac patches could induce an improved outcome in terms of inhibiting unwanted pathophysiological remodeling and boosting cardiac regeneration by preventing further damage to cardiomyocytes.[52] This has been additionally confirmed by Wall et al.[53] in a theoretical simulation model. Considering that a very stiff patch may lead to diastolic dysfunction, Wall et al. showed that patches significantly stiffer than cardiac muscle are preferable to matrices with higher elasticity. This might be due to the fact that stiffer patches could more effectively reduce cardiac wall stress.

At the microscopic level, nanoindentation showed that the modulus of elasticity (E_{IT}) of the surface (hpcECM) and the indentation hardness (H_{IT}; force divided by contact area under load) decreased with increasing hpcECM concentration ($p < 0.001$) (Figure 3i–k, Table 4). All this confirms that the coating could provide a mechanically softer microenvironment for the cells, which might potentially support the mechanosensitive signaling pathways.[54,55] Pooling the data resulted in a strong correlation (R^2 = 0.940) between the hardness and modulus of elasticity. The indentation positions on the surface are shown in Figure 3l. The position of Pooling the data resulted in a strong correlation (R^2 = 0.940) between the hardness and modulus of elasticity (Figure 3m).

This confirms the accuracy of the measurement in micro/nano-scale. Since the ECM gel contains more than 40% collagen (mainly type I and III collagen),[35] this component could have a substantial role in defining the mechanics/stiffness of the constructs. Collagen fibrils present a stiffness ranging from 300 MPa to 1.2 GPa.[56] However, the stiffness of a reconstituted collagen type I gel could drop down to tens or hundreds of Pascals in both micro- and macro-scales.[57] Kolliopoulos et al.[58] have shown that introducing the chorion extracts to a mineralized collagen matrix could reduce the stiffness from 1.5 MP to less than 0.5 MPa. In this study, macro mechanical (unidirectional tensile strain) and micromechanical (nano-indentation) measurements suggest that the PCL 3D-printed construct with high UTS, and high modulus of elasticity is responsible for the bulk mechanical behavior of the patch, whereas hpcECM with a lower modulus of elasticity provides a soft microenvironment for cell adhesion and proliferation comparable to cardiac tissue in microscale.

3.3. Biocompatibility, cell attachment and hemocompatibility assessment

Various cell types, apart from cardiomyocytes, are involved in remodeling during cardiac regeneration. Endothelial cells and fibroblasts both play crucial roles in maintaining tissue function and homeostasis. Fibroblasts are the main production source of the extracellular matrix (ECM) with high type 1 collagen and fibronectin content.[59] The activation and migration of fibroblast cells are crucial for physiological processes related to angiogenesis. They have the capability to induce the formation of capillary-formed structures in the presence of endothelial cells.[59,60] Likewise, endothelial cells have substantial angiogenic characteristics in addition to the capability to transdifferentiate into cardiac muscle tissue.[61]

Here, primarily, the cell viability and proliferation of fibroblasts and endothelial cells were studied and compared by utilizing both HFFs and HUVECs. Live/dead staining of the HFFs and relevant SEM images revealed that all three groups of uncoated and coated PCL induced no cytotoxic effects. However, the patches coated with higher concentration of ECM supported the HFF cell proliferation more and cells presented a more elongated morphology in the dense populations (Figure 4a and 4b). XTT assay

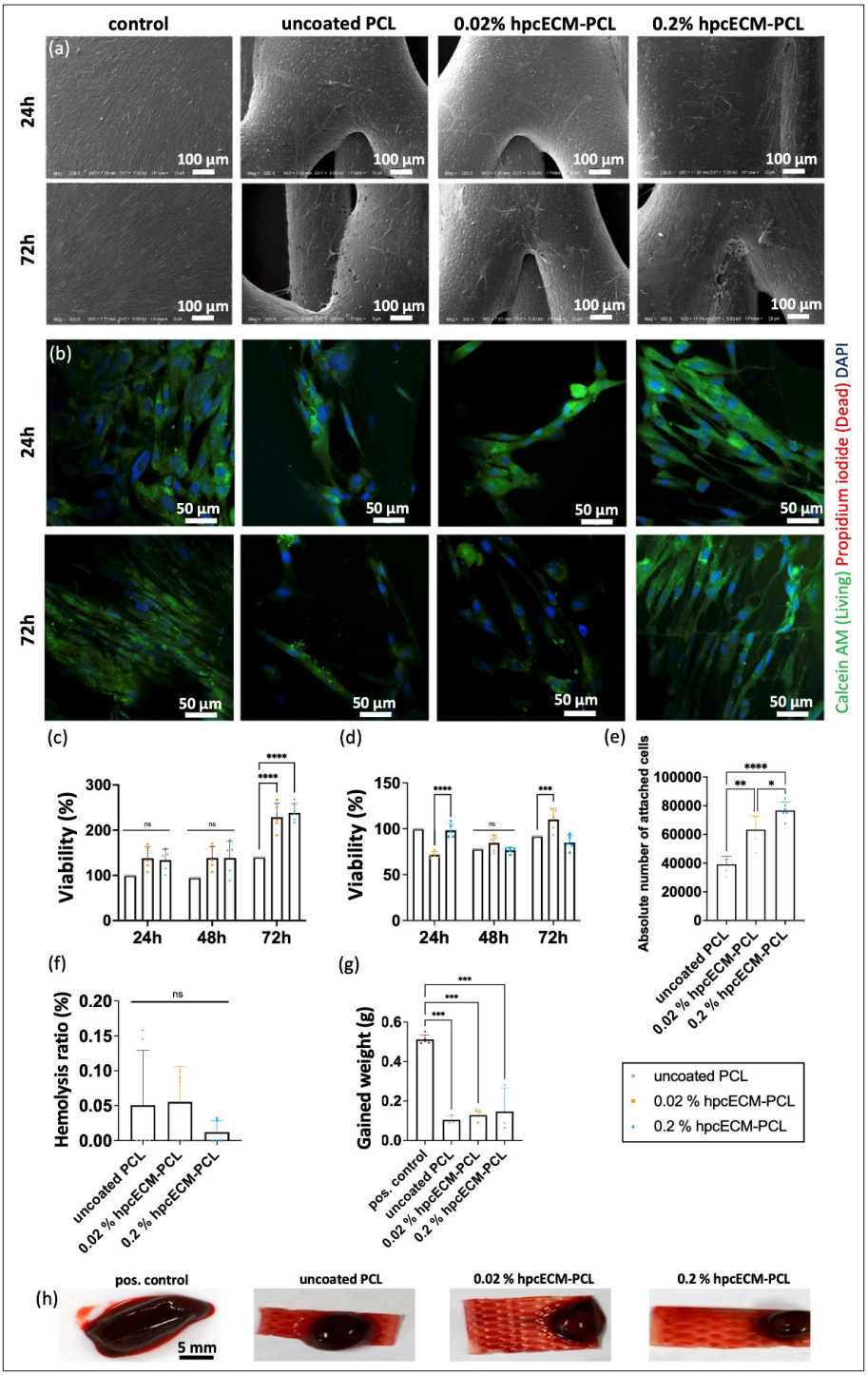

Figure 4. Biocompatibility, cell attachment, and hemocompatibility assays. (a) SEM images and (b) live/dead staining of patches cultured with HFFs for 24 and 72 hours. Patches significantly supported cell attachment. Most of the cells were viable (green cells) and only a limited number of cells were dead (almost no red cells). Both hpcECM-coated PCL samples supported cell proliferation significantly. (c–d) Determination of HFFs and HUVECs proliferation on coated and uncoated samples via XTT assay. Coating with hpcECM increased HFF proliferation after 48 and 72 hours. (e) Cell attachment assay revealed an evident, significant increase of HUVECs' initial attachment in coated samples 30 min after seeding. (f) Hemolysis ratio of tested samples. (g, h) Blood clot formation assay. Blood clot formation was significantly lower in the specimens than in the positive control. No significant difference in clot weight was detectable between coated and uncoated samples; in other words, the tested groups did not induce hemolysis. Abbreviations: HFFs: Human foreskin fibroblasts; hpcECM: Human chorion placenta extracellular matrix; HUVECs: Human umbilical vein endothelial cells; PCL: Poly-ε-caprolactone; SEM: Scanning electron microscopy.

confirmed that first the uncoated PCL patch along with the hpcECM-coated samples were biocompatible, and they did not show any cytotoxicity effect on both HUVECs and HFFs, which proliferated continuously within 24, 48, and 72 hours (Figure 4c and 4d). However, HFFs seeded on 0.2% and 0.02% hpcECM-coated samples promoted the proliferation significantly more than the uncoated groups. This confirms the capability of hpcECM to provide cells with an environment with higher cell affinity, promoting the proliferation and metabolic activity of the cells. The initial cell attachment assay confirmed significant improvement in HUVECs attachment in the coated patches after 30 min of seeding (Figure 4e). Afterward, the proliferations were promoted mainly in 0.02% hpcECM-coated groups after 72 hours (Figure 4d).

The difference in proliferation rate between various cell types was observed during the myocardial infarct repair process.[62] This could be due to the fact that, in general, fibroblasts are constantly producing ECM and they effectively generate their individual preferable environment that promotes growth and proliferation.[63] Myofibroblasts and endothelial cells proliferate and migrate into the infarct region, and they attempt to substitute the necrotic tissue with provisional granulation tissue. It has been shown that the proliferation of myofibroblasts is around 5% higher compared to endothelial cells at the beginning of the repair process.[62] However, as repair progressed, the proliferation rate of both cell types decreased but the trend stayed similar.[62] Furthermore, fibroblasts support and modulate endothelial migration and proliferation in various spheroid co-culture setups.[64]

Hemocompatibility of the PCL patches coated with 0.2% and 0.02% hpcECM was assessed via blood clot formation and hemolysis assays in a static set-up (Figure 4f–h). Figure 4h shows the actual thrombus formed in the presence of the patches. Results revealed that there were significant differences between the positive control and all other coated and uncoated PCL batches. HpcECM coating by itself did not induce any significant alteration in terms of the formed thrombus weight (uncoated PCL: 0.105 ± 0.016; 0.02% hpcECM-PCL: 0.129 ± 0.023; 0.2% hpcECM-PCL: 0.147 ± 0.077; Figure 4g). However, this assay is capable of providing an estimation regarding the hemocompatibility of the uncoated and coated patches. Hemolysis assay provided a more precise assessment in terms of studying the degree of red blood cells (RBCs) destruction induced by the PCL and hpcECM materials. All coated and uncoated groups showed a very low hemolysis rate (all data are below 0.5%, threshold of the hemolysis in humans is approximately 10%),[65] confirming the non-hemolytic characteristics of the pure PCL and the ECM coating (Figure 4f).

3.4. EPCs attachment and adhesion molecule expression

EPCs are circulating cells that contribute to vascular and cardiac repair.[66] They could adhere to the endothelium in ischemic regions in the myocardium and participate in vascularization of the tissue, modulation of immune response and ECM deposition, promoting cardiac microenvironment development.[67,68] In our study, the adhesion of the EPCs to the hydrophobic patches and the role of hpcECM in promoting an endothelial layer were investigated. To do so, freshly isolated EPCs were cultivated on the uncoated PCL and coated patches (0.02% hpcECM-PCL and 0.2% hpcECM-PCL). Fibronectin-coated samples served as controls. It has previously been shown that fibronectin alone or in combination with other ECM proteins such as collagen, elastin, and laminin (in the form of either protein or bifunctional peptide) could support endothelialization.[69-71]

Figure 5a and 5c show that prominin-1 (Prom-1) positive cells were detectable after one week. It was shown that significantly less EPCs attached to fibronectin and uncoated samples (Figure 5b). Furthermore, all attached cells were counted (Prom-1+ and Prom-1- cells) and uncoated samples showed the lowest level of Prom-1 compared with hpcECM and fibronectin coated samples(Figure 5c). This could potentially indicate an increased EPCs recruitment on the coated samples and higher crosstalk between EPCs and other cardiac cell populations such as ECs and cardiac fibroblasts. Furthermore, the influence of hpcECM on the expression level of some key cell adhesion molecules, namely ICAM-1, VCAM-1, and PECAM-1, was further studied (Figure 5d). ICAM-1 and VCAM-1 facilitate inflammation and promote leukocyte migration in an inflammatory state.[72] Further, they support forming endothelial barriers while providing structural support and a binding platform for ECM components. PECAM-1 plays a main role in restoring the vascular permeability barrier following the endothelial cell junction disorder.[73]

Our study demonstrated no significant influence in the expression of ICAM-1, VCAM-1, and PECAM-1 in both the hpcECM-coated and uncoated groups. This absence of ICAM-1 and VCAM-1 overexpression in hpcECM could highlight the role of the hpcECM hydrogel in hindering leukocyte adherence to endothelial cells in an inflammatory state.[72] These findings are in conformance with the results of previous studies[35,74] showing that adhesion and growth of endothelial cells could be promoted without raising the expression of inflammatory cytokines (ICAM-1 and VCAM-1) and selectins. The enhanced adhesion of endothelial cells was complemented by substantial volumetric enlargement of the cells and a prominent

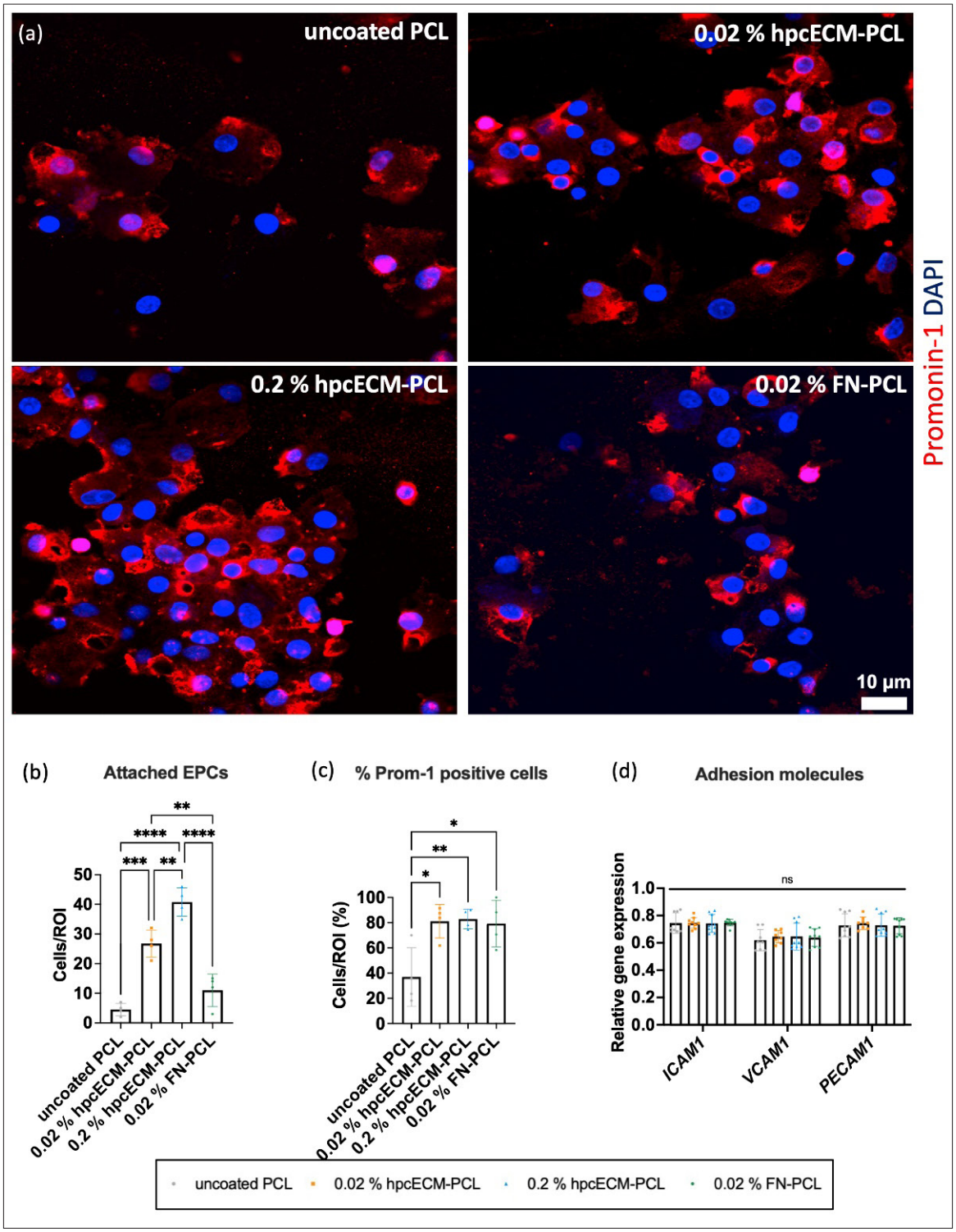

Figure 5. Attachment of endothelial progenitor cells and the activation and gene expression of adhesion molecules. (a, b) The presence of hpcECM coating significantly supported EPCs attachment compared to uncoated and fibronectin-coated patches. (c) The number of Prom-1 positive cells confirmed the activated state of EPCs in both hpcECM- and fibronectin-coated groups. (d) *ICAM1, VCAM1, and PECAM1* gene expression levels showed no significant differences between the groups, implying the role of some other adhesion binding receptors such as integrins in promoting the endothelial cells adhesion. Abbreviations: EPCs: Endothelial progenitor cells; hpcECM: Human chorion placenta extracellular matrix; ICAM-1: Intercellular adhesion molecule 1; PCL: Poly-ε-caprolactone; PECAM-1: Platelet endothelial cell adhesion molecule 1; Prom-1: Prominin 1; VCAM-1: Vascular cell adhesion molecule 1.

presence of cytoskeletal vimentin. These play a substantial role in supporting intercellular contacts and endothelial monolayer integrity. All these could suggest the possible role of other proteins such as vimentin or integrins in cell binding to hpcECM, as integrin $\alpha_5\beta_1$ and $\alpha_v\beta_3$ could stabilize ECM and are mediators of EPCs adhesion to fibrin.[74,75]

3.5. Viability and proliferation of undifferentiated and retinoic acid-differentiated H9c2 cells

Cardiomyocytes, the muscle cells responsible for the contraction and relaxation, are the largest cell fraction by volume in heart. H9c2 cells are originally derived from embryonic rat ventricular tissue[76] and are currently used *in vitro* to mimic skeletal and cardiac muscle. H9c2 cells share abundant characteristics with primary cardiomyocytes, such as membrane morphology, G-protein signaling expression, and electrophysiological properties, although they have lost their ability to beat.[77]

Furthermore, it has been shown that the differentiation of H9c2 cells via RA induces a predominant presence of cell types with an adult cardiac muscle phenotype, characterized by the overexpression of cardiac proteins such as troponin I and troponin T.[78] This confirms that RA induces the differentiation of the H9c2 cells toward a more cardiac-like phenotype, involving mitochondrial function remodeling. However, the majority of recent studies have utilized undifferentiated H9c2 myoblasts, raising concerns regarding the significance and relevance of the obtained results when compared to primary cardiomyocytes.[78,79]

In this study, both undifferentiated and RA-differentiated H9c2 cells were cultivated on coated and uncoated PCL patches (0.02% hpcECM-PCL and 0.2% hpcECM-PCL). The successful differentiation procedure was confirmed via troponin T staining. RA-differentiated cells clearly expressed troponin T protein (red dots), which was however absent in undifferentiated cells (Figure 6b and 6f). The morphology of the cells was also shown via SEM images in Figure 6a and 6e. XTT assay and live/dead staining confirmed the role of hpcECM in supporting attachment and proliferation of the H9c2 cells in both differentiated and undifferentiated stage, but this was statistically significant only in the RA-differentiated cells after 72 hours in 0.2% hpcECM-PCL patches (Figure 6c, 6d, 6g, and 6h). This finding further confirmed the positive potential of hpcECM on the differentiation and proliferation of differentiated H9c2. Previously, it was shown that nano copper oxide-loaded gelatin as well as graphene oxide as a coating composite on a 3D-printed PCL cardiac scaffold could support H9c2 cell attachment after 24 hours. However, the proliferation of these cells at longer time points and the utilization of differentiated H9c2 cells remained unexplored.[40] Additionally, carboxymethyl cellulose (CMC)/gelatin)/graphene oxide-based 3D-printed cardiac scaffolds showed acceptable biocompatibility for H9c2 cells in the formulation with higher CMC concentration. However, this scaffold showed a 65% reduction in H9c2 cell viability compared to the control, confirming the sensitivity of these cells to the microenvironment and the superiority of the hpcECM compared to CMC.[80]

3.6. Inflammatory and immune modulatory potential assessment via primary peripheral blood macrophages

Macrophage polarization has a central role in orchestrating the immunomodulatory behavior of a bioconstruct. This behavior is defined by the activation state of the polarized macrophage, which includes classically activated pro-inflammatory (M1) and alternatively activated anti-inflammatory (M2) phenotype.[81] In this study, polarized expression levels of pro-inflammatory (CCR7, CD80, IL-1α, and TNF-α) and anti-inflammatory (CD163, CD206, and IL-10) macrophages and cytokine markers were assessed (Figure 7). A high donor-to-donor variability in mRNA levels was apparent as it was reported elsewhere.[81,82] In general, a moderate inflammatory gene expression was observed in all groups. In detail, slight pro-inflammatory gene expressions were shown in all groups at 24 hours and this was more significant at 72 hours. However, the expression of C-C chemokine receptor type 7 (CCR7) and CD80 decreased after 72 hours and this was significant in CCR7 expression between 72 hours and 1 week in 0.2% hpcECM groups (CCR7 vs CD206 expression on 0.2% hcpECM-PCL at 72h, $p = 0.02$; CCR7 expression on 0.2% hcpECM-PCL at 72 hours vs 1 week, $p = 0.0071$). After one week, a higher anti-inflammatory gene expression (CD163 and CD206) in both uncoated and in the 0.2% hpcECM groups was observed (Figure 7a). Regarding the cytokine expression levels, expression of tumor necrosis factor alpha (TNF-α) and interleukin (IL)-1 α were higher in the hpcECM-coated samples at 24 and 72 hours (with no statistical differences) (Figure 7b). This was in accordance with the previous findings of Kolliopoulos et al.[58] showing that chorion extract had a high level of cytokines, inducing an initial pro-inflammatory response. However, at later time points (1 week), a significant anti-inflammatory cytokine expression was induced by the 0.2% hpcECM group via high expression of IL-10 (IL-10 expression on PCL vs 0.02% hcpECM-PCL at 1 week, $p = 0.0107$). To conclude, a mild inflammatory reaction was shown in all samples. An initial pro-inflammatory response was induced in the chorion-coated samples. However, this proinflammatory expression declined and was compensated by a significant inflammatory expression of IL-10 in the 0.2% hpcECM groups after one week.

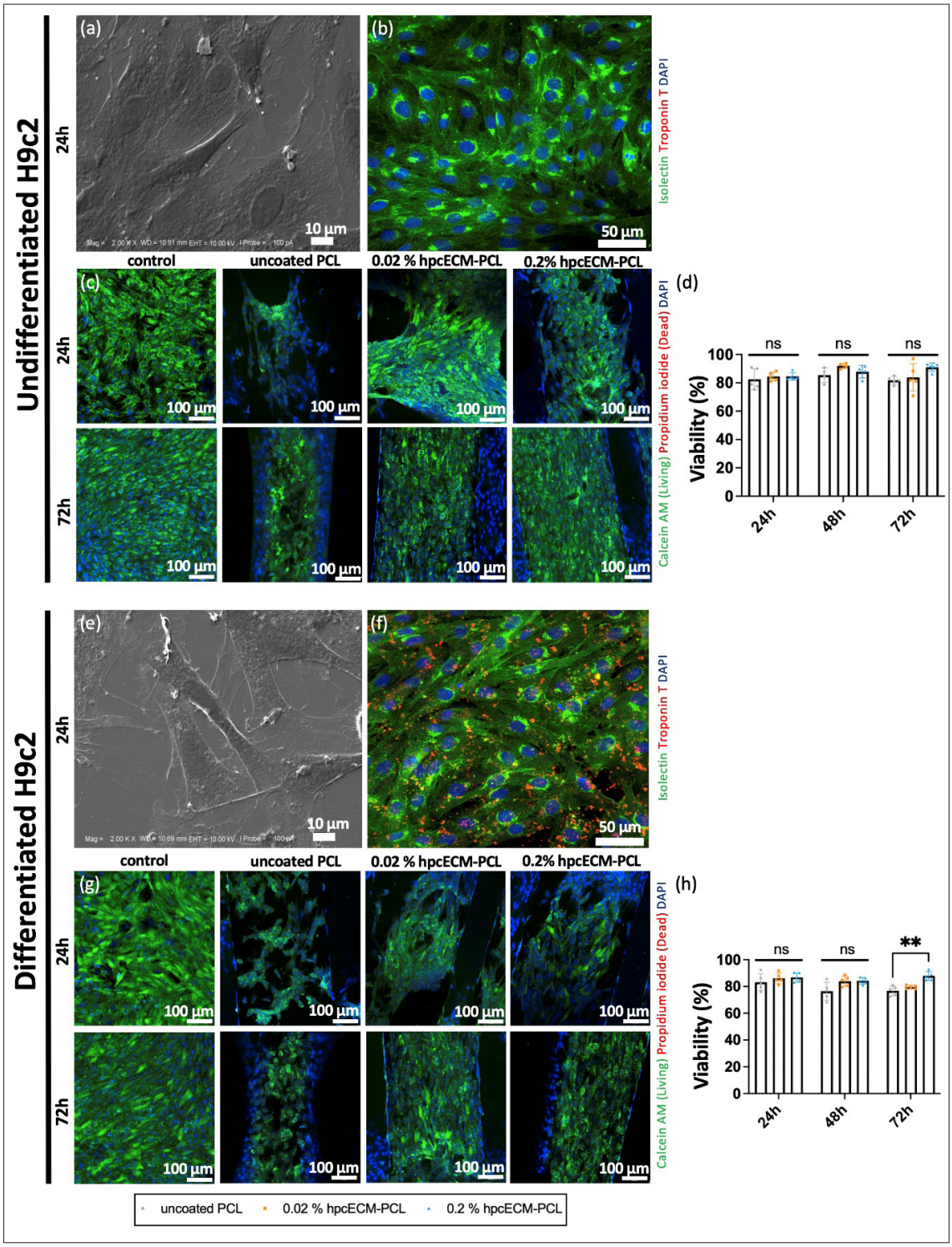

Figure 6. SEM, troponin T staining, live/dead staining and XTT assay of undifferentiated and RA-differentiated H9c2 cells. (a, e) SEM of the undifferentiated and differentiated H9c2 cells. (b, f) Troponin T staining confirmed the successful differentiation of H9c2 cells using RA. Differentiated cells clearly expressed troponin T (red dots). (c, g) Live dead (LD)-stained patches cultured with undifferentiated and RA-differentiated H9c2 cells for 24 and 72 hours. HpcECM clearly supported H9c2 cell attachment. Most cells were viable (green cells), whereas only some dead cells were detectable (almost no red cells). (d, h) Comparison of undifferentiated and RA-differentiated H9c2 cell proliferation on coated and uncoated samples detected by XTT assay. In general, hpcECM coating mainly increased proliferation specifically after 72 hours in RA-differentiated cells for the 0.2% hpcECM-PCL group. Abbreviations: hpcECM: Human chorion placenta extracellular matrix; PCL: Poly-ε-caprolactone; SEM: Scanning electron microscopy.

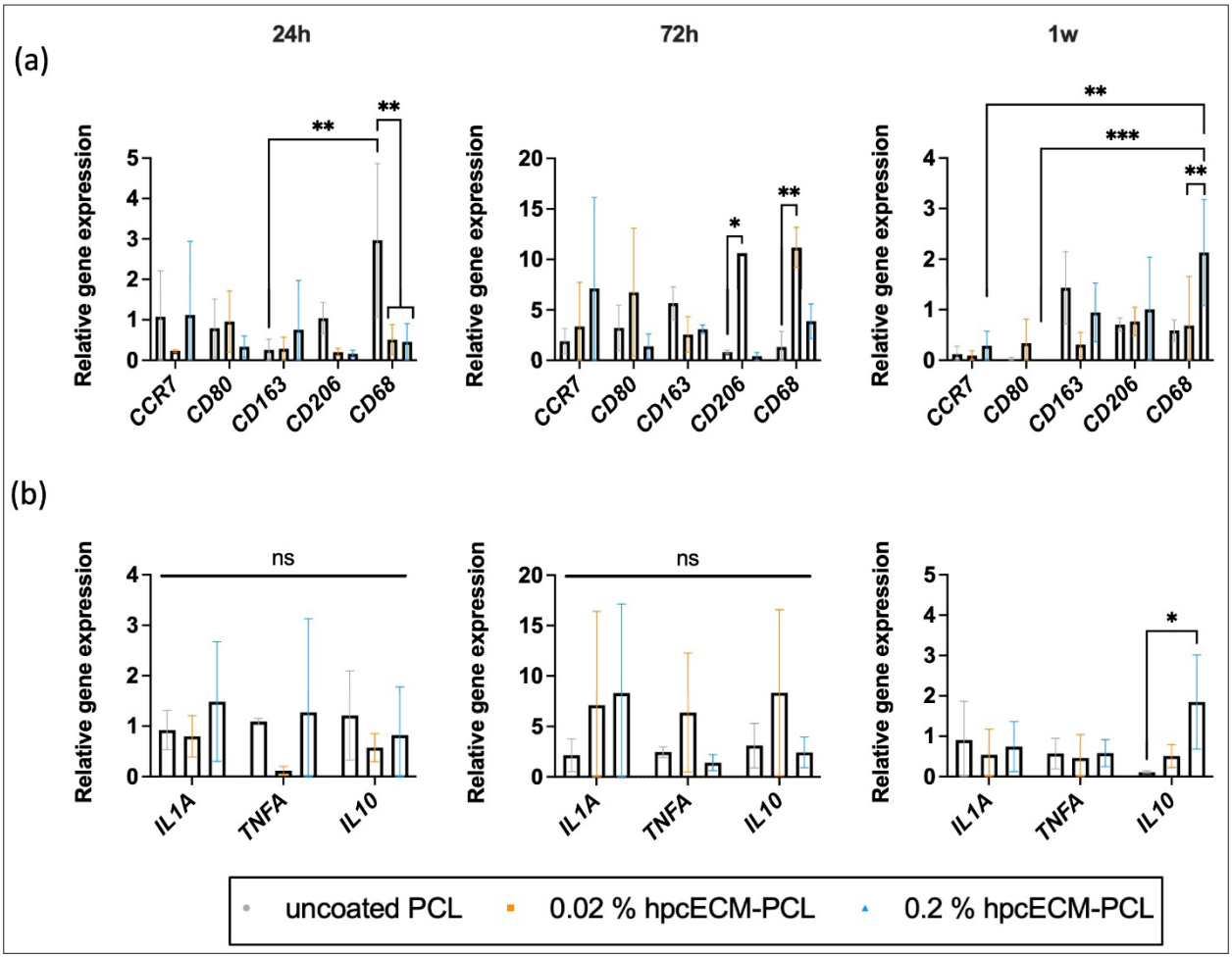

Figure 7. qPCR gene expression of anti-/pro-inflammatory macrophages *(CD68, CD80, CCR7, CD206, and CD163)* (a) and cytokine markers (*IL1A*, *TNFA* and *IL10*) (b) for the 0.2% hpcECM-PCL, 0.02% hpcECM-PCL and uncoated samples after 24 hours, 72 hours, and 1 week of cell culture. *GAPDH* was used as a housekeeping gene. Data are expressed mean ± standard deviation. $*p < 0.05$, $**p < 0.001$, $***p < 0.0001$. The graphs show $2^{-\Delta\Delta Ct}$ values of RT-qPCR runs performed on 6 samples derived from 3 donors. Error bars indicate 95% confidence intervals. Abbreviations: CCR7: Gene for C-C chemokine receptor type 7; hpcECM: Human chorion placenta extracellular matrix; *IL1A*: Gene for interleukin 1α; *IL10*: Gene for interleukin 10; PCL: Poly-ε-caprolactone; *TNFA*: Gene for tumor necrosis factor alpha.

3.7. Limitations and outlook

The current study demonstrated the positive influence of hpcECM on the adhesion and proliferation of cells on 3D-printed regeneration-supporting constructs. In general, ECM can regulate cell behavior through different mechanisms: (1) through direct cell-surface receptors and thus cell anchorage, or (2) via noncanonical growth factors and enzymes leading to the release of functional fragments.[83] Since a considerable amount of growth factors were not detectable in our hpcECM (data not shown), the second mechanism can be ruled out in future studies. Thus, further works on studying the mechanism of cell binding and identifying the activated receptors including ECM-integrin interaction will provide valuable insights.

ECM is considered a dynamic microenvironment for cardiac stem cells.[84] In this study, several cell types playing a critical role in cardiac repair such as endothelial cells, fibroblasts, EPCs, H9c2 undifferentiated and RA-differentiated cells, and macrophages were used. However, utilization of human induced pluripotent stem cells (hiPSCs) and investigation of hpcECM's ability to induce tissue-specific differentiation of hiPSCs to cardiomyocytes were not conducted in this study, warranting practical attempts in future works. Furthermore, functionality of these patches needs to be tested in an *in vivo* setting.

4. Conclusion

The developed hydrogel from human chorionic placenta (with high GAG, elastin and collagen content) is suitable as a cardiac cell-compatible coating agent for synthetic hydrophobic constructs due to its multiple excellent properties. The nanomechanical characterizations confirmed

the important role of hpcECM in providing a softer matrix with lower elastic modulus and hardness at the nanoscale, which has a positive effect on cell physiology. In addition, hpcECM could significantly promote the attachment and proliferation of important heart-related cells such as fibroblasts, endothelial cells, EPCs, and undifferentiated and RA-differentiated H9c2 cells. Our findings showed that the attachment of EPCs and the activation state of these cells were significantly improved, as indicated by the high expression of Prom-1. In addition, the differentiated H9c2 cells were able to proliferate significantly in more concentrated hpcECM (0.2%). HpcECM was able to convert early pro-inflammatory responses into anti-inflammatory responses after 1 week through high IL-10 expression. The results of this study indicate that compared to common coating agents such as fibrin used in cardiac regeneration, hpcECM is a successful candidate to enhance cardiac cell adhesion, proliferation and activation and to support the regeneration of extremely hydrophobic constructs.

Acknowledgements

We would like to thank the personnel of the Department of Obstetrics and Gynaecology, MUW for the retrieval of placentas. Moreover, we appreciate the help of the Imaging Core Facility at the Medical University of Vienna. We also acknowledge the support of Dr Thomas Chudoba (ASMEC GmbH) for nanoindentation.

Funding

This study was partly funded by the Ludwig Boltzmann Institute for Cardiovascular Research and by the Optiflow 3D project funded by the Austrian Research Promotion Agency (FFG) Nr. FO999891239.

Conflict of interest

The authors declare that they have no known competing financial interests or personal relationships that could have appeared to influence the work reported in this paper.

Author contributions

Conceptualization: Marjan Enayati, Karl H. Schneider, Helga Bergmeister

Data curation: Marjan Enayati, Christopher Riedmüller, Sabrina Rohringer, Felix Pointner, Luis Pichelkastner, Marta Bonora, Ewald Unger, Emir Benca

Funding acquisition: Marjan Enayati, Bruno K. Podesser, Helga Bergmeister

Investigation: Marjan Enayati, Christopher Riedmüller, Sabrina Rohringer, Felix Pointner, Lukas Weber, Emir Benca, Marvin Dötzlhofer, Ana Isabel Antunes Goncalves

Methodology: Francesco Moscato

Supervision: Marjan Enayati

Writing–original draft: Marjan Enayati, Christopher Riedmüller, Sabrina Rohringer, Helga Bergmeister

Writing–review and editing: Christopher Riedmüller, Sabrina Rohringer, Francesco Moscato, Bruno K. Podesser, Karl H. Schneider, Helga Bergmeister

Ethics approvals and consent to participate

All the procedures were approved by the Institutional Ethics Committee of the Medical University of Vienna (EK-Nr. regarding the placenta tissue: 1602/2018) and (EK-NR. regarding donated human blood: 2321/2020). Briefly, the donated placentas were obtained from cesarean sections performed at the Department of Obstetrics and Gynecology at the Medical University of Vienna (Austria), after written informed consent of the mothers and approval by the Medical University of Vienna ethics committee (EK:1602/2018). Additionally, the healthy male and female volunteers without anti-coagulant therapy were subjected to venepuncture after verbal informed consent of the blood donor and after approval of the Medical University of Vienna ethics committee (EK: 2321/2020).

Consent for publication

Not applicable.

Availability of data

Data will be made available from the corresponding author upon reasonable request.

References

1. Tsao CW, Aday AW, Almarzooq ZI, et al. Heart disease and stroke statistics—2022 update: a report from the American heart association. *Circulation*. 2022;145(8):e153-e639. doi: 10.1161/CIR.0000000000001052

2. Frangogiannis NG. The extracellular matrix in myocardial injury, repair, and remodeling. *J Clin Invest*. 2017;127(5): 1600-1612. doi: 10.1172/jci87491

3. Nielsen SH, Mouton AJ, DeLeon-Pennell KY, Genovese F, Karsdal M, Lindsey ML. Understanding cardiac extracellular matrix remodeling to develop biomarkers of myocardial infarction outcomes. *Matrix Biol*. 2019;75-76:43-57. doi: 10.1016/j.matbio.2017.12.001

4. Richbourg NR, Peppas NA, Sikavitsas VI. Tuning the biomimetic behavior of scaffolds for regenerative medicine through surface modifications. *J Tissue Eng Regen Med*. 2019;13(8):1275-1293. doi: 10.1002/term.2859

5. Sutthiwanjampa C, Hong S, Kim WJ, Kang SH, Park H. Hydrophilic modification strategies to enhance the surface biocompatibility of poly(dimethylsiloxane)-based biomaterials for medical applications. *Adv Mater Interf*. 2023;10(12):2202333.
doi: 10.1002/admi.202202333

6. Ghaedamini Sl, Karbasi S, Hashemibeni B, Honarvar A, Rabiei A. PCL/Agarose 3D-printed scaffold for tissue engineering applications: fabrication, characterization, and cellular activities. *Res Pharm Sci*. 2023;18(5):566-579.
doi: 10.4103/1735-5362.383711

7. Rashidi N, Najmoddin N, Tavakoli AH, Samanipour R. 3D printed hetero-layered composite scaffold with engineered superficial zone promotes osteogenic differentiation of pre-osteoblast MC3T3-E1 cells. *Surf Interfaces*. 2024;51:104683.
doi: 10.1016/j.surfin.2024.104683

8. Rezaei H, Matin AA, Mohammadnejad M. Cold atmospheric plasma treated 3D printed polylactic acid film; application in thin film solid phase microextraction of anticancer drugs. *Talanta*. 2024;266:125064.
doi: 10.1016/j.talanta.2023.125064

9. Ebrahimi Z, Irani S, Ardeshirylajimi A, Seyedjafari E. Enhanced osteogenic differentiation of stem cells by 3D printed PCL scaffolds coated with collagen and hydroxyapatite. *Sci Rep-UK*. 2022;12(1):12359.
doi: 10.1038/s41598-022-15602-y

10. García AJ, Reyes CD. Bio-adhesive surfaces to promote osteoblast differentiation and bone formation. *J Dent Res*. 2005;84(5):407-413.
doi: 10.1177/154405910508400502

11. Sarker M, Park S, Kumar V, Lee CH. Micro-thin hydrogel coating integrated in 3D printing for spatiotemporal delivery of bioactive small molecules. *Biofabrication*. 2025;17(1): 015019.
doi: 10.1088/1758-5090/ad89fe

12. Pei M, Hwangbo H, Kim G. Hierarchical fibrous collagen/poly(ε-caprolactone) structure fabricated with a 3D-printing process for tissue engineering applications. *Comp B Eng*. 2023;259:110730.
doi: 10.1016/j.compositesb.2023.110730

13. Loyo C, Palza H, Saavedra M, et al. Electrospun polycaprolactone/graphene oxide scaffolds with secondary surface porosity and gelatin-coating. *Mater Today Commun*. 2024;39:109057.
doi: 10.1016/j.mtcomm.2024.109057

14. Zhu J, Li Z, Zou Y, et al. Advanced application of collagen-based biomaterials in tissue repair and restoration. *J Leather Sci Eng*. 2022;4(1):30.
doi: 10.1186/s42825-022-00102-6

15. Lukin I, Erezuma I, Maeso L, et al. Progress in gelatin as biomaterial for tissue engineering. *Pharmaceutics*. 2022;14(6):1177.
doi: 10.3390/pharmaceutics14061177

16. Al-Yafeai Z, Yurdagul A, Peretik JM, Alfaidi M, Murphy PA, Orr AW. Endothelial FN (Fibronectin) deposition by α5β1 integrins drives atherogenic inflammation. *Arterioscler Thromb Vasc Biol*. 2018;38(11):2601-2614.
doi: 10.1161/atvbaha.118.311705

17. Kang BJ, Kim H, Lee SK, et al. Umbilical-cord-blood-derived mesenchymal stem cells seeded onto fibronectin-immobilized polycaprolactone nanofiber improve cardiac function. *Acta Biomater*. 2014;10(7):3007-3017.
doi: 10.1016/j.actbio.2014.03.013

18. Neishabouri A, Soltani Khaboushan A, Daghigh F, Kajbafzadeh AM, Majidi Zolbin M. Decellularization in tissue engineering and regenerative medicine: evaluation, modification, and application methods. *Front Bioeng Biotechnol*. 2022;10:805299.
doi: 10.3389/fbioe.2022.805299

19. Dwivedi R, Kumar S, Pandey R, et al. Polycaprolactone as biomaterial for bone scaffolds: review of literature. *J Oral Biol Craniofac Res*. 2020;10(1):381-388.
doi: 10.1016/j.jobcr.2019.10.003

20. Hu Z, Luo Y, Ni R, et al. Biological importance of human amniotic membrane in tissue engineering and regenerative medicine. *Mater Today Bio*. 2023;22:100790.
doi: 10.1016/j.mtbio.2023.100790

21. Kim JT, Kim KW, Mun SK, Chun YS, Kim JC. Transplantation of autologous perichondrium with amniotic membrane for progressive scleral necrosis. *The Ocular Surface*. 2019;17(3):571-577.
doi: 10.1016/j.jtos.2019.05.004

22. DiDomenico LA, Orgill DP, Galiano RD, et al. Use of an aseptically processed, dehydrated human amnion and chorion membrane improves likelihood and rate of healing in chronic diabetic foot ulcers: a prospective, randomised, multi-centre clinical trial in 80 patients. *Int Wound J*. 2018;15(6):950-957.
doi: 10.1111/iwj.12954

23. Jiang Y, Sun SJ, Zhen Z, et al. Myocardial repair of bioengineered cardiac patches with decellularized placental scaffold and human-induced pluripotent stem cells in a rat model of myocardial infarction. *Stem Cell Res Ther*. 2021;12(1):13.
doi: 10.1186/s13287-020-02066-y

24. Francis MP, Breathwaite E, Bulysheva AA, et al. Human placenta hydrogel reduces scarring in a rat model of cardiac ischemia and enhances cardiomyocyte and stem cell cultures. *Acta Biomater*. 2017;52:92-104.
doi: 10.1016/j.actbio.2016.12.027

25. Duan Y, Huang W, Zhan B, et al. Bioink derived from human placenta supporting angiogenesis. *Biomed Mater*. 2022;17(5).
doi: 10.1088/1748-605X/ac7b5b

26. Schneider KH, Goldberg BJ, Hasturk O, et al. Silk fibroin, gelatin, and human placenta extracellular matrix-based

composite hydrogels for 3D bioprinting and soft tissue engineering. *Biomater Res.* 2023;27(1):117. doi: 10.1186/s40824-023-00431-5

27. Khosrowpour Z, Bashiri Z, Jafari D, et al. Translation prospects of a novel ECM-silk fibroin/alginate 3D-printed scaffold for treatment of full-thickness skin wounds: an *in vitro* and *in vivo* study. *Polym Adv Technol*. 2024;35(11):e6637. doi: 10.1002/pat.6637

28. Lakkireddy C, Vishwakarma SK, Raju N, et al. Fabrication of decellularized amnion and chorion scaffolds to develop bioengineered cell-laden constructs. *Cell Mol Bioeng*. 2022;15(1):137-150. doi: 10.1007/s12195-021-00707-7

29. Patel HN, Vohra YK, Singh R, Thomas V. HuBiogel incorporated fibro-porous hybrid nanomatrix graft for vascular tissue interfaces. *Mater Today Chem*. 2020;17: 100323. doi: 10.1016/j.mtchem.2020.100323.

30. Lei J, Priddy LB, Lim JJ, Koob TJ. Dehydrated human amnion/chorion membrane (dHACM) allografts as a therapy for orthopedic tissue repair. *Tech Orthop*. 2017;32(3):149-157. doi: 10.1097/bto.0000000000000229

31. Go YY, Chae SW, Song JJ. Osteogenic effects of exosomes derived from human chorion membrane extracts. *Biomater Res*. 2021;25(1):16. doi: 10.1186/s40824-021-00218-6

32. Flores-Espinosa P, Méndez I, Irles C, et al. Immunomodulatory role of decidual prolactin on the human fetal membranes and placenta. *Frontiers in Immunology*. 2023;14:1212736. doi: 10.3389/fimmu.2023.1212736

33. McQuilling JP, Vines JB, Kimmerling KA, Mowry KC. Proteomic comparison of amnion and chorion and evaluation of the effects of processing on placental membranes. *Wounds*. 2017;29(6):E36-E40.

34. Schneider KH, Enayati M, Grasl C, et al. Acellular vascular matrix grafts from human placenta chorion: impact of ECM preservation on graft characteristics, protein composition and *in vivo* performance. *Biomaterials*. 2018;177:14-26. doi: 10.1016/j.biomaterials.2018.05.045

35. Rohringer S, Schneider KH, Eder G, et al. Chorion-derived extracellular matrix hydrogel and fibronectin surface coatings show similar beneficial effects on endothelialization of expanded polytetrafluorethylene vascular grafts. *Mater Today Bio*. 2022;14:100262. doi: 10.1016/j.mtbio.2022.100262

36. Kaniuk E, Lechowska-Liszka A, Gajek M, et al. Correlation between porosity and physicochemical and biological properties of electrospinning PLA/PVA membranes for skin regeneration. *Biomater Adv*. 2023;152:213506. doi: 10.1016/j.bioadv.2023.213506

37. Grasl C, Bergmeister H, Stoiber M, Schima H, Weigel G. Electrospun polyurethane vascular grafts: *in vitro* mechanical behavior and endothelial adhesion molecule expression. *J Biomed Mater Res A*. 2010;93a(2):716-723. doi: 10.1002/jbm.a.32584

38. Janssen D, De Palma R, Verlaak S, Heremans P, Dehaen W. Static solvent contact angle measurements, surface free energy and wettability determination of various self-assembled monolayers on silicon dioxide. *Thin Solid Films*. 2006;515(4):1433-1438. doi: 10.1016/j.tsf.2006.04.006

39. Thaler B, Baik N, Hohensinner PJ, et al. Differential expression of Plg-R(KT) and its effects on migration of proinflammatory monocyte and macrophage subsets. *Blood*. 2019;134(6):561-567. doi: 10.1182/blood.2018850420

40. Silvestri A, Boffito M, Sartori S, Ciardelli G. Biomimetic materials and scaffolds for myocardial tissue regeneration. *Macromol Biosci*. 2013;13(8):984-1019. doi: 10.1002/mabi.201200483

41. Liu T, Hao Y, Zhang Z, et al. Advanced cardiac patches for the treatment of myocardial infarction. *Circulation*. 2024;149(25):2002-2020. doi: 10.1161/CIRCULATIONAHA.123.067097

42. Kakabadze Z, Kakabadze A, Chakhunashvili D, et al. Decellularized human placenta supports hepatic tissue and allows rescue in acute liver failure. *Hepatology*. 2018;67(5):1956-1969. doi: 10.1002/hep.29713

43. Kim BS, Kim H, Gao G, Jang J, Cho DW. Decellularized extracellular matrix: a step towards the next generation source for bioink manufacturing. *Biofabrication*. 2017;9(3):034104. doi: 10.1088/1758-5090/aa7e98

44. Prince E, Kumacheva E. Design and applications of man-made biomimetic fibrillar hydrogels. *Nat Rev Mater.* 2019;4(2):99-115. doi: 10.1038/s41578-018-0077-9

45. Schneider KH, Aigner P, Holnthoner W, et al. Decellularized human placenta chorion matrix as a favorable source of small-diameter vascular grafts. *Acta Biomater*. 2016;29:125-134. doi: 10.1016/j.actbio.2015.09.038

46. Ferreira SA, Motwani MS, Faull PA, et al. Bi-directional cell-pericellular matrix interactions direct stem cell fate. *Nat Commun.* 2018;(1):4049. doi: 10.1038/s41467-018-06183-4

47. Huebsch N, Arany PR, Mao AS, et al. Harnessing traction-mediated manipulation of the cell/matrix interface to control stem-cell fate. *Nat Mater*. 2010;9(6):518-526. doi: 10.1038/nmat2732

48. Simmons CA, Alsberg E, Hsiong S, Kim WJ, Mooney DJ. Dual growth factor delivery and controlled scaffold degradation enhance *in vivo* bone formation by transplanted bone marrow stromal cells. *Bone*. 2004;35(2):562-569. doi: 10.1016/j.bone.2004.02.027

49. Tang J, Vandergriff A, Wang Z, et al. A regenerative cardiac patch formed by spray painting of biomaterials onto the heart. *Tissue Eng Part C Methods*. 2017;23(3):146-155. doi: 10.1089/ten.TEC.2016.0492

50. Rebollar E, Frischauf I, Olbrich M, et al. Proliferation of aligned mammalian cells on laser-nanostructured polystyrene. *Biomaterials*. 2008;29(12):1796-1806. doi: 10.1016/j.biomaterials.2007.12.039

51. Paragkumar T, Edith ND, Six JL. Surface characteristics of PLA and PLGA films. *Appl Surf Sci*. 2006;253(5):2758-2764. doi: 10.1016/j.apsusc.2006.05.047

52. Kapnisi M, Mansfield C, Marijon C, et al. Auxetic cardiac patches with tunable mechanical and conductive properties toward treating myocardial infarction. *Adv Funct Mater*. 2018;28(21):1800618. doi: 10.1002/adfm.201800618

53. Wall ST, Walker JC, Healy KE, Ratcliffe MB, Guccione JM. Theoretical impact of the injection of material into the myocardium: a finite element model simulation. *Circulation*. 2006;114(24):2627-2635. doi: 10.1161/circulationaha.106.657270

54. Saraswathibhatla A, Indana D, Chaudhuri O. Cell–extracellular matrix mechanotransduction in 3D. *Nat Rev Mol Cell Biol*. 2023;24(7):495-516. doi: 10.1038/s41580-023-00583-1

55. Yang B, Wei K, Loebel C, et al. Enhanced mechanosensing of cells in synthetic 3D matrix with controlled biophysical dynamics. *Nat Commun*. 2021;12(1):3514. doi: 10.1038/s41467-021-23120-0

56. Gautieri A, Vesentini S, Redaelli A, Buehler MJ. Hierarchical structure and nanomechanics of collagen microfibrils from the atomistic scale up. *Nano Lett*. 2011;11(2):757-766. doi: 10.1021/nl103943u

57. Vader D, Kabla A, Weitz D, Mahadevan L. Strain-induced alignment in collagen gels. *PLoS One*. 2009;4(6):e5902. doi: 10.1371/journal.pone.0005902

58. Kolliopoulos V, Dewey MJ, Polanek M, Xu H, Harley BAC. Amnion and chorion matrix maintain hMSC osteogenic response and enhance immunomodulatory and angiogenic potential in a mineralized collagen scaffold. *Front Bioeng Biotechnol*. 2022;10:1034701. doi: 10.3389/fbioe.2022.1034701

59. Soundararajan M, Kannan S. Fibroblasts and mesenchymal stem cells: two sides of the same coin?. *J Cell Physiol*. 2018;233(12):9099-9109. doi: 10.1002/jcp.26860

60. Costa-Almeida R, Gomez-Lazaro M, Ramalho C, Granja PL, Soares R, Guerreiro SG. Fibroblast-endothelial partners for vascularization strategies in tissue engineering. *Tissue Eng Part A*. 2015;21(5-6):1055-1065. doi: 10.1089/ten.TEA.2014.0443

61. Loureiro J, Miguel SP, Galván-Chacón V, et al. Three-dimensionally printed hydrogel cardiac patch for infarct regeneration based on natural polysaccharides. *Polymers*. 2023;15(13):2824. doi: 10.3390/polym15132824

62. Virag JI, Murry CE. Myofibroblast and endothelial cell proliferation during murine myocardial infarct repair. *Am J Pathol*. 2003;163(6):2433-2440. doi: 10.1016/S0002-9440(10)63598-5

63. Caneparo C, Baratange C, Chabaud S, Bolduc S. Conditioned medium produced by fibroblasts cultured in low oxygen pressure allows the formation of highly structured capillary-like networks in fibrin gels. *Sci Rep-UK*. 2020; 10(1):9291. doi: 10.1038/s41598-020-66145-z

64. Kunz-Schughart LA, Schroeder JA, Wondrak M, et al. Potential of fibroblasts to regulate the formation of three-dimensional vessel-like structures from endothelial cells *in vitro*. *Am J Physiol Cell Physiol*. 2006;290(5):C1385-C1398. doi: 10.1152/ajpcell.00248.2005

65. Amin K, Dannenfelser RM. *In vitro* hemolysis: guidance for the pharmaceutical scientist. *J Pharm Sci*. 2006;95(6): 1173-1176. doi: 10.1002/jps.20627

66. Huang H, Huang W. Regulation of endothelial progenitor cell functions in ischemic heart disease: new therapeutic targets for cardiac remodeling and repair. *Front Cardiovasc Med*. 2022;9:896782. doi: 10.3389/fcvm.2022.896782

67. Du F, Zhou J, Gong R, et al. Endothelial progenitor cells in atherosclerosis. *Front Biosci (Landmark Ed)*. 2012;17(6): 2327-2349. doi: 10.2741/4055

68. Yoder MC. Human endothelial progenitor cells. *Cold Spring Harb Perspect Med*. 2012;2(7):a006692. doi: 10.1101/cshperspect.a006692

69. Clauder F, Czerniak AS, Friebe S, Mayr SG, Scheinert D, Beck-Sickinger AG. Endothelialization of titanium surfaces by bioinspired cell adhesion peptide coatings. *Bioconjug Chem*. 2019;30(10):2664-2674. doi: 10.1021/acs.bioconjchem.9b00573

70. Ardila DC, Liou JJ, Maestas D, et al. Surface modification of electrospun scaffolds for endothelialization of tissue-engineered vascular grafts using human cord blood-derived endothelial cells. *J Clin Med*. 2019;8(2):185. doi: 10.3390/jcm8020185

71. Sgarioto M, Vigneron P, Patterson J, Malherbe F, Nagel MD, Egles C. Collagen type I together with fibronectin provide a better support for endothelialization. *C R Biol*. 2012;335(8):520-528. doi: 10.1016/j.crvi.2012.07.003

72. Kaur R, Singh V, Kumari P, Singh R, Chopra H, Emran TB. Novel insights on the role of VCAM-1 and ICAM-1: potential biomarkers for cardiovascular diseases. *Ann Med Surg (Lond)*. 2022;84:104802. doi: 10.1016/j.amsu.2022.104802

73. Lertkiatmongkol P, Liao D, Mei H, Hu Y, Newman PJ. Endothelial functions of platelet/endothelial cell adhesion molecule-1 (CD31). *Curr Opin Hematol*. 2016;23(3):253-259. doi: 10.1097/moh.0000000000000239

74. Bačáková L, Mareš V, Lisá V, Švorčík V. Molecular mechanisms of improved adhesion and growth of an endothelial cell line cultured on polystyrene implanted with fluorine ions. *Biomaterials*. 2000;21(11):1173-1179. doi: 10.1016/S0142-9612(00)00009-0

75. Post A, Wang E, Cosgriff-Hernandez E. A review of integrin-mediated endothelial cell phenotype in the design of cardiovascular devices. *Ann Biomed Eng*. 2019;47(2):366-380. doi: 10.1007/s10439-018-02171-3

76. Kimes BW, Brandt BL. Properties of a clonal muscle cell line from rat heart. *Exp Cell Res*. 1976;98(2):367-381. doi: 10.1016/0014-4827(76)90447-x

77. Watkins SJ, Borthwick GM, Arthur HM. The H9C2 cell line and primary neonatal cardiomyocyte cells show similar hypertrophic responses *in vitro*. *In Vitro Cell Dev Biol Anim*. 2011;47(2):125-131. doi: 10.1007/s11626-010-9368-1

78. Branco AF, Pereira SP, Gonzalez S, Gusev O, Rizvanov AA, Oliveira PJ. Gene expression profiling of H9c2 myoblast differentiation towards a cardiac-like phenotype. *PLoS One*. 2015;10(6):e0129303. doi: 10.1371/journal.pone.0129303.

79. Branco AF, Sampaio SF, Wieckowski MR, Sardão VA, Oliveira PJ. Mitochondrial disruption occurs downstream from β-adrenergic overactivation by isoproterenol in differentiated, but not undifferentiated H9c2 cardiomyoblasts: differential activation of stress and survival pathways. *Int J Biochem Cell Biol*. 2013;45(11):2379-2391. doi: 10.1016/j.biocel.2013.08.006

80. Arıcı Ş, Kamali AR, Ege D. CMC/Gel/GO 3D-printed cardiac patches: GO and CMC improve flexibility and promote H9C2 cell proliferation, while EDC/NHS enhances stability. *Biofabrication*. 2025;17(1):015025. doi: 10.1088/1758-5090/ad8e87

81. Bertani FR, Mozetic P, Fioramonti M, et al. Classification of M1/M2-polarized human macrophages by label-free hyperspectral reflectance confocal microscopy and multivariate analysis. *Sci Rep-UK*. 2017;7(1):8965. doi: 10.1038/s41598-017-08121-8

82. Rey-Giraud F, Hafner M, Ries CH. *In vitro* generation of monocyte-derived macrophages under serum-free conditions improves their tumor promoting functions. *PLoS One*. 2012;7(8):e42656. doi: 10.1371/journal.pone.0042656

83. Yue B. Biology of the extracellular matrix: an overview. *J Glaucoma*. 2014;23(8 Suppl 1):S20-S23. doi: 10.1097/ijg.0000000000000108

84. Mehanna RA, Essawy MM, Barkat MA, et al. Cardiac stem cells: current knowledge and future prospects. *World J Stem Cells*. 2022;14(1):1-40. doi: 10.4252/wjsc.v14.i1.1

ACCSCIENCE PUBLISHING

International Journal of Bioprinting

RESEARCH ARTICLE

Establishing a framework for the design and fabrication of patient-specific scaffolds targeting partial meniscal defects

Francklin Trindade da Silva[1†], Willian Gonçalves Tsumura[2†], Millena de Cassia Sousa e Silva[3], Anderson Oliveira Lobo[3*], and Thiago Domingues Stocco[2*]

[1]Department of Internal Medicine, Faculty of Medical Sciences, State University of Campinas, Campinas, Brazil

[2]BioRegenera.Lab, Bioengineering Program, Scientific and Technological Institute, Brazil University, São Paulo, SP, Brazil

[3]Interdisciplinary Laboratory for Advanced Materials, Materials Science & Engineering Graduate Program, Federal University of Piauí, Teresina, PI, Brazil

(This article belongs to the *Special Issue: Advances in Bioprinting and Organ-on-a-chip and Applications for Precision Medicine*)

Abstract

Meniscal injuries are a leading cause of knee dysfunction and are commonly treated with partial meniscectomy, which often leads to altered joint biomechanics and early onset osteoarthritis. Current meniscal implants and scaffolds fail to address patient-specific anatomical variations, particularly for partial defects, limiting their clinical effectiveness. This pioneering study introduces the first methodology specifically designed to develop patient-specific scaffolds tailored to partial meniscal injuries, representing a groundbreaking advancement in the field. By using medical imaging and computer-aided design, precise 3D models of injured and intact menisci were created, leveraging the contralateral meniscus as a reference. Scaffolds were fabricated through extrusion-based 3D printing to enable accurate replication of the defect geometry. *Ex vivo* analyses demonstrated the scaffolds' adaptability to diverse defect types and their morphological fidelity to the native tissue. Quantitative assessments revealed minimal deviations, underscoring the precision of the proposed method. This innovative methodology provides a robust framework for developing anatomically precise scaffolds, paving the way for personalized regenerative strategies. Beyond its current application, this method holds potential for creating cell-laden scaffolds, acellular implants, or permanent prosthetic devices, addressing critical challenges in meniscal repair and advancing patient-specific tissue engineering.

Keywords: Bioprinting; Meniscus; Patient-specific modeling; Tissue engineering; Tissue scaffold

†These authors contributed equally to this work.

***Corresponding authors:**
Thiago Domingues Stocco (thiago.stocco@ub.edu.br)

Anderson Oliveira Lobo (lobo@ufpi.edu.br)

Citation: da Silva FT, Tsumura WG, Silva MCS, Lobo AO, Stocco TD. Establishing a framework for the design and fabrication of patient-specific scaffolds targeting partial meniscal defects. *Int J Bioprint*.2025;11(1):556-572. doi: 10.36922/ijb.8109

Received: December 21, 2024
Revised: January 11, 2025
Accepted: January 14, 2025
Published Online: January 15, 2025

Copyright: © 2025 Author(s). This is an Open Access article distributed under the terms of the Creative Commons Attribution License, permitting distribution, and reproduction in any medium, provided the original work is properly cited.

Publisher's Note: AccScience Publishing remains neutral with regard to jurisdictional claims in published maps and institutional affiliations.

1. Introduction

The meniscus plays a pivotal role in knee biomechanics, acting as a critical load distributor, shock absorber, and stabilizer during joint movement. Its biomechanical

properties are intrinsically linked to its unique anatomical geometry, biochemical composition, and extracellular matrix architecture.[1,2] Unfortunately, meniscal injuries are highly prevalent and represent one of the leading causes of knee dysfunction worldwide, often resulting from trauma or degenerative conditions. Due to the meniscus's limited vascularization, particularly in its inner regions, these injuries exhibit a markedly reduced intrinsic healing capacity, presenting a persistent challenge in orthopedic practice.[1,3] Thus, meniscal surgeries rank among the most frequently performed orthopedic procedures globally.[4]

Despite advancements in meniscal repair techniques, such as suturing, these interventions are not universally applicable, often being unfeasible in cases involving poor tissue quality or unfavorable tear locations. As a result, partial meniscectomy remains the standard surgical approach, aiming to alleviate symptoms while preserving as much healthy tissue as possible.[5,6] However, this procedure fundamentally disrupts knee biomechanics, increasing contact pressures on the underlying cartilage and expediting degenerative changes. Thus, while providing short-term symptomatic relief, partial or total meniscectomy is strongly associated with the development of early onset osteoarthritis (OA), one of the most prevalent joint disorders globally, impacting millions of individuals and constituting a leading cause of physical disability worldwide.[7–11] These long-term complications underscore the urgent need for new therapies capable of restoring meniscal function and mitigating the progression of joint degeneration.

Meniscal substitutes and scaffolds have emerged as promising solutions to overcome the inherent limitations of conventional treatments for meniscal injuries. These approaches aim to restore the structural integrity of the meniscus and support joint biomechanics, providing alternatives to mitigate the long-term impact of meniscal loss. While they can offer some degree of articular cartilage protection over varied durations, these interventions are often accompanied by incomplete or compromised regeneration of meniscal tears, alterations in knee biomechanics, and suboptimal restoration of joint function. These strategies have been found to be insufficient to prevent the progression of OA at later stages.[12,13]

The limitations of these approaches vary depending on the type of intervention. For instance, meniscal transplants, often considered for extensive injuries, are hindered by challenges such as the risk of allograft infections, immune rejection, and limited donor availability.[14] Conversely, engineered meniscal scaffolds or implants, while more accessible, frequently exhibit issues such as inadequate mechanical properties and durability, lack of bioactivity, and poor integration with native tissue.[12,13] However, a limitation common to all these strategies is their inability to achieve precise anatomical conformity to the patient's meniscus. For example, current FDA(Food and Drug Administration)-approved meniscal implants, fabricated from natural materials like collagen[15] or synthetic polymers such as polyurethane,[16] are designed with a generic one-size-fits-all approach. These implants often require intraoperative manual shaping to fit the patient's anatomy. This lack of anatomical conformity poses a critical limitation, particularly for partial meniscal defects, where precise size and shape matching are essential for successful outcomes. Thus, generic implants fail to replicate the specific anatomical and morphological characteristics of the native meniscus. This lack of conformity can disrupt joint alignment, increase localized stresses on the articular cartilage, and compromise the meniscus's biomechanical roles of load distribution and stabilization.[2,3,13] Such deviations not only accelerate joint degeneration but also hinder functional recovery, highlighting the critical need for patient-specific solutions tailored to the unique geometry of each meniscus.

Although advancements in patient-specific approaches for meniscal scaffolds have been made, these strategies predominantly focus on total meniscal replacements.[17–19] While full meniscal reconstruction represents an important step forward, it is less aligned with clinical realities, as partial meniscal injuries and subsequent partial meniscectomy are far more prevalent.[20] Despite the potential of these advances, no existing methodology currently addresses the specific needs of partial meniscal defects with patient-specific scaffolds tailored to fit the precise anatomical and morphological characteristics of the lesion site.

Thus, this study aims to introduce the first step-by-step methodology for generating patient-specific scaffolds precisely tailored to partial meniscal defects. By integrating medical imaging, computer-aided design (CAD)-based digital modeling, and 3D printing, the proposed approach establishes a systematic framework that prioritizes anatomical accuracy and clinical relevance. The primary focus of this study is not to assess scaffold performance or material properties but to provide a detailed foundation for developing scaffolds adaptable to various applications, including regenerative strategies that may incorporate cellular components, bioactive materials, or durable structural designs. This methodology, outlined schematically in Figure 1, offers a pathway for advancing personalized solutions in meniscal repair and tissue engineering.

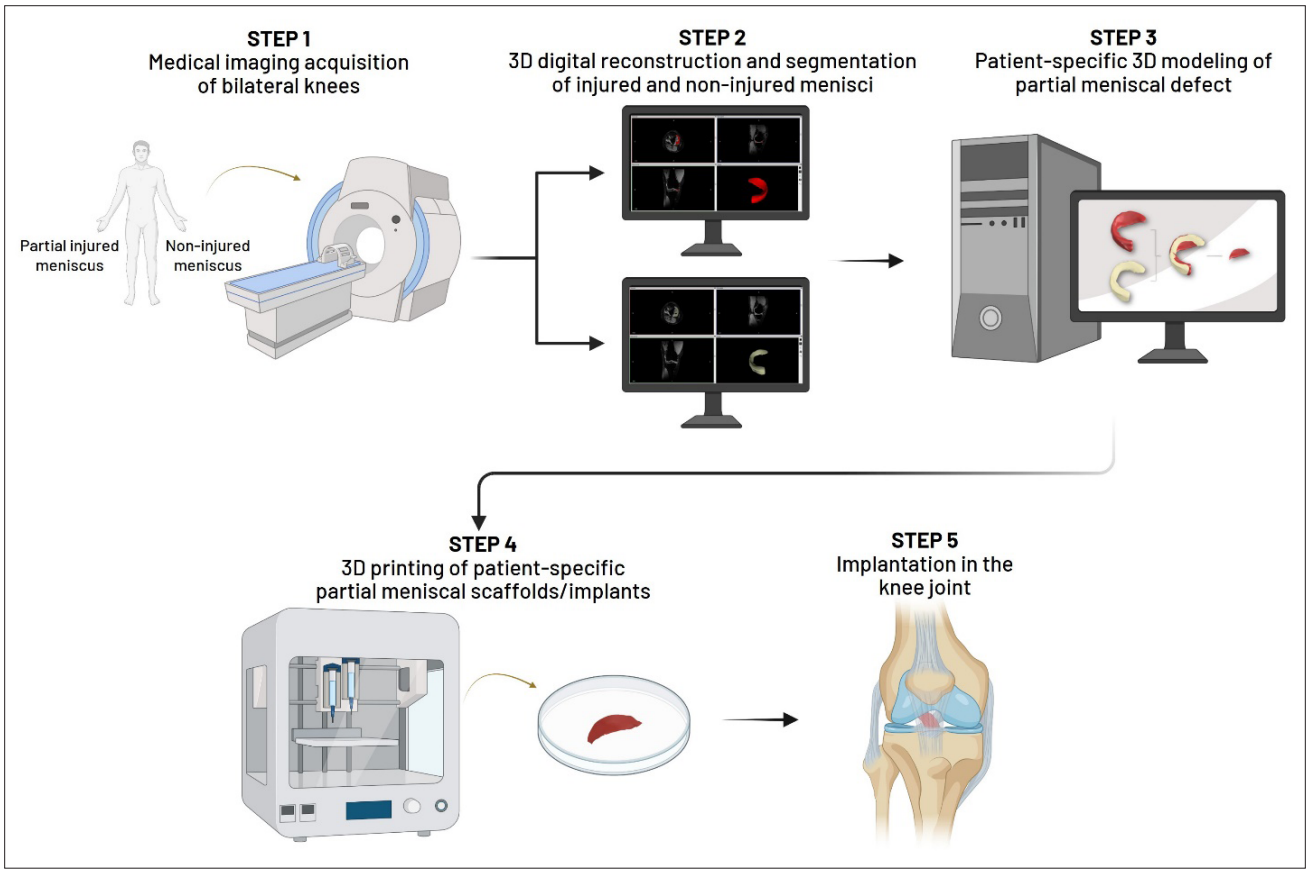

Figure 1. Workflow for developing patient-specific scaffolds/implants for partial meniscal defects. The methodology begins with medical imaging acquisition of bilateral knees to capture both injured and non-injured menisci. The next step involves 3D digital reconstruction and segmentation of the menisci, followed by patient-specific 3D modeling of the partial meniscal defect using the intact contralateral meniscus as a reference. Subsequently, the scaffold/implant is fabricated using 3D printing. The final step is the intended application of the patient-specific scaffold/implant in the knee joint, demonstrating the clinical potential of this approach.

2. Materials and methods

2.1. Digital 3D model generation of partial meniscal defect

The primary objective at this stage is to create a 3D digital model that captures the patient-specific morphology of the medial meniscus, particularly focusing on partial lesions. This process employs magnetic resonance imaging (MRI) images and CAD techniques to translate anatomical data into a customized digital model, accurately reflecting the unique geometry of the meniscal defect. By converting these medical images into a detailed 3D structure, this stage establishes the foundational model required to fabricate a scaffold that closely replicates the native tissue's anatomy and morphology, supporting precision in subsequent biofabrication steps.

2.1.1. Bilateral segmentation and 3D digital reconstruction of menisci

To accurately construct a 3D digital model of the human menisci, a Digital Imaging and Communications in Medicine (DICOM) dataset from a high-resolution bilateral MRI scan of the knee joints (left and right) of an unidentified 30-year-old subject provided by an anonymized database. The MRI included one knee that had undergone partial medial meniscectomy and an intact, uninjured contralateral knee. This dataset was processed using InVesalius (CTI Renato Archer, Brazil) a free, open-source software designed for the visualization, analysis, and 3D reconstruction of medical images from DICOM files. Automatic threshold segmentation was initially applied to identify the meniscal regions, followed by detailed manual adjustments to ensure anatomical precision. The

final 3D reconstructions of the menisci were exported in STL format to facilitate further computational analysis and biofabrication processes.

2.1.2. 3D modeling of partial meniscal scaffold

Following the generation of digital models for both menisci, the next step involved the precise 3D modeling of the partial meniscal defect. This process was performed using Fusion 360 software (Autodesk, USA), which enables detailed manipulation of CAD structures to create an anatomically accurate representation of the lesion site. Initially, both STL files (representing the intact and injured menisci) were aligned centrally within the workspace to ensure consistent orientation. Each STL file was then converted to a solid-body format to enable manipulation required for precise modeling. The healthy meniscus model was subsequently mirrored to match the anatomical side of the injured meniscus. By using Fusion 360's *Combine* function, the overlapping regions between the two models were subtracted, effectively isolating the area of the targeted partial defect. This allowed for the creation of a patient-specific digital scaffold model that accurately represents the missing or damaged portion of the meniscus, providing a foundation for the subsequent stages in the biofabrication process.

2.2. Fabrication of patient-specific partial meniscal scaffold

This step focuses on fabricating a patient-specific scaffold that recaptulates the complex morphology of the meniscal defect previously modeled in three dimensions. Due to the intricate anatomical structure of the meniscus, extrusion-based printing of hydrogel biomaterials was chosen for its ability to achieve controlled deposition and high structural fidelity, essential for reproducing detailed meniscal geometry. This technique is comparatively straightforward and cost-effective, utilizing a pneumatic or mechanical system to dispense the bioink precisely onto the substrate, building sequential layers that form a cohesive three-dimensional structure.[21,22]

2.2.1. Biomaterial ink formulation

Gelatin methacryloyl (GelMA) was selected as the biomaterial matrix for ink formulation due to its favorable properties for bioprinting applications. GelMA, derived from gelatin, a collagen derivative and primary component of the fibrocartilaginous extracellular matrix, is biocompatible, biodegradable, and photocrosslinkable in the presence of a photoinitiator, allowing for extensive customization of its physical and chemical properties.[23,24]

GelMA synthesis was conducted following a previously established protocol, successfully applied, and characterized in our prior studies.[25–27] In brief, type A gelatin from porcine skin (Sigma-Aldrich, USA) was dissolved in phosphate-buffered saline (PBS; Sigma-Aldrich) at 50 °C, with continuous stirring until a homogeneous solution was obtained. Methacrylic anhydride (Sigma-Aldrich, USA) was then added dropwise, and the mixture was stirred for an additional 3 h at 50 °C. The solution was subsequently diluted with preheated PBS, stirred briefly, and then dialyzed against deionized water at 40 °C for 7 days using dialysis tubing (Spectrum Lab Inc., USA) with daily water changes. After dialysis, the solution was lyophilized to yield GelMA as a white solid.

For the final ink formulation, GelMA was dissolved in PBS at a concentration of 100 mg/mL, a concentration shown to support both good printability and cell viability in bioprinting applications.[24,28] To complete the formulation, lithium phenyl-2,4,6-trimethylbenzoylphosphinate (LAP) was added as the photoinitiator at a concentration of 5 mg/mL, ensuring suitability for subsequent bioprinting processes.[29]

2.2.2. Slicing process and adjustment of 3D printing parameters

The next step in the 3D printing process involved slicing the 3D digital model, in which the model was divided into horizontal 2D layers and converted into a G-code file format, a programming language compatible with 3D printers, with precise instructions that guide the bioprinter's movements and material deposition according to user-defined parameters. This slicing was performed using PrusaSlicer 2.8.1 (Prusa Research, Czech Republic), with parameters set as follows: the print head was maintained at 20 °C, the nozzle moved at a speed of 6 mm/s, the layer height was set at 0.2 mm, and an infill density was configured at 40%.

2.2.3. 3D printing of scaffold

The 3D printing process was conducted using the patient-specific digital model of the partial meniscal defect. The GelMA-based biomaterial ink was loaded into 10 mL plastic syringes fitted with conical plastic needles with an inner nozzle diameter of 0.40 mm. An extrusion-based bioprinter (BioEnder Thermo, BioEdTech, Brazil) was employed to fabricate the scaffold structure. During the printing process, the scaffold was exposed to a 405 nm wavelength light source for on-the-spot photocrosslinking to ensure initial structural stability. Following completion of the printing process, the structure was further exposed to the same light source for an additional 2 min to finalize the photocrosslinking of the hydrogel.

2.3. Scanning and quantitative morphological analysis of printed scaffold

To evaluate the printed scaffold's accuracy in replicating the patient-specific meniscal defect, a quantitative morphological comparison was conducted between the nominal 3D digital model and the scanned printed scaffold. The printed meniscal scaffolds were scanned using a structured-light 3D scanner (Dolphin, RVS3D, Brazil), featuring a scanning accuracy of 0.04 mm and a point spacing of 0.06 mm. Each scaffold was scanned in 3 orientations and across 12 rotational positions on a turntable platform to capture a comprehensive representation of the structure. The resulting 3D digital model (in STL format) was then imported into GOM Inspect (GOM GmbH, Germany), a metrology-grade software, to conduct a 3D deviation analysis relative to the nominal model derived from medical imaging data. After fitting and alignment, the morphological similarity of the two models was analyzed using the CAD Comparison tool, with results displayed as a deviation chromatogram, providing a detailed quantitative assessment of morphological fidelity between the printed scaffold and the original digital model.

2.4. Proof-of-concept *ex vivo* implantation analysis

To validate the proposed technique, an *ex vivo* study was conducted, providing essential insights for a successful transition from laboratory development to potential clinical applications (Figure 2).

Initially, bilateral intact porcine knee joints were obtained from a local butcher, and menisci were

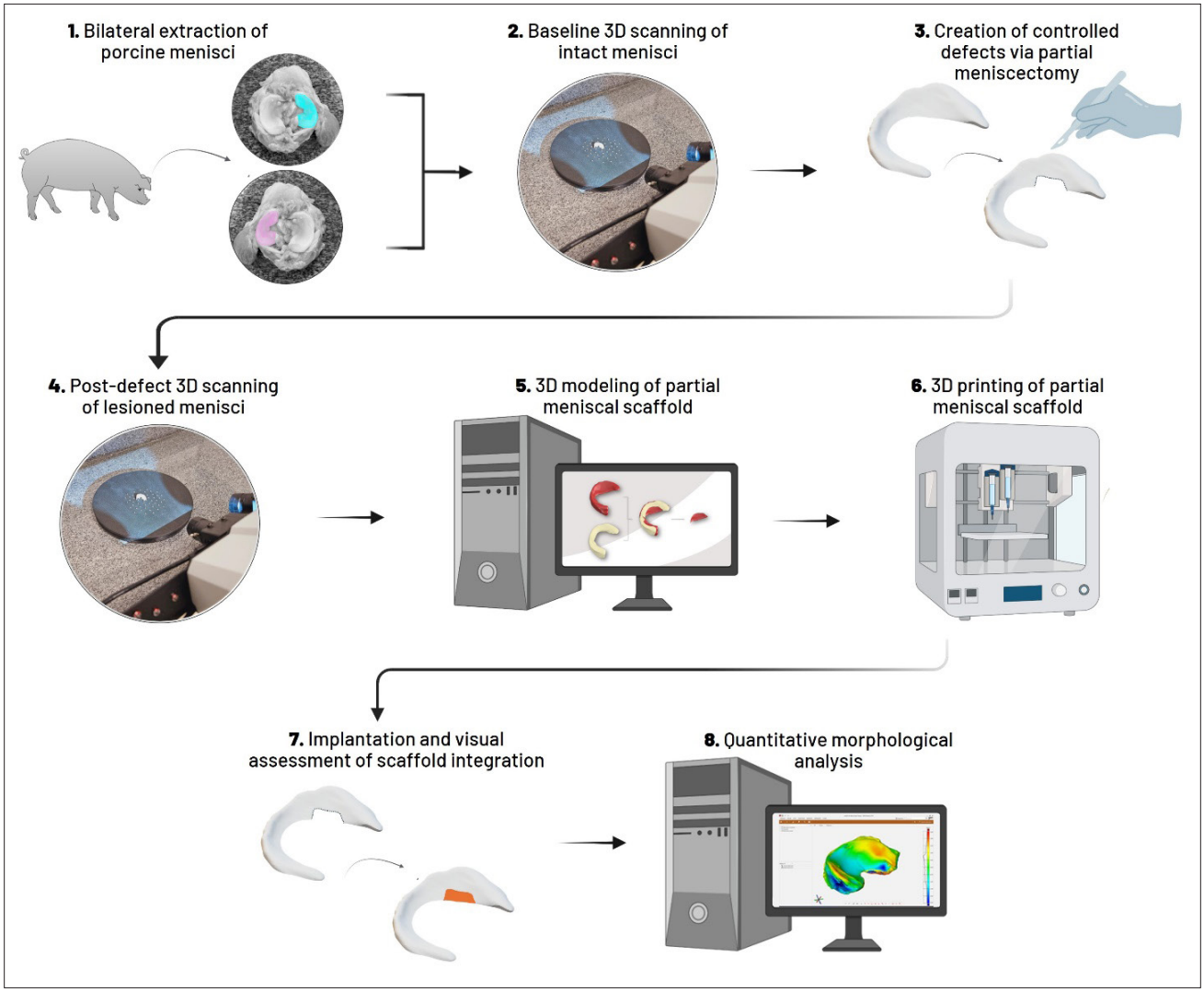

Figure 2. Schematic diagram illustrating the proof-of-concept *ex vivo* study for the initial validation of the proposed methodology for fabricating patient-specific partial meniscal scaffolds.

carefully extracted under sterile conditions to preserve their structural integrity. Each meniscus was scanned using a structured-light 3D scanner as described in **Section 2.3** to establish baseline 3D models of the intact meniscal structures.

Next, a partial meniscectomy was performed on one meniscus from each pair, creating a controlled defect to serve as a receptacle for the patient-specific scaffold implant. The lesioned menisci were then rescanned, and the acquired 3D digital images were processed following the method outlined in **Section 2.1.2**. Then, using the intact contralateral meniscus as a reference, the digital model of the meniscal defect was reconstructed to guide the creation of the scaffold structure tailored to the defect's dimensions and morphology.

Following the modeling stage, 3D printing of the patient-specific scaffold was conducted according to the protocol in **Section 2.2**, resulting in a custom-fit implant designed to restore the meniscus's anatomical continuity. Each scaffold was subsequently implanted into the defect site, and a visual assessment was performed to evaluate the fit and integration of the scaffold across different lesion types, including medial and lateral menisci, as well as varying defect sizes and complexities, such as large, small, and multi-lesion scenarios. This macroscopic analysis provided a qualitative assessment of the scaffold's adaptability to different meniscal geometries and defect profiles, with photographic documentation capturing various fit outcomes.

Finally, quantitative morphological analyses were conducted on the implanted scaffolds to assess their structural fidelity. The scaffold-implanted menisci were scanned post-implantation, and a comparative analysis was performed against the baseline 3D digital model of the intact meniscus using GOM Inspect, as described in **Section 2.3**. This comparison evaluated the precision of scaffold integration by examining deviation patterns between the original, uninjured meniscus and the scaffold-implanted structure, confirming the proposed technique's effectiveness, and identifying areas for potential optimization.

3. Results and discussion

The segmentation and 3D reconstruction of the medial menisci from bilateral MRI scans were successfully performed using InVesalius (CTI Renato Archer) (Figure 3A and B), a free and versatile software tool widely applied in various medical fields. Similar tools for medical segmentation and reconstruction include 3D Slicer, Mimics, and OsiriX[30]; however, InVesalius has been increasingly recognized for its accessibility and functionality, particularly in applications that require precise anatomical modeling, such as craniofacial[31] and brain tissue reconstruction.[32] In previous studies, our research group has effectively employed InVesalius for meniscal segmentation, demonstrating its capability for generating accurate digital models for musculoskeletal applications.[19]

Despite the overall success of the segmentation, we observed limitations in the automatic thresholding feature of InVesalius for this application. While automatic threshold segmentation provided a starting point, significant manual adjustments were necessary to accurately delineate meniscal boundaries, requiring a high level of anatomical expertise to ensure model precision. This need presents a limitation not only for efficiency in larger studies but also for the clinical applicability and translational potential of this methodology. Enhancements to automatic thresholding algorithms, as well as the development of new automated tools, could streamline the segmentation process, reducing the need for extensive manual corrections and improving reproducibility in both research and clinical settings.

In this study, we used high-resolution isotropic MRI images, a sequence type that typically provides slice thicknesses between 0.5 and 1 mm and yields a higher number of slices depending on the anatomical area and settings (our dataset contained 135 slices). This isotropic sequence enables the acquisition of voxels with equal dimensions in all directions, allowing for accurate spatial resolution and high-definition 3D reconstruction.[33] However, conventional MRI protocols for routine knee joint imaging generally employ thicker slices of 3–5 mm, resulting in only 20–40 slices per sequence, and leading to significant anatomical information loss.[34,35] Our preliminary tests using these routine MRI data confirmed that the wider slice spacing introduces continuity issues that hinder accurate 3D modeling. Although high-resolution isotropic MRI addresses these limitations, it is generally impractical for routine use due to time and resource limitations in clinical settings. Future improvements may leverage artificial intelligence (AI) strategies to enhance segmentation accuracy and streamline model reconstruction, including deep learning techniques such as convolutional neural networks (CNNs) and generative adversarial networks (GANs), which have shown promise in super-resolution applications.[36–38] For meniscal imaging specifically, such models could be trained to predict and reconstruct missing spatial information, bridging the gap between clinical imaging limitations and the precision required for patient-specific applications.

The final 3D digital models of the segmented menisci are displayed in Figure 3C and D, accurately representing

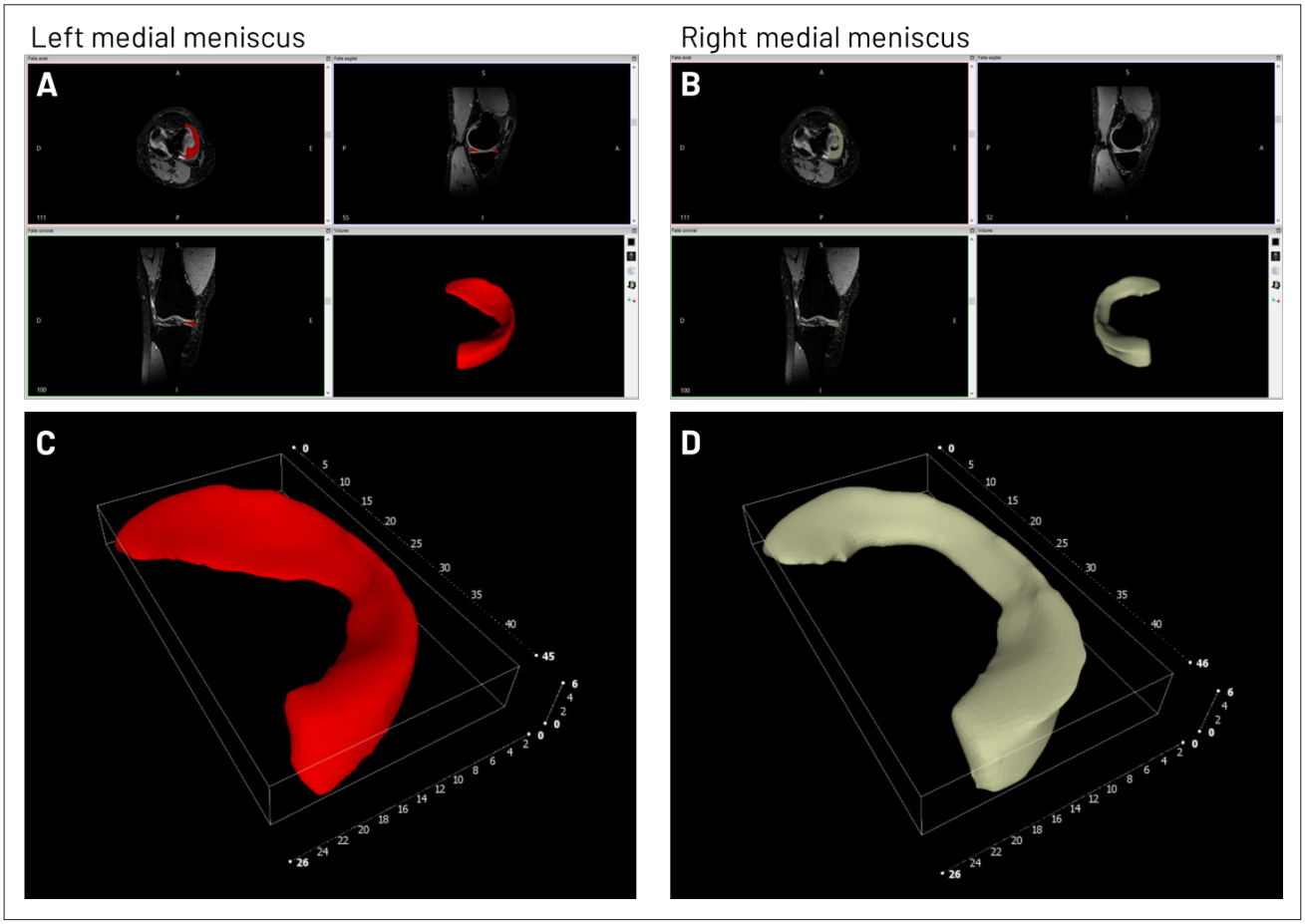

Figure 3. Magnetic resonance imaging (MRI) segmentation and 3D reconstruction of medial menisci from bilateral knee scans. Segmentation and initial 3D reconstruction process of the intact (A) and injured (B) medial menisci. Final 3D digital models of the intact (C) and injured (D) menisci (dimensions displayed in millimeters, mm).

their anatomical structure. Table 1 summarizes the dimensional measurements of the digital meniscus models obtained from each side. Analysis of these dimensions reveals a high degree of morphological similarity between the contralateral menisci, consistent with previous findings in the literature.[39] This previously reported symmetry supports our methodology, using the intact contralateral meniscus as a foundational guide for reconstructing defects in the injured meniscus.

Table 1. Dimensional measurements of 3D reconstructed medial meniscus models for bilateral knee joints

Measurement	Left medial meniscus (intact) (mm)	Right medial meniscus (injured) (mm)
Anterior-posterior length (*x*-axis)	25.65	25.98
Medial-lateral width (*y*-axis)	44.87	45.82
Superior-inferior thickness (*z*-axis)	5.26	5.77

The 3D modeling of the partial meniscal defect was performed to create a patient-specific scaffold that accurately replicates the lesion site, as illustrated in Figure 4A. The digital reconstruction process involved multiple steps to isolate the defective area and generate a custom scaffold model. Figure 4A-I and A-II depict the individual 3D models of the medial menisci: the intact left meniscus (Figure 4A-I) and the partially injured right meniscus (Figure 4A-II). These initial models served as the foundation for aligning, mirroring, and subtracting overlapping regions to generate the final scaffold.

To achieve accurate modeling, both meniscal models were aligned centrally within Fusion 360 software (Autodesk) to ensure consistent orientation, followed by the conversion of STL files to a solid-body format, allowing precise manipulation. In Figure 4A-III, the intact and injured menisci are shown superimposed, providing a

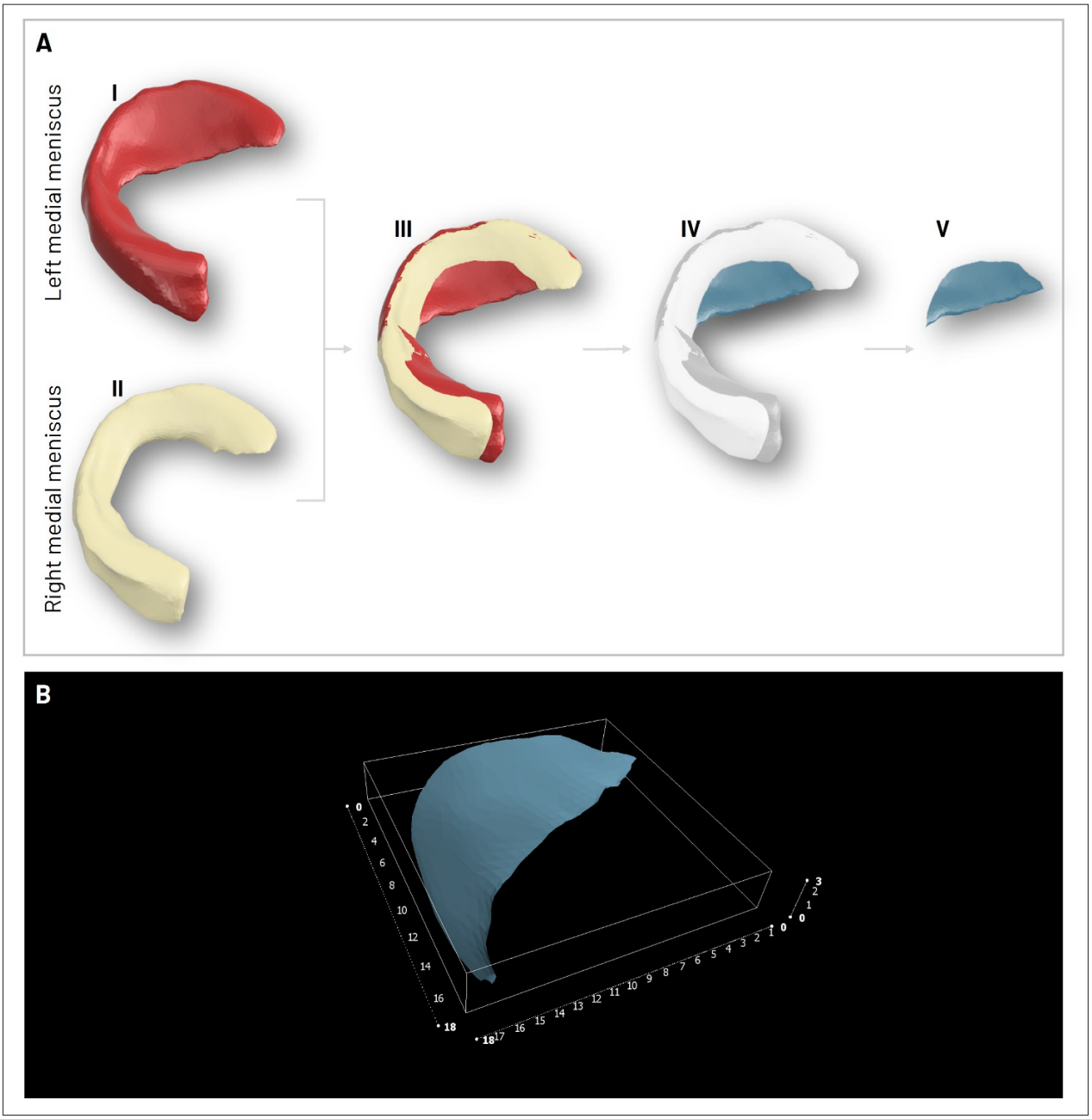

Figure 4. Digital reconstruction and modeling process for a patient-specific meniscal scaffold. (A) Step-by-step modeling of the partial meniscal defect. (I) 3D digital model of the intact left meniscus; (II) 3D model of the partially injured right meniscus; (III) superimposed models of the intact and injured menisci to highlight overlapping regions; (IV) isolation of the partial defect area by subtracting the intact meniscus from the injured one; (V) final extracted defect region used as the foundation for scaffold design. (B) Final patient-specific scaffold model (dimensions displayed in millimeters, mm).

clear view of the overlapping regions. By using the *Combine* function in Fusion 360, we isolated the area of partial meniscectomy by subtracting the intact meniscus from the injured one. This subtraction step is crucial, as it enables the identification of the precise region where tissue loss has occurred, specifically in the inner section of the meniscus, which is highlighted in Figure 4A-IV. Only this region, representing the partial defect, was retained, with other minor discrepancies between the menisci disregarded to maintain anatomical accuracy.

The final output, shown in Figure 4A-V, represents the extracted defect area that will serve as the basis for the scaffold design. The result of the modeling process,

illustrated in Figure 4B, showcases the patient-specific scaffold with precise measurements: a total length of 17.46 mm, a width of 17.19 mm, and a height of 2.69 mm. These dimensions are crucial for ensuring that the scaffold will provide an accurate fit within the lesion site, offering structural support to facilitate meniscal repair.

By using the intact meniscus as a template, we ensured that the scaffold design closely mimics the missing tissue. This approach serves as a potential alternative to other patient-specific modeling strategies, such as freehand digital design or generic templates, which do not use the native tissue as a guide.[40–42] While such methods have their applications, they do not always achieve the anatomical fidelity needed for accurately replicating certain complex structures in the human body, where even small deviations from the original geometry can have a considerable impact on functionality. For meniscal repair, in particular, achieving a high degree of anatomical accuracy is critical, as any discrepancy may impact joint stability and load distribution.[43,44]

Fusion 360 was selected for this study due to its user-friendly interface and interactive tools, facilitating precise alignment and subtraction operations essential for scaffold design. Although a free license for Fusion 360 is currently available for students and educators on a limited basis, the software's commercial nature poses a limitation for broader accessibility. Therefore, to enhance accessibility in future applications, similar modeling routines could be developed using free and open-source software, such as Blender.[45] This adaptation would broaden the applicability of our protocol and make patient-specific scaffold design more attainable in diverse research and clinical settings.

The process of 3D printing the meniscal scaffold is illustrated in Figure 5. Figure 5A shows the 3D model after slicing, ready for extrusion-based printing, while Figure 5B

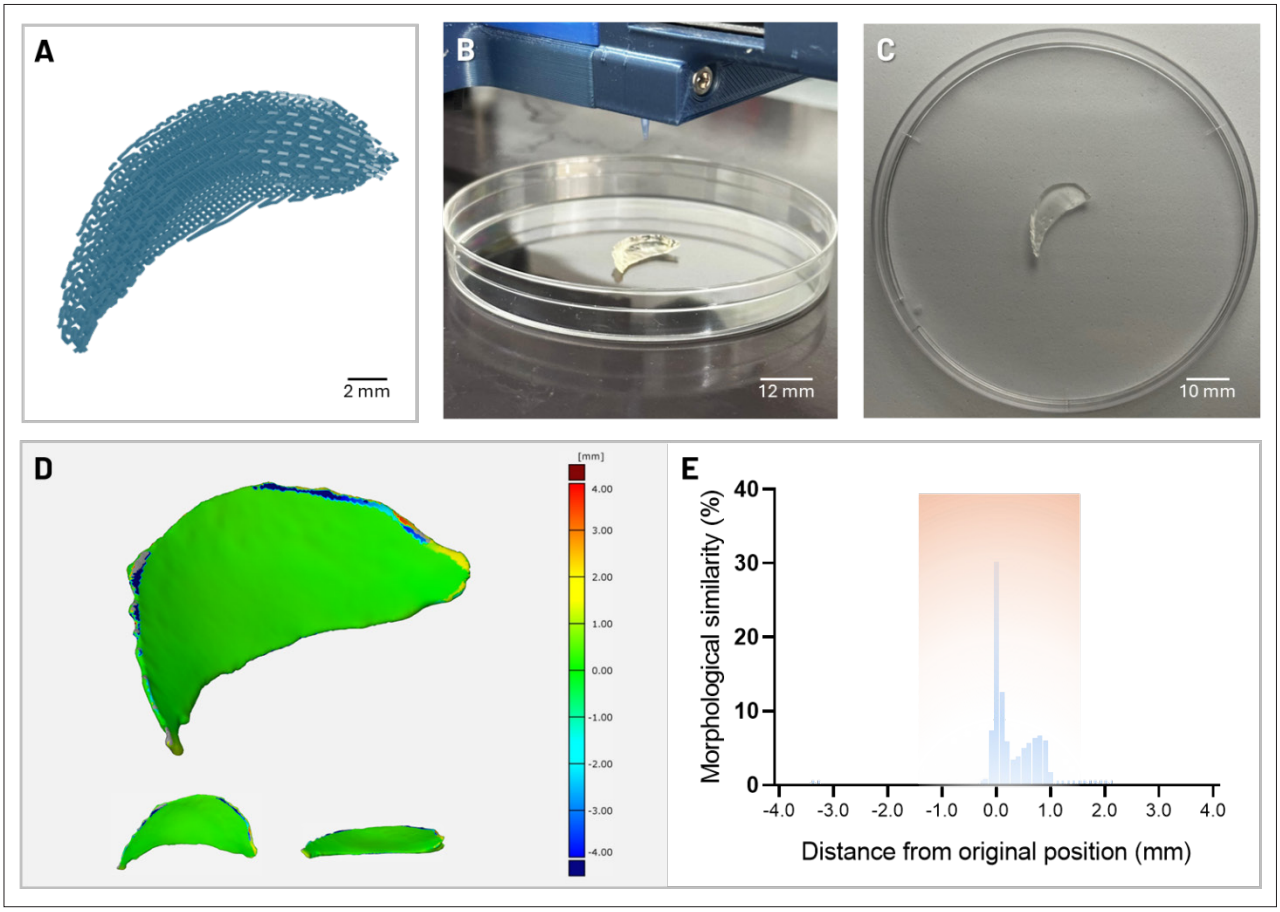

Figure 5. Stages of 3D printing and dimensional accuracy analysis of the meniscal scaffold. (A) Sliced 3D model prepared for extrusion-based printing. (B) Scaffold during the printing process. (C) Final printed scaffold. (D) Color-coded deviation chromatogram generated by GOM Inspect, displaying point-by-point distance deviations between the scanned, printed scaffold, and the nominal digital model (green regions indicate minimal deviation, while blue and red regions highlight areas where the printed scaffold diverges from target dimensions). (E) Histogram quantifying surface deviation (an orange shadow is present in the background of the graph, visually emphasizing and limiting deviations within ±1.5 mm).

captures the scaffold during the printing process, and Figure 5C presents the final printed scaffold. The 3D deviation analysis conducted using GOM Inspect (Figure 5D) provides a color-coded deviation chromatogram, illustrating the point-by-point distance between the 3D model obtained from the scanned, printed scaffold, and the nominal digital model originally designed for printing. This analysis measures the spatial discrepancies at each surface point, enabling us to visualize how closely the printed structure aligns with the intended design. In the chromatogram, green regions indicate minimal deviation, showing that most points on the scaffold's surface align closely with the digital model, while blue and red regions denote negative and positive deviations, respectively, highlighting areas where the printed scaffold deviates from target dimensions. Although this approach provides both quantitative and qualitative insights into scaffold structural accuracy, facilitating high-resolution shape characterization, it remains underexplored for applications in tissue engineering and scaffold validation. This technique is particularly valuable for evaluating scaffold dimensional accuracy and identifying potential areas for refinement, which are crucial for enhancing the precision and reliability of 3D bioprinting in complex tissue constructs. Additionally, its non-destructive nature is especially advantageous for assessing biofabricated tissues, as it allows for precise dimensional verification without compromising the integrity of the scaffold, an essential factor prior to clinical application.

The histogram in Figure 5E quantifies this deviation, showing that 96.84% of the scaffold's surface points deviate by less than ±1.5 mm, underscoring the high fidelity of our 3D printing process. This level of accuracy highlights the effectiveness of our biofabrication process in achieving a structure that closely replicates the digital model. The extrusion-based hydrogel printing method proved effective for fabricating the meniscal partial scaffold. Additionally, this technique permits the incorporation of cells and other components that support the development of functional living tissues and regenerative implants, making it suitable for applications in personalized tissue engineering.[21,22] However, this technique presents challenges, requiring a steep learning curve to achieve consistent results. Factors such as environmental conditions (e.g., temperature and humidity) and variations in the rheological properties of the biomaterial ink add complexity to standardizing the printing process. Currently, we are also actively exploring alternative printing methods, such as digital light processing (DLP), which offers enhanced precision in structural details and could reduce the impact of operator skill and environmental variability on outcomes.[46] Additionally, the extrusion-based approach may encounter significant difficulties when fabricating more complex, patient-specific scaffolds, especially those without a flat base, due to gravitational effects that can distort soft hydrogel structures during printing. Overcoming this limitation may involve exploring other advanced bioprinting strategies, such as freeform reversible embedding of suspended hydrogels (FRESH)[47] and volumetric 3D bioprinting,[48] both of which provide supportive matrices that allow for more intricate scaffold geometries and mitigate gravitational distortion.

Given that evaluating bioink properties was not within the scope of this study, we opted for GelMA hydrogel, a well-established biomaterial for extrusion-based bioprinting. GelMA offers suitable printability and supports cell encapsulation and viability, making it an effective choice for scaffold fabrication in tissue engineering applications.[23] However, GelMA has known limitations regarding mechanical strength, restricting its capacity to mimic the load-bearing properties of native meniscal tissue.[2,49] Both literature data and our previous studies indicate that the mechanical properties of GelMA-based scaffolds could be significantly enhanced through the integration of reinforcing agents, such as nanomaterials, to meet the specific biomechanical demands of meniscal tissue repair.[26,49] Future research could, therefore, focus on optimizing the composition of GelMA or exploring alternative hydrogels to enhance mechanical robustness without compromising biological compatibility within this biofabrication protocol.

The *ex vivo* implantation analysis aimed to validate the proposed technique's clinical potential by testing patient-specific scaffolds within meniscal defects under controlled conditions. Bilateral porcine knee joints were procured, and intact menisci were carefully dissected to preserve structural integrity, serving as reference models for the creation of partial defects. These defects were primarily created in the inner regions of the meniscus (white-white zone), aligning with clinical practice where such areas are most commonly affected and pose greater challenges due to their lack of vascularization and intrinsic healing capacity. Conversely, lesions in the outer regions (red-red zone) were not explored, as their vascular supply allows for better healing potential when repaired through suturing.[6] These defects were varied in terms of location, size, and meniscal region to enable assessment of scaffold adaptability across diverse clinical scenarios. Figure 6 illustrates the visual results of this implantation process across three distinct defect types (column I shows the intact meniscus, column II displays the meniscectomized state, and column III presents the meniscus with the patient-specific scaffold implanted). Figure 6A depicts a large horizontal defect in the inner third of the lateral meniscus; Figure 6B shows a substantial lesion encompassing the anterior horn region

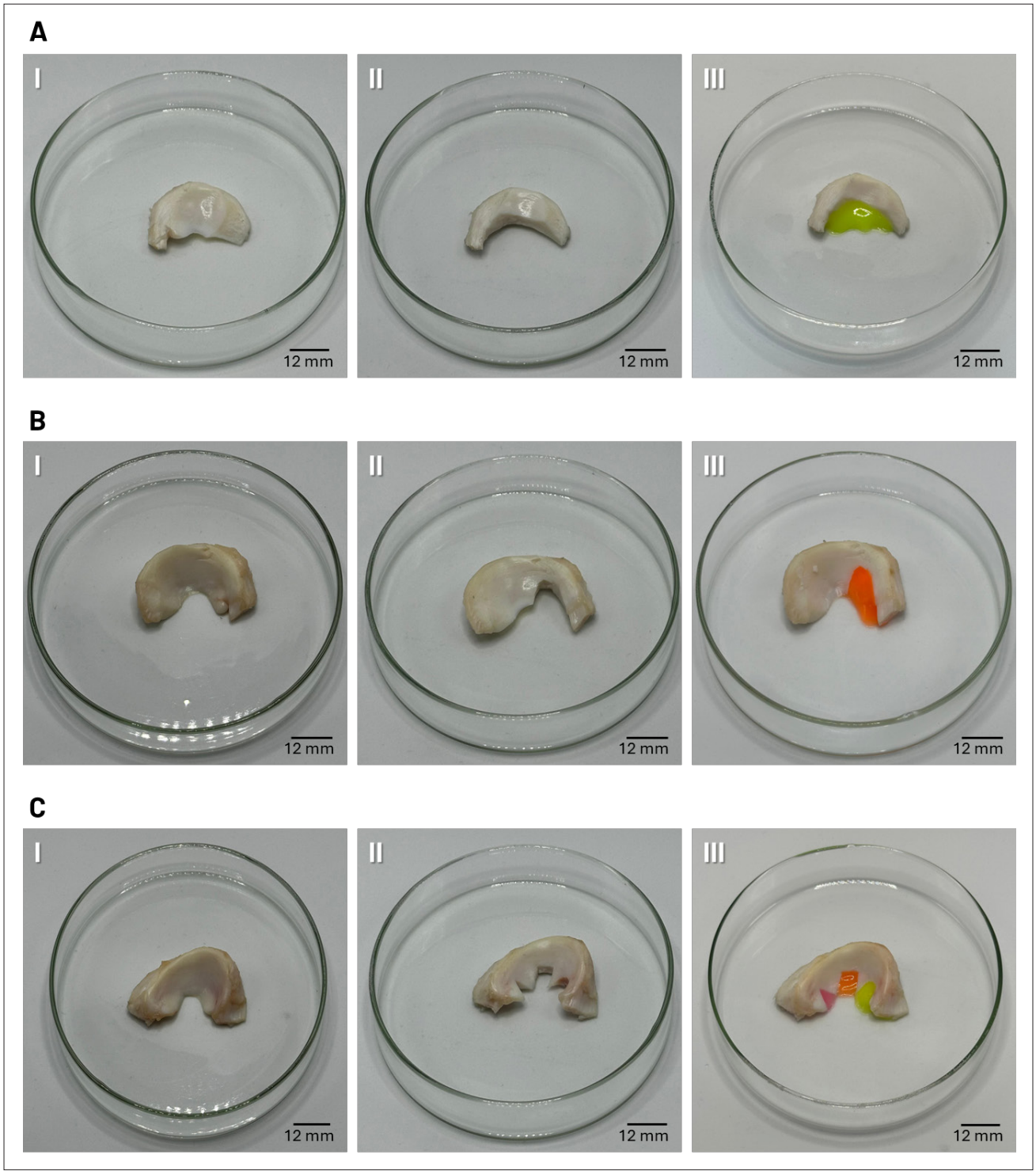

Figure 6. *Ex vivo* implantation of patient-specific scaffolds within partial meniscal defects created in porcine menisci. (A) Large horizontal defect in the inner third of the lateral meniscus. (B) Substantial lesion in the medial third encompassing the anterior horn of the medial meniscus. (C) Multiple smaller lesions in the lateral meniscus, including triangular, rectangular, and circular shapes. Images I show the intact meniscus before lesion creation; Images II display the meniscectomized state; and Images III present the meniscus with the implanted patient-specific scaffold (water-based food dye was applied to scaffolds to enhance visual contrast).

of the medial meniscus; and Figure 6C demonstrates a lateral meniscus with multiple smaller lesions in various shapes (triangular, rectangular, and circular). A water-based food dye was applied to the scaffolds for enhanced visual contrast, facilitating clearer assessment of scaffold integration within each defect.

An additional visual inspection of the scaffold–tissue interface was conducted using optical microscopy to provide a closer look at the contact between the implanted scaffold and the meniscal tissue (Figure 7). The magnified insets in Figure 7 illustrate the boundary for each defect type, suggesting a generally well-aligned interface between the scaffold and native tissue. The visual continuity observed at the scaffold–tissue junction implies that the scaffold conforms reasonably well to the complex contours of each defect, supporting its adaptability in diverse meniscal geometries.

Quantitative morphological assessments of scaffold fidelity are provided in Figure 8. This analysis compared the scaffold-implanted menisci against the baseline 3D model of the intact meniscus. Figure 8A, C, and E displays deviation chromatograms for the scaffold-implanted menisci corresponding to Figure 6A, B, and C, respectively. The color-coded maps illustrate spatial deviations between the scanned, implanted menisci, and the original intact models. Figure 8B, D, and F present histograms quantifying these deviations, offering a clearer understanding of scaffold fidelity. Notably, the deviation analysis across the scaffold surfaces demonstrated high morphological fidelity in each case, with the majority of surface points deviating within ±1.5 mm. Specifically, 94.92% of surface points on the scaffold-implanted lateral meniscus with the large horizontal defect (Figure 8B), 91.48% on the medial meniscus with the extensive anterior horn defect (Figure 8D), and 95.66% on the lateral meniscus with multiple smaller lesions (Figure 8F) remained within this threshold. The morphological analysis in Figure 8 reveals that the scaffold for the anterior horn defect (Figure 8D) exhibited a broader deviation distribution compared to the other cases. This result suggests that anatomical areas with intricate geometries, such as the anterior horn, may pose additional challenges for scaffold accuracy. The increased deviation in this region could be attributed to the scaffold's limited structural support in complex contours, potentially leading to minor misalignment during implantation.

A potential limitation of our methodology for fabricating patient-specific scaffolds is its reliance on the contralateral meniscus as a reference model. This dependency could restrict the approach's applicability in cases where the contralateral meniscus is compromised or unavailable due to bilateral injury or degeneration. Additionally, extrapolating this methodology to other tissues may not always be feasible, particularly for structures or organs that lack a contralateral counterpart. For instance, in organs with a unique anatomical presence within the body, the absence of a mirrored structure limits the ability to generate a patient-specific scaffold based solely on anatomical symmetry. While the current study demonstrates the feasibility of the proposed methodology, further validation with additional datasets, encompassing variations in patient demographics, would enhance its applicability across diverse anatomical features and clinical scenarios. Moreover, further steps are necessary to transition this work toward full *in vivo* validation. This transition will require optimizing the mechanical properties of the scaffold material to withstand physiological loads and integrating biological components to evaluate cellular

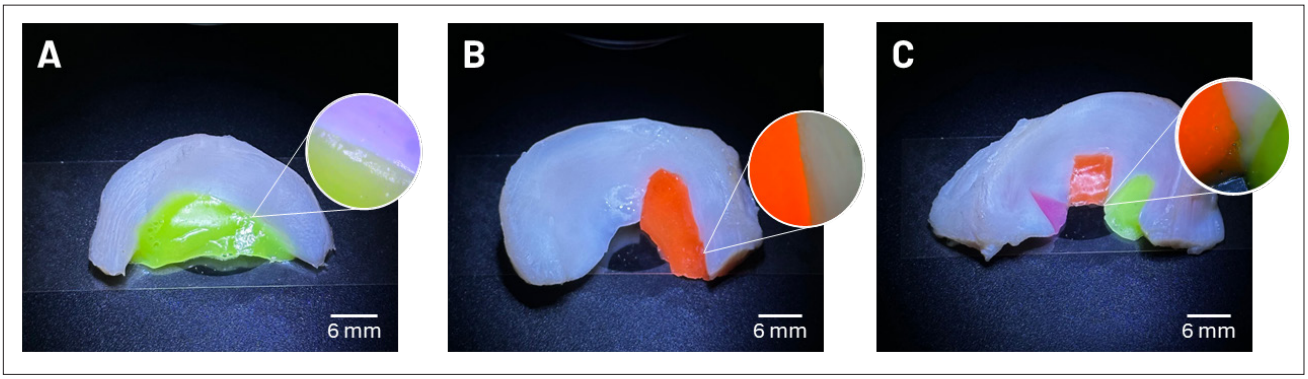

Figure 7. Visual inspection of the scaffold–tissue interface in partial meniscal defects. (A) Large horizontal defect in the inner third of the lateral meniscus. (B) Substantial lesion in the medial third encompassing the anterior horn. (C) Multiple smaller lesions in various shapes within the lateral meniscus. Each image includes a magnified inset captured at 500× magnification using optical microscopy, highlighting the scaffold–tissue interface and demonstrating close contact between the scaffold and meniscal tissue (a water-based dye was applied to the scaffolds to improve visual contrast and facilitate assessment of scaffold integration).

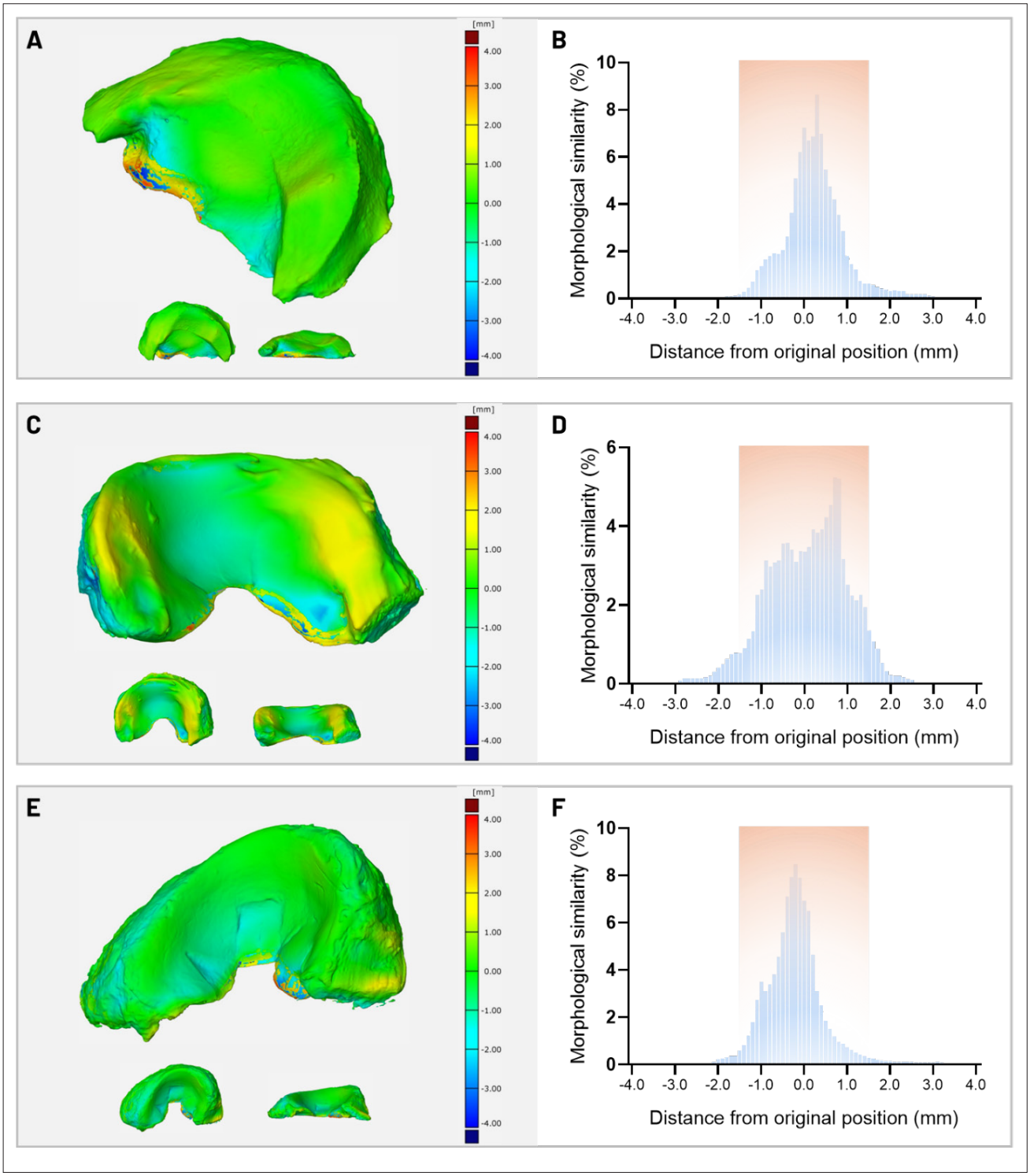

Figure 8. Quantitative morphological analysis of scaffold fidelity using deviation chromatograms and histograms. Deviation chromatograms and corresponding histograms are shown for each scaffold-implanted meniscus: (A, B) lateral meniscus with a large horizontal defect, (C, D) medial meniscus with an extensive defect encompassing the anterior horn, and (E, F) lateral meniscus with multiple smaller lesions. The color-coded maps in the chromatograms illustrate spatial deviations between the scaffold-implanted menisci and their intact 3D models (areas in green represent minor deviation, while blue and red indicate regions where the scaffold deviates more significantly from the intended dimensions), while the histograms quantify the distribution of these deviations (an orange shadow in the background of each histogram highlights and limits deviations within ±1.5 mm).

responses. Expanding these validations will not only strengthen the methodology's clinical applicability but also address critical parameters for its translational potential. Future studies are warranted to address these aspects, building on the foundational work presented here to ensure the methodology's scalability, adaptability, and robustness for broader clinical applications.

Although advances have been made in the field of patient-specific meniscus scaffolds, previous studies have predominantly focused on creating entire meniscal replacements rather than addressing localized, partial defects.[17–19] While some studies have explored scaffolds specifically targeting partial meniscal lesions, these approaches lacked true patient-specific customization in terms of size and morphology.[44,50,51] Therefore, our methodology bridges this gap by combining the patient-specific design of scaffolds with a focus on partial defects. As mentioned above, clinically, partial meniscal injuries are significantly more common, with partial meniscectomy, rather than complete meniscus removal, being the primary surgical intervention.[52] Thus, by developing scaffolds tailored to specific defect sites, our method aligns closely with current clinical practice, aiming to preserve healthy meniscal tissue while minimizing surgical impact. This represents a pioneering step in creating defect-targeted, patient-specific scaffolds for knee menisci with direct clinical relevance.

4. Conclusion

This study successfully presented a novel methodology for creating patient-specific, defect-targeted meniscal scaffolds, addressing a critical gap in regenerative strategies for partial meniscal injuries. By combining medical imaging and CAD-based digital reconstruction, we generated precise 3D models of meniscal defects, enabling the design and fabrication of scaffolds tailored to fit specific lesion sites. The *ex vivo* implantation analysis demonstrated the adaptability of these scaffolds across various defect types and highlighted their morphological fidelity, with quantitative deviation analyses indicating a high degree of structural conformity with the native tissue.

Acknowledgments

The authors gratefully acknowledge BioEdTech company for providing the extrusion-based bioprinter used in this study.

Funding

This work was supported by the National Council for Scientific and Technological Development (CNPq), the Department of Science and Technology of the Ministry of Health (Decit/SECTICS/MS), and the National Program for Genomics and Precision Health (Genomas Brasil) (CNPq: 444141/2023-5). Anderson Oliveira Lobo thanks to CNPq (403890/2023-3 and 310883/2020-2).

Conflict of interest

Thiago Domingues Stocco serves as the Editorial Board Member of the journal and Anderson Oliveira Lobo is the guest editor of the special issue: *Advances in Bioprinting and Organ-on-a-chip and Applications for Precision Medicine*, but did not in any way involve in the editorial and peer-review process conducted for this paper, directly or indirectly. All authors declare that they have no competing interests.

Author contributions

Conceptualization: Thiago Domingues Stocco, Willian Gonçalves Tsumura

Formal analysis: Thiago Domingues Stocco, Francklin Trindade da Silva, Willian Gonçalves Tsumura, Anderson Oliveira Lobo

Funding acquisition: Thiago Domingues Stocco

Investigation: Thiago Domingues Stocco, Francklin Trindade da Silva, Willian Gonçalves Tsumura

Methodology: Thiago Domingues Stocco, Francklin Trindade da Silva, Willian Gonçalves Tsumura, Millena de Cassia Sousa e Silva

Supervision: Thiago Domingues Stocco

Writing–original draft: Thiago Domingues Stocco, Francklin Trindade da Silva, Willian Gonçalves Tsumura, Anderson Oliveira Lobo

Writing–review & editing: Thiago Domingues Stocco, Anderson Oliveira Lobo

Ethics approval and consent to participate

Not applicable.

Consent for publication

Not applicable.

Availability of data

The data that support the findings of this study are openly available on Mendeley Data (http://doi.org/10.17632/zw4b28gpf5.1).

References

1. Fox AJS, Wanivenhaus F, Burge AJ, Warren RF, Rodeo SA. The human meniscus: a review of anatomy, function, injury, and advances in treatment. *Clin Anat*. 2015;28(2):269-287. doi: 10.1002/ca.22456

2. Schwer J, Ignatius A, Seitz AM. The biomechanical properties of human menisci: a systematic review. *Acta Biomater*. 2024;175:1-26.
doi: 10.1016/j.actbio.2023.12.010

3. Pasiński M, Zabrzyńska M, Adamczyk M, et al. A current insight into human knee menisci. *Transl Res Anat*. 2023;32:100259.
doi: 10.1016/j.tria.2023.100259

4. Adams BG, Houston MN, Cameron KL. The epidemiology of meniscus injury. *Sports Med Arthrosc*. 2021;29(3): e24-e33.
doi: 10.1097/JSA.0000000000000329

5. Bergstein VE, Ahiarakwe U, Haft M, Mikula JD, Best MJ. Decreasing Incidence of Partial Meniscectomy and Increasing Incidence of Meniscus Preservation Surgery From 2010 to 2020 in the United States. *Arthroscopy*. 2024: S0749-8063(24)00558-9.
doi: 10.1016/j.arthro.2024.07.030

6. Ozeki N, Seil R, Krych AJ, Koga H. Surgical treatment of complex meniscus tear and disease: state of the art. *J ISAKOS*. 2021;6(1):35-45.
doi: 10.1136/jisakos-2019-000380

7. Ha AY, Shalvoy RM, Voisinet A, Racine J, Aaron RK. Controversial role of arthroscopic meniscectomy of the knee: a review. *World J Orthop*. 2016;7(5):287.
doi: 10.5312/wjo.v7.i5.287

8. Roemer FW, Kwoh CK, Hannon MJ, et al. Partial meniscectomy is associated with increased risk of incident radiographic osteoarthritis and worsening cartilage damage in the following year. *Eur Radiol*. 2017;27(1):404-413.
doi: 10.1007/s00330-016-4361-z

9. Abram SGF, Judge A, Beard DJ, Price AJ. Adverse outcomes after arthroscopic partial meniscectomy: a study of 700 000 procedures in the national Hospital Episode Statistics database for England. *Lancet*. 2018;392(10160):2194-2202.
doi: 10.1016/S0140-6736(18)31771-9

10. Courties A, Kouki I, Soliman N, Mathieu S, Sellam J. Osteoarthritis year in review 2024: epidemiology and therapy. *Osteoarthr Cartil*. 2024;32(11):1397-1404.
doi: 10.1016/j.joca.2024.07.014

11. Hunter DJ, Schofield D, Callander E. The individual and socioeconomic impact of osteoarthritis. *Nat Rev Rheumatol*. 2014;10(7):437-441.
doi: 10.1038/nrrheum.2014.44

12. Bian Y, Cai X, Zhou R, et al. Advances in meniscus tissue engineering: towards bridging the gaps from bench to bedside. *Biomaterials*. 2025;312:122716.
doi: 10.1016/j.biomaterials.2024.122716

13. van Minnen BS, van Tienen TG. The current state of meniscus replacements. *Curr Rev Musculoskelet Med*. 2024;17(8):293-302.
doi: 10.1007/s12178-024-09902-1

14. Kani KK, Porrino JA, Chew FS. Meniscal allograft transplantation: a pictorial review. *Curr Probl Diagn Radiol*. 2022;51(5):779-786.
doi: 10.1067/j.cpradiol.2021.09.008

15. Lucidi GA, Grassi A, Agostinone P, et al. Risk factors affecting the survival rate of collagen meniscal implant for partial meniscal deficiency: an analysis of 156 consecutive cases at a mean 10 years of follow-up. *Am J Sports Med*. 2022;50(11):2900-2908.
doi: 10.1177/03635465221112635

16. Accadbled F, Pham TT, Thevenin Lemoine C, Sales de Gauzy J. Implantation of an Actifit® polyurethane meniscal scaffold 18 months after subtotal lateral meniscectomy in a 13-year-old male adolescent. *Am J Case Rep*. 2020; 21:e920688.
doi: 10.12659/AJCR.920688

17. Cengiz IF, Pitikakis M, Cesario L, et al. Building the basis for patient-specific meniscal scaffolds: from human knee MRI to fabrication of 3D printed scaffolds. *Bioprinting*. 2016;1-2:1-10.
doi: 10.1016/j.bprint.2016.05.001

18. Filardo G, Petretta M, Cavallo C, et al. Patient-specific meniscus prototype based on 3D bioprinting of human cell-laden scaffold. *Bone Joint Res*. 2019;8(2):101-106.
doi: 10.1302/2046-3758.82.BJR-2018-0134.R1

19. Stocco TD, Moreira Silva MC, Corat MAF, Gonçalves Lima G, Lobo AO. Towards bioinspired meniscus-regenerative scaffolds: engineering a novel 3D bioprinted patient-specific construct reinforced by biomimetically aligned nanofibers. *Int J Nanomedicine*. 2022;17:1111-1124.
doi: 10.2147/IJN.S353937

20. Jha V. Editorial commentary: rate of meniscal repair versus meniscectomy has improved and should continue to improve. *Arthrosc J Arthrosc Relat Surg*. Published online October 2024: S0749-8063(24)00787-4.
doi: 10.1016/j.arthro.2024.10.006

21. Zhang YS, Haghiashtiani G, Hübscher T, et al. 3D extrusion bioprinting. *Nat Rev Methods Prim*. 2021;1(1):75.
doi: 10.1038/s43586-021-00073-8

22. Huang G, Zhao Y, Chen D, et al. Applications, advancements, and challenges of 3D bioprinting in organ transplantation. *Biomater Sci*. 2024;12(6):1425-1448.
doi: 10.1039/D3BM01934A

23. Das S, Valoor R, Jegadeesan JT, Basu B. 3D bioprinted GelMA scaffolds for clinical applications: promise and challenges. *Bioprinting*. 2024;44:e00365.
doi: 10.1016/j.bprint.2024.e00365

24. Dobrisan MR, Lungu A, Ionita M. A review of the current state of the art in gelatin methacryloyl-based printing inks in bone tissue engineering. *Virtual Phys Prototyp*. 2024;19(1):e2378003.
doi: 10.1080/17452759.2024.2378003

25. Afewerki S, Bassous N, Harb SV, et al. Engineering multifunctional bactericidal nanofibers for abdominal hernia repair. *Commun Biol*. 2021;4(1):233. doi: 10.1038/s42003-021-01758-2

26. e Silva M de CS, de Sousa GF, das Virgens Santana M, Tsumura WG, Stocco TD, Lobo AO. Tailoring mechanical properties of printed GelMA scaffolds with multilayers of PLA/Laponite nanocomposite fibers. *Mater Lett*. 2024;364:136314. doi: 10.1016/j.matlet.2024.136314

27. Montesdeoca CYC, Afewerki S, Stocco TD, et al. Oxygen-generating smart hydrogels supporting chondrocytes survival in oxygen-free environments. *Colloids Surfaces B Biointerfaces*. 2020;194:111192. doi: 10.1016/j.colsurfb.2020.111192

28. Rajabi N, Rezaei A, Kharaziha M, et al. Recent advances on bioprinted gelatin methacrylate-based hydrogels for tissue repair. *Tissue Eng Part A*. 2021;27(11-12):679-702. doi: 10.1089/ten.tea.2020.0350

29. Elkhoury K, Zuazola J, Vijayavenkataraman S. Bioprinting the future using light: a review on photocrosslinking reactions, photoreactive groups, and photoinitiators. *SLAS Technol*. 2023;28(3):142-151. doi: 10.1016/j.slast.2023.02.003

30. Buffinton CM, Baish JW, Ebenstein DM. An introductory module in medical image segmentation for BME students. *Biomed Eng Educ*. 2023;3(1):95-109. doi: 10.1007/s43683-022-00085-0

31. Yap Abdullah J, Manaf Abdullah A, Zaim S, et al. Three-dimensional analysis of reconstructed skulls using three different open-source software versus commercial software. *Proc Inst Mech Eng Part H J Eng Med*. 2024;238(1):55-62. doi: 10.1177/09544119231212034

32. Gür Y. Masked stereolithography 3D printing of a brain tissue from an MRI data set. *Alexandria Eng J*. 2024;98:302-311. doi: 10.1016/j.aej.2024.05.002

33. Bajaj S, Chhabra A, Taneja AK. 3D isotropic MRI of ankle: review of literature with comparison to 2D MRI. *Skeletal Radiol*. 2024;53(5):825-846. doi: 10.1007/s00256-023-04513-2

34. Ai T, Zhang W, Priddy NK, Li X. Diagnostic performance of CUBE MRI sequences of the knee compared with conventional MRI. *Clin Radiol*. 2012;67(12):e58-e63. doi: 10.1016/j.crad.2012.07.020

35. Parkar AP, Adriaensen MEAPM. ESR essentials: MRI of the knee—practice recommendations by ESSR. *Eur Radiol*. 2024;34(10):6590-6599. doi: 10.1007/s00330-024-10706-7

36. Heckel R, Jacob M, Chaudhari A, Perlman O, Shimron E. Deep learning for accelerated and robust MRI reconstruction. *Magn Reson Mater Physics, Biol Med*. 2024;37(3):335-368. doi: 10.1007/s10334-024-01173-8

37. Zhang H, Shinomiya Y, Yoshida S. 3D MRI reconstruction based on 2D generative adversarial network super-resolution. *Sensors*. 2021;21(9):2978. doi: 10.3390/s21092978

38. Küstner T, Qin C, Sun C, Ning L, Scannell CM. The intelligent imaging revolution: artificial intelligence in MRI and MRS acquisition and reconstruction. *Magn Reson Mater Physics, Biol Med*. 2024;37(3):329-333. doi: 10.1007/s10334-024-01179-2

39. Yoon JR, Jeong HI, Seo MJ, et al. The use of contralateral knee magnetic resonance imaging to predict meniscal size during meniscal allograft transplantation. *Arthroscopy*. 2014;30(10):1287-1293. doi: 10.1016/j.arthro.2014.05.009

40. Nimeskern L, Feldmann EM, Kuo W, et al. Magnetic resonance imaging of the ear for patient-specific reconstructive surgery. In: Najbauer J, ed. *PLoS One*. 2014;9(8):e104975. doi: 10.1371/journal.pone.0104975

41. Laubach M, Suresh S, Herath B, et al. Clinical translation of a patient-specific scaffold-guided bone regeneration concept in four cases with large long bone defects. *J Orthop Transl*. 2022;34:73-84. doi: 10.1016/j.jot.2022.04.004

42. Holz J, Spalding T, Boutefnouchet T, et al. Patient-specific metal implants for focal chondral and osteochondral lesions in the knee; excellent clinical results at 2 years. *Knee Surgery, Sport Traumatol Arthrosc*. 2021;29(9):2899-2910. doi: 10.1007/s00167-020-06289-7

43. Mameri ES, Dasari SP, Fortier LM, et al. Review of meniscus anatomy and biomechanics. *Curr Rev Musculoskelet Med*. 2022;15(5):323-335. doi: 10.1007/s12178-022-09768-1

44. Veronesi F, Di Matteo B, Vitale ND, et al. Biosynthetic scaffolds for partial meniscal loss: a systematic review from animal models to clinical practice. *Bioact Mater*. 2021;6(11):3782-3800. doi: 10.1016/j.bioactmat.2021.03.033

45. Martínez Cendrero A, Franco Martínez F, Solórzano Requejo WG, Díaz Lantada A. Open-source library of tissue engineering scaffolds. *Mater Des*. 2022;223:111154. doi: 10.1016/j.matdes.2022.111154

46. Li W, Wang M, Ma H, Chapa-Villarreal FA, Lobo AO, Zhang YS. Stereolithography apparatus and digital light processing-based 3D bioprinting for tissue fabrication. *iScience*. 2023;26(2):106039. doi: 10.1016/j.isci.2023.106039

47. Shiwarski DJ, Hudson AR, Tashman JW, Feinberg AW. Emergence of FRESH 3D printing as a platform for advanced tissue biofabrication. *APL Bioeng*. 2021;5(1):010904. doi: 10.1063/5.0032777

48. Bernal PN, Delrot P, Loterie D, et al. Volumetric bioprinting of complex living-tissue constructs within seconds. *Adv Mater*. 2019;31(42):e1904209.
doi: 10.1002/adma.201904209

49. Guo A, Zhang S, Yang R, Sui C. Enhancing the mechanical strength of 3D printed GelMA for soft tissue engineering applications. *Mater Today Bio*. 2024;24:100939.
doi: 10.1016/j.mtbio.2023.100939

50. Bandyopadhyay A, Mandal BB. A three-dimensional printed silk-based biomimetic tri-layered meniscus for potential patient-specific implantation. *Biofabrication*. 2019;12(1):015003.
doi: 10.1088/1758-5090/ab40fa

51. Bandyopadhyay A, Ghibhela B, Shome S, Pal D, Nandi SK, Mandal BB. Silk-based injectable photocurable hydrogel loaded with autologous growth factors for patient-specific repair of meniscal defects in vivo. *Appl Mater Today*. 2024;37:102111.
doi: 10.1016/j.apmt.2024.102111

52. Avila A, Vasavada K, Shankar DS, Petrera M, Jazrawi LM, Strauss EJ. Current controversies in arthroscopic partial meniscectomy. *Curr Rev Musculoskelet Med*. 2022;15(5):336-343.
doi: 10.1007/s12178-022-09770-7

ACCSCIENCE PUBLISHING

International Journal of Bioprinting

RESEARCH ARTICLE

Biomimetically hierarchical scaffolds drive critical-sized osteochondral tissue regeneration

Farnaz Ghorbani[1,2,3*], Joaquim Miguel Oliveira[4,5*], Zhi Qian[1,6†], Chongjing Zhang[2†], Yi Zhang[7†], Behafarid Ghalandari[8], Dejian Li[2], Zeyuan Zhong[2,9], Zichen Liu[2,10], Yuanyuan Liu[7,11,12], and Baoqing Yu[1*]

[1]Department of Orthopaedics, Seventh People's Hospital of Shanghai, University of Traditional Chinese Medicine, Shanghai, China

[2]Department of Orthopedics, Shanghai Pudong Hospital, Fudan University Pudong Medical Center, Shanghai, China

[3]Department of Translational Health Sciences, Bristol Medical School, University of Bristol, Bristol, United Kingdom

[4]3B's Research Group, I3Bs – Research Institute on Biomaterials, Biodegradables and Biomimetics, University of Minho, Headquarters of the European Institute of Excellence on Tissue Engineering and Regenerative Medicine, AvePark, Parque de Ciência e Tecnologia, Zona Industrial da Gandra, Barco, Guimarães, Portugal

[5]ICVS/3B's–PT Government Associate Laboratory, Braga, Guimarães, Portugal

[6]Department of Orthopaedics, Institute of Bone and Joint Disease, Zhangye People's Hospital affiliated to Hexi University, Gansu, China

[7]School of Mechatronic Engineering and Automation, Shanghai University, Shanghai, China

[8]Division of Surgery and Interventional Science, Department of Surgical Biotechnology, University College London, London, United Kingdom

[9]Department of Orthopedics, Ruijin Hospital, Shanghai JiaoTong University School of Medicine, Shanghai, China

[10]Department of Materials Science and Engineering, School of Materials Science and Engineering, University of Shanghai for Science and Technology, Shanghai, China

[11]National Center for Translational Medicine (Shanghai) SHU Branch, Shanghai University, Shanghai, China

[12]Wenzhou Institute of Shanghai University, Wenzhou, Zhejiang, China

(This article belongs to the *Special Issue*: *Bioprinting of in Vitro Tissue and Disease Models*)

Abstract

This study presents a pioneering approach utilizing hierarchically functionalized scaffolds to foster anisotropic osteochondral tissue regeneration, leveraging the integration of distinct yet interconnected layers. We developed 3D-printed polydopamine-modified polycaprolactone (PCL) scaffolds, which were subsequently covered with a layer of electrospun PCL-gelatin fibers, and then functionalized with gelatin-bone morphogenetic protein-2 (BMP-2) following oxygen plasma surface treatments, creating a hierarchically organized multi-phasic architecture. This interconnected porous microstructure enabled controllable degradation while maintaining mechanical integrity and hydroxyapatite mineralization. *In vitro* assessments demonstrated that the scaffolds provided superior support for rat bone marrow mesenchymal stem cells, marked by their enhanced adhesion, viability, and proliferation. Increased alkaline phosphatase activity and osteocalcin expression over 14 days indicated that the scaffolds enhanced osteogenic performance, likely due to BMP-2 interaction with serum proteins, as supported by simulation studies, augmenting growth factor bioavailability. *In vivo* investigations in rabbit critical-

[†]These authors contributed equally to this work.

***Corresponding authors:**
Baoqing Yu
(doctorybq@163.com)

Farnaz Ghorbani
(farnaz.ghorbani@bristol.ac.uk)

Joaquim Miguel Oliveira
(miguel.oliveira@i3bs.uminho.pt)

Citation: Ghorbani F, Oliveira JM, Qian Z, et al. Biomimetically hierarchical scaffolds drive critical-sized osteochondral tissue regeneration. *Int J Bioprint*. 2025;11(1):573-597. doi: 10.36922/ijb.5104

Received: October 9, 2024
1st revised: November 27, 2024
2nd revised: December 27, 2024
3rd revised: January 7, 2025
Accepted: January 7, 2025
Published Online: January 7, 2025

Copyright: © 2025 Author(s). This is an Open Access article distributed under the terms of the Creative Commons Attribution License, permitting distribution, and reproduction in any medium, provided the original work is properly cited.

Publisher's Note: AccScience Publishing remains neutral with regard to jurisdictional claims in published maps and institutional affiliations.

sized osteochondral defects at 4- and 12-week post-implantation demonstrated that the multi-phasic scaffolds notably promoted secretion of type I and II collagen, neo-tissue formation, and integration with surrounding tissue, with significant results observed at 12 weeks. These findings indicate the potential of multi-phasic scaffolds for osteochondral tissue regeneration.

Keywords: 3D printing; Biomimetic scaffolds; Electrospinning; Hierarchical scaffolds; Osteochondral tissue; Tissue engineering

1. Introduction

Osteoarthritis and osteochondritis dissecans are debilitating joint diseases resulting from the degeneration of cartilage and subchondral bone.[1] The avascular nature of cartilage, along with molecular mechanisms and a deficiency of reparative cells and bioactive factors, limits the self-regenerative capabilities of osteochondral tissue.[2] Surgical treatments and joint replacements often result in fibrocartilage formation and insufficient biomechanical restoration.[3] In recent decades, the spotlight has shifted to the exploration of tissue engineering as a potential therapeutic avenue. Nevertheless, the intricate nature of anisotropic osteochondral tissue, compounded by distinct tissue lineage and variations in physicochemical and biological properties across the layers, underscores the persistent challenge of achieving effective repair. Thus, there is an urgent need to develop multi-material, multi-phasic hierarchical scaffolds that better mimic osteochondral tissue to facilitate regeneration.

In response to the complex chemical structure of osteochondral tissue, recent research endeavors have focused on developing multi-material design strategies.[4] Among the biomaterials for bone healing, biodegradable polycaprolactone (PCL) stands out for excellent elongation at break and favorable cell adhesion and proliferation.[5] Nonetheless, PCL application is hindered by a lack of inherent bioactive properties. This limitation has prompted exploration into innovative solutions, such as the incorporation of bioactive components like mussel-inspired polydopamine (PDA), which further promote cell adhesion and osteogenic differentiation, and facilitate hydroxyapatite crystal formation for efficient subchondral bone regeneration.[6] In parallel, given the stratified architecture of osteochondral tissue, hydrogels have emerged as a crucial strategy for cartilage layer regeneration. Hydrogels, hydrated viscoelastic matrix, exhibit bioactive properties that support cellular proliferation and differentiation.[7] Specifically, hydrogels derived from gelatin have emerged as a foremost candidate in cartilage regeneration, primarily owing to exceptional swelling capacity, biocompatibility, and structural mimicry of native cartilage composition.[8]

Integrating multi-phasic design strategies with advanced scaffold fabrication techniques is critical for accurately mimicking the native osteochondral extracellular matrix (ECM) architecture. Such fidelity is essential for providing the necessary physico-mechanical support and effectively modulating cellular activities. Recently, three-dimensional (3D) printing has emerged as a transformative method for fabricating precise and personalized scaffolds, particularly those replicating subchondral bone-like layer. This layer-by-layer fabrication process allows precise control over pore geometry and interconnectivity, thereby enhancing cellular functionality and internal vascularization. However, given the multi-phasic architecture of osteochondral tissue, it is necessity to replicate the cartilage layer's structure accurately. Electrospinning technique enables the fabrication of micro/nanofiber layers with a high specific surface area, strategically engineered to mimic the organization of collagen fibers in native cartilage.[9] Integrating 3D-printed scaffolds with embedded electrospun fibers represents an advanced approach, demonstrating superior efficacy in promoting stem cell adhesion and proliferation compared to mono-phasic 3D-printed scaffolds.[10] This integration achieves structural intricacy, provides topographical advantages, and creates a conducive microenvironment for osteochondral tissue regeneration.

Surface modification is crucial for optimizing multi-material and multi-phasic scaffolds functionality. Notably, low-temperature plasma surface modification generates a chemically reactive surface by oxidizing it, adjusting the scaffold's physicochemical properties.[11] This method also provides an active substrate for immobilizing signaling and bioactive molecules, thereby selectively altering biochemical activities. In addition, it addresses challenges associated with the rapid dissolution and instability of bioactive molecules seen in conventional coatings, while enhancing cellular adhesion, proliferation, and differentiation.[12,13] The synergistic utilization of surface modification techniques and the immobilization of bioactive molecules can be examined by immobilization of bone morphogenetic protein-2 (BMP-2), a bioactive growth factor and signaling protein to stimulate bone and cartilage formation.[14–16]

BMP-2 is well-documented for its dual role in promoting both osteogenic and chondrogenic differentiation. This dual functionality is critical for the effective repair of osteochondral tissue, where the integration of bone and cartilage layers depends on synergistic biochemical and structural cues. We hypothesize that immobilizing BMP-2 onto scaffolds, especially after low-temperature plasma surface modification, can significantly increase the bioavailability and sustained efficacy of the growth factor, potentially accelerating the healing of full-thickness osteochondral defects.

In this study, we developed biomimetic hierarchical scaffolds tailored for applications in osteochondral defect regeneration. These scaffolds comprised distinct layers, with the bottom subchondral bone-like layer constructed from 3D-printed PCL decorated with PDA, and the upper cartilage-like layer crafted from electrospun PCL-gelatin. Subsequently, the top layer underwent functionalization through the immobilization of gelatin-BMP-2, following an oxygen plasma surface treatment. Physico-chemical and mechanical analyses were conducted to determine the potential superiority of multi-phasic scaffolds over mono-phasic ones, encompassing morphology observation, compressive strength, interfacial bonding strength, hydrophilicity, absorption capacity, degradation behavior, and *in vitro* bioactivity. Furthermore, both *in vitro* and *in vivo* studies were performed to delineate an optimal structure for the regeneration of injured osteochondral tissue. Our findings revealed that the biomimetic multi-phasic scaffolds, with unique spatial design, successfully met the requirements of osteochondral tissue. Notably, rat bone marrow mesenchymal stem cells, modulated by BMP-2, exhibited osteogenic differentiation. The regenerative capacity of multi-phasic scaffolds was corroborated by the secretion of type I and II collagen, showcasing efficacy in the repair of osteochondral defects in rabbit models. Consequently, the concept of multi-material and multi-phasic scaffolds introduced in this study presents a promising solution for addressing the demands of osteochondral tissue regeneration.

2. Materials and methods

2.1. Materials

PCL filaments (diameter 1.75 mm) was purchased from Esun Co. (Shenzhen, China). Dopamine hydrochloride (DOPA-HCl, Mw 189.64 g/mol) and (3-glycidyloxypropyl) trimethoxysilane (GPTMS, Mw 236.34 g/mol) were purchased from Rhawn Co. (Shanghai, China). Bone morphogenic protein-2 (BMP-2) was purchased from Peprotech Co. (NJ, USA). Gelatin (Mw 40–50 kDa) was purchased from Sigma-Aldrich Co. (MO, USA). An extended list of materials and reagents used in this study is shown in the Supplementary File.

2.2. Preparation of mono-phasic scaffolds

To produce 3D-printed scaffolds, 3D designs and .STL files were prepared using SIMPLIFY3D software (Version 4.0.1, Cincinnati, OH, USA) and manufactured employing biodegradable PCL filaments via a fused deposition modeling (FDM) 3D printer (HORI Z500, Beijing Huitianwei Technology Co., Beijing, China) equipped with a 200 μm diameter nozzle, operating at a feeding rate of 0.14 mm/s. The print bed and nozzle temperatures were maintained at 20 and 115 °C, respectively. Layer-by-layer fabrication of the matrices occurred at 0° and 90° angles with a layer thickness of 0.2 mm. Subsequently, scaffolds measuring 7 × 7 × 3 mm^3 in dimension were subjected to drying in an oven (DHG-9050A, Shanghai Huitai Instrument Manufacturing Co., Shanghai, China) at 36 ± 0.5 °C for 24 h. These fabricated scaffolds are abbreviated as PC.

Mono-phasic scaffolds were prepared by immersing the 3D-printed PC scaffolds in a solution of dopamine hydrochloride (2 mg/mL in a 10 mM of Tris buffer) under gentle stirring at ambient temperature. The prepared mono-phasic scaffolds are abbreviated as PCD.

2.3. Preparation of multi-phasic scaffolds

The PCD scaffolds were covered by a layer of electrospun PCL-gelatin fibers. For the preparation of the electrospinning solution, PCL and gelatin were solubilized in 1,4-trifluoroethanol at a weight ratio of 8:2, achieving a concentration of 10% w/v. Upon complete dissolution, GPTMS was introduced into the polymeric solution at a concentration of 20 wt.%, followed by stirring for 2 h to ensure homogeneity. The resultant hybrid solution underwent electrospinning at a flow rate of 3 mL/hour and a voltage of 5 kV, maintaining a distance of 13 cm between the needle and the PCD scaffold. Subsequently, all specimens were subjected to overnight drying at a controlled temperature of 36 ± 0.5 °C.

The electrospun fibers underwent a surface modification process involving the deposition of a thin gelatin-BMP-2 layer after exposure to oxygen plasma. Specifically, the scaffolds were subjected to a controlled oxygen flow rate of 0.9 L/h for a duration of 90 s within a plasma generator (Zepto, Diener electronic, Ebhausen, Germany), operated at 100 W and maintained at a pressure of 0.76 mbar. Subsequently, the top layer of scaffolds was immersed in a gelatin-BMP-2 solution for a period of 30 min. The coating solution was formulated by dissolving gelatin (2% w/v) and BMP-2 (1 μg/mL) in deionized water. Following coating, the scaffolds were rinsed with deionized water and subjected to drying at 36 ± 0.5 °C. The

resulting composite scaffolds, herein named PCDE, exhibit a multi-phasic structure.

2.4. Characterization

The microstructural characterization of scaffolds was conducted utilizing field emission scanning electron microscopy (FE-SEM; Nova NanoSEM 450, FEI Co., OR, USA) operating at an accelerating voltage of 3 kV after gold sputtering.

Chemical characterization was carried out with a Fourier transform infrared spectroscopy (FTIR; Nicolet Is50, Thermo Fisher Scientific, MA, USA) system in the wavenumber of 400–4000 cm^{-1}.

For mechanical assessment, a compression strength test (Landmark Servohydraulic Test System, MTS Systems Corporation Co., MN, USA) equipped with a 100 N load cell and operating at a crosshead speed of 0.5 mm/min was used to establish stress–strain relationships and determine compressive strength/modulus of the scaffolds. The interfacial bonding strength of multi-phasic constructs was evaluated using a tensile strength test system (WDW-1 Universal Testing Machine, Shanghai Songdun Instruments Manufacturing Co., Shanghai, China) at a displacement rate of 1 mm/min. Scaffolds were affixed to testing stubs utilizing Loctite 406 glue (Henkle, China) with mechanical grips attached to the top (coated electrospun layer) and bottom (3D-printed) surfaces, and tensile force applied along the vertical axis of the scaffolds.

Hydrophilicity assessment of the constructs was carried out by measuring water droplet contact angles using a sessile drop method at ambient temperature (SL200KS, KINO Scientific Instrument Co., MA, USA).

To investigate phosphate-buffered saline (PBS) absorption, scaffolds were immersed in 50 mL of PBS solution at 37 ± 0.5 °C. Dry weight (W_0) of samples was initially determined, followed by subsequent measurements of wet weight after 2, 4, 6, and 24 h of incubation in PBS solution (W). PBS absorption rate was calculated using Equation I.[17]

$$\text{Swelling ratio (\%)} = [(W - W_0) / W_0] \times 100 \quad \text{(I)}$$

The degradation kinetics of the scaffolds were assessed through *in vitro* experimentation, wherein the samples were immersed in 50 mL of PBS solution for a duration of 6 weeks at a controlled temperature of 37 ± 0.5 °C. The initial dry weight (W_0) and subsequent weekly weights (W) of the constructs were meticulously recorded, facilitating the calculation of the degradation ratio as per **Equation II**.[18] The enzymatic degradation process was carried out using a similar method in which PBS solution was replaced with PBS solution containing 4 mg/mL of trypsin.[19] Subsequently, FE-SEM was employed to observe the morphological alterations of the degradable scaffolds at 6 weeks post-incubation.

$$\text{(Bio)degradation ratio (\%)} = |[(W - W_0)/W_0]| \times 100 \text{ (II)}$$

To investigate the *in vitro* biomineralization of scaffolds, the specimens were submerged in 50 mL of a 10× concentrated simulated body fluid (SBF) solution at 37 ± 0.5 °C for 12 h, with the solution being refreshed every 2 h. The deposition of hydroxyapatite-like layers was characterized using a combination of FE-SEM, attenuated total reflection Fourier transform infrared spectroscopy (ATR-FTIR), and X-ray diffraction spectroscopy (XRD). ATR-FTIR spectroscopy (Nicolet 560, Thermo Fisher Scientific, MA, USA) was conducted within the wavenumber range of 400–4000 cm^{-1}. XRD analysis, performed using a X-ray diffractometer (PW3710, Philips Co., the Netherlands) with Cu Kα radiation (λ = 1.5418 Å), encompassed the angular range of 2θ from 10° to 80°. The acquired XRD patterns were cross-referenced with the JCPDS standards to ascertain the crystalline phases present.

2.5. Molecular docking simulation

Molecular docking simulations were undertaken to assess the theoretical preservation and stability of BMP-2 upon interaction with two prominent serum proteins—human serum albumin (HSA) and alpha-2 macroglobulin (MACA)—within the serum milieu. HSA and MACA, being pivotal constituents of bone serum, are known to engage in crucial interactions with various biomolecules. Accordingly, molecular docking simulations were carried out using the HDOCK server to understand the possible interactions.[20,21] The crystallographic structures of BMP-2 (PDB ID: 1REW), HSA (PDB ID: 1AO6), and MACA (PDB ID: 4ACQ) were retrieved from the Protein Data Bank.[22] Subsequent to file preparation, the molecular docking simulations were analyzed utilizing the VMD package,[23] ultimately discerning the optimal binding mode of BMP-2 with HSA and MACA within a radius of 4 Å.

2.6. Cell–scaffolds interactions

In vitro experiments were conducted with rat bone marrow mesenchymal stem cells (rBMSCs) (see Supplementary File). To investigate cell attachment, rBMSCs were seeded onto sterile scaffolds (see Supplementary File) at a concentration of 10^4 cells/mL in Dulbecco's Modified Eagle Medium (DMEM) supplemented with 10% v/v fetal bovine serum and 100 U/mL penicillin-streptomycin.

The cultures were then incubated for 3 days at 37 ± 0.5 °C, 5% CO_2, and 95% humidity. Subsequently, the cells were fixed, followed by PBS washing, dehydration with increasing ethanol concentrations, immersion in isoamyl acetate:ethanol (1:1) for 10 min, and drying at room temperature. The morphology of adhered cells was examined using FE-SEM.

Cell viability assay was conducted using calcein-AM (emission: 515 nm, excitation: 490 nm) and propidium iodide (emission: 617 nm, excitation: 535 nm) at days 1, 3, and 5 of cell culture. Cell-seeded scaffolds were incubated in PBS containing 24 μM calcein-AM, and 4.5 μM propidium iodide for 30 min at 37 ± 0.5 °C, 5% CO_2, and 95% humidity. Following PBS washing, cell viability was evaluated using fluorescence microscopy.

Cell proliferation on the scaffolds was assessed via a Cell Counting Kit-8 (CCK-8) assay after 1, 3, and 5 days of culture. rBMSCs were seeded at a density of 5×10^4 cells/mL and incubated in DMEM supplemented with 10% CCK-8 for 4 h at 37 ± 0.5 °C, 5% CO_2, and 95% humidity. Subsequently, 100 μL of the mixed medium was transferred to a 96-well plate, and optical density (OD) was measured at 450 nm using a microplate reader (BioTex, Cube Biotech, Germany).

To evaluate osteoblastic activity, alkaline phosphatase (ALP) activity was measured using an ALP assay kit after 3, 7, and 14 days of culture. Cells were lysed in RIPA lysis buffer (100 μL/well) and centrifuged at 2000 rpm for 10 min, and the supernatant was incubated with p-nitrophenyl phosphate (p-NPP) for 30 min. ALP activity was determined by measuring absorbance at 405 nm, and results were normalized using a bicinchoninic acid protein assay kit (Life Technologies, USA) to determine total protein content.

Secretion of osteocalcin (OC) protein by cultured cells was quantified after 3, 7, and 14 days using an enzyme-linked immunosorbent assay (ELISA) kit, according to the manufacturer's instructions. Briefly, scaffolds were transferred to fresh wells with PBS and gently agitated to extract secreted proteins. The supernatant was collected, centrifuged at 2000 rpm for 10 min, and transferred to an ELISA plate pre-coated with an anti-osteocalcin antibody. After sequential incubations with primary and biotinylated secondary antibodies, followed by streptavidin-HRP conjugate, substrate solution was added. The reaction was stopped, and OD was measured at 450 nm. OC protein concentration was determined utilizing a standard correlation curve ($n = 5$).

All cell experiments were conducted utilizing a scaffolds-free cell culture plate as a control.

2.7. In vivo experiments

The animal experimentation protocols were approved by the Animal Care and Use Committee at the Fudan University Hospital Medical Center (code 2021-DS-Q-16). The study was conducted in strict adherence to the ethical principles outlined by the National Institutes of Health (NIH) regarding the care and utilization of laboratory animals.

Sixteen male New Zealand white rabbits, each aged 6 months and weighing between 2.2 and 2.6 kg, were organized into four distinct experimental cohorts in this investigation: control (no treatment), PC scaffolds, mono-phasic PCD scaffolds, and multi-phasic PCDE scaffolds. Anesthesia was induced via intravenous injection of Zoletil50™ (Tiletamine & Zolazepam, 0.4 mL/kg) prior to surgical interventions. Osteochondral defects measuring 3 mm in diameter and depth were meticulously created at the trochlear center of the femur utilizing an osteoelectric drill system. The bone debris was removed by continuously flushing with 0.9% saline. The scaffolds were cut with a diameter of 3 mm and implanted into the defect. Following surgical closure, rabbits received intramuscular injections of gentamicin (80,000 units/day) and penicillin (80,000 units/day). Postoperatively, rabbits were housed individually in cages with continuous health surveillance. Upon completion of the 4- and 12-week postoperative intervals, rabbits were sacrificed using pentobarbital sodium (20–60 mg/kg) to facilitate knee specimen retrieval.

Non-destructive micro-computed tomography (μCT) scan (Skyscan1172, Bruker, Kontich, Belgium) was performed to assess the newly formed bone near the defect. The specimens were scanned at 50 kV and 500 μA at a voxel size of 25 μm. Subsequent to 3D image reconstruction, original defect circumferences were delineated to facilitate calculation of bone volume fraction (BV/TV), bone density (BD), connectivity density, trabecular number, trabecular thickness, and trabecular separation utilizing Hounsfield units.

Histological analyses were undertaken through the application of hematoxylin-eosin (HE) and Safranin staining techniques. To facilitate this, the specimens were subjected to a 14-day decalcification process, starting with fixation in a 4% w/v formalin solution, followed by immersion in a 10% w/v ethylenediaminetetraacetate (EDTA)-buffered saline solution (Leagene Biotechnology, Beijing, China). Subsequently, the specimens underwent dehydration using a series of ethanol solutions, were embedded in paraffin (Yiyang Instrument Co., Shanghai, China), sectioned into 4 mm slices, and subjected to HE and Safranin staining.

Immunohistochemical analysis was employed to detect type I and type II collagen. Following sectioning, the samples were subjected to sequential immersion in ascending concentrations of ethanol at a controlled temperature of 37 ± 0.5 °C, followed by rinsing with PBS. Endogenous peroxidase activity was quenched using a 3% hydrogen peroxide solution for 30 min. Subsequently, the sections were treated with 5% w/v bovine serum albumin for 30 min at room temperature to block nonspecific binding sites.

The sections were then incubated at 4 °C overnight with mouse anti-type I collagen primary monoclonal antibody (dilution rate: 1:200; ab6308, Abcam Co., Cambridge, UK) and mouse anti-type II collagen primary monoclonal antibody (dilution rate: 1:200; MA1-37493, Invitrogen Co., MA, USA). Following primary antibody incubation, sections were washed thrice with PBS and then incubated with a secondary anti-mouse IgG antibody (Goat Anti-Mouse IgG H&L, ab150113, Abcam Co., Cambridge, UK) for 30 min at room temperature. Post-immunostaining, sections underwent further dehydration in ascending ethanol concentrations, followed by xylene treatment (Sigma-Aldrich Co., MO, USA) for clarification and sealing.

2.8. Statistical analysis

In vitro and *in vivo* experiments were repeated five times, and the reported values are expressed as mean ± standard deviation of five experiments. The significance of the average values was calculated using a standard software program (GraphPad Prism version 9.2.0, San Diego, CA, USA), and a significance level of $p \leq 0.05$ was considered significant ($^{*}p \leq 0.05$; $^{**}p < 0.01$; $^{***}p < 0.001$).

3. Results and discussion

3.1. Characterization of scaffolds

The principal aim of this investigation was to develop stratified zonal scaffolds and assess potential for osteochondral defect regeneration, illustrated schematically in Figure 1. Similar strategies for the development of multi-material and multi-phasic scaffolds have been explored previously in the context of ligament/tendon-bone region regeneration.[24,25]

In the proposed hierarchical scaffolds, a fibrous layer is intricately linked to a lower zone characterized by higher stiffness and tubular-like pores. Subsequently, this layer is immobilized with a growth factor-hydrogel complex upon exposure to low-temperature oxygen plasma. Figure 2A–F present FE-SEM micrographs of the 3D-printed PCL matrices, both decorated and undecorated with PDA. The obtained results indicate reduced shrinkage in interconnected porous scaffolds as compared to the 3D model. Additionally, the FE-SEM micrographs reveal filaments aligned in parallel in both horizontal and vertical directions, resulting in a meticulously designed internal geometry. Also, the development of cubic-shaped pores within the scaffold's microstructure has been demonstrated to potentially enhance mesenchymal stem cell enrichment, differentiation, as well as gene and protein expression. The uniformity and regularity of these cubic pores allow for optimal cell attachment and colonization, thus ensuring that a higher number of cells are in direct contact with each scaffold.[26] Following DOPA-HCl polymerization, the previously smooth surface of the PC scaffolds was overshadowed and homogeneously covered with PDA, offering additional anchorage sites for cells. Also, PDA exhibits a high affinity for proteins and bioactive molecules, promoting adsorption and creating a localized concentration gradient that stimulates cellular responses.[27] The 3D-printed scaffolds exhibited an average porosity of approximately 60% and approximate pore size of 300–500 μm (see Figure S1B in the Supplementary File), which is adequate for conferring mechanical integrity and fostering cell–scaffold interactions, vascularization, and bone regeneration.[28] Given that an optimal pore size falling within the range of 100–500 μm is known to facilitate cell and tissue growth, oxygenation, *in vivo* osteogenesis performance, and bone repair,[29] the developed scaffolds provide a suitable microarchitecture for supporting subchondral bone repair.

Electrospun PCL-gelatin fibers were collected onto the 3D-printed substrate to simulate the cartilage layer. Subsequently, a layer of gelatin hydrogel enriched with BMP-2 was immobilized on the surface, presenting a promising strategy for interfacing the layers and improving the regenerative potential. It is expected that the immobilization of the gelatin-BMP-2 complex on the surface will support the physical attachment of cells, fostering directional cell growth, proliferation, and differentiation.[30] Thus, the concept of hierarchical scaffolds is poised to provide a robust support for cellular functions and facilitate osteochondral tissue regeneration. FE-SEM micrographs depicting the electrospun PCL-gelatin layer before and after the immobilization of gelatin-BMP-2 are presented in Figure 2G–K. These images delineate the formation of a cartilage-like layer with an approximate thickness of 100 μm. Notably, the results underscore the development of homogeneous, bead-free PCL-gelatin fibers, characterized by an average diameter of 2 ± 0.5 μm. We found that direct immobilization of gelatin-BMP-2 onto oxygen-plasma-modified fibers resulted in a significant increase in fiber diameters to 3 ± 0.8 μm, without compromising uniformity, attributed to fiber

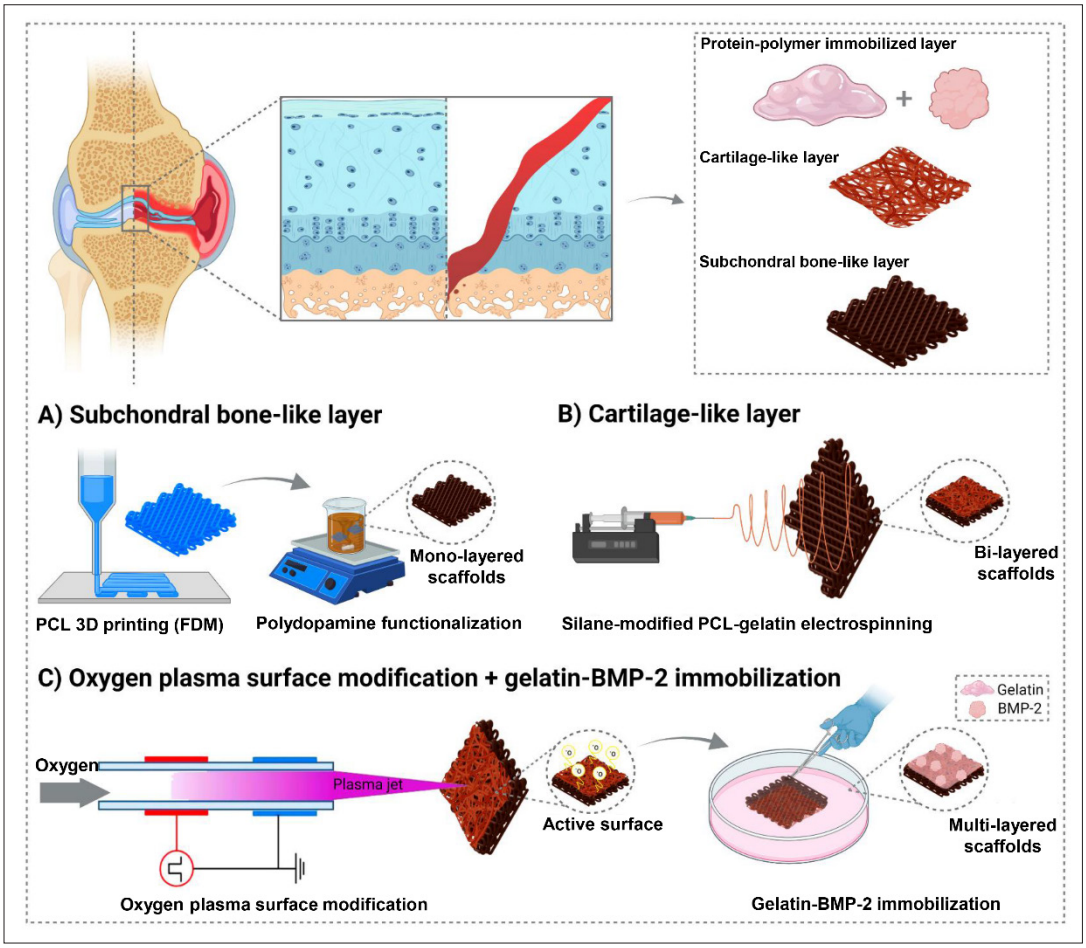

Figure 1. Schematic representation depicting the sequential fabrication steps of multi-phasic scaffolds tailored for the regeneration of critical-sized osteochondral defects. (A) Fabrication of the subchondral bone-like layer utilizing 3D-printed PCL functionalized with PDA. (B) Construction of the cartilage-like layer comprising electrospun PCL-gelatin composite. (C) Surface modification through immobilization of gelatin-BMP-2 post oxygen plasma surface treatment, thereby augmenting regenerative efficacy. This innovative scaffold architecture is devised to effectively address the intricate structure of osteochondral tissue, offering a promising strategy for the repair and regeneration of critical-sized osteochondral defects. Illustration generated with www.biorender.com. Abbreviations: BMP-2, bone morphogenetic protein-2; PCL, polycaprolactone; PDA, polydopamine.

connections and a reduction in void spaces (see Figure S1C in the Supplementary File). This network structure is anticipated to enhance the overall integrity and mechanical strength of the scaffolds. Cross-sectional images of multi-phasic PCDE scaffolds reveal fibers in close contact with the 3D-printed layer, indicative of robust connectivity and adhesion between different layers (Figure 2J and K), which is expected to establish stronger links between the layers.

The detailed chemical characterization of both raw materials and hierarchical scaffolds is provided in the Supplementary File (see Figure S2, Supporting Information). In this study, PC scaffolds were decorated with a thin layer of PDA, which was acquired through the spontaneous oxidation of dopamine hydrochloride in an alkaline solution. The attachment of PDA to the PCL surface is expected to involve a combination of covalent bonds and non-covalent interactions.[31] The upper surface of the multi-phasic scaffolds underwent immobilization with hydrogel-growth factor complexes following oxygen plasma surface treatment. Resulting from the oxygen plasma treatment, the chemical groups on the surface are subjected to bombardment by free radicals or ionized species, generating carbon radicals and unstable peroxides. This transformation is further confirmed by the FTIR spectrum, which attests to the breakdown of the CH linkage and the formation of oxygen-containing functional groups, particularly C=O. Concurrently, the active radicals on the surface of the fibers promptly interact with the hydrogens of the gelatin-BMP-2 complex, thereby enhancing the

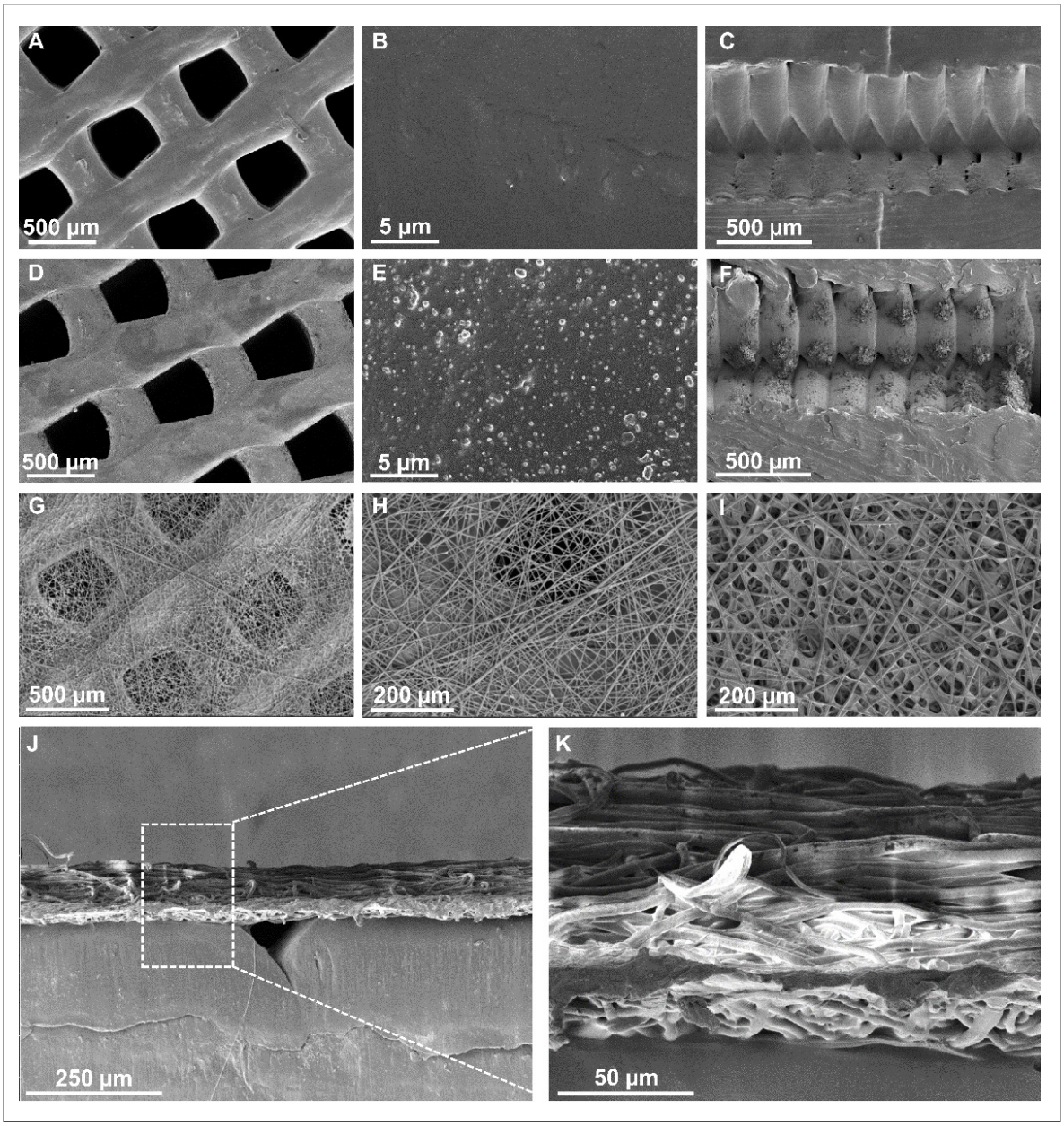

Figure 2. Morphology and microstructure of scaffolds. FE-SEM micrographs of 3D-printed (A–C) PC and (D–F) PCD scaffolds ([A, B, D, E] perpendicular surface, [C, F] cross-section), (G–I) electrospun PCL-gelatin on top of PCD scaffolds (G, H) before and (I) after immobilization of gelatin-BMP-2. (I–K) Multi-phasic PCDE matrices ([I] perpendicular surface, and [J, K] cross-section). Abbreviation: FE-SEM, field emission scanning electron microscopy.

immobilization of the new layer. In addition to hydrogen bonds established between the oxygen-rich surface and gelatin-BMP-2, a covalent bond may form between methyl groups in the electrospun layer and hydroxyl groups in the gelatin-BMP-2 complex. This covalent linkage contributes to the augmented integrity and stability of the immobilized layer, aligning with similar findings reported in other studies.[32–34] The covalent immobilization of growth factors, such as BMP-2, represents a more localized and targeted approach, amplifying the stability and retention of the growth factors. This leads to reduced diffusion or degradation, thereby maintaining bioactivity for an extended duration[35] and fostering enhanced osteogenic/chondrogenic differentiation of rBMSCs. This sustained delivery mechanism ensures that the cells receive a consistent and effective dose of the growth factors over time, a critical factor in promoting desired cellular responses.

Mechanical tests, including assessments of compressive strength, compressive modulus, and toughness of the scaffolds, were conducted in this study. These parameters are particularly important for osteochondral scaffolds as they directly relate to the ability of the scaffolds to withstand compressive loads, maintain mechanical stability, and endure physiological forces in the joint environment. Cartilage tissue experiences dynamic and repetitive loading during movement, and the compressive modulus provides a measure of the scaffold's stiffness, which should closely match the mechanical properties of native cartilage to avoid stress shielding or failure. Similarly, toughness reflects the energy the scaffold can absorb before failure, ensuring durability under repeated mechanical stresses. Figure 3 presents the stress–strain curves, compressive strength, compressive modulus, and interfacial bonding strength of the constructs. Toughness values derived from the stress–strain curves were measured at 17.5 ± 0.1, 15 ± 0.1, and 24 ± 0.005 kJ/mm^3 for PC, PCD, and PCDE scaffolds, respectively. The results indicate a slight reduction in toughness following the coating of PC scaffolds with PDA. This reduction may be attributed to intermolecular interactions within the PC matrices. PDA has the potential to interact with functional groups present in PCL, as observed in FTIR spectra (see Supplementary File), disrupting the molecular arrangement and internal structure of the PC scaffolds, thereby impairing the capacity for deformation and energy absorption. Besides, the multi-phasic PCDE samples, characterized by a larger surface area in the stress–strain curves, demonstrate an enhanced ability to absorb energy through plastic deformation before reaching the point of fracture.

PCD scaffolds demonstrated compressive strength and modulus values that were 1.07 and 0.98 times

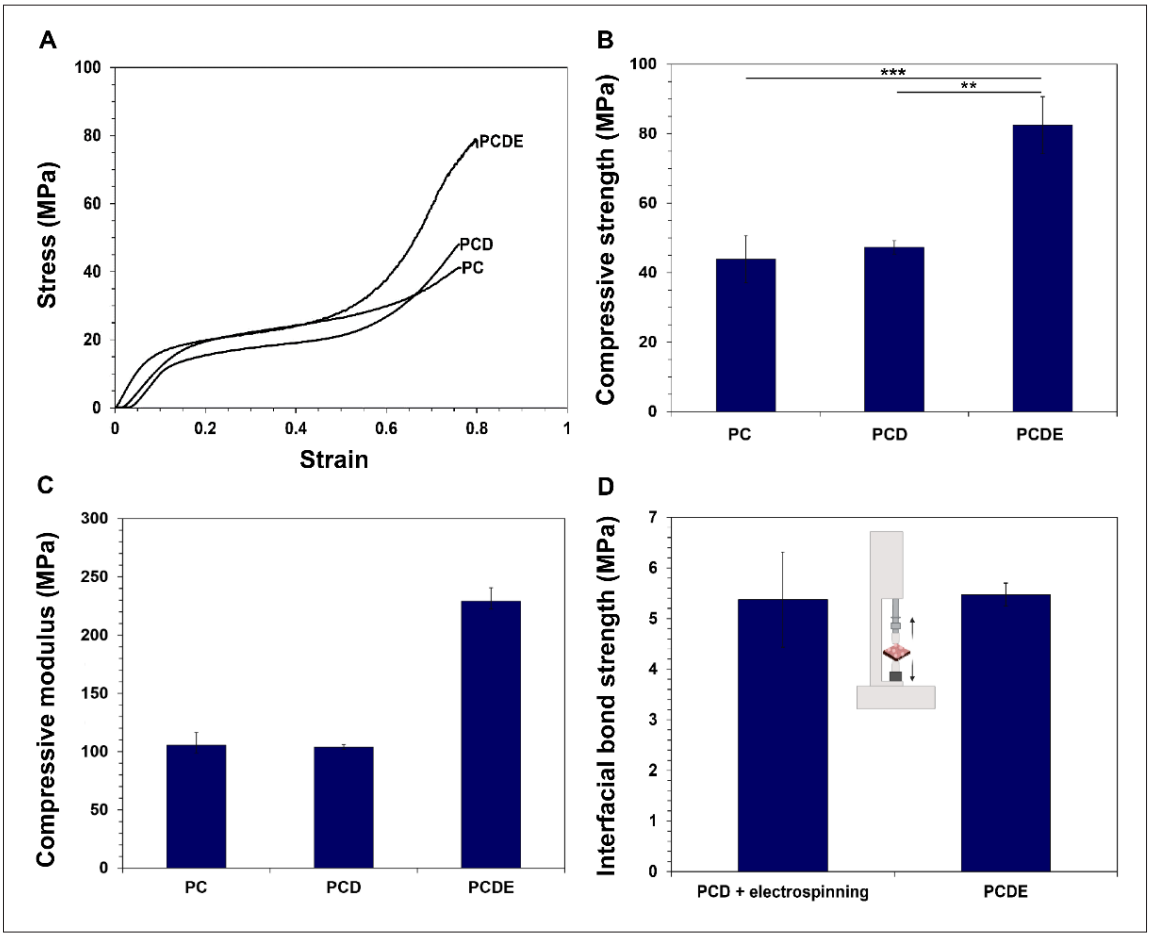

Figure 3. Mechanical behavior of scaffolds. (A) Stress–strain curves, (B) compressive strength, and (C) compressive modulus of PC, mono-phasic PCD, and multi-phasic PCDE scaffolds. (D) Interfacial bonding strength of scaffolds after electrospinning the PCL-gelatin on top of PCD layer (PCD + electrospinning) and following immobilization of gelatin-BMP-2 on oxygen plasma modified fibers (multi-phasic PCDE). $^{**}p < 0.01$; $^{***}p < 0.001$. Abbreviations: BMP-2, bone morphogenetic protein-2; PCL, polycaprolactone.

higher, respectively, than those of the PC scaffolds. This improvement is potentially attributed to PDA deposition, reduced pore size, and increased strand width. Notably, multi-phasic PCDE matrices exhibited a significant increase in compressive strength compared to both PC and mono-phasic PCD scaffolds, with values 1.9 and 1.7 times greater, respectively. The compressive modulus of PCDE scaffolds followed a similar trend, being 2.1 and 2.2 times higher than those of PC and PCD, respectively, due to the multi-phase design. The multi-phasic scaffolds displayed mechanical properties comparable to those of the osteochondral unit. Given the critical role of subchondral bone in providing the mechanical requirements of the entire osteochondral unit, the mechanical properties of the multi-phasic construct are more analogous to subchondral bone tissue. Considering that native cartilage tissue has a compressive modulus of 0.2–6.44 MPa and a compressive strength ranging from 0.005 to 4 MPa,[36] and subchondral bone exhibits a compressive modulus of 1–900 MPa[36] and a compressive strength ranging from 1.5 to 45 MPa,[37] the compressive modulus of multi-phasic PCDE scaffolds aligned more closely with native tissue than previously reported PCL matrices, which have moduli ranging from 2 to 10 MPa.[38,39] The enhanced compressive strength of multi-phasic PCDE scaffolds is anticipated to improve load-bearing capacity. This mechanical robustness is expected to provide mechanical cues that influence cell morphology, promote osteogenesis through the stimulation of extracellular signal-regulated kinase activity, and facilitate tissue reconstruction.[40,41]

A notable challenge associated with multi-phasic scaffolds is inherent weakness in interfacial bonding strength, which elevates the risk of delamination. Accordingly, this study evaluated the interfacial bonding strength to ensure the mechanical integrity of the scaffold layers. This is crucial in osteochondral scaffolds, as weak interfacial bonding could lead to delamination or failure under load, compromising the regeneration process. Ensuring robust bonding between the layers is essential for seamless integration and coordinated regeneration of cartilage and subchondral bone.

To address this concern, we employed an electrospinning technique to deposit a combination of PCL and gelatin onto the surface of 3D-printed PCL-PDA scaffolds. The similar composition of the layers, along with the compatibility of polymer chains and the presence of hydrophilic components in both layers, facilitated effective intermolecular bonding and improved cohesion at the interface, as extensively discussed in the existing literature.[42] The introduction of gelatin and PDA in layers, acting as a bio-adhesive, emerges as a promising factor contributing to enhanced interfacial adhesion. The quinone groups from the PDA may potentially form covalent bonds with the amine groups of gelatin via Michael-type addition, a phenomenon documented in previous literature.[43] This covalent interaction significantly strengthens the binding force between layers. Additionally, possible non-covalent forces operating between gelatin and PDA play a substantial role in reinforcing interfacial adhesion. The cumulative effect of these forces serves to fortify the bond between layers. Furthermore, the electrospinning process imparts a fibrous structure with a high surface area, facilitating increased interlocking between layers. This physical interlocking, combined with the chemical interactions between the components, results in heightened interfacial adhesion, thereby mitigating the risk of delamination. In addition, the immobilization of gelatin-BMP-2 hydrogel on the top surface acts as a bio-glue, further enhancing interlayer bonding. The multi-phasic PCDE constructs (Figure 3D) distinctly exhibited a robust bond between layers, which was 250 times stronger than the previously reported constructs as compared to a previously reported literature.[3] As a result, the stratified scaffolds can provide excellent integrity for osteochondral tissue regeneration, eliminating concerns of layer separation or implant failure.

Interactions between water and scaffolds play a crucial role in enhancing cell function, promoting ECM secretion, increasing protein absorption, providing adhesive ligands, and expediting vascularization and tissue growth.[44] Based on the wettability test, the PC, mono-phasic PCD, and multi-phasic PCDE matrices displayed average contact angles of 86° ± 1°, 53° ± 1.5°, and 83° ± 0.5°, respectively, reflecting the hydrophilicity of all groups (Figure 4A). Time-dependent absorption of PBS by the scaffolds revealed varying degrees among the experimental groups (Figure 4B). Notably, the PDA-modified PC matrices showed higher hydrophilicity and absorption potential, attributable to the enriched surface with hydrophilic functional groups, including catecholamines and hydroxyls, as well as the potential for hydrogen bonds with water molecules. In addition, the hierarchical multi-phasic matrices displayed relatively high-water uptake within the first 2 h (12–28%), followed by a gradual increase over 24 h under a steady gradient. This enhanced absorption capacity can be attributed to the high surface area/volume and interconnected tubular pores present in both electrospun and 3D-printed layers, facilitating the efficient transfer of biological fluid and thereby improving cellular nutrition and tissue regeneration. However, multi-phasic PCDE scaffolds exhibited reduced wettability and absorption capacity compared to mono-phasic scaffolds, a consequence of the inclusion of GPTMS in their chemical composition. While GPTMS plays a crucial role in

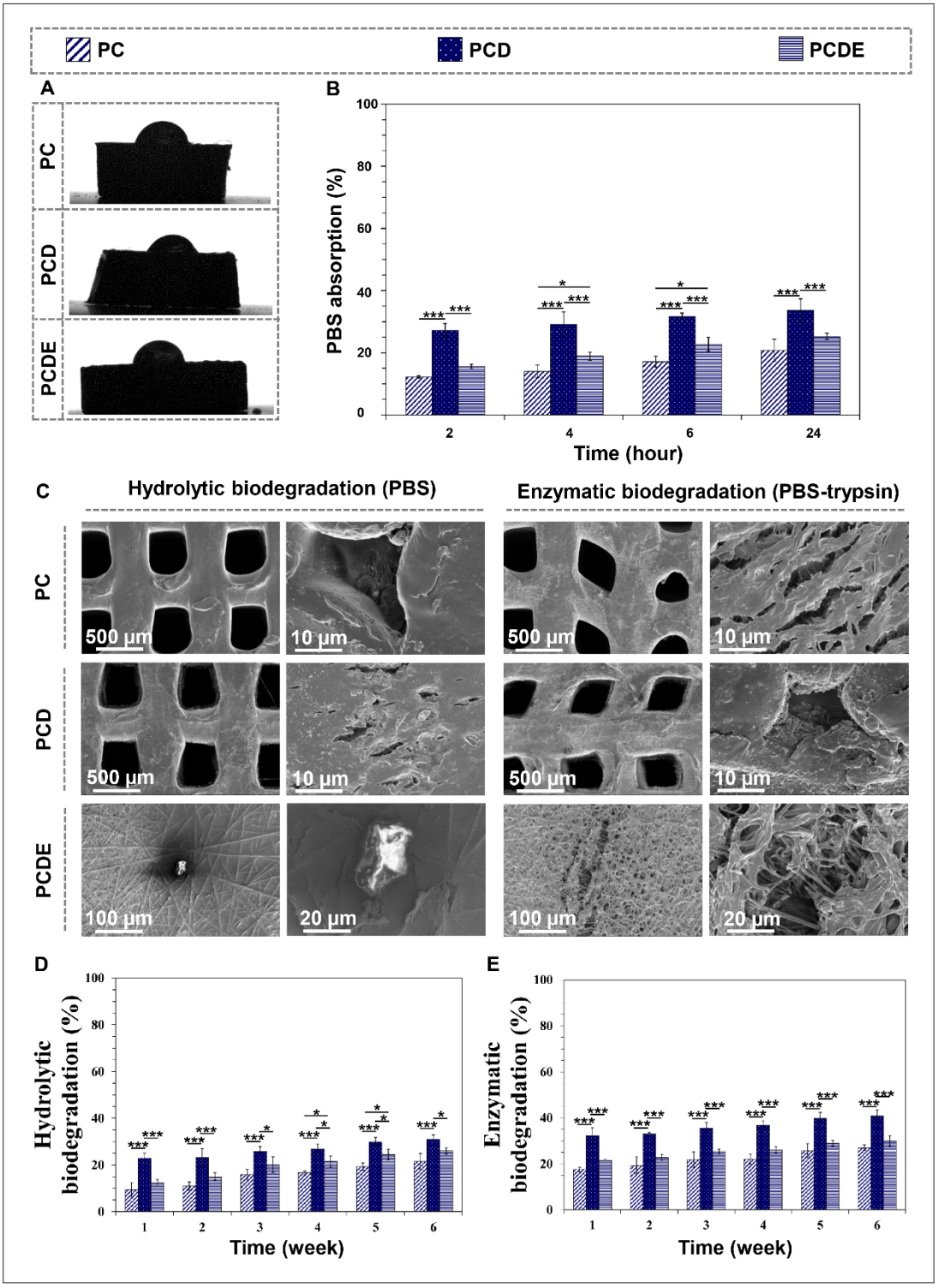

Figure 4. Water–scaffold interactions. (A) Hydrophilicity of PC, mono-phasic PCD, and multi-phasic PCDE scaffolds using water-drop contact angle method. (B) PBS absorption capacity of scaffolds as a function of time. (C) FE-SEM micrographs of degraded scaffolds after 6 weeks of immersion in the PBS and PBS-trypsin solutions. (D) Hydrolytic and (E) enzymatic degradation ratio of scaffolds as a function of incubation time in the PBS and PBS-trypsin solutions, respectively. *$p \leq 0.05$; ***$p < 0.001$. Abbreviations: BMP-2, bone morphogenetic protein-2; FE-SEM, field emission scanning electron microscopy; PCL, polycaprolactone.

mineralization and osteogenic differentiation, and provides higher stability,[45] its slight impact on hydrophilicity has been overlooked. The higher hydrophilicity and absorption of PCDE scaffolds over PC ones can be elucidated by the presence of unreacted amine and hydroxyl functional groups in the immobilized layer as well as enrichment of the surface with oxygen-containing functional groups following oxygen plasma treatment. Thus, functionalized surfaces with higher hydrophilicity are expected to absorb proteins more effectively and facilitate cell adhesion.[46] Overall, all scaffolds demonstrated adequate interaction with water molecules, but multi-phasic PCDE matrices showed superior performance across a set of specific physicochemical and mechanical features.

Degradation of scaffolds following a 6-week immersion in PBS and PBS-trypsin indicated that scaffolds remained stable during this period (Figure 4C–E). However, hydrolytic degradation led to the formation of excessive pores to form and the breakdown of fibers, while enzymatic degradation resulted in more significant deformations of pores and fiber arrangements, ultimately compromising the structural integrity of the scaffolds. Degradation rates as a function of incubation time are depicted in Figure 4D and E. The observed values indicate a gradual degradation over time, with degradation rates in both media remaining below 40% after 6 weeks. The degradation rate of the scaffolds appears to align with the rate of osteochondral tissue formation. Osteochondral tissue regeneration is a complex and dynamic process that initiates with the formation of a cartilaginous callus in the damaged osteochondral tissue, typically occurring within 2 weeks and completing within 2 months through bone remodeling, continuous resorption, and formation of bone tissue mediated by osteoclasts and osteoblasts, respectively.[47] Thereafter, cartilage tissue begins to form through the cloning and cultivation of chondrocytes. Over approximately 6 months, the regenerated cartilage tissue gradually matures and integrates with the surrounding tissue, contributing to the restoration of joint function.[48] In this regeneration process, the migration of MSCs from the surrounding soft tissues and bone marrow is critical for the development of callus tissues. This cell migration is regulated by a complex interplay of signaling molecules and growth factors that are released from the damaged tissues. Notably, BMP-2 is one such molecule that plays a crucial role in the initiation of healing,[49] it is expected that multi-phasic PCDE scaffolds containing BMP-2 exhibit superior performance in the regeneration of defective osteochondral tissue.

In addition to the tubular-like pores contributing to the long-term durability of scaffolds, the chemical composition also significantly influences their degradation characteristics. In this study, the PC scaffolds exhibited the lowest degradation rate compared to other scaffold types. The superior degradation resistance of PCL can be attributed to its semi-crystalline nature and semi-hydrophobic properties. Notably, the PCD scaffolds demonstrated significantly higher degradability than their PC counterparts, attributable to the hydrophilic nature of PDA. Despite the degradation of PDA, its expected stability during bone regeneration is anticipated to effectively support the regeneration process. According to the results, the degradation of stratified PCDE scaffolds was observed to be slower than that of PCD ones, potentially due to the presence of the hydrophobic GPTMS. This controlled degradation behavior is advantageous in osteochondral tissue regeneration, ensuring the structural integrity and longevity of the scaffolds, providing sustained support to cellular processes over an extended period. Additionally, the relatively faster degradation of PCDE matrices as compared to pure PC ones may be explained by unreacted hydrophilic groups in gelatin and oxygen-containing groups resulting from surface modification, thus serving as active sites for rapid hydrolysis.

The biomimetic formation of hydroxyapatite, crucial for scaffold attachment to the surrounding osteochondral tissue, was investigated by immersing the scaffolds in a 10× SBF solution. A schematic illustration of hydroxyapatite formation is shown in Figure 5A. In general, the scaffolds' hydrophilicity enhances the absorption of SBF solution, expediting the biomimetic hydroxyapatite formation. In addition, the negatively charged surfaces, stemming from catechols, hydroxyls, and carboxylic acids, create an optimal substrate for the absorption of calcium ions and the nucleation of hydroxyapatite. The dipole interaction and ionic conduction between the PDA-containing surfaces and the 10× SBF solution play a significant role in hydroxyapatite formation. In this context, charge repulsion at the surfaces promotes the absorption of metal ions from the 10× SBF, reducing the system's energy. Accordingly, the release of H^+ from hydroxyl groups of PDA acts as a nucleation site for the exchange of HCO^{3-} and HPO_4^{2-}, resulting in the precipitation of calcium ions and the formation of a calcium phosphate layer. Furthermore, in multi-phasic scaffolds, the synergistic contribution of mussel-inspired PDA and GPTMS to the biomineralization of scaffolds is observed. GPTMS-containing matrices facilitate the mineralization of hydroxyapatite through electrostatic interactions between the silanol groups and the ions present in the 10× SBF solution. This is followed by precipitation of calcium and phosphate ions on surfaces, leading to the mineralization of hydroxyapatite.

After a 12-h immersion of the scaffolds in a 10× SBF solution, monotonic nucleation of hydroxyapatite-like

layers was observed. Nano-spherical particles covered the surface of mono-phasic PCD scaffolds and multi-phasic PCDE scaffolds, while a lower density of mineralized particles was observed on the surface of PC matrices (Figure 5B). The hydroxyapatite layer formation was confirmed by ATR-FTIR and XRD spectra (Figure 5C and D). According to the ATR-FTIR spectra, peaks at 3100–3500 and 1610 cm^{-1} were identified, corresponding to O—H stretching and water molecules in the mineralized layers. Additionally, peaks observed at 582 and 819 cm^{-1} represented the bending vibrations of P–O and C–O bonds, respectively. Carbonate bonds, indicative of carbonate hydroxyapatite formation with a high degree of similarity to physiological ones, were found between 1410 and 1455 cm^{-1}. Based on XRD spectra, mineralization of the hydroxyapatite led to a reduction in the intensity of the broad peak (around 10°–25°) corresponding to the amorphous phase of polymers. New peaks associated with hydroxyapatite mineralization appeared at 27.27°, 31.55°, 39.65°, 45.62°, and 49.53°, corresponding to crystalline plate reflections (2 1 0), (2 1 1), (3 1 0), (2 2 2), and (2 1 3). The highest intensity of the peaks in XRD spectrum of

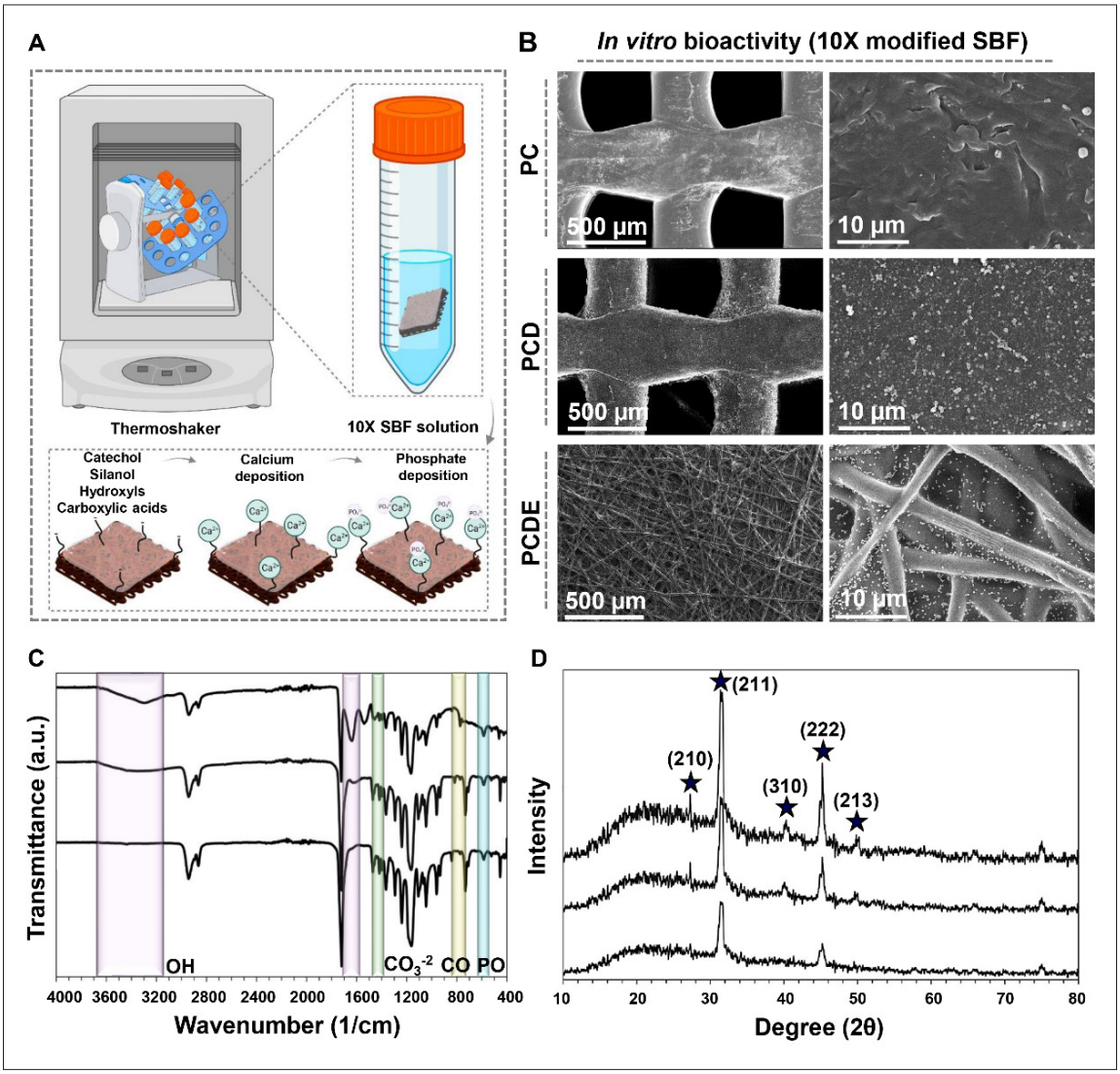

Figure 5. *In vitro* bioactivity evaluation. (A) Schematic illustration of hydroxyapatite formation on scaffolds (created with www.biorender.com). (B) FE-SEM micrographs of precipitated hydroxyapatite on the PC, mono-phasic PCD, and multi-phasic PCDE scaffolds after 12 h of incubation in the 10× SBF solution. (C) ATR-FTIR spectra and (D) XRD spectra of biomimetic hydroxyapatite on the surface of matrices. Abbreviations: ATR-FTIR, attenuated total reflection Fourier transform infrared spectroscopy; FE-SEM, Field emission scanning electron microscopy; SBF, simulated body fluid; XRD, X-ray diffraction spectroscopy.

multi-phasic PCDE scaffolds indicates a higher level of hydroxyapatite precipitation and underscores the greater potential of these scaffolds for biomineralization.

3.2. Protein interaction

Molecular docking simulations were employed to investigate the interaction of BMP-2 with serum proteins, elucidating its persistence in the biological environment following exposure to serum. The two most abundant bone serum proteins, HSA and MACA, were identified as significant physiological targets. Theoretical findings indicated that BMP-2 binds to HSA and MACA at theoretical energy levels of −195.38 and −281.70 kJ/mol, respectively. In both target proteins, the interaction process is spontaneous, with hydrogen bonds and hydrophobic interactions predominantly occurring in the binding site (Figure 6). These interactions contribute to the stability of the BMP-2-serum protein complexes, impacting the release of BMP-2 from the multi-phasic scaffolds and maintaining a localized concentration. The control release of BMP-2 from the multi-phasic scaffolds, facilitated by interactions with serum proteins, particularly HSA and MACA, suggests a potential role in enhancing the BMP-2 availability for cells. The molecular docking simulation conducted in this study, coupled with chemical characterization (see Supplementary File), provides evidence for the long-term presence of BMP-2 through the interaction with scaffolds and serum proteins. It is noteworthy that these findings are based on computational simulations, and further validation was conducted through *in vitro* cell culture and *in vivo* studies to comprehensively assess the biological performance of the developed scaffolds and evaluate the impact of the immobilized BMP-2.

3.3. Cell–scaffold interactions

The attachment, viability, proliferation, and differentiation of rBMSCs on mono-phasic and multi-phasic scaffolds were examined. FE-SEM micrographs (Figure 7A) captured after 3 days of cell culture showed that the scaffolds provided favorable, non-toxic substrates for

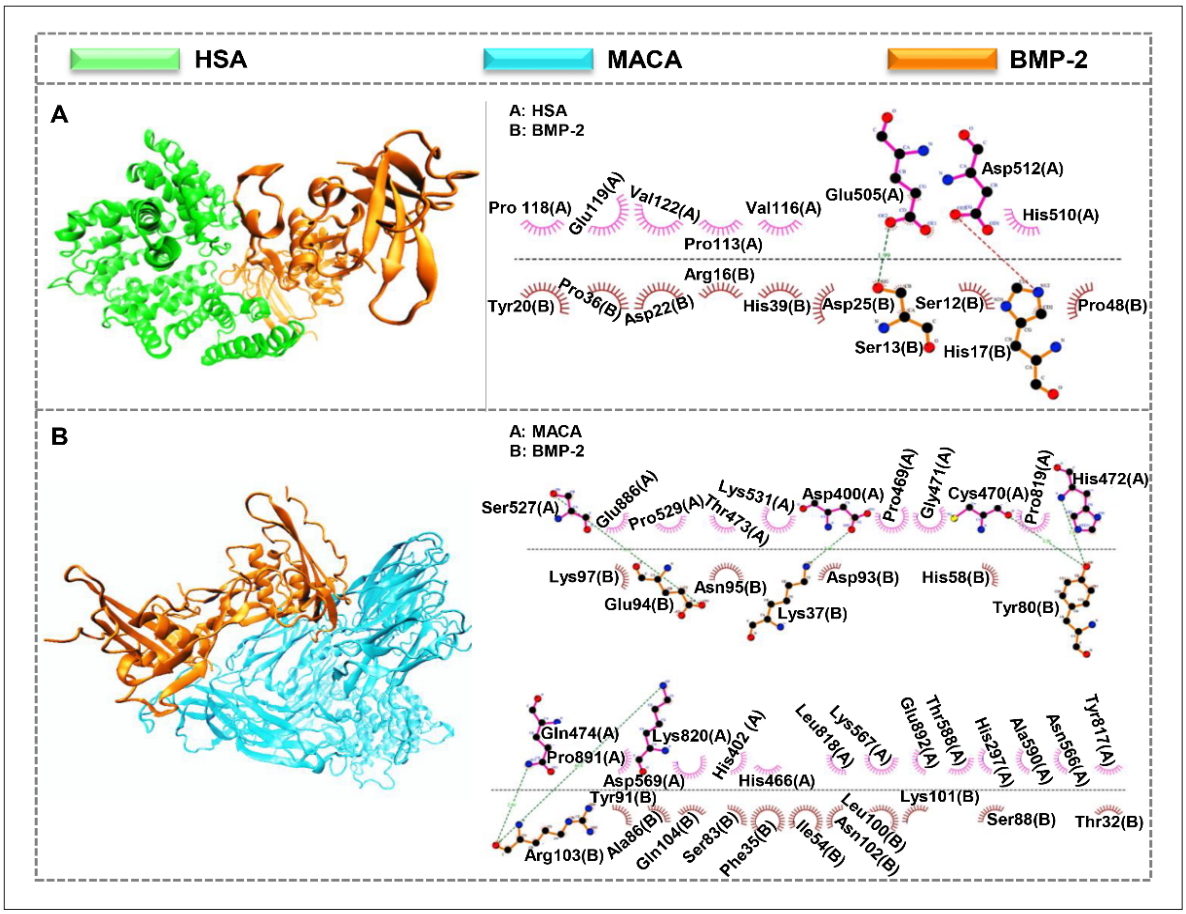

Figure 6. BMP-2 binding with serum proteins. Molecular docking simulations and the depiction of the best mode of BMP-2 interaction with (A) HSA and (B) MACA. BMP-2 interaction process with both target proteins is spontaneous, and the hydrogen bonds and hydrophobic interactions are the main driving forces in the binding site. Abbreviations: BMP-2, bone morphogenetic protein-2; HSA, human serum albumin; MACA, alpha-2 macroglobulin.

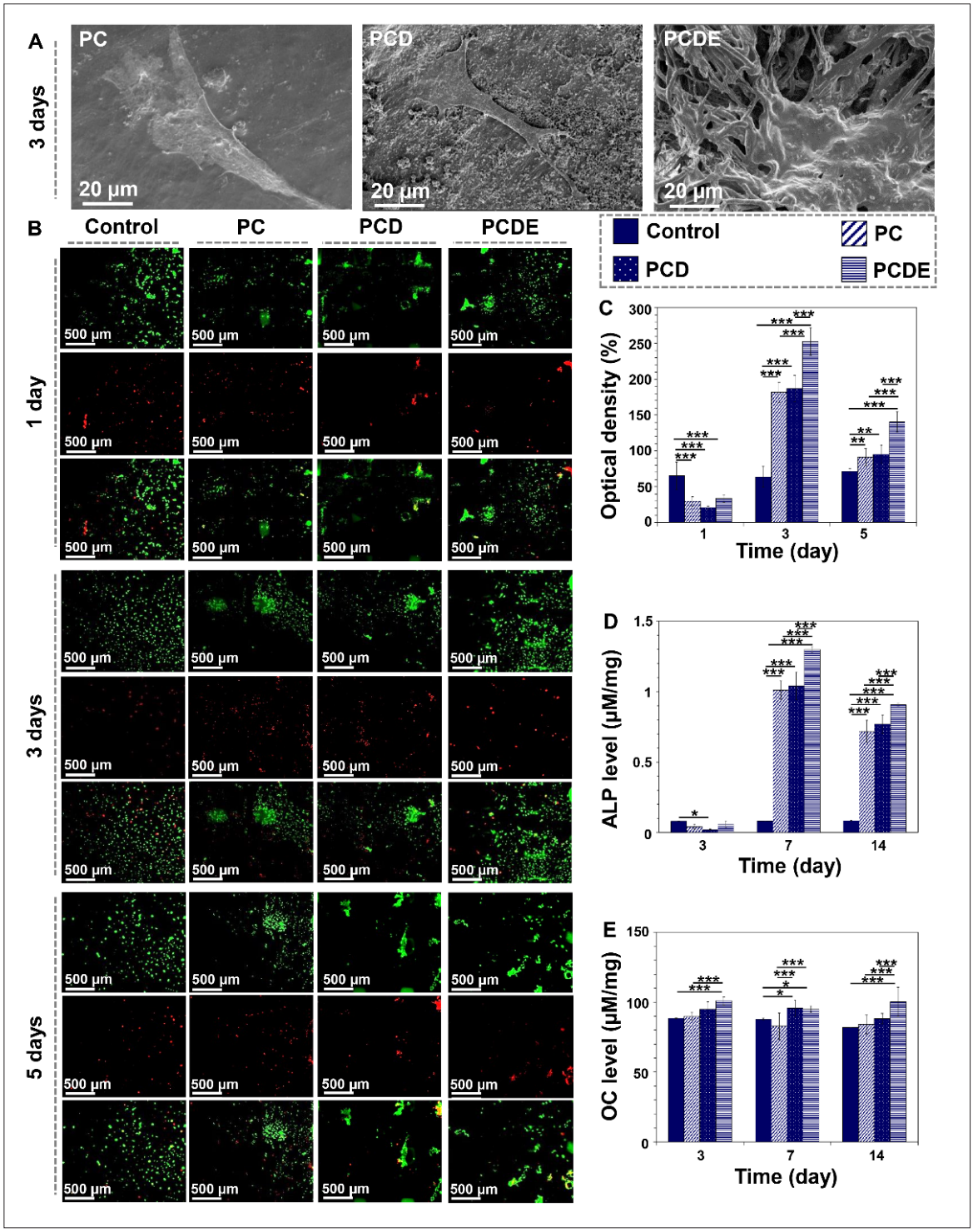

Figure 7. rBMSCs–biomimetic hierarchic scaffolds interactions. (A) rBMSCs adhesion on the surface of PC, mono-phasic PCD, and multi-phasic PCDE scaffolds after a 3-day culture. (B) Live/Dead staining of rBMSCs after 1-, 3-, and 5-day culture on the scaffolds. (C) Proliferation of rBMSCs on the scaffolds as a function of incubation time. (D) ALP activity and (E) OC protein expression after culture of rBMSCs on the surface of scaffolds for 3, 7, and 14 days. *$p \leq 0.05$; **$p < 0.01$; ***$p < 0.001$. Abbreviations: ALP, alkaline phosphatase; OC, osteocalcin; rBMSCs, rat bone marrow mesenchymal stem cells.

cell anchorage, as evidenced by the presence of adherent cells on the surface. This may originate from the porous and hydrophilic microstructures of the scaffolds, which played a crucial role in facilitating oxygenation and fluid transfer, critical for sustaining cell viability and function. Interestingly, the incorporation of PDA onto PC scaffolds induced the development of elongated cells, suggesting that PDA promotes cellular elongation and extensions, indicative of enhanced cell adhesion and spreading. The hydrophilic nature of PDA likely contributed to improved cell–substrate interactions, facilitating cell attachment and spreading on the surface. Furthermore, the multi-phasic PCDE scaffolds exhibited a notably robust attachment and spread of cells, characterized by the presence of lamellipodia and filopodia, surpassing other test groups. This may come from immobilization of BMP-2 on the surface and its influence on cell adhesion.

As evidenced by live/dead cell staining results (Figure 7B), the scaffolds exhibited excellent cytocompatibility, with varying density and distribution across the surface of the constructs. Notably, multi-phasic scaffolds that include a layer of BMP-2 on top showed the highest density of viable cells. This observation aligns with our hypothesis that the scaffold's surface properties and structure significantly influence cellular response. Over time, the development of cell clusters was observed, suggesting early signs of chondrogenesis in rBMSCs.[50] Cell proliferation, as indicated by CCK-8 results (Figure 7C), demonstrated significant differences between the test groups and the control group. After 3 days of incubation, all experimental groups exhibited a marked increase in viable cell numbers, suggesting scaffolds provide a conducive environment for cell growth. Notably, proliferation peaked at day 3, then declined by Day 5, but remained above 80% compared to the control group, highlighting the constructs' potential for tissue engineering applications. The decrease in cell numbers by Day 5 may be due to scaffold degradation (10–25% within the initial days), potentially causing cell removal or stress-induced apoptosis. The initial delay in proliferation, with a peak at Day 3 instead of Day 1, suggests factors like scaffold hydrophobicity and silicon ions[51] in the chemical composition (see Figure S2, Supporting Information) influence early cell adhesion and proliferation. Further analysis showed that PCD scaffolds improved cell–scaffold interactions compared to PC scaffolds, emphasizing PDA's role in enhancing adhesion and proliferation. While there were no significant differences between the multi-phasic PCDE and PC scaffolds after 1 day, extended incubation significantly increased cell proliferation in PCDE scaffolds. Among the experimental groups, the multi-phasic scaffolds exhibited the highest cell viability and proliferation rates, attributed to BMP-2 immobilization, which enhances cell performance by binding to receptors like integrins, affecting biochemical pathways, and accelerating proliferation.[52]

The rBMSCs can differentiate into osteoblastic or chondrocytic lineages in response to specific stimuli.[3] We assessed the impact of constructs on ALP activity, a primary marker of bone formation, and OC protein expression, a key biomarker of osteogenesis, as shown in Figure 7D and E. After a 3-day culture, ALP activity was low but significantly increased with prolonged incubation. Considering that ALP activity is crucial for osteogenic differentiation, our findings indicate that scaffolds effectively promote early-stage rBMSC differentiation. Both mono-phasic PCD and multi-phasic PCDE matrices showed higher ALP levels than PC scaffolds, with multi-phasic scaffolds demonstrating superior osteogenesis. OC protein expression was higher in all test groups compared to the control group, though it decreased in PC scaffolds with longer incubation. In contrast, PCD and PCDE constructs maintained enhanced osteoblastic expression throughout. Notably, multi-phasic scaffolds containing BMP-2 exhibited excellent OC protein expression after 14 days.

Overall, the hydrophilicity of scaffolds facilitates interactions with serum proteins and growth factors, thereby improving cell attachment, migration, and spreading. The mechanism underlying the cell–PDA interaction and the provision of adhesion sites by PDA can be explained through the reaction between the amine- or thiol-functionalized molecules of serum proteins, forming covalent bonds through Shiff-base or Michael addition chemistry.[53] Bio-adhesive PDA-decorated scaffolds have been shown to improve cell adhesion, proliferation, and osteogenic differentiation by preventing protein denaturation and maintaining essential growth factors.[54] In multi-phasic PCDE scaffolds, GPTMS also acts as a signaling molecule, enhancing osteoproductive behavior and increasing scaffold stability and rigidity, which supports cell proliferation through improved attachment and spreading.[55] We also explored BMP-2's role in promoting osteogenic differentiation in rBMSCs within a non-osteogenic medium. Considering that BMP-2 is a key osteoinductive protein that modulates cell–scaffold interactions and induces bone formation by differentiating precursor cells into mature osteoblasts,[56] immobilized BMP-2 allowed for spatial and temporal control of its presentation. This immobilization strategy prevented internalization post-receptor binding, potentially enhancing its biological activity. Consequently, the aforementioned factors synergistically influenced cell activity and protein expression in multi-phasic PCDE scaffolds, mimicking osteochondral ECM and promoting tissue regeneration.

3.4. *In vivo* study

Developing translational strategies and integrating regeneration of cartilage and subchondral bone is a challenge due to the interdependence and complexity of osteochondral tissue, as well as the distinct microenvironments of the tissue layers.[57] Current commercial products lack regenerative potential, adaptability to tissue changes, and fail to restore joint functions, leading to antigenic incompatibility and weak fibrocartilage. Additionally, new tissues struggle with integration, causing uneven surfaces.[58] To evaluate the integrated repair effect of stratified scaffolds, we established an osteochondral defect model in rabbit knees. The study encompassed four groups: control (no treatment), PC scaffolds, mono-phasic PCD scaffolds, and multi-phasic PCDE scaffolds. Post-implantation of scaffolds into rabbit joints showed no signs of infection or inflammation. Figure 8A displays μCT scans of rabbit distal femurs in the coronal, axial, and sagittal planes at 4- and 12-week post-surgery, characterizing the newly developed subchondral bone tissue. μCT images revealed newly formed subchondral bone in the scaffolds-treated defects, whereas the control group exhibited insufficient healing, resulting in concave defect surfaces. Notably, multi-phasic PCDE scaffolds exhibited more extensive calcified tissue compared to control group, PC, and mono-phasic PCD scaffolds at the 4-week post-implantation. Over 12 weeks, both mono-phasic PCD scaffolds and multi-phasic PCDE ones demonstrated increased neo-calcified tissue. Particularly in PCDE scaffolds, the boundary between the repaired and adjacent native tissue was indistinct, indicating robust subchondral bone ingrowth with smooth surfaces capable of offering mechanical support for hyaline cartilage regeneration.

Bone volume/total volume (BV/TV) measurements after 4- to 12-week post-implantation (Figure 8B) revealed no increase in the control group, while scaffold-treated defects displayed enhanced bone volume, particularly at 12 weeks post-surgery. Interestingly, PCD scaffolds had greater bone volume than PC ones, likely attributable to the osteogenic effects of PDA. Nevertheless, multi-phasic PCDE scaffolds demonstrated remarkable bone formation compared to other experimental groups, suggesting a synergistic effect between PDA and BMP-2 in scaffold layers, contributing to enhanced osteochondral regeneration. The combination of these factors, along with the structural cues provided by the multi-phasic matrices, likely facilitated significant tissue formation. Following 4- and 12-week post-implantation, statistical analysis demonstrated significantly higher bone mineral density and connectivity density (Figure 8C and D) in multi-phasic PCDE scaffolds compared to the control or mono-phasic scaffolds. The higher connectivity density suggests that the scaffold's internal structure promoted better tissue organization, which are crucial for bone regeneration. Additionally, the neo-tissues formed by the multi-phasic scaffolds were successfully integrated into the surrounding tissue.

The trabecular number (Tb.N) was significantly higher in the multi-phasic PCDE scaffolds compared to the control and mono-phasic scaffolds at both 4 and 12 weeks post-implantation (Figure 8E). This enhancement in trabecular formation can be attributed to the synergistic effects of BMP-2 and PDA within the scaffold, which are known to promote osteoblast differentiation and bone matrix deposition. Significant increases in trabecular thickness (Figure 8F) were observed in the PCDE group compared to other scaffold treatments. The enhanced trabecular thickness suggests that the multi-phasic scaffolds not only promote bone formation but also contribute to the maturation of the newly formed bone. This could be due to the release of BMP-2, which likely facilitated the development of larger, stronger trabeculae, while PDA's ability to promote osteointegration may have improved the structural connectivity between bone and scaffold. The increased trabecular thickness in the multi-phasic PCDE scaffolds indicates their potential for enhancing bone strength and stability, which is crucial for long-term osteochondral repair. The trabecular separation (Tb.Sp) was significantly reduced in the PCDE scaffold group compared to the control and mono-phasic scaffold groups (Figure 8G), indicating more compact and integrated bone tissue formation. A decrease in trabecular separation is generally associated with increased bone density and improved mechanical properties, which are essential for effective osteochondral regeneration.

Histological assessment at 4- and 12-week post-surgery, employing HE, Safranin O, and immunohistochemical staining of type I and II collagen (Figures 9 and 10), evaluated scaffolds efficiency in cartilage and subchondral bone regenerating. HE staining showed no acute inflammation or necrosis in any groups post-implantation, indicating adequate host tissue integration and scaffold biocompatibility. These findings highlight the positive tissue response to the scaffolds, supporting their potential for osteochondral tissue regeneration. HE and Safranin O staining results revealed inadequate repair of the osteochondral defect in the control group, characterized by a residual void space indicating insufficient new tissue formation. Irregular granulation tissue was present, signifying a disorganized and non-specific healing response. Notably, there was no development of articular cartilage within the defect. The observed lack of natural, complete repair in the control group underscores the limitations

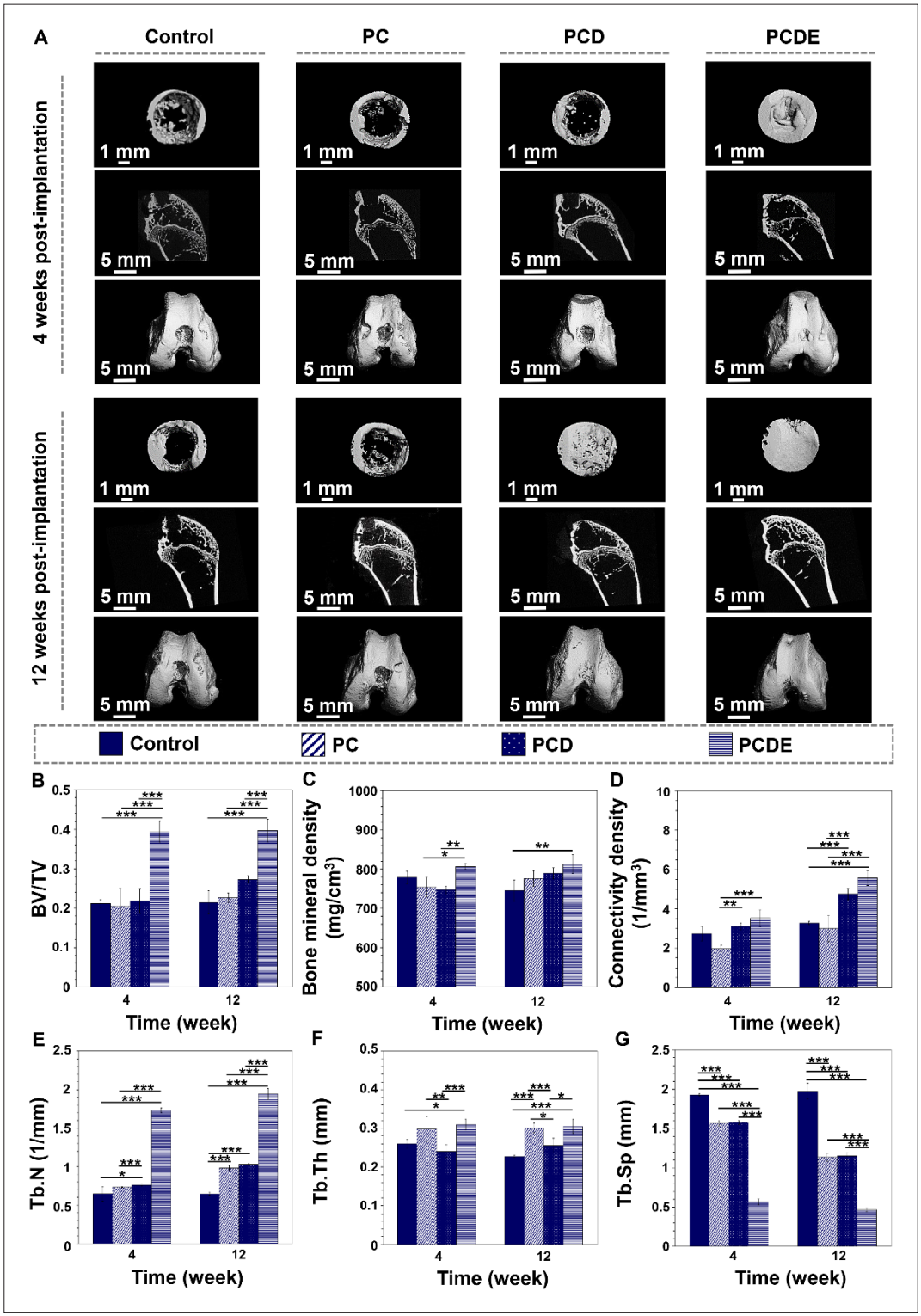

Figure 8. *In vivo* evaluation of scaffolds performance. (A) Micro-computed tomography (μCT) evaluation of *in vivo* rabbit models at 4 and 12 weeks post-implantation, comparing the control group (no treatment), PC scaffolds, mono-phasic PCD scaffolds, and multi-phasic PCDE scaffolds. (B) Bone volume/total volume (BV/TV), (C) bone mineral density, (D) connectivity density, (E) trabecular number (Tb.N), (F) trabecular thickness (Tb.Th), and (G) trabecular separation (Tb.Sp) for four experimental groups. $^{*}p \leq 0.05$; $^{**}p < 0.01$; $^{***}p < 0.001$.

of the body's intrinsic healing mechanisms in addressing severe osteochondral injuries. This highlights the critical role of scaffolds in promoting proper tissue regeneration and restoring the functional properties of the joint.[59] After 12-week post-surgery, the defective area treated with PC scaffolds was filled with neo-bone tissue. However, the neo-tissue exhibited a disorganized structure devoid of subchondral plates, indicating that the PC scaffolds did not provide a conductive substrate for osteochondral tissue regeneration. The disorganized structure suggests a lack of proper organization of the bone matrix, which is essential for the functional properties of the regenerated tissue. The absence of subchondral plates further indicates incomplete regeneration, as these plates are a critical component of the osteochondral unit, providing support and stability to the overlying cartilage. Following the implantation of the mono-phasic PCD scaffolds, there was partial regeneration of cartilage observed; nevertheless, fibrous connective tissues were also present in the defect area. The presence of fibrous connective tissue in the context of cartilage regeneration suggests that complete and fully functional cartilage regeneration may not have been achieved using the mono-phasic PCD scaffolds. A noteworthy positive finding was the absence of delamination between the newly formed articular cartilage and the subchondral plate, underscoring the efficacy of PDA surface functionalization. This outcome implies that PDA modification facilitated the successful bonding between the new cartilage and the underlying bone, which is essential for the overall stability and functionality of the joint. The results of the *in vivo* study using multi-phasic PCDE scaffolds for osteochondral tissue regeneration showed progressive improvements over time. At the conclusion of the 4-week post-surgery period, the presence of new cartilage structures was detected, indicating the potential of the multi-phasic scaffolds to support cartilage formation. However, at this early stage, the newly formed cartilage exhibited an uneven surface and had a significantly lower thickness compared to the surrounding native cartilage. Additionally, there was a lack of subchondral bone structure and inadequate trabecular filling within the bone defect area. These findings suggest that at 4 weeks post-implantation, the processes of scaffolds integration and maturation were still ongoing, and complete tissue regeneration had not yet been achieved. However, by 12 weeks post-implantation, significant improvements were observed. The multi-phasic PCDE scaffolds facilitated the formation of a smooth hyaline cartilage structure within the defect area. Importantly, the defect areas were filled with trabecular bone and subchondral bone structures, and the presence of a clearly visible tide mark was noted. The initial formation of cartilage structures, though uneven and thinner than native tissue, evolved over time into a smoother and more mature hyaline cartilage structure. The formation of subchondral bone provides mechanical support for effective cartilage repair and is crucial for the overall stability and function of the joint.[60] These findings underscore the progressive nature of the tissue regeneration process mediated by the multi-phasic PCDE scaffolds. Immunohistochemical evaluation revealed differential secretion levels of type I collagen in neo-tissues across various experimental groups, indicating varying extents of bone formation. Notably, type II collagen was detected exclusively in neo-tissues within PCD and PCDE scaffolds, particularly in the multiphasic PCDE scaffolds. Considering that type II collagen is a key component of hyaline cartilage, its presence indicates the formation of cartilage tissue. Importantly, the structure of the repaired tissues in these groups closely resembled that of the surrounding hyaline cartilage, suggesting successful cartilage regeneration. Histological analysis using HE and Safranin O staining, along with immunohistochemical assays, confirmed that smooth and thick hyaline cartilage formed in defects treated with hierarchical multi-phasic PCDE scaffolds, as opposed to mono-phasic constructs. This finding indicates effective osteochondral tissue regeneration. Furthermore, the neo-tissues within the multi-phasic scaffolds exhibited ECM components characteristic of cartilage, such as glycosaminoglycan.

Taken together, the histological results, including Safranin O and type II collagen staining, clearly demonstrate the progressive osteochondral repair promoted by the multi-phasic PCDE scaffolds. Specifically:

- *Cartilage regeneration (Safranin O staining)*. The PCDE group showed a Safranin O-stained area as compared to the control group at 12 weeks post-implantation, indicating the formation of a more proteoglycan-rich cartilage matrix in the former group. The difference in staining between 4 and 12 weeks in the PCDE group reflects the progression of tissue maturation, consistent with expected biological timelines.
- *Type II collagen expression*. The expression of type II collagen, a hallmark of hyaline cartilage, was more prominent in the PCDE group compared to controls, particularly at 12 weeks post-implantation. This increase highlights the formation of cartilage-like tissue and its maturation over time.
- *Subchondral bone formation*. The histological results also revealed robust subchondral bone regeneration at 12 weeks pots-implantation in the PCDE group, supporting the overlying cartilage and demonstrating the multi-phasic scaffold's ability to promote integrated osteochondral repair.

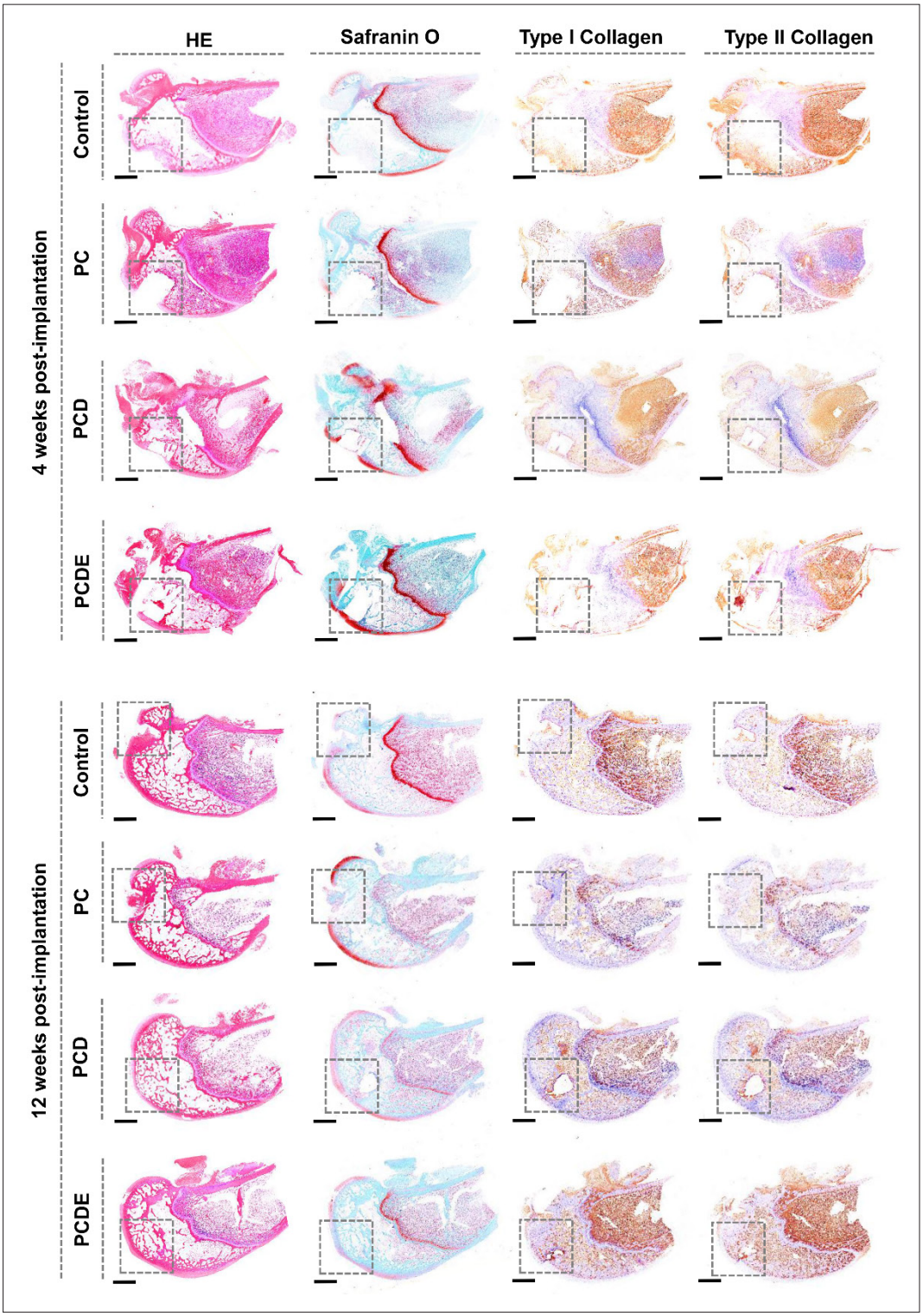

Figure 9. Micrographs of histological and immunohistochemical staining depict neo-tissue formation. Hematoxylin-eosin (HE) staining, Safranin O staining, and immunohistochemical staining of type I and II collagen in control group without any treatment, PC scaffolds, mono-phasic PCD scaffolds, and multi-phasic PCDE scaffolds at 4 and 12 weeks post-implantation. Scale bar = 2.5 mm.

Osteochondral tissue repair is a time-dependent process. At 4 weeks, early signs of tissue formation were evident, such as increased Safranin O staining in the PCDE group compared to controls. By 12 weeks, the tissue had matured significantly, as demonstrated by more substantial cartilage and subchondral bone formation. This aligns with the natural progression of osteochondral regeneration and underscores the scaffold's efficacy in facilitating both initial repair and long-term maturation. In addition to histological evidence, the μCT data provided further validation of the repair effects. The PCDE group exhibited complete defect filling with higher tissue density at 12 weeks, indicative of mineralized tissue formation. These findings are consistent with the qualitative histological data and reinforce the scaffold's role in promoting osteochondral regeneration.

4. Conclusion

This study successfully engineered multi-phasic scaffolds, employing a combination of 3D printing, electrospinning, and protein immobilization following low-temperature oxygen plasma surface modification. The stratified scaffolds were designed for simultaneous regeneration of anisotropic osteochondral tissue, considering key characteristics such as compression strength, interfacial bonding strength, hydrophilicity, absorption capacity, hydrolytic and enzymatic degradation, and bioactivity potential. The biomimetic hierarchical scaffolds demonstrated excellent cytocompatibility, evidenced by the adhesion, viability, and proliferation of rBMSCs. Simulation results indicated that the interaction of serum proteins with BMP-2 can effectively

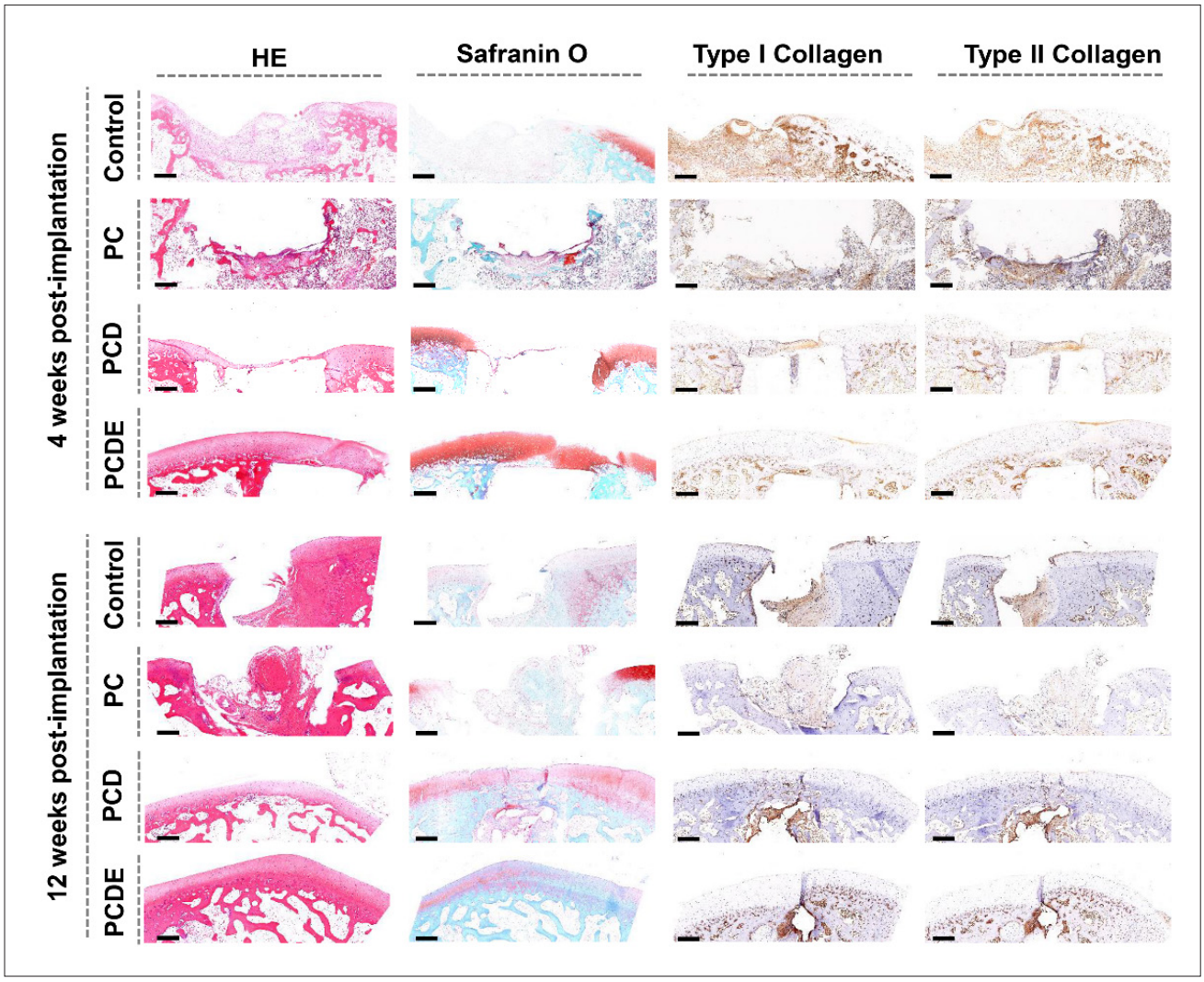

Figure 10. Enlarged micrographs of histological and immunohistochemical staining depict neo-tissue formation. Hematoxylin-eosin (HE) staining, Safranin O staining, and immunohistochemical staining of type I and II collagen in control group without any treatment, PC scaffolds, mono-phasic PCD scaffolds, and multi-phasic PCDE scaffolds at 4 and 12 weeks post-implantation. Scale bar = 500 μm.

increase its availability to cells. Additionally, the expression of relevant early and late osteogenic markers underscored the scaffolds' adequate osteogenic performance for tissue reconstruction. In the *in vivo* experiment conducted on a rabbit model, neo-tissue formation demonstrated a suitable integrity level, accompanied by the secretion of type I and II collagen—indicative of osteochondral tissue ingrowth.

The findings confirm the scaffolds' osteogenic potential through ALP activity and osteocalcin secretion, supported by *in vivo* results demonstrating subchondral bone regeneration. For chondrogenic capacity, the *in vivo* results provided robust evidence, with Safranin O staining and type II collagen expression clearly indicating successful cartilage regeneration at the defect site. These data collectively highlight the scaffolds' ability to promote both osteogenesis and chondrogenesis in biologically relevant contexts. *In vivo* experiments uniquely replicate the biological complexity of an organism, including immune responses, vascularization, and mechanical loading—factors that cannot be fully captured in *in vitro* settings. The outcomes observed *in vivo*, such as improved tissue repair under clinically relevant conditions, offer a comprehensive and realistic understanding of scaffold performance. Both sets of *in vitro* and *in vivo* data provide a clinically relevant and comprehensive demonstration of the scaffolds' dual functionality in regenerating subchondral bone and cartilage. In summation, this study introduces a promising approach for osteochondral tissue repair utilizing stratified multi-phasic and patient-specific scaffolds.

Acknowledgments

None.

Funding

This work was supported by the new quality specialty program of peak plateau clinical medicine of Pudong new area health commission (2024-PWXZ-21); the Program of key medicine of Shanghai Municipal Health Commission (2024ZDXK0038); the Demonstration pilot project of central financial support for the inheritance and innovation of traditional Chinese medicine (YC-2023-0202).

Conflict of interest

Joaquim Miguel Oliveira serves as the Editorial Board Member of the journal and the guest editor of the special issue: *Bioprinting of In Vitro Tissue and Disease Models*, but did not in any way involve in the editorial and peer-review process conducted for this paper, directly or indirectly. The authors have no affiliations with or involvement in any organization or entity with any financial interest, or non-financial interest in the subject matter or materials discussed in this manuscript. The authors declare they have no competing interests.

Author contributions

Conceptualization: Farnaz Ghorbani, Joaquim Miguel Oliveira, Yuanyuan Liu, Baoqing Yu
Data curation: Farnaz Ghorbani
Formal analysis: Farnaz Ghorbani
Funding acquisition: Baoqing Yu
Investigation: Farnaz Ghorbani, Behafarid Ghalandari, Zhi Qian, Chongjing Zhang, Yi Zhang, Dejian Li, Zeyuan Zhang, Zichen Liu
Methodology: Farnaz Ghorbani, Behafarid Ghalandari
Project administration: Baoqing Yu
Supervision: Joaquim Miguel Oliveira, Baoqing Yu
Validation: Farnaz Ghorbani, Joaquim Miguel Oliveira
Visualization: Farnaz Ghorbani, Behafarid Ghalandari
Writing–original draft: Farnaz Ghorbani, Behafarid Ghalandari
Writing–review & editing: Farnaz Ghorbani, Joaquim Miguel Oliveira, Behafarid Ghalandari

Ethics approval and consent to participate

The animal experiment protocols were approved by the Animal Care and Use Committee at the Fudan University Hospital Medical Center (code 2021-DS-Q-16). The study was conducted in strict adherence to the ethical principles outlined by the National Institutes of Health (NIH) regarding the care and utilization of laboratory animals.

Consent for publication

Not applicable.

Availability of data

The data that support the findings of this study are available from the corresponding author upon reasonable request.

References

1. Yue S, Zhai G, Zhao S, et al. The biphasic role of the infrapatellar fat pad in osteoarthritis. *Biomed Pharmacother*. 2024;179:117364.
doi: 10.1016/j.biopha.2024.117364

2. Fang J, Liao J, Zhong C, Lu X, Ren F. High-strength, biomimetic functional chitosan-based hydrogels for full-thickness osteochondral defect repair. *ACS Biomater Sci Eng*. 2022;8(10):4449-4461.
doi: 10.1021/acsbiomaterials.2c00187

3. Liu J, Li L, Suo H, Yan M, Yin J, Fu J. 3D printing of biomimetic multi-layered GelMA/nHA scaffold for osteochondral defect repair. *Mater Des*. 2019;171:107708.

doi: 10.1016/j.matdes.2019.107708

4. Pagan E, Stefanek E, Seyfoori A, et al. A handheld bioprinter for multi-material printing of complex constructs. *Biofabrication*. 2023;15(3):035012. doi: 10.1088/1758-5090/acc42c

5. He M, Li L, Liu Y, et al. Decellularized extracellular matrix coupled with polycaprolactone/laponite to construct a biomimetic barrier membrane for bone defect repair. *Int J Biol Macromol*. 2024;276:133775. doi: 10.1016/j.ijbiomac.2024.133775

6. Ghalandari B, Yu Y, Ghorbani F, et al. Polydopamine nanospheres coated with bovine serum albumin permit enhanced cell differentiation: fundamental mechanism and practical application for protein coating formation. *Nanoscale*. 2021;13(47):20098-20110. doi: 10.1039/D1NR07469E

7. Ghorbani F, Ghalandari B, Khajehmohammadi M, et al. Photo-cross-linkable hyaluronic acid bioinks for bone and cartilage tissue engineering applications. *Int Mater Rev*. 2023;68(7):901-942. doi: 10.1080/09506608.2023.2167559

8. Yakufu M, Wang Z, Li C, et al. Carbene-mediated gelatin and hyaluronic acid hydrogel paints with ultra adhesive ability for arthroscopic cartilage repair. *Int J Biol Macromol*. 2024;273:133122. doi: 10.1016/j.ijbiomac.2024.133122

9. Gu Z, Wang J, Fu Y, et al. Smart biomaterials for articular cartilage repair and regeneration. *Adv Funct Mater*. 2023;33(10):2212561. doi: 10.1002/adfm.202212561

10. Lee SJ, Nowicki M, Harris B, Zhang LG. Fabrication of a highly aligned neural scaffold via a table top stereolithography 3D printing and electrospinning. *Tissue Eng Part A*. 2017;23(11-12):491-502. doi: 10.1089/ten.tea.2016.0353

11. Zarei M, Shabani Dargah M, Hasanzadeh Azar M, et al. Enhanced bone tissue regeneration using a 3D-printed poly(lactic acid)/Ti6Al4V composite scaffold with plasma treatment modification. *Sci Rep*. 2023;13(1):3139. doi: 10.1038/s41598-023-30300-z

12. Teimouri R, Abnous K, Taghdisi SM, Ramezani M, Alibolandi M. Surface modifications of scaffolds for bone regeneration. *J Mater Res Technol*. 2023;24:7938-7973. doi: 10.1016/j.jmrt.2023.05.076

13. Ghorbani F, Kim M, Ghalandari B, et al. Architecture of β-lactoglobulin coating modulates bioinspired alginate dialdehyde-gelatine/polydopamine scaffolds for subchondral bone regeneration. *Acta Biomater*. 2024;181:188-201. doi: 10.1016/j.actbio.2024.04.028

14. Lin S, Maekawa H, Moeinzadeh S, et al. An osteoinductive and biodegradable intramedullary implant accelerates bone healing and mitigates complications of bone transport in male rats. *Nat Commun*. 2023;14(1):4455. doi: 10.1038/s41467-023-40149-5

15. Kim P, Park J, Lee DJ, et al. Mast4 determines the cell fate of MSCs for bone and cartilage development. *Nat Commun*. 2022;13(1):3960. doi: 10.1038/s41467-022-31697-3

16. Yang X, Tian S, Fan L, et al. Integrated regulation of chondrogenic differentiation in mesenchymal stem cells and differentiation of cancer cells. *Cancer Cell Int*. 2022;22(1):169. doi: 10.1186/s12935-022-02598-8

17. Nokoorani YD, Shamloo A, Bahadoran M, Moravvej H. Fabrication and characterization of scaffolds containing different amounts of allantoin for skin tissue engineering. *Sci Rep*. 2021;11(1):16164. doi: 10.1038/s41598-021-95763-4

18. Montes A, Valor D, Delgado L, Pereyra C, Martínez de la Ossa E. An attempt to optimize supercritical CO2 polyaniline-polycaprolactone foaming processes to produce tissue engineering scaffolds. *Polymers (Basel)*. 2022;14(3):488. doi: 10.3390/polym14030488

19. Cai Q. Enzymatic degradation behavior and mechanism of Poly(lactide-co-glycolide) foams by trypsin. *Biomaterials*. 2003;24(4):629-638. doi: 10.1016/S0142-9612(02)00377-0

20. Yan Y, Tao H, He J, Huang SY. The HDOCK server for integrated protein–protein docking. *Nat Protoc*. 2020;15(5):1829-1852. doi: 10.1038/s41596-020-0312-x

21. Yan Y, Zhang D, Zhou P, Li B, Huang SY. HDOCK: a web server for protein–protein and protein–DNA/RNA docking based on a hybrid strategy. *Nucleic Acids Res*. 2017;45(W1):W365-W373. doi: 10.1093/nar/gkx407

22. Protein data bank, www.rcsb.org. www.rcsb.org

23. Naghshineh A, Dadras A, Ghalandari B, et al. Safranal as a novel anti-tubulin binding agent with potential use in cancer therapy: an in vitro study. *Chem Biol Interact*. 2015;238:151-160. doi: 10.1016/j.cbi.2015.06.023

24. Micalizzi S, Russo L, Giacomelli C, et al. Multimaterial and multiscale scaffold for engineering enthesis organ. *Int J Bioprinting*. 2023;9(5):763. doi: 10.18063/ijb.763

25. Criscenti G, Longoni A, Di Luca A, et al. Triphasic scaffolds for the regeneration of the bone–ligament interface. *Biofabrication*. 2016;8(1):015009. doi: 10.1088/1758-5090/8/1/015009

26. Song Y, Zhang Y, Qu Q, et al. Biomaterials based on hyaluronic acid, collagen and peptides for three-dimensional cell culture and their application in stem cell differentiation. *Int J Biol Macromol*. 2023;226:14-36.

doi: 10.1016/j.ijbiomac.2022.11.213

27. Harati J, Tao X, Shahsavarani H, et al. Polydopamine-mediated protein adsorption alters the epigenetic status and differentiation of primary human adipose-derived stem cells (hASCs). *Front Bioeng Biotechnol*. 2022;10:934179. doi: 10.3389/fbioe.2022.934179

28. Zhang Y, Sun N, Zhu M, et al. The contribution of pore size and porosity of 3D printed porous titanium scaffolds to osteogenesis. *Biomater Adv*. 2022;133:112651. doi: 10.1016/j.msec.2022.112651

29. Maji K, Pramanik K. Electrospun scaffold for bone regeneration. *Int J Polym Mater Polym Biomater*. 2022;71(11):842-857. doi: 10.1080/00914037.2021.1915784

30. Escobar Jaramillo M, Covarrubias C, Patiño González E, Ossa Orozco CP. Optimization by mixture design of chitosan/multi-phase calcium phosphate/BMP-2 biomimetic scaffolds for bone tissue engineering. *J Mech Behav Biomed Mater*. 2024;152:106423. doi: 10.1016/j.jmbbm.2024.106423

31. Alfieri ML, Weil T, Ng DYW, Ball V. Polydopamine at biological interfaces. *Adv Colloid Interface Sci*. 2022;305:102689. doi: 10.1016/j.cis.2022.102689

32. Kim YJ, Kang IK, Huh MW, Yoon SC. Surface characterization and in vitro blood compatibility of poly(ethylene terephthalate) immobilized with insulin and/or heparin using plasma glow discharge. *Biomaterials*. 2000;21(2):121-130. doi: 10.1016/S0142-9612(99)00137-4

33. Yoshinyari M, Hakawa T, Matsuzaka K, et al. Oxygen plasma surface modification enhances immobilization of simvastatin acid. *Biomed Res*. 2006;27(1):29-36. doi: 10.2220/biomedres.27.29

34. Adipurnama I, Yang MC, Ciach T, Butruk-Raszeja B. Surface modification and endothelialization of polyurethane for vascular tissue engineering applications: a review. *Biomater Sci*. 2017;5(1):22-37. doi: 10.1039/C6BM00618C

35. Pohl TLM, Schwab EH, Cavalcanti-Adam EA. Covalent binding of BMP-2 on surfaces using a self-assembled monolayer approach. *J Vis Exp*. 2013;(78):e50842. doi: 10.3791/50842

36. Oliveira JM, Ribeiro VP, Reis RL. Advances on gradient scaffolds for osteochondral tissue engineering. *Prog Biomed Eng*. 2021;3(3):033001. doi: 10.1088/2516-1091/abfc2c

37. Ginebra MP. Cements as bone repair materials. In: *Bone Repair Biomaterials*. Elsevier; 2009:271-308. doi: 10.1533/9781845696610.2.271

38. Auyson K, Koomsap P, Chanthakulchan A, Supaphol P. Investigation of applying electrospinning in fused deposition modeling for scaffold fabrication. In: *High Value Manufacturing: Advanced Research in Virtual and Rapid Prototyping*. CRC Press; 2013:149-154. doi: 10.1201/b15961-28

39. Kim G, Son J, Park S, Kim W. Hybrid process for fabricating 3D hierarchical scaffolds combining rapid prototyping and electrospinning. *Macromol Rapid Commun*. 2008;29(19):1577-1581. doi: 10.1002/marc.200800277

40. Khatiwala CB, Peyton SR, Metzke M, Putnam AJ. The regulation of osteogenesis by ECM rigidity in MC3T3-E1 cells requires MAPK activation. *J Cell Physiol*. 2007;211(3):661-672. doi: 10.1002/jcp.20974

41. Kim K, Yeatts A, Dean D, Fisher JP. Stereolithographic bone scaffold design parameters: osteogenic differentiation and signal expression. Tissue Eng Part B Rev. 2010;16(5):523-539. doi: 10.1089/ten.teb.2010.0171

42. Lee SJ, Heo DN, Park JS, et al. Characterization and preparation of bio-tubular scaffolds for fabricating artificial vascular grafts by combining electrospinning and a 3D printing system. Phys Chem Chem Phys. 2015;17(5):2996-2999. doi: 10.1039/C4CP04801F

43. Alfieri ML, Panzella L, Napolitano A. Multifunctional coatings hinging on the catechol/amine interplay. Eur J Org Chem. 2024;27(1):e202301002. doi: 10.1002/ejoc.202301002

44. Ebrahimi Z, Irani S, Ardeshirylajimi A, Seyedjafari E. Enhanced osteogenic differentiation of stem cells by 3D printed PCL scaffolds coated with collagen and hydroxyapatite. *Sci Rep*. 2022;12(1):12359. doi: 10.1038/s41598-022-15602-y

45. Yang Z, Xi Y, Bai J, et al. Covalent grafting of hyperbranched poly-L-lysine on Ti-based implants achieves dual functions of antibacteria and promoted osteointegration in vivo. *Biomaterials*. 2021;269:120534. doi: 10.1016/j.biomaterials.2020.120534

46. Buck E, Lee S, Stone LS, Cerruti M. Protein adsorption on surfaces functionalized with COOH groups promotes anti-inflammatory macrophage responses. *ACS Appl Mater Interfaces*. 2021;13(6):7021-7036. doi: 10.1021/acsami.0c16509

47. Marsell R, Einhorn TA. The biology of fracture healing. *Injury*. 2011;42(6):551-555. doi: 10.1016/j.injury.2011.03.031

48. Behrens P. Matrixgekoppelte Mikrofrakturierung. *Arthroskopie*. 2005;18(3):193-197. doi: 10.1007/s00142-005-0316-0

49. Hettiaratchi MH, Krishnan L, Rouse T, Chou C, McDevitt TC, Guldberg RE. Heparin-mediated delivery of bone morphogenetic protein-2 improves spatial localization of bone regeneration. *Sci Adv*. 2020;6(1):aay1240. doi: 10.1126/sciadv.aay1240

50. Franco RAG, McKenna E, Shajib MS, et al. Microtissue culture provides clarity on the relative chondrogenic and hypertrophic response of bone-marrow-derived stromal cells to TGF-β1, BMP-2, and GDF-5. *Cells*. 2023;13(1):37. doi: 10.3390/cells13010037

51. Tonda-Turo C, Gentile P, Saracino S, et al. Comparative analysis of gelatin scaffolds crosslinked by genipin and silane coupling agent. *Int J Biol Macromol*. 2011;49(4):700-706. doi: 10.1016/j.ijbiomac.2011.07.002

52. Kim BR, Nguyen TBL, Min YK, Lee BT. In vitro and in vivo studies of BMP-2-loaded PCL–gelatin–BCP electrospun scaffolds. *Tissue Eng Part A*. 2014;20(23-24):3279-3289. doi: 10.1089/ten.tea.2014.0081

53. Sy KHS, Ho LWC, Lau WCY, Ko H, Choi CHJ. Morphological diversity, protein adsorption, and cellular uptake of polydopamine-coated gold nanoparticles. *Langmuir*. 2018;34(46):14033-14045. doi: 10.1021/acs.langmuir.8b02572

54. Firoozi N, Kang Y. Immobilization of FGF on poly(xylitol dodecanedioic Acid) polymer for tissue regeneration. *Sci Rep*. 2020;10(1):10419. doi: 10.1038/s41598-020-67261-6

55. Ghosh S, Scott AK, Seelbinder B, et al. Dedifferentiation alters chondrocyte nuclear mechanics during in vitro culture and expansion. *Biophys J*. 2022;121(1):131-141. doi: 10.1016/j.bpj.2021.11.018

56. Baek JW, Kim KS, Park H, Kim BS. Marine plankton exoskeletone-derived hydroxyapatite/polycaprolactone composite 3D scaffold for bone tissue engineering. *Biomater Sci*. 2022;10(24):7055-7066. doi: 10.1039/D2BM00875K

57. Lee J, Lee S, Huh SJ, Kang B, Shin H. Directed regeneration of osteochondral tissue by hierarchical assembly of spatially organized composite spheroids. *Adv Sci*. 2022;9(3): 2103525. doi: 10.1002/advs.202103525

58. Qin C, Ma J, Chen L, et al. 3D bioprinting of multicellular scaffolds for osteochondral regeneration. *Mater Today*. 2021;49:68-84. doi: 10.1016/j.mattod.2021.04.016

59. Wang Z, Le H, Wang Y, et al. Instructive cartilage regeneration modalities with advanced therapeutic implantations under abnormal conditions. *Bioact Mater*. 2022;11:317-338. doi: 10.1016/j.bioactmat.2021.10.002

60. Yang T, Tamaddon M, Jiang L, et al. Bilayered scaffold with 3D printed stiff subchondral bony compartment to provide constant mechanical support for long-term cartilage regeneration. *J Orthop Transl*. 2021;30:112-121. doi: 10.1016/j.jot.2021.09.001

ACCSCIENCE PUBLISHING

International Journal of Bioprinting

RESEARCH ARTICLE

3D-printed artificial cornea featuring aligned fibrous structure and enhanced mechanical strength

Priyanka Chaudhary[1], Dun-Heng Tan[1,2], Chia-Hsien Lee[1], Chun-Yu Chang[3], Ting-Han Lin[4], Ming-Chung Wu[4,5], Wei-Fang Su[1,2], Meng-Fang Lin[1]*, and Yu-Ching Huang[1,4,5]*

[1]Department of Materials Engineering and Biochemical Technology R&D Center, Ming Chi University of Technology, New Taipei City 24301, Taiwan

[2]Department of Materials Science and Engineering, National Taiwan University, Taipei City 10617, Taiwan

[3]Bachelor Program in Semiconductor Materials and Fabrication, Ming Chi University of Technology, New Taipei City 24301, Taiwan

[4]Center for Sustainability and Energy Technologies, Chang Gung University, Taoyuan 33302, Taiwan

[5]Department of Chemical and Materials Engineering, Chang Gung University, Taoyuan 33302, Taiwan

(This article belongs to the *Special Issue*: *Made-to-order Organ*)

Abstract

The global shortage of donor eye bank tissue has significantly impeded advancements in biomaterial for corneal implantation. To address this issue, we have developed a three-dimensional (3D)-printed artificial cornea using a composite scaffolds of sodium alginate (SA) and cellulose nanofibers (CNF), crosslinked with poly-L-lysine-co-L-glutamic acid ($PLL_{80}GA_{20}$, PG) and calcium chloride ($CaCl_2$, CC). The 2 wt% SA/CNF composite scaffolds offer several advantages, including low toxicity, cost-effectiveness, excellent printability, and high mechanical strength, even with low crosslinker concentrations. The PG was synthesized via ring-opening polymerization of L-glutamate N-carboxyl anhydride (BGNCA) and L-lysine N-carboxyl anhydride (CBZNCA). The purity of the monomers was verified through differential scanning calorimetry analysis, revealing a melting point of 97°C. The molecular weight of the synthesized PG was determined to be 47 kDa. A dual crosslinking strategy was employed, starting with electrostatic crosslinking, followed by ionic crosslinking using varying concentrations of PG and CC at different effective charge concentrations of 6.25 12.25, and 25 mM.The hydrogel and 3D-printed cornea were comprehensively evaluated for chemical structure, surface functional groups, water content, mechanical strength, orientation, cytotoxicity, biocompatibility, and transparency. Notably, the inclusion of PG significantly enhanced the mechanical properties of the 3D-printed cornea, with the hydrogel achieving a storage modulus of 2,360 kPa at 6.25 mM of PG/CC, while maintaining over 95% water content. The artificial cornea demonstrated 86% transparency, and the cell viability showed 96% viable on day 7 with degradation rate of 35.9% in 28 days. The superior hydrophilicity, transparency, and mechanical strength of the printed scaffolds highlights their potential for the development of full-thickness corneal structures, making them a promising candidate for future corneal implants.

***Corresponding authors:**
Meng-Fang Lin
(mflin@mail.mcut.edu.tw)

Yu-Ching Huang
(huangyc@mail.mcut.edu.tw)

Citation: ChaudharyP, TanD-H, LeeC-H, et al. 3D-printed artificial cornea featuring aligned fibrous structure and enhanced mechanical strength. *Int J Bioprint*. 2025;11(1):598-613. doi: 10.36922/ijb.4687

Received: August 29, 2024
Revised: October 15, 2024
Accepted: October 28, 2024
Published Online: October 28, 2024

Copyright: © 2024 Author(s). This is an Open Access article distributed under the terms of the Creative Commons Attribution License, permitting distribution, and reproduction in any medium, provided the original work is properly cited.

Publisher's Note: AccScience Publishing remains neutral with regard to jurisdictional claims in published maps and institutional affiliations.

***Keywords*:** Scaffold; Poly-L-lysine-co-L-glutamic acid; 3D bioprinting; Artificial cornea

1. Introduction

The cornea is a transparent and well-structured tissue that plays a crucial role in the majority of the eye's refractive power.[1] Damage to the cornea, whether from bacterial infections or injuries, can lead to cell failure, visual impairment, and even blindness.[2,3] Globally, over 10 million people are affected by various corneal issues each year.[4] Due to its high short-term success rate, penetrating keratoplasty is the most utilized grafting method to restore vision in cases of severe corneal disorders.[5] However, the availability of donor corneal tissue is insufficient to meet global demand. Alternative treatments, such as artificial keratoprostheses, decellularized animal corneal tissue (*e.g.*, pig cornea), and human amniotic membrane, have been explored, but these methods often suffer from low success rates or are not universally approved for tissue transplantation.[6,7]

Biodegradable and biocompatible polymers have emerged as critical components in biomedical engineering, especially in three-dimensional (3D) printing applications such as tissue regeneration scaffolds and drug delivery systems. These biomaterials are of significant attention in cartilage and tissue engineering because they can replicate the properties of the native extracellular matrix, promoting cell adhesion, proliferation, and differentiation. Among the wide variety of polymers used in 3D printing, notable examples include gelatin/gelatin methacryloyl (GelMA), zein, bovine serum albumin, ultra-high molecular weight polyethylene, and polylactic acid. However, each of these materials presents specific limitations concerning mechanical properties, biodegradation rates, and biocompatibility.[8,9] Additional polymers such as poly(methyl methacrylate) cover both natural and synthetic origins, including collagen, gelatin, chitosan, silk, polyethylene glycol, polycaprolactone, poly(lactic-co-glycolic acid) (PLGA), and poly(2-hydroxyethyl methacrylate). These materials can be used individually or in combination to optimize performance. Polyethylene glycol diacrylate (PEGDA) and GelMA, for example, are photocurable gels that can be crosslinked using visible light irradiation with Lithium phenyl-2,4,6-trimethylbenzoylphosphinate (LAP).[10-13] In a study by Patel et al.[14], a GelMA-LAP bio-ink system was developed to fabricate 3D-printed osteogenic models using a volumetric approach, where 2D light patterns were synchronously irradiated while rotating.[15] However, these synthetic materials often fail due to poor host-implant integration, leading to inflammation and implant extrusion.[16] Clinical reports indicate that less than half of patients retain their original keratoprosthesis after follow-up. Biological and biosynthetic materials, such as silk or crosslinked collagen, have shown promise due to their excellent optical transparency and biocompatibility. Despite this, their mechanical integrity is often compromised, requiring overlay sutures instead of standard interrupted sutures. These materials also lack the fibril arrangement of collagen lamellae found in the corneal stroma, which offers low mechanical strength.[16,17]Another way to enhance the mechanical strength of the hydrogel is dual crosslinking, which combines two forms of crosslinks to create a tough and flexible material. For example, one type of crosslink canprovide elasticity while the other adds strength.

Researchers are also working to recreate the complicated lamellar structure of the cornea using biomaterials.[18] Layer-by-layer structural implants have been created using corneal fibroblasts and various substrates, such as gelatin,[19] collagen film,[20] silk fibrins, CNF,[21] and peptide amphiphile.[22] Corneal fibroblasts secrete stromal extracellular matrix within the biomaterial scaffold, creating a corneal stromal equivalent.[23] CNF, a nontoxic fibrous material, has shown promise in tissue engineering due to its alignment and high mechanical strength. Previous studies on CNF-containing hydrogels have reported various mechanical properties. For example, Dong etal.[24] reported that a 61.25 wt% 2,2,6,6-tetramethylpiperidine-1-oxyl radical-mediated oxidized (TEMPO)CNF hydrogel crosslinked with Ca^{2+}, Zn^{2+}, Cu^{2+}, Fe^{3+}, and Al^{3+} exhibited a storage modulus ranging from 0.2 to 2 kPa. Yang et al.[25] also investigated CNF-based composite hydrogels, finding that a0.2–2wt% TEMPO-CNF/Tetra-arm polyethylene glycol hydrogel displayed a storage modulus of 0.2–1 kPa. Yu et al.[26] investigated CNF/polypeptide hydrogel for the first time, analyzing their physical, chemical, and mechanical properties. The crosslinker was utilized at varied concentrations of 50 and 200 mM with the addition of only 12.5 mM of PLGA is Poly-L-lysine-co-L-glutamic acid (PLLGA) resulting in a storage modulus of 34 kPa for 1.91 wt% CNF/PLLGA hydrogel.[26] Their study demonstrated that the mechanical properties of CNF-containing hydrogels are heavily influenced by the crosslinking density. CNF-containing hydrogel, crosslinked with a poly-L-lysine-co-L-glutamic acid ($PLL_{80}GA_{20}$, PG) through hydrogen bonding, exhibited significantly improved mechanical strength. While synthetic corneal equivalents with corneal fibroblasts offer structural similarities to the original cornea, they are not clinically feasible due to

their limited thickness and complex fabrication methods. These materials have also been used to fabricate artificial corneas using techniques such as hydrogel fabrication, 3D printing,[11] and electrospinning.[27] However, their clinical use has been limited by postoperative difficulties, including host tissue rejection, vision obstructions, and persistent epithelial defects.[28]

Over the last few decades, tissue engineering and regenerative medicine have provided alternative methods for forming tissues and organs to overcome the shortage of organ transplants. 3D printing of biomaterials offers a promising solution for producing human tissues and organs, potentially alleviating donor shortage. 3D bioprinting technology enables the fabrication of customizable corneal implants tailored to each patient's unique eye shape and size, increasing the likelihood of success and comfort.[29,30] This adaptability of this technology allows for the integration of various biocompatible materials, such as hydrogels, biopolymers, and composites, facilitating the development of corneal implants that mimic the mechanical and optical properties of the natural cornea while promoting tissue integration and healing.[18]

However, there are limitations to previously reported scaffolds, including low transparency, reduced mechanical strength, high costs, prolonged testing before transplantation, susceptibility to tearing or wrinkling during suturing, and toxicity associated with poor material alignment.[31] Therefore, developing alternative solutions for corneal transplantation, such as cell-based therapies and bioengineered constructs, is critical and urgent.[32] Recently, alginate-based scaffolds have gained attention in tissue engineering due to their superior biocompatibility, biodegradability, non-toxicity, flexibility, and chelating ability. However, alginate alone has limitations, including high viscosity, low solubility, and poor degradability, which restrict its biological applications. To overcome these issues, various natural or synthetic biomaterials have been integrated into alginate structures. Alginate's excellent printability also makes it suitable for 3D printing applications.[33-35]

In this study, we developed a 3D-printed artificial cornea using 2 wt% sodium alginate (SA) and CNF composite scaffolds with dual crosslinking. During the fabrication of the hydrogel, two types of crosslinkers were employed: PG and calcium chloride ($CaCl_2$,CC), which were essential for maintaining the corneal shape following the 3D printing process. This innovative material demonstrates significant mechanical strength, low toxicity, and excellent hydrogel orientation. The PG was synthesized through a ring-opening polymerization method, and the composite hydrogel was fabricated.PG significantly improved the mechanical strength of the hydrogels, with lysine playing a role in human protein synthesis and glutamate-promoting cell proliferation.[36] The potential of the synthesized polymer crosslinked SA/CNF composite hydrogel was evaluated by examining light transmittance, composite hydrogel orientation, and cytocompatibility. Since the mechanical properties of bio-ink were used for 3D printing cornea. Even at low concentrations, the 3D-printed PG-crosslinked hydrogel exhibited high mechanical strength, reaching a storage modulus of 2360 kPa.

2. Materials and methods

Triphosgene (98%, Sigma–Aldrich), benzyl amine (99%, Alfa Aesar), hydrobromic acid solution (33 wt% in acetic acid; 47 wt%, Sigma–Aldrich), L-glutamate(bz)-OH (≥99.0%, Sigma–Aldrich), L-lysine (Cbz)-OH (≥99.0%, Fluorochem), and SA (M_w 150-250 kDa) salt were obtained from Acros organics, and all solvents were purchased from Sigma–Aldrich. Detailed synthesis methods for L-glutamate N-carboxyl anhydride (BGNCA), L-lysine N-carboxyl anhydride (CBZNCA), and PG are provided in the Supplementary File as Figures S1, S2, and S3, respectively. The PG was synthesized using the traditional ring opening polymerization method, with the procedure described in section S1 of the Supplementary File. The preparation of bio-ink and printing procedure has been given in section S1.5.

The synthesized BGNCA, CBZNCA, and PG were confirmed using differential scanning calorimetry (DSC), nuclear magnetic resonance spectroscopy (NMR), and Fourier transform infrared spectroscopy (FTIR) analysis. The fabricated hydrogels were investigated using polarized optical microscope (POM), scanning electron microscopy (SEM), and rheological analysis. Detailed methods of preparation and the information of the instruments used for every analysis are provided in Supplementary File, sections S2 from S2.1 to S2.10

3. Results and discussion

First, the BGNCA and CBZNCA were confirmed by DSC analysis presented in Figure S4a, and then they were used to polymerize the PG. The surface functional group confirmed by the FTIR, as shown in Figure S4b. The surface charges of the SA, CC, and PG were confirmed by the zeta potential before the gelation, and the data are presented in Figure S4c in Supplementary File with detailed explanation. Figure S4d showing the storage modulus of the control group hydrogel as SA and CC. The surface charge of SA was -32.76 mV, and that of the PG was 47.62 mV. The NMR representing the chemical structure of the monomers and polymers is shown in Figure S5a–c (in Supplementary File). The surface charge of SA was

-32.76 mV, and that of the PG was 47.62 mV. The hydrogels were prepared dual crosslinking based on their effective charge concentration of the crosslinker. According to our previous research, the toxicity of using PG with CC was lower at 25 mM effective charge concentration; therefore, in current research, we proposed the lowest molarity (effective charge concentration).[26] Concentrations of 6.25, 12.25, and 25 mM are the concentrations for the fabrication of hydrogels. To produce the hydrogel, we made the solutions and bio-ink, as depicted in Figure 1a, through the individual preparation of a 2 wt% SA aqueous solution and a CNF aqueous solution. Subsequently, we combined both composites and let them homogenize for 2 h. Following that, the composite solution was stirred at 300 rpm overnight. Aqueous solutions of the PG were prepared with effective charge concentrations of 6.25, 12.25, and 25 mM, respectively. The fabrication of hydrogels can be achieved through two distinct techniques: the dropped and co-injection methods. In the dropped method, the SA/CNF mixture was first mixed overnight, and then the crosslinker solution was carefully added dropwise. The ratio of SA/CNF solution to PG was maintained at 1:2. Although gelation initiates within a second, complete gelation necessitates an overnight immersion of the mixture in the crosslinker solution. Following the removal of the crosslinker solution, the hydrogels were placed in deionized water for an additional night under ambient conditions. This method, however, tends to result in uneven or bowl-shaped contact. In the co-injection method, a dual syringe system obtained from Nordon-medical was utilized, along with a 6 cm glass capillary to ensure proper fiber alignment. One syringe was filled with the SA/CNF solution, while the other contained the crosslinker solution. The co-injection gels were created by simultaneously extruding both solutions through the dual syringe. The mixture was allowed to rest overnight within the capillary, resulting in a rod-like texture. The amount of CNF was 2 wt%, but the volume of the CNF optimized according to enhancement of the transparency of hydrogel. CNF is considered for its high fiber content, which results in minimal transparency attributed to its bundled structure. Consequently, after optimization with various volumes, 0.2 mL was selected for the hydrogel formation. The crosslinking mechanism during the hydrogelation is shown in Figure 1b(i). SA is the polymer chain included carboxyl groups (-COO^-), which bind with divalent cations, such as Ca^{2+} in CC and NH_3^+ in PG of the formation of a crosslinked network and gel. The crosslinking mechanism is shown in Figure 1b(ii). It can be observed that the SA provides the negative charges (COO^-), while the PG acts as a crosslinker with positive charges (NH_3^+), and CNF is used to align the hydrogel structure. Physical crosslinking takes place throughout the hydrogelation process by the dropped and co-injection methods. During the 3D printing process, dual crosslinking was employed, starting with physical crosslinking followed by chemical crosslinking. The second stage of crosslinking was achieved through the addition of Ca^{2+}, resulting in covalent chemical bond formation, which provides chemical crosslinking as shown in Figure 1b(iii). The composition and nomenclature of the hydrogel on their effective charge concentrations are tabulated in Table 1.

Table1. Composition of hydrogel with its nomenclature

Sample name	Crosslinker	Sample code	Effective charge concentration (mM) of crosslinker
$PLL_{80}GA_{20}$	-	PG-1	6.25
		PG-2	12.50
		PG-3	25
CNF	$CaCl_2$	CNF/CC-1	6.25
		CNF/CC-2	12.50
		CNF /CC-3	25
CNF	$PLL_{80}GA_{20}$	CNF/PG-1	6.25
		CNF/PG-2	12.50
		CNF/PG-3	25
SA/CNF	$PLL_{80}GA_{20}$	SA/CNF/PG-1	6.25
		SA/CNF/PG-2	12.50
		SA/CNF/PG-3	25
3D-printed SA/CNF	$PLL_{80}GA_{20}/CaCl_2$	SA/CNF/PG/CC-1	6.25
		SA/CNF/PG/CC-2	12.50
		SA/CNF/PG/CC-3	25

Abbreviations: CC: calcium chloride; CNF: cellulose nanofibers; PG: poly-L-lysine-co-L-glutamic acid ($PLL_{80}GA_{20}$); SA: sodium alginate.

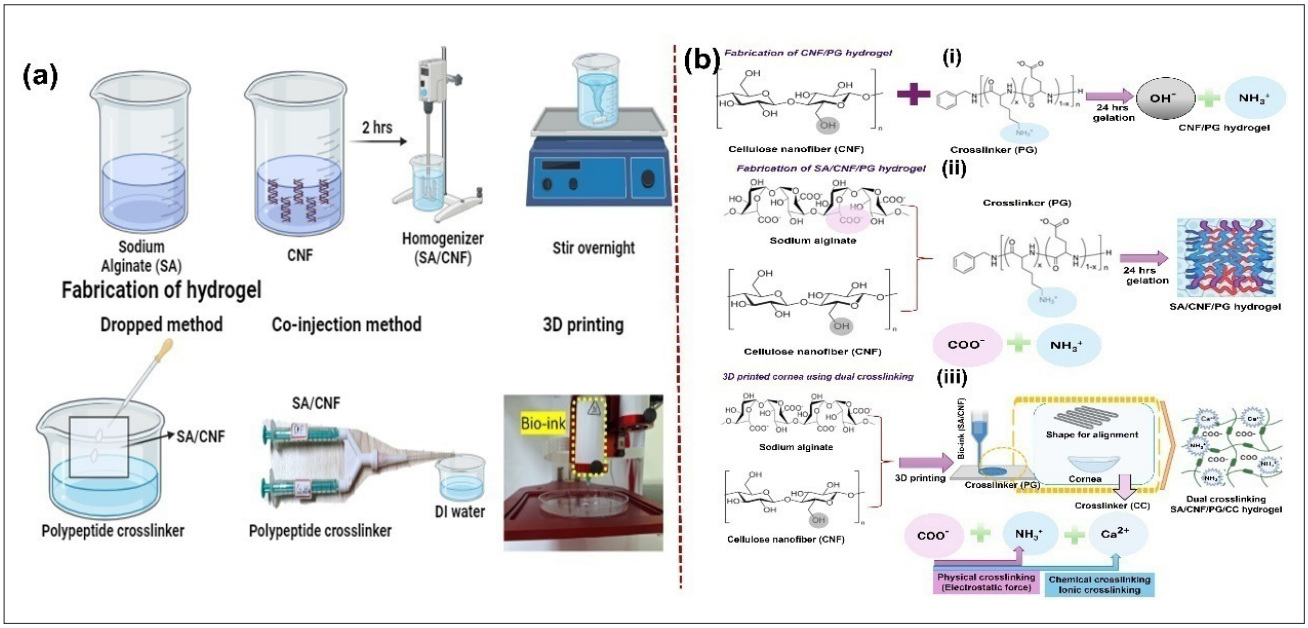

Figure 1. Preparation method of bio-ink with crosslinking mechanism before and after 3D printing. (a) Schematic for the preparation of solutions and bio-inks for the fabrication of hydrogel. (b) Crosslinking mechanism of the CNF/PG hydrogel (i), crosslinking mechanism of the SA/CNF/PG hydrogel (ii), 3D -printed dual crosslinking mechanism of the SA/CNF/PG/CC hydrogel (iii). Abbreviations: CC: calcium chloride; CNF: cellulose nanofibers; PG: poly-L-lysine-co-L-glutamic acid ($PLL_{80}GA_{20}$); SA: sodium alginate.

The mechanical properties of the hydrogels are presented in Figure 2a–d, with detailed parameters tabulated in Table 2**,** including the water content calculated by **Equation S1** (see Supplementary File). All hydrogels demonstrated a water content exceeding 96%, indicating their hydrophilic nature and potential suitability for tissue engineering applications. Figure 2a shows the viscoelastic behavior of the hydrogels, where higher viscosity indicates increased crosslink density. In contrast, decreased viscosity suggests fewer crosslinks, which allows for easier flow. Fewer crosslinks reduce the interaction between polymer chains, increasing their mobility and lowering internal friction. Conversely, more crosslinks restrict the movement of polymer chains, increasing internal friction and, as a result, viscosity. The compositions of CNF/CC-1, CNF/CC-2, CNF/CC-3, CNF/PG-1, CNF/PG-2, and CNF/PG-3 displayed good viscosity, but printing was challenging due to the bundle structure of CNF, which caused clogging in the 3D printer needle. To address this, SA was introduced into the composite hydrogel, resulting in good printability with high viscosity. The SA/CNF/PG-1, SA/CNF/PG-2, and SA/CNF/PG-3 exhibited higher viscosity of 657.12 ± 12.89 Pa·s, 987.10 ± 10.21 Pa·s, and 1064.21 ± 40.12 Pa·s, respectively. Figure 2b presents the storage modulus of the fabricated hydrogel, which depends on the crosslink density and mechanism. The values of the storage modulus of CNF/CC-1, CNF/CC-2, and CNF/CC-3 were 4.74 ± 0.26 kPa, 8.86 ± 1.46 kPa, and 20.07 ± 1.33 kPa, respectively. For the PG-containing crosslinker (SA/CNF/PG-1 to SA/CNF/PG-6), the storage modulus ranged from 19.44 ± 0.53 kPa to 87.18 ± 0.21 kPa, showing higher values than those with CC crosslinker. To investigate and confirm the effect of enhanced ionic crosslinking on mechanical strength, as shown in Figure S4d with corresponding values tabulated in Table S1, the mechanical properties of hydrogel can be significantly enhanced by increasing the degree of ionic crosslinking between SA and CC. The storage modulus can be enhanced through the precise regulation of the concentrations of Ca^{2+} as effective charge concentrations (6.25, 12.25, and 25 mM). The storage modulus of the produced hydrogel depends upon the crosslink density and mechanism. The storage modulus values for SA/CC-1, SA/CC-2, and SA/CC-3 were 18.31 ± 1.39 kPa, 38.01 ± 0.89 kPa, and 42.76 ± 0.52 kPa, respectively. The dual crosslinking mechanism, involving ionic interactions between CNF and CC and electrostatic interactions between CNF and PG, significantly enhanced the mechanical strength of hydrogen. In this process, Ca^{2+} from CC interact with negatively charged hydroxyl groups on CNF, forming ionic bonds that strengthen and stabilize the CNF network. Additionally, electrostatic interactions between CNF and PG further contribute to crosslinking. The PG participates in the network formation; however, its contribution to the storage modulus is far less pronounced than ionic crosslinking provided by Ca^{2+}. Whereas PG may participate in some physical interactions with both

the alginate and CNF components, these interactions are much weaker than the ionic bonds formed by the Ca^{2+}. Therefore, the substantial improvement in the storage modulus observed in the SA/CNF/PG/CC system cannot be explained solely by the presence of PG. The main factor contributing to the increased storage modulus in the SA/CNF/PG/CC systems is the presence of Ca^{2+}, which provides ionic crosslinks within the SA matrix. These CC are believed to form a complex network of strong ionic bonds with the guluronic acid in SA, significantly reinforcing the rigidity of the gel network. When the Ca^{2+} crosslink with the SA chains in the SA/CNF/PG/CC system, they form a so-called "egg-box" structure with the G-blocks, resulting in a compact and highly crosslinked network.[37] This increased crosslinking decreases the moving ability of the polymer chains, leading to greater stiffness and a higher storage modulus. In contrast, the SA/CNF/PGsystem, lacking Ca^{2+}, is stabilized solely through weaker physical interaction among SA, CNF, and PG. The absence of ionic crosslinking provided by Ca^{2+} results in a more flexible polymer network with reduced rigidity, leading to a lower storage modulus in comparison to GA/CNF/(EP–g-GMA). While the Ca^{2+} in the SA/CNF/PG/CC material offers multiple ways to enhance the storage modules, such as forming a denser network structure and increasing the crosslinking density. Therefore, the ionic crosslinking process develops a more rigid and densely packed structure, restricting the mobility of polymer chains and CNFs within the matrix. As a result, the material exhibits greater resistance to deformation under shear stress, leading to an improved storage modulus. Calcium ions significantly increase the crosslinking density within the SA matrix, directly enhancing its mechanical strength and ability to store elastic energy during deformation. This explains why the storage modulus is much higher in SA/CNF/PG/CC than in SA/CNF/PG.

Figure 2c shows the evidence of the higher storage modulus of the 3D-printed SA/CNF-containing hydrogels, where dual crosslinking hydrogels improved mechanical strength by more than two orders of magnitude with the same concentration as PG crosslinkers. The SA/CNF/PG/CC-1, SA/CNF/PG/CC-2, and SA/CNF/PG/CC-3 compositions exhibited storage modulus of 2360 ± 125.78 kPa, 4065 ± 109.23 kPa, and 7065 ± 129.32 kPa, respectively. These behaviors could be attributed to the molecular weight and chemical composition of PG. First, due to their polymeric structure, the size of PG is more than ten times larger than metal cations, contributing to stronger interactions. Second, hydrogen bond provides an additional contact force between SA/CNF and PG. The carbonyl groups on PG act as hydrogen bond acceptors, interacting with the hydroxyl groups of CNF, while the amine groups on PG function as hydrogen bond donors, interacting with carbonyl or hydroxyl groups. These interactions enable PG to efficiently connect SA/CNF, thereby increasing the stiffness of the network. Figure 2d illustrates the curve between storage modulus and oscillation strain in compression mode, demonstrating the viscoelastic properties of hydrogel. Various techniques have been developed for the fabrication of scaffolds, but most of these techniques are not very efficient due to complications in fabricating scaffolds that allow 3D healing and vascularization of blood vessels inside the scaffold.[38] The degradability of the scaffold material denies the need for its post-healing removal and hence negates the side effects related to residual material in the host. Yue et al.[39] reported the cellulose nanofibrils and SA as compound matrix based on double crosslinking strategy and introduced the boric acid/Ca^{2+}; through this method, they found the mechanical properties of 22.8 kPa. Zander et al.[41] have demonstrated that PEG-based hydrogels exhibit storage moduli from 20,000 to 28,000 Pa. *In vivo* studies, for example, illustrated that the addition of cellulose nanocrystals to maleic anhydride-grafted poly(lactic acid) scaffolds resulted in scaffolds with compressive strengths in the range of 0.025 and 0.4 MPa with elastic moduli in the range of 0.04 and 0.15 MPa.[42] Kim et al.[43] fabricated composite scaffolds using polymeric materials with nano-hydroxyapatite. The prepared scaffold improved mechanical properties, such as compressive modules at 4.5 MPa and tensile modulus at 27 MPa. The sample with 20 wt% hydroxyapatite/PLGA exhibited better mechanical properties, compressive strength of 2.31 MPa,[44] a very good viability of osteoblasts, and enhanced stability *in vitro* degradation. Significantly, the mass loss for the maleic anhydride-grafted poly(lactic acid) scaffold after one month was 46.5 wt%, while that for the cellulose nanocrystal-PLA scaffold was 40 wt%. According to the literature, our SA/CNF scaffolds establish the advantage of the usage of exclusively biocompatible and biodegradable materials, reducing the possibility of an inflammatory or immune response in relation to their synthetic counterparts. The environment, which provides ground totally conducive to the growth and regeneration of cells in terms of performance, is due to the biocompatibility of SA, in addition to the minimum molarity of PG that possesses 2,360 kPa of mechanical strength, along with degradation of 35.9% in 28 days. The fibrous structure of the corneal cells possibly matches or even outperforms the performance of collagen-based scaffolds conventionally used. The SA/CNF scaffold, in summary, presently shows a very good balance of transparency, strength, and biocompatibility, with much promise in comparison to other test materials in corneal tissue engineering.

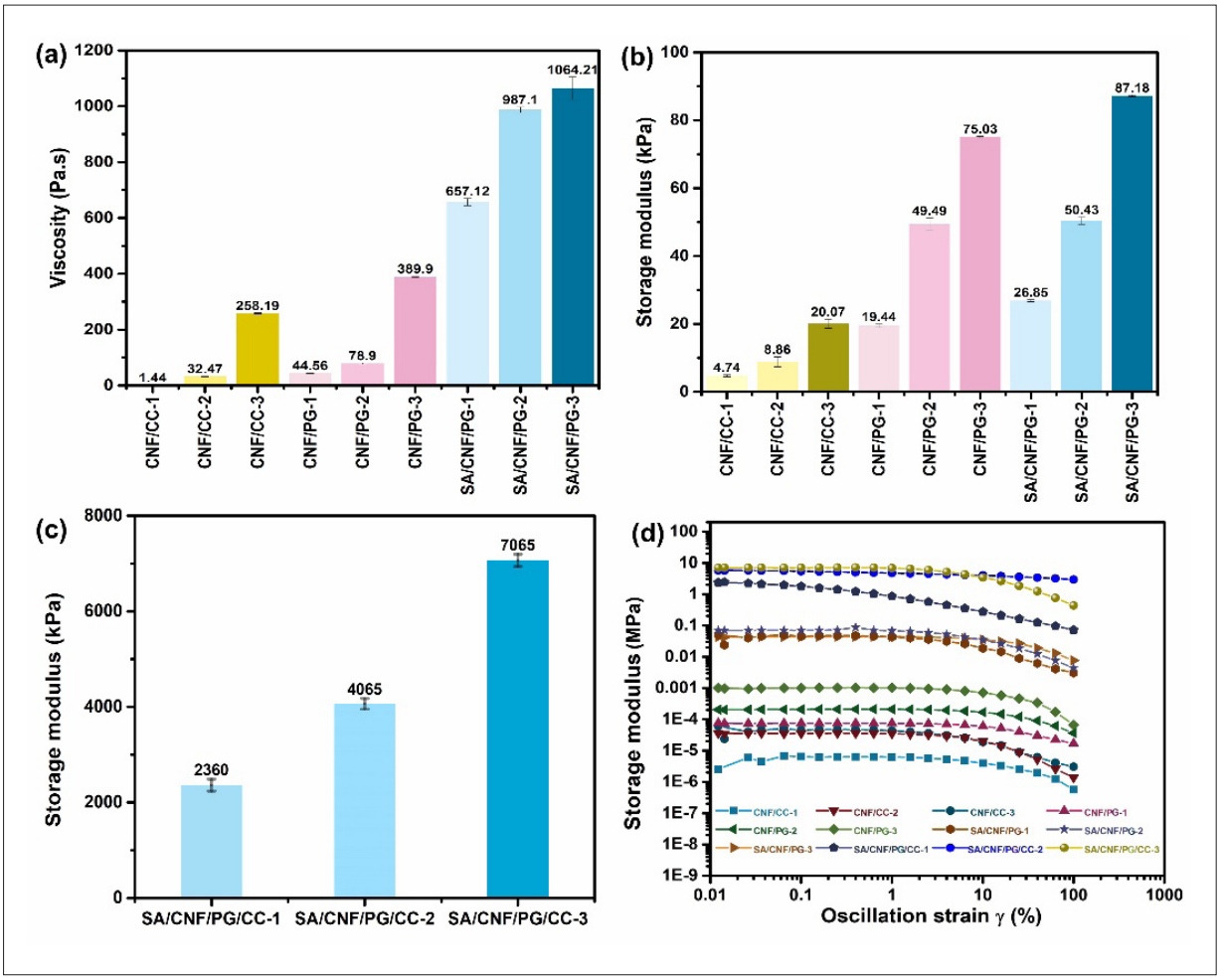

Figure 2. Mechanical properties of the hydrogel before and after printing. (a) Viscosity of the hydrogel. (b, c) Storage modulus of the hydrogel (b) andt he 3D-printed cornea (c), respectively. (d) Viscoelastic behavior of the hydrogel and 3D-printed cornea. Abbreviations: CC: calcium chloride; CNF: cellulose nanofibers; PG: poly-L-lysine-co-L-glutamic acid ($PLL_{80}GA_{20}$); SA: sodium alginate.

Table 2. Mechanical properties of composite hydrogel and 3D-printed hydrogel

Sample code	Viscosity (Pa·s) (n = 3)	Water content (wt%)	Storage modulus G' (kPa) (n = 3)
CNF/CC-1	1.44 ± 0.45	98.32 ± 0.14	4.74 ± 0.26
CNF/CC-2	32.47 ± 1.4	97.10 ± 0.20	8.86 ± 1.46
CNF /CC-3	258.19 ± 1.78	96.18 ± 0.70	20.07 ± 1.33
CNF/PG-1	44.56 ± 1.1	98. 67 ± 0.20	19.44 ± 0.53
CNF/PG-2	78.90 ± 1.9	98.42 ±0.43	49.49 ± 1.69
CNF/PG-3	389.90 ± 2.1	97.83 ± 0.50	75.03 ± 1.34
SA/CNF/PG-1	657.12 ± 12.89	97.09 ± 0.49	26.85 ± 0.28
SA/CNF/PG-2	987.10 ± 10.21	98.31 ± 0.12	50.43 ± 1.04
SA/CNF/PG-3	1064.21 ± 40.12	97.49 ± 0.25	87.18 ± 0.21
SA/CNF/ PG/CC-1	-	97.31 ± 0.17	2360 ± 125.78
SA/CNF /PG/ CC-2		96.09 ± 0.48	4065 ±109.23
SA/CNF/PG/CC-3		97. 67 ± 0.31	7065 ± 129.32

Abbreviations: CC: xalcium chloride; CNF: cellulose nanofibers; PG: poly-L-lysine-co-L-glutamic acid ($PLL_{80}GA_{20}$); SA: sodium alginate.

The alignment of the fabricated hydrogels is presented in Figure 3a–l. A polarized microscope was used to observe the fibrous hydrogel, and the alignment was measured in two modes: (i) cross-polar, and (ii) cross-polar + compensator, where the polarized and analyzer are perpendicular to each other so that birefringent phases can be identified. The image resembles a standard optical microscope when the polarizer and analyzer are aligned in the same polarization direction. The mode reveals the shape and density variations between different phases of the hydrogel.[45] When a compensator is added, birefringent phases with varying orientations display different colors. In Figure 3a–b, the CNF/PG-1 hydrogel fabricated using the droppred method shows a fibrous structure under cross-polar light, but no orientation was observed after adding the compensator, as indicated by the blue and orange colors in the image. Figure 3c–d shows a sample fabricated by the co-injection method, displaying a thin and fibrous morphology under cross-polar light. After adding the compensator, an orange color was observed, indicating the hydrogel's alignment in the southeast direction and confirming a well-aligned hydrogel structure. Figure 3a demonstrates that the hydrogels containing SA/CNFs, made using the dropped method, exhibited a non-uniform microstructure under cross-polar light. This uneven surface may result from the instability caused by the dropped method and the chemical structure of the PG, which contributed to hydrogen bonding. When the compensator was added (Figure 3b), the hydrogel exhibited birefringence, but no clear alignment was observed, as indicated by the blue and orange colors typically used to label orientations (northeast-southwest or northwest-southeast). In Figure 3e–f, the SA/CNF/PG-1 hydrogel, fabricated using the co-injection method, shows an uneven and thick morphology under cross-polar light, likely due to the higher viscosity of SA-containing hydrogel after gelation. Although no orientation was observed in the dropped method, the fibrous structure was evident. Figure 3g–h exhibits the aligned hydrogel produced using the co-injection method, showing a rod-like structure and

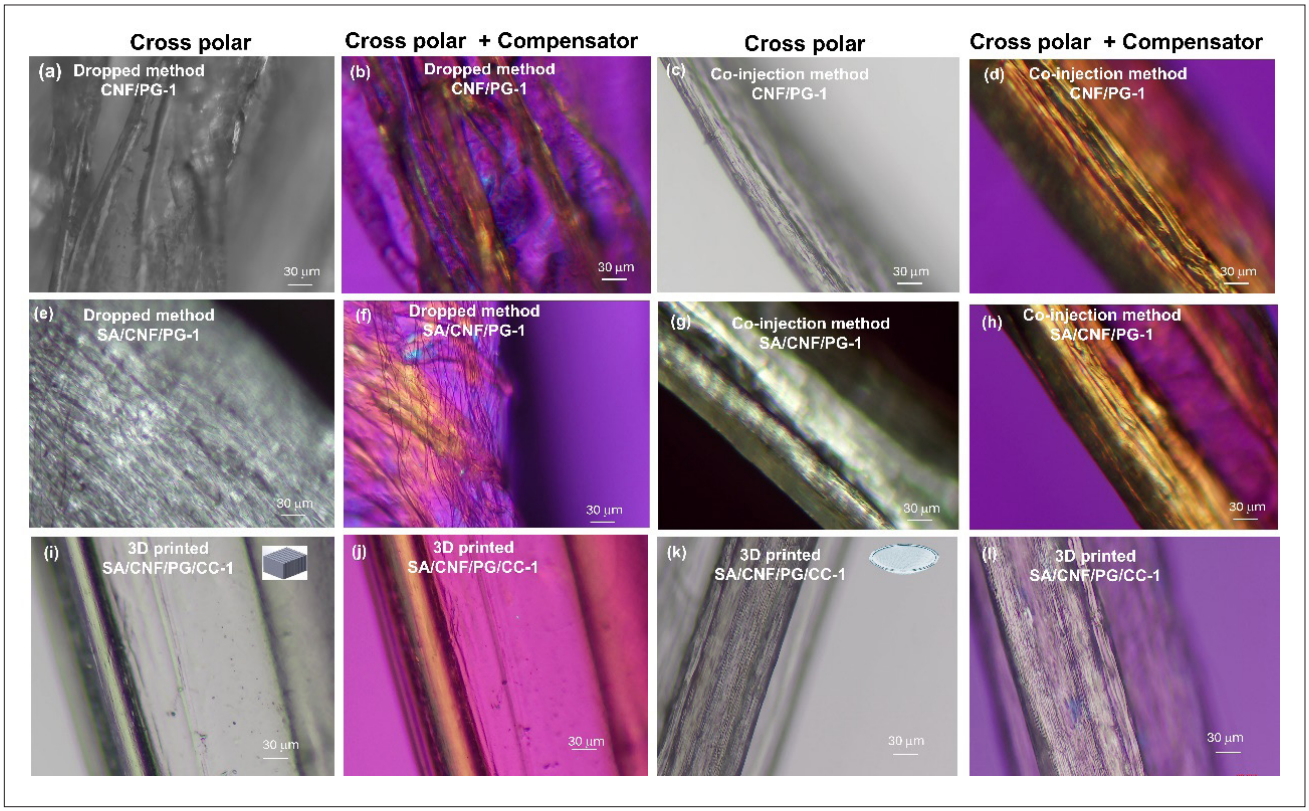

Figure 3. POM images to study orientation. (a) Cross-polar CNF/PG-1, and (b) cross-polar + compensator CNF/PG-1 by dropped method. (c) Cross-polar CNF/PG-1, and (d) cross-polar + compensator CNF/PG-1 by co-injection method. (e) Cross-polar SA/CNF/PG-1, and (f) cross-polar + compensator SA/CNF/PG-1 by dropped method. (g) Cross-polar SA/CNF/PG-1, and (h) cross-polar + compensator SA/CNF/PG-1 by co-injection method. (i) Cross-polar SACNF/PG/CC-1, and (j) cross-polar + compensator SA/CNF/PG/CC-1 by 3D printing of hydrogel in parallel shape. (k) Cross-polar SA/CNF/PG/CC-1, and (l) cross-polar + compensator SA/CNF/PG/CC-1 by 3D printing of hydrogel in cornea shape. Magnification: ×100__. Abbreviations: CC: calcium chloride; CNF: cellulose nanofibers; PG: poly-L-lysine-co-L-glutamic acid ($PLL_{80}GA_{20}$); SA: sodium alginate.

uniformity in the fiber-containing hydrogel. This material holds significant promise for future applications in tissue engineering; it demonstrates how an effectively high-aspect ratio of CNF can align during the extrusion process. Figure 3i–j shows the 3D-printed SA/CNF/PG/CC-1 hydrogel in a rectangular shape, confirming the hydrogel's alignment and even morphology after the printing process. Finally, Figure 3k–l displays the 3D-printed cornea hydrogel undercross-polar mode and cross-polar + compensator modes, revealing a very thin, uniform hydrogel with good orientation. These results are promising for cornea applications, as the hydrogel provides high mechanical strength, and replicates the lamellar structure present within the cornea.

The most important property of the cornea is its transparency, as it refracts light onto the lens before it reaches the retina. To evaluate this property in the hydrogel-based 3D-printed cornea, the transmittance of PG solutions (6.25, 12.25, and 25 mM), CNF, and SA were measured both before and after gelation. Initially, the transparency was about 90% in the 500–700 nm range before the gelation. However, the transparency reduced because of the aggregation of CNF after the gelation, which is highly fibrous and can reduce transparency. The transmission spectrum is recorded between 300 and 700 nm, as shown in Figure 4a–b. Based on the transmittance of 6.25, 12.25, and 25 mM, the 6.25 mM crosslinker concentration was selected for the 3D printing. As shown in Figure 4b, the transmittance of the SA/CNF composite is more than 90% in the visible range (400–700 nm). Figure 4c illustrates the transmittance of the 3D-printed artificial cornea, which achieved over 82% transparency in the visible range, with 86% transmittance at 550 nm. According to the previous literature[46-53] (Figure 4d), the transparency of the 3D-printed cornea has been improved

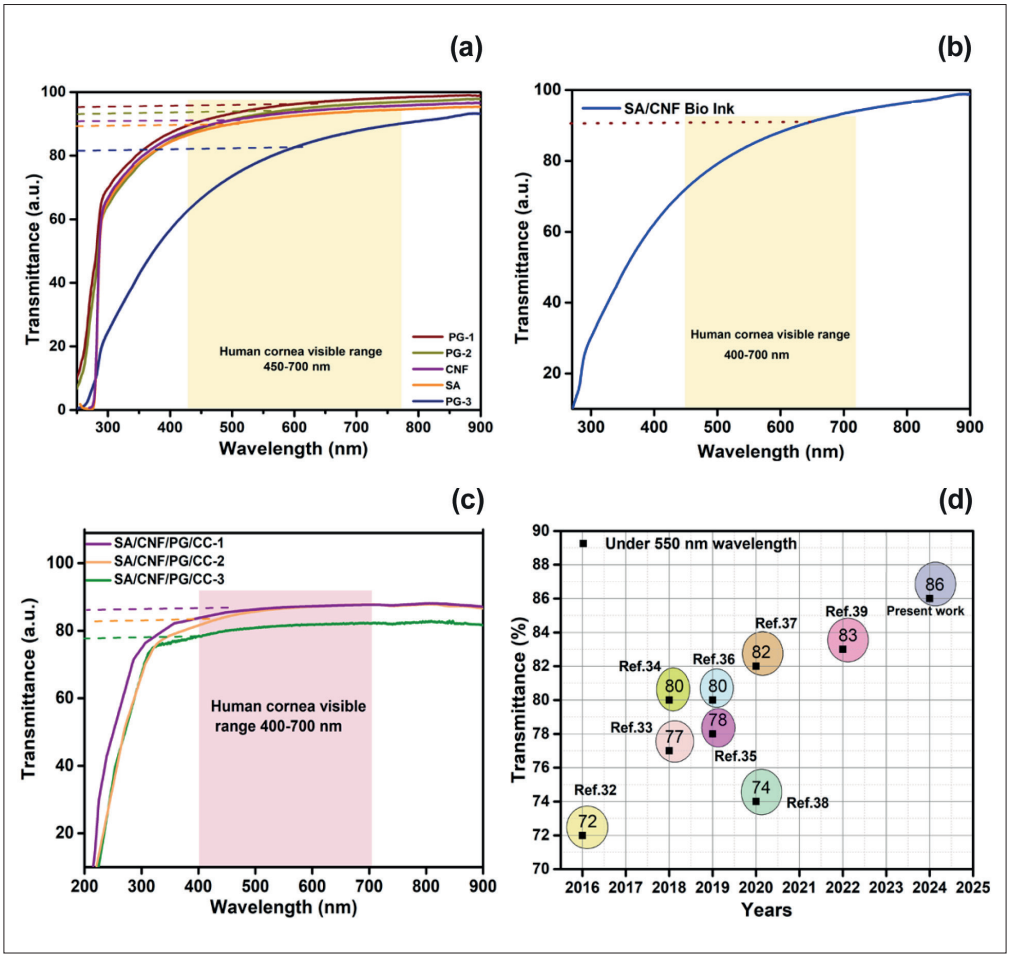

Figure 4. Optical properties of hydrogel before and after printing. (a–c) Transmittance of the solution before printing (a), the SA/CNF composite (b), and the printed artificial cornea (c). (d) Reported transmittance value at 550 nm from the literature.[XX] Abbreviations: CC: calcium chloride; CNF: cellulose nanofibers; PG: poly-L-lysine-co-L-glutamic acid ($PLL_{80}GA_{20}$); SA: sodium alginate.

by this formulation. It has been found that the optical transmittance in human cornea tissue typically ranges from 50% to 60% between 400 and 550 nm and from 60% to 75% between 550 and 700 nm.[54] In the 300–400 nm range, which corresponds to the UVA and UVB regions, transparency decreases, resulting in lower transmittance.

The bio-ink preparation involves two steps. First, an aqueous solution of SA (3 mL) and CNF (0.8 mL) was mixed at room temperature using a magnetic stir until completely dissolved, resulting in a homogeneous solution. In the second step, the PG aqueous solution was prepared. The compositional ratios between SA/CNF and PG were 1:2. The printing specifications for the parallel-shaped mold were optimized to ensure proper alignment of the hydrogel. After printing, a 6.25 mM CC solution was applied dropwise onto the printed structure. A dual crosslinking step was utilized during the 3D printing to maintain the structure integrity of the cornea shape. The surface morphology of 3D-printed cornea hydrogel was analyzed by SEM. For this analysis, a dried cornea-shaped hydrogel was used. As shown in Figure 5a–c, the surface shows the fibrous structure with uniformity, resulting in a high crosslink density. This uniform morphology was achieved due to the fibrous bio-ink. Figure 5d–f further demonstrates the alignment of the printed hydrogel with a fibrous structure. It also shows the 3D-printed cornea shape without fibrous material. The control group SA/PG/CC-1 exhibited no uniformity after printing, highlighting the importance of the fibrous material in achieving the desired structural characteristics, as shown in Figure S6a–c. The transparency and shape of the cornea are shown in Figure S6d.

Cytocompatibility of the SA/CNF/PG/CC-1, SA/CNF/PG/CC-2, and SA/CNF/PG/CC-3 compositions was studied, which were selected based on the mechanical properties of the hydrogels. PC-12 cells were cultured, and live dead cells assays were performed after 7 days. The detailed protocol of the cytotoxicity and cell viability given in section S2.8 (see Supplementary File). The cytotoxicity was performed by using Live/Dead assay on day 7 after seeding cells on the fabricated hydrogel. Two staining solutions, calcein-AM and ethidium homodimer-1 (EthD-1), were used for the Live/Dead assays, respectively. The green-colored cells indicate the live cells and the red ones are the dead cells. As shown in Figure 6a–f, the cornea is nontoxic at both low and high molarity of the PG. Furthermore, the dual crosslinking method enhanced cell adhesion due to the hydrogel's increased stability in

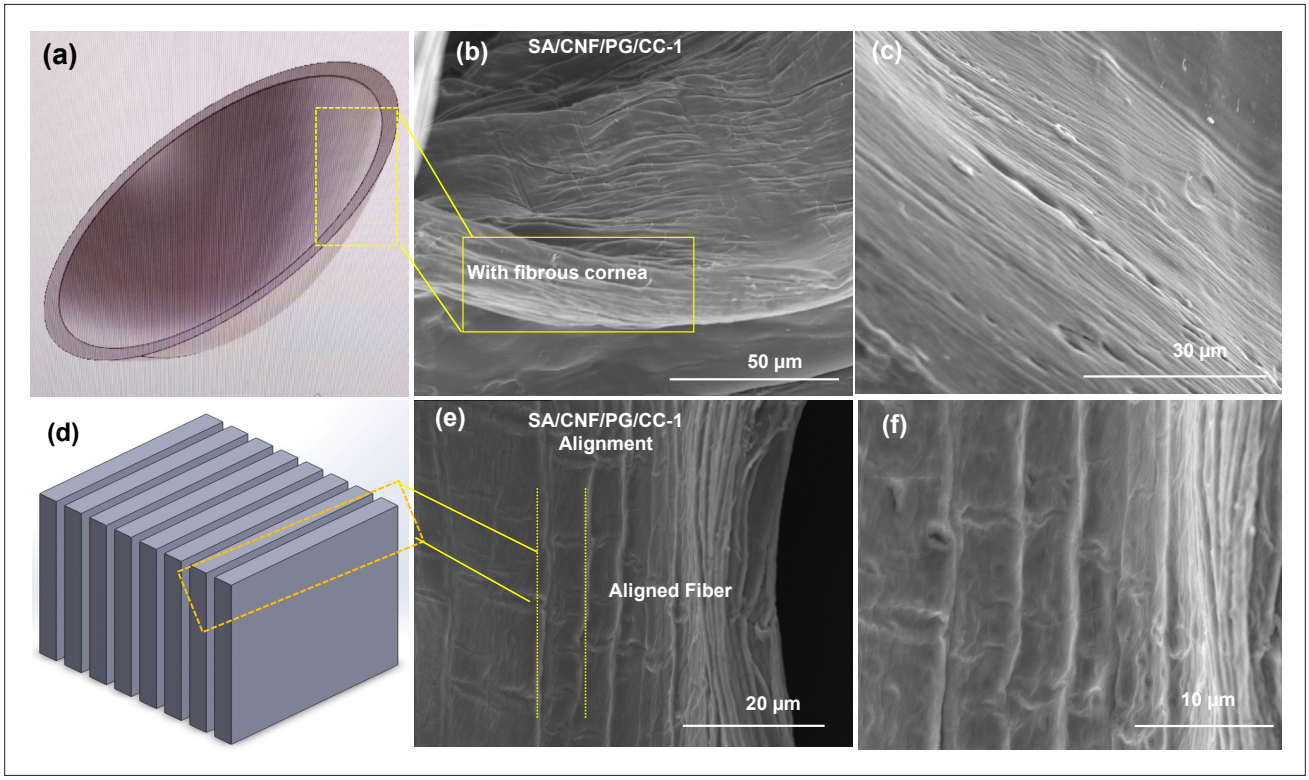

Figure 5. Surface morphology of the 3D-printed cornea and aligned shape. (a–c) Surface morphology of the 3D-printed cornea at 50 µm scale and 30 µm scale. (d–f) Aligned fibrous structure of the 3D-printed hydrogel at 50 µm scale and 30 µm. Magnification: b (x1000), c (x2500), e (x2000), f (x3000). Abbreviations: CC: calcium chloride; CNF: cellulose nanofibers; PG: poly-L-lysine-co-L-glutamic acid ($PLL_{80}GA_{20}$); SA: sodium alginate.

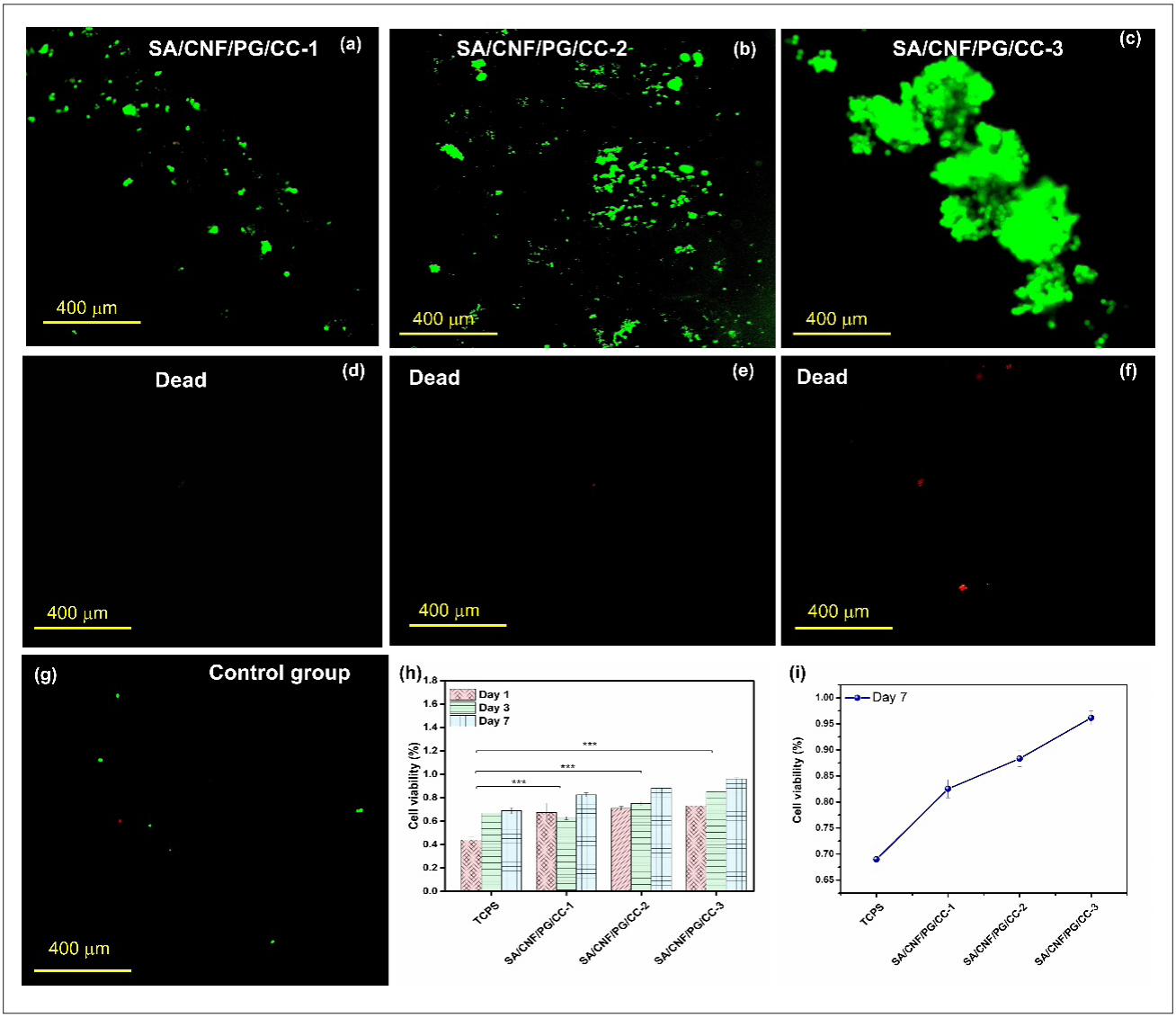

Figure 6. Cell culture studies. (a–c) Livecell study of the SA/CNF/PG/CC-1, SA/CNF/PG/CC-2, and SA/CNF/PG/CC-3 hydrogels. (d–f) Dead cell study of the SA/CNF/PG/CC-1, SA/CNF/PG/CC-2, and SA/CNF/PG/CC-3 hydrogels. (g) Overlay of the control group. (h) Cell viability study of SA/CNF/PG/CC-1, SA/CNF/PG/CC-2, and SA/CNF/PG/CC-3 hydrogels on days1 ,3, and 7, where $P < 0.001$. (i) Comparison of cell viability of SA/CNF/PG/CC-1, SA/CNF/PG/CC-2, and SA/CNF/PG/CC-3 hydrogels on day 7. Abbreviations: CC: calcium chloride; CNF: cellulose nanofibers; PG: poly-L-lysine-co-L-glutamic acid ($PLL_{80}GA_{20}$); SA: sodium alginate.

phosphate-buffered saline (PBS). The hydrogel, containing PG crosslinkers, plays various critical roles in cell culture, particularly in supporting cell growth, differentiation, and function. The PG is composed of glutamate and lysine. Glutamate, an amino acid, influences various aspects of cellular metabolism and function, while lysine is essential to produce antibodies and other immune proteins, aiding immune cell cultures in generating these crucial proteins. Additionally, cell adhesion was improved by the incorporation of PG, which enhanced the interaction between the scaffold and the cells, providing a more favorable environment for cell attachment and proliferation. Based on the results, we conclude that the cornea is biocompatible at the highest effective PG concentration of 25mM. The images show less dead cells because the PC12 cell line employed in this research is derived from a rat adrenal tumor called a pheochromocytoma, which is less vulnerable to cell death. These cells thrive in a controlled environment to grow, for instance, in a high-glucose RPMI-1640 medium supplemented with horse serum and fetal bovine serum. Optimal culture conditions, such as a temperature of 37°C and a CO_2 concentration of 5% along with saturating humidity composition, contribute to enhanced cell survival and decreased cell death rates

in laboratory settings. The cells tend to form clusters and exhibit viability under confluence levels over extended periods of time. When utilizing hydrogel after a week's time frame, for instance, a noticeable decrease in cell mortality would be observed, which sustains their longevity. A not-too-crowded environment, with cells in the culture setting and space and resources for them to grow without feeling overwhelmed or strained, results in a decrease in cell death rates. Figure 6g shows the images of the control group obtained from each specimen (n = 3), which were used for analysis and compared to those cultured on tissue culture polystyrene (TCPS) as a control. The overlay image shows the adhesion of cells with live and dead cells. In general, two ways prevail to categorize a material as low-cytotoxic or biocompatible. The first condition is that the cell viability needs to be over 1 on days 3 and 7. The second condition is that the percentage of live cells should be more than 50%. Generally, low cytotoxicity is observed in the various combinations of synthetic polymers such as the hydrogels with SA/PG/CNF/CC-1 prepared via dual crosslinking. Results from the alamarBlue cell viability test indicate that these constructed objects, through the gel, increased the viability rate from 67% on day 1 to 82% for the SA/PG/CNF/CC-1 hydrogel, from 70% to 88% for the SA/PG/CNF/CC-2 hydrogel, and from 73% to 96% for the SA/PG/CNF/CC-3 hydrogel, with the rate calculated using **Equation S2** (see Supplemetary File). In contrast, hydrogels produced with reduced concentration also evidenced the fact that, due to over 50% cell viability, they boast higher cell viability rates compared to others. The ANOVA test showed the most considerable differences in cell density among the three timepoints recorded in this study, *i.e.*, a significant increase of live cell density from 67% on day 3% to 96% on day 7 for SA/PG/CNF/CC-1, SA/PG/CNF/CC-3, and SA/PG/CNF/CC-3 hydrogels, with respect to control samples (Figure 6h). The SA/PG/CNF/CC-1 hydrogel featured a 67% increase in cell density with respect to control (P<0.001), and the SA/PG/CNF/CC-3 hydrogel showcased a 96% increase with respect to control (P<0.001). From the ANOVA test results, the P-values recorded are less than 0.001. The concentration of PG is important for affecting cell viability in the hydrogel lattice, possibly through elastic modulus and cell adhesion to the matrix. The Live/Deadcell viability assay results further confirm the observations made based on the alamarBlue staining results, indicating a high density of live cells, with a 96% increase of live cell number in the SA/CC/PG/CNF-3 hydrogel, suggesting that 25 mM of SA/CC/PG/CNF-3 is not only cytocompatibility but also non-toxic to the material. However, contraryto the alamarBlue findings, Live/Deadassay showed that in crosslinked PG hydrogels, cell viability was significantly affected by PG concentration since only the hydrogels containing the least amount of PG were less attaches the cells. Based on the cell viability study by Paul et al.[55] that poly-L-lysine is somewhat toxic to the cells and mammals, we argue that very low levels of lysine prove biocompatible for the cells. Also, Paul et al.[56] demonstrated that culturing on variable cationic polyelectrolyte concentration-coated surfaces would trigger the initiation of apoptosis in HepG2 cells. Figure 6i shows that the cell viability increased with the molarity of PG in the SA/CNF/PG/CC-1, SA/CNF/PG/CC-2, and SA/CNF/PG/CC-3 hydrogels on day 7.

The degradation study was conducted over 1.524 days using dried hydrogel scaffolds, and the detailed explanations are presented in section S2.9 (see Supplementary File). Figure 7a displays the degradation rates of scaffolds containing the PG crosslinker. The data revealed that CNF/PG-1, CNF/PG-2, and CNF/PG-3 hydrogels exhibited significant weight loss within a shorter duration. Specifically, the CN/PG-1 degraded by 14%, while the SA/CNF/PG/CC-1 hydrogel at same molarity degraded by only 7.87% after 3 days. This difference is attributed to the higher crosslink density in the SA/CNF/PG/CC-1 hydrogel than in the CNF-based hydrogel. The CNF/PG-1 hydrogel, being softer and thinner, degraded more rapidly compared to the SA-based hydrogel.

The degradation curve shows that the SA/CNF/PG/CC-1 composite hydrogel degraded by 28% after 21 days, while CNF/PG-1 degraded by 45%, and the degradation rate was calculated by **Equation S3**. Previous studies have reported that the SA containing hydrogel typically degraded by 35.9%.[57] The results indicate that incorporating SA can effectively reduce the degradation rate of porous scaffolds, likely due to the increased crosslink density and the formation of an interpreting network. Figure 7b, c, e, and f show the surface morphology of the hydrogel before and after degradation, clearly illustrating the degradation of the scaffold. Figure 7d presents a comparative analysis of the degradation percentages. The SA/CNF scaffold primarily comprises natural biocompatible polymers, significantly reducing the risk of immune rejection or inflammatory reactions. This unique attribute makes it suitable for long-term tissue integration in corneal implants and tracheal stents. Another important advantage is their biodegradability; the scaffold degrades progressively over time as it is replaced by host tissue, eliminating the need for surgical removal, both for tracheal stents and potentially for corneal applications. The intrinsic properties of nanofibers, including their antimicrobial action and controlled degradation, can reduce post-surgical infection or other complications often associated with synthetic scaffolds. However, there are limitations to consider. The structural stability of the SA/CNF ink could present a disadvantage. While the scaffold initially exhibits

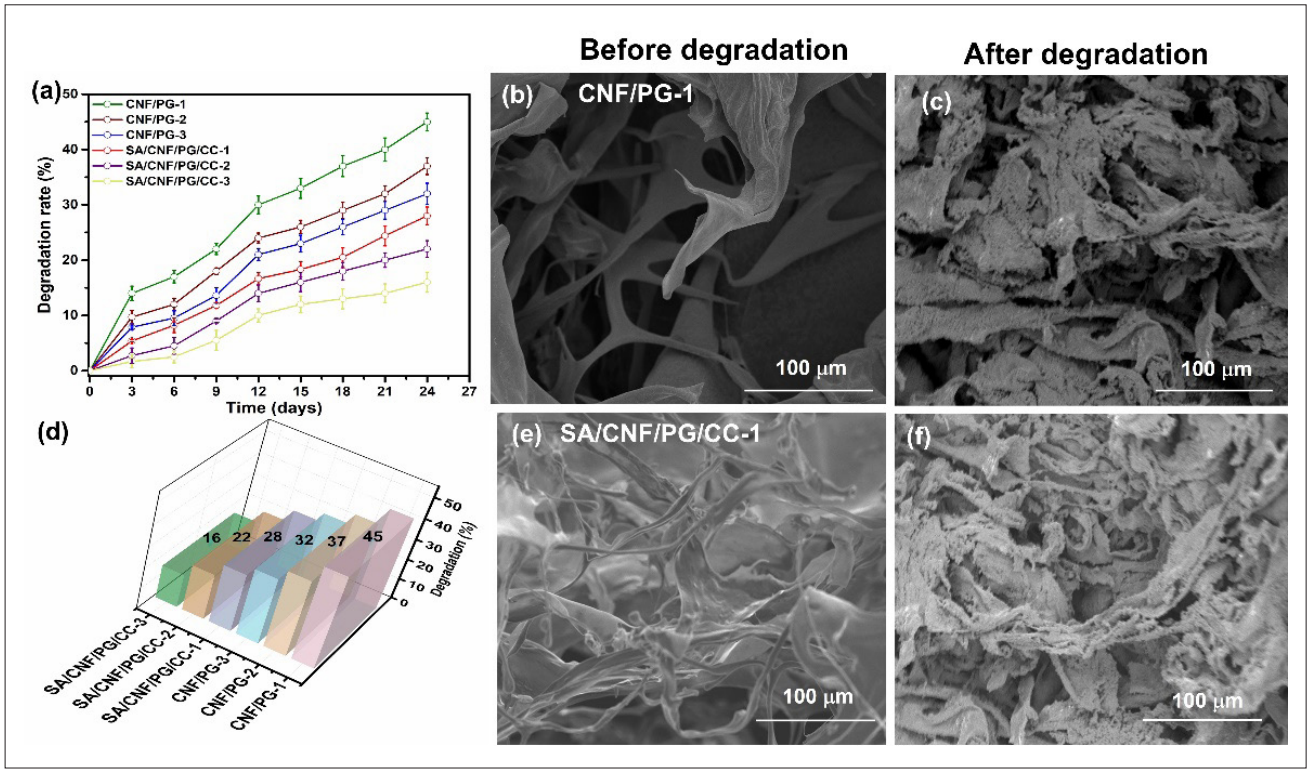

Figure 7. Degradation studies (a) Degradation study of CNF/PG-1, CNF/PG-2, CNF/PG-3, SA/CNF/PG/CC-1, SA/CNF/PG/CC-2, and SA/CNF/PG/CC-3 hydrogels over 3, 6, 9, 12, 15, 18, 21, and 24 days. (b,c) Surface morphology of CNF/PG-1 before (b) and after degradation (c), respectively. (d) Comparison of the hydrogel's degradation level. (e, f) Surface morphology of SA/CNF/PG/CC-1 before (e) and after degradation (f), respectively. Abbreviations: CC: calcium chloride; CNF: cellulose nanofibers; PG: poly-L-lysine-co-L-glutamic acid ($PLL_{80}GA_{20}$); SA: sodium alginate.

a good balance of flexibility and strength, questions may arise regarding its durability in mechanically demanding environments, such as the interior of the trachea, over extended periods. Additionally, for corneal applications, the sustainability of performance during continuous eye movements and exposure to tears and light may pose further challenges.

Rheological tests and preliminary degradation results gave promising signs for an assurance in stability and integrity of the SA/CNF artificial cornea scaffold. Degradation studies have been performed in which, under controlled conditions, the SA/CNF scaffold indeed degrades, an important aspect of its function in the healing of the cornea. Given the seemingly promising initial results on the SA/CNF artificial cornea scaffold, our current understanding of this material holds great promise for future clinical trials.

The cornea is a highly hydrated fibrous tissue, containing about 78% water. Individual collagen fibrils have a diameter in the range of 22.5–35 nm, with inter-fibril spacing of about 41.5 nm. The collagen fibrils in one lamella lie orthogonally to adjacent lamellae. This precise arrangement and hydration give the cornea particular mechanical strength, allowing it to refract light by 80%. In one of the studies done on normal subjects, Young's modulus was stated to be 0.29 ± 0.06 MPa. In this study, we successfully attained the values required for functionality of a native cornea, as per the literature currently available concerning this subject.[58]

4. Conclusion

In this study, we successfully synthesized the PG with a molecular weight of 47 kDa and developed a fibrous bio-ink (SA/CNF) that achieved high mechanical strength, exhibiting a storage modulus of 2360 kPa after dual crosslinking. The initial transparency of the bio-inks was over 92%, and this was maintained at 86% after 3D-printing the cornea. The dual crosslinking process significantly improved both the storage modulus and degradation rate of the hydrogel. Cell culture results demonstrated that the fabricated hydrogel at both low and high molarity exhibited good cytotoxicity and excellent biocompatibility. Additionally, cell adhesion improved due to PG enhancing the interaction between the scaffold and the cells, providing a more favorable environment for attachment and proliferation. Cell viability data showed that more than 50% of cells were viable after

days 1, 3, and 7. The highly statistically significant results (*i.e.*, $P < 0.001$) attained in the ANOVA test indicate that the cell viability rate stood astoundingly at 96% in the SA/CNF/PG/CC-3 hydrogels on day 7. Degradation analysis of the SA-containing hydrogel revealed a degradation rate of 35.9% over 28 days, indicating the hydrogel's stability. To the best of our knowledge, no prior studies have exhibited 3D-printed artificial cornea using aligned fibrous bio-ink. The inclusion of PG effectively improved the mechanical strength of the hydrogel, allowing it to be implanted in the cornea without causing an inflammatory effect. This work further illustrates that the low molarity PG can easily crosslink after 3D printing, enhancing surface morphology and mechanical properties without compromising transparency. In the future, 3D-printed cornea could potentially be used for clinical applications.

Acknowledgments

The authors are thankful to Yu-Ting Lin for helping during cell experiments.

Funding

The financial support from National Science and Technology Council (NSTC), Taiwan (Grant Nos. 111-2221-E-131-019-MY3, 111-2221-E-182-040-MY3, 111-2221-E-002-029, 112-2622-E-131-001, 112-2628-E-131-001-MY4, 113-2628-E-182-001-MY4), is highly appreciated. The author expresses gratitude for the financial support provided by Chang Gung University (URRPD2N0011 and URRPD2N0031).

Conflict of interest

The authors declare they have no conflicts of interests.

Author contributions

Conceptualization: Wei-Fang Su, Meng-Fang Lin, Yu-Ching Huang
Formal analysis: Priyanka Chaudhary, Chun-Yu Chang, Ting-Han Lin, Ming-ChungWu
Funding Acquisition: Ming-Chung Wu, Meng-Fang Lin, Yu-Ching Huang
Investigation: Priyanka Chaudhary, Chia-Hsien Lee
Methodology: Priyanka Chaudhary, Dun-Heng Tan
Resource: Meng-Fang Lin, Yu-Ching Huang
Supervision: Wei-Fang Su, Meng-Fang Lin, Yu-Ching Huang
Writing – original draft: Priyanka Chaudhary, Meng-Fang Lin
Writing – review & editing: Wei-Fang Su, Meng-Fang Lin, Yu-Ching Huang

Ethics approval and consent to participate

Not applicable.

Consent for publication

Not applicable.

Availability of data

The data included in this study is available upon reasonable request from the corresponding author.

References

1. Kong B, Chen Y, Liu R, et al. Fiber reinforced GelMA hydrogel to induce the regeneration of corneal stroma. *Nat Commun.* 2020;11(1):1435. doi: 10.1038/s41467-020-14887-9.
2. Ahn J-I, Kuffova L, Merrett K, et al. Crosslinked collagen hydrogels as corneal implants: effects of sterically bulky vs. non-bulky carbodiimides as crosslinkers. *Acta biomaterialia.* 2013;9(8):7796-7805. doi: 10.1016/j.actbio.2013.04.014.
3. Griffith M, Hakim M, Shimmura S, et al. Artificial human corneas: scaffolds for transplantation and host regeneration. *Cornea.* 2002;21:S54-S61. doi: 10.1097/01.ico.0000263120.68768.f8.
4. Gain P, Jullienne R, He Z, et al. Global survey of corneal transplantation and eye banking. *JAMA ophthalmology.* 2016;134(2):167-173. doi: 10.1001/jamaophthalmol.2015.4776.
5. Bentley E, Murphy CJ, Li F, Carlsson DJ, Griffith M. Biosynthetic corneal substitute implantation in dogs. *Cornea.* 2010;29(8):910-916. doi: 10.1097/ICO.0b013e3181c846aa.
6. Liu L, Kuffová L, Griffith M, et al. Immunological responses in mice to full-thickness corneal grafts engineered from porcine collagen. *Biomaterials.* 2007;28(26):3807-3814. doi: 10.1016/j.biomaterials.2007.04.025.
7. San Choi J, Williams JK, Greven M, et al. Bioengineering endothelialized neo-corneas using donor-derived corneal endothelial cells and decellularized corneal stroma. *Biomaterials.* 2010;31(26):6738-6745. doi: 10.1016/j.biomaterials.2010.05.020.
8. Armitage WJ, Goodchild C, Griffin MD, et al. High-risk corneal transplantation: recent developments and future possibilities. *Transplantation.* 2019;103(12):2468-2478. doi: 10.1097/TP.0000000000002938.
9. Grigoryan B, Paulsen SJ, Corbett DC, et al. Multivascular networks and functional intravascular topologies within biocompatible hydrogels. *Science.* 2019;364(6439):458-464. doi: 10.1126/science.aav9750
10. Orash Mahmoud Salehi A, Heidari-Keshel S, Poursamar SA, et al. Bioprinted membranes for corneal tissue engineering: a review. *Pharmaceutics.* 2022;14(12):2797. doi: 10.3390/pharmaceutics14122797.

11. Alam F, Elsherif M, AlQattan B, et al. 3D printed contact lenses. *ACS Biomater Sci Eng.* 2021;7(2):794-803. doi: 10.1021/acsbiomaterials.0c01470

12. Alam F, Alsharif A, AlModaf FO, El-Atab N. 3D-printed smartwatch fabricated via vat photopolymerization for UV and temperature sensing applications. *ACS Omega.* 2024;9(13):14830-14839. doi: 10.1021/acsomega.3c07411.

13. Bernal PN, Delrot P, Loterie D, et al. Volumetric bioprinting of complex living-tissue constructs within seconds. *Adv Mater.* 2019;31(42):1904209. doi: 10.1002/adma.201904209

14. Patel AP, Wu EI, Ritterband DC, Seedor JA. Boston type 1 keratoprosthesis: the New York Eye and Ear experience. *Eye (Lond).* 2012;26(3):418-425. doi: 10.1038/eye.2011.325

15. Zhang X, Zhang X, Li Y, Zhang Y, et. Al. Applications of Light-Based 3D Bioprinting and Photoactive Biomaterials for Tissue Engineering. Materials. 2023;16(23):7461 doi: 10.3390/ma16237461

16. Riau AK, Venkatraman SS, Dohlman CH, Mehta JS. Surface modifications of the PMMA optic of a keratoprosthesis to improve biointegration. *Cornea.* 2017;36:S15-S25. doi: 10.1097/ICO.0000000000001352

17. Ma T-L, Yang S-C, Cheng T, et al. Exploration of biomimetic poly (γ-benzyl-l-glutamate) fibrous scaffolds for corneal nerve regeneration. *J Mater Chemy B.* 2022;10(33): 6372-6379. doi: 10.1038/s41536-017-0038-8

18. Islam MM, Buznyk O, Reddy JC, et al. Biomaterials-enabled cornea regeneration in patients at high risk for rejection of donor tissue transplantation. *NPJ Regen Med.* 2018;3(1):2. doi: 10.1038/s41536-017-0038-8

19. Mimura T, Amano S, Yokoo S, et al. Tissue engineering of corneal stroma with rabbit fibroblast precursors and gelatin hydrogels. *Mol Vis.* 2008;14:1819.

20. Crabb RA, Chau EP, Evans MC, Barocas VH, Hubel A. Biomechanical and microstructural characteristics of a collagen film-based corneal stroma equivalent. *Tissue Eng.* 2006;12(6):1565-1575. doi: 10.1089/ten.2006.12.1565

21. Lawrence BD, Marchant JK, Pindrus MA, Omenetto FG, Kaplan DL. Silk film biomaterials for cornea tissue engineering. *Biomaterials.* 2009;30(7):1299-1308. doi: 10.1016/j.biomaterials.2008.11.018

22. Gouveia RM, González-Andrades E, Cardona JC, et al. Controlling the 3D architecture of Self-Lifting Auto-generated Tissue Equivalents (SLATEs) for optimized corneal graft composition and stability. *Biomaterials.* 2017;121:205-219. doi: 10.1016/j.biomaterials.2016.12.023.

23. Wang S, Ghezzi CE, Gomes R, Pollard RE, Funderburgh JL, Kaplan DL. In vitro 3D corneal tissue model with epithelium, stroma, and innervation. *Biomaterials.* 2017;112:1-9. doi: 10.1016/j.biomaterials.2016.09.030

24. Dong H, Snyder JF, Williams KS, Andzelm JW. Cation-induced hydrogels of cellulose nanofibrils with tunable moduli. *Biomacromolecules.* 2013;14(9):3338-3345. doi: 10.1021/bm400993f

25. Yang J, Han C-R, Duan J-F, et al. Studies on the properties and formation mechanism of flexible nanocomposite hydrogels from cellulose nanocrystals and poly (acrylic acid). *J Mater Chem.* 2012;22(42):22467-22480. doi: 10.1039/C2JM35498E

26. Yu TY, Tseng YH, Wang CC, et al. Three-level hierarchical 3D network formation and structure elucidation of wet hydrogel of tunable-high-strength nanocomposites. *Macromol Mater Eng.* 2022;307(5):2100871. doi: 10.1002/mame.202100871

27. Rafat M, Li F, Fagerholm P, et al. PEG-stabilized carbodiimide crosslinked collagen–chitosan hydrogels for corneal tissue engineering. *Biomaterials.* 2008;29(29):3960-3972. doi: 10.1016/j.biomaterials.2008.06.017

28. Wang J, Gao C, Zhang Y, Wan Y. Preparation and in vitro characterization of BC/PVA hydrogel composite for its potential use as artificial cornea biomaterial. *Mater Sci Eng C.* 2010;30(1):214-218. doi: 10.1016/j.msec.2009.10.006

29. Brunette I, Roberts CJ, Vidal F, et al. Alternatives to eye bank native tissue for corneal stromal replacement. *Prog Retin Eye Res.* 2017;59:97-130. doi: 10.1016/j.preteyeres.2017.04.002

30. Nie X, Tang Y, Wu T, et al. 3D printing sequentially strengthening high-strength natural polymer hydrogel bilayer scaffold for cornea regeneration. *Regen Biomater.* 2024;11:rbae012.

31. Romo-Valera C, Guerrero P, Arluzea J, Etxebarria J, de la Caba K, Andollo N. Cytocompatibility and suitability of protein-based biomaterials as potential candidates for corneal tissue engineering. *Int J Mol Sci.* 2021;22(7):3648.

32. Liu J, Huang Y, Yang W, et al. Sutureless transplantation using a semi-interpenetrating polymer network bioadhesive for ocular surface reconstruction. *Acta Biomater.* 2022;153:273-286. doi: 10.1016/j.actbio.2022.09.049

33. Rastogi P, Kandasubramanian B. Review of alginate-based hydrogel bioprinting for application in tissue engineering. *Biofabrication.* 2019;11(4):042001. doi: 10.1088/1758-5090/ab331e

34. Logan CM, Fernandes-Cunha GM, Chen F, et al. In situ-forming collagen hydrogels crosslinked by multifunctional polyethylene glycol as a matrix therapy for corneal defects: 2-month follow-up in vivo. *Cornea.* 2023;42(1):97-104.

doi: 10.1097/ICO.0000000000003104

35. Raus RA, Nawawi WMFW, Nasaruddin RR. Alginate and alginate composites for biomedical applications. *Asian J Pharm Sci.* 2021;16(3):280-306. doi: 10.1016/j.ajps.2020.10.001

36. Zarrintaj P, Ghorbani S, Barani M, et al. Polylysine for skin regeneration: a review of recent advances and future perspectives. *Bioeng Transl Med.* 2022;7(1):e10261. doi: 10.1002/btm2.10261

37. Wang L, Zhang HJ, Liu X, et al. A physically cross-linked sodium alginate–gelatin hydrogel with high mechanical strength. *ACS Appl Polym Mater.* 2021;3(6):3197-3205. doi: 10.1021/acsapm.1c00404

38. Reddy MSB, Ponnamma D, Choudhary R, Sadasivuni KK. A comparative review of natural and synthetic biopolymer composite scaffolds. *Polymers.* 2021;13(7):1105. doi: 10.3390/polym13071105

39. Yue X, Deng W, Zhou Z, Xu Y, He J, Wang Z. Reinforced and flame retarded cellulose nanofibril/sodium alginate compound aerogel fabricated via boric acid/Ca2+ double cross-linking. *J Polym Environ.* 2023;31(3):1038-1050.

40. Zander ZK, Hua G, Wiener CG, Vogt BD, Becker ML. Control of mesh size and modulus by kinetically dependent cross-linking in hydrogels. *Adv Mater.* 2015;27(40):6283. doi: 10.1002/adma.201501822

41. Kim S-S, Park MS, Jeon O, Choi CY, Kim B-S. Poly (lactide-co-glycolide)/hydroxyapatite composite scaffolds for bone tissue engineering. *Biomaterials.* 2006;27(8):1399-1409. doi: 10.1016/j.biomaterials.2005.08.016

42 Donnaloja F, Jacchetti E, Soncini M, Raimondi MT. Natural and synthetic polymers for bone scaffolds optimization. *Polymers.* 2020;12(4):905. doi: 10.3390/polym12040905

43. Cui Y, Liu Y, Cui Y, Jing X, Zhang P, Chen X. The nanocomposite scaffold of poly (lactide-co-glycolide) and hydroxyapatite surface-grafted with L-lactic acid oligomer for bone repair. *Acta Biomater.* 2009;5(7):2680-2692. doi: 10.1016/j.actbio.2009.03.024

44. Wang S, Li T, Chen C, et al. Transparent, anisotropic biofilm with aligned bacterial cellulose nanofibers. *Adv Funct Mater.* 2018;28(24):1707491. doi: 10.1002/adfm.201707491

45. Wang X, Majumdar S, Soiberman U, et al. Multifunctional synthetic Bowman's membrane-stromal biomimetic for corneal reconstruction. *Biomaterials.* 2020;241:119880. doi: 10.1016/j.biomaterials.2020.119880

46. Kong B, Sun W, Chen G, et al. Tissue-engineered cornea constructed with compressed collagen and laser-perforated electrospun mat. *Sci Rep.* 2017;7(1):970. doi: 10.1038/s41598-017-01072-0.

47. Majumdar S, Wang X, Sommerfeld SD, et al. Cyclodextrin modulated type I collagen self-assembly to engineer biomimetic cornea implants. *Adv Funct Mater.* 2018;28(41):1804076. doi: 10.1002/adfm.201804076

48. Lei X, Jia Y-G, Song W, et al. Mechanical and optical properties of reinforced collagen membranes for corneal regeneration through polyrotaxane cross-linking. *ACS Appl Bio Mater.* 2019;2(9):3861-3869. doi: 10.1021/acsabm.9b00464

49. Zhang J, Sisley AM, Anderson AJ, Taberner AJ, McGhee CN, Patel DV. Characterization of a novel collagen scaffold for corneal tissue engineering. *Tissue Eng Part C Methods.* 2016;22(2):165-172. doi: 10.1089/ten.TEC.2015.0304

50. Long Y, Zhao X, Liu S, et al. Collagen–hydroxypropyl methylcellulose membranes for corneal regeneration. *ACS Omega.* 2018;3(1):1269-1275. doi: 10.1021/acsomega.7b01511

51. Fernandes-Cunha GM, Chen KM, Chen F, et al. In situ-forming collagen hydrogel crosslinked via multi-functional PEG as a matrix therapy for corneal defects. *Sci Rep.* 2020;10(1):16671. doi: 10.1038/s41598-020-72978-5

52. Lei M, Zhang S, Zhou H, et al. Electrical signal initiates kinetic assembly of collagen to construct optically transparent and geometry customized artificial cornea substitutes. *ACS Nano.* 2022;16(7):10632-10646. doi: 10.1021/acsnano.2c02291

53. Mallet JD, Rochette PJ. Wavelength-dependent ultraviolet induction of cyclobutane pyrimidine dimers in the human cornea. *Photochem Photobiol Sci.* 2013;12(8):1310-1318. doi: 10.1039/c3pp25408a.

54. Paul A, Eun C-J, Song JM. Cytotoxicity mechanism of non-viral carriers polyethylenimine and poly-l-lysine using real time high-content cellular assay. *Polymer.* 2014;55(20):5178-5188. doi: 10.1016/j.polymer.2014.08.043

55. Arnold Jr L, Dagan A, Gutheil J, Kaplan N. Antineoplastic activity of poly (L-lysine) with some ascites tumor cells. *Proc Natl Acad Sci.* 1979;76(7):3246-3250.

56. Liu S, Huang D, Hu Y, et al. Sodium alginate/collagen composite multiscale porous scaffolds containing poly (ε-caprolactone) microspheres fabricated based on additive manufacturing technology. *RSC Adv.* 2020;10(64):39241-39250. doi: 10.1039/d0ra04581k

57. Formisano N, van der Putten C, Grant R, et al. Mechanical properties of bioengineered corneal stroma. *Adv Healthc Mater.* 2021;10(20):2100972. doi: 10.1002/adhm.202100972.

ACCSCIENCE PUBLISHING

International Journal of Bioprinting

RESEARCH ARTICLE

Primitive regenerated-tissue evolution *in situ* after implantation of a 3D-printed tracheal graft

Sen-Ei Shai[1,2,3†*], Yi-Ling Lai[1†], Yi-Wen Hung[4,5], Chi-Wei Hsieh[6], Kuo-Chih Su[7], Chun-Hsiang Wang[7], Te-Hsin Chao[8], Yung-Tsung Chiu[9], Chia-Ching Wu[6,10], and Shih-Chieh Hung[11,12]

[1]Department of Surgery, Division of Thoracic Surgery, Taichung Veterans General Hospital, Taichung, Taiwan

[2]Department of Applied Chemistry, Faculty of Science and Technology, National Chi Nan University, Nantou, Taiwan

[3]Department of Medicine, Institute of Clinical Medicine, National Yang-Ming Chiao-Tung University, Taipei, Taiwan

[4]Animal Radiation Therapy Research Center, Central Taiwan University of Science and Technology, Taichung, Taiwan

[5]Terry Fox Cancer Research Laboratory, Translational Medicine Research Center, China Medical University Hospital, Taichung, Taiwan

[6]Department of Medicine, School of Medicine, National Cheng Kung University, Tainan, Taiwan

[7]Department of Medical Research, Three-Dimensional Printing Research and Development Group, Taichung Veterans General Hospital, Taichung, Taiwan

[8]Division of Colon and Rectal Surgery, Department of Surgery, Chiayi and Wangiao Branch, Taichung Veterans General Hospital, Chiayi, Taiwan

[9]Department of Medical Research and Education, Taichung Veterans General Hospital, Taichung, Taiwan

[10]Department of Cell Biology and Anatomy, College of Medicine, National Cheng Kung University, Tainan, Taiwan

[11]Integrative Stem Cell Center, China Medical University Hospital, Taichung, Taiwan

[12]Institute of New Drug Development, China Medical University, Taichung, Taiwan

[†]These authors contributed equally to this work.

***Corresponding author:**
Sen-Ei Shai
(sse@vghtc.gov.tw)

(This article belongs to the Special Issue: *3D printing for tissue engineering and regenerative medicine - Series 2*)

Citation: Shai SE, Lai YL, Hung YW, et al. Primitive regenerated-tissue evolution *in situ* after implantation of a 3D-printed tracheal graft. *Int J Bioprint*. 2025;11(1):614-630. doi: 10.36922/ijb.5178

Received: October 17, 2024
Revised: November 4, 2024
Accepted: November 12, 2024
Published Online: November 12, 2024

Copyright: © 2024 Author(s). This is an Open Access article distributed under the terms of the Creative Commons Attribution License, permitting distribution, and reproduction in any medium, provided the original work is properly cited.

Publisher's Note: AccScience Publishing remains neutral with regard to jurisdictional claims in published maps and institutional affiliations.

Abstract

Tissue-engineered trachea offers a potential solution for patients needing long-segment tracheal resections. In our research, robust neotissue growth, including cartilage, muscle, adipose, and glands, was observed on the external surface of three-dimensional (3D)-printed tracheal grafts transplanted into a 3-month-old large-scale porcine, noticeable after 7 days. This study is the first to categorize the regeneration stages in detail, aiming for a clearer understanding of the cell development process, as previous studies have not fully elucidated the mechanisms of chondrogenesis and glandogenesis. We have identified four stages of chondrogenesis based on chondrocyte numbers, protein expression, and perichondrium presence. Muscle cells evolved from a fibroblast-like state, confirmed by alpha-smooth muscle actin and smooth muscle-myosin heavy chain markers, while initial adipose tissue resembling brown fat diminished over time. Gland development, marked by a change in MUC5B expression, paralleled the findings in native trachea epithelium and submucosal glands. Transforming growth factor-β1 and type XII collagen were key indicators in the emerging neotissue post-transplant.

***Keywords*:** Primitive regenerated-tissue evolution; Vivid neotissue growth; Glandogenesis; Tracheal graft transplantation

1. Introduction

In the case of extensive tracheal resection, a variety of reconstructive options have been explored, ranging from autografts and allografts to prosthetics,[1–4] but none have been proven fully effective.[5] Consequently, tissue-engineering strategies are being rigorously investigated as viable alternatives. A sustainable, tissue-engineered trachea offers a potential solution for patients needing long-segment tracheal resections.[6] Research involving small animal models has contributed to the design of bioengineered tracheas and grafts.[7–10] Yet, the limited size of these models poses challenges for *in vivo* examination, as small airways often cannot accommodate bronchoscopic cameras.[11] This limitation underscores the necessity of utilizing large animal models, which more closely approximate human airways in size.[12] Tracheal transplantation in large-scale animal models is crucial and represents a more accurate reflection of human clinical applications, notwithstanding the challenges associated with postoperative care and monitoring due to smaller sample sizes. The advancement of three-dimensional (3D) printing technology has enhanced the capability to customize objects that are anatomically and functionally similar to the human trachea for clinical use.[13,14] The concept of *in situ* tissue engineering has become a viable approach, with structures being fabricated *in vivo* rather than *in vitro*, leveraging the body's innate healing capacity for tracheal reconstruction.[6] The prevailing theory in *in vivo* studies suggests that this approach encourages progenitor or stem cell recruitment, fostering the formation of neocartilage and positioning the organism as a natural bioreactor for airway tissue engineering.[15,16] Previous research has predominantly focused on the formation of cartilage and tracheal epithelium in regenerative tissue following 3D-printed tissue-engineering implantation. Our research extends further, revealing an in-depth look at the entire neotissue layer *in situ*, encompassing cartilage, muscle, adipose, and gland tissues originating from mesenchymal cells. We highlight a phenotypic shift by utilizing various tissue stains to trace the evolution of chondrogenesis, glandogenesis, myogenesis, and adipogenesis, providing a detailed account of cell development within the regenerative tissue. Transforming growth factor-β (TGF-β) has been implicated as a crucial player in cellular processes that lead to airway remodeling. It is associated with epithelial alterations, subepithelial fibrosis, airway muscle remodeling, and microvascular adaptations.[17] The effect of TGF-β on fibroblasts is significant, affecting their proliferation, migration, survival, and gene expression, and thus has a considerable impact on extracellular matrix (ECM) remodeling. The nature of the newly formed tissue not only validates the regenerative process but also highlights the potential to overcome immune responses linked to surgery-induced infection and inflammation, resonating with embryogenesis and organ morphogenesis, which are typically difficult to study due to ethical constraints. To our knowledge, a comprehensive understanding of the processes and mechanisms of chondrogenesis and glandogenesis has not been presented in previous studies. We aim to innovatively classify regenerative tissue chronologically, enabling a detailed interpretation of cellular development through specific cell morphology and staining techniques.

2. Materials and methods

2.1. Experimental animals

LY male porcines (n = 10) were obtained from Pinguan Modern Livestock Co., Ltd (Taiwan). These animals were approximately 3 months old, and each weighed 25–40 kg. The experimental protocols received approval from the Institutional Experimentation Committee of Taichung Veterans General Hospital (Animal Welfare Protocol Number: La-1101785; dated May 11, 2021) (Figure S1, **Supporting Information**). A small sample size was used due to the complexities and challenges of working with large-scale animal models. Moreover, the regenerated tissue during the embryogenesis stage was too diminutive for effective analysis in its initial phases. Our team has amassed considerable experience in tracheal transplantation, conducting over 40 experiments with various materials for 3D-printed grafts on large-scale animal models.

2.2. Graft design and preparation prior to tracheal transplantation

We utilized a simulated tracheal implant made from silicone due to its non-toxic nature and inert properties within the body. We crafted silicone tracheal grafts, based on designs created with SolidWorks software, Dassault Systèmes SolidWorks Corporation, USA. specifically for large-scale animal tracheal transplantation. Moreover, silicone offers superior ease of surgical anastomosis with the native trachea, ensuring air-tightness while preserving excellent elasticity. This characteristic is crucial for providing structural support to the trachea, thus preventing

its collapse post-transplantation. Consequently, silicone implants have become a common choice for tracheal stents.[18] A S050 silicone 3D printer (San Draw Inc., United States of America [USA]) was employed in this study. The fabrication process began with the layer-by-layer extrusion of SIL28 (San Draw Inc., USA), a medical-grade silicone, at a thickness of 2 mm per layer to form the graft. The complete fabrication required 3–4 h. The implant achieved optimal flexibility with dimensions of 20 mm in length, 20 mm in diameter, and a wall thickness of 1.5 mm, with a 90% infill. The resilience of these grafts was verified using a JSV-H1000 instrument (Japan Instrumentation System Co., Japan). The tests confirmed that these grafts possess physical stress properties akin to those of the native trachea in 3-month-old pigs. Prior to transplantation, the grafts underwent surface polishing and were then sterilized in an autoclave. Only aseptically 3D-printed grafts in optimal condition were selected for implantation.

2.3. Surgical intervention and postoperative care

Each porcine was anesthetized through induction using Zoletil 50 (8 mg/kg, XXX [intramuscular injection, IM]; Virbac, France), followed by intubation with a 7-mm endotracheal tube, with anesthesia maintained under 4% isoflurane. Each animal was positioned supine, the neck area shaved, and then sterilized with povidone-iodine and 75% alcohol, before being draped with a disposable sterile towel. A cervical midline incision was made, and the strap muscles beneath were separated to expose the upper trachea. A 2-cm- long circumferential segment of the trachea was marked, surgically removed, and replaced with a 3D-printed tracheal graft (Figure S2 and Video S1, Supporting Information). Cross-table ventilation was utilized during the creation of the proximal end anastomosis, and the same procedure was applied to both the proximal and distal ends. After completing the proximal end and the lower posterior half of the distal anastomosis with a 3-O Prolene continuous running suture, the endotracheal tube was repositioned through the graft into the distal trachea. The anterior half of the distal anastomosis was then completed with 4-O Prolene using interrupted sutures placed above the tube. Traction sutures were applied at both ends to relieve tension over the anastomosis sites, and an airtight seal was verified before closing the strap muscles. A silicone Penrose drain was inserted, and the wound was closed in layers (Video S1: Procedures for Surgical Intervention, Supporting Information). Animals were extubated in the operating room and recovered without incidents within 12 h, resuming normal activities and diet. Postoperative care included pain relief (diclofenac potassium, 25 mg), antibiotic (ampicillin, 500 mg), and a mucolytic (bromhexine hydrochloride, 2 mg/mL), all administered with food under veterinary supervision.

Ten male LY porcines participated in the study; however, seven were excluded due to undetected cartilage regeneration (one porcine), wound infection (two porcines), and unexpected death (four porcines). Consequently, three animals were evaluated, providing 15 tissue specimens and 2 native tracheal tissues from 3- and 6-month-old porcines each for comparative analysis.

2.4. Postoperative bronchoscopic examination and laser ablation

The tracheal lumen was examined using intraluminal telescopic visualization (bronchoscopy, Olympus, BF-260/CV-260/CLV-260; Yuan Yu Industry Co., Ltd., Taiwan), approximately weekly after tracheal graft transplantation using a 4.9 mm 0° endoscope (Figure S3, Supporting Information). The degree of stenosis was assessed by comparing the diameter of stenosed and non-stenosed tracheal sections.[19] In cases of significant granulation tissue at the anastomosis site, argon-plasma coagulation (FiAPC probe 1500A/VIO200D; Soma Technology, Inc., Taiwan) was applied to maintain the tracheal lumen, supplied by Era Bioteq Enterprise Co., Ltd.

2.5. Regenerated tracheal cartilage tissue analyzed by hematoxylin and eosin and other stains

Following the death or euthanasia of the animals, autopsies were conducted to harvest graft-related tissues. The tissue samples underwent a gross examination before being fixed in 10% formalin and embedded in paraffin. Histological staining for glycosaminoglycans (GAGs) was performed using hematoxylin and eosin (H&E), alcian blue (ScyTek, ANC250), and safranin O/fast green (Cat. #8348a/Cat. #8348b). Photomicrographs were captured using NDP. view 2.6.8 software (Hamamatsu Photonics K.K., Japan). Chondrocyte counts were determined from the H&E-stained sections using Image J software, and the contents of the neocartilage matrix (GAGs) were analyzed from sections stained with alcian blue and safranin O/fast green. The total pixel area within an H&E-stained cartilage section was calculated based on the distinct morphology of the lacuna. The findings of neocartilage and native tracheal cartilage from the experimental subjects were summarized and compared to those from a 6-month-old mature porcine with stationary tracheal cartilage (Stage IV).

2.6. Process of chondrogenesis analysis based on immunohistochemistry stains

Chondrocyte markers (Sox9, type II collagen, and aggrecan) were identified using a proliferating cell nuclear antigen (PCNA) assay for assessing cell proliferation. TGF-β1 and type XII collagen served as markers for analyzing regenerative neotissue, following tracheal graft transplantation. CD31, indicative of blood vessels in

the neocartilage, was used to characterize angiogenesis via the UltraVision LP Detection System HRP Polymer & DAB Plus Chromogen (TL-060-HD; Thermo Fisher Scientific, USA). Photomicrographs were obtained using NDP.view 2.6.8 software. Cumulative pixel areas within Sox9, aggrecan, and PCNA-stained cartilage sections were quantified based on positively stained chondrocytes in immunohistochemistry (IHC) using Image J software.

2.7. Process of chondrogenesis analysis based on immunohistochemistry stains

The images from each slide were randomly screened and analyzed by an individual blinded to the study objectives. Data (presented as the mean ± standard error of the mean [SEM]) were statistically analyzed using the Kruskal Wallis/analysis of variance (ANOVA) test, with the Dunn–Bonferroni test/Bonferroni test applied for comparing chondrocyte numbers across different tissues. A p-value < 0.05 is considered statistically significant. The outcomes of these staining and protein expressions across different neocartilages were compared, leading to the proposition of various stages in cartilage development. Additionally, four distinctive stages were proposed to characterize the regenerative behavior of chondrogenesis in tracheal cartilages.

3. Results

3.1. Specimen regeneration after tracheal graft transplantation

In all animal subjects, newly regenerated neotissues, comprising varied structures such as cartilage, adipose, muscle, and glands, were observed on the exterior of the tracheal grafts, as evidenced by a continuous layer of neotissue formed post-transplantation (Figure 1). Tissue regeneration was notably characterized by circumferential neotissue completely enveloping the tracheal grafts, suggesting an integrated regenerative process. Remarkably,

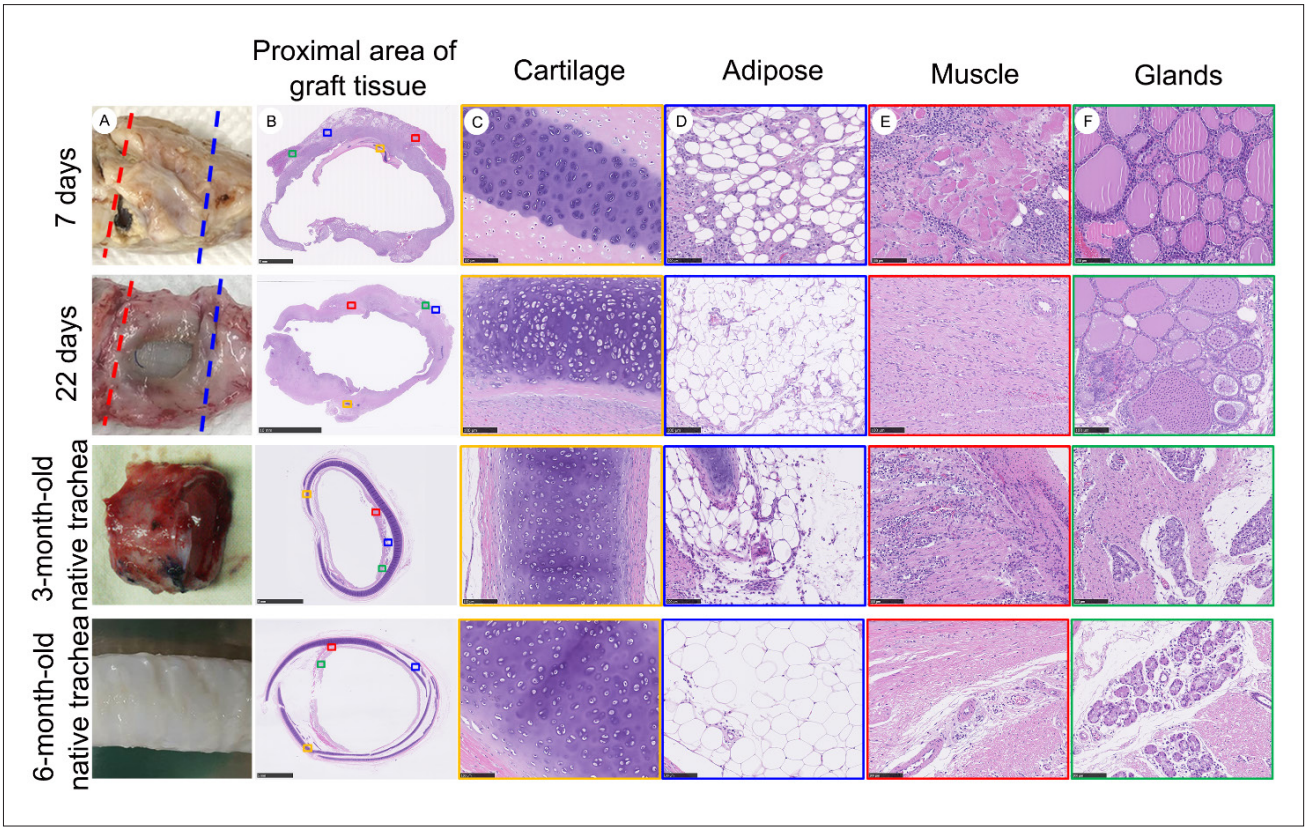

Figure 1. The gross specimen of tissue regeneration outside the graft manifested by hematoxylin and eosin (H&E) staining after tracheal graft transplantation. (A) The gross specimen of neotissue on days 7 and 22 after tracheal graft transplantation, and 3-/6-month-old native porcine trachea. The red dotted line indicates the proximal area of the graft neotissue; the blue dotted line indicates the distal area of the graft neotissue. (B) Section of the proximal area of tubular graft neotissue on days 7 and 22 after tracheal graft transplantation and that of 3-/6-month-old native porcine trachea. (C–F) The proximal area of tubular graft neotissue involves neogrowth of diverse cartilage (C), adipose (D), muscle (E), and submucosal gland (SMG; F) on days 7 and 22. A 3-month-old native porcine trachea was harvested and resected before transplantation. A 6-month-old native pig trachea was acquired from a listed pig and stored in normal saline at 4°C. H&E stains were magnified at 200×. Scale bars: 100 μm in C–F.

within 7 days or less, a heterogeneous, tubular soft neotissue layer emerged around the grate. This layer, incorporating elements such as cartilage, muscle, adipose tissue, and glands, exhibited pronounced inflammatory cell infiltration along its margins and in proximity to the grafts. The differentiation and composition of this tissue varied with time, evolving as the restructuring process progressed (Figure 1). The observed pattern of sequential growth from top to bottom might be attributed to a richer blood supply in the graft's proximal region compared to other areas.

To assess the tracheal lumen and the anastomotic at both ends, we employed a flexible bronchoscope (Figure S2, Supporting Information). It proved challenging to prevent the formation of granulation tissue, a common issue encountered despite various applied methodologies. Notably, active angiogenesis and dense immune cell populations were present in the granulation tissue around the proximal and distal ends of the tracheal anastomosis. The clinical outcomes and findings from the examination of the transplanted grafts were consistent with those reported in our previous research.[20] The presence of lucid angiogenesis and condensed immune cells at these granulation sites indicates a robust, albeit complex, regenerative response following tracheal transplantation.

3.2. Rapid chondrogenesis and maturation after graft transplantation

Neocartilage formation was evident in the tubular tissue's proximal region outside the graft just 7 days post-implantation. This new cartilage exhibited a disorganized pattern of chondrocytes, bearing resemblance to native tracheal cartilage, as confirmed by positive staining with safranin O/fast green, alcian blue, and type II collagen (Figure S6A–D, Supporting Information). By day 22, the middle region of the neotissue displayed a pronounced increase in chondrocyte density, evident through similar staining techniques and variable IHC stains (Figure S4E–H, Supporting Information). Conversely, the distal region displayed neither prominent chondrocyte proliferation nor staining with safranin O/fast green or alcian blue (Figure S4I–K, Supporting Information), except for type II collagen expression (Figure S4L, Supporting Information). This pattern suggests that neocartilage tissue tends to grow sequentially from the proximal end toward the distal end. In the proximal region, neocartilage was present within a week of implantation, characterized mainly by type II collagen. In the distal region, it was identifiable at 22 days post-implantation, exclusively indicated by type II collagen expression.

During the chondrogenesis of neocartilage, both perichondrial papillae (PP) and vascular canals (VCs), crucial for cartilage development regulation, were observed in granulation areas at the tracheal anastomosis. Chondrocyte matrix degradation products, namely alcian blue and type II collagen, were discovered within the blood vessels of VCs/PP. Matrix erosion was evidenced by pre-resorptive layers (PRLs) and intravascular matrix degradation products.[21] Furthermore, the proliferating cell nuclear antigen (PCNA) assay highlighted actively proliferating cells in the neocartilage external to the grafts and in the anastomosis zones adjacent to both the proximal and distal tracheal cartilage, particularly at the neocartilage tips. Notably, varying stages of chondrogenesis were noted throughout the developing cartilage. Concurrently, numerous new blood vessels, indicated by CD31 expression, were found within the neocartilage's perichondrium and in areas adjacent to the proximal/distal tracheal neocartilage, in contrast to the native tracheal cartilage.[20]

3.3. Incipient stage with ectopic cartilage island and/or template formation following rapid growth of chondrocytes

In the developing neotissue, cartilage formation could be observed progressing through sequential stages of chondrogenesis, which were identifiable by a variety of chondrocyte markers and the presence of GAGs. Initially, there was a noticeable proliferation of chondrocytes, which clustered in cartilage islands or appeared as disorganized templates without clear lacuna formation (Figure 2A). During this primitive stage, the staining for the cartilage's GAG matrix was not pronounced (Figure 2E and I), despite the marked expression of Sox9, aggrecan, type II collagen, and PCNA protein. A significant number of these chondrocytes exhibited strong expression of these proteins, both centrally and peripherally in the cartilage tissue, even in the absence of perichondrium coverage at the edges (Figure 2M, Q, U, and Y). As chondrogenesis progressed, the chondrocytes began to form discernible lacuna, though their quantity appeared to decrease (Figure 2B). This maturation phase was characterized by a robust GAG stain, indicating the cell matrix's gradual accumulation (Figure 2F and J). With time, the expression of chondrocyte proteins became less apparent around the edges of the neocartilage and more concentrated in the center, which was confirmed by positive staining (Figure 2N, R, V, and Z1).

3.4. Perichondrium formation with increasing GAG concentration

As chondrogenesis progressed within the neotissue, clusters of chondrocytes, known as isogenous groups, were loosely dispersed within the matrix (Figure 2C and D), exhibiting increased GAG staining (Figure 2G, H, K, and L). Consequently, the perichondrium developed

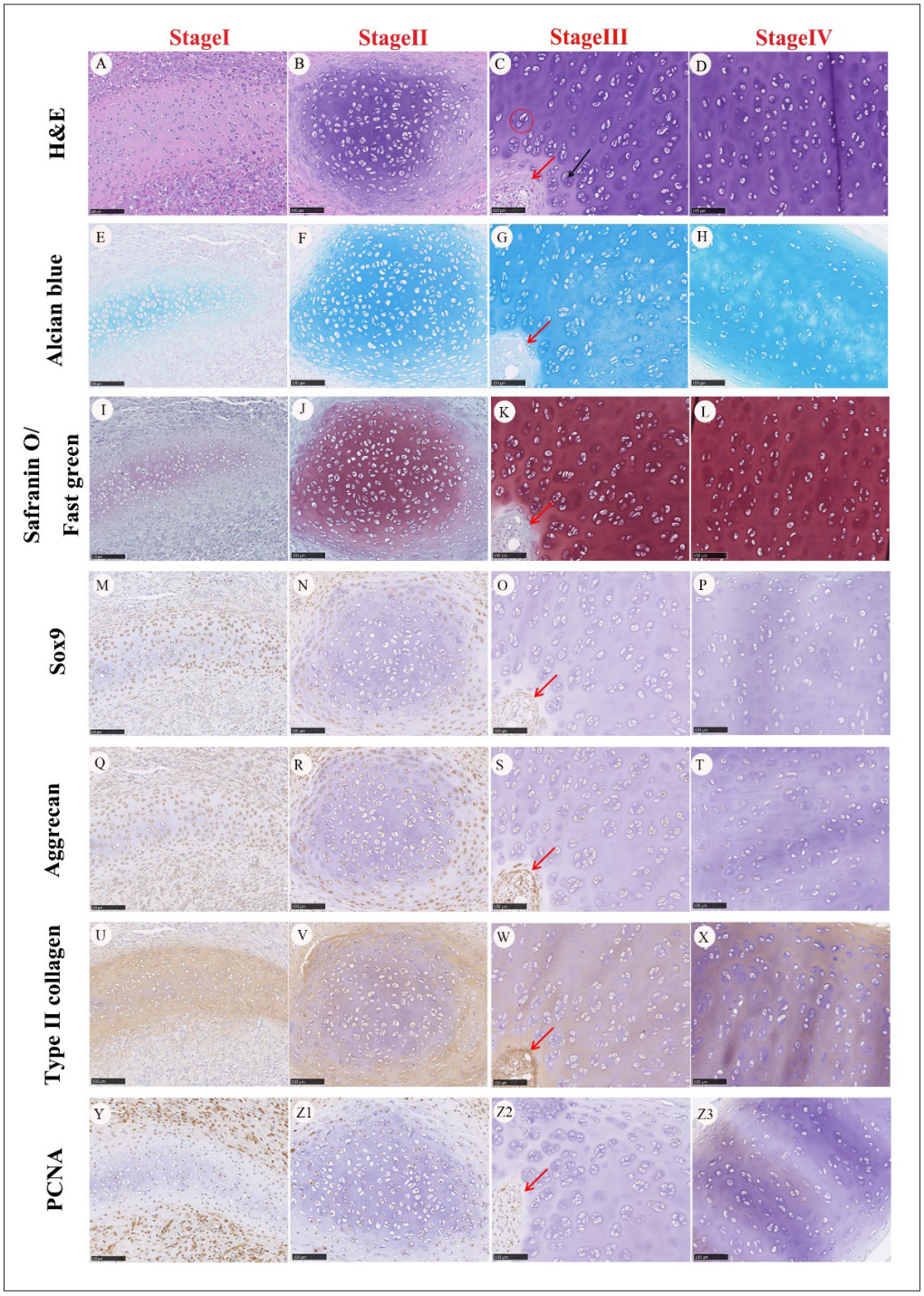

Figure 2. The four stages of chondrogenesis observed within neotissue outside the graft by hematoxylin and eosin (H&E), alcian blue, safranin O/fast green, and immunohistochemistry (IHC; type II collagen, Sox9, aggrecan, and proliferating cell nuclear antigen [PCNA] antibodies) stain. **H&E staining (A–D):** General tissue structure showing progressive chondrocyte development and matrix organization characteristic of cartilage. **Alcian Blue staining (E–H):** Visualization of glycosaminoglycans in cartilage extracellular matrix, with increasing intensity correlating with matrix maturation. **Safranin O/ Fast Green staining (I–L):** Identification of proteoglycan-rich cartilage tissue, evident by the red staining in stages III and IV. **Sox9 (M–P):** Nuclear staining of Sox9, a transcription factor critical for chondrocyte differentiation, predominantly in early stages. **Aggrecan (Q–T):** Immunohistochemical staining demonstrating progressive deposition of aggrecan, a major cartilage proteoglycan. **Type II Collagen (U–X):** Gradual accumulation of type II collagen, a marker of mature cartilage tissue. **PCNA (Y–Z3):** Proliferative activity observed in early stages, reflecting active chondrocyte proliferation during cartilage formation. Scale bars: 100 μm.

at the cartilage edge. Throughout this process, protein expression by the chondrocytes gradually decreased and was predominantly located near the perichondrium edge. Simultaneously, neocartilage formation, characterized by significant GAG concentration, occurred alongside chondro-modulators, such as PP, PRLs, and VCs (Figure 2G and K). These structures, emerging from the perichondrium, played a crucial role in regulating cartilage development by adjusting the number of chondrocytes (Figure 2O, S, W, and Z2). Meanwhile, the expression of key chondrocyte markers, such as Sox9, aggrecan, and PCNA, began to wane at the cartilage center. The developmental process is expected to reach a static phase at maturity, mirroring the state of a 6-month-old native trachea (Figure 2D, H, L, P, T, X, and Z3). This mature stage represents the culmination of cartilage development, where chondrocyte activity stabilizes, and the tissue resembles the structure and composition of native tracheal cartilage.

3.5. Four-stage development model for chondrogenesis in tracheal cartilage regeneration

A four-stage development model was proposed to elucidate the evolving behavior of neocartilage, utilizing histological patterns derived from H&E, alcian blue, and safranin O stains, alongside the IHC results for specific chondrocyte markers. The discrete stages of neocartilage development were characterized by variations in chondrocyte number, the presence of perichondrium, GAG stain intensity, and the existence of chondro-modulators (PP, PRL, and VC). Using Image J software, we quantified H&E-stained chondrocytes and those expressing proteins (Sox9, aggrecan, and PCNA) (n = 4 for each group). The chondrocyte count (mean ± SEM) revealed that Stage I had significantly more chondrocytes than subsequent stages in a 6-month-old native trachea: Stage I (173.25 ± 7.16), Stage II (115.50 ± 3.78), Stage III (53.75 ± 2.66), and Stage IV (51.00 ± 0.71) (Figure S5A, Supporting Information). The 3-month-old porcine specimens exhibited a higher number of smaller-sized chondrocytes compared to the larger-sized chondrocytes (Figure S5E and G, Supporting Information), but a more defined lacuna was observed in the 6-month-old specimens (Figure S5F and H, Supporting Information). The chondrocyte count in the native trachea (n = 4 in each group) was significantly higher in 3-month-olds than in 6-month-olds (95.0 ± 1.68 vs. 51.0 ± 0.71; $p < 0.0001$) (Figure S5I, Supporting Information). Sox9 expression demonstrated a decreasing trend through the stages (Stage I: 97.06 ± 0.29; Stage II: 66.40±2.66; Stage III: 10.34±1.19; Stage IV: 16.15 ± 0.41) (Figure S5B, Supporting Information). Aggrecan expression was highest in Stage I, with subsequent stages reporting comparable levels (Stage I: 97.19 ± 0.83; Stage II: 69.04±3.93; Stage III: 65.02±3.87; Stage IV: 57.36 ± 3.86). (Figure S5C, Supporting Information). PCNA-positive cells, indicative of proliferation, were more abundant in the early stages and diminished over time (Stage I: 85.60 ± 3.75; Stage II: 45.71 ± 4.88; Stage III: 20.22 ± 3.55; Stage IV: 13.73 ± 1.68) (Figure S5D, Supporting Information). Taken together, the initial stage (Stage I) exhibited the highest counts of chondrocytes and expressions of Sox9, aggrecan, and PCNA, but lacked perichondrium and interim chondro-modulators; Stage II displayed slightly reduced expressions but exhibited similar characteristics; Stage III demonstrated a stabilization in chondrocyte count and protein expressions compared to Stage II, featuring the emergence of perichondrium and modulators structures; by Stage IV, in the 6-month-old native trachea, chondrogenesis reached homeostasis, with the disappearance of chondro-modulators, illustrating the completion of the developmental process.

3.6. Evolution of new adipose tissue

In the native trachea, fat tissue is relatively rare, typically situated between cartilage segments. During the initial stage of neotissue development, we observed a significant proliferation of adipose tissue, featuring smaller adipocytes (brown fat-like cells). This was evident across the entire tissue section just 7 days post-transplantation (Figure 3A–C). Over time, there was a noticeable reduction in adipocyte prevalence, as they were gradually replaced by connective tissue across all regions—proximal, middle, and distal—indicating a decline in both the number and distribution of adipocytes following implantation (Figure 3D–F). However, it should be noted that these cells undergo rapid regression post-transplantation, indicating a transient phase in tissue development. This suggests that the regenerative process initially involves a diverse range of cell types, including those typically not associated with adult porcine physiology, which may contribute to early healing and tissue integration phases.

3.7. Muscle tissue regeneration with αSMA expression in early neomuscle tissue

The formation of new muscle tissue within the graft was examined 7 days post-transplantation (Figure 4B–D). Notably, a significant presence of inflammatory cells was observed within the inner layers of the neotissue, particularly in the middle area adjacent to the graft (Figure 4B). Additionally, a variety of muscle bundles were identified in the tissue's middle area (Figure 4C–D), whereas the outer layer predominantly featured larger muscle bundle cells (Figure 4D). By day 22, the tissue exhibited denser muscle formations interspersed with elastic fibers (Figure 4F–H), akin to the muscle tissue found in the native trachea (Figure 4A and E). Most of the newly formed muscle tissues were identified by the early muscle cell marker alpha-smooth muscle actin (αSMA),

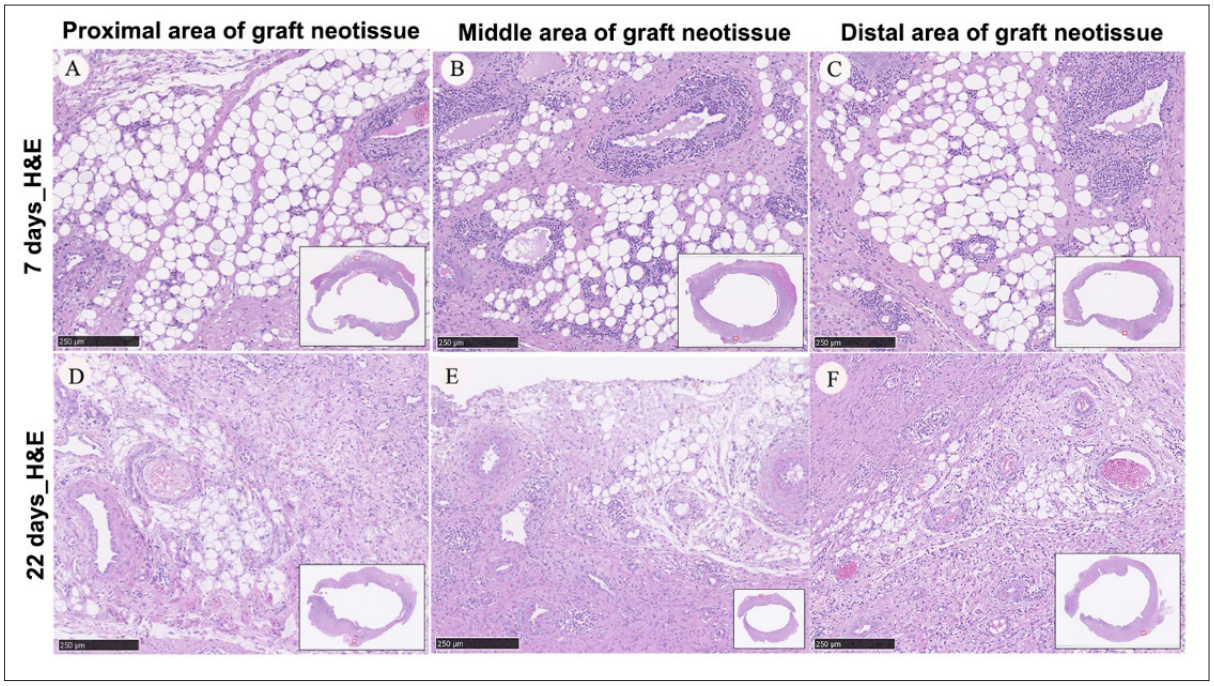

Figure 3. Evolution of neogrowth of adipose tissue in the proximal, middle, and distal area outside the graft after tracheal graft implantation. The distribution of adipose tissue within the proximal (A and D), middle (B and E), and distal (C and F) area of graft tissue was analyzed by hematoxylin and eosin (H&E) staining after 7 (A–C) and 22 days (D–F) after tracheal transplantation. The abundance of adipocyte-like brown fat cells regressed with time by number and distribution. Magnification: 100×. Scale bars: 250 μm.

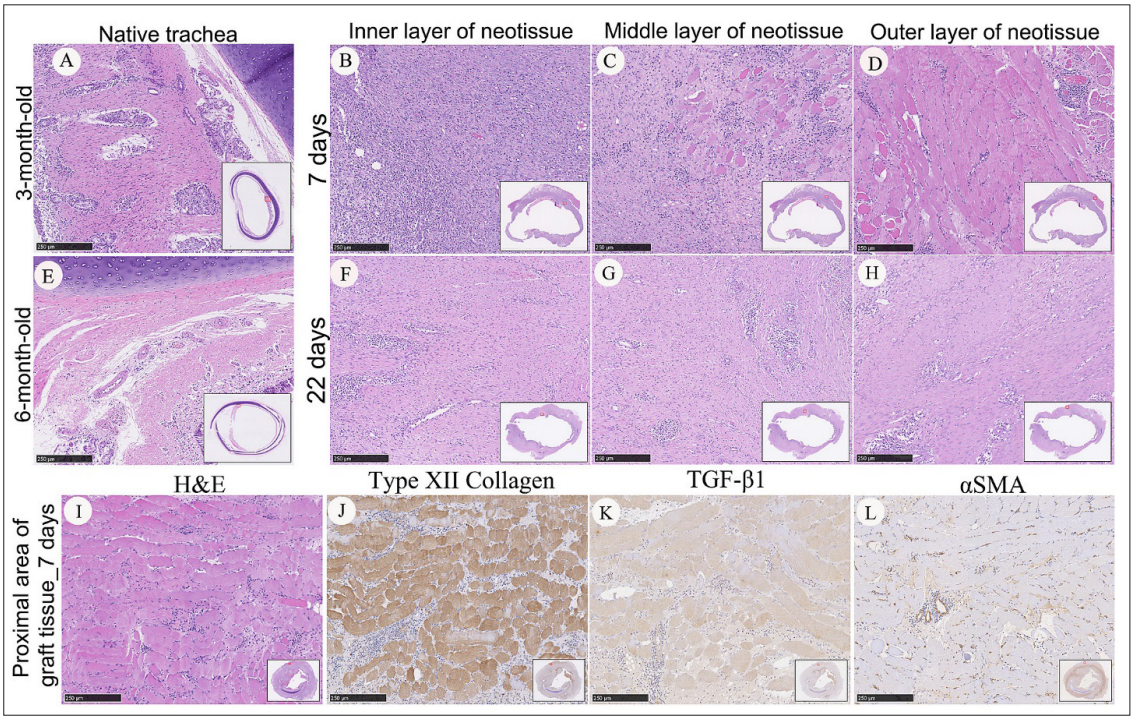

Figure 4. Evolution of neogrowth of muscle tissue based on the expression of type XII collagen, TGF-β1, and αSMA proteins in different areas. Muscle morphology of 3- and 6-month-old native trachea (A and E, respectively), compared to neomuscle within the middle area of neotissue outside the graft, were investigated by hematoxylin and eosin (H&E) staining after 7 (B–D) and 22 days (F–H) from transplantation. (I–L) H&E staining, type XII collagen, TGF-β1, and αSMA marker expression for muscle cells were detected within the proximal area of graft neotissue 7 days after transplantation. Proteins are indicated in brown color by immunohistochemistry (IHC). Magnification: 100×. Scale bars: 250 μm.

rather than the late-state marker smooth muscle myosin heavy chain (SM-MHC), at both 7 and 22 days post-transplantation (Figure S6, Supporting Information). The expression of αSMA in early-stage muscle cells indicates the growth of new muscle tissues around the implanted graft at these time points. Staining for the SM-MHC marker, which signifies later stages of muscle cell differentiation, revealed that only a minority of the new tissue exterior to the implant constituted muscle cells in advanced differentiation stages, regardless of the observation time post-transplantation. The presence of αSMA was prominent in myofibroblast components involved in regeneration, including blood and lymphatic vessels, muscle tissues, and submucosal glands (SMGs). Protein expression analyses highlighted strong type XII collagen expression and subdued staining for TGF-β1 and αSMA within the graft's proximal area 7 days after implantation (Figure 4J–L). This detailed examination underscores the dynamic process of muscle tissue neoformation in the context of graft integration, marked by varied cellular components and protein expressions reflective of ongoing tissue regeneration and remodeling.

3.8. Evolution of neoglands with MUC5AC, MUC5B, and TGF-β1 expression

Resident glands within the epithelium and submucosa of 3- and 6-month-old native trachea, as well as submucosal neoglands following graft transplantation, demonstrated expression of MUC5AC and MUC5B (Figure 5A–T). MUC5AC was primarily expressed in the goblet cells of the epithelium, while MUC5B was predominantly found in the SMG and, to a lesser extent, in the superficial epithelia of the human trachea.[22] Notably, MUC5AC expression was absent in the submucosal neoglands across the proximal, middle, and distal areas of the graft neotissue (Figure 5C–E and H–J). In contrast, MUC5B was detected with significant intensity in both long- and short-term neoglands (Figure 5M–O and R–T). Additionally, a strong expression of TGF-β1 was observed in the neotissue surrounding the tracheal grafts (Figure 5Z3–Z5). TGF-β1, a factor associated with fibrosis, indicated the fibrotic process occurring in the regenerative tissue post-implantation. In the tracheas of 3-month-old porcines, gland clusters were evenly distributed across the submucosa, exhibiting pronounced MUC5B and TGF-β1 expression. Conversely, in 6-month-old porcines, gland clusters were localized to the submucosa on the esophageal side, with glands diminishing in other areas.

The initial morphology of the neoglands resembled that of large follicular cells found in the thyroid, characterized by a clear, pale eosinophilic, or vacuolar cytoplasm, distributed throughout the gland. By postoperative days 7 and 22, cuboidal morphology of varying sizes was evident throughout the neotissue (Figure 6A–H). Observation of individual glands revealed immature follicles and vascular cytoplasm in the peripheral zone undergoing maturation over time (Figure 6I–K). Follicles in this zone contained numerous endocytic vacuoles at the margin of the colloid-filled lumen and vesicular cytoplasm.[23] Over time, the shrunken neoglands matured and clustered within the submucosa adjacent to the esophageal site in the native trachea of the 6-month-old porcine (Figure 6L).

4. Discussion

Chondrogenesis was observed at its early stage in neocartilage outside the graft from 7 to 22 days post-transplantation, suggesting that tracheal graft implantation triggers a significant inflammatory response alongside myogenesis, glandogenesis, and adipogenesis, leading to cartilage formation outside the tissues (Table 1). The development of chondrogenesis, myogenesis, and adipogenesis was associated with mesenchymal stem cell (MSC) migration to the graft area for regeneration.[24] Our findings indicated that neocartilage developed from the proximal to middle and distal areas of the tracheal grafts, likely due to the abundant blood supply in the proximal area facilitating tissue growth. MSCs have the potential to fully regenerate tissue injury through their capacity to modulate the inflammatory niche, leading to granulation tissue formation, particularly by releasing growth factors like TGF-β.[25,26] The perichondrium, containing chondro-progenitor cells and chondroblasts, played a crucial role in enhancing chondrogenesis. This was further elaborated by examining the interim chondro-modulators (PP, PRL, and VC), which regulated the excessive number of chondrocytes. These modulators, originating from the perichondrium and migrating towards the cartilage center, facilitated chondrolysis. The PP, PRL, and VC were essential for cartilage maturation through cartilage erosion, followed by the removal of degraded products.[27] These structures provided metabolism modulation for the excessive chondrocytes in the cartilage center and the removal of matrix degradation products. PPs and VCs, as chondro-modulators, were found near the proximal and distal granulation areas of the tracheal graft anastomosis at least 2 weeks post-transplantation, playing major roles in cartilage development through processes of erosion and matrix degradation via chondrolysis to achieve homeostasis. Matrix degradation products (alcian blue and type II collagen stains) were detected in the VCs **(Figure 2G and W)**, allowing for their transport out of the PPs/VCs.[20] Markers of chondrocytes (Sox9 and aggrecan) and significant proliferation (PCNA) within these structures indicated the active growth of primitive chondrocytes modulated by PPs/VCs during chondrogenesis **(Figure 2O, S, and Z2)**. VCs were observed in regenerative

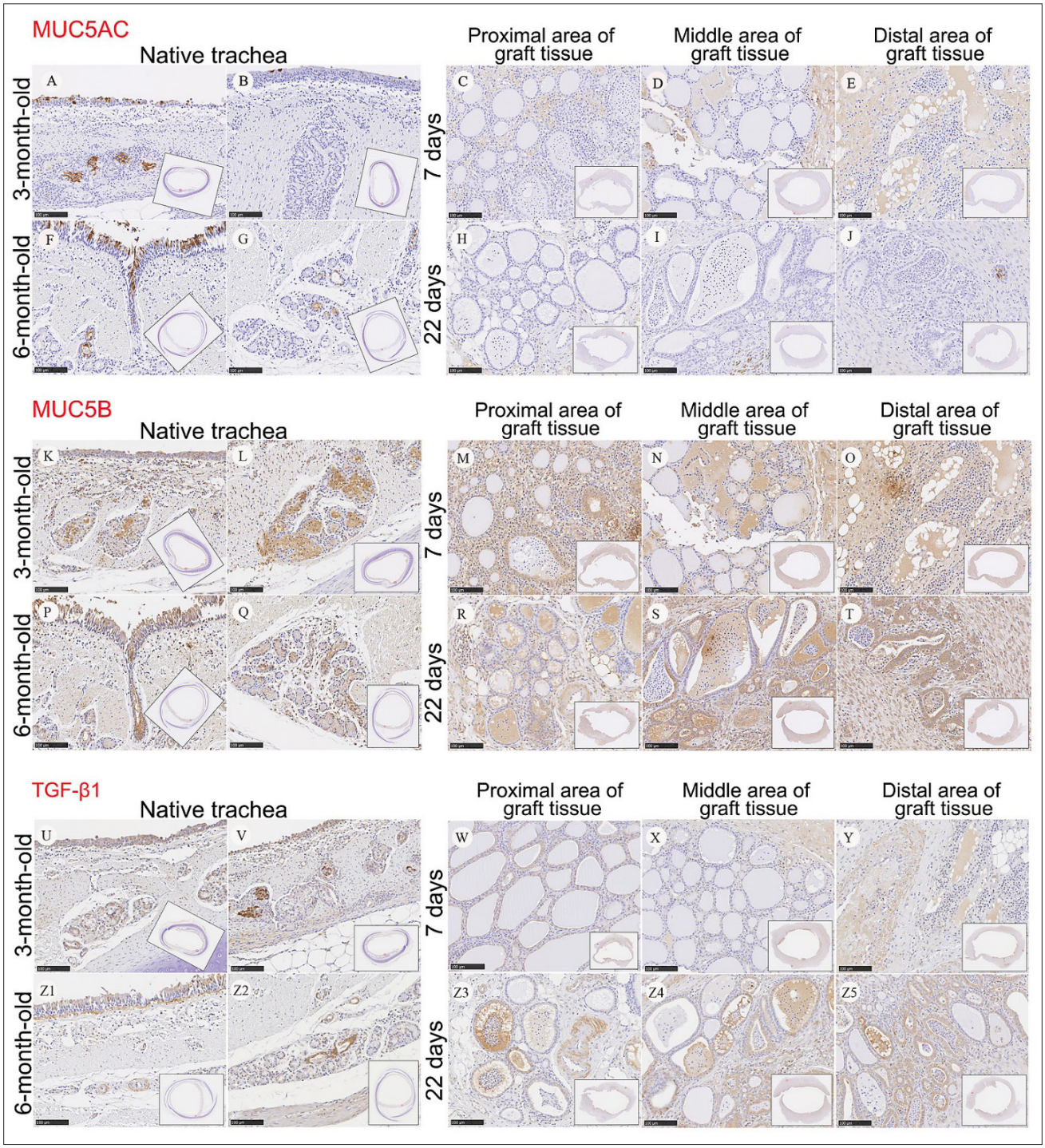

Figure 5. The evolution of neoglands in submucosal glands (SMGs) based on MUC5AC, MUC5B, and TGF-β1 expressions on days 7 and 22 in the neotissue of 3- and 6-month-old native trachea. The images of the native trachea were respectively focus on airway's epithelium (left) and SMG (right). (A–J) MUC5AC protein expression of SMGs in 3- (A and B) and 6-month-old (F and G) native trachea, as well as neoglands in the proximal (C and H), middle (D and I), and distal (E and J) areas outside graft tissue. (K–T) MUC5B expression of SMGs in 3- (K and L) and 6-month-old (P and Q) native trachea, as well as neoglands in the proximal (M and R), middle (N and S), and distal (O and T) areas outside graft tissue. (U–Z5) TGF-β1 expression of SMGs in 3- (U and V) and 6-month-old (Z1 and Z2) native trachea, as well as neoglands in the proximal (W and Z3), middle (X and Z4), and distal (Y and Z5) areas outside graft tissue. MUC5AC, MUC5B, and TGF-β1 proteins were detected in brown color. Magnification: 100×. Scale bars: 100 μm.

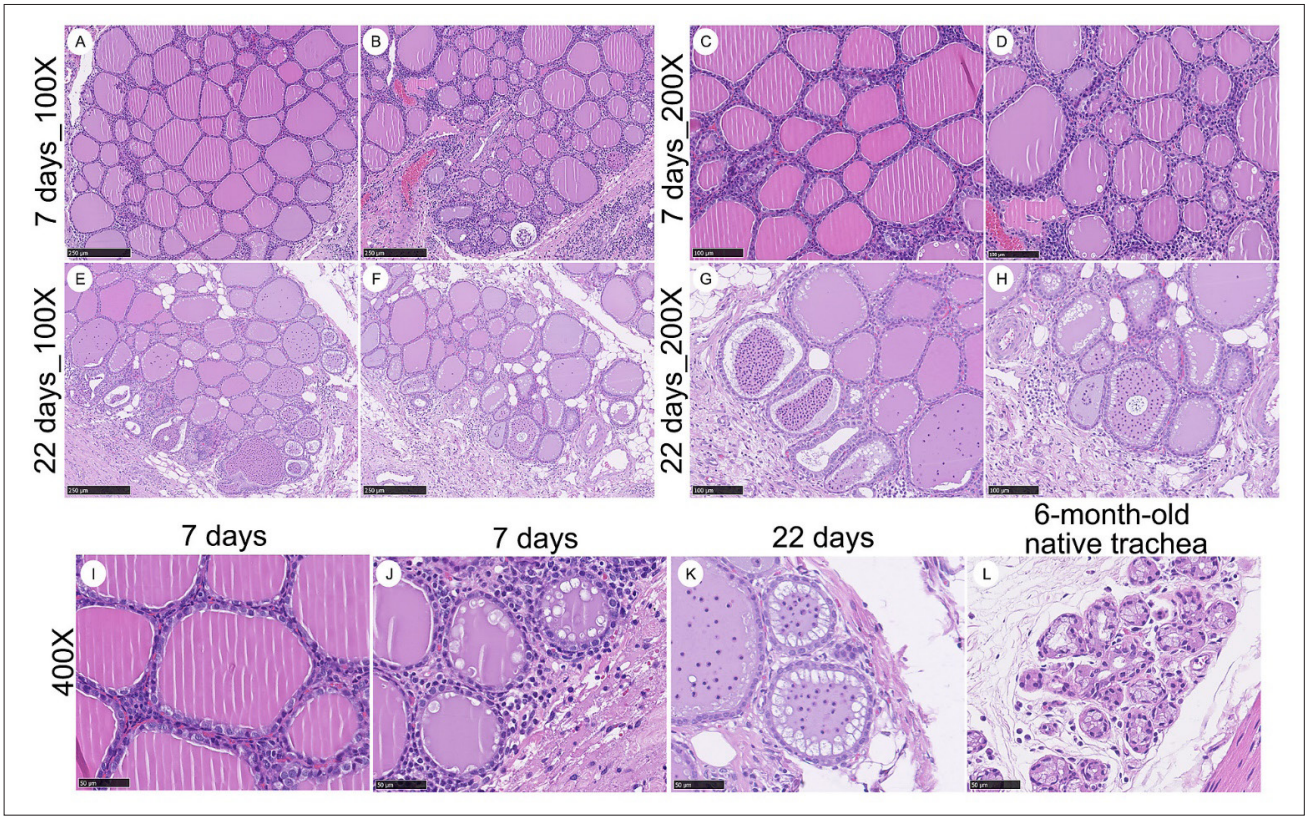

Figure 6. Phenotypic shifts of initial neoglands mimic follicle cell-like of the thyroid in neotissue at the proximal area outside the graft at 7 and 22 days after graft transplantation, with mature submucosal glands (SMGs) from 6-month-old native trachea visualized using hematoxylin and eosin (H&E) staining. (A–D) The neoformation of mimic follicle cell-like thyroid glands 7 days after graft transplantation. (E–H) The neoformation of glands 22 days after graft transplantation. (I–L) The neoglands outside graft neotissue with phenotype transformation (I–K) and maturation of SMG in 6-month-old native trachea (L). Magnification: 100× (A, B, E, and F); 200× (C, D, G, and H); 400× (I, J, K, and L). The scale bars: 250 μm in A–H, and 50 μm in I–L.

tracheal cartilages 2 weeks post-transplantation, with PPs, PRLs, and VCs participating in cartilage development through corrosion and matrix degradation processes. Degradation debris was found on the surface of granulation tissue, particularly in the proximal trachea.[20] The density and distribution of chondrocytes varied across porcine native trachea of different ages (6.5-month-old and 3-month-old), neocartilage outside the graft, and neocartilage at the graft anastomosis ends. Histological analysis revealed more oval-shaped and larger cells in 6-month-old native porcine tracheal cartilage compared to the 3-month-old counterpart. Staining with H&E, safranin O, alcian blue, and type II collagen displayed similarities in 3-month-old native tracheal cartilage but was particularly weak in posterior tracheal cartilage and tracheal islands.[20] PCNA expression was higher in neocartilage outside the grafts, suggesting a higher proliferation potential compared to native tracheal cartilage, with a more pronounced and distinct perichondrium in native cartilage than in regenerative neocartilage.[20] The neocartilage was identified through low levels of staining, indicating weak matrix formation even in mature chondrocytes, (Figure 2A–H). PCNA expression was higher in neocartilage outside the grafts, suggesting a higher proliferation potential compared to 3-month-old native trachea than in regenerative neocartilage (Figure 2Z2 and Z3).[20]

The initial neoglands closely resembled large thyroid follicular cells, marked by their clear, pale eosinophilic or vacuolar cytoplasm. This appearance likely results from the absorption of intraluminal colloids. By postoperative days 7 and 22, the neotissue displayed varied, primarily cuboidal morphology. Towards the peripheral zone, immature follicles were observed to mature over time (Figure 6I–K), with these follicles in the peripheral zone containing numerous endocytic vacuoles at the colloid-filled lumen's margin and in the vesicular cytoplasm.[23] As the glands matured, they decreased in size and clustered in the submucosa of the 6-month-old porcine native trachea (Figure 6L). In the resident SMG, MUC5B was expressed, unlike MUC5AC. MUC5B also exhibited extensive expression across the superficial epithelia of the airways,

Table 1. Summary of regeneration of cartilage, adipose, muscle tissue, and submucosal gland (SMG) in graft neotissue for short- and long-term tracheal transplantation

Tissue	Parameter	Neotissue outside the graft						Native trachea[#]	
		7 days post-implantation			22 days post-implantation			3-month-old	6-month-old
Neocartilage	Location	Proximal	Middle	Distal	Proximal	Middle	Distal	Native cartilage	Native cartilage
	Distribution	Discrete	No	No	Discrete	Discrete	Discrete	Circumferential	Circumferential
	Cell size	Smaller cells with vague lacuna	N/A	N/A	Smaller cells with vague lacuna	Smaller cells with vague lacuna	Smaller cells with vague lacuna	Smaller cells with vague lacuna	Bigger cells with obvious lacuna
	Number	Outnumber	N/A	N/A	Outnumber	Outnumber	Few	Outnumber	Moderate
	HE staining	++++	N/A	N/A	++++	++	-	++++	++++
	Safranin O	++++	N/A	N/A	++++	++++	-	++++	++++
	Alcian blue	++++	N/A	N/A	++++	++++	-	++++	++++
	IHC_Type II collagen	++++	N/A	N/A	++++	++++	++++	++++	++++
	IHC_Type XII collagen	+++	N/A	N/A	N/A			N/A	N/A
	IHC_TGF-β1	+++	N/A	N/A	N/A			-	-
	IHC_Aggrecan	++	N/A	N/A	++	++	++	+	+
	IHC_PCNA	+++	N/A	N/A	+++	+++	+++	++	+
Neoadipose	Location	Proximal	Middle	Distal	Proximal	Middle	Distal	Within cartilages	Within cartilages
	Distribution	Evenly	Evenly	Evenly	Discrete	Discrete	Discrete		
	Number	Many	Many	Many	Few	Few	Few	Few	Few
Neomuscle	Location (all)[@]	Inner	Middle	Outer	Inner	Middle	Outer	N/A	N/A
	Phenotype	Spindle-like (myofibroblast)	Mixed spindle-like and columnar -like	Columnar -like	Spindle-like (myofibroblast)	Spindle-like (myofibroblast)	Spindle-like (myofibroblast)	N/A	N/A
	IHC_α-SMA	+++	++	+	+++	+++	+++	N/A	N/A
	IHC_SM-MHC	+	+	+	+	+	+	N/A	N/A
	IHC_Type XII collagen	++++			N/A			N/A	N/A
	IHC_TGF-β1	+			N/A			N/A	N/A

(Continued...)

doi: 10.36922/ijb.5178

Table 1. Continued...

Neogland	Location	Proximal	Middle	Distal	Proximal	Middle	Distal	Submucosa	Submucosa
	Distribution	Discrete	Discrete	No	Discrete	Discrete	Discrete	Circumferential	Discrete (esophageal side)
	Phenotype	Follicular cell-like gland	Follicular cell-like gland	N/A	Follicular cell-like gland	Follicular cell-like gland	Follicular cell-like gland	Seromucinous gland	Seromucinous gland
	Size	Larger	Larger	N/A	Larger	Larger	Larger	Smaller	Smaller
	Number	Many	Many	N/A	Many	Many	Many	Cluster	Cluster
	IHC_MUC5AC	-	-	N/A	-	-	-	+	+
	IHC_MUC5B	+++	+++	N/A	+++	+++	+++	++++	+++
	IHC_TGF-β1	-	-	N/A	++	++	++	+	+
Epithelium	Location	No			No			Epithelial	Epithelial
	Thickness (μm)	N/A			N/A			26.6 ± 1.1	50 ± 1.9
	IHC_MUC5AC	N/A			N/A			++	++
	IHC_MUC5B	N/A			N/A			++++	++++

Note: # denotes XXX; @ denotes XXX; +: ; ++: XXX; +++: XXX; ++++: XXX; -: XXX. Abbreviations: HE: XXX; …

being the predominant secretory mucin alongside SMG. MUC5B and MUC5AC expression characterize CCSP-positive secretory cells in the superficial airway epithelia.[22] Each mucin has unique functions and expressions specific to certain sites. MUC5AC and MUC5B are the main gel-forming mucins in human airways.[28–31] Traditionally, MUC5AC is associated with secretion by superficial epithelial goblet cells, while MUC5B predominantly originates from SMG.[29,32–35] MUC5AC is known as a "response mucin," regulated by various inflammatory stimuli[36–38], suggesting vital innate immune roles during airway stress.[22]

Neocartilages and glands regenerated and extended from the proximal to the distal area within the vibrant tubular tissue of the tracheal grafts. Initial neocartilage growth was observed in the proximal area 7 days post-transplantation, expanding to the proximal, middle, and distal areas by 22 days. Neoglands appeared in the neotissue of both proximal and middle areas at 7 days and extended to all three areas by 22 days. Neomuscle and neoadipose tissue were noted at both 7 and 22 days, indicating earlier regeneration compared to cartilages and glands. Over time, the muscle, adipose tissue, and glands underwent shrinking, remodeling, and maturation. The formation of larger neomuscle tissue was explored in graft tissue 7 days post-transplantation (Figure 4B–D), evolving into condensed muscle bundles with elastic fibers by 22 days (Figure 4F–H), akin to the native trachea (Figure 4A and E). At both 7 and 22 days, neomuscle predominantly expressed the early muscle cell marker αSMA rather than the late marker SM-MHC, highlighting that most neomuscle tissues, including those at 7 or 22 days post-transplantation, were in a primitive stage (Figure S6, Supporting Information). The activation of fibroblast could induce contractile myofibroblast formations, identified by αSMA expression.[39] Smooth muscle cells (SMCs), known for their roles in proliferation, contraction, and ECM deposition, retain significant plasticity.[40] TGF-β has been reported to enhance MSC differentiation into SMCs[41,42], and its stimulation causes fibroblasts to differentiate into myofibroblasts, a process marked by αSMA and associated with accelerated wound healing. This was corroborated by a notable increase in αSMA expression in myofibroblasts by day 7, suggesting that TGF-β might promote granulation tissue formation, primarily featuring active myofibroblast expressing αSMA.[39]

In the native trachea, fat is typically situated between cartilages. Early on, significant growth of adipose tissue, characterized by smaller adipocytes, was observed throughout the tissue section **(Figure 3A–C)**. Over time, the adipose tissue diminished, as it was replaced by connective tissue (Figure 3D–F), indicating a decrease

in fat tissue across proximal, middle, and distal regions post-implantation. The discovery of tissues (adipocytes) resembling adipose tissue in 2- to 3-month-old porcines suggests that such finding could enhance understanding of non-shivering thermogenesis control.[43]

At 7 days post-implantation, TGF-β1 was prominently detected in cartilage, fat, and muscle tissues, but only minimally in glands (Figure S7A–D, Supporting Information). TGF-β1 presence was noted in the tracheal epithelium, vessels, SMG, and muscle endothelium of porcines. A 3-month-old porcine trachea displayed disrupted epithelium and basement membrane integrity, along with increased SMG around the submucosa with intense TGF-β1 expression. Conversely, a 6-month-old native trachea exhibited intact epithelium and basement membrane, fewer SMG in the dorsal submucosa, and weaker TGF-β1 expression (Figures 5 and S8, Supporting Information). Predominantly, type XII collagen was found in muscle tissue, with lesser expression in cartilage, fat, and glands (Figure S7E–H, Supporting Information), indicating that early transplantation inflammatory reactions might relate to the fibrosis process. Type XII collagen is essential for more than maintaining bone and muscle integrity; it may also play a role in early-stage hyaline cartilage development by aiding chondrocyte re-differentiation.[44]

Despite the complexities and challenges of using a large animal model, we advocate for their essential role in preliminary research to validate tracheal prosthesis integration criteria: mechanical stability without inflammatory rejection, and successful tissue colonization and vascularization. Understanding and inhibiting microbial adhesion at the biomaterial-tissue interface is crucial, considering variables like the pH, air, and humidity in the larynx and trachea that can cause corrosion, oxidation, and microbial growth.[45] Mechanical stress at anastomoses and granulation tissue development, due to foreign body, inflammation, and infection responses, alongside mechanical issues like substrate stiffness or wound tension, remain significant challenges. While silicone-supported ECMs have prevented graft malacia by maintaining open lumens, addressing intraluminal granulation tissue, especially in circumferential grafts, requires further research.[46] The persistent formation of granulation tissue at anastomotic sites underscores the need for more in-depth investigations to understand its mechanism and management strategies.[47–49] Technical difficulties in large animal experimental logistics and postoperative care also present challenges that future research can address, focusing on mitigating excessive granulation tissue formation.[46]

A significant limitation encountered in large animal surgery includes the challenges associated with postoperative care, particularly in preventing neck extension and addressing postoperative complications. Our survival rates could have been markedly improved had we possessed the same capacity to manage postoperative issues, such as granulation tissue formation, through standard endobronchial interventions. These interventions, routinely applied in human patients, are logistically unfeasible in animal subjects.

5. Conclusion

3D-printed pure silicone tracheal grafts have demonstrated the potential to foster *de novo* vivid tissue growth with stent-sparing anastomosis. However, they have yet to achieve successful transplantation outcomes in large-scale porcine models. The regeneration of cartilage, muscle, adipose, and glands *in situ* has provided valuable insights into the application of advanced 3D printing technology for creating customized and size-matched tissues. This approach emerges as a promising and feasible solution for enhancing the adaptability of tracheal grafts.

Acknowledgments

The authors sincerely appreciate the assistance provided by the Biostatistics Task Force, the Center for Translational Medicine, the 3D Printing Research and Development Group, and the Department of Medical Research at Taichung Veterans General Hospital, Taiwan. The authors would also like to express their gratitude to both Yuan Yu Industry Co., Ltd., Taiwan, and Era Bioteq Enterprise Co., Ltd., Taiwan.

Funding

This research was funded by the Ministry of Science and Technology, Taiwan (Grant No. MOST 110-2314-B-075A-013-1); Yen Tjing Ling Medical Foundation, Taiwan (Grant No. CI-112-9); Taichung Veterans General Hospital and National Yang-Ming University, Taiwan (Grant No. TCVGH-YM1100104); Taichung Veterans General Hospital and National Yang-Ming University, Taiwan (Grant No. TCVGH-YM1110105); and Taichung Veterans General Hospital, Taiwan, (Grant No. TCVGH-1104701C).

Conflict of interest

The authors declare they have no competing interests.

Author contributions

Conceptualization: Sen-Ei Shai

Data curation: Sen-Ei Shai, Yi-Ling Lai, Yung-Tsung Chiu
Formal analysis: Sen-Ei Shai, Yi-Ling Lai
Funding acquisition: Sen-Ei Shai, Yi-Ling Lai
Investigation: Sen-Ei Shai, Yi-Ling Lai, Yi-Wen Hung
Methodology: Sen-Ei Shai, Yi-Ling Lai, Yi-Wen Hung
Project administration: Sen-Ei Shai, Yi-Ling Lai, Yi-Wen Hung, Chi-Wei Hsieh
Resources: Sen-Ei Shai, Yi-Ling Lai
Software: Yi-Ling Lai, Chi-Wei Hsieh, Kuo-Chih Su, Chun-Hsiang Wang
Supervision: Te-Hsin Chao, Chia-Ching Wu, Shih-Chieh Hung
Validation: Sen-Ei Shai
Visualization: Sen-Ei Shai
Writing – original draft: Sen-Ei Shai, Yi-Ling Lai
Writing – review & editing: Sen-Ei Shai

Ethics approval and consent to participate

Ethical clearance for the experimental protocols was provided by the Institutional Experimentation Committee of Taichung Veterans General Hospital (Animal Welfare Protocol Number: La-1101785; approved on May 11, 2021).

Consent for publication

Not applicable.

Availability of data

All data have been presented in the article and supplementary file.

References

1. Nakanishi R. Cryopreservation of the tracheal grafts: review and perspective. *Organogenesis*. 2009;5(3):113-118. doi: 10.4161/org.5.3.9494
2. Han Y, Lan N, Pang C, Tong X. Bone marrow-derived mesenchymal stem cells enhance cryopreserved trachea allograft epithelium regeneration and vascular endothelial growth factor expression. *Transplantation*. 2011;92(6):620-626. doi: 10.1097/TP.0b013e31822a4082
3. Martinod E, Seguin A, Radu DM, et al. Airway transplantation: a challenge for regenerative medicine. *Eur J Med Res*. 2013;18(1):25. doi: 10.1186/2047-783x-18-25
4. Candas F, Gorur R, Haholu A, et al. Is tracheal transplantation possible with cryopreserved tracheal allograft and hyperbaric oxygen therapy? An experimental study. *Ann Thorac Surg*. 2016;101(3):1139-1144. doi: 10.1016/j.athoracsur.2015.09.018
5. Al-Ayoubi AM, Rehmani SS, Sinclair CF, Lebovics RS, Bhora FY. Reconstruction of anterior tracheal defects using a bioengineered graft in a porcine model. *Ann Thorac Surg*. 2017;103(2):381-389. doi: 10.1016/j.athoracsur.2016.10.034
6. Ott LM, Weatherly RA, Detamore MS. Overview of tracheal tissue engineering: clinical need drives the laboratory approach. *Ann Biomed Eng*. 2011;39(8):2091-2113. doi: 10.1007/s10439-011-0318-1
7. Zhao L, Sundaram S, Le AV, et al. Engineered tissue-stent biocomposites as tracheal replacements. *Tissue Eng Part A*. 2016;22(17-18):1086-1097. doi: 10.1089/ten.TEA.2016.0132
8. Weidenbecher M, Tucker HM, Gilpin DA, Dennis JE. Tissue-engineered trachea for airway reconstruction. *Laryngoscope*. 2009;119(11):2118-2123. doi: 10.1002/lary.20700
9. Komura M, Komura H, Kanamori Y, et al. An animal model study for tissue-engineered trachea fabricated from a biodegradable scaffold using chondrocytes to augment repair of tracheal stenosis. *J Pediatr Surg*. 2008;43(12): 2141-2146. doi: 10.1016/j.jpedsurg.2008.08.038
10. Luo X, Liu Y, Zhang Z, et al. Long-term functional reconstruction of segmental tracheal defect by pedicled tissue-engineered trachea in rabbits. *Biomaterials*. 2013;34(13):3336-3344. doi: 10.1016/j.biomaterials.2013.01.060
11. Gao M, Zhang H, Dong W, et al. Tissue-engineered trachea from a 3D-printed scaffold enhances whole-segment tracheal repair. *Sci Rep*. 2017;7(1):5246. doi: 10.1038/s41598-017-05518-3
12. Yahaya B. Understanding cellular mechanisms underlying airway epithelial repair: selecting the most appropriate animal models. *Sci World J*. 2012;2012:961684. doi: 10.1100/2012/961684
13. Rehmani SS, Al-Ayoubi AM, Ayub A, et al. Three-dimensional-printed bioengineered tracheal grafts: preclinical results and potential for human use. *Ann Thorac Surg*. 2017;104(3):998-1004. doi: 10.1016/j.athoracsur.2017.03.051
14. Park JH, Ahn M, Park SH, et al. 3D bioprinting of a trachea-mimetic cellular construct of a clinically relevant size. *Biomaterials*. 2021;279:121246. doi: 10.1016/j.biomaterials.2021.121246
15. Martinod E, Chouahnia K, Radu DM, et al. Feasibility of bioengineered tracheal and bronchial reconstruction using stented aortic matrices. *JAMA*. 2018;319(21):2212-2222. doi: 10.1001/jama.2018.4653
16. Martinod E, Paquet J, Dutau H, et al. In vivo tissue engineering of human airways. *Ann Thorac Surg*. 2017;103(5):1631-1640. doi: 10.1016/j.athoracsur.2016.11.027

17. Halwani R, Al-Muhsen S, Al-Jahdali H, Hamid Q. Role of transforming growth factor-β in airway remodeling in asthma. *Am J Respir Cell Mol Biol*. 2011;44(2):127-133. doi: 10.1165/rcmb.2010-0027TR

18. Lee P, Kupeli E, Mehta AC. Airway stents. *Clin Chest Med*. 2010;31(1):141-150, Table of Contents. doi: 10.1016/j.ccm.2009.08.002

19. Shai SE, Lai YL, Hsieh CW, Hung SC. A modified procedure of T-tube maneuver to treat tracheal total obstruction involving ablative bronchoscopy sparing open surgical intervention. *JTCVS Tech*. 2023;22:317-330. doi: 10.1016/j.xjtc.2023.09.004

20. Shai SE, Lai YL, Hung YW, et al. De novo cartilage growth after implantation of a 3-D-printed tracheal graft in a porcine model. *Am J Transl Res*. 2020;12(7):3728-3740.

21. Ponte AL, Marais E, Gallay N, et al. The in vitro migration capacity of human bone marrow mesenchymal stem cells: comparison of chemokine and growth factor chemotactic activities. *Stem Cells*. 2007;25(7):1737-1745. doi: 10.1634/stemcells.2007-0054

22. Okuda K, Chen G, Subramani DB, et al. Localization of secretory mucins MUC5AC and MUC5B in normal/healthy human airways. *Am J Respir Crit Care Med*. 2019;199(6):715-727. doi: 10.1164/rccm.201804-0734OC

23. Lee J, Yi S, Chang JY, et al. Regeneration of thyroid follicles from primordial cells in a murine thyroidectomized model. *Lab Invest*. 2017;97(4):478-489. doi: 10.1038/labinvest.2016.158

24. Sun H, Mei L, Song C, Cui X, Wang P. The *in vivo* degradation, absorption and excretion of PCL-based implant. *Biomaterials*. 2006;27(9):1735-1740. doi: 10.1016/j.biomaterials.2005.09.019

25. Gao F, Chiu SM, Motan DA, et al. Mesenchymal stem cells and immunomodulation: current status and future prospects. *Cell Death Dis*. 2016;7(1):e2062. doi: 10.1038/cddis.2015.327

26. Tracy LE, Minasian RA, Caterson EJ. Extracellular matrix and dermal fibroblast function in the healing wound. *Adv Wound Care (New Rochelle)*. 2016;5(3):119-136. doi: 10.1089/wound.2014.0561

27. Gabner S, Häusler G, Böck P. Vascular canals in permanent hyaline cartilage: development, corrosion of nonmineralized cartilage matrix, and removal of matrix degradation products. *Anat Rec (Hoboken)*. 2017;300(6):1067-1082. doi: 10.1002/ar.23537

28. Kesimer M, Kirkham S, Pickles RJ, et al. Tracheobronchial air-liquid interface cell culture: a model for innate mucosal defense of the upper airways? *Am J Physiol Lung Cell Mol Physiol*. 2009;296(1):L92-l100. doi: 10.1152/ajplung.90388.2008

29. Buisine MP, Devisme L, Copin MC, et al. Developmental mucin gene expression in the human respiratory tract. *Am J Respir Cell Mol Biol*. 1999;20(2):209-218. doi: 10.1165/ajrcmb.20.2.3259

30. Kirkham S, Sheehan JK, Knight D, Richardson PS, Thornton DJ. Heterogeneity of airways mucus: variations in the amounts and glycoforms of the major oligomeric mucins MUC5AC and MUC5B. *Biochem J*. 2002;361(Pt 3):537-546. doi: 10.1042/0264-6021:3610537

31. Kesimer M, Ehre C, Burns KA, Davis CW, Sheehan JK, Pickles RJ. Molecular organization of the mucins and glycocalyx underlying mucus transport over mucosal surfaces of the airways. *Mucosal Immunol*. 2013;6(2):379-392. doi: 10.1038/mi.2012.81

32. Audie JP, Janin A, Porchet N, Copin MC, Gosselin B, Aubert JP. Expression of human mucin genes in respiratory, digestive, and reproductive tracts ascertained by in situ hybridization. *J Histochem Cytochem*. 1993;41(10):1479-1485. doi: 10.1177/41.10.8245407

33. Groneberg DA, Eynott PR, Oates T, et al. Expression of MUC5AC and MUC5B mucins in normal and cystic fibrosis lung. *Respir Med*. 2002;96(2):81-86. doi: 10.1053/rmed.2001.1221

34. Groneberg DA, Eynott PR, Lim S, et al. Expression of respiratory mucins in fatal status asthmaticus and mild asthma. *Histopathology*. 2002;40(4):367-373. doi: 10.1046/j.1365-2559.2002.01378.x

35. Hovenberg HW, Davies JR, Carlstedt I. Different mucins are produced by the surface epithelium and the submucosa in human trachea: identification of MUC5AC as a major mucin from the goblet cells. *Biochem J*. 1996;318 (Pt 1):319-324. doi: 10.1042/bj3180319

36. Young HW, Williams OW, Chandra D, et al. Central role of Muc5ac expression in mucous metaplasia and its regulation by conserved 5' elements. *Am J Respir Cell Mol Biol*. 2007;37(3):273-290. doi: 10.1165/rcmb.2005-0460OC

37. Bonser LR, Zlock L, Finkbeiner W, Erle DJ. Epithelial tethering of MUC5AC-rich mucus impairs mucociliary transport in asthma. *J Clin Invest*. 2016;126(6):2367-2371. doi: 10.1172/jci84910

38. Park JA, Tschumperlin DJ. Chronic intermittent mechanical stress increases MUC5AC protein expression. *Am J Respir Cell Mol Biol*. 2009;41(4):459-466. doi: 10.1165/rcmb.2008-0195OC

39. Darby IA, Laverdet B, Bonté F, Desmoulière A. Fibroblasts and myofibroblasts in wound healing. *Clin Cosmet Investig Dermatol*. 2014;7:301-311. doi: 10.2147/ccid.S50046

40. Alexander MR, Owens GK. Epigenetic control of smooth muscle cell differentiation and phenotypic switching in

vascular development and disease. *Annu Rev Physiol*. 2012;74:13-40.
doi: 10.1146/annurev-physiol-012110-142315

41. Seeger T, Hart M, Patarroyo M, Rolauffs B, Aicher WK, Klein G. Mesenchymal stromal cells for sphincter regeneration: role of laminin isoforms upon myogenic differentiation. *PLoS One*. 2015;10(9):e0137419.
doi: 10.1371/journal.pone.0137419

42. Shi N, Chen SY. From nerve to blood vessel: a new role of Olfm2 in smooth muscle differentiation from human embryonic stem cell-derived mesenchymal cells. *J Biomed Res*. 2015;29(4):261-263.
doi: 10.7555/jbr.29.20150027

43. Dauncey MJ, Wooding FB, Ingram DL. Evidence for the presence of brown adipose tissue in the pig. *Res Vet Sci*. 1981;31(1):76-81.

44. Taylor DW, Ahmed N, Parreno J, et al. Collagen type XII and versican are present in the early stages of cartilage tissue formation by both redifferentating passaged and primary chondrocytes. *Tissue Eng Part A*. 2015;21(3-4):683-693.
doi: 10.1089/ten.TEA.2014.0103

45. Nakamura T, Sato T, Araki M, et al. In situ tissue engineering for tracheal reconstruction using a luminar remodeling type of artificial trachea. *J Thorac Cardiovasc Surg*. 2009;138(4):811-819.
doi: 10.1016/j.jtcvs.2008.07.072

46. Weber JF, Rehmani SS, Baig MZ, Jadoon Y, Bhora FY. Successes and failures in tracheal bioengineering: lessons learned. *Ann Thorac Surg*. 2021;112(4):1089-1094.
doi: 10.1016/j.athoracsur.2020.10.021

47. Kastanos N, Estopá Miró R, Marín Perez A, Xaubet Mir A, Agustí-Vidal A. Laryngotracheal injury due to endotracheal intubation: incidence, evolution, and predisposing factors. A prospective long-term study. *Crit Care Med*. 1983;11(5):362-367.
doi: 10.1097/00003246-198305000-00009

48. Dooms C, De Keukeleire T, Janssens A, Carron K. Performance of fully covered self-expanding metallic stents in benign airway strictures. *Respiration*. 2009;77(4):420-426.
doi: 10.1159/000203364

49. Sarper A, Ayten A, Eser I, Ozbudak O, Demircan A. Tracheal stenosis aftertracheostomy or intubation: review with special regard to cause and management. *Tex Heart Inst J*. 2005;32(2):154-158.

Our Journals

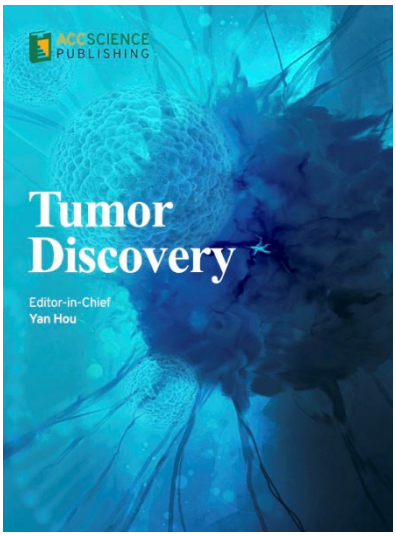

Tumor Discovery is a peer-reviewed and open-access journal that aims to present new cancer research with strong emphasis on fundamental and translational studies. *Tumor Discovery* covers topics, including but not limited to the following:

- Etiology and pathogenesis of cancer
- Mechanisms and molecular pathways underlying cancer initiation and progression
- Tumor metastasis
- Tumor evolution and heterogeneity
- Tumor microenvironment and tumor-host interactions
- Cancer genetics and genomics
- Cancer characterization using omics approaches
- Discovery and validation of cancer biomarker
- Discovery of new therapeutic targets
- New approaches of diagnostic and treatment modalities
- Statistical methods in cancer research

Global Translational Medicine is a quarterly journal that focuses on medicine, biological sciences, and biomaterials engineering. The goal of *Global Translational Medicine* is to provide a platform to researchers for showcasing their latest research works in translational medicine so as to advance the field towards the betterment of human health. Despite the advancement of omics and new technologies, the process of transforming these technologies and scientific research results into effective therapies and putting them into clinical use still has a long way to go. *Global Translational Medicine* provides a platform to fill the gaps in preclinical and inter-disciplinary research, to promote clinical translation of scientific research results, and to contribute to the conception of new and improved preventive measures as well as diagnostic and therapeutic techniques of diseases.

Global Translational Medicine covers the following themes: cardiovascular disease, metabolism/diabetes/obesity, neuroscience/neurology, cancer, biomaterials and their applications in medicine, proteomics/metabolomics, pharmacogenomics, biomarkers, bioinformatics and data mining, animal and clinical research, and medical methods arising from interdisciplinary crossover.

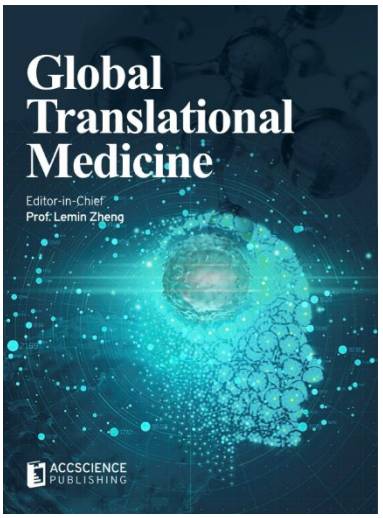

Start a new journal

Write to us via email if you are interested to start a new journal with AccScience Publishing. Please attach your CV, professional profile page and a brief pitch proposal in your email. We shall inform you of our decision whether we are interested to collaborate in starting a new journal.

Contact: info@accscience.com

https://accscience.com/journal/IJB

ACCSCIENCE PUBLISHING

ACCSCIENCE PUBLISHING

Contact
www.accscience.com
8 Burn Road, #15-03 Trivex, Singapore 369977
Email: editorial@accscience.com
Phone: +65 8182 1586